ELASTIC-PLASTIC FRACTURE

Second Symposium

VOLUME II
Fracture Resistance Curves and Engineering Applications

Shih/Gudas
editors

ASTM
STP 803

ELASTIC-PLASTIC FRACTURE: SECOND SYMPOSIUM, VOLUME II—FRACTURE RESISTANCE CURVES AND ENGINEERING APPLICATIONS

A symposium
sponsored by ASTM
Committee E-24 on
Fracture Testing
Philadelphia, Pa. 6-9 Oct. 1981

ASTM SPECIAL TECHNICAL PUBLICATION 803
C. F. Shih, Brown University, and
J. P. Gudas, David Taylor Naval Ship
R&D Center, editors

ASTM Publication Code Number (PCN)
04-803002-30

1916 Race Street, Philadelphia, Pa. 19103

Library of Congress Catalog Card Number: 82-83520

NOTE

The Society is not responsible, as a body,
for the statements and opinions
advanced in this publication.

Printed in Baltimore, Md (b)
November 1983

Foreword

The Second International Symposium on Elastic-Plastic Fracture Mechanics was held in Philadelphia, Pennsylvania, 6-9 Oct. 1981. This symposium was sponsored by ASTM Committee E-24 on Fracture Testing. C. F. Shih, Brown University, and J. P. Gudas, David Taylor Naval Ship Research and Development Center, presided as symposium chairmen. They are also editors of this publication.

Related ASTM Publications

Fracture Mechanics (13th Conference), STP 743 (1981), 04-743000-30

Fractography and Materials Science, STP 733 (1981), 04-733000-30

Crack Arrest Methodology and Applications, STP 711 (1980), 04-711000-30

Fracture Mechanics (12th Conference), STP 700 (1980), 04-700000-30

Elastic-Plastic Fracture, STP 688 (1979), 04-688000-30

A Note of Appreciation to Reviewers

The quality of the papers that appear in this publication reflects not only the obvious efforts of the authors but also the unheralded, though essential, work of the reviewers. On behalf of ASTM we acknowledge with appreciation their dedication to high professional standards and their sacrifice of time and effort.

ASTM Committee on Publications

ASTM Editorial Staff

Janet R. Schroeder
Kathleen A. Greene
Rosemary Horstman
Helen M. Hoersch
Helen P. Mahy
Allan S. Kleinberg
Virginia M. Barishek

Acknowledgments

The editors would like to acknowledge the assistance of Professor G. R. Irwin, Dr. J. D. Landes, Professor P. C. Paris, and Mr. E. T. Wessel in planning and organizing the symposium. We are grateful for the support provided by the ASTM staff, particularly Ms. Kathy Greene and Ms. Helen M. Hoersch. The timely submission of papers by the authors is greatly appreciated. Finally, this publication would not have been possible without the tremendous effort and dedication that was put forth by the many reviewers. Their high degree of professionalism ensured the quality of this publication. The editors also wish to acknowledge the diligent assistance of Ms. Susan Beigquist, Ms. Ann Degnan, Mr. Steven Kopf, and Mr. Mark Kirk in preparing the index.

J. P. Gudas
C. F. Shih

Contents

TEST METHODS AND GEOMETRY EFFECTS

CYCLIC PLASTICITY EFFECTS AND MATERIAL CHARACTERIZATION

Introduction

In October 1981, ASTM Committee E24 sponsored the Second International Symposium on Elastic-Plastic Fracture Mechanics which was held in Philadelphia, Pennsylvania. The objective of this meeting was to provide a forum for review of recent progress and introduction of new concepts in this field. The impetus for this symposium was the historical development of elastic-plastic fracture technology. Concepts such as the J-Integral, COD, and HRR field generated tremendous interest which led to the First International Symposium held in 1977. The presentation and publication of works on such topics as J-controlled crack growth, tearing instability, and numerical description of crack tip fields, among others, led to major, broad-based research activities and application-oriented developments. This sustained growth provided the motivation for another meeting devoted solely to elastic-plastic fracture.

The call for papers for the Second International Symposium generated an overwhelming response. This was reflected by the number of papers presented, and the attendance which exceeded 300 participants. The papers submitted to this symposium underwent rigorous review. The works contained in these two volumes reflect the high degree of interest in this subject and the quality of the efforts of the individual authors.

In the first ASTM publication devoted to elastic-plastic fracture (ASTM STP 668), there were three major groupings including elastic-plastic fracture criterion and analysis, experimental test techniques and fracture toughness data, and applications of elastic-plastic methodology. The present collection of papers shows substantial growth in theoretical and analytical areas which now include topics ranging from fundamental analysis of crack growth under static and dynamic conditions, finite strain effects at the crack tip, elevated temperature effects, visco-plastic crack analysis, and tractable treatments of fully plastic crack problems and surface flaws. These theoretical and analytical developments, combined with progress in test method development and ductile fracture toughness characterization led to substantial growth in engineering application of elastic-plastic fracture methodologies as evidenced by the large selection of papers on this topic.

The papers in these two volumes have been grouped into six topic areas including elastic-plastic crack analysis, fully plastic crack and surface flaw analysis, visco-plastic crack analysis and correlation, engineering applications, test methods and geometry effects, and cyclic plasticity effects and ma-

terial characterization. The first grouping contains papers on crack propagation under static and dynamic conditions, crack growth and fracture criteria, finite strain effects on crack tip fields, and plasticity solutions for important crack geometries and structural configurations. Fully plastic crack solutions, elastic-plastic line-spring models, approximate treatment of surface flaws, and surface flaw crack growth correlations are the focus of the second grouping of papers. An area not addressed in the first symposium and which has since attracted significant attention is crack growth at elevated temperature, and time dependent effects. Papers on this topic address theoretical aspects of creeping cracks, computational procedures, microstructural modelling, creep crack growth correlations, and materials characterization.

The second volume of this publication begins with the major section on engineering applications. This includes several papers on tearing instability, J-based design curves, evaluations of several fracture criteria, further developments of fracture analysis diagrams, and flawed pipe analyses. This is followed by a series of papers on test methods and geometry relationships. A majority of the papers focus on J_{Ic} and J_I-R- curve test procedures and computations, and several papers address the test specimen geometry dependence of these parameters. In the last section several papers are devoted to prior load history effects, crack growth in the elastic-plastic regime under cyclic loading, and micromechanism studies of the fracture process.

The collections of papers from this and the previous symposium contain many of the major works in the rapidly evolving subject of elastic-plastic fracture. It is hoped that these two volumes will serve to stimulate further progress in this field.

J. P. Gudas

David Taylor Naval Ship Research and Development Center, Annapolis, Md. 21401; symposium chairman and editor.

C. F. Shih

Division of Engineering, Brown University, Providence, R.I. 02912; symposium chairman and editor.

Engineering Applications

Paul C. Paris[1] *and Richard E. Johnson*[2]

A Method of Application of Elastic-Plastic Fracture Mechanics to Nuclear Vessel Analysis

REFERENCE: Paris, P. C. and Johnson, R. E., **"A Method of Application of Elastic-Plastic Fracture Mechanics to Nuclear Vessel Analysis,"** *Elastic-Plastic Fracture: Second Symposium, Volume II—Fracture Resistance Curves and Engineering Applications, ASTM STP 803*, C. F. Shih and J. P. Gudas, Eds., American Society for Testing and Materials, 1983, pp. II-5–II-40.

ABSTRACT: The primary purpose of this work was to develop analytical relationships which could be used to assess the safety of irradiated nuclear reactor pressure vessels against unstable fracture. The need for such a calculation occurs when the Charpy upper-shelf energy of the vessel steel is predicted to fall below the required 50 ft · lb (67.8 J) level from accumulated neutron radiation damage. The method used was based on "tearing instability" concepts under "*J*-controlled growth" conditions for the crack stability criterion. The aforementioned purpose was served by developing fracture mechanics methods of wider applicability than previously available and applying them in analyses at upper-shelf conditions (above the transition temperature). Elastic-plastic fracture mechanics concepts were used to extend recognized linear elastic fracture mechanics flaw analysis equations for through-the-thickness flaws and surface flaws into the plastic range. The approach also made use of J-R curve characterization of the material fracture resistance.

A crack stability diagram in the form of J as a function of T plot was shown to be useful in demonstrating safe levels of loading (applied J) by comparison with the material J-R curve, reduced onto the same diagram. Consequently, a safe level of applied load, J_{50} [for $J/T = 50$ in. · lb/in.^{2} (8.756 kJ/m^2)], was suggested and the possibility of its correlation with upper-shelf Charpy energy values discussed.

KEY WORDS: fracture mechanics, elastic-plastic fracture, analysis, J-integral, J-R curve, tearing modulus, pressure vessel, surface flaw, through-wall flaw, crack growth instability, yielding, Charpy (energy), upper shelf (energy)

Nomenclature

a Crack length (for through-thickness cracks) or crack depth (for surface cracks)

[1]Professor of mechanics, Washington University, St. Louis, Mo. 63105; Fracture Proof Design Corporation, St. Louis, Mo., 63108.

[2]Task manager, U.S. Nuclear Regulatory Commission, Washington, D.C. 20555.

a_{eff} Effective crack size with a plastic zone correction added
a_0 Initial crack size prior to growth
Δa Crack length change
b Uncracked ligament size
c Half the surface length of a surface crack
E Modulus of elasticity
$f(a/c)$ A surface flaw geometry correction
f^* A coefficient in a hardening stress bracket
$F(a/c)$ A coefficient in a hardening stress bracket
$g(a/t)$ A coefficient in a hardening stress bracket
$G(a/t)$ A coefficient in a hardening stress bracket
G^* A coefficient in a hardening stress bracket
J Rice's J-integral
J_{appl} Intensity of the crack-tip field, J, applied
J_{mat} Material's resistance value of J for an observed crack length change, Δa
K Intensity of an elastic crack-tip field
n A hardening exponent (for describing material properties)
P Applied load
r Radial distance from a crack front
r_y A plastic zone correction to be added to crack length
R Radius of a pressure vessel
s Arc length on a contour around a crack tip
t Wall thickness of a pressure vessel
T Tearing modulus
T_{appl} Applied tearing modulus
T_{mat} Material's resistance to tearing modulus for an observed crack length change, Δa
T_i Applied traction (stress)
u_i Displacement corresponding to an applied traction
U Pseudo-elastic system energy stored (corresponding to deformation plasticity theory)
W Pseudo-strain-energy density
x,y Rectangular coordinates measured perpendicular and parallel to a crack surface
Y A geometrical correction for crack-tip field intensity in shells (a function of $\lambda = a/\sqrt{Rt}$).
$\bar{\alpha}$, $\bar{\bar{\alpha}}$ Coefficients in hardening laws for stress-strain curves
β Stress state (plane stress versus plane strain) coefficient in a plastic zone correction
γ A coefficient adjusted for stress state in relating δ to J
Γ A contour around a crack tip
δ Crack opening stretch (displacement)
δ_p Load-point displacement

Δ Applied displacement (loading)
ϵ Strain
ϵ_0 Flow strain
ϵ_{ij} Components of strain
E_{ij}, $\bar{\Sigma}_{ij}$ Functions of θ and n in power-hardening fields of strain and stress
θ Angular coordinate measure from the extension of a crack plane
λ A shell parameter, $a/\sqrt{Rt}$
σ Applied (tension) stress
σ_{ij} Components of stress
σ_0 Flow stress (in tension)
σ_{eff} Net ligament nominal (effective) stress
ϕ_0 A complete elliptic integral (of the second kind [*19*])
ψ^* A coefficient in a hardening stress bracket
ω Hutchinson's J-controlled growth validity assurance parameter
$'$ Prime derivative with respect to the argument
{ } Stress brackets or factors in equations for J and T applied
[ ] Geometry brackets or factors in equations for J and T applied

The American Society of Mechanical Engineers (ASME) Boiler and Pressure Vessel Code for nuclear reactor pressure vessels has for some time permitted the use of linear elastic fracture mechanics (LEFM), specifically in Appendix A of Section XI. This has allowed clear and conservative evaluations of any potential danger due to flaws found in inspections of reactor vessels. However, LEFM, as incorporated in the Code, has a limited range of direct applicability without large and perhaps undue conservatism. Moreover, the Code version of LEFM makes use of the $K_{\text{Ic}} - K_{\text{Id}}$ concept of impending failure (little or no crack growth), instead of more advanced concepts of flaw or crack stability permitting limited stable flaw growth. Under the use of LEFM, the Code itself acknowledges ranges of inapplicability such as well above the transition temperature where LEFM cannot produce applicable quantitative results. Appendix A provides no specific criteria for upper-shelf toughness; the situation was discussed earlier [*1*].[3] In Title 10 of the Code of Federal Regulations, Part 50 (10 CFR 50), a lower limit is imposed on Charpy upper-shelf energy (USE), namely, 50 ft · lb (67.8 J); for materials of less USE, unspecified methods must be used to assure safety. On the other hand, the current ASME Code provisions using fracture mechanics have served very well in cases of appropriate quantitative applicability.

In recent years, a great deal of progress has been made in J-integral based elastic-plastic fracture mechanics (EPFM). In particular, a more advanced crack stability criterion has been developed [*2,3*] and widely accepted [*4,5*] which depends on the whole J-integral R-curve for material characterization (rather than a single value such as K_{Ic}, which is more limited). These and

[3]The italic numbers in brackets refer to the list of references appended to this paper.

other advances in EPFM make possible the suggestion of new methods for application to nuclear vessels.

The new methodology presented in this paper is proposed on its own merit but is phrased with the existing Code in mind in order to supplement it with alternative methods in areas such as upper-shelf conditions where the existing Code seems lacking. Indeed, the most realistic postulated vessel failure conditions are usually well within the elastic range for gross section stresses but may include occasional cases of large-scale yielding. Therefore, only modest modifications of current methods of vessel flaw stress analysis will be suggested. On the other hand, more ductile, perhaps fully plastic, failures are characterized by significant amounts of stable flaw growth. Therefore a more advanced (R-curve) stability concept will be suggested, especially for material property evaluation purposes. The new methodology can be considered as an extension of the existing Code methods written in terms of J-integral EPFM, for which LEFM is simply a special case.

Indeed, the only really new embellishment to be presented herein is the use of a J versus T diagram to assess crack instability. It is simply a new diagramatic representation of J-R curve material representation and applied J-T curves from established methods. It is proposed to clarify situations which will lead to crack instability, to simply delineated regions of rigorous applicability of the analytic concepts, to clearly demonstrate safety margins for approaching instability, etc. However, the use of J versus T diagrams involves no new assumption, it is just a new representation method which clarifies many matters. One further result, which will be demonstrated, is that the limiting allowable J-values suggested herein to avoid crack instability on the J versus T diagram have, so far, shown good correlation with Charpy upper-shelf energies. This can be of great practical significance where only Charpy data are available.

The Plane-Strain J-Integral R-Curve

According to developments by Hutchinson [6] and Rice and Rosengren [7] (HRR), the value of the J-integral (or J_{applied}) can be seen to be a parameter characterizing the intensity of the plastic stress-strain field surrounding the crack tip. Their results lead to the following form for the stress-strain field, the HRR field

$$\sigma_{ij} = \sigma_0 \left(\frac{J}{r\epsilon_0\sigma_0} \right)^{1/n+1} \tilde{\Sigma}_{ij}(\theta, n)$$

$$\epsilon_{ij} = \epsilon_0 \left(\frac{J}{r\epsilon_0\delta_0} \right)^{n/n+1} \tilde{E}_{ij}(\theta, n) \tag{1}$$

plus higher-order terms (negligible near a crack tip). The coordinates r and θ are the usual cylindrical coordinates measured from the crack tip. The analysis was based on adopting a deformation theory of plasticity for a stress-strain curve whose latter portion (well beyond the elastic range) can be represented by a power law or

$$\frac{\epsilon}{\epsilon_0} = \left(\frac{\sigma}{\sigma_0}\right)^n \tag{2}$$

then $\bar{\Sigma}_{ij}$ and $\bar{E}_{ij}$ are particular specified functions for the distribution of stresses and strains surrounding the crack tip.

The preceding approach assumes that two different cracks in the same material will have identical stress-strain fields surrounding the crack tips if loaded to the same intensity, J. It follows that if the stress and strain fields for the two cracks are identical, then what happens within them is identical, such as increments of extension, Δa, of the tips of the cracks. Hence, it is argued that a plot of J versus Δa, the J-R-curve, is a unique plot of a material's crack extension characteristics. Indeed, this is the very same argument upon which LEFM is based for K-controlled crack-tip fields. Though the logical basis of the J-R curve is equivalent to that of LEFM, the assumptions, conditions, and limitations should be clearly specified since they are less familiar than those for LEFM. Unless otherwise specified, they are

1. that conditions in the material's crack-tip fracture process zone are plane-strain,
2. that conditions which disrupt the HRR field are avoided, such as avoiding concentrated slips direct from the crack tip to nearby boundaries or cross-slip (slip at 45 deg through the thickness),
3. that crack growth does not disrupt the HRR fields, and
4. that cleavage does not intercede on the J-R curve.

Indeed, J-R curves produced by the types of test conditions proposed by ASTM Committee E-24 for standards at least attempt to be sufficient to avoid Conditions 1 and 2 as problems. Indeed, Condition 4 is thought not to be a problem at temperatures exceeding 100°C (212°F) above the transition temperature (beginning of upper shelf); but more data on this point may be needed. Finally, Condition 3 is not a problem under conditions proposed by Hutchinson [2], which are

$$\omega = \frac{dJ}{da}\frac{b}{J} \gg 1 \tag{3}$$

and

$$\Delta a \ll b$$

Hutchinson [3] showed by differentiating Eq 1, obtaining the increments of the strain, $d\epsilon_{ij}$, that these increments $d\epsilon_{ij}$ are sufficiently proportional ϵ_{ij} to assure appropriate use of deformation theory. The use of J itself here is also based on having conditions sufficiently appropriate for deformation theory. Hence Eq 3 also assures sufficient conditions for the definitions of J in its integral forms to follow. [It should be noted that sufficient conditions are distinct from necessary conditions and therefore Eqs 3 may not always be *required* for appropriate use of J.]

Therefore, under the given conditions the applicability of "strict deformation theory" is appropriate, the conditions for so called "J-controlled crack growth" are met, and J may be defined with equal validity either by its contour integral or compliance counterparts, which are [8] (see also [Ref 9] for details)

$$J = \int_\Gamma W dy - T_i \frac{\partial u_i}{\partial x} ds$$

(Γ is any contour around the crack tip), or

$$J = -\int \frac{\partial P}{\partial a} d\delta_p = \int \frac{\partial \delta_p}{\partial a} dP \tag{4}$$

Consequently, the "plane strain J-R curve" as shall be adopted here is assumed to be produced under appropriate conditions as discussed under the preceding four conditions. J should be measured by a method consistent with applying Eqs 4, including crack length change, Δa, corrections. The J-R curve is then a plot of J versus Δa points as loading progresses on a cracked specimen of the material at a given temperature.

Further, the J-R curves available may not always have been produced under ideal conditions (often undersized test specimens). This will not rule out their use if they can be shown to be conservative. For example, slightly subsized specimens or the use of side grooves or both with appropriate data reduction methods have been shown to give conservative J-R curves for bending-type tests. As used here, conservatism is taken with respect to safety when using the test results to evaluate applications by the methods developed later in this paper.

The Tearing Instability Criterion

In the previous section in Eqs 1 it was noted that J is the intensity of the crack-tip stress and strain field. Moreover, with proportional straining as guaranteed by meeting the conditions of Eqs 3 it can be argued that appropriate use of "strict deformation theory" and "J-controlled crack growth" will result. Therefore, at least under these conditions, the second definition of J in Eqs 4 implies that

$$J_{\text{applied}} \sim \frac{dU}{da} \tag{5}$$

where U is pseudo-elastic energy per unit thickness stored (that is, for the nonlinear elastic analog to an elastic-plastic material) by applying loads or deformation to the cracked body of interest. Regarding crack length change, da, as a displacement, J_{applied} takes on the connotation of a generalized force and J_{material} may be regarded as the material's resistance to that force. Consequently, a statement of equilibrium with respect to crack extension is

$$J_{\text{applied}} = J_{\text{material}} \tag{6}$$

The stability of the equilibrium expressed by Eq 6 can be found by examining the second derivative of system energy. Using Eq 5 the stability criterion can be written

$$\frac{d^2U}{da^2} \sim \frac{dJ_{\text{applied}}}{da} \lessgtr \frac{dJ_{\text{material}}}{da} \tag{7}$$

For convenience, the tearing modulus, T, is defined as

$$T = \frac{dJ}{da}\frac{E}{{\sigma_0}^2} \tag{8}$$

where E is elastic modulus and σ_0 the flow stress. Then the stability criterion, Eq 7 may be expressed in nondimensional terms by

$$T_{\text{applied}} \lessgtr T_{\text{material}} \quad \begin{matrix}\text{(stable)}\\ \text{(indifferent)}\\ \text{(unstable)}\end{matrix} \tag{9}$$

Now, J_{applied} may be found from the stress analysis solution for the cracked body, applying Eqs 4 to make the determination. Consequently J_{applied} will depend on applied loads, P, or deformations, Δ, and crack size, a, hence

$$J_{\text{applied}} = J_{\text{applied}}(P, a) \text{ or } J_{\text{applied}}(\Delta, a) \tag{10}$$

On the other hand, J_{material} depends on the materials' resistance or its J-R curve, which is a plot of J versus Δa characterizing the material's resistance to crack extension. Consequently

$$J_{\text{material}} = J_{\text{material}}(\Delta a) \tag{11}$$

Therefore, when derivatives d/da are taken of Eqs 10 and 11 to form T_{applied} and T_{material} as indicated in Eq 8, it should be noted that T_{material} may be

formed from the slope of the J-R curve, $dJ_{material}/da$, taken at a given level of J. That is to say

$$T_{material} = T_{material}(J) \tag{12}$$

On the other hand

$$\frac{dJ_{applied}}{da} = \frac{\partial J_{applied}}{\partial P} \cdot \left(\frac{\partial P}{\partial a}\right) + \frac{\partial J_{applied}}{\partial a}$$

or

$$= \frac{\partial J_{applied}}{\partial \Delta} \cdot \left(\frac{\partial \Delta}{\partial a}\right) + \frac{\partial J_{applied}}{\partial a} \tag{13}$$

where the partial derivatives of $J_{applied}$ on the right side of Eqs 13 are found from $J_{applied}$ solutions in the form of Eqs 10. The other ( ) partial derivatives in Eqs 13 depend on the load application system compliance and must be evaluated accordingly. Furthermore, assuming that the quantities in Eqs 13 are properly evaluated, it is observed that

$$T_{applied} = T_{applied}(P, a)$$

or

$$= T_{applied}(\Delta, a) \tag{14}$$

Regarding Eqs 10 and 14 as parametric equations for $J_{applied}$ and $T_{applied}$, the loading parameter P or Δ may be eliminated between them. Making use of the statement of equilibrium from Eq 6

$$J_{applied} = J_{material} = J$$

then

$$T_{applied} = T_{applied}(J, a) \tag{15}$$

The result is that both $T_{applied}$ and $T_{material}$ in Eqs 12 and 15 may be thought of as functions of J, where increasing J is viewed as the variable indicating increasing load or deformation applied to the body. Moreover, the crack size, a, in Eq 15 may be regarded as the initial crack size, a_0, plus the change in crack size, Δa, from the increase in J as determined from Eq 11 or the material's J-R curve. That is to say that

$$a = a_0 + \Delta a$$

where

$$\Delta a = \Delta a(J) \tag{16}$$

is determined by the J-R curve (for Δa may be negligible compared with a_0 in some cases). Therefore as loading progresses and J increases, $T_{applied}$ may be computed by Eq 15 with Eq 16 and $T_{material}$ by Eq 12 then compared, according to Eq 9, to determine the first value of J or the loading which causes instability.

This approach to determining instability will be exploited graphically in the next section where J versus T diagrams will be used as a method of exploring crack instability problems.

The J Versus T Stability Diagram

Consider a schematic representation of $J_{material}$ and $T_{material}$ on a J versus T diagram, using a side-by-side plot of the material's J-R curve, Fig. 1. Given the material's J-R curve, the left-hand diagram of Fig. 1, at any J such as indicated by the arrow, the slope, $dJ_{material}/da$, may be determined. As defined by Eq 8

$$T_{material} = \frac{dJ_{material}}{da} \frac{E}{\sigma_0^2} \tag{17}$$

which establishes a point on the J versus T diagram on the right in Fig. 1. Repeating the procedure at various J-values will result in the J versus T material curve. Note that below J_{Ic} no crack extension takes place, so that $T_{material}$ is very large (that is, off scale). In this way J-R curves can be transformed directly into the J versus T-mat curves.

In a typical J-R test, the remaining uncracked ligament, b, is the proper dimension to determine ω as defined by Eq 3. Therefore, dividing $J_{material}$ by $T_{material}$

$$\frac{J}{T_{material}} = \frac{J\sigma_0^2}{(dJ/da)E} = \frac{\sigma_0^2 b}{E\omega} \tag{18}$$

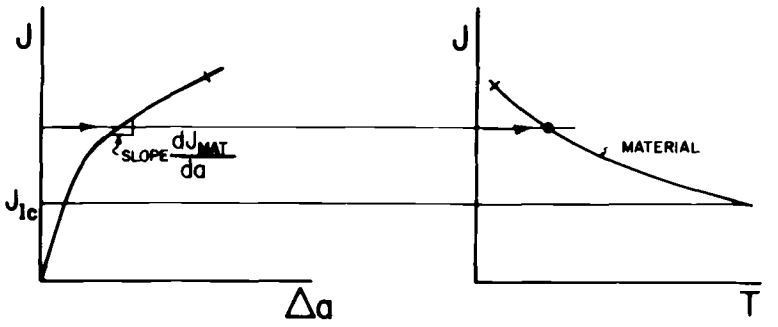

FIG. 1—*A material's* J-R *curve replotted on a* J-T *diagram.*

Consider the conditions of assured validity, Eqs 3. As shown in Fig. 1, a crack extension limit ($\Delta a \ll b$) may be placed on the R-curve with a corresponding mark at the same J-level on the J versus T-mat curve. Another limit (from Eq 3) can be represented as in Fig. 2 by a line of slope $\sigma_0^2 b/E\omega$ through the origin representing Eq 18. The actual material properties (σ_0 and E), specimen size (b), and smallest acceptable ω (perhaps five or smaller) determine the slope and, therefore, the intersection with the ω-limit of, the materials curve. Therefore the J versus T-mat curve may be doubtful above the lower of these two limits. (It is presumed that all other J-R curve test requirements and practices are met satisfactorily.)

All J versus T material curves which have been plotted to date have shown concave upward behavior. Physical reasons why this should be observed will be omitted here. Accepting this empirically observed behavior, the material curve from below the limit marks at least could be extrapolated upward as a straight-line extension of the valid curve to determine a safe J versus T loading region as shown in Fig. 3. That is to say that if a cracked specimen of the same material is loaded to a certain J-level, and the applied ($J_{applied}$, $T_{applied}$) point is in the "safe region" as shown in Fig. 3, then for that J-level, $T_{applied} < T_{material}$ and the crack is stable according to Eq 9.

It remains to determine the trace of the ($J_{applied}$, $T_{applied}$) points for $T_{applied}$ (J)-curve, as loading or J increases starting with no load. However, it is sufficient to observe that for the applications to be considered here,[4] the $T_{applied}$ curves always increase monotonically with J whereas the $T_{material}$ curves decrease monotonically with J, so the intersection of the two curves uniquely indicates the onset of instability; that is, no prior instabilities (intersections) can occur. This is illustrated in Fig. 4.

Analysis of typical $T_{applied}$ curves for the applications of interest will follow to demonstrate the monotonic increasing J versus $T_{applied}$ behavior.

On the other hand, there are other applications such as testing for which

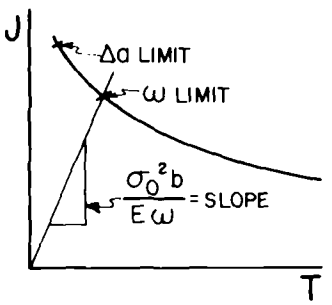

FIG. 2—*Assured validity limits noted on a* J-T *diagram.*

[4]Cracks in pressure vessel walls primarily loaded with internal pressure are considered here.

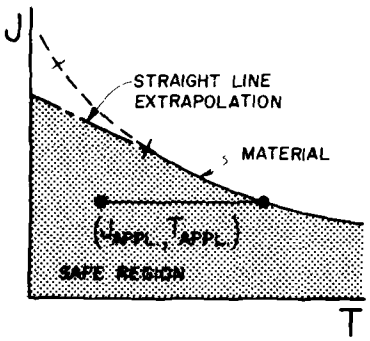

FIG. 3—*The safe region* (J_{appl}, T_{appl}) *for a given material.*

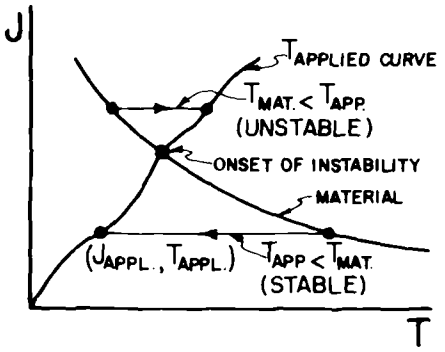

FIG. 4—*A schematic T-applied curve extending to instability.*

always stable conditions are sought (in bending where $T_{applied}$ = negative). These are treated in earlier studies [*2*] sufficiently for the objectives of this current work. Nevertheless, it is noted and the reader is warned that other relevant considerations must be made where widely different loading conditions and crack configurations exist, such as plastic bending of nuclear piping with through cracks. However, for the normal conditions and postulated flaws for pressure vessels, the J versus $T_{applied}$ behavior will follow a consistent pattern, as will be shown.

Analysis of *J* Versus *T* Applied Curves for Through Cracks in Pressure Vessel Walls

Under the actual pressures expected in nuclear pressure vessels, the shell stresses remain linear elastic and LEFM conditions apply. At a temperature high enough to be well into the Charpy upper-shelf region and for flaw sizes of

interest, it may take stresses approaching yield or higher to cause actual crack instabilities. Moreover, in assessing measured crack instabilities in model or full-scale vessel tests, the necessary pressures resulted in stresses near or exceeding the yield of the material. Therefore, along with the previously developed J versus T diagram, stability analysis, and material characterization, it is necessary to develop analytical equations for $J_{applied}$ and $T_{applied}$ which are accurate when applied in the LEFM range and also can be applied in the range where stresses exceed the yield strength. Thus factors of safety or results of vessel tests or both may be assessed at least approximately.

Linear-Elastic Format

In the linear-elastic range it is noted that

$$J = \frac{K^2}{E} \tag{19}$$

where for a cylindrical shell of radius, R, and thickness, t, with a through crack of length, $2a$, the applied stress intensity factor, K, may be written

$$K = \sigma\sqrt{\pi a} \cdot Y(\lambda) \tag{20}$$

where $\lambda = a/\sqrt{Rt}$ and Y is a geometrical correction factor for the effect of shell curvature and bending. Substituting Eq 20 into Eq 19 and rearranging leads to a convenient form

$$J_{applied} = \frac{\sigma_0^2 a}{E}\left\{\frac{\pi\sigma^2}{\sigma_0^2}\right\}[Y^2] \tag{21}$$

where we define

$\{\ \}$ = stress bracket
$[\ ]$ = geometry bracket

for the purposes to follow. For examining crack stability under constant pressure or load (that is, σ constant), the first form of Eq 13 applies with $\partial P/\partial a = 0$; hence following the definition of Eq 8

$$T_{applied} = \frac{dJ_{applied}}{da}\frac{E}{\sigma_0^2} = \frac{\partial J_{applied}}{\partial a}\frac{E}{\sigma_0^2} \tag{22}$$

Putting Eq 21 into Eq 22 leads to

$$T_{applied} = \left\{\frac{\pi\sigma^2}{\sigma_0^2}\right\} \cdot [Y^2 + 2\lambda Y \cdot Y'] \tag{23}$$

which contains the same stress bracket as Eq 21 but a new geometry bracket. To identify the implied $J_{applied}$ versus $T_{applied}$ curve on a J versus T diagram by eliminating load or σ, simply divide Eq 21 by Eq 23, to obtain

$$\frac{J_{applied}}{T_{applied}} = \frac{\sigma_0^2 a}{E} \cdot \left[\frac{1}{1 + 2\lambda Y'/Y}\right] \tag{24}$$

For constant crack size, a, and for a given material, the ratio of $J_{applied}$ to $T_{applied}$ is a constant according to Eq 24, which can be represented as a straight line through the origin on a J versus T diagram as in Fig. 5.

As loading occurs, that is, as stress σ is applied, from Eq 21, J applied starts from zero (the origin of Fig. 3) and proceeds to increase with the square of the applied stress. If J exceeds J_{Ic} crack extension, Δa (actual) begins to occur so the trace of $J_{applied}$ versus $T_{applied}$ would depart slightly from a straight line. But the crack length changes prior to the onset of instability are likely to be small in heavy sections so this slight departure will be neglected for the moment.[5]

It remains to show how the $J_{applied}$ versus $T_{applied}$ curve behaves as stresses exceed the range of applicability of LEFM. But first it is relevant to establish values for the geometry brackets as given in Eqs 21, 23, and 24.

Shell Correction Factors or Geometry Brackets for Through Cracks in Cylindrical Shells with Internal Pressure

The shell correction factors for longitudinal through cracks in shells as developed first by Folias [*10*] and modified by Erdogan and Kibler [*11*] and

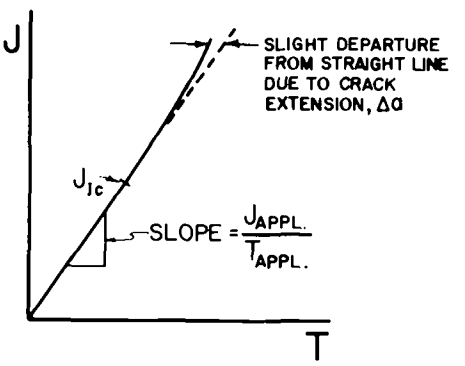

FIG. 5—*A typical* J *versus* T *applied curve (almost straight).*

[5]Even if they are not small, their effects can easily be incorporated into the analysis, as a perturbation.

verified by Krenk [*12*] are perhaps most conveniently shown in Rooke and Cartwright's work [*13*]. For the longitudinal crack they can be empirically expressed over the range of interest by the approximations (± 1 percent)

$$Y = (1 + 1.25\lambda^2)^{1/2} \text{ for } (0 \leq \lambda \leq 1)$$

$$= (0.6 + 0.9\lambda) \text{ for } (1 \leq \lambda \leq 5)$$

where as before

$$\lambda = \frac{a}{\sqrt{Rt}} \tag{25}$$

Similar expressions may be developed for circumferential cracks—again see Ref *13*—but are of lesser interest since the applied longitudinal stresses are a factor of 2 less than the hoop stresses, and longitudinal cracking is favored.

Using expressions such as Eq 25 or curves from [Ref *13*], the geometry brackets required in Eqs 21, 23, and 24 have been computed and are given here graphically in Fig. 6-9 for both longitudinal and circumferential through cracks.

In the following discussion it will be of special interest to note that the geometry bracket associated with Eq 24 (dashed curves in Figs. 6-9) is always a number smaller than 1 and greater than ⅓. Indeed for most vessels, $R/t \cong 10$ and the usual leak-before-break assumption of $a = t$ gives $\lambda \cong 0.31$ and the [ ] is between 1 and 0.8, that is, always nearly 1 in Eq 24.

Plastic Zone Corrected LEFM Conditions

Historically the first attempts to extend LEFM toward the elastic-plastic range included correcting the crack length for the plastic zone at the crack tip to obtain an effective crack size, a_{eff}, that is

$$a_{\text{eff}} = a + r_y$$

where

$$r_y = \frac{1}{\beta\pi}\left(\frac{K^2}{\sigma_0{}^2}\right) = \frac{JE}{\beta\pi\sigma_0{}^2} \tag{26}$$

where

$\beta \cong 2$ (for plane stress)
$\cong 6$ (for plane strain)

In applying the plastic zone correction to Eq 21, for example, the crack size, a, might be replaced by a_{eff}, both where it appears explicitly and in Y. However, its use here shall be restricted to relatively low nominal stress

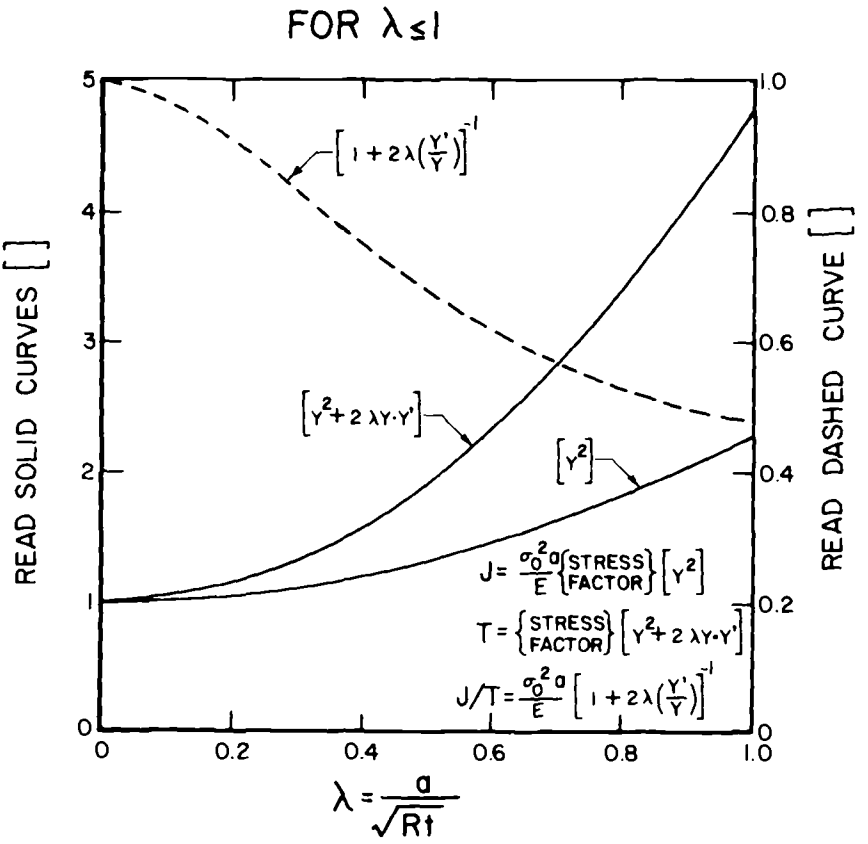

FIG. 6—*Shell correction factors for longitudinal cracks in cylinders (for low λ).*

levels, for example, $(\sigma/\sigma_0) < 2/3$, so $r_y \ll a$, so that its effect on the value of the geometry bracket $[Y^2]$ and others will be small and can be neglected. Correcting only the explicit appearance of "a" in Eq 21 and rearranging gives

$$J_{\text{applied}} = \frac{\sigma_0^2 a}{E} \left\{ \frac{\pi (\sigma/\sigma_0)^2}{1 - (Y^2/\beta)(\sigma/\sigma_0)^2} \right\} [Y^2] \tag{27}$$

For through cracks in nuclear vessels, where instability is approached at stress levels of 2/3 yield or less, the crack-tip plastic zone stress state will be closer to plane strain than plane stress. Hence, to simplify the stress bracket in Eq 27 taking $Y^2 = 1$ (but using the actual values from curves) for the geometry bracket and $\beta = 2$ (*plane stress* thus conservative), a conservative estimate of J_{applied} is achieved

$$J_{\text{applied}} = \frac{\sigma_0^2 a}{E} \left\{ \frac{\pi (\sigma/\sigma_0)^2}{1 - 1/2 (\sigma/\sigma_0)^2} \right\} [Y^2] \tag{28}$$

Indeed, most often the 1/2 in the stress bracket might be too conservative but it can be no less than 1/6. For the range of interest Fig. 10 shows a plot of these extremes for the stress bracket. Using the conservative value 1/2 also compensates for the slight underestimate of the geometry bracket, $[Y^2]$, by neglecting the plastic zone correction in it.

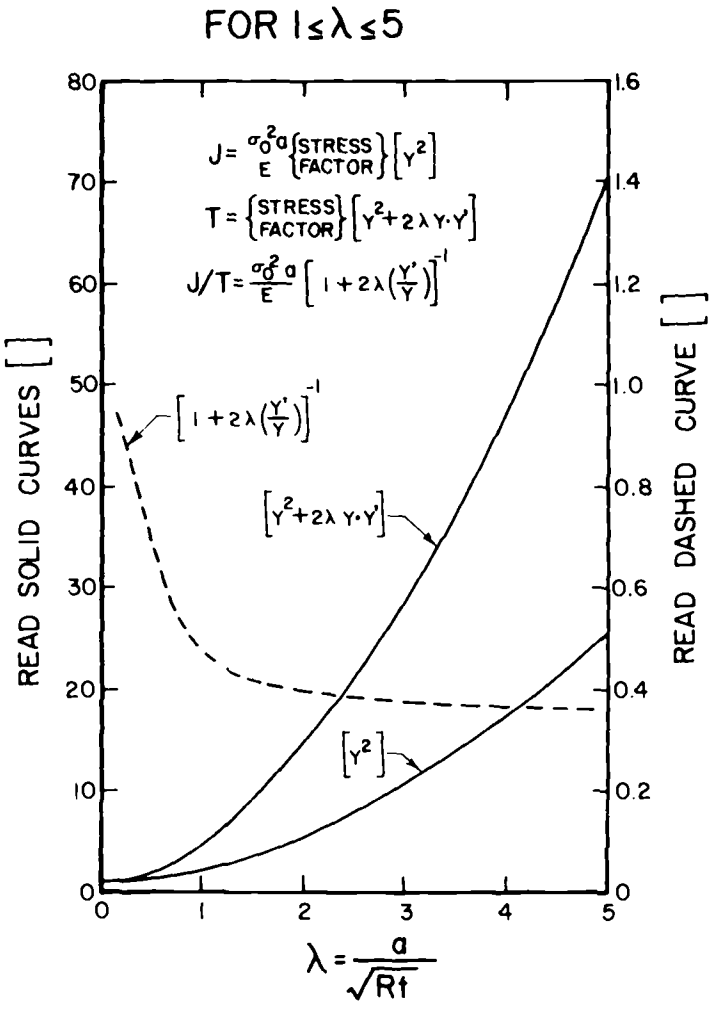

FIG. 7—*Shell correction factors for longitudinal cracks in cylinders (for high λ but with $\sigma/\sigma_0 \leq 0.67$).*

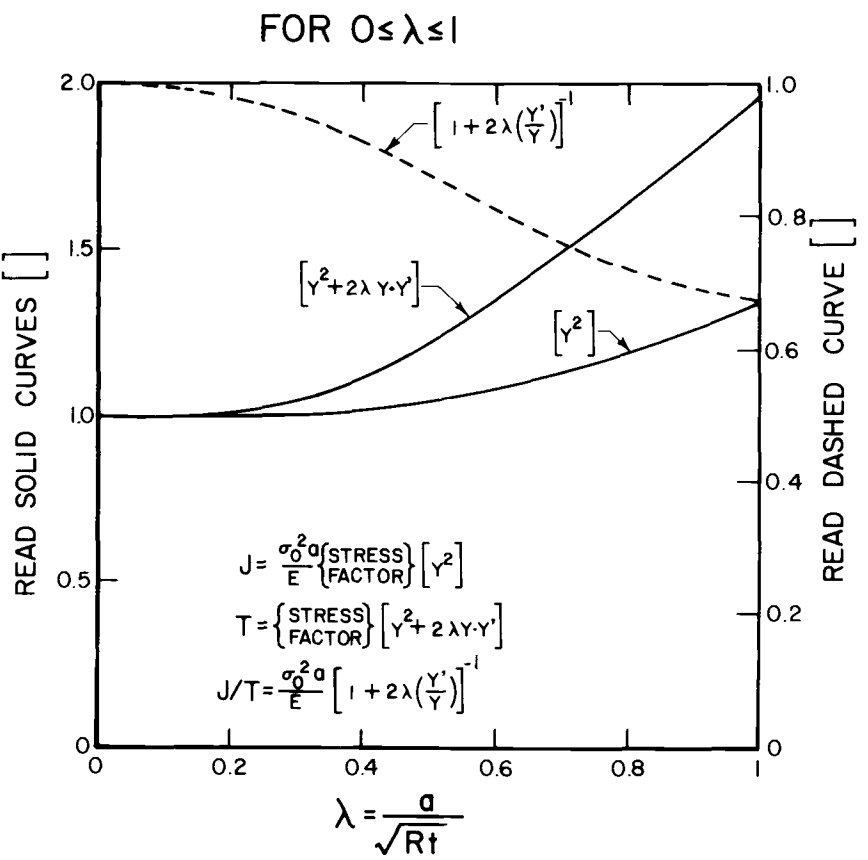

FIG. 8—*Shell correction factors for circumferential cracks in cylinders (for low λ).*

Finally, it is noted that the simplifying assumptions leading to Eq 28 not only result in a good (perhaps slightly conservative) approximation for $J_{applied}$, but *most importantly* result in an especially convenient format. The stress bracket and geometry brackets in Eq 28 completely separate the stress and geometry effects on $J_{applied}$ into independent factors. Because of the separation and following the analysis represented by the sequence Eq 21 to Eqs 23 and 24, operating on Eq 28, the results are

$$T_{applied} = \left\{ \frac{\pi(\sigma/\sigma_0)^2}{1 - \frac{1}{2}(\sigma/\sigma_0)^2} \right\} [Y^2 + 2\lambda YY'] \tag{29}$$

and

$$\frac{J_{applied}}{T_{applied}} = \frac{\sigma_0^2 a}{E} \left[\frac{1}{1 + 2\lambda Y'/Y} \right] \tag{30}$$

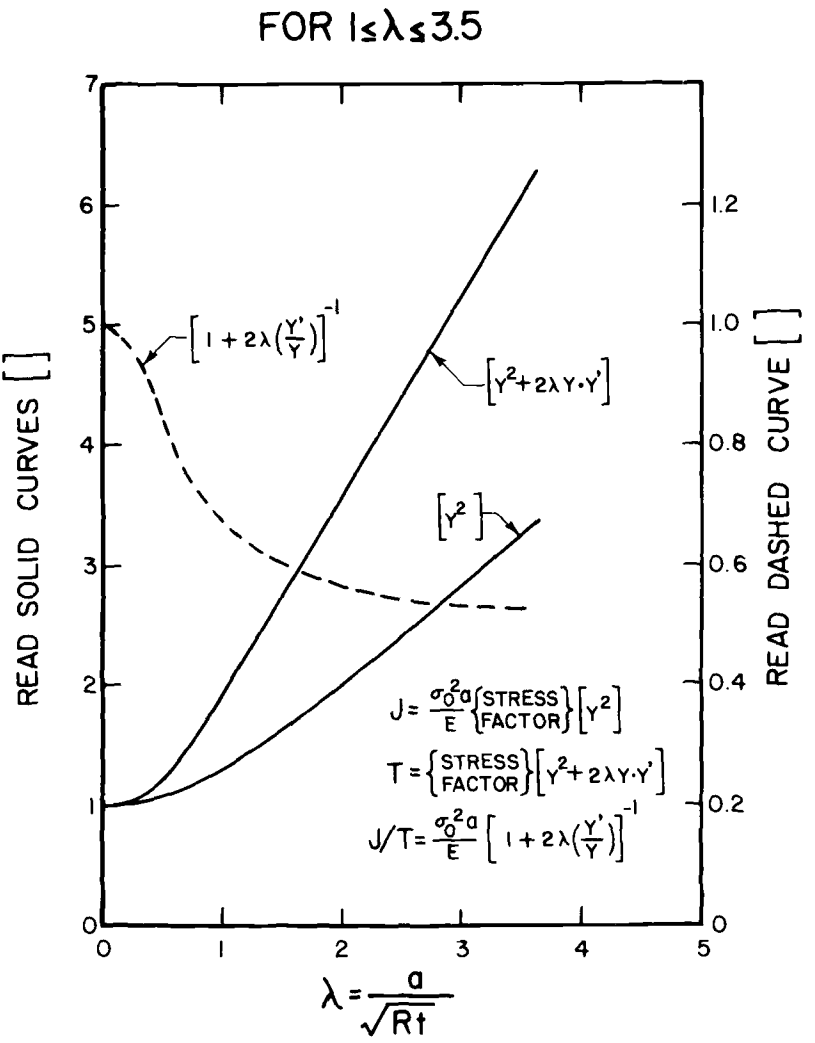

FIG. 9—*Shell correction factors for circumferential cracks in cylinders (for high* λ *but with* $\sigma/\sigma_0 \leq 0.67$*).*

It should be noted that the final result Eq 30, is identical to Eq 24, which implies that on the J versus T diagram, Fig. 5, the same $J_{\text{applied}} - T_{\text{applied}}$ trace or loading line is followed, whether the plastic zone correction is used or not! Consequently, as discussed earlier, the loading line is a straight line through the origin of the J versus T diagram of a slope given by

$$\text{slope} = \frac{J_{\text{applied}}}{T_{\text{applied}}} = \frac{\sigma_0{}^2 a}{E}\,[\text{order of 1}] \cong \frac{\sigma_0{}^2 a}{E} \tag{31}$$

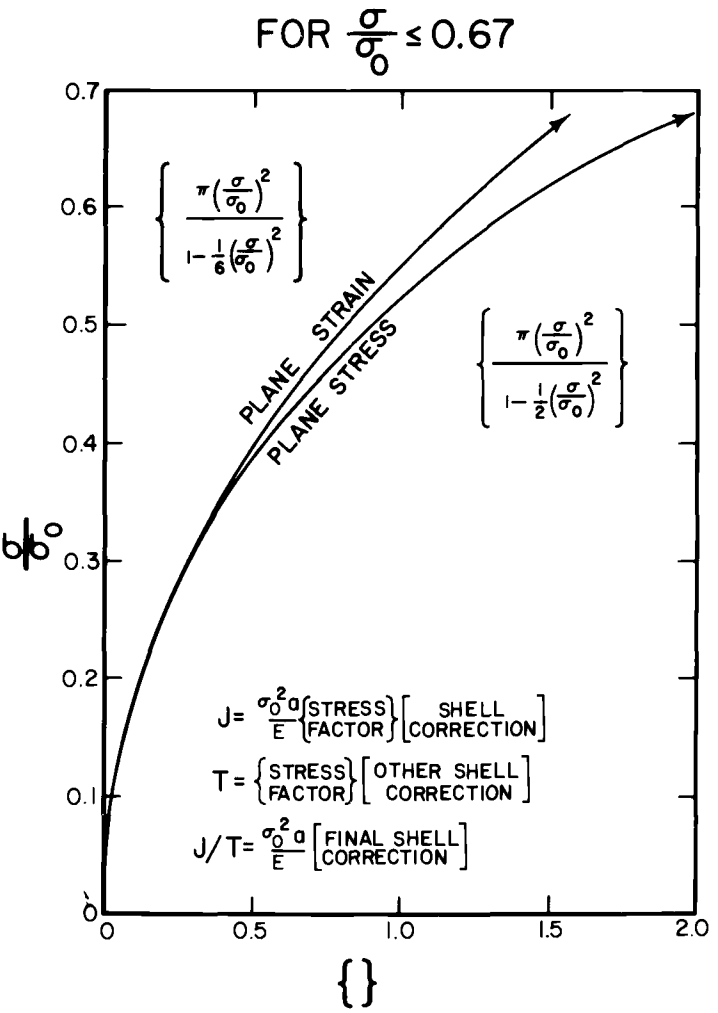

FIG. 10—*Stress correction factors for* J *and* T *for low stress,* $\sigma/\sigma_0 \leq 0.67$.

A Note on Further Extrapolation of the Stress Bracket

The analysis of actual nuclear vessels at nominal stress levels above 2/3 yield is not realistically associated with any known operating or even faulted conditions. However, for the purpose of comparison of analytical methods with test results from model vessel tests pressurized to crack instability, extrapolation of the foregoing methods to obtain fair approximations is relevant.

Moreover, at stress levels higher than 2/3 yield, interest becomes centered on rather short through cracks, $a \ll t$, so that $\lambda \ll 1$ and the geometry correction effects become small. Under such conditions, the separation as in Eq

28 to independent stress brackets and geometry brackets is no less justified; thus it need not be discussed further here. For the stress bracket functions derived in the following, it must be noted that they should be applied only for low λ ($\lambda < 1$) so Figs. 6 and 8 will be relevant but Figs. 7 and 9 should be excluded.

The Strip Yield Model Stress Bracket

Using the so-called Dugdale strip yield model to develop the stress bracket, the development of the function follows Eqs 21, 23, and 24 or equally well Eqs 28-30, repeated here for emphasis

$$J_{\text{applied}} = \frac{\sigma_0{}^2 a}{E}\{\quad\}[Y^2]$$

and (32)

$$T_{\text{applied}} = \{\quad\}[Y^2 + 2\lambda YY']$$

and

$$\frac{J_{\text{applied}}}{T_{\text{applied}}} = \frac{\sigma_0{}^2 a}{E}\left[\frac{1}{1 + 2\lambda Y'/Y}\right]$$

where $\{\quad\}$ is the stress bracket.

From the solution for the strip yield model for a center through-cracked plate—for example, see Ref *14*— and comparing results with the first of Eqs 32, the stress bracket *for strip yielding* is

$$\{\quad\} = \left\{\left(\frac{8}{\pi\gamma}\right)\ell\text{n}\sec\left(\frac{\pi}{2}\frac{\sigma}{\sigma_0}\right)\right\} \tag{33}$$

where 0.7 (for plane strain) $\leq \gamma \leq 1$ (for plane stress).

This stress bracket might be used for stress levels from 2/3 yield up to (but not including) the yield strength (it assumes elastic-perfectly plastic nonhardening material). It is appropriate to go on to hardening solutions for extrapolation of the stress bracket for stresses at or above the yield strength.

The Power-Hardening Stress Bracket

For a power-hardening approximation of a material's stress strain curve by

$$\frac{\epsilon}{\epsilon_0} = \bar{\alpha}\left(\frac{\sigma}{\sigma_0}\right)^n \tag{34}$$

the numerical solutions for center-cracked plates under both plane stress and plane strain have been presented by Hutchinson and co-workers [*15*]. Their results were compiled and applied to develop tearing instability parameters by Zahoor [*16*] and tabulated by Tada [*17*]. Taking their plane stress results in the same form as the first of Eqs 32, the stress bracket becomes

$$\{\quad\} = \left\{\bar{\alpha} f^* \left(\frac{\sigma}{\sigma_0}\right)^{n+1}\right\} \tag{35}$$

where

$$\begin{aligned} f^* &= \pi \quad (n = 1) \quad = 9.2 \quad (n = 7) \\ &= 5.5 \quad (n = 3) \quad = 11.3 \quad (n = 10) \\ &= 7.5 \quad (n = 5) \quad \text{etc.} \end{aligned}$$

The power-hardening model, Eq 34, is a fair approximation only above yield for nominal stresses. Therefore its use is limited. However, if only the above-yield range is of interest in certain applications, some further simplifications may be invoked. Dividing Eq 35 by Eq 34 and rearranging

$$\{\quad\} = \left\{f^* \left(\frac{\sigma}{\sigma_0}\right)\left(\frac{\epsilon}{\epsilon_0}\right)\right\} \tag{36}$$

Above yield the stress is always near the yield stress $\sigma \cong \sigma_0$ (or Eq 34 can be adjusted). Hence in the above-yield range the stress bracket is almost proportional to the strain or more properly the stress times the strain. Substituting Eq 36 into the first of Eqs 32

$$J_{\text{applied}} = f^* \sigma \epsilon a [Y^2] \tag{37}$$

Noting that in this relationship J_{applied} varies approximately linearly with nominal stress, σ, with nominal strain, ϵ, and with crack size, a, is of considerable assistance in intuitively understanding the role in loading deformation and size as variables affecting J_{applied}.

However, the simple power-hardening model of a material's stress-strain curve, Eq 34, is inadequate to represent the detailed behavior of both the elastic range and the hardening range. A better representation is found through the Ramberg-Osgood approximation.

The Ramberg-Osgood Stress Bracket

The Ramberg-Osgood representation of a material's stress-strain behavior is

$$\frac{\epsilon}{\epsilon_0} = \frac{\sigma}{\sigma_0} + \bar{\bar{\alpha}} \left(\frac{\sigma}{\sigma_0}\right)^n \tag{38}$$

Again, from Hutchinson's results [*15*] as compiled by others [*16,17*], comparing terms in the same form as the first of Eqs 32, the stress bracket may be written

$$\{\quad\} = \left\{\Psi^* \left(\frac{\sigma}{\sigma_0}\right)^2 + \bar{\bar{\alpha}}\, G^* \left(\frac{\sigma}{\sigma_0}\right)^{n+1}\right\} \tag{39}$$

The parameters Ψ^* and G^* vary in a complex way with $\bar{\bar{\alpha}}$ and n, which can be determined from analysis in Refs *16* and *17*. The limiting case for elastic material, $\bar{\bar{\alpha}} = 0$, is $\Psi^* = \pi$ ($G^* \neq \infty$, $n \neq \infty$). Thus Eq 39 is seen to reduce to a form proper for insertion in Eq 21. At the other limit with the stress above yield, $\sigma > \sigma_0$, the Ψ^*-term is negligible and then $\bar{\bar{\alpha}}\, G^* \cong \alpha f^*$, which produces agreement with Eq 35.

It would be cumbersome to present stress-strain curve-fitting considerations using Eq 38, as well as corresponding determinations of Ψ^* and G^*, for all materials here. More to the point is to consider a typical material, A533B, at 93°C (200°F) for which Shih [*18*] obtained the following curve-fitting results

$$\begin{aligned} \sigma_0 &= 60 \text{ ksi} \\ E &= 29 \times 10^3 \text{ ksi} \\ \bar{\bar{\alpha}} &= 1.115 \\ n &= 9.7 \end{aligned}$$

Following Refs *16* and *17* for plane stress and using these results, one obtains

$$\begin{aligned} \Psi^* &= 4.3 \\ \bar{\bar{\alpha}}\, G^* &= 11.8 \end{aligned}$$

which, when substituted in Eq 39, gives

$$\{\quad\} = \left\{4.3\left(\frac{\sigma}{\sigma_0}\right)^2 + 11.8\left(\frac{\sigma}{\sigma_0}\right)^{10.7}\right\} \tag{40}$$

for a typical nuclear vessel material. Plotting the stress bracket, Eq 40, for $\frac{2}{3} < (\sigma/\sigma_0) < 1$ and fairing it into the stress bracket from Eq 28 for $(\sigma/\sigma_0) < \frac{2}{3}$ resulted in the curve of Fig. 11. Again, the reader is reminded that the higher end of the curve in Fig. 11 is appropriate for situations only where $\lambda \ll 1$, so the elastically determined geometry brackets must not be used inappropriately in the fully plastic range.

Summary on Through-Crack Analysis

In summary, a method has been developed to analyze through cracks in nuclear pressure vessels to determine J_{applied}, T_{applied}, and $J_{\text{applied}}/T_{\text{applied}}$.

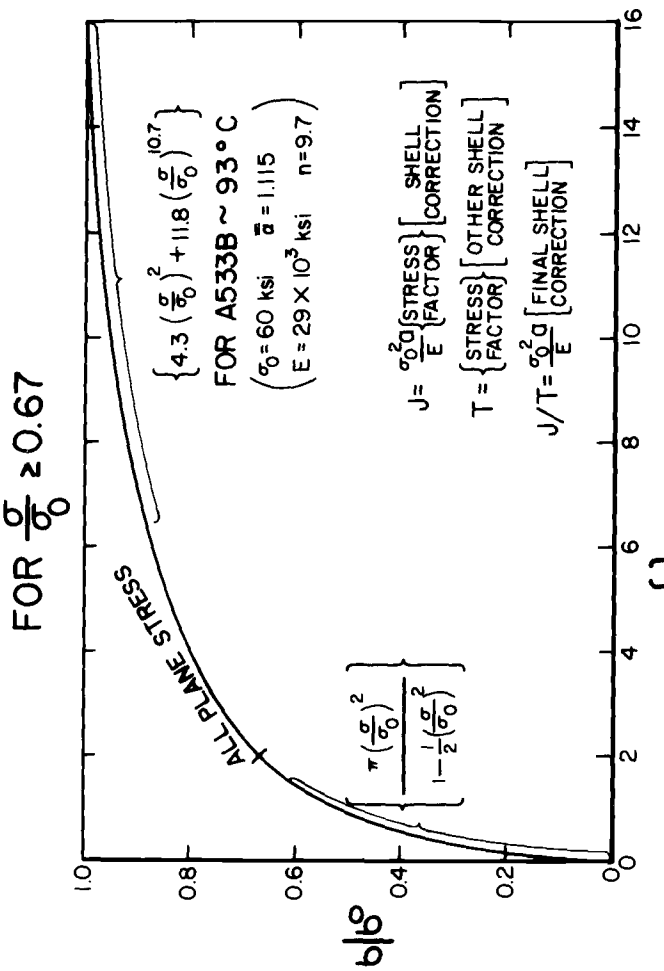

FIG. 11—*Stress correction factors for J and T extended to high stress (for low λ only) (1 ksi = 6.90 MPa).*

Neglecting both a plastic zone correction to the geometry factor and geometry correction to the stress factor forced a separation of effects which was compensated by developing stress factors for plane stress (conservative). For application at stress levels below $\frac{2}{3}$ yield *or* low values of λ ($\lambda \ll 1$), the method is accurate and slightly conservative. At stresses above $\frac{2}{3}$ yield or with high $\lambda(\lambda > 1)$, but not both, the method will give good approximations. This permits comparison of analytical predictions with many test results. [The method is not intended to treat long through cracks ($\lambda > 1$) concurrent with high nominal stresses (approaching or above yield), but this combination is never encountered in nuclear vessel analysis.]

The resulting equations for all cases were reduced to Eqs 32. The geometry brackets were given in Figs. 6-9 and the stress brackets in Fig. 11 (and Fig. 10).

Finally, the loading line on a J versus T diagram for the trace of J_{applied} versus T_{applied} is effectively a straight line through the origin of slope equal to $\sigma_0^2\, a/E$ times a factor which ranges from 0.5 to 1. This result is independent of the stress bracket model employed.

Surface Flaw Analysis

For a surface flaw of depth, a, and length, $2c$, in a vessel wall of thickness, t, the form of the elastic solution for K is often given as

$$K = \frac{\sigma\sqrt{\pi a}}{\phi_0(a/c)} f(a/c) \cdot g(a/t) \tag{41}$$

where ϕ_0 is the elliptical shape factor as computed from the complete elliptic integral of the second kind [*19*]

$$\phi_0 = \int_0^{\pi/2} \left[1 - \frac{c^2 - a^2}{c^2} \sin^2\theta\right]^{1/2} d\theta$$

and where $f(a/c)$ is a front surface correction factor, and $g(a/t)$ a back surface correction.

One may combine ϕ_0 and f into F by

$$F(a/c) = \left(\frac{f(a/c)}{\phi_0(a/c)}\right)^2$$

LEFM Surface Flaw Equations

Writing J_{applied} directly from the preceding

$$J_{\text{applied}} = \frac{K^2}{E} = \frac{\sigma_0^2\, a}{E} \left\{\pi \frac{\sigma^2}{\sigma_0^2}\right\} F(a/c)\, G(a/t) \tag{42}$$

where

$$G(a/t) = [g(a/t)]^2 \quad \text{and} \quad G'(a/t) = \frac{dG}{d(a/t)}$$

for subsequent use.

Differentiating under constant pressure stress, σ, as before to obtain T_{applied} gives

$$T_{\text{applied}} = \{\quad\} F(a/c)[G(a/c) + (a/t)G'(a/t)] \tag{43}$$

where the derivatives of F are neglected since they are slightly negative for increasing "a" compared with "c." This gives a conservative result for T_{applied}. Proceeding as before, dividing Eq 42 by Eq 43

$$\frac{J_{\text{applied}}}{T_{\text{applied}}} = \frac{\sigma_0{}^2 a}{E} \cdot \left[\frac{1}{1 + a/t \cdot G'/G}\right] \tag{44}$$

Notice that the form of this result is identical to those for through flaws. Indeed, taking G to be the often-employed "secant correction" [*14*] or

$$G(a/t) = \sec \frac{\pi a}{2t}$$

the geometry bracket in Eq 44 is given by

$$[\quad] = \left[\frac{1}{1 + \frac{\pi a}{2t} \tan \frac{\pi a}{2t}}\right] \tag{45}$$

which for $0 \leq (a/t) \leq \frac{1}{2}$ takes on values which range from 1 to 0.57. Hence, as before, the geometry bracket in Eq 44 is slightly less than but nearly equal to 1 for cases of interest. This result is also independent of adjustments to the stress bracket, does not enter Eq 44, and is independent of the crack shape aspect ratio; that is, it does not include the function $F(a/c)$. This elastic analysis should be tentatively restricted to avoid yielding of the uncracked remaining ligament, $t - a$, behind the crack. It is certainly acceptable if

$$\sigma/\sigma_0 < (1 - a/t)$$

For additional reasons associated with corrections of the form of the foregoing elastic analysis, it is prudent to restrict its use to a/t-values equal to or less than $\frac{1}{2}$.

Surface Flaw with Yielding Remaining Ligament

Consider the case where a/t is greater than ½ and where

$$1 > \sigma/\sigma_0 > (1 - a/t)$$

The ligament behind the crack will surely yield, but the uncracked regions of the vessel wall will be elastic. Following the analysis of the yielded ligament behind a surface flaw as in Ref *2*, that is, as an elastic through crack with the remaining ligament supplying distributed closing forces equal to the flow stress over the net section area, the displacement at the center of the crack is taken to be equal to the crack opening stretch, δ, or

$$\delta = \gamma \frac{J}{\sigma_0} = \frac{2\sigma_{\text{eff}}(2c)}{E} = \frac{4c}{E}[\sigma - \sigma_0(1 - a/t)] \tag{46}$$

Solving for J_{applied} gives

$$J_{\text{applied}} = \frac{\sigma_0^2 a}{E}\left(\frac{4c}{\gamma a}\right)\left(\frac{\sigma}{\sigma_0} - 1 + a/t\right) \tag{47}$$

Note that stress and geometry effects are necessarily mixed here. However, T_{applied} can be computed again by differentiating with constant nominal pressure stress or

$$T_{\text{applied}} = \frac{4c}{\gamma t} \tag{48}$$

This result was found in Ref *2*. Continuing, we divide Eq 47 by Eq 48, resulting in

$$\frac{J_{\text{applied}}}{T_{\text{applied}}} = \frac{\sigma_0^2 a}{E}(t/a)\left(\frac{\sigma}{\sigma_0} - 1 + a/t\right) \tag{49}$$

Under the conditions stated in the foregoing, the final parenthesis in Eq 49 is positive but less than a/t. Therefore the product of the final two parentheses is less than but nearly 1. Hence, comparing the form of Eq 49 to Eq 44 and earlier results, such as the last of Eq 32, shows that all can be described by

$$\frac{J_{\text{applied}}}{T_{\text{applied}}} = \frac{\sigma_0^2 a}{E}[\sim 0.5 \text{ to } 1] \tag{50}$$

Figure 12 shows the values of the [ ] factor from Eqs 49 and 45 faired together from high a/t to low a/t, respectively, consistent with the limitations of these equations.

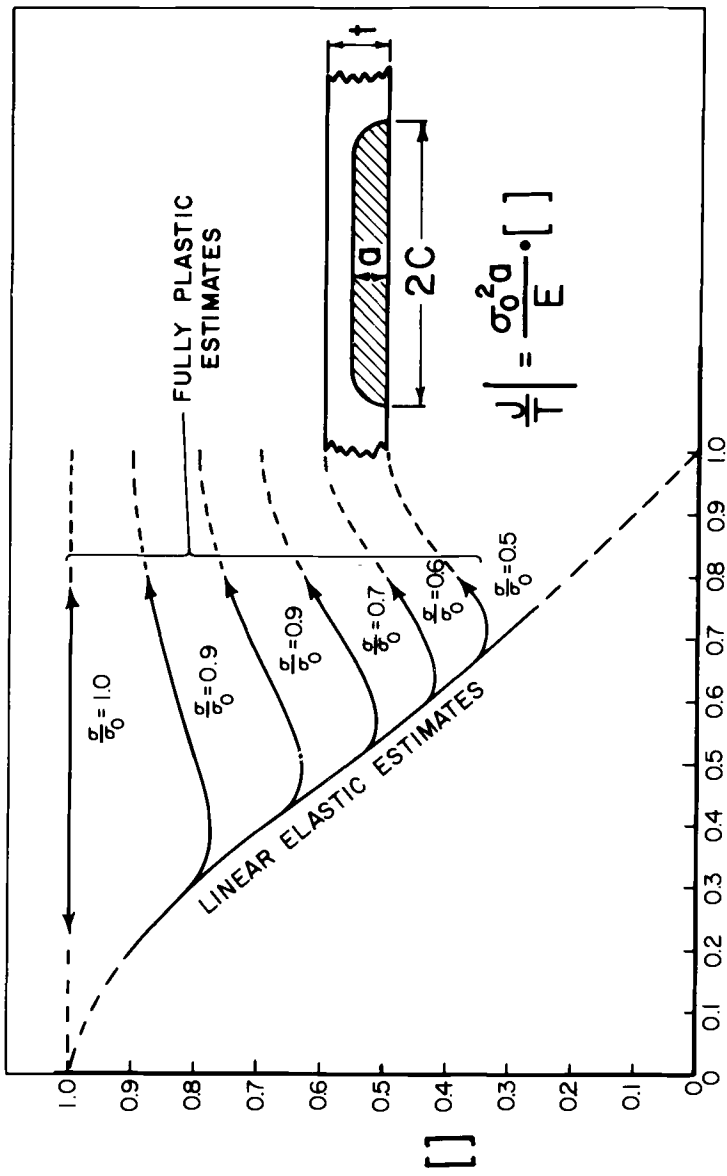

FIG. 12—*The J/T geometry correction [ ] for surface flaws for elastic and plastic ligaments.*

The discussion has established that Eq 50 applies to surface flaws as well as through flaws. However, the analysis is recommended currently only for reasonably shallow surface flaws, that is, $a/t \leq 1/2$. Moreover, for good precision over a wide range of stress levels, the stress bracket should be further developed.

Stress Bracket for Surface Flaw

The geometry corrections for the surface flaw, that is, $F(a/c)$ and $G(a/t)$ in Eq 42, are adequately represented by the curves in Appendix A of Section XI of the Nuclear Pressure Vessel Code. The curves for $\sigma/\sigma_0 = 0$ are uncorrected for plastic zone effects and are most appropriate here (not overly conservative), since the plastic zone correction and other higher stress level effects shall be treated by modifying the stress bracket.

First, consider a plastic zone correction for the surface flaw formula, Eq 42. As noted previously, since $F(a/c)$ diminishes for increasing "a," its effect somewhat cancels the increase in $G(a/t)$. Thus a small plastic zone correction will have little effect on the values of the combined geometry correction terms. On the other hand, the explicit appearance of "a" in Eq 42 can be plastic zone corrected, using Eq 26 for plane strain. Up to stress levels of 2/3 of yield this can be accomplished by adopting the plane-strain stress bracket correction as plotted in Fig. 10, or

$$\{\quad\} = \left\{\frac{\pi(\sigma/\sigma_0)^2}{1 - 1/6\,(\sigma/\sigma_0)^2}\right\} \tag{51}$$

The (1/6) coefficient in the stress bracket could be corrected for geometry effects but, in the stress range of applicability and for $a/t \leq 1/2$, this correction is small and applies to a term of small influence; thus it well may be neglected. Especially so since it is a greater convenience to avoid mixing stress and geometry factors.

As was done before for through-thickness flaws, the stress bracket correction approach may be accomplished most appropriately for higher stress levels by employing the hardening results of Hutchinson and co-workers [*15*]. In this case, plane-strain Ramberg-Osgood hardening analysis was employed. Indeed, for very shallow ($a/t \ll 1/2$) but long ($a/c \ll 1$) surface flaws, their results for center-cracked plates are accurately appropriate. Hence, for $a/t \leq 1/2$ and $a/c \ll 1$, their results will give fair approximations for the high-stress-level range, that is, $\sigma/\sigma_0 > 2/3$.

Following the same Ramberg-Osgood analysis associated with Eqs 38 and 39, but for plane strain, and again adopting Shih's [*18*] parameters for A533B steel at 93°C (200°F) (that is: $\sigma_0 = 60$ ksi, $E = 29 \times 10^3$ ksi, $\bar{\bar{\alpha}} = 1.115$ and $n = 9.7$) results in

$$\{\quad\} = \{3.3(\sigma/\sigma_0)^2 + 3.5(\sigma/\sigma_0)^{10.7}\} \tag{52}$$

Fairing the stress bracket, Eq 52, together with the former Eq 51 near $\sigma/\sigma_0 = \frac{2}{3}$, provided the results in the "Plane Strain" column in Table 1. The other column, "Plane Stress," gives tabular results for through cracks for comparison. The Table 1 results were consistently similar even though the plane-stress values eventually deviated from the plane strain values; therefore the methodology was extended to surface flaws in uniform stress fields in vessel walls.

Analysis of Surface Flaws into Nonuniform Stress Fields

Though the pressure stresses in a nuclear vessel wall induce (almost) uniform unperturbed stress fields, secondary stresses such as residual stresses, thermal transient stresses, and faulted conditions result in high stress gra-

TABLE 1—*Stress correction factors for J for plane stress (through flaws) and plane strain (surface flaws) with Ramberg-Osgood hardening. See Ref* 17.

For use with the stress-strain law

$$\frac{\epsilon}{\epsilon_0} = \frac{\sigma}{\sigma_0} + \overline{\overline{\alpha}}\left(\frac{\sigma}{\sigma_0}\right)^n$$

for typical A533B steel at 93°C (199°F); then σ_0 = 414 MPa (60 ksi); $\overline{\overline{\alpha}}$ = 1.115, and n = 9.7 (see Ref 5)

σ/σ_0	{Plane Stress} (for Through Flaws)	{Plane Strain} (for Surface Flaws)
0	0	0
0.2	0.134	0.127
0.4	0.546	0.516
0.5	0.898	0.819
0.6	1.38	1.20
0.7	2.05	1.65
0.8	3.39	2.35
0.9	7.35	3.78
1.0	16.1	6.80
1.05	24.6	9.54
1.10	37.9	13.6
1.15	58.3	19.9
1.20	89.1	29.3

where

$$J = \frac{\sigma_0^2\, a}{E} \cdot \{\quad\} \cdot [\text{geometric correction}].$$

dients through the wall. The secondary stresses are of great concern only in combination with pressure stresses; they cause yielding locally (at the surface of the wall). The foregoing methods are inadequate to handle this situation accurately and other analytic methods are not available currently to develop a method of equal accuracy. However, an approximate and conservative method may be advanced (as suggested to the present authors by Riccardella [*20*]).

As noted with Eq 37, J_{applied} is roughly proportional to applied strain. Consequently, if thermal stresses (or other secondary stresses) are determined by elastic analysis, the stress values are much too high (yielding should have occurred) but the implied strains are nearly correct. Therefore, computing implied strains, averaging them over the crack area of a surface flaw, and then transforming them back to equivalent stresses by the Ramberg-Osgood relation, Eq 38, for insertion into the preceding surface flaw analysis should give reasonable results. Tentatively, the results of such a superposition are judged to be a conservative method of handling secondary stresses. This matter bears some further study.

Consistent with the proportionality of J_{applied} to strain, Reuter [*21*], in performing a sensitivity analysis of the effect of variation of the stress-strain curves on stress brackets, also noted this proportionality to strain. Indeed, for high stress levels (σ/σ_0 equal to or greater than yield) he has shown that rewriting the stress bracket in terms of strain has some merit. That observation is consistent with the suggestion here of using superimposed strain to treat superimposed secondary stress circumstances.

Application of *J* Versus *T* Diagram to Nuclear Pressure Vessel Conditions and Materials

As explained in the text with Fig. 4, crack instability occurs when the J-T_{applied} curve intersects the J-T_{material} curve. In discussing both the surface flaw and through flaw from the LEFM range into the fully plastic range, it was noted by Eqs 24, 30–32, 44, and 50 that J-T_{applied} is a nearly straight line through the origin of a J versus T diagram. Summarizing all those equations, the slope is

$$\frac{J_{\text{applied}}}{T_{\text{applied}}} = \frac{\sigma_0^2 a}{E} \text{ [0.5 to 1]} \tag{53}$$

On the other hand, the region of the J versus T diagram for which the material property data are absolutely assured to be accurate by "J-controlled growth" critera, Eq 18, is

$$\frac{J_{\text{applied}}}{T_{\text{material}}} = \frac{\sigma_0^2 a}{E\omega} \tag{54}$$

where $\omega \geq 5 \gg 1$.

In practice, the postulated flaw sizes, a, for analytical purposes are likely to be the order of ¼ to 1 times the vessel wall thickness for surface and through-flaw sensitivity studies, whereas the remaining uncracked ligaments, b, in experimental specimens are likely to be a much smaller fraction of the vessel wall thickness. Thus, to compare Eqs 53 and 54 it is noted that

$$a[0.5 \text{ to } 1] \gg b/\omega \tag{55}$$

or the loading line for J_{applied} versus T_{applied} will not intersect the materials curve in the region where $\omega \geq 5$. However, both the J-T_{material} analysis and J-T_{applied} analyses are assured to be correct up to the experimental J-levels where $\omega \geq 5$. Therefore at that level there is still an assured safety margin factor on T, in fact by the inequality Eq 55; that is

$$\text{margin} = \frac{T_{\text{material}}}{T_{\text{applied}}} = \frac{a[0.5 \text{ to } 1]\omega}{b} \gg 1 \tag{56}$$

which is a safety margin against instability considering Eq 9.

Alternatively, it can be argued that since there is a fair margin against instability at the J-level where $\omega \to 5$ in the test data, loading would necessarily have to increase further, raising the apparent J, in order for instability to occur. Using the linear (cummulative) extrapolation of the data as suggested in Fig. 3, loading would at least progress beyond the point where the extrapolated data intersect the line representing Eq 54, with b replaced by a. At that point the analysis of the postulated vessel flaw is at a J-level where $\omega \geq 5$ so the analysis is still accurate. The load or pressure corresponding to J at that point can be found from the J_{applied} equations. Some further unknown margin exists at still greater loads since instability has not yet ensued even though at high loads neither "J-controlled growth" nor the analysis method are absolutely assured.

Application to End of Life by Irradiation Damage to Actual Vessels

Considering the preceding discussion, the former (more conservative) criteria rather than the alternative will be adopted here as a limiting (safe) J-level for purposes of safety assessments. Both the available data on irradiation damaged material and prospects of data from surveillance and other programs are limited to test specimen sizes of uncracked remaining ligaments, b, of slightly over 25 mm (1 in.). Inserting that size into Eq 54 along with other typical irradiation-damaged material properties—for example, $\sigma_0 > 85$ ksi, $E = 30 \times 10^3$ ksi, with $\omega = 5$—gives

$$\frac{J_{\text{material}}}{T_{\text{material}}} = \frac{\sigma_0^2 b}{E\omega} = \frac{(85)^2(1)}{30(5)} \approx 50 \frac{\text{in.} \cdot \text{lb}}{\text{in.}^2} \tag{57}$$

Figure 13 is a J versus T diagram showing some of the available irradiated J-R curve data, as well as some low-toughness unirradiated data. The curves shown were reported by Loss [22] and the experimental details and the method of development can be found in that publication. It is sufficient to note here that in the opinion of the present authors they are properly obtained data meeting the conditions for "J-controlled growth" over the full range for which the curves are plotted.

A $J/T = 50$ line was plotted on Fig. 13 intersecting the material data curves. Each curve has associated with it a number, which is the Charpy impact upper-shelf energy (in. ft · lb) from tests of the same material and condition. Thus in the neighborhood of the Code-significant Charpy energy of 50 (that is, the range 35 to 78 ft · lb), it was noted that the J-levels at the inter-

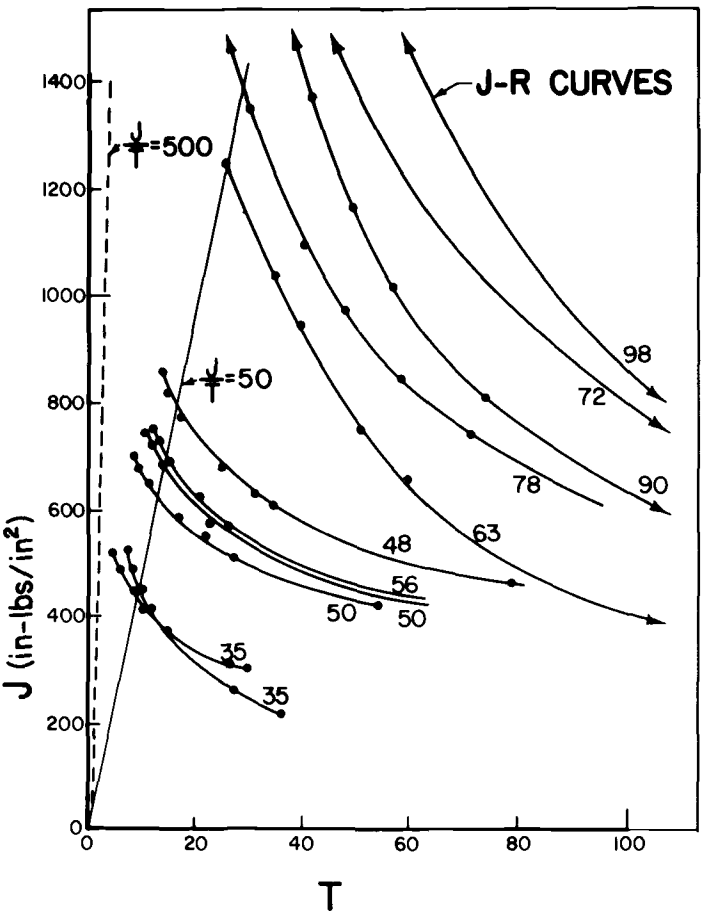

FIG. 13—*Typical data from Loss (NRL) on irradiated nuclear vessel materials (upper-shelf Charpy V-notch noted on each curve) [22] (1 in. · lb/in.^{2} = 0.17512 kJ/m^2).*

sections varied significantly. Also it was noted that these intersections with $J/T = 50$ were at J-levels considerably above the critical, J_{Ic}, values for these materials (sometimes as much as three times). Hence, J_{Ic} is far too conservative and not directly connected to crack instability for reasonable judgments of actual reactor safety for upper-shelf conditions.

On the other hand, linear extrapolation of the material data curves from the $J/T = 50$ line to loading J/T-curves for vessel postulations (usually $J/T > 500$) indicated a modest increase in J for instability above the $J/T = 50$ values. Consequently, the $J/T = 50$ intersection values, denoted J_{50} in further discussion here, appear to be reasonable (slightly conservative) for use in reactor vessel analysis. That is to say that these J_{50}-values, established from J-R curve tests of actual vessel material, including weld metal, are proposed and recommended as reasonable limiting values for vessel analysis for the current state of the art.

The Possibility of a Charpy Correlation with J_{50}-Values

The previous discussion recommending J_{50}-values measured directly from a plane-strain J-Integral R-curve test did so for very relevant reasons. The test directly measures crack extension (Δa) behavior for increases in applied J under rigorous J-controlled conditions. The results are directly applicable for estimating the instability of crack extension under local crack-tip conditions of plane strain with J-controlled growth for postulated vessel cracks. Short of extensive testing of *full scale* vessels with cracks, it is the most direct and rigorous approach available.

Correlations or data extrapolations, though tempting, do not have an important role except in cases where no other avenue of approach exists, and even then only with a vast amount of statistical data available to illustrate exceptions. One potential case is that of existing reactors with doubtful material chemistries, including welds, whose surveillance capsules do not contain material samples from which proper J-R curves may be obtained. Some capsules only have Charpy bars and no other way to establish J-R curve properties.

For such an extreme case the question is, Can the Charpy test in some way be correlated to the relevant property for analytical judgments, J_{50}, no more, no less? As a consequence, Loss's data were plotted on Fig. 14 to explore this possibility. For both irradiated and unirradiated base metal and weld metal a scatterband of data resulted. The scatterband was fairly broad but its lower boundary seemed well enough defined to provide hope that such a correlation may be possible for use where J-R curves are impossible to obtain.

It is noted that the data are from a single source and are not a very numerous (statistically significant) sample. So as hopeful as one may view this attempt at correlation, it remains to be firmly established.

Indeed if it is established as a correlation, it remains from statistical considerations to determine an adequate margin between the lower boundary of

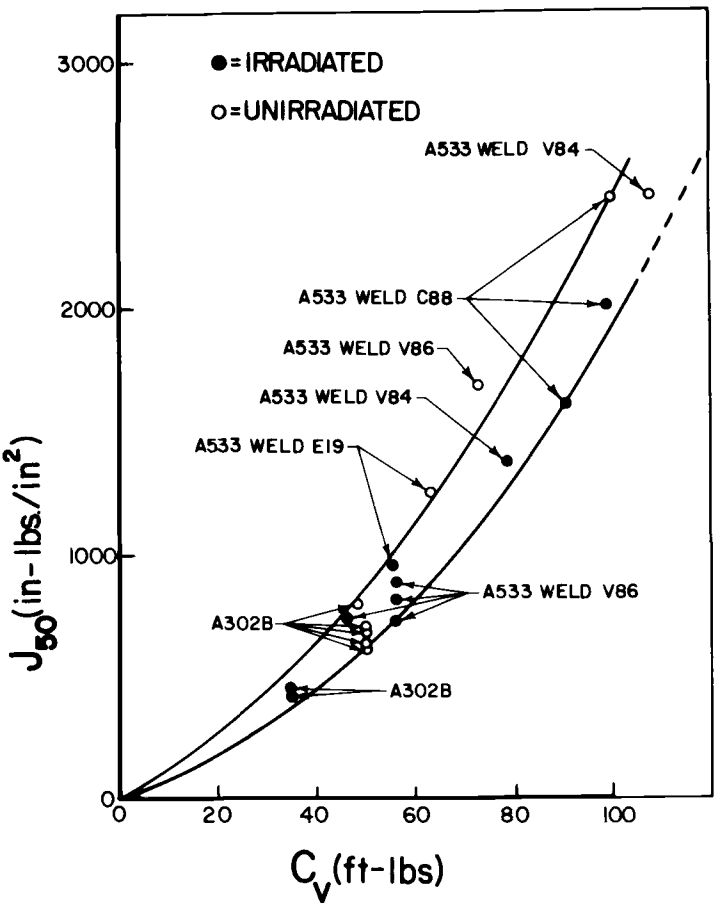

FIG. 14—*An attempted correlation of J_{50}-values with Charpy upper-shelf values from data by Loss [22]. (1 in. · lb/in.^{2} = 0.17512 kJ/m^2) (1 ft · lb = 1.356 J).*

the data and acceptable J_{50}-values for use in analysis to assure safe utilization. This judgment is left for others after an adequate data base has become available.

Discussion and Conclusions

The analysis methods developed herein have attempted to combine several objectives. The methods suggested are the first logical extensions of LEFM Code methods for flaw analysis in nuclear pressure vessels, that make use of established elastic plastic fracture mechanics methodology so as to be quantitatively applicable to above-transition-temperature conditions. This has been done by making use of "tearing instability" concepts under "*J*-controlled growth" conditions to formulate crack instability criteria which are not overly

conservative. The method is integrated with the use of *J-R* curves, which are the only available and widely accepted direct quantitative fracture properties characterization for above-transition-temperature conditions.

Staying within the *J*-controlled growth region for material properties tests, specifically for bend or compact-specimen J-R curves, is shown to suggest limiting the loading on postulated vessel cracks to an applied *J*-level, J_{50}, where the test data intersect $J/T = 50$. This assures conservatively avoiding crack instability by the tearing mode. At near or below the transition temperature the cleavage mode bears other considerations. On the other hand, well above the transition temperature, which is usually consistent with nuclear vessel normal operating conditions, cleavage is avoided. As a further expedient for situations such as some surveillance programs where only Charpy specimens are available, it is shown that upper-shelf Charpy energies seem to correlate with J_{50}-values. This correlation and other data requirements suggest developing a broader data base.

The analysis and resulting equations developed here for applied J, T, and J/T are appropriate approximations permitting the separation of stress level effects and geometrical effects into independent factors. This has led to clearly delineating the regions of interest on J versus T diagrams for the location of potential crack instability points for postulated vessel cracks at or above about $J/T = 500$. Thereafter, once a safe value is selected such as limiting J to a value J_{50} (for $J/T \leq 50$), the approximations have served their purpose. Nevertheless, they are clearly and conservatively developed herein and are suggested as sufficiently accurate for broad usage with the advantages of simplicity and familiarity to fracture mechanics practitioners.

Acknowledgments

This analysis has been developed and the paper produced under a subcontract (K-8195) between the Del Research Corp. (P. Paris, president) and EG&G, Idaho (Nuclear) Inc. The encouragement and suggestions of the staff of the Nuclear Regulatory Commission (NRC) are gratefully acknowledged as essential to this work. Their continued guidance, experienced prospectives, and earlier direct technical support have been most effective and are due the utmost thanks. The financial support of other programs at Washington University (St. Louis) by the NRC Operating Reactors Division contributed effectively to the origins of the analysis herein. The use of J versus T diagrams, as developed here, was originated in earlier unpublished work with Societe Technigaz, as well as in Ref *2*.

References

[*1*] "Flaw Evaluation Procedures," American Society of Mechanical Engineers Section XI Task Group on Flaw Evaluation, T. V. Marston, Ed., Electric Power Research Institute Special Report NP-719-SR, Palo Alto, Calif., Aug. 1978.

[*2*] Paris, P. C., Tada, H., Zahoor, A., and Ernst, H., "A Treatment of the Subject of Tearing

Instability," NUREG 0311, Nuclear Regulatory Commission, Washington, D.C., Aug. 1977; see also *Elastic-Plastic Fracture, ASTM STP 668*, J. D. Landes, J. A. Begley, and G. A. Clarke, Eds., American Society for Testing and Materials, 1968, pp. 5-36.

[3] Hutchinson, J. W. and Paris, P. C. in *Elastic-Plastic Fracture, ASTM STP 668*, J. D. Landes, J. A. Begley, and G. A. Clarke, Eds., American Society for Testing and Materials, 1968, pp. 37-64.

[4] *Proceedings*, CSNI Meeting on Plastic Tearing Instability, compiled by P. C. Paris, NUREG/CR-0100, Nuclear Regulatory Commission, Washington, D.C., Jan. 1980.

[5] Shih, C. F. in *Proceedings*, CSNI Meeting on Plastic Tearing Instability, compiled by P. C. Paris, NUREG/CR-0100, Nuclear Regulatory Commission, Washington D.C., Jan. 1980.

[6] Hutchinson, J. W., *Journal of the Mechanics and Physics of Solids*, Vol. 16, No. 1, Jan. 1968.

[7] Rice, J. R. and Rosengren, G. F., *Journal of the Mechanics and Physics of Solids*, Vol. 16, No. 1, Jan. 1968.

[8] Rice, J. R., *Transactions*, American Society of Mechanical Engineers, *Journal of Applied Mechanics*, Vol. 35, 1968, pp. 379-386.

[9] Paris, P. C. in *Flaw Growth and Fracture, ASTM STP 631*, American Society for Testing and Materials, 1977.

[10] Folias, E. S., *International Journal of Fracture Mechanics*, Vol. 1, 1965, p. 104.

[11] Erdogan, F. and Kibler, J. J., *International Journal of Fracture Mechanics*, Vol. 5, 1969, p. 229.

[12] Krenk, S., *Transactions*, Fourth International Conference on Structural Mechanics in Reactor Technology, San Francisco, 1977, Paper G5/3.

[13] Rooke, D. P. and Cartwright, D. J., *Compendium of Stress Intensity Factors*, Her Majesty's Stationery Office, London, 1976.

[14] Tada, H., Paris, P., and Irwin, G. R., *The Stress Analysis of Cracks Handbook*, Del Research Corp., St. Louis, Mo., 1973.

[15] Hutchinson, J. W., Needleman, A., and Shih, C. F. in *Fracture Mechanics*, N. Perrone et al., Eds., University Press of Virginia, Charlottesville, Va., 1978.

[16] Zahoor, A. In "Further Results on the Subject of Tearing Instability," prepared by H. Tada and P. C. Paris, NUREG/CR-1220, Nuclear Regulatory Commission, Washington, D.C., Jan. 1980.

[17] Tada, H. and Paris, P. C., "Tearing Instability Analysis Handbook," NUREG/CR-1221, Nuclear Regulatory Commission, Washington, D.C., Jan. 1980.

[18] Shih, C. F. and Hutchinson, J. W., *Transactions*, American Society of Mechanical Engineers, *Journal of Engineering Materials and Technology*, Vol. 98, No. 4, Oct. 1976.

[19] Burrington, R. S., *Handbook of Mathematical Tables and Formulas*, 3rd ed., Handbook Publishers, Sandusky, Ohio, 1949.

[20] Riccardella, P. in "Resolution of the Reactor Vessel Materials Toughness Safety Issue," NUREG-0744, Nuclear Regulatory Commission, Washington, D.C., Vol. 2, June 1981.

[21] Reuter, W. in "Resolution of the Reactor Vessel Materials Toughness Safety Issue," NUREG-0744, Nuclear Regulatory Commission, Washington, D.C., Vol. 2, June 1981.

[22] Loss, F. in "Resolution of the Reactor Vessel Materials Toughness Safety Issue," NUREG-0744, Nuclear Regulatory Commission, Washington, D.C., Vol. 2, June 1981.

Karl Kussmaul[1] *and Lothar Issler*[2]

Evaluation of the Elastic-Plastic Fracture Mechanics Methodology on the Basis of Large-Scale Specimens

REFERENCE: Kussmaul, K. and Issler, L., **"Evaluation of the Elastic-Plastic Fracture Mechanics Methodology on the Basis of Large-Scale Specimens,"** *Elastic-Plastic Fracture: Second Symposium, Volume II—Fracture Resistance Curves and Engineering Applications, ASTM STP 803*, C. F. Shih and J. P. Gudas, Eds., American Society for Testing and Materials, 1983, pp. II-41-II-57.

ABSTRACT: Within the scope of the cooperative project "Integrity of Components" (FKS) which is a part of the German Nuclear Safety Research Programme of the Federal Minister for Research and Technology, the theoretical and experimental investigation on ductile fracture is of decisive importance. The FKS is mainly concentrated on tearing tests on large-scale heavy-section specimens, in both the base material and welded conditions. Universal facilities up to 100 MN are available to test large-scale round and flat bars containing sharp defects in the form of machined notches, fatigue cracks, and natural flaws, such as segregation and heat-affected zone cracking. The dimensions are chosen so that it is possible to realize the significant technological states of material and stress over all conditions in the light-water reactor pressure vessel. The tested materials similar to A508 Class 2 and 3 cover a wide range of ductility (C_V upper-shelf toughness-40 to 200 J, crack initiation J_i = 50 to 200 kN/m, T-modulus = 10 to 300).

KEY WORDS: elastic-plastic fracture, toughness, static loading, large-scale and full-scale heavy-section testing, elastic limit, plastic limit, natural heat-affected zone cracking, size effect

The test results are mainly analyzed with the J-integral and crack-opening displacement (COD) concepts. The relevant ductile fracture criteria are determined on small-scale specimens and calculated with finite-element methods as well as with the estimation scheme developed by General Electric under an Electric Power Research Institute (EPRI) contract. The R-curve technique, including the tearing instability diagram and modified failure assess-

[1]Director and full professor, Staatliche Materialprüfungsanstalt (MPA), University of Stuttgart, D 7000 Stuttgart, West Germany.
[2]Professor, Fachhochschule für Technik, D 7300 Esslingen, West Germany.

ment diagram, are used for assessing crack initiation, stable crack propagation, and instability.

In addition to the comparative application of the elastic-plastic fracture mechanics concepts, the large-scale tests are intended to indicate the limits of conventional approaches, for example, the plastic limit load. Furthermore, the correlations between fracture stress and classical toughness characteristics, such as C_V-toughness and reduction of area, are investigated.

For the present, it can be stated that the tools applied open a reliable access to the understanding and quantification of ductile fracture. However, further developments of testing, measuring, and calculation methods of the J and COD concepts are necessary. These demands concern both the application to component and operational conditions as well as the degree of conservatism of R-curves determined on small-scale specimens. There are still considerable uncertainties in the application of the ductile fracture approaches with special regard to the analysis of natural cracking. On the other hand, an engineering assessment approach on the basis of classical material characteristics shows good promise of handling the problem of ductile fracture in practice.

The large-scale-and full-scale testing philosophy has been representing for decades an important part of a reliable strategy for fracture-safe materials and design [*1.2*].[3] It soon became evident that with respect to then existing flaws, which, however, remained undetected, the fracture resistance was only sufficient if the ductility exceeded a certain level. The requirements for toughness were firstly derived from the tension test characteristics, elongation, and reduction of area (RA) at fracture. It is interesting to note that the notched-bar impact test with a ligament size of 15 by 15 mm^2 was introduced to the German pressure vessel code just 50 years ago.

Nowadays the results of the large-scale tests being performed in the frame of the German reactor safety research program "Integrity of Components" (FKS) serve the following:

1. Evaluation of the overall states of stresses, toughness [nil-ductility transition temperature (NDTT) transition range, upper-shelf range], and flaws ranging from most favorable to worst-case conditions.
2. Review of the current fracture mechanics approaches (small-scale specimens) with respect to the component (large- and full-scale specimens), Fig. 1.
3. Development of an engineering approach to ductile fracture by introducing simplified numerical methods and conventional material characteristics (C_V, RA).
4. Supporting the so-called "basis safety strategy" in the field of nuclear engineering and design, the tenor of which is the break with the postulate of catastrophic failure not only for the reactor pressure vessel (RPV) but also for the other safety-related components [*3-5*].

[3]The italic numbers in brackets refer to the list of references appended to this paper.

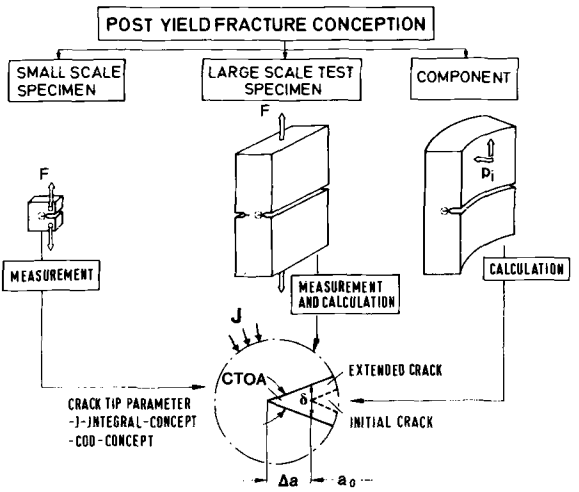

FIG. 1—Large-scale specimens as a link for transferability.

The characteristic feature of the FKS, when considering the whole range of ductility, is to shed light on both the quality of the elastic-plastic fracture mechanics (EPFM), linear elastic fracture mechanics (LEFM), and plastic limit load (PLLA) analysis, and on the possibility of applying the conventional (C_V, RA) toughness characteristics as fracture-controlling parameters. The toughness spectrum of the FKS materials provides experimental results for the whole range of EPFM and the well-established boundaries LEFM and PLLA which, in turn, firmly support the still problematic EPFM methods, Fig. 2.

The new additional requirements for "basis safe materials" are for all locations and directions:

$C_V \geq 100\,J$	upper-shelf energy (USE), single value
RA ≥ 45 percent	room temperature

The results of the test-and-analysis program address the following main topics:

static mechanical loading,
base materials and weldments both with natural cracks, machined notches, and fatigue cracks,
effect of configuration and size of specimens, and
effect of temperature and level of USE.

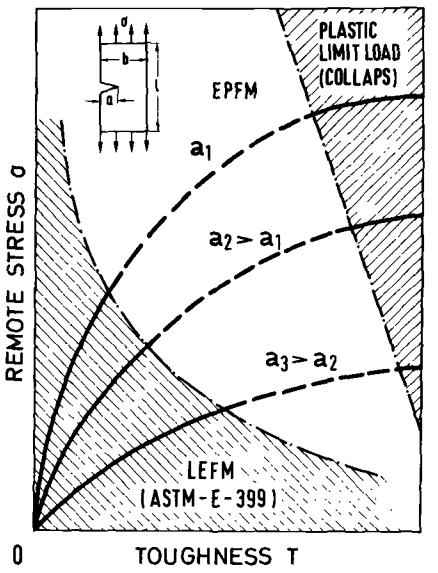

FIG. 2—*Fracture mechanics methods.*

The data developed for this paper were derived from an RPV shell course material (fabricated for a 1200-MWe pressurized water reactor (PWR) plant and rejected during fabrication) as well as special heats, up to 200 t in the as-forged condition. Segregation and segregation cracking effects were not specifically included in the results obtained.

Materials Characteristics

Chemical Composition

The basic chemical composition of the materials corresponds more or less to the nuclear grade steels 22Ni-Mo-Cr37 (A508 Class 2) and 20Mn-Mo-Ni55 (A508 Class 3, A533B Class 1). Unfavorable toughness conditions were achieved by selection of the upper or the lower bounds of the percentage of the alloying elements sometimes exceeding the specified limits, and a high content of accompanying elements and residuals. These elements are also responsible for segregation cracking and heat-affected zone (HAZ) embrittlement and cracking.

Strength and Toughness

The strength and toughness characteristics are given in Table 1 and Figs. 3-6. KS 01 (A508 Class 2) is a rejected flange ring; KS 07 (A508 Class 2, mod-

TABLE 1—*Specimen strength and toughness characteristics.*

	Room Temperature												350°C											
	$R_{p0.2}$, N/mm^2			R_m, N/mm^2			A_5, %			Reduction of Area, %			$R_{p0.2}$, N/mm^2			R_m, N/mm^2			A_5, %			Reduction of Area, %		
Material	L	T	S	L	T	S	L	T	S	L	T	S	L	T	S	L	T	S	L	T	S	L	T	S
KS 01	439	438	446	590	586	588	26	25	22	71	55	52	373	379	372	544	552	538	25	20	18	69	45	38
KS 07 A+B	598	611	611	764	777	777	19	13	10	60	23	14	430	545		709	722		18	9		54	11	
KS 14		484			649			25			65			429			586			19			63	
KS 15	478	497	502	650	665	663	19	19	15	65	56	35	421	431	425	589	594	589	16	15	12	65	50	32

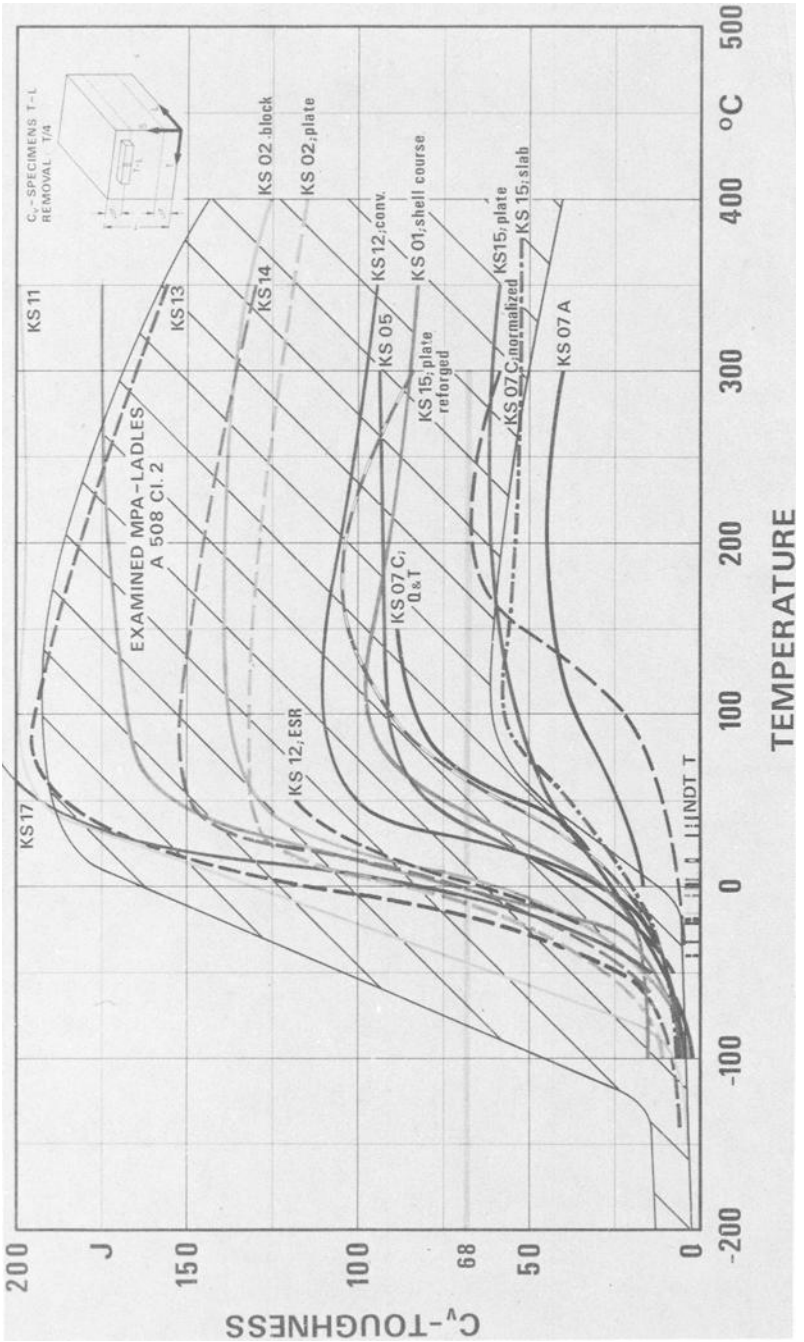

FIG. 3—C_V toughness of FKS materials.

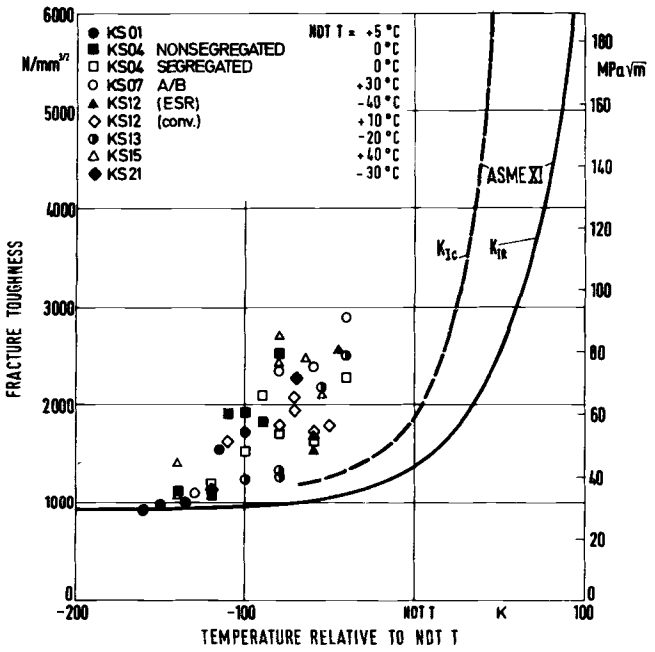

FIG. 4—*Fracture toughness of FKS materials.*

ified) indicates a forged slab. KS 14 (A533B Class 1) denotes a forged plate, whereas KS 15 (A533B Class 1, modified) represents again a forged slab.

Weldments

Multilayer submerged-arc techniques were employed for the fabrication of the V-shaped weldments up to a thickness of 250 mm. To cover the range of quality (toughness, HAZ cracking), both optimum welding parameters as well as unfavorable welding conditions and heat history were applied. Extended coarse grain zones and micro/macro cracking are typical for the worst-case condition.

Specimen Design

The configuration of specimens and type of flaws correspond to compact tension (CT), double-edge-notched (DEN), double-edge-cracked (DEC), and single-edge-notched (SEN) specimens, Fig. 7. Single-edge-cracked (SEC) specimens with natural HAZ cracking were tested under tension and three-point bending.

The size of large-scale specimens is characterized by a thickness B range

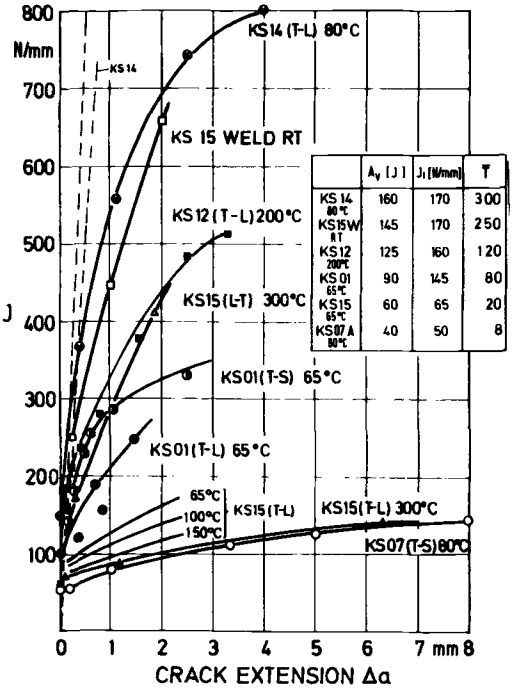

	A_v [J]	J_i [N/mm]	T
KS 14 80°C	160	170	300
KS15W RT	145	170	250
KS12 200°C	125	160	120
KS01 65°C	90	145	80
KS15 65°C	60	65	20
KS07A 80°C	40	50	8

FIG. 5—*J-R curves of FKS materials.*

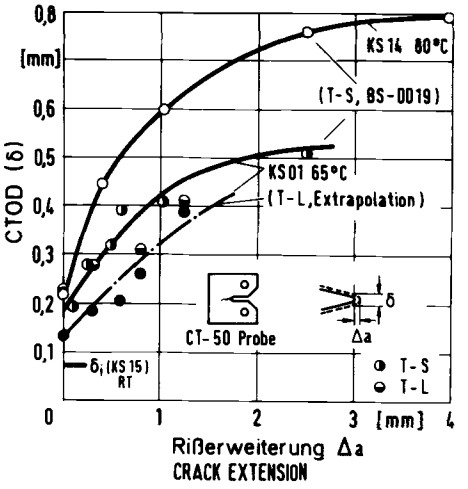

FIG. 6—*Crack-tip opening displacement of FKS materials.*

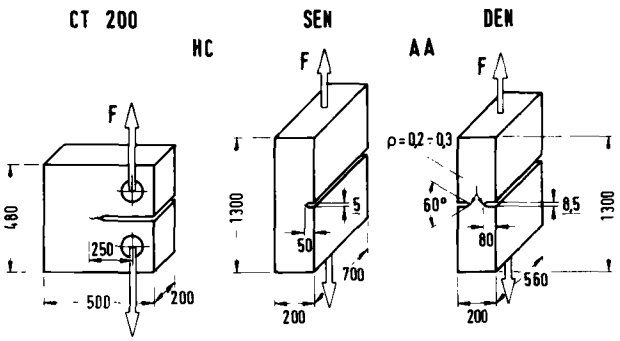

FIG. 7—*Large-scale specimens (base material).*

(defect length) 10 to 700 mm and a maximum ligament width ($W - a$) of 500 mm, where a is the defect depth. The scaling factor for medium-size specimens is 1:5.

Test Procedure and Evaluation

The J-R curve was derived from small CT25 and CT50 specimens (single- and multiple-specimen technique). The initiation value J_i has been defined as the intersection of the curved J-R line with the blunting line. The J versus load functions for all tested specimens were calculated assuming dead load by the two-dimensional (plane strain, plane stress) and three-dimensional finite-element methods, by the estimation scheme [*6*] (plane strain, plane stress) and by η-factor estimation [*7*]. The crack-tip opening displacement (CTOD) for small-and large-scale specimens was determined by all available methods (rotation factor BS 5762:1979, endoscopy, inserted clip gages, metallographic cuts, replica technique, measuring grid, Moiré). The COD versus load functions were calculated by finite-element and estimation scheme methods.

Determination of the initiation load for large-scale tests was tried by heat-tinting, acoustic emission, the ultrasonic difference method, and potential probe methods.

The instability point, Fig. 8, was evaluated by the R-curve/driving force tangency [*8*], the tearing instability diagram [*9*], and the J_{50} method [*10*].

Results

Correlation of Toughness Properties (Small-Scale Specimens)

J_i and J_{50} versus C_V toughness plots, Fig. 9, indicate a linearity for initiation and a progressive increase for instability. The J_i-values fit the added scatter-

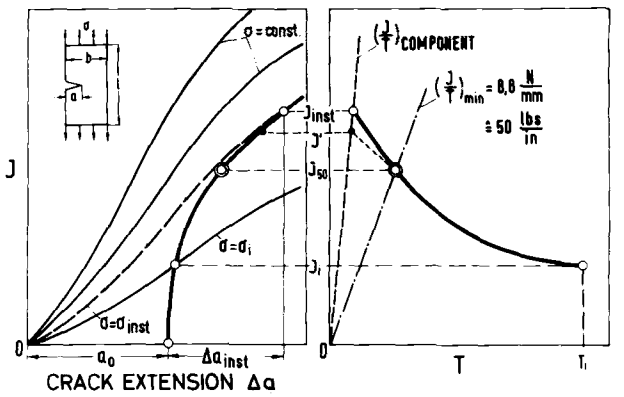

FIG. 8—*Determination of instability by R-curve and J_{50}-method.*

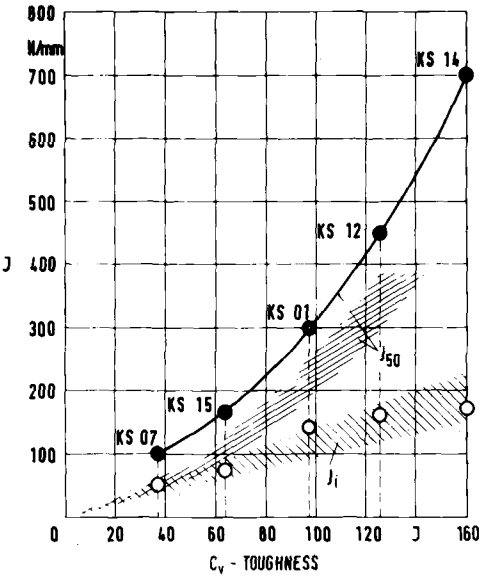

FIG. 9—J_i *and* J_{50} *as a function of* C_V *toughness.*

band for the empirical evaluation in the literature; the J_{50}-values of the FKS tests are about 10 percent higher than the results derived from unirradiated and irradiated specimens [*11*].

Correlation of Failure Stress and Toughness (Large-Scale Specimens)

The foregoing relationship is established by means of the J-C_V correlation, Fig. 9, and the calculated J driving-force diagram for the respective compo-

nent represented by large-scale specimens, Fig. 10. An example of this procedure to predict initiation and instability is shown in Fig. 11. The experimental instability stress of a large-scale SEN specimen is in good agreement with the theoretical solution.

Experimental results for the instability of DEN, Fig. 12, show again that

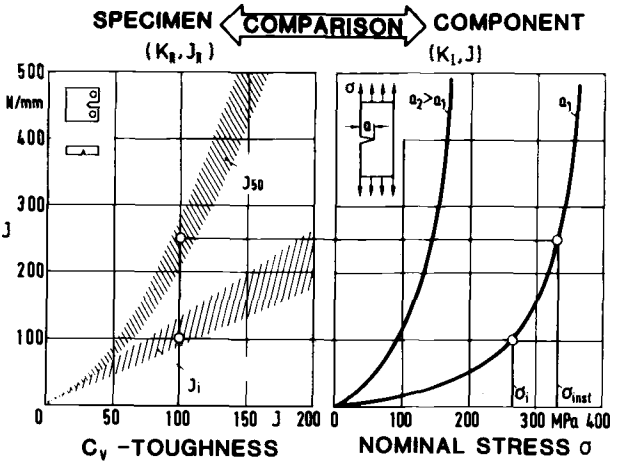

FIG. 10—*Loading capacity as a function of* C_V *toughness.*

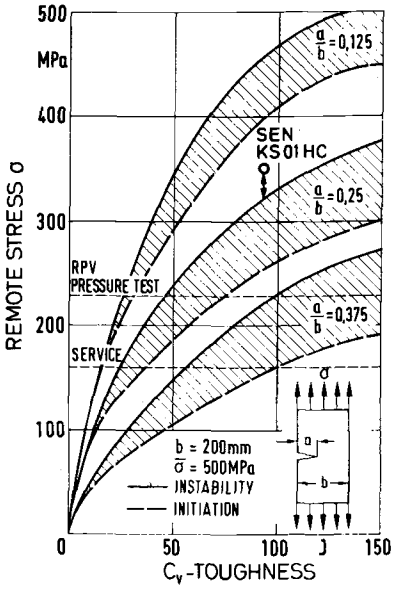

FIG. 11—*Failure analysis for an SEC large-scale specimen.*

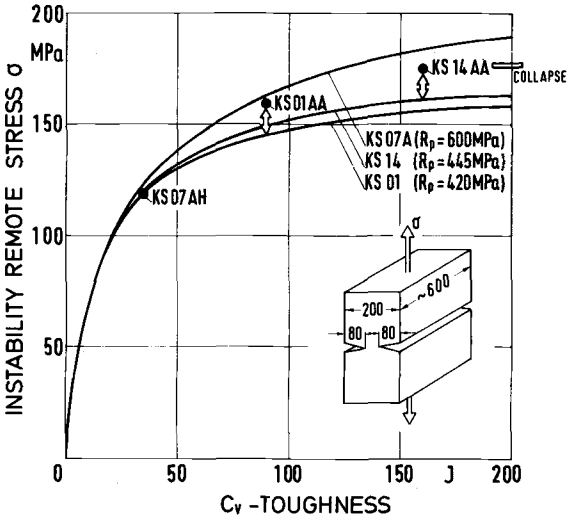

FIG. 12—J_{50} *analysis for DEN-panel (DENP) compared with large-scale specimen results.*

the J_{50} method gives a suitable approximation. Above 100 J, the fracture stress of the DEN specimen is on a level with the calculated collapse stress after [*12*]. Moreover, the analysis of an SEN large-scale specimen in the tearing instability diagram, Fig. 13, indicates that the application of the estimation scheme and the J_{50} method to predict instability is promising (see also Fig. 11).

Size Effect

The CT25 to CT200 scaling tests, Fig. 14, show that J_i can be regarded as an initiation-controlling property. However, the problem of the definition of the initiation point and the proper size requirements for the slope of the J-R curve still exists. It is remarkable to note that the 20 percent side-grooved CT50 specimen represents a lower bound even for the CT200 without side grooves.

Another example for the scaling effect, demonstrated in the failure assessment diagram (FAD), Fig. 15, and the J-σ plot, Fig. 16, shows the higher fracture stress and the collapse mode of failure for the smaller specimens, whereas the large-scale specimens due to the (absolute) large crack size generate a high-stress intensity and a crack-tip controlled fracture in the elastic-plastic regime.

The thickness effect can be seen in Fig. 17. The ductile material shows an increasing loading capacity with increasing thickness up to a saturation level (B = 300, theoretical and experimental constraint factor = 2.3 and 2.1, respectively). The lower-bound weldments with HAZ cracking reach the saturation level at the same thickness.

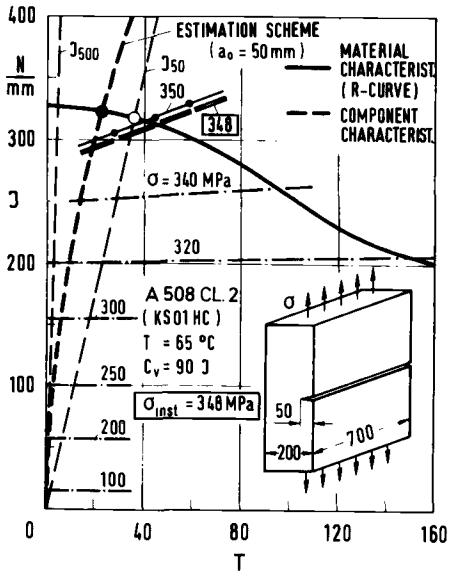

FIG. 13—*Tearing instability diagram for an SEN large-scale specimen.*

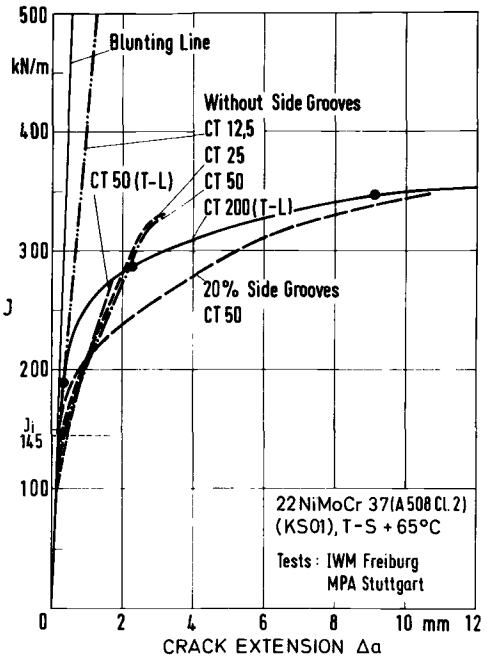

FIG. 14—*J-R curves for different CT-specimens (A508 Class 2).*

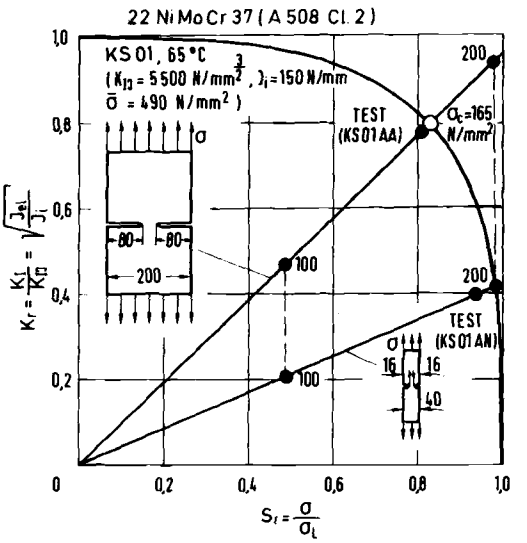

FIG. 15—*Analysis of scaled DENP in the FAD.*

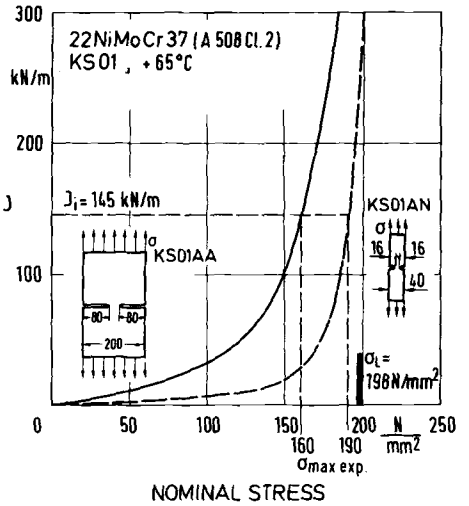

FIG. 16—*Analysis of scaled DENP in terms of J.*

Type of Flaw

No significant difference in fracture stress of large-scale specimens of the ductile materials KS14 was measured when comparing sharp notches and fatigue cracks, despite the different J-R curves with higher J_i and T for the as-notched condition.

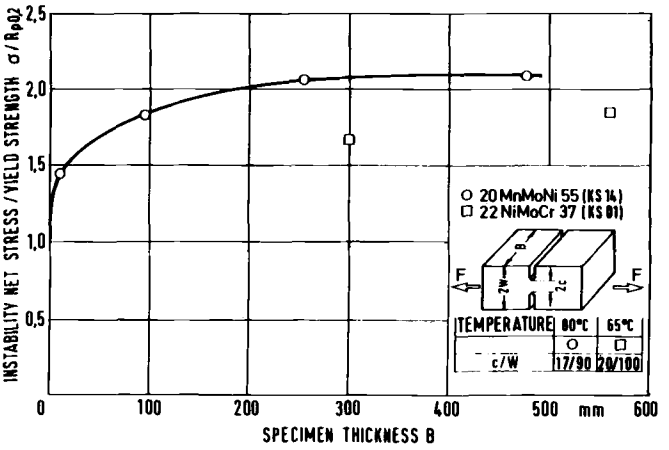

FIG. 17—*Effect of specimen thickness for A533 B Class 1.*

Natural HAZ Cracking

The tension and bending tests were evaluated both by J (Fig. 18) and COD, Fig. 19. The crack path did not follow the HAZ but branched to the base material. Therefore, the failure analysis is first related to the toughness characteristics of the base material. Both J_i and δ_i are reliable tools to describe the measured (ultrasonic method) initiation. However, the scattering of the COD analysis (numerical and experimental) is significant. With respect to J it can be noted that, when using the instability crack length, the calculated driving force corresponds to the experimentally determined J. The J_{50} instability analysis is conservative even if the stable crack extension is neglected. Crack initia-

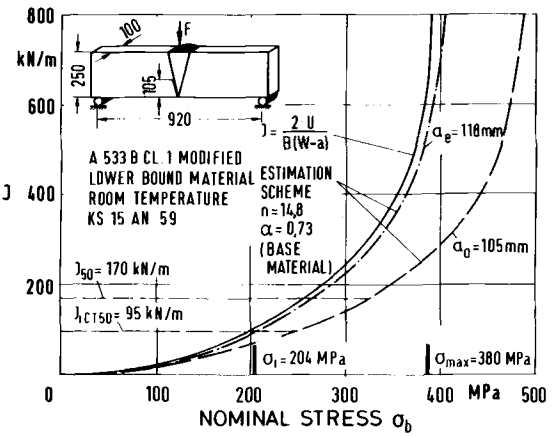

FIG. 18—J-*analysis of a natural HAZ crack.*

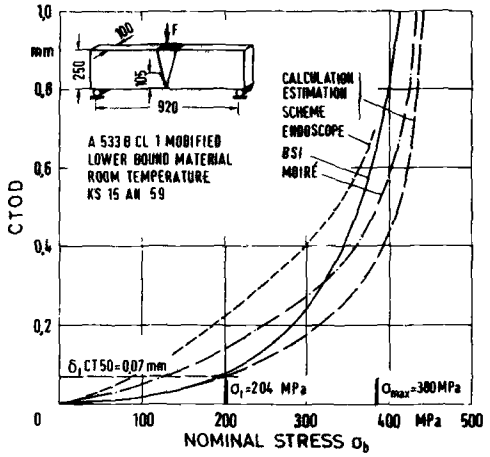

FIG. 19—*COD-analysis of a natural HAZ crack.*

tion of the large-scale tension specimen with HAZ cracking again could be satisfactorily calculated with the help of the J and COD methods.

Concluding Remarks

The following conclusions are based upon our manifold work on the safety of the LWR pressure vessel.

1. Large-scale specimens proved to be a powerful basis for the critical evaluation of the current EPFM methods embedded in the LEFM and PLLA.
2. The currently available FM methods are in principle suitable for the quantification of the safety margin of cracked components under static mechanical loading.
3. The preceding statement applies not only to the onset of stable crack growth but, within certain limits, also to instability.
4. J and COD can apparently be regarded as equivalent criteria; however, the J-method has the advantage of facilitating the applicability.
5. The engineering assessments, including the plastic collapse analysis, based upon the conventional toughness characteristics are suitable for the interpretation of ductile fracture and open the field for extended practical use.
6. The "basis safety strategy" for high-toughness materials (USE $\geq$ 100 J) could be further validated.

Acknowledgments

This research was supported by the Minister of Research and Technology of the Federal Republic of Germany and the Nuclear Industry (steel and component makers, nuclear steel supply system vendors, utilities).

References

[1] Kussmaul, K. and Sturm, D., "Research Activities at the MPA Stuttgart in the Field of Nuclear Pressure Vessel Technology," Paper No. 12, Sixth Annual Information Meeting, HSST-Program, Oak Ridge National Laboratory, Oak Ridge, Tenn., 1972.

[2] Wellinger, K., Krägeloh, E., Kussmaul, K., and Sturm, D. in *Proceedings*, First International Conference on Structural Mechanics in Reactor Technology, Berlin, 20-24 Sept. 1971; and *Nuclear Engineering and Design*, Vol. 20, 1972, pp. 215-235.

[3] Kussmaul, K. and Blind, D. in *Trends in Reactor Pressure Vessel and Circuit Development*, R. W. Nichols, Ed., Applied Science Publishers, London, 1980, pp. 1-14.

[4] Kussmaul, K. et al in *Proceedings*, Fourth International Conference on Structural Mechanics in Reactor Technology, 15-19 Aug. 1977, San Francisco; and *VGB-Kraftwerkstechnik*, Vol. 58, No. 6, June 1978, pp. 439-448; also *International Journal of Pressure Vessels and Piping*, Vol. 8, 1980, pp. 323-346.

[5] Kussmaul, K., "Developments in Nuclear Pressure Vessel and Circuit Technology in the Federal Republic of Germany," Smirt-6, Post Conference Seminar No. 8, Paris, 24-25 Aug., 1981.

[6] Shih, C. F. and Kumar, V., "Estimation Technique for the Prediction of Elastic-Plastic Fracture of Structural Components," General Electric Co. Semiannual Reports for EPRI, Poughkeepsie, N.Y., 1979/1980.

[7] Turner, C. F., in *Post Yield Fracture Mechanics*, D. G. H. Latzko, Ed., Applied Science Publishers, London, 1979.

[8] Shih, C. F., "An Engineering Approach for Examining Crack Growth and Stability in Flawed Structures," Committee on the Safety of Nuclear Installations (CSNI) of the Organization for Economic Cooperation and Development (OECD) Specialists Meeting on Plastic Tearing Instability, NUREG/CP-0010, CSNI Report No. 39, 1979.

[9] Paris, P. C., "A Treatment of the Subject of Tearing Instability," NUREG-0311, Washington University, Nuclear Regulatory Agency, 1977.

[10] Paris, P. and Johnson, R. E., "A Method of Application of Elastic-Plastic Fracture Mechanics on Nuclear Vessel Analyses," Nuclear Regulatory Agency Report, to be published.

[11] Loss, F., "Contribution on Resolution of the Reactor Vessel Materials Toughness Safety Issue," USNRC Report NUREG-0744, Nuclear Regulatory Agency, Vol. II, June 1981.

[12] Ewing, D. J. F. and Hill, R. *Journal of the Mechanics and Physics of Solids*, Vol. 15, 1967.

Sten Kaiser[1] *and A. Janne Carlsson*[1]

Studies of Different Criteria for Crack Growth Instability in Ductile Materials

REFERENCE: Kaiser, S. and Carlsson, A. J. **"Studies of Different Criteria for Crack Growth Instability in Ductile Materials,"** *Elastic-Plastic Fracture: Second Symposium, Volume II—Fracture Resistance Curves and Engineering Applications, ASTM STP 803,* C. F. Shih and J. P. Gudas, Eds., American Society for Testing and Materials, 1983, pp. II-58-II-79.

ABSTRACT: A general instability condition of solid mechanics, valid for a nonlinear structural component in an otherwise elastic system, is shown to be inherent in the T-modulus concept of instability. This condition involves the slope of the descending part of the load-displacement curve of the nonlinear component. It is shown that this slope can be used to evaluate T_{appl} at instability; T_{appl} can then be used to give a simple estimation of T_{mat} without the need for exact crack length determination.

In this paper such evaluations for large panel specimens and smaller bend and CT specimens are reported for three structural steels. The obtained data are in good agreement with conventionally determined data. However T-evaluations for tension-type specimens give values which are higher by a factor of two than those calculated for bend-type specimens. This indicates that T is not geometry independent, but that T from bend and CT specimens gives a lower bound.

A method is discussed of analyzing the instability of a large structure with a cracked, ductile component using the slope of the load-displacement curve and the general instability criteria of mechanics without recourse to fracture parameters.

KEY WORDS: tearing modulus, unstable crack growth, crack-driving force diagram, J-R curves, load-displacement records, tearing instability, elastic-plastic fracture

Several concepts have been proposed for studying instability in structures with extensive plastic deformation and stable crack growth. All these require elaborate testing and test evaluation. Most experimental results are obtained with specimens or components tested under displacement control in a stiff testing machine.

One interesting question in the application of these results is to transfer them to cases when the specimen or component is part of an otherwise elastic

[1]Research assistant and professor, respectively, Department of Strength of Materials and Solid Mechanics, Royal Institute of Technology, Stockholm, Sweden.

system. A second, more interesting question is to transfer the results to other specimens, components, or structures with plastic deformation and stable crack growth.

The first question does not, as will be discussed, require introduction of fracture parameters. The problem can be solved using the load-displacement curve of the non-linear specimen or component. Especially the slope of the descending part of the curve is then of importance. Its inverse will be referred to as the rebound "compliance." The second question requires introduction of a fracture parameter. In this paper three such proposed parameters are used to evaluate experimental studies of instability in different specimens. These parameters are the T-modulus by Paris et al [*1*],[2] the η-factor concept by Turner [*2*], and the Electric Power Research Institute (EPRI) estimation scheme by Shih et al [*3*] and Shih and Hutchinson [*13*].

The rebound "compliance" mentioned in the preceding is shown to be an interesting measure for the determination of the material property T_{mat}, as is demonstrated in the following.

The rebound compliance of a nonlinear component may also be used to predict instability of this component in an otherwise elastic system. A treatment of instability of a large structural system can then be based on fracture tests on a specimen similar to the nonlinear part of the system and simple structural calculations for the elastic parts of the system.

Simple Instability Analysis for a Nonlinear Component in an Elastic System

Consider a cracked specimen or component connected to an elastic system, in Fig. 1 simplified to a spring in series with the specimen.

The total deformation of the spring and the specimen is given through

$$\Delta_{tot} = C_{ext} P + \Delta \tag{1}$$

where Δ is composed of one elastic and one plastic part.

In tests with stable crack growth in a specimen, one often observes that the load-displacement curve after maximum load is almost linear; see Fig. 2 and also Ref *1*. This motivates introduction of a rebound "compliance" C_r such that

$$d\Delta = -C_r dP \tag{2}$$

Here C_r is a function not only of plastic properties but also of crack elongation. If the unloading curve is not linear, C_r depends also on displacement.

[2]The italic numbers in brackets refer to the list of references appended to this paper.

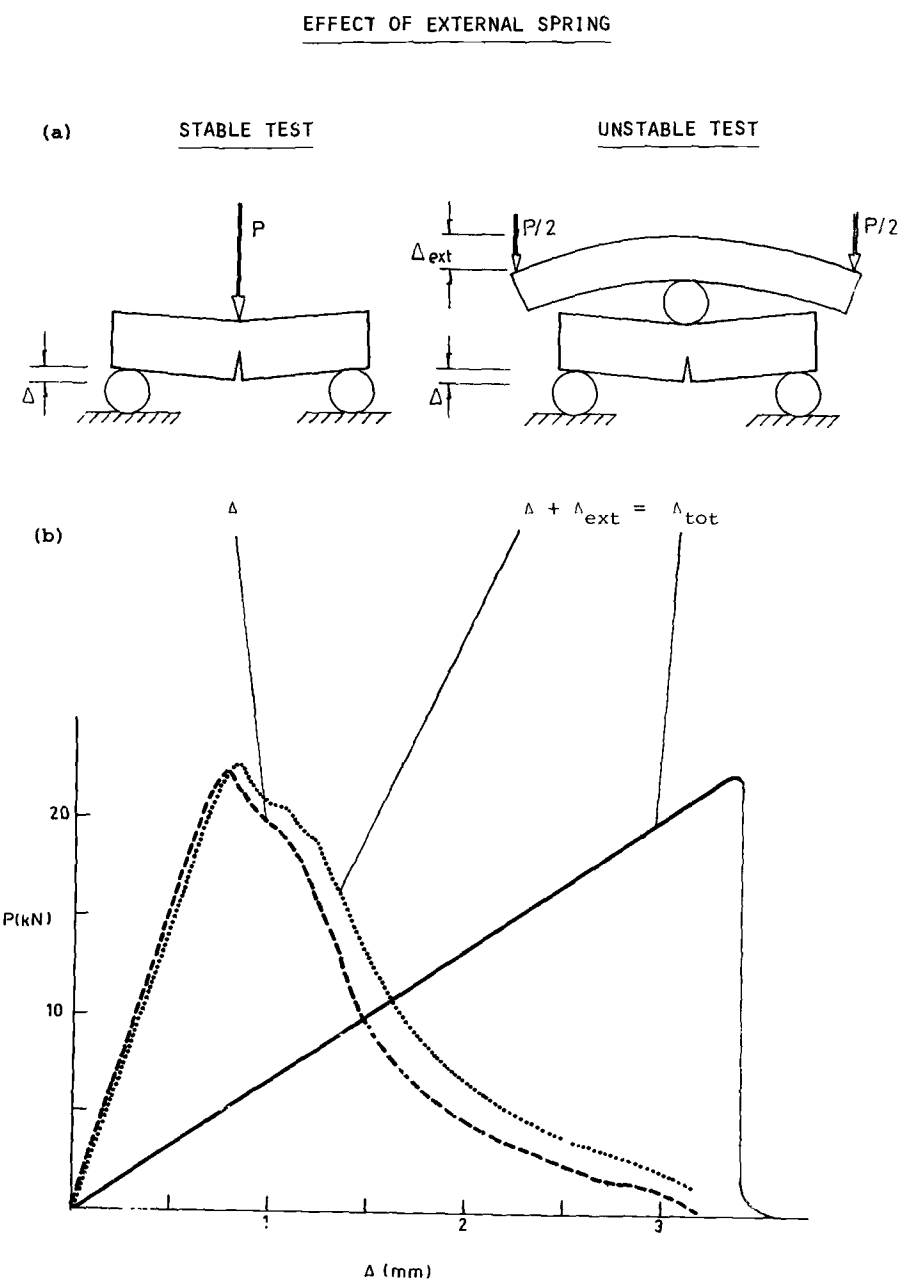

FIG. 1—P-Δ *curves for specimens under stable and unstable conditions, respectively, and the* P-Δ_{tot} *curve for the unstable setup (spring in series with the specimen).*

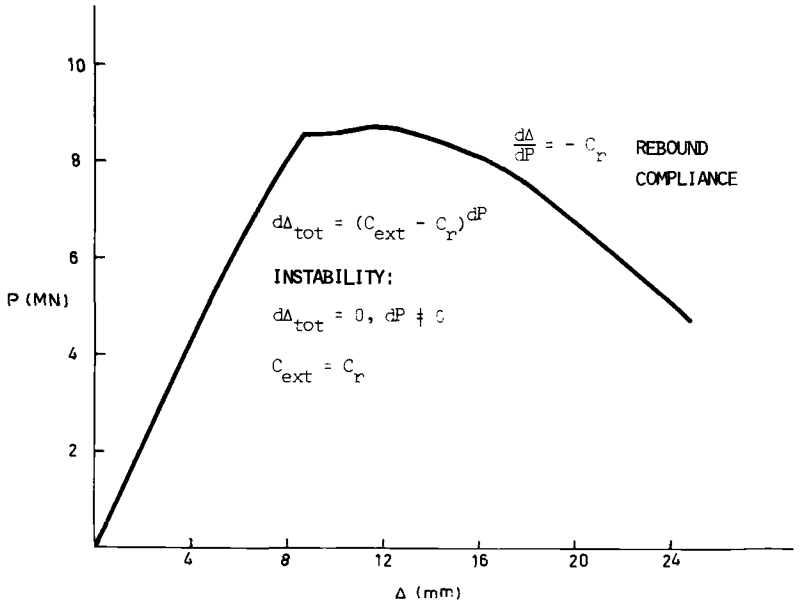

FIG. 2—*A* P-Δ *curve for a CC panel.*

If the specimen is connected in series with an external spring with compliance C_{ext} as in Fig. 1*b*, one has from Eqs 1 and 2

$$d\Delta_{tot} = (C_{ext} - C_r)dP = -C_m dP \tag{3}$$

where $C_m = -C_{ext} + C_r$ is the measured rebound "compliance" in the test with spring. Instability occurs for $d\Delta_{tot} = 0$, $dP \neq 0$, that is

$$C_{ext} \geq C_r = -\frac{d\Delta}{dP} \tag{4}$$

This relation is well known from literature on the common tension test [*4*]. In ductile rate-independent materials with extensive stable crack growth, the preceding relations are valid also during the unstable phase of crack elongation if this is slow enough so that inertia effects may be neglected. This means that the $P - \Delta$ relation is the same for a specific specimen type in a stable test under perfect displacement control ($C_{ext} = 0$) and in an unstable test under combined load-displacement control ($C_{ext} \neq 0$). Under the unstable phase of crack growth the specimen displacement (elongation), Eq 2, is compensated for by the displacement (shortening) of the spring, $C_{ext}\, dP$, so that in Eq 1, Δ_{tot} = constant.

This is demonstrated in Fig. 1, where results of measurements on a test setup with a bend specimen and a spring in series with the specimen are shown. The figure shows load versus total displacement Δ_{tot} and load versus specimen displacement Δ for an unstable test [$C_{ext} > -(d\Delta/dP)$]. It also shows a stable test ($C_{ext} = 0$) of an identical specimen under displacement control.

A conclusion to be drawn from the foregoing discussion is that the result of tests on identical specimens in series with springs of different compliance is predictable from Eq 4 as it concerns the slope of the descending part of the load-displacement curve and possible instability. Sufficient information for such a prediction is obtained from one test with displacement control or with known spring loading. No recourse has to be made to fracture mechanics parameters.

Reanalyzing the records given in Ref *1* for bend specimens in series with springs of different compliance, one finds the value of C_{ext} and C_m given in Table 1 (specimens with $a/W \approx 0.51$). Using Eq 3, C_r is then computed and the results in Table 1 obtained. For all unstable tests reported, $C_{ext} > 7 \cdot 10^{-4}$, and for all stable tests reported, $C_{ext} < 5.4 \cdot 10^{-4}$. This confirms the instability condition, Eq 4, as does several tests of our own on different specimen geometries.

Relating T-Modulus to Descending Portion of Load-Displacement Curves

From a fracture mechanical point of view it is interesting to transfer fracture-controlling parameters from one specimen geometry to another or to structures. The possibility to do this is referred to as the geometry independence of the parameter.

The T-modulus has been proposed by Paris to be such a parameter for stable crack growth and for instability [*5*]. The T-concept has since been extensively investigated theoretically and experimentally [*6, 7*]. Several methods exist to determine the material property T_{mat} from experimental data.

Here, one comment will be made regarding the relation of T_{mat} to the load-displacement record of a test with stable crack growth.

Consider the J-integral and the load P in a test setup according to Fig. 1 as a function of crack length and specimen displacement Δ.

TABLE 1—*Bend specimen values.*

Test	C_m, mm/N	C_{ext}, mm/N	C_r, mm/N	Stable/Unstable
A2	4.13×10^{-4}	1.90×10^{-4}	6.03×10^{-4}	stable
B2	1.97×10^{-4}	4.37×10^{-4}	6.34×10^{-4}	stable
B4	0.8×10^{-4}	5.39×10^{-4}	6.10×10^{-4}	stable

The variations of J and P are

$$dJ = \frac{\partial J}{\partial a}\bigg|_{\Delta} da + \frac{\partial J}{\partial \Delta}\bigg|_{a} d\Delta \tag{5}$$

$$dP = \frac{\partial P}{\partial a}\bigg|_{\Delta} da + \frac{\partial P}{\partial \Delta}\bigg|_{a} d\Delta \tag{6}$$

The tearing modulus of the material is by definition, and from Eqs 5 and 6

$$T_{\text{mat}} = \frac{E}{\sigma_0^2}\frac{dJ}{da} = \frac{E}{\sigma_0^2}\left\{\frac{\partial J}{\partial a}\bigg|_{\Delta} - \frac{\partial J}{\partial \Delta}\bigg|_{a} \frac{\dfrac{\partial P}{\partial a}\bigg|_{\Delta}}{-\dfrac{dP}{d\Delta} + \dfrac{\partial P}{\partial \Delta}\bigg|_{a}}\right\} \tag{7}$$

The applied tearing modulus is obtained from Eqs 1, 5, and 6 and the condition $d\Delta_{\text{tot}} = 0$

$$T_{\text{appl}} = \frac{E}{\sigma_0^2}\frac{\partial J}{\partial a}\bigg|_{\Delta \text{tot}} = \frac{\mathrm{E}}{\sigma_0^2}\left\{\frac{\partial J}{\partial a}\bigg|_{\Delta} - \frac{\partial J}{\partial \Delta}\bigg|_{a} \frac{\dfrac{\partial P}{\partial a}\bigg|_{\Delta}}{\dfrac{1}{C_{\text{ext}}} + \dfrac{\partial P}{\partial \Delta}\bigg|_{a}}\right\} \tag{8}$$

Comparing Eqs 7 and 8, it is seen that the general mechanical instability condition Eq 4 is equivalent to the instability condition

$$T_{\text{appl}} \geq T_{\text{mat}} \tag{9}$$

T_{appl} may also be determined from the variation of J due to a virtual crack elongation at constant Δ_{tot}. Therefore in the derivation of T_{appl} it is formally preferable to write Eqs 5 and 6 in variational form, for example

$$\delta J = \frac{\partial J}{\partial a}\delta a = \left(\frac{\partial J}{\partial a}\bigg|_{\Delta} + \frac{\partial J}{\partial \Delta}\bigg|_{a}\frac{d\Delta}{da}\right)\delta a \tag{10}$$

The expression in Eq 8 for T_{appl} is obtained also in this case.

Condition Eq 4 is not geometry independent whereas the condition Eq 9 is expected to be that under certain conditions [*8*].

Results of experimental studies of this geometry independence are reported later.

Going back again to Eqs 7 and 8, one can conclude that T_{mat} can be deter-

mined from the rebound compliance, $C_r = -\mathrm{d}\Delta/dP$, of a stable tearing test by putting $C_{ext} = C_r = -d\Delta/dP$ in the explicit formula for T_{appl} derived from Eq 8 for the actual specimen geometry.

This method for determination of T_{mat} is applied in the following to different specimen geometries and different steels.

Experimental Work—Materials

In the experimental part of this investigation, three Swedish structural steels were used; OX 540, which is a pressure vessel steel; OX 802, an extra-high-strength quenched-and-tempered pressure vessel steel; and OX 812, an extra-high-strength quenched-and-tempered structural steel. The composition and conventional material properties of these steels are given in Tables 2 and 3. The values given for J_{Ic} and T in Table 3 are determined by the recommended conventional technique [*9,10*].

Determination of T_{appl} at Instability from Rebound Compliance: Compact Tension and Bend Specimens

As discussed earlier, the T-modulus for a specimen can be evaluated from a displacement-controlled test measuring the rebound "compliance," that is, $C_r = -d\Delta/dP$, and inserting it in the appropriate expression for T_{appl}.

TABLE 2—*Composition of experimental steels.*

Steel	C	Si	Mn	P	S	Mo	B
OX 540	<0.20	0.15 to 0.5	<1.8	0.035	<0.035	...	...
[a]OX 802	0.12	0.37	1.34	0.013	0.007	0.64	...
OX 812	<0.16	0.15 to 0.70	<1.5	<0.202	...	...	<0.005
	Cu	Al	Nb	V	N		
OX 540	...	>0.02	<0.05	...	<0.009		
[a]OX 802	0.08	0.040	0.035	0.003	...		
OX 812	...	...	...	...	...		

[a] Actual values.

TABLE 3—*Mechanical properties.*

Material	σ_y, MPa	σ_u, MPa	σ_0, MPa	J_{Ic}, KN/m	T_m
OX 540	375	600	475	250	400
OX 802	800	836	800	200	10 to 20
OX 812	750	860	800	200	170

Several such expressions exist. For three-point bend specimens, Paris and Hutchinson [8] give

$$T_{appl} = \frac{4P^2E}{\sigma_0^2 b^2 B}\left\{\frac{C}{1 + C\dfrac{\partial P}{\partial \Delta_c}\Big|_a}\right\} - \frac{JE}{\sigma_0^2 b} \qquad \text{(3PB)} \qquad (11)$$

where σ_0 is the flow stress and C the external and elastic specimen (no crack) compliance C_{nc}. The values used for σ_0 in this paper are given in Table 3. The thickness of the specimen is B and the ligament b. Further, Δ_c is the displacement due to the crack. Equation 11 can be simplified by assuming $(\partial P/\partial \Delta)_a = 0$, which is expected to be a good approximation at limit load.

Further approximations are to put P = limit load and to assume the ideal plastic value of J.

This leads to

$$T_{appl} = \frac{8b^2EB}{L^2}C - \frac{\Delta_c E}{W\sigma_0} \qquad \text{(3PB)} \qquad (12)$$

where L is the length between supports and W the width (height) of the specimen.

To evaluate T_{appl} from the preceding relations, b has to be measured or estimated. This was done using the key curve method [11]. A P-Δ relation for constant crack length was obtained from a specimen with a blunt notch and ligament b_0. A power-law expression

$$\frac{PW}{b_0^2} = k\left(\frac{\Delta_{pl}}{W}\right)^n \qquad (13)$$

was fitted to the P-Δ_{pl} curve by appropriate choice of k and n.

In specimens with extending cracks, the current crack length was calculated from Eq 13

$$b = \left(\frac{P \cdot W^{n+1}}{k\,\Delta_{pl}{}^n}\right)^{1/2} \qquad (14)$$

The accuracy was found to be as good as for other existing methods for crack length measurement.

Another advantage of this method is that

$$\frac{\partial P}{\partial \Delta_{pl}}\Big|_a = \frac{nP}{\Delta_{pl}} \qquad (15)$$

can be directly estimated from the blunt-notch test. This quantity together with $(\partial P/\partial \Delta_{el})_a$, enters Eq 11.

Estimations of T using this procedure and Eqs 11 and 12 are shown in Figs. 4, 5, and 6 for OX 812 (Specimens $W = 40$ mm and $B = 20$ mm). The figures also show the scatterband of the conventionally determined T_{mat} (Table 3 and Fig. 3). Figure 4 refers to Eq 11, Fig. 5 to Eq 11 with $(\partial P/\partial \Delta)_a = 0$, and Fig. 6 to Eq 12. In Eq 11 (Figs. 4 and 5) a C varying with Δ was used. This variation was described by fitting a fifth-degree polynomial to the descending portion of the P-Δ curve and adding the elastic specimen compliance C_{nc}. Thus $C = C(\Delta) = C_r(\Delta) + C_{nc}$.

In Eq 12, C is put equal to a constant value C_0 taken from the final linear

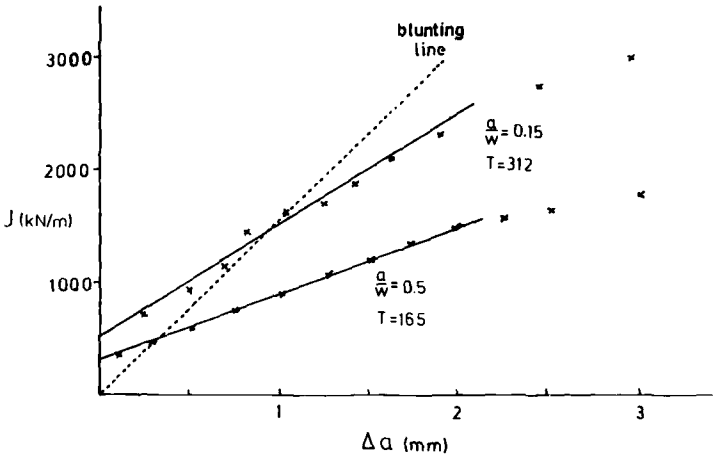

FIG. 3—*Conventionally determined* J *versus* Δa *curves for OX 812.*

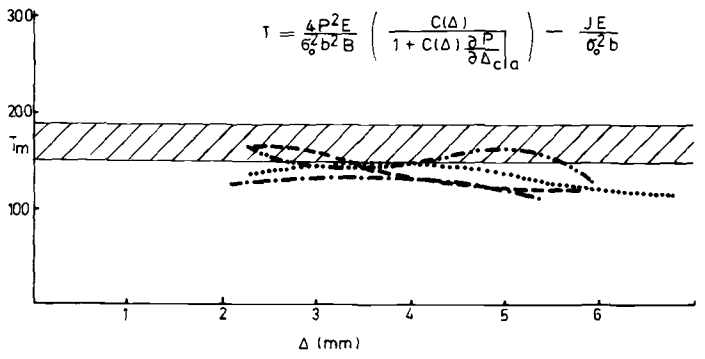

FIG. 4—T_{appl} *at instability for four bend specimens of OX 812, using Eq 11.*

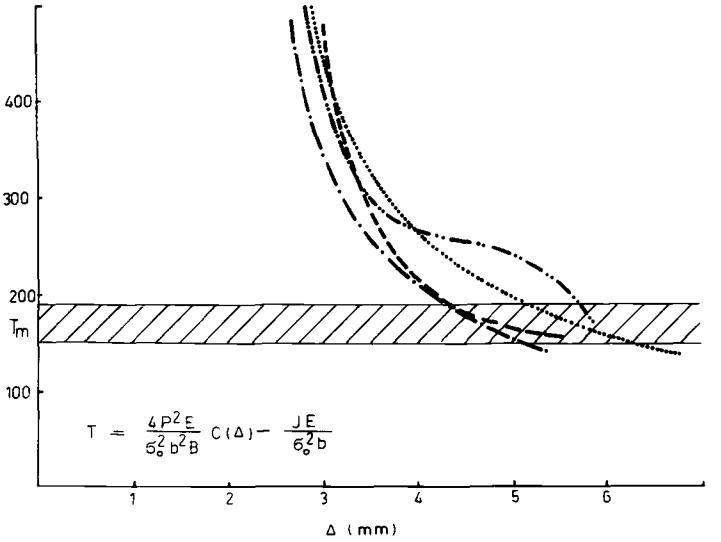

FIG. 5—T_{appl} *at instability for four bend specimens of OX 812, using Eq 11 and* $(\partial P/\partial \Delta_c)_a = 0$.

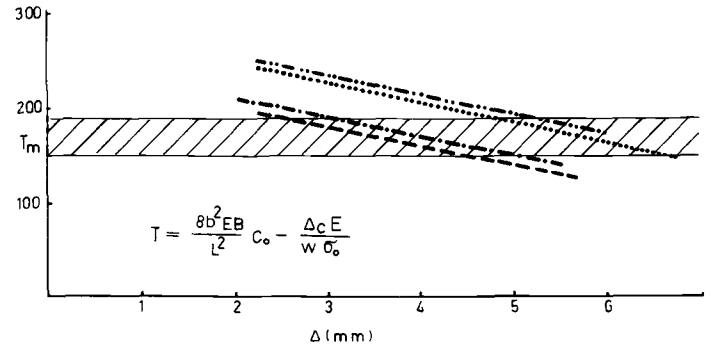

FIG. 6—Γ_{appl} *at instability for four bend specimen of OX 812, using Eq 12 and constant value for* C.

part of the descending P-Δ curve and adding the elastic specimen compliance C_{nc}. Thus $C_0 = C_r + C_{nc}$ with C_r = constant.

The similar approach by Turner [2, 7] using the η-factor was also applied. The corresponding expression for T_{appl} is

$$T_{appl} = 2.12\pi F_1^2 x(1-x)^3\left(\frac{9}{4}\eta_{pl} + \frac{9}{2}\frac{\eta_{pl}}{\eta_{el}}(\eta_{pl} - \eta_{el})\right) \qquad \text{(3PB)} \quad (16)$$

where

$$\eta_{el} = \frac{b}{C}\frac{dC}{da} \qquad \eta_{pl} = 2$$

$$x = \frac{a}{W} \qquad a = W - b$$

$$K_I = \sigma\sqrt{\pi a}F_1 \quad \text{defines } F_1$$

Using the variable value for C and Eq 16, the curves in Fig. 7 were obtained. Figures 4 through 7 refer to four different test specimens of OX 812.

A conclusion is that the proposed method of determination of T_{appl} at instability gives values in good agreement with T_{mat} conventionally determined. This is especially true when Eq 11 is used, Fig. 4. The deviations at lower displacements in Figs. 5–7 are due to the approximations in the corresponding expressions for T_{appl}. The true value of T_{mat} is reached asymptotically at large Δ in Figs. 5–7. Further, one can conclude that Eqs 12 and 16 are almost equivalent.

A corresponding evaluation was made using CT specimens. The relation corresponding to Eq 12 as regards the degree of approximation then reads (Appendix I)

$$T_{appl} = 2.12\,EB\left(1 - \frac{\sqrt{2}x}{\sqrt{1+x^2}}\right)^2 C - 2.06\,\frac{E\Delta_{pl}}{\sigma_0 W(1+x^2)^{3/2}} \qquad (17)$$

The η-factor approach leads to (Appendix II)

$$T_{appl} = 2.12\,\alpha^2 F_1{}^2 x(1-x)\eta_{pl}\left(\frac{2\eta_{pl}}{\eta_{el}} - 1\right) \qquad (18)$$

where

$$\eta_{pl} = 2\frac{1+\alpha}{1+\alpha^2}, \qquad \alpha = \left[4\left(\frac{a}{b}\right)^2 + 4\left(\frac{a}{b}\right) + 2\right]^{1/2} - \left(2\frac{a}{b} + 1\right)$$

Five 20-mm-thick specimens of OX 812 were tested and evaluated using Eqs 17 and 18 and the same procedure as for the bend specimens. Figures 8 and 9 shows the results obtained using Eq 17 with C variable and constant, respectively. Figure 10 shows the result obtained using Eq 18.

The conclusion to be drawn is the same as for the bend specimens. The difference between small and large CT specimens is partly due to difference in elastic displacement and partly to the prescence of more shear lips in the large specimens. The agreement between T determined from 3PB and CT specimen data is good, as expected.

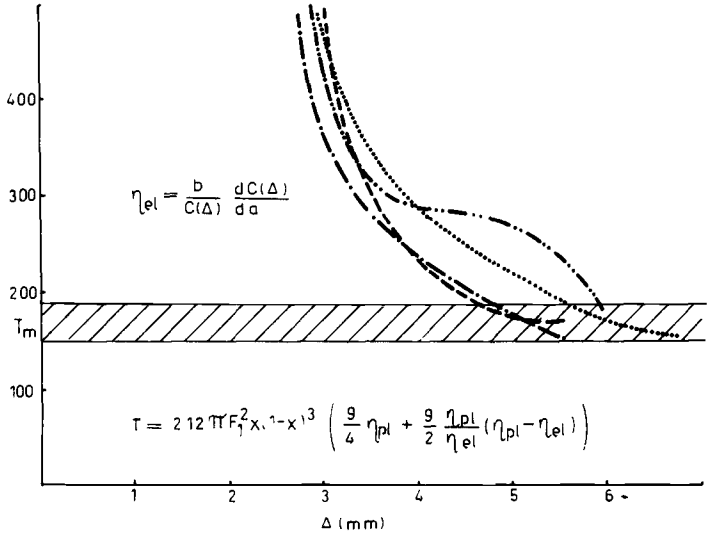

FIG. 7—T_{appl} *at instability for four bend specimen of OX 812, using Eq 16.*

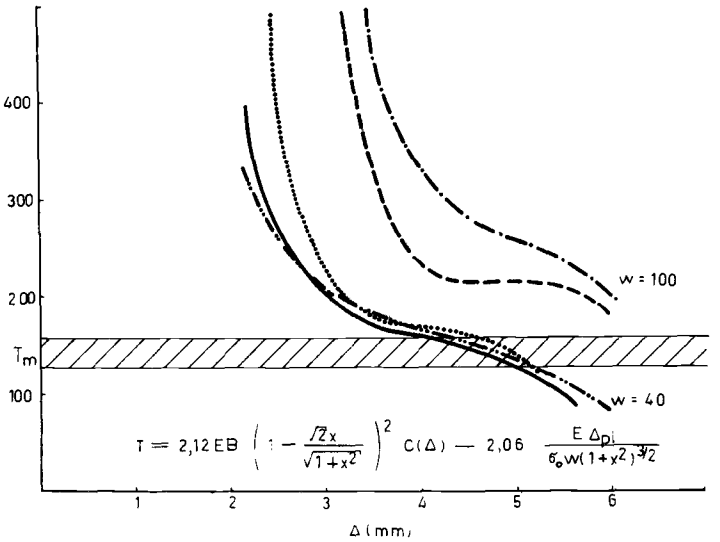

FIG. 8—T_{appl} *at instability for five CT specimens of OX 812, using Eq 17.*

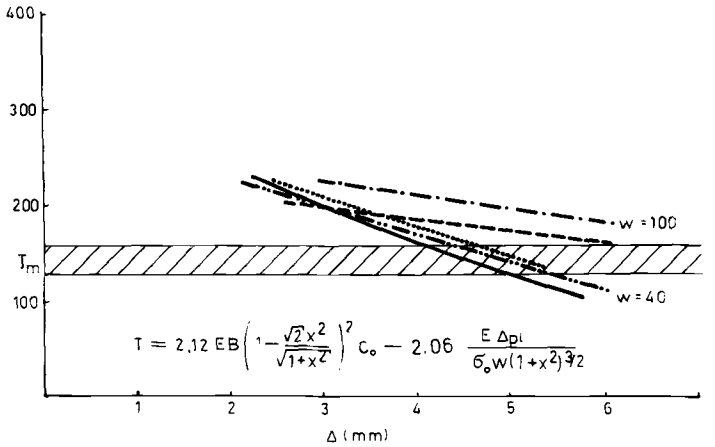

FIG. 9—T_{appl} *at instability for five CT specimens of OX 812, using Eq 17 and constant value for* C.

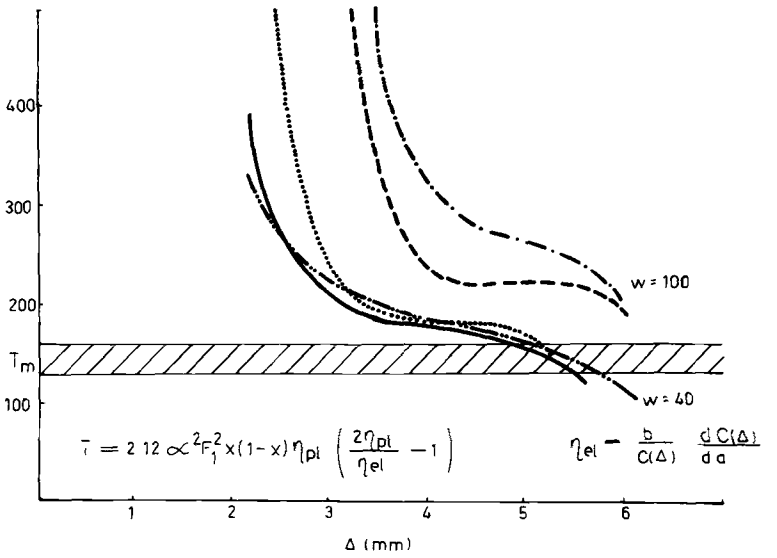

FIG. 10—T_{appl} *at instability for five CT specimens of OX 812, using Eq 18.*

Geometry Independence of T

In order to study the geometry independence of T, test records from earlier J_{Ic}-measurements on double edge-cracked and center-cracked panels were used. To evaluate T_{appl} the rebound "compliance" of these records was mea-

sured. No records of crack extension were available. Therefore, only the limit load expression for T could be used. It has in plane stress the form [5]

$$T_{appl} = 2ABEC \tag{19}$$

and does not include crack length. Here $A = 1$ for center-cracked (CC) panels and $4/3$ for double-edge-cracked (DEC) panels, and $C = C_{el} = L/WBE$. In this case $C = C_r + C_{el}$ was used with C_r being the rebound compliance as in previous cases.

The panels were 20 mm thick of dimensions 900 by 1000 mm with cracks of lengths $2a = 350$ to 500 mm. The material was OX 802, which is similar to OX 812. However, it has a much lower T_{mat}-value. A typical load-displacement curve is shown in Fig. 2. In these tests, contrary to other tests in this paper, Δ is measured on the loading piston head. It therefore includes the displacement of a part of the test machine. This is the reason for the large Δ in the P-Δ record and has been accounted for in the evaluation of C. The result of the evaluation for six tests is shown in Fig. 11. The actual rebound compliance $C_r = C_r(\Delta)$ is used in Eq 19. As can be seen, a constant level of T_{appl} with rather low specimen scatter is reached at large displacements.

To study geometry independence, CT specimens of the same material were tested. For these, T_{appl} was evaluated using Eq 17, and T_{mat} using an EPRI estimation scheme. Results are given in Fig. 12. As discussed in the preceeding paragraph, the asymptotically reached value of T_{appl} at large Δ is of in-

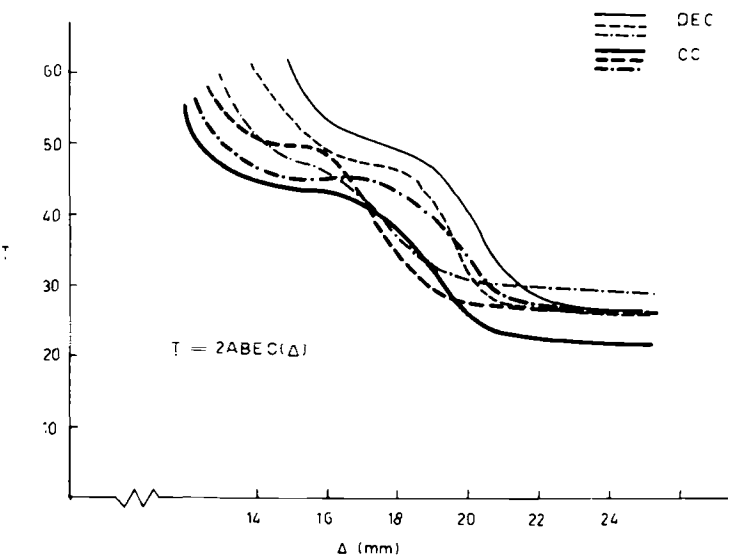

FIG. 11—T_{appl} *at instability for three CC and three DEC panels of OX 802, using Eq 19.*

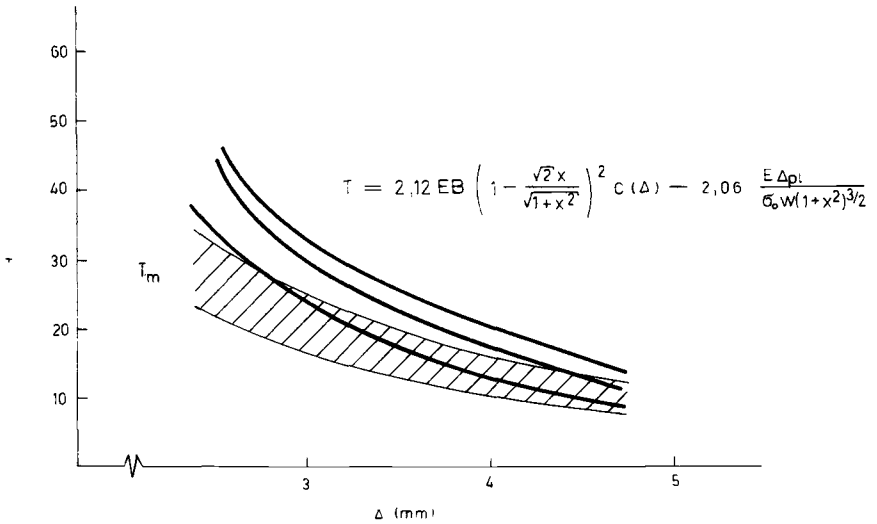

FIG. 12—T_{appl} *at instability for three CT specimens of OX 802, using Eq 17 and* T_{mat} *determined by an EPRI estimation scheme.*

terest. As can be seen, this value for the CT specimens is about half of that for the CC and DEC specimens. This is in agreement with the general conception that the bending-type specimens give a lower bound for T_{mat}.

OX 812: Short Cracks in Bending

The expressions for J and T for bending are derived under the condition that the crack is deep enough to ascertain a J-dominated field. They also require that the bending moment can be separated in one part which depends only on crack length and one which is a function of rotation only, $M = b^2 f(\theta)$.

In Fig. 13 (OX 812) it is seen that the latter condition is satisfied at least down to $a/W = 0.15$. Still, T seems to be dependent on initial crack length for a/W around 0.15, perhaps because the J-dominance is lost.

In Fig. 3 the material J-R curve is shown for a long $[(a_0/W) \approx 0.5]$ crack and a relatively short $[(a_0/W) \approx 0.15]$ crack. The slope of the latter is almost twice that of the former, giving a doubling of T_{mat}. This seems to be, if not consistent, at least nice and conservative, but if one looks at the T_{appl} at instability using Eq 11, the picture is somewhat different, Fig. 14. T for the long cracks is, as already seen in Fig. 4, approximately constant for a wide range of plastic deformation.

For the short cracks, however, $T_{appl} \approx T_{mat}$ at maximum load, but then T_{appl} decreases drastically with deflection. This means that the increase in T_{mat} for shorter cracks predicts the increase in plastic deflection at maximum

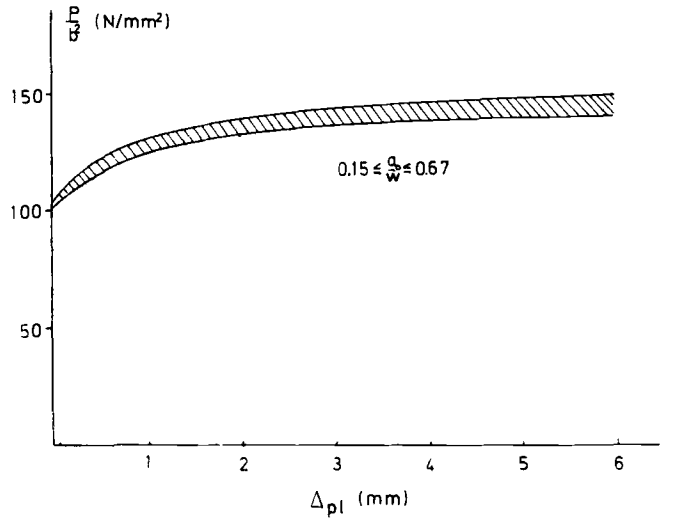

FIG. 13—P/b^2 *(actual ligament length) versus plastic deflection for ten bend specimens of OX 812.*

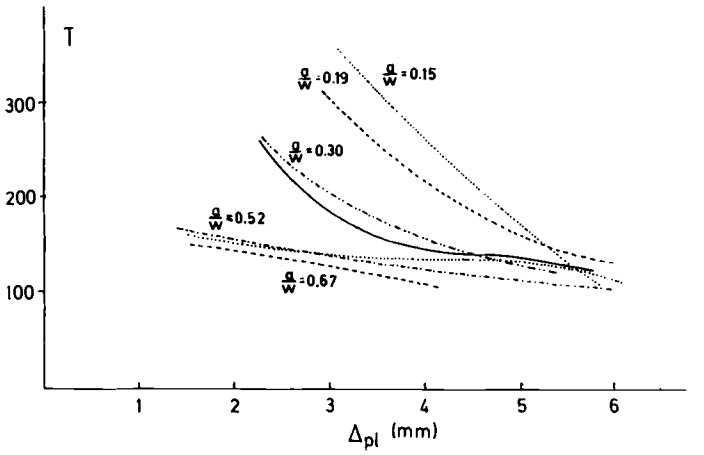

FIG. 14—T_{appl} *at instability for seven bend specimens of OX 812, using the "exact" Eq 11.*

load, but it does not necessarily give conservative estimations of the external compliance needed to create instability.

This is not an invalidation of the T-theory since the conditions for J-controlled crack growth perhaps are not fulfilled; however, it is a warning not to always interpret an increase in T_{mat} as a conservative result when going outside these conditions.

Application to Dead-Load Conditions

One of the materials tested, OX 540, had a very high T-modulus (~ 400) and a rising P-Δ curve up to substantial crack extension ($\Delta a \approx 0.05b$) and was stable even under dead-load conditions almost as long as the T-concept is considered being applicable. For this reason it was not meaningful to use limit load expressions for T-evaluation.

Applications of the EPRI "crack driving force" diagram [3] shows that stability prevails under dead-load conditions for a 3PB specimen test of this material, Fig. 15.

Dead-load conditions are equivalent to $C_{ext} = \infty$ in Fig. 1. If this value is inserted in Eq 11 together with $(dP/d\Delta)_a$ from a blunt-notch specimen as discussed earlier, T_{appl} increases with Δ according to Fig. 16. T_{appl} reaches T_{mat} at $\Delta \approx 4.25$ mm. This value agrees excellently with the deflection at maximum load in the test. The T-modulus can thus be used to predict instability also under load control.

EPRI Estimation Scheme

The results for OX 540 and OX 812 just given were verified using the EPRI crack driving force diagram for instability analysis. The material is there described by a Ramberg-Osgood power hardening law. The fully plastic conditions are given by [3]

$$\frac{\epsilon}{\epsilon_0} = \alpha\left(\frac{\sigma}{\sigma_0}\right)^n \tag{20}$$

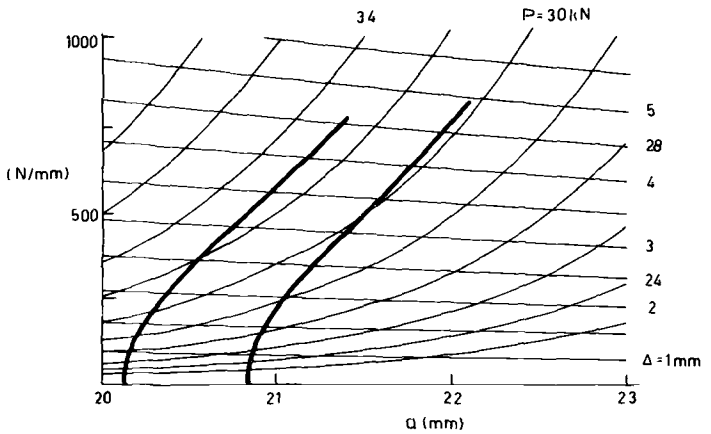

FIG. 15—*Crack-driving force diagram for two bend specimens of OX 540.*

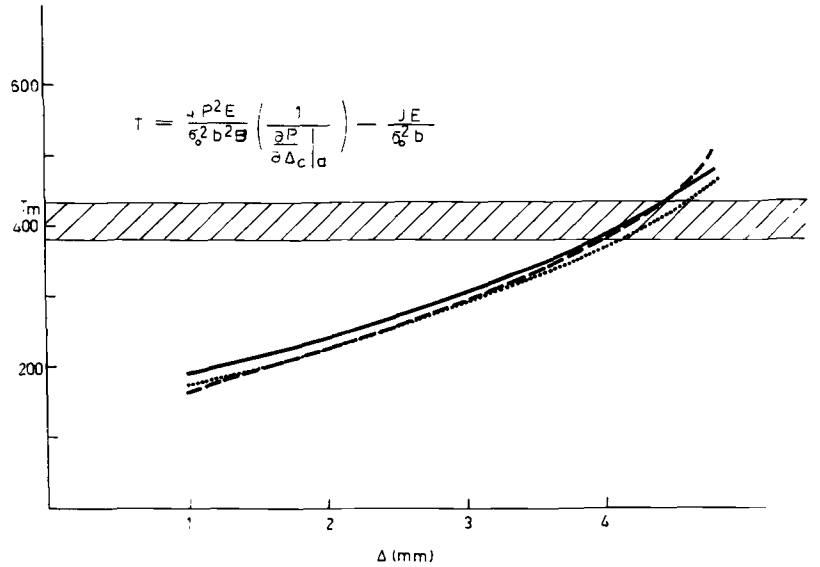

FIG. 16—T_{appl} *under dead-load conditions for three bend specimens of OX 540.*

$$J_{pl} = \alpha\sigma_0\epsilon_0 b h_1 \left(\frac{P}{P_0}\right)^{n+1} \tag{21}$$

$$\Delta_{pl} = \alpha\epsilon_0 a h_3 \left(\frac{P}{P_0}\right)^{n} \tag{22}$$

Here h_1 and h_3 are tabulated functions of n and (a/W) given for different geometries.

To the foregoing solution one can add the linear elastic solution as given, for example, in Ref *12*. Introducing a spring with compliance C_{ext} in series with the specimen, the total displacement is

$$\Delta_{tot} = \alpha\epsilon_0 a h_3 \left(\frac{P}{P_0}\right)^{n} + \frac{PF_3}{E} + C_{ext}P \tag{23}$$

where F_3 is to be taken from Ref 12. Plotting J for controlled total displacement, the crack driving force diagrams in Figs. 17 and 18 are obtained for some of the bend- and CT-specimens analyzed in Figs. 6 and 9. The C_{ext} used is equal to C_0 measured from the respective P-Δ curve.

In Figs. 17 and 18 the J-Δa curves of the tests are also plotted. These are taken from conventional T-modulus determinations [*9*]. As can be seen, the

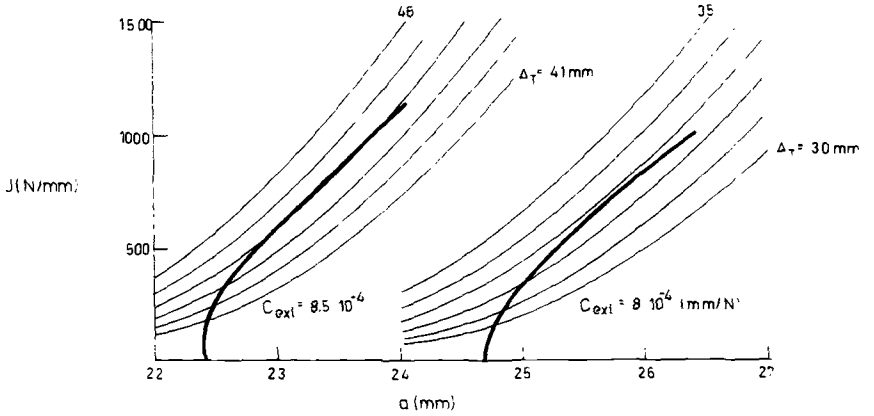

FIG. 17—*Crack-driving force diagram for two bend specimens of OX 812 in series with springs,* $C_{ext} = C_T$ *from Fig. 6.*

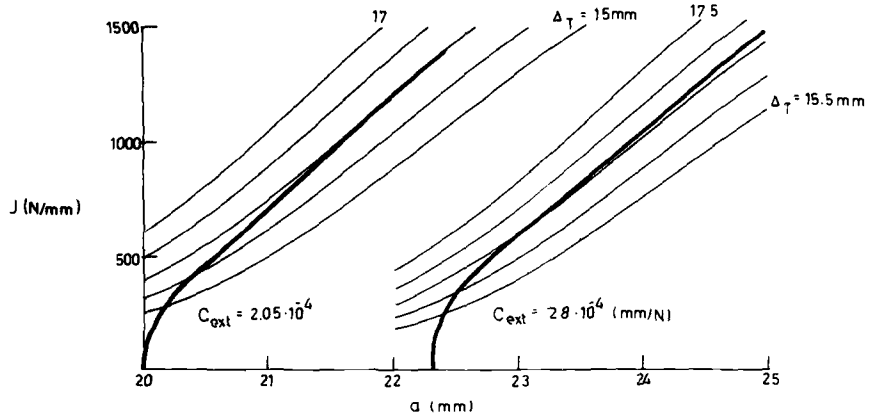

FIG. 18—*Crack-driving force diagram for two CT specimens of OX 812 in series with springs,* $C_{ext} = C_T$ *from Fig. 9.*

crack driving force curves and the J-Δa curves are parallel over a large range of crack extension, as they should be.

Discussion

The proposed method using the rebound compliance to determine T_{appl} at instability and thus also T_{mat} has proved to give reliable results compared with conventional methods. It does not require independent crack length measurements but allows all necessary information to be extracted from a

few simple tests. In the present study the method has been applied to materials with high tearing modulus but should be possible to use on less tough materials.

For the materials studied the T-modulus is constant over a very large range of crack elongation exceeding the generally accepted limits of validity of the T-concept.

The geometry dependence of T observed between CC- and DEC-panels on one hand and bend-type specimens on the other is to be expected. The fact that the bend-type specimens define a lower bound for T_{mat} gives confidence in applications of the T-concept to problems of crack growth instability.

At the same time it motivates questioning the use of the T-concept and the evidently equivalent η-factor concept compared with other simpler procedures of instability analysis.

One such more-direct procedure would be to use the rebound compliance of a cracked specimen or component test to determine the allowable compliance of the elastic part of a larger structure containing an identical nonlinear component. This of course requires that the part of the structure which qualitatively and quantitatively governs the plastic deformation at the crack can be identified and also is small enough to be tested.

This method of instability analysis proved to work in the present study for the limited number of simple cases where it was applied.

At the presentation of this paper at the Philadelphia symposium it came to our attention that Ernst et al [*14*] earlier had pointed out that the T-modulus instability criterion is equivalent to a simpler instability criterion, Eq 4. We were not aware of this work, which was not published by the time of the 1981 symposium.

Acknowledgment

The authors wish to thank Mr. Hans Öberg for sharing his profound knowledge of the laboratory and for valuable discussion. The support of the Swedish Board for Technical Development, Project 80-3850, is also gratefully acknowledged.

APPENDIX I

The limit load conditions for a CT specimen can be expressed as

$$P_L = 1.455\,\sigma_0\,\alpha b B = 1.455\,\sigma_0 B[\sqrt{2(w^2 + a^2)} - (w + a)]$$

$$J_{pl} = -\frac{\Delta_{pl}}{B}\frac{\partial P_L}{\partial a} = 1.455\,\sigma_0\Delta_{pl}\left(1 - \frac{\sqrt{2}a}{\sqrt{w^2 + a^2}}\right)$$

$$\frac{dJ}{da} = 1.455\,\sigma_0\left(1 - \frac{\sqrt{2}\,a}{\sqrt{w^2 + a^2}}\right)\frac{d\Delta_{pl}}{da} - 1.455\,\sigma_0\Delta_{pl}\frac{\sqrt{2}w^2}{(w^2 + a^2)^{1.5}}$$

At instability

$$d\Delta_{pl} + d\Delta_{el} + d\Delta_{ext} = 0 \qquad d\Delta_{pl} = -C\,dP_L$$

(if $C = C_{el} + C_{ext}$ and $P_L\,dC_{el}$ is small).

$$\frac{d\Delta_{pl}}{da} = -C\frac{dP_L}{da} = C\,1.455\,\sigma_0 B\left(1 - \frac{\sqrt{2}a}{\sqrt{w^2 + a^2}}\right) \qquad \left(x = \frac{a}{w}\right)$$

$$\frac{dJ}{da} = 1.455^2\,\sigma_0{}^2 B\left(1 - \frac{\sqrt{2}a}{\sqrt{w^2 + a^2}}\right)^2 C - 1.455\,\sigma_0\Delta_{pl}\frac{\sqrt{2}w}{(w^2 + a^2)^{1.5}}$$

$$T = \frac{E}{\sigma_0{}^2}\frac{dJ}{da} = 2.117\,EB\left(1 - \frac{\sqrt{2}\,x}{\sqrt{1 + x^2}}\right)^2 C - 2.058\frac{E\Delta_{pl}}{\sigma_0 w(1 + x^2)^{1.5}}$$

APPENDIX II

Following Turner in Ref 2, one gets:

$$I = G - \frac{\Delta_{el}}{B}\left(1 - \frac{\eta_{el}}{\eta_{pl}}\right)\frac{\partial P_L}{\partial a} \qquad \text{(elastic energy release)}$$

$$I \geq \frac{b}{\eta_{pl}}\left(\frac{dJ}{da}\right)_R \qquad \text{(instability criteria)}$$

$$P_L = 1.455\,b\sigma_0\alpha B \qquad \text{(CT specimen)}$$

$$\frac{\partial P_L}{\partial a} = -\eta_{pl}\frac{P_L}{b} \qquad \Delta_{el} = CP_L \qquad (C = C_{el} + C_{ext})$$

$$\Rightarrow \frac{\eta_{pl}}{b}G + \eta_{pl}\frac{P_L}{Bb^2}(\eta_{pl} - \eta_{el})C \geq \frac{dJ}{da}$$

$$\left\{G = \frac{K_I{}^2}{E}\eta_{el} = \frac{b}{C}\frac{dC}{da} = \frac{b}{C}\frac{2B(K_I/P)^2}{E} = \frac{b2aF_1{}^2}{CBw^2E}\right\}$$

$$2.117\alpha^2 F_1{}^2 x(1-x)\eta_{pl}\left[\frac{2\eta_{pl}}{\eta_{el}} - 1\right] \geq \frac{E}{\sigma_0{}^2}\frac{dJ}{da} = T_{mat}$$

$$\eta_{pl} = 2\frac{1+\alpha}{1+\alpha^2}, \qquad \alpha = \sqrt{4\left(\frac{a}{b}\right)^2 + 4\frac{a}{b} + 2} - \left(2\frac{a}{b} + 1\right)$$

F_1 is the linear elastic fracture mechanics shape function from Ref *12*.

References

[1] Paris, P., Tada, H., Ernst, H., and Zahoor, A. in *Elastic-Plastic Fracture, ASTM STP 668* J. D. Landes, J. A. Begley, and G. A. Clarke, Eds., American Society for Testing and Materials, 1979, pp. 251-265.

[2] Turner, C. E. in *Advances in Elastic-Plastic Fracture*, L. H. Larsson, Ed., Applied Science Publishers, London 1979, pp. 139-164.

[3] Shih, C. F., Kumar, V., and German, M. D., "Estimation Technique for the Prediction of Elastic-Plastic Fracture of Structural Components of Nuclear Systems, Third Semiannual Report, General Electric Co., Schenectady, N.Y., 1980.

[4] McClintock, F. and Argon, A., *Mechanical Behaviour of Materials*, Addison-Wesley, Reading, Mass., 1966.

[5] Paris, P., Tada, H., Zahoor, A., and Ernst, H. in *Elastic-Plastic Fracture, ASTM STP 668*, J. D. Landes, J. A. Begley, and G. A. Clarke, Eds., American Society for Testing and Materials, 1979, pp. 5-36.

[6] *Elastic-Plastic Fracture, ASTM STP 668*, J. D. Landes, J. A. Begley, and G. A. Clarke, Eds., American Society for Testing and Materials, 1979.

[7] *Fracture Mechanics, ASTM STP 667*, C. W. Smith, Ed., American Society for Testing and Materials, 1979.

[8] Hutchinson, J. W. and Paris, P. C. in *Elastic-Plastic Fracture, ASTM STP 668*, J. D. Landes, J. A. Begley, and G. A. Clarke, Eds., American Society for Testing and Materials, 1979, pp. 37-64.

[9] Carlsson, J., Kaiser, S., Markström, K., Wüthrich, C., and Öberg, H. in *Advances in Fracture Research*, D. Francois, Ed., Pergamon Press, Oxford, U.K., 1980, p. 863.

[10] Carlsson, J. and Markström, K. in *Fracture 1977*, Fourth International Conference on Fracture, Waterloo, Ont., Canada, Vol. 1, 1977.

[11] Joyce, J. A., Ernst, H., and Paris, P. C. in *Fracture Mechanics, ASTM STP 700*, American Society for Testing and Materials, 1979, pp. 222-236.

[12] Tada, H., Paris, P. C., and Irwin, G., *The Stress Analysis of Cracks Handbook*, Del Research Corp. Hellertown, Pa., 1973.

[13] Shih, C. F. and Hutchinson, J. W. in *Transactions*, American Society of Mechanical Engineers, *Journal of Engineering Materials and Technology*, Vol. 98, No 4, 1976, pp. 289-295.

[14] Ernst, H. A., Paris, P. C., and Landes, J. P. in *Fracture Mechanics, ASTM STP 743*, Richard Roberts, Ed., American Society for Testing and Materials, 1981, pp. 476-502.

Cedric E. Turner[1]

Further Developments of a *J*-Based Design Curve and Its Relationship to Other Procedures

REFERENCE: Turner, C. E., **"Further Developments of a *J*-Based Design Curve and Its Relationship to Other Procedures,"** *Elastic-Plastic Fracture: Second Symposium, Volume II—Fracture Resistance Curves and Engineering Applications, ASTM STP 803*, C. F. Shih and J. P. Gudas, Eds., American Society for Testing and Materials, 1983, pp. II-80–II-102.

ABSTRACT: The existing so-called *J*-design curve is based on shallow-notch data ($a/W \leq 0.1$) and in many other ways is in a less-developed form than the corresponding crack-opening displacement and R-6 procedures. A specific though simplified relationship between the three methods of assessment is pointed out and a modified *J*-estimation method is then proposed. The features of load or displacement control, shallow or deep notches, stress concentrations, and residual stresses are discussed and proposals made to encompass them within the revised procedure. The normalized *J*, $JE/Y^2\sigma_Y{}^2a$ is expressed as a function of an effective structural strain that depends upon notch depth. One equation is used to describe the load-controlled region of linear elastic fracture mechanics and contained yield, and another, the strain-controlled regime at or above ligament limit load.

KEY WORDS: fracture mechanics, *J*-contour integral, structural design, residual stresses, and strain concentration, elastic-plastic fracture

Methods for design against fracture can be briefly categorized into three degrees of complexity. The simplest is just avoidance of brittle fracture by selection of material, perhaps by the Charpy V or similar test. This should be coupled with avoidance of ductile fracture by design against plastic collapse, perhaps using limit analysis. A more complicated though still simple procedure is the use of a so-called "design curve" against fracture, typified by the (COD)[2] [*1*],[3] R-6 [*2*], and *J* [*3*] methods. The essence here is that brittle behavior is recognized as an interaction between material property and structural mechanics to be treated by linear elastic fracture mechanics (LEFM),

[1]Professor of materials in mechanical engineering, Imperial College, London, U.K.

[2]ASTM usage refers to the "crack-tip opening displacement" (CTOD), but the design method referenced [*1*] uses the U.K. terminology "crack opening displacement" (COD) throughout.

[3]The italic numbers in brackets refer to the list of references appended to this paper.

while ductile fracture, though less well agreed, is treated by elastic-plastic fracture mechanics (EPFM) analyses in terms of COD or J, with due regard to plastic collapse as an alternative mode of failure. Various procedures, such as the two-parameter, equivalent energy, and gross strain procedures (many of which are summarized in Ref *3*), offer alternative views of EPFM. A third level of complexity is offered by individual computations, in principle encompassing elastic-plastic behavior in three dimensions, though in practice often restricted to two dimensions. The extent to which such studies can be condensed into a predigested form remains to be seen [*4*].

A point not to be overlooked is that design against fracture and assessment of the significance of defects involve many aspects other than either selection of material or estimation of a fracture parameter. For some structures these further matters are codified—for example, the well-known American Society of Mechanical Engineers (ASME) rules for pressure vessels. In other areas the rules are less formalized and it is here that "design curves" are employed which embody both procedures for estimating the applied severity of fracture parameter and also proposals for treating the many other aspects of the whole problem—for example, the effects of defects other than cracks and choice of appropriate values of toughness. The procedure best developed and documented in this respect appears to be the COD method [*1*]. The R-6 documentation [*2*] is specific but less embracing and J literature is as yet poorly organized into a design methodology. The early history of the methods is described elsewhere [*3,5–7*].

The object of this paper is firstly to show the schematic relationship between COD, R-6, and J-"design curves" and then to make suggestions for the continued development of a simple J-based methodology for design and assessment problems. Only the J-estimation procedure is in question here. As already remarked, the embodiment of an estimation procedure into a design or assessment methodology is a much broader issue and it is supposed that supporting rules such as already embodied in the COD or R-6 documents would be developed.

Elastic-plastic methods other than COD, R-6, and J are dismissed rather summarily with the statement that the more they are developed, the nearer they are seen to be interpolations between LEFM and collapse, which in principle are encompassed by the three procedures, COD, R-6 and J [*8*]. There may of course be points of practice or correlation that warrant more attention than given here, but the theories as such do not seem to offer anything more embracing than J.

A Schematic Relationship Between COD, R-6, and J-Design Curves

The relationship between the estimation procedures currently used for COD, R-6, and J-design curves are examined schematically. The basic curves for all three methods are shown in Figs. 1*a*-1*c* and described by Eqs 1-3

Equations for COD (ferritic material):

$$\Phi = \delta/2\pi e_y \bar{a} = (e/e_y)^2 \quad \text{for } e/e_y \leq 0.5 \tag{1a}$$

$$= (e/e_y) - 0.25 \quad \text{for } e/e_y \geq 0.5 \tag{1b}$$

where

$e_y = \sigma_y/E$,
δ = COD,
$\bar{a}$ = equivalent crack that is acceptable in an infinite plate.

Equation for R-6

$$K/K_{Ic} = \{(8/\pi^2)(S_c/S)^2 \ell n \sec(\pi S/2S_c)\}^{-1/2} \tag{2}$$

where S is the load and S_c the *nominal* collapse load.

Equations for J:

$$J/G_y = (e/e_y)^2 \quad \text{for } e/e_y \leq 0.85 \tag{3a}$$

$$= 5\{(e/e_y) - 0.7\} \quad \text{for } 0.85 \leq e/e_y \leq 1.2 \tag{3b}$$

$$= 2.5\{(e/e_y) - 0.2\} \quad \text{for } e/e_y \geq 1.2 \tag{3c}$$

where

$G_y = Y^2\sigma_y{}^2 a/E$,
$K = Y\sigma\sqrt{\bar{a}}$, and
a = crack length.

It is not suggested that all features can be related rigorously. Nevertheless, a particular algebraic relationship is formulated since it allows certain major features to be highlighted.

The key point of the formulation is not, however, the algebraic form adopted here, but the assumption that the variables of geometry and degree of deformation are separable. This assumption will be reexamined later. For the present purpose it is convenient to observe that typical load-deformation relationships for components can be represented not unreasonably by an expression in the normalized form

$$q = Q_0 \phi \tan(Q/Q_0) \tag{4a}$$

where

Q = load,
q = displacement, and
ϕ = elastic compliance of the cracked body, that is, $\phi = dq/dQ$ as $Q \to 0$.

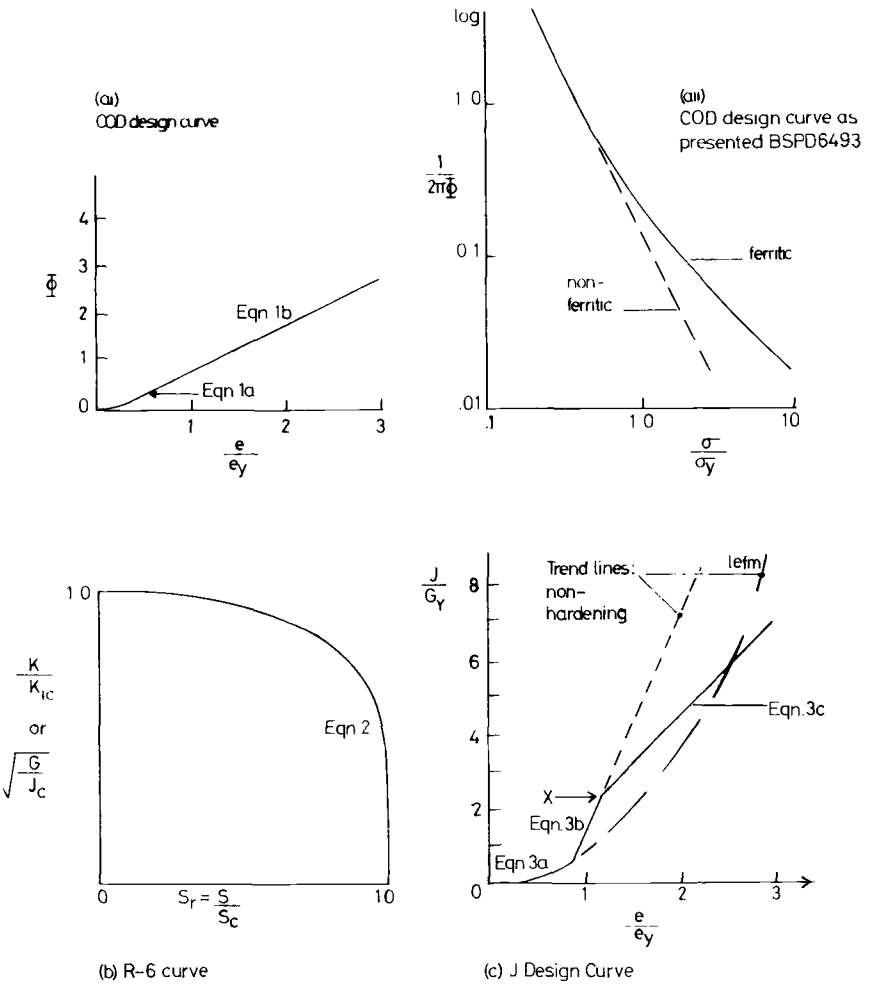

FIG. 1—Present so-called design curves: (a) COD, (b) R-6, (c) J. (see Eqs 1, 2, and 3 for definition of the diagrams).

It is supposed this expression can also be written

$$q = Q_0 \phi \tan(\pi\sigma/2f) \tag{4b}$$

thus implying

$$Q_0 = (Q/\sigma)(2f/\pi); \qquad q_0 = Q_0\phi \tag{5}$$

where σ is the usual stress in the uncracked body and f the maximum stress attainable. If f is a material property such as yield stress, then the separation

of variables is maintained, but the maximum load may be unrealistic. If f models the maximum load, it would usually be a function of crack size. The potential energy is $P = Qh + w$, where w is work done and h is the height of the load above some arbitrary datum such that $dh = -dq$. Thus, $dP/da = -dC/da$ where C is complementary energy

$$C = \int q\, dQ = \phi Q_0^2\, \ell n \sec (Q/Q_0) \tag{6}$$

Therefore

$$BJ = (\partial C/\partial a)|_Q = Q_0^2\, (d\phi/da)\, \ell n \sec (Q/Q_0) \tag{7}$$

Using the LEFM relationship for G and denoting G at $\sigma = f$ by G_f

$$BG = (Q^2/2)\, (d\phi/da) \tag{8}$$

then

$$J = 2G(Q_0/Q)^2\, \ell n \sec (Q/Q_0) \tag{9a}$$

or

$$J = G_f (8/\pi^2)\, \ell n \sec (\pi\sigma/2f) \tag{9b}$$

If, in Eq 9*b*, G_f is taken from LEFM for the infinite-plate case with $f = \sigma_y$

$$J = (8\sigma_y^2\, a/\pi E)\, \ell n \sec (\pi\sigma/2\sigma_y) \tag{10}$$

If δ is defined as J/G_y, consistent with the well-known Dugdale model, then from Eq 10

$$\delta E/\pi\sigma_y a = (8/\pi^2)\, \ell n \sec (\pi\sigma/2\sigma_y) \tag{11}$$

$$= (\sigma/\sigma_y)^2 \{1 + (\pi^2/24)\, (\sigma/\sigma_y)^2 + \ldots\} \tag{12}$$

A COD-Type Design Curve

As is well-known [5], the COD curve of Eqs 1*a* and 1*b* does not follow the quasi-elastic strains given by the Dugdale analysis. However, if the normalized δ, Eq 11, is plotted against q/q_0 from Eq 4*b*, then as seen in Fig. 2*a*, the resulting curve has a form broadly similar to Fig. 1*a*. The relationship is not exact, of course, since in reality the COD curve was defined by experimental measurement of COD and gage length displacement, not by analysis of load-displacement records. Perhaps more importantly, as seen by comparing Eq 1*a* and the first term of Eq 12, the value of COD given by Eq 1*a* is twice that given by Eq 12, which is itself consistent with LEFM, so that in the use of the

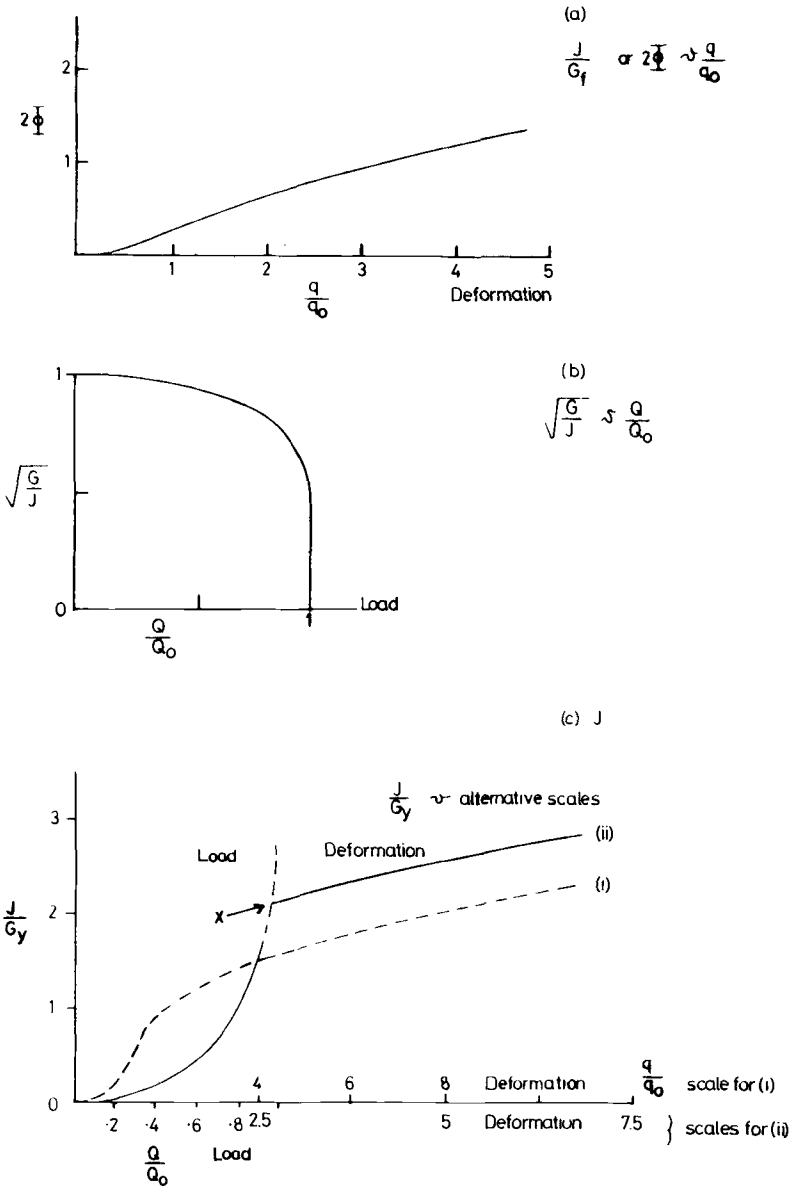

FIG. 2—*Schematic forms for an estimate of* J *from Eq 4 versus various abscissas: (a) to simulate COD, (Fig. 1a(i); (b) to simulate R-6 (Fig. 1b); (c) to simulate* J *(Fig. 1c).*

COD design curve [*1*] there is an intentional factor of conservatism of twofold in the LEFM regime. This dominates the differences between Eqs 1*a*, *b* and the particular analytical model chosen in the foregoing, but nevertheless it is clear that schematically the COD design curve corresponds to an estimate of J/σ_y versus applied deformation.

An R-6 Type Curve

A curve of $\sqrt{G/J}$ versus Q/Q_0 using Eq 9*a* has the same functional form as Eq 2, although the normalized load is here Q/Q_0, whereas the R-6 method uses S/S_c, where $S \equiv Q$, but S_c is the nominal collapse load in a ligament of area $B \times (B + L)$ where B is thickness and L is the surface length of a part-through thickness crack. If it is argued, as it was when R-6 was formulated, that the ℓn sec term must become large as the load tends to collapse, then Q/Q_0 must be interpreted as Q/Q_c, where Q_c is collapse load, although as just noted, R-6 uses a particular arbitrary definition of collapse of a ligament. However, Q_c or S_c is a function of crack size and so cannot be introduced into Eq 4*a* without breaking the simple variables-separable form assumed. Thus, the change from Q/Q_0 to Q/Q_c must be made in an ad hoc manner after Eq 9 has been derived, if the simple mathematical development given here is to be followed. The ratio Q/Q_c is also not strictly the value σ/f required to pass from Eq 9 to Eq 9*b*. Nevertheless, with these restrictions the present simple derivation gives a curve, Fig. 2*b*, closely similar to R-6 based on the same load-displacement diagram as for the COD curve, Fig. 2*a*.

A J-Based Curve

If J/G_y is plotted against strain in the uncracked body using Eqs 10 and 4*b*, then a curve is found, Fig. 2*c*, similar to Fig. 1*c*. Again, a precise derivation cannot be given, since the Eqs 4 onward relate to a cracked body. This makes little difference in the elastic regime (at least for shallow cracks) but greatly affects the plastic displacements. The curve is shown plotted in two ways. The overall load is shown as J/G_y versus q/q_0 for the cracked body and that is similar to the COD curve apart from the terms and scales on the ordinate. The same data are also plotted in two steps: (1) with strain in the near elastic region estimated as Q/Q_0, followed by (2) strain in the plastic regime estimated as the strain at 10 percent less load to simulate a 10 percent crack as typical of those used in the original computations [*3*]. The point X for the junction of the two regimes is taken arbitrarily as $Q/Q_0 = 0.95$. Again, the point is not the numerical values obtained, since in reality the computed data are used, but the fact that, starting with the given Eq 4*a*, the various forms of design curves emerge in a self-consistent manner.

An EPRI-Type Curve

Equation 4*a* does not, of course, fit the linear plus power-law representation used [*4*], but the schematic relationship between [*4*] and the foregoing simple model can be pointed out. If the *J*-based values of Fig. 2*c* are normalized as J/G rather than J/G_y, then Fig. 3*a* is obtained. The load-based abscissa in the near LEFM regime gives a near parabolic curve and the strain-based abscissa gives the linear "tail." The distinction is that the *J*-based diagram of Fig. 2*c* and Fig. 3*a* expresses the large deformation regime beyond ligament yield in terms of deformation, whereas the Electric Power Research Institute (EPRI) diagram proper expresses it in terms of

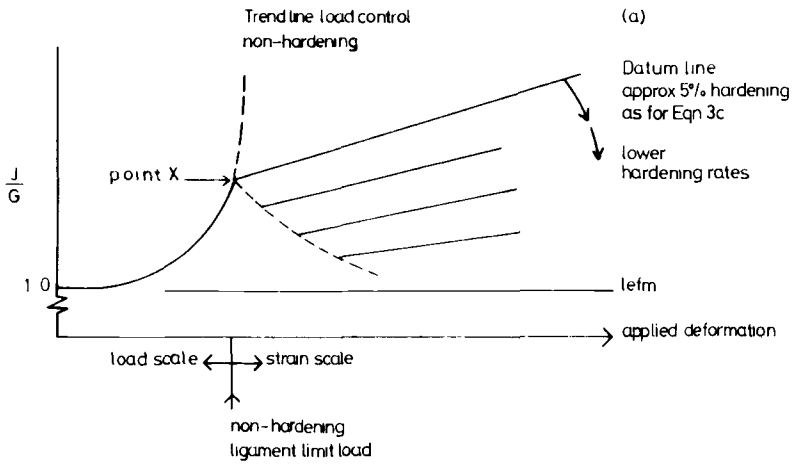

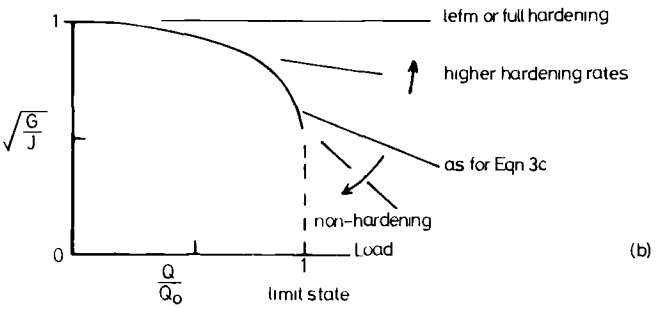

FIG. 3—*Schematic J-estimation diagram re-expressed against a combined load/strain axis: (a)* J/G *(following Figs. 1c and 2c); (b) as* $\sqrt{G/J}$ *(following Figs. 1b and 2b).*

work-hardening load. The effect of work-hardening is allowed for in COD, R-6, and the *J*-based diagram, only in terms of an increase of yield stress to an effective flow stress when defining f, in Eqs 4*b* and 5, but the effect of hardening is shown schematically, Fig. 3*a*, where no hardening reduces to the R-6 diagram terminating at ligament yield and complete (linear) hardening would simply extend LEFM with $J = G$. If Fig. 3*a* is then inverted and the ordinate square-rooted, the EPRI diagram of "R-6 with tail" is found, Fig. 3*b*, subject to whether the post-net yield regime is expressed in terms of strain or load.

It is not, of course, demonstrated that Eq 4 is a good representation of all cases, and hence that Figs. 2*a*, 2*b*, and 2*c* are good representations of J for all cases. Indeed, unless f is related to collapse, Eq 4*b* cannot be satisfactory and, as pointed out in the presentation of the *J*-design curve [*3*], the computed data do not fall on one curve, Eqs 3*a*-3*c* being an upper bound to the cases then studied, defined by the tension data with the bending data falling somewhat below. In short, the relationship between Figs. 1*a*, 1*b*, and 1*c*, and Figs. 2*a*, 2*b*, and 2*c*, and Figs. 3*a* and 3*b* remains schematic rather than precise. Nevertheless, it is sufficiently instructive on the comparison between the methods to justify the simplifications made.

A Simple *J*-Based Estimation Procedure

Overall Scope

The *J*-estimation curve as currently presented is based on two-dimensional (2D) elastic-plastic plane-strain finite-element computations for a variety of configurations, including tension, bending, cracks emanating from a stress concentration, and a crack in a thick cylinder, all with $a/W \leq 0.1$. These are collectively called the reference cases. Most of the calculations include a mild degree of work-hardening representative of structural carbon-manganese (C-Mn) steels, and are detailed Ref *3*. It is also noted that Eqs 3 were developed explicitly for the elastic-plastic fracture regime. Nothing was said about plastic collapse, or indeed, LEFM-based methods, on the grounds that satisfactory procedures existed for those topics. Although it is recognized that J is not strictly relevant to residual stress, a modification to include yield level residual stress was suggested [*9*]. Reaction stresses were treated as applied loads, but for self-equilibrating residual stresses it was proposed that the ordinate be increased by unity, so that, for example, whereas at $e/e_y = 1.2$, Eq 3*c* gives $J/G_y = 2.5$ with the addition of yield level residual stresses, a value of $J/G_y = 3.5$ would be appropriate. A number of features of these equations for J are now discussed and modifications suggested. It should be clearly stated that the equations derived for the purposes of the schematic comparison in the first part of this paper are not used for the proposals now being developed other than by way of illustration. The justification for the

present equations must rest on the reference cases data already described [*3,9*], other data mentioned herein, and experimental evidence yet to be adduced.

Some Desirable Features of a J-Estimation Curve

Clearly normalized terms are required if a variety of circumstances is to be covered. Condensation to a single curve is an end point which, though desirable, may not be feasible beyond the idealized relationships already stated. Thus, either a degree of approximation must be accepted with the proposed single curve erring on the side of conservatism, or several relationships must be proposed, each applicable to some defined circumstances. The R-6, COD, and *J*-"design curve" methods clearly follow the former course. In at least broad terms the "*J*-handbook method" [*4,10*] appears to follow the latter. The immediate point is that in proposing a single curve, compromises must be made so that even the rather obvious desiderata listed here cannot necessarily be met, one being in conflict with the other to some extent:

1. The cracked region of a body may experience plasticity that is controlled by load, deformation, or by its own interaction with the surrounding parts of the structure, but the abscissa of the diagram must be in terms of the elastic stress and strain in the uncracked body since these are the only terms likely to be directly available.

2. Degeneration to LEFM seems essential. One obvious route is to recognize that J degenerates to G and then to normalized to give J/G_y as in Eqs 3. Equation 9*b* would follow this scheme if f were taken as σ_y. Alternatively, using J/G leads to $J/G = 1$ for LEFM, whence it is implied that any function could be chosen for the second axis of a diagram. Equation 9*a* and R-6 use this scheme. Departure from strict LEFM should be compatible with accepted procedures for plastic zone correction. If this is not so, then some conflict will arise in well-contained yield.

3. The circumstances of "general plasticity" at which J becomes very large must be defined. If there is true limit-state behavior, J will then depend upon deformation, and even if a limit state is only conceptual (because of work-hardening or change of geometry), load is a rather insensitive measure of a near-horizontal load-deflection behavior. There are two related issues:

(*a*) Is net ligament yield to be avoided as a design criterion in its own right? This must be so for regular usage but may not be so for "avoidance of catastrophe" where plastic collapse without separation may be highly desirable.

(*b*) Can strains larger than those implied by net ligament yield be tolerated without in fact causing plastic collapse of the structure? For two-dimensional configurations such as conventional tension or bending specimens, the two phenomena of ligament yield and plastic collapse would be

the same were it not for work-hardening of the ligament. However, for three-dimensional problems (for example, a crack in the corner of a vessel head to flange joint) a nominal net yield of the ligament area may be far less than the load to cause true plastic collapse, primarily for reasons of strain control by adjacent material, although also restricted by the effect of work-hardening.

4. Allowance must be made for practical aspects commonly met with, such as the existence of residual or thermal stresses and regions of local stress concentration. Any less commonly met special cases not adequately dealt with should be noted and embargoed.

These points are discussed first in rather general terms, to outline the arguments on which the later particular proposals are made.

Choice of Axes

The forces or deformations that control a crack, that is, those which would be applied to a test coupon cut to model the cracked region, are here called the "cracked body structural stress (cbsσ) or strain (cbse)." The problem is to relate these terms to the known stresses or strains in the uncracked body while offering reasonable continuity with LEFM and also guarding against failure by plastic collapse. These two limiting conditions are usually treated in different ways, LEFM requiring the nominal (gross section) stress σ often normalized by yield stress to give σ/σ_y, whereas collapse requires a net section stress, σ_n, normalized to a collapse stress, σ_c, that makes allowance for constraint, work-hardening, and a section modulus that differs for tension or bending. It would be feasible to define a term that interpolated between these two limits, although that would still exclude the strain-controlled regime beyond ligament yield which may be entered in some extreme solutions. In the embryo *J*-design curve [*3*] the problem was avoided because discussion was limited to shallow-notch cases where uncracked body values were taken as adequate estimates of applied severity, be it for collapse or for entry into the design curve. The following is now proposed:

1. In the near-LEFM regime the abscissa should become an effective strain ratio $e_f/e_y = \sigma/\sigma_y$, where σ is the stress in the uncracked body, just as in LEFM, and this regime should incorporate both Eqs 3*a* and 3*b*, with a plastic zone correction included.

2. In the extensive plasticity regime the abscissa should become an effective strain ratio defined by cbse, itself expressed as either some simple function of the uncracked body stress, where there is adjacent material which prevents general plasticity, or of the uncracked body deformation, where general yield occurs.

3. If Regime 1 is exceeded, a separate check must be made on the risk of

plastic collapse, but where circumstances merit it, entry can then be made into the strain-controlled Regime 2.

4. The ordinate should remain J/G_y as at present.

The scheme proposed here is examined in outline and refined in connection with various special problems, notably deep notches and stress concentrations, in the following sections. Residual stresses and biaxial stresses are also considered rather more briefly. It remains to be seen whether there are as yet unperceived drawbacks to these proposals, or whether some other scheme, perhaps one of those already discussed [*1,2,4*] is preferable.

Notch Depth

The difficulty of finding a basis for the abscissa in strain-controlled cases when notches are deep has already been outlined in the opening discussion of a *J*-estimation curve. All that is added here is a brief description of the method of analyzing the deep-notch computed data used to support the present argument. There is of course an implication that in practice the cbse should be estimated in a compatible way. The effective strain for entry to the abscissa (that is, the cbse) is identified as the uncracked body strain e times a multiplication factor that is notionally the ratio of the length required to reach the undisturbed elastic field to the length of the severely disturbed field that might be modeled by a test panel. This ratio is taken as W/b, although more evidence on an appropriate value and what factors affect it would be welcome.

Thus, for the deep-notch displacement-controlled crack beyond yield

$$\text{Effective } e/e_y = (\text{cbse})/e_y = (W/B)(e/e_y) \tag{13a}$$

where e is the uncracked body strain, itself probably elastic. This value $(\text{cbse})/e_y$ is proposed as the entry to the abscissa for problems that enter general yield under conditions of displacement control. However, when

$$(\text{cbse})/e_y > 1 \quad \text{or} \quad b/W < 0.5 \tag{14a}$$

the problem should be examined explicitly in terms of limit behavior both to evaluate ligament limit load and to confirm whether or not restriction to such a load is a design requirement in its own right. More case data are needed to better justify or refute this proposal but, on the evidence so far examined, it appears conservative relative to the shallow-notch cases that define the estimation curve, as shown later. This procedure, applied as just described, results in a discontinuity between the near-elastic and post-ligament yield regime. It would in fact be more logical to apply the cbse concept to the

plastic component of deformation only. That further refinement is described in Ref *13* but the improvement obtained is added to Fig. 6 here.

Three-Dimensional Problems

All the elastic-plastic computations on which the so-called *J*-design curve is based have been made in two dimensions. For application to three-dimensional (3D) problems, two suggestions are made:

1. The LEFM shape factor appropriate to three dimensions is used in determining G_y ($=Y^2\sigma_y{}^2a/E$) so that, by implication, the effect of plasticity is accounted for in the estimation equations for J/G_y, and in particular, by the point at which they are entered.

2. In the common 3D cases of a semi-elliptical flaw, net ligament yield is well below true plastic collapse because of the adjacent elastic material "in parallel" with the crack. Entry into a strain-controlled regime of crack behavior is therefore quite feasible in an emergency, but the cbse term argued in the previous section would now be B/b rather than W/b.

Thus, Eqs 13*a* and 14*a* can also be interpreted

$$(\text{cbse})/e_y = (B/b)(e/e_y) \tag{13b}$$

and if

$$(\text{cbse})/e_y > \quad \text{or} \quad b/B < 0.5 \tag{14b}$$

then collapse should be checked explicitly.

Proposal 1 is similar to the usage of both COD and R-6, although in practice different results may be obtained for COD because in evaluating the real crack size, a, from the equivalent crack $\bar{a}$, Ref *1* supplies its own formulas or graphs of shape factors, which do not always agree with the accepted LEFM shape factor Y, notably for semi-elliptical cracks in bending where the basis of the diagram in Ref *1* appears to be the tensile Y-factors.

Stress Concentrations

The treatment of stress concentration cases in both COD and R-6 procedures is to use elastic estimates. Thus, both imply acceptance for short cracks of the relationship

$$K = Yk_t\sigma\sqrt{a} \tag{15}$$

where the local stress is $k_t\sigma$, k_t being the elastic stress concentration factor. The COD procedure estimates e/e_y as $k_t\sigma/\sigma_y$, whereas the R-6 procedure uses the value of K directly as a function of σ. For larger cracks the methods

are broadly comparable in that R-6 continues to use the most appropriate estimate for K (for example, the Bowie solutions for a crack emanating from a hole) whereas COD accepts the nominal value of $k_t\sigma/\sigma_y$ for e/e_y but includes rules for turning the effective crack length $\bar{a}$ into a real crack length a. In the published J-design curve [3] the use of $e/e_y = k_t\sigma/\sigma_y$ is accepted, together with use of the most appropriate Y-factor in the ordinate $JE/Y^2\sigma_y{}^2a$, implying, of course, that the shape factor Y is itself independent of degree of plasticity, since the latter is accommodated by the specified equations for J/G_y. This method was adopted in the light of the computation for cracks at a hole in plate [12] as a compromise between giving a reasonable estimate and simplicity. Further analysis of the same results [13] shows that for long cracks (for example, $a/R \simeq 1.0$) or low stresses (for example, $\sigma/\sigma_y < 0.6$) the method is adequate. For short cracks (for example, $a/R < 0.1$) and high stresses (for example, $\sigma/\sigma_y > 0.6$) the method is not conservative. The diagram should then be entered at the true local strain at the region of concentration in the uncracked body, which can be found either by elastic-plastic computation for the uncracked body, or by use of Neuber's rule

$$k_\sigma k_e = k_t{}^2 \tag{16}$$

k_σ is here the plastic stress concentration factor and k_e the plastic strain concentration factor, so that the diagram is entered at $k_e\sigma/\sigma_y$ where σ is the conventional "remote" elastic stress in the body as used in LEFM. This method was proposed in Ref 7 although that estimation curve differed from the present one. The Neuber estimation, although not rigorous, seems satisfactory, provided the notch region remains in contained yield. The value of J derived from Eq 3c entered at the true plastic strain in the uncracked body falls slightly above the value of J computed for the actual cracked configuration for the present data and is thus conservative. It must be cautioned that the only cases analyzed refer to $k_t = 3$ with various values of a/R. Higher or lower values of stress concentration have not been studied. Data for short cracks are shown in Fig. 4; data for larger cracks are given in Refs 12 and 13, where it is concluded that for contained yield an LEFM estimate of K with correction for plastic zone size gives the most appropriate value.

Residual Stresses

In the COD procedure a term is added to the abscissa of value e_r/e_y where $e_r = \sigma_r/E$, and σ_r is the residual stress. In an unstress-relieved body, σ_r may be taken as σ_y so that unity is added to the abscissa. In the R-6 procedure the K-values for mechanical and residual stresses are added. The abscissa S/S_c is not altered although a correction to the ℓn sec relation has been suggested for these cases in the latest supplements to Ref 2. To obtain the combined K-value, the combined value of stress $\sigma_m + \sigma_r$ could, of course, be used if it

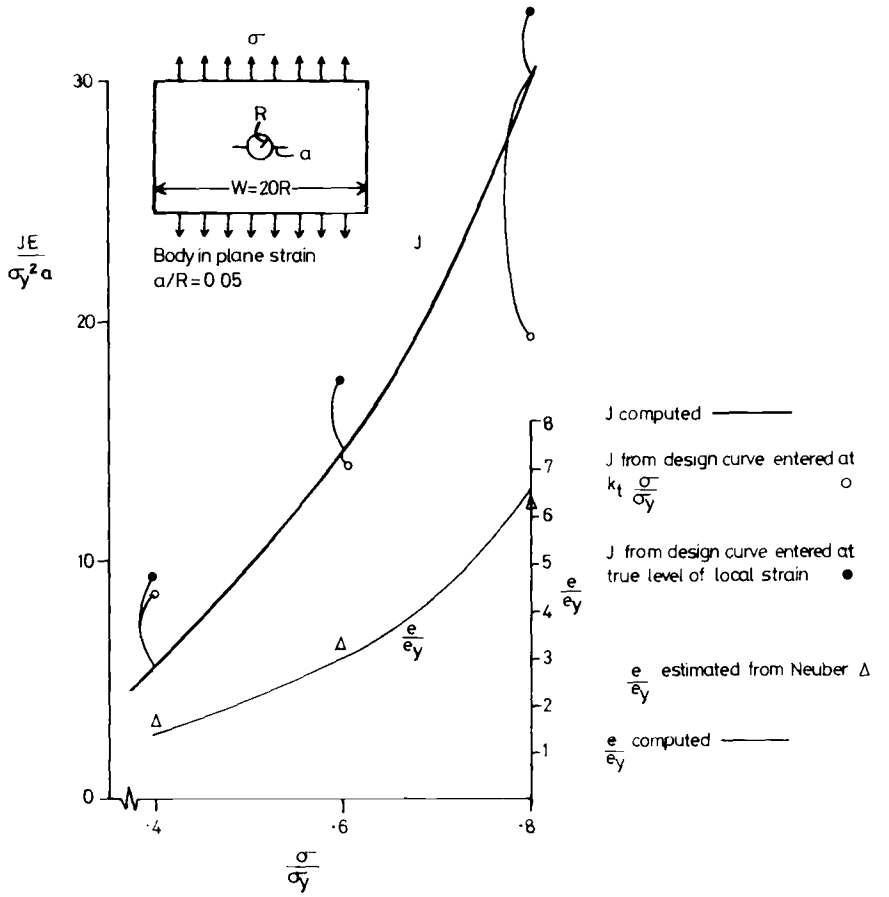

FIG. 4—*Estimates of strain at a stress concentration using the Neuber relationship and subsequent estimate of* J *for a short crack* (a/R = *0.05) emanating from a hole in a plate under tension.*

were assumed that the distributions of mechanical and residual stress across the section were the same. In the existing *J*-procedure the suggestion has so far covered only residual stress of yield level where unity is added to the ordinate of J/G_y, and reaction stresses, if any, are treated as applied loads [*9*]. It is realized that *J* is not strictly relevant to residual stresses, but, if that rigorous view is taken, *J* ceases to be useful for many practical problems. The close affinity between *J*, COD, and R-6 methods clearly implies that what is feasible by one method is feasible by the other and will in practice be used, whether rigorous or not.

It is now proposed that to allow for residual stresses other than yield level, and also to ensure compatibility with LEFM, some fractional power of the mechanical and residual terms J_m and J_r must be added such that if all

stresses, including the summation, $\sigma_m + \sigma_r$, are still elastic, then $J^{1/2}$ terms are added (that is, K is added as in LEFM) but if either or both terms are fully plastic, then J itself is added. No explicit procedure to cover all cases is given here. In essence the (known) value of residual stress is normalized as σ_r/σ_y or e_r/e_y and the abscissa is entered at the appropriate point. The normalized value of J relevant to the residual stress is then read off the ordinate. A similar procedure will have been carried out for the mechanical stresses. The two values of J are then combined by adding such that

$$J = (J_m^{1/\alpha} + J_r^{1/\alpha})^\alpha \tag{17}$$

As a rule of thumb, perhaps $1/\alpha = 0.5 + s/2\sigma_y$ could be used where $s = \sigma_m + \sigma_r$. The author has some doubts whether even this complexity is justified in view of the many uncertainties, but adding J-values is not conservative in LEFM and adding $J^{1/2}$-values after yield seems overconservative. Whether a yet further term as in Ref *9* for reaction residuals stresses (induced, for example, if a patch were heated or stretched before welding into a rigid surrounding structure) is needed seems doubtful unless both local discontinuity and reaction stresses remain elastic. If either reaches yield, the other is reduced, although residual strains that might be damaging remain. The whole subject appears to justify a much more thorough discussion if any rule other than the simplest is to be proposed. Meanwhile, the inclusion of a plastic zone correction in the present proposals implies that at $\sigma_r = \sigma_y$ a term 1.5 rather than 1.0 is added to the value of J/G_y, thereby introducing additional conservatism.

Thermal and Biaxial Stresses

In the sense that thermal stresses are self-equilibrating or possibly reactionary in respect of an adjacent component, treatment as for residual stress seems appropriate and is not further discussed here. Possible repeated plastic thermal strains would require separate study. Insofar as equibiaxial stresses can readily be developed (for example, at the bore of a thick cylinder with a temperature gradient across the wall), then a more careful study of biaxial effects may be justified. Unfortunately, the effect of biaxial stress on fracture is not well understood, and is not discussed in the COD or R-6 procedures. Several computational studies relevant to the estimation of the applied severity under biaxial loading, be it J, COD, or other, were reviewed in Ref *3*. In summary, it was argued that an applied biaxial stress altered the value of J from the uniaxial case, but that for a given value of J, the crack tip field, however induced, was still characterized by J.

It is difficult to disentangle the latter statement from the effect of biaxiality (or even triaxiality) on the micromechanisms of fracture, which topic is beyond the scope of the present paper, though extremely relevant to the

"right-hand side" of the design equation J (applied) $< J$ (material). A very tentative method of estimating J for the biaxial case was outlined in Ref *3*, p. 107. There is a large effect on the collapse load in plane strain, and hence on the load at which J becomes large. It is important to note that in plane strain, for a given axial load, an equibiaxial stress reduces the value of J (though increasing the triaxiality), whereas for a given axial displacement the J-value is increased (Fig. 5). Thus, biaxial-induced thermal strains seem potentially unconservative, whereas biaxial pressure stresses may be less so, in respect of ductile crack initiation for which the uniaxial case has been taken as datum.

Revised *J*-Estimation Curve: Statement and Summary

A statement of the revised curve has been delayed until this point because so many of the foregoing factors interact. The proposal is clearly a compromise so that if viewed in the light of only one argument it may seem unsatisfactory. In the revised form, Eqs 3*a* and 3*b* for LEFM and contained yield are combined into Eq 18*a*. Equation 3*c* for deformation beyond yield is retained as Eq 18*b* but with a reinterpretation of the abscissa as effective strain (cbse). The curve is shown in Fig. 6. The equations are

$$J/G_y = (e/e_y)^2(1 + 0.5(e/e_y)^2) \quad \text{for } e/e_y \leq 1.2 \tag{18a}$$

where e/e_y can be estimated from the elastic value of σ/σ_y in the absence of stress concentrations or residual stresses. The coordinate of the junction point X (Fig. 2*c*) is retained as $J/G_y = 2.5$ for $e/e_y = 1.2$ in conformity with the original data and this is satisfied to within 1 percent by Eq 18*a*. In the post-yield regime

$$J/G_y = 2.5\{(e/e_y) - 0.2\} \quad \text{for } e/e_y \geq 1.2 \tag{18b}$$

The interpretation of e/e_y is here the term (cbse)/e_y already introduced, Eq 13, whereby the abscissa remains as with Eq 3*c* for $a/W \to 0$, but is altered to cover deep-notch cases by use of the effective-strain term, which is strain e/e_y times W/b or B/b (as appropriate for the through or part-through cracks). An additional requirement, Eq 14, is now introduced, so that if

$$\begin{aligned} &\text{(cbse)}/e_y > 1 \text{ (that is, if } (e/e_y)(W/b) \quad \text{or} \quad (e/e_y)(B/b) > 1) \\ &\text{or if } b/W \text{ (or } b/B) < 0.5 \\ &\text{or if } y/\sqrt{\pi} > W/b \text{ (or } B/b) \end{aligned} \tag{18c}$$

then limit state behavior must be examined explicitly.

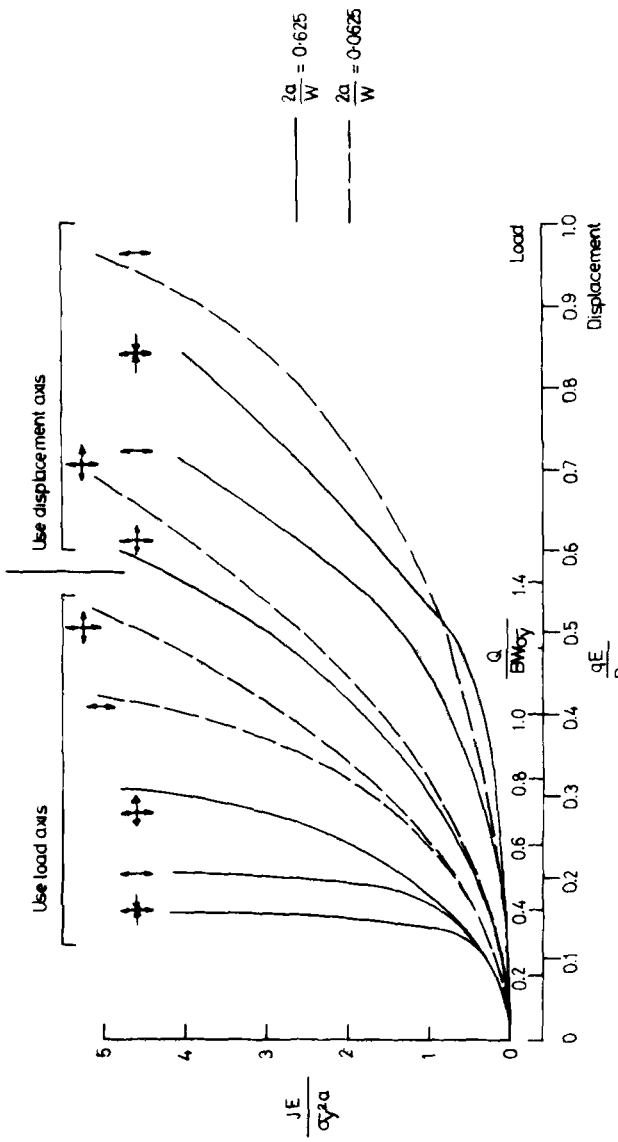

FIG. 5—*Effect of biaxial loading on the value of* J *induced in shallow-notch and deep-notch center-cracked tension (finite-element studies in plane strain; mildly work-hardening).*

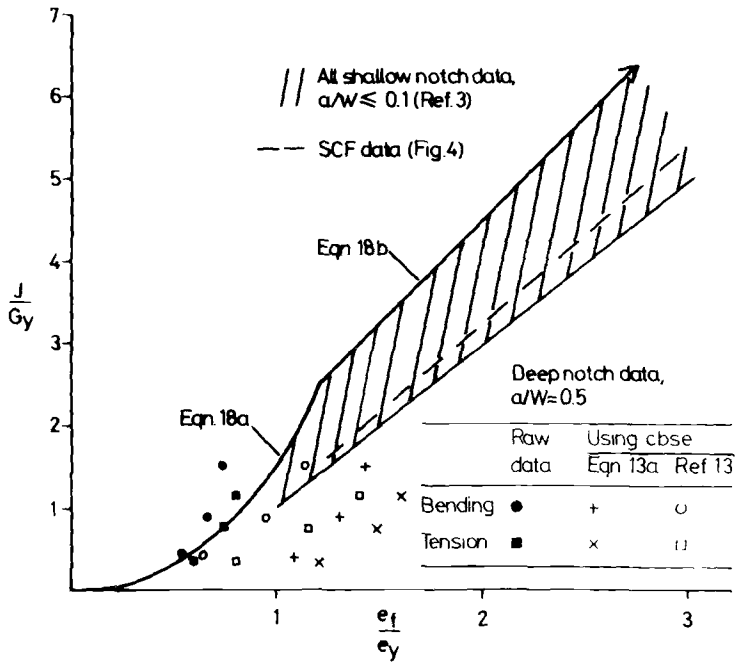

FIG. 6—*Revised J-estimation curve defined by Eq 18, together with deep-notch tension data interpreted using the cbse concept.*

The meaning of e/e_y for stress concentration cases is σ/σ_y while in contained yield (say $\sigma/\sigma_y \leq 0.8$) since a plastic zone correction is incorporated in Eq 18*a*. The Neuber relations can be used for more extensive yield (say up to $e/e_y \leq 1.2$) and e/e_y is then the actual strain so estimated. The latter is more conservative notably for short cracks and high stresses where the uncracked body plastic zone is extensive in relation to crack size.

For problems with residual stresses the ordinate has to be assessed twice, once for mechanical stress alone and once for residual stress alone. The two values are combined according to Eq 17.

Fracture Toughness in Terms of J

As just noted in connection with biaxial stresses, it is beyond the scope of this paper to discuss whether a critical value of J exists at fracture and how it is best measured. Nevertheless, it must be pertinent to ask what the value estimated by the proposed procedure might be equated to. In the R-6 procedure J (applied) is expressed as an equivalent K-value and limited to K_{Ic}, or perhaps J (applied) is equated to J_{Ic}, which is identified as K_{Ic} so that the

ordinate taken as $\sqrt{G/J}$ in connection with Eq 9 becomes K/K_{Ic} in use. The COD method allows various interpretations of COD at initiation or up to maximum load according to circumstance and agreement, but it must be recalled that full section test specimens are used, primarily to match the risk of cleavage in the test specimen to that in the structure. Clearly, the most conservative treatment here is to write $J < J_{Ic}$ without further entering the argument of whether truly $J_{Ic} = J_i$ (at initiation) or some larger value, allowing for a blunting line and a small amount of stable tear. In short, "initiation toughness" is implied as a concept, however, in fact, it may be measured. If appreciable crack growth is to be permitted, alternative assessments of instability can be made in terms T [*14*], I [*3,15*], or dJ/da [*10,16,17*] that are related but not identical. Such analyses may be necessary for severe problems but seem inconsistent with a simple design curve approach, unless indeed simple instability procedures are developed. As a brief statement in connection with a J-estimation procedure, the author has suggested [*15*] that a post-initiation value of toughness can be used, expressed in terms of J, up to the value of J at instability of the test specimen, as indeed have Refs *1* and *19*, but with the proviso

$$(b/\eta) \text{ component} \geq (b/\eta) \text{ test specimen} \tag{19}$$

where b is ligament, $\eta = JBb/w$, and w is work done. This guards against ductile instability occurring in the component prior to the value of J measured in the test specimen if the J_R-curve is indeed a material property. Where doubt exists, a side-grooved specimen can be used to ensure that the R-curve is not augmented by shear lips in the test specimen to a greater extent than in the component. To guard against cleavage, many advocate use of full-thickness specimens, as in the COD procedure, or as proposed for J-testing [*19*]. The point is not pursued here other than to draw attention to its relevance, including the effects of biaxial stress which, at the root of a semi-elliptic thumbnail crack, will act parallel to the line of the crack front, or what is conventionally called the "z-direction" [*20*]. It has also been re-questioned recently [*21*] whether there can be significant time-dependent effects particularly after initiation, and more particularly where the ligament has yielded. The effect of prestrain is also in question, some arguing that the possible effects of starting crack growth more than outweigh alleged beneficial effects of inducing favorable residual stress, and, of course, eliminating "rogue"components, and that there is no beneficial effect if the pattern of loading service differs from that used for pre-straining. Clearly, all these topics play an important role in turning an estimation procedure into a design procedure and several may be less well understood and of more significance than the uncertainties of the estimation procedure. All these points are acknowledged. Some are discussed further in Ref *23*.

Discussion

Only a few general points relating to the overall proposal will be mentioned. Since the overall form of the equations has not been substantially altered, no further evidence in support is given beyond that discussed in Refs *3* and *9*. The close relationship with COD and R-6 methods pointed out in the opening section implies that much of the experimental evidence used to support these methods [*5,6*] would equally well support the present one. The differences in procedure are within the uncertainties of much of the experimental data in which, for example, toughness may be inferred without direct measurement and ambiguities exist on the meaning of failure between initiation and instability. One main modification from the previous proposal is the coverage of deep notches. The general trend of deep-notch cases so far reexamined falls conservatively, as here described as shown in Fig. 5. The use of cbse is seen as an alternative to the procedure of recategorization used in Refs *1* and *2* for cracks that cause local yield of a ligament.

Perhaps the most important point is the retention of strain in the abscissa. Changing to load, Q/Q_c, inevitably requires a change of ordinate to J/G as already discussed. There is no doubt the present data would correspond closely to the R-6 line (with ordinate left as $\sqrt{G/J}$, without J identified as a critical value to K_{Ic}^2/E). The difficulty lies in how then to locate Point X (Fig. 1*c*) beyond which strain-controlled behavior occurs. The abscissa beyond X must be strain and it may be possible to devise a dual axis of both effective strain and normalized stress for the load-controlled regime. For high work-hardening rates J/G must tend towards LEFM so that a scheme such as shown in Fig. 3 emerges. The axes and locating point X have been derived only for the shallow-notch data aided by speculation, so that scales have been omitted deliberately. However, when plotted with axes already square-rooted and with the ordinate inverted, Fig. 3*b*, not only is the first part of the diagram identical to R-6 (subject to the definition used for "collapse" load) but the second or strain-controlled part reflects the proposals of Bloom [*22*] and the data shown by Shih et al ([*10*], Fig. 16), although their description uses a work-hardened flow stress rather than strain as the abscissa above "collapse." The formulation and description of diagrams in the style of Fig. 3 will be examined further in a separate paper. An immediate point is the role of work-hardening not hitherto discussed here. On a diagram such as Fig. 3 work-hardening must reduce the diagram toward the LEFM line $J/G = 1$, as also shown by Shih et al ([*10*], Fig. 15). In terms of the present axes of J/G_y and strain, it is noted that the use of a flow stress increases the estimate of J in the strain-controlled region above X, Fig. 1*c*, since the effect of replacing σ_y by σ_{fl} in the ordinate more than offsets the reduction in the abscissa. This is contrary to behavior in LEFM where there is no effect and in the load-controlled small-yield regime where reduction of plastic zone size reduces J. A distinction may be required between the case of a high work-

hardening rate that continues indefinitely and a high work-hardening ratio (for example, ultimate tensile strength/yield) which saturates.

In the latter case, it seems that by appropriate choice of an augmented value of σ_y the J-displacement relationship that is being mapped is very little affected for the cases so far studied. Thus, with reservations for load-controlled behavior, together with the limiting cases of either continued high hardening *rate* (where the LEFM parabola would continue above Point X, Fig. 1*c*) or *no* work-hardening, perhaps including the case of a long yield plateau (where the fully plastic regime has a linear slope greater than Eq 3*c*), the present curve is retained, and bounds all the actual work-hardening cases computed. This point will also be further discussed elsewhere.

Meanwhile, a comparative study has been made of COD, R-6, and J-methods, and the difference between them discussed at some length [*24*]. The major conclusion is that the unspecified steps of engineering judgment may swamp the differences in procedure, and that if the judgments are agreed upon (though they may not necessarily be correct!) the difference between the three methods was rather small for the cases studied.

Conclusions

The existing procedure for estimating J for design or assessment purposes has been re-phrased and extended to cover deep notches as well as shallow, to incorporate better rules for stress concentration and residual stress cases, and to distinguish explicitly between load and strain-controlled behavior near the ligament limit state. The proposal is publicized in its present form with the intention of encouraging confirmatory or condemnatory evidence from the many other sources that exist. A relationship between COD, R-6, and J methods has been shown explicitly using a simplified model. The major differences are not in the estimation of COD or J per se, but in the method of specifying the stresses or strains which the cracked body is subjected to in terms of the known uncracked body analysis and the implied engineering judgments that may be contained therein.

Acknowledgments

Much of the work drawn upon here was supported by grants for computational studies from the Science and Engineering Research Council, U.K., over a period of several years.

References

[*1*] *Guidance on Some Methods for the Derivation of Acceptance Levels for Defects in Fusion Welded Joints.* British Standards Institution, PD6493, 1980.

[*2*] Harrison, R. P., Loosemore, K., and Milne, I., "Assessment of the Integrity of Structures

Containing Defects," CEGB Report R/H/R6, Central Electricity Generating Board, Leatherhead, Surrey, U.K., 1976 and Supplements, 1979, 1981.

[3] Turner, C. E. in *Post-Yield Fracture Mechanics*, D. G. H. Latzko, Ed, Applied Science Publishers, London, 1979, Chapter 2.

[4] "EPRI Ductile Fracture Research Review Document," D. M. Norris et al Eds., Electric Power Research Institute, Palo Alto, Calif., Dec. 1980.

[5] Burdekin, F. M. and Dawes, M. G. in *Practical Application of Fracture Mechanics to Pressure Vessel Technology*, Institution of Mechanical Engineers, London, 1971, pp. 28-37.

[6] Dowling, A. R. and Townley, C. H. A., *International Journal of Pressure Vessels and Piping*, Vol. 3, 1975, pp. 77-107.

[7] Begley, J. A., Wilson, W. K., and Landes, J. D. in *Fracture Analysis, ASTM STP 560*, American Society for Testing and Materials, 1974, pp. 155-169.

[8] Turner, C. E. in *Proceedings*, International Colloquium on the Practical Applications of Fracture Mechanics to the Prevention of Failure of Welded Structures, International Institute of Welding, Bratislava, Czechoslovakia, 1979, pp. 293-304.

[9] Turner, C. E. in *Advances in Elasto-Plastic Fracture*, L. H. Larsson, Applied Science Publishers, London, 1980, pp. 301-318.

[10] Shih, C. F., German, M. D., and Kumar, V., *International Journal of Pressure Vessels and Piping*, Vol. 9, 1981, pp. 159-196.

[11] Parks, D. M., "A Line-Spring for Ductile Fracture," EPRI Report No. RP1237-3, Electric Power Research Institute, Palo Alto, Calif., Dec., 1980.

[12] Sumpter, J. D. G. and Turner, C. E. in *Proceedings*, Second International Conference on Pressure Vessel Technology, American Society of Mechanical Engineers, Vol. 2, 1973, pp. 1095-1104.

[13] Turner, C. E. submitted to the *Journal of Strain Analysis*. Institute of Mechanical Engineers, London, 1982.

[14] Paris, P. C., Tada, H., Zahoor, A., and Ernst, H. in *Elastic-Plastic Fracture, ASTM STP 668*, J. D. Landes, J. A. Begley, and G. A. Clarke, Eds., American Society for Testing and Materials, 1979, pp. 5-36.

[15] Turner, C. E. in *Fracture Mechanics, ASTM STP 677*, American Society for Testing and Materials, 1979, pp. 614-628.

[16] Garwood, S. J. in *Fracture Mechanics. ASTM STP 677*. American Society for Testing and Materials, 1979, pp. 511-532.

[17] Shih, C. F., deLorenzi, H. G., and Andrews, W. R. in *Elastic-Plastic Fracture, ASTM STP 668*, J. D. Landes, J. A. Begley, and G. A. Clarke, Eds., American Society for Testing and Materials, 1979, pp. 65-120.

[18] Turner, C. E. in *Proceedings*, Fifth International Conference on Fracture, Cannes, France, Vol. 3, 1981, pp. 1167-1189.

[19] Towers, O. C. and Garwood, S. J. *Welding Institute Research Bulletin*, Vol. 20, No. 10, Oct. 1979, pp. 292-299.

[20] Sumpter, J. D. G. and Turner, C. E. in *Cracks and Fracture, ASTM STP 601*, American Society for Testing and Materials, 1976, pp. 3-18.

[21] Ziebs, J. et al, *International Journal of Pressure Vessels and Piping*, Vol. 9, 1981, pp. 221-232.

[22] Schulze, H. D. and Fuhlrott, H. *International Journal of Pressure Vessels and Piping*, Vol. 8, 1980, pp. 131-142.

[23] Turner, C. E. in *Proceedings*, Conference on the Fitness for Purpose Validation of Welded Construction, Welding Research Institute, Abington, Cambridge, U.K., Nov. 1981.

[24] Bloom, J. E., "Applications of the CEGB R-6 Method," EPRI Report No. RP1237-2, Electric Power Research Institute, Palo Alto, Calif., Dec. 1980.

[25] Burdekin, F. M. et al, in *Proceedings*, Conference on the Fitness for Purpose Validation of Welded Construction, Welding Research Institute, Abington, Cambridge, U.K., Nov. 1981.

Ludvik Hodulak[1] *and Johann G. Blauel*[1]

Application of Two Approximate Methods for Ductile Failure Assessment

REFERENCE: Hodulak, L. and Blauel, J. G., **"Application of Two Approximate Methods for Ductile Failure Assessment,"** *Elastic-Plastic Fracture: Second Symposium. Volume II—Fracture Resistance Curves and Engineering Applications, ASTM STP 803*, C. F. Shih and J. P. Gudas, Eds., American Society for Testing and Materials, 1983, pp. II-103-II-114.

ABSTRACT: Test results of large-scale specimens are analyzed on the basis of the tearing instability concept. The "Engineering Approach" of Shih et al and the extended "Failure Assessment Diagram" of Milne are used together with crack resistance J-R curves obtained from small-scale compact specimens to evaluate the loads at crack initiation and instability and the amount of stable crack growth. A detailed parameter study is conducted to show the sensitivity of the numerical results to the variation of input data such as stress-strain law, limit load, and the material resistance curve.

KEY WORDS: failure assessment, elastic-plastic fracture, crack initiation, stable crack growth, tearing instability

The analysis of the failure of components in the elastic-plastic regime of material behavior is widely based on the J-integral as the controlling parameter. A criterion for fracture can then be formulated similar to that in linear elastic fracture mechanics (LEFM) by comparing the applied loading with the material toughness—both in terms of J, that is, fracture if $J_{applied} \geq J_{Ic}$. But the loads resulting in this way for the onset of crack extension can underestimate appreciably the actual load-carrying and deformation capacity of the component. More realistic predictions of failure loads can be expected if stable crack growth is taken into account and a tearing instability concept [*1*][2] is adopted.

[1] Senior scientist and head of Metallic Materials Group, respectively, Fraunhofer-Institut für Wöhlerstrasse, West Germany.

[2] The italic numbers in brackets refer to the list of references appended to this paper.

The crack instability analysis requires material characterization by a J-resistance curve, that is, $J_{material}$ as a function of increase Δa of crack length through ductile tearing, and a description of crack-tip loading in terms of $J_{applied}$. Besides elaborate finite-element calculations, several approximate methods can be used to obtain $J_{applied}$ as a function of load and crack size for a specific geometry.

The objective of this paper is to examine the applicability of two approximate procedures—the "Engineering Approach" (EA) developed by Shih and co-workers [*2,3*] and the Central Electricity Generating Board "Failure Assessment Diagram" (FAD) as modified by Milne [*4*]—for the analysis of the failure behavior of large-scale specimens which have been tested in the framework of the German reactor safety program [*5,6*].

For calculation of loads at crack initiation and instability and of stable crack extension, the material is characterized by a J-resistance curve generated by the method of partial unloading from small compact specimens (2T). To test the methods rather than to make a conservative safety assessment as required for a structural component, an attempt was made to predict the critical loads as precisely as possible. For this goal a parameter study was conducted to show the sensitivity of the calculational results to the uncertainties of material and stress analysis input data.

Material and Specimens

In Fig. 1 the dimensions of two types of large-scale specimens investigated and of the 50-mm-thick (2T) compact specimens for generation of a J-resistance curve are shown. The specimens were machined from a 240-mm-thick ring of a rejected forging of the reactor pressure vessel steel 22NiMoCr37 with low base material toughness.

The single-edge notched (SEN) and small compact specimens have been notched in T-S direction, while the 8T compact specimen is in a T-L orientation.

The mechanical properties of the material at the test temperature of 65°C are yield stress $\sigma_Y = 420$ MPa, ultimate tensile stress $\sigma_u = 560$ MPa, Young's modulus $E = 210$ GPa (see full stress-strain curve in Fig. 5), Poisson's ratio $\nu = 0.3$, and Charpy energy 80 J (for LT) and 150 J (for TL). The J-resistance curve shown in Fig. 2 was measured by the method of partial unloading compliance [*7*] on two small (2T) compact specimens with 20 percent side grooves using an expression for J with crack growth correction as in Ref *8*. The critical J-value for the onset of crack extension is $J_i = 145$ kJ/m^2. The tearing modulus T decreases with increasing crack extension from an initial value of about 100 to about 10 at $\Delta a = 8$ mm. For the T-L direction, slightly smaller values have been found.

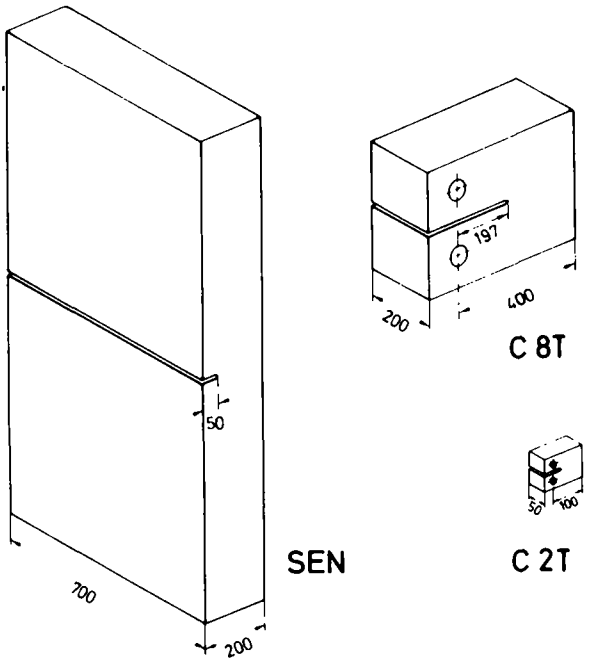

FIG. 1—*Geometry of large-scale specimens SEN and C8T tested by MPA Stuttgart [5,6] and of the C2T specimens used for generation of J-resistance curve; all dimensions in millimetres.*

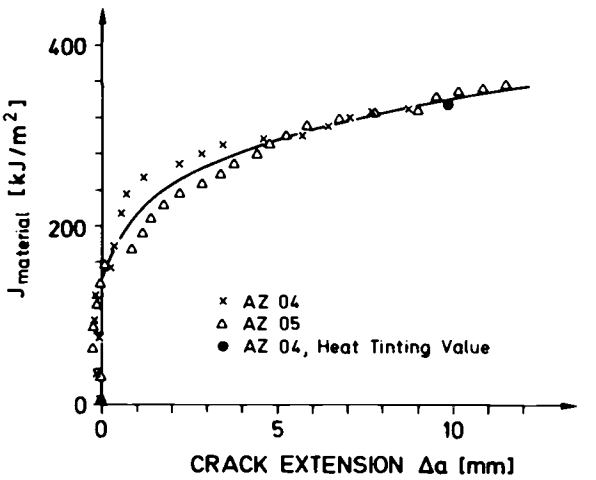

FIG. 2—*Crack resistance curve for the material 22NiMoCr37 (T-S orientation) used in this investigation, obtained from small (2T) compact specimens with 20 percent side grooves tested at 65°C:* $J_i \approx 145\ kJ/m^2$, $10 < T < 100$.

Calculation Methods

Using the description of the stress-strain field in the vicinity of the crack tip in terms of $J_{applied}$, the material resistance to crack extension Δa may be characterized by a J-resistance curve, $J_{material}$ (Δa). While the onset of crack extension occurs at a specific value of $J_{applied}$

$$J_{applied} = J_{material} (= J_i) \tag{1}$$

further increase of loading may be necessary for the crack to become unstable. Under conditions of "J-controlled crack growth" the instability is reached at [9]

$$\frac{dJ_{applied}}{da} \geq \frac{dJ_{material}}{da} \tag{2}$$

The Engineering Approach for an approximate calculation of $J_{applied}$ assumes the material obeying a Ramberg-Osgood stress-strain law

$$\frac{\phi}{\phi_0} = \frac{\sigma}{\sigma_0} + \alpha \left(\frac{\sigma}{\sigma_0} \right)^n \tag{3}$$

where

ϕ and σ = true strains and stresses,
index o = reference stress/strain, and
α and n = material constants describing strain hardening.

Then is was shown (see for instance Ref 3) that $J_{applied}$ could be approximately calculated as the sum of a linear elastic strain energy release rate

$$G = \frac{K^2}{E'} = f_1 (a_{eff}) \frac{F^2}{E'} \tag{4}$$

calculated for a plasticity-corrected effective crack length a_{eff} and a fully plastic solution with the functions h_1 $(a/t, n)$ being tabulated in Refs 2 and 10 for some cases

$$J_{applied} = f_1 (a_{eff}) \frac{F^2}{E'} + \alpha \cdot \sigma_0 \cdot \phi_0 \cdot c \cdot h_1 (a/t, n) \left(\frac{F}{F_L} \right)^{n+1} \tag{5}$$

where

F = applied load,
F_L = limit load of cracked specimen based on σ_0 as material parameter,
c = geometric constant,

K = stress-intensity factor,
t = specimen width,
a = crack length,
E = Young's modulus,
ν = Poisson's ratio, $E' = E\,(1 - \nu^2)$ for plane strain, and $E' = E$ for plane stress.

Having $J_{applied}$ from Eq 5 (h_1 linearly interpolated for intermediate values of a/t) and $J_{material}$ (Δa) being known, the stable growth of a crack in a specific geometry may now be analyzed numerically step by step as sketched in Fig. 3*a*: Extend the crack incrementally, check the instability condition (Eq 2) at constant load, increase the load to such value (iteration) that $J_{applied}$ $(\sigma, a + \Delta a) = J_{material}$ (Δa), and repeat crack extension steps up to the instability point.

The FAD procedure [*11*] avoids explicit calculation of $J_{applied}$ by characterizing the cracked structure through the limiting cases of linear elastic and plastic collapse behavior, and—by comparing it in a normalized diagram with a semi-empirical failure curve—statements on safe or unsafe loads can be derived. Including stable crack growth by the generalized parameters [*4*]

$$K_r = \frac{K(a + \Delta a)}{\sqrt{J_{material}\,(\Delta a)/E'}} \tag{6a}$$

$$S_r = \frac{F_{applied}}{F_{Limit}(a + \Delta a)} \tag{6b}$$

instability loads can be determined following a suggested graphical method or numerically as in Fig. 3*b*: the load is increased and the crack is extended step by step in such a way that the normalized crack loading curve follows the assessment line

$$K_r = S_r \left[\frac{8}{\pi^2} \ell n \sec \left(\frac{\pi}{2} S_r \right) \right]^{-1/2} \tag{7}$$

up to the instability point. Following the derivation of an assessment line from J-controlled growth in Ref *12*, the procedure of the instability load assessment using FAD [*4*] can be considered as an approximate determination of the tearing instability load from Eq 2.

Sensitivity Study

Simplifying assumptions concerning the stress analysis of the cracked component have to be made for the application of either one of the methods described in the preceding paragraph, and the material input data are usu-

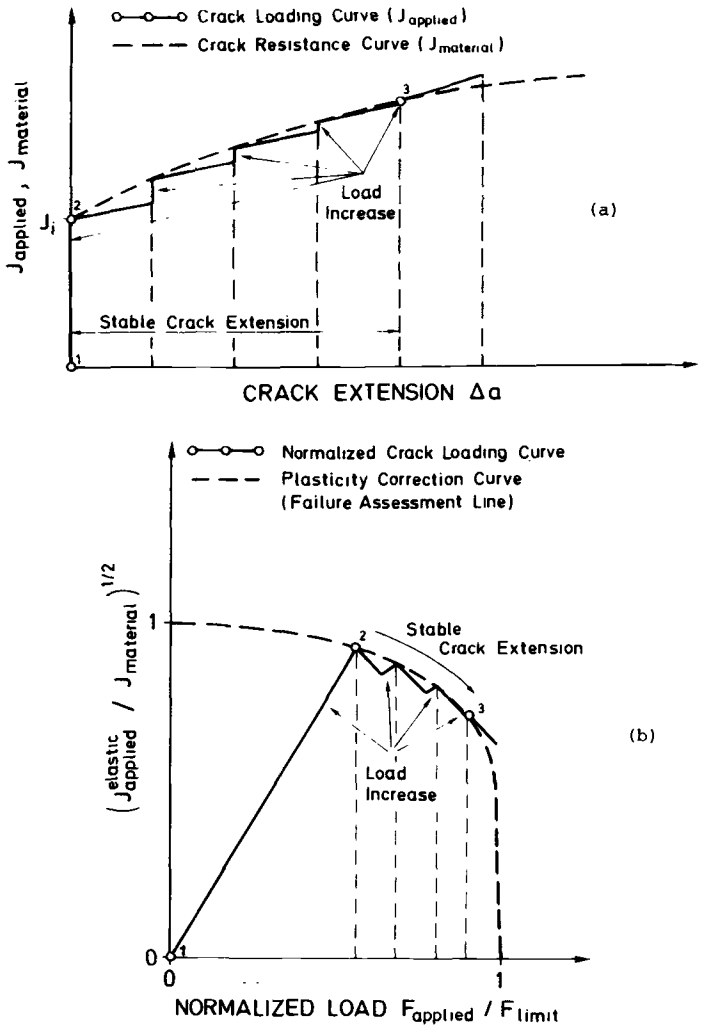

FIG. 3—*Stepwise calculation of crack initiation, stable crack growth, and tearing instability, using* (a) J *versus* Δ a *diagram,* (b) *failure assessment diagram:* o^1 *onset of loading;* o^2 *crack initiation;* o^3 *tearing instability.*

ally known only with a limited accuracy. Therefore a sensitivity study was conducted to establish their influence on the predictions of failure behavior.

The influence of limit load calculation when using the FAD method is demonstrated in Fig. 4 for the specimens of Fig. 1. From Refs *2* and *13* different solutions for the limit stress σ_L under conditions of either plane strain or plane stress are listed for the SEN and C specimens in Fig. 4 and are used to evaluate the critical loads for crack initiation and tearing instability. The

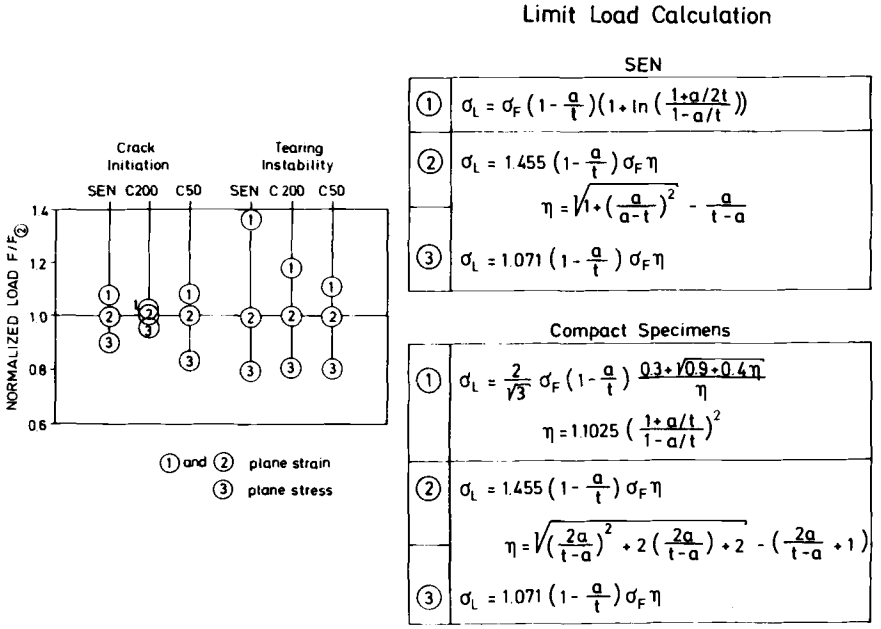

FIG. 4—*Influence of limit load calculation on the loads for crack initiation and tearing instability evaluated with FAD procedure for specimens of Fig. 1.*

flow stress $\sigma_F = (\sigma_Y + \sigma_u)/2$ was used to account for strain hardening in an at least approximate manner; stress-intensity factors were calculated from Ref *14*

SEN specimen:

$$K = \left[\frac{2t}{\pi a}\tan\frac{\pi a}{2t}\right]^{1/2}\frac{0.752 + 2.02\,(a/t) + 0.37\,[1-\sin(\pi a/2t)]^3}{\cos(\pi a/2t)}\,\sigma\sqrt{\pi a} \tag{8}$$

C specimens:

$$K = \left[29.6 - 185.5\frac{a}{t} + 655.7\left(\frac{a}{t}\right)^2 - 1017\left(\frac{a}{t}\right)^3 + 638.9\left(\frac{a}{t}\right)^4\right]\sigma\sqrt{a} \tag{9}$$

CCP specimen:

$$K = \left[1 - 0.025\left(\frac{a}{t}\right)^2 + 0.06\left(\frac{a}{t}\right)^4\right]\left[1/\sqrt{\cos\frac{\pi a}{2t}}\right]\sigma\sqrt{\pi a} \tag{10}$$

The variations of results in Fig. 4 for initiation and instability depend on specimen type and size; large differences in the case of the SEN specimen are possible and call for an improved stress analysis by finite-element-techniques.

If the EA method is used for determination of $J_{applied}$ the problem arises of an appropriate determination of the constants α, n, and σ_0 in a Ramberg-Osgood representation of the material stress-strain curve. Figure 5 demonstrates that for the steel used for the large-scale tests an uniformly good representation of the measured curve (crosses in Fig. 5) is not possible; Sets one and three of the parameters α and n give a fairly good description only in the linear elastic and in the strain-hardening regime, respectively. Parameter Set two is chosen as a compromise and the corresponding results from a J-Δa diagram analysis are used to normalize the critical loads for initiation and instability. The same reference stress $\sigma_0 = \sigma_Y$ is used for all three cases. Figure 5 shows for the specimens investigated differences of less than 10 percent for the extreme curve fits compared with the mean. For a safety assessment, Parameter Set three would guarantee conservativeness. The problem of determining the material constants is also discussed in Ref *15*.

In a tearing instability analysis with any method the results are influenced by the accuracy of the $J_{material}$ curve. Therefore artificial $J_{material}$ curves with $J_i = 145$ KJ/m^2 and different constant slopes were used to calculate the

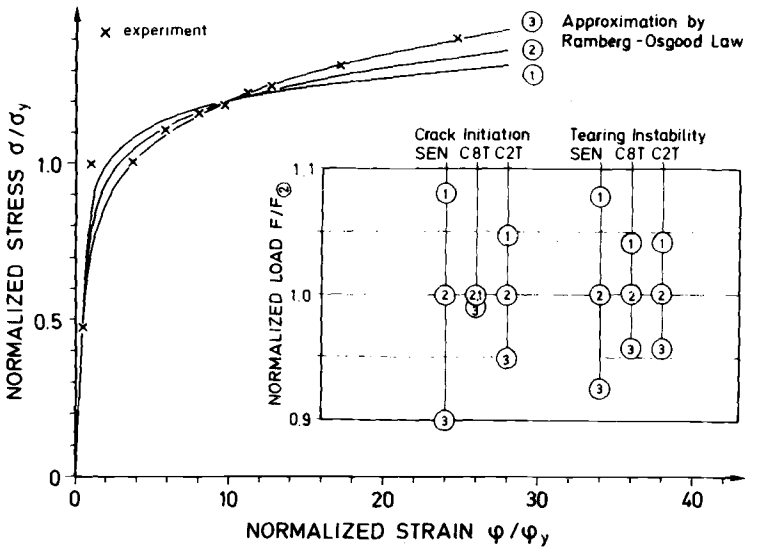

FIG. 5—*Influence of the Ramberg-Osgood approximation of the material stress-strain curve on the loads at crack initiation and tearing instability calculated from the* J-Δa *diagram using the Engineering Approach for specimens of Fig. 1.* $\sigma_0 = \sigma_y = 420$ *MPa. one:* $\alpha = 1$, n = *12;* two: $\alpha = 1.85$, n = *8.7; three:* $\alpha = 2.7$, n = *6.5.*

curves in Fig. 6 with the EA method. Resulting tearing instability loads are normalized by the respective initiation loads. The dependence of the instability loads on the slope of the $J_{material}$ curve (or the tearing modulus) is more pronounced for the C8T-specimen than for the SEN and the C2T specimens; differences in load reserve from crack initiation to instability are obvious. Also shown in Fig. 6 is the influence of the slope of the $J_{material}$ curve on the amount of stable crack growth. The numerical results demonstrate the complex interaction of material resistance and loading; in terms of load increase and extent of stable growth, tearing instability is induced close to or far after crack initiation for specimens of different geometry and size.

Comparison of Calculated and Measured Loads

For the evaluation of critical loads of the large-scale tests, rather than conservative assumptions the following most plausible stress analysis solutions and material data were used:

1. $J_{material}$ curve from 2T compact specimens with 20 percent side grooves (Fig. 2).
2. Ramberg-Osgood description of material stress-strain curve with $\alpha = 1.35$, $n = 10$, and $\sigma_0 = \sigma_y$, similar to two in Fig. 5.
3. $\sigma_F = (\sigma_y + \sigma_u)/2$ for limit load calculation in the FAD method.

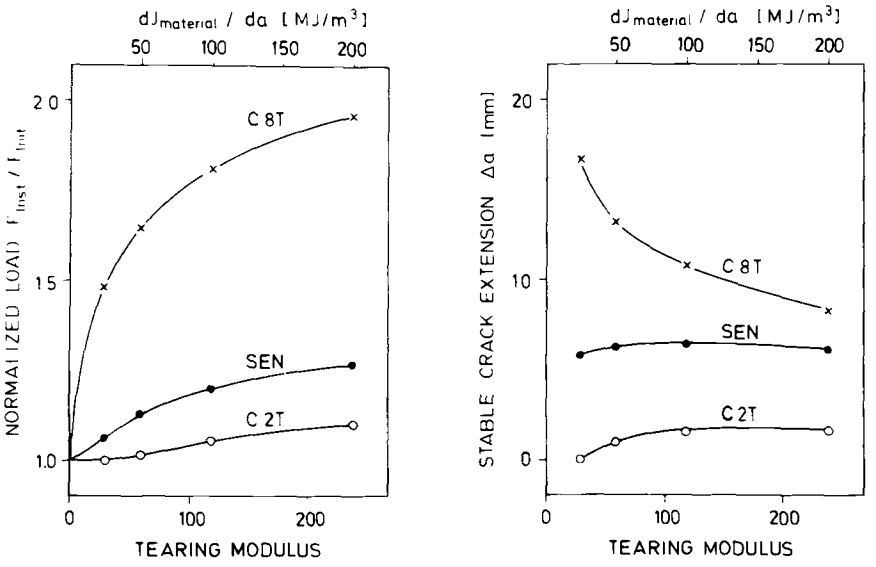

FIG. 6—*Influence of the tearing modulus on the loads at instability* F_{Inst} *and on the stable crack growth* Δa *for specimens of Fig. 1; Engineering Approach used.*

4. Plane-strain conditions for evaluation of limit loads (Eqs 2 in Fig. 4) and fully plastic solutions h_1 $(a/t, n)$
5. Stress-intensity factors from Eqs 8–10.
6. For the CCP specimen the limit load formula

$$\sigma_L = \frac{2}{3}\left(1 - \frac{a}{t}\right)\sigma_F \tag{11}$$

Results for crack initiation and instability of two large-scale specimens are shown in Fig. 7 normalized with the actual failure loads from the tests. Good agreement of the instability loads calculated by the EA and FAD methods with the measured ultimate load is found for the 8T compact specimen. A margin of safety of 25 percent compared with crack initiation is predicted. The result may, however, be influenced by the different crack orientations in the C8T tests and in the J-R curve evaluation.

The agreement is less satisfactory for the SEN specimens. Since the bending is partly restricted in the experiment, another evaluation was made using the center-cracked panel (CCP) with $a/t = 0.25$ and $2t = 400$ mm as a model. This should give an upper bound for the description of the instability behavior. Figure 7 shows the mean value of the two instability predictions still lying somewhat below the observed failure load. A reason for this may be the use of the J_{material} curve of Fig. 2, which is expected to be conservative for this tension loaded-type of specimen (see for instance Ref *16*). As a whole the results from the FAD calculation appear less reliable for this case than those

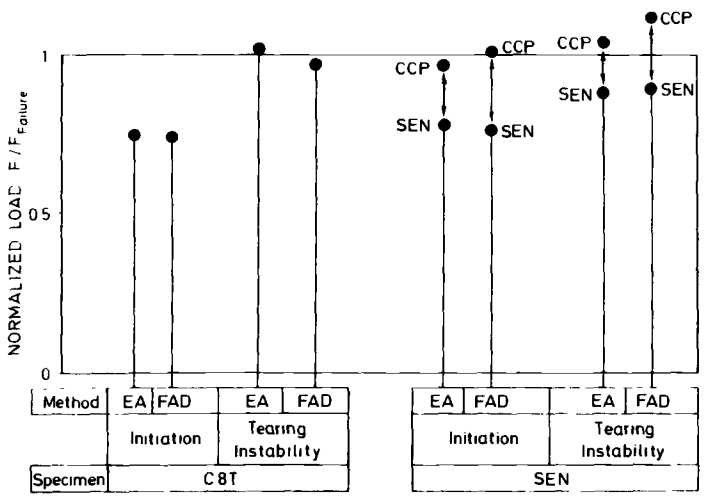

FIG. 7—*Comparison of calculated loads at crack initiation and tearing instability with failure loads obtained experimentally for large-scale specimens of Fig. 1.*

from the EA method because the SEN specimen failed near limit load; the limit load depends on strain hardening, which is taken into account only in a very approximate way in the FAD method.

Discussion

Serious problems may be encountered if EA or FAD is used in a tearing instability analysis. There may be uncertainties of the input data not only due to limited accuracy of material data ($J_{material}$ curve, stress-strain curve), but also due to options like choice of stress state, equations for limit load, and description of stress-strain curve. Therefore full agreement of calculated instability loads with measured failure loads cannot generally be expected and an experimental validation of methods should be based on as large a number of experiments as possible.

In case of a safety assessment all uncertainties can be covered by conservative assumptions and procedures. In order to reduce conservativeness and to check the validity of the methods of tearing instability analysis, especially the following points of uncertainty need further investigation:

1. Geometry dependence of $J_{material}$ curve and range of J-controlled crack growth.
2. Appropriate description of material stress-strain curve through Ramberg-Osgood law.
3. Choice of plane-stress or plane-strain conditions for prevailing test situation.

Conclusions

Evaluation of the failure behavior of two types of large-scale specimens using the "Engineering Approach" by Shih and the "Failure Assessment Diagram" generalized by Milne allows the following conclusions:

1. Failure loads obtained by each of the methods agree reasonably well with measured ones.
2. Results of instability analyses are very sensitive to some input data and parameters, which are known with only a limited accuracy. Consequently a limited accuracy of resulting instability loads has to be expected.
3. A conservative assessment of failure loads can be made.
4. A final judgment on the accuracy and the ease of use of the two methods is not yet possible.

Acknowledgments

The authors acknowledge financial support by the Government of the Federal Republic of Germany and by Materialprüfungsanstalt Stuttgart

through Contract FKS-82 0115-185 IWM 0480/80, and would like to thank Dr. L. Issler for fruitful discussions.

References

[1] Paris, P. C. et al in *Elastic-Plastic Fracture, ASTM STP 668*, American Society for Testing and Materials, 1979, pp. 5-36.

[2] Shih, C. F. and Kumar, V., "Estimation Technique for the Prediction of Elastic-Plastic Fracture of Structural Components," First Semiannual Report for the Electric Power Research Institute, Palo Alto, Calif., 1 June 1979.

[3] Kumar, V. and Shih, C. F. in *Fracture Mechanics: Twelfth Conference, ASTM STP 700*, American Society for Testing and Materials 1980, pp. 406-438.

[4] Milne, I., *Material Science and Engineering*, Vol. 39, 1979, pp. 65-79.

[5] Krägeloh, E., Issler, L, and Zirn, R., "Analyse von Grossprobenversuchen mit Zähbruchkonzepten," Elastic-Plastic Fracture Concepts, 6th Seminar of the Staatliche Materialprüfungsanstalt (MPA), Stuttgart, Vol. 6, Oct. 1980.

[6] Kussmaul, K. and Issler, L., this publication, pp. II-41-II-57.

[7] Clarke, G. A., et al in *Mechanics of Crack Growth, ASTM STP 590*, American Society for Testing and Materials, 1975, pp. 27-42.

[8] Standard Test for J_{Ic}, A Measure of Fracture Toughness, ASTM Designation E 813-81, *Book of Standards*, Part 10, American Society for Testing and Materials, 1982.

[9] Hutchinson, J. W. and Paris, P. C., in *Elastic-Plastic Fracture, ASTM STP 668*, American Society for Testing and Materials, 1979, pp. 37-64.

[10] Kumar, V., German, M. D., and Shih, C. F., "An Engineering Approach for Elastic-Plastic Fracture Analysis," EPRI Report NP-1931, Electric Power Research Institute, Palo Alto, Calif., July 1981.

[11] Harrison, R. P., Milne, I., and Loosmore, K., "Assessment of the Integrity of Structures Containing Defects," Central Electricity Generating Board Report R/H/R6, Revision 1, Leatherhead, Surrey, U.K., 1977.

[12] Shih, C. F., German, M. D., and Kumar, V., "An Engineering Approach for Examining Crack Growth and Stability in Flawed Structures," General Electric Co. Report No. 80 CRD 205, Schenectady, N.Y. Sept. 1980.

[13] Chell, G. G., in *Developments in Fracture Mechanics I*, G. G. Chell, Ed., Applied Science Publishers, London, 1979.

[14] Tada, H., Paris, P. C., and Irwin, G. R. in *The Stress Analysis of Cracks Handbook*, Del Research Corp., Hellertown, Pa. 1973.

[15] Issler, L., Birk, R., and Hund, R., "Anwendung eines neuen Näherungsverfahren aus den USA zur Zähbruchanalyse," Elastic-Plastic Fracture Concepts, 6th Seminar of the Staatliche Materialprüfungsanstalt (MPA), Stuttgart, Oct. 1980.

[16] Garwood, S. J. in *Fracture Mechanics: Twelfth Conference, ASTM STP 700*, American Society for Testing and Materials, 1980, pp. 271-295.

Theodore U. Marston,[1] *Robin L. Jones,*[1] *Melvin F. Kanninen,*[2] *and Donald F. Mowbray*[3]

Development of a Plastic Fracture Methodology for Nuclear Systems

REFERENCE: Marston, T. U., Jones, R. L., Kanninen, M. F., and Mowbray, D. F., **"Development of a Plastic Fracture Methodology for Nuclear Systems,"** *Elastic-Plastic Fracture: Second Symposium, Volume II—Fracture Resistance Curves and Engineering Applications, ASTM STP 803,* C. F. Shih and J. P. Gudas, Eds., American Society for Testing and Materials, 1983, pp. II-115–II-132.

ABSTRACT: This paper describes research conducted to develop a fundamental basis for flaw tolerance assessment procedures suitable for components exhibiting ductile behavior. The research was composed of an integrated combination of stable crack growth experiments and elastic-plastic analyses. A number of candidate fracture criteria were assembled and investigated to determine the proper basis for plastic fracture mechanics assessments. The results demonstrate that many different fracture criteria can be used as the basis of a resistance curve approach to predicting stable crack growth and fracture instability. While all have some disadvantages, none is completely unacceptable. On balance, the best criteria were found to be the J-integral for initiation and limited amounts of stable crack growth and the local crack-tip opening angle for extended amounts of stable growth. A combination of the two, which may preserve the advantages of each while reducing their disadvantages, also was suggested by these results. The influence of biaxial and mixed flat/shear fracture behavior was investigated and found to not alter the basic results. Further work in the development of simplified ductile fracture analyses for routine engineering assessments of nuclear pressure vessels and piping evolving from this research is also described.

KEY WORDS: fracture, crack propagation, J-integral, elastic-plastic fracture methodology, crack-tip opening angle, crack opening displacement, 2219-T87 aluminum, A533B steel, elastic-plastic fracture

A key element in nuclear component structural integrity assessments that has been lacking until recently is the ability to account accurately for the presence of flaws. The linear elastic fracture mechanics (LEFM) procedures

[1]Electric Power Research Institute, Palo Alto, Calif. 94303.
[2]Battelle, Columbus, Ohio 43201.
[3]General Electric Co., Schenectady, N.Y.

currently embodied in the American Society of Mechanical Engineers (ASME) Boiler and Pressure Vessel Code and in the Code of Federal Regulations are based upon essentially brittle fracture behavior. Hence, they can seriously underestimate the flaw tolerance of nuclear pressure boundary components (for example, load estimates can differ by as much as a factor of three) that are often chosen specifically for their exceptional toughness and ductility. Analysis methods that treat the ductile fracture mode therefore are needed to obtain accurate flaw tolerance assessments for components made from such materials.

Nonlinear fracture mechanics techniques taking direct account of inelastic material behavior have been proposed that could be applied to nuclear plant components. However, in the mid-1970's when the research described in this report was conceived, the most appropriate approach was not known. Accordingly, the Electric Power Research Institute (EPRI) developed a research effort to provide a fundamental basis for such assessments. This was done through companion research programs conducted at Battelle's Columbus Laboratories [*1*][4] and General Electric's Research and Development Laboratory [*2*]. The approach used and the key results obtained in these efforts, which formed the spearhead of EPRI's plastic fracture analysis group [*3*], are described in this paper.

Objectives of the Research

Nuclear plant components could be subjected to pressure and thermal stresses well beyond normal working levels during accident conditions such as a loss-of-coolant accident (LOCA) and an anticipated transient without scram (ATWS). Present design analyses include an assessment of the safety margin for postulated accidents via LEFM. But, because crack extension is accompanied by large-scale plastic deformation in the tough, ductile materials used in nuclear applications, LEFM-based analysis procedures are not applicable. The stable crack growth that precedes fracture instability generally confers an added margin of safety, but adds further complexity. The objective of this research was to develop a firm basis for a plastic fracture methodology in place of LEFM that could be used to obtain realistic assessments of the risk of failure in flawed nuclear pressure vessels and piping.

Fracture analysis in the plastic regime must address a number of complications not present in the elastic case. Foremost are the inherent nonlinearities in the material deformation and large geometry changes together with the fact that flaws will propagate in a stable manner prior to final fracture. Hence, a plastic fracture methodology must explicitly treat crack initiation and the subsequent stable crack growth to the onset of the ultimate unstable crack propagation. These events are illustrated schematically in Fig. 1.

[4]The italic numbers in brackets refer to the list of references appended to this paper.

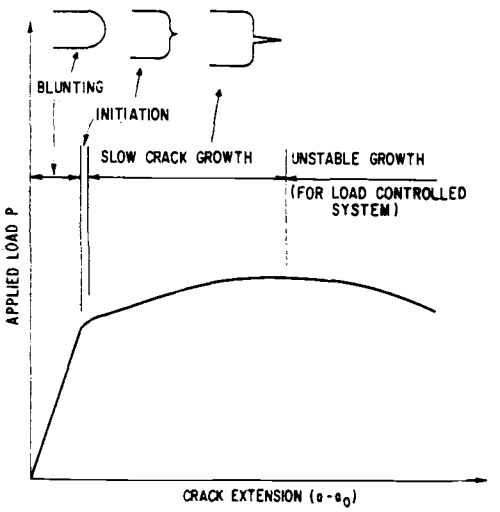

FIG. 1—*Schematic illustration of ductile fracture progression [2].*

The onset of unstable growth in the compliant loading systems that typify actual engineering structures will likely occur beyond the maximum load; see Fig. 1. Hence, a system-dependent technique for determining the point of fracture instability is an important aspect in the development of a plastic fracture methodology. Further complications involve the possibility of a mixed-character fracture process (that is, crack extension in both the flat and shear modes) and of multiaxial states of loading. All of these factors were addressed in this research.

General Approach and Results

The key element in the development of a plastic fracture methodology surely is a crack-tip criterion valid in the presence of large-scale plastic deformation. A variety of candidates was judged in a research program that proceeded through three main phases. First, a list of candidate fracture parameters was selected and assembled. The second and third phases involved a combination of experimentation and analysis using laboratory test specimens of A533B steel and a "toughness-scaled" aluminum alloy to obtain data on crack growth initiation, stable growth, and fracture instability. This provided a basis for judging the candidate parameters. The parameters selected for examination in this research are given in Table 1.

Specifically, "generation-phase" initial filter analyses were performed to obtain confirmation of the candidate fracture parameters by comparing experiments with analyses. In these analyses the observed applied stress versus stable crack growth data were used as input to a finite-element model. This

TABLE 1—*Candidate fracture criteria for the basis of a plastic fracture methodology*

Criterion Symbol	Identification	Designation of Critical Value
G	LEFM energy release rate	R
$J(T)$	J-integral (tearing modulus)	$J_c(T_{mat})$
$\mathcal{S}$	generalized energy release rate	$\otimes$
COA	average crack opening angle	$(COA)_c$
CTOA	crack-tip crack opening angle	$(CTOA)_c$
F	finite element crack tip node force	F_c
G_0	elastic-plastic energy	G_{0c}
G_Z	computational process zone energy release rate	G_{Zc}

procedure simultaneously generated critical values of each candidate criterion. Then, "application-phase" evaluation analyses were performed to evaluate the fracture parameters and the corresponding concepts. These used a particular criterion to predict initiation, stable growth, and fracture instability for several different geometries and loading conditions for which experimental results were available. The general procedure is illustrated in Fig. 2.

The candidate parameters that were selected represented a measure of the stress/strain state at the crack tip and should therefore be independent of initial crack length and geometry. The evaluation of crack-growth parameters

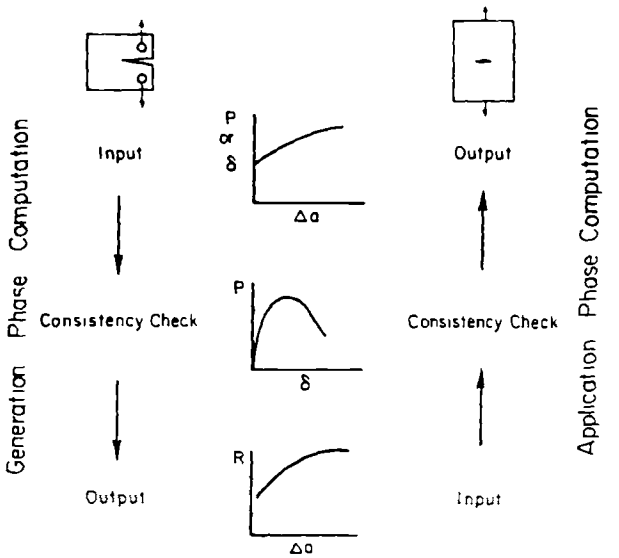

FIG. 2—*Development of a plastic fracture methodology using finite-element analysis and experimental crack growth measurements [1].*

considered the aforementioned parameters plus their rate of change with respect to crack length. Several additional requirements that were placed on the parameters included (1) a minimal sensitivity to the finite-element mesh and load increment size, (2) reasonable computational costs, and (3) applicability to three-dimensional geometries and mixed-mode fracture problems.

Implementation of the preceding strategy required several novel developments in both the computational and the experimental portions of the research. Appropriate crack-tip elements were established for characterizing the singular deformation fields of stationary and propagating cracks in plastically strained material. Special routines were devised for computing the J-integral over a number of integration paths. Also, means for extending cracks across a finite-element grid by node shifting and release techniques were established. In the experimental research, highly sensitive measurement techniques were developed for detecting crack-tip opening displacements and crack extensions during the testing of large fracture specimens. Also, side-grooved specimens were utilized to promote flat, plane-strain fracture and their applicability was justified through analysis and experiments.

Results typical of those obtained in the generation-phase or initial filter stage of the program are shown in Figs. 3, 4, and 5. Figure 3 shows the prescribed and simulated load-line displacement versus crack extension curves for General Electric's Test T-52, a 4T compact specimen having a 25 percent depth side groove (the experimental data are also shown). The finite-element simulation can be seen to accurately follow the prescribed data. Figure 4 shows the calculated load versus load-line displacement curve. The calculated result is in excellent agreement with the experimental results, indicating that the plane-strain modeling of side-grooved specimens is appropriate. Figure 5 shows a comparison between the J-resistance values obtained from this specimen and a number of other 4T, 25 percent side-grooved compact tension specimen experiments.

Characteristic results for the two parameters generally considered to be the most useful—J and crack-tip opening angle (CTOA)—are shown in Figs. 6 and 7. These were obtained from Battelle's compact tension tests on the "toughness-scaled" aluminum alloy 2219-T87,[5] and they display behavior very similar to that obtained by General Electric (GE) in A533B steel, indicating the universality of the results being obtained. Of particular interest, the monotonically increasing behavior of the J-resistance curve can be contrasted with the constancy achieved by the CTOA-resistance curve after an initial transient.

A detailed appraisal of the collection of candidate plastic fracture parameters considered in this study is beyond the scope of this paper. Those results have to some extent already been disseminated—see Refs *4–9*. It will suffice

[5]Toughness scaling implies that the thickness of the test specimens was small enough that the characteristic ratio $(K_{Ic}/t\sigma_Y)$, where t is the plate thickness and σ_Y the yield strength, was comparable to that of A533B steel used in actual applications.

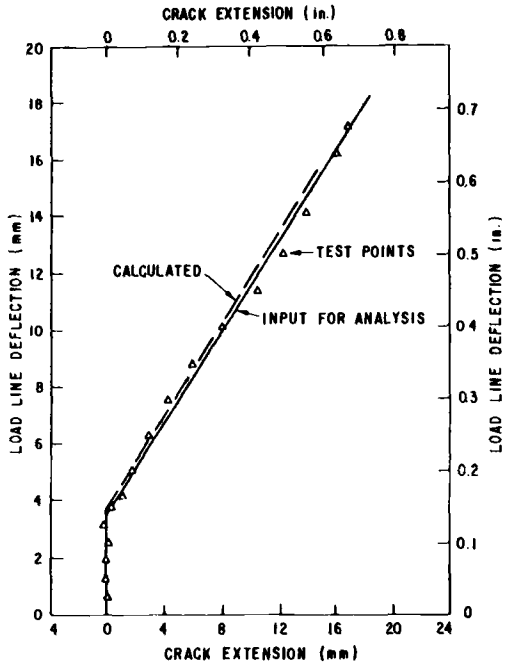

FIG. 3—*Load-line displacement versus crack extension curves for GE A533B steel compact-tension specimen T-52 [2].*

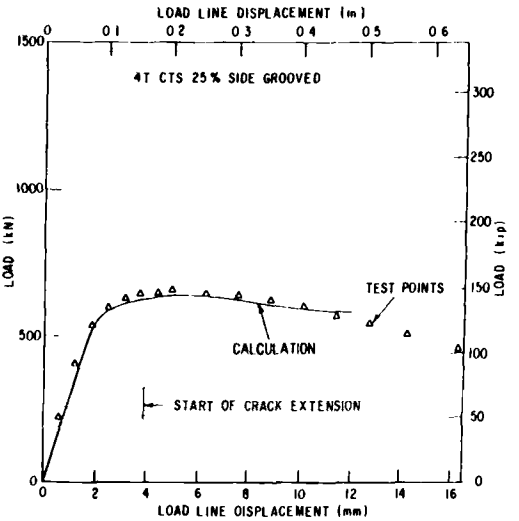

FIG. 4—*Load versus load-line displacement for GE A533B steel compact-tension specimen T-52 [2].*

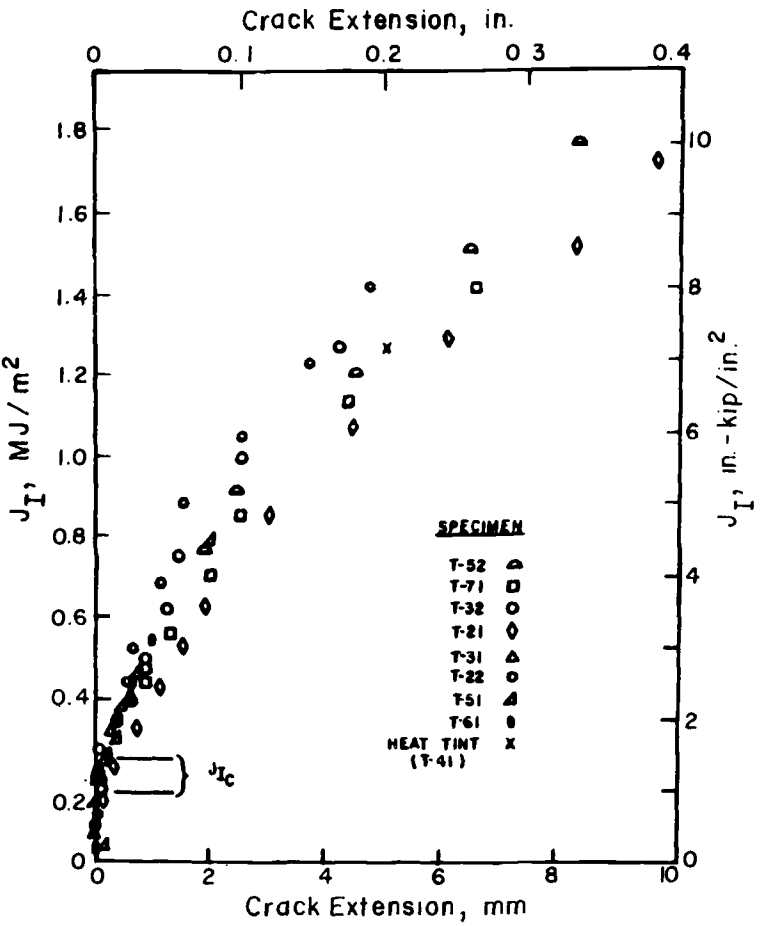

FIG. 5—*J-resistance data for GE A533B steel 4T compact-tension specimens with 25 percent side grooves [2].*

to say here that all the parameters appearing in Table 1 have merit and none can be unequivocally rejected. The energy release rate parameters (see Ref *4* for the various permutations that exist), despite the fundamental objection raised first by Rice [*10*], can be made to work [*19*]. Nevertheless, it now appears that two of the candidate parameters are superior: *J* and CTOA. These will be pursued in the following.

Theoretical Basis for *J* and CTOA as Plastic Fracture Parameters

The theoretical basis for the use of *J* and CTOA as plastic fracture parameters stems from the asymptotic crack-tip stress and strain field solutions orig-

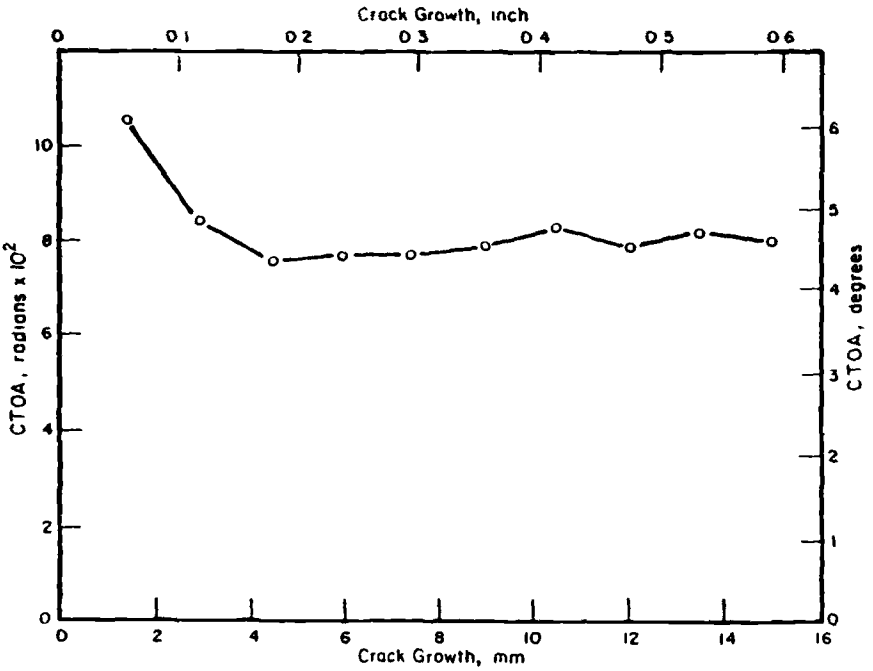

FIG. 6—*Crack-tip opening angle resistance curve for 2219-T87 aluminum generated from a Battelle compact-tension specimen [1].*

inating in the work of Hutchinson [*11*] and of Rice and Rosengren [*12*]. These are referred to as the "HRR" field equations. For stationary cracks, they have the form

$$\sigma_{ij} = \sigma_0 \left[\frac{EJ}{\sigma_0^2 I_n r} \right]^{1/n+1} \tilde{\sigma}_{ij}(\theta, n) \tag{1}$$

$$\epsilon_{ij} = \frac{\sigma_0}{E} \left[\frac{EJ}{\sigma_0^2 I_n r} \right]^{n/n+1} \tilde{\epsilon}_{ij}(\theta, n) \tag{2}$$

where

n and σ_0 = material flow parameters (the strain-hardening exponent and yield strength, respectively),
r and θ = polar coordinates centered at the crack tip,
I_n = integration constant depending on n only, and
$\tilde{\sigma}_{ij}$ and $\tilde{\epsilon}_{ij}$ = dimensionless functions of θ and n.

Equations 1 and 2 show that J is the amplitude of the crack-tip singularity fields. Thus, the strain-energy density has a $1/r$ singularity for a stationary

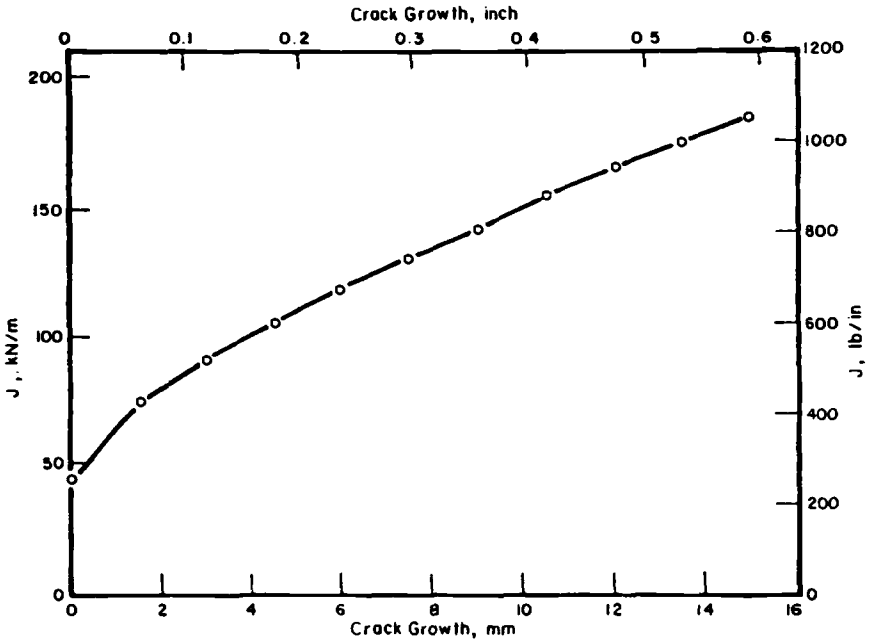

FIG. 7—*J-resistance curve for 2219-T87 aluminum generated from a Battelle compact-tension specimen [1].*

crack. Similar relationships and meaning can be obtained for the crack-tip opening displacement δ_t, since J and δ_t for a stationary crack are simply related by

$$\delta_t = d_n \frac{J}{\sigma_0} \tag{3}$$

where d_n is a function of the strain-hardening exponent and the stress state [9].

To the extent that J and δ_t characterize the stationary crack-tip field, the onset of crack extension can be identified with critical values of J and δ_t (for example, J_{Ic} and δ_{Ic}). Single-parameter descriptions such as these will be valid as long as the HRR singularity dominates the fracture process zone. To assure this condition, requirements must be imposed on the degree of plane-strain constraint that is maintained at the crack tip. Computational and experimental studies were conducted in the GE research to assist in defining these requirements.

During stable crack growth, the crack-tip fields are far more complex than for stationary cracks. Rice [13] has shown that the singularity in the strain field is milder, of the form $\ell n(1/r)$. Analysis of these fields shows that, if the

HRR field increases in size more rapidly than it advances due to stable crack growth, the crack-tip environment can be described by dJ/da or $d\delta_t/da$. Finite-element simulations of growing cracks were used to more explicitly define the limitations of these parameters.

The finite-element computational work employed general-purpose codes with suitable modifications for fracture analyses. Specifically, computational routines were established for calculating the J-integral over a number of integration paths during each load step in a nonlinear analysis. Also, the codes were modified to permit the propagation of cracks through the finite-element mesh while the nonlinear step-by-step calculation is performed, and to permit the rate of the propagation to be controlled by a specified parameter. The crack growth was accomplished by node shifting and node release.

The elastic-plastic finite-element analyses were carried out using two-dimensional elements, assuming plane-strain or plane-stress behavior. Plane-strain models of actual three-dimensional problems were possible because side grooves were employed in many of the fracture test specimens. Side-groove depths of about 25 percent were sufficient to promote flat fracture with straight crack fronts in the experiments, as required for the modeling to correctly simulate the desired physical behavior. Also supporting this position are results from elastic three-dimensional finite-element analyses on specimens of varying side-groove depth [*2*]. These results show a 25 percent side-groove depth to be optimum in that the stress-intensity factor and plane-strain constraint are nearly uniform through the thickness and of the same magnitude as that for idealized plane-strain deformation.

The use of a J-resistance curve is subject to some limitations, as pointed out by Hutchinson and Paris [*14*]. Further analytical and numerical studies [*7,8*] have shown that several requirements must be met to ensure that crack growth can be characterized by J or δ_t. There is a section or ligament size requirement which basically guarantees sufficient constraint to maintain the dominance of the HRR field. This requirement is dependent upon the geometry and applied load system. For bending load cases such as the compact specimen, the ligament and thickness must exceed 25 times J_{Ic}/σ_0, while for tensile loading of the center-cracked panel (CCP) specimen, the size requirement is 200 times J_{Ic}/σ_0. Additionally, the normalized slopes of the resistance curves must be sufficiently large. Mathematically, these can be stated as [*14*]

$$\frac{b}{J_{Ic}}\frac{dJ}{da} >> 1.0 \tag{4}$$

and

$$\frac{\sigma_0}{E}\frac{d\delta_t}{da} >> 1.0 \tag{5}$$

where b is the uncracked ligament length and E the modulus of elasticity.

The path-dependence of J must be considered when evaluating it as a plastic fracture parameter. The GE work [2] determined values for J on a set of integration paths that ranged from one very near the crack tip to one fairly remote from the crack tip. The results were designated J_2, J_3, ... where J_2 is evaluated in the region dominated by the HRR singularity while the higher-number subscripts denote evaluation along progressively more remote contours. The analytical studies show that J_{MC}, the value of the J-integral calculated using the Merkle-Corten relation [20], is the value of J measured experimentally using load-displacement records. The variation of these parameters with crack extension is illustrated in Fig. 8.

Figure 8 shows that while J_{MC} continues to increase, J_2 begins to level off after some crack extension [2]. Thus, (dJ_2/da) falls to zero and thereby violates one of the requirements for J-controlled growth; see Eq 4 inequality. On the other hand, the crack-opening angle, after an initial transient, remains

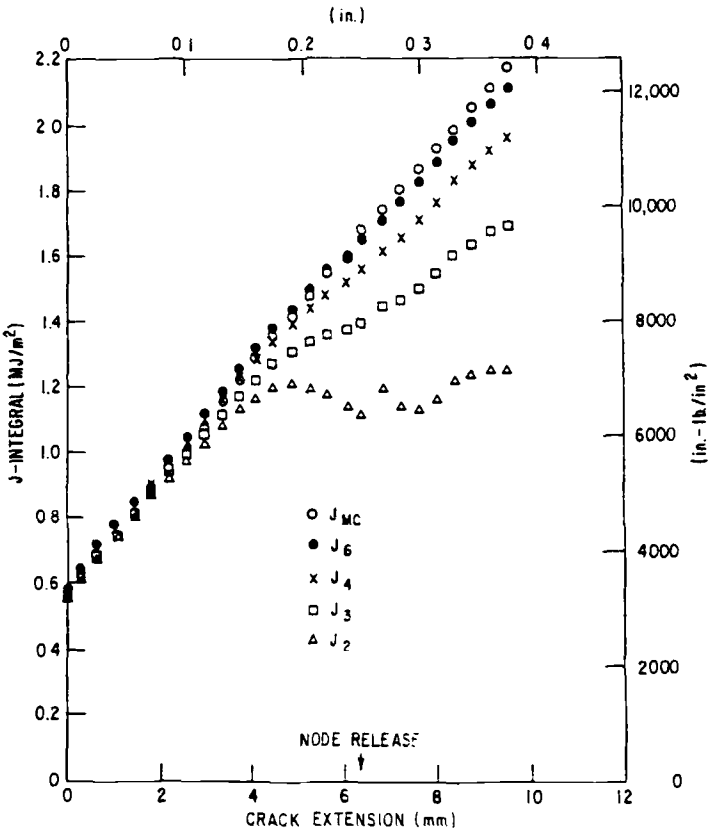

FIG. 8—*J-resistance curves evaluated at different contours on the GE A533B steel compact-tension specimen T-52 [2].*

constant for a considerable range of crack growth [2]. This satisfies the requirement for CTOA-controlled growth specified by Eq 5 inequality. It also appears that, beyond the initial stage of crack growth, a constant critical value of the CTOA may be employed to characterize stable growth. This is not unexpected since the CTOA can be derived from more fundamental considerations.

A key calculation was performed by Battelle to predict the load-crack growth behavior in a wide center-cracked panel of 2219-T87 aluminum using criteria determined from compact-tension (CT) test results. The results are shown in Fig. 9. It can be seen that the predictions using J and CTOA are both reasonable. However, the combination of J and CTOA designated as J/CTOA in Fig. 9 is clearly the most accurate. In all calculations, initiation was specified to occur at the J_{Ic}-value determined in the CT tests. Also, the

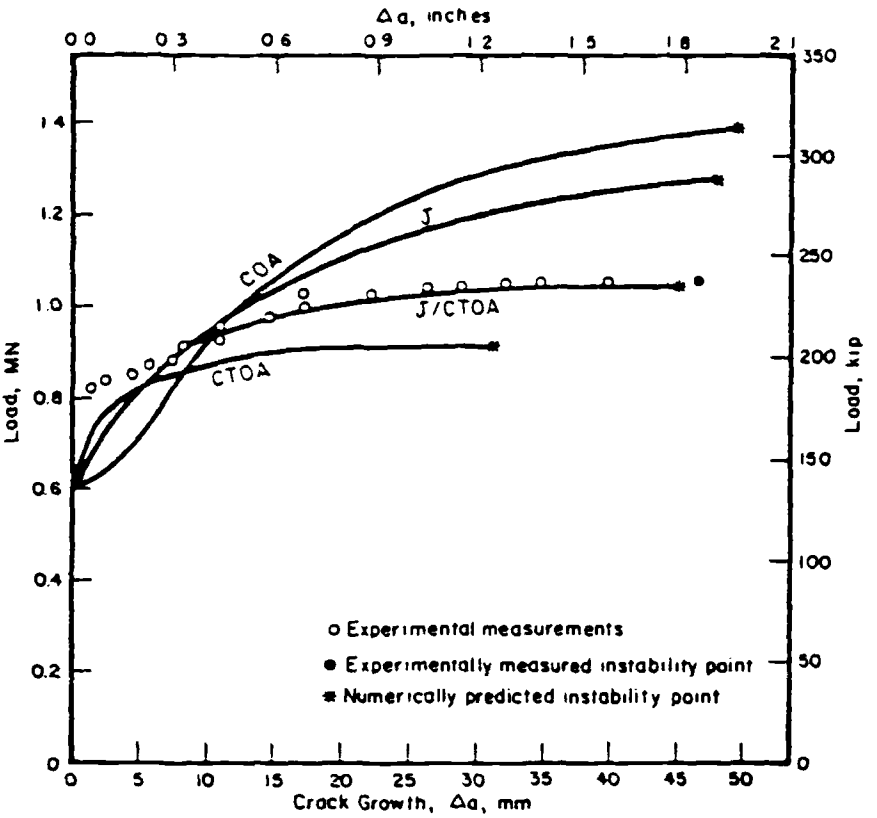

FIG. 9—*Critical comparison of plastic fracture criteria by application-phase analysis of a wide center-cracked panel using resistance curves determined from CT specimen tests on 2219-T87 aluminum [1].*

CTOA resistance curve was a constant value corresponding to the measured plateau value.

In the combined *J*/CTOA approach, the *J*-resistance curve was used for initiation and some amount of stable crack growth with an internally computed CTOA-value used thereafter. This procedure seems most promising as it takes full advantage of the *J*-resistance curve approach without suffering from its restriction to small amounts of crack growth. It also uses the observed constancy of CTOA while circumventing the complications of the initial transient in this parameter. Yet, because the critical CTOA to be used for extensive growth is one that is *calculated* during the early stages of crack growth, the combined-parameter approach does not require any further experimental measurements.

Influence of Biaxial and Mixed-Character Loading on the Plastic Fracture Parameters

Although a significant amount of work has been addressed to the effects of biaxial loading on fracture under LEFM conditions, little was known about the importance of biaxial loading on stable crack growth accompanied by extensive crack-tip plasticity. Clearly, such effects, if any, must be known to use a plastic fracture analysis effectively. In particular, a plastic fracture mechanics crack growth parameter (for example, *J*-resistance curve) determined from a laboratory test specimen cannot exhibit substantial biaxial loading dependence if it is to be useful in assessing structural performance.

To examine this question, a number of experiments on thin 2219-T87 aluminum panels were performed by Battelle [*1,15*]. In the thickness and specimen geometry examined, extensive stable crack growth with large-scale plasticity was obtained. The experiments were performed for a range of biaxiality ratios and initial crack lengths. It was found that, while some differences in the early stages of stable crack growth occurred, biaxial loading has little effect on the failure loads for the panels. It was also found that the crack opening displacement is proportional to the nominal strain and can be directly related to the biaxiality ratio.

While it is often true that shear fracture propagation can require greater energy than does flat ductile fracture, these differences may not be large. If the absence of significant differences between the flat ductile and shear types can be confirmed, the analysis of mixed-type fractures in these materials could be greatly simplified. To obtain a quantitative assessment of this possibility, experiments were carried out by Battelle on A533B steel to compare the resistance to shear fracture with that for flat fracture.

Shear fractures were obtained with slant-notch CT specimens in which the machined notch and fatigue precracks were in the same plane as the subsequent shear fracture. Flat fractures were obtained with side-grooved CT specimens. A finite-element model was used to simulate the experimentally

observed stable crack growth and, thereby, to determine values of various crack-tip parameters to characterize the fracture toughness. Of most interest were the *J*-resistance curve and the crack opening angle parameter. These results are shown in Figs. 10 and 11 where the Battelle slant-notch specimen results on A533B steel denoted by SR are compared with General Electric's flat fracture mode test T-52.

It can be seen from Fig. 10 that the CTOA-value determined for A533B steel is essentially independent of specimen geometry and of fracture type, that is, flat or slant shear. Moreover, following an initial transient, it is constant for large amounts of crack growth. In Fig. 11 the *J*-resistance curve is similarly seen to be specimen-independent provided limit load conditions are not reached. (Under limit load conditions, the *J*-resistance becomes somewhat specimen dependent.) Hence, under conditions where the *J*-resistance parameter or the CTOA parameter provides effective characterizations of the resistance to stable crack growth, these studies indicate that the differences between flat and slant shear fractures in A533B steel are not significant [*15*].

Development and Application of an Engineering Methodology

While the present program was successful in developing a methodology for predicting ductile fracture response, the calculations necessary to apply the methodology to the flawed structures of interest required the use of sophisti-

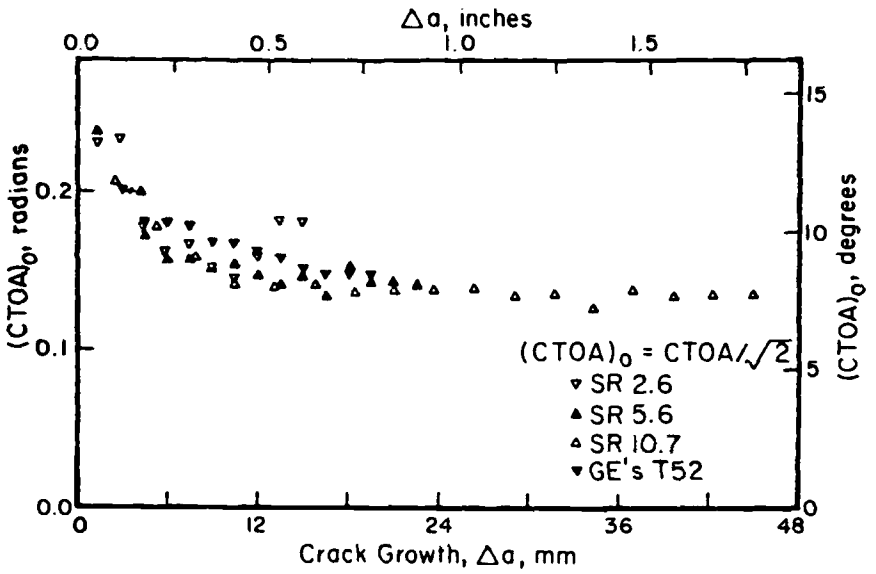

FIG. 10—*Crack-tip opening angle (CTOA), consistently defined, for flat and shear fracture in A533B steel [1].*

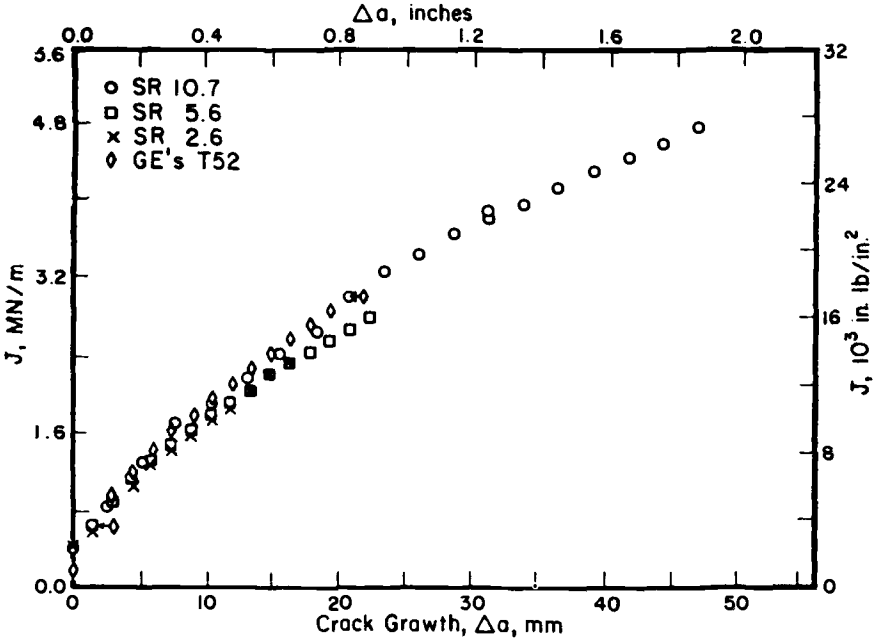

FIG. 11—*J-resistance curve for flat and shear fracture in A533B steel [1].*

cated finite-element analyses. This is expensive and time-consuming. To circumvent these requirements, the technology developed in this program has been utilized by General Electric to develop a simpler and less-expensive ductile fracture analysis procedure [*16*]. This "engineering approach" is based on considering crack driving forces and material resistance in terms of J or crack opening displacement (COD) or both. The approach consists of the following elements:

1. a handbook of fully plastic crack solutions for flawed structural components,
2. an estimation procedure which enables one to construct crack-driving force solutions for any level of loading by combining known elastic solutions with the newly developed fully-plastic solutions, and
3. a simple, graphical procedure for predicting the onset of crack growth, the extent of stable growth, and fracture instability by combining the driving force estimates with the appropriate resistance curve on a common diagram.

An example illustrating the mechanics of the approach for compact specimen test T-52 is shown in Fig. 12 [*17*].

Figure 12 shows the diagram combining the driving force and resistance curves on coordinates of J versus crack length (COD versus crack length

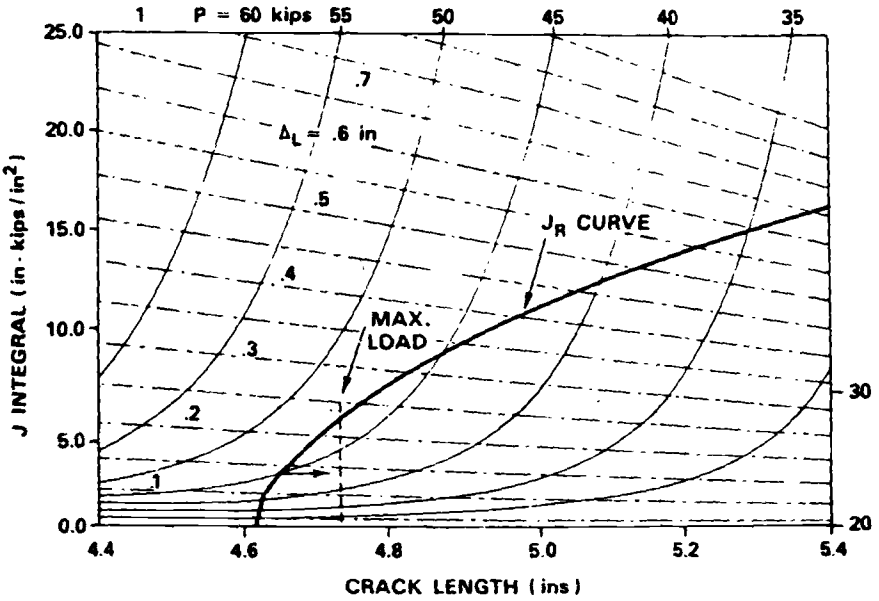

FIG. 12—*Application of a simplified ductile fracture analysis, GE specimen T-52 [2].*

could also be used). Driving force curves are shown for both constant applied load and constant displacement. The resistance curve overlays on the diagram with the zero point corresponding to the initial crack length. The extent of stable crack growth for a given applied load (or displacement) is read from the resistance curve at the point of intersection of the appropriate driving force curve. The fracture instability point is determined at the point of tangency of the driving force and resistance curves. Predictions for T-52 and numerous other specimens using this approach have shown encouraging agreement with experiments [*16,17*].

Discussion

The objective of this research was to provide the basis for a fracture assessment methodology accounting for the large-scale plasticity and stable crack growth phenomena involved in the fracture of nuclear pressure vessels and piping. The work sought to identify appropriate criteria to characterize the onset of crack extension (crack initiation), stable crack growth, and fracture instability (the onset of unstable crack extension). It is believed that the project successfully attained its principal objectives. Specifically, the results provide a convincing justification for the use of J and CTOA as crack-tip characterizing parameters in a plastic fracture mechanics resistance curve approach.

As a result, a fundamental basis for the application of fracture mechanics to ductile and tough materials—particularly where significant amounts of crack-tip plastic deformation and stable crack growth can precede general instability—has been established.

A host of problems is now facing the nuclear industry—for example, see Stahlkopf [*18*]. Application of the methodology developed in this research to flawed nuclear plant components will greatly assist in resolving them. But, before this can be done, it must be recognized that a number of unresolved issues still exist [*19*]. Among these is the paucity of demonstrations that any plastic fracture criterion evaluated on a simple test specimen can give an accurate prediction of fracture instability in an actual full-scale component. Also, the geometry and constraint dependence of J and CTOA and their practical implications must yet be evaluated. The use of simple estimation schemes for plastic fracture conditions clearly needs to be broadened.

Conclusions

This research demonstrated that, while many different ductile fracture parameters can serve as the basis of a resistance curve approach, J and CTOA are definitely superior. When the amount of stable crack growth preceding fracture instability is small, J is the more useful. The constancy of CTOA over extended amounts of stable crack growth is intriguing but has yet to be exploited in a practical manner. The effect of biaxial loading and the differences associated with flat and slant shear fracture do not appear to complicate the current plastic fracture mechanics approaches based upon Mode I conditions. A simplified engineering methodology for predicting ductile fracture has been formulated for application to nuclear plant problems.

Acknowledgment

The authors are greatly indebted to their colleagues at Battelle's Columbus Laboratories and General Electric's Corporate Research and Development Laboratory who performed the research reported in this paper. These include G. T. Hahn, D. Broek, R. B. Stonesifer, C. W. Marschall, I. S. Abou-Sayed, and A. Zahoor at Battelle, and C. F. Shih, V. Kumar, W. R. Andrews, H. G. deLorenzi, M. D. German, and R. G. Van Stone at General Electric.

References

[*1*] Kanninen, M. F., Hahn, G. T., Broek, D., Stonesifer, R. B., Marschall, C. W., Abou-Sayed, I. S., and Zahoor, A., *Development of a Plastic Fracture Methodology*, Battelle's Columbus Laboratories Report to the Electric Power Research Institute on RP601-1, EPRI NP 1734, Columbus, Ohio, March 1981.

[*2*] Shih, C. F., Andrews, W. R., deLorenzi, H. G., German, M. D., Van Stone, R. H., and Mowbray, D. F., *Methodology for Plastic Fracture*, General Electric Co. Corporate Re-

search and Development Division Report to the Electric Power Research Institute on RP601-2, EPRI NP 1735, Schenectady, N.Y., March 1981.

[3] *EPRI Ductile Fracture Research Review Document*, D. M. Norris, Jr., et al, Eds., Electric Power Research Institute Report NP-80-10-LD, Palo Alto, Calif., Dec. 1980.

[4] Kanninen, M. F., Broek, D., Hahn, G. T., Marschall, C. W., Rybicki, E. F., and Wilkowski, G. M., *Nuclear Engineering and Design*, Vol. 48, 1978, pp. 117-134.

[5] Hahn, G. T., Broek, D., Marschall, C. W., Rosenfield, A. R., Rybicki, E. F., Schmueser, D. W., Stonesifer, R. B., and Kanninen, M. F., *Tolerance of Flaws in Pressurized Components*, Mechanical Engineering Publications, Ltd., London, 1978, pp. 37-46.

[6] Hahn, G. T., Broek, D., Marschall, C. W., Rosenfield, A. R., Rybicki, E. F., Schmueser, D. W., Stonesifer, R. B., and Kanninen, M. F. in *Elastic-Plastic Fracture, ASTM STP 668*, J. D. Landes, J. A. Begley, and G. A. Clarke, Eds., American Society for Testing and Materials, 1979, pp. 121-150.

[7] Shih, C. F., deLorenzi, H. G., and Andrews, W. R. in *Elastic-Plastic Fracture, ASTM STP 668*, J. D. Landes, J. A. Begley, and G. A. Clarke, Eds., American Society for Testing and Materials, 1979, pp. 65-120.

[8] Andrews, W. R. and Shih, C. F. in *Elastic-Plastic Fracture, ASTM STP 668*, J. D. Landes, J. A. Begley, and G. A. Clarke, Eds., American Society for Testing and Materials, 1979, pp. 426-450.

[9] Shih, C. F., *Journal of the Mechanics and Physics of Solids*, 1981.

[10] Rice, J. R. in *Proceedings*, 1st International Conference on Fracture, Japanese Society for Strength and Fracture, Tokyo, Vol. 1, 1966, p. 309.

[11] Hutchinson, J. W., *Journal of the Mechanics and Physics of Solids*, Vol. 16, 1968, pp. 13-31 and pp. 337-347.

[12] Rice, J. R. and Rosengren, G. F., *Journal of the Mechanics and Physics of Solids*, Vol. 16, 1968, pp. 1-12.

[13] Rice, J. R. in *Proceedings*, Conference on the Mechanics and Mechanisms of Crack Growth, Cambridge, U.K., April 1973, M. J. May, Ed., British Steel Corp. Physical Metallurgy Centre Publication, 1975, pp. 14-39.

[14] Hutchinson, J. W. and Paris, P. C. in *Elastic-Plastic Fracture, ASTM STP 668*, J. D. Landes, J. A. Begley, and G. A. Clarke, Eds., American Society for Testing and Materials, 1979, pp. 37-64.

[15] Abou-Sayed, I. S., Marschall, C. W., and Kanninen, M. F. in *Advances in Fracture Mechanics*, D. Francois, et al, Eds., Pergamon Press, New York, 1980, pp. 227-234.

[16] Kumar, V., German, M. D., and Shih, C. F., "An Engineering Approach for Elastic-Plastic Fracture Analysis," General Electric Co. Corporate Research and Development Report to Electric Power Research Institute on RP1237-1, EPRI NP 1931, Schenectady, N.Y., July 1981.

[17] Kumar, V. and Shih, C. F. in *Fracture Mechanics, ASTM STP 700*, American Society for Testing and Materials, 1980, pp. 406-438.

[18] Stahlkopf, K. E., "Light Water Reactor Pressure Boundary Components: A Critical Review of Problems," Electric Power Research Institute Report, Palo Alto, Calif., Sept. 1981.

[19] Kanninen, M. F., Popelar, C. H., and Broek, D., *Nuclear Engineering and Design*, Vol. 67, 1981, pp. 27-55; see also NUREG/CR-2110, May 1981.

[20] Merkle, J. G. and Corten, H. T., *Journal of Pressure Vessel Technology*, 1974, pp. 286-292.

Hugo A. Ernst[1]

Some Salient Features of the Tearing Instability Theory

REFERENCE: Ernst, H. A., **"Some Salient Features of the Tearing Instability Theory,"** *Elastic-Plastic Fracture: Second Symposium, Volume II—Fracture Resistance Curves and Engineering Applications, ASTM STP 803,* C. F. Shih and J. P. Gudas, Eds., American Society for Testing and Materials, 1983, pp. II-133-II-155.

ABSTRACT: In this work the problem of the stability of a system deformed under displacement and load-controlled conditions is examined. The instability conditions are found from the load versus displacements, P-δ, characteristics of the system and the stiffness of the structure, K_M, on a completely general basis. The analysis is performed for the system in series with a spring under displacement control and for the system in parallel with the spring under load-controlled conditions.

In addition it is shown that the conditions for instability found for both situations using the tearing instability theory are in complete agreement with those obtained under a completely general basis. As a result the tearing instability theory is proven to be always valid in the sense that instability will occur if and only if $T_{app} > T_{mat}$.

Finally, a small experimental program on a nickel-chromium-molybdenum-vanadium rotor steel was conducted in order to prove that structures can be designed to assure stable crack growth under load-controlled conditions beyond maximum load.

KEY WORDS: systems, instability, fracture, mechanics, plasticity, tearing, T, J, R-curves, load, displacement, elastic-plastic fracture

It has become common practice in recent years to characterize a materials resistance to crack growth by means of the J-integral [*1-3*].[2]

First, J was accepted as a valid parameter to characterize the onset of crack growth as a result of the work of Begley and Landes [*4-5*]. Later, as a natural extension of the early K versus Δa resistance curves, J was tentatively used as a measure of the material toughness for stable crack growth by means of the J-resistance or J-Δa curve, although the theoretical basis for its use was not very clear. The theoretical basis for the J-Δa curve was later pro-

[1]Senior engineer, Materials Engineering Department, Westinghouse R&D Center, Pittsburgh, Pa. 15235.

[2]The italic numbers in brackets refer to the list of references appended to this paper.

vided by the analysis of Hutchinson and Paris [6], where they proved that if a certain criterion regarding the percentage of crack growth, the slope of the J-R curve and J itself, is met, there is indeed a J-controlled crack growth regime.

Although the J-R curve concept is growing in acceptance and its use becoming common practice, the question of whether a crack will grow in a stable or unstable manner remained unresolved until very recently. It was recognized that instability results from a lack of balance between the rate of increase of the applied drive force and that of the material resistance to crack growth.

Recently, the basic implications of this concept were further explored by Paris et al [7-8] and as a result it was demonstrated that the overall characteristics of the structure play a major role in instability and its effects have to be included in the rate balance mentioned. In their work they introduced a nondimensional quantity called the tearing modulus, T, that in general has the form

$$T = \frac{E}{\sigma_0^2} \frac{dJ}{da} \tag{1}$$

where E is the elastic modulus and σ_0 the flow stress. If Eq 1 is evaluated using the J-resistance curve of the material, the resulting T is the material tearing modulus T_{mat}. If instead, dJ/da in Eq 1 is calculated as the rate of change of crack drive or the applied J, per unit virtual crack extension, with the condition of total displacement, δ_{tot}, kept constant (or other similar conditions specified), the resulting T is the applied tearing modulus T_{app}. Following Ref 7 and 8, instability will occur when

$$T_{app} \geq T_{mat} \tag{2}$$

Using the condition of total displacement constant, the compliance of the structure, C_M, is introduced into the analysis and T_{app} becomes a function of C_M. Consequently, according to Eq 2, conditions for instability can be predicted provided the values of T_{mat} and expressions for T_{app} are known. In their original work, Paris et al developed formulas for T_{app} for different configurations assuming perfect plasticity and crack growth under limit-load conditions. They also performed the first experimental evaluation of the theory. In their tests of three-point-bend specimens loaded in series with a spring bar of adjustable length, the compliance of the system, C_M, was varied from test to test, producing stable or unstable behavior in complete agreement with the theory.

The results were originally shown in a T_{mat} versus T_{app} plot, Fig. 1. Each test is represented by its T_{mat} and T_{app} values. Open points correspond to unstable crack growth while filled points correspond to stable crack growth.

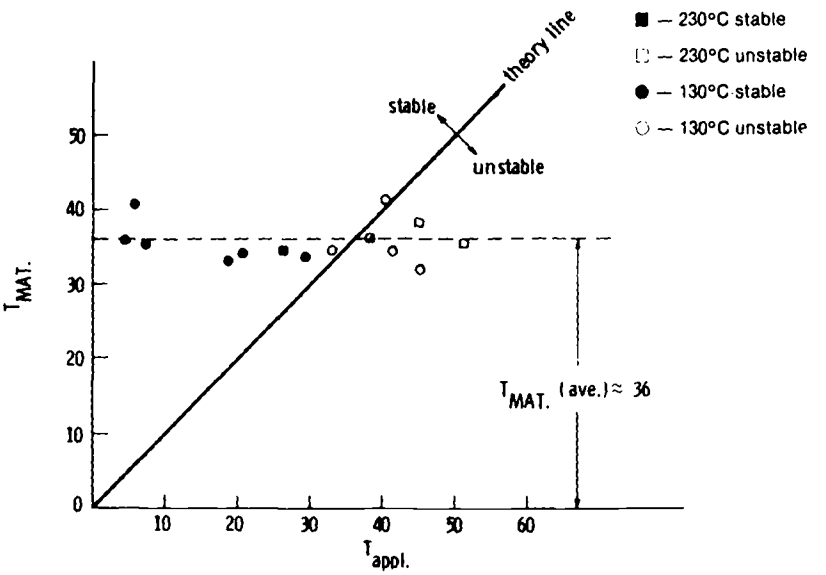

FIG. 1—T_{mat} *versus* T_{app} *for NiCrMoV three-point-bend specimens after Paris et al [8].*

Ideally, according to the theory, all open points (unstable) should lie to the right of the 45-deg line (region where $T_{app} > T_{mat}$), while the filled points (stable) should lie to the left of the 45-deg line (region where $T_{mat} > T_{app}$). The excellent agreement shown in Fig. 1 was the first experimental verification of the tearing instability theory.

Since this first work, significant effort was devoted to extending the basic concepts in different directions. Hutchinson and Paris [6] presented a more general expression for T_{app} for a specimen loaded in series with a spring simulating the structure

$$T_{app} = \frac{E}{\sigma_0^2}\left\{\left.\frac{\partial J}{\partial a}\right|_P - \left.\frac{\partial J}{\partial P}\right|_a \left.\frac{\partial \delta}{\partial a}\right|_P \left(\frac{1}{C_M + \left.\frac{\partial \delta}{\partial P}\right|_a}\right)\right\} \tag{3}$$

where δ is the displacement due to the crack and C_M is the compliance of the spring. All the terms appearing in the Eq 3 are calibration functions, that is, they don't bear any information regarding the material response to crack growth. These functions can be obtained from finite-element analysis or experimentally from blunt-notch specimen tests; no "real" crack growth test is needed for their determination. This scheme has been used [7,8] to obtain T_{app} for different configurations of practical interest and, as was mentioned, instability can be predicted by comparing the value of T_{app} obtained from Eq 2 with the experimentally obtained T_{mat}.

In related work Ernst et al [9] developed general formulas to evaluate both T_{app} and T_{mat} directly from a load-displacement ($P - \delta$) test record giving

$$T_{mat} = \frac{E}{\sigma_0^2}\left\{\left.\frac{\partial J}{\partial a}\right|_\delta - \left.\frac{\partial J}{\partial \delta}\right|_a \left.\frac{\partial P}{\partial a}\right|_\delta \left(\frac{1}{\left.\frac{\partial P}{\partial \delta}\right|_a - \frac{dP}{d\delta}}\right)\right\} \tag{4}$$

$$T_{app} = \frac{E}{\sigma_0^2}\left\{\left.\frac{\partial J}{\partial a}\right|_\delta - \left.\frac{\partial J}{\partial \delta}\right|_a \left.\frac{\partial P}{\partial a}\right|_\delta \left(\frac{1}{\left.\frac{\partial P}{\partial \delta}\right|_a + K_M}\right)\right\} \tag{5}$$

This formulation allows a direct comparison between the two T-values (see later) and also gives T_{app} as a function of T_{mat} by combining Eqs 4 and 5

$$T_{app} = \frac{E}{\sigma_0^2}\left\{\left.\frac{\partial J}{\partial a}\right|_\delta - \left.\frac{\partial J}{\partial \delta}\right|_a \left.\frac{\partial P}{\partial a}\right|_\delta \times \left(\frac{1}{K_M + \frac{dP}{d\delta} + \frac{1}{B}\frac{(\partial J/\partial \delta)^2}{\left(\frac{\sigma_0^2}{E}T_{mat} - \frac{\partial J}{\partial a}\right)}}\right)\right\} \tag{6}$$

where B is the specimen thickness.

At the same time, significant effort was also devoted to experimentally verifying the tearing instability theory. Joyce et al [10], Vassilaros et al [11], and Kanninen et al [12] conducted several experimental programs to do this. Their basic approach has been the same as the one used in the initial work of Paris et al [7,8]: This entails the selection of a certain material-specimen geometry combination to conduct a series of displacement-controlled tests where specimens are loaded in series with a spring whose compliance could be changed from test to test. Values of T_{mat} were obtained as the normalized slope of the J-R curves and T_{app}-values were obtained using some of the different schemes [6-9].

At the beginning, the results were reported in a T_{mat} versus T_{app} plot similar to that of Fig. 1; later, it was realized that in general neither T_{mat} nor T_{app} was constant in a given test. As a consequence, the results were plotted in a J-T format as shown in Fig. 2. Slopes of the J-R curves were obtained at different J levels; these were normalized and replotted in a J versus T_{mat} format. At the same time, using some of the schemes mentioned in the preceding [6-9], values of T_{app} were obtained for different J levels and also plotted in the J-T frame. Instability was expected to occur at the intersection of these

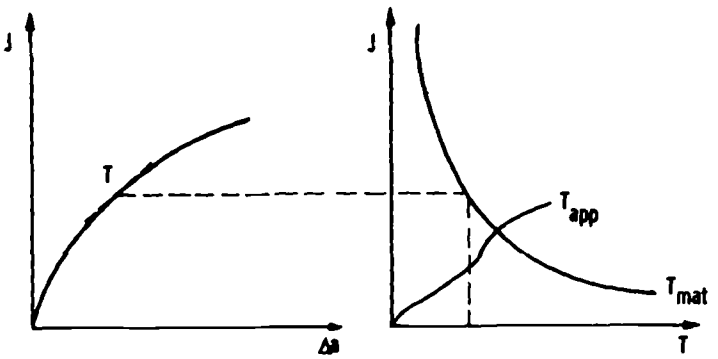

FIG. 2—J-T *plot.*

two curves; if the test was stable, the two curves should not intersect. If this approach was successful, instability was properly predicted by the tearing instability theory and thus it was said to be validated.

In the present work the problem of instability is approached from a different point of view, that of emphasizing the role of the P-δ record. The conditions for instability are shown to be predicted directly from the P-δ record characteristics and the compliance of the structure C_M. It is also shown that these conditions are completely consistent with those of the tearing instability theory. Thus tearing instability theory is proven to be *always valid* in that unstable crack extension will occur if and only if $T_{app} > T_{mat}$.

Finally, the results of a small number of critical experiments using a nickel-chromium-molybdenum-vanadium (Ni-Cr-Mo-V) rotor steel are presented completely validating the aforementioned concepts.

Stability Under Total Displacement-Controlled Conditions

Consider the P-δ record of a specimen tested under displacement control as shown in Fig. 3*a*. Suppose now that an identical specimen is tested in series with a spring of compliance C_M (or stiffness $K_M = C_M^{-1}$). It can be seen that the load held by the specimen P and the load held by the spring, P_M, are equal to the total externally applied load P_{tot}

$$P = P_M = P_{tot} \tag{7}$$

Also, according to the principle of equilibrium, the displacement applied to the specimen δ plus the displacement on the spring δ_M gives the total externally applied displacement δ_{tot}

$$\delta_{tot} = \delta + \delta_M \tag{8}$$

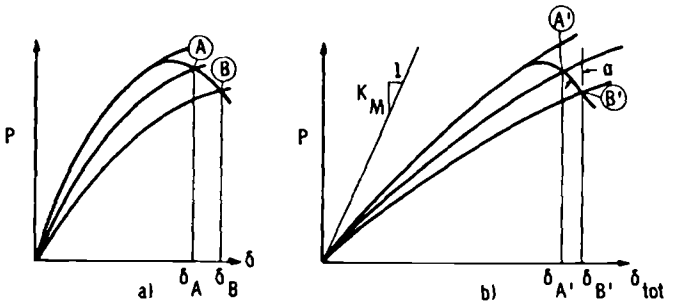

FIG. 3—*Test record of identical specimens* (a) *without and* (b) *with spring in series.*

Consequently, the second specimen test record (P-δ_{tot}) will be the result of just shifting every point of the original P-δ record to the right by an amount

$$\delta_M = PC_M \tag{9}$$

In particular, consider two generic points A and B in Fig. 3*a*, given by their coordinates (δ_A, P_A) and (δ_B, P_B), respectively. By the addition of the spring, they will be shifted to (δ'_A, P_A) and (δ'_B, P_B), respectively, Fig. 3*b*, where

$$\begin{aligned} \delta'_A &= \delta_A + P_A C_M \\ \delta'_B &= \delta_B + P_B C_M \end{aligned} \tag{10}$$

Furthermore, these equations can be combined to give

$$(\delta'_B - \delta'_A) = (\delta_B - \delta_A) + C_M (P_B - P_A) \tag{11}$$

The foregoing expression can be regarded as the fundamental instability equation. If Points A and B are in the rising part of the test record with $P_B > P_A$, the addition of the spring will cause an *increase* in the relative displacement

$$(\delta'_B - \delta'_A) > (\delta_B - \delta_A) \tag{12}$$

because the second term on the right-hand side of Eq 11 is positive. Instead, if Points A and B are in the decreasing portion of the record with $P_A > P_B$, then the relative displacement will be *diminished* by the addition of the spring

$$(\delta'_B - \delta'_A) < (\delta_B - \delta_A) \tag{13}$$

because the second term on the right-hand side of Eq 11 is negative. As a direct consequence, if enough compliance, C_M, is added to the system, the new relative displacement can be made as small as one wishes. Eventually it can be negative, that is, B′ lying to the left of A′ with $\delta'_B < \delta'_A$. If this were the case, the displacement would have to decrease to pass through B′, but obviously this is not compatible with the boundary condition which asks for a monotonically increasing displacement. Thus the test record approaches B′ as close as is physically possible (vertical drop) corresponding to unstable crack growth at that point.

The condition for instability can be expressed as

$$\begin{aligned} (\delta'_B - \delta'_A) < 0 \quad &\text{unstable} \\ (\delta'_B - \delta'_A) > 0 \quad &\text{stable} \end{aligned} \tag{14}$$

Combining Eqs 11 and 14 gives the instability condition

$$(\delta'_B - \delta'_A) = (\delta_B - \delta_A) + C_M(P_B - P_A) < 0$$

or

$$-(P_B - P_A)/(\delta_B - \delta_A) = -dP/d\delta > K_M = C_M{}^{-1} \tag{15}$$

where $-dP/d\delta$ refers to the slope of the test record of the specimen alone. Thus, instability is expected if and only if the negative of the slope of the specimen test record is greater than the stiffness of the spring (structure). Note that as a consequence, instability cannot occur in the rising part of the P-δ record. In fact, for this portion, $dP/d\delta$ is positive, thus $-dP/d\delta < 0$, and Eq 15 can never be satisfied (K_M being always positive). These features are illustrated in Fig. 4, where a schematic P-δ record has been replotted in terms of the parameter $Q = -dP/d\delta$ versus δ; different spring stiffnesses K_M are also shown. Initially, from Points A to B, Q is essentially constant and negative (corresponding to linear elastic slope); later plasticity or crack extension, or both, begins and Q starts to increase, passes through zero, Point C (corresponding to maximum load), increases to a maximum value at Point F and then starts to decrease.

If a similar specimen in series with a spring is tested under displacement control, different situations can arise depending on the value of K_M. If K_M is very big (very rigid spring), the whole Q versus δ record is well below the K_M1 line and no instability is expected to take place. For a smaller value of K_M, that is, K_M2, the Q versus δ record crosses the K_M2 line at Point E, and thus instability is expected to take place at the corresponding displacement δ_E. For an even smaller value of K_M, that is, K_M3, the crossing occurs even earlier, at Point D, thus instability is expected at δ_D. Finally, for a very soft spring, $K_M \approx 0$, instability will occur close to Point C. This result agrees completely with the

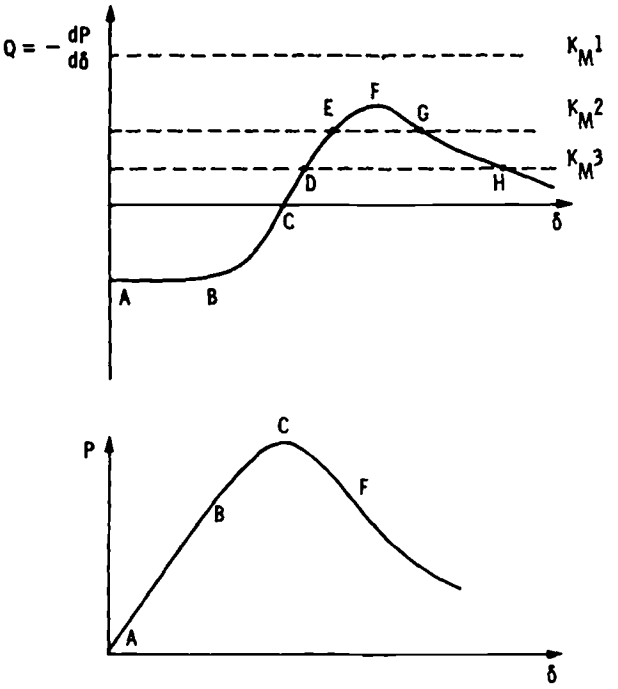

FIG. 4—*Load and* $Q = -dP/d\delta$ *versus displacement* δ.

well-known fact that, under load control, instability occurs at maximum load, and in fact an infinitely soft spring in series with the specimen means essentially that the latter is under load-controlled conditions.

Note that for the portion of the record, A to C, no instability is possible because $Q < 0$ and K_M cannot be negative, thus Q is always smaller than K_M.

A final word is in order here regarding the end of instability.

Equation 15 is expected to accurately predict the point of onset of instability because it is based on nothing else but the principle of equilibrium. On the other hand, the Q versus δ plot may cross the K_M line, a second time at Points G and H for example, and that should indicate the end of instability for those values of K_M. However, in this analysis, inertia effects have not been taken into account and thus the point of "arrest of instability" is not expected to be very accurately described by Eq 15, although the latter may serve as a starting point for an in-depth study of this matter.

In conclusion, the condition for instability (partial or total) has been found from the test record characteristics. It is based on nothing else but equilibrium; thus it is completely general (it is assumed that the addition of the spring does not change the mechanism of deformation or fracture). Note that *no mention of* J *or crack length,* a, *was made throughout the analysis.* In

fact, the instability condition of Eq 15 applies to any system for which the load-displacement record is known. Given a test record, the remaining compliance capacity (C_{CR}) [9] or the additional compliance needed to cause instability in a similar test can be determined from Eq 15

$$C_{CR} = (K_M)^{-1} = \left(-\frac{dP}{d\delta}\right)^{-1} \tag{16}$$

The foregoing methodology can be applied even if the system in question were an uncracked body or the general conditions were such that no parameter such as J could be defined, or both.

Tearing Instability Theory for Displacement-Controlled Conditions

The conditions for instability can also be found using the tearing modulus concept of Paris et al [7,8], given in Eq 1. Without any loss in generality, J can be expressed as a function of displacement due to the crack, δ, and crack length, a

$$J = J(a, \delta) \tag{17}$$

Differentiating

$$dJ = \left.\frac{\partial J}{\partial a}\right|_{\delta} da + \left.\frac{\partial J}{\partial \delta}\right|_{a} d\delta \tag{18}$$

Then the material tearing modulus T_{mat} is [9]

$$T_{\text{mat}} = \frac{E}{\sigma_0{}^2}\left.\frac{dJ}{da}\right|_{\text{mat}} = \frac{E}{\sigma_0{}^2}\left.\frac{\partial J}{\partial a}\right|_{\delta} + \left.\frac{\partial J}{\partial \delta}\right|_{a}\frac{d\delta}{da} \tag{19}$$

where the term $d\delta/da$ is to be evaluated following the actual crack growth. Also, the load P can be expressed as

$$P = P(a, \delta) \tag{20}$$

and differentiating

$$dP = \left.\frac{\partial P}{\partial a}\right|_{\delta} da + \left.\frac{\partial P}{\partial \delta}\right|_{a} d\delta \tag{21}$$

or

$$\frac{d\delta}{da} = -\frac{\left.\dfrac{\partial P}{\partial a}\right|_{\delta}}{\left(\left.\dfrac{\partial P}{\partial \delta}\right|_{a} - \dfrac{dP}{d\delta}\right)} \tag{22}$$

where the term $dP/d\delta$ is to be evaluated from the P-δ record. The foregoing equation can be substituted in Eq 18 to give a completely general expression for T_{mat}

$$T_{mat} = \frac{E}{\sigma_0^2}\left\{\left.\frac{\partial J}{\partial a}\right|_\delta - \left.\frac{\partial J}{\partial \delta}\right|_a \left(\frac{\left.\frac{\partial P}{\partial a}\right|_\delta}{\left.\frac{\partial P}{\partial \delta}\right|_a - \frac{dP}{\delta\delta}}\right)\right\} \tag{23}$$

or using

$$\left.\frac{\partial J}{\partial \delta}\right|_a = -\frac{1}{B}\left.\frac{\partial P}{\partial a}\right|_\delta \tag{24}$$

$$T_{mat} = \frac{E}{\sigma_0^2}\left\{\left.\frac{\partial J}{\partial a}\right|_\delta + \frac{\left(\left.\frac{\partial P}{\partial a}\right|_\delta\right)^2}{B\left(\left.\frac{\partial P}{\partial \delta}\right|_a - \frac{dP}{d\delta}\right)}\right\} \tag{25}$$

On the other hand, the applied tearing modulus T_{app} is defined as the rate of change of J with crack length under the condition that the overall displacement is kept constant. Thus T_{app} is given by

$$T_{app} = \frac{E}{\sigma_0^2}\left\{\left.\frac{\partial J}{\partial a}\right|_\delta + \left.\frac{\partial J}{\partial \delta}\right|_a \left.\frac{d\delta}{da}\right|_{\delta_{tot}}\right\} \tag{26}$$

The condition δ_{tot} = constant is equivalent to $d\delta_{tot} = 0$, or separating the total displacement into a part due to the crack, δ, and a part due to the rest of the structure (uncracked body part), δ_M

$$\begin{aligned} d\delta_{tot} &= d\delta + d\delta_M = 0 \\ &= d\delta + C_M dP = 0 \end{aligned} \tag{27}$$

where $C_M = (K_M)^{-1} = d\delta_M/dP$ can be associated with the linear compliance of the system (spring + testing machine + uncracked specimen) as before. T_{app} then can be calculated using Eqs 17, 20, and 27 to give

$$T_{app} = \frac{E}{\sigma_0^2}\left\{\left.\frac{\partial J}{\partial a}\right|_\delta - \left.\frac{\partial J}{\partial \delta}\right|_a \frac{\left.\frac{\partial P}{\partial a}\right|_\delta}{\left(\left.\frac{\partial P}{\partial \delta}\right|_a + K_M\right)}\right\} \tag{28}$$

or

$$T_{app} = \frac{E}{{\sigma_0}^2}\left\{\left.\frac{\partial J}{\partial a}\right|_{\delta} + \frac{\left(\left.\frac{\partial P}{\partial a}\right|_{\delta}\right)^2}{B\left(\left.\frac{\partial P}{\partial \delta}\right|_{a} + K_M\right)}\right\} \tag{29}$$

which are completely general expressions for T_{app}. The instability condition can now be found directly; defining

$$\Delta T = T_{mat} - T_{app} \tag{30}$$

instability will result when

$$\Delta T < 0 \tag{31}$$

or using Eqs 22 and 28

$$\Delta T = -\frac{E}{{\sigma_0}^2}\left\{\left.\frac{\partial P}{\partial a}\right|_{\delta}\left.\frac{\partial J}{\partial \delta}\right|_{a}\frac{1}{B}\left(\frac{1}{\left(\left.\frac{\partial P}{\partial \delta}\right|_{a} - \frac{dP}{d\delta}\right)} - \frac{1}{\left(\left.\frac{\partial P}{\partial \delta}\right|_{a} + K_M\right)}\right)\right\} < 0 \tag{32}$$

Note that

$$\left.\frac{\partial P}{\partial a}\right|_{\delta} < 0 \tag{33}$$

and then

$$\Delta T < 0$$

if and only if

$$-dP/d\delta > K_M$$

for the instability condition.

Thus according to the theory, instability will be ensured when $\Delta T < 0$ and that will happen if and only if $-dP/d\delta > K_M$. This condition is exactly the same as that one of Eq 15 which was found on a completely general basis, with no need to mention J or crack length. As a result, the condition $\Delta T < 0$ implies instability and, vice versa, the instability event implies $\Delta T < 0$. Thus, the tearing instability theory has been proven to be always valid in that it correctly predicts unstable crack growth.

Furthermore, the generality of the approach leading to Eq 15 allows the use of any parameter X, $X = X(\delta, a)$, instead of J if desired. In fact if a parameter X, such as crack opening displacement (COD), crack opening angle (CTOA), or any other physical quantity, is used instead of J in Eqs 22 and 27 the resulting X-based tearing moduli, T_{matX} and T_{appX} will provide an automatically validated tearing instability condition. In other words, instability will be always correctly predicted by $T_{appX} > T_{matX}$ because in fact this condition is dictated by the more general one $-dP/d\delta > K_M$.

The choice of X should not be based then on its suitability for instability predictions (all of them work) but rather on physical grounds; that is, on the convenience of its experimental determination and the degree of independence of the corresponding R-curve of constraint, geometry, and loading conditions.

Stability Under Total Load-Controlled Conditions

It is well recognized that the structural member is normally constrained by the structure in such a way that neither an exclusively load-controlled nor displacement-controlled situation is realistic, but more likely a mixed one where the stiffness of the rest of the structure K_M has to be taken into account. In the last section it was shown that, by adding a spring in series with the specimen in a displacement-controlled test, the structure can be simulated and in fact the whole range from load control to displacement control can be covered by just changing the stiffness of the spring K_M. Nevertheless, that is not the only possible way of covering this range. In fact, there are situations where the structure has an intermediate loading condition which cannot be represented by the aforementioned model. These would be redundant structures where several members are sharing the overall applied load; namely, stiffened plates or pipes, sets of structural supporters, or cables. The crack growth stability problem for these types of structures was the subject of a recent paper by Paris et al [*13*], who developed the so-called fracture-proof design concept. According to this concept structural parts can be designed in such a way as to guarantee stable crack growth even under load-controlled conditions.

In the present work this stability problem is examined in an absolutely general way, following the spirit of the previous sections, and a complete tearing modulus analysis is performed.

Consider the P-δ record of a specimen tested under displacement-controlled conditions as shown in Fig. 5*a*. Suppose that an identical specimen is tested, this time in parallel with a spring of stiffness K_M. The displacement imposed on the specimen, δ, and that of the spring, δ_M, are equal

$$\delta = \delta_M \tag{34}$$

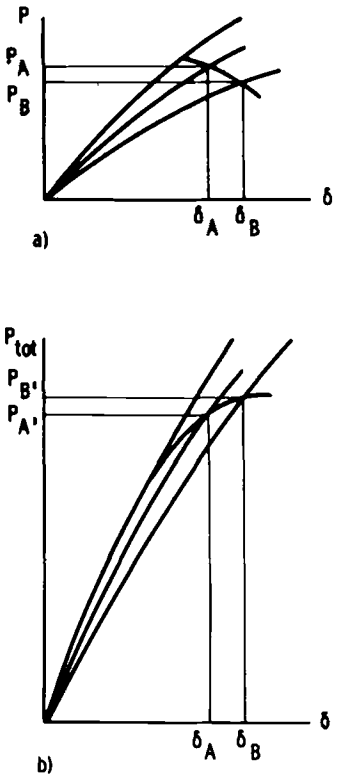

FIG. 5—*Test record of identical specimens* (a) *without and* (b) *with spring in parallel.*

On the other hand, according to the principle of equilibrium, the load on the specimen, P, plus the load on the spring, P_M, equals the total externally applied load P_{tot}

$$P_{tot} = P + P_M \tag{35}$$

As a consequence, the second specimen test record (P_{tot}, δ), shown in Fig. 5*b*, will be just the result of shifting every point of the original P-δ record up in load by an amount

$$P_M = K_M \delta \tag{36}$$

As before, if two generic points, A and B, in Fig. 4*a* are considered, with coordinates (δ_A, P_A) and (δ_B, P_B), respectively, the addition of the spring will shift them to (δ_A, P_A') and (δ_B, P_B'), with

$$P'_A = P_A + K_M \delta_A$$

$$P'_B = P_B + K_M \delta_B \tag{37}$$

Combining the foregoing equations, one gets

$$(P'_B - P'_A) = (P_B - P_A) + K_M(\delta_B - \delta_A) \tag{38}$$

The foregoing expression can be regarded as the fundamental instability equation for load-controlled systems. If Points A and B were in the rising portion of the P-δ record ($P_A < P_B$), the addition of the spring would cause an increase in the load difference due to the fact that the second term on the right-hand side of Eq 38 is positive

$$(P'_B - P'_A) > (P_A - P_B) \tag{39}$$

If Points A and B were in the decreasing portion of the P-δ record ($P_A > P_B$), the addition would also cause an increase in the load difference for the same reason as before

$$(P'_B - P'_A) > (P_B - P_A) \tag{40}$$

In fact, if the second term on the right-hand side of Eq 38 were big enough, the relative difference in load would become positive $P'_B - P'_A > 0$, and that means *a continual increase in load*. The required value of K_M to produce this behavior can be obtained from Eq 38

$$(P_B - P'_A) = P_B - P_A) + K_M(\delta_B - \delta_A) > 0$$

or

$$-\frac{P_B - P_A}{\delta_B - \delta_A} < K_M \tag{41}$$

$$-dP/d\delta < K_M$$

to produce a monotonically increasing load curve.

Note that if the resulting P_{tot}-δ record is monotonically increasing, it is irrelevant whether the test is run under load or displacement-controlled conditions; that is, the test will be stable regardless of these conditions. Thus, Eq 41 represents the fundamental condition for stable behavior under load-controlled conditions, and the minimum value of K_M that satisfies it is the minimum value of stiffness required to produce a monotonically increasing curve and thus prevent instability. As a result the instability conditions are

$$-dP/d\delta < K_M \quad \text{stable}$$

$$-dP/d\delta > K_M \quad \text{unstable} \tag{42}$$

Note that this condition is exactly the same as that one of Eq 15 derived for a completely different situation; in both cases stable behavior will be guaranteed if and only if

$$-dP/d\delta < K_M \tag{43}$$

This similarity allows a discussion completely analogous to that of the previous section that will not be repeated here in whole for the sake of brevity. In conclusion, under load control, instability cannot occur before $Q = 0$ (maximum load) and beyond that point instability can be prevented if the stiffness of the structure in parallel with the cracked body is greater than $-dP/d\delta$.

Note again that this condition has been derived using only the principle of equilibrium; thus it is completely general. No mention was made of crack length or any field parameter.

Tearing Instability Theory for Total Load-Controlled Conditions

The conditions for stable/unstable behavior of a specimen in parallel with a spring under load-controlled conditions can also be obtained using the tearing modulus concept.

The material tearing modulus, T_{mat}, being independent of the loading conditions, will still be given by Eq 23

$$T_{\text{mat}} = \frac{E}{{\sigma_0}^2}\left\{\left.\frac{\partial J}{\partial a}\right|_\delta - \left.\frac{\partial J}{\partial \delta}\right|_a \frac{\left.\dfrac{\partial P}{\partial a}\right|_\delta}{\left(\left.\dfrac{\partial P}{\partial \delta}\right|_a - \dfrac{dP}{d\delta}\right)}\right\} \tag{44}$$

The applied tearing modulus, T_{app}, can be defined as the rate of change of J per unit virtual crack extension, with the condition of total load P_{tot} kept constant; thus using Eqs 16 and 17

$$T_{\text{app}} = \frac{E}{{\sigma_0}^2}\left.\frac{dJ}{da}\right|_{P_{\text{tot}}} = \frac{E}{{\sigma_0}^2}\left\{\left.\frac{\partial J}{\partial a}\right|_\delta + \left.\frac{\partial J}{\partial \delta}\right|_a \left.\frac{d\delta}{da}\right|_{P_{\text{tot}}}\right\} \tag{45}$$

The condition $P_{\text{tot}} = \text{constant}$ means $dP_{\text{tot}} = 0$, or using Eq 35

$$dP_{\text{tot}} = dP_M + dP = 0 \tag{46}$$

with

$$P_M = \delta_M K_M$$

$$P = P(a, \delta) \tag{47}$$

Differentiating Eqs 47 and substituting in Eq 46 give

$$d\delta_M K_M + \left.\frac{\partial P}{\partial \delta}\right|_a d\delta + \left.\frac{\partial P}{\partial a}\right|_\delta da = 0 \tag{48}$$

Noting that from Eq 34

$$d\delta_M = d\delta \tag{49}$$

Eq 48 gives

$$\frac{d\delta}{da} = -\frac{\left.\frac{\partial P}{\partial a}\right|_\delta}{\left.\frac{\partial P}{\partial \delta}\right|_a + K_M} \tag{50}$$

Combining Eqs 45 and 50 gives

$$T_{app} = \frac{E}{{\sigma_0}^2}\left\{\left.\frac{\partial J}{\partial a}\right|_\delta - \left.\frac{\partial J}{\partial \delta}\right|_a \frac{\left.\frac{\partial P}{\partial \delta}\right|_\delta}{\left(\left.\frac{\partial P}{\partial \delta}\right|_a + K_M\right)}\right\} \tag{51}$$

This equation is the general expression for T_{app} for a specimen in parallel with a spring (structure) under load-controlled conditions.

The instability condition can be obtained by comparing Eqs 44 and 51, giving

$$\Delta T = T_{mat} - T_{app} < 0 \tag{52}$$

if and only

$$-dP/d\delta > K_M$$

for instability

This condition obtained from the tearing instability theory agrees with Eq 42 obtained on a completely general basis, based on nothing else but the principle of equilibrium.

As a result, the tearing instability theory is proven to be always valid for load-controlled conditions in that instability will occur if and only if $\Delta T < 0$. Note that, as before, if any other parameter $X = X(\delta, a)$ were used instead of J, the resulting X-based tearing moduli, T_{matX} and T_{appX}, would provide an automatically validated tearing instability condition.

Finally, it is to be noted that Eqs 33 and 52 *are identical* although they represent completely different situations. The former was obtained for a specimen in series with the spring under displacement control, whereas the latter was obtained for a specimen in parallel with the spring under load-controlled conditions. This "symmetry" allows full use of the methodology and discussion presented in the early sections for both cases.

Experimental Program

In order to demonstrate the validity of the concepts of the last sections, a critical experimental program was conducted. Specimens of different crack length were tested under displacement-controlled conditions. From the P-δ records the minimum stiffness needed in parallel to prevent instability was calculated from Eq 42, and finally similar specimens were tested in parallel with springs to obtain *stable crack growth under load-controlled conditions beyond maximum load*. A detailed description of the program follows.

Material

The material used was a nickel-chromium-molybdenum-vanadium (NiCrMoV) rotor steel. This material was subjected to extensive testing by Logsdon [*14*], and was the one used by Paris et al [*8*].

Specimen Geometry

The test specimen configuration used was the three-point-bend geometry with full span $L = 10.16$ cm (4 in.), total width $W = 2.54$ cm (1 in.), and thickness $B = 1.27$ cm (½ in.).

Testing Conditions

The specimens were tested in air at a test temperature of 230°C (446°F) so as to be well above the transition temperature of the material to avoid cleavage.

Experimental Procedure and Results

The experimental program consisted first of testing three specimens of different a/W, namely, 0.5, 0.6, and 0.7, under displacement control, measuring load and ram displacement in a standard MTS servo-hydraulic testing

machine. From the P-δ records an average slope for the decreasing $dP/d\delta$ was measured in each case. The results are given in Table 1.

Next, similar specimens were tested, this time in parallel with two spring bars under load-controlled conditions. The testing arrangement is shown in Figs. 6 and 7.

The stiffness of the spring bar in parallel with the cracked body was changed from test to test by either using bars of different thickness or changing their span or both. In each test, the characteristics of both spring bars (thickness and span) were kept the same for symmetry purposes.

Using this procedure, two more specimens of each a/W (total of six more) were tested in parallel with bars whose stiffness was bigger than the corresponding value of $-dP/d\delta$ previously obtained from the P-δ records. The results are summarized in Table 2. In Fig. 8 the P-δ test records of three specimens of $a/W = 0.5$ and stiffness $K_M = 0$; 359 and 449 MPa (52 and 65 ksi) are shown. In all cases, the crack growth was stable, even beyond the point of maximum load.

In conclusion, it was demonstrated that instability under load-controlled conditions can, indeed, be prevented, provided the stiffness of the structure in parallel with the cracked body is greater than $-dP/d\delta$, in complete agreement with Eq 42.

TABLE 1—*Test results.*

a/w	$Q = -dP/d\delta$, klb/in.
0.5	27
0.6	17
0.7	7.5

1 klb/in. = 175 kN/m.
= 0.75 MPa·m.

TABLE 2—*Test results.*

	K_M, klb/in.	Stable?
$a/w = 0.5$	65.1	yes
$Q = 27$	51.8	yes
$a/w = 0.6$	32	yes
$Q = 17$	21.4	yes
$a/w = 0.7$	16.8	yes
$Q = 7.5$	10.6	yes

1 klb/in. = 175 kN/m.
= 0.75 MPa·m.

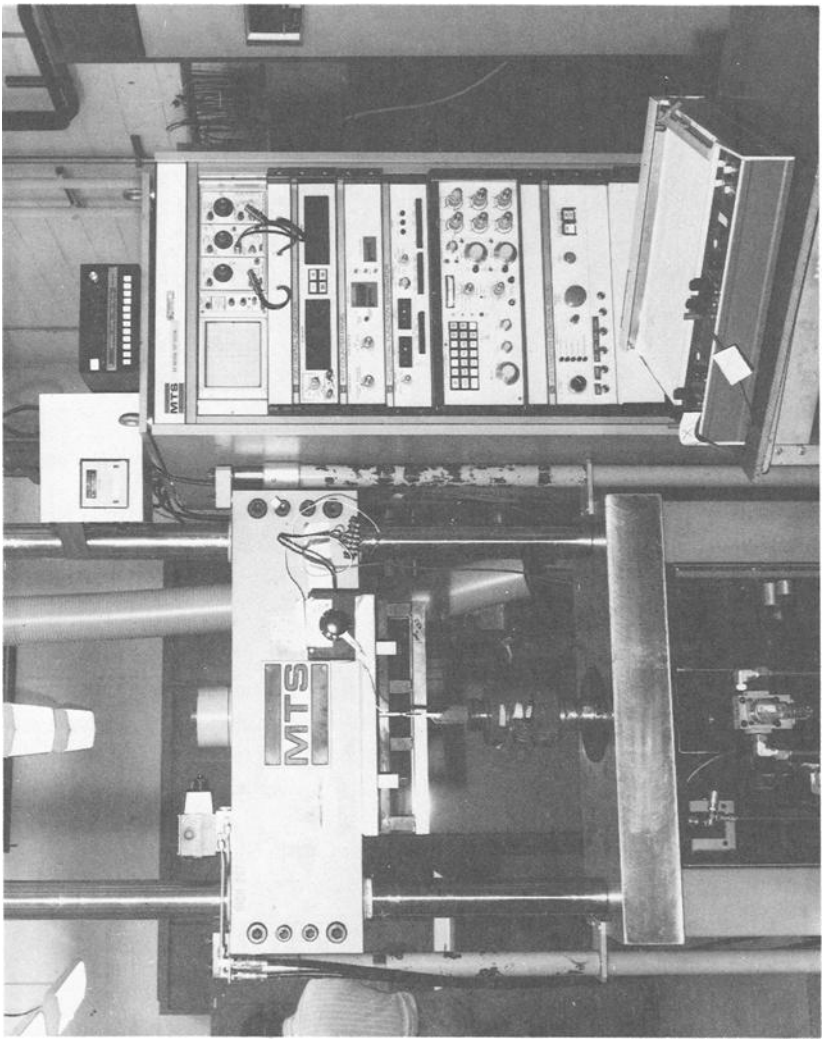

FIG. 6—*Experimental setup.*

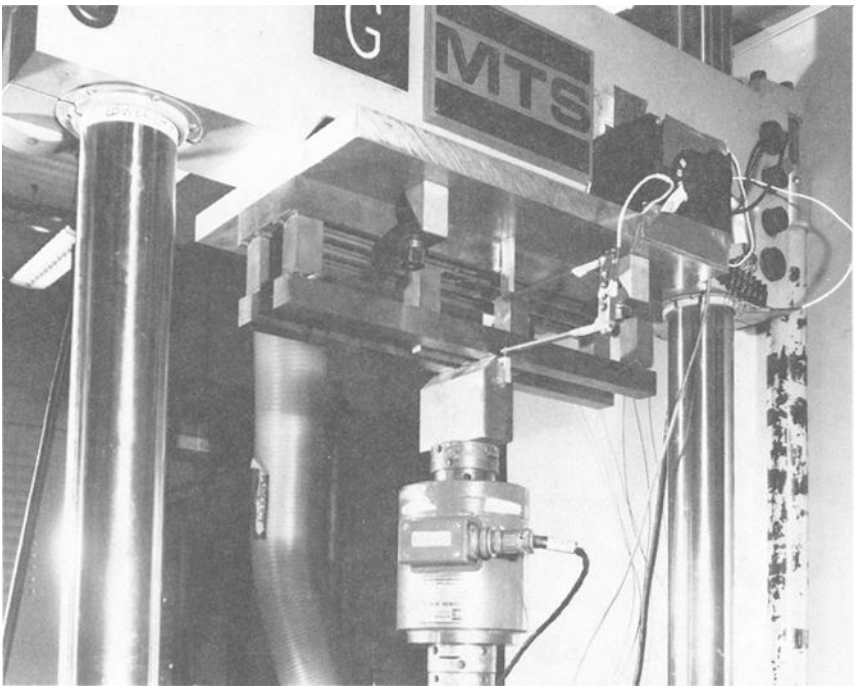

FIG. 7—*Experimental setup.*

Final Comment

In this work the conditions for instability of a system were found from the P-δ characteristics, based only on the principle of equilibrium. The system can be considered as a black box to which displacement is being applied (or load) and load (or displacement) is measured as the response. The conditions for instability were obtained for a spring in series with the black box under displacement control and for a spring in parallel with the black box under load-controlled conditions. In both cases, stable behavior will be guaranteed if and only if

$$K_M > -dP/d\delta$$

Also, for the particular system consisting of a cracked body, the instability conditions for both cases based on the tearing modulus theory were found to be completely consistent with the foregoing equation. Furthermore, any parameter $X = X(\delta, a)$ can be used for instability predictions and the X-based tearing moduli will provide the correct instability condition. In particular, if modified versions of the J-integral as proposed by Rice et al [*15*]

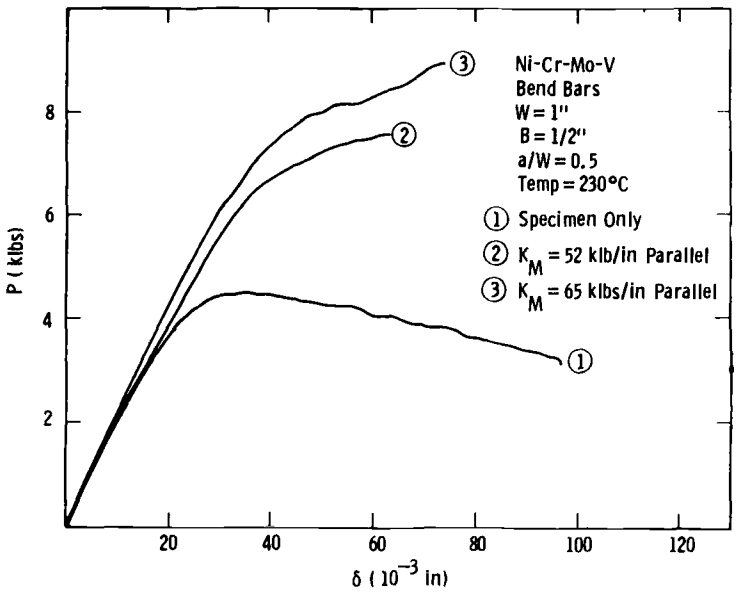

FIG. 8—*Experimental test records (1 klb/in. = 175 kN/m = 0.75 MPa·m; 1 in. = 2.54 cm; 230°C = 446°F).*

and Herman and Rice [*16*] and generalized by Ernst [*17*] are used to describe the crack growth process, the instability condition will still be correctly assessed by the corresponding tearing moduli.

So far, it has been demonstrated that instability can be predicted using the aforementioned concepts, or the C_{CR} [*9*], for a given configuration. Nevertheless, it is of much greater interest to be able to predict instability in an untested geometry. This also can be accomplished using the C_{CR} concept. In fact combining Eqs 22 and 33 gives

$$C_{CR}^{-1} = K_M > -\frac{dP}{d\delta} = -\left.\frac{\partial P}{\partial \delta}\right|_a - \left.\frac{\partial J}{\partial \delta}\right|_a \frac{\left.\frac{\partial P}{\partial a}\right|_\delta}{\left(\frac{\sigma_0^2}{E} T_{\text{mat}} - \left.\frac{\partial J}{\partial a}\right|_\delta\right)}$$

as the stability condition for any configuration. Note that as mentioned $\partial P/\partial \delta|a$, $\partial P/\partial a|\delta$, $\partial J/\partial \delta|a$, and $\partial J/\partial a|\delta$ are calibration functions and the additional information needed is T_{mat}, which supposedly can be obtained from other specimen tests. Thus instability can be predicted in a given geometry with calibration functions and "universal material properties" without having to actually test it. Thus, the importance of such a universal J-R curve is apparent. It is clear then, that future effort should not be devoted so much

to instability predictions, but rather to exploring and understanding the influence of specimen geometry, size, type of loading, and constraint on the different candidate parameters to provide a truly universal material resistance curve.

Acknowledgment

This work was partially supported by the Electric Power Research Institute under Contract No. RR 1238-2, Dr. Douglas M. Morris, project manager. The author wants to thank his colleagues from Westinghouse R&D Center, D. E. McCabe and J. D. Landes for their valuable help.

References

[1] Rice, J. R., *Transactions*, American Society of Mechanical Engineers, "A Path Independent Integral and the Approximate Analysis of Strain Concentration by Notches and Cracks," *Journal of Applied Mechanics*, Vol. 35, 1968, pp. 379-386.

[2] Hutchinson, J. W., "Singular Behavior at the End of Tensile Crack in a Hardening Material," *Journal of the Mechanics and Physics of Solids*, Vol. 16, No. 1, 1968, pp. 13-31.

[3] Rice, J. R. and Rosengren, C. F., "Plane Strain Deformation Near a Crack Tip in a Power Law Hardening Material," *Journal of the Mechanics and Physics of Solids*, Vol. 16, No. 1, 1968, pp. 1-12.

[4] Begley, J. A. and Landes, J. A., "The J Integral as a Fracture Criterion," in *Fracture Toughness, ASTM STP 514*, American Society for Testing and Materials. 1972, pp. 1-23.

[5] Landes, J. D. and Begley, J. A., "The Effect of Specimen Geometry on J_{IC}," in *Fracture Toughness, ASTM STP 514*, American Society for Testing Materials, 1972. pp. 24-39.

[6] Hutchinson, J. W. and Paris, P. C., "Stability Analysis of J-Controlled Crack Growth," in *Elastic-Plastic Fracture, ASTM STP 668*, J. D. Landes, J. A. Begley, and G. A. Clarke, Eds., American Society for Testing and Materials, 1979, pp. 37-64.

[7] Paris, P. C., Tada, H., Zahoor, A., and Ernst, H. A., "The Theory of Instability of the Tearing Mode of Elastic-Plastic Crack Growth," in *Elastic-Plastic Fracture, ASTM STP 668*, J. D. Landes, J. A. Begley, and G. A. Clarke, Eds., American Society for Testing and Materials, 1979, pp. 5-36.

[8] Paris, P. C., Tada, H., Ernst, H., and Zahoor, A., "An Initial Experimental Investigation of Tearing Instability Theory," in *Elastic-Plastic Fracture, ASTM STP 668*, J. D. Landes, J. A. Begley, and G. A. Clarke, Eds., American Society for Testing and Materials, 1979, pp. 251-265.

[9] Ernst, H. A., Paris, P. C., and Landes, J. D. in *Fracture Mechanics: 13th Conference, ASTM STP 743*, "Estimations on J-Integral and Tearing Modulus T from a Single Specimen Test Record," 13th National Symposium on Fracture Mechanics, ASTM STP, American Society for Testing and Materials, 1981, pp. 476-502.

[10] Joyce, J. A., and Vassilaros, M. G. in *Fracture Mechanics: 13th Conference, ASTM STP 743*, "An Experimental Evaluation of Tearing Instability Using the Compact Specimen," 13th National Symposium on Fracture Mechanics, ASTM STP, American Society for Testing and Materials, 1981, pp. 525-542.

[11] Vassilaros, M. G., Joyce, J. A., and Gudas, J. P. in *Fracture Mechanics: 14th Conference, ASTM STP 791*, "Experimental Verification of the Tearing Instability Phenomena for Structural Materials," presented at the 14th National Symposium on Fracture Mechanics, Los Angeles, CA July 1981. American Society for Testing and Materials, 1983, pp. I-65-I-83.

[12] Kanninen, M. F., Zahoor, A., Wilkowski, G. M., Abou-Sayed, I. S., Marschall, C. W., Broek, D., Sampath, S. G., Rhee, H. D., and Ahmad, J., "Instability Predictions for Circumferentially Cracked Type 304 Stainless Steel Pipes Under Dynamic Loading," Battelle

Columbus Laboratories Final Report to the Electric Power Research Institute on T118-2, Columbus, Ohio, in preparation, June 1981.

[*13*] Paris, P. C., Tada, H., and Baldini, S. E., "Fracture Proof Design," CSNI Specialists Meeting on Plastic Tearing Instability held at the Center for Fracture Mechanics, Washington University, St. Louis, Mo., 25–27 Sept. 1979; U.S. Nuclear Regulatory Commission Report NUREG CP-0010, Washington, D.C., Jan. 1980.

[*14*] Logsdon, W. A. in *Mechanics of Crack Growth, ASTM STP 590,* American Society for Testing and Materials, 1976, pp. 43–61.

[*15*] Rice, J. R., Drugan, W. J., and Sham, T. L. in "Elastic Plastic Analysis of Growing Cracks," *Fracture Mechanics: Twelfth Conference, ASTM STP 700,* American Society for Testing and Materials, 1980, pp. 189–221.

[*16*] Herman, L., Rice, J. R., "Comparison of Experiment and Theory for Elastic-Plastic Plane Strain Crack Growth," Brown University Report No. 76, Providence, R.I., Feb. 1980.

[*17*] Ernst, H. A., this publication, pp. I-191–I-213.

Shu S. Tang,[1] *Peter C. Riccardella,*[1] *and Roland Huet*[2]

Verification of Tearing Modulus Methodology for Application to Reactor Pressure Vessels with Low Upper-Shelf Fracture Toughness

REFERENCE: Tang, S. S., Riccardella, P. C., and Huet, R., **"Verification of Tearing Modulus Methodology for Application to Reactor Pressure Vessels with Low Upper-Shelf Fracture Toughness,"** *Elastic-Plastic Fracture: Second Symposium, Volume II—Fracture Resistance Curves and Engineering Applications, ASTM STP 803*, C. F. Shih and J. P. Gudas, Eds., American Society for Testing and Materials, 1983, pp. II-156–II-178.

ABSTRACT: A significant number of operating reactor pressure vessels in the United States are anticipated to undergo, during their design lifetime, reductions in upper-shelf fracture toughness below the minimum values currently prescribed in the Code of Federal Regulations. This reduction occurs in the beltline region of the vessels adjacent to the reactor core due to neutron irradiation effects. A methodology has been developed by Paris to apply tearing modulus methodology to quantitatively establish the minimum upper-shelf toughness levels required to maintain an acceptable margin of safety in such vessels.

The proposed analytical techniques and data base are compared with test data and alternative analytical results in order to verify the validity of the methodology. The method is used to predict failure conditions in a series of large pressure vessels and tension bar experiments containing large crack-like defects. The analytical method is also compared with a three-dimensional nonlinear finite-element analysis of a typical pressurized water reactor vessel containing a beltline defect. The method is shown to accurately predict the test failure conditions and to agree well with the finite-element analysis results.

KEY WORDS: tearing modulus, elastic-plastic fracture, J-integral, flaw, vessel, fracture toughness

During plant operation, reactor pressure vessels of water-cooled reactor power plants are subject to continuous neutron irradiation. This irradiation

[1]Senior engineer and senior director, respectively, NUTECH, San Jose, Calif. 95119.
[2]Metallurgical engineer, Failure Analysis Associate, Palo Alto, Calif. 94303.

will reduce the material fracture toughness. To maintain an adequate factor of safety against fracture, the Code of Federal Regulation (10-CFR-50) and the American Society of Mechanical Engineers (ASME) Boiler and Pressure Vessel Code specify minimum Charpy upper-shelf impact energy requirements. Under current regulations reactor vessel material must have minimum Charpy upper-shelf energy of 102 J (75 ft-lb) initially and must maintain a minimum of 68 J (50 ft-lb) throughout the plant design life. High-energy neutron irradiation tends to reduce the Charpy upper-shelf energy, as shown in Fig. 1. It also increases the reference nil-ductility temperature (RT_{ndt}) of the reactor pressure vessel material. In some plants, the upper-shelf energy is projected to drop below the preceding limits during their design lifetime.

The minimum requirement for upper-shelf material toughness for reactor pressure vessels and associated safety margins has been identified as an unresolved safety issue by the U.S. Nuclear Regulatory Commission (NRC). It is generic issue A-11, "Reactor Vessel Material Toughness," and a task action plan has been implemented to resolve this issue [*1*].[3] One of the objectives of the task action plan is to develop an engineering methodology to quantitatively establish the minimum upper-shelf toughness level required to maintain acceptable margins of safety in reactor pressure vessels. The engineering methodology is based on the tearing instability concept developed by Paris [*2*]. This concept was further developed by Paris [*3*] for application to the reactor vessel fracture toughness issue.

In this paper, the engineering methodology and data base proposed in Ref *1* are compared with large-scale test data and alternative analytical techniques

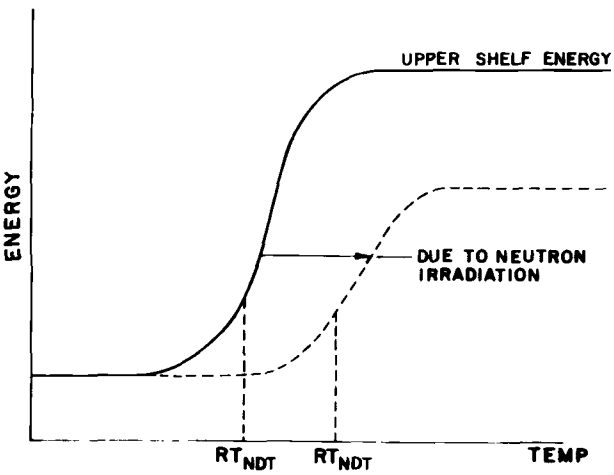

FIG. 1—*Schematic showing change in material upper-shelf energy due to neutron irradiation.*

[3]The italic numbers in brackets refer to the list of references appended to this paper.

to verify the validity of the proposed methodology. The method is used to predict failure conditions in a series of large pressure vessel and tension bar tests in which large crack-like defects have been introduced into the components. The analytical method is also compared with a three-dimensional finite-element analysis of a typical pressurized water reactor (PWR) vessel containing a large beltline defect. Finally, additional verification needs are identified and overall conclusions are drawn regarding the validity of the method for its intended purposes.

Theoretical Background

It has been shown that in the linear elastic regime, the J-integral can be related to the stress intensity factor K_I as

$$J = \frac{K_I^2}{E'} \tag{1}$$

where

$$E' = E \text{ (plane stress)}$$

$$= \frac{E}{1 - \nu^2} \text{ (plane strain)}$$

For the elastic case, the stress-intensity factor for a part-through surface flaw can be expressed as [*4*]

$$K_I = \sigma_m M_m \sqrt{\frac{\pi a}{Q}} \tag{2}$$

Introducing the flow stress σ_0, substituting Eq 2 into Eq 1 (with $\sigma = \sigma_m$), and rearranging, we get

$$\begin{aligned} J &= \frac{\sigma_0^2 a}{E'} \left[\pi \left(\frac{\sigma}{\sigma_0} \right)^2 \left(\frac{M_m}{Q} \right)^2 \right] \\ &= \frac{\sigma_0^2 a}{E'} F\left(\frac{\sigma}{\sigma_0} \right) G(a/t, a/l) \end{aligned} \tag{3}$$

In order to expand the applicability of Eq 3, using an approximate strip yield and crack opening stretch approach, Paris [*3*] has developed an approximate value $F(\sigma/\sigma_0)$ for shallow part-through flaws into the plastic region under the assumption of Ramberg-Osgood stress-strain law of the form

$$\frac{\epsilon}{\epsilon_0} = \frac{\sigma}{\sigma_0} + \bar{\bar{\alpha}}\left(\frac{\sigma}{\sigma_0}\right)^n \tag{4}$$

For empirically determined values of $\bar{\bar{\alpha}} = 1.115$ and $n = 9.7$ the stress correction function F for plane stress and plane strain is presented in Fig. 2 [3]. Considering the approximate nature of the analysis, it is assumed that the geometric correction factor $G(a/t, a/l)$ does not vary significantly from the elastic value as the analysis is extended into the plastic range. Therefore, differentiating Eq 3 to determine the tearing modulus T yields

$$\begin{aligned} T &= \frac{E'}{\sigma_0^2}\frac{\partial J}{\partial a} \\ &= F\left(\frac{\sigma}{\sigma_0}\right) G(a/t, a/l) + aF\left(\frac{\sigma}{\sigma_0}\right)\frac{d}{da}[G(a/t, a/l)] \end{aligned} \tag{5}$$

Once again considering the approximate nature of the analysis, it is assumed that the second term in Eq 5 is negligible. Using Eqs 3 and 5, the quotient J/T can be expressed simply as

$$\frac{J}{T} = \frac{\sigma_0^2 a}{E'} \tag{6}$$

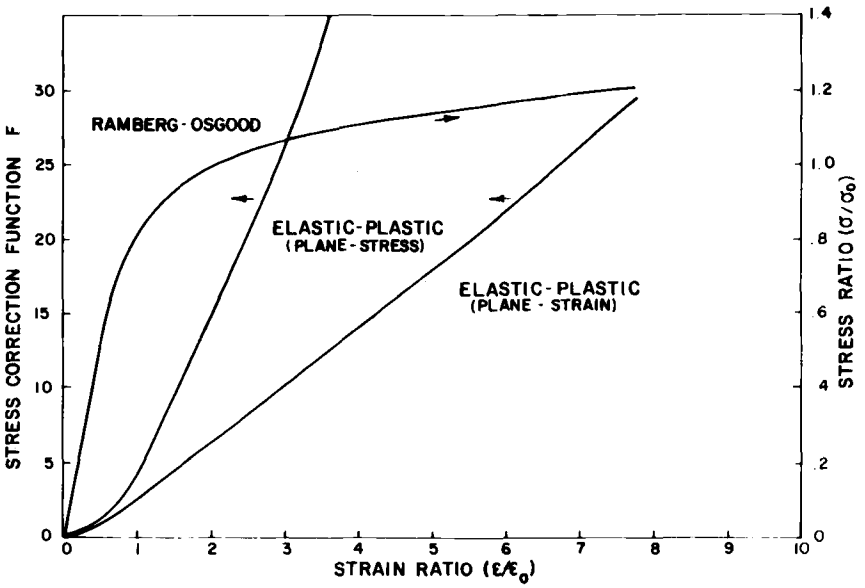

FIG. 2—*Stress correction function for part-through flaw [3] and Ramberg-Osgood stress-strain law.*

Values of applied J and T computed by the foregoing equations are used as the basis for comparison with the material fracture toughness properties $J_{material}$ and $T_{material}$ to develop failure predictions.

As shown in Fig. 3 [*3*], the critical J for instability can be determined from the intersection between the $J_{applied}$-$T_{applied}$ curve and the $J_{material}$-$T_{material}$ curve. Given a crack depth, a, and applied stress, σ, with Eqs 3 to 6, stress or strain corresponding to the critical J at instability can be determined.

Test Results Used for Verification

Heavy Section Steel Technology (HSST) Test Vessels

A series of intermediate-sized test pressure vessels was constructed and tested under the NRC-sponsored HSST Program [*5–7*]. The test vessels were made from low-alloy steel forging, plate, and weld material typical of those used in nuclear pressure vessel construction. Large cracks were artificially introduced in the vessels. The vessels were then pressurized to failure at various test temperatures ranging from lower transitional to upper-shelf temperature regimes for the low-alloy steels from which the vessels were fabricated. Figure 4 illustrates the overall configurations and dimensions of the intermediate test vessels.

Table I summarizes the specific vessel test conditions and results. Failure pressures were all in the 172 to 207-MPa (25 to 30 ksi) range, approximately three times the 67-MPa (9.7 ksi) nominal design pressure. Failure strains, however, varied extensively from close to yield strain to considerable gross plastic strain. As expected, a trend of higher failure strains for vessels tested at higher temperatures and with smaller flaw sizes was observed. Two distinct failure modes also were observed. Some vessels exhibited stable crack

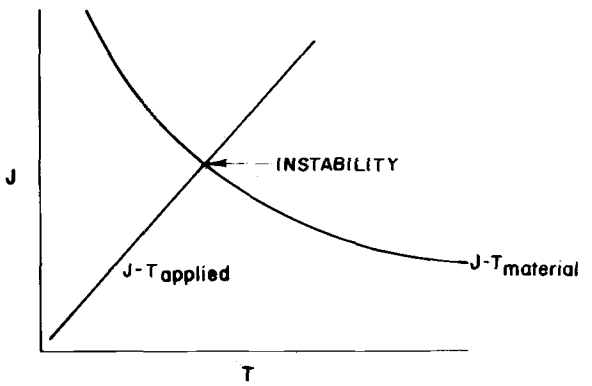

FIG. 3—*Tearing instability for stable crack growth.*

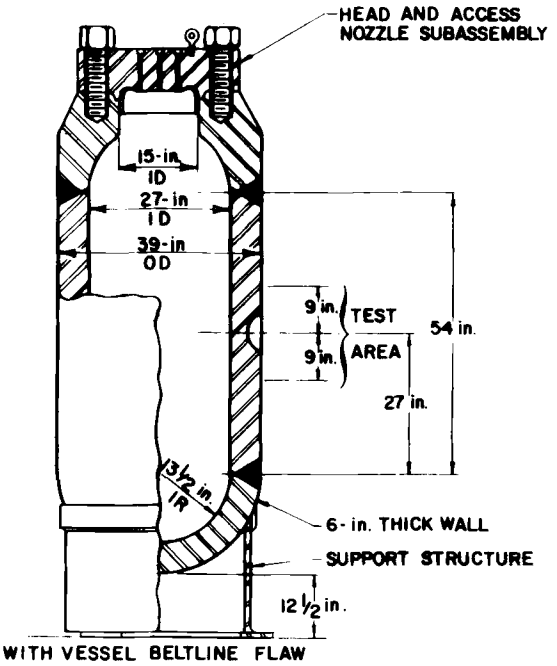

FIG. 4—*HSST intermediate pressure vessels (ITV's) (1 in. = 2.54 cm).*

TABLE 1—*Summary of test results from five 152-mm thick (6 in.) HSST intermediate test vessels.*

Vessel	Test Temperature, °C (°F)	Flaw Dimensions, mm (in.) Depth	Length	Flaw Location[a]	Fracture Pressure, MPa (ksi)	Nominal Fracture Strain,[b] %
V1	54 (130)	65 (2.56)	210 (8.25)	base metal (o)	198 (28.8)	0.92
V2	0 (32)	64 (2.53)	211 (8.30)	base metal (o)	192 (27.9)	0.19
V3	54 (130)	54 (2.11)	216 (8.50)	weld metal (o)	214 (31.0)	1.47
V4	24 (75)	75 (2.95)	208 (8.20)	weld metal (o)	183 (26.5)	0.17
	24 (75)	79 (3.12)	205 (8.05)	base metal (o)	183 (26.5)	0.17
V6	88 (190)	48 (1.87)	133 (5.25)	weld metal (o)	220 (31.9)	2.0
	88 (190)	34 (1.34)	132 (5.20)	base metal (o)	220 (31.9)	2.0
	88 (190)	49 (1.94)	135 (5.30)	weld metal (i)	220 (31.9)	2.0

[a]Letter o = outside surface; i = inside surface.
[b]Outside circumferential strain on centerline of vessel remote from flaw.

extension, finally leading to a leaking through-wall crack and others exhibited gross unstable fracture of the entire vessels. The magnitude and diversity of the data base generated by the HSST program provided an excellent opportunity for application and verification of the tearing modulus concepts proposed for application to the Task A-11 generic issue.

Southwest Research Institute (SWRI) Large Tension Specimen Tests

The 6¾ million kg (15 million lb) tension test facility at SWRI was used to test a series of large tension specimens for the HSST program [*8*]. Large cracks were machined in the specimens before testing. Figure 5 [*8*] shows the geometry of the specimens and cracks. The specimens made of low-alloy steel plate material typical of nuclear pressure vessel construction were tested at various temperatures ranging from 5 to 104°C (40 to 220°F), covering the lower- to upper-shelf temperature regimes for this material. Table 2 summarizes the specific test conditions and results. Failures occurred at strains ranging from well below yield to well beyond gross plastic deformation of the specimens. The results show the expected trend of higher failure stresses and strains for specimens tested at higher temperatures or having smaller flaws.

Material Toughness Estimation

Material toughness properties, J_{material} versus T_{material}, are needed in order to make test failure predictions. These material toughness properties were obtained using two approaches [*1*]:

(1) use of large-specimen test data for the material and test temperature of interest to develop J_{material} and T_{material} directly from J-R curves, and
(2) extrapolation of small-specimen test data using a power-law J-R curve approximation, with parameters in the power-law approximation obtained from empirial correlations of Charpy and tension test data for the material and test temperature of interest.

The latter approach was not needed for the present experimental comparisons, since actual large-specimen J-R curves were available. However, it is included to permit an evaluation of the power-law approach for cases in which large-specimen data are not available.

In contrast to the low upper-shelf fracture toughness material to which the A-11 issue is directed, the intermediate test vessels were fabricated from material with relatively high upper-shelf fracture toughness. Only limited upper-shelf J-R data are available for this class of material since the focus of J-R testing has been the low upper-shelf materials of main interest to the A-11 issue. Figure 6 presents J-R curve data for two sets of large-specimen tests of material similar to those used in the intermediate test vessels. A series of 4T compact tension specimens tested by General Electric Co. [*9*] yielded

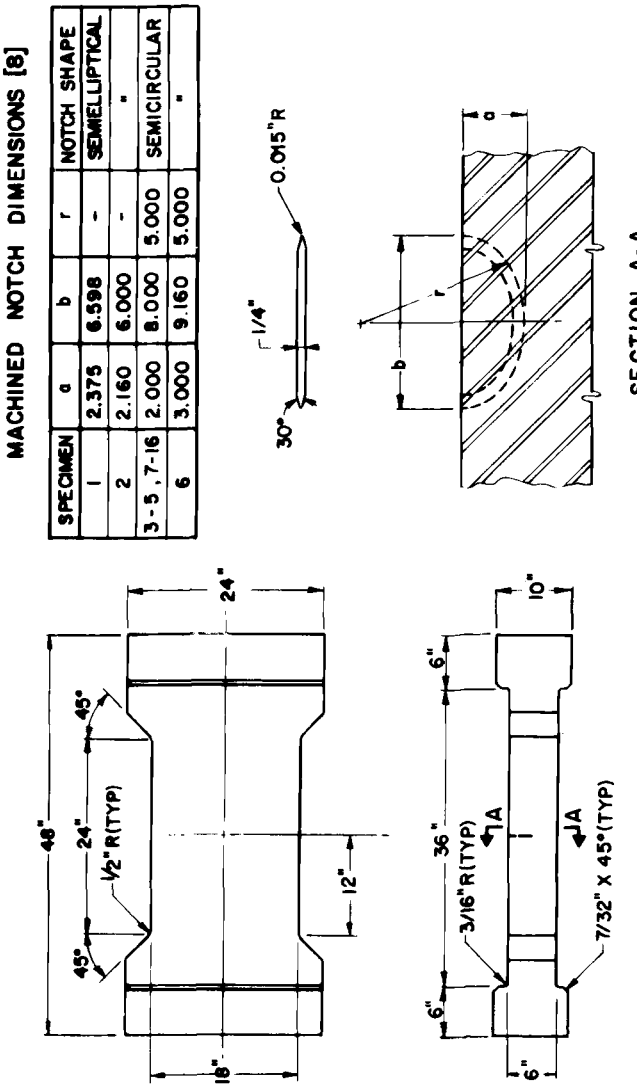

FIG. 5—*Dimensions of SWRI large tension specimens [8] (1 in. = 2.54 cm).*

TABLE 2—*Test results from SWRI tension specimen tests.*

Specimen	Test Temperature, °C (°F)	Avg Strain at Ultimate, %	Avg Strain at Fracture, %
1	102 (215)	...	8.50
2	104 (220)	3.83	9.60
3	10 (50)	0.24	0.24
4	38 (100)	4.10	7.90
5	24 (75)	0.35	0.35
6	38 (100)	0.48	0.48
14	93 (200)	1.81	4.22

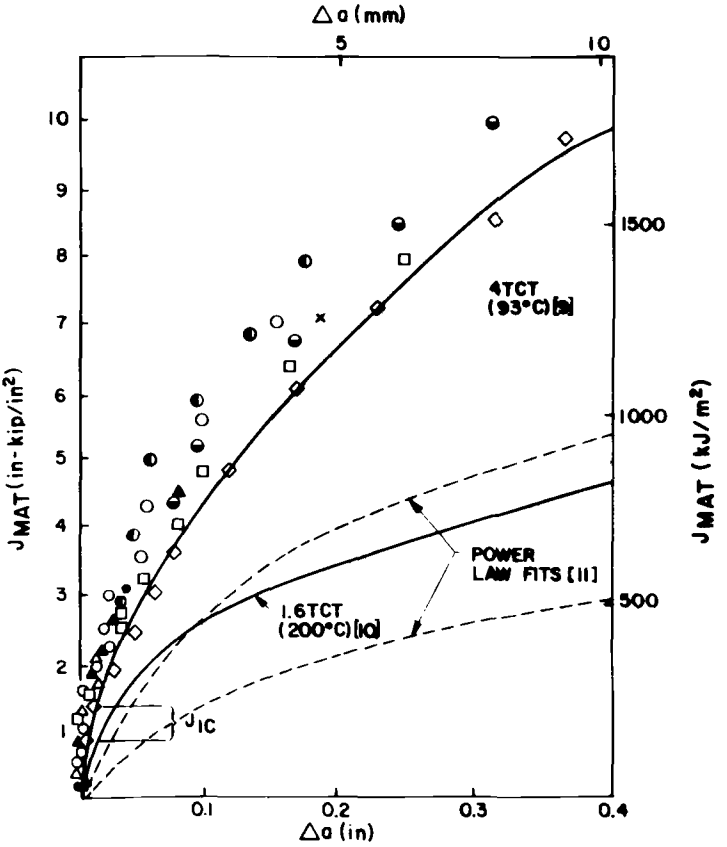

FIG. 6—*J-R curves for materials similar to intermediate test vessel material (1 in. = 2.54 cm).*

the upper solid curve. A 1.6T compact specimen tested by the Naval Research Laboratory [*10*] yielded the lower solid curve. A second estimate of material J-R curve can be obtained from a power-law R-curve approximation in conjunction with an empirical correlation of Charpy and tension test data for the vessel material [*11*]. The resulting J-R curves are also shown in Fig. 6. Differentiating these curves yields the $J_{material}$ versus $T_{material}$ curves in Fig. 7. Other J-T curves [*10*] for low upper-shelf fracture toughness material are also given in Fig. 7 for comparison.

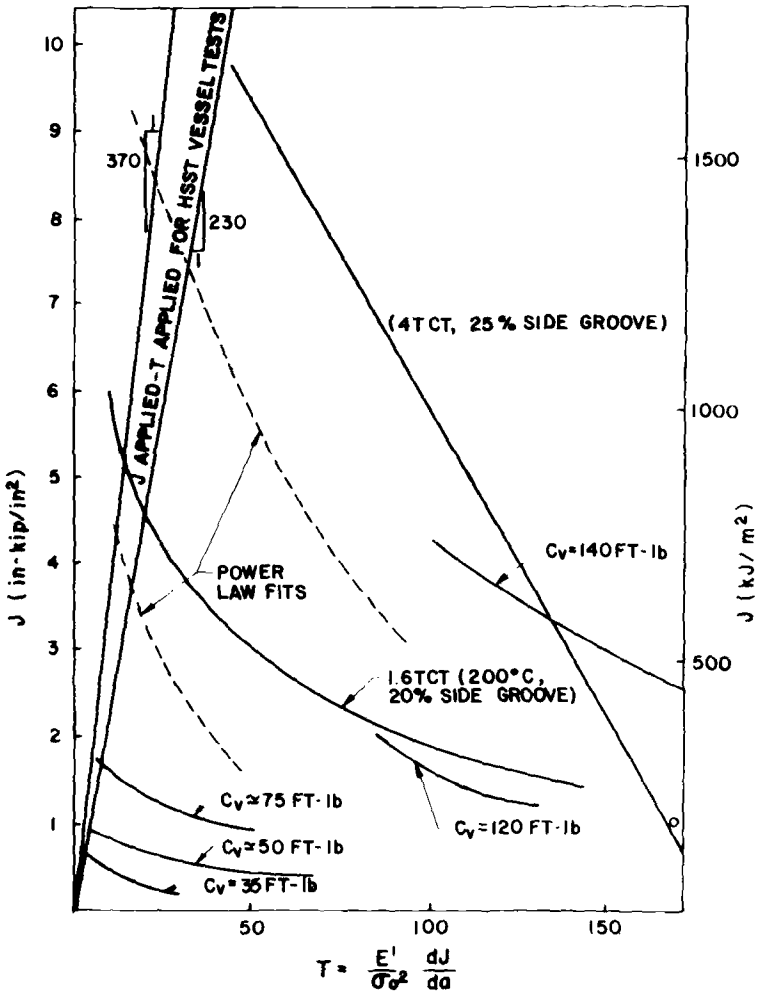

FIG. 7—J_{MAT} *versus* J_{MAT} *curves for the J-R curves of Fig. 6 (1 ft·lb = 0.1383 kg·m).*

Analysis Results

HSST Intermediate Test Vessels

Using Eq 6, assuming σ_o = 413 MPa (60 ksi) and E = 199 520 MPa (29 × 10^6 psi), the $J_{applied}/T_{applied}$ for the intermediate test vessels V1, V2, V3, V4, and V6 was calculated to be from 230 to 370. The $J_{applied}/T_{applied}$ curves for all five vessels are plotted as a near vertical band in Fig. 7. The intersection of this band with the appropriate $J_{material} - T_{material}$ curve represents the prediction of critical J-value at instability for the vessels. In the case of Vessels V1, V3, and V6, the intersection for J-critical falls somewhere between 875.6 and 1751.3 kJ/m^2 (5000 and 10 000 in.·lb/in.^{2}) using 4T and 1.6T compact tension specimen test data. Alternatively, using the power-law R-curve approximations, the critical J-value at instability is found to lie between 700.5 and 1401.0 kJ/m^2 (4000 to 8000 in.·lb/in.^{2}). These are in essentially the same range as the critical J-values obtained from the 1.6T and 4T compact tension test specimens, indicating reasonable agreement between the toughness estimates obtained by the two approaches.

Figure 8 presents plots of J versus strain for the five vessels using Eqs 3 and 4. The J-calculations are based on the thin shell approximation of uniform stress and strain through the wall thickness. The actual vessels are relatively thick and would sustain substantial through-thickness strain gradients. Also,

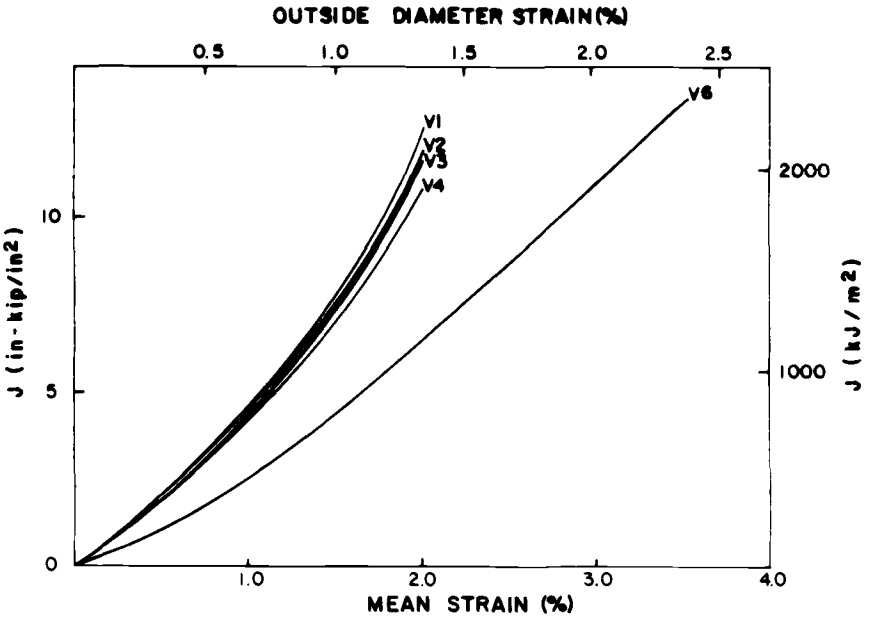

FIG. 8—J *versus mean and outside strain for test vessels.*

the strain gages in the vessel tests were mounted on the vessel outside surface, remote from the crack. Thus a second strain scale giving outside surface strain is also shown in Fig. 8 to account for the through-wall strain gradient. $J_{critical}$ can be entered into this figure to determine the predicted failure strain.

Table 3 summarizes the results of the analyses of the surface-flawed test vessels. For Vessels V2 and V4, which were tested in the transitional regime, the failure strains were predicted based on material fracture toughness J_{Ic} = 210.2 kJ/m^2 (1200 in.·lb/in.^{2}) in Fig. 6. Entering Fig. 8, this yields outer surface strain predictions of 0.21 and 0.18, which are in excellent agreement with the actual failure strains. For Vessels V1, V3, and V6, which were tested in the upper-shelf regime, values of J_{crit} for instability were determined based on the applied J-T band intersections with the material J-T curves. Since material toughness properties were obtained using large-specimen test data and power-law fit curves, failure strains were also determined based on both methods. Using large compact tension specimen data, the J_{crit} was found to be 876 kJ/m^2 (5000 in.·lb/in.^{2}) using 1.6T compact tension specimen test data and 1751 kJ/m^2 (10 000 in.·lb/in.^{2}) using 4T compact tension specimen data. Using power-law fits curves, the J_{crit} was found to be 700 kJ/m^2 (4000 in.·lb/in.^{2}) for the lower-bound curves and 1401 kJ/m^2 (8000 in.·lb/in.^{2}) for the upper-bound curve. Entering the J versus strain curves of Fig. 8, failure strains were determined; these are presented in Table 3. The predicted failure strains using large compact tension specimen data and power-law fit curves both provide reasonable estimates of the actual test failure conditions for the tests conducted in the upper-shelf regime. Likewise, the crack initiation approach ($J = J_{Ic}$) gives reasonable estimates for the tests conducted in the transitional regime. Considering the magnitude of some of the approximations used in these analyses, the accuracy of these predictions is highly encouraging.

Large Tension Specimen Tests

The approximate analysis for part-through flaws used in the HSST test vessels was again employed to estimate the $J_{applied}/T_{applied}$ curves for the SWRI large tension specimens. However, this analysis neglects the effect of the bending stress introduced by the presence of the crack. Therefore, it is only valid as a first approximation for these tension specimens. Table 4 presents the geometrical parameters [*8*] and the J/T-value for the various tests performed. The stress function $F(\sigma/\sigma_o)$ [*3*] was used to calculate the J versus strain curve for the tension specimens tested.

For tests performed at 24°C (75°F) or lower (that is, in the transitional regime), the failure criterion was chosen to be material fracture toughness J_{Ic} = 210.2 kJ/m^2 (1200 in.·lb/in.^{2}). For the other tests performed in the upper-shelf regime, the J_{crit} for failure prediction was determined to be similar to

TABLE 3—*Comparison of actual and predicted failure conditions for HSST test vessels Nos. 1 to 4 and 6.*

Vessel	Test Temperature, °C (°F)	Regime	Actual Failure Conditions, %	Crack Initiation ($J = J_{Ic}$)		Instability ($J = J_{crit}$ from Fig. 7)			
						Large Compact-Tension Specimen Data		Power-Law Fits	
				J_{Ic}, kJ/m^2 (in.·lb/in.^{2})	Strain, %	J_{crit}, kJ/m^2 (in.·lb/in.^{2})	Strain, %	J_{crit}, kJ/m^2 (in.·lb/in.^{2})	Strain, %
V2	0 (32)	transition	0.19	210 (1200)	0.21	...	...	...	...
V4	24 (75)	transition	0.17	210 (1200)	0.18	...	...	...	...
V1	54 (130)	upper shelf	0.92	...	...	876 (5000) 1751 (10 000)	0.71 1.19	700 (4000) 1401 (8000)	0.60 1.04
V3	54 (130)	upper shelf	1.47	...	...	876 (5000) 1751 (10 000)	0.74 1.24	700 (4000) 1401 (8000)	0.62 1.06
V6	88 (190)	upper shelf	2.0	...	...	876 (5000) 1751 (10 000)	1.09 1.85	700 (4000) 1401 (8000)	0.93 1.59

TABLE 4—*Crack dimensions of the SWRI large tension specimen at ultimate load.*

Specimen No.	Crack Depth, mm (in.)	Crack Length, mm (in.)	J/T, kJ/m^2 (in.·lb/in.^{2})
1	...	...	...
2	73 (2.86)	150 (5.91)	59 (338)
3	52 (2.05)	213 (8.37)	42 (242)
4	88 (3.45)	204 (8.02)	71 (407)
5	64 (2.53)	208 (8.26)	52 (299)
6	110 (4.33)	260 (10.25)	89 (511)
14	74 (2.90)	199 (7.85)	60 (342)

that for the HSST test vessels. Using 4T compact-tension specimen test data, the J_{crit} was determined to be 1751 kJ/m^2 (10 000 in.·lb/in.^{2}) and 876 kJ/m^2 (5000 in.·lb/in.^{2}) from the 1.6T compact-tension specimen test data. Using power-law fit J-R curves, the upper-bound and lower-bound values were found to be 700 kJ/m^2 (4000 in.·lb/in.^{2}) and 1401 kJ/m^2 (8000 in.·lb/in.^{2}), respectively. These values are identical to those used in the HSST vessel tests because the material J-T curves are the same, and the $J_{applied}/T_{applied}$ lines are similar. For the preceding J_{crit}-values, the failure strain is determined from the appropriate curve in Fig. 10 for the various large tension specimen tests. The results are given in Table 5. The predicted strains grossly underpredict the actual ultimate strains, except for the tests which were performed at temperatures near transistion regime. The predictions are conservative because the analyses assumed plane-strain conditions, rather than the plane-stress conditions which were most likely obtained in the tests.

To account for plane-stress conditions, Paris [*12*] suggested an approximate modification to the J_{mat}-T_{mat} curves of doubling the J-values in Fig. 9. J_{mat}-T_{mat} curves, modified in this manner for plane-stress conditions, are shown in Fig. 11, along with the J_{app}/T_{app} band for the large tension tests. In this condition, the J_{crit} was determined to be 1401 kJ/m^2 (8000 in.·lb/in.^{2}) and 3152 kJ/m^2 (18 000 in.·lb/in.^{2}) from the large compact tension specimen test data. From the power-law fit curves, J_{crit} is found to be 1225 kJ/m^2 (7000 in.·lb/in.^{2}) and 2276 kJ/m^2 (13 000 in.·lb/in.^{2}) for the two curves shown. Taking the foregoing J_{crit}-values as input into Fig. 10 again, a second set of predicted strains was found under the assumption of plane stress. The results are given in Table 6. These new predicted strains are in better agreement with, but higher than, the experimental ultimate strains in the majority of the test cases, indicating that the actual specimen behavior is between plane stress and plane strain. The exception is the tests conducted in the transitional regime in which the plane-strain crack initiation predictions are more accurate. It is also noteworthy that one of the 38°C (100°F) tests (Specimen 6) was better characterized by the crack initiation methodology, while the other (Specimen 4) agrees well with the instability prediction. This observation indi-

TABLE 5—*Comparison of predicted and actual strains at failure for SWRI large tension specimens (assumed plane-strain condition).*

Specimen No.	Strain, %		Test Temperature, °C (°F)	Crack Initiation, $J = J_{Ic}$		Instability ($J = J_{crit}$ from Fig. 9)			
						Large Compact-Tension Specimen Data		Power-Law Fits	
	at Ultimate	at Fracture		J_{Ic}, kJ/m^2 (in.·lb/in.^{2})	Strain, %	J_{crit}, kJ/m^2 (in.·lb/in.^{2})	Strain, %	J_{crit}, kJ/m^2 (in.·lb/in.^{2})	Strain, %
1	...	8.50	102 (215)	...	...	876 (5000)	1.3	700 (4000)	1.1
						1751 (10 000)	2.3	1401 (8000)	1.9
2	3.83	9.60	104 (220)	...	...	876 (5000)	1.4	700 (4000)	1.2
						1751 (10 000)	2.6	1401 (8000)	2.1
3	0.24	0.24	10 (50)	210 (1200)	0.28	...	...	...	...
4	4.10	7.90	38 (100)	...	...	876 (5000)	1.1	700 (4000)	0.94
						1751 (10 000)	2.0	1401 (8000)	1.6
5	0.35	0.35	24 (75)	210 (1200)	0.28	...	...	...	...
6	0.48	0.48	38 (100)	...	...	876 (5000)	0.94	700 (4000)	0.88
						1751 (10 000)	1.6	1401 (8000)	1.3
14	1.81	4.22	93 (200)	...	...	876 (5000)	0.94	700 (4000)	0.88
						1751 (10 000)	1.7	1401 (8000)	1.4

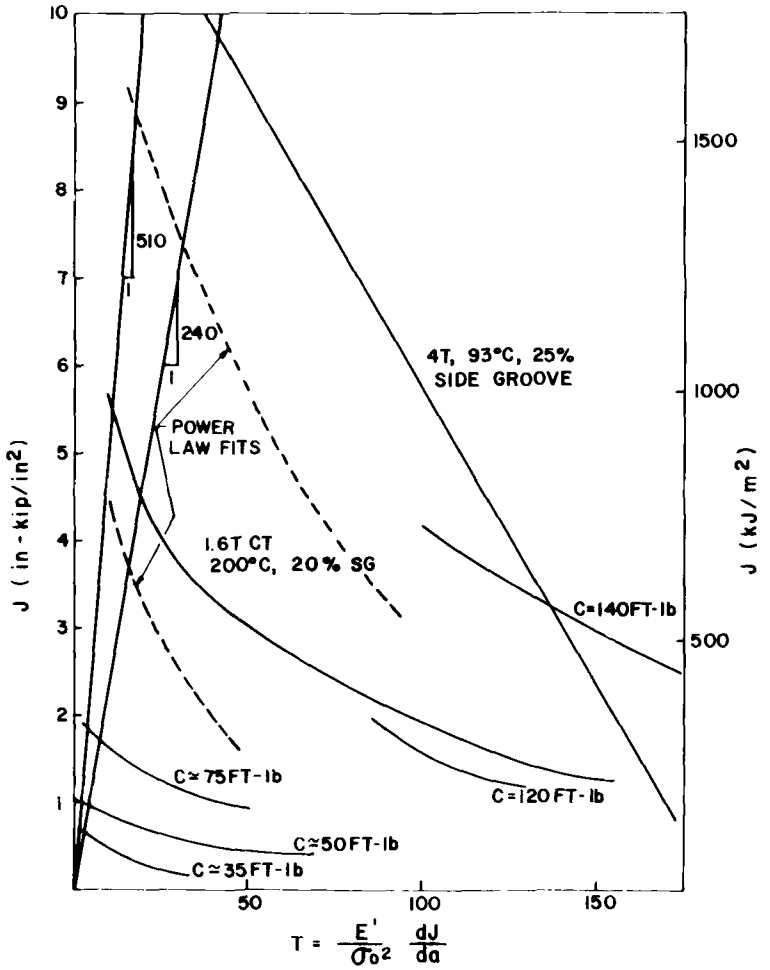

FIG. 9—J *versus* T *curves for the large tension tests (plane strain assumed) (1 ft·lb = 0.1383 kg·m).*

cates that 38°C (100°F) may be the approximate boundary between transitional and upper-shelf behavior in those tests.

Comparison with Three-Dimensional Finite-Elements Analysis

The stress function F (σ/σ_0) [*3*] was also used to calculate the energy release rate and compared with finite-element analyses results. General Electric Co., under Electric Power Research Institute (EPRI) sponsorship, has conducted a detailed three-dimensional elastic-plastic finite-element analysis

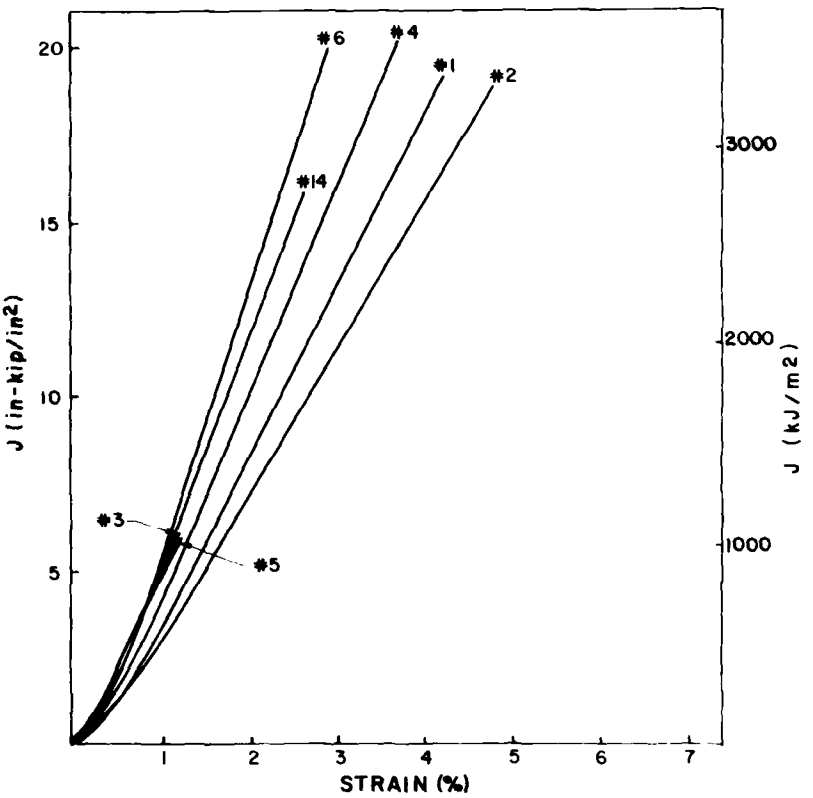

FIG. 10—$J_{APPLIED}$ *versus strain for the large tension specimens.*

of a typical PWR reactor vessel containing a beltline flaw [*13*]. Vessel geometry and crack detail are illustrated in Fig. 12. The elastic-plastic stress-strain curve is shown in Fig. 13.

Assuming Tresca flow theory and zero radial stress, the stress acting on the crack is the standard hoop stress in the thin-wall cylindrical shell:

$$\sigma = \frac{Pr}{t} \tag{7}$$

Considering the total strain to consist of elastic and plastic components, the stress-strain curve in Fig. 13 was rewritten as

$$\frac{\epsilon}{\epsilon_0} = \frac{\sigma}{\sigma_0} + 1.4\left(\frac{\sigma}{\sigma_0}\right)^{8.6} \tag{8}$$

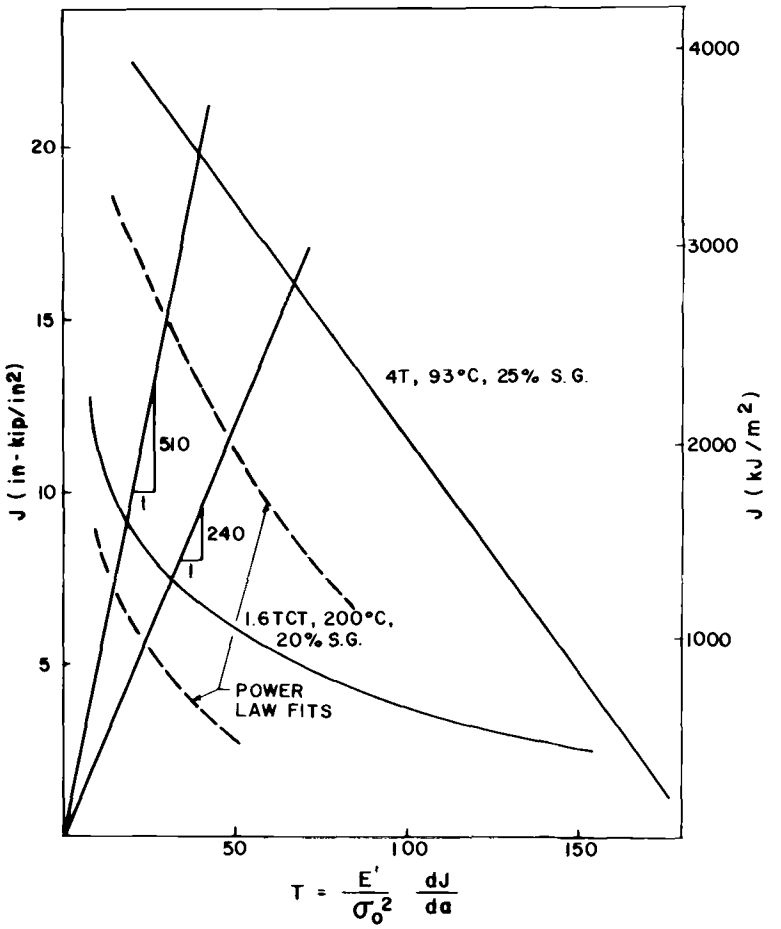

FIG. 11—J *versus* T *curves for the large tension specimens corrected for plane stress.*

This equation is the same as the Ramberg-Osgood form used earlier but with slightly different values of the parameters α and n. For the flaw configuration shown in Fig. 12, the geometric correction factor $G\,(a/l,\ a/t)$ can be determined using the standard linear elastic fracture mechanics methodology of ASME Code, Section XI, Appendix A [*4*], as follows:

$$a/l = 0.167$$
$$a/t = 0.25$$
$$M_m = 1.19$$
$$Q = 1.20$$
$$G\,(a/l,\ a/t) = \frac{M_m{}^2}{Q} = 1.18$$

TABLE 6—*Comparison of predicted and actual strains at failure for SWRI large tension specimens (assumed plane-strain condition).*

Specimen No.	Strain, %		Test Temperature, °C (°F)	Crack Initiation, $J = J_{Ic}$		Instability ($J = J_{crit}$ from Fig. 11)			
						Large Compact-Tension Specimen Data		Power-Law Fits	
	at Ultimate	at Fracture		J_{Ic}, kJ/m^2 (in.·lb/in.^{2})	Strain, %	J_{crit}, kJ/m^2 (in.·lb/in.^{2})	Strain, %	J_{crit}, kJ/m^2 (in.·lb/in.^{2})	Strain, %
1	...	8.50	102 (215)	...	...	1401 (8000)	1.9	1225 (6000)	1.50
						3152 (18 000)	3.6	2276 (13 000)	2.88
2	3.83	9.60	104 (220)	...	...	1401 (8000)	2.1	1225 (6000)	1.69
						3152 (18 000)	4.5	2276 (13 000)	3.31
3	0.24	0.24	10 (50)	420 (2400)	0.53	...	...	...	...
4	4.10	7.90	38 (100)	...	...	1401 (8000)	1.6	1225 (6000)	1.31
						3152 (18 000)	3.3	2276 (13 000)	2.44
5	0.35	0.35	24 (75)	420 (2400)	0.53	...	...	...	...
6	0.48	0.48	38 (100)	...	...	1401 (8000)	1.3	1225 (6000)	1.06
						3152 (18 000)	2.7	2276 (13 000)	1.94
14	1.81	4.22	93 (200)	...	...	1401 (8000)	1.4	1225 (6000)	1.13
						3152 (18 000)	2.9	2276 (13 000)	2.19

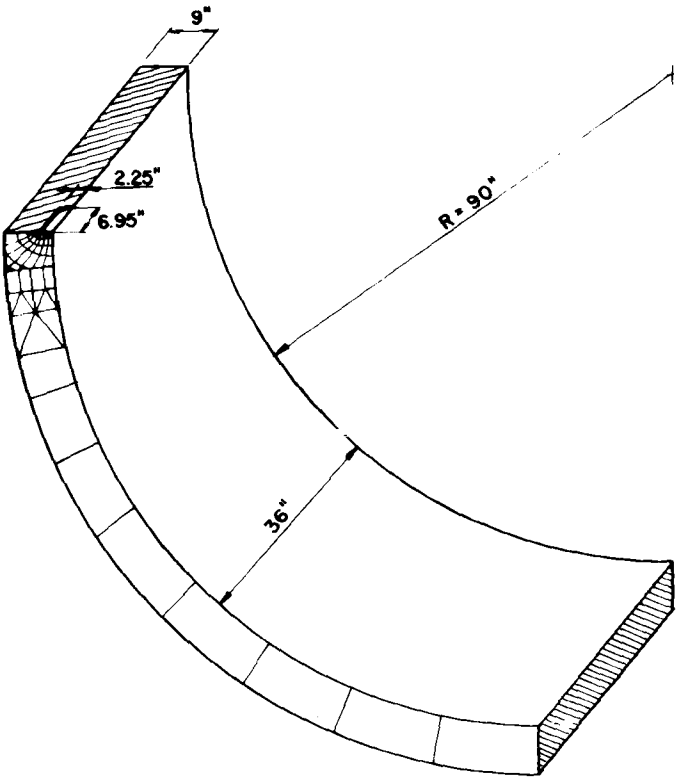

FIG. 12—*Finite-element model of vessel with beltline axial flaw [13] (1 in. = 2.54 cm).*

Using the geometry correction factor G, stress function F, Eqs 3 and 7, the values of J versus internal pressure are plotted in Fig. 14. The results from the finite-element analysis [*13*] are also presented in Fig. 14. The agreement between the two approaches is excellent for the entire range of pressures over which the finite-element analyses have been performed.

This agreement further verifies the approximate surface flaw methodology developed [*3*] for application to the NRC Task A-11 issue. It also indicates a lack of sensitivity of the stress correction function F to the particular stress-strain law since it has now been demonstrated for two different stress-strain curves.

Conclusions

Analyses are presented which demonstrate the validity of the proposed tearing modulus methodology by Paris [*3*] for application to the reactor vessel fracture toughness generic safety issue (A-11). The method is shown to

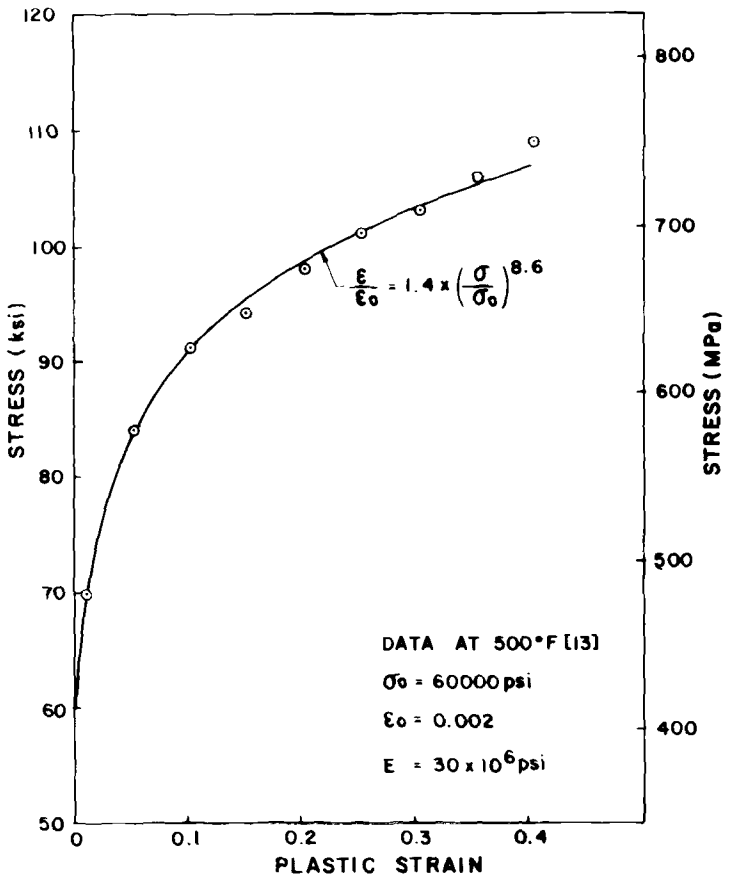

FIG. 13—*Plastic flow curve for A533B.*

accurately predict the failure conditions in all beltline-flawed HSST intermediate test vessels. It also conservatively predicted the failure conditions in the SWRI large tension bars. The conservatism in this case is believed to be primarily due to the lack of full triaxial constraint in the vicinity of the cracks, and a plane-stress approximation is introduced which appears to correct for this effect. The methodology also agrees extremely well with three-dimensional nonlinear finite-element analysis results for a typical PWR reactor vessel containing a large beltline crack.

Although the verification program discussed herein has demonstrated the viability of the proposed NRC Task A-11 methodology, there is a need for additional testing to complete the verification. A large body of experimental $J_{material}$-$T_{material}$ data exists for the relatively low upper-shelf fracture toughness materials of interest in the A-11 program. However, all of the

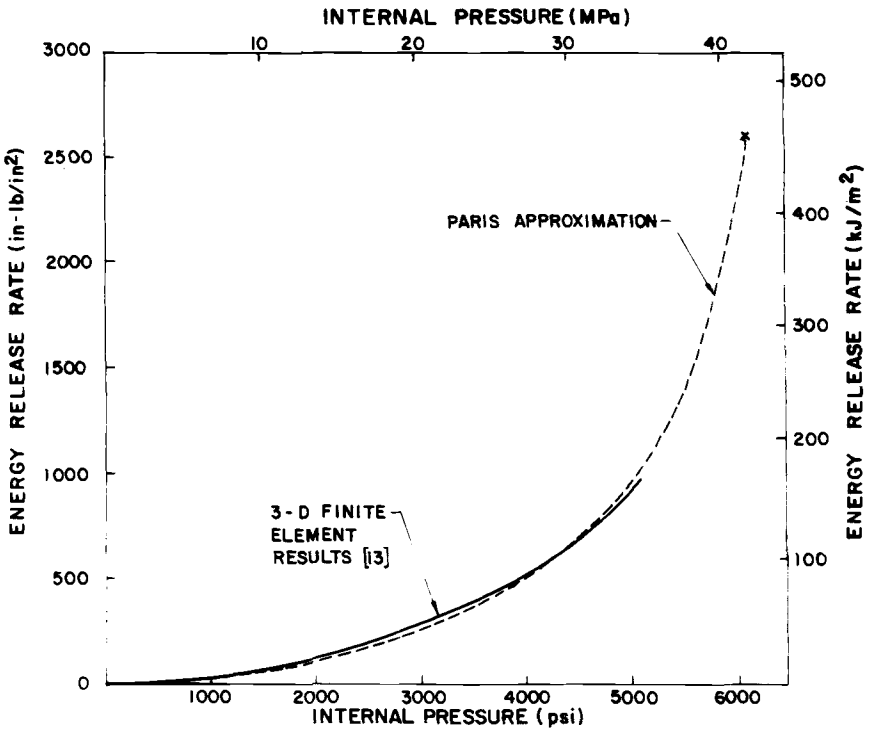

FIG. 14—*Variation of energy release rate with internal pressure.*

verification tests to date have been conducted with relatively high upper-shelf toughness materials for which only a small amount of $J_{material}$-$T_{material}$ data exists. Thus to fully prove out the methodology, additional $J_{material}$-$T_{material}$ testing of high upper-shelf materials as well as a verification test on low upper-shelf material is recommended.

Acknowledgments

The authors gratefully acknowledge the financial support of this work by the Oak Ridge National Laboratory and the technical guidance and support provided by Prof. Paul C. Paris of Washington University and Dr. Richard E. Johnson of the U.S. Nuclear Regulatory Commission.

References

[1] Johnson, R. E. et al, "Resolution of Reactor Vessel Materials Toughness Safety Issue A-11," U.S. Nuclear Regulatory Commission Report NUREG-0744, issued for comments, Washington, D.C., Sept. 81.

[2] Paris, P. C., Tada, H., Zahoor, A., and Ernst, H., "A Treatment of the Subject of Tearing

Instability," U.S. Nuclear Regulatory Commission Report NUREG-0311, Washington, D.C., Aug. 1977.

[3] Paris, P. C. and Johnson, R. E., this publication, pp. II-5–II-40.

[4] *ASME Boiler and Pressure Vessel Code*, American Society of Mechanical Engineers, Section 11, 1977.

[5] Derby, R. W. et al, "Test of Six-Inch Thick Pressure Vessels, Series 1: Intermediate Test Vessels V1 and V2," ORNL-4895, Oak Ridge National Laboratory, Oak Ridge, Tenn., 1974.

[6] Bryan, R. H. et al, "Test of Six-Inch Thick Pressure Vessels, Series 2: Intermediate Test Vessels V3, V4, and V6," ORNL-5059, Oak Ridge National Laboratory, Oak Ridge, Tenn., 1975.

[7] Merkle, J. G. et al, "Test of Six-Inch Thick Pressure Vessels, Series 3: Intermediate Test Vessels V7," ORNL/NUREG-1, Oak Ridge National Laboratory, Oak Ridge, Tenn., 1976.

[8] Grigory, S., *Nuclear Engineering and Design*, Vol. 17, 1971, pp. 161–169.

[9] Shih, C. F. et al, "Methodology for Plastic Fracture—Final Report," EPRI, RG-601-2, Electric Power Research Institute, Palo Alto, Calif., March 1981.

[10] Loss, F. J., Menke, B. H., Hiser, A. L., and Watson, H. E., this publication, pp. II-777–II-795.

[11] Merkle, J. G., to be published.

[12] Paris, P. C., private communication.

[13] Kumar, V. et al, "Estimation Technique for the Prediction of Elastic-Plastic Fracture of Structural Components of Nuclear Systems—Semi-Annual Report," EPRI Contract RP-1237-1, Electric Power Research Institute, Palo Alto, Calif., to be published.

Graham G. Chell[1] *and Ian Milne*[1]

Ductile Tearing Instability Analysis: A Comparison of Available Techniques

REFERENCE: Chell, G. G. and Milne, I., **"Ductile Tearing Instability Analysis: A Comparison of Available Techniques,"** *Elastic-Plastic Fracture: Second Symposium, Volume II—Fracture Resistance Curves and Engineering Applications, ASTM STP 803*, C. F. Shih and J. P. Gudas, Eds., American Society for Testing and Materials, 1983, pp. II-179-II-205.

ABSTRACT: A comparison is made between the major proposals recently developed for assessing the stability of a structure which is cracking by ductile mechanisms. These proposals all have in common the concept that stability is ensured if the crack driving force is less than the material's resistance to cracking. They differ, however, in how they define and evaluate the necessary parameters.

The four basic procedures discussed are:

1. Direct graphical comparisons, using the J-integral as a fracture parameter. Different methods of estimating the applied J are discussed, together with techniques for comparing the slopes of the applied J and the material's resistance curve.
2. An energy-based method which compares the elastic energy release rate and the plastic work dissipation rate during crack extension.
3. Assessment diagram approaches. These include the Central Electricity Generating Board procedure and methods that incorporate strain-hardening effects.
4. Maximum load crack-opening displacement.

The information needed to perform each analysis and its relevance to the practical problem when viewed against the uncertainties inherent in any structural analysis are discussed. Emphasis is given to the treatment of thermal and residual stresses. It is concluded that the confidence obtained in the results varies from procedure to procedure, but this can be greatly enhanced if certain safeguards are applied during the analysis. The safeguards necessary depend upon which approach is adopted.

KEY WORDS: ductile tearing, instability analysis, J-integral, η-factor, crack-opening displacement, crack growth, resistance curve, failure assessment diagram, tearing modulus, strain hardening, stress-intensity factor, plastic collapse load, strip yielding model, J estimation schemes, design curves, thermal stresses, residual stresses, elastic-plastic fracture

[1]Fracture Mechanics Project leader and research officer, respectively, General Electricity Research Laboratories, Central Electricity Generating Board, Kelvin Avenue, Leatherhead, Surrey, U.K.

In recent years several proposals have been developed which are aimed at assessing the stability of a structure when it is cracking by ductile mechanisms. All of these techniques use the same concept, namely, that stability is ensured if the crack driving force is less than the resistance of the material to cracking. They have, however, either different ways of defining this condition or different ways of calculating it. This paper is intended to review the different proposals for performing this type of analysis with the objective of highlighting the suitability of each technique with particular regard to the amount and type of information required to perform each analysis. The techniques reviewed are those which have been developed specifically for handling the problem of ductile crack growth in thick structures. The possibility of fracture by brittle mechanisms and time-dependent effects is not considered here.

General Philosophy

Ductile failure of a structure containing a defect generally occurs in the following sequence:

1. A crack initiates from the defect,
2. the crack extends, lowering the plastic collapse load of the structure, and
3. failure occurs at a point when the structure ceases to perform its design function.

Structural failure may be either by unstable or stable mechanisms, that is, it may be progressive and therefore controllable, or disruptive. Unstable failure invariably arises in load-controlled structures, where the instability condition inevitably coincides with the structure's maximum tolerable load. Unstable failure may also arise under displacement control, but in this case it may occur after some unloading, depending on the gage length over which the displacements are imposed. In neither case is the instability point related solely to the amount of crack growth. Depending upon the form of the crack driving force, instability may coincide with the initiation of cracking, or it may occur after the crack has grown a considerable distance.

The basic characteristic of all the approaches to be described here is that the applied crack extension force is judged against the material's resistance to cracking. If this is exceeded, the crack extends until the applied force is balanced by the resistance. If a point of balance cannot be attained, then the ensuing cracking is unstable. At the present time there are three proposed classes of resistance parameters. They are based upon the J-integral (J_R), the crack-tip opening displacement (COD), and the plastic work absorption rate. In the former two the applied values of J, J_A, and COD, δ_A, represent the crack-tip driving force, while in the latter the driving force is the elastic energy release rate.

The principle behind the analysis is shown schematically in terms of J in Fig. 1. At load L_1, J_A intersects the J_R-curve at a point above J_{Ic}, the initiation value. Before this intercept the crack extension force is greater than the material's resistance to cracking, so the crack will extend here. Beyond the intercept the crack extension force is lower than the resistance to cracking, so the crack cannot extend here. The intercept of the two curves, J_A and J_R, defines the point of stability in terms of initial crack length, the crack extension, and the loading conditions. At L_3, J_A is everywhere above J_R, so at this load the structure is unstable. The limit of stability is defined at L_2, where J_A is tangential to J_R. The condition for stable growth is expressed mathematically as

$$J_A = J_R \tag{1a}$$

$$\frac{dJ_A}{da} < \frac{dJ_R}{da} \tag{1b}$$

Use of a resistance curve concept in the manner idealized in Fig. 1 therefore involves two aspects: (1) choice of the resistance toughness (taken as J_R in Fig. 1) and (2) evaluation of a crack driving force consistent with the choice of resistance parameter. It is in the detail of these two aspects, and how they are combined in applying equations similar to Eq 1, that the following techniques differ, not in their fundamental concepts.

Direct Comparison of J_A and J_R Curves

This is the most obvious and direct procedure to follow as it simply means superimposing J_A-curves over a J_R-curve,[2] as depicted in Fig. 1. J_A is evaluated as a function of crack length, a, at the applied load or displacement of interest and the J_R-curve is plotted for crack extension Δa with respect to the crack lengths of interest, a_0, where $\Delta a = a - a_0$. If Eq 1 is satisfied, this will be visually obvious and the structure will be stable. The limiting condition for stability is given as the solution to the equations[3]

$$J_A(a) = J_R(a - a_0) \tag{2a}$$

$$\frac{dJ_A}{da} = \frac{dJ_R}{da} \tag{2b}$$

[2]Unless otherwise stated, the J used is evaluated from deformation theory. In experiments a so-called far-field value of J may be obtained from the total area under the load-displacement curve uncorrected for crack growth. In both theory and experiment the deformation value of J_R saturates after some growth while the far-field value continues to increase [*43,19*].

[3]Note that the solution to Eq 2 is dependent on the compliance of the cracked structure. For example, in a noncompliant system, such as a displacement imposed over a short gage length, dJ_A/da, may be negative. This implies that such a structure is inherently stable in the ductile regime.

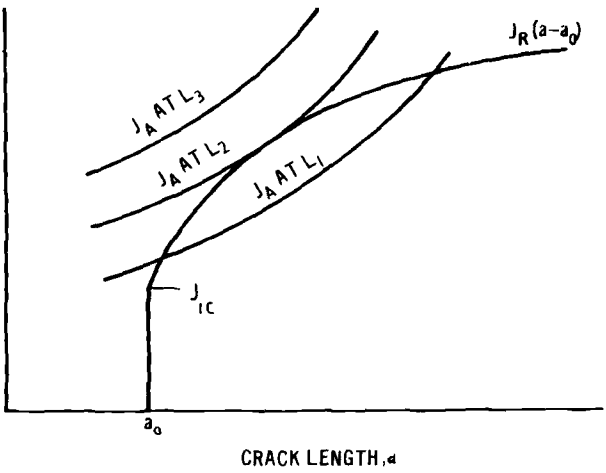

FIG. 1—*Principle of resistance curve analysis.*

These equations can be solved graphically for the instability load for a given initial crack size a_0 by re-evaluating and replotting J_A for different loads as a function of a until the tangency point is obtained with the J_R-curve as in Fig. 1. To determine the instability crack length for a constant load, J_R is plotted as a function of Δa for different values of the initial crack size a_0 until the tangency point is found. (For example, in Fig. 1 the instability crack length at L_1 can be obtained by displacing the J_R-curve along the abscissa until it becomes tangent to the J_A-curve for L_1.) Consequently, all the information required of an analysis can be obtained from these types of plot.

Unfortunately the evaluation of J_A is seldom straightforward. The J-integral should be evaluated as a function of crack size and load for any given material and structural geometry. If finite-element methods are used, then the accuracy of the results should be confirmed, for example, by independent calculations using different finite-element meshes.[4] Finite-element methods can clearly become impractical if it is necessary to cover the range of properties commonly observed in structural materials, as well as a range of structural geometries. Consequently, a number of simpler ways have been developed.

Approximate Estimates of J_A

There are two major types of J estimation procedures; those which attempt to provide an explicit estimate of J for any given structure, and those which

[4]Comparison of the results of elastic-plastic finite-element analyses of cracked three-point bend specimens show that the calculated values of J are very sensitive to the type of element and mesh used in the computations [*44,45*]. This sensitivity implies that there could be large errors in J computations in the elastic-plastic regime unless the results are validated, as suggested in the text.

use an approximate equation for J which is expressed in a form which is applicable to any geometry. Examples of the latter include the solution to the strip yielding model [*1,2*][5] suitably modified for structural geometry effects [*3*] and interpreted in terms of J [*4*]. This solution forms the basis of the Central Electricity Generating Board's (CEGB) defect assessment procedure (hereafter referred to as R6), which is discussed later.

Another approximate estimate of J_A can be obtained from the J design curve proposed by Turner [*9*]. This curve was derived as an upper bounding line to a number of finite-element solutions for J and is shown in Fig. 2. The ordinate is expressed in normalized units of J, $JE'/Y^2\,\sigma_y{}^2\,a$, where $Y = K/\sigma_A a^{1/2}$, σ_A being the applied stress, K the linear elastic stress-intensity factor for the crack of length a, E' Young's modulus divided by $(1 - \nu^2)$, where ν is Poisson's ratio, and σ_y the yield stress. The abscissa is expressed in terms of the applied strain in the uncracked body, e, normalized by the yield strain, e_y. The solution is applicable to short cracks which are less than 10 percent of the wall thickness. For deeper cracks, and particularly where plastic collapse of the net section is approached, it is unlikely to provide an upper-bound J-estimate. The design curve bounds J-values obtained for a crack emanating from a hole in a plate subject to a uniform tensile stress [*10*]. For this type of geometry, where there is a strain gradient associated with a stress concentrator, the applied strain is that measured local to the root of the concentrator.

Paris and his co-workers have developed analytical techniques for estimating J_A after general yielding of the uncracked ligament has occurred. These

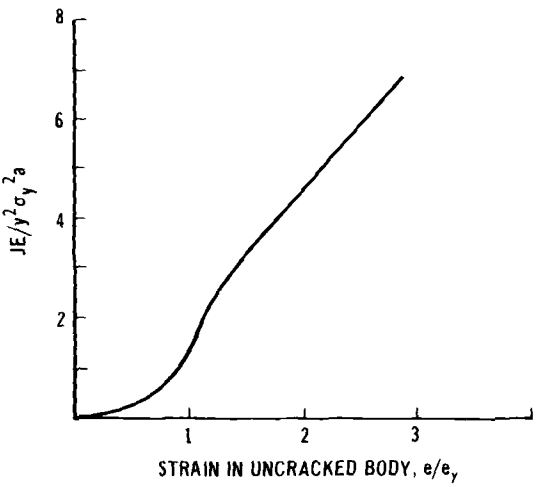

FIG. 2—J *design curve proposed by Turner [9].*

[5]The italic numbers in brackets refer to the list of references appended to this paper.

methods have been used to calculate approximate J-values for a number of cracked structural geometries (for example, Refs 5-8). Plastic limit relationships are exploited in order to simplify the analyses and make them tenable. The methods provide solutions to J_A in a regime where finite-element techniques appear to be at their weakest.

Other explicit estimates of J_A can be obtained from energy considerations using the geometric η-factors of Turner [11]. These factors relate the elastic and plastic components of J to the work done on the structure through the equations

$$G = \eta_e W_e/(w - a)B \tag{3a}$$

$$J_{FP} = \eta_p W_p/(w - a)B \tag{3b}$$

$$J = G + J_{FP} \tag{3c}$$

where

η_e and η_p = elastic and plastic values of η,
W_e and W_p = elastic and plastic components of work,
$w - a$ = uncracked ligament,
B = thickness,
G = elastic strain energy release rate, and
J_{FP} = plastic component of J.

In using Eqs 3 to estimate J_A, not only must the η-factors be known, but W_e and W_p must also be estimated.[6] For pin-loaded geometries, such as standard test specimen designs, evaluation of η_p is relatively straightforward [11]. However, this is not generally the case for structures where load-displacement curves are often unknown or not easily defined (for example, as in pressurized components). Here it may be easier to evaluate J directly using appropriate numerical techniques.

Shih and his co-workers (for example, see Refs 12 and 13) have developed another method for estimating J_A which enables a compendium of solutions to be constructed in a similar manner to the compendia at present available for K solutions. This is achieved by evaluating J from two terms

$$J = J_{FOP} + J_{FP} \tag{4a}$$

where J_{FP} is a fully plastic solution having the general form (compare Ref 6)

$$J_{FP} = \alpha e_y \sigma_y (w - a) h_1(n, a/w, P_0)(P/P_0)^{n+1} \tag{4b}$$

[6] W_e is not explicitly required, of course, because G is defined once the applied stress-intensity factor is known.

where α and n are obtained from fitting the Ramberg-Osgood equation to the material's stress strain curve,

P = applied load,
P_0 = reference load based upon σ_y (and not to be confused with the plastic collapse load), and
h_1 = function determined by fitting J_{FP} to a fully plastic finite element J solution for the geometry in question.

Values for h_1 have been tabulated in Ref *13* as a function of n for a number of geometries.

J_{FOP} is a linear elastic solution for J corrected for small-scale plasticity using a modification of Irwin's first order plastic zone size correction. It has the form $J_{FOP} = K^2(a_e)/E'$, where $K(a_e)$ is the elastic stress intensity at the applied load P, and a_e the corrected crack length. This latter parameter is given by $a_e = a + \phi r_y$ where $\phi = 1/[1 + (P/P_0)^2]$ and

$$r_y = \frac{1}{\beta\pi}\,\frac{n-1}{n+1}\left(\frac{K}{\sigma_0}\right)^2$$

β being 6 for plane strain and 2 for plane stress. The inclusion of the factor ϕ reduces the plastic zone size correction term to half of its usual value when $P = P_0$. The reason for this is unclear to the present authors since the estimation scheme is simply a parametric fit to the appropriate finite-element solution. The approach bears some similarities to that of Turner (compare Eqs 3*c* and 4*a*), but differs significantly from it in the way that J_{FP} is evaluated and in the inclusion of the first-order plastic correction in J_{FOP}.

The accuracy of the solution depends upon obtaining a good fit of the parameters α, σ_y, e_y, n, h_1 $(a/w, P_0, n)$, and $P_0(\sigma_y, a/w)$ to the material and structural parameters they represent. This is not always straightforward. For example, for a given stress-strain curve, the values of α and n depend upon the value chosen for σ_y, that part of the curve chosen for the best fit, and which stress strain curve is used, true stress/true strain or the engineering curve [*14*]. Inappropriate choices for α and n can result in large errors in the estimated J_A especially for materials such as austenitic steels, which have a high capacity for strain hardening [*15*].

Tearing Modulus Approach

Paris et al [5] nondimensionalized Eq 1*b* by dividing each side by σ_0^2/E' to define two tearing moduli, the material's modulus, T_m, and the applied modulus T_A. Thus, for stability of crack growth, Eq 1 is rewritten as

$$J_A = J_R \qquad (5a)$$

$$T_A < T_m \tag{5b}$$

This concept was originally restricted to the regime of J-controlled crack growth defined by Hutchinson and Paris [*16*]. This limits its application to structures and specimen geometries in which the deformation is in plane strain and where the extent of the crack growth is such that

$$\omega = \frac{w - a}{J_R} \frac{dJ_R}{da} \gg 1 \tag{6a}$$

and

$$\Delta a < R \tag{6b}$$

where R is some small fraction of the crack length or uncracked ligament. The minimum acceptable values for these parameters have yet to be defined. Nevertheless, for restricted amounts of crack growth under large-scale yielding conditions, dJ_R/da is experimentally found to be constant so that T_m can be considered to be a material constant. Under these conditions the analysis should be rigorous according to deformation theory. Under small-scale yielding conditions, however, this theory is not entirely consistent with the experimental and theoretical work of Rice and co-workers, who found that J_R reaches a saturation value after a small amount of crack growth[7] [*17–19*].

Note that in practice the limitations imposed by Eq 6*a* and 6*b* will tend to exclude shallow and very deep cracks. The ω-criterion of Eq 6*a* is also dependent on the geometry of the structure, being favored by large uncracked ligaments. This criterion is most easily satisfied for large values of dJ_R/da where, for most practical purposes, instability is coincident with plastic collapse (see, for example, Ref *20*.)

The diagrammatic technique for determining the crack instability conditions shown schematically in Fig. 1 can be simplified by reinterpreting the procedure in terms of a J-T diagram (for example, see Ref *21*). Here a locus of points (J_R, T_m) representing the material's resistance to cracking is drawn with respect to a set of axes with J as the ordinate and T as the abscissa (Fig. 3). Another curve representing the locus of points (J_A, T_A) is also drawn, either with crack length held constant, and the load increased, or vice versa. The instability conditions are defined by the intersection of the two curves (Point F in Fig. 3). Thus, provided the points (J_A, T_A) fall inside the material's resistance curve, the structure is predicted to be stable; if they fall outside, the structure is predicted to be unstable. The diagram is attractive in concept;

[7]It should be noted that in the crack-tip model of Rice and co-workers, J appears only as a parameter which defines the externally applied load. The assumption that J characterizes the crack-tip deformation fields is not required and hence in principle there is no restriction on the amount of growth for which a J analysis is valid. However, the actual definition of J is subject to certain conditions (see, for example, Ref *18*).

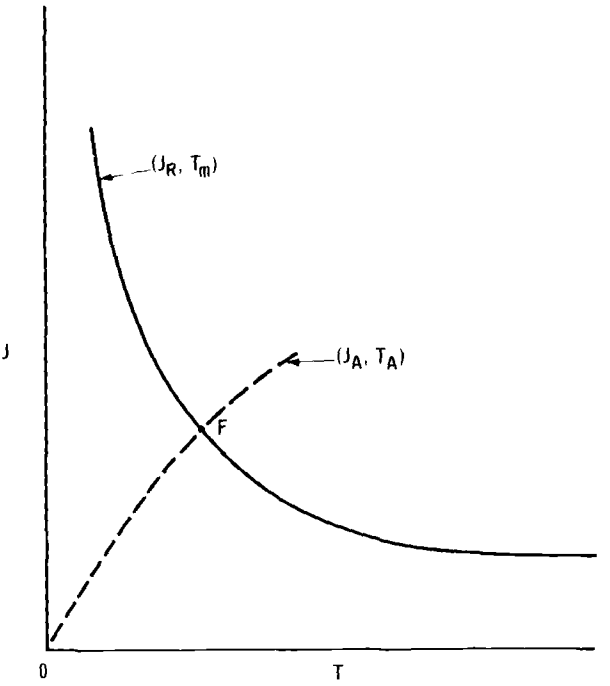

FIG. 3—*J-T diagram.*

the instability point is well defined and the diagrammatic format lends itself to a sensitivity analysis. However, it does not bypass the need to evaluate J_A as a function of both load and crack size. Furthermore the evaluation of T_A should be performed as a function of crack size over a region large enough to span the crack size of interest by a considerable margin. This is especially important in geometries and stress fields where J_A is sensitive to crack size. The reason for this is demonstrated in Fig. 4. At a_0, T_A is well below T_m and stability is predicted. At a_1, however $T_A = T_m$. The difference between a_1 and a_0 may not be large enough to cover the range of uncertainties present in the analysis (for example, uncertainties on crack sizes, material properties, or estimation of T_m).

Figure 4 also raises a further point: Despite the fact that for a crack length a_0 the difference between T_A and T_m is large enough to imply that the structure is highly stable, it could in practice take only a very little increase in load to cause instability. This may not be so readily apparent from a J-T diagram, so that in order to expose this kind of feature in any analysis it is necessary to repeat the calculations to cover a wide range of the major variables. When using finite-element techniques, this more complete form of analysis is extremely involved; it would be more easily performed using the approximate techniques outlined earlier.

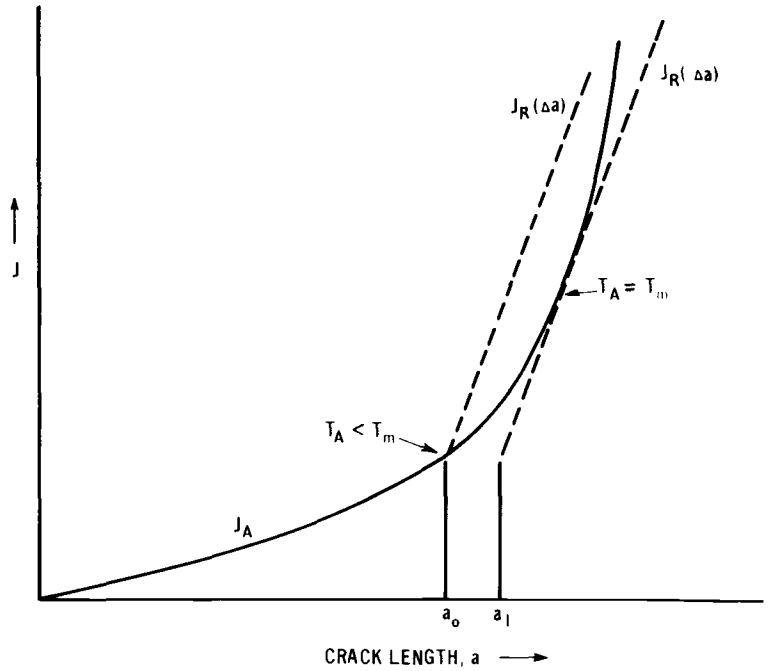

FIG. 4—*Example of the sensitivity of an instability analysis to crack length.*

Turner's Theory

Turner [*22*] has defined instability during ductile crack growth as the point where the elastic energy release rate, I, exceeds the plastic work dissipation rate. This concept derives from a proposal by Orowan [*23*]. The analytical work in evaluating I is at present confined to displacement loading at plastic collapse. Under these conditions

$$I = G(2\eta_p/\eta_e - 1) \tag{7}$$

where G is Irwin's elastic energy release rate and η_e and η_p are the geometric terms relating G and J_{FP} to the elastic and plastic areas under a load displacement curve as defined earlier. In going from a_0 to a at the plastic limit load, the plastic work rate is given by

$$\frac{dW_p^*}{da} = \frac{w - a}{\eta_p}\frac{dJ_R}{da} - J_R/\eta_p \tag{8}$$

The asterisk signifies that W_p is the plastic work expended in the structure

during crack growth, and this is determined by the material parameter J_R and the structural geometry through the equation

$$J_R = \eta_p W_p^*/(w - a)$$

If the criteria [*16*] for *J* dominated growth are satisfied, then the second term on the right-hand side of Eq 8 is small, and Turner's criterion for instability, defined as

$$I > dW_p^*/da \tag{9a}$$

becomes

$$\eta_p \frac{I}{(w - a)} > \frac{dJ_R}{da} \tag{9b}$$

This compares with Eq 2*b* provided $\eta_p I/(w - a) = dJ/da$. Turner has calculated η_e and η_p for a number of geometries and because the theory is formulated under displacement loading, η_e is dependent on the compliance of the uncracked body (that is, the gage length over which the displacements are imposed). As in the *J*-based theories, Turner assumes that the resistance curve, J_R, is a material constant for small amounts of growth and is independent of structural geometry and loading system, and that it should be calculated by assuming deformation theory [*24*]. In principle, therefore, J_R could be measured on the actual structure using the values of J_A calculated during growth. Implicit in this statement is the fact that *J* is the controlling parameter. Thus there appears to be a basic inconsistency in Turner's approach in that stability is defined in terms of *J*, yet instability is defined with respect to the parameter *I*.

Although the concept was developed at plastic collapse, there appears to be no reason why it should not be more generally applicable.

Failure Assessment Diagrams

The CEGB Diagram (R6)

The resistance curve concept of Fig. 1 can be interpreted in terms of the CEGB failure assessment diagram (R6), Fig. 5, by generalizing the coordinates in the following way [*25*]

$$S_r = \frac{P}{P_1} \tag{10a}$$

$$K_r = \sqrt{\frac{G}{J_R}} = \frac{K_1}{K_\Omega} \tag{10b}$$

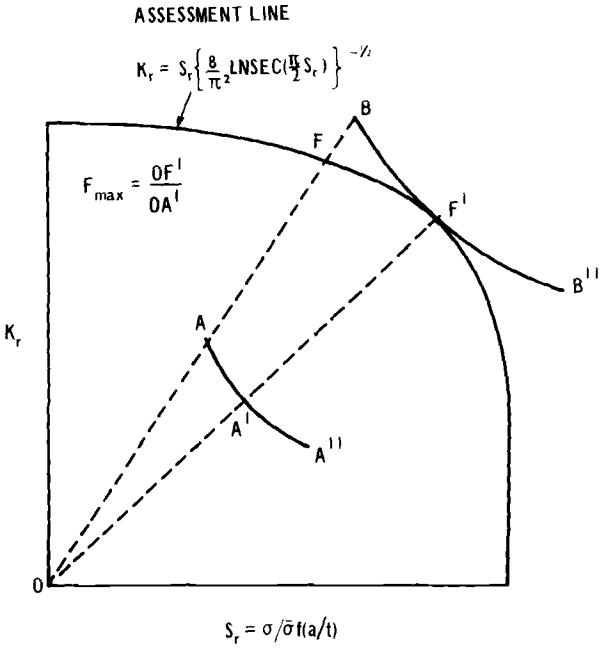

FIG. 5—*Resistance curve analysis on failure assessment diagram.*

where

P_1 = plastic collapse load,
K_1 = linear elastic stress-intensity factor, and
$K_\Omega = \sqrt{E'J_R}$.

A constant load locus (AA'A" in Fig. 5) is plotted on the diagram as a function of postulated crack growth and is judged with respect to the failure assessment line of Harrison, Loosemore, and Milne [*26*]. This assessment line uses a form of the Bilby, Cottrell, Swinden [*2*] solution to interpolate between the two limiting criteria, plastic collapse at $S_r = 1$ and linear elastic failure at $K_r = 1$. It can be considered to define the boundary between the stable and unstable states of a structure. Thus, on the failure assessment diagram the tangency point between a locus of assessment points BF'B" and the assessment line (as shown in Fig. 5) corresponds, for example, to the tangency point of the J_R-curve and the J_A curve for L_2 in Fig. 1 [*20*].

The use of K-ratios in Eq 10*b* has the advantage of making the analysis linear in load. Thus the instability load point is easily evaluated by determining the maximum value of the load factor F as a function of Δa defined as

$$F(\Delta a) = \frac{\text{Load to position assessment point on assessment line}}{\text{Applied load}}$$

$$= \frac{OF}{OA}, \frac{OF'}{OA'} \text{ etc.}$$

in Fig. 5, or

$$F(\Delta a) = \frac{2}{\pi S_r(\Delta a)} \cos^{-1} \exp\left(-\frac{\pi^2 S_r^2(\Delta a)}{8K_r^2(\Delta a)}\right) \tag{11}$$

If the applied load is P, and the maximum value of F is F_{max}, the instability load is given simply by the product $P \cdot F_{max}$.

The analysis is straightforward once the required elastic and plastic solutions are known. The plastic limit is the most difficult one to assess, especially in complicated structural geometries. Nevertheless, in the absence of specific solutions for a given geometry it is generally possible to estimate the plastic collapse load using lower-bound plastic limit theories. More realistic estimates are obtainable from scale-model tests of the structure. P_1 is normally evaluated in terms of a flow stress, which is the arithmetic mean of the yield and ultimate tensile stresses of the material, and this has proved to be satisfactory for most ferritic steels [*15*]. When accurate estimates of P_1 can be made, a very precise prediction of ductile instability can be obtained [*27*].

This approach has several advantages. First, the analysis is simple. Apart from the J_R-curve, only simply obtained material properties are needed. If these are unknown, they can generally be deduced from specifications and experience.

Second, it has the important attribute that a good level of understanding is obtained about the predicted behavior of the structure. The diagrammatic representation of the analysis produces a visual image which clearly indicates the most important parameters in the analysis—for example, J_R, flow properties or crack size—and hence where the most effort is needed, for example, in refining the analysis or improving material properties.

Third, the procedure is very flexible. Since the coordinates have a simple relationship to all variables, a very quick sensitivity analysis can be performed [*28*].

When analyzing systems loaded under fixed displacements, the analysis has to be performed using loads resulting from constant displacement rather than constant load and taking appropriate account of the gage length [*29*]. This presents no special problem if the structure remains elastic, as it does in most cases. Where large-scale plasticity occurs, the plastic compliance of the system must be evaluated in order to determine the effective loading. In such cases a pessimistic analysis may be performed by evaluating the effective load

using linear elasticity theory. If this results in an apparent elastic load which coincides with or exceeds the limit load, that is, $S_r > 1$, this method cannot provide a useful solution. Under these circumstances an alternative procedure must be employed, for example, by utilizing the plastic limit load techniques of Paris and co-workers [*7,8*].

The use of the Bilby, Cottrell, and Swinden [*2*] model solution for the interpolation formula may be questioned on two counts:

1. The strip yielding plastic zone is an unrealistic physical representation of real plastic zones.
2. The model was derived only for an infinite plate geometry and should not therefore be applied to real physical geometries of complex shape.

It should be remembered, however, that the CEGB procedures were evolved to solve practical problems with all their concomitant uncertainties, not to predict the detailed behavior of well-categorized laboratory test specimens. To this end, theoretical rigor was sacrificed for practical convenience. Nevertheless, experience with a variety of test and structural geometries has shown that the procedures are capable of predicting maximum loads to within the tolerance of any engineering assessment for all types and sizes of plastic zone, and for cracks initiating at all stress levels [*27*]. Indeed experimental observations on ferritic structures have yet to produce any major feature which is not consistent with the failure assessment line. Moreover, in comparing the R6 diagram with the *J*-estimates of Kumar et al [*12*], Milne [*15*] demonstrated that for all practical purposes the two approaches will give equivalent results for ferritic steel structures. However, for structures made of austenitic steels, a procedure which makes explicit allowance for the high strain-hardening capacity of these materials may be preferred.

Strain-Hardening Assessment Diagrams

For certain materials, in particular austenitic steels, the strain-hardening capacity is so large that the simple flow stress criterion adopted for the R6 procedures may be inappropriate. Under these conditions some allowance must be made for the strain-hardening properties of the material.

The simplest way of developing a strain-hardening assessment diagram is to use a known solution for J, based upon a suitable strain-hardening law. K_r can then be defined as

$$K_r = \left(\frac{G}{J}\right)^{1/2}$$

with S_r defined as before. In practice such J solutions are normally evaluated with respect to a reference stress, such as σ_y. In these cases it is then more appropriate to define S_r in terms of this reference stress

$$S_r = \frac{\sigma}{\sigma_y f(a/t)}$$

where $f(a/t)$ is the appropriate collapse stress function and σ the applied stress.

Using the estimation schemes of Kumar et al [*12*] for a through crack in an infinite plate, Bloom [*30*] derived the following equation for an assessment line which includes strain hardening

$$\frac{1}{K_r^2} = 1 + \frac{2}{9}\frac{n-1}{n+1}\frac{S_r^2}{1+S_r^2} + \frac{3\alpha h_1(0,n) S_r^{n-1}}{4\pi(1-\nu^2)} \tag{12}$$

where α and n are obtained from the Ramberg-Osgood strain-hardening law, and $h_1(0,n) = z(0,n)[1.13 - 0.15/n + 1]$ with $z(0,n) = 3.85\sqrt{n}(1 - 1/n) + \pi/n$. Note that $h_1(0, n)$ is a special case of $h_1(a/W, n, P_0)$ and is used by Bloom to define a geometry-independent assessment line. An example of such an assessment line is shown in Fig. 6. The position of the line is of course dependent upon the parameters α and n, and a new line has to be plotted for each new value of these. In all cases, however, the assessment line approaches the S_r-axis asymptotically. This is an artifact of the Ramberg-Osgood strain-hardening law [*15*] and implies that structures can support an infinite load if the toughness is high enough or if there is no crack.

The infinite-plate solution of Eq 12 tends to be an excessively pessimistic representation of the J solutions of Kumar et al [*12,13*] for some specific geometries. Where this is so, Bloom [*31*] has used the geometry-dependent J solutions of Kumar et al. In these cases new assessment curves should be gener-

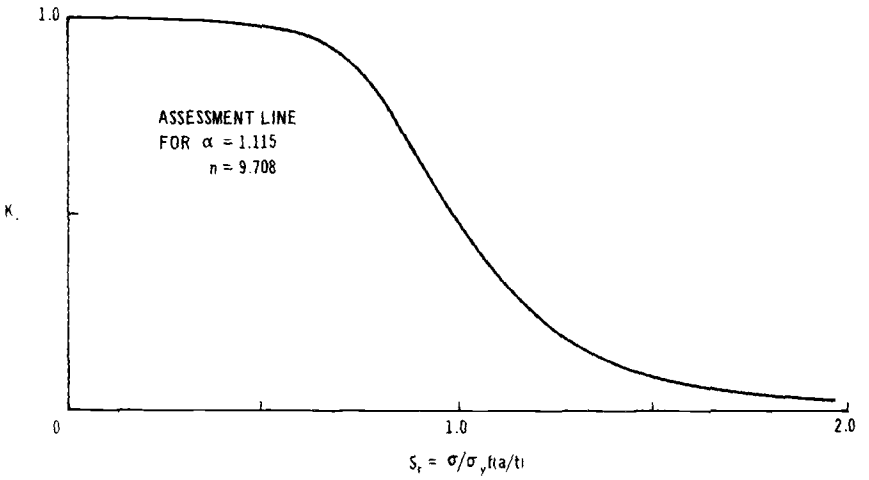

FIG. 6—*Strain-hardening assessment line, after Bloom [30].*

ated, not only for the specific α and n obtained from the stress-strain curve, but also for each geometry, including crack length, using the appropriate value of h_1 for the chosen value of P_0. Assessment lines generated in this way have been plotted for a number of geometries by Bloom and Kumar et al which show this apparent geometry dependence. However, in their case, P_0 and P_1 are different functions of a/t and they defined S_r as P/P_0. If S_r is defined as P/P_1, this geometry dependence largely disappears and for ferritic steels, at least, the curves lie close to the R6 line, as demonstrated in Fig. 7 (see also Refs *15* and *27*). Alternatively, the apparent geometry dependence can be included via P_0, and the analysis referred to a set of curves plotted for a given material and a range of crack length intervals, as proposed by Bloom [*31*].

For austenitic steels, the picture is somewhat different. Here, the strain-hardening assessment lines depend sensitively upon how closely the Ramberg-Osgood law can be made to fit the stress-strain curve of the material. For a typical austenitic steel, a reasonable fit over the high strain region of the stress-strain curve is generally obtained only with values of $\alpha > 3$ and $n < 4$. These values predict excessive strains at stress levels close to σ_y and result in large plasticity effects in the estimates for J at net section stress levels well below yield. The strain-hardening assessment line for a compact tension specimen (Curve 1) is compared with experimental data derived from the load-displacement curve of the specimen in Fig. 8 [*15*]. Also shown in Fig. 8 is an assessment line generated using values of α and n obtained by fitting the Ramberg-Osgood equation at stress levels close to yield (at $S_r = 1$) (Curve 2). This provides a better description of the specimen behavior near to general yield. It is clear that, for materials with a high capacity for strain hardening,

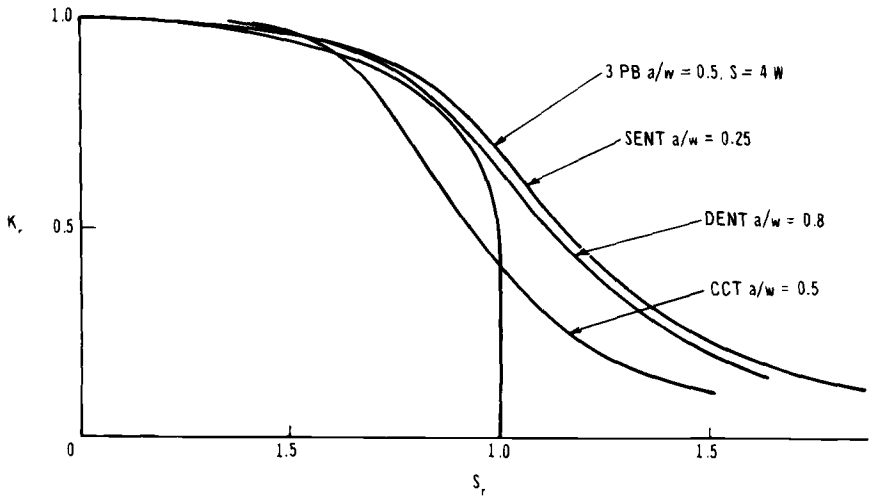

FIG. 7—*Comparison of strain-hardening assessment lines for four geometries with R6.*

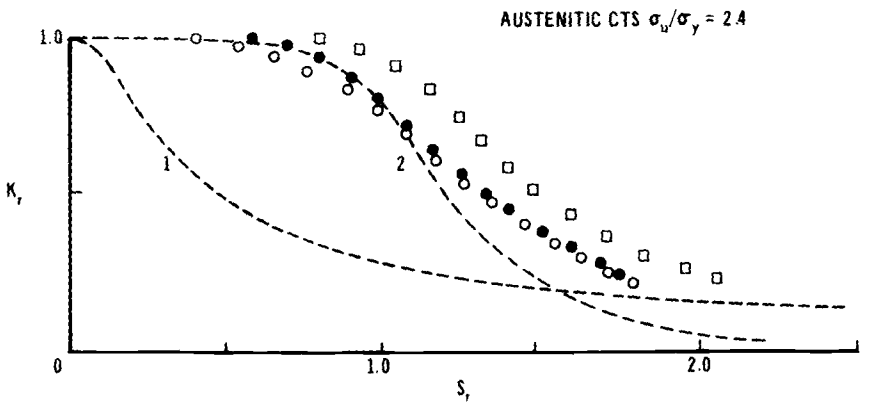

FIG. 8—*Comparison of test data with J-estimates from Ramberg-Osgood law: (1) fitted over total stress-strain curve; (2) fitted at low strains. Symbols as in Fig. 9.*

any procedure which uses the Ramberg-Osgood law should be treated with caution.

An alternative way of dealing with strain hardening, which avoids the problems created by the Ramberg-Osgood law, is that recently proposed by Milne [*15*][*27*]. This still uses the strip yielding model to interpolate between linear elastic and fully plastic behavior, but the effects of strain hardening are incorporated in the collapse limit by redefining the equation of the assessment line as

$$S_r = \frac{\sigma}{\sigma_y} + (1 - K_r^{1/2})\left(\frac{\sigma_u}{\sigma_y} - 1\right)$$

$$K_r = \frac{\sigma/\sigma_y}{\sqrt{\frac{8}{\pi^2} \ln \sec \frac{\pi}{2} \frac{\sigma}{\sigma_y}}}$$

where σ_u is the ultimate tensile stress. This solution has the property that plasticity effects are related to the yield stress in the small-scale yielding regime, the flow stress at intermediate levels of plasticity, and the ultimate tensile stress at very high levels of plastic deformation. For ferritic steels this solution produces results comparable to the formal R6 procedures, and to the *J*-estimates of Kumar et al [*12,13*]. It is also a good fit to the experimental data for the austenitic steel shown in Fig. 9 [*27*]. It has the added attraction that the plastic limit load is still incorporated in the analysis explicitly, thus avoiding the physically unacceptable behavior predicted by strain-hardening

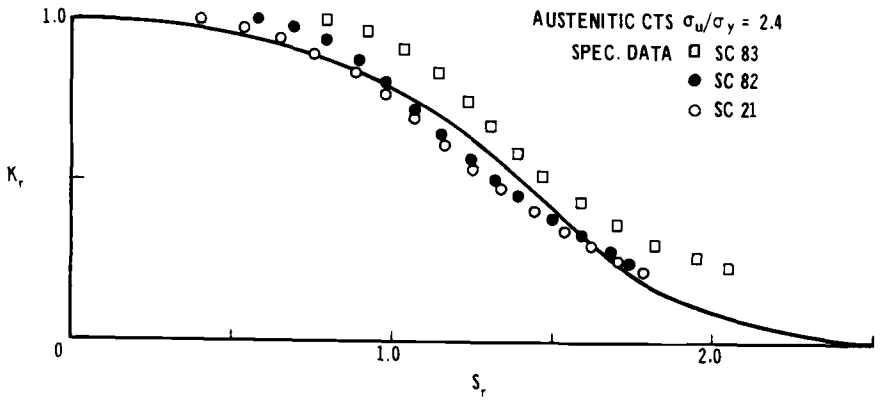

FIG. 9—*Comparison of test data with proposed R6 strain-hardening line. Data from Ref [15].*

solutions which become asymptotic to the S_r-axis.[8] Furthermore, the solution can be plotted in a form which is particularly suitable for code applications, Fig. 10.

Crack-Opening Displacement Criteria

J and the crack-opening displacement, δ, provide an equivalent descriptions of ductile crack growth insofar as they are related by the simple equation $J = m\sigma_y \delta$ where m is a constant dependent on work-hardening capacity and structural geometry. However, despite the fact that in principle both driving force and resistance curves can be determined in terms of δ, in practice it can be a very difficult exercise to define either of these.

The COD design curve (Fig. 11) [*32*] is based upon the gross section strain rather than the applied stress. The curve is empirically based on the fracture analysis of wide-plate test data [*33*]. The J-design curve of Turner [*9*] is an extension of the COD design curve philosophy to a J-analysis (compare Fig. 2 and Fig. 11) but, at present, without the same level of experimental validation.

It is recommended practice to determine the critical COD at fracture from tests performed on three-point bend specimens equal in thickness to that of the structure. The mouth-opening displacement is measured and converted to a COD using a geometrically based analysis [*34*]. Towers and Garwood [*35*] have argued that by following this procedure the COD measured on a three-point bend specimen at maximum load, δ_m, if used as the critical failure parameter in an assessment, should always provide an underestimate of the load-carrying capacity of a structure subjected to tensile loading. One of the requirements for this to be true is that the crack driving force must be

[8]To avoid this asymptotic behaviour, Bloom has recently introduced a cutoff in the strain-hardening solutions based upon the plastic collapse stress calculated using the ultimate tensile stress.

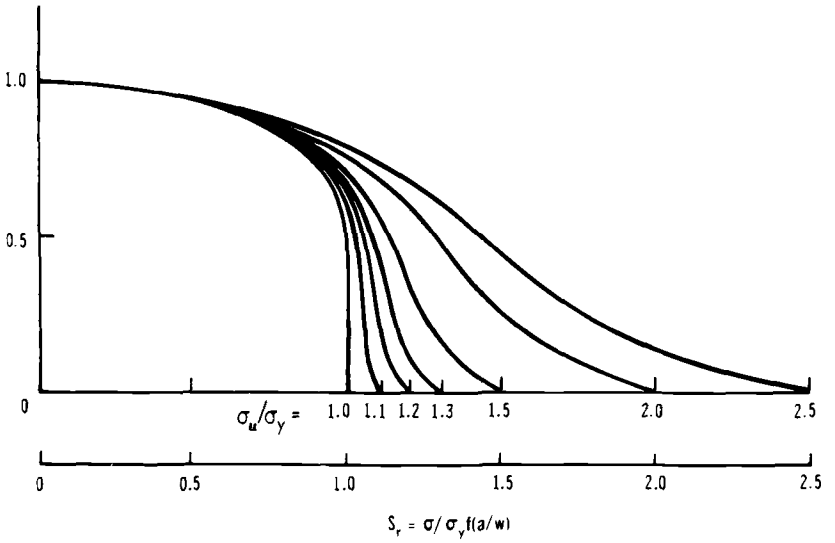

FIG. 10—*Proposed R6 strain-hardening diagram [15].*

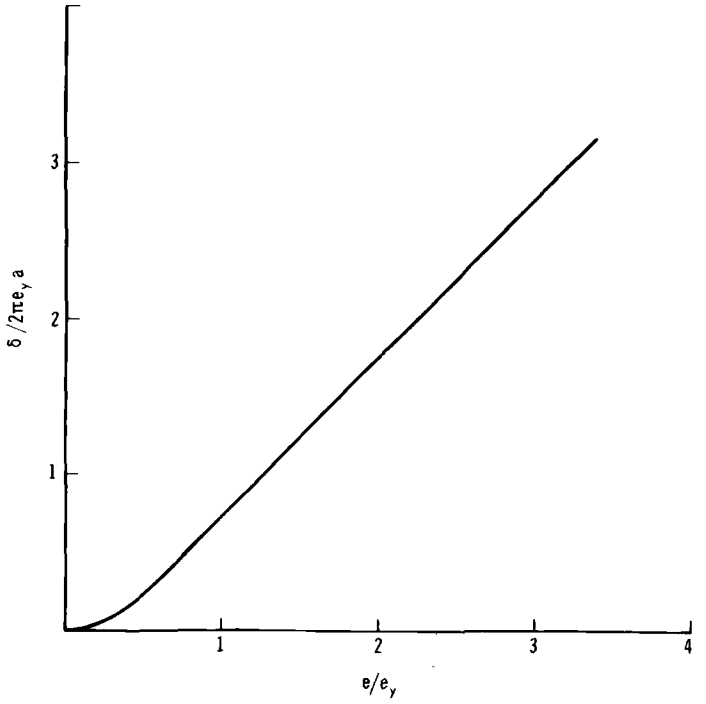

FIG. 11—*COD design line, after Dawes [32].*

greater in the specimen than in the structure. To satisfy this criterion the crack in the structure must be shorter than the crack in the specimen. Another requirement is that the plastic constraint, measured in terms of stress triaxiality must be lower in the structure than in the specimen. For most practical problems these requirements would normally be satisfied. However, if high residual or thermal stresses are present in the structure, this may produce a constraint on plastic deformation which exceeds that encountered in a three-point bend test. Geometric discontinuities in the structure may produce similar effects. For these situations it is not obvious that assessing against the maximum-load COD measured in a bend test would lead to underestimation of the load-bearing capacity, and a more elaborate approach may be required.

The maximum-load COD method has the advantage of requiring only conventional material flow properties, as in the CEGB technique, together with a COD fracture analysis. Neither J_R nor COD resistance curves are explicitly required, obviating the need for the large number of specimens which are required to develop these curves. There are, however, some distinct drawbacks.

First, the technique provides only limited information about the state of a cracked structure. It is not possible to judge whether the crack has just initiated at the maximum-load COD or whether it has grown a substantial amount. Moreover, it is often desired to limit applied load levels during operation so that crack growth does not occur, and to judge safety factors against the predicted instability load conditions. Clearly this type of knowledge is unavailable unless crack initiation is also monitored during the COD test. Second, because the method does not require crack driving force curves to be compared with resistance curves, the level of safety implied by the analysis will vary significantly with crack size. In particular, shallow cracks will be assessed more pessimistically than deep cracks. This pessimism adds to that which is already inherent in the COD design curve. Thus the acceptable sizes of shallow cracks may be severely underestimated, perhaps to below the limit required for detection by nondestructive testing techniques. Third, the COD analysis requires that full section thickness tests be performed. This is possible only for modest sections. For heavy section structures it is generally possible to test only subsized specimens. In such cases the maximum-load COD analysis could not be considered to be an acceptable technique. Fourth, although the COD design line was derived to cater for residual loading, it is not clear that the analysis would still be acceptable when the maximum-load COD based on a primary load test is used as the critical failure parameter.

Analysis in the Presence of Thermal and Residual Stresses

Although these stresses can result in elastic-plastic effects, they do not contribute to failure in the plastic collapse regime [*36,37*]. Thus residual and thermal stresses require a treatment different from mechanically induced stresses.

The COD approach was of course originally developed to include effects of residual stresses [*38*]. Such stresses are added on to the mechanical stresses, converted to strains, and treated via the COD design line. The design line has been experimentally shown to produce safe estimates in as-welded structures provided the residual stresses are assumed to be of yield stress magnitude [*32*]. In stress-relieved structures, or in the presence of thermal stresses, there is no similar experimental validation, and an uncertainty exists as to how best to include these stresses. Certainly, taking the peak value of the thermal stresses, as is recommended, will be severely overpessimistic in the majority of cases.

The R6 procedures incorporate elastic-plastic effects using a modified Irwin-type first-order plasticity correction [*39,40*] which is added as an extra term to the K_r-axis. Since plasticity from thermal and residual stresses does not affect the plastic collapse loads, this should provide a reasonably accurate analysis for most practical purposes. Experimental validation is difficult, however, and only a limited amount of data are available [*41*]. This procedure is nevertheless applicable to any analysis which is expressed in the form of an assessment diagram. If the empirical strain-hardening modification to R6 suggested by Milne [*15*] is used, then the first-order plasticity correction should be based upon σ_y.

A numerical evaluation of J will automatically incorporate the effects of thermal and residual stresses, provided the analysis makes adequate allowance for the presence of initial strains [*42*]. J_A can also be estimated from Turner's J design line. Here the effects of the residual stresses are incorporated along the strain axis, and J_A is estimated from a design line displacement upwards [*9*].

Although the preceding methods address the problem imposed by thermal and residual stresses explicitly, other methods, which rely upon a specific estimate of J_A, have so far ignored these. For example, the J estimation procedure of Kumar et al [*12,13*] cannot be used in the presence of thermal and residual stresses without modification. Basically this is because this procedure has been developed as a multivariable fit to finite-element solutions, and the variables have been chosen to be equivalent to some easily identifiable parameters. This makes it difficult to adjust the solution for situations where these parameters need to be modified, as in the case of thermal and residual stresses. Similarly if J is estimated using η-factors [*11*] it is unclear how these would be calculated for thermal and residual loading.

Information Required for the Analysis and Necessary Safeguards

Information Required

Since the purpose of a failure analysis is to define the safe working conditions of a cracked structure, it is worth reviewing what information is required for each of the techniques discussed in the foregoing, and what reliance can be

placed on this information and the ensuing results. Certain information is common to all forms of analysis, for example, the loading conditions and resultant stress levels, the crack sizes and shapes, the geometry of the structure, the temperature of operation. This information will be available to a variable degree of accuracy depending upon the type of structure. In particular, stress gradients may be difficult to evaluate accurately—especially in the proximity of welds, whether stress-relieved or not—and crack sizes and shapes may be difficult to assess. Moreover, an irregular-shaped crack must be idealized before it can be evaluated by any technique. Thus there are inherent uncertainties in input data used for any analysis and this fact may sometimes obviate the need to use oversophisticated techniques. This point should be borne in mind when choosing which form of analysis to adopt for any particular problem.

The COD technique is the only form of analysis which does not explicitly require a resistance curve. In this sense it stands apart from the other techniques. It does, however, require an estimate of the maximum-load COD from a three-point bend specimen whose thickness is that of the structure under analysis. Load-displacement curves for three-point bend specimens that fail near plastic collapse often have extended maxima. This makes it difficult to define unequivocally a maximum-load COD.

The other techniques can be divided into two basic groups: those in which J is explicitly evaluated and those which may be interpreted in terms of J. This latter grouping includes the diagrammatic procedures of R6 and Bloom [*30*].

Five methods have been mentioned for estimating J_A explicitly: finite-element computations, the Kumar et al [*12,13*] estimation scheme, the techniques of Paris and co-workers [*5-8*], the J design curve of Turner [*9*], and the evaluation of J_A through η-factors [*11*]. The first two require a well-defined stress-strain curve, and some form of idealization of this curve. The idealization adopted by Kumar et al [*12,13*] is the Ramberg-Osgood equation. The methods of Paris and co-workers exploit the analytical simplifications that occur under limit load conditions. They require good estimates of the plastic collapse load. The material properties required to use Turner's J design curve are only the yield stress and yield strain, while use of η-factors depends upon knowing the work done on the cracked structure by the external loading, generally via the plastic collapse load of the structure.

The R6 approach also requires an estimate of the plastic collapse load. This is normally evaluated in terms of a flow stress based upon the average of the yield and ultimate tensile stresses of the material. The strain-hardening modifications require either the total stress-strain behavior as needed for a detailed J solution [*30*] or, if the simpler proposal of Milne [*15*] is adopted, the yield and ultimate tensile stresses.

Sources of Error

The potential sources of error in the aforementioned procedures arise from two features: (1) errors or inaccuracies in the input data, including the scatter

in the material properties, and (2) the ability of the procedure(s) to model correctly the load-crack growth or load-displacement behavior of the structure. As far as material properties are concerned, the scatter in resistance curve data appears to be relatively small compared with, for example, the scatter in cleavage fracture toughness. What is more, for structures which display a high tolerance to ductile cracking, the instability load is relatively insensitive to the resistance curve [*20*]. In this situation the flow properties of the material govern instability. Yield and ultimate tensile strengths can vary by as much as 10 percent across the thickness of a heavy section plate, and the strain to failure by somewhat more than this, depending upon the geometry of the tension specimen. It is therefore unreasonable to expect an accuracy of better than 10 to 20 percent in any failure assessment.

Procedures which use a geometry-independent curve (R6, *J* design curve, COD design curve) cannot be expected to model load-crack growth behavior as precisely as those which use a more detailed estimate of J_A. However, when establishing how accurately J_A can be estimated, account must be taken of the variability in flow properties of the material. Inaccurate modeling of the stress-strain curve will inevitably lead to inaccurate estimates of J_A.

The areas of weakness in one procedure are often areas of strength in another. Thus, a high level of confidence can be obtained from any analysis by applying safeguards appropriate to that form of analysis. These can be itemized as follows:

1. Explicit estimates of J_A should be checked to see if they give the expected behavior near the plastic limit load. This check should also be applied to the COD design curve approach.
2. All the techniques should be applied at load levels slightly higher than the load of interest and over a range of crack sizes spanning the crack size of interest. This will give valuable information regarding the sensitivity of the analysis to input data.
3. All procedures which adopt a geometry independent-curve—that is, R6, Turner's *J* design curve, and the COD design curve—should be compared with *J* solutions of proven accuracy. This will establish confidence in their use and help define their regime of applicability. If the difference in the two solutions is unacceptably large, then the reason for this should be determined, and the most appropriate solution used with suitable justification.

General Summary

Several ways of addressing the problem of ductile crack growth have been discussed herein. None of these has universal appeal; the choice of which to apply will depend upon the type of problem addressed, the data available for the analysis, and the accuracy required of the result. The more elaborate techniques are generally more rigorous, but in failure assessments rigor is invariably compromised by the uncertainties in the input data. This often means that the confidence in the predicted instability conditions is generally

no greater than that obtained from simpler procedures. Nevertheless, elaborate procedures are often necessary, if only in establishing confidence in the use of alternative ones.

A direct analysis can be obtained by comparing graphically an applied J with the materials J resistance curve or, more definitively, by using the J-T diagrams described by Paris [*21*]. J_A and T_m can be evaluated using numerical methods, or more conveniently by using approximate methods.

The J estimation schemes of Kumar et al [*12,13*] take strain-hardening effects explicitly into account. The success of this method depends upon how well the Ramberg-Osgood law fits the material's stress-strain curve. The fit is generally satisfactory for ferritic steels like A533B, but not for austenitic steels. For the latter case, excessive plasticity effects can be predicted at low stress levels (about $0.25\ \sigma_y$) when they are not observed in practice [*15*]. The solutions are nevertheless pessimistic at these stress levels; that is, they overestimate J. The nature of the Ramberg-Osgood law also causes optimistic predictions at high stress levels, and structures can be predicted to carry a load at stress levels well above ultimate. For this reason it is prudent to evaluate independently the plastic limit load of a structure. This method, as well as the other J estimation methods outlined herein, have not, at the present time, satisfactorily addressed the problem of thermal and residual stresses.

Of the assessment diagram approaches, the R6 diagram based upon a flow stress criterion is the simplest to apply. For most practical situations involving ferritic materials, use of this assessment line is compatible with the currently known J solutions [*27*]. For unusual geometries however, it is, prudent to compare this line with alternative solutions for J where they are available.

For materials with a high capacity for strain hardening, use of a flow stress criterion together with the R-6 diagram can be nonconservative at stress levels close to general yielding. This may be avoided either by using a yield stress criterion or by using an assessment line which incorporates strain-hardening effects. The yield stress criterion is the simplest to apply, requiring no adjustment of the assessment line, but it may be highly pessimistic. Strain-hardening assessment lines can be derived from any J solution which incorporates strain-hardening effects [*30*] or by using a simple interpolation formula as suggested by Milne [*15*].

Assessment diagram approaches to elastic plastic fracture provide the easiest and most comprehensive means of performing an analysis. This stems from the simple functional relationships which exist between the coordinates S_r and K_r and the major variables in an analysis. Thus effects due to thermal and residual stresses can be relatively easily incorporated, but they can be kept separate from those due to mechanical stresses. A comprehensive solution to the problem can be very quickly obtained.

Such a comprehensive solution, however, can be obtained only if sufficient materials properties data are available—in particular the resistance curve. While such data may be available, or obtainable, for new or specialized items

of plant, they are usually not available for older plant or for the vast majority of engineering structures. In such instances the maximum-load-COD approach may be the only technique which can be applied.[9] This is especially true for as-welded structures, where residual stress levels are unknown and only an empirically based solution can be applied. However, as for the other solutions, certain checks should be performed to ensure that areas of the structure do not experience a higher state of plastic constraint than the specimen, and that the crack depth in the specimen is greater than that in the structure.

Acknowledgments

This work was performed at the Central Electricity Research Laboratories and is published by permission of the Central Electricity Generating Board.

References

[1] Dugdale, D. S., *Journal of the Mechanics and Physics of Solids*, 1960, Vol. 8, p. 100.
[2] Bilby, B. A., Cottrell, A. H., and Swinden, K. H. in *Proceedings of the Royal Society of London*, Vol. A272, 1963, p. 304.
[3] Dowling, A. R. and Townley, C. H. A., *International Journal of Pressure Vessels and Piping*, Vol. 3, 1975, p. 77.
[4] Chell, G. G. in *Developments in Fracture Mechanics—7*, G. G. Chell, Ed., Applied Science, London, 1979, p. 67.
[5] Paris, P. C., Tada, H., Zahoor, Z., and Ernst, H. in *Elastic-Plastic Fracture, ASTM STP 668*, J. D. Landes, J. A. Begley, and G. A. Clarke, Eds., American Society for Testing and Materials, 1979, pp. 5-36.
[6] Zahoor, A. and Paris, P. C. in *Proceedings*, Specialist Meeting on Elastoplastic Fracture Mechanics, Daresbury, U.K., CSNI Report 32, 22-24 May 1978, Paper 10.
[7] Tada, H., Musicco, G., and Paris, P. C. in *Proceedings*, Specialist Meeting on Elastoplastic Fracture Mechanics, Daresbury, U.K., CSNI Report 32, 22-24 May 1978, Paper 16.
[8] Tada, H., Paris, P. C., and Gamble, R. M. in *Fracture Mechanics: Twelfth Conference, ASTM STP 700*, American Society for Testing and Materials, 1980, p. 296.
[9] Turner, C. E. in *Advances in Elasto-Plastic Fracture Mechanics*, L. H. Larsson, Ed., Applied Science, London, 1979, p. 301.
[10] Sumpter, J. D. G., "Elastic-Plastic Fracture Analysis and Design Using the Finite Element Method," Ph.D. Thesis, Imperial College, London, 1973.
[11] Turner, C. E. in *Fracture Mechanics: Twelfth Conference, ASTM STP 700*, American Society for Testing and Materials, 1980, p. 314.
[12] Kumar, V., German, M. D., and Shih, C. F., "Estimation Technique for the Prediction of Elastic-Plastic Fracture of Structural Components of Nuclear Systems," General Electric Co. Report SRD-80-094, Schenectady, N.Y., 1980.
[13] Kumar, V., German, M. D., and Shih, C. F., "An Engineering Approach for Elastic-Plastic Fracture Analysis," EPRI Report NP-1931, Electric Power Research Institute, Palo Alto, Calif., July 1981.
[14] Issler, L., Birk, R., and Hund, R. in *Proceedings*, 6th MPA Seminar, Stuttgart, 1980.

[9]The maximum-load COD technique can be adapted for other approaches by, for example, evaluating to a maximum load J_R and K_Ω obtained using three-point bend specimens. However, a major principle of the COD technique is that the specimen thickness should equal that of the structure. In addition, large and variable factors of safety are incorporated in the COD design line which are absent from the other approaches.

[15] Milne, I., "Failure Assessment Diagrams and J Estimates: A Comparison for Ferritic and Austenitic Steels," *International Journal of Pressure Vessels and Piping*, Vol. 13, 1983, p. 107.
[16] Hutchinson, J. W. and Paris, P. C., in *Elastic-Plastic Fracture, ASTM STP 668*, J. D. Landes, J. A. Begley, and G. A. Clarke, Eds., American Society for Testing and Materials, 1979, pp. 37-64.
[17] Rice, J. R., and Sorensen, E. P., *Journal of the Mechanics and Physics of Solids*, 1978, Vol. 26, p. 163.
[18] Rice, J. R., Drugam, W. J., and Sham, T. L., in *Fracture Mechanics: Twelfth Conference, ASTM STP 700*, American Society for Testing and Materials, 1980, p. 189.
[19] Hermann, L., and Rice, J. R. in *Proceedings*, Conference on Micromechanisms of Crack Extension, Cambridge, U.K., 1980, Paper No. 1.
[20] Chell, G. G. and Milne, I. in CSNI Report No. 39, Nuclear Regulatory Commission Report NUREG/CP-0010, 1979, p. 376.
[21] Paris, P. C., this publication, pp. II-5-II-40.
[22] Turner, C. E. in *Fracture Mechanics, ASTM STP 677*, American Society for Testing and Materials, 1979, p. 614.
[23] Orowan, E., *Journal of Applied Physics*, Vol. 26, 1955, p. 900.
[24] Garwood, S. J., Robinson, J. N., and Turner, C. E., *International Journal of Fracture*, Vol. 11, 1975, p. 528.
[25] Milne, I., *Materials Science Engineering*, Vol. 39, 1979, p. 65.
[26] Harrison, R. P., Loosemore, K., and Milne, I., "Assessment of the Integrity of Structures Containing Defects," 1976, CEGB Report No. R/H/R6, Central Electricity Generating Board, Leatherhead, Surrey, U.K.; see also CEGB Report No. R/H/R6-Rev 2., Revision 2 of the foregoing, 1980.
[27] Milne, I., "Experimental Validation of Resistance Curve Analysis," CEGB Report No. RD/L/2044/N81, Central Electricity Generating Board, Leatherhead, Surrey, U.K., 1982. 1982.
[28] Milne, I., Harrison, R. P., and Dowling, A. R. in *Proceedings*, Fourth International Conference on Pressure Vessel Technology, Institution of Mechanical Engineers, London, 1980, Vol. 1, Paper C11/80, p. 25.
[29] Chell, G. G. and Milne, I. in *Fracture and Fatigue*, J. C. Radon, Ed., Pergamon Press, Oxford, U.K., 1980, p. 97.
[30] Bloom, J. M., *International Journal of Fracture*, Vol. 16, 1980, p. R73.
[31] Bloom, J. M. in *Proceedings*, Ductile Fracture Public Meeting, Electric Power Research Institute, Palo Alto, Calif. Dec. 1980.
[32] Dawes, M. G., *Welding Journal Research Supplement*, Vol. 53, 1974, p. 369.
[33] Dawes, M. G. and Kamath, M. S. in *Proceedings*, Conference on the Significance of Flaws in Pressurised Components, Institution of Mechanical Engineers, London, May, 1978.
[34] Dawes, M. G., "The Application of Fracture Mechanics to Brittle Fracture in Steel Weld Metals," Ph.D. Thesis, The Welding Institute, London, 1976.
[35] Towers, O. L. and Garwood, S. J. in *Fracture and Fatigue*, J. C. Radon, Ed., Pergamon Press, Oxford, U.K., 1980, p. 57.
[36] Chell, G. G. and Ewing, D. J. F., *International Journal of Fracture*, Vol. 13, 1977, p. 467.
[37] Formby, C. L. and Griffiths, J. R. in *Proceedings*, International Conference on Residual Stresses in Welded Construction and Their Effects, The Welding Institute, London, 1977, p. 359.
[38] Burdekin, F. M. and Dawes, M. G. in *Proceedings*, Conference on Application of Fracture Mechanics to Pressure Vessel Technology, Institution of Mechanical Engineers, London, May 1971.
[39] Chell, G. G. in *Elastic-Plastic Fracture, ASTM STP 668*, J. D. Landes, J. A. Begley, and G. A. Clarke, Eds., American Society for Testing and Materials, 1979, pp. 581-605.
[40] Milne, I., *5th Transactions of Conference on Structural Mechanics in Reactor Technology*, Berlin, T. A. Jaeger and B. A. Boley, Eds., North Holland, 1979, Paper G1/3.
[41] Formby, C. L., "Comparability of the CEGB Procedure for the Assessment of the Integrity of Structures (R6) with Experimental findings in the presence of Residual Stress," CEGB North West Region Report NW/SSD/RN116/79, Central Electricity Generating Board, Leatherhead, Surrey, U.K., 1980.

[42] Ainsworth, R. A., Neale, B. K., and Price, H. in *Proceedings*, Conference on the Tolerance of Flaws in Pressurised Components, Institution of Mechanical Engineers, London, 16 May 1978.
[43] Shih, C. F., deLorenzi, H. G., and Andrews, W. R. in *Elastic-Plastic Fracture, ASTM STP 668*, J. D. Landes, J. A. Begley, and G. A. Clarke, Eds., American Society for Testing and Materials, 1979, pp. 65–120.
[44] Wilson, W. K., and Osias, J. R., *International Journal of Fracture*, Vol. 14, 1978, p. R95.
[45] Larsson, L. H. in *Proceedings*, Sixth International Conference on Structural Mechanics in Reactor Technology, Paris, Aug. 1981, Paper G3/2.

Joseph M. Bloom[1]

Validation of a Deformation Plasticity Failure Assessment Diagram Approach to Flaw Evaluation

REFERENCE: Bloom, J. M., **"Validation of a Deformation Plasticity Failure Assessment Diagram Approach to Flaw Evaluation,"** *Elastic-Plastic Fracture: Second Symposium, Volume II—Fracture Resistance Curves and Engineering Applications, ASTM STP 803*, C. F. Shih and J. P. Gudas, Eds., American Society for Testing and Materials, 1983, pp. II-206–II-238.

ABSTRACT: This paper is based upon work done to establish the validity of a simple engineering approach to assess ductile fracture. The approach is based upon the ideas of the British Central Electricity Generating Board's (CEGB) R-6 Failure Assessment Diagram (FAD) and the deformation plasticity solutions developed by General Electric. The FAD approach is an easy way to visualize a complex elastic-plastic analysis of a specimen or structure. The FAD is a safety/failure plane defined by the stress-intensity factor/fracture toughness ratio, K_r, as the ordinate and the applied stress/plastic collapse ratio, S_r, as the abscissa. For a particular stress level and flaw size, the coordinates (S_r', K_r') are determined. If the assessment point (S_r', K_r') lies on or outside of the failure assessment curve (FAC), the structure will fail. Design loads or margins of safety are readily determined graphically due to the unique linear proportionality of the diagram's axes. The FAC is constructed by taking the fully plastic solution results of deformation plasticity developed by Shih and Kumar along with Shih's estimation scheme to derive a curve in terms of (S_r, K_r) coordinates of the FAD. The validation of the deformation plasticity FAD was based upon the use of a Babcock & Wilcox-modified version of the incremental plasticity finite-element computer program ADINA (Automatic Dynamic Incremental Nonlinear Analysis). Since the FAC's are based upon the deformation plasticity J-integral, the validation of these curves is also a validation of the J-integral. Compact, center-cracked plate, double-edge-cracked plate, and single-edge-cracked plates were among the fracture configurations which were evaluated using the ADINA computer program. The additional validation of the FAD approach from experimental data of five test programs is also a validation of the elastic-plastic J-integral/J-resistance curve approach. These test programs included six different materials and five different test configurations. Based upon the assessment results the deformation plasticity failure assessment approach and the elastic-plastic J-integral/J-resistance curve approach appear to provide an excellent predictive method for determining specimen load behavior.

[1]Technical advisor, Fracture Mechanics, Applied Mechanics Section, Babcock & Wilcox, A McDermott Company, Research and Development Division, Alliance, Ohio 44601.

KEY WORDS: fracture, plastic collapse, ductile fracture, failure assessment diagram, ductile tearing, deformation plasticity, estimation procedures, J-integral, Ramberg-Osgood stress-strain curves, elastic-plastic fracture

There is a need for a simple engineering approach to assess ductile fracture.[2] Under most design loading conditions, nuclear reactor coolant pressure boundary ferritic materials will behave in a ductile manner. The Nuclear Regulatory Commission (NRC) in 10CRF50 requires adequate margins of safety on the pressure-retaining components of the reactor coolant pressure boundary of water-cooled power reactors. This regulation also establishes design criteria which will assure that these pressure-retaining components behave in a nonbrittle manner when stressed under operating, maintenance, testing, and postulated accident conditions. Currently no elastic-plastic procedure exists in the American Society of Mechanical Engineers (ASME) Codes for determining margins of safety for these accident conditions. In addition, present safety margins based on linear elastic fracture mechanics (LEFM) analyses for normal operating or accident conditions could lead to conclusions which may result in the shutdown of some nuclear plants. Therefore, the availability of a simple but accurate engineering assessment procedure would be most valuable in avoiding costly repair procedures and in establishing adequate safety margins.

One approach to this problem is a failure assessment procedure which recognizes both fracture and plastic collapse. The proposed failure assessment procedure is based upon the concepts of the British Central Electricity Generating Board's (CEGB) two-criteria assessment diagram known as the R-6 Failure Assessment Diagram (FAD) [*1*][3] and the deformation plasticity solutions from the *Plastic Fracture Handbook* [*2*] developed by General Electric under Electric Power Research Institute (EPRI) Contract RP1237-1. The FAD approach is an easy way to visualize a complex elastic-plastic analysis of a specimen or structure. The FAD is a safety/failure plane defined by the stress-intensity factor/fracture toughness ratio, K_r, as the ordinate and the applied stress/plastic collapse ratio, S_r, as the abscissa.

Flawed structures can be evaluated in terms of the FAD through the coordinates (S_r', K_r') of an assessment point, where

$$K_r' = K_I/K_{Ic} \quad \text{and} \quad S_r' = \sigma/\sigma_1 \tag{1}$$

where

K_I = stress-intensity factor for the structure to be assessed,
K_{Ic} = fracture toughness of the material,

[2]The term "ductile" is used in this paper to refer to the physical character of the fracture zone, and the term "elastic-plastic" is used to refer to the state of stress and strain in the structure.

[3]The italic numbers in brackets refer to the list of references appended to this paper.

σ = applied stress on the structure, and
σ_1 = plastic collapse stress.

For a particular stress level and flaw size, the coordinates (S_r', K_r') can be determined. If this assessment point (S_r', K_r') lies on or outside of the failure assessment curve (FAC), the structure will fail. For ductile tearing, the assessment points for a structure which is displacement-controlled lie on the failure assessment curve. In addition, design loads or margins of safety are readily determined graphically due to the unique linear proportionality of the diagram's axes.

The first use of the FAD approach was based upon the extension of the CEGB two-criteria approach of Dowling and Townley [*3*]. Their two-criteria approach stated that structures will fail by either of two mechanisms—brittle fracture or plastic collapse—and that these two mechanisms are connected by a transition curve which allows one to go directly from LEFM behavior to plastic instability or collapse. The CEGB transition curve was based upon the Dugdale strip yield model.

Harrison et al [*1*] of CEGB reformulated the two-criteria approach into a failure assessment diagram referred to in Britain as the R-6 Failure Assessment Diagram with coordinates (S_r', K_r'). The equation of the R-6 FAC is given by

$$K_r = S_r \left\{ \frac{8}{\pi^2} \ell n \sec (\pi S_r/2) \right\}^{-1/2} \tag{2}$$

Points calculated from Eq 1 which lie inside the FAC dictate that the structure is safe from failure as illustrated in Fig. 1.

Later work by CEGB [*4*] has shown that this procedure works well for cleavage fracture as well as ductile fracture, up to the point of crack initiation. For ductile fracture analysis, K_r' can be redefined in terms of an equivalent J-integral by

$$K_r' = \sqrt{J_{IE}(a)/J_{Ic}} \tag{3}$$

where J is given by

$$J_{IE} = \frac{K_I^2 \cdot (1 - \nu^2)}{E} \tag{4}$$

for the case of plane strain where E and ν are Young's modulus and Poisson's ratio, respectively and J_{Ic} is the J-value associated with the initiation of ductile tearing.

The discussion of the extension of the FAD approach to account for stable crack growth (ductile tearing) beyond initiation is presented later in the section on experimental validation for ductile tearing behavior.

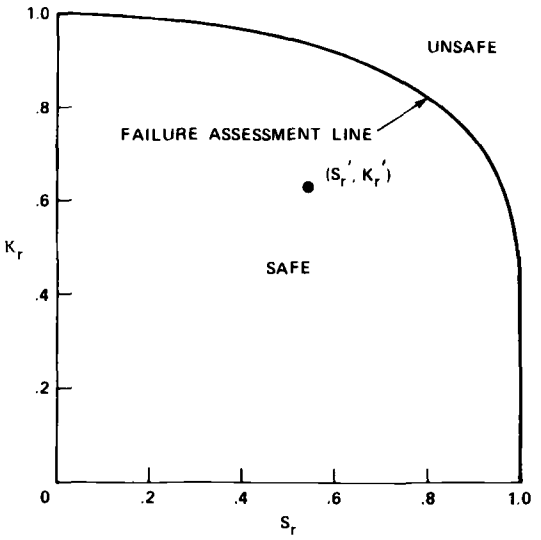

FIG. 1—*R-6 failure assessment diagram.*

The CEGB R-6 FAD as illustrated in Fig. 1 is based upon the strip yield model [*5,6*] and therefore does not take into account either geometry or material strain-hardening effects, so that the establishment of validity in general of the R-6 FAD is most difficult. Therefore, this paper presents work done under EPRI Contract RP1237-2, The Two Criteria Failure Assessment Procedure [*7*], which validates both the deformation plasticity failure assessment approach and the elastic-plastic J-integral approach using both finite-element incremental plasticity results and experimental test data from configurations which have undergone ductile tearing.

Deformation Plasticity Failure Assessment Diagrams

Recent efforts in elastic-plastic failure analysis have concentrated on the development of a *Plastic Fracture Handbook* [*2*] which contains fully plastic solutions based upon deformation plasticity for both fracture mechanics specimens and flawed cylindrical configurations. A finite-element deformation plasticity computer program developed by Needleman and Shih [*8*] was used to generate these fully plastic solutions. Provided that a material can be represented by a power-law hardening model, Ilyushin's principle [*9*] can be used to show that the resulting plasticity solutions are scalable and the results of the deformation plasticity theory will give exact solutions to flow theory of plasticity problems. Expressions for the J-integral can then be written in terms of the strain-hardening exponent. By exploiting the functional forms of both the fully plastic solution and the linear elastic solution, Shih and Hutch-

inson [*10*] first showed that a simple approximate estimate for the complete range of applied stress and strain on a structure can be formulated in terms of the total J-integral, which can be written as

$$J = J^e(a_{\text{eff}}) + J^P(a, n) \tag{5}$$

where J^e is the elastic contribution based on Irwin's plasticity-adjusted crack length (a_{eff}) and J^P is the deformation plasticity solution in terms of the J-integral. The deformation plasticity failure assessment curve in terms of $\sqrt{J_{\text{elastic}}/J}$ versus σ/σ_1 or (S_r, K_r) coordinates is constructed from Eq 5. The essence of the assessment diagram is that it is made up of a combination of an elastic parameter normalized with respect to the same parameter evaluated using elastic-plastic theory and the ratio of the applied load to limit load of the structure. Figure 2 illustrates this concept schematically in terms of the J-integral parameter for crack growth initiation only.

The straight line

$$y_1 = \sqrt{J_{\text{elastic}}/J_{\text{Ic}}} \tag{6}$$

is linearly proportional to the elastic K calibration (in terms of J) and therefore increases linearly with stress level. The curve

$$y_2 = \sqrt{J_{\text{elastic}}/J} \tag{7}$$

is based on the elastic-plastic structural response and therefore decreases with increasing stress level, since the denominator (J) becomes quite large

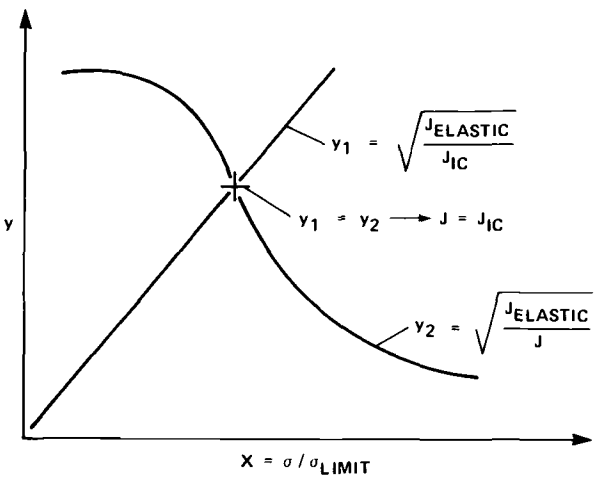

FIG. 2—*Schematic of failure assessment diagram approach (initiation only).*

near limit load. When the load on the structure for a given flaw size is increased such that $y_1 = y_2$, the crack initiates and $J = J_{Ic}$ (or $J = J_R$ if ductile tearing occurs). Furthermore, the load path for a fixed crack size is such that any point on the line y_1 is directly proportional to load. The distance of a point on y_1 to the intersection of y_1 with y_2 is a measure of the margin of safety of the structure to be assessed. Depending on what failure model is chosen, the function $J_{elastic}/J$ can take on various forms. Derived expressions for deformation plasticity-based FAC's are given in the Appendix for compact, double-edge-notched, single-edge-notched, center-cracked, and precracked bend specimens.

Finite-Element Incremental Plasticity Validation

The validation of the deformation plasticity FAD and the elastic-plastic J-integral using finite-element analyses was based upon the use of a Babcock & Wilcox-modified version of the computer program ADINA (Automatic Dynamic Incremental Nonlinear Analysis). This program is based upon an incremental small-strain-solution approach using the von Mises criteria of plasticity with isotropic hardening. The configurations of interest are loaded under displacement control, and an average of three J-integral paths versus the remote stress is calculated. The results are then recalculated in terms of (S_r', K_r') coordinates and plotted on the theoretically derived deformation plasticity FAC's (see Appendix). A number of finite element runs were made for various crack configurations using a Ramberg-Osgood stress-strain curve defined by

$$\epsilon = \sigma/E + \frac{\alpha\sigma_0}{E}(\sigma/\sigma_0)^n \tag{8}$$

where

E = 200 000 (N/mm^2).
α = 1,
n = 10, and
σ_0 = 400 (N/mm^2).

To check convergence, two finite-element grids were run for a compact specimen with $a/w = 0.58$ under plane-strain conditions. It can be seen in Fig. 3 that the more refined grid (102 elements, 424 nodes) and the estimation approach results in terms of S_r, K_r are much improved. The discrepancy between the two approaches appears to be reduced by a factor of 2 using the more refined grid. In addition, although not shown, the same grid was used for Ramberg-Osgood materials with low values of n ($n < 4$) to check out the validity of the deformation plasticity FAC. The agreement with the derived deformation plasticity FAC was excellent. The small discrepancy of the

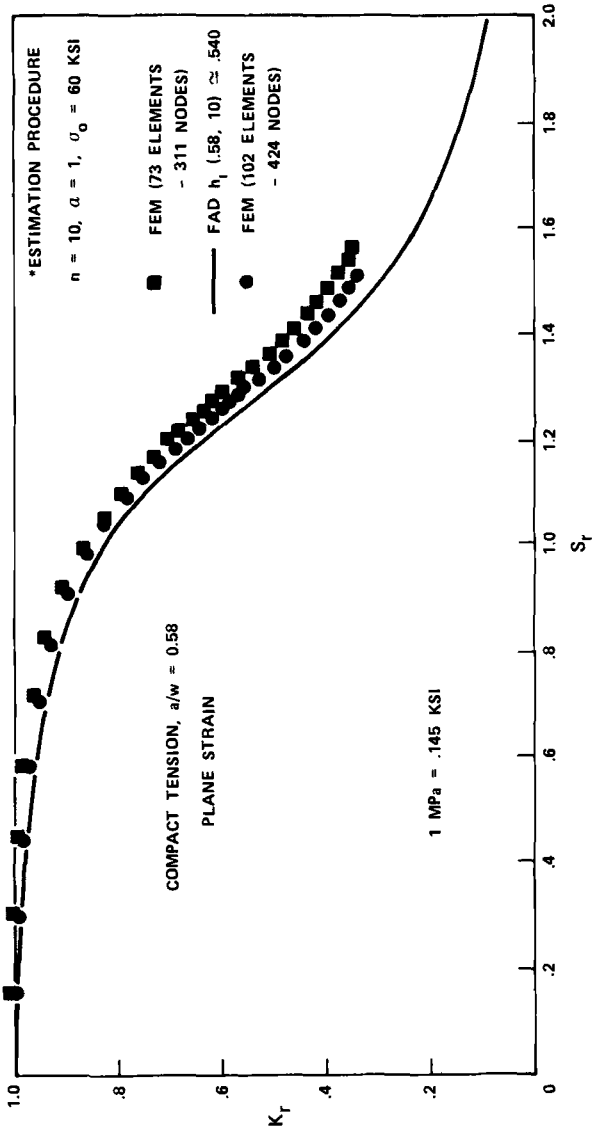

FIG. 3—*Comparison of ADINA finite-element solution and deformation plasticity FAD for a compact specimen under plane strain in terms of* (S_r, K_r) *coordinates.*

finite-element results in almost all the computer runs for large S_r is thought to be due to the cruder grid used over the remaining ligament in the present incremental finite-element analysis using ADINA compared with the grids used in Ref *2* for the generation of the deformation plasticity results.

Figure 4 shows the results of the comparison of the incremental plasticity solution for a center-cracked panel (CCP) with $a/w = 0.05$ under plane-strain conditions. Here the agreement in the range of small S_r-values ($S_r < 0.6$) is excellent. For this case "quarter-point" elements [*11*] simulating the elastic stress singularity were used at the crack tip during the complete loading of the specimen. Subsequent incremental plasticity computer runs provided no special treatment of the crack-tip singularity since in the plastic region the actual crack-tip singularity would be a function of the strain-hardening exponent [*12*]. Figure 5 illustrates the comparison between finite-element computer runs and the derived deformation plasticity FAC (see Appendix) for the double-edged-cracked plate (DECP) for two finite-element grids. The first corresponds to an L/W of 2.5. The grid consisted of 134 eight-note isoparametric elements with 757 degrees of freedom. The uncracked ligament consisted of a total of nine elements with a 2-by-2 Gaussian integration used to generate the stiffness matrix. Four triangles, formed by degenerating the eight-node quadratic elements, made up the crack-tip region. No special treatment of the crack-tip singularity was attempted. Due to the difference between the finite-element results for $L/W = 2.5$ and derived FAC, a second analysis was run based upon a similar grid but with a length-to-width ratio of $L/W = 5.0$. Note the minor effect shown in Fig. 5 of Shih's plastic zone adjustment correction, ϕ [*13*], to the overall results. The maximum difference between the two approaches occurs in the transition region between the elastic behavior and the fully plastic behavior. Shih [*14*] attributed this discrepancy to the use of the Ramberg-Osgood representation of the stress-strain curve in the estimation scheme. The single-edge-cracked plate under uniform tensile loading with $a/b = 0.75$ was run using ADINA for a Ramberg-Osgood material curve with $\alpha = 1$, $n = 10$. The grid used consisted of 952 nodes and 270 elements. The results are shown compared with the derived deformation plasticity FAC in Fig. 6. In comparisons of some of the other geometries discussed earlier in this paper, quarter-point elements were used around the crack tip. In this computer run, only conventional isoparametric elements were used around the crack tip. This is why in the elastic region ($K_r \sim 1.0$), the finite-element solution is on the high side; that is, the stress-intensity factor is lower than it should be.

Lastly, a comparison was made between the failure assessment approach and a finite-element elastic-plastic simulation of stable crack growth for a double-edge-notched tensile plate (DECP), Fig. 7, which was tested by Materialprufungsanstalt (MPA)-Stuttgart as part of the German Component Safety Program [*15*]. Both approaches used as input a material J_R-resistance curve determined by tests at Babcock & Wilcox, Alliance Research Center,

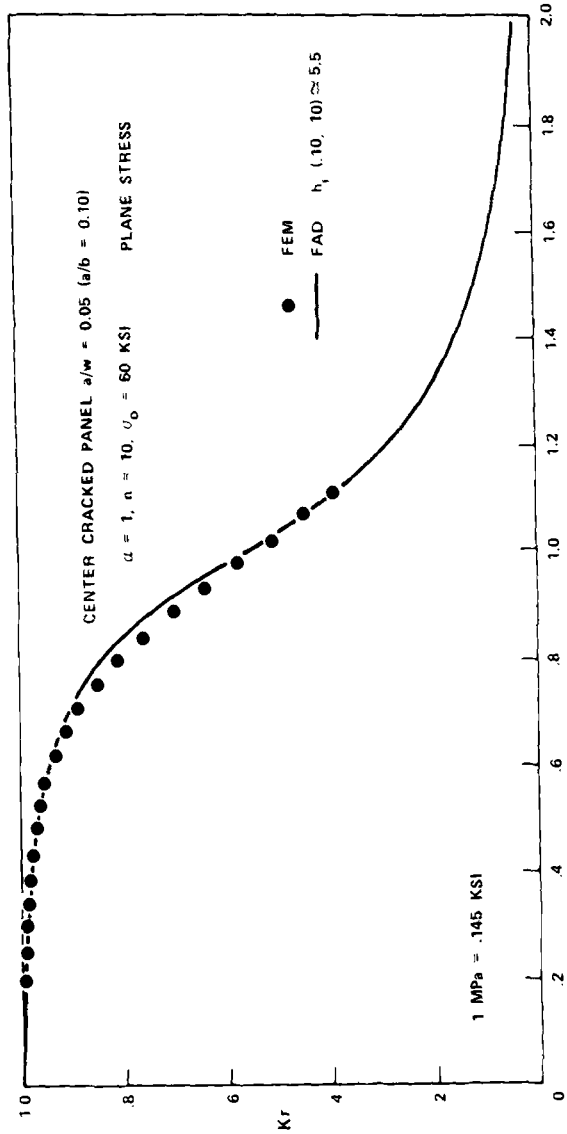

FIG. 4—*Comparison of ADINA finite-element solution and deformation plasticity FAD for a center-cracked panel under plane stress in terms of* (S_r, K_r) *coordinates.*

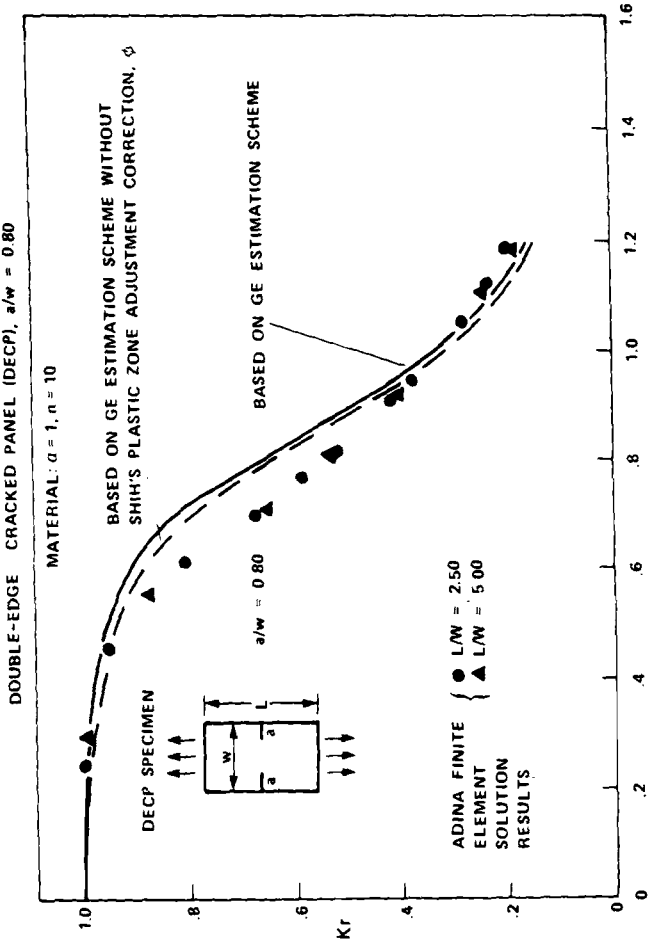

FIG. 5—*Comparison of ADINA finite-element solution and deformation plasticity FAD for a double-edge-cracked panel under plane strain in terms of* (S_r, K_r) *coordinates.*

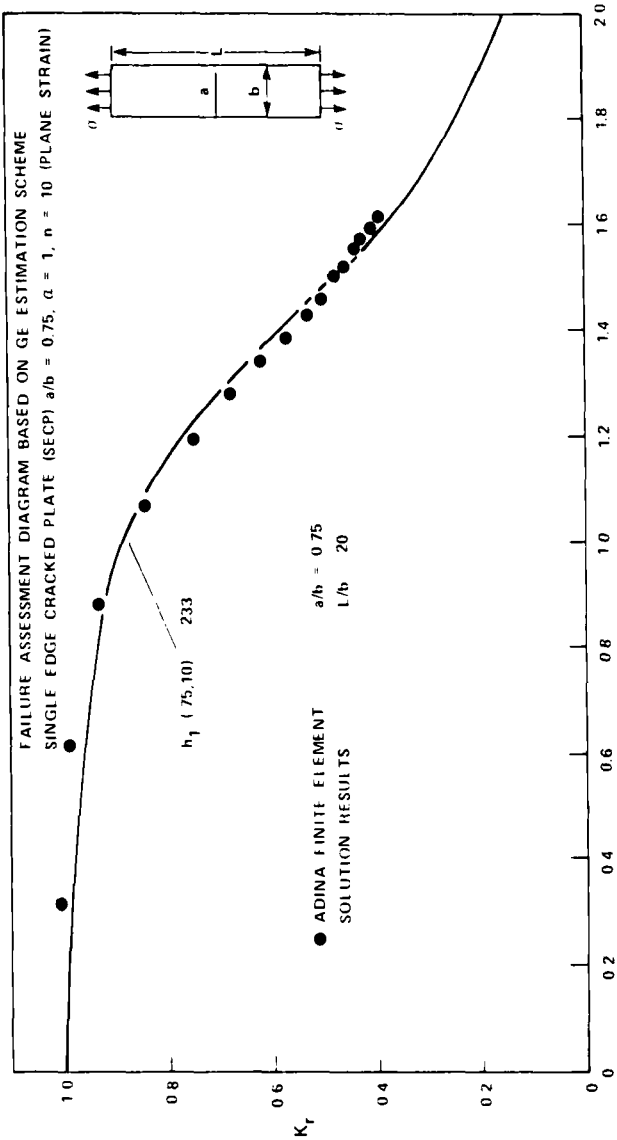

FIG. 6—*Comparison of ADINA finite-element solution and deformation plasticity FAD for a single-edge-cracked plate under plane strain in terms of* (S_r, K_r) *coordinates.*

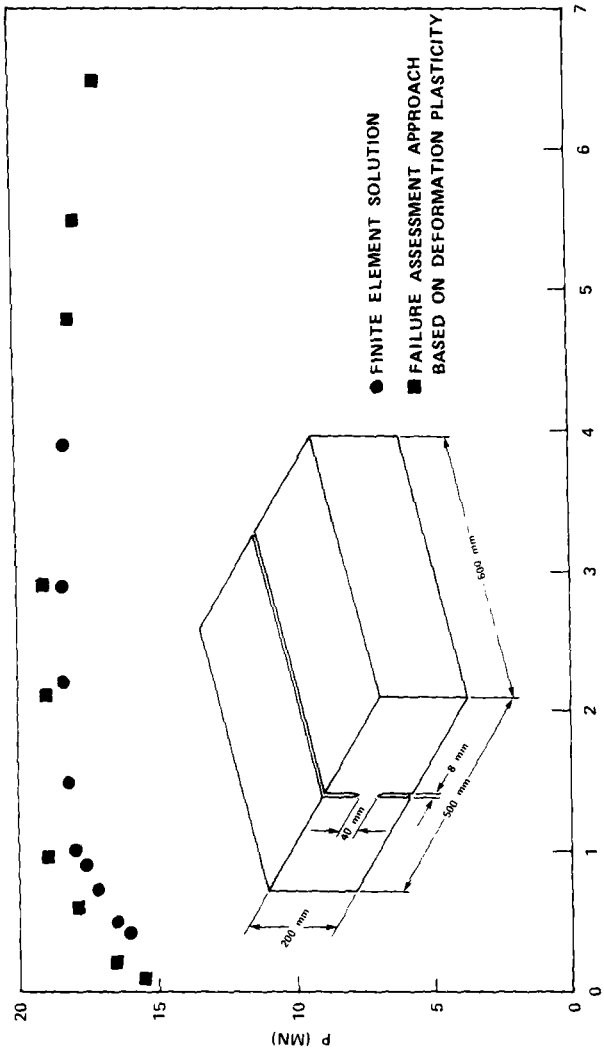

FIG. 7—Comparison of load behaviors from finite-element solution and failure assessment approach for double-edge cracked plate.

of three 2T compact fracture specimens tested at 80°C using the single-specimen J-integral test procedure. In addition, the plate material was also tested to determine the stress-strain curve of the material. Values of α and n found (see Appendix) were used both for the derivation of the FAD and the constants of the Ramberg-Osgood expression (Eq 8) used in the finite-element formulation. Figure 7 shows a comparison in terms of load versus crack extension between the failure assessment diagram approach and the rigorous finite-element crack growth analysis using ADINA.

The elastic-plastic finite-element analysis was made using a Babcock & Wilcox-modified version of ADINA. This program simulates stable crack growth by growing the crack when the average of three J-integral path values exceeds the J_R materials curve input into the computer code. The solution approach is an incremental small plasticity analysis based on the von Mises criteria with isotropic hardening. The finite-element grid for the plane-strain double-edge-cracked specimen model consisted of 482 nodes and 137 eight-node isoparametric elements. In Fig. 7, note the excellent agreement in load prediction from crack initiation to past the maximum load point. The difference in maximum load between the two approaches was less than 4 percent. The approach using the failure assessment diagram was to derive the FAD for a DECP with $a/b = 0.80$, $\alpha = 3.53$, $n = 7.63$, and $\sigma_0 = 611$ N/mm based upon both the K_I elastic solution from Tada et al [*16*] and the deformation plasticity solution from Ref *17*. The material resistance curve J_R was then used to calculate K_r'-values and the limit load expression was used to determine S_r'-values for an assumed remotely applied load. The load level of each point of the resulting (S_r', K_r') locus of points generated was increased (ratioed up) such that each point fell on the failure assessment curve. The ratioing factors then gave the values of the applied load for each (S_r', K_r') point as a function of crack extension as shown in Fig. 7.

This last finite-element run discussed shows that the failure assessment diagram is equivalent to a rigorous finite-element crack growth analysis, provided that the *J*-controlled crack growth is maintained in the structure up to the point of maximum load.

Experimental Validation for Ductile Tearing Behavior

As additional validation of the FAD approach and the elastic-plastic J-integral/J-resistance curve approach, experimental test data from configurations which have undergone ductile tearing will be presented.

Milne [*4*] extended the interpretation of the FAD to account for stable crack growth beyond initiation as given by Eqs 3 and 4 discussed earlier. Now for ductile tearing the position of the assessment point (S_r', K_r') relative to the failure assessment curve determines how close the structure is to the initiation of ductile tearing, as shown in Fig. 8 by the point L_1'. Now, since both S_r', K_r' are directly proportional to applied load (L), the load can be in-

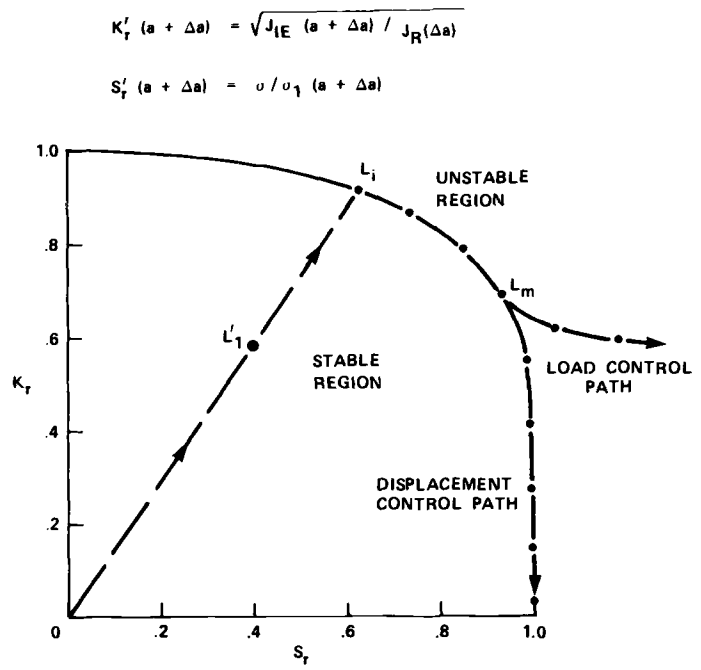

FIG. 8—*Failure assessment diagram in terms of stable crack growth.*

creased and the point L_1' moves radially from the origin of the diagram to the point L_i, which is the initiation point of ductile tearing. After initiation of ductile tearing, the locus of (S_r', K_r') points will follow the failure assessment curve between the initiation load (L_i) and the maximum load point (L_m), and thus define the region between stable and unstable crack growth as shown in Fig. 8. Note that the R-6 FAD is used in Fig. 8 for illustrative purposes only. For displacement-controlled structures, the path follows the failure assessment line. For load-controlled structures, the path will go outside the assessment curve after the maximum load point (L_m) has been reached, indicating that the structure has become unstable.

In order to calculate the locus of points which follow the failure assessment line, K_r' and S_r' must be defined as follows

$$K_r'(a + \Delta a) = \sqrt{J_{IE}(a + \Delta a)/J_R(\Delta a)} \tag{9}$$

and

$$S_r'(a + \Delta a) = \sigma/\sigma_1(a + \Delta a) \tag{10}$$

where now J_{IE}, J_R, and σ_1 are functions of the amount of slow stable crack growth. J_R is the experimentally measured J-resistance curve plotted as a

function of slow stable crack growth, Δa. J_{IE} is calculated as before from the elastic stress-intensity factor for the current crack length, $a + \Delta a$.

The condition that the assessment points must follow the FAC can alternatively be expressed as

$$J_R(\Delta a) = J(a, P) \tag{11}$$

where $a = a_0 + \Delta a$ is the current crack length and P is the remotely applied load. $J_R(\Delta a)$ is the crack growth material resistance and $J(a, P)$ is analogous to the crack driving force but expressed in terms of the J-integral.

The first test program which will be discussed is due to the work of General Electric (GE) sponsored under the EPRI contract RP601-2 [*18*] which included tests on compact specimens (CS), double-edge-cracked plates (DECP), and single-edge-cracked plates (SECP) of A533B steel. Figure 9 illustrates the derived FAD curves for plane-strain compact specimens of $a/w = 0.625$ and 0.750 (see Appendix for equations of these curves) along with the (S_r', K_r') points calculated from the actual test data of the GE/EPRI A533B 4T compact specimens [*18*]. The test results were given in terms of (J_R, Δa, P) data sets. The coordinate points (S_r', K_r') were determined from Eqs 9 and 10 where the applied stress σ is the experimentally measured value and σ_1 is the plastic collapse stress for a crack of length $a + \Delta a$. Note that both the assessment curve and the GE data points have been calculated in terms of the material yield strength instead of a flow stress, which is usually used instead in the application of the CEGB R-6 approach. The limit load expression used here for the definition of S_r is based upon the expression developed by Rice [*19*]; therefore, the "$h_1(a/w, n)$" functions obtained from Ref *2* must be modified accordingly in order that the comparisons be consistent. This is discussed in detail in the Appendix. It can be seen that the compact failure assessment curves form a lower bound to the actual test data. This is consistent with the findings given in Ref *20*.

The DECP and SECP specimens tested by General Electric under the EPRI program RP601-2 [*18*] were assessed using the FAD approach. That test program provided complete test results in terms of load and J-resistance curves, and, therefore, plots of actual data points in terms of (S_r', K_r') points were possible. These data points were then compared directly with the derived FAC's (see Appendix). Figure 10 compares the test results of three DECP specimens (Nos. 11, 14, and 18) with the FAC for a DECP with $a/b = 0.80$. Both plane-stress and plane-strain FAC's were developed. On closer examination, however, it appeared that the test data were more representative of plane-stress behavior. Additional comparisons not shown indicated that data points for Specimens 13, 15, 16, and 17 fall slightly above the plane-stress-derived FAC. This could indicate that the test data behavior may be more typical of mixed-mode or even plane-strain conditions. These data comparisons seem to indicate that the DECP configurations tested by

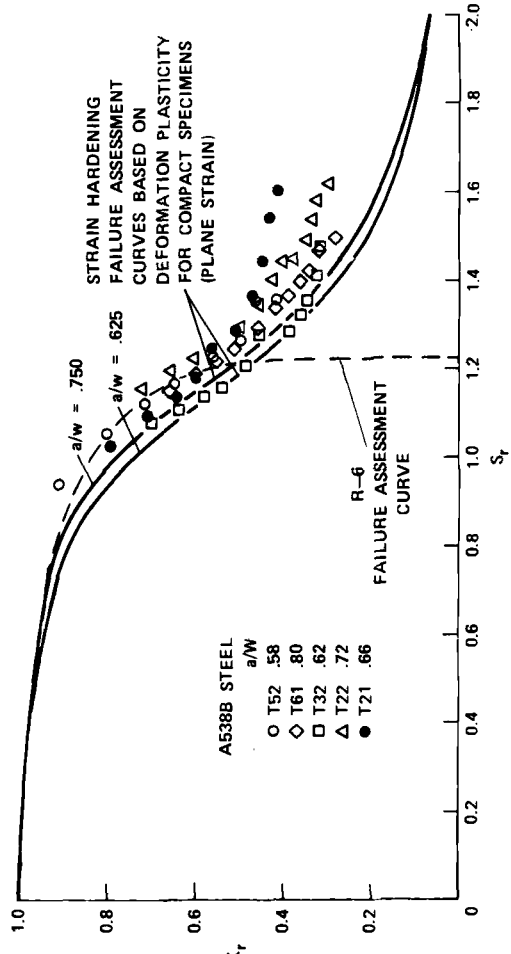

FIG. 9—*Failure assessment of EPRI/GE A533B 4T compact specimens.*

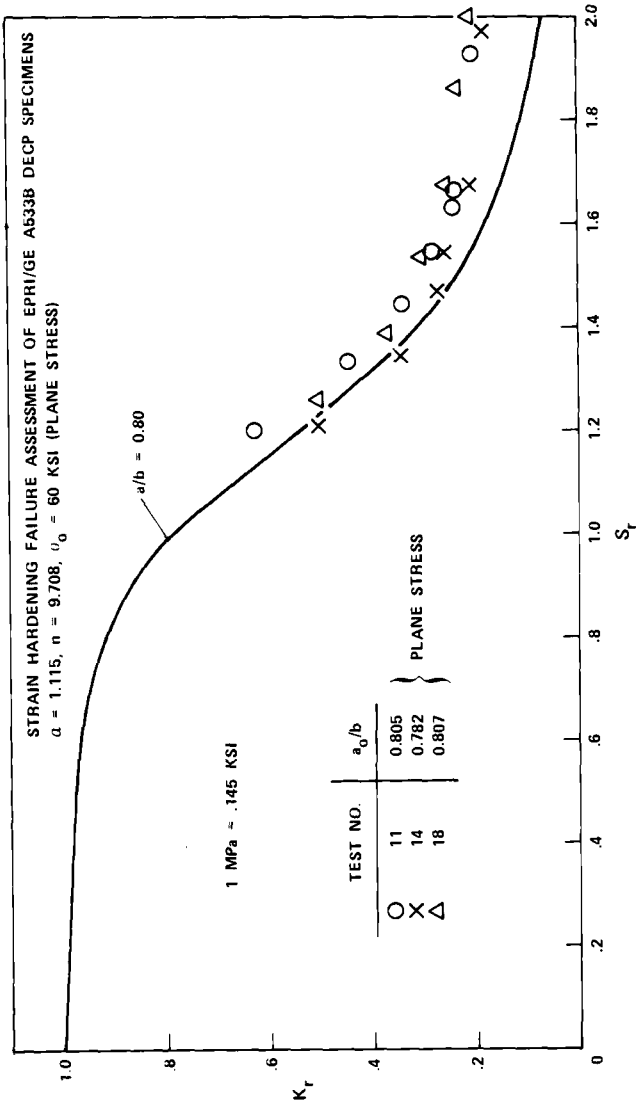

FIG. 10—*Failure assessment of GE/EPRI A533B double-edge-cracked plates in plane stress,* a/b = *0.80.*

General Electric were not constrained enough to produce a pure plane-strain test condition. Figure 11 shows similar comparisons of data for SEN specimens. The single-edge-notched specimens were loaded in such a way as to simulate the displacement and load conditions of a CCP specimen. Therefore, these SEN specimens were analyzed as CCP specimens. The FAC shown in Fig. 11 was derived from the plane-stress deformation plasticity solution for $a/b = 0.75$ from Ref *2*. The agreement with the derived FAC for Test Nos. 3–8 were excellent, while Test No. 9's results (not shown) tended to fall slightly below the derived FAC. Test No. 9 had an initial a/b ratio of 0.5875, while the rest of the tests had a/b ratios greater than 0.67.

The task group on Application of Fracture Analysis Methods (ASTM E24.06.02) conducted a predictive round robin to experimentally verify whether the fracture analysis methods currently being used can or cannot predict failure (maximum load or instability load) of complex structural components containing cracks from compact fracture test specimens of the same thickness of material. The experimental test program was conducted by the National Aeronautics and Space Administration (NASA-Langley) and the Westinghouse Research Laboratory. The comparisons of data with the derived FAD's were limited to two compact specimens [12.7 mm (½ in.) thick of 203 mm (8 in.) and 102 mm (4 in.) in width] of 2024-T351 aluminum and 304 stainless steel compacts of the same dimensions. The specimen data in terms of (S_r', K_r') coordinates were limited to these four specimens since these were the only specimens tested where complete resistance curves were given. Figure 12 shows a comparison of the two 2024-T351 compact aluminum specimens with the derived deformation plasticity FAD for compact $a/w = 0.50$ specimens with Ramberg-Osgood properties of $\alpha = 0.2511$, $n = 8.53$, and $\sigma_{flow} = 276$ MPa (40 ksi). Note the excellent agreement of the data with the derived FAD. The drop-off of data points is due to the formation of large shear lips, and thus possibly a breakdown of J-controlled crack growth. Figure 13 also illustrates the excellent agreement of the 304 stainless steel compact specimen test data in terms of (S_r, K_r) coordinates with the derived deformation plasticity FAC. Here it is seen that the R-6 FAC is definitely nonconservative. The 304 stainless steel material has considerable strain-hardening properties which cannot be accounted for using the R-6 based Dugdale model.

In cases where only a compact specimen J-resistance curve was available, the FAD approach was used in conjunction with the derived FAC for the specimen and material of interest to predict the maximum load either in another similar compact specimen or in another type specimen of the same material.

The J-resistance curves found experimentally from the compact specimens of 2024-T351 aluminum from the ASTM round robin were used to predict the maximum failure load of four 12.7-mm-thick (½ in.) center-cracked panels using the deformation plasticity derived FAC generated for a center-

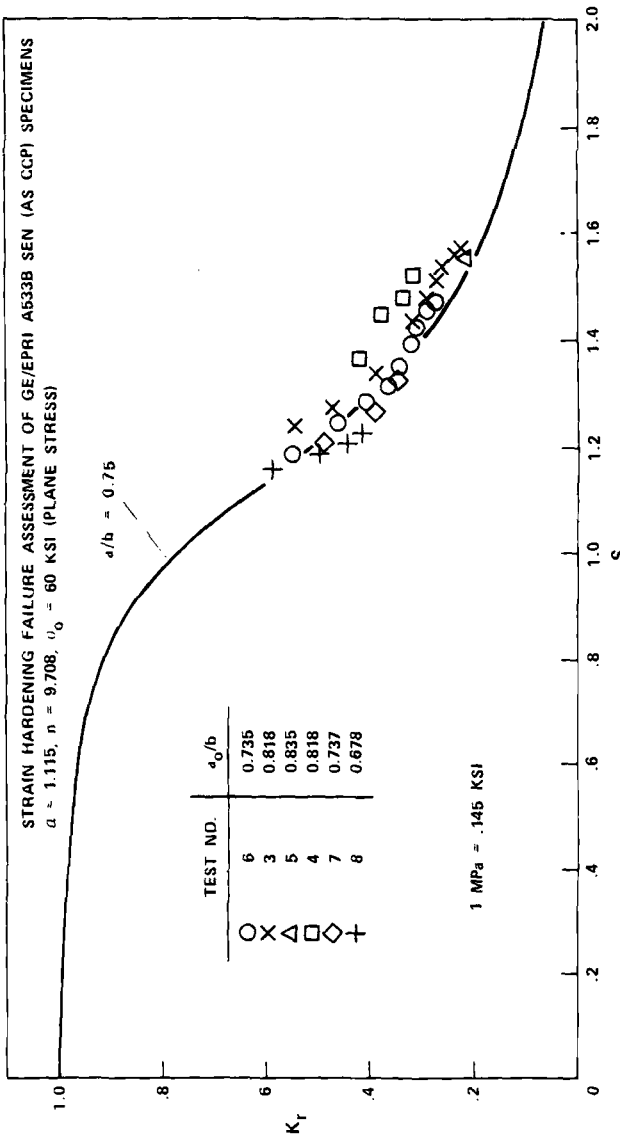

FIG. 11—*Failure assessment of GE/EPRI A533B single-edge-notched specimens acting as center-cracked plates in plane stress, a/b = 0.75.*

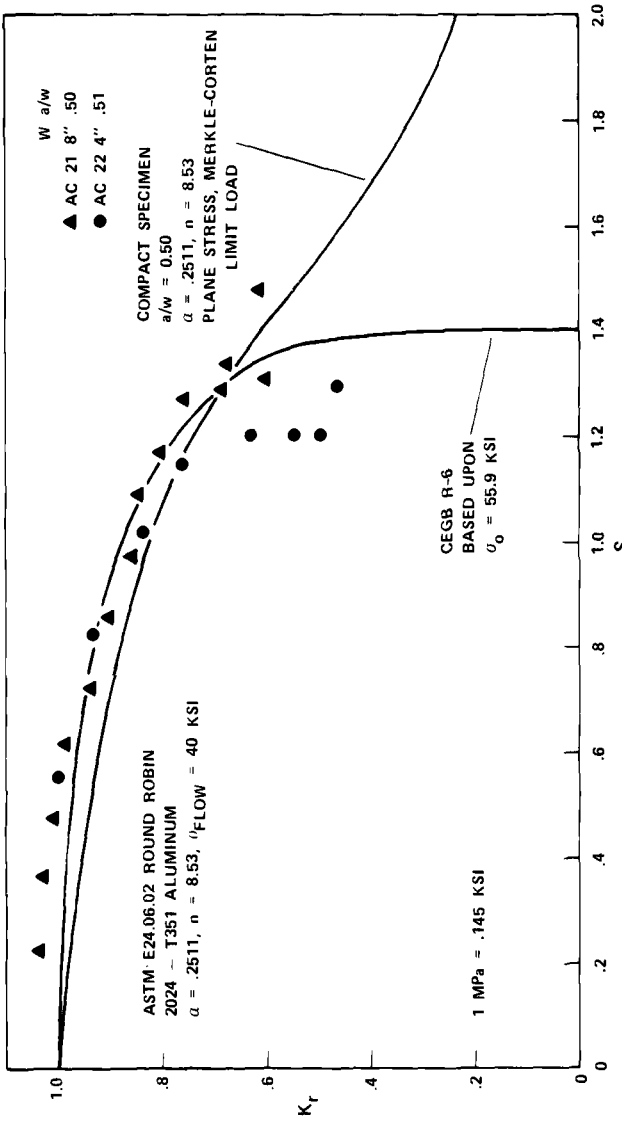

FIG. 12—*Failure assessment of ASTM E24.06.02 round-robin 2024-T351 aluminum compact specimens (AC21 and AC22).*

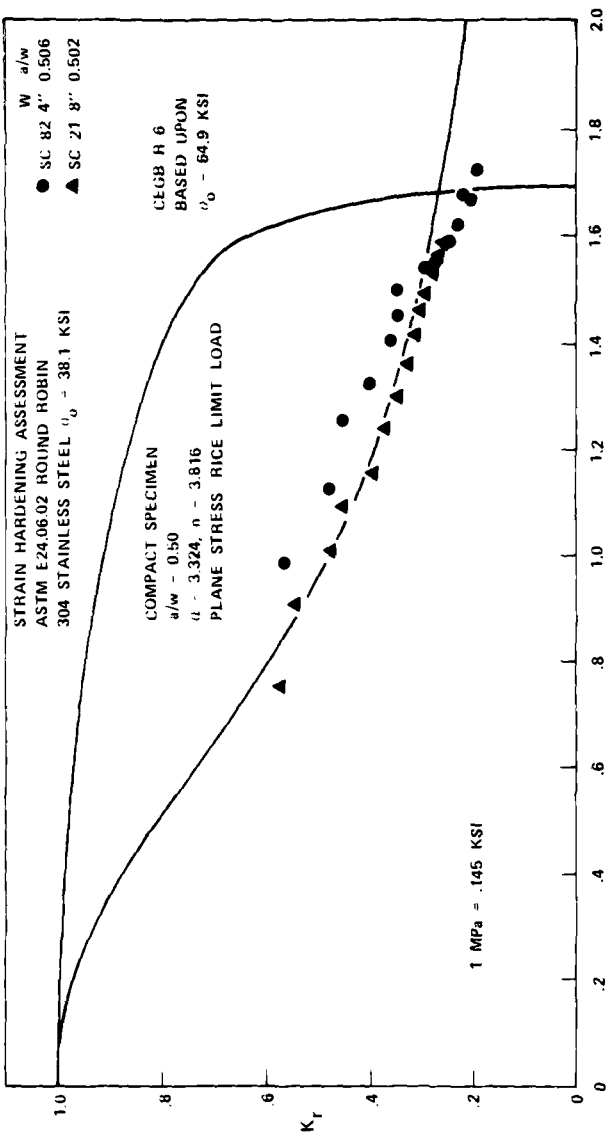

FIG. 13—*Failure assessment of ASTM E24.06.02 round-robin 304 stainless steel compact specimens (SC82 and SC21).*

cracked panel of $a/w = 0.40$ and $\alpha = 0.2511$, $n = 8.53$. The results are given in Table 1 with the overall standard error for all four specimens of 1.9 percent.

In addition to the 304 stainless steel compact specimen data analyzed and shown in terms of (S_r', K_r') coordinates in Fig. 13, twenty-five additional 304 stainless steel compact specimens tested under the ASTM round robin were also analyzed in terms of their maximum loads. These additional compacts were predicted to within a standard error of 5.2 percent. The J-resistance curves used to determine these maximum loads were taken from tests of two different-sized compact specimens, one 102 mm (4 in.) wide and the other 203 mm (8 in.) wide. Lastly, four Type 304 stainless steel center-cracked plates (CCP) were analyzed using the J-resistance curve taken from the experimental results of SC21 [the 203-mm (8 in.) width compact specimen] of the same thickness [$t = 12.7$ mm (0.5 in.)] as that of the CCP's. Table 2 gives the results of these predictions. The overall standard error for all four CCP's was 5.6 percent, which is comparable to that found from the compact specimen results.

Six large-scale test specimens tested under the German large component test program by MPA-Stuttgart [*21*] were evaluated using the deformation plasticity failure assessment approach. The J-resistance curve determined from a non-face-grooved 50-mm-thick (2 in.) (CT50) compact specimen was used to predict the maximum load for a 200-mm-thick (~8 in.) compact specimen (CT200), two DECP, and two SECP specimens. FAD's were developed for the CS, DECP, SECP, and CCP configurations, and, in conjunction with the J-resistance curve of the CT50 specimen, were used to predict the maximum loads of the specimens. The results of the predictions are summarized in Table 3.

The SECP specimens were initially evaluated as SECP configurations, but after discussions with Dr. Issler of MPA it was determined that in fact these specimens were loaded in such a way as to simulate the boundary conditions of a CCP specimen. All the predictions appear to validate the use of a com-

TABLE 1—*Prediction of* P_{max} *for the ASTM E24.06.02 round-robin 2024-T351 aluminum center-cracked tension specimens.*

Specimen No.	B, in.	W, in.	a_0, in.	P_{max}, Maximum Failure Load, kips	
				Experimental	Predicted
AH91	0.495	5	1.030	67.9	68.8
AH92	0.495	5	0.992	70.0	71.4
AH3	0.495	10	2.016	130.7	133.7
AH6	0.495	10	2.050	129.0	131.4
				standard error = 1.9%	

1 kip = 4.448 kN.
1 in. = 25.4 mm.

TABLE 2—*Prediction of P_{max} for the ASTM E24.06.02 round-robin stainless steel 304 center-cracked tension specimens.*

Specimen No.	B, in.	W, in.	a_0, in.	P_{max}, Maximum Failure Load, kips	
				Experimental	Predicted
SH91	0.536	5	1.029	103.0	107.1
SH92	0.536	5	1.031	105.5	107.1
SH6	0.530	10	1.971	198.4	210.2
SH10	0.536	10	2.000	197.5	210.2
				standard error = 5.6%	

1 kip = 4.448 kN.
1 in. = 25.4 mm.

TABLE 3—*Prediction of P_{max} for the German large-component test specimens tested at MPA-Stuttgart.*

Specimen Type	Designation	Predicted Maximum Load, MN	Experimental Maximum Load, MN	Percent Difference
CS	CT50	0.232	0.224	3.6
CS	CT200	3.13	3.1	1.0
DECP	KS 01 AA	20.2	17.9	12.8
DECP	KS 01 AW 64	1.01	0.90	12.0
SECP	KS 01 HC	42.9	48.8	−12.1
SECP	KS 01 GC	46.4	53.8	−13.7
SECP(CCP)	KS 01 HC	49.6	48.8	1.6
SECP(CCP)	KS 01 GC	51.1	53.8	−5.0

1 kip = 4.448 kN.

pact specimen-generated J-resistance curve for the prediction of other-type specimen behaviors. The overprediction of maximum load for the DECP configurations appears to be due to the use of a non-face-grooved compact specimen (which had some resulting shear lips producing a greater J-resistance) for the prediction of a highly constrained plane-strain DECP specimen (which had no shear lips). If the compact specimen (CT50) had face grooves, the resistance curve would be much lower and the resulting prediction of the DECP's maximum load would have been much lower.

In order to evaluate the sensitivity of both the R-6 FAC and the deformation plasticity FAC, two additional materials were investigated. Two high-strength HY 130 side-grooved 25.4-mm-thick (1 in.) (1T) standard ASTM E 399[4] compact specimens were tested at the Babcock & Wilcox Alliance Research Center (ARC) [22] and evaluated in terms of the failure assessment

[4]ASTM Test for Plane-Strain Fracture Toughness of Metallic Materials.

diagram. The specimens were tested using the single-specimen J-integral unloading compliance procedure. The test results in terms of J and load P versus stable crack growth, Δa, were used to determine (S_r', K_r') points as shown in Fig. 14. The assessment points (S_r', K_r') were compared with the CEGB R-6 curve based on the average of the yield and ultimate strengths, and with the estimation scheme for Ramberg-Osgood stress-strain properties of $\alpha = 1.651$ and $n = 33.72$ based upon a power-law fit of the yield and ultimate strength of the HY 130 material. On inspection of Fig. 14, it can be seen that the data can easily fit either the more exact deformation plasticity FAC or the R-6 FAC. This is in agreement with earlier observations made in Ref *22* that the CEGB R-6 FAD is a good representation for materials with little or no strain hardening.

A modified ferritic steel obtained from MPA-Stuttgart, 22Ni-Mo-Cr37, similar to SA 508 Class 2, was tested using the single-specimen J-integral unloading compliance procedure at the Babcock & Wilcox ARC [*7*]. Three 2T compact specimens of this material were tested and a J_R-curve was determined. The equivalent (S_r', K_r') points were calculated and plotted on the corresponding deformation plasticity FAD. Figure 15, representing the KS 37 specimen only, is typical of the results of all the compact specimens. In all three specimens after the maximum load point (for KS 37 this point is represented by No. 9 in Fig. 15), the (S_r', K_r') points drop below the FAC. Subsequent examinations after the test when the specimens were broken open showed that the crack surfaces were irregular and that there were many untorn ligaments, out-of-plane crack growth, and nonuniform crack growth. Physically the material had many laminations, and the crack was trying to propagate perpendicular to these laminations. The unloading compliance method gave crack growth measurements which were in error by as much as 100 percent. The (S_r', K_r') points which fell below the failure assessment curve were recalculated by changing the amount of slow stable crack growth in the calculations such that these resultant recalculated points fell on the FAC. The resulting "equilibrium Δa's" were found to be consistent with the physically measured crack growth made after the specimens were broken open.

A similar type of behavior was shown by the ASTM E24.06.02 round-robin 2024-T351 aluminum compact specimen AC 22 (see Fig. 12). In that case the AC 22 specimen developed large shear lips at about the same point where the (S_r', K_r') points dropped below the FAC for the compact specimen.

In both these cases the place where the points deviate from the FAC is where the J-controlled crack growth became invalid. Note it was only after the specimens were broken open that physical evidence was obtained. This strongly suggested that the FAD might be useful in detecting a loss of J-controlled crack growth due either to irregular crack growth or a breakdown of the crack growth measurement.

The expression for the failure assessment curve for a three-point-bend specimen was based upon the deformation plasticity solution in Ref *2* and the

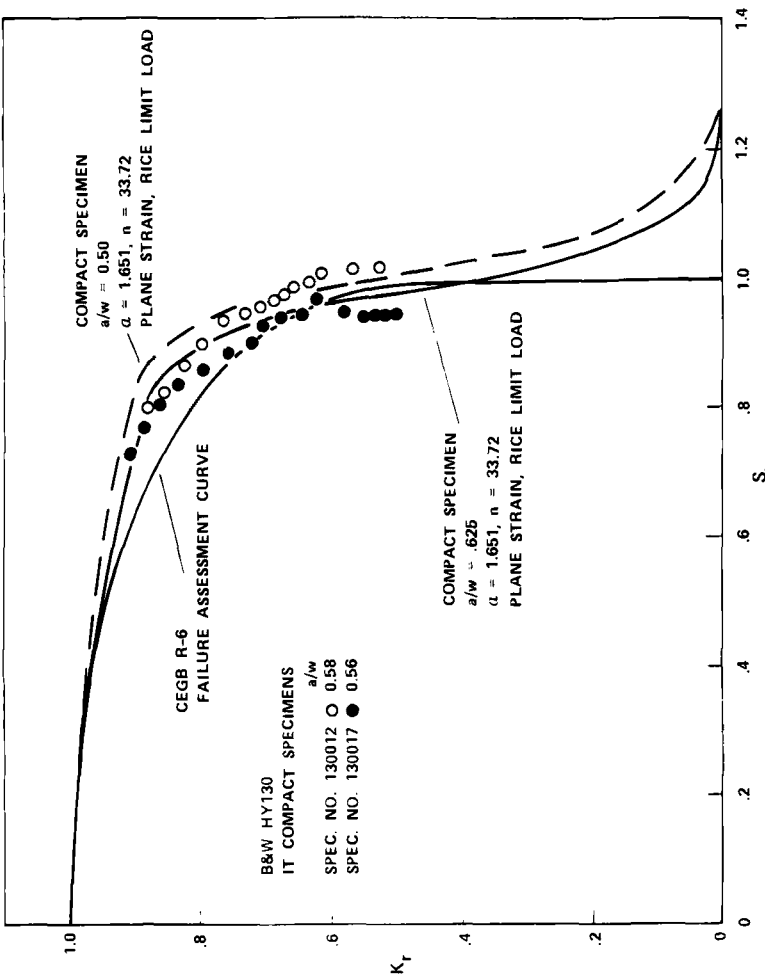

FIG. 14—*Failure assessment of Babcock & Wilcox-tested HY130 compact specimens (130012 and 130017).*

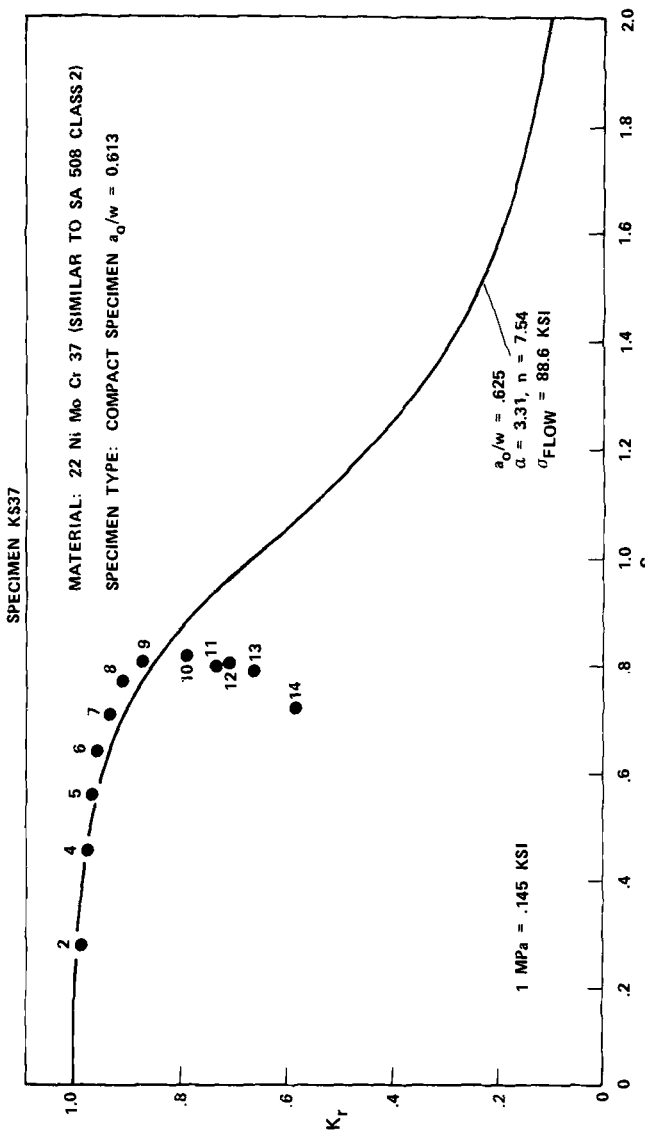

FIG. 15—*Failure assessment of Babcock & Wilcox-tested 22Ni-Mo-Cr37 (modified) steel compact specimen KS37.*

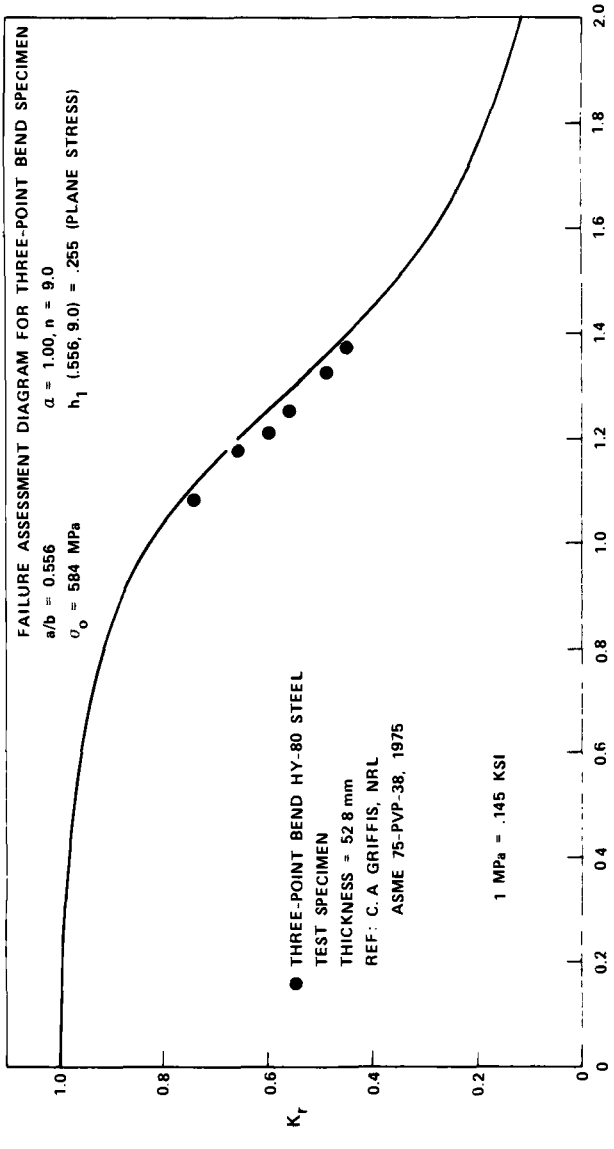

FIG. 16—*Failure assessment of NRL HY80 steel three-point-bend specimen in plane stress,* a/b = *0.556.*

linear elastic solution from Ref *16*. Test data [*23*] from the Naval Research Laboratories of three-point-bend HY-80 steel specimens were evaluated in terms of S_r, K_r and plotted as shown in Fig. 16. The agreement between the experimental data and the derived failure assessment curve is excellent.

Conclusions

Compact, center-cracked plate, double-edge-cracked plate, and single-edge-cracked plates were among the fracture configurations which were evaluated using the ADINA incremental plasticity computer program. Material properties simulating both ferritic and austenitic materials were used. In all cases the comparisons between the finite-element results and the derived deformation plasticity FAC's were excellent.

Results of actual experimental test data in terms of (S_r', K_r') coordinates compared favorably with the derived deformation plasticity FAC's. Results of the predictions of maximum load of noncompact configurations using J_R resistance curves developed from compact specimens were usually within 6 percent of the actual experimental test results, with the exception of a few tests where the greater deviation from experimental results could be reasonably explained.

Based on the assessment results presented in this paper of several different materials:

A533B steel,
304 stainless steel,
22Ni-Mo-Cr37 modified and unmodified steel,
2024-T351 aluminum, and
HY130 and HY80 high-strength steels,

several different specimen configurations:

compact,
double-edge-notched,
single-edge-notched,
center-cracked, and
precracked bend,

the deformation plasticity failure assessment approach and the elastic-plastic J-integral/J-resistance curve approach appear to provide an excellent predictive method for determining specimen load behavior.

Acknowledgments

The author wishes to acknowledge the support of this work by the Electric Power Research Institute, Palo Alto, Calif. under Contract RP 1237-2. The author also wishes to acknowledge both Drs. S. Malik and M. Schroedl (now with the Naval Research Laboratories) of the Babcock & Wilcox Research and

Development Division for their work on the development and running of the finite-element validations using the computer program ADINA as well as R. Futato of the Babcock & Wilcox Research and Development Division for his cooperation in supplying the Research and Development Division's compact specimen test data. Additional thanks is also offered for the encouragement and helpful discussions from both Drs. P. Sensmeier of the Babcock & Wilcox Research and Development Division and K. Yoon of the Babcock & Wilcox Nuclear Power Generation Division. Lastly, thanks is extended to Dr. D. Norris of EPRI without whose support this work would not have been possible.

APPENDIX

Deformation Plasticity-Derived FAC Expressions

The author has taken the deformation plasticity solutions results from Ref *2* along with General Electric's proposed estimation scheme [*13*] and derived failure assessment expressions for the following specimens

Center-Cracked Plate (Plane Strain and Plane Stress)

$$J/J_{\text{elastic}} = 1/K_r^2 = ae/a\ \frac{\sec(\pi/2\, ae/a\, a/b)}{F_1^2} + \frac{\alpha h_1 S_r^{n-1}}{\pi(1-f\nu^2)F_1^2\Lambda^2(1-a/b)} \tag{12}$$

where

$$ae/a = 1 + 1/\beta\frac{(n-1)}{(n+1)}F_1^2\Lambda^2(1-a/b)^2\frac{S_r^2}{1+S_r^2} \tag{13}$$

and $\beta = 6$ for plane strain and $\beta = 2$ for plane stress; $\Lambda^2 = 4/3$ for plane strain and $\Lambda^2 = 1$ for plane stress; $f = 1$ for plane strain and $f = 0$ for plane stress, and $F_1^2 = \sec(\pi/2\, a/b)$, where

$$P_{\text{limit}}{}^* = \frac{4c\sigma_0}{\sqrt{3}}\ \text{(plane strain)} \quad \text{and} \quad K_I = \sigma\sqrt{\pi a \sec\frac{\pi a}{2b}}$$

or

$$P_{\text{limit}} = c\sigma_0\ \text{(plane stress)} \tag{14}$$

*where c is defined as the remaining ligament in all the expressions to follow or $c = b - a$.

Double Edge-Cracked Plate (Plane Strain)

$$J/J_{\text{elastic}} = \frac{1}{K_r^2} = \frac{\left(1 - 3/8\frac{ae}{a}a/b\right)^2}{(1 - ae/a\ a/b)}\ \frac{(1-a/b)}{(1-3/8\ a/b)^2}\ ae/a + \frac{4\alpha\, h_1 S_r^{n-1}}{\pi(5.94)^2(1-\nu^2)(1-3/8\, a/b)^2\, a/b} \tag{15}$$

where

$$ae/a = 1 + \frac{(5.94)^2}{24}\,\frac{n-1}{n+1}\,(1 - \tfrac{3}{8}\,a/b)^2\,(1 - a/b)\,\frac{S_r^2}{1 + S_r^2} \tag{16}$$

and

$$\begin{aligned} P_{\text{limit}} &= 5.94\,\sigma_0(b-a) \\ K_1 &= \sigma\sqrt{\pi a}\;\frac{(1.01 - 0.375\,a/b)}{\sqrt{1 - a/b}} \qquad a/b \geq 0.50 \end{aligned} \tag{17}$$

Compact Specimen (Plane Strain)

$$\begin{aligned} J/J_{\text{elastic}} = \frac{1}{K_r^2} &= \frac{(2 + a/w\,ae/a)^2}{(1 - a/w\,ae/a)^3}\,\frac{(1 - a/w)^3}{(2 + a/w)^2} \\ &\quad + \frac{\alpha h_1'(a/w, n) S_r^{n-1}}{(1 - \nu^2)F_1^2\Lambda^2 a/w(1 - a/w)} \end{aligned} \tag{18}$$

where

$$ae/a = 1 + \frac{1}{6\pi}\,\frac{n-1}{n+1}\,F_1(a)^2\Lambda^2(1 - a/w)^2\,\frac{S_r^2}{1 + S_r^2} \tag{19}$$

$$F_1(a) \cong \frac{2(2 + a/w)}{(1 - a/w)^{3/2}}\,\frac{1}{\sqrt{a/w}} \times (0.663) \tag{20}$$

$$\Lambda = \frac{2}{\sqrt{3}}\left[\frac{0.3 + \sqrt{0.9 + 0.4\zeta}}{\zeta}\right] \tag{21}$$

$$\zeta = 1 + 1.1025\left[\frac{1 + a/w}{1 - a/w}\right]^2 \tag{22}$$

where

$$P_{\text{limit}} = \Lambda\sigma_0 c \quad \text{(based on Rice's limit load)} \tag{23}$$

and

$$K_1 = \sigma\sqrt{\pi a}\,F_1(a), \qquad a/b \geq 0.60$$

Single-Edged-Notched Plate (Plane Strain)

$$\begin{aligned} J/J_{\text{elastic}} = \frac{1}{K_r^2} &= \left[\frac{0.878 + 0.244\,ae/a\;a/b}{0.878 + 0.244\,a/b}\right]^2\left[\frac{1 - a/b}{1 - ae/a\;a/b}\right]^3\frac{ae}{a} \\ &\quad + \frac{\alpha(1 - a/b)^2 h_1 S_r^{n-1}}{\pi(0.878 + 0.244\,a/b)^2(1 - \nu^2)\Lambda^2} \end{aligned} \tag{24}$$

where

$$\Lambda = 1.455\left\{\left[1 + \left(\frac{1}{(b/a - 1)}\right)^2\right]^{1/2} - \left(\frac{1}{b/a - 1}\right)\right\} \tag{25}$$

$$ae/a = 1 + \frac{1}{6}\frac{(n-1)}{(n+1)}\frac{(0.878 + 0.244\,a/b)^2}{(1 - a/b)}\frac{\Lambda^2 S_r^2}{(1 + S_r^2)} \tag{26}$$

where

$$P_{\text{limit}} = \Lambda\sigma_0 c$$

and (27)

$$K_I = \sigma\sqrt{\pi a}\,\frac{(0.878 + 0.244\,a/b)}{(1 - a/b)^{3/2}}, \qquad a/b \geq 0.5$$

Three-Point-Bend Specimen (Plane Strain)

$$J/J_{\text{elastic}} = \frac{1}{K_r^2} = \left[\frac{1 - a/b}{1 - ae/a\;a/b}\right]^3\left[\frac{0.59 - 0.22\,a/b\;ae/a}{0.59 - 0.22\,a/b}\right]^2\frac{ae}{a} + \frac{\alpha h_1 S_r^{n-1}}{9\pi(1-\nu^2)a/b(0.59 - 0.22\,a/b)^2\Lambda^2} \tag{28}$$

where

$$ae/a = 1 + \frac{3}{2}\frac{n-1}{n+1}(1 - a/b)(0.59 - 0.22\,a/b)^2\Lambda^2\frac{S_r^2}{1 + S_r^2} \tag{29}$$

$$\Lambda = 0.728$$

$$P_{\text{limit}} = \Lambda\sigma_0 c^2/L$$

and

$$K_I = \sigma\sqrt{\pi a}\,(0.59 - 0.22\,a/b)(1 - a/b)^{-3/2}$$

for (30)

$$S/b = 4 \quad \text{and} \quad a/b \geq 0.60$$

Ramberg-Osgood Stress-Strain Representation

All the foregoing deformation plasticity-derived FAD expressions are based on the representation of the material stress-strain curve by the Ramberg-Osgood equation

$$\epsilon/\epsilon_0 = \sigma/\sigma_0 + \alpha(\sigma/\sigma_0)^n \tag{31}$$

where α and n are defined in the preceding and σ_0 and ϵ_0 are chosen for convenience as the engineering yield strength and engineering yield strain, respectively, of the material. The constants α and n are determined by a least-squares best fit of the *true* plastic stress-*true* plastic strain plotted on log-log paper. The constants (α' and n') which give the best fit to the equation

$$\log \epsilon_p = \log \alpha' + n' \log \sigma_p \tag{32}$$

are used in the derivation of the deformation plasticity FAD's.

Determination of the Deformation Plasticity Constants "h_1"

The constants "h_1" used in the derived deformation plasticity FAC expressions can be taken directly from Ref *2* noting that they are functions of the a/b ratio of the configuration, the strain-hardening exponent n, and the stress state, that is, plane strain or plane stress. However, it must further be noted that these h_1 values are dependent upon the reference limit load expression used in Ref *2*. If for some reason a different reference limit load is used in a FAD analysis, a modified h_1 value must be used. As an example, the 4T compact A533B GE/EPRI specimens (see Fig. 9) were analyzed using the limit load expression due to Rice [*19*]. The expression given in this Appendix is also based on the Rice expression. Therefore the h_1' $(a/w, n)$ values used must be derived from the h_1 $(a/w, n)$ values given in Ref *2*. The h_1 values given in Ref *2* are based on a limit load of Merkle and Corten [*24*].

By equating the deformation plasticity J-integral solutions based on Rice and Merkle-Corten limit loads, the required h_1' $(a/w, n)$ Rice limit load-based values are obtained as

$$h_1'(a/w, n) = h_1(a/w, n)\left(\frac{P_{\text{Rice}}}{P_{\text{M-C}}}\right)^{n+1} \tag{33}$$

where P_{Rice} is the limit load due to Rice and $P_{\text{M-C}}$ is the limit load due to Merkle and Corten. Note that the limit load constraint factor Λ is based on Rice's limit load and is consistent with the use of the h_1' values in the foregoing.

Note that for the DECP analyses, the h_1 values used were based upon an earlier version of the *Plastic Handbook* [*17*] where

$$p_{\text{limit}} = 5.94\sigma_0(b - a) \tag{34}$$

while the more recently released version [*2*] has different h_1 values corresponding to a different reference limit load.

References

[*1*] Harrison, R. P., Loosemore, K., and Milne, I., "Assessment of the Integrity of Structures Containing Defects," CEGB Report No. R/H/R6, Central Electricity Generating Board, U.K., 1976.

[*2*] Kumar, V., German, M. D., Shih, C. F., "An Engineering Approach for Elastic-Plastic Fracture Analysis," EPRI Topical Report NP-1931, Research Project 1237-1, Electric Power Research Institute, Palo Alto, Calif., July 1981.

[*3*] Dowling, A. R. and Townley, C. H. A., *International Journal of Pressure Vessel and Piping*, Vol. 3, 1975, p. 77.

[*4*] Milne, I., *Materials Science and Engineering*, Vol. 39, 1979, p. 65.

[*5*] Dugdale, D. S., *Journal of the Mechanics and Physics of Solids*, Vol. 8, 1960, p. 100.

[*6*] Bilby, B. A., Cottrell, A. H., and Swinden, K. H., "Plastic Yielding from Sharp Notches," *Proceedings of the Royal Society*, London, Vol. A272, 1963, p. 304.

[*7*] Bloom, J. M. and Malik, S. N., "A Procedure for the Assessment of the Integrity of Nuclear Pressure Vessels and Piping Containing Defects," EPRI Topical Report NP-2431, Research Project 1237-2, Electric Power Research Institute, Palo Alto, Calif., June 1982.

[*8*] Needleman, A. and Shih, C. F., "Finite Element Method for Plane Strain Deformations of Incompressible Solids," *Computer Methods in Applied Mechanics and Engineering*, 1978, p. 223.

[*9*] Ilyushin, A. A., *Prikadnaia Matematika i Mekhanika*, Vol. 10, 1946, p. 347.

[*10*] Shih, C. F. and Hutchinson, J. W., *Transactions*, American Society of Mechanical Engi-

neers, *Journal of Engineering Materials and Technology*, Series H, Vol. 98, No. 4, Oct. 1976, p. 289.

[*11*] Bloom, J. M., *International Journal of Fracture*, Vol. 2, Aug. 1975, p. 705.

[*12*] Rice, J. R. and Rosengren, G. F., *Journal of the Mechanics and Physics of Solids*, Vol. 16, No. 1, Jan. 1968, p. 1.

[*13*] Kumar, V. and Shih, C. F. in *Fracture Mechanics, ASTM STP 700*, American Society for Testing and Materials, 1980, p. 406.

[*14*] Shih, C. F., private communication, Plastic Fracture Analysis Group Meeting at Battelle-Columbus Laboratories, 9 Sept., 1980.

[*15*] Bloom, J. M., "Elastisch-Plastische Versagensanalyse (Elastic-Plastic Failure Analysis)," Sixth MPA Seminar, Staatliche Mateiralprufungsanstalt-Universität, Stuttgart, Paper No. 9, 9/10 Oct. 1980.

[*16*] Tada, H., Paris, P. C., Irwin, G. R., *The Stress Analysis of Cracks Handbook*, Del Research Corp., Hellertown, Pa., 1973.

[*17*] Kumar, V., German, M. D., and Shih, C. F., "Estimation Technique for the Prediction of Elastic-Plastic Fracture of Structural Components of Nuclear Systems," EPRI Combined Second and Third Semiannual Report, Feb. 1, 1979 to Jan. 31, 1980, Research Project 1237-1, Electric Power Research Institute, Palo Alto, Calif., 1 June 1980.

[*18*] Shih, C. F., Andrews, W. R., deLorenzi, H. G., German, M. D., Van Stone, R. H., and Mowbray, D. F., "Methodology for Plastic Fracture," Final Report to EPRI, Contract No. RP601-2, General Electric Co., Schenectady, N.Y., Aug. 1980.

[*19*] Rice, J. R., *The Surface Crack: Physical Problems and Computational Solutions*, J. F. Swedlow, Ed., American Society of Mechanical Engineers, New York, 1972.

[*20*] Shih, C. F. and Kumar, V., "Estimation Technique for the Prediction of Elastic-Plastic Fracture of Structural Components of Nuclear Systems," First Semi-annual Report, EPRI Contract RP 1237-1, Electric Power Research Institute, Palo Alto, Calif., 1 June 1979.

[*21*] Issler, F., Birk, R., and Hund, R., "Anwendung eines neuen Nëherungsverfahrens aus den USA zur Zähbruchanalyse (Application of a New Estimation Technique from the USA for the Prediction of Ductile Fracture)," Sixth MPA Seminar, Staatliche Materialprufungsanstalt-Universität, Stuttgart, Paper No. 8C, 9/10 Oct. 1980.

[*22*] Bloom, J. M., *International Journal of Pressure Vessels and Piping*, May-June 1980, p. 215.

[*23*] Griffis, C. A., "Elastic-Plastic Fracture Toughness: A Comparison of J-Integral and Crack Opening Displacement Characterizations," *ASME Paper No. 75-PVP-38*, American Society of Mechanical Engineers, 1975.

[*24*] Merkle, J. G. and Corten, H. T., *Transactions*, American Society of Mechanical Engineers, *Journal of Pressure Vessel Technology*, Vol. 96, 1974, p. 286.

C. Fong Shih,[1] *Virendra Kumar,*[2] *and Marjorie D. German*[2]

Studies on the Failure Assessment Diagram Using the Estimation Method and *J*-Controlled Crack Growth Approach

REFERENCE: Shih, C. F., Kumar, V., and German, M. D., **"Studies on the Failure Assessment Diagram Using the Estimation Method and *J*-Controlled Crack Growth Approach,"** *Elastic-Plastic Fracture: Second Symposium, Volume II—Fracture Resistance Curves and Engineering Applications, ASTM STP 803*, C. F. Shih and J. P. Gudas, Eds., American Society for Testing and Materials, 1983, pp. II-239–II-261.

ABSTRACT: The failure assessment diagram procedure for assessing the integrity of flawed structures evolved from the "two criteria" approach due to Dowling and Townley. The present form of the diagram, also referred to as the R-6 diagram, is due to Harrison, Loosemore, and Milne. Chell and Milne generalized the approach to account for thermal and residual stress and for crack growth problems, respectively. The failure assessment curve is obtained by using the Dugdale solution to interpolate between brittle fracture governed by K_{Ic} and plastic collapse governed by the limit load P_o. This leads to a single failure curve in the R-6 approach. However, it should be noted that the Dugdale solution is intended for a finite crack in a thin infinite sheet subjected to remote tension and also assumes that the material is elastic-perfectly plastic.

Failure assessment diagrams can be determined directly using the estimation method and the *J*-controlled crack growth approach. The essential elements for constructing the diagrams are the elastic crack solutions (available in several elastic crack handbooks) and the fully plastic crack solutions for the specific crack configurations. It will be shown that the failure assessment equation can be obtained by rearranging the crack growth equilibrium equation associated with the J_R-curve approach. The more precise derivations show that the shape and position of the failure assessment curve depend on crack configuration, the relative size of the crack, type of loading, and material deformation properties. Explicit equations for failure curves are derived for elastic-strain hardening material and for elastic-strain hardening material with saturation stress.

Failure curves are constructed for several fracture test specimens and for axially and circumferentially flawed cylinders. The curves are generated for a practical range of deformation properties and crack length-to-width ratios. The usage of these curves is il-

[1]Visiting associate professor of engineering, Division of Engineering, Brown University, Providence, R.I. 02912.

[2]Mechanical engineers, Corporate Research and Development, General Electric Co., Schenectady, N.Y. 12301.

lustrated with several problems. Load-deformation and crack growth behavior of flawed structures can be determined (albeit indirectly!) from the failure curves for the specific structures being evaluated.

KEY WORDS: elastic-plastic fracture, failure assessment diagram, crack growth, J-integral, thermal stress, residual stress, J_R-curve

The failure assessment diagram procedure for assessing the integrity of flawed structures evolved from the "two criteria" approach due to Dowling and Townley [*1*].[3] The present form of the diagram, also referred to as the R-6 diagram, is due to Harrison, Loosemore, and Milne [*2*]. Chell [*3*] and Milne [*4*] generalized the approach to account for thermal and residual stress and for crack growth problems, respectively. The failure assessment curve is obtained by using the Dugdale solution to interpolate between brittle fracture governed by K_{Ic} and plastic collapse governed by the limit load P_o. This leads to a single failure curve in the R-6 approach. However, it should be noted that the Dugdale solution in intended for a finite crack in an infinite sheet subjected to remote tension. The solution also assumes that the material is elastic-perfectly plastic and that the plane-stress condition is applicable. The general validity of the R-6 diagram is discussed in this paper.

Crack growth stability based on *J*-controlled crack growth has been treated by Paris et al [*5*] and Hutchinson and Paris [*6*]. Along these lines Bloom [*7*] and Shih, German, and Kumar [*8*] determined the failure assessment curve for a number of crack configurations. The studies reported in Ref *8* revealed that there is no unique failure line, but that the shape and position of the failure line depends on the geometry of the cracked body, the type of loading, and material deformation properties. In this paper the failure assessment curves are derived from the crack growth equilibrium equation (under *J*-controlled growth conditions) for two material models. Several applications with these curves are also discussed.

Derivation of Failure Curves for J-Controlled Crack Growth

Failure curves can be constructed from elastic-plastic solutions for the particular crack configuration and taking into account the strain hardening property of the material. An essential component for the analyses is the so-called fully plastic solutions; a catalog of fully plastic solutions for a number of crack configurations is available in Ref *9*. The methodology for constructing elastic-plastic solutions from basic solutions is discussed in Refs *8–12*. The methodology exploits the functional forms of the fully plastic solutions and the linear elastic solutions to construct simple formulas for the J-integral, crack opening displacement δ, and remote displacement (due to crack) Δ_c which are accurate for the complete range of elastic-plastic deformation.

[3]The italic numbers in brackets refer to the list of references appended to this paper.

The crack driving force J, which depends on the applied load P and crack length a, is the sum of the elastic (based on an adjusted crack length) and fully plastic contribution. From the estimation method [*8–12*]

$$J = J^e(a_e, P) + J^p(a, n, P) = \hat{J}(a_e)[P/P_o]^2 + \hat{J}(a, n)[P/P_o]^{n+1} \quad (1)$$

where

a_e = adjusted crack length,
n = material hardening exponent, and
P_o = reference load or limit load based on the yield stress σ_o for the particular crack configuration under consideration.

Under J-controlled crack growth conditions, equilibrium of crack growth requires the crack driving force to equal the resisting force, i.e.,

$$J(a, P) = J_R(\Delta a) \quad (2)$$

where J_R is the material resistance which depends only on the amount of crack extension Δa. Using the estimation scheme (that is, Eq. 1) the equality may be rewritten as

$$\hat{J}(a_e)[P/P_o]^2 + \hat{J}(a, n)[P/P_o]^{n+1} = J_R(\Delta a) \quad (3)$$

The latter equation can be rearranged to the desired form

$$\frac{J^e(a, P)}{\hat{J}(a_e)[P/P_o]^2 + \hat{J}(a, n)[P/P_o]^{n+1}} = \frac{J^e(a, P)}{J_R(\Delta a)} \quad (4)$$

where J^e is the elastic crack driving force and has the form

$$J^e(a, P) = \hat{J}(a)[P/P_o]^2 \quad (5)$$

By definition J^e is related to the elastic stress-intensity factor K by

$$J^e = K^2/E' \quad (6)$$

where $E' = E$ for plane-stress problems and $E' = E/(1 - \nu^2)$ for plane-strain problems.[4] By virtue of Eq 6, $\hat{J}(a)$ can be determined directly from available solutions for K. A consequence of J-controlled growth is [*6,8*]

$$E' J_R(\Delta a) = K_R^2(\Delta a) \quad (7)$$

[4] E is Young's modulus and ν is Poisson's ratio.

where the material K_R-curve is obtained under small-scale yielding conditions. The equality (or identity) holds at the same amount of physical crack growth and is valid for either limiting plane-strain or plane-stress states, as long as J-controlled growth conditions are met.

Now introduce the stress ratio S_r defined by the ratio of the applied load P to the reference load P_o, that is

$$S_r = P/P_o \tag{8}$$

Further introduce ratios of the elastic force to the resisting force defined by

$$K_r = K(a, P)/K_R(\Delta a) \tag{9}$$

$$J_r = J^e(a, P)/J_R(\Delta a) \tag{10}$$

It follows from Eqs 6 and 7 that

$$K_r^2(a, P, \Delta a) = J_r(a, P, \Delta a) \tag{11}$$

Substituting Eqs 8 through 11 into Eq 4 gives

$$\frac{S_r^2}{H_e S_r^2 + H_n S_r^{n+1}} = J_r = K_r^2 \tag{12}$$

where

$$H_e = \hat{J}(a_e)/\hat{J}(a) \tag{13}$$

and

$$H_n = \hat{J}(a, n)/\hat{J}(a) \tag{14}$$

Equation 12 describes a curve in the space of K_r and S_r where the crack driving force (under dead-load condition or load-controlled situation) is in equilibrium with the material resistance. It is clear that the shape and location of the equilibrium curve depends on the crack configuration and material properties, including the hardening exponent, since H_e and H_n depend on these quantities.

The curve described by Eq 12 defines the equilibrium crack growth states in terms of the applied load P and the crack length a for a given amount of crack extension. For example, if we choose to define crack initiation as failure (that is, setting $\Delta a = 0$ in the preceding considerations), then $K_R = K_{Ic}$ and $J_R = J_{Ic}$, and the elastic driving force, given by Eqs 9 and 10, is normalized by the respective crack initiation resistance values. In this case Eq 12 defines the equilibrium states for crack initiation in terms of P and a. By considering several values of Δa, Eq 12 specifies the family of equilibrium states for a given crack configuration undergoing crack extension.

In the place of the elastic-plastic driving force (Eq 1), the Dugdale solution for J, namely

$$J(a, \sigma^{\infty}) = \frac{8}{\pi} \sigma_0 \epsilon_0 a \ell n \left[\sec\left(\frac{\pi}{2} \frac{\sigma^{\infty}}{\sigma_0} \right) \right] \tag{15}$$

may be used as the crack driving force in Eq 2. For this model the equilibrium curve (Eq 12) reduces to the failure line of Harrison, Loosemore, and Milne [2] for crack initiation and Milne [4] for crack growth, namely

$$\frac{S_r^2}{\frac{8}{\pi^2} \ell n \left[\sec\left(\frac{\pi}{2} S_r \right) \right]} = J_r = K_r^2 \tag{16}$$

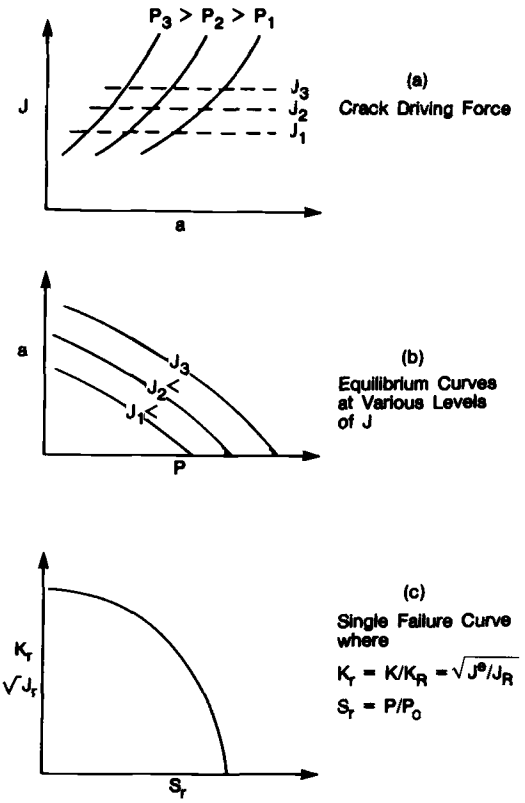

FIG. 1—*Construction of failure assessment diagram from J-integral crack driving force. Generalized coordinates* K_r *and* S_r *collapse crack growth curves into single failure curve.*

In Refs *1-4*, the Dugdale solution is assumed to be the appropriate crack driving force for all crack configurations and for strain-hardening materials as well. This gives rise to a single failure line in the space of K_r and S_r, as described by Eq 16. The more appropriate failure curves described by Eq 12 do not lead to a unique failure line. However, the failure curves for some configurations and for certain range of crack length-to-width ratio based on Eq 12 may be quite similar.

A failure curve may also be derived from an R-curve analysis based on δ, measured at the original crack tip. For this case, H_e and H_n will be given in terms of the appropriate dimensionless quantities $\hat{\delta}(a)$ and $\hat{\delta}(a, n)$.

Equation 12 is a restatement of the equilibrium condition for crack growth (Eq 2) in terms of the stress ratio S_r and elastic force K_r or J_r. A graphical interpretation of the developments thus far is appropriate. For a given crack configuration, Fig. 1*a* shows J as a function of crack length a with applied load P held fixed. Let J_1 denote the value of J at crack initiation. It is possible to identify the values (a_1, P_1), (a_2, P_2) and (a_3, P_3) that will cause the crack to initiate as indicated in Fig. 1*a*. This information can be replotted in another diagram with a and P as the coordinates. Now the points (a_1, P_1), (a_2, P_2), (a_3, P_3) can be connected to form a curve in the space of a and P. The value of J associated with this curve is J_1; that is, the curve is a contour for $J = J_1$. Since J_1 is also the value of J at crack initiation, the following interpretation may be made. Any combination of crack length and applied load which falls on the curve will cause crack initiation in the crack configuration under consideration. The process may be repeated for larger values of J, for example, J_2, J_3 etc. to correspond to different amounts of crack growth. The family of equilibrium curves tagged as J_1, J_2, J_3, etc. (corresponding to different amounts of crack growth) are shown in Fig. 1*b*. By appropriately normalizing the ordinate and abscissa of the diagram through the parameters K_r and S_r, the family of curves in Fig. 1*b* collapses into a single crack growth curve as indicated in Fig. 1*c*. In other words, certain information obtainable from the J_R-curve analyses could be compressed into a single curve via the generalized coordinates K_r and S_r. The latter curve is unique only to the particular crack configuration and material deformation property employed.

Failure Curve for Strain-Hardening Material with Saturation Stress

The failure diagram can be generalized to include materials which strain-harden and eventually reach a saturation stress σ_s. Consider a uniaxial stress-strain law of the form

$$\epsilon/\epsilon_0 = \sigma/\sigma_0 + \alpha(\sigma/\sigma_0)^n + \beta(\sigma/\sigma_s)^m \tag{17}$$

where α and β are material constants and $m/n \gg 1$. There are primarily three regimes of deformation. For applied stress σ less than σ_0, the strain is

essentially elastic. In the range between σ_0 and σ_s, the primary contribution to the strain comes from the strain-hardening term, that is, the second term on the right-hand side of Eq 17. For σ greater than σ_s, the strain is dominated by the last term in Eq 17; in fact, the material behaves like a perfectly plastic material in the latter regime. This material behavior is depicted in Fig. 2. Thus Eq 17 describes an elastic strain-hardening material with a saturation stress. Let μ be defined by

$$\mu = \frac{\sigma_s}{\sigma_0} \tag{18}$$

and let the limit load and stress ratio be defined in terms of σ_s, that is

$$P_s = \Lambda \, c \, \sigma_s \tag{19}$$

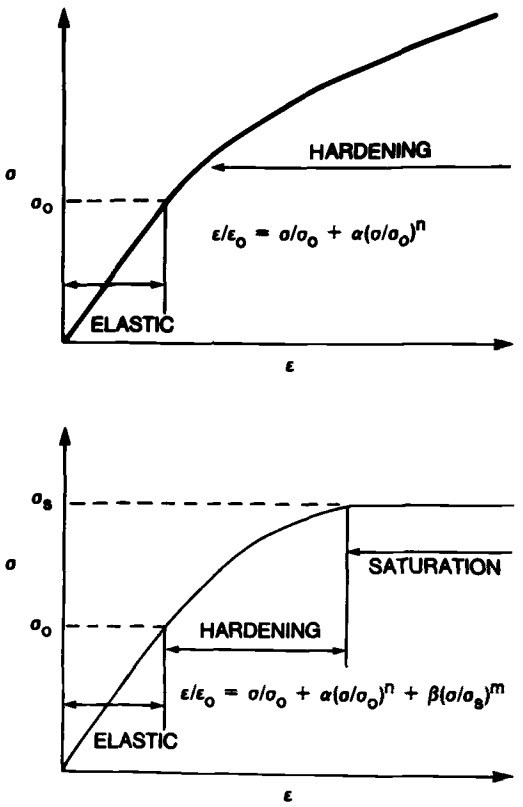

FIG. 2—*Elastic-strain-hardening material and elastic-strain hardening with saturation stress material.*

$$S_r = \frac{P}{P_s} \tag{20}$$

where Λ is the constraint factor and c the uncracked ligament. Using the estimation method, the failure line for a material obeying Eq 17 is [*8*]

$$\frac{S_r^2}{H_e(\mu S_r)^2 + H_n(\mu S_r)^{n+1} + H_m S_r^{m+1}} = J_r = K_r^2 \tag{21}$$

where

$$H_m = \hat{J}(a, m)/\hat{J}(a) \tag{22}$$

and H_e and H_n are as given by Eqs 13 and 14, respectively.

There is some support for the saturation stress model. The true-stress/true-strain data for 304 stainless steel [*13*] when corrected for necking using Bridgman correction indeed suggests a saturation stress. Norris [*14*] reanalyzed the foregoing data using a more accurate iterative method discussed in Ref *15*. The resulting curve, which supports a saturation stress concept, is shown in Fig. 3.

Failure Curves for Several Crack Configurations

Strain-Hardening Model

The basic input to the construction of the failure assessment diagram is the linear elastic and the fully plastic crack solutions for the relevant crack configuration. The fully plastic solutions are given in Refs *9–12* while a good source of elastic solutions is Ref *16*.

The failure line for a strain-hardening material of the Ramberg-Osgood type is given by Eq 12. As discussed previously, the shape and position of the failure line in the space of K_r and S_r are dependent upon crack configuration and deformation properties. To illustrate the point, we examine the failure line for the plane-stress and plane-strain center-cracked panel (CCP). The plane-stress failure curve for several hardening exponents is shown in Fig. 4*a*. The failure curve for the elastic-perfectly plastic material ($n = \infty$) and the Dugdale or R-6 curve are also indicated. The curves intersect the ordinate at unity and approach the abscissa asymptotically for hardening materials. In the case of the elastic-perfectly plastic material and the R-6 curve, they intersect the abscissa at unity. It is apparent that the failure curves are dependent on deformation properties. The corresponding plane-strain curves are shown in Fig. 4*b*. While the plane-stress and plane-strain curves are rather similar, the curves are strongly dependent on the hardening exponent. In many engineering applications, the limit load (or reference

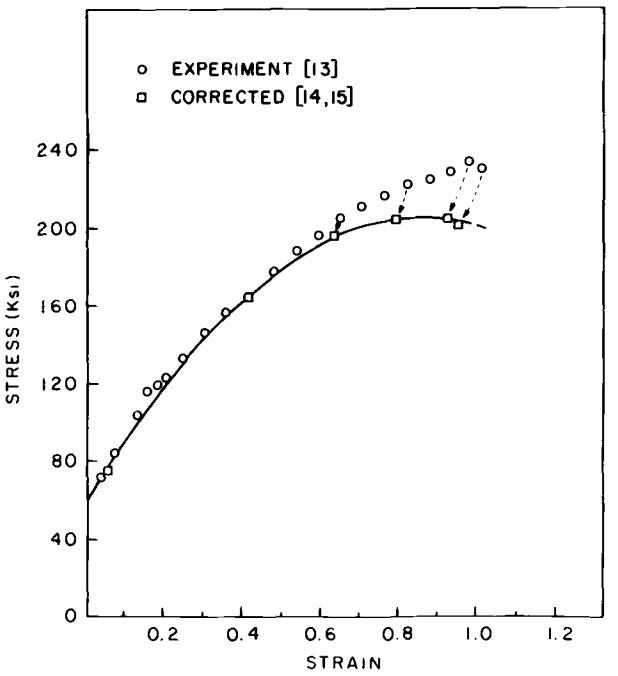

FIG. 3—*Stress-strain curve for Type 304 stainless steel (taken from Ref* 14*).*

load) is computed on the basis of the flow stress σ_f. Thus if S_r is defined from the latter limit load, then the equilibrium curves for the strain-hardening materials will shift toward the R-6 and the elastic perfectly plastic curves. Consequently the failure curves would appear to be less strongly dependent on n.

The dependence of the failure curves on the crack length-to-width (a/b) ratios is shown in Fig. 4*c*. The curves are only slightly dependent on relative crack lengths. This suggests that in the analyses of small amounts of crack growth where the failure assessment diagram is employed, a failure curve based on the original crack length should yield information within acceptable engineering accuracy.

Failure curves for the compact specimen are shown in Fig. 5. In general the observations concerning the CCP are also applicable here. However, the plane-strain and plane-stress curves are more dissimilar. This is in part due to the rather different limit load and slipline field associated with the plane-strain and plane-stress configuration under bending. The greater degree of similarity between plane-strain and plane-stress failure curves for the CCP can be attributed to the similarity in the respective limit load and slipline field. A direct illustration of this point is given in Fig. 6.

Failure curves are also generated for the single-edge-cracked panel (SECP)

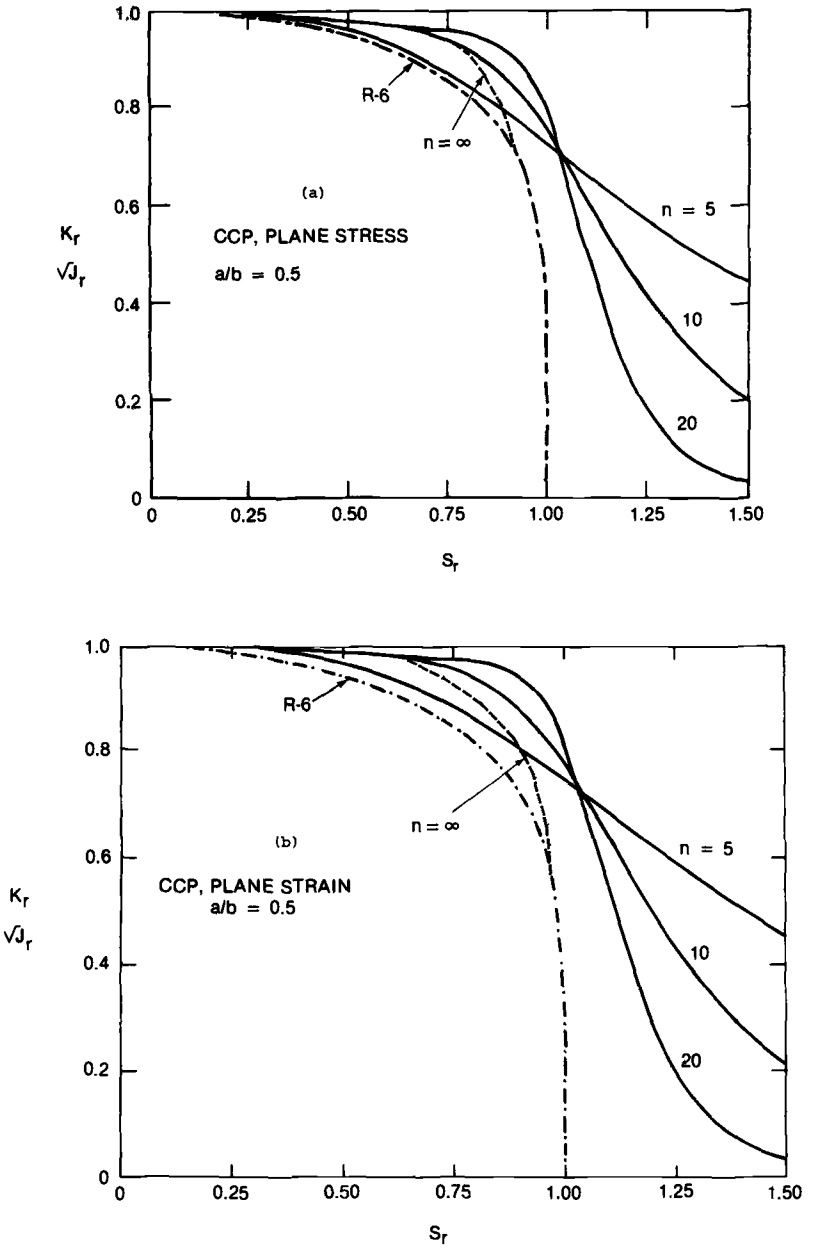

FIG. 4—*Plane-stress and plane-strain failure curves for center-cracked panel for several strain-hardening exponents and crack length-to-width ratios.*

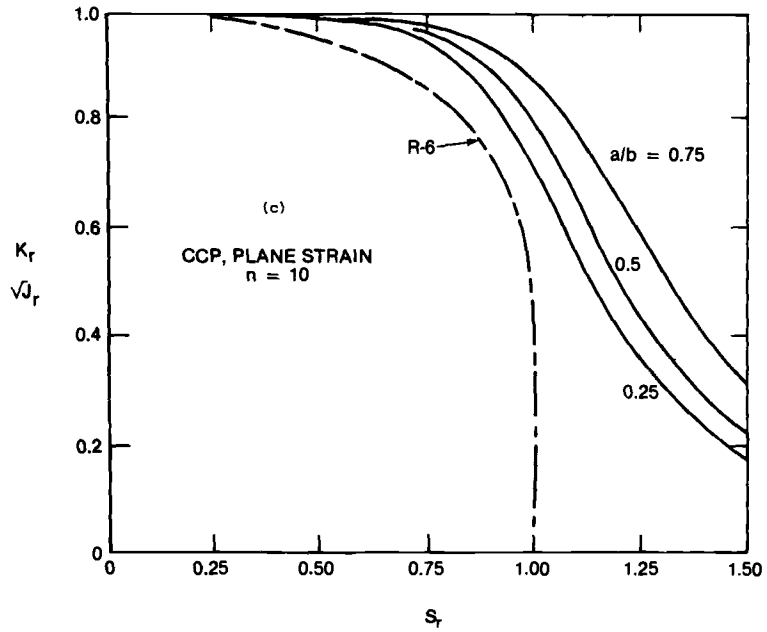

FIG. 4—*Continued.*

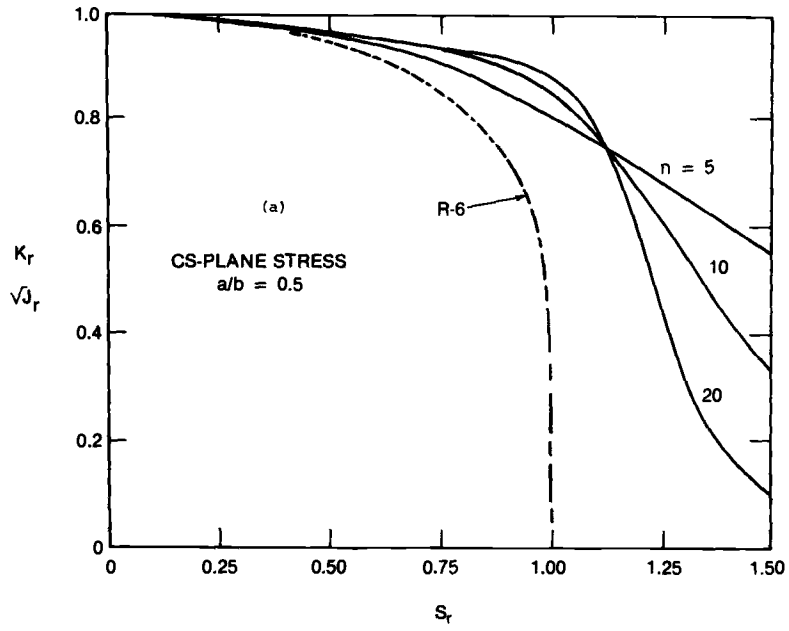

FIG. 5—*Plane-stress and plane-strain failure curves for compact specimen for several strain-hardening exponents and crack length-to-width ratios.*

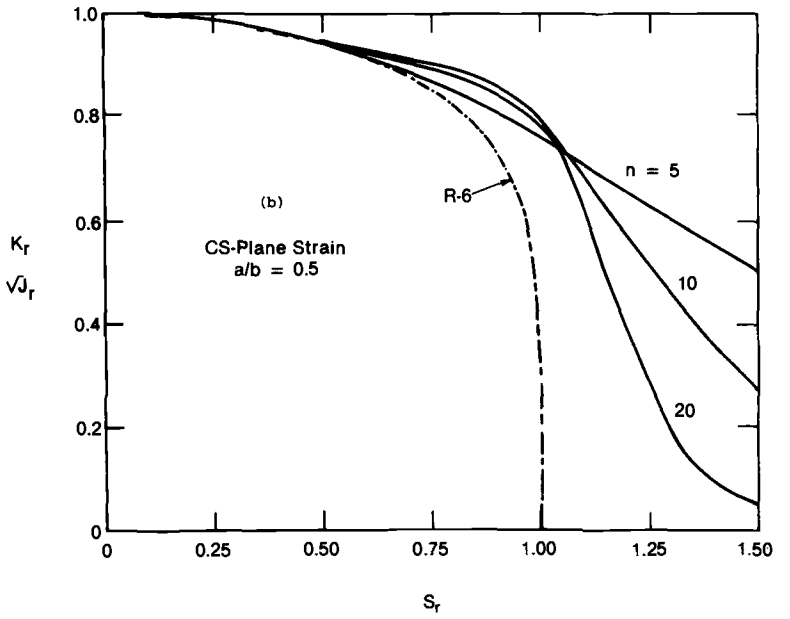

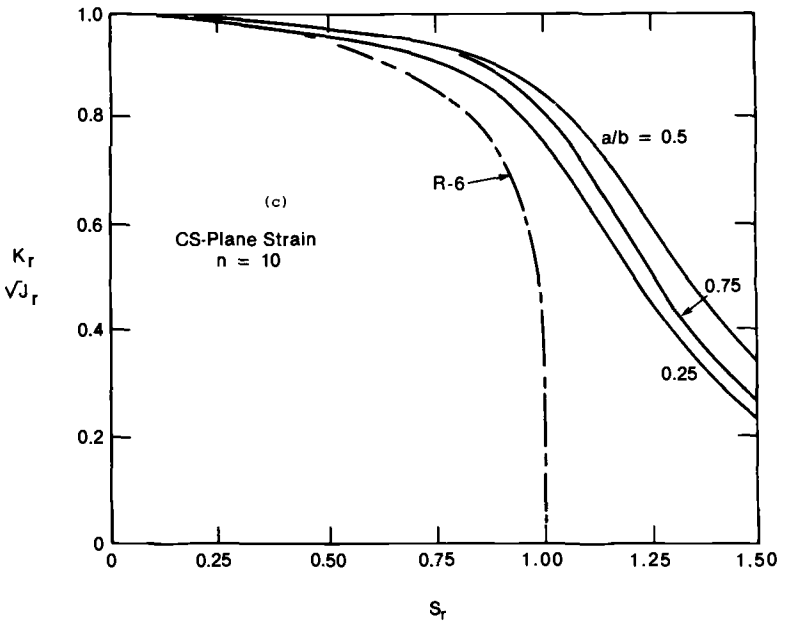

FIG. 5—*Continued.*

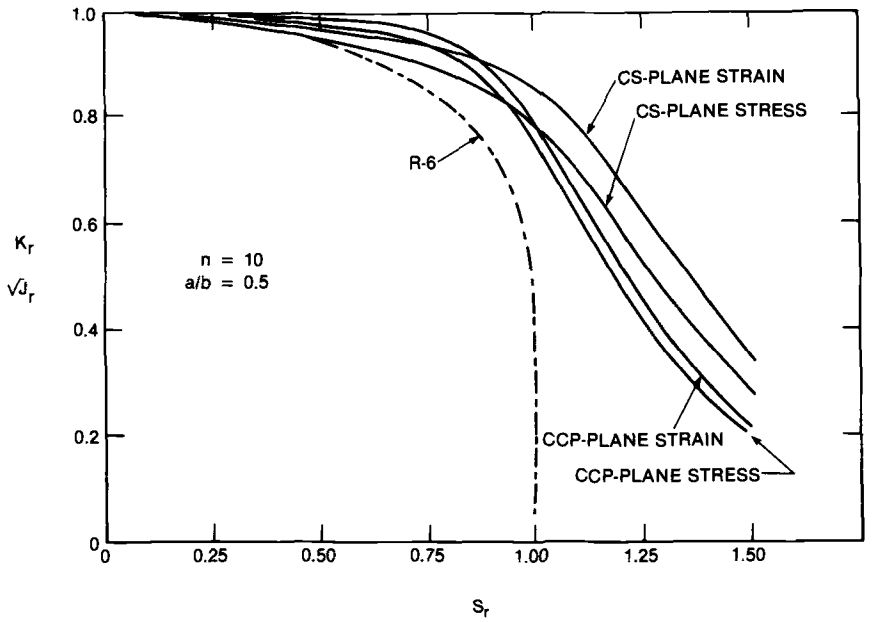

FIG. 6—*Comparison of plane-strain and plane-stress failure curves for center-cracked panel and compact specimen.*

subjected to remote tension. The curves for three a/b ratios and n of 10, which is typical of A533B steels, are shown in Fig. 7*a*. Similar curves are plotted in Fig. 7*b* for an $n = 5$ material which is representative of 304 stainless steel. The R-6 curve is also included in the figure.

Failure assessment diagrams are readily generated for flawed pipes. The fully plastic solutions, or the h functions for these configurations, are available in Ref *9*. From these fully plastic solutions, the crack growth equilibrium curves or the failure curves are determined according to Eq 12 or Eq 21. The failure curves for axially and circumferentially cracked cylinders are shown in Fig. 8 for A533B steel and 304 stainless steel. The crack length-to-width ratio of 1/4 was chosen to match the deepest relative crack depth for the maximum postulated flaw size in the ASME Pressure Vessel and Pipe Code. Also included in the figure is the R-6 curve.

Saturation Stress Model

For the very ductile materials where fracture or plastic collapse develops at large plastic strains, the failure curve described by Eq 21 may be the more appropriate to employ for purposes of analyses. The failure curve will intersect the abscissa at unity; in other words, fracture instability or plastic col-

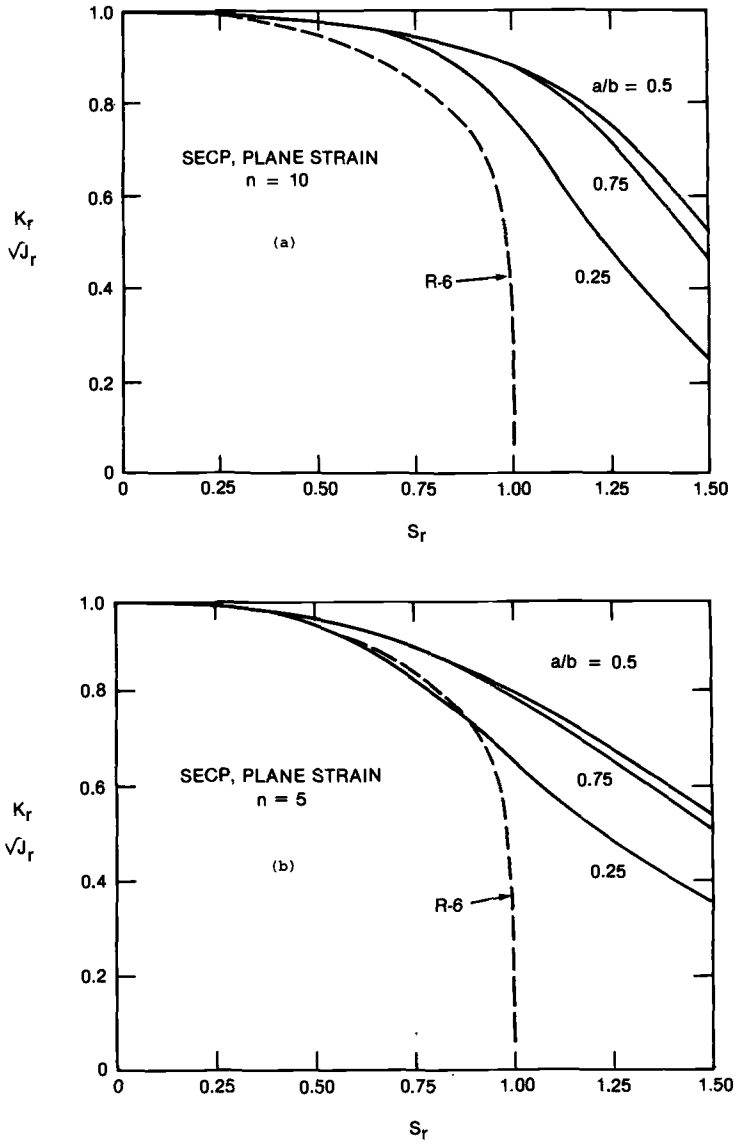

FIG. 7—*Plane-strain failure curves for single-edge-cracked panel for* n = *10 and* n = *5 materials.*

lapse will occur when the limit load for the flawed structure is attained. This assumes of course that the structure is subjected to load-controlled loading. The failure curves for the hardening material with saturation stress contain the strain hardening and the R-6 curves described in the preceding para-

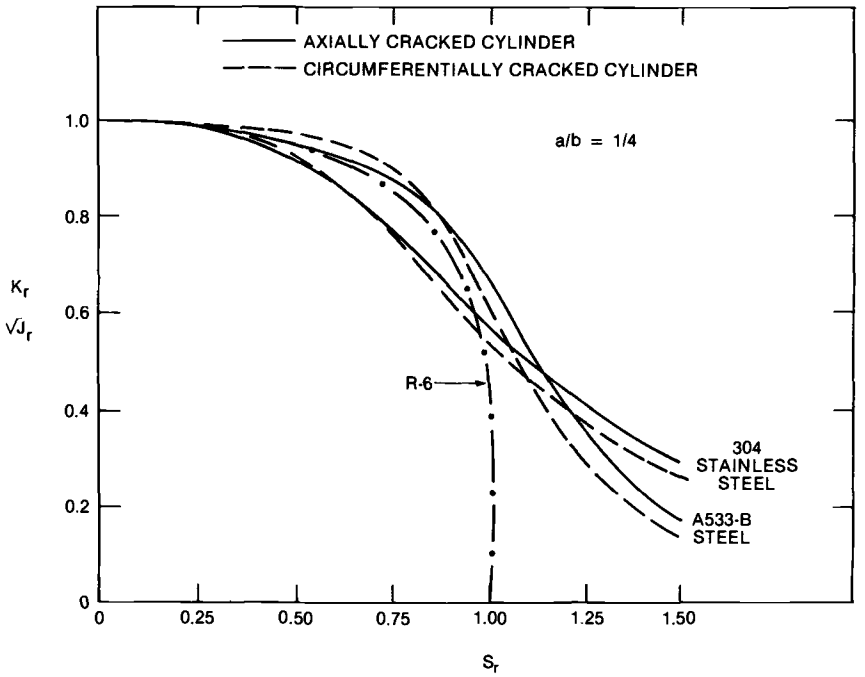

FIG. 8—*Failure curves for axially and circumferentially cracked cylinders.*

graphs as special cases. Failure curves are constructed for the compact specimen configuration for a material with a saturation stress which is 33 percent higher than the yield stress (typical of A533B steels). The diagrams for two crack length-to-width ratios are shown in Fig. 9. In the first case, the curve is quite similar to the R-6 curve. In the other, the differences are significant.

Similar curves using the saturation stress model are shown in Fig. 10 for the circumferentially cracked cylinder. The curves appropriate to A533B steel fall below the R-6 curve. These curves are at odds with suggestions that the R-6 curve may constitute a lower-bound failure line for defect tolerance analyses of structures. However, it may be noted that a lower-bound R-6 curve could still be obtained if the value of the flow stress is adjusted for the crack configuration.

Steel piping fabricated from 304 stainless steel is rather ductile. In most situations, crack growth in 304 stainless steel piping will occur only at fully yielded conditions close to the limit load for the configuration. The stress-strain curve for the material also appear to saturate at large strains [*14*]. Thus the failure diagram using the saturation stress model (Eq 21) could be employed for the analyses of flawed stainless steel piping [*17*].

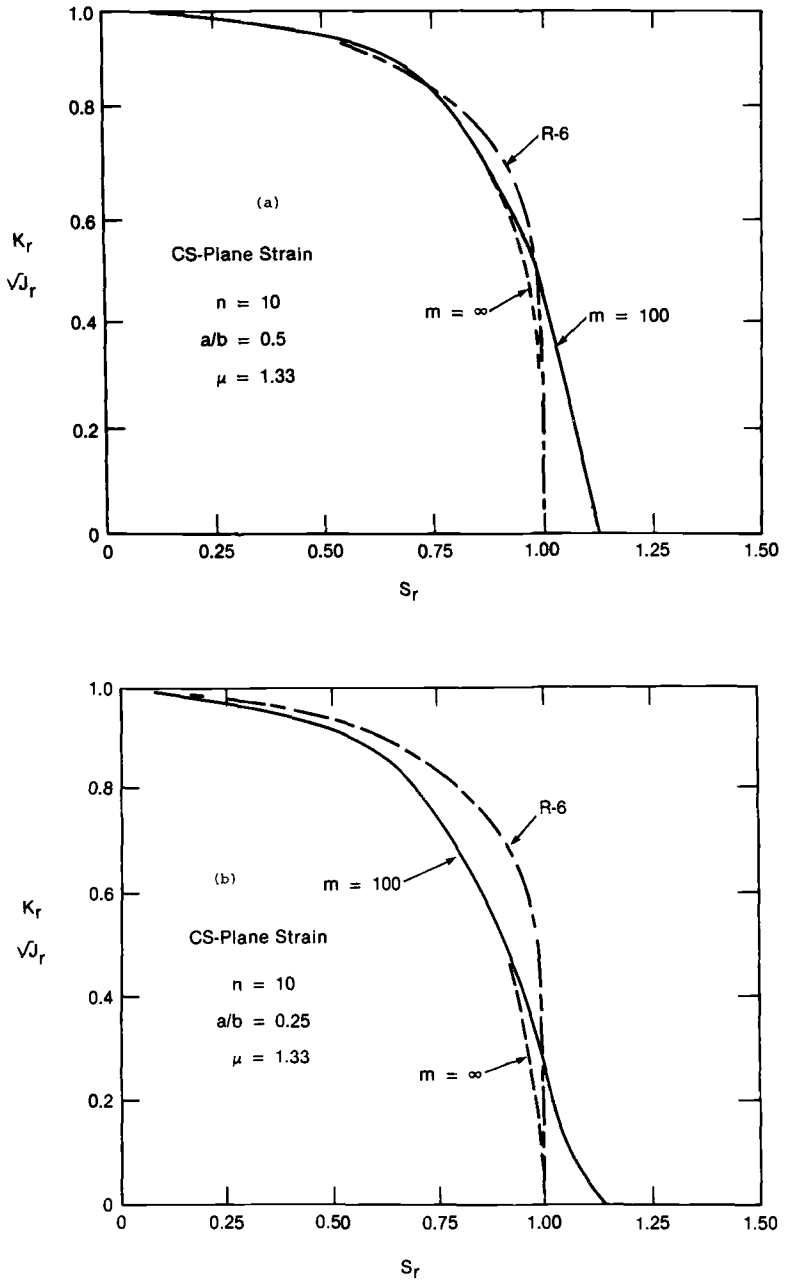

FIG. 9—*Plane-strain failure curves for strain-hardening material with saturation stress. Compact specimen* a/b *equals 0.5 and 0.25.*

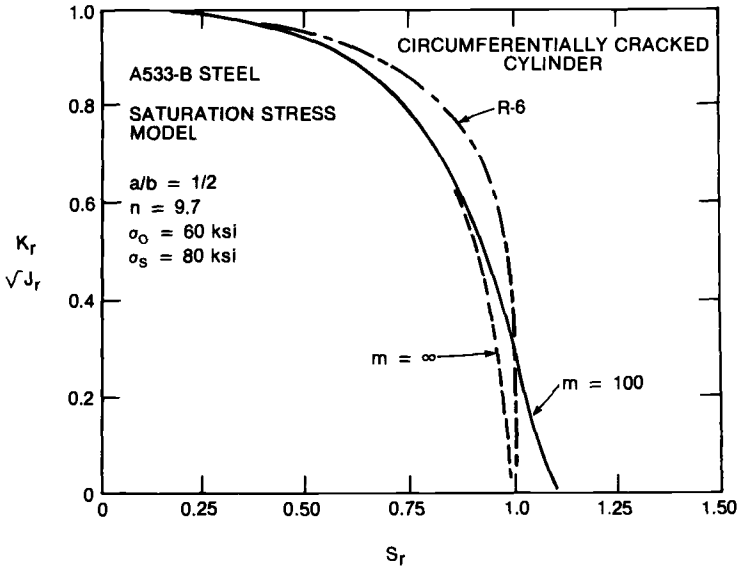

FIG. 10—*Failure curves for circumferentially crack cylinders using saturation stress model.*

Failure Curves for Variable Crack Length

The failure curves in Figs. 4 through 10 are constructed for constant crack length-to-width ratios. As noted in the preceding sections, the variation in the curves due to small variation in crack size is relatively insignificant. Where there are substantial amounts of crack growth, the failure line should be reconstructed to account for the change in crack length. To illustrate this point, we examine the plane-strain compact specimen which is allowed to undergo substantial stable crack growth. In Fig. 11, the dashed lines correspond to failure curves for the plane-strain compact specimen with constant crack length-to-width ratio of 0.25, 0.50, and 0.75. For large amounts of crack growth, the change in the crack length-to-width ratio is significant and therefore the equilibrium curve will shift.

Consider a 4T compact specimen of A533B steel with an initial crack length-to-width ratio a_0/b of 0.5. The mean J_R-curve is given in Fig. 3 of Ref *8* and the experimental data are reported in Ref *19*. For this crack configuration and the specific J_R-curve, the failure curve or the crack growth equilibrium curve is indicated by the solid line in Fig. 11. This curve is obtained by adjusting the value of the quantities H_e and H_n in Eq 12 according to the "updated" crack length determined from the J_R-curve. Similarly, equilibrium curves for different initial crack length can be obtained. A curve for $a_0/b = 0.25$ is also included.

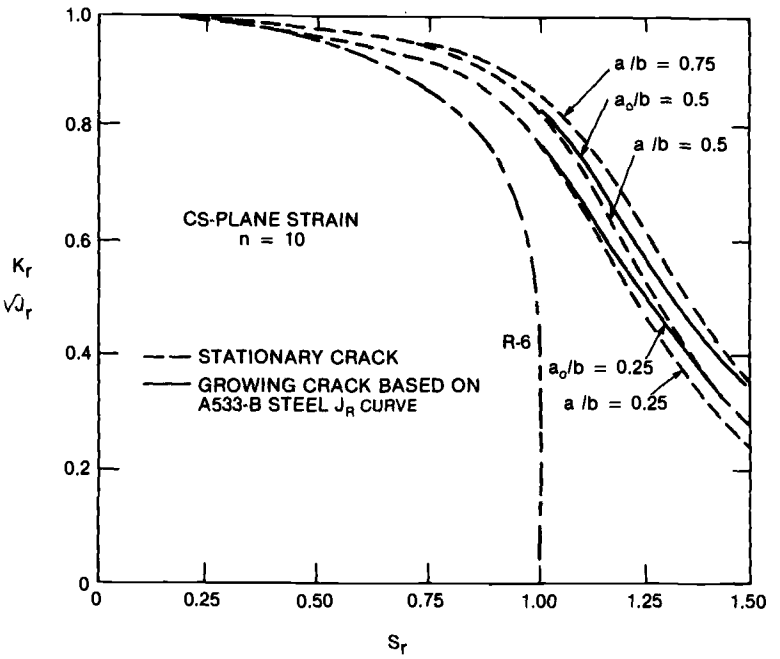

FIG. 11—*Plane-strain failure curves for A533B steels with initial crack length-to-width ratios of 0.25 and 0.5, respectively.*

Applications of Failure Assessment Diagrams

To employ the failure assessment diagram for structural integrity analyses, the following steps should be taken:

1. The failure line for the specific crack configuration should be constructed using Eqs 12 or 21 (whichever is the more appropriate). The h-functions for the given material deformation properties can be obtained from the tabulation in Ref *9*.

2. For the given crack configuration, and initial crack length a_o, K (or J^e) is computed using the tabulation in Ref *16*. This value is normalized by K_{Ic} (or J_{Ic}) to obtain K_r. The stress ratio S_r is obtained by normalizing the applied load P by the limit load (or reference load) for the crack configuration being examined.

3. The point K_r, S_r is now placed on the failure assessment diagram. There are two possible situations. If the point lies inside the region bounded by the axes and the failure curve, the structure is safe. If the point falls on or beyond the failure curve, the crack in the structure will initiate. If failure is defined on the basis of crack "initiation," then the structure is unsafe or has failed. If

the design will allow for crack growth, the load-carrying capacity of the structure can be evaluated further.

4. For the case where the load point falls beyond the safe region, the crack in the structure is incremented by an amount Δa. The reference or limit load for the structure is recomputed using the current crack length $a_0 + \Delta a$. The applied load normalized by the reference load defines the updated stress ratio S_r. Based on the current load and crack length, the updated K (or J^e) is also computed. The value of K_R (or J_R) corresponding to crack growth of a is directly obtained from the resistance curve for the material; K_r is given by the ratio $K(a_0 + \Delta a)$ and $K_R(\Delta a)$.

5. The updated point K_r, S_r is again placed on the diagram and the preceding steps 3 and 4 are repeated.

By the foregoing process, the crack growth behavior and the load-carrying capacity of the structure can be determined. If there is substantial stable crack growth, then the failure curve (or equilibrium curve) itself should be updated to correspond to the updated crack lengths. In general, changes in the failure curve itself are negligible for small amounts of crack growth. The foregoing procedure assumes load-controlled conditions or a dead-load system. The procedure can be modified to accommodate a displacement-controlled system with finite compliance [*4*]. However, the procedure becomes a little more complex for displacement-controlled systems and it may be easier to obtain similar information directly from the R-curve analyses using the crack driving force diagrams discussed in Refs *8* and *9*. A discussion of the determination of stable crack growth and the point of instability in more general terms (that is, for finite compliance systems) is given in Refs *5-8*.

Estimating the Load-Deformation and Crack Growth Behavior from the Failure Assessment Diagram

The crack growth equilibrium relationship Eqs 12 and 21 provide an implicit relationship between the applied load, the initial crack length, and the amount of crack growth for a given crack configuration and material J_R-curve. In other words, if the J_R-curve is known (or measured from a test specimen) the load crack growth behavior of the structure under examination can be determined from Eq 12 or Eq 21 in the following manner. For the given crack configuration, material deformation properties, and initial crack length a_0, the quantities H_e and H_n are computed. At the onset of crack growth the value of J_R is equal to J_{Ic}. Now Eq 12 is a nonlinear equation in S_r which can be solved by say the Newton-Raphson method. The solution gives the value of S_r (or applied load P) at crack initiation. Suppose the crack is extended by an amount Δa. The quantities H_e and H_n are recomputed for the new crack length $a_0 + \Delta a$; the value of J_R is taken from the resistance curve

data for the given amount of crack growth. The nonlinear equation can again be solved for the new value of S_r. By repeating this procedure for additional values of a, the complete load crack growth behavior is determined. Alternatively, the same information can be obtained more directly from the crack driving force diagram by following the J_R-curve. This has been discussed in Refs *8*, *9*, and *12*.

Using the foregoing procedure, the crack growth behavior for a series of 4T A533B steel compact specimens was obtained. All the specimens had side grooves of 12.5 percent with the exception of T51, which had 25 percent side grooves. A comparison of the predicted behavior and the experimental results is given in Fig. 12. The estimated curve generally falls slightly below the actual measurements and this is in accord with earlier studies on crack growth behavior under J-controlled crack growth conditions [*19*].

Similarly the load-versus displacement behavior of the structure cannot be determined directly from the failure assessment diagram. The information discussed in the preceding paragraph (for example, the results presented in Fig. 12) may be employed in the estimation method formula for the displacement, which depends on the applied load and crack length. The consequence of these computations is the load versus displacement behavior for the structure [*8,9*].

The experimental data obtained from compact specimens are plotted on the failure assessment diagram in Fig. 13. Most of the points are closely clustered and the data band is provided instead. The data band does fall between the equilibrium curves determined from Eq 12.

It should again be emphasized that the information concerning the load crack growth behavior and the load deformation behavior is more readily obtained from the crack driving force diagrams. These latter diagrams provide all the information for the analyses of crack growth and the load deformation behavior.

Discussion

In general the shape and position of the failure assessment curve as described by Eqs 12 or 21 depend on crack configuration, crack length-to-width ratio, type of loading, material deformation property, and whether plane-strain or plane-stress conditions are applicable. For certain crack geometries and type of loading, the curves may not depend too strongly on the hardening exponent and crack length-to-width ratios. The J-integral crack driving force employed to arrive at Eqs 12 and 21 is obtained by the estimation scheme discussed in Refs *8–12*. These earlier investigations also demonstrated that the estimation scheme formulas for J and other relevant crack parameters are rather accurate, at least for the crack configurations examined. Results from these earlier investigation support the use of these formulas to determine the failure assessment curve. Indeed the results sum-

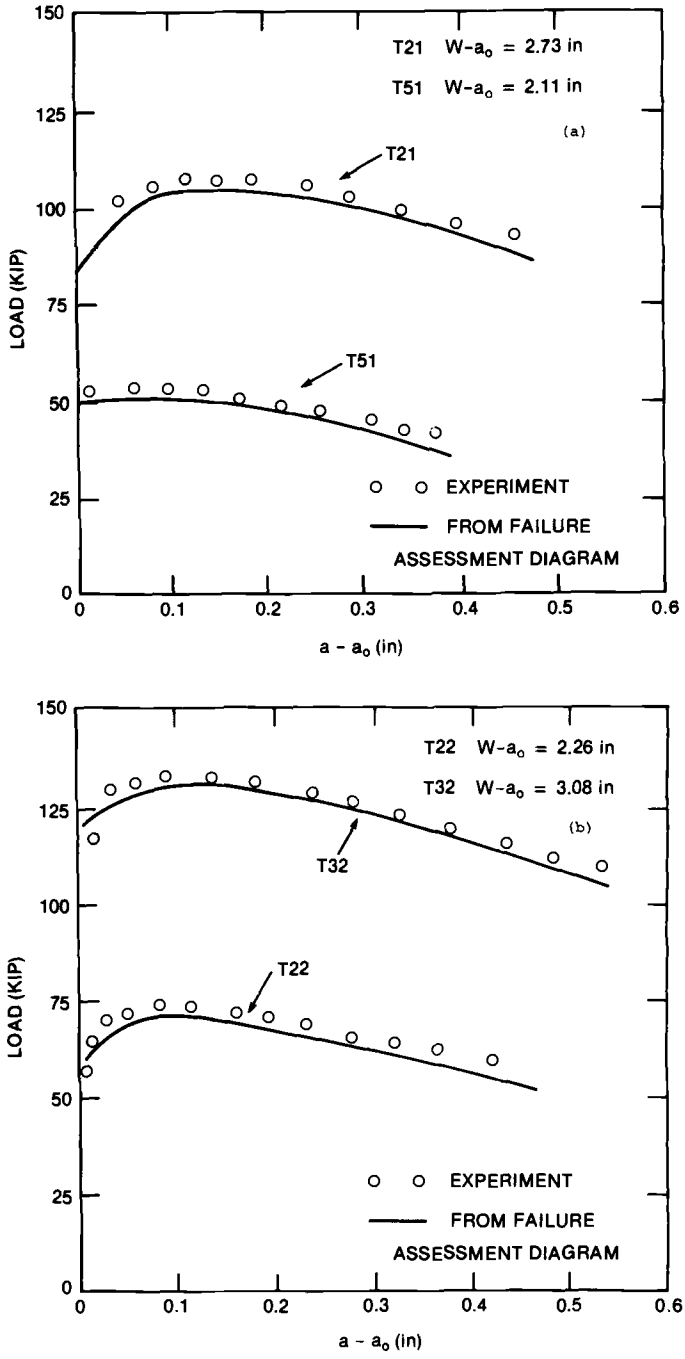

FIG. 12—*Load crack growth behavior for 4T compact specimens T21, T51, T22, and T32.*

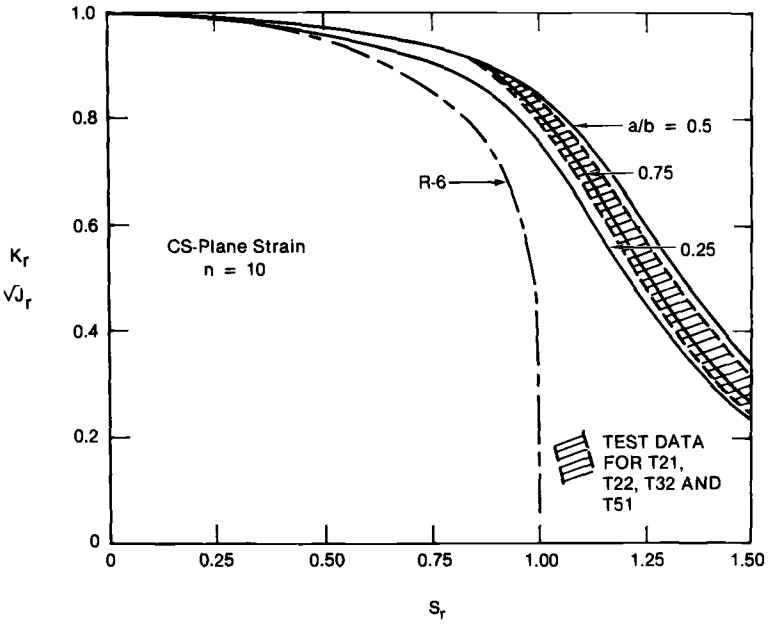

FIG. 13—*Experimental data for compact specimens T21, T22, T32, and T51 are summarized in the failure assessment diagram. The solid lines are the equilibrium curves computed from the estimation method.*

marized in Figs. 12 and 13 validate the determination of failure assessment curves using the estimation scheme.

The R-6 failure assessment line [*1–4*] is obtained by using the Dugdale solution, which is derived for a finite crack in an infinite sheet subject to remote tension. The solution also assumes that the material is elastic-perfectly plastic and that plane-stress conditions prevail [*20*]. Thus it is not expected that the R-6 curve should have general applicability. However, through appropriate adjustments of the material flow stress and limit load, the R-6 curve may be rather useful, especially for crack configurations where the normalized crack driving force does not depend too strongly on the hardening exponent and relative crack size.

It is also apparent that the failure assessment diagram offers a simple procedure for a quick first evaluation of the safety margin of flawed structure subjected to load-controlled boundary conditions. However, the procedure becomes more complex for displacement-controlled systems, and it may be easier to obtain similar information directly from the crack driving force diagram analysis [*8, 9*].

Acknowledgment

This work was supported by the General Electric Research and Development Center, Schenectady, N.Y. In the final preparation of the manuscript C. F. Shih was supported by the Materials Research Laboratory at Brown University through Contract No. DMR79-23257. The helpful comments of Dr. D. M. Norris of the Electric Power Research Institute are gratefully acknowledged.

References

[1] Dowling, A. R. and Townley, C. H. A., *International Journal of Pressure Vessels and Piping*, Vol. 3, 1975, pp. 77-137.

[2] Harrison, R. P., Loosemore, K., and Milne, I., "Assessment of the Integrity of Structures Containing Defects," CEGB Report No. R/H/R6, Central Electricity Generating Board, U.K., 1976.

[3] Chell, G. G. in *Elastic-Plastic Fracture, ASTM STP 668*, J. D. Landes, J. A. Begley, and G. A. Clarke, Eds., American Society for Testing and Materials, 1979, pp. 581-605.

[4] Milne, I., *Materials Science and Engineering*, Vol. 39, No. 1, 1979, pp. 65-79.

[5] Paris, P. C., Tada, H., Zahoor, A., and Ernst, H. in *Elastic-Plastic Fracture, ASTM STP 668*, J. D. Landes, J. A. Begley, and G. A. Clarke, Eds., American Society for Testing and Materials, 1979, pp. 5-36.

[6] Hutchinson, J. W. and Paris, P. C. in *Elastic-Plastic Fracture, ASTM STP 668*, J. D. Landes, J. A. Begley, and G. A. Clarke, Eds.. American Society for Testing and Materials, 1979, pp. 37-64.

[7] Bloom, J. M., this publication, pp. II-206-II-238.

[8] Shih, C. F., German, M. D., and Kumar, V., *International Journal of Pressure Vessels and Piping*, Vol. 9, 1981, pp. 159-196.

[9] Kumar, V., German, M. D. and Shih, C. F., "An Engineering Approach for Elastic-Plastic Fracture Analysis," EPRI Topical Report NP-1931, Electric Power Research Institute, Palo Alto, Calif., July 1981.

[10] Shih, C. F. in *Mechanics of Crack Growth, ASTM STP 590*, American Society for Testing and Materials, 1976, pp. 3-22.

[11] Shih, C. F. and Hutchinson, J. W., *Transactions*, American Society of Mechanical Engineers, *Journal of Engineering Materials and Technology*, Vol. 98, 1976, pp. 289-295.

[12] Kumar, V. and Shih, C. F. in *Fracture Mechanics, ASTM STP 700*, American Society for Testing and Materials, 1980, pp. 406-438.

[13] Hartley, C. S., Jenkins, D. A., and Lee, J. J., *Transactions*, 5th International Conference on Structural Mechanics in Reactor Technology, Vol. C, Paper C3/13, North Holland Publishing Co., Amsterdam, 1979.

[14] Norris, D. M., private communication, 1979.

[15] Norris, D. M., Jr., Moran, B., Scudder, J. K., and Quinones, D. F., *Journal of the Mechanics and Physics of Solids*, Vol. 26, 1978, pp. 1-19.

[16] Tada, H., Paris, P. C., and Irwin, G. R., *The Stress Analysis of Cracks Handbook*, Del Research Corp., Hellertown, Pa., 1973.

[17] Shih, C. F., German, M. D., Andrews, W. R., deLorenzi, H. G., Hussain, M., and Mowbray, D. F., "Crack Opening and Stability Analyses for Flawed Stainless Steel Piping," 1st Semiannual Report to Electric Power Research Institute, Contract No. T118-8, General Electric Co., Schenectady, N.Y., 1980.

[18] Kumar, V., German, M. D., and Shih, C. F., this publication, pp. II-239-II-261.

[19] Shih, C. F., deLorenzi, H. G. and Andrews, W. R. in *Electric-Plastic Fracture, ASTM STP 668*, J. D. Landes, J. A. Begley, and G. A. Clarke, Eds., American Society for Testing and Materials, 1979, pp. 65-120.

[20] Dugdale, D. S., *Journal of the Mechanics and Physics of Solids*, Vol. 8, 1960, pp. 100-104.

H. Okamura,[1] *K. Kageyama,*[2] *and Y. Takahata*[3]

Lower-Bound Solutions and Their Application to the Collapse Load of a Cracked Member Under Axial Force and Bending Moment

REFERENCE: Okamura, H., Kageyama, K., and Takahata, Y., **"Lower-Bound Solutions and Their Application to the Collapse Load of a Cracked Member Under Axial Force and Bending Moment,"** *Elastic-Plastic Fracture: Second Symposium, Volume II—Fracture Resistance Curves and Engineering Applications, ASTM STP 803*, C. F. Shih and J. P. Gudas, Eds., American Society for Testing and Materials, 1983, pp. II-262–II-277.

ABSTRACT: The lower bound of collapse load of an edge-cracked member subjected to axial force and bending moment is remarkably improved by introducing the statically admissible stress field in plane-strain and plane-stress conditions. A procedure for the calculation of collapse load of a member with a surface flaw is also proposed. In addition, a method of evaluation of the J-integral for compact specimen is derived by using the aforementioned lower-bound solution. Finally, the applicability of the failure assessment diagram through the collapse load and fracture toughness is confirmed experimentally and numerically under the combined loading of bending and tension, as long as the J_{Ic} criterion is valid.

KEY WORDS: fracture (materials), cracks, plasticity, plastic deformation, collapse load, surface flaw, compact specimen, J-integral, elastic-plastic fracture, fracture mechanics, failure assessment diagram, limit analysis

In some structural design codes such as the American Society of Mechanical Engineers (ASME) Pressure Vessel Code Section III, the design of structural components is usually and essentially based on the collapse load in uncracked state of the members, and partly referred to the strength for brittle

[1]Professor, Department of Mechanical Engineering, Faculty of Engineering, University of Tokyo, 7-3-1 Hongo, Bunkyo-ku, Tokyo, 113 Japan.
[2]Material Properties Division, Mechanical Engineering Laboratory, Agency of Industrial Science and Technology, MITI, Ibaraki, Japan.
[3]Yanmar Diesel Engine Co. Ltd., Osaka, Japan.

fracture in its cracked state. The criterion for brittle fracture has been well established, and we can predict the fracture strength of a cracked member with heavy section by the fracture toughness, K_{Ic}, in the small-scale yielding condition. In the design of most structural components, however, it might be important to evaluate the strength of a cracked member in the elastic-plastic regime. A reasonable and convenient failure criterion for the cracked member in the fully plastic regime will be given by the collapse load. And the strength of the cracked member in the elastic-plastic regime might be estimated, it is hoped, by the two-criteria approach [*1*][4] using K_{Ic} and the collapse load.

The lower bound of collapse load is more important in the structural design and safety assessment than the upper bound from the stand-point of conservative estimation. But a well-known lower-bound solution of an edge-cracked member is not so useful because it underestimates the collapse load in comparison with the experimental results. In the present paper, the improved lower-bound solutions of the collapse load of an edge-cracked member under axial force and the bending moment are obtained in conditions of both plane strain and plane stress. The collapse limit diagram for structural design is obtained and compared with the ASME Pressure Vessel Code.

In addition, a three-dimensional analysis of collapse load is carried out and a lower bound of collapse load of the member with surface flaw subjected to the axial force and bending moment is obtained.

Consideration of the collapse load of a cracked member is important not only in structural design based on limit analysis but also in elastic-plastic fracture mechanics. Merkle and Corten [*2*] proposed an estimation procedure of the J-integral for the compact-tension specimen by using a well-known lower-bound solution in order to consider the axial force as well as the bending effect. The lower-bound solution is remarkably improved in the present paper and the result is applied to the estimation of the J-integral of the compact specimen.

As a fracture criterion from small-scale yielding to the fully plastic regime, the failure assessment diagram (FAD) was proposed by Harrison et al [*3*], based on the two-criteria approach using K_{Ic} and the collapse load. In the present paper, the FAD is applied to the combined loading of bending and tension, and the effect of the combined loading is studied by using an eccentric tension specimen of A533B Class 1 steel and the finite-element method.

Improved Lower-Bound Solutions in Plane Strain

Lianis and Ford [*4*] introduced the statically admissible stress field as shown in Fig. 1 and obtained the lower bound of collapse moment of an edge-cracked strip under pure bending in plane strain. The fundamentals of the following limit analysis may be found in several textbooks on plasticity such

[4]The italic numbers in brackets refer to the list of references appended to this paper.

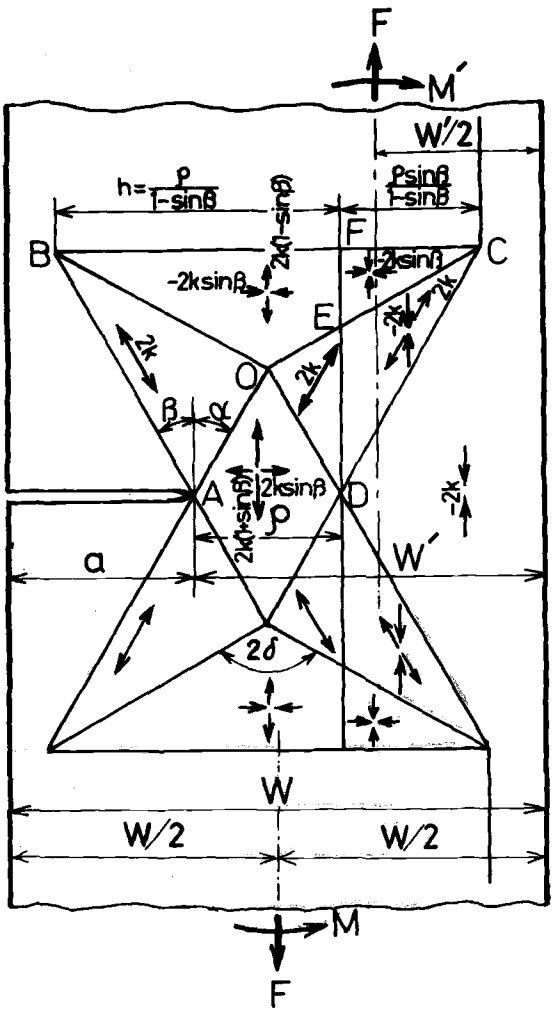

FIG. 1—*Statically admissible stress field in plane strain.*

as Prager-Hodge's [*13*]. In the present paper, the effect of axial force on the stress field is considered and the solution of the lower bound is extended to the case of combined loading of axial force and bending moment [*5*].

To an edge-cracked strip with width W, crack length a, and thickness B, the membrane stress P'_m and the bending stress P'_b in the sense of stress intensity are defined as follows, by using the ligament width $W' = W - a$, the axial force F, and the bending moment M' referred to the centerline of the ligament width (see Fig. 1)

$$P'_m = F/BW', \qquad P'_b = 6M'/BW'^2 \tag{1}$$

The membrane stress P_m and the bending stress P_b are also defined as for full thickness W

$$P_m = F/BW, \qquad P_b = 6M/BW^2 \tag{2}$$

where M is the bending moment referred to the centerline of full thickness.

Case of Deep Crack

The stress field in Fig. 1 is statically admissible when

$$\alpha = \pi/4 - \beta/2 \tag{3}$$

$$\delta = \pi/2 - \alpha \tag{4}$$

$$0 \leqq \beta \leqq \pi/6 \tag{5}$$

Equations 3 and 4 are derived from the equilibrium of the region ABFD, and Eq 5 is necessary not to break the yield criterion in the region CDE. The applied load exists in equilibrium with the stress field and F and M' are given as

$$F = 2kB\{\rho(2 + \sin\beta) - W'\} \tag{6}$$

$$M' = kB\rho(W' - \rho)(2 + \sin\beta) \tag{7}$$

where k is the shear yield stress and ρ the length AD. The most suitable lower bound of collapse is obtained under the condition that Point C remains within the strip, as follows

$$P'_b/3k = \begin{cases} -4(P'_m/2k - 1/4)^2/5 + 5/4, & (-1 \leqq P'_m/2k \leqq 1/4) \\ \dfrac{4(1 + P'_m/2k)\{(1 + \sqrt{5 - 4P'_m/2k})/2 - P'_m/2k}{3 + \sqrt{5 - 4P'_m/2k}}, & (1/4 \leqq P'_m/2k \leqq 1) \end{cases} \tag{8}$$

For pure bending ($P'_m = 0$), $P'_b/3k = 1.20$ and it coincides with the constraint factor obtained by Lianis and Ford [*4*].

Critical Crack Depth

Equation 8 is applicable when crack depth ratio a/W is larger than the following critical value $(a/W)_c$, because crack depth is required to satisfy the condition in which Point B exists in the strip

$$\left(\frac{a}{W}\right)_c = \begin{cases} (1 + P'_m/2k)/(7/2 + P'_m/2k), & (-1 \leqq P'_m/2k \leqq 1/4) \\ (3 - 2P'_m/2k - \sqrt{5 - 4P'_m/2k})/2(1 - P'_m/2k), & (1/4 \leqq P'_m/2k \leqq 1) \end{cases} \tag{9}$$

Case of Shallow Crack

In the case that a/W is less than the foregoing $(a/W)_c$, the most suitable lower bound of collapse is also obtained as follows

$$\frac{P'_b}{3k} = 2\left(1 + \frac{P'_m}{2k}\right) \times \left[1 - \frac{1 + P'_m/2k}{2 + \frac{1}{2}\left\{\sqrt{\left\{\frac{P'_m}{2k}\left(\frac{W}{a} - 1\right) + \frac{W}{a}\right\}^2 + 8} - \frac{P'_m}{2k}\left(\frac{W}{a} - 1\right) - \frac{W}{a}\right\}}\right] \tag{10}$$

Collapse Limit Diagram in Plane Strain

The results of Eqs 8-10 are summarized in Fig. 2, the collapse limit diagram. The maximum $(a/W)_c$ in Eq 9 is 1/3, and Eq 8 is applicable in all combinations of the axial force and the bending moment in the range of $a/W \geqq 1/3$. As a/W decreases, the collapse limit asymptotically converges to the true solution with no crack, namely

$$P'_b/3k = 1 - (P'_m/2k)^2 \tag{11}$$

The upper-bound solutions for the deep edge crack are also shown in Fig. 2. The broken line is the extension of Green's solution by Okamura et al [6] and Shiratori et al [7]. Results of the dashed-dotted curve are obtained by using the circular slipline assumed by Rice [8] and Ewing [9]. A well-known lower-bound solution coincides with the lower-bound curve of $a/W = 0$. As seen from the diagram, the lower bound of the collapse is improved remarkably, and the present analysis decreases the difference between the upper and the lower bounds, especially in the range of the small $P'_m/2k$ for the deep crack. It

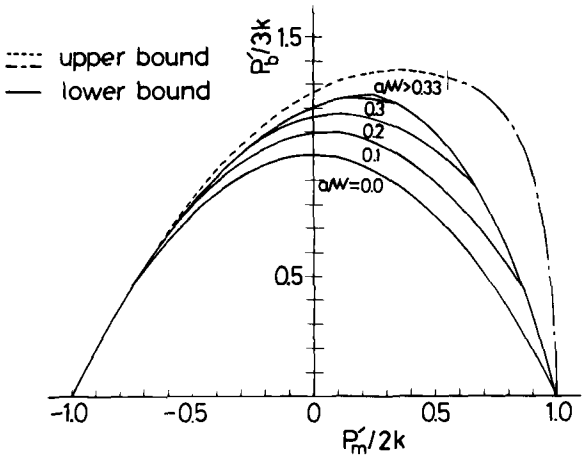

FIG. 2—*Collapse limit diagram in plane strain.*

might be emphasized that the improved lower-bound solution can be applied to the member with an arbitrary crack depth ratio; on the other hand, the upper-bound solution is restricted to the deeply cracked member.

Improved Lower-Bound Solution in Plane Stress

Ford and Lianis [*10*] obtained the lower bound of collapse moment of the edge-cracked strip under pure bending in plane stress by introducing the statically admissible stress field which is similar to the stress field of plane strain shown in Fig. 1. The effect of the axial force can be considered [*11*] in the same manner as the plane-strain problem. In the plane-stress problem, it makes a large difference in the solution whether the yield criterion is von Mises' or Tresca's. The von Mises yield criterion is assumed in the following results.

Case of Deep Crack

The result of the lower bound of collapse of a deeply edge-cracked strip under axial force and bending moment is obtained in the range that the membrane stress is not large

$$\frac{P_b'}{1.5S_y} = 1.072\left(1+\frac{P_m'}{S_y}\right)^2 - 2\frac{P_m'}{S_y}\left(1+\frac{P_m'}{S_y}\right), \qquad \left(-1 \leqq \frac{P_m'}{S_y} < 0.5475\right) \quad (12)$$

where S_y is the tensile yield stress. The range of P'_m/S_y is required to satisfy a condition in which Point C in Fig. 1 remains within the strip. In the case that P'_m/S_y is larger than 0.5475, the solution could not be obtained in the closed form. The optimum values of α, β, and δ were obtained numerically and the final results are shown in Fig. 3. In the case of pure bending, P'_b/S_y is equal to 1.072 and coincides with the constraint factor obtained by Ford and Lianis [*10*].

Critical Crack Depth

Equation 12 is applicable under the condition in which the crack depth ratio is larger than the following critical value $(a/W)_c$

$$\left(\frac{a}{W}\right)_c = 0.1540\left(1+\frac{P'_m}{S_y}\right)\Big/\left(1+0.1540\frac{P'_m}{S_y}\right), \qquad \left(\frac{P'_m}{S_y}<0.5475\right) \tag{13}$$

In the range where P'_m/S_y is larger than 0.5475, $(a/W)_c$ is given numerically by the geometrical condition in which Point B remains within the strip. The maximum value of $(a/W)_c$ is 0.220 and Eq 12 is valid in all combination of the axial force and bending moment as long as $a/W \geqq 0.220$.

Collapse Limit Diagram in Plane Stress

In the case that a crack is shallower than the critical depth, the most suitable lower bound of collapse load is obtained by calculating numerically the statically admissible angles α, β, and δ.

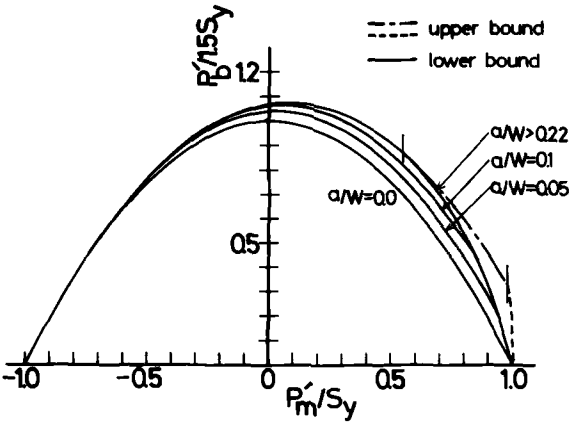

FIG. 3—*Collapse limit diagram in plane stress.*

The results of lower bound of collapse limit in plane stress are shown in Fig. 3 with the upper bounds for a deep crack obtained by Ewing and Richard [9]. The lower bound given by Eq 12 coincides with the upper bound in the range where $-1 \leqq P'_m/S_y < 0.5475$ and $a/W > 0.220$, and the result gives the true solution. As the crack depth ratio decreases, the collapse limit asymptotically converges to the true solution with no crack, namely

$$\frac{P'_b}{1.5S_y} = 1 - \left(\frac{P'_m}{S_y}\right)^2 \tag{14}$$

If we assume Tresca's yield criterion, the true solution is given by Eq 14.

Collapse Limit Diagram for Structural Design

The lower bound of collapse load is more important in structural design and safety assessment than the upper bound from the standpoint of conservative estimation. But there is still a question whether the lower bound is too conservative or reasonable in the sense of a structural design criterion. In order to confirm the applicability of the improved lower-bound solution, the collapse load was experimentally studied by using a mild steel. The edge-cracked specimens were eccentrically pulled by pins under several combination of axial force and the bending moment. The crack depth ratios a/W were nearly equal to 0.5. The results are compared in Fig. 4 with the theoretical solutions of plane strain. Assuming the von Mises yield criterion to apply, we use k for $S_y/\sqrt{3}$. It is concluded from the experimental results that the improved lower-bound solution can be used as a reasonable design criterion of the collapse of an edge-cracked member.

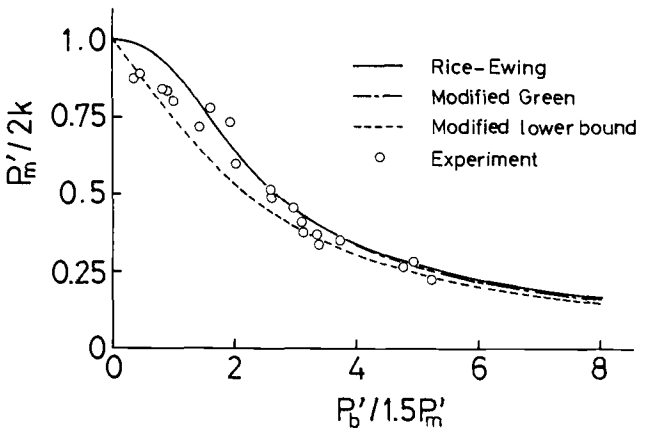

FIG. 4—*Experimental results of collapse load of edge-cracked specimen in comparison with the theoretical curves.*

In the design of structural components, it might be important to reveal how the collapse load varies when a given length of crack is induced. The lower-bound curves are shown in Fig. 5 as a function of crack depth ratio a/W on a P_m versus $P_m + P_b$ diagram. The plane-strain condition is assumed, and P_m and P_b in the uncracked state are defined by Eq 2. The inner hexagon shows the ASME Pressure Vessel Code Section III design limit in the normal operating condition. The collapse limit diagram indicates that the member can sustain the design load without appreciable plastic deformation as long as crack depth ratio is smaller than 0.15, if the member is designed according to the preceding design code.

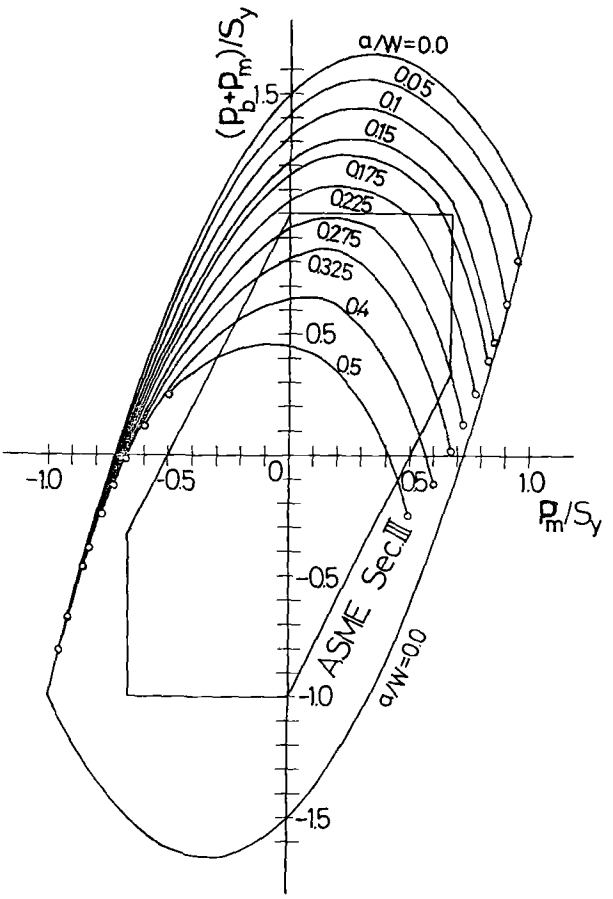

FIG. 5—*Collapse limit diagram for structural design.*

Lower Bound of Collapse Limit for Surface Flaw

The lower-bound solution in plane stress can be applied to the three-dimensional analysis of the collapse limit of a member with a surface flaw under axial force and the bending moment. The shape of a flaw is assumed to be rectangular with depth a and width c. If we circumscribe the rectangular with a real flaw, the assumption of the shape might be reasonable from the standpoint of conservative estimation.

The member is divided into two plates, the cracked plate with thickness c and the uncracked plate with thickness B-c as shown in Fig. 6. The statically admissible stress field in plane stress is assumed in both plates. The stresses are not continuous on the boundary between the cracked plate and the uncracked plate. But the equilibrium condition is satisfied on the boundary because the tractions acting on the boundary are zero in the plane-stress condition. Therefore, the stress field of the member with a surface flaw, which is shown in Fig. 6*b*, is statically admissible and gives the lower bound of the collapse load.

The two plates share the applied load F and M between them, and the collapse limit of the member with surface flaw is obtained by combining Eq 12 of the cracked plate and Eq 14 of the uncracked plate as follows

$$\frac{P_b}{1.5\,S_y} = -\zeta^2(1-\xi)^2\left\{\frac{2-L_0}{\zeta}+\frac{1}{1-\zeta}\right\}\left(\frac{P'_{mc}}{S_y}\right)^2 + 2\zeta(1-\xi)\left\{L_0(1-\xi)-1+\frac{P_m/S_y}{1-\zeta}\right\}\left(\frac{P'_{mc}}{S_y}\right) + (1-\zeta)+L_0\zeta(1-\xi)^2-\frac{1}{1-\zeta}\left(\frac{P_m}{S_y}\right)^2 \tag{15}$$

where $\xi = a/W$, and $\zeta = c/B$. P'_{mc} is the membrane stress acting on the ligament section of the cracked plate and L_0 is the constraint factor 1.072 for pure bending. From Eq 15 the optimum P'_{mc} which makes the collapse moment maximum is revealed to be given by the relation

$$\frac{P'_{mc}}{S_y} = \frac{(1-\zeta)\{L_0(1-\xi)-1\}+P_m/S_y}{(1-\xi)\{2-L_0+(L_0-1)\zeta\}} \tag{16}$$

Therefore the most suitable lower bound of collapse moment for a surface flaw is obtained as Eq 17 under the conditions of Eq 18

$$\frac{P_b}{1.5\,S_y} = (1-\zeta) + L_0\zeta(1-\xi)^2 + \frac{\zeta(1-\zeta)\{L_0(1-\xi)-1\}^2}{2-L_0+(L_0-1)\zeta}$$

$$+ \frac{2\zeta\{L_0(1-\xi)-1\}}{2-L_0+(L_0-1)\zeta}\left(\frac{P_m}{S_y}\right) - \frac{2-L_0}{2-L_0+(L_0-1)\zeta}\left(\frac{P_m}{S_y}\right)^2 \quad (17)$$

$$\frac{a}{W} > 0.220, \quad -1 \leqq \frac{P'_{mc}}{S_y} < 0.5475, \quad -1 \leqq \frac{P_{mB}}{S_y} \leqq 1 \quad (18)$$

P_{mB} is the membrane stress of the uncracked plate. When P'_{mc}/S_y becomes less than -1 in Eq 16, the most suitable lower bound is given by substituting the relation $P'_{mc}/S_y = -1$ into Eq 15.

As an example, the result of collapse moment of the member with surface flaw under pure bending is shown in Fig. 7.

Estimation of the J-Integral for a Compact Specimen Based on the Improved Lower-Bound Solution

Analysis of the collapse limit of a cracked member plays an important role in elastic-plastic fracture mechanics. An application is the J-integral analysis for a compact specimen. Merkle and Corten [*2*] calculated the J-integral of

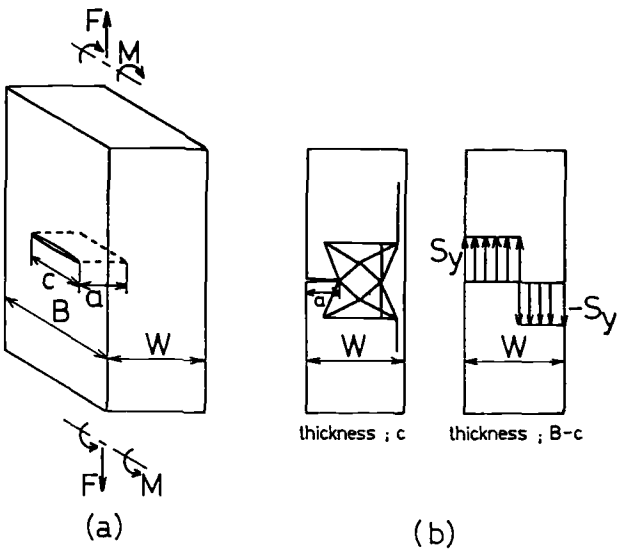

FIG. 6—(a) *Member with a surface flaw;* (b) *stress field assumed in the member.*

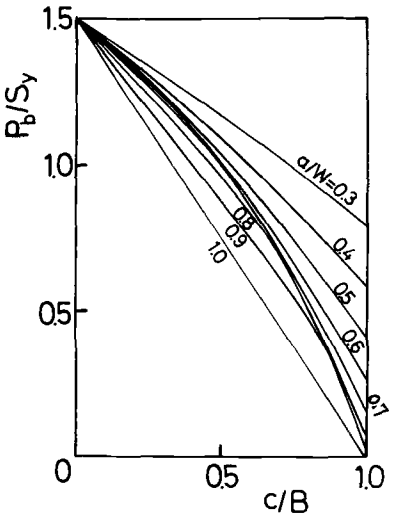

FIG. 7—*Collapse moment of a member with a surface flaw under pure bending.*

the specimen and proposed a formula of estimation in which a single load-displacement curve is used. In their analysis the stress distribution corresponding to a statically admissible stress field to get a well-known lower-bound solution of Eq 11 is used in order to consider the axial force as well as the bending effect. The lower-bound solution is considerably improved in the present paper and the collapse load can be estimated more precisely. This result is applied to the estimation of the J-integral of the compact specimen.

In the case of a deep crack, the lower bound of collapse limit in plane strain is given by Eq 8. In much the same way as proposed by Merkle and Corton, the J-integral for the compact specimen is obtained as Eq 19, by using the applied load F and the load-line displacement Δ.

$$J=(\eta_r\phi_r+\eta_c\phi_c)/W', \quad \text{where} \quad \phi_r=\int_0^{\Delta}\left(\frac{F}{B}\right)d\Delta, \quad \phi_c=\int_0^{F/B}\Delta d\left(\frac{F}{B}\right) \tag{19}$$

η_r and η_c are obtained by the authors [5], Merkle and Corten [2] and Shiratori and Miyoshi [7], and all the results can be expressed in the same form as follows

$$\eta_r=\frac{L_0r(1-\xi)}{(r+\xi)\{2r+(2-L_0)(\xi-1)\}}, \qquad \eta_c=\frac{\xi(1-\xi)}{\xi^2+2/L_0-1} \tag{20}$$

where

$$\xi = a/W, \qquad r = \{L_0(\xi^2 - 1)/2 + 1\}^{1/2} - \xi$$

$$L_0 = \begin{cases} 1.20 \text{ (present analysis)} \\ 1.00 \text{ (Merkle and Corten)} \\ 1.261 \text{ (Shiratori and Miyoshi)} \end{cases}$$

A new expression of η_r and η_c in Eq 20 is chosen so that L_0 coincides with the constraint factors of the stress field assumed for pure bending. In the expression, a and W are defined by the distances from the load line according to the convention for compact specimens. The result of Shiratori and Miyoshi is derived from the extended Green's solution [*6, 7*], which gives an upper bound of collapse limit. Table 1 compares the factors η_r and η_c. There is a small difference between the factors of the authors' lower bound and Shiratori-Miyoshi's upper bound. As formulated in Eq 20, η_r and η_c are the functions of the constraint factor L_0 for pure bending. It might be emphasized that the true values of η_r and η_c for real L_0 may lie in a narrow range between the results of the authors and Shiratori et al.

Failure Assessment Diagram as an Elastic-Plastic Failure Criterion

The two-criteria approach has been proposed by Dowling and Townley [*1*] as an elastic-plastic failure criterion in which the stress-intensity factor and the collapse load are used, and we can conveniently evaluate the strength of a cracked member in the elastic-plastic regime by using linear fracture mechanics, limit analysis, and the assessment curve based on the approach. In the present paper, the validity of the failure assessment diagram (FAD) [*3*] is examined from the standpoint of a J-integral evaluation for a cracked member under bending and tension.

Converting J into the equivalent stress-intensity factor K_p by the relation $K_p = \sqrt{E'J}$ where E' is E, Young's modulus, for plane stress or $E/(1 - \nu^2)$

TABLE 1—*Comparison of the factors* η_r *and* η_c *for lower and upper bounds.*

a/W	η_r	η_r'	η_r''	η_c	η_c'	η_c''
0.45	2.385	2.290	2.418	0.285	0.206	0.313
0.50	2.348	2.265	2.377	0.273	0.200	0.299
0.55	2.311	2.239	2.336	0.255	0.190	0.278
0.60	2.274	2.212	2.294	0.234	0.176	0.253
0.65	2.237	2.186	2.254	0.209	0.160	0.225
0.70	2.200	2.159	2.214	0.182	0.141	0.195

η_r', η_c' by Merkle-Corten; η_r'', η_c'' by Shiratori-Miyoshi.

for plane strain, we get the following assessment curve which is similar to the FAD but that does not depend on K_{Ic}.

$$\frac{K}{K_p} = S_r \left\{ \frac{8}{\pi^2} \ln \sec \left(\frac{\pi}{2} S_r \right) \right\}^{-1/2} \tag{21}$$

where S_r is the applied load/collapse load. K_p or J will be estimated from both S_r and K, the stress-intensity factor by elastic analysis. Equation 21 is derived from the Dugdale model of an infinite inner-cracked plate subjected to uniform tensile stress at infinity, and the effects of the finite boundaries and the bending stress are not accounted for. The applicability of Eq 21 is investigated experimentally and analytically in case of the edge-cracked member under combined bending and tensile loading.

The material tested is a pressure vessel steel JIS SQV2A, equivalent to ASTM A533B Class 1. In order to apply both the membrane stress and bending stress simultaneously, the edge-cracked specimens with various eccentricity e and crack length a were pulled by pins. The J-integral was determined from the elastic behavior of the specimens by a specimen compliance method generalized by Begley and Landes [*12*]. The collapse load was defined as the onset of gross deformation by the criterion of twice compliance, in which the collapse point is determined by the intersection of the load-displacement curve and the straight line whose compliance is twice as large as that in the proportional range of the load-displacement curve. The results are plotted on the assessment diagram. The ranges of e/W and a/W are 0.01 ~ 0.66 and 0.2 ~ 0.25, respectively. The numerical analysis by the finite-element method (FEM) was also carried out for the edge-cracked specimen with a/W of 0.25 under the various ratios of P_b/P_m.

The experimental and numerical results are compared in Fig. 8 with the theoretical curve of Eq 21, which is derived from the Dugdale model. It is concluded that, within the range of the present analysis, the J-integral under a combined loading of bending and tension can be estimated from the failure assessment curve in Eq 21 with a certain accuracy and that the elastic-plastic failure stress of a cracked member can be determined by the FAD as long as the J_{Ic} criterion is valid.

Conclusions

1. Improved lower-bound solutions of an edge-cracked strip subjected to axial force and bending moment are analytically derived in conditions of both plane strain and plane stress. The present analysis decreases the difference between the upper and the lower bounds of collapse limit for deep crack under plane-strain conditions, especially in the range that the membrane stress is small. The lower-bound solution of the plane stress is proved to be the exact solution in the range of $a/W \geqq 0.22$ and $-1 \leqq P'_m/S_y < 0.5475$.

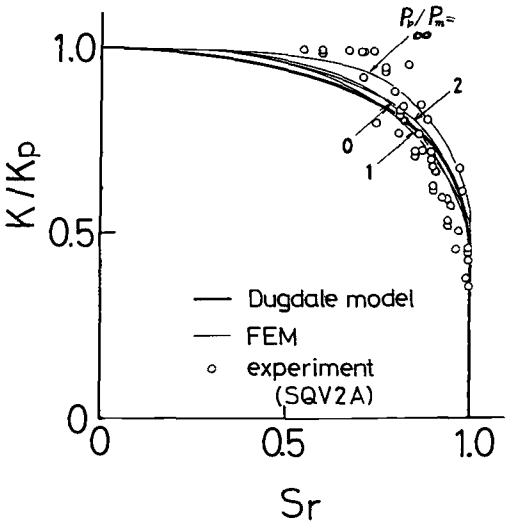

FIG. 8—*Failure assessment diagram in comparison with experimental and numerical results.*

2. The collapse load of the edge-cracked specimen of a pressure vessel steel was experimentally studied and the experimental results agree quite well with the improved lower bound. The lower-bound solution of collapse limit is more important in safety assessment than the upper bound because of conservative estimation.

3. The collapse limit diagram of lower bound for structural design can be obtained and compared with the design limit by the ASME Pressure Vessel Code.

4. A procedure is proposed for the calculation of the collapse limit of a structural member with a surface flaw under axial force and bending moment.

5. An estimation procedure of the J-integral for a compact specimen is proposed, based on the improved lower-bound solution. The factors η_r and η_c in the formula are shown as the functions of the constraint factor for pure bending, and η_r and η_c for the true constraint factor are between the results of the present authors and those of Shiratori and Miyoshi.

6. The applicability of the FAD is confirmed experimentally and analytically under the combined loading of bending and tension. The FAD is a useful design criterion of elastic-plastic failure of a cracked member as long as the J_{Ic} criterion is valid.

References

[1] Dowling, A. R. and Townley, C. H. A., *International Journal of Pressure Vessel and Piping*, Vol. 3, No. 3, 1975, p. 77.

[2] Merkle, J. G. and Corten, H. T., *Journal of Pressure Vessel Technology, Transactions*, American Society of Mechanical Engineers, Vol. 96, No. 4, 1974, pp. 286-292.
[3] Darlaston, B. J. L. in *Developments in Pressure Vessel Technology*, R. W. Nichols, Ed., Applied Science Publisher, London, Vol. 1, 1979, pp. 97-114.
[4] Lianis, G. and Ford, H. in *Proceedings*, 9th International Congress for Applied Mechanics, Congrés International de Mechanique, Appliquée, Brussels, Vol. 8, No. 12, 1957, pp. 235-238.
[5] Okamura, H., Takahata, Y., and Kageyama, K., "Collapse Load of Cracked Member under Axial Force and Bending Moment and Its Application—1st Report; Plane Strain Problem," *Transactions*, Japan Society of Mechanical Engineers (JSME), Series A to be published; Reprint of the JSME, No. 807-2, 1980, pp. 95-98 (in Japanese).
[6] Okamura, H., Watanabe, K., and Takano, T., *Engineering Fracture Mechanics*, Vol. 7, No. 3, 1975, pp. 531-539.
[7] Shiratori, M. and Miyoshi, T., *Transactions*, Japan Society of Mechanical Engineers, Series A, Vol. 45-389, 1979, pp. 50-56 (in Japanese).
[8] Rice, J. R. in *Proceedings*, Surface Flaw Symposium, American Society of Mechanical Engineers Winter Annual Meeting, 1972, p. 171.
[9] Ewing, D. J. F. and Richards, C. E., *Journal of the Mechanics and Physics of Solids*, Vol. 22, 1974, pp. 27-36.
[10] Ford, H. and Lianis, G., *Zeitschrift für Angewandte Mathematik und Mechanik*, Vol. 8, 1957, pp. 360-382.
[11] Okamura, H., Takahata, Y., and Kageyama, K., "Collapse Load of Cracked Member under Axial Force and Bending Moment—2nd Report; Plane Stress Problem and Collapse Load of Surface Flawed Member," *Transactions*, Japan Society of Mechanical Engineers, to be published (in Japanese).
[12] Begley, J. A. and Landes, J. D. in *Fracture Toughness, ASTM STP 514*, American Society for Testing and Materials, 1972, pp. 1-20.
[13] Prager, W. and Hodge, P. G., *The Theory of Perfectly Plastic Solids*, Wiley, New York, 1951.

Ian Milne[1] *and David A. Curry*[2]

Ductile Crack Growth Analysis Within the Ductile-Brittle Transition Regime: Predicting the Permissible Extent of Ductile Crack Growth

REFERENCE: Milne, I. and Curry, D. A., **"Ductile Crack Growth Analysis Within the Ductile-Brittle Transition Regime: Predicting the Permissible Extent of Ductile Crack Growth,"** *Elastic-Plastic Fracture: Second Symposium, Volume II—Fracture Resistance Curves and Engineering Applications, ASTM STP 803*, C. F. Shih and J. P. Gudas, Eds., American Society for Testing and Materials, 1983, pp. II-278–II-290.

ABSTRACT: The ductile-brittle transition in ferritic steels is reviewed using data from pressure vessel steels A533B, A508, BS1501-271, and their associated weld metals and heat-affected zones in a variety of conditions. A schematic model is presented which provides a rational basis for understanding the phenomenon and making predictions. This model, which is consistent with the predictions obtained from physical models of cleavage fracture, contains the following important features.

1. If in the transition regime, K_{Ic} is defined as the fracture toughness at the onset of the brittle mode of fracture and K_{IJ} is defined as the fracture toughness at the onset of ductile crack growth, then $K_{Ic} > K_{IJ}$.
2. The ductile crack extension obtained between the initiation of ductile crack growth and the onset of brittle fracture is defined by the elastic-plastic crack growth resistance curve.
3. K_{Ic} cannot be reached without generating the appropriate amount of ductile crack extension.

It follows that, when performing a failure analysis in this temperature regime, the choice of K_{IJ} as a failure criterion is unnecessarily pessimistic and inconsistant with the choice of K_{Ic} as a failure criterion below these temperatures. A procedure is presented which allows the permissible extent of crack growth to be obtained.

KEY WORDS: ductile-brittle transition, ferritic steels, phenomenological model, fracture toughness, J_R-curve, ductile crack extension, permissible extent of crack growth, elastic-plastic fracture

[1]Research officer, Central Electricity Research Laboratories, Central Electricity Generating Board, Leatherhead, Surrey, U.K.

[2]Project leader, Schlumberger Cambridge Research, Cambridge, U.K.

In ferritic steels the transition in fracture mode from metallurgically brittle to metallurgically ductile mechanisms has been recognized for some considerable time. In Charpy impact test data it coincides with a general increase in the energy absorbed, the steepness of the increase depending upon the difference between the upper and lower shelf energy levels and the temperature range over which the transition occurs. In fracture toughness test data it occurs in the temperature range where the brittle fracture toughness is increasing rapidly. In both types of test, within the transition temperature range, a crack may propagate initially in the ductile mode but change to the brittle mode after some, often small, amount of crack extension. Since ductile fracture is often stable and brittle fracture is generally unstable, a fracture mechanics analysis which predicts ductile stable crack growth in the transition regime, and which does not allow for this possible mode change, may be unconservative. There is therefore a need to estimate whether, in the transition regime, any ductile crack growth can be permitted and, if so, how much. This paper reviews our current knowledge of the ductile-brittle transition in ferritic steels and develops a phenomenologically descriptive model which allows estimation of the amount of ductile crack growth permissible at any temperature in the transition temperature range.

Description of Transition

The ductile-brittle transition in fracture toughness is shown schematically as a function of temperature in Fig. 1. Here the toughness at the initiation of brittle fracture is designated K_{Ic} and is signified by the heavy line. The lighter line signifies the initiation of ductile fracture and is designated K_{IJ}. Typically K_{Ic} increases rapidly over a limited temperature range while K_{IJ} remains relatively constant. The lower limit to the transition occurs where these two lines intersect, at DBL. Below this temperature, neglecting size effects, which are covered later, all fracture mechanisms are brittle (cleavage). Immediately above this temperature, cracks initiate and grow a small amount by ductile mechanisms whereupon brittle fracture intervenes. Within this regime K_{Ic} continues to increase with temperature until a point is reached where for all practical purposes K_{Ic} is unattainable. Eventually cleavage becomes impossible because crack-tip blunting limits the maximum attainable stress to less than the cleavage stress [*1*].[3] This is the upper limit to the ductile-brittle transition temperature range, DBU, and beyond this cracking can be by ductile mechanisms only.

The behavior depicted in Fig. 1 is, in practice, confused by scatter in material properties. For K_{Ic} this can be greater than a factor of two, and is exaggerated by size effects. The size effects may be explained in terms of statistical sampling which results from the scatter in K_{Ic} [*2*] and in terms of

[3]The italic numbers in brackets refer to the list of references appended to this paper.

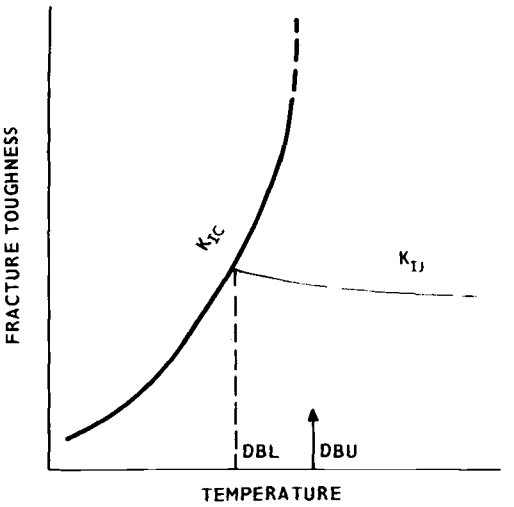

FIG. 1—*Ductile-brittle transition (schematic).*

the loss in triaxiality which occurs when testing small specimens [*3*]. Nevertheless, provided certain reservations are made regarding K_{Ic} and K_{IJ}, (see the following), the schematic model in Fig. 1 is consistent with all the observations which have been made concerning this phenomenon. These observations cover a vast range of ferritic materials but are rarely documented fully. For present purposes, however, it is sufficient to note the observations of Wessel [*4*], Begley and Toolin [*5*], Logsdon [*6, 7*], Sumpter [*8*], Logsdon and Begley [*9*], Loss et al [*10*], Milne and Curry [*11, 12*], and Curry et al [*13*]. The materials examined in these investigations include pressure vessel steels A533B, A508, BS1501-271, and their associated weldments in various conditions including as-tempered, after post-weld heat treatment, after irradiation, and after strain-aging. All these observations have been made using fracture toughness specimen geometries. The phenomenon has also been demonstrated on a structural geometry, the intermediate test vessel V-9 in the Heavy Section Steel Technology (HSST) program [*14*]. The description in Fig. 1 is also consistent with the mechanistic model of brittle cleavage fracture proposed by Ritchie et al [*1*] insofar as the mechanistic model predicts the temperature dependence of K_{Ic} shown in Fig. 1, and hence the competition between the ductile and cleavage mechanisms at temperatures close to DBL [*3, 8*].

The Meaning of K_{Ic} and K_{IJ}

The brittle fracture toughness is designated as K_{Ic} in Fig. 1. This implies that it must be derived from data which are valid by the relevant standard

testing procedures, the ASTM Test for Plane-Strain Fracture Toughness of Metallic Materials (E 399-78a) and BS5447. Linear elastic fracture mechanics (LEFM) valid tests present no practical difficulties at low toughness levels but, at the levels of toughness commonly observed in the transition range, valid tests are rarely possible. Indeed the size requirements for high-toughness material are such that in only a few instances have upper-shelf values of K_{Ic} have been reported for ferritic steels. For example, Begley and Toolin [5] required 203-mm (8 in.) compact tension specimens to measure the upper-shelf K_{Ic} of a 3½ percent nickel-chromium-molybdenum-vanadium (3½NiCrMoV) steel.

The LEFM validity criteria were empirically derived to ensure that the resulting K_{Ic} would be size independent. This requires that the test be performed in plane strain under nominally linear elastic conditions. Thus below DBL a valid K_{Ic} corresponds to the critical stress intensity factor at the onset of brittle fracture (cleavage). Although an invalid test below DBL still characterizes the same event, cleavage, the size effect mentioned earlier often raises the fracture toughness to a level above the valid K_{Ic} [2,15] in such a way that it is possible to plot a series of fracture toughness curves as a function of temperature at different specimen sizes [3,8]. Thus the effect may be represented as a shift in the temperature-dependent part of the brittle fracture toughness curve so that invalid specimens have a lower DBL than valid ones as shown in Fig. 2. There is some limited evidence that this size effect diminishes for cleavage above DBL [12] so in this range the invalid curve is represented by a broken line in Fig. 2. Nevertheless, in this temperature range the fracture toughness at the onset of brittle fracture still characterizes the cleavage initiation albeit after some variable amount of ductile crack extension.

When cracks initiate and propagate by ductile mechanisms the event is

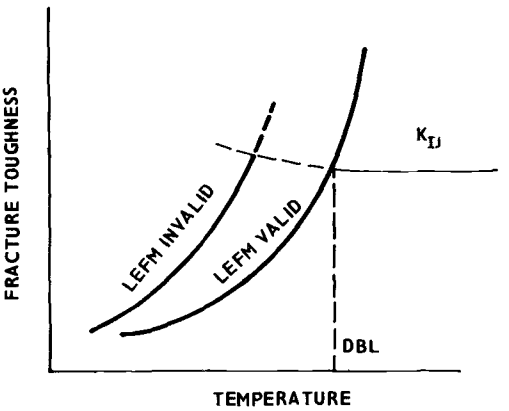

FIG. 2—*Effect of invalid-sized specimens on the ductile brittle transition (schematic).*

seldom discrete enough to be unambiguously measurable. In such cases it is conventional to measure the material's resistance to crack growth, generally in terms of J, and to plot this against the crack extension, Δa, to give a J-resistance curve. This curve is extrapolated to zero crack growth where the initiation toughness, J_{Ic} is defined. J_{Ic} can be converted to units consistent with plane-strain stress-intensity factors, that is, K_{IJ}, through the equivalence $K_{IJ} = \sqrt{E'J_{Ic}}$, where $E' = E/1 - \nu^2$, E being Young's modulus and ν Poisson's ratio. In practice the point on the J-resistance curve which defines zero crack growth is in dispute [*16*] as is the form of analysis used to fit a curve through the experimental data. However, these conflicts need not concern us for the present, except insofar as we recognize that by any system of measurement J_{Ic} will be a point on the early part of the resistance curve. Since this part of the J_R-curve is, within limits [*17,18*], geometry- and size-independent J_{Ic} will be a material parameter.

Between DBL and DBU, the fracture toughness at the onset of brittle fracture is defined by the point on the resistance curve corresponding to the extent of the ductile crack growth that precedes the brittle instability [*10.12*]. Close to DBL, the crack growth required for this is small, but it increases rapidly with temperature. Consequently, larger specimens are required in order to obtain a cleavage instability at temperatures approaching DBU than just above DBL. Nevertheless, at any temperature between DBL and DBU it is theoretically possible to test a specimen which is so large that, at the brittle fracture event, an LEFM valid K_{Ic} will be obtained. In this case the amount of ductile crack extension will be less than 2 percent of the original crack depth. Thus in LEFM the term K_{Ic} has the same meaning at all temperatures up to DBU, both in terms of the standards and in terms of the event it characterizes: the initiation of brittle fracture. On the other hand, in LEFM invalid tests this parameter can be taken only as characterizing cleavage initiation. If, however, in this regime the parameter is size independent, the LEFM value for K_{Ic} will still be obtained, despite the test being invalid.

Mechanisms of the Transition

The transition from ductile stable crack growth to brittle unstable crack growth can be understood with reference to Figs. 3 and 4. In Fig. 3 the transition region of the toughness temperature diagram is shown exaggerated. The left-hand ordinate is scaled in units of toughness and the right-hand ordinate in units of crack extension, Δa. The origin for the right-hand ordinate has been chosen to correspond with K_{IJ} on the left-hand ordinate at the appropriate temperature, T_1. Figure 4 is a schematic J-resistance curve, plotted at T_1 in terms of K (called K_Ω).

When a specimen is tested at T_1, the initial stages of loading stretch the crack tip to the extent defined by the blunting line in Fig. 4. At K_{IJ} the crack is on the point of resharpening and growing. This point is labeled A in Fig. 3.

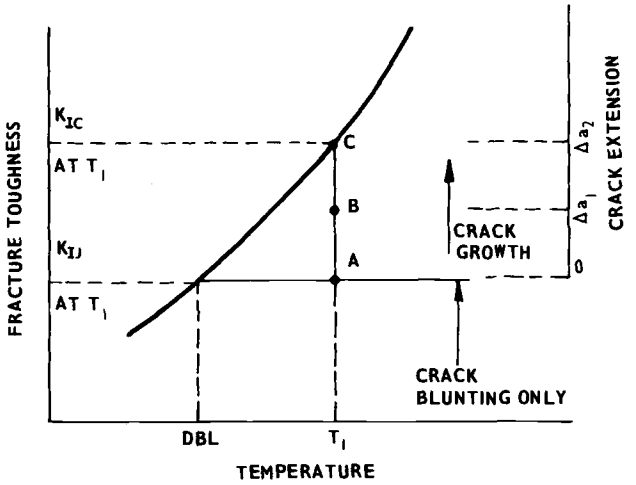

FIG. 3—*Ductile crack extension and fracture toughness-temperature relationship (schematic).*

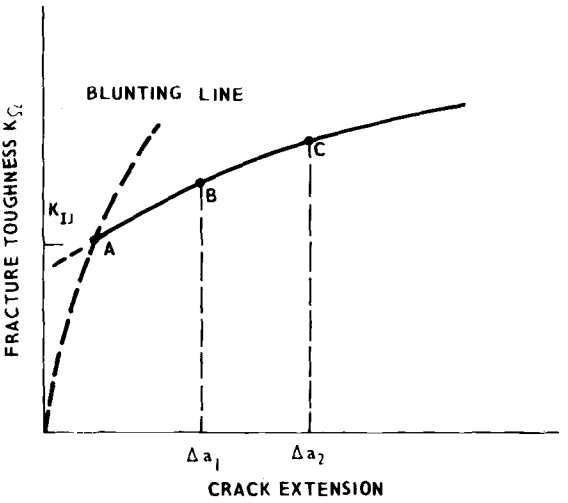

FIG. 4—*Resistance curve between DBL and DBU.*

Further loading causes the crack to extend in a stable manner, following the resistance curve in Fig. 4. For example, after a crack extension of Δa_1, the resistance toughness K_Q has risen to the level defined at B in Fig. 4. This toughness level has also been plotted on Fig. 3 at B. Loading until the crack extends to Δa_2 raises the measured toughness to the level defined at C in Fig. 4, which from Fig. 3 coincides with K_{Ic} at T_1. At this point brittle fracture is initiated and the specimen fails.

This schematic model is entirely consistent with the concept of a competition between the ductile and brittle mechanisms within this temperature range [*3,8*] and also with the mechanistic model for cleavage fracture proposed by Ritchie et al [*1*]. In this model cleavage cannot occur until the local condition is satisfied that the cleavage stress is exceeded over a metallurgically significant distance. The cleavage stress is relatively temperature independent, while the yield stress decreases with temperature. Thus at low temperatures the condition for cleavage is satisfied at nominal stress levels which are modest compared with the yield stress, but in the temperature range where the yield stress drops well below the cleavage stress, the increased plasticity makes this condition more difficult to achieve [*3*]. In this temperature range the cleavage condition can be satisfied only at high nominal stress levels and this is reflected in the temperature dependence of K_{Ic}.

Above DBL the conditions for ductile crack growth are satisfied before those for cleavage. However, the ductile crack cannot propagate without the stress in the remaining ligament increasing. In this situation, even though the crack is growing in a stable mode, the conditions for cleavage are still capable of being satisfied. If the crack can grow far enough for this to occur a cleavage instability will ensue. At any temperature between DBL and DBU the crack extension required to satisfy the cleavage condition depends upon the difference between K_{Ic} and K_{IJ}.

There are two important corollaries of this model. First, in the presence of ductile crack growth, even when K_{Ic} determines the load capacity of the specimen, it is the resistance curve which defines the crack extension up to this point. Second, K_{Ic} cannot be reached without extending the crack by this amount.

There is considerable experimental evidence in support of this model [*4-13*] even though much of it is confused by scatter and most of it has not been plotted in terms of resistance curves. Resistance curves are available in Refs *10*, *12*, and *13*, however, the latter two containing toughness-temperature plots also. It is clear from these that at toughness levels above K_{IJ} the brittle fracture toughness rises very steeply with temperature. Indeed in tests on BS1501-271 steel, Milne and Curry [*12*] observed a rise so steep that the size effect manifest in the cleavage toughness below K_{IJ}, represented by a shift in DBL, was lost above K_{IJ}. This is partly a consequence of the curve being steeper, whereby large differences in toughness correspond to smaller differences in temperature, and partly a consequence of mechanistic features which are unavoidable in ductile crack growth. These include sharpening of the crack as it extends from the blunted stretch zone, which will cause an instantaneous elevation of the local stress intensification, propagation of the crack into a strain hardened matrix, and an increase in the nominal applied stress in the load-bearing ligament as the crack propagates.

Fracture toughness is of course a material property that is particularly prone to scatter, and this tends to be exaggerated in the temperature depen-

dent part of the toughness-temperature curve. An extreme case of scatter was observed by Curry et al [*13*] and is shown in Fig. 5*a*. However, it is an implicit feature of the model that each specimen will belong to a particular toughness temperature curve, in the manner demonstrated in Fig. 5*b* where a number of curves have been drawn to pass through the data of Fig. 5*a*. Each curve is exactly the same shape, but is drawn at different positions along the temperature axis. The shape was determined by the American Society of Mechanical Engineers (ASME) XI K_{Ic} reference curve below 200 MPa$\sqrt{m}$ and above this by an eyeline fit to the bulk of the data in the temperature range between −10 and −15°C.

It should be emphasized that there is little to justify the exact shape of these curves. Although they often connect data from the same-sized specimens, because of scatter, data from other sizes of specimen may also fall on any given curve. They are presented only to demonstrate that the scatter in fracture toughness can be represented by a scatter in DBL of a master curve. It is readily demonstrated that this conclusion would be obtained regardless of the shape chosen for the master curve. Note that the right-hand ordinate is scaled in terms of crack extension with an origin corresponding to about 270 MPa$\sqrt{m}$. All the data above this toughness level were evaluated at the point where cleavage followed ductile crack extension, and they all fell on the same J_R-curve, regardless of specimen size or temperature [*13*]. The crack extension was measured only in macroscopic terms and is an average of the ductile crack extension observed over the total area of the specimen ahead of the fatigue crack tip.

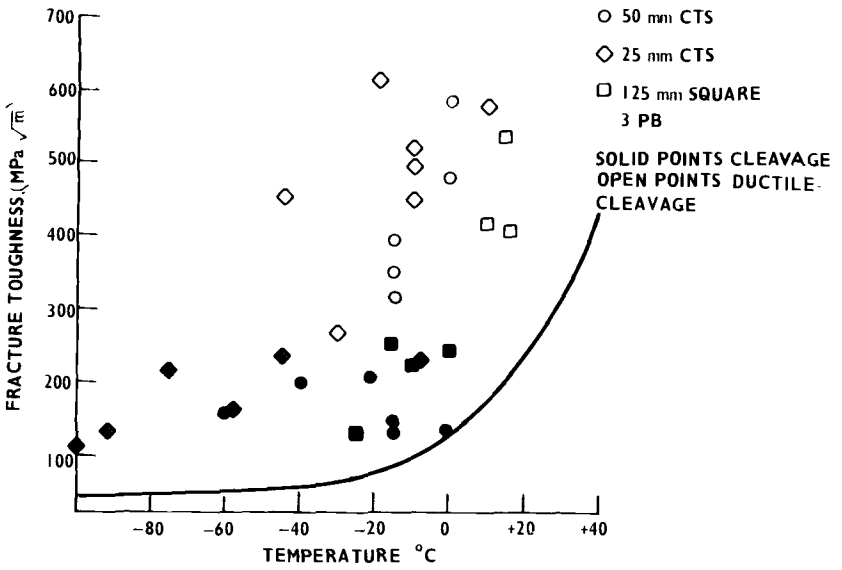

FIG. 5*a*—*Fracture toughness data as a function of temperature for A533B plate material.*

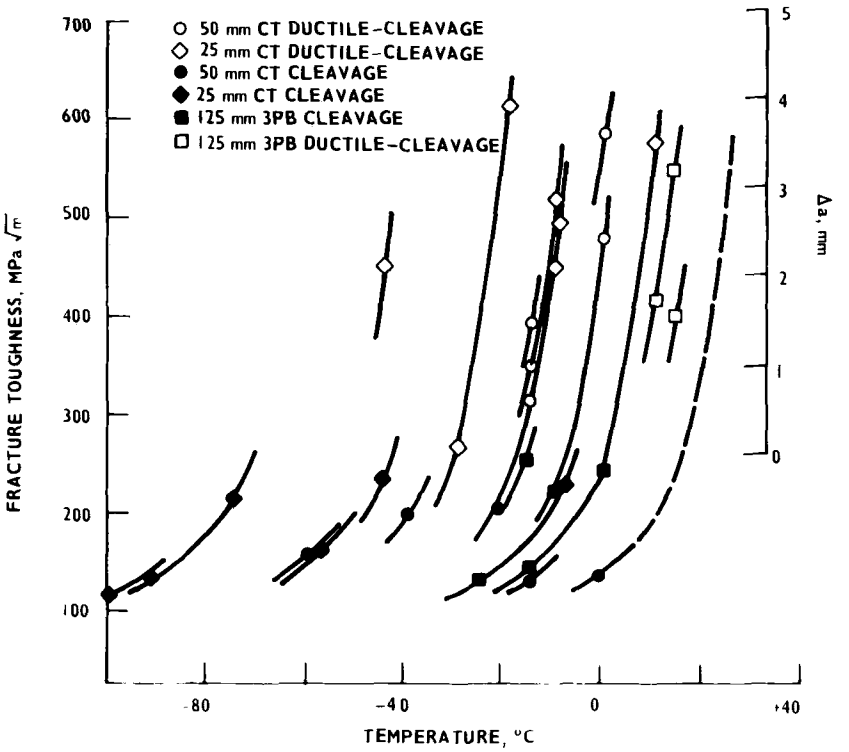

FIG. 5*b*—*Scatter in fracture toughness-temperature curves along temperature axis (all data LEFM invalid).*

In macroscopic terms, K_{IJ} therefore corresponds to a toughness level of 270 MPa$\sqrt{m}$. When cleavage occurs below this toughness level, as it does for the solid points in Figs. 5*a* and 5*b*, the scatter can be represented in terms of the cleavage fracture toughness only. On the other hand, when cleavage occurs above this toughness level, open points in Fig. 5*a* and 5*b*, scatter can also be observed in the crack extension obtained prior to cleavage. This is clear from Fig. 5*b* where at 0°C, for example, the crack extension at cleavage ranged from 0 to 3.7 mm. This scatter in crack extension before cleavage is of course automatically allowed for in the model. Note that for this specific material, the highest temperature at which a cleavage transition has been observed is +13°C, for a 125-mm-thick specimen. The dashed line in Fig. 5*b* has been drawn through the lowest data point obtained in this series of tests. Since this curve extends to temperatures of 25 to 30°C, the model suggests that the possibility of a ductile-cleavage transition must be admitted at these temperatures, even though none has been observed here.

Application to Structures

When performing an analysis of a structure which is operating within its ductile-brittle transition temperature, there is clearly the possibility that the crack growth mechanism will change from a stable ductile to an unstable brittle process if the crack is allowed to grow far enough. One way of avoiding this is to avoid crack growth altogether by using K_{IJ} as the assessment criterion. Another way is to perform a resistance curve analysis in the normal manner, but to limit the crack extension to that permitted by the difference between K_{Ic} and K_{IJ}. This second option is obviously the more appropriate, since it is based upon a truer assessment of what influences the load capacity of the structure. It is also consistent with the two corollaries noted in the preceding, and with a standard assessment at toughness below K_{IJ} which uses K_{Ic} as the failure criterion.

An example of an analysis where this philosophy has been followed has been presented by Milne [*19*]. In this example the HSST intermediate vessel test V9 [*14*] was analyzed using three J_R-curves, each limited by the same amount of crack extension that was observed in the actual test. An alternative limit, which is more consistent with the preceding philosophy, is to limit the J_R-curves at the same level of toughness. Choosing 560 MPa$\sqrt{m}$ for this (equivalent to $J_R = 1414$ kNm^{-1}), the three J_R-curves, and the analysis used in Ref *19*, the following three results are obtained for the cleavage pressure, P_c

For $J_R = 220 + 188\,\Delta a$, $P_c = 192$ MPa after 6.35 mm of crack extension
For $J_R = 220 + 94\,\Delta a$, $P_c = 189$ MPa after 12.7 mm of crack extension
For $J_R = 220 + 47\,\Delta a$, $P_c = 184$ MPa after 25.4 mm of crack extension

The measured values were 185 MPa after 12.7 mm of crack extension [*14*].

In erecting a safety case the major objective of an analysis is to be confident of avoiding failure rather than predicting it. In this respect there are two aspects to the use of toughness data relevant to possible transitions from ductile to brittle fracture, the scatter in the materials property data base and the validity of it.

For the first of these, it is conventional below K_{IJ} to allow for scatter in K_{Ic} by using a lower bound to the data base. This convention is no less applicable above K_{IJ}, and a glance at Fig. 5*b* demonstrates that in this regime the use of lower-bound cleavage fracture toughnesses will also correspond to the lower bound of the permitted crack extension. Such an analysis will therefore be pessimistic in the same way than an analysis to a lower bound K_{Ic} is pessimistic.

For the second of these, there are two general requirements of validity to consider. The most restrictive of these, K_{Ic} as defined by the standards, will be satisfied only rarely and so it must be accepted that the analysis will in general

be based upon an elastic-plastic failure criterion. Under these circumstances it would be prudent to limit the analysis to the regime of *J*-controlled growth despite the fact that at temperatures higher than the ductile-brittle transition range it appears to be safe to exceed these limits [*19*]. Provided the conditions for *J*-controlled growth in both the structure and the specimen test data are satisfied, the safe amount of ductile crack extension can be established as the lower of the two limits

1. six percent of the crack length or ligament width, or
2. the crack growth obtained between K_{IJ} and the cleavage toughness (K_{Ic}) along the resistance curve,

these two limits being applied to both the test specimens and the structures. K_{Ic} is definable above K_{IJ} by specimens large enough to demonstrate that specimen size has an insignificant influence on the temperature range of this part of the toughness-temperature curve. If this requires only modest-sized specimens, the safe amount of crack growth will be dominated by specimen size, not the size of the structure.

Figure 6 demonstrates the operation of the scheme on a plot of K_{Ic} versus temperature. It has been assumed that K_{Ic} has been established, as indicated in the foregoing, taking into account the influence of possible strain aging effects and other forms of hardening. The right-hand ordinate is scaled in terms of millimetres of crack growth with the origin corresponding to K_{IJ} at T_s, the service temperature, using the resistance curve data obtained when establishing the K_{Ic} curve. It is assumed that these J_R data satisfy the conditions for *J*-controlled growth and that Δa limitations imposed by specimen size are more severe than those imposed by structure size. The resultant crack growth

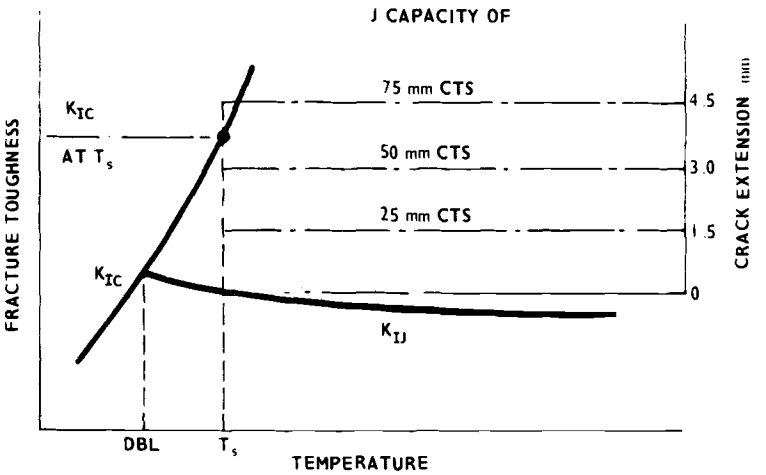

FIG. 6—*Determination of crack extension permitted in transition region.*

limits are plotted on this diagram for compact tension specimens 25, 50, and 75 mm thick. At the service temperature, T_s, ductile crack growth is permitted up to 1.5 mm by the J capacity of the 25-mm specimen, 3-mm by the J capacity of the 50-mm specimen, and 3.5 mm by the transition to brittle fracture at K_{Ic}. This latter crack extension is within the J capacity of the 75-mm specimen.

Finally, it should be emphasized that permitting crack growth at temperatures between DBL and DBU is entirely consistent with conventional fracture mechanics criteria. Under linear elastic conditions, the criterion would be K_{Ic}. Between DBL and DBU this cannot be attained without allowing the crack to grow the required amount, and this is recognized in the standard testing procedures. It is also consistent with resistance curve analysis, since the crack extension is determined by the resistance curve between K_{IJ} and K_{Ic}. Consequently the scheme outlined in Fig. 6 represents no major departure from current practice in failure analysis.

Conclusions

In ferritic steels, if the ductile-brittle transition is characterized by a change in fracture mode from stable ductile tearing to unstable brittle fractures, K_{Ic} can be defined as the fracture toughness at the onset of brittle fracture and K_{IJ} as the fracture toughness at the onset of ductile fracture. In the transition temperature regime:

1. $K_{Ic} > K_{IJ}$.
2. The ductile crack extension obtained between K_{IJ} and K_{Ic} is defined by the elastic-plastic crack growth resistance curve.
3. K_{Ic} cannot be reached without extending the crack the appropriate amount by ductile mechanisms.
4. In this temperature regime, crack growth can be permitted in a failure analysis provided the extent of crack growth is limited to that determined by the smaller of the two criteria: (1) the crack growth between K_{IJ} and K_{Ic}, and (2) the conditions for J-controlled growth.

Acknowledgments

This work was performed at the Central Electricity Research Laboratories and is published by permission of the Central Electricity Generating Board.

References

[1] Ritchie, R. O., Knott, J. F., and Rice, J. R., *Journal of the Mechanics and Physics of Solids*, Vol. 21, 1973, p. 395.
[2] Landes, J. D. and Schaffer, D. H. in *Fracture Mechanics: Twelfth Conference, ASTM STP 700*, American Society for Testing and Materials, 1980.
[3] Milne, I. and Chell, G. G. in *Elastic-Plastic Fracture, ASTM 668*, J. D. Landes, J. A.

Begley, and G. A. Clarke, Eds., American Society for Testing and Materials, 1979, pp. 358–377.

[4] Wessel, E. T. in *Practical Fracture Mechanics for Structural Steels*, U.K. Atomic Energy Authority, 1969, Paper H1.

[5] Begley, J. A. and Toolin, P. R., *International Journal of Fracture*, Vol. 9, 1973, p. 243.

[6] Logsdon, W. A. in *Mechanics of Crack Growth, ASTM STP 590*, American Society for Testing and Materials, 1976, p. 43.

[7] Logsdon, W. A. in *Elastic-Plastic Fracture, ASTM STP 668*, J. D. Landes, J. A. Begley, and G. A. Clarke, Eds., American Society for Testing and Materials, 1979, pp. 515–536.

[8] Sumpter, J. D. G., *Metal Science*, Vol. 10, 1976, p. 354.

[9] Logsdon, W. A. and Begley, J. A., *Engineering Fracture Mechanics*, Vol. 9, 1977. p. 461.

[10] Loss, F., Menke, B. H., Gray, R. A., and Hawthorne, J. R. in *Proceedings*, CSNI Specialists Meeting on Plastic Tearing Instability, Committee on the Safety of Nuclear Installation, Report No. 39, NUREG/CP-0010, 1979, p. 292.

[11] Milne, I. and Curry, D. A. in *Proceedings*, Fourth International Conference on Pressure Vessel Technology, Institution of Mechanical Engineers, 1980, Paper C56/80.

[12] Milne, I. and Curry, D. A. in *Proceedings*, Third European Conference on Fracture and Fatigue, Pergamon Press, Oxford, U.K., 1980, p. 39.

[13] Curry, D. A., Milne, I. and Akhurst, K. in *Fracture and the Role of Microstructure, Proceedings*, Fourth European Conference on Fracture, K. L. Maurer and F. E. Matzer, Eds., EMAS, Cradley Health, U.K., 1982, pp. 236–243.

[14] Merkle, J. G. in *Elastic-Plastic Fracture, ASTM STP 668*, J. D. Landes, J. A. Begley, and G. A. Clarke, Eds., American Society for Testing and Materials, 1979, pp. 674–702.

[15] Munz, D. and Keller, H. P. in *Proceedings*, Third European Conference on Fracture and Fatigue, Pergamon Press, Oxford, U.K., 1980, p. 105.

[16] Ingham, T. and Moreland, E. in *Proceedings*, CSNI Specialists Meeting on Plastic Tearing Instability, Committee on the Safety of Nuclear Installations, Report No. 39, NUREG/CP-0010, 1979, p. 330.

[17] Hutchinson, J. W. and Paris, P. C. in *Elastic-Plastic Fracture, ASTM STP 668*, J. D. Landes, J. A. Begley, and G. A. Clarke, Eds., American Society for Testing and Materials, 1979, pp. 37–64.

[18] Shih, C. F., deLorenzi, H. G., and Andrews, W. R. in *Elastic-Plastic Fracture, ASTM STP 668*, J. D. Landes, J. A. Begley, and G. A. Clarke, Eds., American Society for Testing and Materials, 1979, pp. 65–120.

[19] Milne, I., this publication, pp. II-657–II-685.

Akram Zahoor[1] *and M. F. Kanninen*[2]

Ductile Fracture of Circumferentially Cracked Pipes Subjected to Bending Loads

REFERENCE: Zahoor, A. and Kanninen, M. F., **"Ductile Fracture of Circumferentially Cracked Pipes Subjected to Bending Loads,"** *Elastic-Plastic Fracture: Second Symposium, ASTM STP 803, Volume II—Fracture Resistance Curves and Engineering Applications*, C. F. Shih and J. P. Gudas, Eds., American Society for Testing and Materials, 1983, pp. II-291–II-308

ABSTRACT: A plastic fracture mechanics methodology is presented for part-through cracks in pipes under bending. A previous analysis result on the behavior of part-through cracks in pipes is reviewed. Example quantitative results for the initiation and instability of radial growth of part-through cracks are presented and compared with the experimental data to demonstrate the applicability of the method. The analyses in our previous work are further developed to include the instability of circumferential growth of part-through cracks. Numerical results are then presented for a compliant piping system, under displacement controlled bending, which focus on (1) instability of radial growth (unstable wall breakthrough) and (2) instability of circumferential growth of the resulting through-the-thickness crack. The combined results of the above two types of analyses are presented on a safety assessment diagram. This diagram defines a curve of critical combination of length and depth of part-through cracks which delineates leak from fracture. The effect of piping compliance on the leak-before-break assessment is discussed.

KEY WORDS: ductile fracture, degraded piping, part-through cracks, J-integral/tearing modulus, *J*-resistance curve, unstable wall breakthrough, leak-before-break, safety assessment diagram, elastic-plastic fracture

Periodically over the past several years, cracks have been discovered in small to medium-size-diameter piping at operating boiling water reactor (BWR) facilities. The lines found to have cracks include recirculation bypass piping, core spray lines, reactor-water-cleanup lines, and control rod drive

[1]Supervising engineer, EDS Nuclear Inc., 7910 Woodmont Ave., Bethesda, Md. 20814; formerly with Fracture Proof Design Corp., St. Louis, Mo.
[2]Research leader, Battelle Columbus Laboratories, 505 King Ave., Columbus, Ohio 43201.

return lines [*1,2*].[3] Almost all cracking incidents have been found to occur in the heat-affected zones (HAZ's) of girth welds in Type 304 stainless steel piping. These cracks are typically at the inner surface of the pipe wall and are oriented circumferentially.

Type 304 stainless steel is a highly ductile and tough material and the potential for pipe break resulting from the presence of these cracks is considered low as evidenced by the service experience. However, service experience for cracks subjected to large loads is not available because of very low rate of occurrence of such loads. It is, therefore, desirable to obtain a quantitative determination of the potential for pipe rupture under large loads to insure the integrity of the piping system.

Experimental observations on flawed Type 304 stainless steel pipes subjected to bending indicated that the cross section containing a crack usually undergoes general yielding before the initiation of crack growth. This observation originally suggested the "net-section failure stress" criterion for predicting the strength of flawed BWR pipes [*3*]. This criterion is quite useful in predicting limit loads which, for load-controlled loadings, give a reasonable prediction of fracture. But, this simple criterion cannot be applied for displacement-controlled (or compliant loading) situations where stable crack growth and fracture instability are to be predicted. A discussion of the limitations of this approach can be found in Ref *4*.

An approach that allows fracture instability to occur after some amount of stable crack growth is the J-integral/tearing modulus approach. The first application of this approach to the analysis of part-through cracks in reactor piping was reported recently by Zahoor and Kanninen [*5*], who considered the stability of radial growth of surface cracks in rigid piping systems. The present paper discusses first the significant results of the work in Ref *5* relating to the fracture mechanics-based leak-before-break analysis, that is, the propensity of part-through cracks to grow predominantly radially through the pipe wall. Following this, the stability analysis of a part-through crack in a compliant piping system is presented. This analysis, although a direct extension of our earlier papers [*5,6*], provides the necessary tools for the analysis of the mathematically more difficult problem of a variable-depth part-through crack in a pipe under bending. Using the analysis of Ref *5*, the predictions are made for the load and displacement at initiation of part-through cracks to show the predictive capability of the method. Additional results are then presented which show that reasonably accurate predictions for wall breakthrough can be made using the method presented in this paper. Following this, numerical analyses for stability of radial and circumferential growth are presented for two different piping compliance systems. The combined results of the two types of analyses provided an assessment of leak-before-break for flawed piping systems.

[3]The italic numbers in brackets refer to the list of references appended to this paper.

Part-Through Cracks in Bending

In this section we review briefly an analysis result from our earlier work [5] on the behavior of part-through cracks in pipes under large bending loads. Figure 1 shows the cross section of the flawed pipe. As shown, the part-through crack is assumed in the circumferential plane. For simplicity of illustration, the bending moment is assumed to have been applied through a four-point-bend loading system as shown in Fig. 2. (Notice that the spring shown is not required for this discussion, but it is required for the analysis of compliant piping systems that is discussed in a later section.) The pipe is oriented such that the flaw is loaded symmetrically in bending. Consistent with the observed behavior of Type 304 stainless steel, it is assumed that the applied load P is so large that it produces gross yielding of the flawed section (Fig. 1). To further simplify the development, it is assumed that $+\sigma_0$ acts on the tension side and $-\sigma_0$ on the compression side of the flawed section where σ_0 is the flow stress.

Under fully plastic bending, the elastic contribution to the load-point displacement may be small compared with its plastic contribution. Hence, the former can be neglected. Assuming that this is the case, the J-integral may be estimated as [5]

$$J = -\frac{2dP_l}{dA}\,\delta_{pl} \tag{1}$$

where

P_l = limit load,
δ_{pl} = load-point displacement due to the plasticity confined in the cracked section, and
A = part-through crack area.

Notice that the foregoing expression for J in Ref 5 does not contain the factor 2. This is an error in our earlier work [5,6]. All J expressions and the first

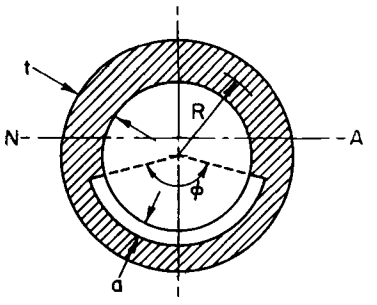

FIG. 1—*Cross section of the crack plane in a circumferentially cracked pipe.*

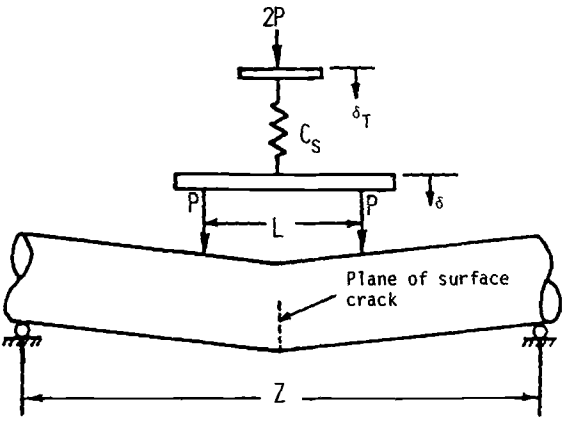

FIG. 2—*Circumferentially cracked pipe in a compliant four-point-bend loading system.*

term in dJ/da must be multiplied by a factor of 2 in order for the analyses in Refs 5 and 6 to be correct. This error, however, does not change any of the conclusions reached in these papers.

Because there are two crack fronts associated with a part-through crack, the change in area, dA, is equal to Rtd (ϕx) for a thin-walled pipe; x is a non-dimensional crack depth defined as fraction of pipe thickness. The foregoing crack area is for a uniform-depth part-through crack; other cases such as a variable-depth crack can be analyzed in exactly the same manner with added mathematical complexity. For a part-through crack, one of the most important question is: What is the relative magnitude of J along the circumferential and radial crack front? If it is assumed that a virtual crack extension occurs at either crack front, then Eq 1 gives simple but useful estimates of J for circumferential and radial crack fronts [5]

$$J_r = 2\beta_1 P_l \delta_{pl}$$

and (2)

$$J_\phi = 2\beta_2 P_l \delta_{pl}$$

where β_1 and β_2 depend upon flaw and pipe dimensions. The interesting feature of this result is that J_r and J_ϕ have identical form and they differ in magnitude only through β-functions.

The relative magnitudes of J_ϕ and J_r can now be determined by dividing their respective expressions. Figure 3 shows the variation of J_ϕ/J_r with crack length ϕ and crack depth a/t [5]. It can be noted from this figure that the ratio J_ϕ/J_r is always less than 1 and decreases monotonically as crack length increases. This result shows the propensity for a predominantly radial growth

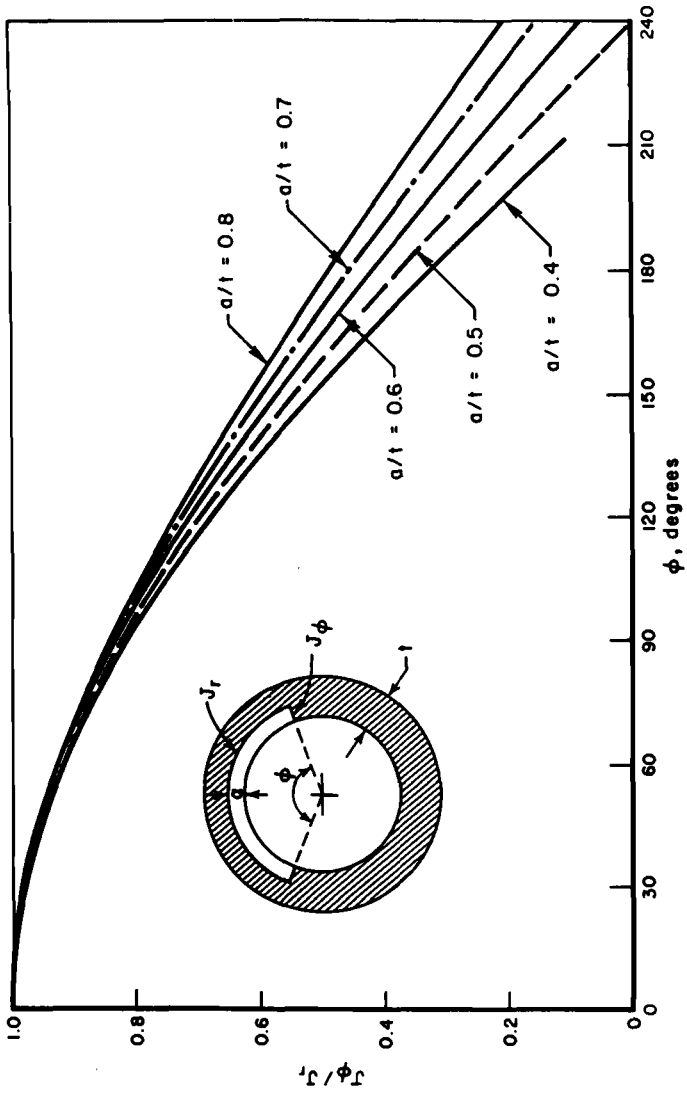

FIG. 3—*Curves of* J_ϕ/J_I *versus* ϕ *[5].*

for part-through cracks in pipes under bending. In a recent work [7], a similar behavior has been shown also for part-through cracks in pipes under tension. This conclusion of predominantly radial growth agrees qualitatively with the experimental data on Type 304 stainless steel [4].

The preceding analysis result suggests that the leak-before-break is very likely for part-through cracks in pipes. But, any approach for quantitative assessment of this possibility must consider crack growth and relative potential for instability of both crack fronts and must include the compliance of piping system. This aspect will be addressed later in this paper.

Comparison of Crack Initiation Predictions with Experimental Data

The motivation for the analysis presented in this section was to check the predictive capability of Eq 2. As discussed in the foregoing section, a circumferential part-through flaw in a pipe subjected to bending would first initiate in the radial direction. Hence Eq 2 for J_r is appropriate for making predictions of radial growth initiation. Specifically, analysis predictions of load and load-point displacements will be made for comparison with the experimental data of Ref 4.

Several experiments on circumferentially cracked 102-mm-diameter (4-in.) Type 304 stainless steel pipes were conducted by Wilkowski [4]. The surface crack experiments were conducted in a rigid four-point-bend loading system under displacement-controlled bending (Fig. 2, without spring). The part-through cracks were located at the inside wall and were of uniform depth. The specimen preparation and testing procedures are described in adequate detail by Wilkowski [4]. Here, major elements of the experimental work will be described briefly for completeness of this discussion. The surface cracks were machined by either a 0.254-mm-thick slitting saw, or by electric discharge machining (EDM). The EDM process used a 10-deg tapered electrode which gave a notch root radius of 0.076 to 0.127 mm. Past experience has shown that these notch radii are sufficient to represent sharp cracks in Type 304 stainless steel.

Three surface crack experiments were selected for prediction. For each case, the data recorded included load, crosshead displacement, crack-mouth-opening displacement at the center of the surface crack, and the electric potential across the center of the surface crack. The electric potential method was used to define crack initiation, maximum load, and stable growth. The details of the method and measurement technique are beyond the scope of this paper. The three surface cracks selected had constant depths of about 60 percent of the pipe thickness and lengths of 25 and 50 percent of the circumference (Table 1). The analysis procedure for load and load-point-displacement predictions was as follows: The limit load was predicted from

$$P_l = 8\sigma_0 R^2 t\{\cos(x\phi/4) - 0.5x \sin(\phi/2)\}/(Z - L) \tag{3}$$

TABLE 1—*Analysis predictions of initiation of radial growth of circumferential part-through wall cracks in 102-mm-diameter Schedule 80 Type 304 stainless steel pipes subjected to bending.*

Experiment	x, Depth/ Thickness	Length, Fraction Circumference	Load, kN			Crosshead Displacement, mm		
			Experimental	Predicted	% Error	Experimental	Predicted	% Error
3S	0.595	0.50	57.51	50.35	−12.4	39.4	35.6	−9.7
6S	0.608	0.25	58.00	64.41	+11.0	42.4	36.8	−13.2
10S	0.575	0.50	55.64	56.31	+1.2	39.0	36.3	−7.2

A flow stress σ_0 of 482 MN/m^2 was assumed. Z and L in the experiment were 1.524 and 0.406 m, respectively. Values of the predicted load P_l are given in Table 1. As shown, good agreement between the predicted and experimental load was found. It should be noted that all part-through crack pipe data reported in Ref *4* indicated the initiation to be very near the maximum load.

The load-point displacement prediction required a value of J at crack initiation. This becomes obvious by examining J_r in Eq 2, giving

$$\delta_{pl} = J_{Ic}/2\beta_1 P_l \tag{4}$$

where

$$\beta_1 = \frac{\sin(x\phi/4) + 2/\phi \sin(\phi/2)}{4Rt\{\cos(x\phi/4) - 0.5x \sin(\phi/2)\}} \tag{5}$$

The initiation J-value for Type 304 stainless steel has been reported by several investigators; the values greatly depend upon the patience of individual investigators, the method used, and the accuracy of the measurement system to detect initiation of growth from severely blunted crack tip [*4,8*]. Moreover, the plastic straining needed to achieve initiation in surface-cracked pipes would be different from what is required for a through-crack geometry whether compact tension, center-cracked panel, or pipe specimen. The values reported for J_{Ic} vary from 0.600 to 2.802 MN/m. We assume a value of 2.802 MN/m, which is felt to be realistic for part-through cracks and piping application.

The elastic contribution to the load-point displacement was calculated from

$$\delta_{ep} = C_{ep} P_l \tag{6}$$

where $C_{ep} = (Z - L)^2 (Z + 2L)/24EI$ is the elastic compliance of the uncracked pipe in four-point bending where I is the moment of inertia of the pipe. The load-point displacement δ was then calculated by adding δ_{ep} and δ_{pl}. This means that the elastic contribution to δ due to the presence of the crack was presumed to be negligible. Because the test fixture was very rigid

compared with the surface cracked pipe, the load-point displacement gives a fairly accurate estimate of the crosshead displacement. The predictions are given in Table 1. Here again, the agreement between the predicted and experimental values is good. It should be noted that δ predictions have about the same accuracy as those of P_l. The agreement given in Table 1 clearly suggests that the J-estimates developed in Ref 5 are reasonably accurate.

Prediction of Wall Breakthrough

Encouraged by the results of crack initiation, it was decided to make prediction of wall breakthrough; that is, the displacement at which a part-through crack would grow unstably to become a through-wall crack. This type of prediction requires the computation of applied dJ_r/da. In this section, we present a method that can be used to develop predictive curves of displacement at wall breakthrough for part-through cracks. The length of the part-through crack was selected to be 50 percent of the pipe circumference ($\phi = \Pi$). In order to compare the prediction with experimental data, Experiment No. 10S [4] for which initiation was predicted in the preceding section was selected.

Figure 4 shows the load-displacement record of Experiment 10S [4]. The various stages of crack growth are shown: initial flaw at one, onset of radial instability at two, end of instability or through-crack development at three, and through-crack development to entire length of the surface crack at four. This experiment was conducted in displacement-controlled bending. Our interest is to predict the displacement at the onset of radial instability. The prediction was based upon a comparison of the applied dJ_r/da against its material counterpart.

The material J-resistance curve used is shown in Fig. 5. This curve was developed using surface flawed pipe experimental data on 102-mm-diameter pipes [4]. Because the surface cracks did not grow uniformly in the radial direction, an average radial growth was defined assuming equal growth all along the length of the surface flaw and it is denoted as $\widetilde{\Delta a}$. Radial crack growth was measured by heat-tinting of the flaw during experiments. The J-values were calculated, using appropriate expression in Eq 2. The J-$\widetilde{\Delta a}$ data points from several experiments were used to develop the resistance curve shown in Fig. 5. Further details can be found in Ref 4.

The expression used to calculate applied dJ_r/da was taken from Ref 5

$$\frac{dJ_r}{da} = 2R\phi c_{ep}(\beta_1 P_l)^2 + \frac{\gamma_r}{t} J_r \tag{7}$$

Figure 6 shows a plot of dJ/da versus J for crack growth in the radial direction. The solid curves shown are for crack depths ranging from 10 to 90 percent of the thickness. The calculations were performed as follows. First, J_r

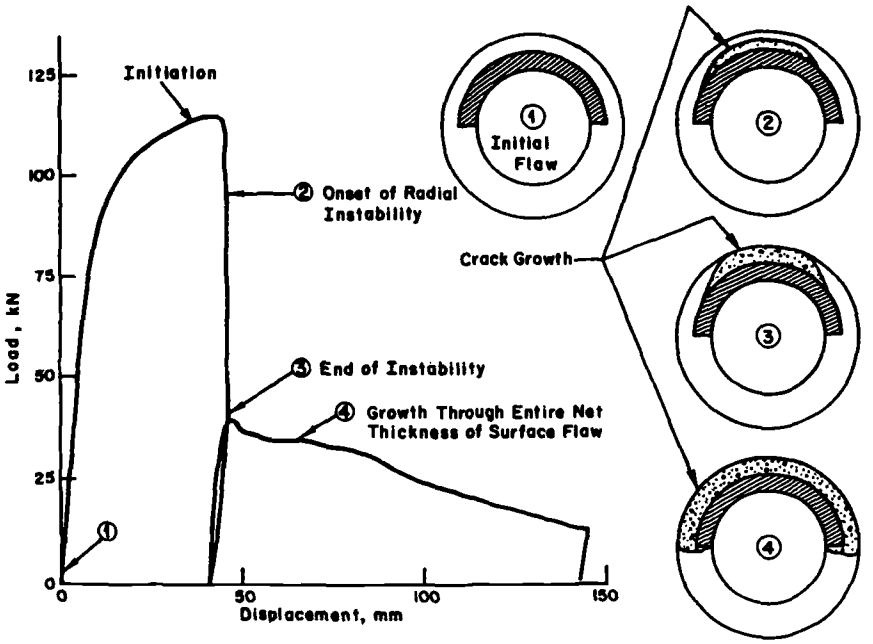

FIG. 4—*Load-displacement record of a 57.5 percent depth part-through-wall cracked pipe in four-point-bend loading [4].*

was calculated from Eq 2 using a σ_0-value of 482.5 MN/m^2 and assuming increasing values of δ_{pl}. It was then substituted into Eq 7 and dJ_r/da was obtained. The distances Z and L in the four-point bend loading system were 1.524 and 0.406 m, respectively. The calculational pairs for each crack depth were plotted giving straight lines as shown in Fig. 6. The material crack growth resistance behavior is shown by the dashed curve. This curve was derived from the J-resistance curve shown in Fig. 5.

The intersection of the applied curve with the material curve gave a critical value of J for each x at which unstable radial crack growth is predicted. These critical J_r-values were then used in Eqs 2, 3, and 6, giving load-point displacements at wall breakthrough. The results are shown in Fig. 7. It can be seen that the predicted result for 50 percent circumference and 57.5 percent depth part-through crack agrees with the experimental data shown in Fig. 4.

Stability of Growth of Part-Through Cracks

In our earlier work [*5*], we considered the stability of radial growth of part-through cracks. Here, we extend the analysis to include the stability of circumferential growth of part-through cracks. Additionally, crack stability is

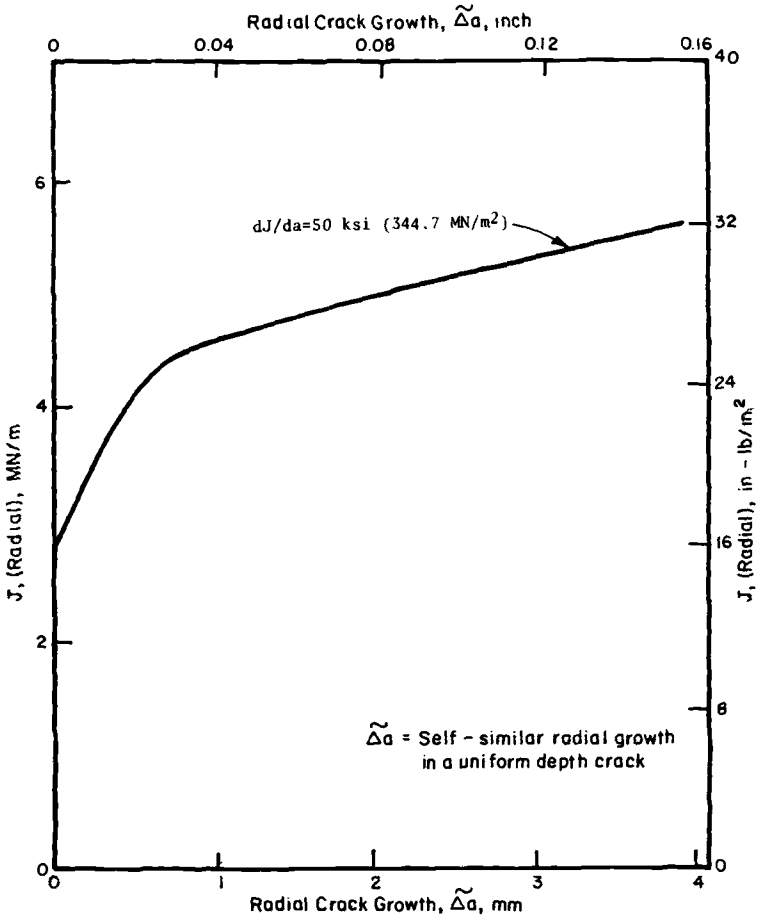

FIG. 5—*Type 304 stainless steel J-resistance curve for radial growth of part-through-wall cracks in pipes.*

now derived in terms of crack area rather than crack length or depth. This allows the consideration of variable depth part-through cracks. The analysis assumes a spring in series with the cracked pipe (Fig. 2). The spring can be interpreted as representing the additional compliance of a piping system. The total displacement, δ_T, can be expressed as (see Fig. 2)

$$\delta_T = \bar{c}P + \delta_{pl} \tag{8}$$

where $\bar{c} = 2c_s + c_{ep}$ where c_s and c_{ep} are the compliance of the linear elastic spring and that of the uncracked pipe, respectively. Assuming fully plastic condi-

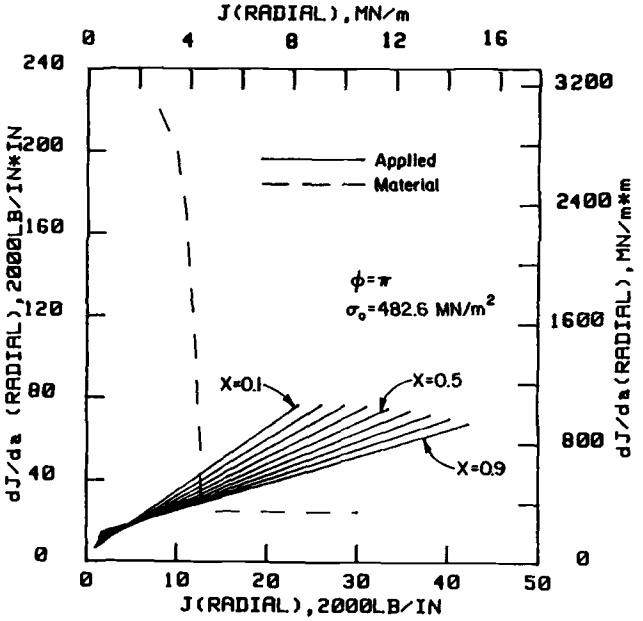

FIG. 6—dJ/da *versus* J *for radial crack growth in a 102-mm-diameter pipe in bending.*

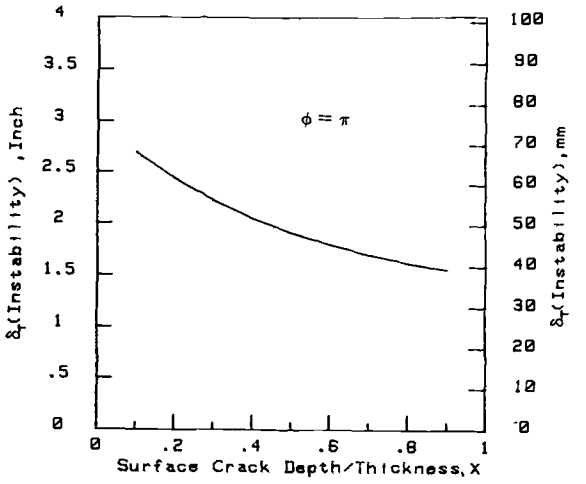

FIG. 7—*Load-point displacement versus* x *for radial crack growth instability in a 102-mm-diameter pipe in bending.*

tions and crack growth under displacement-controlled bending (δ_T = constant) gives

$$\frac{d\delta_T}{dA} = 0 = \bar{c}\,\frac{dP_l}{dA} + \frac{d\delta_{pl}}{dA} \tag{9}$$

where dA denotes the increment in crack area. For the example in Fig. 1, dA is equal to $Rtd\,(\phi x)$. Equation 9 is not restricted to uniform depth cracks. Surface cracks having variable depth can be considered using Eq 9. An example of variable-depth flaws is part-elliptical or part-circular flaws. The quantity $d\delta_{pl}/dA$ can be derived from Eq 1. Equation 9 then becomes

$$\left(\frac{dJ}{dA}\right)_{\delta_T} = \left(\frac{\partial J}{\partial A}\right)_{\delta_{pl}} - \bar{c}\,\frac{dP_l}{dA}\left(\frac{\partial J}{\partial \delta_{pl}}\right)_A \tag{10}$$

For simplicity, let us consider the flaw case shown in Fig. 1. The change in area for circumferential growth is equal to $Rtxd\phi$. The partial derivatives of J can be derived using Eq 1 through 3. The derivation is very similar to that in Ref 5; therefore, it is omitted here. The final result is

$$\frac{dJ_\phi}{d(R\phi/2)} = 4\bar{c}xt(\beta_2 P_l)^2 + \frac{2\gamma_2}{R}J_\phi \tag{11}$$

where

$$\gamma_2 = \frac{\partial F_2/\partial\phi}{F_2}$$

and

$$F_2 = \sin(x\phi/4) + \cos(\phi/2)$$

The foregoing result can be used to develop applied curves for circumferential growth of part-through cracks. Through-wall cracks analysis is a special case of the foregoing result and is easily obtained by substituting $x = 1$ in Eq 11. The result for radial growth in compliant piping can be derived in a similar manner. The only change in Eq 7 is that c_{ep} is replaced by c.

In general, the analysis for stability of growth of part-through cracks requires the determination of applied dJ/da for both the circumferential and radial crack fronts. Previous work [8,9] has considered stability of through-wall cracks with the presumption that all part-through cracks will become through cracks. Because crack growth resistance may be different in radial and circumferential directions, a mere comparison of applied dJ/da for the two directions will not provide enough information about the leak-before-break behavior. Therefore, for each direction (radial and circumferential) a

separate comparison of the applied and material dJ/da is required to determine if instability is possible in either direction. The results of the analysis for each direction can then be combined to define leak-before-break potential for surface cracks. This is explained by a safety assessment diagram defined and developed in the next section.

Development of Safety Assessment Diagram

Consider a part-through crack, growing stably under a fixed or slowly varying displacement-controlled bending, that reaches the radial crack growth instability point. If the resulting through-the-thickness crack is stable, then the pipe will remain intact, at least until the displacement increases further. If this occurs, then a leak-before-break condition has been demonstrated.

The proposed procedure for the development of safety assessment diagram is as follows: First, calculate applied dJ_r/da for several surface cracks and compare them with the material counterpart to determine the instability point. Using this result, compute the load-point displacement from the first of the two expressions in Eq 2. Secondly, calculate the $dJ_\phi/d(R\phi/2)$ for the same cracks using Eq 11 and compare it with its material counterpart to determine instability point, if any. Using this result, calculate the load-point displacement using the second of the two expressions in Eq 2. Finally, compare the displacement pairs to determine whether radial instability occurs first. If it is so, then leak is predicted. If not, break is predicted. This procedure will define certain part-through cracks that will produce a leak and others that will not. It is realized that these results will depend upon $\bar{c}$ because it influences the applied values of dJ/da. Also, relative differences between the resistance curves influence the final result.

The safety assessment diagrams were developed for two piping compliances. The first example considered a 102-mm-diameter Schedule 80 Type 304 stainless steel piping system. For illustration purposes a straight pipe with two hangers, symmetrically placed, was considered. This example is identical to the four-point bend system of Fig. 2 but without spring. The second example considered a spring in series with the pipe as in Fig. 2. The compliance of the spring was chosen to be about two times that of the pipe.

In the first example, the pipe length was assumed as 6.4 m. The spacing between the hangers was assumed as 4.27 m, which is the maximum allowable spacing in 102-mm-diameter lines of stainless steel construction [*10*]. These dimensions are then Z and L, respectively, for our analysis purpose. Analyses such as those depicted in Fig. 6 were performed for $\phi = \Pi/6$, $\Pi/3$, $\Pi/4$, $\Pi/2$, and Π. The results are shown by the solid curves on Fig. 8.

The dashed curve resulted from a similar analysis for crack instability of through-the-thickness cracks. The J-resistance curve used in this analysis is shown in Fig. 9. The details of the method and data used in the development of this resistance curve can be found in Ref *6*. It should be noted that the

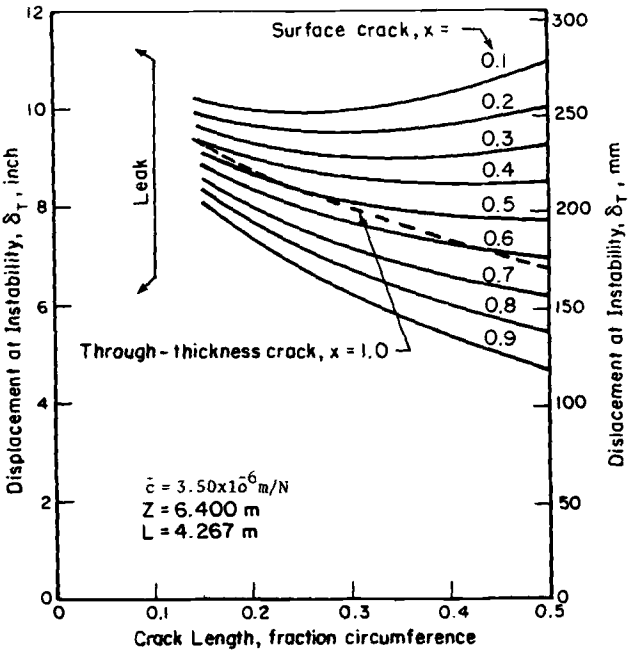

FIG. 8—*Instability predictions for part-through-wall and through-wall cracks in 102-mm-diameter pipes.*

J-values shown on this figure are corrected for the factor 2, which was missed due to an error in our earlier work [*6*]. The procedure used for through-crack instability prediction is as follows: For each assumed ϕ, J_ϕ was chosen to be equal to J_c, the J-value for initiation of through-the-thickness crack. Then, $dJ_\phi/d(R\phi/2)$ was calculated using Eq 11. Next, a small amount of crack growth was assumed and the applied J_ϕ was obtained via the J-resistance curve using the statement of equilibrium. The crack functions were computed using crack growth and substituted into Eq 11 to obtain $dJ_\phi/d(R\phi/2)$. This procedure was repeated for other assumed crack growth. Thus, an applied curve was developed for each selected initial crack length which was compared with the material curve of Fig. 9. The critical values of J at instability were then converted into load-point displacements. The predicted load-point displacements and the crack lengths at instability were plotted giving the dashed curve in Fig. 8.

A leak region, marked by the area on left of the vertical line, is shown in Fig. 8. In this region (ϕ less than II/9), any part-through crack is predicted to have stable radial crack growth; that is, applied and material curves do not intersect. The intersection of the part-through crack curves and through-crack curve defines the leak-before-break behavior. That is, the intersection

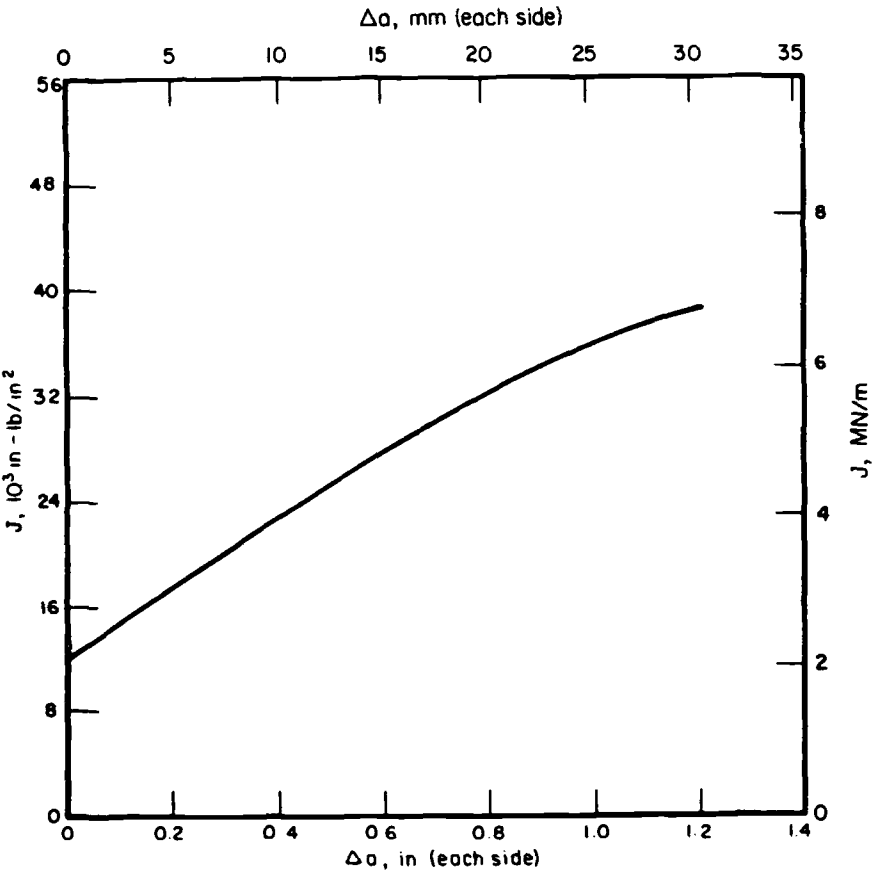

FIG. 9—*Type 304 stainless steel J-resistance curve for circumferential growth of through-wall cracks [6].*

points define combinations of crack length and depth of part-through cracks that are just sufficient to cause fracture. This result is shown in Fig. 10 in the form of a safety assessment diagram. Two regions are defined: In the leak region, when a part-through crack becomes a through crack it will be stable because additional displacement (loading) will be required for growth of through-crack. In the fracture region, a part-through crack that becomes a through crack would become unstable immediately and would result in pipe fracture without any leak warning.

For the purpose of comparing the leak-before-break behavior of different lines, it is convenient to present the result in terms of piping compliance as this is the most important input parameter. For the problem just considered, $\bar{c}$ was calculated as 3.50×10^{-6} m/N. In the second example, a spring having a C_s of 6.295×10^{-6} m/N was assumed in series with the pipe. The di-

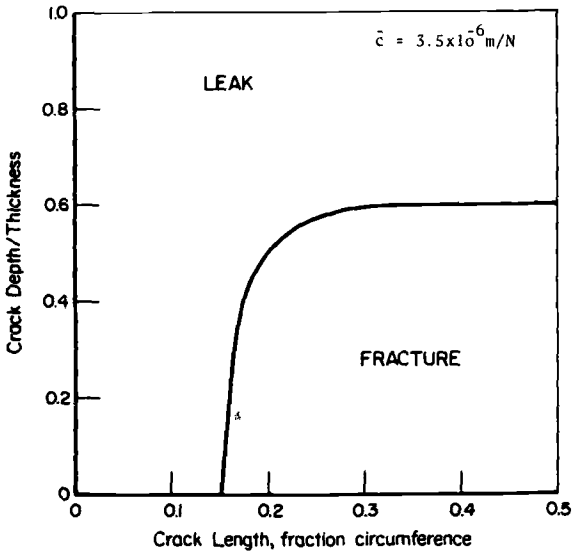

FIG. 10—*Safety assessment diagram for a 6.4-m-long, 102-mm-diameter pipe subjected to displacement-controlled bending.*

mensions of the pipe and other input parameters were exactly the same as in the first example. The spring compliance is approximately two times that of the pipe. This represents a relatively rigid piping system ($\bar{c} = 1.6 \times 10^{-5}$ m/N). A safety assessment diagram was developed using the procedure just described. The final result is compared with the previous example in Fig. 11. As expected, the fracture region increases slightly due to the increase in compliance. Curves such as those shown in Fig. 11 can be developed for several values of $\bar{c}$ representing compliance of real piping systems. The main feature of the proposed safety assessment diagram is that they can be developed in advance for each potential crack location. If a part-through crack is detected during in-service inspection, then it can be quickly evaluated to verify if leak-before-break behavior can be demonstrated.

Discussion and Conclusions

The plastic fracture mechanics methodology elaborated in this paper provides a means of predicting the instability of wall breakthrough and subsequent instability of through cracks. It was shown that accurate predictions are possible for initiation of radial growth and for instability of wall breakthrough. The method clearly delineated the wall breakthrough from final fracture event. This aspect was not considered in any previous work [*8,9*]. Thus, the assessment of leak-before-break in cracked pipes is now possible using a rational and sound method.

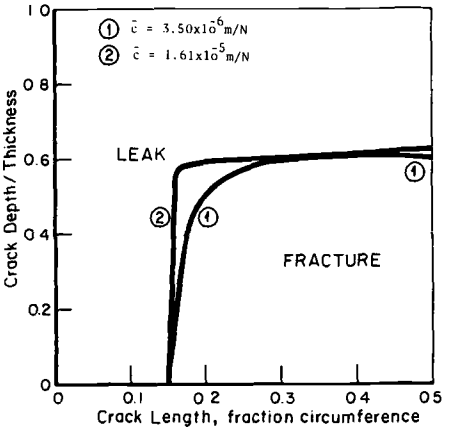

FIG. 11—*Effect of piping compliance on the leak-before-break behavior of part-through cracks.*

There are two aspects that deserve further work in any leak-before-break analysis. One of them is the calculation of compliance of the real piping system which is needed in the form of $\bar{c}$. The other is the issue of J-resistance curves for radial and circumferential growth in pipes. The work by the authors [*4,6*] is the first effort in developing such information directly from pipe specimens. Additional refinements in the analysis techniques and evaluation of data are needed to insure accurate resistance curves and consequently useful predictions. The analysis equations presented in this paper assume fully plastic bending conditions for all part-through cracks. This assumption may not be valid for ferritic piping. Further work is suggested where linear elastic and fully plastic fracture mechanics solutions can be combined. The instability analyses can then be developed along the lines of Refs *4-7, 11*.

Acknowledgments

The work reported in this paper was performed for the Electric Power Research Institute (EPRI) BWR pipe integrity analysis program under project T118-2. The authors would like to thank Dr. D. M. Norris, Jr. of EPRI for his support and encouragement of the work. This work was completed while the first author was associated with Battelle Memorial Institute, Columbus Laboratories.

References

[*1*] "Investigation and Evaluation of Cracking in Austenitic Stainless Steel Piping of Boiling Water Reactor Plants," NUREG-75/067, Pipe Crack Study Group, Nuclear Regulatory Commission, Washington, D.C., 1975.

[2] "Investigation and Evaluation of Stress-Corrosion Cracking in Piping of Light Water Reactor Plants," NUREG/0531, Pipe Crack Study Group, U.S. Nuclear Regulatory Commission, Washington, D.C.

[3] Kanninen, M. F. et al, "Towards an Elastic-Plastic Fracture Mechanics Predictive Capability for Reactor Piping," *Nuclear Engineering and Design*, Vol. 48, 1978, pp. 117–134.

[4] Kanninen, M. F. et al, "Instability Predictions for Circumferentially Cracked Type-304 Stainless Steel Pipes under Dynamic Loadings," EPRI NP-2347, Electric Power Research Institute, Palo Alto, Calif., Vol. 2, April 1982.

[5] Zahoor, A. and Kanninen, M. F., *Transactions*, American Society of Mechanical Engineers, *Journal of Engineering Materials and Technology*, Vol. 103, No. 3, 1981, pp. 194–200.

[6] Zahoor, A. and Kanninen, M. F., *Transactions*, American Society of Mechanical Engineers, *Journal of Pressure Vessel Technology*, Vol. 103, Nov. 1981, pp. 352–358.

[7] Zahoor, A. and Norris, D. M., "Ductile Fracture of Circumferentially Cracked Type-304 Stainless Steel Pipes in Tension," to be presented at the Symposium on Behavior of Circumferential Cracks in Pressure Vessels and Piping, American Society of Mechanical Engineers, June 1983.

[8] Cotter, K. H., Chang, H.-Y., and Zahoor, A., "Application of Tearing Modulus Stability Concepts to Nuclear Piping," EPRI Report NP-2261, Electric Power Research Institute, Palo Alto, Calif., Feb. 1982.

[9] Tada, H., Paris, P. C., and Gamble, R. in *Fracture Mechanics, ASTM STP 700*, American Society for Testing and Materials, 1980, pp. 296–313.

[10] "Pipe Hangers and Supports—Selection and Applications," MSS Standard Practice SP-69, Manufacturer's Standardization Society of the Valve and Fittings Industry, July 1966.

[11] Zahoor, A., "Tearing Instability of Elastic-Plastic Crack Growth," D.Sc. Dissertation, Washington University, St. Louis, Mo., Aug. 1978.

Sampath Ranganath[1] *and Hardayal S. Mehta*[1]

Engineering Methods for the Assessment of Ductile Fracture Margin in Nuclear Power Plant Piping

REFERENCE: Ranganath, S. and Mehta, H. S., **"Engineering Methods for the Assessment of Ductile Fracture Margin in Nuclear Power Plant Piping,"** *Elastic-Plastic Fracture: Second Symposium, Volume II—Fracture Resistance Curves and Engineering Applications, ASTM STP 803*, C. F. Shih and J. P. Gudas, Eds., American Society for Testing and Materials, 1983, pp. II-309–II-330.

ABSTRACT: When a crack is discovered during inspection of a piping component in a nuclear power plant, the decision on replacement is dependent on the available design margin of the pipe in the presence of the crack. This paper describes the development of engineering methods to assess the design margin in cracked pipes. Procedures are outlined to evaluate cracks in piping, using methods consistent with the American Society of Mechanical Engineers (ASME) Code design basis, and to develop failure diagrams for piping. A criterion based on net section collapse is shown to predict adequately the load capability of piping with cracks. The predictions of the net section collapse approach are shown to be consistent with results from elastic-plastic fracture analysis based on J-integral and R-curve methods. Finally, the methodology is used to recommend acceptance criteria for flaws in power plant piping. The proposed criteria assure that the minimum safety margins inherent in the ASME Code are preserved during operation. Since allowable flaw sizes can be determined using information already available in piping stress reports, the proposed criteria offer a simple conservative method for assessing flaws in piping.

KEY WORDS: net-section collapse, circumferential cracks, failure diagrams, nuclear piping, flaw assessment, ductile fracture, J-integral, estimation scheme, elastic-plastic fracture

When a crack is discovered during inspection of a piping component in a nuclear power plant, a decision has to be made whether the repair/replacement of the component is warranted immediately or if it could be deferred until a convenient time when it could be made with minimum impact on plant availability. The decision would be based on the comparison of the discovered

[1]Manager and senior engineer, respectively, Mechanics Analysis Subsection, General Electric Co., San Jose, Calif. 95125.

crack with the critical crack size for given service conditions. For components made of materials in which brittle fracture is the failure mode, the critical crack size can be determined on the basis of linear elastic fracture mechanics (LEFM) methods. However, for piping components made of materials like stainless steel and high-toughness carbon steel, failure is characterized by extensive yielding and subsequent plastic instability. For such ductile materials, therefore, it is necessary to use elastic-plastic fracture mechanics or plastic collapse methods in establishing critical crack sizes for given service conditions. The purpose of this paper is to describe methods for the evaluation of flaws in ductile piping and to develop simple flaw acceptance criteria. The focus will be on part-through and through-wall circumferential cracks since observed field cracks are generally located near the circumferential girth welds in piping.

The methodology used to determine the acceptance flaw size is to first evaluate the critical flaw size for the applied loading conditions. The acceptance flaw size is then determined by requiring a suitable design margin on the critical flaw conditions. The critical flaw size is determined by using limit-load concepts. It is assumed that a pipe with a circumferential crack is at the point of incipient failure when the net section at the crack develops a plastic hinge. Plastic flow is assumed to occur at a critical stress level, σ_f, called the flow stress of the material. The criterion is simple to apply and has been shown to be effective in predicting failure of stainless steel pipes containing circumferential cracks [*1,2*].[2] Using this method, referred to hereafter as the net-section collapse approach, critical flaw parameters can be represented in the form of a failure diagram defining the combination of critical crack depth and length at which collapse occurs for a given applied stress. The advantage of the net-section collapse approach is that it is consistent with the American Society of Mechanical Engineers (ASME) Boiler and Pressure Vessel Code [*3*] (hereafter referred to as "ASME Code" or "Code") piping design basis and uses information already available in piping stress reports. No additional analysis or materials data are required in this assessment. Although the crack assessment procedure used here is based on collapse theory, the existence of a critical net section stress can also be justified by a general yield fracture mechanics analysis [*4*]. To compare the present method with elastic-plastic fracture mechanics criteria, failure predictions were made for (1) crack initiation based on J_{Ic}, and (2) maximum load assuming J-controlled crack growth. Comparisons were made for through-wall cracks and part-through circumferential cracks in both stainless steel and carbon steel piping under axial loads. The elastic-plastic fracture estimation scheme of Shih et al [*5,6*] was used for the J-computations and the crack growth analysis was performed using typical J-R curves for the material. Comparisons were also made with the British two-parameter R-6 criterion [*16*].

[2]The italic numbers in brackets refer to the list of references appended to this paper.

Finally, the failure diagrams developed for different applied stress levels were used to establish acceptance criteria for cracks in piping designed to the ASME Code. The approach used in establishing flaw acceptance standards was to require that the minimum safety margins of the Code be retained throughout plant operation even with cracks. Using this procedure, acceptable flaw sizes can be conveniently determined as a function of stress level for the different plant operating conditions.

Net Section Collapse Formulation

Consider a circumferential crack of length, ℓ, and constant depth, d, located on the inside surface of a pipe (Fig. 1). In order to determine the point at which collapse occurs, it is necessary to apply the equations of equilibrium assuming that the cracked section behaves like a hinge. For this condition, the assumed stress state at the cracked section is as shown in Fig. 1 where the maximum stress is the flow stress of the material, σ_f. Let P_m be the membrane stress in the longitudinal direction in the uncracked section of the pipe and P_b be the bending stress. Equilibrium of longitudinal forces and moments about the axis give the following equations

Case 1: *Neutral axis located such that* $\alpha + \beta < \pi$:

$$\beta = \frac{(\pi - \alpha d/t) - (P_m/\sigma_f)\pi}{2} \tag{1}$$

$$P_b = \frac{2\sigma_f}{\pi}(2 \sin \beta - d/t \sin \alpha) \tag{2}$$

Case 2: *Neutral axis located such that* $\alpha + \beta > \pi$ *(assume crack takes compression)*:

$$\beta = \frac{\pi(1 - d/t - P_m/\sigma_f)}{2 - d/t} \tag{3}$$

$$P_b = \frac{2\sigma_f}{\pi}(2 - d/t) \sin \beta \tag{4}$$

Case 3: *Through-wall crack; pressure loading only*:

$$P_m = \frac{2\sigma_f}{\pi}\left[\frac{\pi}{2} - \frac{\alpha}{2} - \sin^{-1}\left(\frac{\sin \alpha}{2}\right)\right] \tag{5}$$

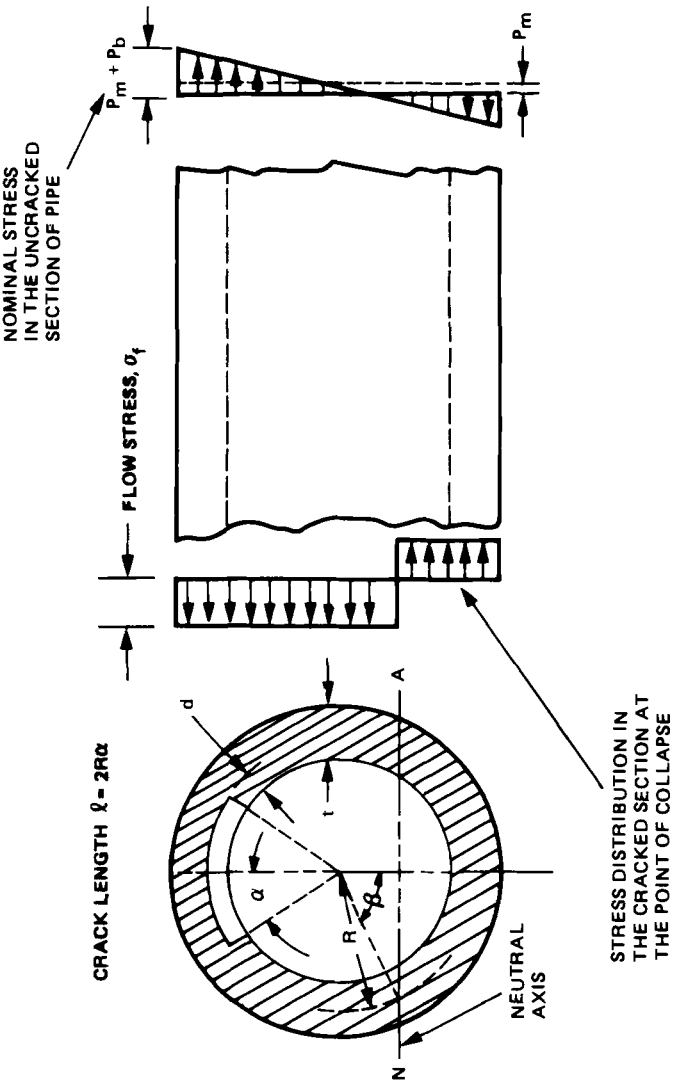

FIG. 1—*Schematic showing stress distribution in a cracked pipe at the point of collapse.*

where

t = pipe thickness,
α = half crack angle as shown in Fig. 1, and
β = angle that defines location of neutral axis.

The foregoing equations together define the combinations of α and d/t for which failure by collapse is predicted under the given applied stresses, P_m and P_b.

It should be noted that only the stresses due to externally applied loads need to be considered in evaluating P_m and P_b. Such loads include pressure, deadweight, seismic inertia, and water hammer, and are defined as primary loads by the ASME Code [3]. Stresses due to temperature gradients and due to thermal expansion loads need not be considered in this analysis since such stresses do not affect the net section collapse load.

The preceding equations can be solved by considering a given value of crack depth, d, and determining the angle α at which collapse is predicted for specified values of P_m, P_b, and σ_f. The material flow stress, σ_f, is in general a function of the yield strength, S_y, and ultimate strength, S_u, of the material.

Figure 2 shows a failure analysis diagram developed for stainless steel piping with the curves shown for two stress levels—one corresponding to the normal operating condition and the other corresponding to the design condition which includes limiting earthquake loads. The value of flow stress was assumed as 331 MPa (48.0 ksi) based on experimental data. For the normal operation condition, the primary stress of interest is the axial membrane stress due to internal pressure. This stress was assumed as 41 MPa (6 ksi). Other primary stresses were negligible. For the design condition (which includes the operating basis seismic loads), the ASME Code [3] stress limit is $(P_m + P_b) = 1.5^3 S_m$ [S_m for stainless steel = 110 MPa (16.0 ksi)]. It should be noted that this is the maximum stress permitted by the Code and, in reality, the calculated stresses are usually well below the Code limits.

The failure analysis diagram of Fig. 2 indicates that stainless steel pipes can tolerate large circumferential cracks without failure. For example, under normal operating conditions, a through-wall crack extending through 55 percent of the circumference is tolerated.

Available field observed data on circumferential cracks in austenitic pipes and safe ends are also shown on the failure analysis diagram (Fig. 2) in order to make a qualitative estimate of typical safety margins. The nominal pipe size in these data varies from 5 to 25 cm (2 to 10 in.). It is seen that the field data on cracks are well within the safe region. Moreover, the data show a tendency for the pipe to leak before the collapse load point is reached, thus indicating a strong trend for a "leak before break" condition. Also, since field

[3] S_m is the design stress-intensity value defined in the ASME Code and is dependent on the minimum yield and ultimate strength of the material.

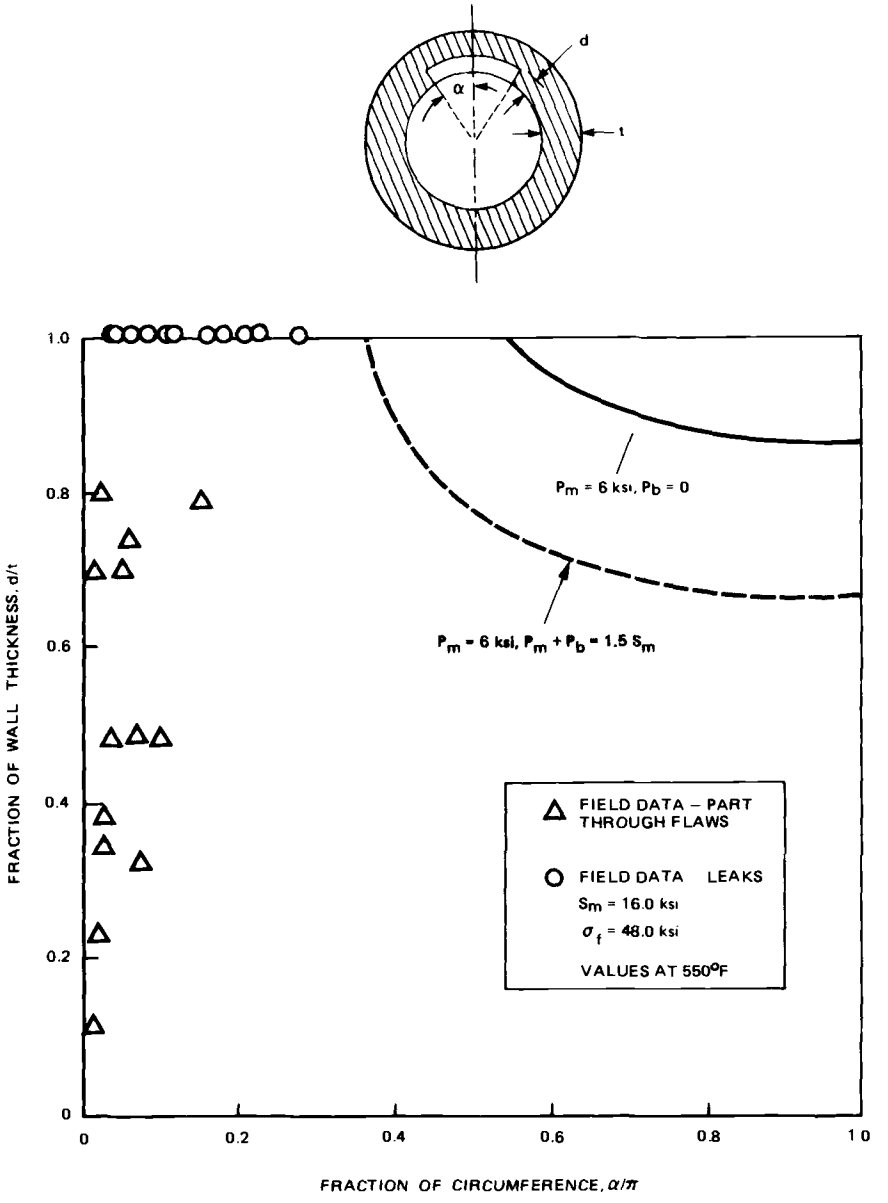

FIG. 2—*Comparison with field data—stainless steel piping (ksi = 6.90 MPa).*

cracks have varying depths and are seldom aligned in the same plane, the idealized representation used here would enhance the conservatism.

Comparison with Elastic-Plastic Fracture Mechanics Predictions

The criterion used in this assessment of the strength of circumferentially cracked pipes is based on the concept of a critical net-section flow stress. The existence of a critical net-section stress for crack initiation in a center-cracked panel (CCP) has been justified by Smith [*4*] using the results of fully plastic solutions developed by Shih et al [*5,6*]. By relating the crack opening displacement, and thereby J, to the net-section stress, Smith concluded that except for a slight panel width dependence, the net-section stress at crack initiation in a CCP is essentially constant for highly ductile materials such as stainless steel. Recently Zahoor and Kanninen [*7*] examined stability of part-through circumferential cracks in pipes subjected to bending loads by developing J-integral expressions based on a critical net-section stress at initiation. Thus, the net-section collapse approach used here to evaluate piping flaws is consistent with elastic-plastic fracture concepts also. To provide additional confirmation that the net-section collapse method is conservative relative to elastic-plastic fracture mechanics (EPFM) predictions, the two methods were compared using two examples—a through-wall crack and a fully circumferential part-through crack in a pipe subjected to axial loading. More general cases of axial and bending loads as well as part-through surface cracks could not be evaluated because of the limited number of EPFM solutions available in the literature for cracks in pipes.

In comparing the net-section collapse method with the EPFM predictions, both initiation, that is, attainment of J_{Ic}, and maximum load, including stable crack growth, were used as the failure criteria. Two high-toughness piping materials—Type 304 stainless steel and SA106 Grade B carbon steel—were considered. The J-integral calculations were performed using the estimation scheme [*8*] in which elastic and fully plastic solutions are added to obtain the value of J-integral in the elastic-plastic range. In computing the elastic-plastic solutions, the material stress-strain curve is characterized by the Ramberg-Osgood form as follows:

$$\left(\frac{\epsilon}{\epsilon_0}\right) = \left(\frac{\sigma}{\sigma_0}\right) + \alpha\left(\frac{\sigma}{\sigma_0}\right)^n \tag{6}$$

The values of the parameters n, α, σ_0, and ϵ_0 used in the J-integral computations are shown in Table 1. Once the applied J-values are computed, failure predictions can be made by comparing the applied J and dJ/da with the material properties: J_{Ic}, the crack initiation toughness measure, and dJ_{MAT}/da, the slope of the J-R curve. The room temperature J_{Ic}-values for Type 304 Stainless Steel reported in the literature [*9,10*] range from 788.0 to 1365.9

TABLE 1—*Material properties used in elastic-plastic fracture mechanics comparison.*

Material	Properties used in Elastic-Plastic Fracture Evaluation	Properties used in Net-Section Collapse Evaluation
Stainless steel type 304	J_{Ic} = 4000 in. · lb/in.^{2} 8000 in. · lb/in.^{2} $\frac{dJ}{da}$ = 13 000 lb/in.^{2} Ramberg-Osgood parameters σ_0 = 30.0 ksi ϵ_0 = 0.001 n = 5.42 α = 1.69	σ_f = 52.5 ksi
Carbon steel SA106 Grade B	J_{Ic} = 1500 in. · lb/in.^{2} $\frac{dJ}{da}$ = 30 000 lb/in.^{2} Ramberg-Osgood parameters σ_0 = 27.0 ksi ϵ_0 = 0.0009 n = 6.98 α = 1.08	σ_f = 47.5 ksi

NOTES:
1 in. · lb/in.^{2} = 0.17512 kJ/m^2
1 lb/in.^{2} = 6.9 kPa.
1 ksi = 6.90 MPa.

kJ/m^2 (4500 to 7800 lb · in./in.^{2}). In comparisons reported here, two values of J_{Ic}, 700.5 to 1401.0 kJ/m^2 (4000 and 8000 lb · in./in.^{2}), were used. Since from the allowable crack size assessment standpoint it is desirable to underpredict the maximum load, a lower-bound dJ/da-value of 93 MPa (13 500 lb/in.^{2}) was selected based on experimentally determined J-R curves for circumferentially cracked stainless steel pipes included in Ref *10*. Note that in some cases such as investigation of stability of part-through circumferential cracks, choice of a lower-bound dJ/da may not be appropriate. The J_{Ic} and dJ/da-values for carbon steel were obtained from Ref *11*. The flow stress σ_f used in the net-section collapse predictions was based on the material yield and ultimate strengths given in the ASME Code. Table 1 shows all the material properties used in the analysis.

In the following sections, details of the comparison between the net-section collapse and the EPFM predictions are presented for two examples: a through-wall flaw and a 360-deg part-through circumferential flaw in a pipe under axial loading.

Through-Wall Flaws: Stainless Steel Pipe

Reference *12* includes a curve of J versus applied axial stress (σ_m) for a 66-cm-diameter (26 in.) pipe with a quarter circumference through-wall flaw. A bilinear stress-strain curve with a yield strength, S_y, of 276 MPa (40 ksi) and a tangent modulus, E_t, of 1152 MPa (167 ksi) was assumed in that analysis. This J-curve is derived directly from a shell model and thus does not involve any shell correction. From that curve, the axial stress corresponding to J of 700.5 kJ/m^2 (4000 in. · lb/in.^{2}) was determined as 152 MPa (22 ksi). Thus, based on crack initiation as failure criterion, the elastic-plastic fracture calculations predict an allowable through-wall flaw size of one quarter of the circumference under an applied axial stress of 152 MPa (22 ksi). This data point is shown in Fig. 3. The net-section collapse failure line corresponding to an axial stress of 152 MPa (22.0 ksi) is also shown in Fig. 3. This failure line is given by Eqs 1-4 with $P_m = 152$ MPa (22 ksi) and $P_b = 0$. It is seen that crack initiation occurs before the onset of net-section collapse. However, when crack growth is accounted for, the maximum load predicted by EPFM is expected to be higher than the net section collapse load.

The foregoing comparison was based on J-solutions for a specific pipe size and crack length. General estimation schemes that permit J-computation for any pipe size and crack lengths are not available at this time. Instead, center-cracked plate solutions with shell correction factors were used to make the comparison between EPFM and net-section collapse predictions for different pipe size and crack length combinations.

Shell correction factors for through-wall circumferential cracks in shells subjected to axial membrane stress are given, among others, by Rooke and Cartwright [*13*] and Delale and Erdogan [*14*]. The shell correction factor in these references is defined as the nondimensional ratio of K in the shell to $\sigma_m \sqrt{\pi a}$, where σ_m is the applied remote axial stress. In this paper, the shell correction factor is defined as the ratio of J in the shell to J in a CCP of width equal to the circumference of the shell. The values in Refs *13* and *14*, which are essentially identical, were reevaluated this way and are plotted in Fig. 4 as a function of the nondimensional parameter λ ($= a\sqrt{Rt}$; a = one-half the crack length, R and t are shell radius and thickness, respectively). While derived on a linear elastic basis, these factors are believed to be applicable in the elastic-plastic range. Paris [*15*] has used similar factors in the elastic-plastic evaluation of postulated cracks in pressure vessels. The bending introduced due to the presence of a through-wall crack is included in these shallow-shell-theory solutions. A good agreement noted between the J-integral values for 66-cm (26 in.) pipe with quarter circumference flaw included in Ref *12* (referred earlier in this subsection) and those obtained using a shell correction factor indicates that this approach is reasonable.

Two pipe sizes—small and large—were considered in this evaluation. The small pipe was a 10-cm (4 in.) Schedule 80 [$D_0 = 11.43$ cm (4.5 in.),

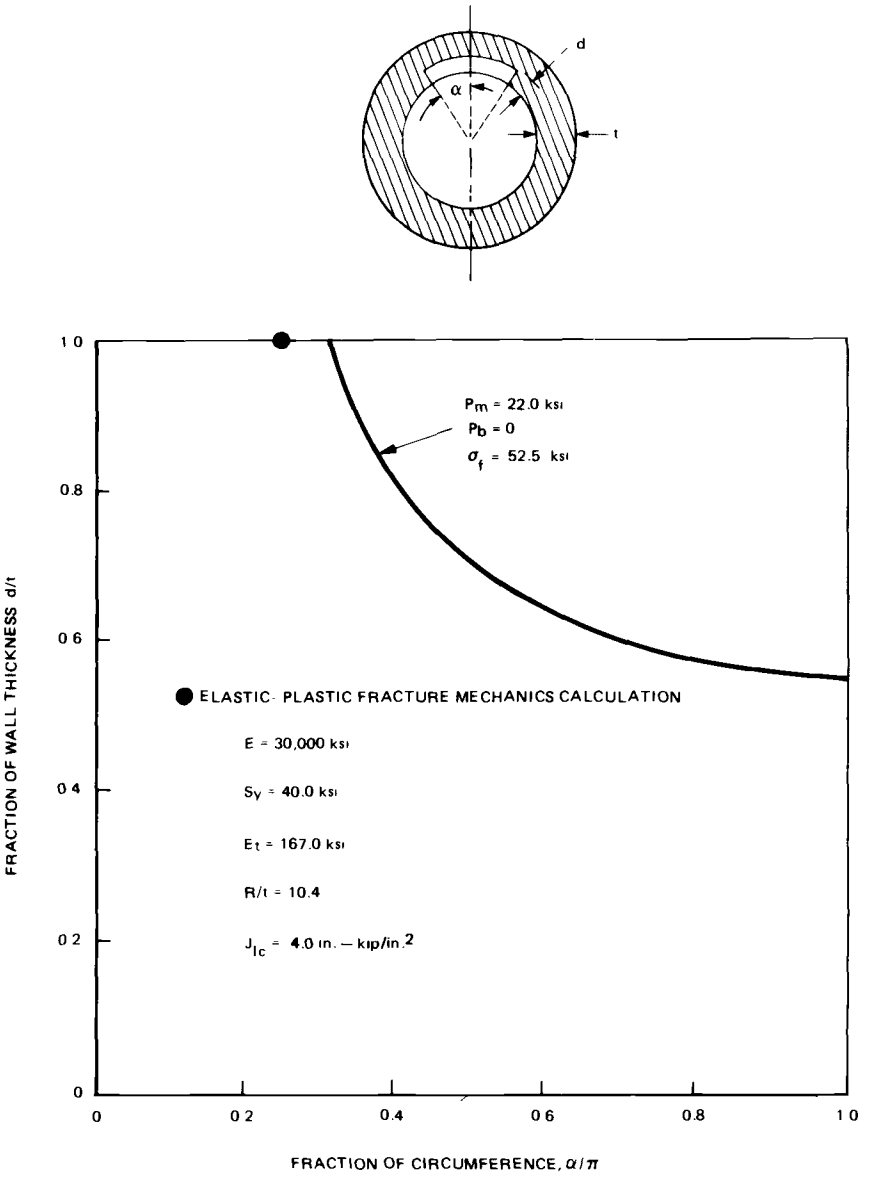

FIG. 3—*Comparison of net-section collapse and elastic-plastic fracture mechanics predictions for a through-wall flaw in 304 stainless steel pipe (ksi = 6.90 MPa).*

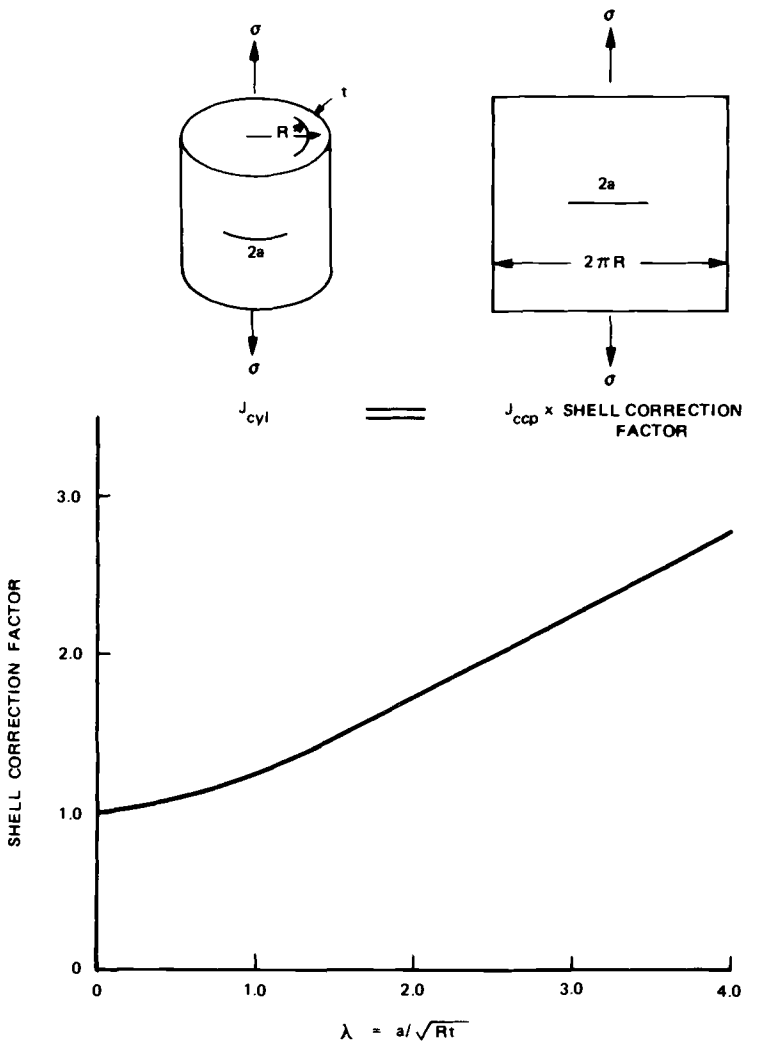

FIG. 4—*Procedure for calculation of J for axially loaded cylinder with a through-wall crack.*

t = 8.559 mm (0.337 in.)] and the large pipe was 50-cm (20 in.) Schedule 80 [D_0 = 50 cm (20 in.), t = 26.187 mm (1.031 in.)]. The J-integral values for the equivalent CCP geometry were obtained using the estimation scheme formulas given in Ref *6* and the stress-strain parameters given in Table 1. These were multiplied by the shell correction factor to determine the applied J. Allowable axial membrane stress was based on comparison with J_{Ic} (that is, crack initiation) for three crack length-to-circumference ratios: 0.125, 0.25, and 0.375. The results are shown in Fig. 5 along with the net-section

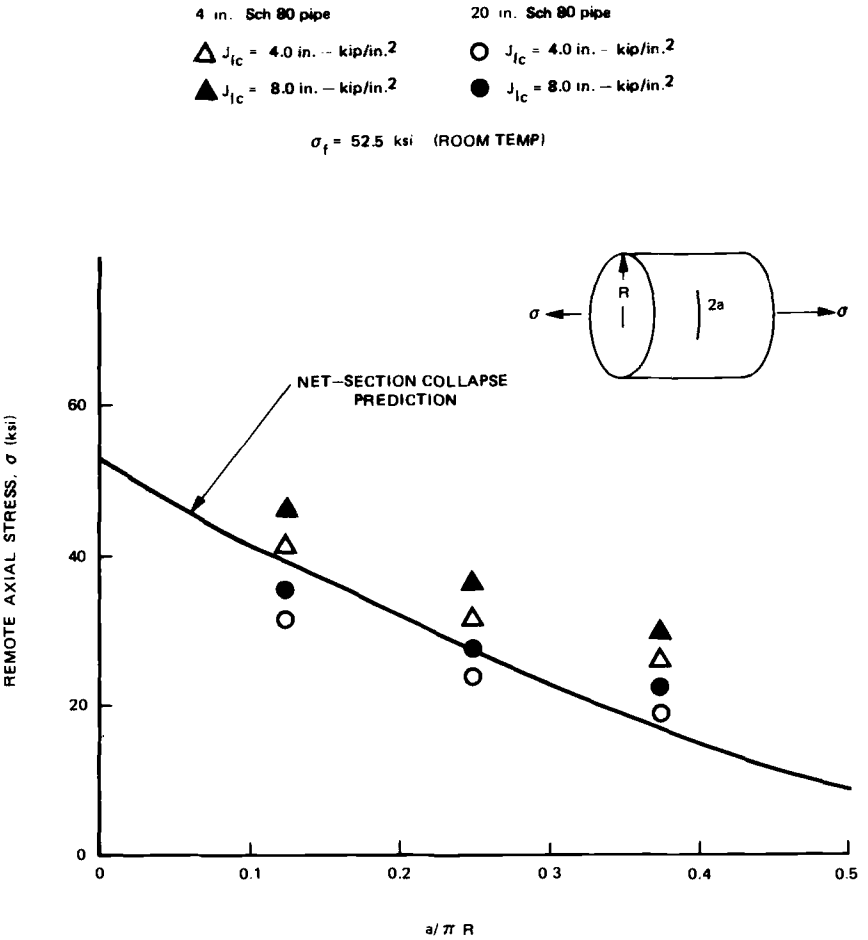

FIG. 5—*Comparison of net-section collapse and estimation scheme (J_{Ic}) load predictions for axially loaded 304 stainless steel pipe with through-wall circumferential crack (1 ksi = 6.90 MPa; 1 in. = 25.4 mm).*

collapse prediction line which was obtained using Eq 5. The EPFM results are in good agreement with the net-section collapse prediction. The differences in the allowable membrane stresses between the 10-cm (4 in.) and 50-cm (20 in.) pipes using the EPFM are as expected due to the built-in crack size effect in the mathematical expression for J. The net-section collapse predictions are independent of pipe size. It is seen that the net section collapse predictions are conservative (that is, predict a lower allowable membrane stress) with respect to EPFM prediction for crack initiation in the 10-cm (4 in.) pipe. In the case of the 50-cm (20 in.) pipe, however, the allow-

able stress by the net-section collapse method is somewhat higher than predicted for crack initiation based on J_{Ic}. As before, if crack growth is included and the maximum load is computed using the material J-R curve, the EPFM prediction for the allowable stress is expected to be higher than that based on the net-section collapse method. Figure 6 shows the comparison based on maximum load assuming J-controlled crack growth. The maximum loads were calculated using a computer program which simulated the graphical procedure depicted in the crack driving force diagram of Ref *6*. The J-R curve was assumed to be a straight line with a slope equal to the value of the

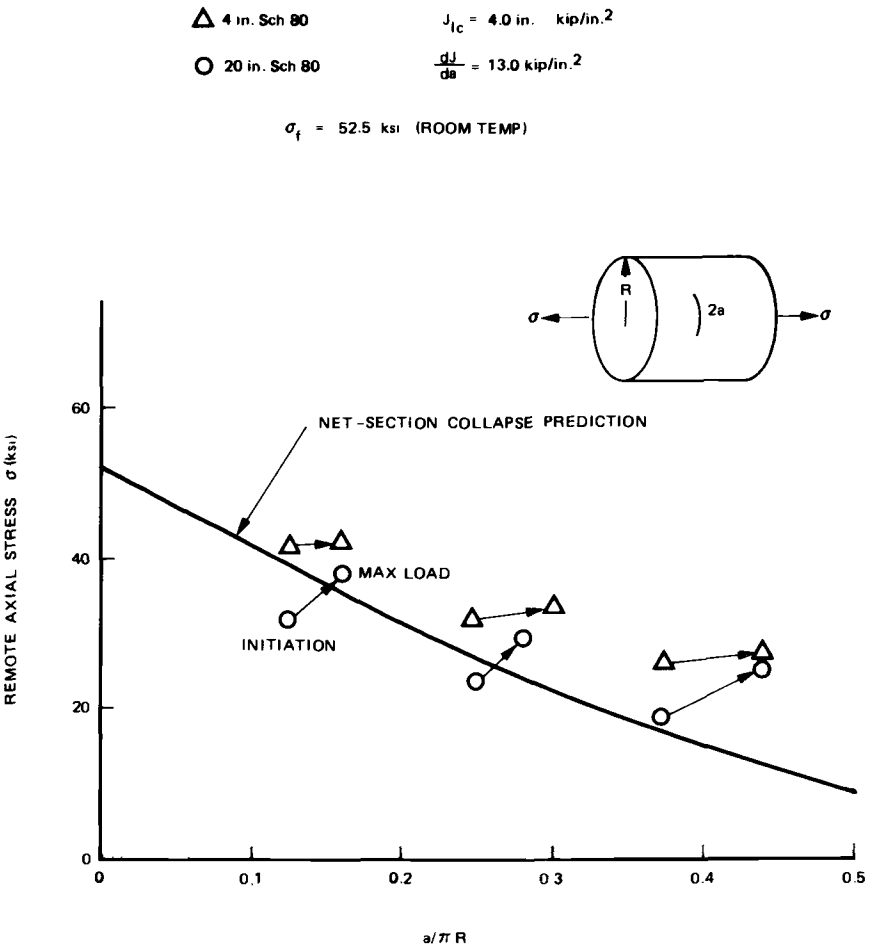

FIG. 6—*Comparison of net-section collapse load and estimation scheme maximum load for axially loaded 304 stainless steel pipe with through-wall circumferential crack (1 ksi = 6.90 MPa; 1 in. = 25.4 mm).*

material dJ/da in Table 1. From Fig. 6, it is seen that when the stable crack growth is taken into account, the EPFM predictions for both the 10- and 50-cm (4 and 20 in.) pipes fall above the net section collapse. Although this comparison for the through-wall flaws is not extensive, it does illustrate the good agreement between the EPFM and the net section collapse predictions.

Fully Circumferential Flaws

Figure 7 shows the allowable axial stress for fully circumferential flaws in stainless steel pipes calculated on a crack initiation (J_{Ic}) basis. As in the through-wall flaw case, the calculations were performed for two pipe sizes. The J-integral values were obtained as a function of axial stress using the esti-

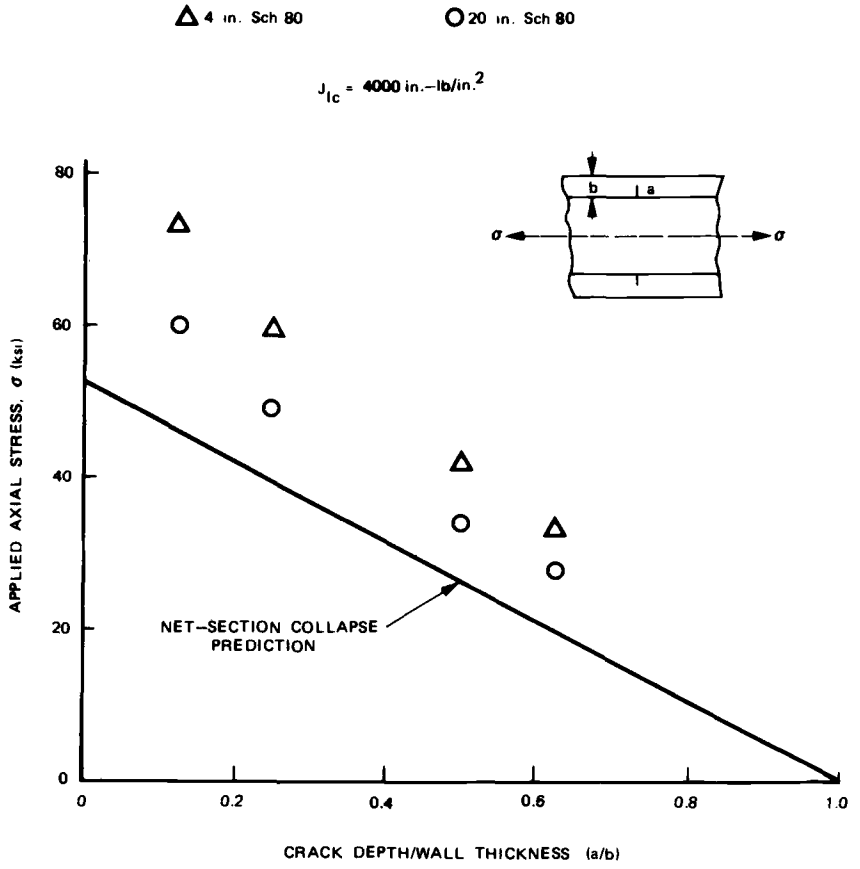

FIG. 7—*Comparison of net-section collapse and estimation scheme (J_{Ic}) load predictions for axially loaded 304 stainless steel pipe with 360-deg circumferential crack (1 ksi = 6.90 MPa; 1 in. = 25.4 mm).*

mation scheme formulas of Ref *8*. A pipe size effect similar to that observed in the through-wall case is also noted here. In this case, however, the EPFM predicted allowable axial stress for both pipe sizes is higher than the net section collapse prediction. Thus, from this limited comparison for stainless steel pipes, it is seen that the net-section collapse predictions are in reasonable agreement with the EPFM calculations.

Comparison with Two-Criteria Failure Assessment Approach

The two-criteria approach or the R-6 diagram has been developed mainly by researchers at the Central Electricity Generating Board (CEGB) for an engineering integrity analysis of flawed structures [*16*]. This diagram enables the safety margin for fracture and limit load failures to be plotted in a failure space defined by the stress-intensity/fracture toughness ratio (K_r) as the ordinate and the applied stress to plastic collapse stress ratio (S_r) as the abscissa. The failure curve is obtained by using the Dugdale solution for a finite crack in an infinite sheet subjected to remote tension. Similar failure assessment curves plotted on $K_r - S_r$ axes have been derived using estimation scheme solutions by Shih et al [*8*] and Bloom [*17*]. Procedures developed by these authors will be used in comparison presented here.

For this comparison, a 15-cm (6 in.) Schedule 80 pipe [$D_0 = 16.827$ cm (6.625 in.), $t = 10.972$ mm (0.432 in.)] of SA 106 Grade B carbon steel was chosen. The pipe was assumed to have a through-wall crack extending through 1/8 of the circumference and subjected to remote axial stress. The pertinent room-temperature material resistance curve data and the stress-strain curve parameters are all given in Table 1. The following formulas from Ref *8* are used to develop the failure assessment line

$$\frac{[\hat{J}(a)]\,(P/P_0)^2}{[\hat{J}(a_e)]\,(P/P_0)^2 + \hat{J}\,(a,\,n)\,(P/P_0)^{n+1}} = \frac{J_e}{J_{ep}} = K_r^2 = J_r \tag{7}$$

$$S_r = P/P_0 \tag{8}$$

where

P = applied load,
P_0 = reference load,
$\hat{J}$ = represents dimensionless functions whose numerical values are listed in Ref *8*,
a_e = Irwin's effective crack length modified to account for strain hardening,
J_e = value of J calculated assuming linear elastic behavior, and
J_{ep} = value of J calculated using the estimation scheme for elastic-plastic behavior.

Equations 7 and 8 describe the failure assessment line in the space of K_r and S_r. The failure assessment line for the subject cracked pipe configuration is shown in Fig. 8. Reference load P_0 was defined as $\sigma_0 \times$ (Area of uncracked ligament at cracked section).

The loading line in Fig. 8 is simply $\sqrt{J_e/J_{Ic}}$, where J_{Ic} is the value of the J-integral at crack initiation, and its intersection with the assessment line indicates the crack initiation point. During the stable ductile crack growth phase the loading point moves along the assessment line as indicated. Although there is a slight increase in the crack length during the ductile tearing phase, the assessment line based the original crack length was considered a reasonable approximation. For comparison purposes, the R-6 line and the

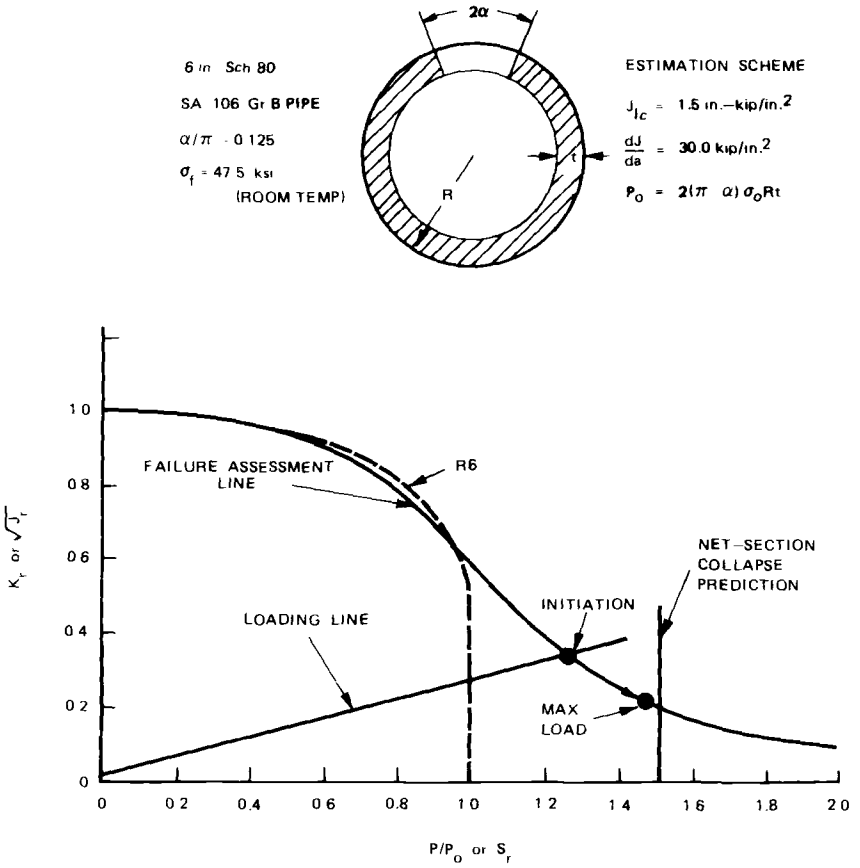

FIG. 8—*Two-criteria (R-6) format comparison of net-section collapse and estimation scheme predictions for axially loaded carbon steel pipe with through-wall crack (1 ksi = 6.90 MPa; 1 in. = 25.4 mm).*

net-section collapse prediction are also indicated in Fig. 8. As expected, the R-6 line, based on yield stress as the flow stress, provides a conservative estimate in the limit load-controlled failure region.

Development of Acceptance Criteria for Cracked Piping

The net-section collapse approach permits determination of the critical flaw size in a stainless steel pipe for a given combination of applied stresses. However, the acceptance flaw size is smaller than this and can be determined by applying a required safety margin on the failure flaw parameters. The acceptance flaw size, a_f, is the maximum size to which a detected flaw can be allowed to grow without the need for repair. In other words, it is the maximum allowable end-of-inspection period flaw size. In order to develop easy-to-apply acceptance flaw tables, the following simplifying assumptions are made.

1. *Membrane Stress*—In calculating the location of the neutral axis (angle β in Eqs 1 and 3), the value of the primary membrane stress is required. Since pipes are generally sized such that the hoop stress at design pressure is less than S_m (Article NB3640, Ref *3*), it is reasonable to assume that the axial membrane stress P_m is $S_m/2$. Parametric studies with different values for P_m have shown that the allowable flaw sizes are not significantly dependent on the assumed value of P_m.

2. *Flow Stress*—Experimental measurements [*1*] and evaluations of General Electric (GE) pipe test data indicated that the assumption of $\sigma_f = 3\,S_m$ is reasonable. This is slightly higher than the average of the Code minimum values of the ultimate strength and yield strength at 288°C (550°F) for Type 304 stainless steel. A flow stress value indexed to S_m is more realistic since different grades of austenitic materials have different strength properties and pipes are designed on the basis of the design stress intensity S_m. Also, the Code minimum properties are for annealed material and do not consider the beneficial effects of strain-hardening. In the vicinity of piping welds where cracks are likely to occur, the strength of the weld heat-affected zone is higher than that of the annealed material. In view of the foregoing reasons, the assumption $\sigma_f = 3\,S_m$ is reasonable.

3. *Safety Factor*—The philosophy in setting the acceptance standards is to preserve the *minimum* safety margin inherent in the ASME Code design basis for *uncracked piping*. For normal conditions, the minimum margin on primary membrane stress is 3 ($P_m < S_m$ is the lower of $S_u/3$ or $0.9\,S_y$). For bending stresses in piping, the margin is slightly lower as seen from the following equation for straight piping (Article NB-3652, Ref *3*)

$$PD/4t + MD/2I \leq 1.5\,S_m \tag{9}$$

where

P = pressure,
t = thickness,
D = outside diameter,
I = moment of inertia, and
M = applied moment including seismic loading.

Considering the case of pure moment loading alone, it is seen that the total safety margin arises from two factors: (1) a ratio of 2 coming from the allowable limit of 1.5 S_m, whereas the flow stress is 3 S_m, and (2) the ratio of the fully plstic moment for a thin pipe ($4\ \sigma_f r^2\ t$) to the moment for just reaching the flow stress on the surface ($\pi\ \sigma_f r^2\ t$) giving a factor of $4/\pi$. (For rectangular cross sections the ratio is 1.5.) Thus, for pipes in bending the overall safety margin is $8/\pi = 2.546$. In setting up the acceptance standards, the safety margin will be imposed on $P_m + P_b$. The required safety factor is the average of the Code minimum safety margins for P_m and $P_b = \frac{1}{2}\ (3.0 + 2.546) = 2.773$.

For faulted conditions, the safety margin is one half of the value for normal conditions, that is, $\frac{1}{2}\ (2.773) = 1.387$. This is also consistent with the Code design basis since the allowable limit to be used in Eq 9 is 3 S_m for faulted conditions.

Based on the foregoing assumptions, flaw assessment diagrams can be developed for different values of $P_m + P_b$ (P_m is assumed to be $S_m/2$ and $\sigma_f = 3\ S_m$). Figure 9 shows the failure diagram for $P_m + P_b = S_m$. The dotted line represents the combination of flaw depth and length defining plastic collapse. Applying a safety factor of 2.773 on $P_m + P_b$, the allowable flaw parameters can also be calculated as shown by the curved solid line. Flaw combinations below this line will preserve the minimum safety margins of the ASME Code. Since through-wall cracks cannot be tolerated (even though sufficient structural margins can be demonstrated), the maximum allowable crack depth is limited to 75 percent of the wall thickness. This is consistent with Appendix A of Section XI, ASME Code [*18*], which requires the crack arrest depth in pressure vessels to be less than 75 percent of the wall thickness. Also, from a practical perspective, it may be more cost effective to repair/replace the pipe for such deep cracks even though adequate structural margins can be shown.

Similar diagrams can be developed for emergency and faulted conditions also, except that the required safety margin is 1.387.

The acceptance flaw sizes shown in Fig. 9 can be determined for a range of applied stresses for both normal and faulted conditions. Tables 2 and 3 show the allowable values for different values of $(P_m + P_b)/S_m$ for normal and faulted conditions. For intermediate values of $P_m + P_b$ the acceptance flaw sizes can be determined by interpolation.

It should be noted that the acceptable flaw, a_f, represents the maximum

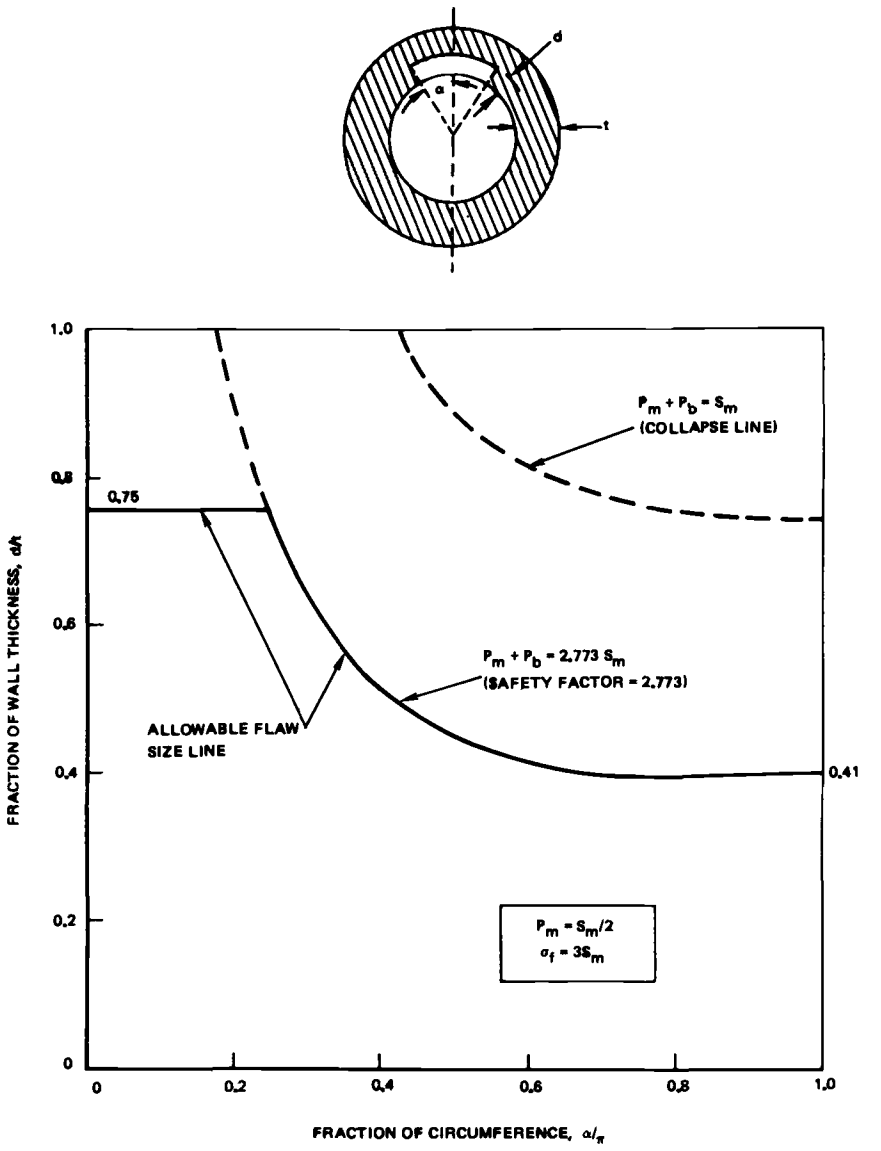

FIG. 9—*Determination of allowable flaw sizes with a safety factor of 2.773 for normal conditions.*

flaw size that can be tolerated at the end of the next inspection interval. To determine the allowable value, a_i, at the previous inspection, it is necessary to subtract the expected crack growth during that interval.

The methodology presented here for evaluating cracks in piping is based on limit-load design concepts which are strictly valid with highly ductile

TABLE 2—*Acceptance flaw size for normal conditions.*

$\frac{P_m + P_b}{S_m}$	Ratio of Length to Circumference, $\ell/2\pi r$				
	0.1	0.2	0.3	0.4	0.5 or more
	a/t				
1.4	0.40	0.21	0.15	0.10	0.10
1.3	0.75	0.39	0.27	0.22	0.19
1.2	0.75	0.56	0.40	0.32	0.27
1.1	0.75	0.73	0.51	0.42	0.34
1.0	0.75	0.75	0.63	0.51	0.41
0.9	0.75	0.75	0.73	0.59	0.47
0.8	0.75	0.75	0.75	0.68	0.53

P_m = primary membrane stress.
P_b = primary bending stress.
S_m = ASME Code design stress.

TABLE 3—*Acceptance flaw size for faulted conditions.*

$\frac{P_m + P_b}{S_m}$	Ratio of Length to Circumference, $\ell/2\pi r$				
	0.1	0.2	0.3	0.4	0.5 or more
	a/t				
2.8	0.40	0.21	0.15	0.10	0.10
2.6	0.75	0.39	0.27	0.22	0.19
2.4	0.75	0.56	0.40	0.32	0.27
2.2	0.75	0.73	0.51	0.42	0.34
2.0	0.75	0.75	0.63	0.51	0.41
1.8	0.75	0.75	0.73	0.59	0.47
1.6	0.75	0.75	0.75	0.68	0.53

P_m = primary membrane stress.
P_b = primary bending stress.
S_m = ASME Code design stress.

materials. They do not explicitly consider failure by brittle fracture or tearing instability. To preclude brittle fracture concerns, the criteria outlined here are restricted to austenitic piping and the associated weld materials and stainless steel castings with low ferrite content. Although tearing instability is not explicitly considered here, tearing instability is not likely since the acceptance criteria developed here assure large margins over hinge formation.

Summary and Conclusions

Simple engineering methods are developed for the evaluation of flaws in ductile piping. Since failure in piping is characterized by gross yielding and plastic instability, it can be assumed that a pipe with a circumferential crack

is at the point of incipient failure when the net section at the crack reaches a critical flow stress and develops a plastic hinge. The results can be presented in the form of a failure diagram defining the combination of critical crack depth and length at which collapse occurs for a given applied stress. The advantage of the net-section collapse approach is that it is consistent with the ASME Code piping design basis and uses information already available in piping stress reports. No additional analysis or materials data are required in this assessment. Failure predictions based on this method are in good agreement with experimental data on both 304 stainless steel and high-toughness carbon steel piping.

Although the crack assessment procedure used here is based on collapse theory, the existence of a critical net-section stress can be justified by a general yield fracture mechanics analysis also. To compare the present method with elastic plastic fracture mechanics criteria, failure predictions were made for (1) crack initiation based on J_{Ic}, and (2) maximum load assuming J-controlled crack growth.

Comparisons were made for through-wall cracks and part-through circumferential cracks in both stainless steel and carbon steel piping under axial loads.

The results show that the predictions of the simple net-section collapse approach are in good agreement with the more detailed elastic-plastic fracture methods for evaluating cracks in piping. This is significant since it demonstrates that the simple engineering methods coupled with information available in stress reports can be used in confidence to assess cracks in piping.

Finally, the failure diagrams developed for different applied stress levels were used to establish acceptance criteria for cracks in piping designed to the ASME Code. The approach used in establishing flaw acceptance standards was to require that the minimum safety margins of the Code be retained throughout plant operation even with cracks. Using this procedure, acceptable flaw sizes can be conveniently determined as a function of stress level for the different plant operating conditions. An important advantage comes from the fact that no special stress analysis or fracture evaluation is required to determine flaw acceptability. Information that is already available in piping stress reports can be used to make the assessment. Specific material properties such as J_{Ic} data, tearing modulus, and J-R curves are not needed for the evaluation. The only material property needed is the flow stress, which can be obtained from minimum-strength properties specified in the Code. Thus, the proposed criteria offer a simple, conservative method for assessing flaws in piping.

Acknowledgments

This work was partly funded by the Electric Power Research Institute (EPRI), Palo Alto, Calif., through Contract T118-1. The authors express

their appreciation to Dr. D. M. Norris of EPRI for his encouragement and useful discussions. The authors also acknowledge the contributions of researchers at the General Electric Corporate Research and Development Center, Schenectady, N.Y., specifically Drs. C. F. Shih (now at Brown University), V. Kumar, and D. Mowbray, in developing the engineering methods of elastic-plastic fracture analysis which were used in this work.

References

[1] "Mechanical Fracture Predictions for Sensitized Stainless Steel Piping with Circumferential Cracks," EPRI Report NP-192, Final Report, Electric Power Research Institute, Palo Alto, Calif., Sept. 1976.

[2] "Review and Assessment of Research Relevant to Design Aspects of Nuclear Power Plant Piping Systems," NUREG-0307, Nuclear Regulatory Commission, Washington, D.C., July 1977.

[3] ASME Boiler & Pressure Vessel Code, Section III, Division 1, Nuclear Power Plant Components, American Society of Mechanical Engineers, 1980 Edition.

[4] Smith, E., *International Journal of Pressure Vessels and Piping*, Vol. 8, No. 4, July-Aug. 1980, pp. 303-311.

[5] Shih, C. F. and Hutchinson, J. W., *Transactions*, American Society of Mechanical Engineers, *Journal of Engineering Materials and Technology*, Series H, Vol. 98, 1976, pp. 289-295.

[6] Shih, C. F. and Kumar, V., "Estimation Scheme for the Prediction of Elastic-Plastic Fracture of Structural Components of Nuclear Systems," First Semi-Annual Report, EPRI Contract RP1237-1, Electric Power Research Institute, Palo Alto, Calif., June 1979.

[7] Zahoor, A. and Kanninen, M. F., *Transactions*, American Society of Mechanical Engineers, *Journal of Engineering Materials and Technology*, Vol. 103, 1981, pp. 194-200.

[8] Kumar, V., German, M. D., and Shih, C. F., "An Engineering Approach for Elastic-Plastic Fracture Analysis," Electric Power Research Institute Report NP-1931, Palo Alto, Calif., July 1981.

[9] Bamford, W. H. and Bush, A. J. in *Elastic-Plastic Fracture, ASTM STP 668*, J. D. Landes, J. A. Begley, and G. A. Clarke, Eds., American Society for Testing and Materials, 1979, pp. 553-577.

[10] Zahoor, A. and Kanninen, M. F., *Transactions*, American Society of Mechanical Engineers, *Journal of Pressure Vessel Technology*, Vol. 103, 1981, pp. 352-358.

[11] Goldberg, A., Streit, R. D. F., and Schott, R. G., "Evaluation of Cracking in Feedwater Piping Adjacent to the Steam Generators in Nine Pressurized Water Reactor Plants," Lawrence Livermore Laboratory Report UCRL-53000, Livermore, Calif., Oct. 1980; also published as NUREG/CR-1603.

[12] Shih, C. F. et al, "Crack Opening and Stability Analyses for Flawed Stainless Steel Piping," First Interim Report to EPRI, Contract No. T118-8, Electric Power Research Institute, Palo Alto, Calif., Sept. 1980.

[13] Rooke, D. P. and Cartwright, D. J., *Compendium of Stress Intensity Factors*, Her Majesty's Stationary Office, London, 1976.

[14] Delale, F. and Erdogan, F., *Quarterly of Applied Mathematics*, Vol. 37, 1979, pp. 239-258.

[15] Paris, P. C., "A Method of Application of Elastic-Plastic Fracture Mechanics to Nuclear Vessel Analysis," Appendix B, NUREG-0744, U. S. Nuclear Regulatory Commission, Washington, D.C., Sept. 1981.

[16] Harrison, R. P., Loosemore, K., and Milne, I., "Assessment of the Integrity of Structures Containing Defects," C.E.G.B. Report No. R/H/R 6, Central Electricity Generating Board, U.K., 1976.

[17] Bloom, J. M., "The Two Criteria Failure Assessment Procedure," Appendix A, EPRI Ductile Fracture Research Review Document NP-80-10-LD, Electric Power Research Institute, Palo Alto, Calif., Dec. 1980.

[18] ASME Boiler and Pressure Vessel Code, Section XI, Rules for In-Service Inspection of Nuclear Power Plant Components, American Society of Mechanical Engineers, 1980 Edition.

Gery M. Wilkowski,[1] *Jalees Ahmad,*[1] *Akram Zahoor,*[1]
Charles W. Marschall,[1] *David Broek,*[1]
Ibraham S. Abou-Sayed,[1] *and Melvin F. Kanninen*[1]

Fracture of Circumferentially Cracked Type 304 Stainless Steel Pipes Under Dynamic Loading

REFERENCE: Wilkowski, G. M., Ahmad, J., Zahoor, A., Marschall, C. W., Broek, D., Abou-Sayed, I. S., and Kanninen, M. F., **"Fracture of Circumferentially Cracked Type 304 Stainless Steel Pipes Under Dynamic Loading,"** *Elastic-Plastic Fracture: Second Symposium, Volume II—Fracture Resistance Curves and Engineering Applications, ASTM STP 803*, C. F. Shih and J. P. Gudas, Eds., American Society for Testing and Materials, 1983, pp. II-331–II-350

ABSTRACT: A program of experimentation and analysis aimed at determining fracture instability in circumferentially cracked Type 304 stainless steel pipes in seismic or water-hammer loadings is described. Experimental work on center-cracked tension panels revealed that dynamic loading does not affect the net-section stress criterion evolved previously for Type 304 stainless steel. Full-scale tests on 100-mm-diameter (4 in.) pipes subjected to a dynamic load nevertheless indicate that a margin of safety exists beyond that predicted by the application of the net-section stress criterion. It is concluded that the finite duration of a dynamic loading together with the system compliance which allows stable crack growth beyond maximum load is primarily responsible. A *J*-based plastic fracture mechanics assessment based upon rate-dependent mechanical and fracture properties of the material was made and found to be consistent with this hypothesis.

KEY WORDS: fracture, dynamic loading, Type 304 stainless steel, nuclear plant piping, elastic-plastic fracture

Previous work has shown that a critical net-section stress criterion can be quite effective for predicting the strength of circumferentially cracked Type 304 stainless steel pipes under quasi-statically applied loads [*1–2*].[2] However, because of the combined effects of a finite load duration and the escalation of the flow stress at high strain rates, this criterion is likely to be overly conser-

[1] Battelle Columbus Laboratories, Columbus, Ohio 43201.
[2] The italic numbers in brackets refer to the list of references appended to this paper.

vative for dynamic loadings. Thus, predictions for seismic, water-hammer, or other such transient events based on current technology could misjudge the actual margin of safety in flawed nuclear piping. The research reported in this paper addresses this concern by a program of combined analyses and experiments. The work includes small-scale specimen testing, a plastic fracture mechanics analysis, and full-scale pipe fracture experiments.

The experiments on small-scale test specimens described herein are of two types: center-cracked tension panel experiments and impact-loaded bend specimen experiments. The former were designed to evaluate the effect of cyclic and other high-rate or transient loading conditions on the net-section stress criterion. The latter were designed to help evaluate the effect of loading rate on the J-resistance curve. A series of four pipe fracture experiments on circumferentially cracked, 100-mm-diameter (4 in.), Type 304 stainless steel pipes under dynamic loading was also conducted. An analysis using a J-integral-based plastic fracture mechanics approach was applied to these experiments. The analysis employed a J-resistance curve taken from the impact experiments and a J-estimation method appropriate for the dynamically loaded circumferentially cracked pipes. Specific application was made to the single experiment in which a significant amount of crack growth was achieved.

Center-Cracked Panel Experiments

The flat-plate test data generated in a previous program [*1–2*] established that sharp fatigue cracks and fine saw cuts in sensitized and nonsensitized Type 304 stainless steel gave essentially the same net-section stresses at maximum load and during stable crack growth. In fact, more recent work [*3*] showed that J_{Ic} -values from bend specimens with stress-corrosion cracks were greater than for fatigue cracks, and comparable to the sharp machined-notch specimens. In addition, cracks located in the heat-affected zone (HAZ) of a weldment showed few differences from the behavior in the base material. Accordingly, the experiments performed in this program used specimens with saw cuts in unsensitized material. In addition, only a few monotonic loading experiments were performed (to correlate with the previous results) in order to concentrate on dynamic loading conditions.

In the test series that was performed, the center-cracked panels were subjected to increasingly complex load histories. In several tests the load was released several times during crack growth in otherwise monotonic loading. In some of these the load was reversed to compression. In subsequent tests, groups of up to 50 constant-amplitude load cycles were applied at various stages of crack growth. Finally, tests were performed in which a simulated seismic load, taken from an actual earthquake record, was applied as a series of loads.

Of most significance is the bearing that these new results have on the critical net-section stress criterion established in the previous work [*1*]. In such an ap-

proach a correlation is sought for the net-section stress acting on the uncracked ligament—that is, $\sigma_{net} = \sigma_\infty W/(W - 2a)$ where σ_∞ is the applied (remote) stress, W the plate width, and $2a$ the crack length—and the point of incipient failure. If such a criterion is to be meaningful, then σ_{net} should be a constant from one test to another. The results shown in Fig. 1 indicate that this is indeed the case.

The results in Fig. 1 show that both the initiation of crack growth (open symbols) and the maximum load (closed symbols) are well correlated by unique net-section stress values. Use of this criterion to predict the results of quasi-static pipe fracture tests obtained in another phase of this research program—see Ref *3*—is shown in Fig. 2. It can be seen that excellent agreement exists with the results for three different pipe diameters. The pipe experiments were performed in bending with the maximum load achieved in the experiment being shown.

Taken together, the results given in Figs. 1 and 2 suggest that perturbations to monotonic loading will not significantly affect the critical net-section collapse criterion for the failure of circumferentially cracked Type 304 stainless

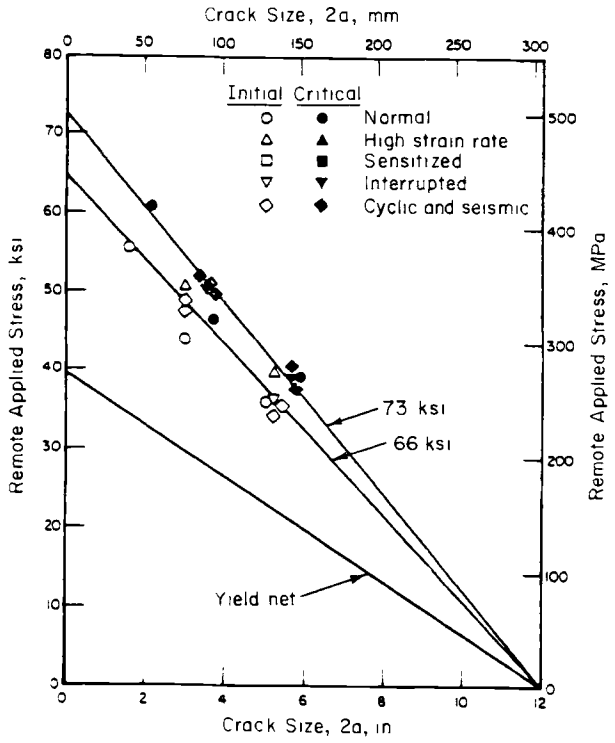

FIG. 1—*Residual strength as a function of crack size for Type 304 stainless steel center-cracked tension panels.*

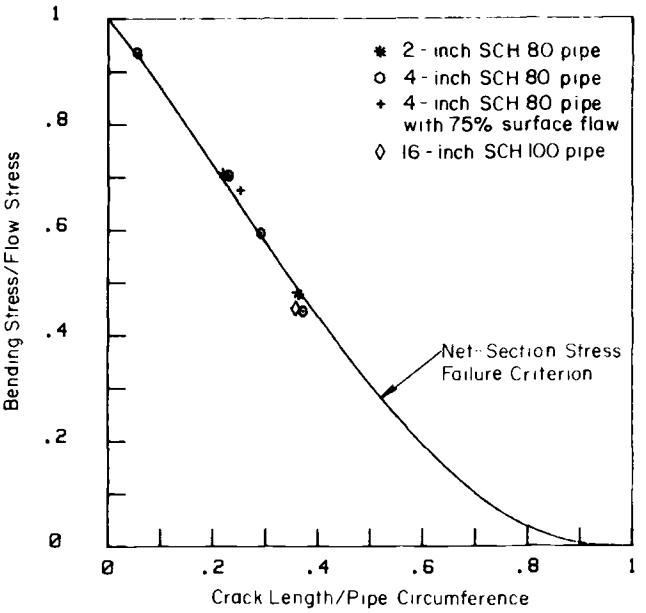

FIG. 2—*Comparison of quasi-statically loaded through-wall cracked Type 304 stainless steel pipe experiments with the net-section stress failure criterion (1 in. = 2.54 cm).*

steel pipe. Hence, a prediction of pipe fracture under load-controlled conditions can be readily made. In nuclear piping systems, however, a dynamic loading would manifest itself more nearly as a displacement- (or rotation) controlled loading. In addition, the finite duration of such loadings will also tend to lessen their severity. To obtain a precise assessment requires a plastic fracture mechanics analysis, which in turn requires appropriate material properties and a crack growth resistance curve. The impact-loaded bend specimen experiments described next were performed to develop these data.

Bend Specimen Experiments

The bend specimen experiments were conducted on two thicknesses of Type 304 stainless steel and at two temperatures. Both quasi-static and interrupted impact loadings were used, the latter increasing the displacement rate by a factor of 2×10^5. The necessary input for the finite-element calculation of J was the experimental crack growth versus load-line displacement data; see Fig. 3. The high-rate experiments were conducted with an instrumented drop-weight tower. An unusual feature of these tests was the control on the amount of crack extension. This was achieved by stopping the falling weight after a predetermined amount of deflection had taken place in the three-point-bend speci-

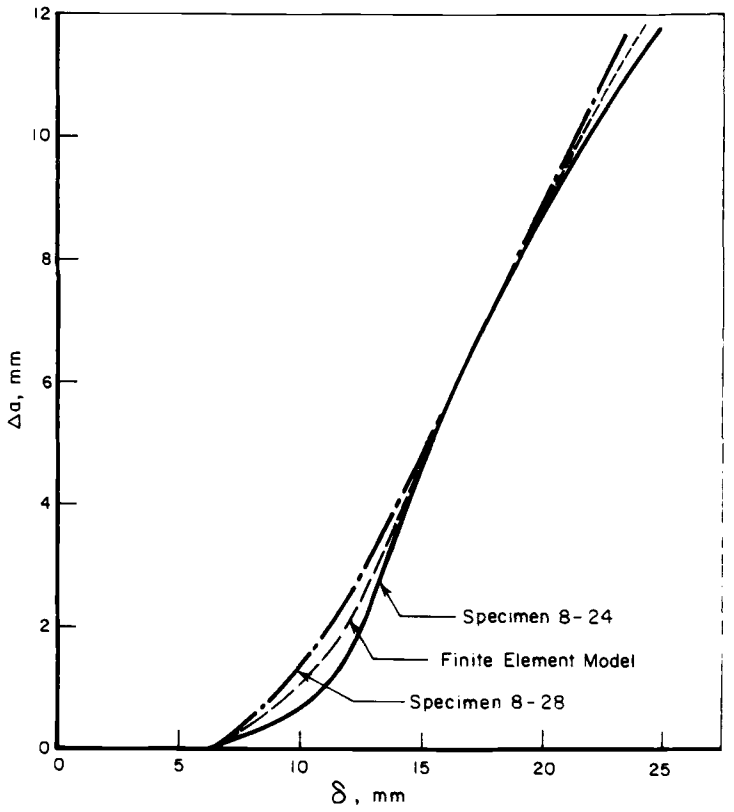

FIG. 3—*Crack growth versus displacement measurements from quasi-static tests of sharp-notched three-point-bend specimens of Type 304 stainless steel (1 mm = 0.04 in.).*

men. The load at the instant the instrumented striker contacted the stop-block was evident from the load/time record; see Fig. 4. Following the impact test, the specimen was photographed to permit later measurement of crack opening displacement (COD) and midspan displacement. It was then heat-tinted and broken open to permit measurement of the average crack extension resulting from impact loading.

Eight to ten specimens were tested to obtain the necessary data for calculating a J-resistance curve. Each specimen had a different level of displacement. These ranged from about 5 to 30 mm (0.2 to 1.2 in.). These displacement levels produced crack extensions that ranged from about 0 to 10 mm (0 to 0.4 in.).

Because of the very large ductility of Type 304 stainless steel, a large deformation elastic-plastic finite-element analysis with special gap-lift-off elements was used to assess the results. This is illustrated by the finite-element simulation of an impact test shown in Fig. 5. The extremely large deformations are

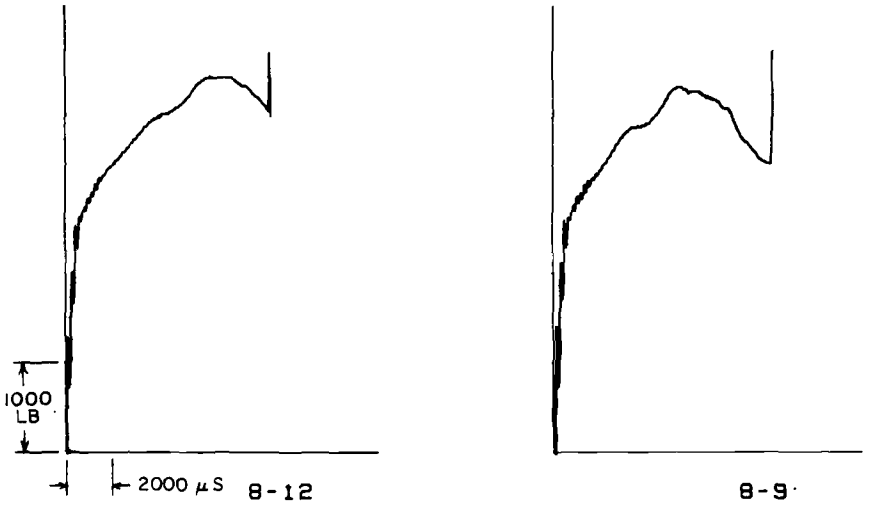

FIG. 4—*Load versus time curves for interrupted impact tests (1 lb = 0.45 kg).*

evident; note that because of symmetry about the crack plane, only half of the specimen is shown.

One complication that immediately arises in these analyses is the inexorable loss of path independence of the J-integral during stable crack growth. Figure 6 shows typical results obtained for an interrupted impact test using five integration contours (see insert in Fig. 6 for the location of the contours). It can be seen that, while the initiation point is virtually identical for all five paths, significant divergence occurs after as little as 1 mm (0.04 in.) of crack growth. Also worthy of note is the apparently inconsistent result obtained on the most remote crack path. This results from the fact that this contour is affected by the plastic deformation occurring around the load point. As a compromise, the value obtained around the fourth path was used in this work. A comparison between the interrupted dynamic results and those obtained under quasi-static loading conditions is shown in Fig. 7.

Perhaps the most important finding in the bend specimen testing pertains to the question of high-rate loading of pipes as might occur in a seismic event. As Fig. 7 shows, a high-loading rate tends to raise the J-resistance curve for Type 304 stainless steel. Hence, tests conducted at low rates will tend to give conservative results. Conversely, specimens tested at 290°C (550°F) exhibited somewhat lower J-resistance curves than those tested at room temperature. This stems primarily from the substantially lower flow stress of Type 304 stainless steel at the higher temperature. These results suggest that a room-temperature test will overestimate the crack growth resistance of boiling water reactor (BWR) piping at its operating temperature while quasi-static testing will provide a conservative estimate of the dynamic fracture behavior.

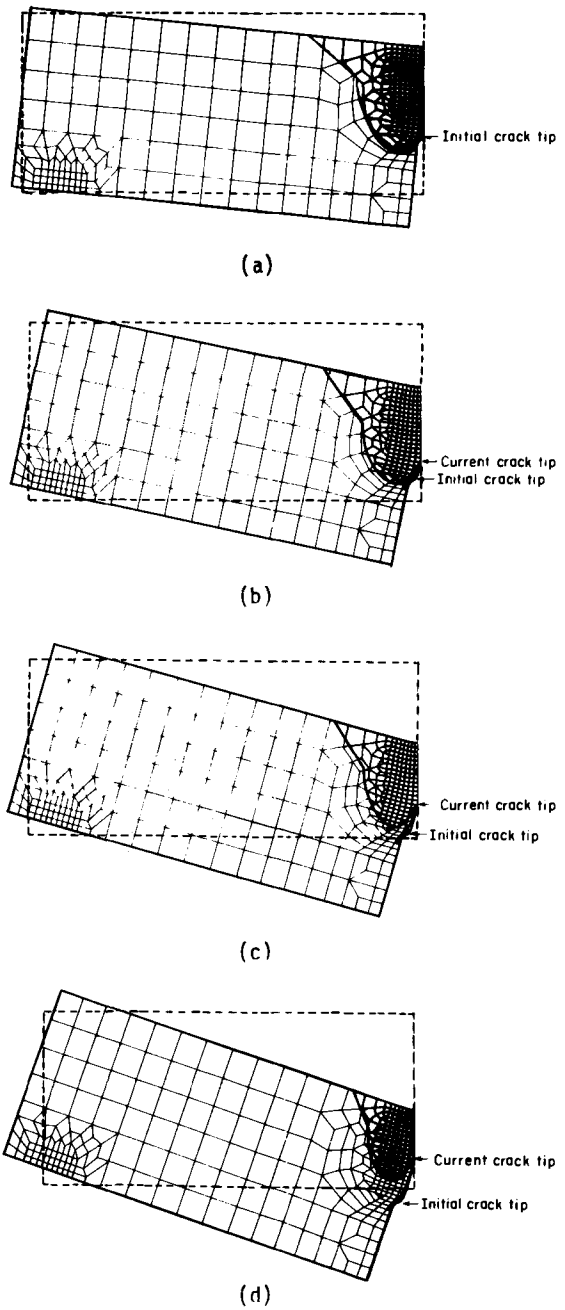

FIG. 5—*The deformed shape and the calculated plastic zone at different stages of crack growth for interrupted impact tests of a sharp-notched three-point-bend specimen of Type 304 stainless steel. Note that only one half of the specimen is shown.*

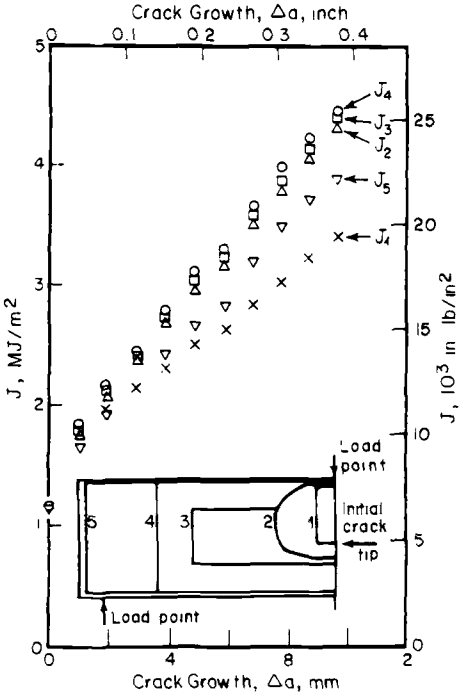

FIG. 6—*The J-integral values computed around five different contours for interrupted impact tests on sharp-notched three-point-bend specimens of Type 304 stainless steel.*

Specimen thickness effects were found to be more pronounced at room temperature than at 290°C (550°F). At both low- and high-displacement rates, the 26-mm (1.03 in.) specimens, characteristic of 10-cm-diameter (4-in.), Schedule 80 pipes, yielded higher J-Δa curves than did the 8.4-mm (0.33 in.) specimens. Although these results indicate that tests conducted on the thinner plate may provide conservative predictions for the performance of the thicker sections that are found in 66-cm-diameter (26 in.) piping, this is not necessarily true. Because the bend tests were conducted on stainless steel from different heats, the toughness variations could also be due to material property variations.

Pipe Fracture Experiments

The results obtained in the bend specimen testing indicated that the J-resistance curves for Type 304 stainless steel pipes subjected to dynamic loading would be elevated above those obtained in conventional slow loading tests. In addition to the effect of piping system inertia, an increased flow stress at higher loading rates and a finite duration of the load exist, all of which tend

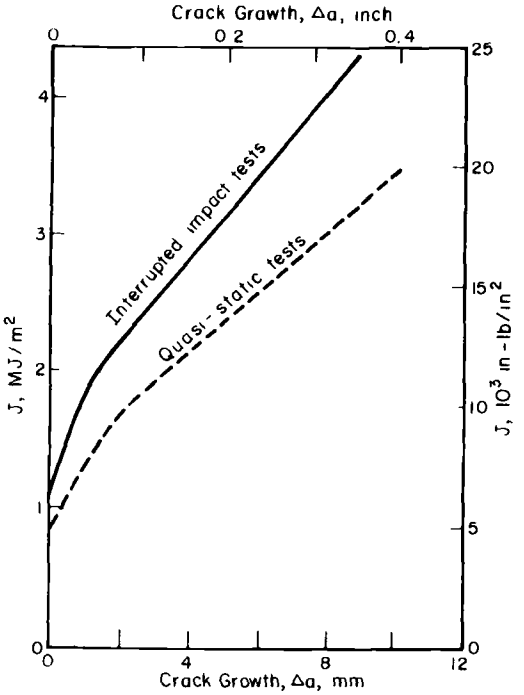

FIG. 7—*J-resistance curves for Type 304 stainless steel generated from sharp-notched three-point-bend specimens tested under quasi-static and impact loading.*

to mitigate the propensity of a dynamically imposed loading to cause pipe fracture. For high-toughness materials, the maximum load the structure can withstand eventually reaches a plateau level corresponding to plastic instability or net-section collapse; that is, a further increase in toughness will not increase the failure stress.[3] This has previously been demonstrated for axially flawed pipe [*4*]. Hence for high-toughness materials such as the seamless Type 304 stainless steel pipe, the increased strain-rate increases both J_{Ic} and the flow stress, but only the increase in the flow stress increases the load-carrying capacity of the pipe.

To study the effect of transient dynamic loading, a series of four dynamic pipe fracture tests was performed. These tests used essentially the same experimental setup—see Fig. 8—but with a different (through-wall) circumferential crack length used in each. Specifically, the crack sizes ranged from zero in the first test up to 50 percent of the circumference in the fourth.

As depicted in Fig. 7, the experiment used a vertical test section with a through-wall crack located near the lower or fixed end. A horizontal section

[3] See Fig. 12.

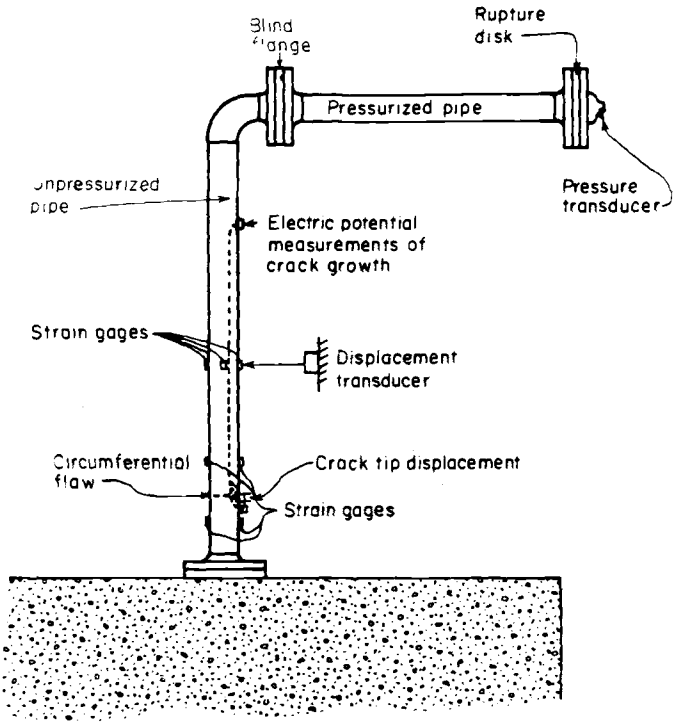

FIG. 8—*Experimental setup for induced transient bending stresses in the dynamic pipe fracture experiments.*

containing pressurized carbon dioxide was attached to the upper end of the column to provide the dynamic loading. To begin the experiment, a rupture disk located at the right-hand end of the horizontal section was burst. This resulted in a lateral thrust being applied to the vertical cracked pipe. It can be seen in Fig. 8 that sufficient instrumentation was included to both monitor crack initiation and growth (if it occurred) and to enable the plastic fracture mechanics analysis described in the following section of this paper to be performed.[4]

To design these experiments, it was necessary to accurately know the time history of the lateral load. These data were obtained from theoretical gas dynamics calculations and from tests in which the pressurized pipe section was mounted on a load cell. The resulting thrusts are shown in Fig. 9*a*. Because of the discrepancy that existed between the experimental measurements and the prediction (primarily due to the inaccuracy of current analyses with regard to two-phase flow problems), post-test calculations were made using the test data

[4]Specific note was taken of the possibility of a torsional contribution due to nonaxisymmetric loading. This was found to be negligible in all four experiments.

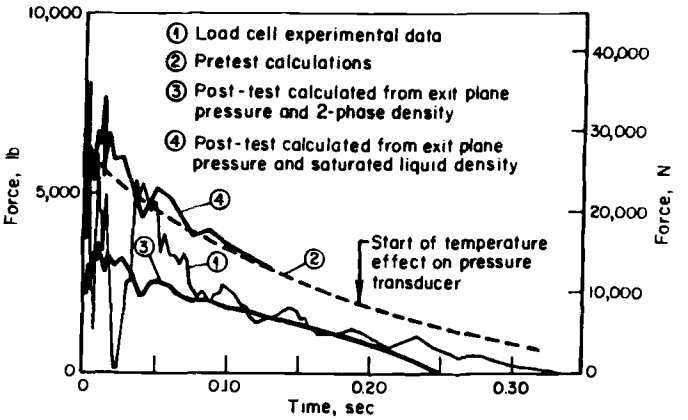

(a) Comparison of measured and predicted loads.

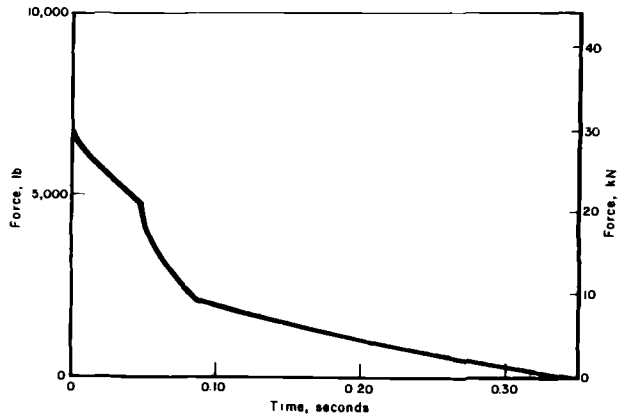

(b) Adjusted load used in design of the experiment.

FIG. 9—*Lateral loads acting in the dynamic pipe fracture experiments.*

to improve the agreement. A combination of Curves 3 and 4 from Fig. 9*a* was then used in the design of the pipe fracture experiments; see Fig. 9*b*.

The adjusted thrust history was used as input to a dynamic elastic-plastic finite-element piping system analysis computation. However, this computation did not allow for the possibility of a cracked section. Hence, the calculated stresses and deformation are nominal values that would occur only for a crack-free system. The bending moments calculated for these conditions at each of several locations along the column are shown in Fig. 10. Note that, because a significant strain-rate effect exists for Type 304 stainless steel—see Fig.

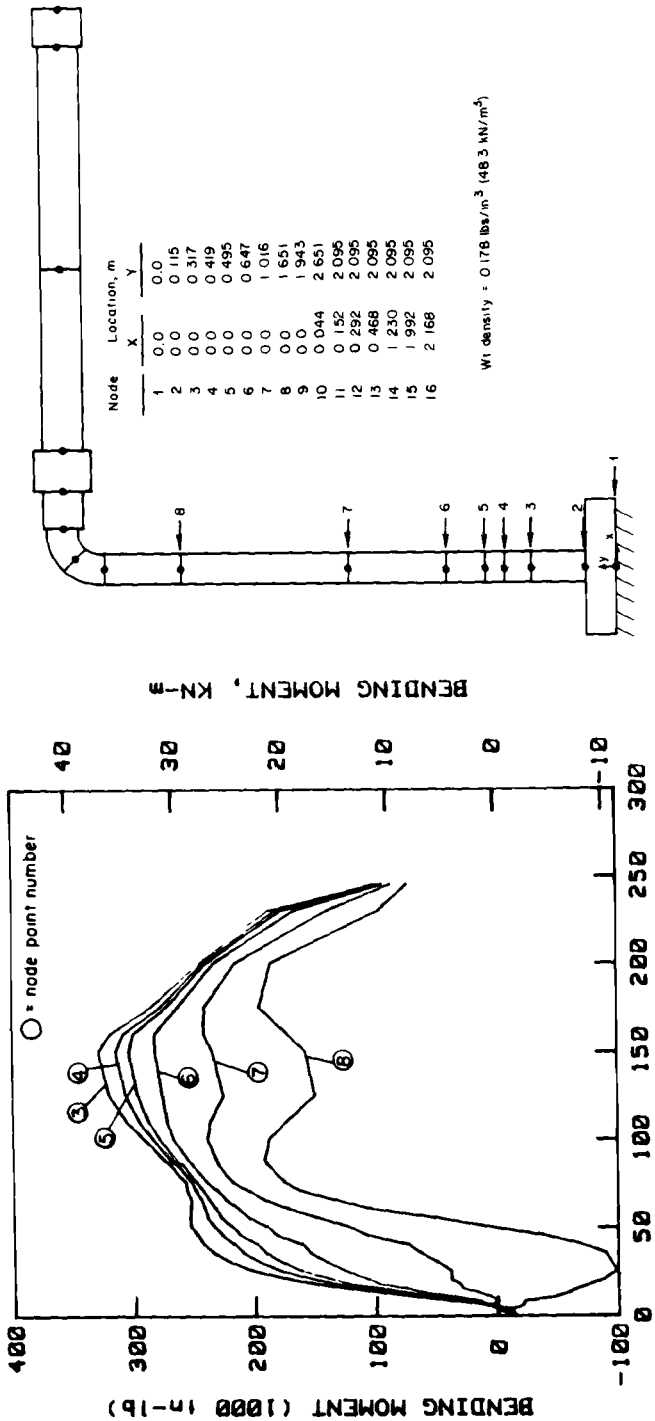

FIG. 10—*Calculated bending moment history for the dynamic uncracked pipe experiments using the thrust history in Fig. 9b and the dynamic stress-strain curve* ($\dot{\epsilon} = 0.076\ s^{-1}$) (*1 m = 3.28 ft*).

11—the stress-strain curve obtained at about the strain rate anticipated in the experiment (that is, $\dot{\epsilon} = 0.076\ s^{-1}$) was used in these computations.[5]

The first dynamic pipe fracture experiment, Experiment No. 1D, did not have a crack. This experiment was performed in order to assess the preliminary design information and, indeed, some adjustments were found to be necessary because of the idealizations contained in the analysis. The second experiment, 2D, was designed such that the initial crack was a through-wall crack with a length of about 15 percent of the circumference. Sharp saw cuts of the same acuity as in the bend specimen and flat-plate tests were employed. This was slightly greater than that required for initiation according to the net-section stress criterion and the uncracked pipe dynamic bending stresses. For a number of reasons (such as the greater compliance of the cracked pipe, the finite load duration, and load-rate effects), crack growth was not expected. And, in fact, crack growth initiation did not occur. The maximum crack-tip opening displacement was 0.254 mm (0.010 in.), whereas the critical COD for initiation was 2.5 mm (0.100 in.). Although this was only one-tenth of the critical COD, it was 80 percent of the load required for crack initiation; see Fig. 12.

To perform the third experiment, the crack length was arbitrarily doubled. Somewhat surprisingly, no crack growth was experienced in this test either. The crack-tip opening displacement was 1.75 mm (0.070 in.), which was 70 percent of the initiation value. This corresponded to a maximum applied load of 85 percent of that necessary for crack initiation; see Fig. 12.[6] It is clear from Fig. 12 that, as the crack length increases, the pipe compliance reduces the dynamic bending moment enough to preclude crack initiation.

A circumferential crack length equal to 50 percent of the circumference was used in the fourth experiment, 4D, to insure crack initiation and growth. In this experiment the crack initiated and grew approximately 3 mm (0.12 in.) at each crack tip before it arrested. This result and the results of the three preceding dynamic pipe fracture experiments, when compared with the quasi-static experiments on the basis of the bending moments calculated for an *uncracked* pipe, suggest a large margin of safety. However, when the reduction of the bending moment due to the compliance of the cracked structure is taken into account—see Fig. 12—this margin is considerably reduced. Nevertheless, because pipe fracture was not achieved even though the net-section stress criterion was exceeded, a margin of safety does indeed exist in dynamic loading. However, the exact amount cannot be determined in the absence of dynamic experiments in which fracture instability is achieved.

[5] The peak bending moments were about 20 percent higher than those calculated using the quasi-static stress-strain curve.

[6] The experimental data in Fig. 12 were obtained by conducting a series of experiments on pipes of different toughnesses.

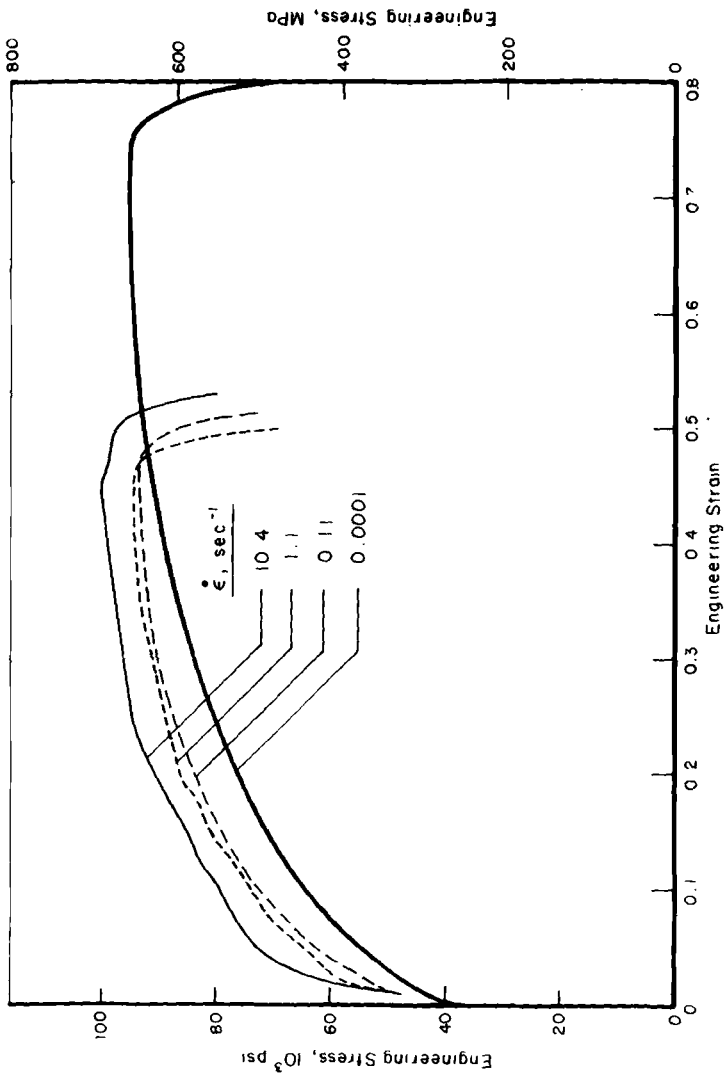

FIG. 11—*Effect of strain rate on stress-strain behavior of 8.4-mm-thick (0.33 in.) Type 304 stainless steel plate tested in tension at room temperature.*

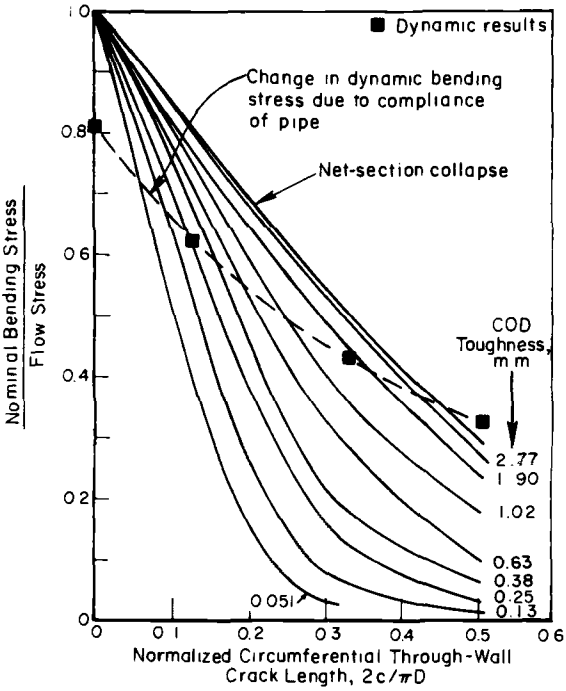

FIG. 12—*Comparison of dynamic loading experimental data with static test data for through-wall circumferentially cracked Type 304 stainless steel pipes in bending.*

Plastic Fracture Mechanics Analysis

Plastic fracture investigations have established that J-integral-based assessments can be highly effective [*5*]. Recent work [*6*] has carried these assessments into the dynamic region. Hence, the dynamic pipe experimental data can be analyzed to obtain an estimate of the applied J-integral as a function of time. Using this result in combination with the experimentally determined point for crack initiation (expressed in time) would then determine the initiation *J*-value for the dynamic loading. The experiment examined was dynamic pipe experiment No. 4D, which contained a 50 percent through-thickness crack, because only in this experiment was crack initiation obtained. Hence, this exercise cannot offer a complete assessment of the applicability of the plastic fracture mechanics analysis procedure. In particular, the tearing modulus fracture instability prediction cannot be tested since instability was not obtained experimentally.

As in the work of Zahoor and Kanninen [*7*], an estimate of the J-integral for a pipe with a circumferential through-thickness crack that is subjected to bending loads can be obtained from

$$J = -\int_0^{\theta_{pl}} \frac{\partial M_L}{\partial(\text{crack area})}\bigg|_{\theta_{pl}} d\theta_{pl} \tag{1}$$

where M_L is the limit moment and θ_{pl} is the rotation of the pipe due to plasticity confined in the crack section. Under the usual assumption that a limit moment exists

$$J = -\int_0^{\theta_{pl}} \frac{dM_L}{d(\text{crack area})}\,\theta_{pl}$$

or

$$J = \beta \int_0^{\theta_{pl}} M_L d\theta_{pl} \tag{2}$$

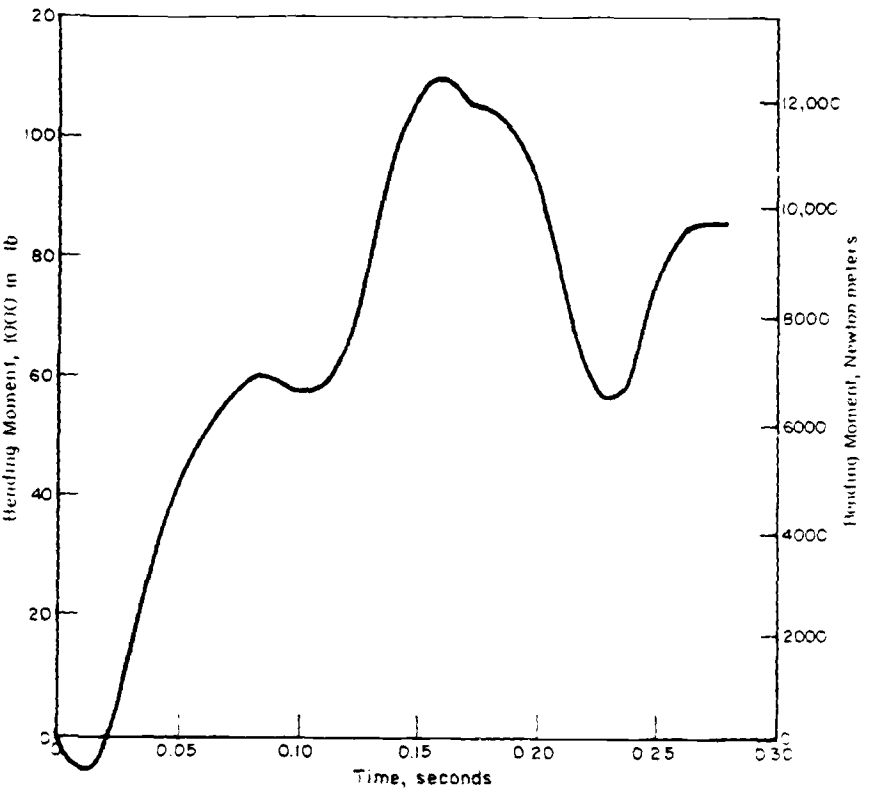

FIG. 13—*Experimental bending moment variation with time in dynamic pipe fracture experiment No. 4D.*

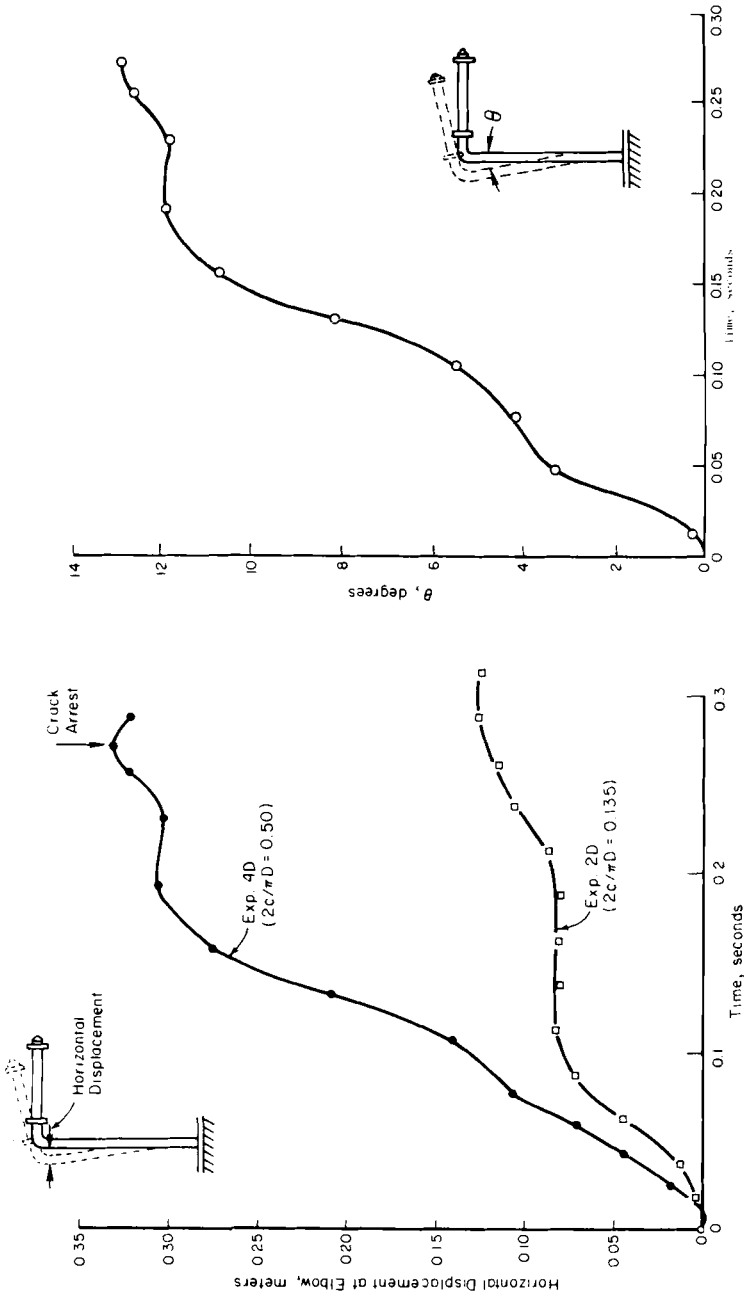

(a) Comparison of horizontal displacements of elbow from experiments and finite element calculations.

(b) Total rotations of pipe above the crack plane during Experiment 4D.

FIG. 14—*Horizontal displacement and pipe rotation in Experiment 4D (1 m = 3.28 ft).*

In Eq 2, β is a geometric function that depends solely on the crack length and the pipe dimensions defined in the foregoing.

In order to make use of Eq 2, data on the limit moment and pipe rotation are required. In the case of dynamic loading, these quantities must be known as a function of time. The experimental bending moment variation with time is shown in Fig. 13. The variation of pipe rotation with time can be extracted from the elbow displacement data. These are given for Experiment 4D in Fig. 14. Equation 2 can then be used to determine J versus time. The result is shown in Fig. 15.

As shown in Fig. 15, the maximum J-value occurs at a time $t = 0.28$ s with a value of 3.590 MN/m (20 500 in. · lb/in.^{2}). It should be noted that the maximum bending moment occurs at a θ_{pl}-value of 0.16 rad (which occurs at time $t = 0.15$ s). The estimated J-integral value at this instant was 1.534 MN/m (8760 in. · lb/in.^{2}). The point where the bending moment drops off very sharply gives a J-value of 3.345 MN/m (19 000 in. · lb/in.^{2}). This is the time when the pipe is experiencing unloading. Based on this information, the initiation is predicted at 1.534 MN/m (8760 in. · lb/in.^{2}) at a time $t = 0.15$ s.

Comparison with Figure 7 shows that the value of $J = 1.53$ MJ/m^2 (8760 in. · lb/in.^{2}) for initiation is consistent with the higher impact specimen generated J-resistance curves. Moreover, because J does fall off rather sharply for

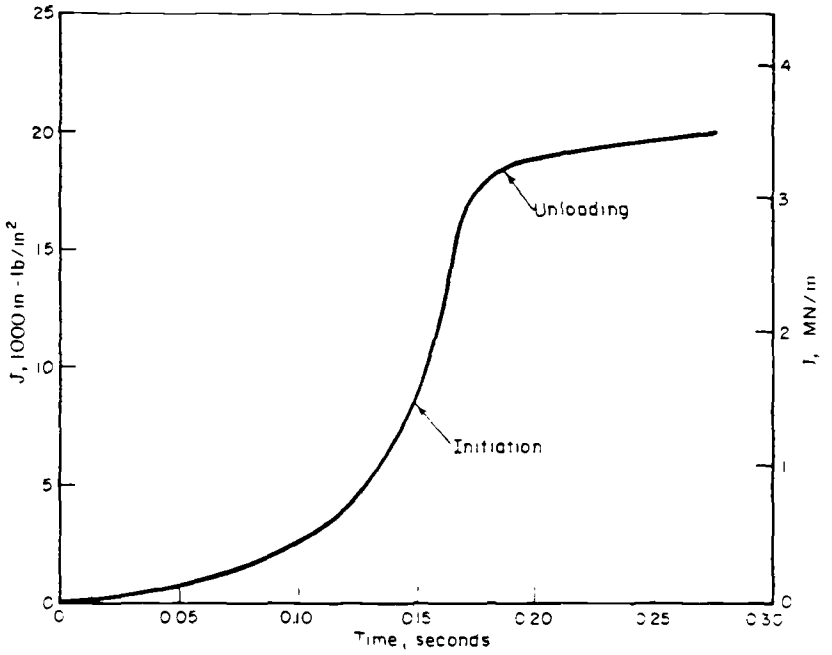

FIG. 15—*Estimated applied J versus time curve for the dynamic pipe fracture experiment No. 4D.*

greater times, the calculation is qualitatively consistent with the observation of crack arrest after a small amount of crack growth. Specifically, the J-value at crack arrest was 3.06 MJ/m^2 (17 500 in. · lb/in.^{2}). This J-value and the experimental crack growth of 3.2 mm (0.125 in.) are compared with the bend specimen J-resistance curve in Fig. 16. The dynamic pipe J-value is slightly above the impact test results, but is in reasonable agreement.

Conclusions

The research reported in this paper has led to three main conclusions. First, the net-section stress failure criterion for Type 304 stainless steel appears to be unaffected by dynamic and nonmonotonic loading. Second, a margin of safety exists in dynamic loading of circumferentially cracked Type 304 stainless steel pipes that is primarily due to the finite duration of the load and the system compliance. Third, plastic fracture mechanics assessments for crack growth and fracture instability under dynamic loading, including the load rate effects on the mechanical and fracture properties of the materials, can give reasonable crack growth and instability/arrest predictions.

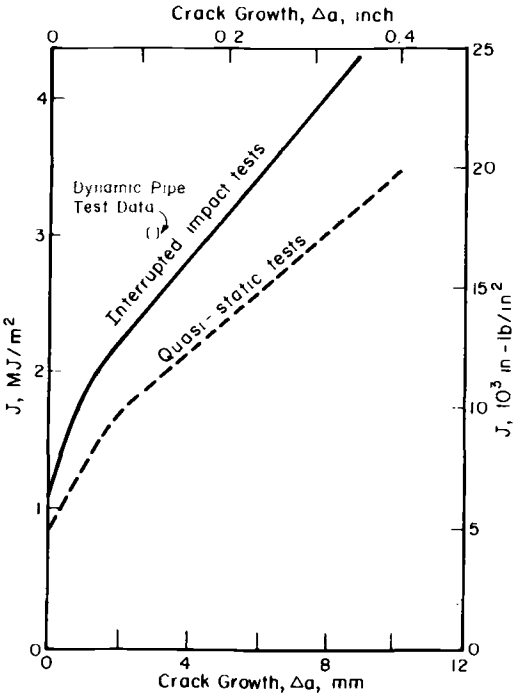

FIG. 16—*Comparison of the dynamic pipe fracture experiment and the J-resistance curves for Type 304 stainless steel generated from sharp-notched three-point-bend specimens tests.*

Acknowledgment

The research reported in this paper was part of project T118-2 supported by the Electric Power Research Institute, Palo Alto, Calif. The authors would like to express their gratitude to Dr. Douglas Norris of EPRI for his encouragement of their work. The high-loading-rate 3-point-bend bar specimen experiments discussed in this paper were performed at the Fracture Control Corp., Goleta, Calif.

References

[1] Kanninen, M. F., Broek, D., Marschall, C. W., Rybicki, E. F., Sampath, S. G., Simonen, F. A., and Wilkowski, G. M., "Mechanical Fracture Predictions for Sensitized Stainless Steel Piping with Circumferential Cracks," EPRI NP-192, Electric Power Research Institute, Palo Alto, Calif., Sept. 1976.

[2] Kanninen, M. F., Broek, D., Hahn, G. T., Marschall, C. W., Rybicki, E. F., and Wilkowski, G. M., *Nuclear Engineering and Design*, Vol. 48, 1978, pp. 117-134.

[3] Kanninen, M. F., Zahoor, A., Wilkowski, G., Abou-Sayed, I., Marschall, C., Broek, D., Sampath, S., Rhee, C., and Ahmad, J., "Instability Predictions for Circumferentially Cracked Type 304 Stainless Steel Pipes Under Dynamic Loading," Battelle's Columbus Laboratories Report to the Electric Power Research Institute on RP T118-2, Columbus, Ohio, 30 June 1981.

[4] Kiefner, J. F., Maxey, W. A., Eiber, R. J., and Duffey, A. A. in *Progress in Flaw Growth and Fracture Toughness Testing, ASTM STP 536*, American Society for Testing and Materials, 1973, pp. 461-481.

[5] Marston, T. U., Jones, R. L., Kanninen, M. F., and Mowbray, D. F., this publication, pp. II-115-II-132.

[6] Ahmad, J., Barnes, C. R., and Kanninen, M. F., this publication, pp. I-214-I-239.

[7] Zahoor, A. and Kanninen, M. F., this publication, pp. II-291-II-308.

Test Methods and Geometry Effects

Donald E. McCabe[1] *and John D. Landes*[1]

J_R-Curve Testing of Large Compact Specimens

REFERENCE: McCabe, D. E. and Landes, J. D., **"J_R-Curve Testing of Large Compact Specimens,"** *Elastic-Plastic Fracture: Second Symposium, Volume II—Fracture Resistance Curves and Engineering Applications, ASTM STP 803*, C. F. Shih and J. P. Gudas, Eds., American Society for Testing and Materials, 1983, pp. II-353-II-371.

ABSTRACT: This paper describes experiences and special testing techniques applied to J_R-curve development using compact specimens ranging in size by factors up to 20. All specimens were 20 percent side-grooved. The material used was A508 Class 2A and the tests were made at 477 K (400°F). Unloading compliance was used to measure crack growth and a special displacement measuring gage having high sensitivity and linearity was developed to detect minute compliance changes of the order of 0.1 percent. High-temperature creep effects were present but these were readily eliminated from interfering with unloading compliance precision by prior partial unloading to below the creep deformation range. Crack growth was calculated using a differential compliance formula and was usually predicted accurately within ±15 percent of the heat tint indicated growth. This was generally true over a wide range of specimen sizes and initial crack sizes.

An example J_R-curve comparison is given, comparing small-specimen versus large-specimen data. Deviation from a common J_R-curve develops when $\Delta a_p \geq 0.06\, b_0$, where b_0 is the initial specimen ligament size. For the smallest specimen data, a modified J calculation was applied which reestablishes comparability between large- versus small-specimen J_R data, and this can be maintained over crack growth that represents a substantial ligament size change.

KEY WORDS: elastic-plastic fracture, J_R-curve, key curve, A508 steel

The fracture toughness behavior of structural materials is now appropriately modeled in terms of the J_R-curve characteristics. Although R-curve concepts and testing techniques had been developed on high-strength materials, the predominant effort is now being put into descriptions for structural grade materials. The development of reproducible and reliable elastic-plastic J_R-curves is not an easy experimental task and this paper is devoted to the consideration of testing techniques and to some of the analytical aspects associated

[1]Senior engineer and advisory engineer, respectively, Materials Research Department, Westinghouse R&D Center, 1310 Beulah Rd., Pittsburgh, Pa. 15235.

with testing methods. An R-curve is a plot of material toughness development, usually expressed in terms of J_R, versus observed stable growth. One problem area that has received considerable attention recently has been the justification for the use of J under growing crack conditions. New or revised computational methods that have been applied is a subject matter that has been covered in a previous paper [*1*].[2]

Experimental Practices

The main focus of attention here will be on the experimental procedures applied to measure slow-stable crack extension, and specifically, unloading compliance [*2*]. The testing procedure was to periodically partially unload the specimen about 10 to 15 percent to obtain unloading slopes. The slopes are completely linear, independent of prior plastic deformation, and related to the existing physical crack size. Careful measurement of changes in slope as the test progresses can be used with known linear elastic compliance calibrations to determine physical crack size. The crack size change of interest to J_R-curve concerns is often-times small relative to the overall specimen dimensions. Hence changes in slope will also be small and it is necessary to attune instrumentation accuracy requirements to this fact [*3*]. To illustrate, Table 1 lists various standard sizes of compact specimens and the change in compliance that 0.13 mm (0.005 in.) of stable crack growth would represent. It is immediately obvious that extraordinary precision in unloading compliance practice is needed for the larger specimens. Transducer signals are handled as is depicted in Fig. 1. The specimen is loaded in clevises which contain flat bottom holes that serve to minimize friction due to pin rotation as the specimen is opened [ASTM Test for Plane-Strain Fracture Toughness of Metallic Materials (E 399-78a)]. Careful specimen alignment is absolutely mandatory. Knife edges made from spot-welded-on razor blades are attached at the specimen load line, and these serve as precision attachment points for the clip gage. The sharp edges give a precise fit which is completely devoid of contact point sliding. The transducers and amplifiers used are carefully calibrated and periodically checked for sensitivity and linearity. The two x-y recorders

TABLE 1—*Compliance change (%) for 0.127 mm (0.005 in.) of crack growth, assuming* $a_0/W = 0.5$.

Size	a_0, in. (mm)	Crack Size Change, %	Compliance, $\Delta C/C_0$, %
1T	1 (25.4)	0.5	1.2
2T	2 (50.8)	0.25	0.6
4T	4 (101.6)	0.12	0.3
10T	10 (254)	0.05	0.13

[2]The italic numbers in brackets refer to the list of references appended to this paper.

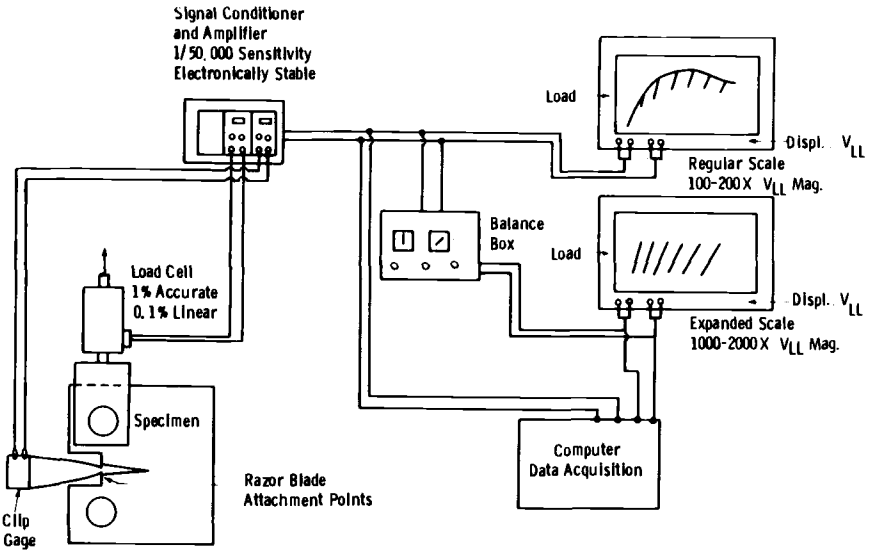

FIG. 1—*Schematic of test system for partial unloading compliance J_R-curve testing.*

shown represent two levels of signal magnification; the smaller scale is for J determination, and the enlarged scale for unloading slope determination of crack size. The appearance of the enlarged scale unloading slopes is usually a key indicator of a successful or appropriately made test setup. The unload and reload slopes should be linear and if the pen is kept down to trace in both directions, a well set-up specimen or test condition will show no separation of the two slopes; namely, no hysteresis loop effects.

Many investigators prefer to digitally compile the load-displacement data in a computer for fully automated J_R-curve determinations, [*4*]. However, this can be a productive venture only if the test specimens used and instrumentation variations are amenable to a routine practice. The wide range of specimen and crack sizes in the present project (to be described) had been judged to be outside of the bounds for easy computer adaptations.

A dominant part of what has been established as recommendations for J_R-curve development has been based on experiences with the testing of 1T-size compact specimens for J_{Ic} [ASTM Determination of J_{Ic}, A Measure of Fracture Toughness (E 813-81)]. Here one is permitted to take a somewhat narrow viewpoint on test method requirements since the identification of the onset of stable crack growth is the primary objective. Of greatest importance is the ability to detect small increments of growth such as in the aforementioned 0.13-mm (0.005 in.) increment example, and the accuracy of crack size measurements to larger crack extensions tends to be somewhat immaterial.

If the objective of the experiment is to characterize the material J_R-curve behavior, the perspective on test method requirements should be revised ac-

cordingly. Less emphasis is needed on the detection of small increments of growth and more emphasis is placed on the accuracy of crack size determination following relatively substantial stable crack growth. Herein resides a new problem, because straight-sided specimens will develop shear lips which (1) tend to pin the crack growth at the surfaces, creating thumbnail shaped crack fronts, and (2) reduce the accuracy of unloading compliance crack size determinations. A solution to this has been to side-groove specimen faces to a depth that will result in straight propagated crack fronts. Generally, this has been found to establish good correlation between compliance indicated and physically measured crack sizes over an extensive amount of crack growth [*5*]. The major penalty, however, is that the apparent material J_R-curve behavior is oftentimes changed and it is not presently known for certain that this change is a real material behavior resulting from plane-strain constraint, or if the new J_R-curve is unique to side-grooving. If the latter is true, the resulting J_R-curve is of no value to design condition considerations.

Material and Equipment

A 3.3-m-diameter (130 in.) by 0.53-m-thick (21 in.) forged tube plate of A508 Class 2A steel was obtained for an investigation to study specimen size and geometry effects on J_R-curve. The sample was extensively evaluated for material property variability and considerable differences were found, particularly in the skin [to about 127 mm (5 in.) depth] and rim [in to about 508 mm (20 in.)] areas. A region of reasonable uniformity of properties was found for specimen selection and the values representative of this zone are listed in Table 2. Specimens were made to plan view dimensions of the standard compact geometry with the test matrix designed to study the effects of variable thicknesses and initial crack sizes on J_R-curve behavior. The dimensional variables of the test matrix are summarized in Table 3: All were 20 percent (10 percent each face) side-grooved. The specimens were precracked prior to the side groove machining and this generally resulted in relatively straight initial crack fronts. In large thick specimens, excellent precrack control was obtained by first precompressing the specimens at a load of equal magnitude to the initial precracking tension load. Fatigue cracks initiate more easily and propagate more uniformly for a short time along a straight crack front. The test matrix is shown in the form of broken specimen halves in Fig. 2.

Specimen Design

ASTM Method E 813 and a present draft method for R-curve determination contain a recommended 1T-size compact specimen design shown in Fig. 3*a*. A large cutout area on the front face is used to accommodate razor blade attachments on the load line. Accordingly, the loading pin hole spacing is rather large, increased by $0.2W$ over that of the Method E 399 compact spec-

TABLE 2—*Material properties A508 Class 2A (center slab position).*

Yield Strength		Tensile Strength		Elongation, %	Reduction of Area, %	Hardness R_B	CVN,[a] ft-lb (J)		FATT,[b] °F	(K)
ksi	(MPa)	ksi	(MPa)							
55	(380)	80	(550)	30	63	87	115	(157)	100	(396)

[a]Charpy V-notch.
[b]Fracture appearance transition temperature.

TABLE 3—*Test matrix for specimen size and dimension effects on J_R-curve.*

Size Code	Plan View Dimensions, in. W	H	Gross Thickness, in.	Relative Initial Crack Size, a_0/W
½T	1	1.2	0.5 and 1.0	0.5
1T	2	2.4	0.5 and 1.0	0.5 and 0.75
2T	4	4.8	0.5 and 2.0	0.5 and 0.875
4T	8	9.6	1.0 and 2.0 and 4.0	0.5 and 0.75 and 0.875
10T	20	24	1.0 and 10.0	0.55

1 in. = 25.4 mm.

imen. This design is quite susceptible to pin-hole failures due to the small under-hole ligament, and this can be particularly troublesome when loads are high due to a_0/W less than 0.6. An improved 1T design was employed herein, Fig. 3*b*. All larger specimens (2T, 4T, and 10T) were made to the E 399 plan view dimensions with a relatively narrow cutout for the load-line gage.

Unloading Compliance Gage

With reference to the information in Table 1, it would appear that in order to detect changes in crack size in larger specimens, extraordinary measures must be taken to optimize both the sensitivity and linearity of the displacement measuring transducers, [*6*]. Sensitivity and linearity in the 0.25 to 0.50 μm (10 to 20 μin.) range would appear to be needed. A gage designed and built to substantially satisfy this need is shown in Fig. 4. The gage has an overall working range of 50 mm (2 in.) and the high sensitivity is obtained with a 1.3-mm (0.05 in.) linear variable differential transducer (LVDT) which according to design specifications is linear to 1.3 μm (50 μin.) over its working range. As a specimen is loaded, the core position is continuously adjusted to an electrical balance position. The gage is used only on unloading and over a small displacement change. Actually, a good working version of this gage was developed only after several design and test iterations involving several

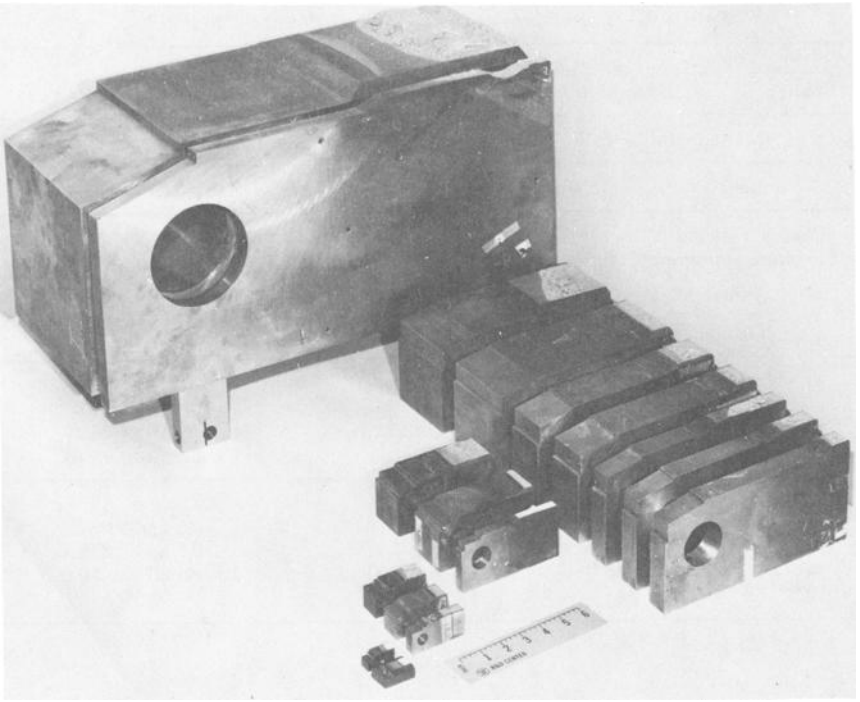

FIG. 2—*Specimen sizes tested in R-curve effects study.*

semi-successful schemes. The key elements which eventually evolved to make an optimum design were

1. A precision ball-bearing type slide bar which is absolutely rigid in the transverse direction and almost friction free to longitudinal motion. Angular displacement is thereby efficiently converted to linear displacement.
2. Point contact is made to the extension arms from the front face of the specimen. Cone type points are seated in Rockwell C indentation points on the extension arms. The leaf springs shown serve only to keep the contact cones firmly in place.
3. No springs are used to force motion. The dead weight of the gage supplies all of the forces necessary.
4. Automatic core positioning with an electrical balance circuitry and motor was considered but this was postponed for later development.

The gage was calibrated against a capacitive-type [0.254-mm (0.010 in.)] LVDT which is sensitive and linear to within 5×10^{-5}-mm (2 μin.). Table 4 gives the comparison made with both systems mounted in parallel in a calibrator. The 10^{-3}-mm (50 μin.) linearity of the 1.3-mm (0.05 in.) LVDT appears to be satisfactory and the suggested precision is adequate to contain at

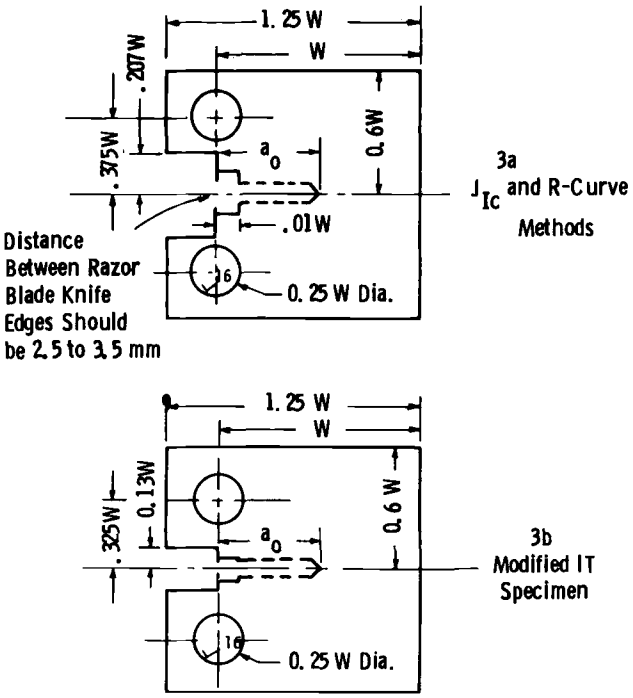

FIG. 3—*Comparison of standard specimen design* (a), *and modified design* (b), *1T size.*

worst 0.25 mm (0.010 in.) of crack growth error in a 10T-size compact specimen. This corresponds to about 0.1 percent error in overall crack size.

Testing Techniques

Elevated Temperature Testing

Prior to committing to the testing of the large specimens, a rather extensive material toughness survey was made with 1T-size compact specimens. As a result, a safe temperature of 477 K (400°F) was established where all possible sizes of specimens could be expected to be safely on the upper shelf of the transition temperature behavior. For such high-temperature conditions, it is not always necessary to heat the entire specimen plus grips assembly. In fact, good temperature control of the test zone can be obtained by heating only the part that projects out behind the clevis and this practice has been used successfully for test temperatures as high as 533 K (500°F). There is an advantage to this from the standpoint that instrumentation placed on the front face of the specimens will not see high temperatures and no special high-temperature capability clip gages are required. Generally, specimens can be fitted

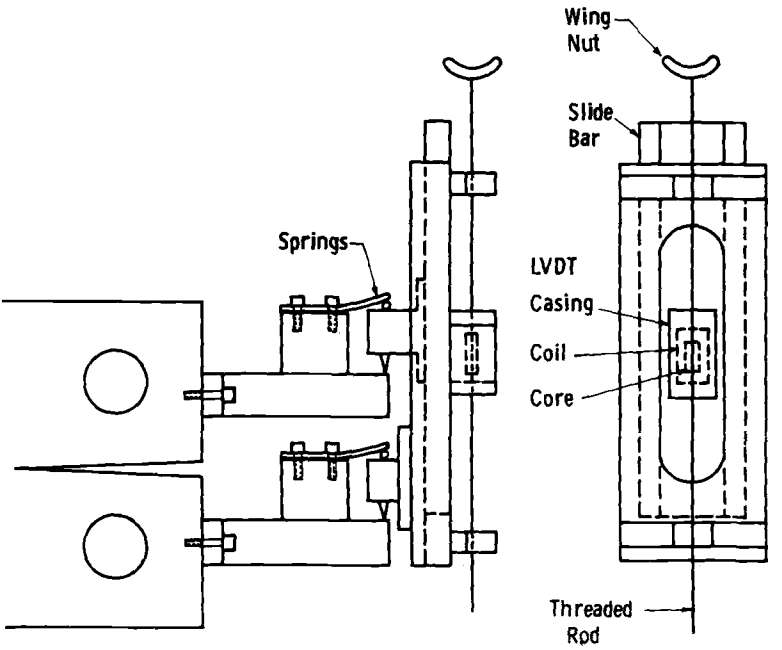

FIG. 4—*Schematic drawing of rezeroing LVDT gage.*

with strip heaters in a similar manner to that shown for a 10T specimen in Fig. 5. Various strip heater sizes are available for different specimen sizes. Test temperature was monitored at four locations on the specimen surfaces and from shielded thermocouples which were embedded inside of the specimens through drilled holes emanating from the top and bottom surfaces of the specimen. Insulating materials can be wrapped around the heater-specimen assemblies to reduce heat loss and to promote temperature uniformity.

Figure 6 represents the family of gages used to test the various specimen sizes ranging from ½T to 10T compacts. The large long-arm clip gage was designed specifically to measure displacements up to 44 mm (1.75 in.) on the load line of the 10T specimen. The smaller clip gage is linear up to 19-mm (0.75 in.) displacement and it was used on all other specimen plan-view sizes ranging from ½T [W = 25.4 mm (1.0 in.)] to 4T [W = 203 mm (8.0 in.)]. These gages were attached to the specimens just outside of the hot zone and no special high-temperature strain gages or strain-gage adhesives were used. However, since the gages were attached with the tips in a hot zone, they tended to develop an elevated temperature gradient in the arms. Ordinary room convection currents will carry the heat away such that the gage body will be at room temperature. However, heat loss develops at an uncontrolled rate in the arms such that the clip gage will continuously and minutely change dimensions and the output will display a slight drift, oftentimes slow, and of small

TABLE 4—*Results of two calibration runs on the rezeroing LVDT gage.*

Run No. 1 Calibrator[a] Set Point, in.	Capacitive[b] LVDT, V	Rezero LVDT Gage, V	Difference, μin.[c]
0	0		
0.001	1.167	1.181	+14
0.002	2.215	2.232	+17
0.003	3.233	3.244	+11
0.004	4.079	4.092	+13
0.005	5.026	4.999	−27
0.006	6.014	5.988	−26
0.007	7.039	7.009	−30
0.008	8.084	8.050	−34
0.009	9.119	9.072	−47
0.010	10.043	10.084	−41
Run No. 2			
0.0010	.996	.993	− 3
0.0020	2.013	1.998	−15
0.0030	3.118	3.100	−18
0.0045	4.405	4.393	−12
0.0055	5.607	5.605	− 2
0.00675	6.766	6.765	− 1
0.0080	7.908	7.900	− 8
0.009	9.046	9.036	−10
0.010	10.131	10.117	−14
0.011	11.189	11.164	−25

[a]2 μin.[c] rated accuracy.
[b]Calibrator set point not carefully controlled because capacitive LVDT is used as reference standard.
[c]1 μin. = 0.0254 μm.

magnitude (in the millivolt range on a 10 V output scale). The drift could easily go unnoticed without special awareness and it would ordinarily be of almost no consequence to J_R determinations. For unloading compliance crack size determinations the errors could be enough to create problems. The remedy is simply to shield the clip gage arms from room convection currents with a lightweight pliable insulating material.

Unloading Slope Determinations

Ductile materials such as A508 have a tendency to display load relaxation behavior when tests are made at elevated temperatures such as 477 K (400°F). If a compact specimen is tested under displacement-controlled loading, and the test is stopped for the development of a partial unloading slope, a period of load relaxation will ensue. If unloading slopes are attempted during this relaxation, the slopes will be affected and a type of hysteresis loop will develop between unloading and reloading (on expanded scale records of the type indicated in Fig. 1). A usual practice to avoid this is to wait for the relaxation to

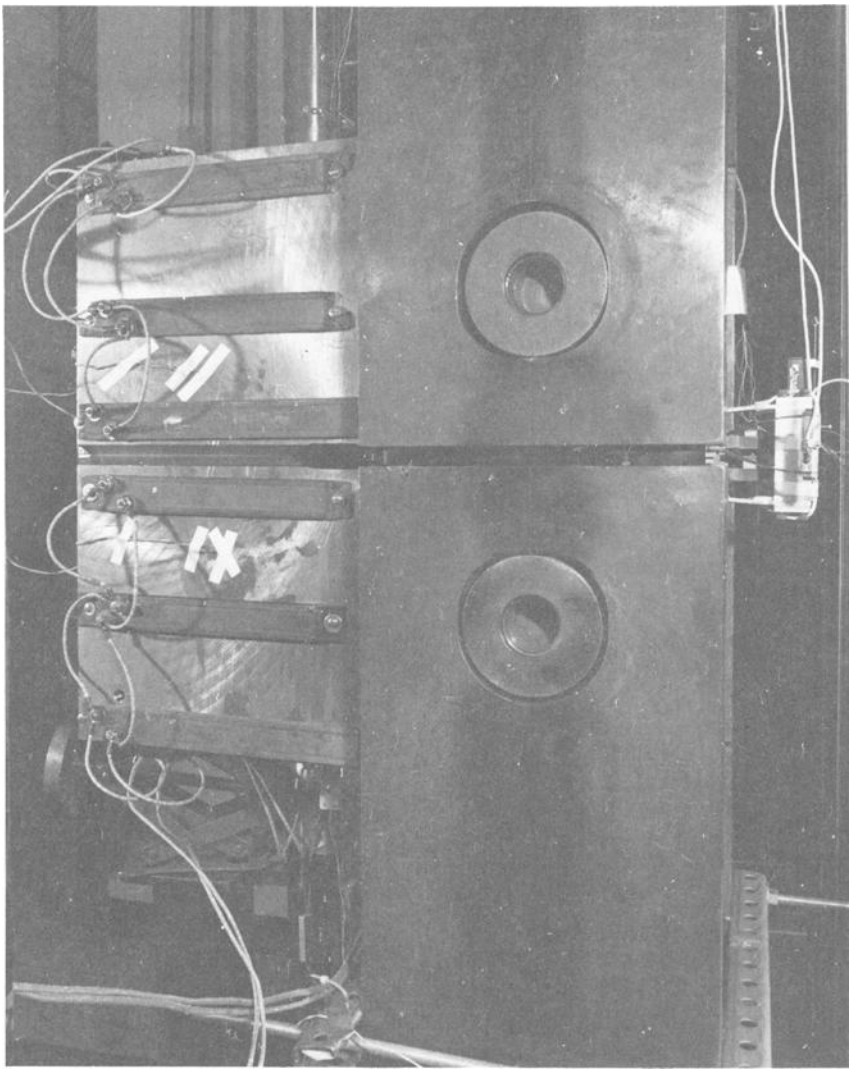

FIG. 5—*10T specimen fitted with sixteen 500-W strip heaters.*

subside, Fig. 7*a*. This can take several minutes, and when 15 to 20 unloading slopes are developed in a single test, the time of test is inconveniently expanded. Furthermore, the return to the original load versus displacement record shows a gap, the interpretation of which (with respect to total energy and J calculation) could be subject to question. An attractive alternative incorporated in the present program was to immediately reverse the applied

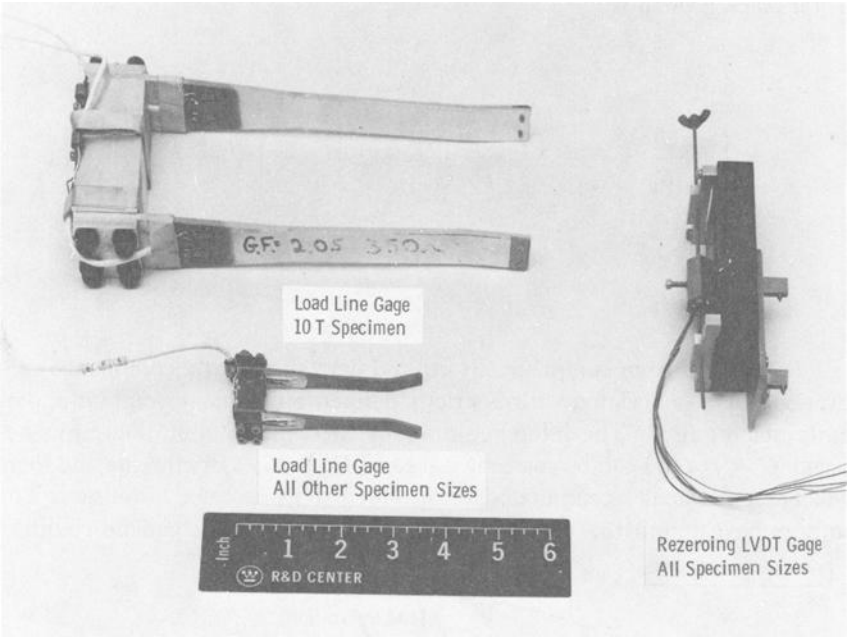

FIG. 6—*Gages used in specimen size effect study.*

displacement such that the load was immediately reduced to below the load relaxation range, Fig. 7*b*. Unloading slopes could then be developed with the assurance that the time-dependent effects were completely absent. Frequently 10 to 20 percent initial unload was necessary to avoid the relaxation at 477 K (400°F).

The A508 of the present project also showed a slight strain aging characteristic at 477 K (400°F). This was evidenced by a slight overshoot in load (from increased strength) immediately following the unloading slope, illustrated in Fig. 7*c*. Therefore, in order to ensure consistent J determinations, it was necessary to space the unloading slopes at intervals sufficient to reestablish the original test record character. The main problem with this was that on large specimens, the extended steps between unloadings caused the spacing on Δa_p increments to be greater than desired.

Crack growth was predicted using differential compliance (ASTM E 813) where

$$da_i = \frac{b_0}{2} \left[\frac{C_i - C_{i-1}}{C_{i-1}} \right] \left[\frac{1 + \alpha^2}{1 + \alpha} \right] \tag{1}$$

Total crack growth is

$$(\Delta ap)_i = \sum_{N=1}^{N=i} da_i$$

$$\alpha = \left[\left(\frac{2a}{b} \right)^2_{i-1} + 2 \left(\frac{2a}{b} \right)_{i-1} + 2 \right]^{1/2} - \left[\left(\frac{2a}{b} \right)_{i-1} + 1 \right]$$

$$b_i = [W - (a_0 + \Delta a_p)]$$

$$b_0 = (W - a_0)$$

Relative change in compliance is utilized here such that a compliance calibration curve, associated with a strictly defined attachment point, is apparently not required. The inference that the theoretical calibration curve behavior $C \approx f(a/w)$ can be correctly traced by Eq 1 is not strictly true and there will be some small accumulated error with extensive crack extension. The authors have found that the continual error accumulation can be counter-

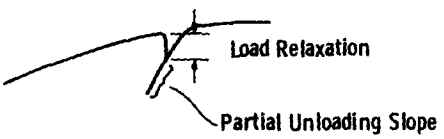

a) Local Test Record Appearance with Fixed Displacement Hold Period

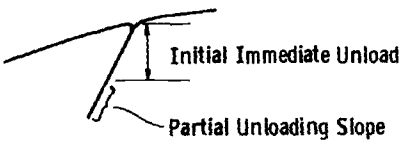

b) Local Test Record Appearance with Immediate Unload Past the Time Dependent Unloading Range

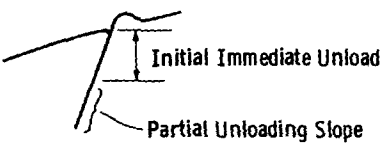

c) Local Test Record Appearance with Overshoot on Recovery

FIG. 7—*Segments of load-displacement records showing time-dependent effects.*

acted through the use of a fixed dimension b_0. Table 5 gives a comparison of crack growth dimensions by 9-point heat tint (E 813) and compliance predicted. Except for four cases, the agreement was within a very acceptable ± 15 percent.

J_R-Determinations

An expression has been recently developed by Ernst [*7*] which corrects deformation theory J for slow-stable crack growth

$$J_{i+1} = \left[J_i + \left(\frac{\eta}{b} \right)_i \frac{A_{i,i+1}}{B_N} \right] \left[1 - \left(\frac{\gamma}{b} \right)_i (a_{i+1} - a_i) \right] \qquad (2)$$

The subscripts i and $i + 1$ relate to test record increments and the parameters; η, γ, and b are updated between each step. These are defined as follows:

$$\eta = 2 + 0.522\, b/W$$
$$\gamma = 1 + 0.76\, b/W$$
$$b = [W - (a_0 + \Delta a_p)]$$

$A_{i,i+1}$ equals the incremental work between Steps i and $i + 1$. If side-grooved specimens are tested, the thickness dimension, B_N, used by most investigators is the net thickness. An experimental observation here was that the 20 percent side-grooved specimens showed increased initial elastic compliance slope of 10 percent over the theoretical non-side-groove compliance calibration. See Table 6. This suggests that elastic J and K_I^2/E will not be equivalent and that a new value of η is required. It therefore is evident that some further developmental work or stronger justifications or both should be applied to the calculation of J_R in side-grooved specimens.

J_R-curve data obtained for the extremes in specimen size covered in the present program are shown in Fig. 8. The open points are deformation theory J calculated by Eq 2 and the solid data points are modified J as has been discussed in Ref *1* and *8*. This new computational suggestion was derived from the observation made by Rice et al [*11*] that for a very special case of pure bend and for specimens with small ligaments, the use of a far-field J as opposed to deformation theory J will develop consistent J_R-curve behavior. Ernst adopted this suggestion and has developed a more generalized form for calculating J for a broader range of test condition circumstances

$$J_m = G + (J_D)_{Pl} + \int_{a_0}^{a} J_{Pl} \frac{\gamma}{b}\, da \qquad (3)$$

$$G = K_I^2/E = J_{el}$$

$(J_D)_{Pl}$ = Eq 2 using δ_{Pl} instead of δ_{total}.

TABLE 5—*Summary compliance predicted crack growth versus 9-point heat tint crack growth.*

Plan View Size	a_0, in.[a]	Δa_p-(in.) Predicted	Δa_p-(in.) 9-Point[b]	% Error
1XWOL	0.527	0.240	0.235	2
Mod WOL	0.525	0.219	0.197	11
½T	0.619	0.133	0.096	38
½T	0.525	0.211	0.193	9
½T	0.535	0.231	0.189	22
1T	1.525	0.135	0.142	5
1T	1.519	0.136	0.141	4
1T	1.552	0.121	0.125	3
1T	1.536	0.099	0.098	1
1T	1.029	0.223	0.244	9
1T	1.019	0.261	0.292	12
1T	1.040	0.183	0.183	0
1T	1.031	0.273	0.273	0
2T	2.010	0.535	0.506	6
2T	3.551	0.032	0.046	44
2T	3.628	0.067	0.066	1
2T	2.040	0.522	0.510	2
2T	2.114	0.595	0.604	1
4T	7.084	0.226	0.215	5
4T	7.074	0.228	0.202	13
4T	7.038	0.117	0.133	14
4T	7.067	0.086	0.098	14
4T	7.111	0.205	0.192	7
4T	7.047	0.142	0.160	13
4T	6.072	0.528	0.529	0
4T	6.080	0.484	0.458	6
4T	4.109	0.974	1.040	7
4T	4.149	0.960	0.982	2
4T	4.084	1.638	1.453	13
4T	4.141	1.057	1.236	17
10T	11.054	2.800	2.880	3
10T	13.596	1.015	1.064	5
10T	11.625	3.091	2.804	10
10T	11.774	3.250	2.890	12

[a]1 in. = 25.4 mm.
[b]Heat tint, 9-point measurement average.

For the larger specimens and where the crack growth is less than 6 percent of the initial ligament dimension, the difference between J calculated with no growth correction, deformation theory J (Eq 2), and modified J (Eq 3) is hardly identifiable. An example comparison is shown in Table 7 for crack growth data that extend to well beyond 0.06 b_0. The apparent similarity between modified J and uncorrected J is not fortuitous because after combining Eqs 2 and 3, we obtain (for the compact specimen geometry)

$$(J_M)_{i+1} = \left[J_i + \left(\frac{\eta}{b} \right)_i \frac{A_{i,i+1}}{B_N} \right] \left[1 - \left(\frac{\gamma}{b} \right)_i (a_{i+1} - a_i) \right]$$

$$+ \int_{a_0}^{a_{i+1}} J_{Pl} \frac{\gamma}{b} da \tag{4}$$

For small $a_{i+1} - a_i$

$$(J_M) = (J_{el} + J_{Pl}) - \int_{a_0}^{a} (J_{el} + J_{Pl}) \frac{\gamma}{b} da + \int_{a_0}^{a} J_{Pl} \frac{\gamma}{b} da \tag{5}$$

If data are taken over small growth increments, $(a_{i+1} - a_i)$, the second and third terms differ essentially by a factor times J elastic and in specimens with small initial ligaments, $J_{el} \ll J_{Pl}$. This suggests a tendency for J_M to be equal to J uncorrected for crack growth in the compact specimen geometry.

Discussion

As discussed in the introduction, J_R-curves have been used for J_{Ic} determinations where a premium has been placed on an ability to detect small growth increments. Furthermore, stable crack growth beyond 1.9 mm (0.07 to 0.08 in.) is somewhat incidental to the objectives and for all intents and purposes the extra data can be ignored. If J_R-curve is the principal objective, the local J_{Ic} data can be misleading as to what the overall J_R-curve behavior of the material might be. Figure 9 (taken from unpublished work) shows an obvious difference in J_R-curve behavior between 10 and 51-mm-thick (0.4 and 2.0 in.) A533B on a J_{Ic} scale of observation. When data points are extended to 12.7 mm (0.5 in.) of crack growth, bottom in Fig. 9, one can no longer be

TABLE 6—*A listing of compliance changes caused by 20% side groove.*

Specimen Size	Gross Thickness, in.[a]	a_0/W	Compliance Increase, %
10T	10	0.589	10.2
10T	10	0.581	15.8
4T	4	0.518	10.8
4T	4	0.510	13.5
4T	1	0.519	6.5
4T	1	0.514	13.6
2T	2	0.529	12.3
2T	2	0.510	7.1
1T	1	0.515	2.8
1T	1	0.520	5.9
1T	0.5	0.510	13.4
1T	0.5	0.515	16.6
0.5T	0.5	0.535	13.1
0.5T	0.5	0.525	7.8
		Avg $\Delta C/C$	10.7%

[a] 1 in. = 25.4 mm.

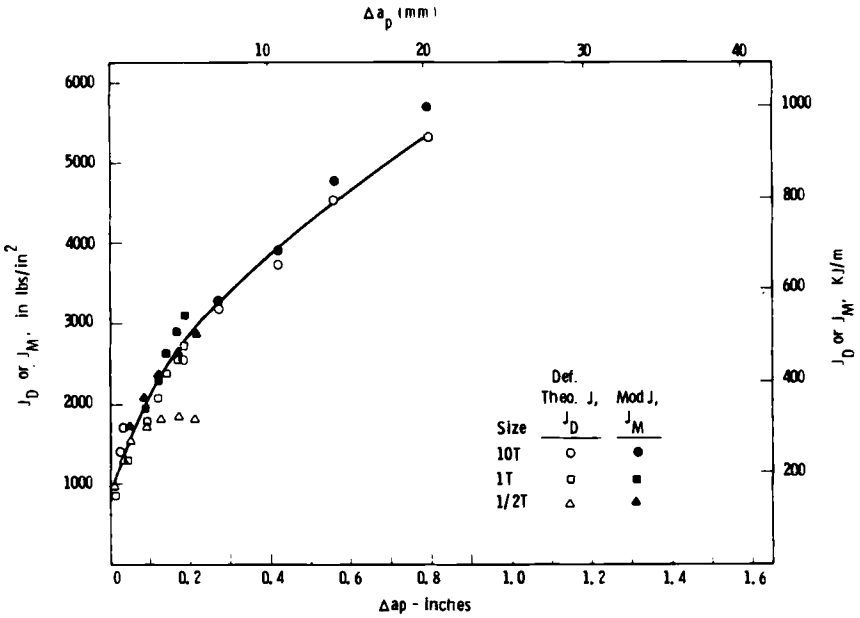

FIG. 8—*J_R-curve data for three sizes of 20 percent side-grooved specimens.*

TABLE 7—*Example: Comparison of* J *calculations.*

Event	Load, kips	(in.) Δa_p	(in.-lb/in²) J_D	(in.-lb/in²) J_M	Uncorrected, $J = \eta A/B_N b$	
1	0.52	0	5	5	5	
2	1.29	0	30	30	30	
3	2.02	0	95	95	95	
4	2.515	0	220	220	220	
5	2.900	0	520	520	520	
6	3.000	0.011	975	1000	1000	
7	2.885	0.028	1285	1365	1375	$\rightarrow \frac{\Delta a}{b_0} \simeq 0.06$
8	2.655	0.050	1535	1710	1715	
9	2.300	0.087	1705	2070	2070	
10	1.950	0.125	1815	2400	2380	
11	1.535	0.168	1835	2705	2650	
12	1.360	0.211	1790	2965	2870	

NOTES: 1 kip = 1000 lb (450 kg).
1 in. = 25.4 mm.
½T standard compact.
W = 1.0 in.
a_0 = 0.525 in.
B = 0.5.
B_N = 0.4.

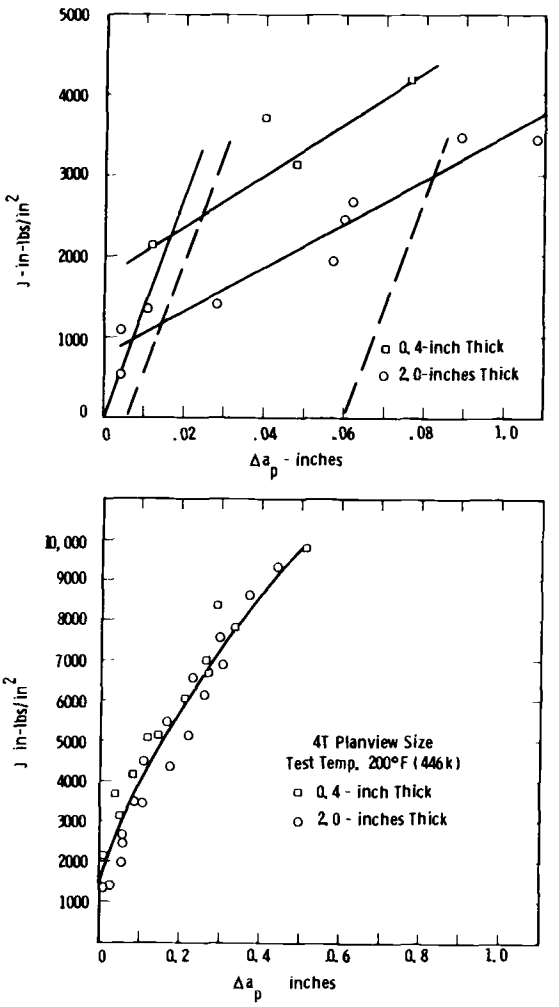

FIG. 9—*J_R-curve behavior of 10.16-mm-thick (0.4 in.) and 50.8-mm-thick (2 in.) A533B.*

convinced with absolute certainty that there is a basic difference in J_R-curve behavior.

Computer data acquisition and processing is commonly used for rapid and nonsubjective J_R-curve development. Even though computer capability was available to this program, it was not employed because of the wide variability of output information generated. This tended to negate the potential time savings advantage. Instead, extra effort was put into the more important test control features such as grips and specimen alignment, transducer precision, linearity, and calibration.

The recently proposed modified *J* calculation shows some potential for ob-

taining J_R-curve data from small specimens that could not possibly meet the validity criteria established for deformation theory J. If adequate material is available, use of larger specimens and deformation theory J is preferred since most analytically developed J-values are deformation theory related. A recommendation for optimum test conditions is to choose a specimen size such that $\Delta a_p < 0.06\, b_0$, ($b_0 = W - a_0$), and the computational method used to calculate J would be somewhat immaterial. In other words, J_D after crack growth, J calculated without growth correction, or modified J would give about the same numerical value of J.

The specimens in the present program were all 20 percent side-grooved and in all cases J was calculated on the basis of B_N to conform with the common practice. However, the experimental elastic compliance behavior of the present specimens would suggest that the present J approximation formulas based on a non-slide-groove dimensional analyses are misapplied in the present case.

Conclusions

In order to develop a fine-tuned unloading compliance method for the detection of small increments of crack extension in large standard compact specimens, a special rezeroing LVDT gage was designed and built. With a 1.27-mm (0.050 in.) LVDT, the gage was calibrated to be linear within 1.27 μm (50 μin).

A compliance change of the order of 0.1 percent was made possible from an instrumentation capability standpoint.

Although a compact specimen with a large cutout in the front face and widely spaced loading pinholes appears in a present draft method of the ASTM working committee on the J_R-curve, it is suggested here that something closer to the E 399 compact specimen design with a much reduced cutout zone be adopted.

For testing situations where there is time-dependent load relaxation when displacement-controlled loading is stopped, immediately reversed displacement to about 10 to 20 percent reduction of load prior to the unloading compliance slope determination is recommended. This offers the advantages of (1) reduced testing time, (2) less ambiguity in the interpretation of test record significance, and (3) unloading slopes that can be clearly obtained with no interference from creep effects.

For small specimens with small initial ligaments, it may be necessary to calculate toughness, J_R, in terms of a nondeformation theory J, (J_M), originally suggested by Rice et al and that was later generalized by Ernst as J_M. Conditions for deformation theory J will be violated and this will result in a premature upper plateau in the J_R-curve. This can be avoided with modified J, J_M. However, the overall significance of J_M is not easily justified and caution on its adoption and use is recommended until the ramifications of the suggestion are fully understood. Perhaps the best policy would be to use spec-

imens where Δap is less than 6 percent of the initial ligament size whenever possible. Here, variability due to computational methods would not be of concern.

Acknowledgment

The work presented in this paper was supported by the Electric Power Research Institute (EPRI) under Contract RP 1238-2. The authors would like to acknowledge Dr. D. M. Norris, Jr., EPRI project manager for this program, who contributed to the planning of the work.

The authors also acknowledge the assistance of their colleagues at Westinghouse: W. H. Pryle, who assisted with material handling and specimen preparations; F. Y. Gradich, who assisted with the equipment development; L. W. Burtner, T. R. Fabis, and W. T. Broush, who helped with the testing; and R. R. Hovan and J. Selchan, who assisted with the preparation of the manuscript.

References

[1] McCabe, D. E. and Ernst, H. A. in *Fracture Mechanics—14th Conference, ASTM STP 791*, American Society for Testing and Materials, 1983.

[2] Clarke, G. A., Andrews, W. R., Paris, P. C., and Schmidt, D. W. in *Mechanics of Crack Growth, ASTM STP 590*, American Society for Testing and Materials, 1976, pp. 27-42.

[3] "Tentative Test Procedure for Determining the Plane-Strain J_I-R Curve," A working document of Committee E24.08.03, Sixth Draft, American Society for Testing and Materials, May 1980.

[4] Joyce, J. A. and Gudas, J. P. in *Elastic-Plastic Fracture, ASTM STP 668*, J. D. Landes, J. A. Begley, and G. A. Clarke, Eds., American Society for Testing and Materials, 1979, pp. 451-468.

[5] Vassilaros, M. G., Joyce, J. A., Gudas, J. P. in *Fracture Mechanics—Twelfth Conference, ASTM STP 700*, American Society for Testing and Materials, 1980.

[6] Clarke, G. A. in *Fracture Mechanics—13th Conference, ASTM STP 743*, American Society for Testing and Materials, 1981, pp. 553-575.

[7] Ernst, H. A., Paris, P. C., and Landes, J. D. in *Fracture Mechanics—13th Conference, ASTM STP 743*, American Society for Testing and Materials, 1981, pp. 476-502.

[8] Ernst, H. A., this publication, pp. I-191-I-213.

[9] Herman, L. and Rice, J. R., "Comparison of Experiment and Theory for Elastic-Plastic Plane Strain Crack Growth," Brown University Report No. 76, Providence, R.I., Feb. 1980.

Anthony A. Willoughby[1] *and Stephen J. Garwood*[1]

On the Unloading Compliance Method of Deriving Single-Specimen R-Curves in Three-Point Bending

REFERENCE: Willoughby, A. A. and Garwood, S. J., **"On the Unloading Compliance Method of Deriving Single-Specimen R-Curves in Three-Point Bending,"** *Elastic-Plastic Fracture: Second Symposium, Volume II—Fracture Resistance Curves and Engineering Applications, ASTM STP 803*, C. F. Shih and J. P. Gudas, Eds., American Society for Testing and Materials, pp. II-372–II-397.

ABSTRACT: The application of unloading compliance for deriving single-specimen R-curves in three-point bending has been examined. Various methods, including the use of a double-clip-gage arrangement, are investigated. Finite-element calculations show that the best estimate of crack length is likely to be obtained from the conventional clip gage/load compliance, using $a/W \geq 0.5$. The results are compared with those from blunt-notched calibration test specimens and with fatigue-cracked specimens, both with and without side grooves, of two pressure vessel steels. It is found that the initial crack length may be estimated accurately, but that the estimate becomes less precise as tearing occurs. Consequently, predictions of crack extension are rather inaccurate. However, there is considerable scope for improvement in the measurement technique employed, and for the use of correction factors.

The use of two clip gages allows good estimates of load-point displacement, crack-tip opening displacement (CTOD) and J to be made, particularly when plastic displacements become significant. It is suggested that the technique could prove valuable in routine measurements of CTOD and J on bend specimens.

KEY WORDS: bend tests, R-curves, fracture toughness, crack-tip opening displacement, J-integral, measurement, compliance, calibration, elastic-plastic fracture

Nomenclature

a	Crack length
a_0, a_f	Initial, final crack length
Δa	Crack extension
B	Test specimen thickness between side grooves (if any)
B_0	Nominal test specimen thickness

[1]Senior research engineer and principal research engineer, respectively, The Welding Institute, Abington, Cambridge CB1 6AL, U.K.

C	Vertical distance between two knife-edge fixtures
CTOD	Crack-opening displacement at crack tip
E'	Effective Young's modulus, $E/(1 - \nu^2)$
J	J-integral
K	Stress-intensity factor
M	Geometrical factor relating J and CTOD
P	Load
q	Displacement of load point
q_v	q evaluated from two clip gages
q_c	component of q due to presence of crack
r	Rotational factor
S	Loading span
T	Tearing modulus
U	Absorbed energy
V	Mouth opening
v_1, v_2	Clip gage displacements at two knife-edge positions
V_1, V_2, V_3, V_4	Clip gage displacements at the positions defined in Fig. 2
$V_{(i)}$	Clip gage displacement at the start of ith unloading
V_{el}, V_P	Elastic and plastic components of clip gage displacement
W	Test specimen width
z_1, z_2	Knife-edge heights above test specimen surface
α_i	Correction factor for ith unloading
δ	CTOD
ν	Poisson's ratio
σ_Y	Yield stress

There has been considerable interest recently in measuring the toughness during crack extension of ductile materials such as medium-strength steels and aluminium alloys (that is, where the crack advances by a mechanism of microvoid coalescence or localized shear). The results are commonly expressed in terms of the crack-growth resistance curve, or R-curve, which is a plot of the toughness, in terms of the crack-tip opening displacement (CTOD) or the J-integral, versus the amount of crack extension. From this curve the toughness at initiation of tearing, δ_i or J_i, and the tearing modulus, T [*1*],[2] may be determined.

The multiple-specimen technique is the most unambiguous method of measuring R-curves, but it is laborious and wasteful of material. Of the single-specimen methods, unloading compliance has been used extensively on compact specimens [*2–4*], with encouraging results. This choice of test specimen has the advantage that the load-point displacement can be measured directly, by appropriate positioning of the knife edges between which the clip gage is fixed.

[2]The italic numbers in brackets refer to the list of references appended to this paper.

In many cases it is desirable to use three-point bend test specimen for measuring fracture toughness, for instance, when testing surface cracks. This investigation was undertaken on two structural steels in order to determine whether an unloading compliance technique could be applied to bend specimens. In addition to the standard displacement/load compliance, a double clip gage arrangement was examined in detail.

Unloading Compliance in Three-Point Bending

Compliance Using a Single Measure of Displacement

In a three-point bend specimen the compliance measure equivalent to that used for a compact tension geometry is the load-point displacement versus load, q/P, compliance. An alternative measurement to q is the mouth opening, V, of the crack. Analytical solutions for these compliances, q/P and V/P, as a function of crack length are available (for example, Tada [5], 1973). In practice, however, q and V are not easily measured. The load-point displacement, q, must either be derived from crosshead displacement corrected for extraneous displacements [6], or measured by means of a calibration beam [7]. The mouth opening, V, is usually measured at points above the specimen surface, using raised knife edges. In this case a simple solution for differing knife-edge thicknesses has not been published, so that individual calibrations are required. Another possible drawback of all displacement/load compliance measurements is that the effective load may vary during a bend test if the outer rollers are allowed to move, as with the standard fixture.

Compliance Using a Double-Clip Gage Arrangement

The double-compliance technique was first used by Heyer and McCabe [8] on crack line, wedge-loaded (CLWL) sheet specimens. By measuring the displacements, v_1 and v_2, at two locations along the crack line for blunt-notched calibration specimens, an experimental elastic relationship was derived between a/W and v_1/v_2. During small unloadings the slope v_1/v_2 was used to estimate the crack length, and the stress-intensity factor, K, was estimated from the maximum values of v_1 and v_2 before each unloading. The CLWL test specimen is effectively loaded in bending, and so it is possible that the same technique can be used on a three-point bend geometry by positioning two clip gages at different heights either above or below the top surface of the specimen.

From the double-clip-gage arrangement it is possible to derive several other parameters of interest by assuming that the test specimen deforms as two rigid halves about a center of rotation. From Fig. 1 it is apparent that the angle of bend, Θ, may be expressed in terms of v_1 and v_2 or q (assuming small angles) as

$$\frac{\Theta}{2} = \frac{q}{S/2} = \frac{(v_2 - v_1)/2}{C}$$

Hence the load-point displacement is given by

$$q = \frac{(v_2 - v_1)S}{4C}$$

$$= (v_2 - v_1)\frac{W}{C} \quad \text{if} \quad S = 4W \tag{1}$$

The rotational factor, r (defined as the ratio of the distance between the crack tip and the center of rotation to the net ligament, $W - a$), may be derived from geometrical considerations

$$\frac{r(W - a) + a + z_1}{v_1} = \frac{r(W - a) + a + z_2}{v_2}$$

where z_1 and z_2 are the knife-edge heights and $C = z_2 - z_1$. Hence

$$r = \frac{v_1(a + z_2) - v_2(a + z_1)}{(v_2 - v_1)(W - a)} \tag{2}$$

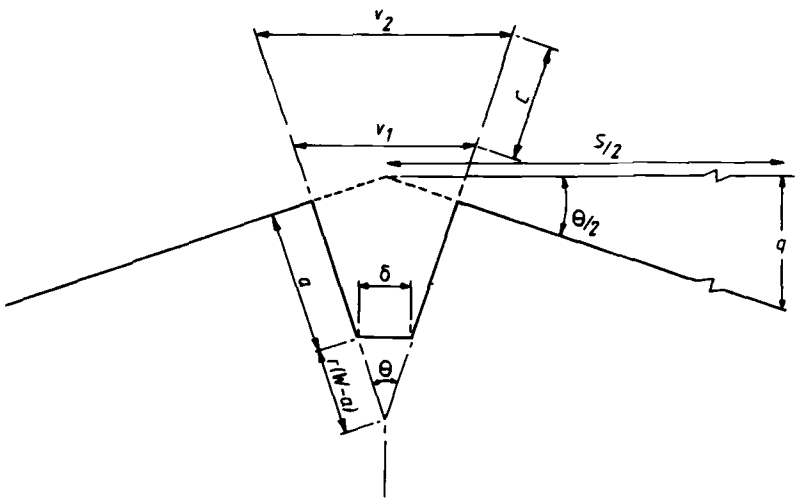

FIG. 1—*Geometrical relationship between clip gage displacement and load-point displacement.*

The CTOD, δ, is given by

$$\frac{v_1 - \delta}{a + z_1} = \frac{v_2 - v_1}{z_2 - z_1}$$

Hence

$$\delta = \frac{v_1(z_2 + a) - v_2(z_1 + a)}{z_2 - z_1} \tag{3}$$

Finally, the absorbed energy, U, and thus the J-integral, may be calculated from the load-point displacement, via [*10*]

$$U = \int P dq \tag{4}$$

and

$$J = \frac{2U}{B(W - a_0)} \tag{5}$$

It should be noted that two different types of behavior occur when performing a test with multiple unloadings. During loading, the material behaves in an elastic-plastic manner, and the relationships given in Eqs 1-5 are calculated using the instantaneous values of v_1 and v_2. During the unloading, the material behaves in an elastic manner, and the crack length is derived from the slope of the unloading line, dP/dq, dP/dV, or dv_1/dv_2, etc.

Experimental Details

Materials

The major part of the test program was carried out on a medium-strength steel, BS 1501-271 (Ducol W30), in the as-received condition. In addition, a limited number of tests was conducted using HY80 steel. The chemical composition and tensile properties of the two materials are given in Table 1.

Test Specimens and Knife Edges

Three-point bend test specimens were used exclusively, with width $W = 50$ mm, span $= 4W = 200$ mm, and nominal thickness $B_0 = 25$ mm. Some specimens were side-grooved to a depth of 5 mm on each side. All test specimens were extracted in the longitudinal orientation, with through-thickness notches (L-T orientation).

The test specimens were notched and fatigue-cracked to a depth of approx-

TABLE 1—*Properties of the materials tested.*

	Chemical Composition, weight %										
	C	S	P	Si	Mn	Ni	Cr	Mo	V	Cu	Al
BS 1501-271 ("Ducol")	0.125	0.015	0.026	0.37	1.17	0.79	0.54	0.27	...	0.10	...
HY80	0.16	0.009	<0.005	0.26	0.34	2.54	1.33	0.34	...	0.06	0.032

	Tensile Properties at +20°C		
	0.2% Proof Stress, N/mm^2	Ultimate Stress, N/mm^2	Elongation, %
BS 1501-271 ("Ducol")	506	675	29
HY80	588	712	22

imately 25 mm ($a/W \simeq 0.5$). A series of 12 blunt-notched calibration specimens, having no fatigue crack, was prepared from the Ducol. These had a/W ratios of 0.45, 0.5, 0.55, 0.6, 0.65, and 0.7, in both the plane-sided and side-grooved conditions.

Two different arrangements of the clip gages were investigated for the double-compliance measurements. In the first, the upper clip gage was attached to the normal knife edges, of thickness 3 mm, above the surface (Position 1 in Fig. 2*a*). The second set was attached by screws on the side of the specimen 20 mm below the top surface (Position 4 in Fig. 2*a*). This location was chosen to be as close as possible to the crack tip while remaining outside the plastic zone. In the second case a special support was designed so that both knife edges were located above the specimen surface, at heights of 6.1 and 53.1 mm

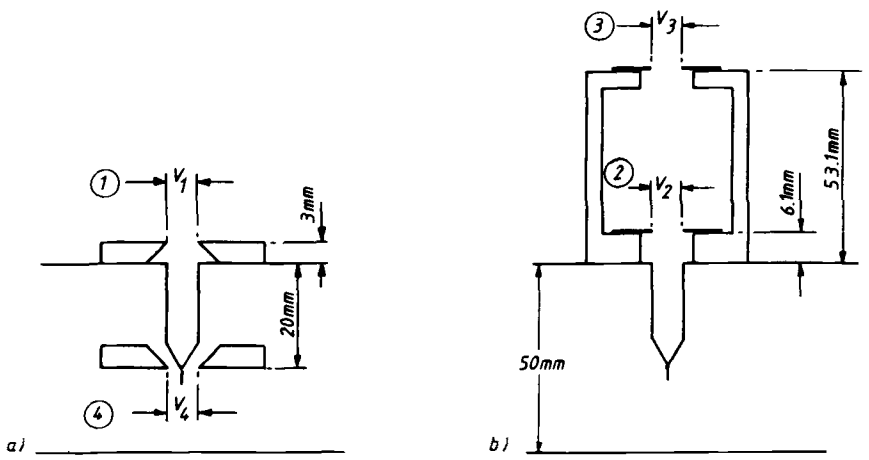

FIG. 2—*Positions 1 to 4 for the knife-edge fixtures.*

(Positions 2 and 3, respectively, in Fig. 2*b*). The arrangement is photographed in Fig. 3. The supports were machined from aluminium, the actual knife edges consisting of sections of razor blades spot-welded to steel inserts. A short-legged clip gage, capable of measuring displacements up to about 4 mm, was used at the lower knife-edge position and a longer-legged variety, which can measure up to 8 mm, at the upper location.

In all cases the knife edges or supports were screwed to the specimen to given an effective gage length of 18 mm for the measurement of the displacement.

Method

Mechanical testing was carried out on a servohydraulic test machine with standard [*11*] bend fixtures. All tests were at room temperature. The test specimens were initially loaded to well below the general yield load and several small unloadings were carried out to determine the initial crack length. Before unloading the test specimen was held at constant displacement until the time-dependent relaxation of the load was observed to cease. This hold period helps to remove any hysteresis in the unloading [*3*]. The unloading was also performed at a lower rate (0.01 mm/s) than the reloading (0.02 mm/s) to assist with data collection.

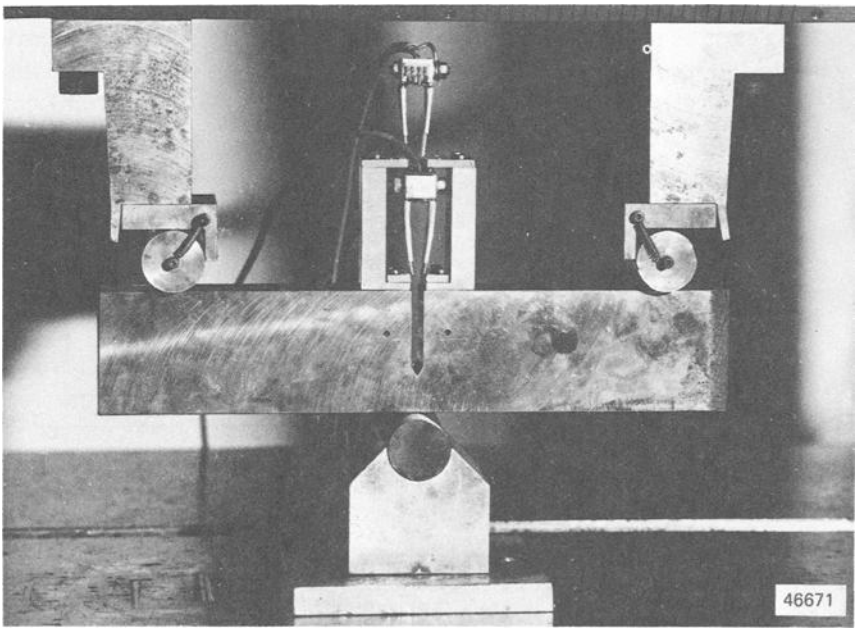

FIG. 3—*Photograph of the raised knife-edge supports on a calibration specimen.*

The test specimens were then given successive increments of displacement, each one being followed by a period at constant displacement, for relaxation of the load, followed by a slow unloading to about 70 percent of maximum load. Finally, the specimens were unloaded fully and broken open at low temperature in the cleavage mode to reveal the extent of tearing. The initial and final crack lengths were measured at five points equally spaced along the fracture face, and the results averaged.

During the course of the test, the load, ram displacement, and the displacements of the two clip gages were monitored continually by means of a computerized data logger. About 40 readings were taken during unloading, from which the unloading slope of load versus clip gage displacement between 95 and 75 percent of the maximum load was calculated by linear regression. The top 5 percent of the unloading was ignored to allow for load relaxation. By substituting the value of $E'B\ v/P$ (where $v = v_1$ or v_2, depending on clip gage position) into a previously obtained calibration polynomial, an indication of the crack length could be obtained at the end of each unloading.

The blunt-notched calibration specimens were cycled successively in the elastic range in order to derive the average compliance as a function of crack length for both plane-sided and side-grooved test specimens. The experimental calibrations were expressed as the crack length in terms of a polynomial in $E'B\ v/P$, where B is the actual thickness, (that is, the net thickness between the side grooves).

Finite-Element Computations

During the partial unloading the test specimen behaves elastically, and the compliances can be compared with published elastic solutions (for example, Tada [5]). However, this only gives solutions in terms of the load versus mouth opening, V, or displacement, q, neither of which is measured readily in a bend test. Therefore it was decided to run a series of elastic finite-element computations on the geometrical configuration employed, using crack lengths in the range $a/W = 0.05$ to 0.7.

The finite-element package used cubic quadrilateral elements, each containing 12 nodes. Special degenerate triangular elements at the crack tip allow the singularities to be modeled closely while employing comparatively few elements. The details are described more fully in Ref *12*.

The meshes used were designed to simulate the specimen geometry chosen, including the knife-edge attachments, with nodes placed at the fixing point for the crack tip knife edge (Position 4 in Fig. 2*a*) and at the knife-edge tips above the top surface (Positions 1, 2, and 3 in Fig. 2*a* and 2*b*). The computation of K and mouth opening V were compared with published results [5] and were found to differ by between 3 and 8 percent. After checking that the stresses in the knife-edge supports were acceptably low, the displacements at

all the knife-edge positions and the compliances were calculated for each a/W ratio. The results are given in detail in the Appendix.

Experimental Results

Variation in Compliance Functions with Crack Length

Several compliance functions were examined for the calibration specimens (during 20 percent unloading) and from the finite-element computation. They are expressed in nondimensional form as $E'BV_1/P$, $E'BV_2/P$, $E'BV_3/P$, $E'Bq_v/P$, V_1/V_4, and V_3/V_2, where the displacements V_1, V_2, V_3, and V_4 are as defined in Fig. 2, and q_v is derived from Eq 1, using the appropriate values of clip gage displacement and knife-edge height.

Figure 4 shows the variation in clip gage compliance $E'BV_1/P$ with the a/W ratio. The trends are identical for the calibration specimens and the finite-element results. However, the plane-sided calibration specimens gave

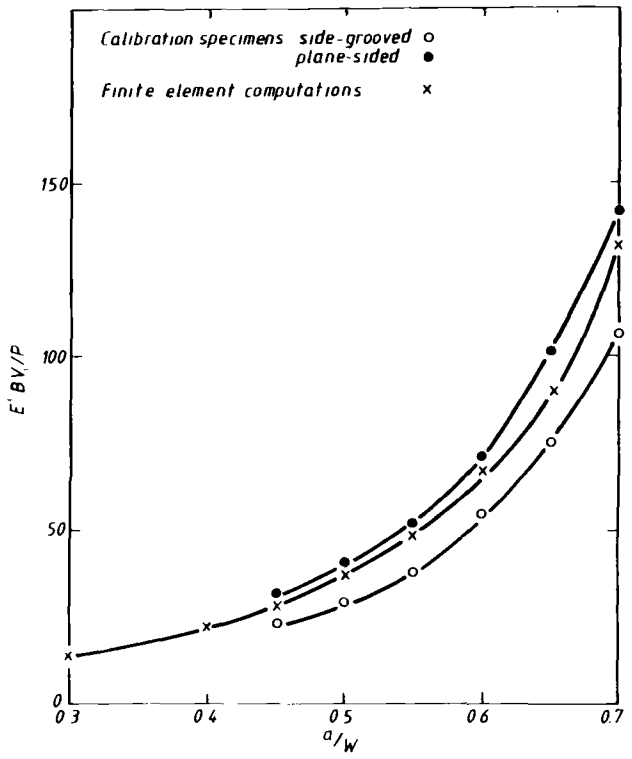

FIG. 4—*Observed variation of clip gage/load compliance, from calibration specimens and finite-element calculations.*

higher compliances than the side-grooved ones, with the finite-element solution lying in between.

The discrepancy between the compliances measured on the plane-sided test specimens and in the finite-element simulation is not surprising, since the latter was found to give a consistent underestimate of mouth opening, with an average error of approximately 5 percent, when compared with Tada's [5] analytical solution. Adjustment of the finite-element results upward by 5 percent would give close agreement with the experimental compliances. For the side-grooved test specimens, it is customary to employ an effective thickness in order to achieve the same value of nondimensional compliance. The average effective thickness was 20.28 mm when the clip gage was in Position 1 (Fig. 2) and 20.35 mm when it was in Position 2. This indicates that for the test specimens a good estimate of effective thickness would be the arithmetic mean of the nominal and net thicknesses, 25 and 15 mm, respectively (that is, 20 mm). The concept of effective thickness applies only to the estimation of crack length from compliance, not to the calculation of toughness.

The variation in load-point displacement compliance $q\,E'B/P$ is depicted in Fig. 5. The load-point displacement, q_v, for the calibration specimens was calculated from the two clip gage displacements, using Eq 1. This is compared with the finite-element computation of q_v and q, and with the elastic solution for q_c from Tada [5]. The latter gives only the extra displacement due to the presence of the crack, whereas q includes the displacement, due to bending and shear, of the uncracked body, and q_v should just include the (small) component due to shear. This explains some of the differences between the various curves, although one would expect q_v to follow q_c more closely, since the shear component included in q_v is less than 20 percent of the bending component.

The variation in double compliances, V_1/V_4 and V_3/V_2, is shown in Fig. 6. Agreement between the finite-element results and the calibration specimens is less good. In the case of the V_1/V_4 compliance, the scatter could be due to bending in the horizontal plane of the calibration specimen (that is, preferential opening of the notch on one side), since this would affect the values of V_4 measured on the side. The reason for the poor agreement between V_3/V_2-values is not clear.

Measurement of Crack Lengths in a Fracture Toughness Test

The purpose of studying the elastic compliance of cracked bodies was to find out how closely the repeated unloadings during the fracture toughness test could be used to infer the crack length. Obviously the results could be compared only with the physical measurement of crack length made on the fracture surfaces for the beginning and end of tearing. The intermediate unloadings could not be checked.

The compliance functions derived from the calibration specimens were

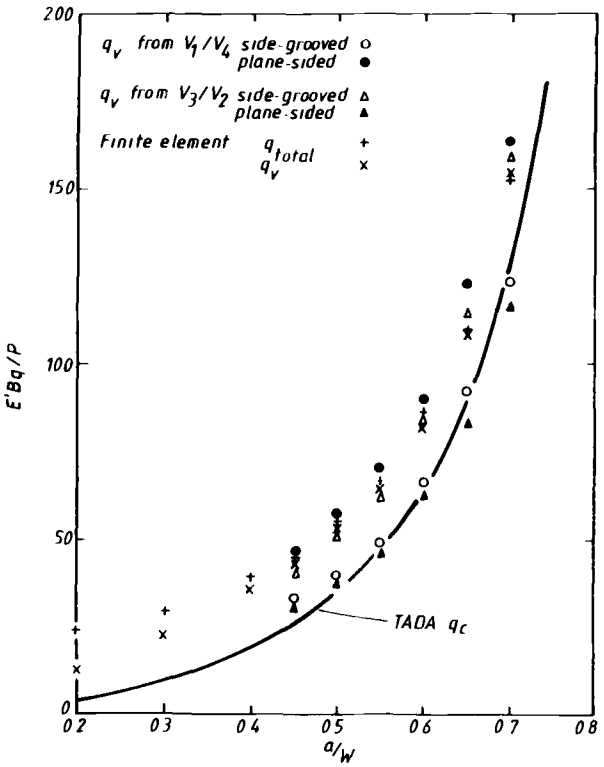

FIG. 5—*Observed variation with* a/W *of load-point displacement/load compliance, from calibration specimens and finite-element computations. Displacement estimated from two clips* (q_v) *and from end displacement* (q_{total}).

stored in the computer in polynomial form, so that the crack length could be estimated from the appropriate unloading slopes. Figure 4 illustrates that the clip gage versus load compliances appear to be fairly well behaved and give an increasing variation with change in a/W ratio at larger crack lengths. Table 2 summarizes the estimates of crack length for the Ducol test specimens. It may be seen that the initial crack length is estimated fairly closely (-1.7 to $+2.5$ percent), the trend being to overestimate the value. The estimate for the final crack length is slightly worse (-5.5 to $+3.3$ percent), with a tendency to underestimate the value.

An error of a few percent in the crack length is not significant for the calculation of toughness, especially bearing in mind the fact that the compliance calibration used may be in error. However, it is important, firstly, that the same crack length should be obtained when several unloadings are performed at a given value of plastic displacement (repeatability), and secondly, that the error should be similar for the initial and final crack lengths, so that the tearing is estimated correctly. On the first point, it was found that the indicated

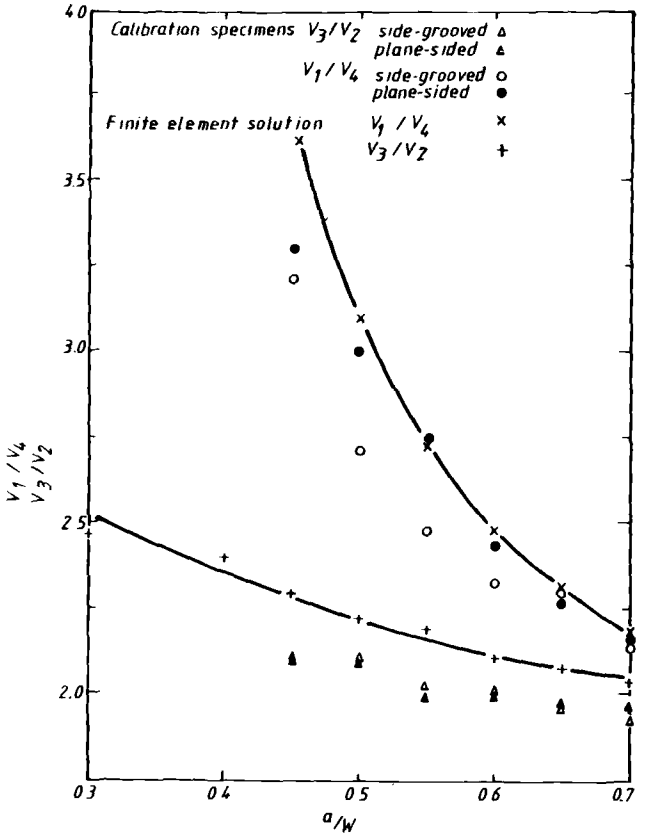

FIG. 6—*Variation of double compliance with* a/W.

crack length would vary by up to ± 0.3 mm (1.3 percent) during the first three unloadings in the elastic range. The variation on Test Specimen No. OEC8, which had an initial a/W of ~ 0.6, was considerably less. On the second point, the general tendency was to overestimate the initial crack length, but underestimate the final length, so that the tearing would be underestimated. This fact is highlighted in Table 2, although the trend is somewhat masked by the fact that the stretch zone was excluded from the measurement of tear length, in common with normal practice in the United Kingdom. The stretch zone width was estimated to be 0.1 to 0.2 mm for the Ducol. It is not clear, however, where this should be allowed for, since the stretch zone would already be partially formed at the first unloading, when the initial crack length was estimated.

The double compliance in terms of V_1/V_4 and V_3/V_2 was also investigated. Figure 6 shows that V_3/V_2 should vary little with crack length, and indeed it proved impossible to estimate reasonable crack lengths using this compliance

TABLE 2—*Comparison of physical crack lengths with those estimated by clip/load compliance,* $E'BV_1/P$ *or* $E'BV_2/P$.

Specimen No.	Material	Type	Initial Crack Length, a_0, mm			Final Crack Length, a_f, mm			Crack Extension, Δa, mm		Clip Position
			Physical	Compliance	Error, %	Physical	Compliance	Error, %	Physical	Compliance	
OEC 2	Ducol	S[a]	25.27	25.58	+1.3	31.32	30.18	−3.6	5.90	4.60	2
3	Ducol	S	24.66	24.23	−1.7	27.37	26.83	−2.0	2.57	2.60	2
4	Ducol	S	24.84	24.95	+1.9	26.75	26.17	−2.2	1.82	1.22	2
6	Ducol	S	24.72	24.78	+0.2	24.90	25.04	+0.6	0.11	0.26	2
7	Ducol	S	21.79	...	...	22.70	22.52	−0.8	0.78	...	2
8	Ducol	S	29.93	30.28	+1.2	31.49	31.69	+0.6	1.49	1.41	2
9	Ducol	S	25.45	26.16	+2.8	25.48	26.31	+3.3	0	0.15	2
10	Ducol	S	24.84	25.40	+2.3	24.93	25.73	+3.2	0	0.33	2
OEC 1A	Ducol	P[b]	22.77	22.85	+0.7	24.78	23.42	−5.5	2.00	0.57	1
3A	Ducol	P	23.84	23.95	+0.5	24.49	24.72	+0.9	0.65	0.77	1
4A	Ducol	P	24.04	23.82	−0.9	25.53	25.49	−0.2	1.49	1.68	1
5A	Ducol	P	25.51	25.60	+0.4	25.84	26.11	+1.0	0.33	0.51	1
6A	Ducol	P	26.14	26.80	+2.5	28.26	28.16	−0.4	2.13	1.36	1
7A	Ducol	P	26.30	26.44	+0.5	27.92	27.17	−2.7	1.62	0.73	1
8A	Ducol	P	23.16	23.11	−0.2	24.13	23.82	−1.3	0.80	0.71	2
9A	Ducol	P	26.69	26.69	0	27.70	27.26	−1.6	0.89	0.57	2
10A	Ducol	P	25.42	25.76	+1.3	26.04	26.13	+0.3	0.51	0.37	2

[a] S = side-grooved.
[b] P = plane-sided.

for the test specimen geometry considered. Slightly more success was achieved with the V_1/V_4 compliance (Table 3). The first series of specimens (6AL series, HY80) had one clip gage attached to Position 4 (Fig. 2*a*), and some variability in V_1/V_4 was experienced which was ascribed to bending of the specimen in the horizontal plane. Therefore, to counteract this effect, the second series (OEC1A, 7A Ducol) had a third clip gage attached to the other side in Position 4, and the displacements from the pair were averaged. This improved the results, as is apparent from the error columns in Table 3. It is also noticeable that for the Ducol test specimen the crack length was overestimated, whereas it was underestimated for the HY80 test specimens. This could be due to an effect of material, but was more probably caused by different conditions being present in the two series; for instance, an error in the clip gage calibration could cause large differences. There is no particular trend to the error in estimated tear lengths, which were wrong by a factor of 2 or 3 in some cases.

Consideration of the errors inherent in the clip gage and load measurements indicates that the expected error in crack length inferred from V_1/P is ± 0.2 to 0.4 mm whereas, using V_1/V_4, the error increases to ± 1 to 2 mm (both at $a/W = 0.5$). This calculation, although highly approximate, shows that the clip gage versus load compliance gives the more accurate results, and that if double compliance is to be used, greater accuracy is required from the clip gages than was attained in this investigation.

Other errors which are inherent in this method of measuring crack extension are the possible variation in elastic compliance caused by the gross plasticity which accompanies tearing [*13*] (apart from the change in crack length), and the curvature of the crack front.

The Measurement of Rotational Factor

Using the double-clip gage technique, the rotational factor may be estimated directly at any value of displacement, via Eq 2. The initial value of crack length, estimated by compliance, was used in the calculation. The total (elastic + plastic) displacements were used and thus the calculation gives the *overall* rotational factor. The results at each unloading for the Ducol test specimens, where the raised knife-edge setup (Fig. 2*b*) was used, are given in Fig. 7 as a function of clip gage displacement. The scatterbands for the side-grooved and plane-sided test specimens contained 36 and 16 data points, respectively. It is apparent that in all cases the overall rotational factor rises rapidly to approximately 0.4, and after some tearing stabilizes in the range 0.45 to 0.5.

Measurement of CTOD

The CTOD at each unloading was calculated by two methods. The first was from the two clip gages, via Eq 3. The second was by means of the formula in BS 5762 [*11*], namely

$$\delta = \frac{K^2}{2E'\sigma_Y} + \frac{V_p \times 0.4(W - a_0)}{0.4W + 0.6a_0 + z} \tag{6}$$

In this case the plastic clip gage opening could be estimated from the total clip gage displacement and the slope of the unloading line. The results are summarized in Fig. 8, where it will be seen that the estimate of CTOD from the two clip gages was larger than the standard formula calculation.

At small CTOD's the difference was proportionately larger—by a factor of ~3 when the standard CTOD was less than 0.02 mm, reducing to ~30 percent when standard CTOD ≃0.1 mm. This discrepancy in the elastic regime could be due to several causes. The precrack flanks were assumed to be linear for the extrapolation from the two clip gage readings, whereas in reality they are curved, thus giving a smaller CTOD. On the other hand, the "standard" formula [*11*] assumes that $M = 2$ in the expression relating CTOD to K

$$K^2/E' = M\sigma_Y \,\text{CTOD} \tag{7}$$

This may be an overestimate for higher-strength materials, giving an underestimate of true CTOD.

As the plastic displacements in the specimen increase, the discrepancy between the two estimates of CTOD becomes proportionally less, reducing to about 20 percent at a "standard" CTOD of 0.7 mm. Once significant plasticity has occurred, the CTOD estimate based on the double-clip-gage extrapolation is likely to be more accurate, because it does not require the assumption of a rotational constant. It was shown in the previous section that the rotational factor is somewhat larger than the value of 0.4 assumed in the standard formulation, which means that the latter will underestimate the true CTOD at large plastic displacements.

Measurement of Load-Point Displacement

The load-point displacement is difficult to measure accurately in three-point bending due to the necessity of correcting for extraneous displacement. The two-clip-gage arrangement, however, allows load-point displacement to be estimated via Eq 1.

Figure 9 shows a comparison between q_v, estimated from the two clip gages, and q_{total}, obtained by subtracting the appropriate extraneous displacement from the ram displacement. The two clip estimates, q_v, are considerably lower than q_{total}, by up to 30 percent, at small displacements, until q_{total} ≃1.6 mm, when good correspondence between the two estimates is obtained. In fact the discrepancy was generally constant for a given test specimen, being ~0.1 mm throughout the range of loading. This could be due to the error due to the bending of the arms not being allowed for in the double-

TABLE 3—*Comparison of physical crack lengths with those estimated by double compliance, V_1/V_4. All test specimens were plane-sided.*

Specimen No.	Material	Initial Crack Length, a_0, mm			Final Crack Length, a_f, mm			Crack Extension, Δa, mm	
		Physical	Compliance	Error, %	Physical	Compliance	Error, %	Physical	Compliance
OEC 4A	Ducol	24.04	24.94	+3.7	25.53	27.97	+9.6	1.49	3.03
5A	Ducol	25.51	26.32	+3.2	25.84	27.70	+7.2	0.33	1.38
6A	Ducol	26.14	26.17	+0.1	28.26	29.44	+4.2	2.12	3.27
7A	Ducol	26.30	28.03	+6.6	27.92	29.58	+5.9	1.62	1.55
6AL 2	HY80	26.48	26.48	0	30.69	29.89	−2.6	4.21	3.41
4	HY80	26.52	22.49	−15.2	27.02	24.21	−10.4	0.5	1.72
5	HY80	26.15	22.57	−13.7	27.26	22.95	−15.8	1.11	0.38
7	HY80	25.85	...	...	26.57	23.01	−13.4	0.72	...
10	HY80	26.62	24.77	−6.9	28.00	25.83	−7.8	1.38	1.06
11	HY80	26.01	23.85	−8.3	29.49	28.25	−4.2	3.48	4.40

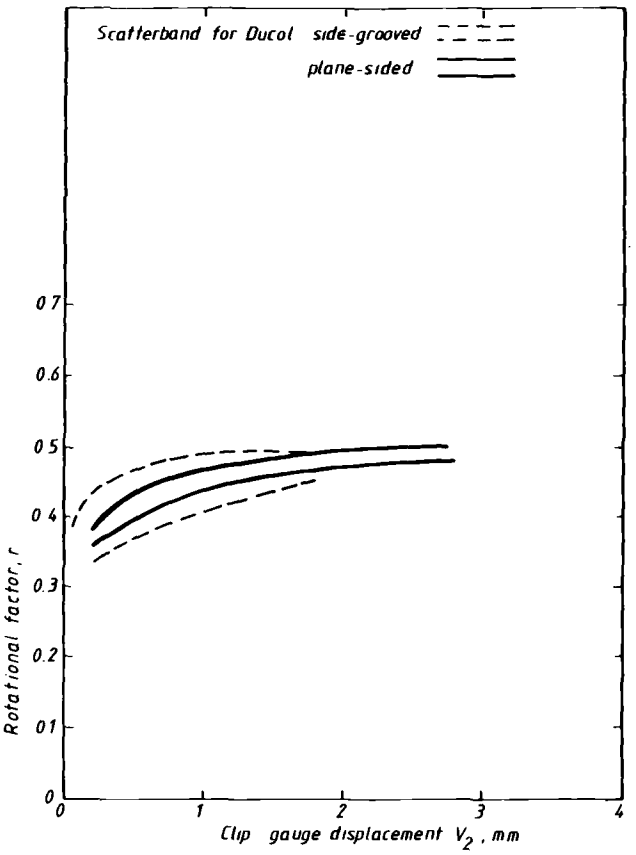

FIG. 7—*Variation of rotational factor with clip gage displacement.*

clip estimates—at a load of 40 kN (near the yield load), this would cause an underestimate of ~0.12 mm. Another factor is the approximate nature of the correction made for extraneous displacement, which could easily be incorrect by 0.1 mm.

It appears therefore that good estimates of the load-point displacement can be obtained by means of the double-clip-gage arrangement, particularly if a correction for the bending of the test specimen arms is employed at small displacements.

The Measurement of R-Curves

It was seen in the previous section that the CTOD can be estimated readily by both the double-clip-gage extrapolation method or by the standard [*11*] formula. Similarly, J could be calculated accurately by integrating the area under the load/load point-displacement record, and applying Eq 5. The load-

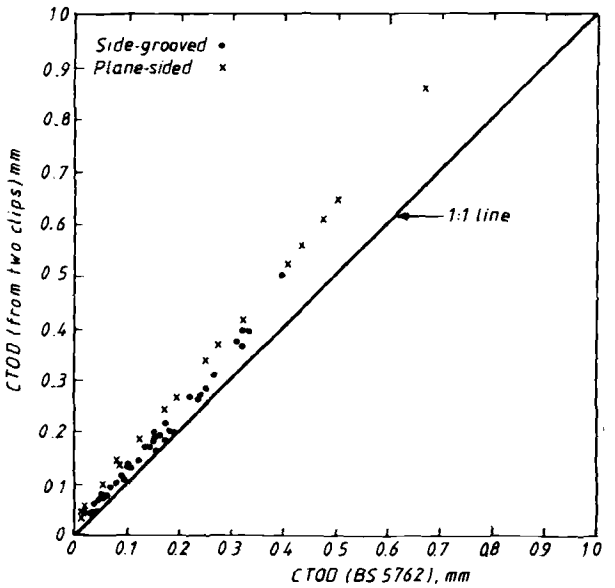

FIG. 8—*Comparison of CTOD's calculated from two clips, and from BS 5762.*

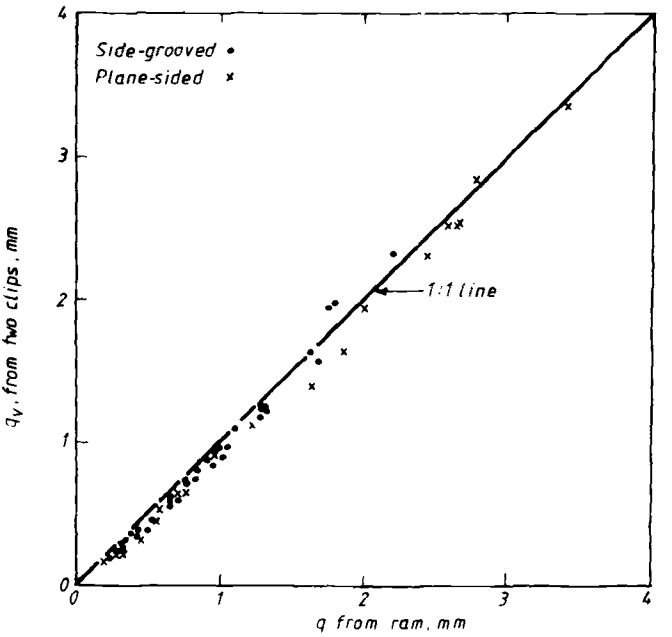

FIG. 9—*Comparison of load-point displacement, estimated from two clips and from corrected ram displacement.*

point displacement could be estimated with good accuracy from the two clip gages, and therefore the calculation of J by the computer is simple and accurate. Thus the toughness, in terms of CTOD or J, can be readily obtained by the computer.

The other parameter required in an R-curve is the crack extension, Δa. It was seen earlier that this could not be inferred with any accuracy by means of the V_1/V_4 compliance given the accuracy of the clip gages used. The clip gage displacement/load compliance offers more promise. Figures 10 and 11 show the J_R-curve for side-grooved and plane-sided Ducol test specimens, respectively, using both the clip gage displacement/load compliance and the multiple-specimen method. The general trend of the compliance R-curve is to overestimate the initial tear length, and underestimate the final one, thus giving a steeper R-curve with an ill-defined initiation point. The initiation point is further confused, for the plane-sided test specimens, Fig. 11, by the tendency to predict negative tear lengths in the early part of the test. However, Fig. 10 does show the necessity for making an allowance for stretch zone formation. This could be accomplished by drawing in a blunting line, but the drawback is that its slope is uncertain. Another alternative would be to measure the stretch zone width of the fracture face after the test, and ignore all measurements which show a lesser amount of crack extension. Given a stretch zone width of 0.1 to 0.2 mm, for the Ducol, this method would eliminate many of

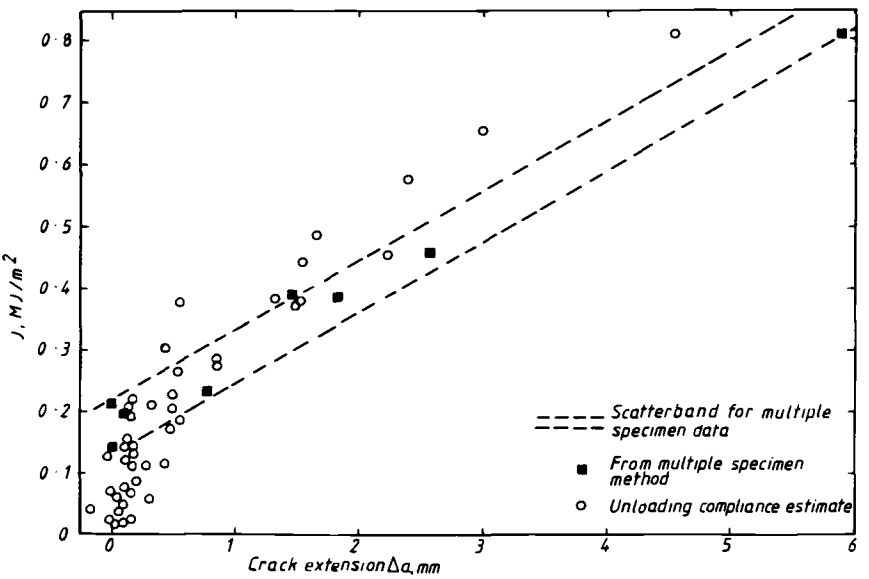

FIG. 10—*J_R-curves from unloading compliance and from multiple-specimen data: side-grooved, Ducol.*

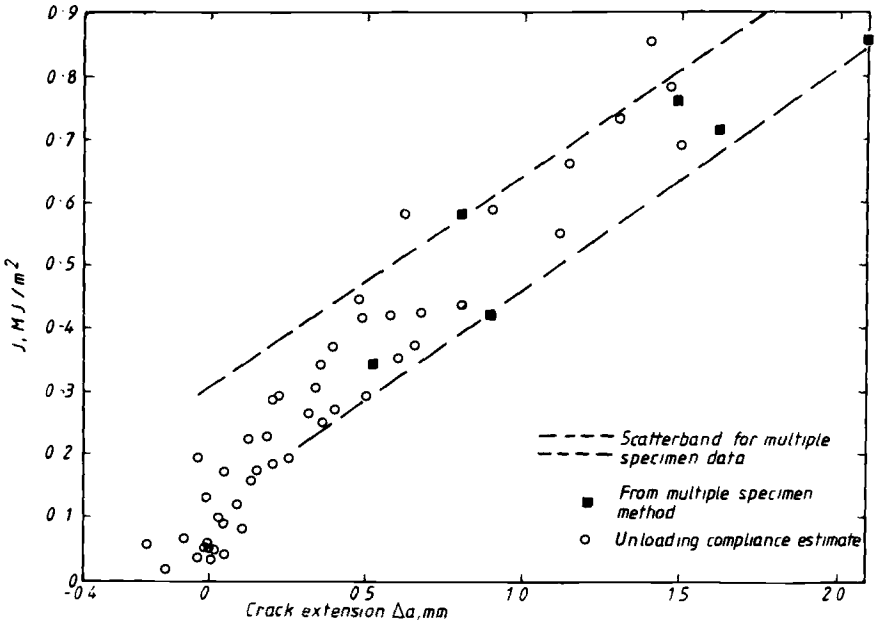

FIG. 11—*J_R-curves: plane-sided, Ducol.*

the lowest data points, but would not allow an unambiguous initiation toughness to be determined for the present set of data.

Discussion

In three-point bending a double-clip-gage arrangement allows good estimates of the following quantities: CTOD (using whichever formula is considered appropriate), rotational factor, load-point displacement, and J. These may be obtained at any point during the test from the instantaneous values of load and displacement of the two clip gages, provided that the initial crack length is known. These estimates are less accurate at very small displacements, within the elastic regime, but in this case corrections based on the load level may be applied. The initial crack length may also be estimated by performing several small unloadings during the elastic loading portion of the test. Using the clip gage/load compliance calibration with the present setup, the initial crack length could be estimated to within ± 2 to 3 percent at an a/W ratio of 0.5, with the error probably reducing to less than 1 percent at $a/W = 0.6$. These errors are well within the limits obtained in normal toughness testing. Shorter crack lengths were not examined but it is apparent that the error for $a/W \simeq 0.3$ would be substantially greater.

The double-clip-gage technique therefore offers considerable advantages for routine fracture toughness testing of three-point bend specimens having $a/W \geq 0.5$, when a small computer is used to collect and analyze the data. The required toughnesses can be calculated immediately upon the conclusion of the test, or even at any level of load and displacement while the test is in progress. The method would be to load the test specimen into the elastic regime (to a load, for instance, of 1 to 2 times the load used in fatigue precracking), while monitoring load and the two clip gage displacements, and then to perform several small (~ 20 percent) unloadings to infer an average value of the initial crack length. This would be calculated from the unloading slope of the clip gage/load line. Loading would then be recommenced, and at the critical point (which will in all cases correspond to a maximum load point) the various toughness parameters of interest can be calculated from the two clip gage displacements and the load. It will still be necessary to examine the fracture surface after the test to measure the tear length (if this is required), and to test for the validity of the fatigue crack, but in the latter case the initial estimate of the crack length should give an indication of whether the precrack has reached a sufficient depth in the center of the specimen.

Extension of the technique to the measurement of single-specimen R-curves, using multiple unloadings, is less clear cut. The main source of error is in the estimation of the tear length. This consists of two parts:

1. a random error on the estimation of crack length of approximately $+0.2$ to 0.4 mm, which causes fluctuation in the predicted crack extension, and
2. a trend to underpredict the crack length as the tearing increases.

This tendency has been noted by other workers [*2,13*] although the magnitude of the effect appears to be reduced by allowing time-dependent relaxation to occur before unloading [*14*].

The technique could be enhanced by obtaining a better estimate of the initial crack length, and this could be achieved by improving the accuracy of the clip gages and their seating on the knife edges. Razor blades were used for the latter, but no precautions were taken in selecting the clip gages for the accuracy of their machined grooves. The underprediction of the tear lengths is probably inherent in the techniques. It has been found to be more serious in plane-sided specimens than in side-grooved ones [*2*], and this may be due to a combination of plane stress effects of the side ligaments and the crack front curvature. However, it should be possible to correct for this systematic error once the random errors have been reduced. Loss [*3*] applies a correction to the initial value of compliance, after the test is completed, to force agreement between the predicted and physical initial crack length, and this method could be extended as follows. The first unloading compliance is written, $\alpha_1 E'BV/P$, and the final (nth) compliance is $\alpha_n E'BV/P$. The correction factors α_1 and α_n are then chosen so that, on substitution into the compliance calibration, the correct values of initial and final crack length are obtained.

The correction factors, α_2, α_3, etc., for the intermediate unloadings would then be calculated so that they scale with the applied displacements, $V_{(2)}$, $V_{(3)}$, that is

$$\alpha_i = \alpha_1 + \frac{V_{(i)} - V_{(1)}}{V_{(n)} - V_{(1)}} (\alpha_n - \alpha_1)$$

This method of correction has been applied to Specimen No. OEC2 (side grooved), which exhibited the greatest amount of tearing, and the results, both before and after correction, are shown in Fig. 12. It is apparent that agreement between the multiple-specimen data and the single-specimen R-curve is greatly improved, particularly after the first millimetre of tearing. The slope of the R-curve could thus be obtained with good accuracy from this one specimen, but the estimate of initiation toughness is less precise.

Both side-grooved and plane-sided test specimens were examined, and a different compliance function, based on the experimental calibration, was used for each. It would obviously be simpler, when testing specimens of different dimensions, to employ a single calibration curve for all geometries. In this case an effective thickness should be employed and it is likely that a correction factor, as outlined in the foregoing, will have to be applied at least for the initial crack length.

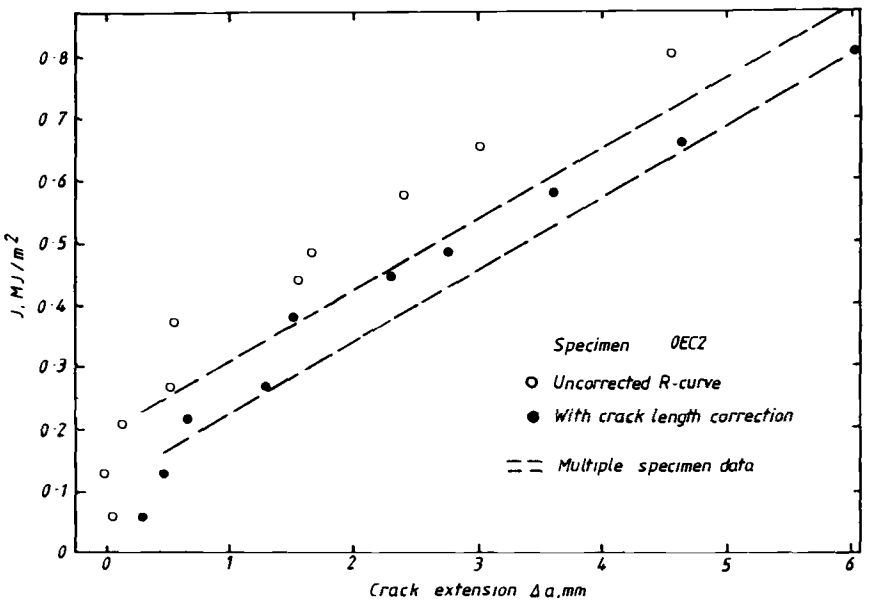

FIG. 12—*Effect on the J_R-curve of correcting the crack lengths (to force agreement between compliance and physical measurements), applied to Test Specimen OEC2 (side-grooved).*

Conclusions

1. Unloading compliance, based on clip gage displacement and load, enabled accurate predictions of initial crack length to be made for three-point bend specimens of medium-strength steel, side-grooved or plane-sided, having $a/W \geq 0.5$.

2. The crack length after tearing had occurred was predicted less accurately, there being a tendency toward underestimation. Consequently, the tear lengths were not predicted very accurately with the present experimental setup.

3. A double clip-gage arrangement enabled accurate estimates of CTOD, load-point displacement, and J to be made once general yield had occurred.

4. The measurement of initiation of tearing and R-curves from a single specimen was found to be rather inaccurate because of the errors involved in the prediction of crack extension. A method of correcting the compliance estimates of crack length substantially improved the prediction of the slope of the R-curve.

Acknowledgments

The authors wish to thank the Engineering Materials Requirements Board and the Research Members of The Welding Institute for providing the financial support for this project. The authors are also grateful to Mr. E. K. Briggs for his untiring work with the minicomputer and to Mr. B. A. Wakefield and his staff to the Brittle Fracture Laboratory. Particular thanks are due to Don McCabe of Westinghouse, whose suggestions helped to initiate this project.

APPENDIX

Finite-Element Computation

The finite-element package, which was used to investigate the effect of crack length on elastic compliance, employed cubic, isoparametric, quadrilateral elements, with special degenerate elements at the crack tip. The package was developed specially for examining the effect of cracks in weldments, and is described in Ref *12*. Relatively few elements are required to model the crack-tip region, and in this case 15 elements were used, including two for the structure supporting the knife edges. Figure 13 shows the mesh chosen for a crack length/width ratio of 0.5. The design of the knife-edge support was chosen to model the shape and location of the mechanical fixture, except that it also contained a node at height 3 mm to model the position of the standard knife edges. In addition a node was located 20 mm below the top surface and 9 mm from the crack plane, for all meshes for which $a/W \geq 0.4$. This was to model the fixing point of the knife edge in Position 4 (Fig. 5*a*). Eleven ratios of a/W, in the range 0.05 to 0.7, were investigated, the mesh in the crack tip region being adjusted accordingly. All calculations were performed in plane strain, with Poisson's ratio $\nu = 0.3$. Values of

TABLE 4—*Nondimensional elastic clip gage and load-point displacements. The clip gage locations are given in Fig. 2.*

a/W	Error in K, %	Error in V, %	$\frac{V_1E'B}{P}$	$\frac{V_2E'B}{P}$	$\frac{V_3E'B}{P}$	$\frac{V_4E'B}{P}$	$\frac{qE'B}{P}$	$\frac{V_1}{V_4}$	$\frac{V_3}{V_2}$
0.05	−1.5	−1.4	2.768	2.991	6.774	...	21.63	...	2.264
0.1	−6.6	−6.1	3.760	4.135	9.583	...	21.70	...	2.317
0.2	+5.9	+3.5	7.49	8.32	20.56	...	24.31	...	2.476
0.3	+5.1	+2.8	13.32	14.65	36.15	...	29.98	...	2.467
0.4	+3.3	+4.5	22.02	24.29	58.05	4.686	39.14	4.70	2.390
0.45	+2.8	+3.8	28.63	31.37	72.06	7.779	46.21	3.680	2.297
0.5	+5.4	+4.8	37.12	40.44	90.74	11.96	55.15	3.103	2.244
0.55	+7.9	+6.8	48.24	52.34	114.67	17.61	66.83	2.740	2.190
0.6	+3.7	+4.7	66.40	71.65	151.16	26.72	86.27	2.484	2.110
0.65	+6.7	+7.5	89.49	96.31	200.22	38.65	110.11	2.315	2.079
0.7	−0.5	+5.4	131.71	141.33	288.2	60.42	153.26	2.180	2.039

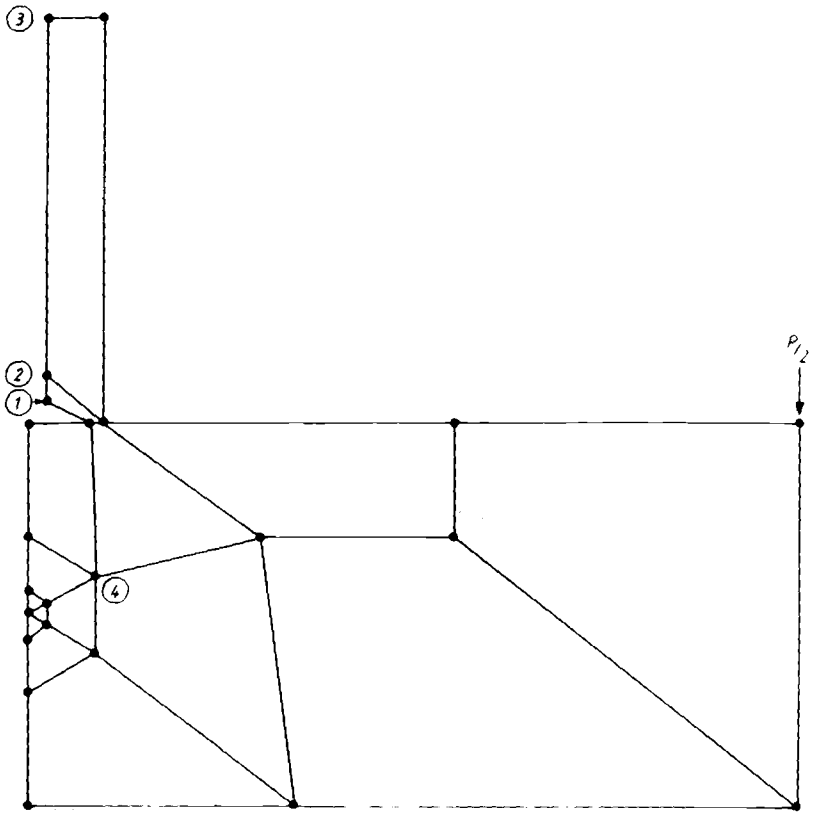

FIG. 13—*Mesh used for* a/W = *0.5. The circled figures refer to the knife-edge positions in Fig. 2.*

stress-intensity factor, K, and mouth opening, V, were compared with the approximation given in Tada [5]. Table 4 shows that the differences were less than 8 percent. In order to check that the knife-edge support was not being distorted, the displacements of the nodes were plotted for $a/W = 0.5$, and it was found that the support remained perpendicular to the top edge of the specimen at the fixing points. The stresses in the two elements comprising the support were also found to average less than 10 percent of those in the neighboring elements in the specimen.

The horizontal displacements (V_1, V_2, V_3, V_4) of the four knife-edge positions, and the vertical displacement, q, of the load point, were calculated and are presented in nondimensional form in Table 4. The results should all be accurate, to better than 8 percent for a/W in the range 0.05 to 0.7. Since the knife-edge support remained undistorted and perpendicular to the top surface of the specimen, it is possible to infer, by interpolation, displacements at any other height above the specimen.

References

[1] Paris, P. C., Tada, H., Zahoor, A., and Ernst, H. in *Elastic-Plastic Fracture, ASTM STP 668*, J. D. Landes, J. A. Begley, and G. A. Clarke, Eds., American Society for Testing and Materials, 1979, pp. 5-36.

[2] Gudas, J. P., Joyce, J. A., and Davis, D. A. in *Fracture-Mechanics—Eleventh Symposium: Part I, ASTM STP 677*, American Society for Testing and Materials, 1977, pp. 474-485.
[3] F. J. Loss (Ed.), NUREG Report/CR 1128, Nuclear Regulatory Commission, Washington, D.C., 1979.
[4] Clarke, G. A., Andrews, W. R., Paris, P. C., and Schmidt, D. W. in *Mechanics of Crack Growth, ASTM STP 590*, American Society for Testing and Materials, 1976, pp. 27-42.
[5] Tada, H., Paris, P. C., and Irwin, G. R., *The Stress Analysis of Cracks Handbook*, Del Research Corp., Hellertown, Pa., 1973.
[6] Dawes, M. G. in *Elastic-Plastic Fracture, ASTM STP 668*, J. D. Landes, J. A. Begley, and G. A. Clarke, Eds., American Society for Testing and Materials, 1979, pp. 307-333.
[7] Dawes, M. G., "A New Method of Measuring Displacements and Rotational Factors in SENB Specimens," Welding Institute Report E72/76, Abington, Cambridge, U.K., 1976.
[8] Heyer, R. H. and McCabe, D. F., *Engineering Fracture Mechanics*, Vol. 4, 1972, pp. 393-413.
[9] Willoughby, A. A., Pratt, P. L., and Turner, C. E. *International Journal of Fracture*, Vol. 17, No. 5, 1981, pp. 449-466.
[10] Rice, J. R., Paris, P. C., and Merkle, J. G. in *Progress in Flaw Growth and Fracture Toughness Testing, ASTM STP 536*, American Society for Testing and Materials, 1973, pp. 231-245.
[11] "Methods for Crack Opening Displacement (COD) Testing," BS 5762, The British Standards Institution, London, 1979.
[12] Smith, I. J. in *Proceedings*, Second International Conference on Numerical Methods in Fracture Mechanics, Swansea, U.K., 1980.
[13] Kamath, M. S. and Harrison, J. D., "Ductile Crack Extension in API 5LX65 and HY130 Steels," Welding Institute Report 36/1977/E, Abington, Cambridge, U.K., 1977.
[14] Todd, J. A., Zackay, V. F., and Parker, E. R., U.S. Department of Energy Report DE-AT03-76ET10699, Washington, D.C., 1980.

Kiyotsugu Ohji,[1] *Akio Otsuka,*[2] *and Hideo Kobayashi*[3]

Evaluation of Several J_{Ic} Testing Procedures Recommended in Japan

REFERENCE: Ohji, K., Otsuka, A., and Kobayashi, H., **"Evaluation of Several J_{Ic} Testing Procedures Recommended in Japan,"** *Elastic-Plastic Fracture: Second Symposium, Volume II—Fracture Resistance Curves and Engineering Applications, ASTM STP 803*, C. F. Shih and J. P. Gudas, Eds., American Society for Testing and Materials, 1983, pp. II-398–II-419.

ABSTRACT: The J_{Ic} testing procedures proposed by the American Society for Testing and Materials (ASTM) and the Japan Society of Mechanical Engineers (JSME) were evaluated using medium-strength heat-treated steels. Among the three multiple-specimen methods investigated, the ASTM R-curve method generally gave the largest J_{Ic}-values, while the JSME R-curve method provided the smallest values. The JSME stretched zone width (*SZW*) method, which was developed with emphasis on accurate identification of the initiation of ductile tearing, yielded relatively high toughness values that were rather close to those by the ASTM method. The ASTM method provided a relatively stable procedure for toughness determination and yielded values higher than that at the onset of ductile tearing for these materials. The JSME R-curve method seemed to give the values closest to the onset of ductile tearing among the three methods investigated. The JSME *SZW* method showed sensitivity to interpretation and definition of the critical values of *SZW*. Development of a stable procedure for determining the critical *SZW* values may be of primary importance for improving reliability of the JSME *SZW* method.

KEY WORDS: J_{Ic} testing, elastic-plastic fracture toughness, J-integral, R-curve method, stretched zone, stretched zone width method, evaluation, standard, round-robin test, medium-strength steel, heat-treated steel, elastic-plastic fracture

Nomenclature

B Specimen thickness
J J-integral

[1]Professor, Department of Mechanical Engineering, Osaka University, Yamada-oka, Suita, Japan 565.
[2]Professor, Department of Iron & Steel Engineering, Nagoya University, Chikusa-ku, Nagoya, Japan 464.
[3]Associate Professor, Department of Physical Engineering, Tokyo Institute of Technology, Meguro-ku, Tokyo, Japan 152.

J_{Ic}	Valid elastic-plastic fracture toughness expressed in terms of J (ASTM and JSME method)
J_{in}	J at the initiation of ductile tearing defined by the intersection of the R-curve with the measured blunting line (JSME method)
J_Q	J at the onset of crack growth defined by the intersection of the R-curve with an assumed blunting line (ASTM method)
dJ/da	Slope of the R-curve (ASTM method)
$(dJ/da)_R$	Slope of the R-curve (JSME method)
$(dJ/da)_B$	Slope of the blunting line (JSME method)
SZW	Stretched zone width (JSME method)
SZW_c	Critical value of the SZW (JSME method)
Δa	Crack extension
Δa_{ASTM}	Crack extension (ASTM method)
Δa_{JSME}	Crack extension (JSME method)
ΔEP	Increment of electric potential
σ_B	Ultimate tensile strength
σ_Y	Effective yield strength $= (\sigma_B + \sigma_{YS})/2$
σ_{YS}	Tensile yield strength, or 0.2 percent offset tensile yield strength

The J-integral as proposed by Rice [*1*][4] would be one of the most promising quantities for the experimental determination of elastic-plastic fracture toughness. The development of a testing method to obtain J_{Ic}-values has been made largely by Landes and Begley [*2–4*], and Rice, Paris and Merkle [*5*]. Based on the R-curve method proposed by Landes and Begley [*4*], a recommended procedure for the determination of J_{Ic} was proposed in 1979 [*6*] by the ASTM Task Group E24.01.09 on Elastic-Plastic Fracture under Committee E-24 on Fracture Testing. After some minor modifications, this proposed method of J_{Ic} testing has been included since August 1981 in the ASTM Standards under the designation of Standard Test for J_{Ic}, A Measure of Fracture Toughness (E 813-81).

One of the most important problems in the standardization of J_{Ic} testing may be how to identify the initiation of slow-stable crack growth correctly and with good reproducibility. Although in the ASTM recommended procedure just mentioned the J-value at the onset of crack growth is given by the intersection point between a best straight-line fit of the data of J versus Δa (R-curve) and an assumed blunting line, some other methods, for example, a fractographic method [*7*], may also be possible. Kobayashi et al [*7*] have proposed a procedure [the stretched zone width (SZW) method] to determine the initiation point of ductile tearing based on the fact that the blunting line terminates when fracture initiates. In this method the blunting line and a critical stretched zone width should be obtained by direct measurements of stretched zone width by a scanning electron microscope. They reported that

[4]The italic numbers in brackets refer to the list of references appended to this paper.

this method was successfully applied to various kinds of material in determining J_{Ic}-values [*7,8*].

In Japan, the Japan Society of Mechanical Engineers (JSME) Committee S781 on Standard Method of Test for Elastic-Plastic Fracture Toughness J_{Ic} (chairman: Professor Hiroshi Miyamoto, Science University of Tokyo) has started with the aim that J_{Ic} testing procedures should be developed not only for the elastic-plastic fracture toughness but also for K_{Ic} estimation by the use of smaller specimens. The final draft was completed in March 1981 after two and a half years of discussion, and this is being published as the JSME Standard in October 1981 under the designation of JSME S 001-1981. The recommended procedure given in this JSME Standard will be the basis to develop a more refined one by accumulating much data, including round-robin test results. The basic philosophy adopted in the JSME method is to determine the J_{Ic}-values of low- and medium-strength, high-toughness materials by obtaining the initiation point of physical tearing as correctly and accurately as possible. From the view that the *SZW* is a good parameter which may reflect direct indications of the physical onset of ductile tearing, the *SZW* method is adopted as well as the R-curve method. In the JSME method, there are also some other points significantly different from the ASTM method, such as actual measurement of the blunting line, the definition of crack extension, and the required conditions for qualifying regression line (R-curve) data.

This paper describes the results of the cooperative tests made on low- and medium-strength steels following the JSME and ASTM procedures.[5]

Outline of the JSME Standard Method of Test for Elastic-Plastic Fracture Toughness J_{Ic} (JSME S 001-1981)

The main features of the JSME method will be described briefly in terms of where and how it differs from the ASTM method, which is now available as the ASTM Method E 813 in worldwide circulation.

Figure 1*a* summarizes schematically the feature of the ASTM method. The initiation point Q of slow-stable crack growth is defined by the intersection point between a linear regression line fit of the R-curve data qualified by this method (9.1.3, 9.3.1, and 9.3.2 in Method E 813) and the assumed blunting line which is calculated by $J = 2\sigma_Y \Delta a$ (9.2.2). As shown in Fig. 1*a*, at least four R-curve data points must exist between Δa_p(min) and Δa_p(max), which are determined by the 0.15-mm and 1.5-mm offset lines. Further, at least one data point should be positioned near the blunting line; the limiting line is given by the $\xi/3$-line parallel to the blunting line. The slope of the regression line must satisfy the following relation (9.3.5.4)

[5]This cooperative test program was started in 1979 and was finished early in 1981 before the final draft of the JSME standard S 001-1981 was completed.

$$dJ/da < \sigma_Y \tag{1}$$

The J_Q-value is considered a valid J_{Ic}-value according to the ASTM method if all the requirements specified in this method are satisfied.

Figure 1*b* shows the feature of the JSME R-curve method. The basic idea that the onset of ductile tearing is identified by the intersection between the

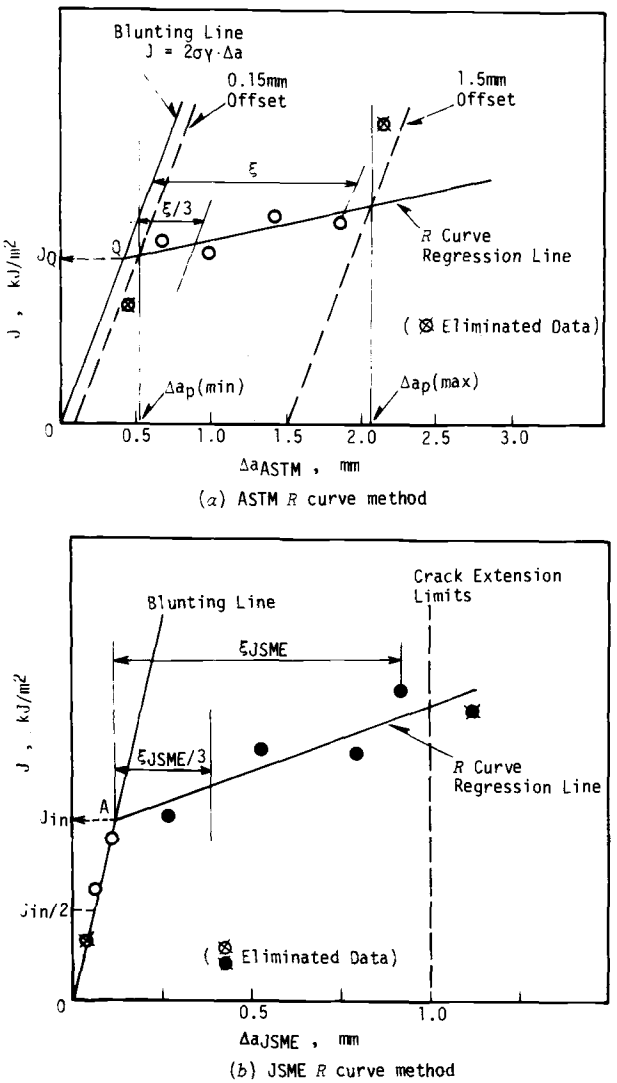

FIG. 1—*Schematic illustrations of the ASTM and JSME R-curve methods and their data qualification.*

linear regression line fit of qualified four or more R-curve data and a blunting line is exactly the same as that in the ASTM method. In the JSME R-curve method, however, modification is made of the procedure for determining both the regression line and the blunting line, in order to find the initiation point of physical ductile tearing as correctly and accurately as possible.

First, the blunting line must be determined by direct observations of the crack tip stretch, that is, *SZW*, by an electron microscope. At least two observed points are required in the range of $J > J_{in}/2$, where J_{in} is the J-value at the onset (Point A in Fig. 1*b*) of ductile tearing identified by the JSME method; J_{in} corresponds to J_Q in the ASTM method.

Secondly, in order to lay emphasis on R-curve data near the crack initiation, the lower limit for crack extension, or the 0.15-mm offset line, is eliminated, and the upper limit for crack extension is lowered to 1 mm instead of the 1.5-mm offset line. For keeping at least one data point near the blunting line, a condition of $\xi_{JSME}/3$ similar to that in the ASTM method is introduced as shown in Fig. 1*b*.

Because of the use of the measured blunting line in the JSME method, the slope requirement is changed from Eq 1 to

$$(dJ/da)_R < (dJ/da)_B/2 \tag{2}$$

The third big difference between the ASTM method and the JSME R-curve method is in measurements of crack extension. Ductile materials usually show thumbnail-shape crack extension in fracture toughness tests. In the JSME method, the crack extension is measured at three or more locations spaced evenly in the central quarter of the specimen thickness, as illustrated in Fig. 2*b*, while the ASTM method uses the measurements at nine or more locations spaced evenly from one side to the other as in Fig. 2*a*. This modification usually yields larger measured values of crack extension than those by the ASTM method, as will be shown later in Table 3 and Figs. 5, 6, 9 and 10, and may magnify, in effect, the sensitivity for detecting the initiation of physical stable tearing.

The JSME method allows the use of the stretched zone width (*SZW*) method, which is not included in the ASTM method. In place of using the regression line of R-curve data, the *SZW* method determines fractographically the terminal point of the blunting process, or the initiation point of ductile tearing, by measuring critical stretched zone widths, SZW_c. Figure 3 illustrates schematically the JSME *SZW* method. At least three values of SZW_c are needed to obtain J_{in}.

The JSME method defines that the *SZW* has reached a critical value SZW_c (or the blunting process has been terminated) if the fractographically identified tear region exceeds 20 percent in length along the front line of the fatigue precrack. When the tear region is less than 20 percent in length, the value of *SZW* is used as the data for the blunting line. The value of *SZW*,

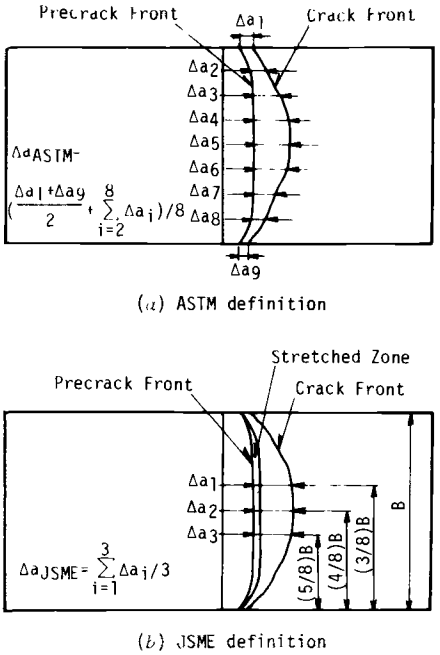

FIG. 2—*The ASTM and JSME definitions of crack extension.*

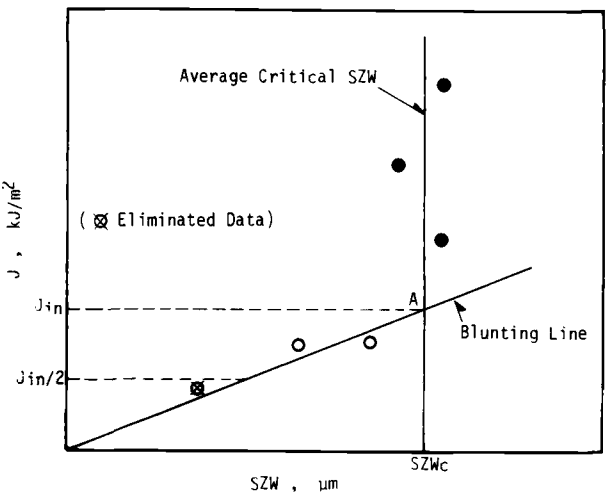

FIG. 3—*Schematic illustration of the JSME SZW method.*

either critical or subcritical, is determined in the central $B/4$ region, as was done for Δa_{JSME} in Fig. 2*b*.

The value of SZW_c may implicitly be understood to remain unchanged after the initiation of crack growth. According to the JSME method, the SZW method is not applicable if SZW_c is found to be a function of J.

The J_{in} thus determined either by the R-curve method or by the SZW method is regarded as a valid J_{Ic} according to the JSME method, if all the requirements prescribed in the JSME method are satisfied.

The requirements in the JSME method are essentially the same as those in the ASTM method, except for those described in the foregoing. The minimum specimen size requirement was somewhat relaxed for specimen width and maximum scatterbands were introduced for qualifying the data for use in blunting line, R-curve, and SZW_c determination.

In the ASTM method the use of single-specimen techniques is allowed in generating the R-curve data. Theoretically this does not cause any contradiction with the multiple-specimen technique. In the JSME method, single-specimen techniques are allowed for use in detecting directly the point of the onset of ductile tearing. This naturally may result in discrepancies of J_{in}-values among the multiple- and single-specimen techniques employed. Therefore, fractographic confirmation of the crack initiation point is required in the JSME method, when any single specimen technique is used.

No rule is given in the JSME method for the case where different J_{Ic}-values are obtained by the R-curve and SZW methods.

Both the ASTM and JSME methods are not recommended in cases where fast (cleavage type) fracture occurs.

Test Program

This research was made in order to collect necessary data to develop the JSME standard and to investigate relationship between the J_{Ic}-values determined by the ASTM and JSME methods.

Three institutes participated in this program; Osaka University (Ohji), Nagoya University (Otsuka), and Tokyo Institute of Technology (Kobayashi). It was planned that the three institutes would conduct the J_{Ic} tests following the ASTM and JSME procedures by using the specimens of the same geometry prepared from the same plate by a single shop. Two medium-strength heat-treated structural steels, HT 80 and HT 60, were selected because it was thought that the J_{Ic} test would be most advantageously applied to materials of these strength levels. In this program the main efforts were focused on the comparison of the J_{Ic}-values determined by the ASTM R-curve method, the JSME R-curve method, and the JSME SZW method. However, in parallel with these efforts, measurements were also made simultaneously to detect the initiation of ductile tearing by using several kinds of single-specimen technique allowed in the JSME method: the electric potential (EP) method at Osaka Uni-

versity and Nagoya University, the ultrasonic (US) method at Tokyo Institute of Technology, and the acoustic emission (AE) method at Osaka University. These results are also briefly described in this paper.

Materials and Specimen Preparation

Materials used are the quench-and-tempered low-alloy steels HT 80 and HT 60. The chemical composition and the mechanical properties of the materials tested are given in Tables 1 and 2, respectively. Specimens (1TCT) as shown in Fig. 4 were machined from the central part of the thickness of a 32-mm-thick rolled plate, in the direction L-T for HT 80 and in the direction T-L for HT 60. All the specimens were machined in the same shop. Each laboratory in this program was supplied with ten specimens for each steel. The fatigue precrack was introduced using procedures which satisfied the conditions of both the ASTM and JSME methods.

Results and Discussion

All the test results obtained in this program are summarized in Table 3, together with a set of data obtained by investigators at Nippon Kokan K.K. (NKK) with the same HT 60 used in this program. It is evident from Table 3 that in almost all cases the JSME definition yields a larger value of crack ex-

TABLE 1—*Chemical composition of materials tested, weight %.*

	HT 80	HT 60
Carbon	0.12	0.13
Silicon	0.26	0.44
Manganese	0.86	1.15
Phosphorus	0.017	0.018
Sulfur	0.007	0.014
Copper	0.17	...
Nickel	...	...
Chromium	0.78	0.18
Molybdenum	0.41	...
Vanadium	0.04	...
Boron	0.09	...

TABLE 2—*Mechanical properties of materials tested.*

Material	σ_{YS}, MPa	σ_B, MPa	σ_Y, MPa	Elongation, %
HT 80	765	814	790	21
HT 60	569	667	618	22

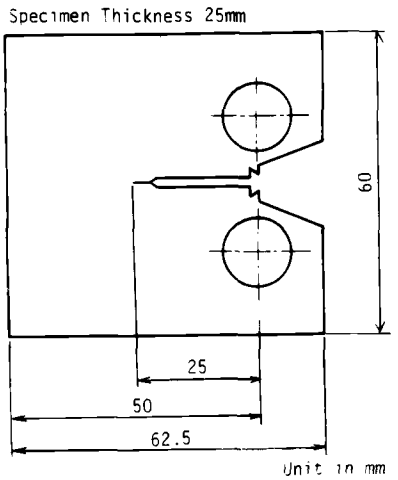

FIG. 4—*Specimen configuration and dimensions.*

tension than the ASTM definition does. This might make it easier to find the initiation of physical ductile tearing.

HT 80 (L-T)

All the test results obtained by the three institutes were processed following the ASTM method. Figure 5 illustrates this procedure. The regression line satisfied the requirement $dJ/da < \sigma_Y$, and J_Q was determined as 293 kJ/m^2. This J_Q-value satisfies the minimum size requirements of the specimen. Therefore the value of 293 kJ/m^2 is a valid J_{Ic} according to the ASTM method.

A set of data obtained at Osaka University (marked by "O" in Fig. 5) alone also gave a valid J_{Ic} of 308 kJ/m^2. Furthermore, the remaining four qualified data obtained at Nagoya University and Tokyo Institute of Technology yielded another valid J_{Ic} of 263 kJ/m^2. These two valid J_{Ic}-values remain within a range of about ± 10 percent of the foregoing J_{Ic}-value of 293 kJ/m^2. It may be said that the ASTM method provides a relatively stable procedure for J_{Ic} determination. However, it is evident from Table 3 and Fig. 5 that the initiation of physical crack growth occurs at a J-value much smaller than the J_{Ic}-values determined by the ASTM method.

The same data were then processed in accordance with the JSME R-curve method. Figure 6 shows all the data obtained in this program, which are plotted following the JSME R-curve method. By determining both the blunting line and the R-curve regression line from the data qualified by this method, the J-value at the intersection of these two lines, J_{in}, was obtained as 174 kJ/m^2. This value satisfied all the requirements prescribed in the JSME

TABLE 3—J_{Ic} *test results on HT 80 and HT 60.*

(*a*) HT 80					(*b*) HT 60				
Specimen No.	J, kJ/m^2	Δa_{ASTM}, mm	Δa_{JSME}, mm	SZW, μm	Specimen No.	J, kJ/m^2	Δa_{ASTM}, mm	Δa_{JSME}, mm	SZW μm
	NAGOYA UNIVERSITY					NAGOYA UNIVERSITY			
1	356	0.47	0.69	c110[a]	1	173	3.48	6.44	c33
2	146	0.08	0.11	73	2	94	0.54	0.98	c36
3	123	0.04	0.05	44	3	36	0.008	0.01	10
4	248	0.27	0.38	c128	4	30	0.007	0.008	8
5	199	0.19	0.24	c109	5	78	0.10	0.11	c24
6	297	0.37	0.60	c139	6	40	0.01	0.011	11
7	251	0.25	0.28	c125	7	48	0.011	0.013	13
8	99	0.033	0.037	37	8	126	2.54	3.72	c29
					9	100	0.67	0.92	c36
	OSAKA UNIVERSITY					OSAKA UNIVERSITY			
1	302	0.30	0.52	c133	1	>400	6.25	10.86	c46
2	174	0.069	0.073	73	2	>400	5.15	8.88	c52
3	328	0.37	0.64	c122	3	145	0.82	1.06	c55
4	386	0.75	1.48	c145	4	43	0.014	0.014	14
5	125	0.053	0.056	56	5	106	0.89	0.92	c47
6	447	0.95	1.75	c119	6	80	0.029	0.027	27
7	473	1.54	3.10	c113	8	129	1.81	2.44	c39
8	214	0.17	0.19	96	9	141	2.53	4.25	c36
9	370	0.59	1.08	c111	10	93	0.55	0.76	c39
10	473	0.92	1.73	c139					
11	350	0.73	1.23	c118					
	TOKYO INSTITUTE OF TECHNOLOGY					TOKYO INSTITUTE OF TECHNOLOGY			
1	523	1.34	2.34	c 90	1	79	...	0.032	32
2	198	...	0.077	77	2	101	1.37	2.04	c36
3	1140	3.79	8.23	c108	3	37	...	0.015	15
4	930	2.38	4.82	c106	4	46	...	0.017	17
5	892	2.39	4.92	c104	5	103	1.64	2.58	c34
6	375	0.82	1.52	c 99	6	125	0.68	0.93	c49
7	118	...	0.042	42	7	124	1.74	3.63	c31
8	278	0.26	0.44	c 92	9	>200	...	...	c33
					10	168	1.86	2.93	c33
						NIPPON KOKAN K.K.			
					12	223	3.98	6.70	...
					13	122	1.78	2.43	...
					14	93	1.09	1.26	...
					15	66	0.23	0.0	...
					16	128	1.22	1.35	...
					18	84	0.54	0.41	...
					19	103	1.01	1.32	...
					20	130	1.53	2.36	...
					21	95	0.67	0.81	...

[a]C = Data after initiation of suctile tearing.

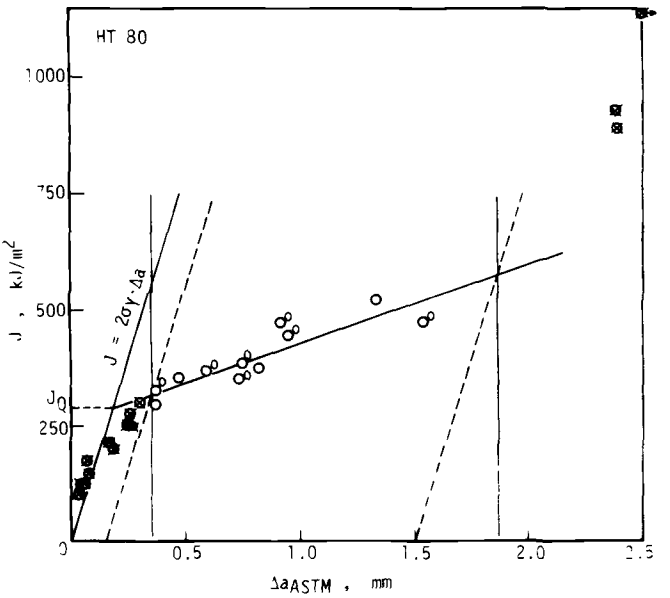

FIG. 5—*Determination of* J_Q *by the ASTM R-curve method (HT 80).*

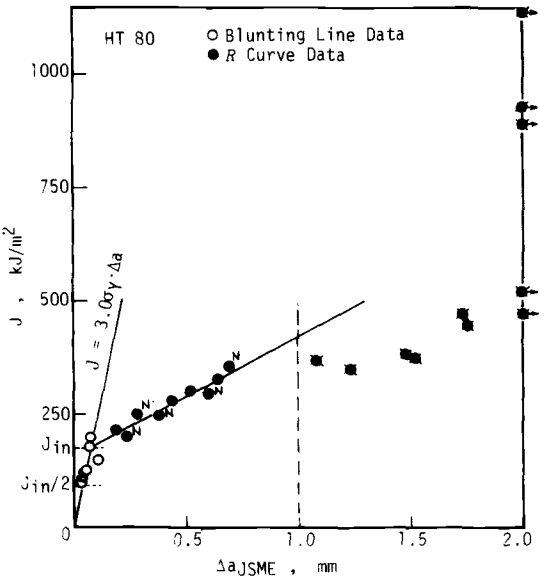

FIG. 6—*Determination of* J_{in} *by the JSME R-curve method (HT 80).*

R-curve method. Therefore this J_{in}-value is a valid J_{Ic} in terms of the JSME method. A set of data obtained at Nagoya University (marked by "N" in Fig. 6) alone also gave a valid J_{Ic} of 168 kJ/m^2 in accordance with the JSME method. A set of the remaining four qualified data for the R-curve regression line, obtained at Osaka University and Tokyo Institute of Technology, gave another valid J_{Ic} of 186 kJ/m^2. The JSME R-curve method may also provide a stable procedure for determining J_{Ic}-values which are much closer to the physical initiation point of ductile tearing than the J_{Ic}-values by the ASTM method, if the qualified R-curve data are widely distributed within the range limited by the maximum crack extension of 1 mm.

By comparing Figs. 5 and 6, it is evident that most of the R-curve data qualified by the JSME R-curve method consist of the data disqualified by the 0.15-mm offset line in the ASTM method; the data that overlap each other are very limited. The JSME method improves nonlinearity in R-curve data in a range of small crack extension by using its own definition of crack extension, while the ASTM method excludes nonlinear data by the 0.15-mm offset line. These two procedures worked very well for the HT 80 used in this program and gave stable J_{Ic} values, as described in the foregoing.

Due to this procedure, however, the J_{Ic}-values in accordance with the ASTM method were larger than the J-value at the onset of physical tearing. In the case of the JSME R-curve method, J_{Ic}-values very close to the initiation of physical tearing were obtained. In reality, however, there could be some possibilities that the nonlinearity in the R-curve data may not completely be removed by the JSME procedure for some ductile materials. In such cases, a J_{Ic}-value that is determined by using R-curve data clustering near the blunting line, but still satisfying the qualification requirement of $\xi_{JSME}/3$ in Fig. 1*b*, may be much smaller than a J_{Ic}-value determined by using R-curve data extensively distributed in the qualified crack extension range. This may result in scatter of the valid J_{Ic}-values and could cause some instability of the JSME procedure. This may be understood from Fig. 6, in which the slope of the R-curve data is decreasing with increase in crack extension beyond the limit of 1 mm.

In Fig. 6 the slope of the measured blunting line was 3.0 σ_Y in the JSME method. If this measured value is used in place of the assumed one in the ASTM method, the J_Q-value reduces slightly to 282 kJ/m^2. The effect of the slope of the blunting line on the ASTM J_{Ic}-value is very small for this material.

The JSME *SZW* method was used to determine J_{Ic}-values from the same data. Figure 7 indicates the measured blunting line (open symbols) and the critical stretched zone width, SZW_c (solid symbols), which may give an initiation point of ductile tearing on the blunting line. As seen in the figure, the data points for the blunting line show a relatively small scatter and their difference among the three institutes is not so remarkable, while discrepancies of the SZW_c measurements are evident among the three institutes. Therefore, a

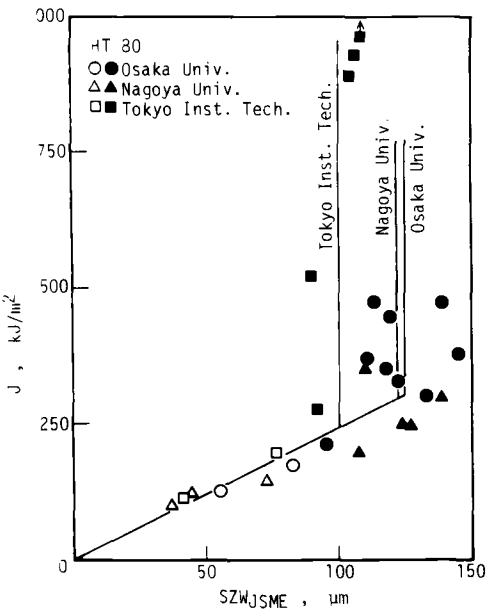

FIG. 7—*Determination of* J_{in} *by the JSME SZW method (HT 80).*

single blunting line was determined by pooling all the data obtained by the three institutes, while the SZW_c-values were averaged separately for each institute. The averaged SZW_c-values were 122 (Nagoya University), 125 (Osaka University), and 100 (Tokyo Institute of Technology) μm. Then the J_{in} values for the three institutes were 287, 294, and 235 kJ/m^2. A considerable difference is observed among these values. These J_{in}-values due to the JSME *SZW* method satisfy the minimum specimen size requirements described in the JSME method, and they are considered as valid J_{Ic}-values in accordance with the JSME method.

Since the difference in the observed SZW_c-values among the three institutes could have resulted mainly from the difference in interpretation of the stretched zone width in fractographs, it was considered that the difference in J_{in} might be improved, to some extent, if the blunting line was also separately determined for each institute. In doing it this way, the J_{in}-values were determined as 278 (Nagoya University), 284 (Osaka University), and 266 (Tokyo Institute of Technology) kJ/m^2, which were averaged to 276 kJ/m^2. Scatter of the J_{in}-values in this case is within ± 4 percent.

In summarizing the foregoing J_{Ic} test results, the JSME R-curve method gave the smallest J_{Ic} and the ASTM R-curve method resulted in the largest values. In between and near to the latter were the values obtained by the JSME *SZW* method. It is felt rather strange that the JSME *SZW* method

yielded much larger J_{Ic}-values than the JSME R-curve method, in spite of the direct observation of the fracture-initiated zone and the use of the quantity which supposedly is most closely connected with the crack initiation process.

The reasons why the *SZW* method gave a considerably larger value than the JSME R-curve method are not quite clear. It might be supposed that the SZW_c of medium-strength high-toughness materials may increase with increase in J even after the initiation of ductile tearing, and that the crack advance due to crack tip blunting may not be linear with respect to J, in particular, at high J-values. The former may further be divided into two cases: (1) the SZW_c itself may increase by its own deformation with increase in J (load) after the initiation of ductile tearing, and (2) with increase in J the uncracked region along the precrack, which has presumably higher local ductility compared with the region already tear-cracked, is progressively tear-cracked at higher local values of critical stretched zone width and in effect this may result in increase in the SZW_c averaged along the crack front. Further studies are needed on these subjects.

Figure 8 shows representative fractographs of tested J_{Ic} specimens. Figure 8*a* illustrates the fracture surface before the initiation of ductile tearing; the specimen was crack-marked by fatigue. The boundaries are clear between the fatigued regions and the stretched zone, and this may result in small scatter in the measurement of the blunting line. Figure 8*b* indicates the fracture surface after the initiation of ductile tearing. In general, the boundary between the dimple region and the stretched zone is fairly clear. Partly, however, there were regions in which dimples were observed in the stretched zone and sometimes it was difficult to determine SZW_c definitely. Furthermore, some difference in interpretation of the stretched zone in these cases may have increased some discrepancies of SZW_c among the three institutes.

In the J_{Ic} tests described in the foregoing, several single-specimen techniques, which used electric potential, ultrasonic, and acoustic emission, were applied in order to detect the initiation of ductile tearing. The details of these test results will be published elsewhere later. Therefore, only a brief description of the results is given here. According to six test results by the electric potential method, the J_{in}-values ranged from 167 to 190 kJ/m^2, with an average of 181 kJ/m^2 and a coefficient of variation of 5 percent, when the J_{in}-values were determined by a bend point on each measured ΔEP-J relation. This average is fairly close to the J_{Ic}-value of 174 kJ/m^2 determined by the JSME R-curve method. When the ultrasonic technique was used, J_{in}-values ranging from 228 to 285 kJ/m^2, and with an average of 262 kJ/m^2, were determined for four specimens with an ultrasonic sensor placed on the top surface of the specimens (top-on). When the sensor was placed on the back surface of the specimen ligament (end-on), the J_{in}-values of three specimens ranged from 235 to 292 kJ/m^2, with an average of 253 kJ/m^2. These averaged values are fairly close to the J_{Ic}-values determined by the JSME *SZW* method.

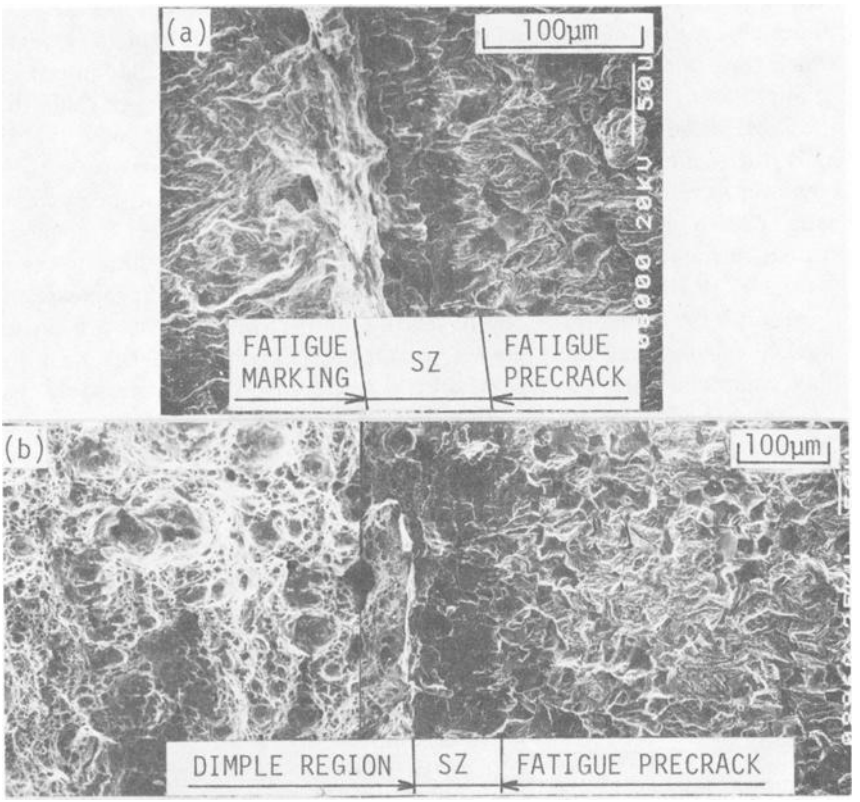

FIG. 8—*Fractographs of stretched zones along the fatigue precrack front of HT 80: (a) during blunting process; (b) after the initiation of ductile tearing.*

In the case of HT 80, no reliable and reproducible J_{in}-value was obtained by means of the AE technique.

In the present study the electric potential and ultrasonic techniques yielded fairly good results as the single-specimen method for J_{Ic} testing. But for checking reliability and reproducibility of these single-specimen methods, more "blind" tests should be done in the future.

HT 60 (T-L)

The open circles in Fig. 9 indicate the test results by the three institutes, which were processed following the ASTM procedure. As seen in the figure, this set of data is invalidated because of data clustering.

This same material was also tested by a group of Nippon Kokan K.K. (NKK) using specimens with exactly the same geometry supplied from the same shop. These data [*9*] are indicated by double circles in Fig. 9. When all

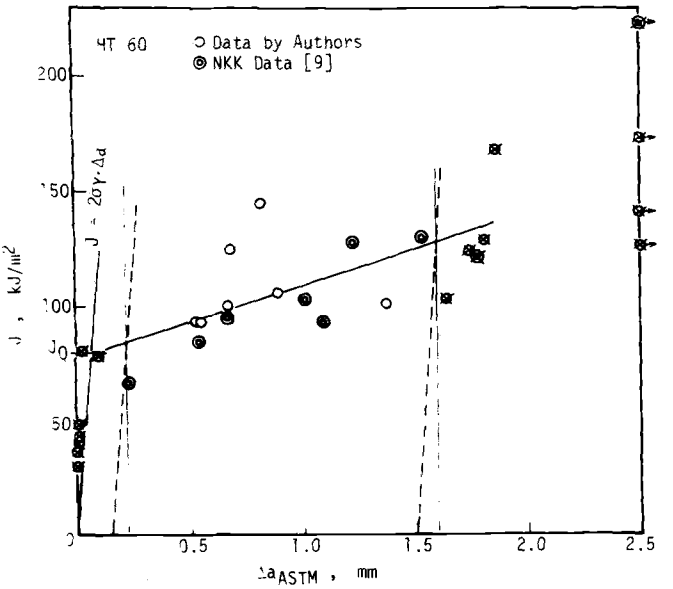

FIG. 9—*Determination of* J_Q *by the ASTM R-curve method (HT 60).*

the data in Fig. 9 are utilized, the rejection criterion of data clustering is cleared, and the J_Q-value is determined as 79 kJ/m^2, which provides a valid J_{Ic} value by the ASTM method. The set of the NKK data alone also provides another valid ASTM J_{Ic}-value of 60 kJ/m^2 [*9*]. The latter is considerably smaller than the former. As will be shown later, fractographs of this material showed a remarkable influence of rolling texture and local inhomogeneity on resistance to ductile tearing. Therefore, the R-curve method, which is a typical multiple-specimen method and is constructed by assuming a moderate material homogeneity, may not be applied satisfactorily to this type of inhomogeneous material.

The same data were next processed in accordance with the JSME R-curve method. Figure 10 shows all the data from the three institutes by open and solid circles as well as those from the NKK group by double circles. By using all these data, J_{in} was determined as 73 kJ/m^2, which provided a valid J_{Ic}-value in terms of the JSME R-curve method. In this case, the set of data by the three institutes alone also gave a valid J_{Ic}-value of 75 kJ/m^2; the contribution from the NKK data happened to be only two points and they little affected the J_{Ic} determination.

Figure 11 shows the results by the JSME *SZW* method. In the blunting process, scatter of the data (open symbols) is inconspicuous and the discrepancies of the data among the three institutes are not noticeable. However, the measured values of SZW_c (solid symbols) are significantly different among

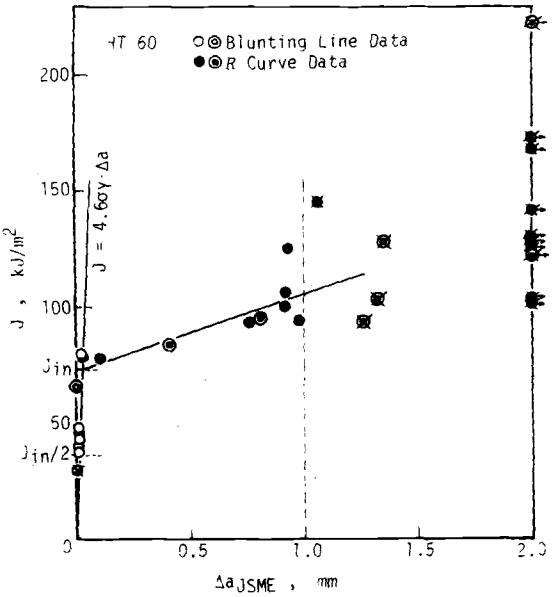

FIG. 10—*Determination of J_{in} by the JSME R-curve method (HT 60).*

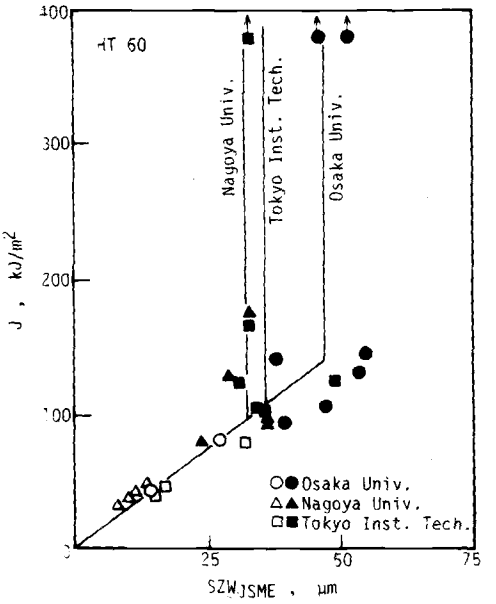

FIG. 11—*Determination of J_{in} by the JSME SZW method (HT 60).*

the three institutes. Therefore, a common single blunting line was used, while the SZW_c-values were averaged separately for each institute, as was done for HT 80 in the foregoing. The SZW_c-values thus determined were 32 (Nagoya University), 36 (Tokyo Institute of Technology), and 45 (Osaka University) μm, and the resulting J_{in}-values were 98, 110, and 138 kJ/m^2, respectively.

The coefficient of variation of SZW_c for each institute was about 20 percent with HT 60 while it was about 10 percent with HT 80. Since no noticeable difference in the blunting line data existed among the three institutes, the causes of increase in scatter with HT 60 may be not in the blunting process, but in the crack initiation process.

According to five measurements by the electric potential technique, the J_{in}-values ranged from 58 to 93 kJ/m^2, with an average of 71 kJ/m^2 and a coefficient of variation of 21 percent. In the case of the ultrasonic technique, J_{in} was detected with three specimens at the top-on position; the J_{in}-values were 70, 77, and 109 kJ/m^2, with an average of 85 kJ/m^2. In the case of the end-on position, J_{in} was detected with four specimens; their values were 74, 78, 94, and 99 kJ/m^2, with an average of 86 kJ/m^2. The J_{in}-values by the electric potential method were fairly close to those by the JSME R-curve method (and also those by the ASTM R-curve method with this material), and the J_{in}-values by the ultrasonic method were between the values by the JSME R-curve method and those by the JSME *SZW* method. This trend is similar to that observed in the foregoing with HT 80.

Figure 12 shows representative fractographs of HT 60. Figure 12*a* shows a stretched zone in a relatively early stage of blunting process. The boundaries between the stretched zone and the fatigue zones (precracked and marked) are relatively clear. It is understood from this photograph why the difference of the blunting line was not noticeable among the three institutes. Figure 12*b* shows a fractograph after the initiation of ductile tearing. Many big dimples elongated in the crack extension direction are observed on the surface, and *SZW* is very much affected by these dimples and varies remarkably along the crack front. It might be understood that the initiation of these big dimples may be playing a decisive role in determining the critical values of *SZW* and their variation.

Summary of the Test Results

Table 4 summarizes the J_{Ic} test results obtained in this investigation. The discrepancies of the valid J_{Ic}-values are evident for different J_{Ic} test methods. The discrepancies of J_{Ic} between the ASTM and JSME R-curve methods resulted primarily from difference of the philosophies underlying the respective methods; the ASTM method seems to aim at a stable and reproducible measurement of the J_{Ic}-value rather than its physical meaning, while the

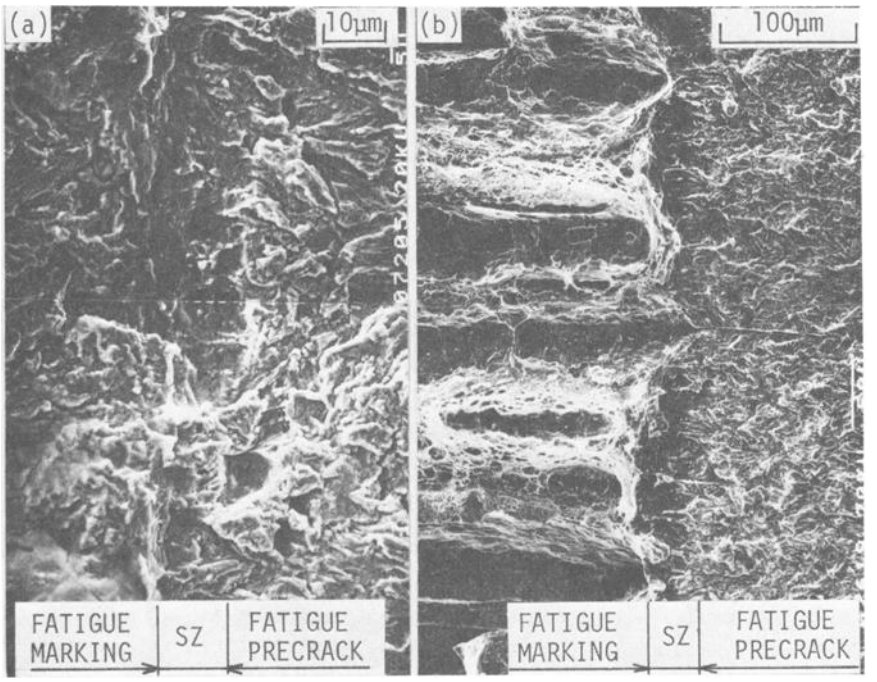

FIG. 12—*Fractographs of stretched zones along the fatigue precrack front of HT 60: (a) during blunting process; (b) after the initiation of ductile tearing.*

TABLE 4—*Summary of test results.*

Material	J_{Ic} kJ/m^2 ASTM R-Curve	JSME R-Curve	JSME-*SZW*	EP[f]	US[f]
HT 80 (L-T)	293	174	...	...	...
	...	168[a]	287[a]	...	...
	308[b]	...	294[b]	181[b]	...
	...	...	235[c]	...	262[c](top-on)
	...	...	...	...	253[c](end-on)
HT 60 (T-L)	...	75	...	...	...
	79[d]	73[d]	...	...	...
	...	...	98[a]	...	...
	...	...	138[b]	71[b]	...
	...	...	110[c]	...	85[c](top-on)
	60[e]	...	...	...	86[c](end-on)

[a]Nagoya University.
[b]Osaka University.
[c]Tokyo Institute of Technology.
[d]NKK data were included.
[e]NKK.
[f]Single-specimen method. No crack growth check was done.

JSME method tries to determine the physical initiation of ductile tearing as accurately as possible. The result that the J_{Ic}-value by the ASTM R-curve method is much larger than that by the JSME method seems to reflect this difference of philosophy between these two methods. Although the *SZW* method is also based on the same philosophy as that of the JSME R-curve method, the J_{Ic}-values obtained by the *SZW* method showed rather larger values than those expected. This rather unexpected result seems to indicate that some problems still remain on defining and measuring the SZW_c.

In any event it is quite embarrassing that an authorized standard test method yields multiple valid test results with noticeable discrepancies for a specific property of a particular material. In order to avoid this embarrassment which could occur in the present JSME method, it is suggested that a required number of measurements be concentrated within a very small range near the initiation point of ductile tearing; this is legitimate in terms of the data qualification in the JSME method for the use of the R-curve, the blunting line, and the critical *SZW* determinations.

If the blunting line can be estimated by some means, the *SZW* method may be used as a single-specimen method. When the measuring method of *SZW* is well established in the future, the *SZW* method could be one of the most reliable and economical J_{Ic} testing methods with a wide range of applications, particularly in the case of accident analysis, where availability of materials is limited both in size and in quantity.

Conclusions

A cooperative research on J_{Ic} test methods was made by using the medium-strength high-toughness steels HT 60 and HT 80, in order to obtain necessary data to evaluate the JSME Standard Method of Test for Elastic-Plastic Fracture Toughness J_{Ic} (JSME S 001-1981) and to investigate its correlation with the ASTM Standard Test for J_{Ic} (E 813-81). The following conclusions were obtained.

1. Significant differences were found between the J_{Ic}-values determined by the ASTM R-curve method and those by the JSME R-curve method, and also between the J_{Ic}-values by the JSME R-curve method and those by the JSME stretched zone width (*SZW*) method, even in cases where all the requirements for a valid J_{Ic} prescribed in the respective methods were satisfied.

2. In the case of HT 80, whose metallurgical structure was homogeneous, the J_{Ic}-value determined by the ASTM R-curve method showed the largest value and that by the JSME R-curve method the smallest. The JSME *SZW* method gave J_{Ic}-values in between and close to the value by the ASTM R-curve method. These results seem to be general in low- and medium-strength homogeneous materials.

3. Scatter of blunting line data was relatively small in general, even in the case of HT 60, whose metallurgical structure was rather inhomogeneous. Scatter of R-curve data for inhomogeneous materials was considered to be caused by the initiation and growth processes of ductile tearing. The use of the R-curve methods for determining J_{Ic}-values may not be appropriate for inhomogeneous materials.

4. Both the ASTM and JSME R-curve methods provide relatively stable procedures for J_{Ic} determination of homogeneous materials. For HT 80 the ASTM method yielded valid J_{Ic}-values considerably higher than the J-value at the onset of ductile tearing, while among the three methods, which include the two R-curve methods (ASTM and JSME) and the *SZW* method, the JSME R-curve method gave the J_{Ic}-values closest to the J-value at the initiation of ductile tearing.

5. The electrical potential and ultrasonic methods are promising. However, significant differences were found in this investigation among the J_{in}-values determined by these single-specimen methods and the multiple-specimen methods. Further work is necessary for obtaining J_{Ic}-values with good reliability and reproducibility by these single-specimen methods.

Acknowledgments

This research was made as a part of the research on "Establishment of Elastic-Plastic Fracture Toughness Testing Method by Means of AE," which was supported by a Grant-in-Aid for Co-Operative Research (A), Japanese Ministry of Education. The authors wish to thank Professor Kitagawa, the head investigator of the aforementioned research project, for permission to publish this paper in separate form. They also thank the Technical Research Center of Nippon Kokan K.K. for permission to use their test data. The assistance of their colleagues in the laboratories of Ohji, Otsuka, and Kobayashi in conducting the J_{Ic} tests in this investigation is acknowledged. In preparing of this paper, the cooperation of Dr. T. Miyata, Nagoya University, and Mr. Sang-Ryung Kang, Osaka University, is also gratefully acknowledged.

References

[1] Rice, J. R., *Journal of Applied Mechanics, Transactions*, American Society of Mechanical Engineers, Vol. 35, June 1968, pp. 379-386.

[2] Begley, J. A. and Landes, J. D. in *Fracture Toughness, ASTM STP 514*, American Society for Testing and Materials, 1972, pp. 1-23.

[3] Landes, J. D. and Begley, J. A. in *Fracture Toughness, ASTM STP 514*, American Society for Testing and Materials, 1972, pp. 24-39.

[4] Landes, J. D. and Begley, J. A. in *Fracture Analysis, ASTM STP 560*, American Society for Testing and Materials, 1974, pp. 170-186.

[5] Rice, J. R., Paris, P. C., and Merkle, J. C. in *Progress in Flaw Growth and Fracture Toughness Testing. ASTM STP 536*, American Society for Testing and Materials, 1973, pp. 231-245.
[6] Clarke, G. A., Andrews, W. R., Begley, J. A., Donald, J. K., Embley, G. T., Landes, J. D., McCabe, D. E., and Underwood, J. H., *Journal of Testing and Evaluation*, Vol. 7, 1979, pp. 49-56.
[7] Kobayashi, H., Hirano, K., Nakamura, H., and Nakazawa, H., *Advances in Research on the Strengh and Fracture of Materials*, Vol. 3B, D. M. R. Taplin, Ed., Pergamon Press, Oxford, U.K., 1978, pp. 583-592.
[8] Kobayashi, H., Nakamura, H., and Nakazawa, H. in *Recent Research on Mechanical Behavior of Solids*, University of Tokyo Press, 1979, pp. 341-357.
[9] Urabe, N. and Akiyama, T., private communication.

Hideo Kobayashi,[1] *Haruo Nakamura,*[1] *and Hajime Nakazawa*[1]

Evaluation of Blunting Line and Elastic-Plastic Fracture Toughness

REFERENCE: Kobayashi, H., Nakamura, H., and Nakazawa, H., **"Evaluation of Blunting Line and Elastic-Plastic Fracture Toughness,"** *Elastic-Plastic Fracture: Second Symposium, Volume II—Fracture Resistance Curves and Engineering Applications, ASTM STP 803*, C. F. Shih and J. P. Gudas, Eds., American Society for Testing and Materials, 1983, pp. II-420–II-438.

ABSTRACT: The Japan Society of Mechanical Engineers (JSME) has made an effort towards standardization of the J_{Ic} test method. The recommended procedure includes two multiple-specimen methods [obtained at the intersections of the experimentally determined *J*-stretched zone width (*SZW*) blunting line and the R-curve, and of the *J-SZW* blunting line and the critical stretched zone width (SZW_c)] and three single-specimen methods (ultrasonic, electrical potential, and acoustic emission). Concerning the blunting line and the R-curve, many experimental data have been accumulated by the present authors in recent years.

In this paper, the evaluation method of the blunting line and of the R-curve and their application to the J_{Ic} test are discussed with special attention to a comparison between two methods recommended by JSME and the American Society for Testing and Materials.

KEY WORDS: elastic-plastic fracture, J-integral, stretched zone, crack initiation, crack extension, blunting line, R-curve, tearing modulus

The Japan Society of Mechanical Engineers (JSME) has made an effort toward standardization of the elastic-plastic fracture toughness (J_{Ic}) test method. The recommended procedure in the JSME standard for the J_{Ic} test method (Standard Method of Test for Elastic-Plastic Fracture Toughness J_{Ic}, JSME S 001-81) includes two multiple-specimen methods and three single-specimen methods. In the former, the J_{Ic}-values are determined as the intersections of the experimentally determined J-integral versus subcritical stretched zone width (*SZW*) blunting line and the *J* versus crack extension (Δa) fracture resistance curve (R-curve), and of the *J-SZW* blunting line and the critical stretched

[1]Associate professor, research associate, and professor, respectively, Department of Physical Engineering, Tokyo Institute of Technology, Ohokayama, Meguro, Tokyo, Japan.

zone width (SZW_c). In the latter, the ultrasonic, electrical potential, and acoustic emission methods are utilized.

Concerning the blunting line and the R-curve, many experimental data have been accumulated by the present authors in recent years. A fractographically derived SZW as a measure of the crack-tip plastic bunting has been examined quantitatively, and a relation between SZW and J has been clarified for various materials, ranging from linear elastic fracture mechanics (LEFM) to elastic-plastic fracture mechanics (EPFM) regimes [*1-5*].[2] Based upon the relation between SZW and J, a new elastic-plastic fracture toughness J_{Ic} test method has been proposed, and its validity and applicability have been confirmed [*1-5*]. This method is the most important one recommended in the JSME standard, where the J_{Ic}-value is determined as the intersection of the J-SZW blunting line and SZW_c.

On the other hand, the recommended procedure in the American Society for Testing and Materials (ASTM) standard for the J_{Ic} test method [ASTM Standard Test for J_{Ic}, A Measure of Fracture Toughness (E 813-81)] has been proposed. There are several differences between two methods recommended by JSME and ASTM.

In this paper, the evaluation methods of the blunting line and of the R-curve and their application to the J_{Ic} test are discussed with special attention to a comparison between two methods recommended by JSME and ASTM. Results show that experimental examination of the J-SZW blunting line and SZW_c, recommended in the JSME standard, is useful for the J_{Ic} test in some materials.

A Proposed Elastic-Plastic Fracture Toughness J_{Ic} Test Method

Recently, a J_{Ic} criterion and its test method have been developed by Begley and Landes [*6*] and ASTM Task Group E24.01.09 [*7*]. Their test method has been adapted into the ASTM Method E 813-81. In the ASTM standard, attention has been directed mainly to processes of ductile tearing, and the following J versus Δa blunting line has been assumed

$$\Delta a = \frac{\text{CTOD}}{2} = \frac{J}{2\sigma_{fs}} \tag{1}$$

where CTOD is the crack-tip opening displacement and σ_{fs} the average of the yield stress (σ_{ys}) in tension (offset = 0.2 percent) and the tensile strength (σ_B). The J_{Ic}-value has been defined as a J-value at the intersection of the R-curve and the blunting line.

The J_{Ic}-value can also be obtained by examination of a relation between SZW and J before and after the initiation of ductile tearing. The procedure is summarized as follows (JSME S 001-81):

[2]The italic numbers in brackets refer to the list of references appended to this paper.

1. Statically load more than two specimens to different displacement values where ductile tearing does not initiate.

2. Unload each specimen and mark the front of the subcritical stretched zone by subsequent fatigue cracking. Then, pull the specimen apart by overload.

3. Measure the three-point average of *SZW*. The fractographic examination should be performed at 3/8B, 4/8B, and 5/8B (B = specimen thickness) where plane-strain conditions exist. Plot *SZW* and *J* and draw a best-fit line through an original point.

4. Pull more than three specimens apart by overload and measure each SZW_c. Determine average SZW_c. The critical stretched zone width (SZW_c) is defined as a critical value of *SZW* when ductile tearing initiates. SZW_c is not affected by any following stable crack growth. So, it is possible to measure SZW_c on the overload fracture surface by the same method as the measurement of *SZW*.

5. Mark J_{Ic} as a *J*-value at the intersection of the line $SZW = SZW_c$ and the extrapolation of the *J* versus *SZW* blunting line.

The R-curve method recommended by JSME is almost identical to that recommended by ASTM except for the following three points:

1. The experimentally determined *J-SZW* blunting line instead of Eq 1 is utilized.

2. The midthickness average (3/8B, 4/8B, and 5/8B, Δa_{three}) instead of the total average (ASTM: two surfaces and seven inners, Δa_{avg}) of crack extension is utilized.

3. Two offset lines concerning Δa in ASTM are somewhat changed as follows: The 0.15-mm lower limit offset line is omitted and the maximum crack extension is limited to 1.0 mm instead of the 1.5-mm offset line in ASTM.

Evaluation of the Blunting Line

For an ideal crack, such as a sawcut crack or a fatigue precrack where the previous fatigue loading effect can be considered negligible compared with the following monotonic load, a relation between CTOD and the stress-intensity factor (K) or the *J*-integral of the form

$$\text{CTOD} = \frac{(1 - \nu^2)K^2}{\lambda E \sigma_{fs}} \tag{2}$$

in the LEFM case or

$$\text{CTOD} = \frac{J}{\lambda \sigma_{fs}} \tag{3}$$

in the EPFM case under plane-strain conditions has been found, where ν is Poisson's ratio, E is Young's modulus, and λ is about 2. A schematic section

profile of the subcritical stretched zone is shown in Fig. 1. The geometric relation between Δa or SZW and CTOD is given by

$$\Delta a = SZW = \frac{\text{CTOD}}{2 \tan \beta} = \frac{J}{2\lambda\sigma_{fs} \tan \beta} \tag{4}$$

where 2β is the crack-tip blunting angle, and the quantity $2 \tan \beta$ has a value between 1.4 and 2.

In recent years, many experimental data of SZW have been accumulated in the results of the J_{Ic} tests carried out by the present authors. Figures 2 to 4 present all the results on a double-logarithmic plot of SZW for various materials as functions of J and J/σ_{fs}. If we assume relationships of two types of form

$$SZW = A_1 J \tag{5}$$

$$SZW = B_1 \frac{J}{\sigma_{fs}} \tag{6}$$

the values of A_1 and B_1 become as given in Table 1.

The present authors [*2,3,5*] have shown that the J-SZW blunting line of the ideal crack depends not on σ_{ys} or on σ_{fs} but on E. As shown by Table 1, the values of B_1 for alloy steels and aluminum alloys show a tendency to become larger as σ_{fs} becomes larger. It should be noted that if J/σ_{ys} instead of J/σ_{fs} is taken as a parameter, dependence on σ_{ys} becomes more remarkable. Therefore, it is evident that the relation between CTOD or Δa and J does not obey Eq 3 or Eq 4. For intermediate-strength steels (304, A533B-1, and 10B35 tempered at 873 K) and aluminum alloys except 7075-T6, however, Eq 3 or Eq 4 can stand and the value of B_1 is

$$B_1 = \frac{1}{4} \tag{7}$$

This value is plausible, since it can be obtained assuming that $\lambda = 2$ and $\beta = 45$ deg in Eq 4.

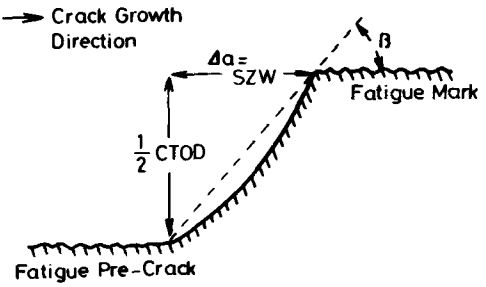

FIG. 1—*Schematic section profile of subcritical stretched zone.*

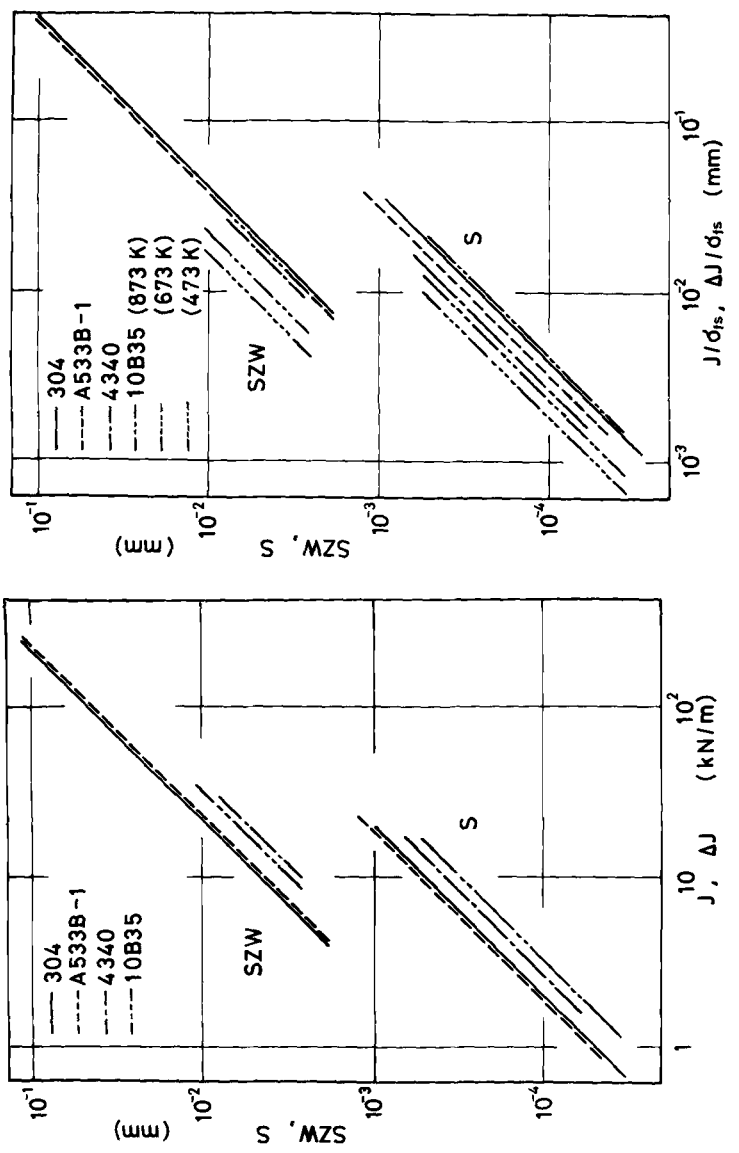

FIG. 2—*Comparison between SZW and S (alloy steels): (a) as functions of J and ΔJ; (b) as functions of* J/σ_{fs} *and* $\Delta J/\sigma_{fs}$.

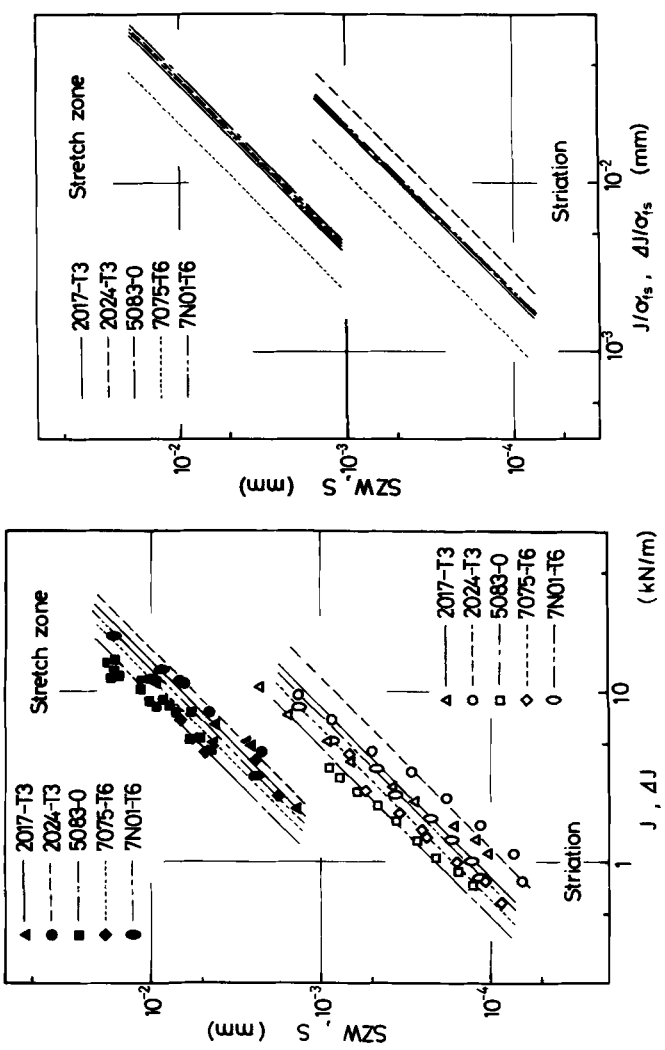

FIG. 3—*Comparison between SZW and S (aluminum alloys): (a) as functions of J and ΔJ; (b) as functions of* J/σ_{fs} and $\Delta J/\sigma_{fs}$.

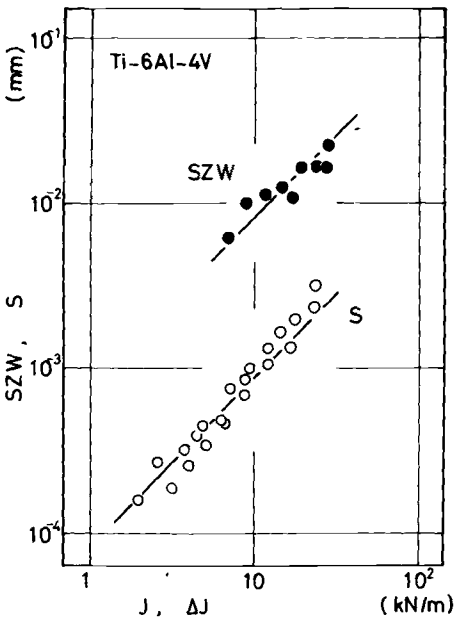

FIG. 4—*Comparison between* SZW *and* S *as functions of* J *and* ΔJ *(Ti-6Al-4V).*

TABLE 1—*Values of* A_1, A_2, B_1, B_2, *and* A_2/A_1.

	σ_{fs}, MPa	A_1, m^2/kN	A_2, m^2/kN	B_1	B_2	A_2/A_1
304	496	0.46×10^{-6}	0.51×10^{-7}	0.23	0.025	0.11
A533B-1	588	0.43×10^{-6}	0.53×10^{-7}	0.25	0.031	0.12
4340	1068	0.27×10^{-6}	0.36×10^{-7}	0.28	0.038	0.13
10B35 (873 K)	755	0.33×10^{-6}	0.31×10^{-7}	0.25	0.023	0.09
(673 K)	1362	0.33×10^{-6}	0.31×10^{-7}	0.44	0.042	0.09
(473 K)	1744	0.33×10^{-6}	0.31×10^{-7}	0.57	0.053	0.09
Average		0.37×10^{-6}	0.43×10^{-7}	0.37	0.035	0.12
2017-T3	384	0.68×10^{-6}	0.123×10^{-6}	0.26	0.047	0.18
2024-T3	411	0.57×10^{-6}	0.083×10^{-6}	0.24	0.034	0.15
5083-O	217	1.08×10^{-6}	0.212×10^{-6}	0.23	0.046	0.20
7075-T6	537	0.82×10^{-6}	0.164×10^{-6}	0.44	0.088	0.20
7N01-T6	321	0.77×10^{-6}	0.138×10^{-6}	0.25	0.044	0.18
Average		0.78×10^{-6}	0.144×10^{-6}	0.28	0.052	0.18
Ti-6Al-4V	970	0.82×10^{-6}	0.087×10^{-6}	0.79	0.084	0.11
Total average		0.67×10^{-6}	0.091×10^{-6}	0.48	0.057	0.13

It seems rather strange that *SZW* formed by crack-tip plastic blunting does not depend on σ_{fs}. However, a characteristic like this is well known in fatigue. In Stage 2*b*, plane-strain LEFM fatigue crack growth, growth rates (da/dN) are in excellent agreement with striation spacings (S) and obey the following expression in the case that the stress ratio (R) is about 0

$$da/dN = S = C_1(1-\nu^2)\left(\frac{\Delta K}{E}\right)^2 \tag{8}$$

where ΔK is the stress-intensity factor range. Experimental investigations show that the constant C_1 is about 9 on the assumption that $\nu = 1/3$ [*8,9*].

For comparison, the striation spacings (S) when R is about 0 are plotted in Figs. 2 to 4 as functions of ΔJ and $\Delta J/\sigma_{fs}$, where ΔJ is the cyclic J-integral converted from ΔK. Note that the use of ΔJ does not mean the EPFM case, as all the data on S satisfy small-scale yielding conditions. If we assume relationships of two types of form

$$S = A_2 \Delta J \tag{9}$$

$$S = B_2 \frac{\Delta J}{\sigma_{fs}} \tag{10}$$

the values of A_2 and B_2 become as given in Table 1. The values of B_2 show the same tendency as B_1. It should be noted that not B_1 but ratio A_2/A_1 or B_2/B_1 becomes the structure-insensitive property, as shown in Table 1.

From the structure-insensitive property of A_2/A_1, it is clear that the values of *SZW* and S for the same J-value are as different as approximately one order of magnitude. The reason for the smaller width of the striation should be attributed to plasticity-induced crack closure under the cyclic load [*10,11*]. The present authors have shown that the fatigue crack acceleration during a single peak overload can be exactly evaluated from the ratio A_2/A_1 [*4,11*]. The result is given by the following expression in the case that R of the previous fatigue load is about 0

$$\frac{GS}{S} = \frac{\alpha \Delta J_0 + (J_1 - J_0)}{\alpha \Delta J_1} \tag{11}$$

where

GS = giant striation spacing formed during a single peak overload,
S = striation spacing formed by cyclic ΔJ_1,
$\alpha = A_2/A_1$,
ΔJ_0 = cyclic ΔJ for previous fatigue load range,
J_0 = monotonic J for previous fatigue load,

J_1 = monotonic J for single peak overload, and
ΔJ_1 = cyclic ΔJ for single peak overload range.

For $J_1 \gg J_0$, *GS* would become *SZW* and the crack can be considered as the ideal crack. This is the reason why the experimentally determined *J-SZW* blunting line is utilized in the JSME recommendation. It may be concluded that Eq 1 should not be used as the blunting line.

Evaluation of the J_{Ic} Test Methods

Two techniques, the stretched zone method and the R-curve method, were used to determine the J_{Ic}-value of an HT80 steel (σ_{fs} = 789 MPa), an HT60 steel (σ_{fs} = 617 MPa), and a 304 stainless steel (σ_{fs} = 432 MPa). The tests were performed in the longitudinal (L-T) orientation for HT80 and 304, and in the transverse (T-L) orientation for HT60. Specimens used were the 25.4-mm compact type. J was calculated from the load-displacement record and specimen dimensions using the equation in the ASTM Method E 813-81.

Stretched Zone Method

The relation between *SZW* and J in HT60 is shown in Fig. 5. Open and solid symbols in Fig. 5 represent data before and after the initiation of ductile tearing, respectively. So, the former means the subcritical stretched zone width (*SZW*) data and the latter means the critical stretched zone width (SZW_c) data. The measurements of *SZW* and SZW_c were performed according to the method in JSME S 001-81. All the data before *SZW* reaches SZW_c fall on a J versus *SZW* blunting line with little variation. On the other hand, a fair

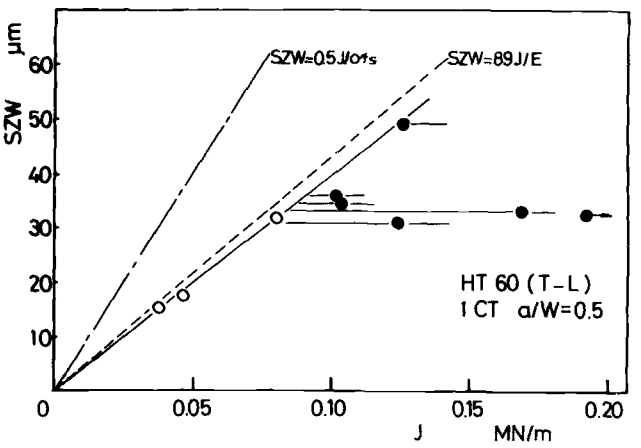

FIG. 5—*Relation between* SZW *and* J *(HT60 steel).*

amount of scatter on SZW_c exists (SZW_c = 32 to 49 μm). Fractographic observation revealed that splitting by elongated and pancaked dimples occurred along the alloy-rich band oriented at right angles to the crack front. Accordingly, the critical stretched zone is divided into several parts. Also, its width, SZW_c, for each specimen has a wide variation due to the material inhomogeneity. The J_{Ic}-value for each specimen, however, can be evaluated exactly at the intersection of the blunting line and each SZW_c (J_{Ic} = 70.6 to 123 kN/m).

Figure 6 shows the result of HT80. In this material, the clear stretched zone was observed and a variation of its width was not so remarkable compared with that in HT60. The J_{Ic}-value (263 kN/m) is in good agreement with that obtained from the R-curve method.

The result of 304 shows that the stretched zone develops to a width of more than 250 μm without the initiation of ductile tearing. Hereafter, microvoids appear throughout the whole stretched region. A conservative value of J_{Ic} = 490 kN/m is obtained fractographically.

R-Curve Method

Figure 7 shows the relation between J and the total average (ASTM: two surfaces and seven inners) crack extension (Δa_{avg}) in HT60 where the blunting line is determined experimentally. After the initiation of ductile tearing, a scatter is observed reflecting the wide variation of J_{Ic} of each specimen as stated earlier. In this case, it is not reasonable to determine one R-curve using multiple specimens. Furthermore, it was difficult to control the Δa-value due to the low value of dJ/da, which resulted in insufficient data being obtained

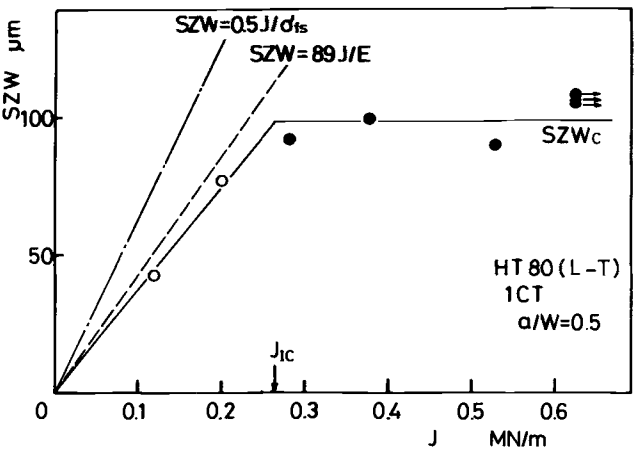

FIG. 6—*Relation between* SZW *and* J *(HT80 steel).*

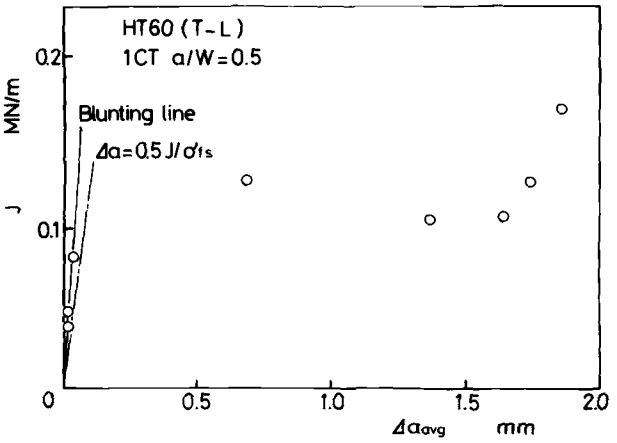

FIG. 7—*J-resistance curve (HT60 steel).*

within the offset line. The R-curve method cannot be applied for this kind of material.

The total average (Δa_{avg}), the midthickness average (JSME: three inners, Δa_{three}), and the maximum (Δa_{max}) crack extensions were measured in HT80. A comparison of the R-curves for three measurement techniques is shown in Fig. 8. It is clear that the three different techniques result in markedly differing Δa-values due to crack tunneling near the midthickness of the specimens. However, this difference has little influence on the J_{Ic}-value. The J_{Ic}-values are 221 and 247 kN/m according to the JSME (experimentally determined blunting line, Δa_{three}) and ASTM (assumed blunting line, Δa_{avg}) methods, respec-

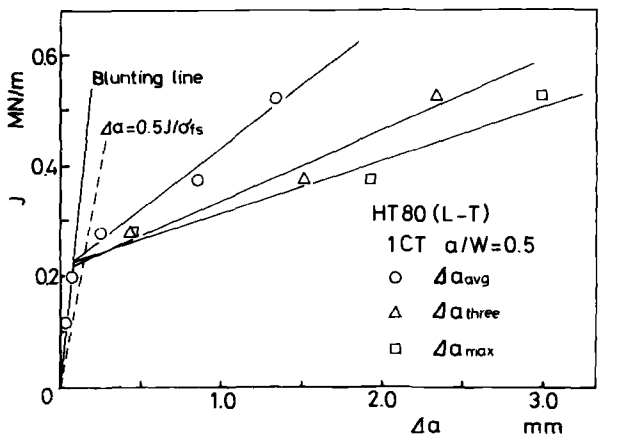

FIG. 8—*J-resistance curve (HT80 steel).*

tively. These two methods give almost the same J_{Ic}-values, although the latter gives a somewhat larger value than the former.

The relation between J and Δa in 304 is shown in Fig. 9. The assumed blunting line given in Eq 1 does not represent the experimentally derived one. The constant value in Eq 1 becomes about 4 rather than 2 as shown in Table 1. It should be noted that crack tunneling does not occur. There is little difference between the slope of the J-Δa_{avg}, the J-Δa_{three} and the J-Δa_{max}. And each slope after the initiation of ductile tearing ($J > 490$ kN/m) is almost identical to that of the blunting line. So, it is not possible to determine J_{Ic} by the R-curve method.

Evaluation of J_{Ic} and J Resistance Curve of A533B-1 Steel

Evaluation of J_{Ic}

The relation between *SZW* and J in A533B-1 is shown in Fig. 10. The difference in specimen sizes (½CT to 2CT) has little influence on the relation. The J_{Ic}-values are 190, 185, and 191 kN/m for ½CT, 1CT, and 2CT specimens, respectively. If Eq 1 is used as a blunting line, it is clear that J_{Ic} is underestimated.

The results of the R-curve methods in JSME S 001-81 and ASTM E 813-81 are shown in Figs. 11*a* and 11*b*, respectively. The JSME method utilizes the data just after the initiation of ductile tearing. So, all the valid data in the

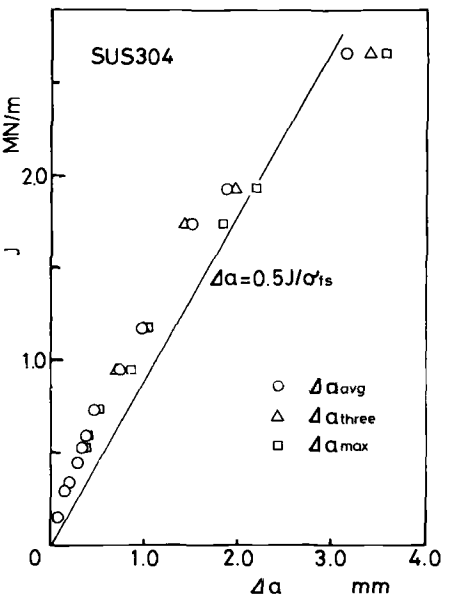

FIG. 9—J-*resistance curve (304 stainless steel).*

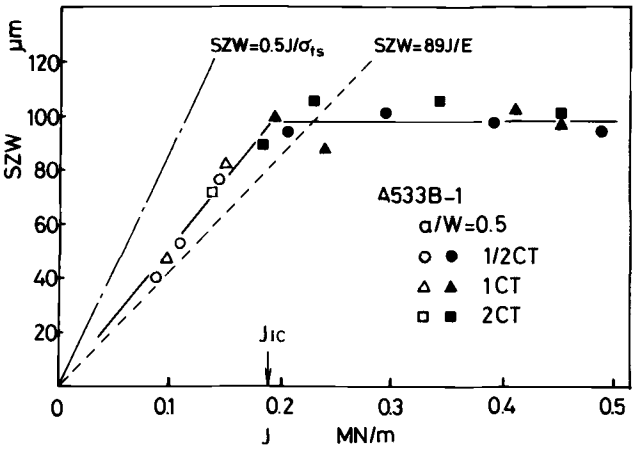

FIG. 10—*Relation between* SZW *and* J *(A533B-1 steel).*

JSME method are regarded as invalid in the ASTM method due to the data limitation of 0.15-mm lower limit offset line. However, the difference between these two methods has little influence on the valid J_{Ic}-values, 180 and 213 kN/m in the JSME and ASTM methods, respectively, which are almost identical to those obtained by the stretched zone method. Strictly, the J_{Ic}-value of the ASTM method is somewhat larger than that of the JSME method, as in the case of HT80. The reason may be attributed to the misfit of Eq 1 for the actual blunting line in the ASTM method.

In the ASTM method, the valid J_{Ic}-value of the ½CT specimen was not obtained due to following specimen size restriction:

$$B, b > \alpha \frac{J}{\sigma_{fs}} \tag{12}$$

where

$\alpha = 15$,
B = specimen thickness, and
b = ligament.

If the restriction of Eq 12 is neglected, the conditional value (J_Q) of the ½CT specimen becomes larger than the valid J_{Ic}-values of the 1CT and 2CT specimens.

On the other hand, according to the JSME method, the J_{Ic}-value of the ½CT specimen can be obtained, because the Δa_{three} data near J_{Ic} are utilized. The R-curves for different specimen sizes obtained in this method have a pivot point at J_{Ic}, although the specimen size may influence on the dJ/da-value. In the JSME method, the restriction of Eq 12 is not needed necessarily for the R-curve data if the J_{Ic}-value satisfies the restriction ($\alpha = 25$ and $J = J_{Ic}$ in Eq

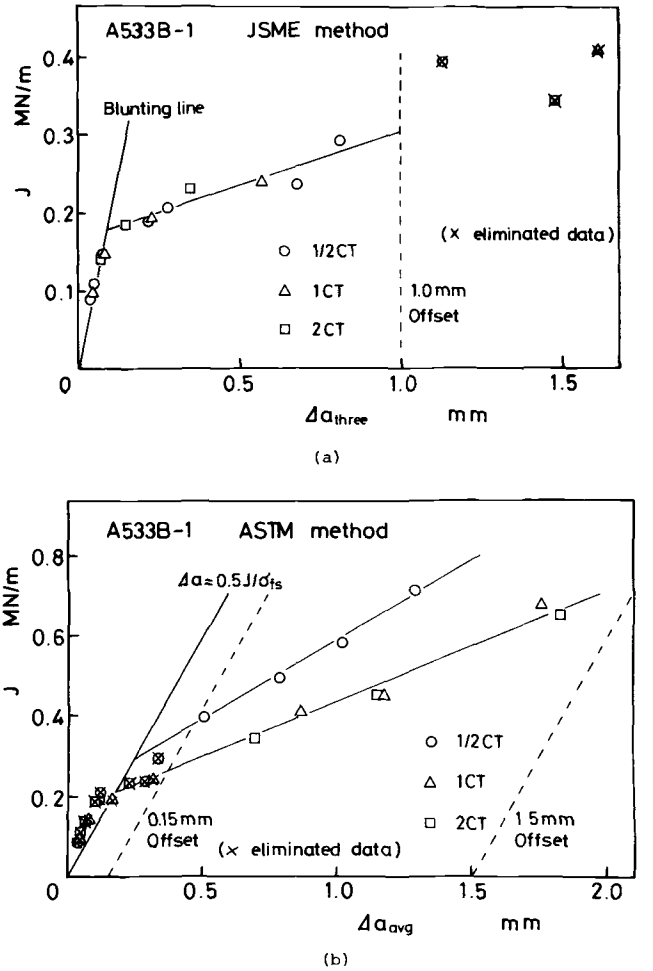

FIG. 11—J-*resistance curve (A533B-1 steel);* (a) *JSME method;* (b) *ASTM method.*

12). So it may be concluded that, according to the JSME method, the J_{Ic}-value can be evaluated using smaller specimen size compared with the ASTM method. Furthermore, the dJ/da value for Δa_{three} is smaller than that for Δa_{avg} and this gives a sharp intersection of the R-curve and the blunting line which results in the clear determination of J_{Ic}.

Figure 12 shows the normalized load versus load-line-displacement curve [*12*], where solid circles represent the onset of general yielding obtained by finite-element method (FEM) analyses. The initiation points of ductile tearing for the ½CT, 1CT, and 2CT specimens differ in stress states (plane stress or plane strain) and yielding conditions (large scale or small scale). However,

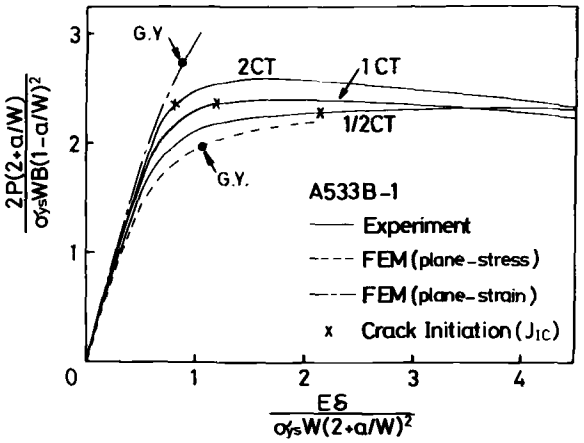

FIG. 12—*Normalized load versus load-line displacement curve.*

these differences have no effect on the valid J_{Ic}-value calculated using the load versus load-line-displacement curve. The specimen size restriction is needed only for the occurrence of the plane-strain-type ductile tearing.

Evaluation of the J Resistance Curve

Figure 13 shows a comparison of the relations between J and Δa_{avg} for the ½CT, 1CT, and 2CT specimens of A533B-1. Compensating some data obtained by a compliance method in ASTM E 813-81 for the R-curve data, the tearing modulus [*13*]

$$T_J = \frac{E}{\sigma_{fs}^2}\frac{dJ}{da} \tag{13}$$

was evaluated. The procedure involves a statistical curve-fitting to the data. The equation form is

$$\Delta a = \sum_{k=0}^{n} C_k J^k \tag{14}$$

where C_k is a constant. Changing n from 2 to 15, the value of n to give the best fit was chosen. The values were n = 9, 6, and 5 for the ½CT, 1CT, and 2CT specimens, respectively. Differentiating and substituting Eq 14 into Eq 13, T_J was obtained as shown in Fig. 14. Although the actual curves showed some oscillation, this was neglected. The plateaus of T_J exist. And the value for the ½CT specimen is larger than that for the 1CT and 2CT specimens, which may suggest that the specimen size restriction of Eq 12 should be met to obtain the size-independent T_J.

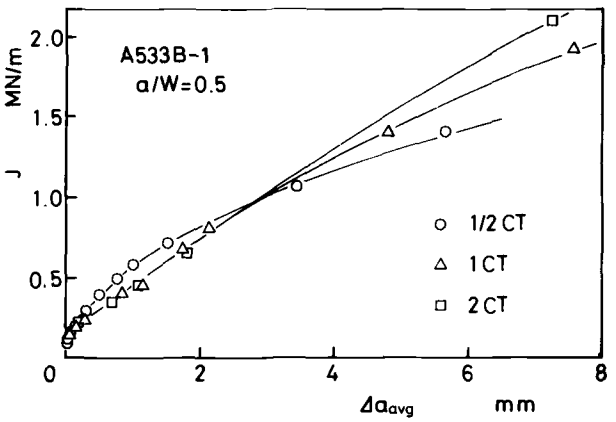

FIG. 13—J-*resistance curve for* ½*CT, 1CT, and 2CT (A533B-1 steel).*

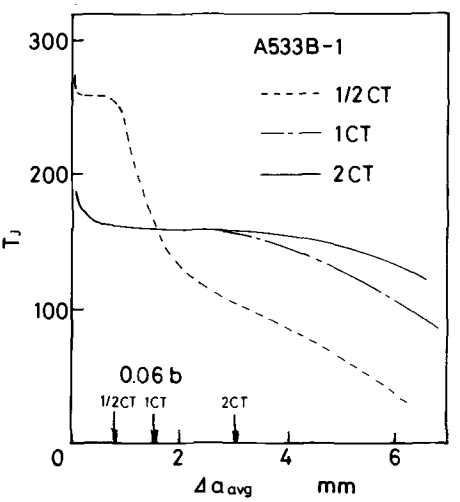

FIG. 14—*Tearing modulus versus crack extension.*

On the other hand, Hutchinson and Paris [*14*] have suggested that a validity criterion for the J-controlled crack growth is given as

$$\omega = \frac{b}{J}\frac{dJ}{da} \gg 1 \tag{15}$$

The constant value of T_J for the 1CT and 2CT specimens satisfies Eq 15 [ω = 19 to 4 (1CT) and 39 to 8 (2CT) for J = 0.2 to 1.0 MN/m]. So, its value may be regarded as a valid measure of material toughness during stable crack growth. Another validity criterion suggested by Shih et al [*15*] is given as

$$\Delta a < 0.06b \tag{16}$$

As shown by Fig. 14, T_J begins to level off after some crack extension. The reason may be attributed to the fact that the data do not satisfy Eq 16 in such a Δa_{avg} range. It should be noted that the range of validity becomes narrower if the Δa-correction developed by Ernst and Paris [*16*] is made as shown in Fig. 15.

Figure 16 is a double-logarithmic plot of Δa_{avg} as a function of J. For comparison, the data of SZW and S are also shown in Fig. 16. It is clear that the dependence of the crack-tip plastic bunting (SZW and S) characteristic on J is quite different from that of the stable crack growth (Δa_{avg}) characteristic. For a wide range of Δa_{avg}, the relation between Δa_{avg} and J is given as

$$\Delta a_{avg} = C_2 J^2 \tag{17}$$

where C_2 is a constant.

Conclusion

The results obtained are as follows:

1. The J-SZW blunting line before the initiation of ductile tearing can be obtained uniquely by use of the electron microscope. This experimentally determined blunting line does not obey the following assumed expression

$$J = 2\sigma_{fs}\Delta a$$

where σ_{fs} is the flow stress. In some low- and intermediate-strength materials, the intersection point of the assumed blunting line and the R-curve does not exist. So, the blunting line should be determined experimentally for each material.

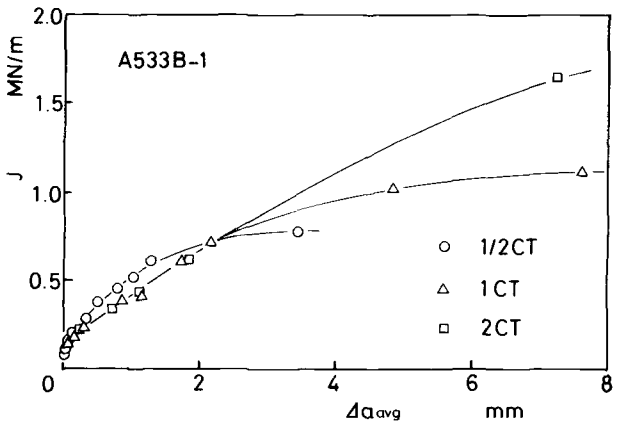

FIG. 15—J-*resistance curve (*Δa *corrected; A533B-1 steel).*

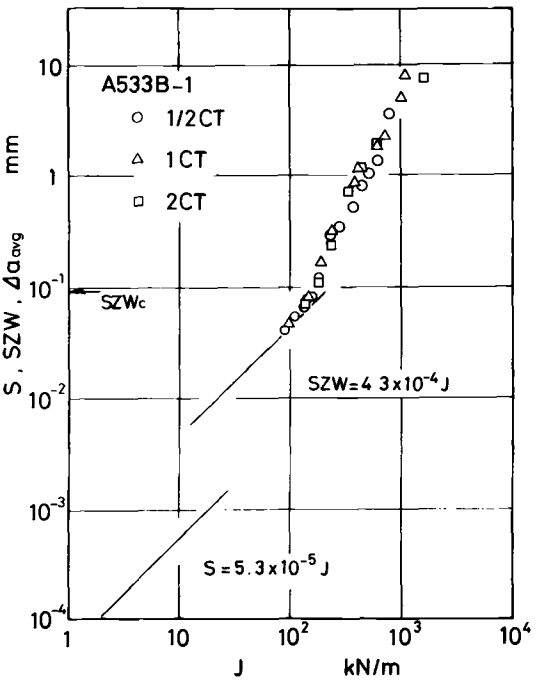

FIG. 16—*Comparison between* Δa, SZW, *and* S *as functions of* J *and* ΔJ.

2. In some materials, J_{Ic}-values determined by the single-specimen method have wide variation due to material inhomogeneity. For these kinds of materials, difficulty arises in determining one R-curve utilizing multiple specimens. It is possible, however, to determine J_{Ic} accurately for each specimen at the intersection of the *J-SZW* blunting line and the line of $SZW = SZW_c$. It should be noted that use of the assumed blunting line instead of an experimentally determined one can give incorrect J_{Ic}-values.

3. According to the JSME method, the J_{Ic}-value can be evaluated using a smaller specimen size compared with the ASTM method.

Acknowledgment

The authors wish to express their thanks to Norio Takashima, a graduate student of Tokyo Institute of Technology, for his help and contribution to this work.

References

[*1*] Kobayashi, H., Hirano, K., Nakamura, H., and Nakazawa, H. in *Advances in Research on the Strength and Fracture of Materials, Proceedings*, Fourth International Conference on Fracture, Vol. 3, Pergamon Press, New York, 1977, pp. 583-592.

[2] Kobayashi, H., Nakamura, H., and Nakazawa, H. in *Recent Research on Mechanical Behavior of Solids*, University of Tokyo Press, 1979, pp. 341-357.

[3] Kobayashi, H., Nakamura, H., and Nakazawa, H. in *Mechanical Behaviour of Materials, Proceedings*, Third International Conference on Mechanical Behaviour of Materials, Vol. 3, Pergamon Press, New York, 1979, pp. 529-538.

[4] Kobayashi, H., Nakamura, H., Hirano, A., and Nakazawa, H. in *Materials, Experimentation and Design in Fatigue, Proceedings*, Fatigue '81, Westbury, Guildford, Surrey, U.K., 1981, pp. 318-327.

[5] Kobayashi, H., Nakamura, H., Hirano, K., and Nakazawa, H. in *Fracture Mechanics of Ductile and Tough Materials and Its Application to Energy Related Structures, Proceedings*, USA-Japan Joint Seminar, Martinus Nijhoff Publishers, The Hague, 1981, pp. 111-120.

[6] Begley, J. A. and Landes, J. D. in *Fracture Toughness, ASTM STP 514*, American Society for Testing and Materials, 1972, pp. 1-23.

[7] Clarke, G. A., Andrews, W. R., Begley, J. A., Donald, J. K., Embley, G. T., Landes, J. D., McCabe, D. E., and Underwood, J. H., *Journal of Testing and Evaluation*, Vol. 7, No. 1, 1979, pp. 49-56.

[8] Bates, R. C., Clark, W. G., Jr., and Moon, D. M. in *Electron Microfractography, ASTM STP 453*, American Society for Testing and Materials, 1969, pp. 192-214.

[9] Kobayashi, H., *Journal of the Japan Society of Mechanical Engineers*, Vol. 80, No. 703, 1977, pp. 492-497.

[10] Elber, W. in *Damage Tolerance in Aircraft Structures, ASTM STP 486*, American Society for Testing and Materials, 1971, pp. 230-242.

[11] Kobayashi, H., Nakamura, H., and Nakazawa, H. in *Mechanics of Fatigue*, AMD-Vol. 47, American Society of Mechanical Engineers, 1981, pp. 133-150.

[12] Andrews, W. R. and Shih, C. F. in *Elastic-Plastic Fracture, ASTM STP 668*, J. D. Landes, J. A. Begley, and G. A. Clarke, Eds., American Society for Testing and Materials, 1979, pp. 426-450.

[13] Paris, P. C., Tada, H., Zahoor, A., and Ernst, H. in *Elastic-Plastic Fracture, ASTM STP 668*, J. D. Landes, J. A. Begley, and G. A. Clarke, Eds., American Society for Testing and Materials, 1979, pp. 5-36.

[14] Hutchinson, J. W. and Paris, P. C. in *Elastic-Plastic Fracture, ASTM STP 668*, J. D. Landes, J. A. Begley, and G. A. Clarke, Eds., American Society for Testing and Materials, 1979, pp. 37-64.

[15] Shih, C. F., deLorenzi, H. G., and Andrews, W. R. in *Elastic-Plastic Fracture, ASTM STP 668*, J. D. Landes, J. A. Begley, and G. A. Clarke, Eds., American Society for Testing and Materials, 1979, pp. 65-120.

[16] Ernst, H. A. and Paris, P. C., "Techniques of Analysis of Load-Displacement Records by *J*-Integral Methods," *U.S. Nuclear Regulatory Commission Report, NUREG/CR-122*, Washington, D.C., Jan. 1980.

James A. Joyce[1]

Instability Testing of Compact and Pipe Specimens Utilizing a Test System Made Compliant by Computer Control

REFERENCE: Joyce, J. A., **"Instability Testing of Compact and Pipe Specimens Utilizing a Test System Made Compliant by Computer Control,"** *Elastic-Plastic Fracture; Second Symposium, Volume II—Fracture Resistance Curves and Engineering Applications, ASTM STP 803*, C. F. Shih and J. P. Gudas, Eds., American Society for Testing and Materials, 1983, pp. II-439-II-463.

ABSTRACT: The aim of this paper is to demonstrate that a computer-controlled test machine can replace a test machine made compliant by a mechanical spring for tearing instability testing of simple compact and cracked pipe geometries. For both geometries tested herein, close agreement was demonstrated between the "computer compliant" and "spring compliant" test systems. The results show that though the computerized system utilized here is slower than the spring machine, this is not a serious drawback for structural materials with low to moderate rate dependence. The "inertia free" response of the computerized system is in fact a positive feature for studying tearing instability arrest and promises to be very useful in further studies in that area.

Experimental results obtained in this study on the circumferentially cracked pipe geometry show that J-R curves from the pipe geometry lie well above J-R curves obtained from subscale compact specimens removed from the pipe wall. Tearing instability occurs in the pipes at crack extension values well in excess of what was obtained from compact specimens of the scale utilized, and a prediction of pipe instability based on the compact J-R curve alone would give very conservative results.

KEY WORDS: elastic-plastic fracture, J-integral, J-R curves, slow crack growth, tearing modulus, tearing instability, compact specimens, circumferentially cracked pipe specimens, computer-controlled testing, tearing instability arrest

During the past few years a major effort in the area of elastic-plastic fracture has gone into the development of the J-integral as a fracture criterion and into the development of the J-R curve both to define an initial J_{Ic} crack

[1]Associate professor, Mechanical Engineering Department, U.S. Naval Academy, Annapolis, Md. 21402.

initiation parameter and as a separate and independent material toughness characterization. Paris and co-workers [*1*][2] have proposed the use of the J-R curve to predict the onset of ductile tearing instability by defining a tearing force, T, where

$$T_{\text{APPLIED}} = \frac{E}{\sigma_0^2}\left(\frac{dJ}{da}\right)_{\text{APPLIED}} \tag{1}$$

and a material tearing resistance

$$T_{\text{MATERIAL}} = \frac{E}{\sigma_0^2}\left(\frac{dJ}{da}\right)_{\text{MATERIAL}} \tag{2}$$

and stating the conditions for tearing instability to be

$$T_{\text{MATERIAL}} > T_{\text{APPLIED}} \text{ stability}$$

$$T_{\text{APPLIED}} \geq T_{\text{MATERIAL}} \text{ instability} \tag{3}$$

Some limited experimental work has been accomplished which verifies the preceding concept for simple bend bar and compact specimen geometries [*2-4*]. This experimental verification is difficult even for simple geometries because highly compliant test machine fixtures must be constructed to generate T_{APPLIED} values large enough to exceed T_{MATERIAL} values for the high-toughness steels typically found in engineering applications. For more complicated geometries, involving, for instance, biaxial loading, the experimental difficulties become immense.

The objective of this task was to utilize a computer-controlled servo-hydraulic test machine to simulate a compliant test machine and to investigate whether identical ductile tearing instabilities could be generated in compact and circumferentially cracked pipe specimens in "spring compliant" and "computer compliant" test machines.

The concept of programming the hydraulic ram to act like a combination of load control and displacement control is very simple, but practical considerations soon show that to avoid wildly unstable machine behavior an experimentally determined amount of "software damping" is required to produce a reasonable approximation of compliant test machine behavior.

Analysis of Tearing Instability

The tearing instability criterion specified in Eqs 1-3 requires evaluation of the material tearing resistance T_{MAT} and the tearing force T_{APP} as a specimen

[2]The italic numbers in brackets refer to the list of references appended to this paper.

or structural member is loaded as a function of load and load-point displacement and including the effects of crack extension. The material tearing resistance can be directly evaluated from the J-R curve of the material by application of Eq 2. In practice a polynomial or other function is fit to the series of J and Δa (crack extension) pairs which make up the J-R curve and then this fitting function is differentiated to get T_{MAT}.

In the present study for the compact specimen, J was evaluated using the equation of Ernst [5] that

$$J_{i+1} = J_i = \left(\frac{\eta}{b}\right)_i A_{i,i+1}\left[1 - \left(\frac{\gamma_i}{b_i}\right)(a_{i+1} - a_i)\right] \tag{4}$$

where i indicates the step of the incremental evaluation process

$$\eta_i = 2 + 0.522 b_i/W \tag{5}$$

$$\gamma_i = 1 + 0.76 b_i/W \tag{6}$$

and

b_i = remaining ligament at the ith step,
$A_{i,i+1}$ = area enclosed by the actual test record and lines of constant displacement at crack-opening displacement (COD) limits δ_i and δ_{i+1},
a_i = crack length at the ith step, and
W = specimen width.

The crack length was measured using an unloading compliance technique like that of Joyce and Gudas [6].

The applied tearing force was calculated using the analysis of Ernst [5] for a compact specimen that

$$T_{APP} = \frac{E}{\sigma_0^2}\left\{-\gamma\frac{J}{b} + \frac{\eta^2 P}{b^2}\frac{1}{\frac{K_M}{P} + \frac{1}{P}\frac{dP}{d\delta} + \frac{\eta^2 P}{b^2}\left(\frac{1}{dJ/da + \gamma(J/b)}\right)}\right\} \tag{7}$$

where

P = load,
σ_0 = flow stress = $\dfrac{(\sigma_{ys} + \sigma_{uts})}{2}$, (8)
E = elastic modulus,

K_M = machine stiffness, and
$dP/d\delta$ = slope of load—load-point displacement record.

The other quantities are as defined previously.

Ernst [5] has also shown that T_{APP} and T_{MAT} can be written in parallel forms as

$$T_{APP} = \frac{E}{\sigma_0^2}\left[-\gamma\frac{J}{b} + \frac{\eta^2 P}{b^2}\left(\frac{1}{\frac{H'}{WH} + \frac{K_M}{P}}\right)\right] \tag{9}$$

and

$$T_{MAT} = \frac{E}{\sigma_0^2}\left[-\gamma\frac{J}{b} + \frac{\eta^2 P}{b^2}\left(\frac{1}{\frac{H'}{WH} - \frac{1}{P}\frac{dP}{d\delta}}\right)\right] \tag{10}$$

where H is defined according to

$$P = \frac{b^2}{W} g(a/W) \cdot H(\delta_{PL}/W) \tag{11}$$

which is an assumed form of the load-displacement record for a compact specimen. The forms for T in Eqs 9 and 10 show that the Paris instability criterion of Eq 3 is equivalent to the requirement that

$$\begin{aligned} -\frac{dP}{d\delta} &< K_M \quad \text{stability} \\ -\frac{dP}{d\delta} &\geq K_M \quad \text{instability} \end{aligned} \tag{12}$$

Recourse to this relationship will be taken later in this work.

The equations of Ernst given in the foregoing are applicable to bend bars but not to the circumferentially cracked pipes that were tested in this work, though the classical slope requirements for instability expressed in Eq 12 certainly apply to the circumferentially cracked pipe configuration. The equations used here for J and T_{APP} for the circumferentially cracked pipe are taken from work by Tada et al [7] and by Zahoor and Kanninen [8]. For reference the notation used to define the pipe geometry is presented in Fig. 1.

The Tada equation for J is simply that

$$J = \sigma_0 R\phi\left(\sin\frac{\theta}{2} + \cos\theta\right) \tag{13}$$

and the equation for T_{APP} (which is really a slight extension of his work to include a test machine compliance) is

$$T_{APP} = \frac{8ER^2t}{\ell^2}\,[1/K_{pipe} + 1/K_M]\left(\sin\frac{\theta}{2} + \cos\theta\right)^2 + \frac{EJ}{2\sigma_0{}^2R}\left(\frac{\cos\frac{\theta}{2} - 2\sin\theta}{\sin\frac{\theta}{2} + \cos\theta}\right) \quad (14)$$

where $1/K_{pipe}$ is the pipe compliance given by

$$\frac{\delta}{P} = \frac{1}{K_{pipe}} = \frac{\ell^2}{EI}\left[\frac{L}{4} - \frac{\ell}{3}\right] \quad (15)$$

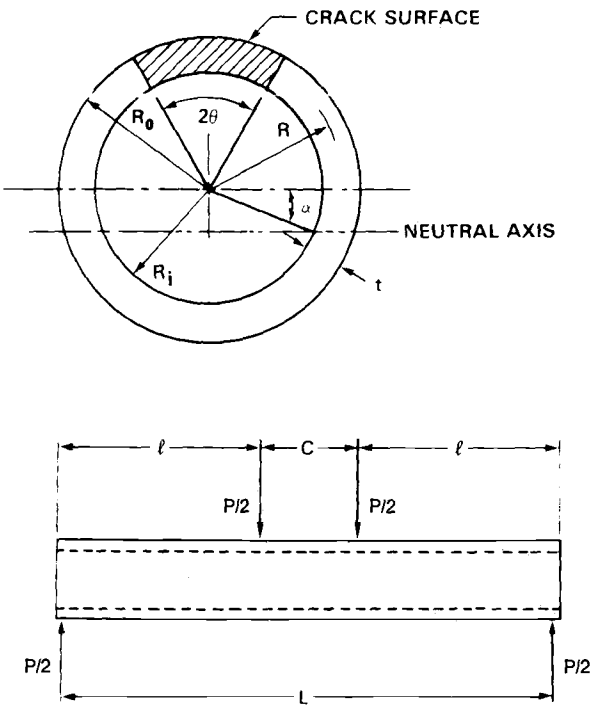

FIG. 1—*Schematic showing notation utilized in analysis of the circumferentially cracked pipe loaded in four-point bending.*

The Zahoor [8] analysis for J starts by assuming a separable load-displacement relationship of the form

$$P = h(2\theta) \cdot F(\delta_{PL}) \tag{16}$$

where δ_{PL} is the plastic component of the load-point displacement. The J can be expressed as

$$\begin{aligned} J &= J_{EL} + J_{PL} \\ &= \frac{K_I^2}{E} + \beta \int_0^{\delta_{PL}} P \, d\delta_{PL} + \int_{\theta_0}^{\theta} 2\gamma J_{PL} \, d\theta \end{aligned} \tag{17}$$

with

$$K_I^2 = \sigma^2 \pi a \, [0.7631 - 1.3511x^2 - 0.3822x^3/(1-x)^3] \tag{18}$$

and

x = through-wall crack length/pipe circumference,
$2a$ = circumferential crack length, and
σ = outer fiber tensile bending stress.

$$\beta = h'(2\theta)/R\text{th}(2\theta) \tag{19}$$

$$\gamma = h''(2\theta)/h'(2\theta) \tag{20}$$

where θ_0 is the initial crack angle and $h(2\theta) = \cos(\theta/2) - \frac{1}{2}\sin\theta$.

The Zahoor equation for T_{APP} for a compliant test machine is

$$T_{APP} = \frac{E}{\sigma_0^2} \left[2t(\beta P)^2 \left(\frac{C_M + C_{PIPE}}{1 + (C_M + C_{PIPE}) \left(\frac{dP}{d\delta_{PL}} \right)_\theta} \right) + \frac{2\gamma}{R} J_{PL} \right] \tag{21}$$

For both of these expressions β and γ were evaluated by Zahoor and Kanninen and presented graphically [8]. The term $(dP/d\delta_{PL})_\theta$ can be evaluated directly from the load-displacement curve of the specimen until the point of crack initiation. After this point, the term is not readily available and for this case it is assumed to be small, giving

$$T_{APP} = \frac{E}{\sigma_0^2} \left[\frac{2t(\beta P)^2}{K_{PIPE}} \left(1 + \frac{K_{PIPE}}{K_M} \right) + \frac{2\gamma}{R} J_{PL} \right] \tag{22}$$

Description of the Experimental Work

Specimen Description

Two specimen types were utilized in this project. The first was a standard ½T compact specimen of geometry shown in Fig. 2 made from HY-130 steel with properties tabulated in Table 1. All compact specimens were machined from 25-mm-thick (1 in.) plate in the T-L orientation. The second specimen type was a circumferentially cracked pipe specimen of 6061-T651 aluminum alloy as shown in Fig. 3 loaded in four-point bending as shown in Fig. 1 with $C = 152$ mm (6 in.). Two compact specimens of the geometry of Fig. 2 were also machined from the pipe with a crack orientation identical to the circumferential crack direction but with a final thickness of 4.62 mm (0.18 in.) [compared with the 6.01-mm (0.24 in.) pipe wall dimension]. These two

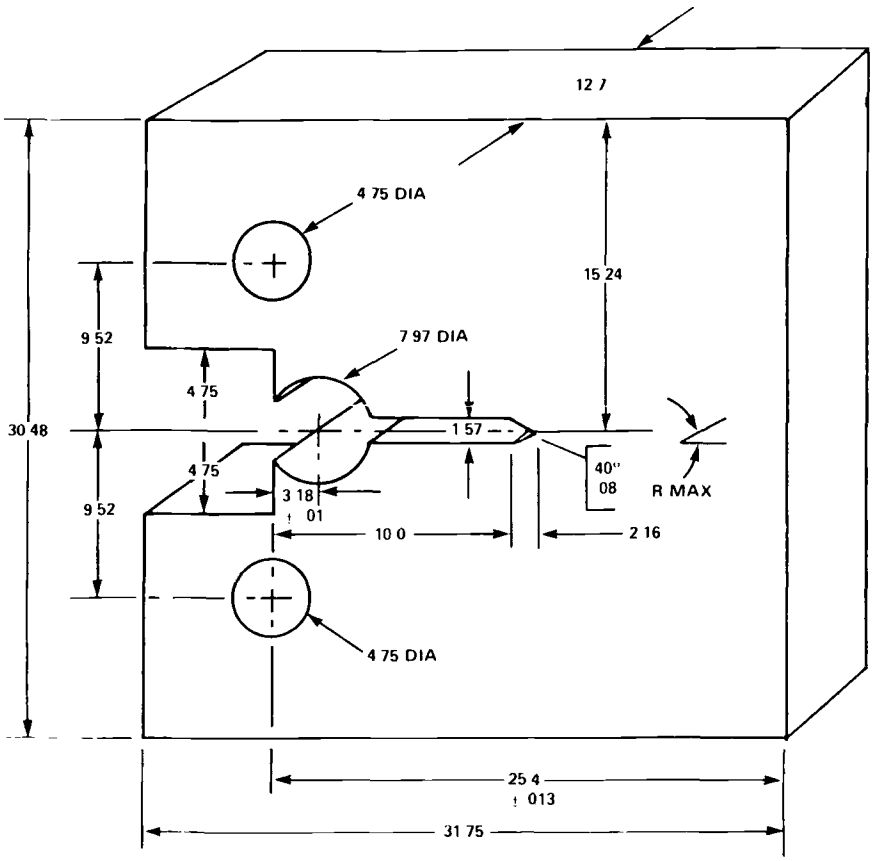

FIG. 2—*Specimen drawing of ½-scale compact specimen. Dimensions are in mm.*

TABLE 1—*Chemical composition and tensile mechanical properties of HY-130 steel.*

Chemical Composition, Weight %												
C	Mn	P	Si	Ni	Cr	Mo	V	S	Cu	Al	Co	Ti
0.11	0.76	0.005	0.03	5.00	0.42	0.53	0.043	0.004	0.022	0.021	0.02	0.008

Tensile Mechanical Properties			
Yield Strength, 0.2% MPa[a]	Ultimate Tensile Strength, MPa	Elongation, % in 2 in.[b]	Reduction of Area, %
937	978	21	55

[a] 1 MPa = 0.145 ksi.
[b] 1 in. = 25.4 mm.

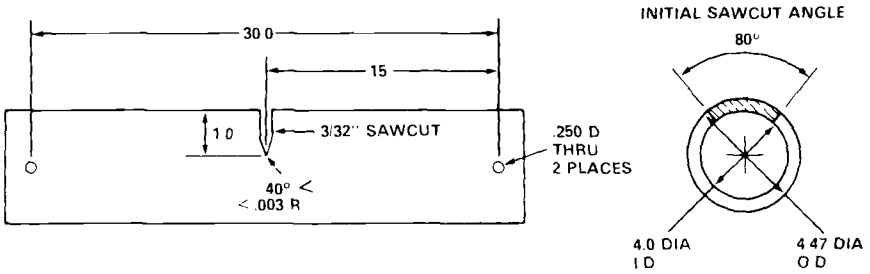

FIG. 3—*Specimen drawing of 10-cm (4 in.) inside diameter pipe specimens. Dimensions are in inches.*

specimens were used to evaluate the J-R curve properties for the aluminum pipes discussed later.

All specimens were fatigue-precracked before testing. Initial crack lengths for compact specimens were such that $a/W = 0.62$, while for pipe specimens x varied from 0.3 to 0.35. Side grooves were not used on the compact specimens and all tests were conducted at static rates at ambient room temperature. Approximately three specimens of each geometry were tested using a mechanically compliant test machine utilizing a titanium leaf spring of variable span. A similar number of specimens were tested in a computer-interfaced servohydraulic test machine made compliant by a software program.

Hardware Description

A schematic of the spring compliant test apparatus utilized for the compact specimens is shown in Fig. 4. A screw-driven displacement-controlled machine is utilized in conjunction with a minicomputer data acquisition system which monitors load, load-line COD displacement, and head displacement and calculates the present crack length, J, and T_{APP} during the course of the test. An on-line plot of load versus COD allows determination of the

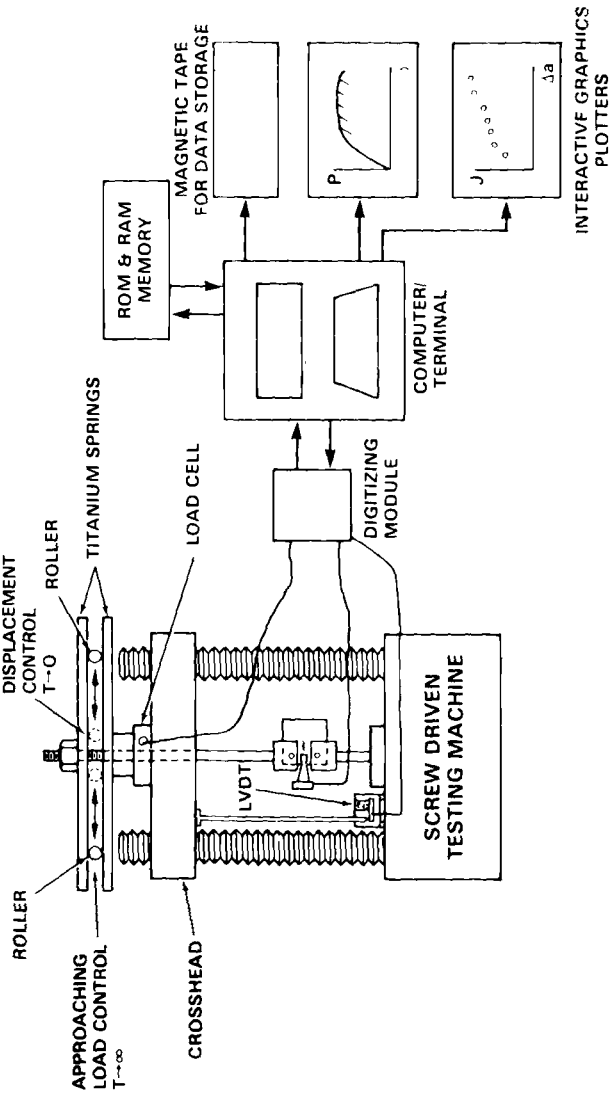

FIG. 4—*Schematic of the spring compliant test apparatus as utilized for compact specimens.*

onset of instability. All data are stored on magnetic cassettes so that they are available for a post-test reanalysis if necessary. The aluminum pipe specimens were loaded by placing the titanium spring on the test machine table, mounting a pipe in a four-point bend apparatus on top of the leaf spring, and then loading the combination in compression utilizing the moveable upper head. For the pipe specimens separate transducers were used to measure the COD displacement and the load-point displacement as well as load and machine stroke.

Both specimen types were loaded in a standard unloading compliance format so that crack length estimates were available at points along the load-displacement record. A sample plot is shown in Fig. 5, which includes load versus COD and load versus load-point displacement for a stable aluminum pipe specimen.

A schematic of the "computer compliant" test apparatus is shown in Fig. 6. The most noticeable change here is that the spring is gone and a servohydraulic test frame is used instead of a screw-controlled machine. The bending strong back is suspended from the load frame to minimize actuator mass and improve the rate of response of the system. The PDP 11/34 controller is utilized in this system to generate the slow time base ram motion of approximately 0.25 mm/min (0.01 in./min) and to superimpose upon this a spring component of stroke proportional to the load drop and the desired machine stiffness. The mechanical machine stiffness was measured for each test setup and a total stiffness was taken as the machine component in series with the

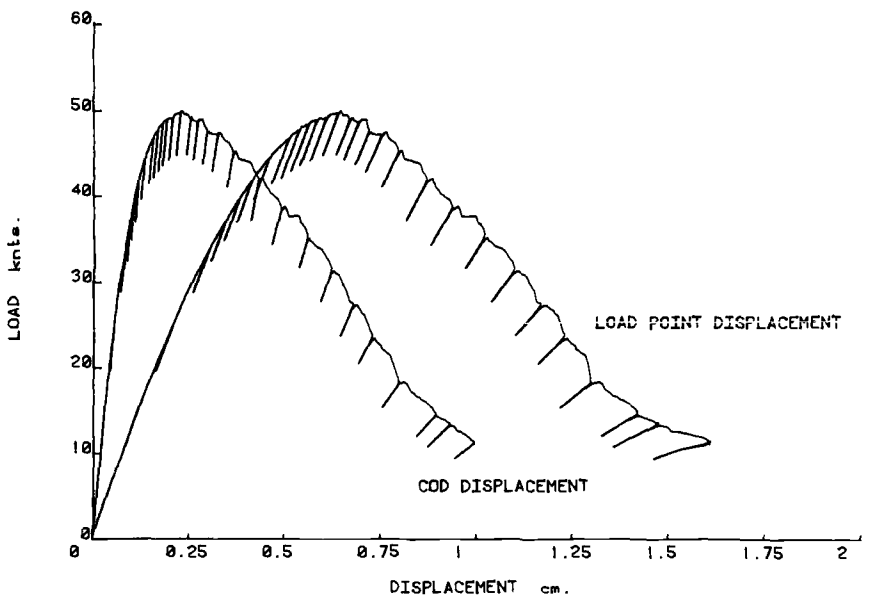

FIG. 5—*Load-versus-displacement records for a circumferentially cracked pipe in four-point bending.*

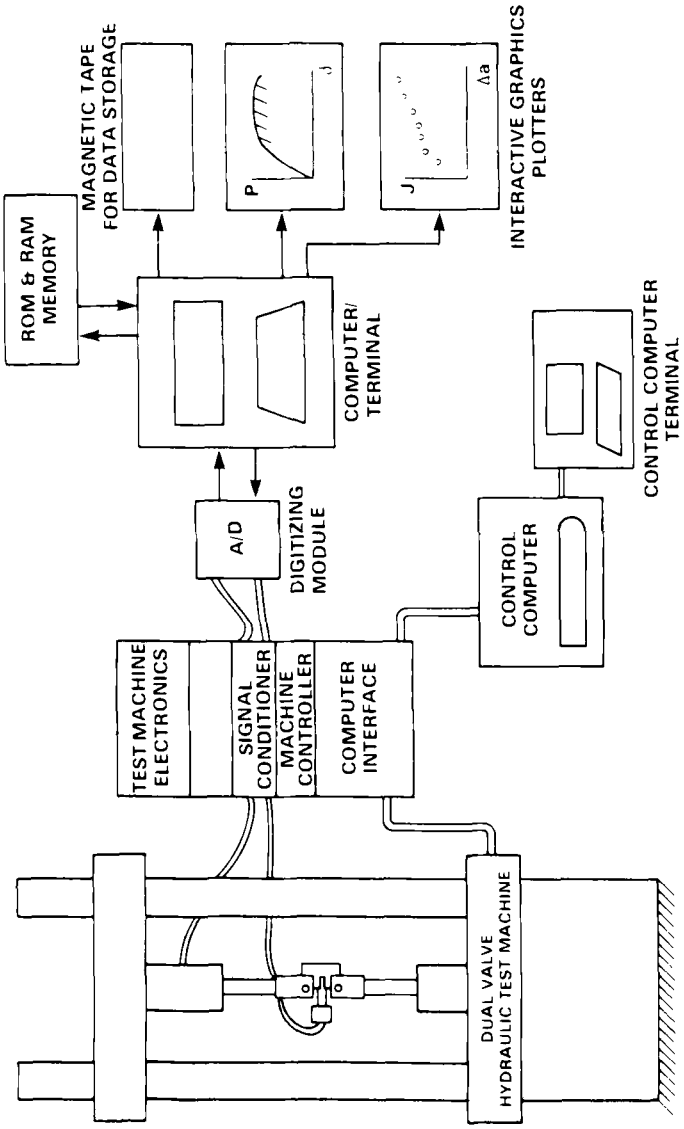

FIG. 6—*Schematic of the computer compliant test apparatus as utilized to test compact specimens.*

superimposed computer-generated component. The PDP 11/34 software is described more fully in the following section.

Data acquisition and analysis were carried out exactly as was done in the spring compliant case. The machine control software allowed unloadings to be applied throughout the test and data taken from the transducers allowed real-time calculation of crack length, J, and T_{APP} by the minicomputer and a real-time plot of load versus COD displacement for the compact specimen or both COD and load-point displacement for the pipe specimens. All data were taken and stored by the minicomputer at about one set per second. The PDP 11/34 was not used to store any data since this would have excessively reduced the machine's response rate.

Software Description

For the computer compliant test system the computer was utilized to generate a stroke displacement given by

$$U_{\text{STROKE}} = (\pm 1)\,\text{Rate} * \text{Time} + \frac{P_{\text{MAX}} - P}{K_C} \tag{23}$$

where

K_C = computer component of machine stiffness,
P_{MAX} = maximum load achieved by specimen,
P = present load,
Rate = calibrated quantity giving a stroke rate of approximately 0.25 mm/min (1 in./min) for compact specimens 0.50 mm/min (2 in./min) for pipe specimens,
Time = elapsed time with a least count of seconds, and
± 1 = utilized to generate unloadings and can be changed during the test by user-definable buttons.

If the present load is greater than the previous P_{MAX}, the second term is set to zero. The program used here is shown in Fig. 7. The language is MTS BASIC and the software is included here simply to demonstrate that no attempt is made to "program" an instability, only to generate realistic compliance conditions. The program lines above line 960 are for program initialization, program lines 960 and 970 generate a HOLD or STOP condition, while lines 980 to 1170 are the operating loop producing the command quantity X2. This loop is completed about 30 times per second by the PDP 11 computer. Lines 1020 to 1100 are needed to stabilize the program behavior and act to allow only 5 percent of total ram travel to be applied per second. This is possibly a little conservative but in early attempts without this "damper" the system noise interpreted as load drop was enough to start unstable ram oscillations which broke the specimens in about five cycles of increasing ram amplitude.

Presentation of the Tearing Instability Test Results

Compact Specimens

Load-displacement records for two ½T compact specimens are shown in Fig. 8. Specimen 65 was tested on the spring compliant test apparatus while Specimen 51 was tested in the "computer compliant" system—both systems were set for stiffnesses in excess of 17.5 kNt/mm (100 000 lb/in.). J-R curves resulting from these tests are shown in Fig. 9. Rotation corrections were included in the crack length calculations here using the formula of Hawthorne et al [*9*]. Clearly comparable results are obtained from the two test systems.

The average slopes of these load-displacement records in the region beyond maximum load to a COD of 2.3 mm (0.092 in.) was estimated to be about −3.5 kNt/mm (−20 000 lb/in.), so specimens were then run on both systems with machine stiffness of about this magnitude. The results in Fig. 10 show that in both cases an instability resulted just beyond maximum load.

Some differences need to be pointed out here, however. The computer compliant system reacted much more slowly and traversed the COD range from 0.1 to 0.23 cm (0.04 to 0.092 in.) in about three seconds, while the spring system traveled to a COD of 0.48 cm (0.192 in.) in less than a second. Also as shown in Figs. 11 and 12, the computer system crack growth arrested as soon as the specimen load-displacement record slope fell to a flatter negative value than the $-K_M$-value applied by the test system, while the spring system crack did not arrest until the load-displacement curve was much lower in slope than the $-K_M$-value applied by the system.

The instability rate for the spring system was conjectured here to be a function of the spring-mass system and not a material property and this was proven by adding to the basic system of Fig. 6 an additional data acquisition system to measure load and displacement data at a high rate during the instability. The system used was programmed to take 200 pairs of load-displacement values per second and was capable of doing this for 30 seconds.

Just beyond maximum load this system was started and the results for Specimen 59 are shown in Fig. 13. Clearly, when the crack jumped ahead, 20 COD readings were measured implying a 0.1 s time interval for the unstable crack to grow approximately 5 mm (0.2 in.).[3] This rate corresponds well with

[3]The high rate data acquisition system took approximately 6000 data pairs with a 12-bit (3½ digit) accuracy—compared with 20-bit (5½ digit) accuracy for the slow data system. Only a small part of the data taken are shown in Fig. 11. The high-speed system noise is shown by the scatter of data points at both ends of the instability—a rather large scatter because of the lower-quality system being used for these data.

The delayed drop in load resulted from the low-frequency response of the load signal conditioning system.

The one circled point is low-speed data taken during the instability and is accurate if it is observed that this system takes COD, then load values, separated by approximately 0.1 s, causing the resulting pair to appear off-set from the high-speed data.

Delays in low-speed data acquisition occur after each unloading during which the computer calculates the specimen stiffness, crack length, J, etc. The larger data acquisition delay at COD ≈ 0.6 mm (0.24 in.) occurred due to both a calculation delay and a cathode ray tube screen copy delay and does not represent a further instability.

```
INSTF1      MTS BASIC V01B-02C

100 CALL "QUIT"
110 CALL "BUTN"(160,1,180,6,250,7,300,8)
120 CALL "EDMP"(1)
130 CALL "TIME"(10)
140 CALL "STAR"
150 GO TO 500
160 F1=9
170 CALL "BUTN"
180 F5=0
190 X0=X2-X5
200 M1=1
210 T1=0
220 CALL "BUTN"
250 F5=1
260 CALL "BUTN"
300 F5=0
310 X0=X2-X5
320 M1=-1
330 T1=0
340 D0=D
350 CALL "BUTN"
500 CALL "BUTN"(1)
520 PRINT
530 PRINT "THIS PROGRAM ATTEMPTS TO USE THE MTS MACHINE"
540 PRINT "TO MODEL A VARIABLY COMPLIANT TEST MACHINE FOR TEARING"
550 PRINT "INSTABILITY TESTING OF CRACKED SPECIMENS."
560 PRINT
570 PRINT "WRITTEN BY J.A.JOYCE AT USNA JUNE 1981"
580 PRINT
590 PRINT
600 PRINT "INPUTING A 'STOP' OR 999 TO ANY INPUT WILL STOP THIS "
610 PRINT "PROGRAM."
620 PRINT
630 PRINT "INPUT THE TEST MACHINE CALIBRATION FACTORS (G,0) FOR"
640 PRINT "STROKE AND LOAD."
650 INPUT G3,03,G2,02
660 IF G3=999 THEN 1180
670 PRINT "INPUT DESIRED MACHINE SPRING CONSTANT FOR THIS TEST"
680 INPUT K9
690 IF K9=999 THEN 1180
700 PRINT
710 PRINT "INPUT THE DESIRED STEP RATE IN  UNITS/SECOND DESIRED FOR"
720 PRINT "THIS SPECIMEN."
730 INPUT S1
740 IF S1=999 THEN 1180
750 F1=0
```

FIG. 7—*Program listing of software used to generate compliant conditions in the computer compliant test system.*

the response time calculated for a single-degree-of-freedom system with $K =$ 3.5 kNt/mm and $M = 30$ kg (66 lb) if a 13.4-kNt (3000 lb) load were suddenly removed, which would be on the order of 0.01 s. Thus though the computer system has a slower response than the spring system, the difference would not be significant for most materials. The computer system response can be increased by transferring to a compiled computer language like CBASIC or FORTRAN, by use of a hardware processing system, and by use of a higher-speed computer processing unit.

The observation that the computer system instability arrests as soon as the load-displacement curve slope falls flatter than the $-K_M$-value corresponds through Eqs 9 and 10 to the statement that instability arrest will occur if

$$T_{MAT} > T_{APP} \tag{24}$$

if the load capacity of the specimen is above the load present in the spring.

```
760 F5=0
770 X0=0
780 X5=0
790 CALL "STIM"(0,0,0)
800 M1=1
810 K5=K9*G3/G2
820 C5=1/K5
830 PRINT "INSTALL THE TEST PIECE - SET UP YOUR DATA "
840 PRINT "ACQUISITION SYSTEM TO THE POINT WHERE YOU ARE READY TO"
850 PRINT "TAKE INITIAL CRACK LENGTH DATA."
860 PRINT
870 PRINT "PUSH THE 'RUN' BUTTON AND BRING UP HIGH PRESSURE "
880 PRINT "TYPE GO/RETURN TO CONTINUE"
890 INPUT A$
900 IF A$="STOP" THEN 1180
910 CALL "EDMP"(1)
920 CALL "MSW1"(2,X0)
930 CALL "GTIM"(T1)
940 CALL "DACQ"(0,P0,0,Z9)
950 CALL "DACQ"(0,D0,2,Z9)
960 IF F5=0 THEN 980
970 GO TO 960
980 CALL "DACQ"(0,P,0,Z9)
990 CALL "DACQ"(0,D,2,Z9)
1000 IF D<D0+3 THEN 1120
1010 IF P>=P0 THEN 1110
1020 X6=(P0-P)*C5
1030 IF X6>X5+3 THEN 1070
1040 IF X6<X5-3 THEN 1090
1050 X5=X6
1060 GO TO 1120
1070 X5=X5+3
1080 GO TO 1120
1090 X5=X5-3
1100 GO TO 1120
1110 P0=P
1120 X2=M1*S1*T1+X0+X5
1130 X=INT(X2)
1150 CALL "FG1"(X)
1160 IF F1=9 THEN 1180
1170 GO TO 960
1180 PRINT "YOU WANT TO STOP - YOU GOT IT "
1190 CALL "MSW1"(0)
1200 CALL "FG1"(0)
1210 END
```

FIG. 7—*Continued.*

Graphically this criterion is displayed in Fig. 11 by drawing a line of slope $-K_M$ from the load-displacement point of instability initiation. Instability arrest is not possible until the specimen load-displacement curve crosses back above this line and has a slope flatter than $-K_M$ that is, $T_{MAT} > T_{APP}$. This arrest criterion is clearly demonstrated in the computer compliant system which demonstrates no inertia effect as shown in Fig. 11. The spring system instability does not arrest until considerably more crack extension occurs as shown in Fig. 12, apparently because system inertia overdrives the expected arrest point.

A T_{MAT}-J plot was developed for this HY-130 material from the J-R curves shown in Fig. 14. No single linear or power law was found to accurately fit these results so a combined fit was used, defined by

$$\begin{aligned} J &= 178\Delta a + 82.9 \qquad 126 \le J \le 314 \qquad \text{kPa·m} \\ J &= 553 - 309/\Delta a \qquad J > 314 \qquad \text{kPa·m} \end{aligned} \tag{25}$$

with Δa in millimetres.

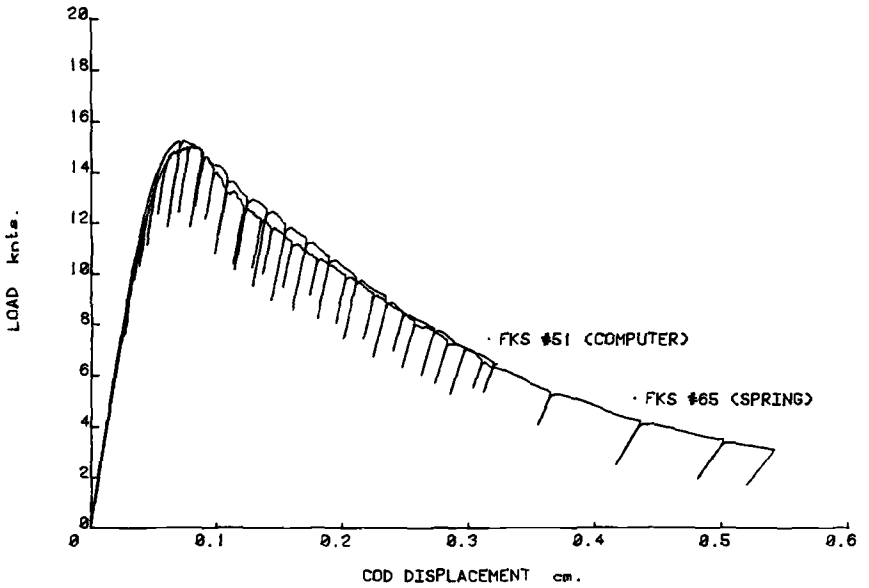

FIG. 8—*Comparison of load-displacement records from compact specimens tested in stiff versions of each test system.*

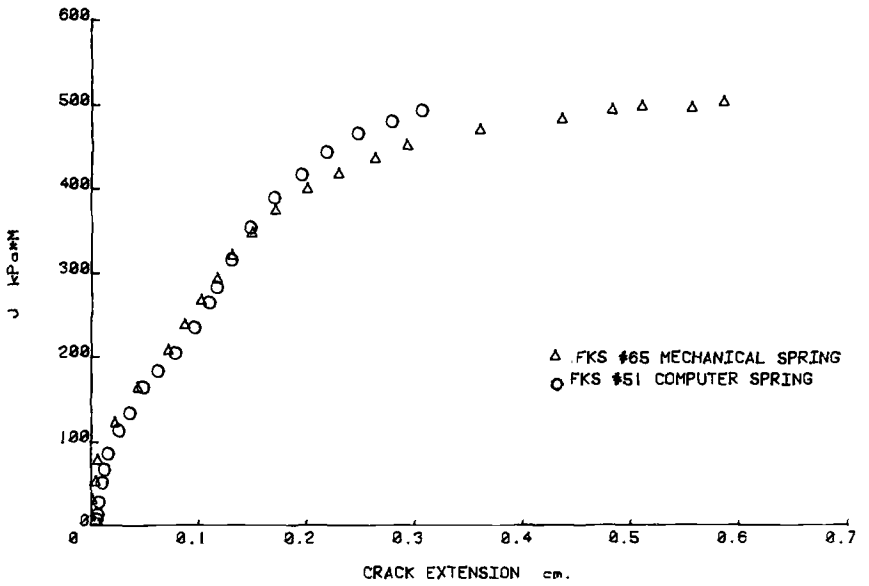

FIG. 9—*Comparison of J-R curves obtained from the compact specimens of Fig. 8.*

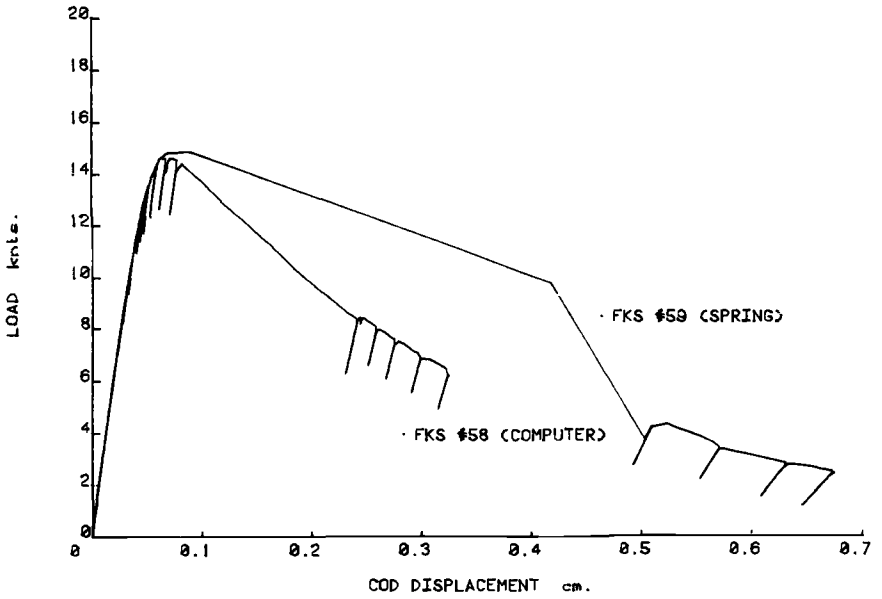

FIG. 10—*Load-displacement records from compact specimens tested under compliant test conditions in the two test systems with* $K_M \approx 3.5$ *kNt/mm.*

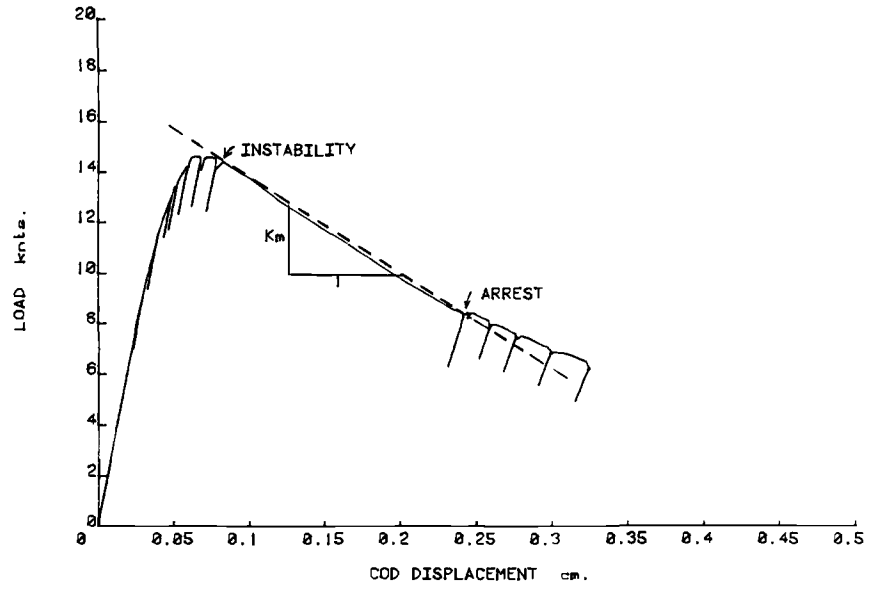

FIG. 11—*Load-displacement record of a compact specimen using the computer compliant test system showing the instability and arrest points in comparison with a line of slope* $-K_M$.

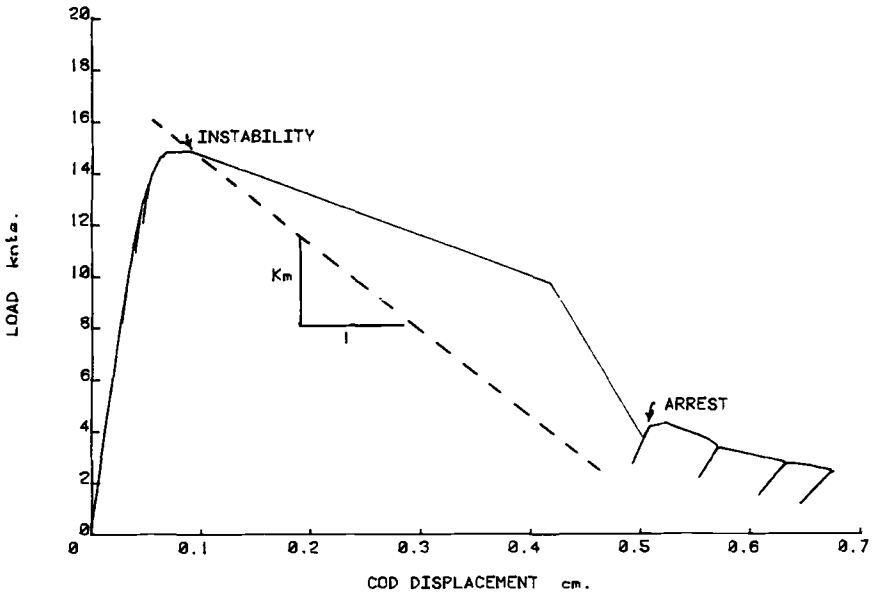

FIG. 12—*Load-displacement record of a compact specimen using the spring compliant test system showing the instability and arrest points in comparison with a line of slope* $-K_M$.

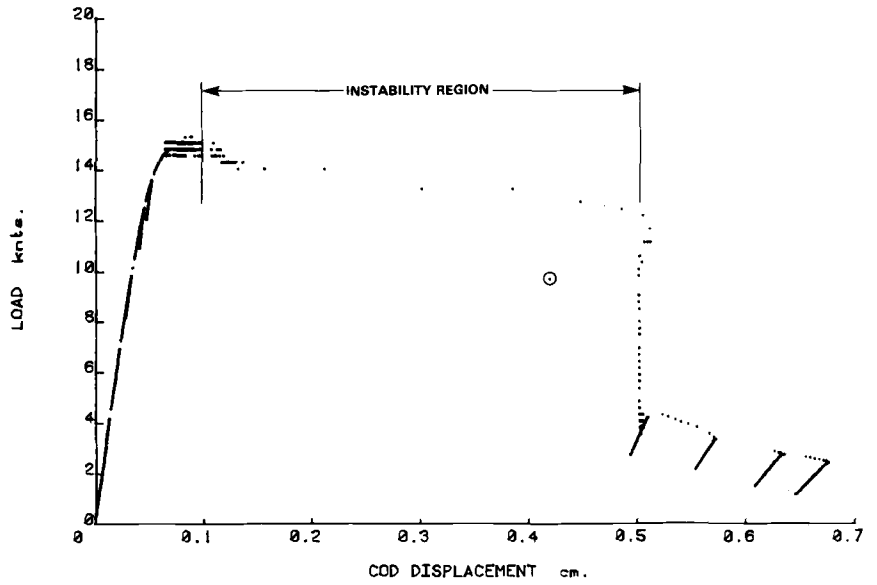

FIG. 13—*Load-displacement record of compact specimen FKS No. 59 tested in the spring compliant system, showing both high-speed and low-speed data.*

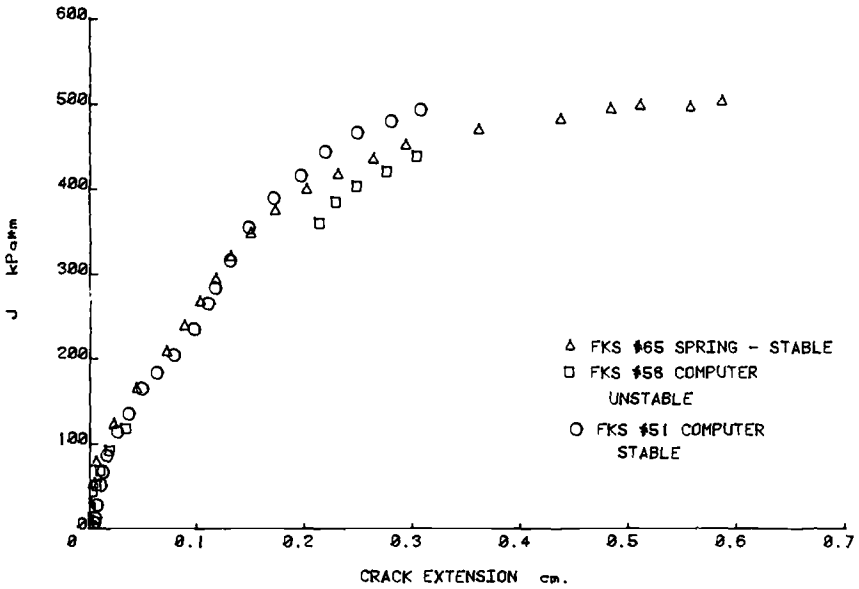

FIG. 14—*A plot of J-R curve records obtained from typical HY-130 FKS compact specimens.*

The resulting plot of T_{MAT} versus J is shown in Fig. 15. Evaluating T_{APP} from the Ernst's Eq 7 for a typical unstable specimen gives results like that of Fig. 15 showing that both instability and arrest are accurately predicted in terms of the tearing force and tearing resistance for this geometry-material combination.

Pipe Specimens

Load-displacement records from stable pipe tests using both systems were found to be similar and the slopes of these curves beyond maximum load implied that tearing instability would result for machine stiffnesses less than 7 kNt/mm (40 000 lb/in.) for these specimens. Load-displacement records for two specimens, one on each system, with $K_M \cong 6.6$ kNt/mm (37 700 lb/in.), are shown in Fig. 16 and clearly comparable results are found in the two tests, except that again the computer system response is slow, approximately 3 s versus < 1 s for the spring system. The differences in initial stiffness and maximum load are due to a slight difference in crack length between these two specimens. Crack arrest was not found in these tests until loads had dropped to a small fraction of maximum load so that no information was gained on these tests with respect to crack arrest in a pipe configuration. Typical J-R curves obtained from the stable pipe tests and the stable portion of the unstable tests are shown in Fig. 17. Both Zahoor [*8*] and Tada [*7*] forms for J are shown for these pipe tests. Instability was not observed in this

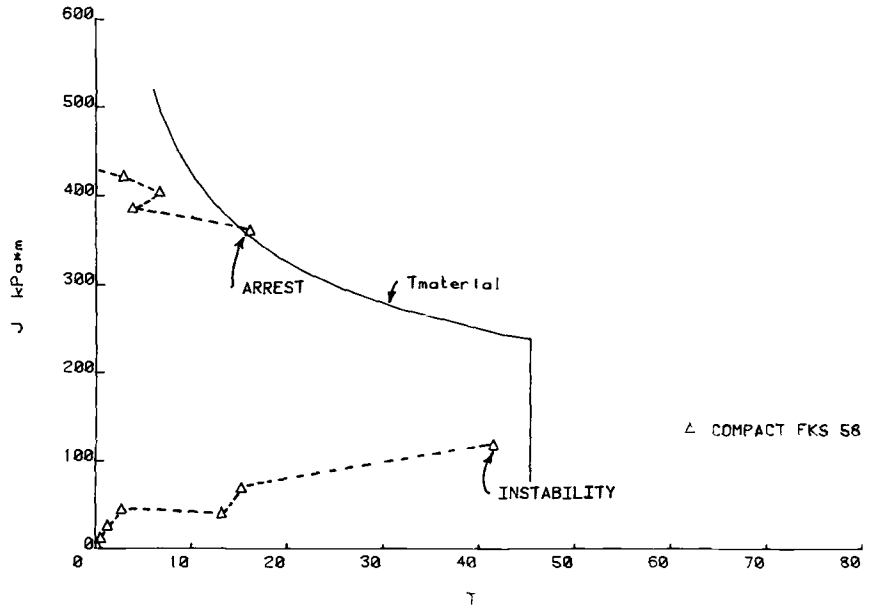

FIG. 15—J-T *plot for compact specimens showing instability and arrest for a typical specimen tested on the computer compliant system.*

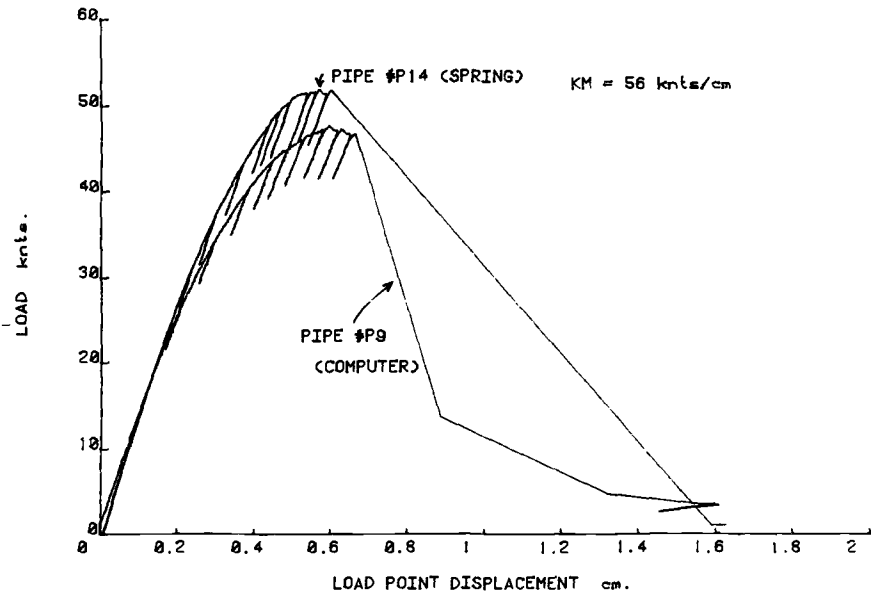

FIG. 16—*Load-displacement records for pipes tested in the spring compliant and computer compliant test systems.*

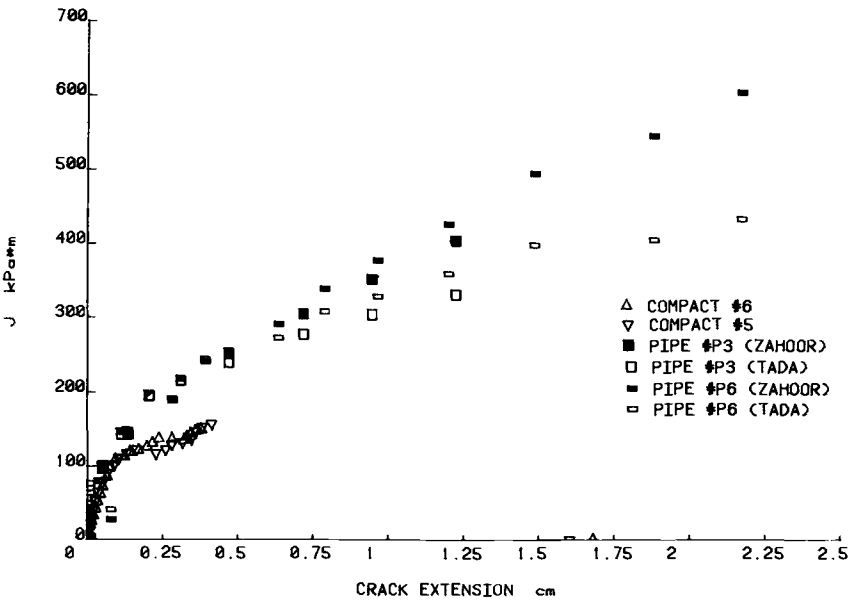

FIG. 17—*Comparison plot of J-R curves for 10-cm (4-in.) inside diameter pipes and subsize compact specimens cut from the 6061 T6 pipe wall.*

specimen geometry until approximately 13 mm (0.52 in.) of stable crack growth per crack tip was present. Also shown on Fig. 17 are the J-R curves obtained from the small compact specimens removed from the pipe wall. These results demonstrate a J_{Ic}-value somewhat below that of the pipe tests, depending to a large extent on what portion of the pipe J-R curve is used to extrapolate to the J_{Ic} point. Similarly, the compact J-R curves fall distinctly below the pipe J-R curves obtained by either the Tada or Zahoor analysis. The fact that the small specimens give lower rather than higher J_{Ic}-values is somewhat surprising. The material tearing resistance, that is, J-R curve slope, measured from the compact specimen does appear to be a reasonably conservative estimate of the pipe tearing resistance in this case.

Fracture surface observation showed that both the compact and pipe specimens demonstrated a triangular crack tunneling effect to about one half the cross-sectional thickness and then a transition to a shear mode of crack extension. For the pipe wall compact specimens the compliance estimates of crack extension were between 5 and 10 percent short of a five-point average optical measurement made after the test—using a post-test fatigue procedure to mark the final crack geometry. Final crack lengths taken on pipe specimens showed a similar tendency to underestimate the measured crack extension but only by about 10 to 15 percent of the total crack extension.

Figure 18 shows that for a typical pipe (No. P9) with $K_M = 5.6$ kNt/mm (32 000 lb/in.) the J at instability is not accurately predicted by either the

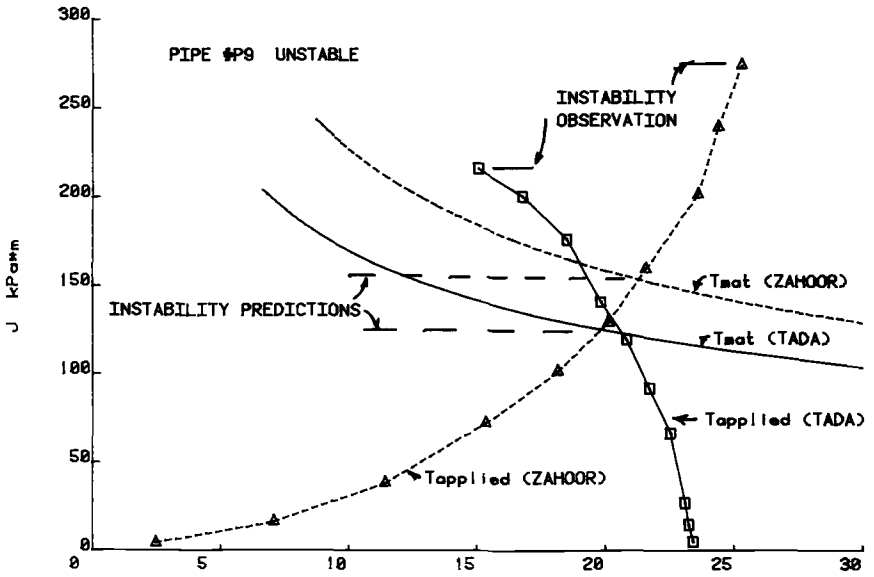

FIG. 18—J-T *plot for 6061 T6 10-cm (4-in.) inside diameter pipes (Pipe No. P9) showing a comparison of Tada [7] and Zahoor [8] analyses for* T_{MAT} *and* T_{APP} *for an unstable fracture test.*

Zahoor or the Tada analysis. Instability would be expected when the T_{MAT} and T_{APP} curves intersect, which occurs at a J-value of between 120 and 145 kPa·m, but the observed instability did not occur until well beyond that point, that is, $J = 270$ kPa·m by the Zahoor analysis or $J = 210$ kPa·m by the Tada analysis. The T_{MAT}-J plot is obtained from the specimen itself by fitting the J-R curve with a power function in the stable region. T_{APP}-values from both the Tada [7] model and the Zahoor [8] model are shown in Fig. 18 and are conservative by factors of from 2 to 4. These formulas are both known to be only estimates of the real T_{APP} and were presented as such by their respective developers. The Tada model assumes rigid plastic behavior, which is not a very good estimate of the behavior of this aluminum pipe. A calculation of limit load using the formula of Tada [7] that

$$M_p = 4\sigma_0 R^2 t\,(\cos\theta/2 - \tfrac{1}{2}\sin\theta) \tag{26}$$

shows that the specimen approached 95 percent or more of its limit load assuming $\sigma_0 = 310$ MPa (45 000 psi). The Tada analysis for J and T assumes that all deformation occurs at the specimen limit load and it thus overestimates J in these pipes in the region before maximum load during which about 1.2 cm (0.48 in.) of crack extension occurs. This overestimation of J also effects both the T_{APP} and T_{MAT} calculations.

The Zahoor model assumes that a specific type of separability exists between crack length and COD dependence in the specimen load-displacement relationship. Such a separability has never been experimentally verified even for a simple compact or bend geometry. These separability assumptions are, however, probably accurate for simple geometries, including pipes, until a reasonable amount of crack extension occurs—but for the pipes tested here, crack extensions of 1.5 cm (0.6 in.) are present before instability occurs and the assumptions of the Zahoor analysis are suspect by this point.

Another possible explanation for the inaccuracy of the present application of the Zahoor analysis is that the quantity $(\partial P/\partial \delta_{PL})_\theta$ in Eq 21 was set to zero since no better estimate was available. Use of an accurate positive value for this quantity, obtained either experimentally or analytically, would shift the Zahoor results in Fig. 18 toward better agreement with the experimental observation.

Figure 19 shows a plot similar to that of Fig. 18 for a pipe which remained stable. Here the prediction is for stable behavior by either analysis technique since the T_{MAT} and T_{APP} curves do not intersect for either analysis technique. This is typical of the results found here in that the technique is conservative if stability is predicted and stable results are obtained, but if instability is predicted it would not occur until later in the test, that is, at J and crack extension values beyond that predicted by the analysis.

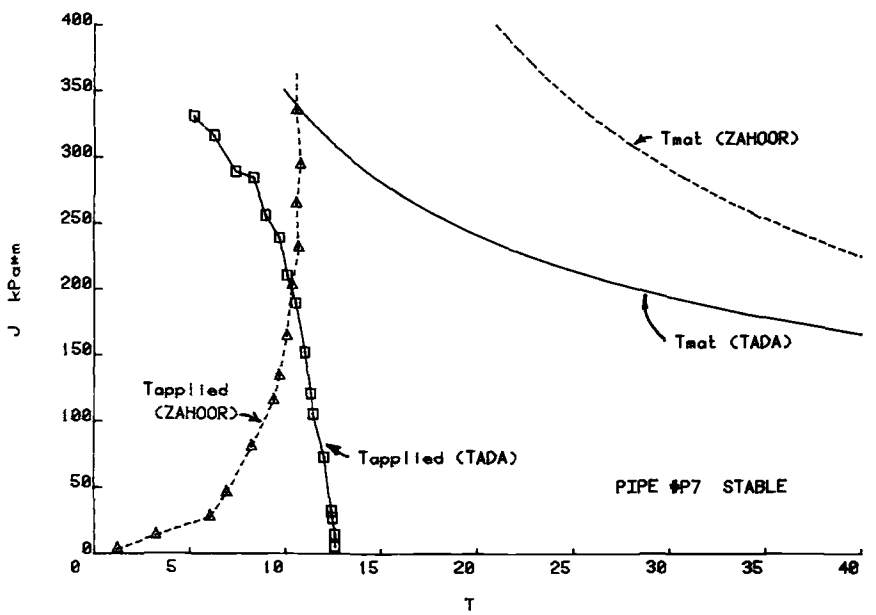

FIG. 19—J-T *plot for a 6061 T-6 10-cm (4 in.) inside diameter (Pipe No. P7) showing a comparison of Tada [7] and Zahoor [8] analyses for* T_{MAT} *and* T_{APP} *for a stable fracture test.*

Utilization of these formulas for order-of-magnitude estimates of whether a piping system is likely to be safe, with inclusion of typical engineering safety factors, would clearly give acceptable results, but attempts to use them to predict the J or crack extension at instability initiation is not to be recommended.

Discussion

The major disadvantage of using a computer-controlled test machine for tearing instability tests is that you have to have a computer-controlled test machine and the expertise to program and operate it. The next important disadvantage is apparently that the test speed is slower during an instability, and for a rate-sensitive material differences might occur between the results of a spring test machine and a computer-controlled machine. This disadvantage will be reduced as minicomputer test machine controller central processing unit speeds are increased and as compiled languages like FORTRAN become available on computer-interfaced test machines.

The advantages of the computer-controlled machine are that expensive compliant test frames do not have to be constructed, inertial effects present in springs are predominately eliminated, and inertial effects can be included to model the real structure inertial effects if these are felt to be important for a given structure. A final, but important, advantage is that the computerized system can more easily be extended to combined loading situations for which construction of mechanical springs would be very expensive and difficult.

Conclusions

A computer compliant system can adequately generate test machine conditions required to generate ductile tearing in instabilities in test specimens. The computer response rate is slower than most springs (unless a very massive system is used) but only about an order of magnitude slower, which will not produce significant differences in most metallic materials. The computer system is inertia-free, which appears to be a valuable attribute for investigation of tearing instability arrest. Inertia effects could, of course, be programmed into the system to more closely model the behavior of a flawed member in a real structure.

Experimental work has also shown that J-R curves obtained from a compact specimen geometry fall below those obtained from a circumferential pipe geometry—a case where both geometries are loaded predominantly in bending and have nearly the same thickness and constraint. The applied tearing force calculated using the Ernst analysis for a compact specimen geometry appears very accurate at predicting both instability initiation and arrest. Similar calculations for the circumferentially cracked pipe geometry were not very successful, apparently overestimating the applied tearing force by a factor of about 2.

Finally, these experiments seem to imply that the conditions for the arrest of a ductile tearing instability are simply, first, $T_{MAT} > T_{APP}$ due to a flattening of the slope of the load-displacement record so that $-(dP/d\delta) < 1/K_M$, and second, the load capacity of the specimen is greater than the load present in the compliant structure at the given load-point displacement corresponding to arrest. If significant structural inertia is present when the previous conditions are satisfied, additional crack extension will result.

References

[1] Paris, P. C., Tada, H., Zahoor, A., and Ernst, H. in *Elastic-Plastic Fracture, ASTM STP 668*, J. D. Landes, J. A. Begley, and G. A. Clarke, Eds., American Society for Testing and Materials, 1979, pp. 5-36.

[2] Paris, P. C., Tada, H., Zahoor, A., and Ernst, H. in *Elastic-Plastic Fracture. ASTM STP 668*, J. D. Landes, J. A. Begley, and G. A. Clarke, Eds., American Society for Testing and Materials, 1979, pp. 251-265.

[3] Joyce, J. A. and Vassilaros, M. G. in *Fracture Mechanics: Thirteenth Conference, ASTM STP 743*, Richard Roberts, Ed., American Society for Testing and Materials, 1981, pp. 525-542.

[4] Vassilaros, M. G., Joyce, J. A., and Gudas, J. P. in *Fracture Mechanics: Fourteenth Conference. ASTM STP 791*, American Society for Testing and Materials, 1983.

[5] Ernst, H. A., Paris, P. C., and Landes, J. D. in *Fracture Mechanics: Thirteenth Conference. ASTM STP 743*, Richard Roberts, Ed., American Society for Testing and Materials, 1981, pp. 476-502.

[6] Joyce, J. A. and Gudas, J. P. in *Elastic-Plastic Fracture, ASTM STP 668*, J. D. Landes, J. A. Begley, G. A. Clarke, Eds., American Society for Testing and Materials, 1979, pp. 451-468.

[7] Tada, H., Paris, P. C., and Gamble, R. M. in *Fracture Mechanics: Twelfth Conference, ASTM STP 700*, American Society for Testing and Materials. 1980, pp. 296-313.

[8] Zahoor, A. and M. F. Kanninen, *Journal of Pressure Vessel and Piping, Transactions*, American Society of Mechanical Engineers, Vol. 103, Nov. 1981, pp. 352-358.

[9] "Evaluation and Prediction of Neutron Embrittlement in Reactor Pressure Vessel Materials, Annual Progress Report for 1978," J. C. Hawthorne, Ed., NRL Report 327, NRL-EPRI Research Program Rp 886-2, Electric Power Research Institute, Palo Alto, Calif., 30 Aug. 1979, p. 40.

W. Alan Van Der Sluys[1] *and Robert J. Futato*[1]

Computer-Controlled Single-Specimen J-Test

REFERENCE: Van Der Sluys, W. A. and Futato, R. J., **"Computer-Controlled Single-Specimen J-Test,"** *Elastic-Plastic Fracture: Second Symposium, Volume II—Fracture Resistance Curves and Engineering Applications, ASTM STP 803*, C. F. Shih and J. P. Gudas, Eds., American Society for Testing and Materials, 1983, pp. II-464-II-482.

ABSTRACT: The development of a computer-controlled single-specimen *J*-test procedure is described. The results of a sensitivity study to determine the effect of analog-to-digital converter resolution and transducer signal noise on elastic unloading compliance crack length measurements are presented. The results are used to estimate the minimum equipment performance specifications needed for successful *J*-test automation. The actual test system is described along with the details of the automated procedure.

A comparison is made between results obtained using the automated procedure and the more conventional heat-tinting technique for HY-130 at room temperature (tested as part of the American Society for Testing and Materials J-Integral R-Curve Round Robin Program) and nuclear pressure vessel grade steels at 200 to 290°C. Good agreement in the generation of J-Δa data was found in all cases. However, some difficulty was encountered in predicting absolute crack lengths by compliance in the round-robin tests, apparently due to specimen design.

KEY WORDS: data acquisition, unloading compliance, elastic-plastic fracture, J-integral test, crack propagation

Nomenclature

a_i	Instantaneous crack length measurement
a_0	Initial crack length measurement
b	Uncracked ligament, w-a
B_e	Effective specimen thickness
B_N	Net specimen thickness
B_T	Total specimen thickness
C	Compliance

[1]Section manager, metallurgy, and research engineer, respectively, Babcock & Wilcox, a McDermott company, Alliance Research Center, Alliance, Ohio 44601.

E Modulus
J J-integral value
P_i Instantaneous load measured by A/D
V_i Instantaneous displacement measured by A/D
w Specimen width
a/w Crack length ratio
$\Delta(a/w)$ Confidence interval in a/w
ΔC Confidence interval in compliance
ΔP Change in load during unloading
ΔV Change in displacement during unloading

Fracture mechanics analysis procedures were first introduced in the American Society of Mechanical Engineers Boiler and Pressure Vessel Code in 1972 when Appendix G to Section III of the Code was first published. Section III presents the design rules for nuclear pressure vessels. With the introduction of fracture mechanics analysis techniques to the design rules, it was appropriate that fracture mechanics test specimens be included in the nuclear pressure vessel surveillance programs, because one of the purposes of the programs is to monitor the effects of irradiation on the mechanical properties of pressure vessel materials. The Babcock & Wilcox Co. (B&W) started including compact fracture specimens in their reactor vessel surveillance program in the mid-1970's. The research division was given the responsibility of developing and maintaining the test procedures for conducting the fracture tests. With the rapid growth in this field in recent years, this requires a continuous effort.

The original test procedure in the reactor vessel surveillance program made use of the multiple-specimen heat-tinting method for determining J_{Ic}. This was eventually replaced by the single-specimen unloading compliance method, and finally most recently by a fully automated unloading compliance procedure for generating the J-R curve.

There are a number of reasons for developing a fully automated fracture test technique. The fracture analysis for pressure vessel design is not yet fully developed, so the most general fracture test techniques and data storage procedures must be used for all testing. The J-R curve will supply the materials information required for any elastic-plastic or fully plastic analysis, and digital data gathering and storage allow for easy reanalysis of the test data as new procedures emerge. In addition, the automated system can produce higher-quality results than manual systems, and is significantly more reliable. Since there are few replicate specimens in a surveillance program, extremely reliable test procedures are needed to insure that all specimens produce usable information.

This paper describes the development of the automated test procedure. Included is a discussion of a sensitivity study which was performed to determine the specifications for the hardware needed to conduct the experiments, as

well as a description of the hardware and software which was developed and some results obtained with the system.

Sensitivity Study

The generation of an entire J-R curve from a single specimen requires the remote detection of small amounts of crack extension with a high degree of confidence. Instrumentation for an automated procedure should therefore be selected based on a consideration of the effect of the measurement technique on the confidence of the results.

When the elastic unloading compliance measurement technique is used, crack lengths are determined from a knowledge of specimen compliance, calculated from load and displacement data obtained during a partial unload of the specimen at various points throughout the test. Consequently, any scatter or uncertainty in measured load or displacement causes a corresponding uncertainty in the calculated compliance and ultimately the calculated crack length. The scatter in measured data, due primarily to electronic signal noise and analog-to-digital (A/D) conversion in an automated test, must therefore be reduced to known acceptable levels.

The effect of A/D conversion and electronic noise on measured data can be modeled as shown in Fig. 1. The A/D conversion process transforms a continuously varying signal into a set of integers varying linearly between zero and $\pm 2^{b-1}$ full scale, where b = A/D word length. (The highest-order bit in the word is generally used to indicate signal polarity.) The minimum resolvable signal change, U, is that causing a change of one bit in the A/D output, so that U = (full-scale signal)/2^{b-1}. The individual (dimensionless) data points generated by the conversion process are therefore a measure of the number of smallest resolvable units, U, composing a signal of any given time, and can be described by the expression

$$\text{A/D output} = \text{integer}\left[\frac{\text{(signal level)}}{U} + 0.5 + \text{noise}\right] \tag{1}$$

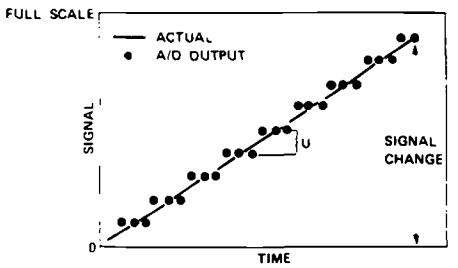

FIG. 1—*Model showing digitization of continuous signal by analog-to-digital (A/D) conversion process.* U = *smallest signal change resolvable by A/D.*

The foregoing expression allows for rounding between bits as well as for the superposition of noise on the true signal.

Using the foregoing model, the effect of A/D conversion and transducer signal noise on crack length confidence can be estimated. Since in general specimen compliance is a function of modulus, specimen thickness, and crack length [*1,2*],[2] the precision in a/w due to the precision of a given compliance measurement can be approximated by the expression

$$\Delta(a/w) = \Delta C \left(\frac{\partial C}{\partial (a/w)} \right)^{-1} \tag{2}$$

for small errors in C and a/w, ignoring changes in modulus or specimen thickness. Further, if a linear regression analysis can be used to calculate compliance, then the precision, ΔC, can be estimated statistically as the percent confidence interval of the compliance, C, given by the expression

$$\Delta C = (t_{(1-\alpha/2)} - t_{(\alpha/2)}) \frac{S_{y \cdot x}}{S_x (n-1)^{1/2}} \tag{3}$$

where

n = total number of points used in compliance calculation,
t = values of t distributions for $n - 2$ degrees of freedom,
$S_{y \cdot x}$ = standard error of estimate, and
S_x = variance of load distribution for a given displacement [3].

For the foregoing equation, percent confidence = $100\,(1 - \alpha)$. Using Eq 1, the individual load and displacement data points measured during an unload, P_i and V_i, respectively, can be described by

$$\begin{aligned} P_i &= U_p \text{ integer} \left[R_P \frac{i}{n} + 0.5 + \text{noise} \right] \\ V_i &= U_V \text{ integer} \left[R_V \frac{i}{n} + 0.5 + \text{noise} \right] \end{aligned} \tag{4}$$

where

$$\begin{aligned} R_P &= \frac{\Delta P}{U_P} = \frac{\Delta P}{\text{load range}} \times 2^{b-1} \\ R_V &= \frac{\Delta V}{U_V} = \frac{\Delta V}{\text{displacement range}} \times 2^{b-1} \end{aligned} \tag{5}$$

[2]The italic numbers in brackets refer to the list of references appended to this paper.

ΔP and ΔV are the total change in load and displacement, respectively, during the unload. Therefore

$$\Delta C = (U_V/U_P)\,\bar{\Delta}C = C(R_P/R_V)\bar{\Delta}C$$

where $\bar{\Delta}C$ is a dimensionless function of R_P, R_V, a/w, n, and noise, and the confidence interval in a/w corresponding to $\bar{\Delta}C$ can be estimated by

$$\Delta(a/w) = (R_P/R_V)(C)(\bar{\Delta}C)\left(\frac{\partial C}{\partial(a/w)}\right)^{-1} = \text{function}\,(R_P, R_V, a/w, n, \text{noise}) \tag{6}$$

Consequently, at a given crack length ratio, the statistical confidence interval in a/w is dependent on the effective resolution, R_P and R_V, and the level of electronic noise.

Several assumptions were made for computational ease in the foregoing analysis. These assumptions are: (1) the crack length versus compliance equations are exact, (2) the variance of the distribution of loads for a given displacement are equal for all displacements, and (3) the distribution of loads for a given displacement is a normal distribution. In addition, Eq 3, used to define the percent confidence interval in compliance, ΔC, is strictly valid only in cases when the load values are known without error. However, since order-of-magnitude estimates of confidence are being sought, the errors due to these assumptions are considered to be negligible.

Confidence intervals calculated according to Eq 6 at the 95 percent confidence level are shown in Fig. 2 as a function of R_P and R_V for $a/w = 0.6$. The calculation assumes displacement measurement on the specimen load line, and that approximately 100 data points are available for the compliance calculation. A constant noise level equal to eight times the digital resolution (± 4 A/D output units) on both the load and displacement signals is also assumed. The noise spectra of the signals are independent and totally random with $\sigma = 1$. Note that when R_P and R_V vary greatly, the smaller determines the size of the confidence interval. In fact, regions of total R_V-control and total R_P-control exist, corresponding to the horizontal and vertical regions of the curves, respectively. In these regions, increases in the effective resolution of the noncontrolling parameter will have little, if any, effect on measurement confidence. Notice also the interchangeability of R_p and R_V, not U_p and U_V, in determining confidence interval size.

Figure 3 shows the effect of slight changes in the noise level on the effective resolution required to produce a confidence interval $\Delta(a/w) = 0.001$. As before, the peak noise level is assumed to be equal on both load and displacement, although the noise spectra of the two signals are independent and totally random. Results of the analysis reveal that a significant increase in

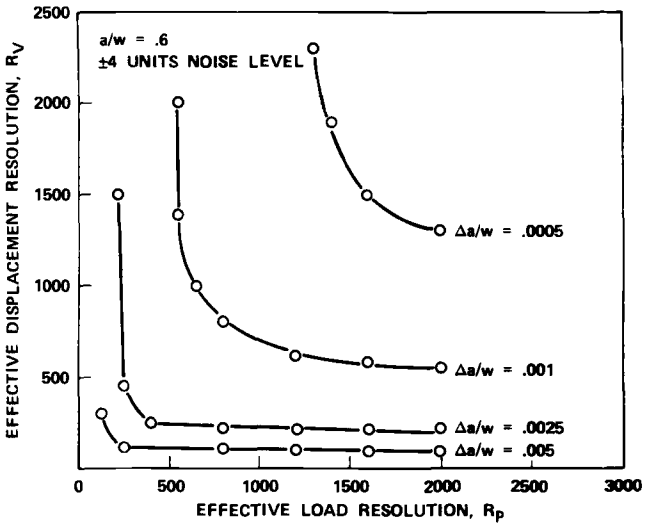

FIG. 2—*Effect of load and displacement signal resolution during unload on crack length measurement confidence,* $\Delta a/w$. $R_p = \Delta P/U_p$ *and* $R_V = \Delta V/U_V$ *for* ΔP *Load Change and* ΔV *Displacement Change During Unload.*

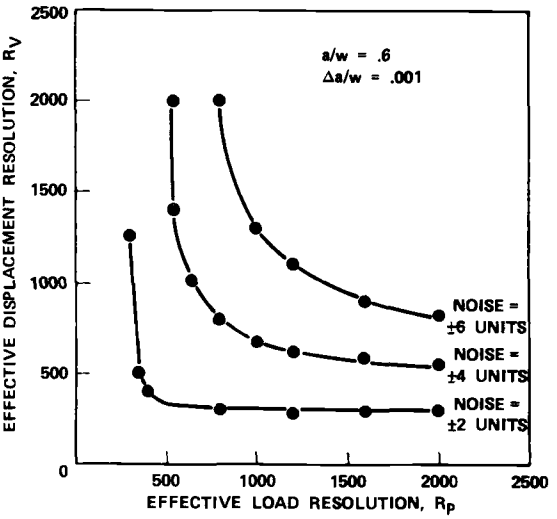

FIG. 3—*Effect of noise on signal resolution required for crack length confidence interval of 0.001* w.

effective resolution is required to offset relatively slight increases in electronic noise. Conversely, electronic noise will sharply limit the statistical confidence in a crack length measurement. Consequently, care must be taken to maintain electronic noise at minimal levels throughout testing.

In designing a system for both automated data acquisition and test control, the need for high-resolution data acquisition must be balanced against the need for short A/D conversion time. It is therefore desirable to use the shortest A/D word length that will supply the necessary resolution. Assuming $R_P = 1500$ and $R_V = 550$ at a ± 4 unit noise level will provide adequate statistical confidence for proper J-R curve generation, then for a typical J-test in which maximum load = 47 kN (10 000 lb) and maximum displacement = 4 mm (0.16 in.) with $\Delta P = 7$ kN (1600 lb) and $\Delta V = 0.08$ mm (0.003 in.) during unloading, a 16-bit A/D can be used provided

$$\text{load range} \leq \frac{7\text{ kN}}{1500} \times 2^{15} = 153\text{ kN (34 000 lb)}$$

$$\text{displacement range} \leq \frac{0.08\text{ mm}}{550} \times 2^{15} = 4.7\text{ mm (0.19 in.)}$$

However, since both R_P and R_V are less than 2^{11} (= 2048), then a 12-bit A/D will work as well, provided

$$\text{load range} \leq \frac{7\text{ kN}}{1500} \times 2^{11} = 9.5\text{ kN (2100 lb)}$$

$$\text{displacement range} \leq \frac{0.08\text{ mm}}{550} \times 2^{11} = 0.3\text{ mm (0.012 in.)}$$

Therefore, while for a typical J-test a 16-bit converter can be used with the standard analog electronics for test control, a 12-bit A/D will provide equal statistical confidence if additional electronic signal amplification is used to expand the unload. In general, a $2^{15}/2^{11}$ (= 16-fold) increase in signal amplification is required to interchange 12-bit and 16-bit A/D converters, when scatter in load and displacement due to electronic noise is kept constant.

Procedure

Description of Hardware

Using the results of the sensitivity study, an automated test system based on a 12-bit word was designed. A schematic representation of the hardware is shown in Fig. 4. The test is conducted using an MTS servohydraulic test ma-

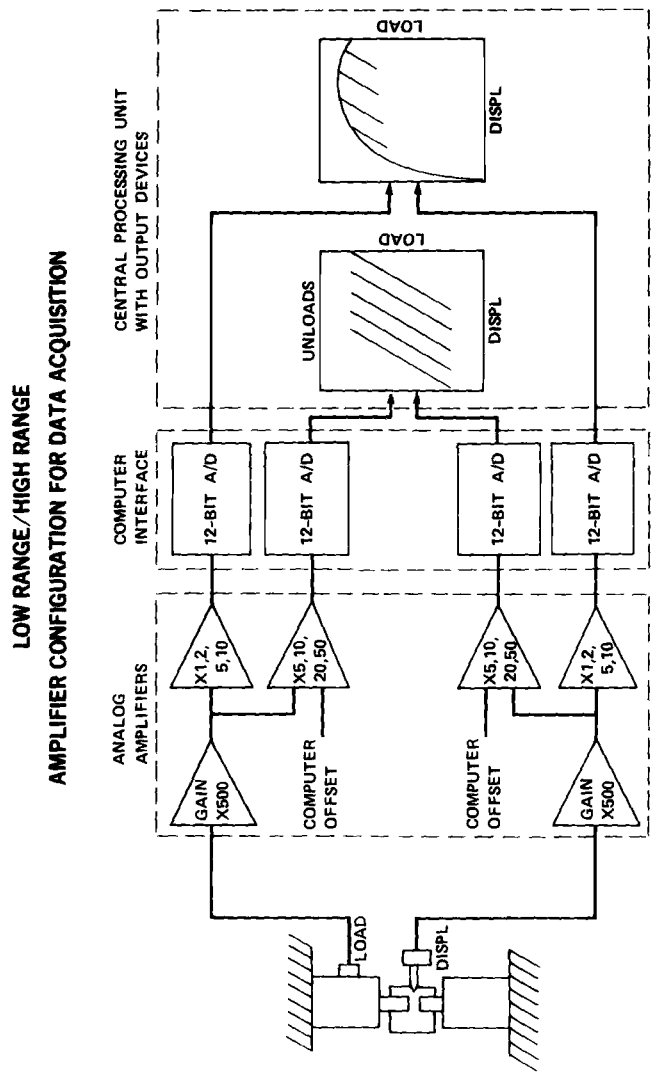

FIG. 4—*Schematic diagram of automated system showing the use of low-gain amplifiers for data acquisition over the entire test range, and high-gain amplifiers for data acquisition during unloading.*

chine with standard analog control electronics. Two relatively low-gain transducer conditioning amplifiers are used for test control and data acquisition over the entire range of the test. In addition, two high-gain amplifiers are used to expand the change in load and displacement during the unloadings and provide the resolution required for precise crack length measurements. All amplifiers are dual-staged, consisting of a fixed-gain preamplifier in series with a variable-gain second stage. Ranging is accomplished in the second stage. Each of the high-gain amplifiers has a digital-to-analog (D/A) converter input to enable offset of the amplifier by the computer during the test. The computer-controlled offset capability is needed to enable re-zeroing of the amplifiers prior to each unloading, since the range of the amplifiers will be exceeded during the course of a test.

Both of the high-gain amplifiers are heavily filtered for noise suppression. Filter roll-off is fairly sharp above 10 Hz, although some attenuation occurs at frequencies as low as 1 Hz. Signal noise at the output is typically ± 0.03 V and appears to be quite random. The filtering network introduces a substantial phase shift between the outputs of the high-gain and low-gain amplifiers. This does not, however, interfere with test results.

The entire test system is under control of a PDP 11/34 minicomputer. Two DEC RKØ5 disk units are used for system file storage as well as permanent storage of all test data. A cathode ray tube (CRT) display with hard-copy unit serves as the system terminal and is used for graphics displays of intermediate and final test results.

Computer control of the specimen loading as well as all data acquisition is provided through an MTS 433 Processor Interface Unit. Timed master/slave data acquisition from all four amplifiers as well as command function generation is possible under complete software control.

Description of Automated Procedure

The JTEST (B&W's automated single specimen J-test procedure) is conducted in three stages: (1) test initiation, (2) test execution, and (3) post-test data analysis. Each level may be run independently of the others provided all preceding levels have been completed. However, automatic sequencing between levels may be used at the discretion of the operator to allow uninterrupted flow of the test. A flow chart of the procedure is shown in Fig. 5.

Because of the total automation of the procedure, a detailed set of test parameters is needed to define the manner in which a particular test is run. The parameters include both material tensile properties and specimen dimensions as well as test control parameters, including: (1) amplifier ranges, (2) increment between crack length measurements, (3) extent of unloading, (4) portion of unload data to be used in compliance calculation, and (5) loading and unloading rates. Parameters entered by the operator when a new test is initiated are permanently stored on a magnetic disk for reference during execu-

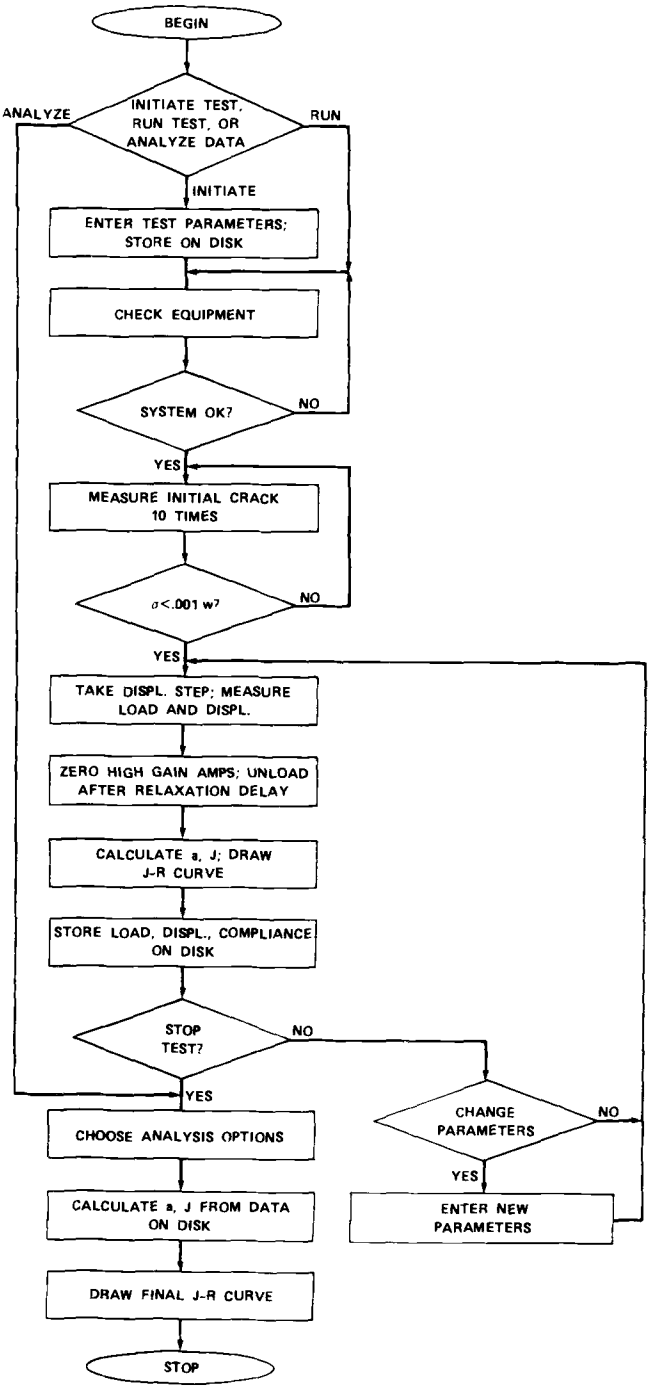

FIG. 5—*Flow chart of automated single-specimen JTEST procedure.*

tion of the test and post-test analysis. To optimize results, however, all test control parameters may be changed during the course of the test at the discretion of the operator.

Crack lengths are measured using the elastic unloading compliance technique, where crack length is related to normalized specimen compliance by the expression [*1*]

$$a/w = 1.000196 - 4.06319(U_{LL}) + 11.242(U_{LL})^2 - 106.043(U_{LL})^3 + 464.335(U_{LL})^4 - 650.677(U_{LL})^5$$

$$U_{LL} = \frac{1}{(B_e EC)^{1/2} = 1}, \qquad B_e = B_T - \frac{(B_T - B_N)^2}{B_T}$$

The effective thickness, B_e, is used to account for the effect of side grooves on specimen compliance [*2*]. Compliance is calculated by a linear regression analysis of load and load-line displacement data obtained from the high-gain amplifiers during elastic loading or unloading. The data acquisition rate is scaled based on the loading rate to give approximately 100 data points over the entire loading or unloading curve. However, regions of the curve can be excluded from the calculation at the discretion of the operator if abnormalities (for example, initial nonlinearity) are observed.

A series of checks is made to determine the accuracy and precision of the system prior to actual testing. The system is checked by the software to insure consistency between the parameters requested when the test was initiated and the actual system configuration. If consistency is found, the specimen is cycled ten times to a load less than that used for precracking, and crack lengths calculated on each half cycle. The difference between the crack lengths measured during the loading and during the unloading are computed, along with the standard deviations and averages of the crack lengths measured during the ten loadings and during the ten unloadings. Experience has shown that proper system performance will be characterized by:

1. agreement of calculated initial crack length with that estimated from precracking data,
2. standard deviations of loading and unloading measurements $< 0.001\,w$, and
3. differences between loading and unloading measurements at a given cycle $< 0.002\,w$.

The *J*-test is executed in a series of load-line displacement steps. Crack lengths are measured after each increment in displacement. To maximize stability past peak load, the servohydraulic test machine is run under control of the extensometer attached to the specimen load line. The incremental change in area corresponding to each step is calculated using a trapezoidal numerical

integration technique on load and load-line displacement data obtained from the low-gain amplifiers during the step. The rate of data acquisition is scaled based on the loading rate to give approximately 100 data points over each increment.

A significant drop in load has been observed in specimens held at constant load-line displacement near maximum load. This relaxation has been found to cause a substantial error in the calculated crack length if incorporated into the unload. Consequently, the unloading must be delayed following the displacement increment until the relaxation has reached an insignificant rate.

To obtain the required delay without unnecessarily increasing testing time, a routine has been added to the software to delay the unloading until the relaxation rate reaches 0.3 percent of the unloading rate. An error analysis of the crack length measurement process reveals this rate to affect less than 0.0005 w error in the resultant calculated crack length for $0.5 \leq a/w \leq 0.8$, judged to be an acceptable error. Delays of typically 3 to 5 min are required.

An intermediate J-R curve is drawn after each crack length measurement to allow the operator to follow the progression of the test and change test control parameters as needed to optimize results. However, only load and displacement data generated during the test and the compliance from each unload are recorded on magnetic disk for post-test analysis.

Data generated during the J-test may be analyzed in several different ways. The available options for analysis include:

1. Modulus correction: a correction factor applied to the normalized compliance calculated at each unload, the magnitude of which is calculated to force the initial crack length estimated by the unloading compliance technique to equal the physical crack length. Used to correct systematic errors in crack length measurements.

2. Rotation correction [4]: correction to measured compliances to account for specimen rotation at large displacements, given by

$$C_{\text{corrected}} = \frac{C_{\text{measured}}}{\left(\frac{H}{R}\sin(\theta) - \cos(\theta)\right)\left(\frac{D}{R}\sin(\theta) - \cos(\theta)\right)}$$

where

H = half-span of applied load points,
R = radius of rotation $(w + a)/2$,
D = distance from crack plane to displacement measurement line with no load on specimen,
$\theta = \sin^{-1}[(\delta_m + D)/(D^2 + R^2)^{1/2}] - \tan^{-1}(D/R)$, and
V_m = load-line displacement from crack plane to measurement line.

3. On-line crack estimate: use of compliances measured during test without correction.

4. Moving crack correction [5]: correction to calculated J-value to account for effect of crack propagation on the measured load-versus-displacement curve, given by

$$J_{(i+1)} = \left[J_i + \left(\frac{\eta}{b}\right)_i \left(\frac{A_{i,i+1}}{B_N}\right)\right]\left[1 - \left(\frac{\gamma}{b}\right)_i (a_{i+1} - a_i)\right]$$

where

$\eta = 2 + 0.522\ \text{b/w}$,
$\gamma = 1 + 0.76\ \text{b/w}$, and
$A_{i,i+1}$ = area under load versus load-line displacement record between lines of constant displacement at Points i and $i + 1$.

5. Merkle-Corten equation [6, 7]: use of Merkle-Corten equation to calculate J, given by

$$\mathrm{J} = \frac{C_1 A}{b_0 \mathrm{B_N}}$$

where

$$C_1 = \frac{2(1 + \alpha)}{(1 + \alpha^2)}$$

$$\alpha = \left[\left(\frac{2a_0}{b}\right)^2 + 2\left(\frac{2a_0}{b}\right) + 2\right]^{1/2} - \left(\frac{2a_0}{b} + 1\right)$$

All crack lengths and J-values are recalculated from raw data on the magnetic disk using the analysis options chosen.

The final J-R curve is constructed using the recalculated J-values and values of crack extension, Δa, calculated by the expression

$$\Delta a = a_i - a_0 + \text{offset}$$

where offset = shift along Δa-axis. An offset is sometimes required due to slight systematic differences between the initial crack length measurement and the crack length measurements made during the J-test. Such differences can be caused by a slight reseating of the extensometer at the start of the test, or by nonlinearity in the initial portion of the load-versus-displacement curve used to measure a_0. In such cases, the offset can be used to align the data in the early portion of the J-R curve with the theoretical blunting line, of importance primarily in the calculation of J_{Ic}. Only offsets less than 1 percent of the initial crack length are considered to be acceptable. Larger systematic errors in crack

extension must be eliminated through a correction applied to compliance, analogous to the modulus correction described earlier.

Results

Results from two testing programs conducted using the automated system are shown in Figs. 6–8. Figure 6 shows the J-R curves generated for HY-130 as part of the American Society for Testing and Materials (ASTM) J-Integral R-Curve Round Robin program [*8*], while Figs. 7 and 8 show some of the results of an internal B&W program to characterize the stable tearing properties of submerged-arc weld metals at upper-shelf temperatures. Compact fracture specimens 25.4 mm (1 in.) thick were used in both programs, with slight variations in notch design. The specimen design shown in Fig. 9, in which the clip gage is attached to knife edges machined in the specimen load line, was used for the weld metal tests for consistency with the design used by B&W in the reactor vessel surveillance program. For the round-robin tests, the loading pinholes were spread apart and the notch region enlarged to enable the replacement of the machined knife edges with razor blades attached to the specimen load-line.

Table 1 gives the initial and final crack length for each test as measured by compliance and by heat tinting after the test. In each case, the heat tint result

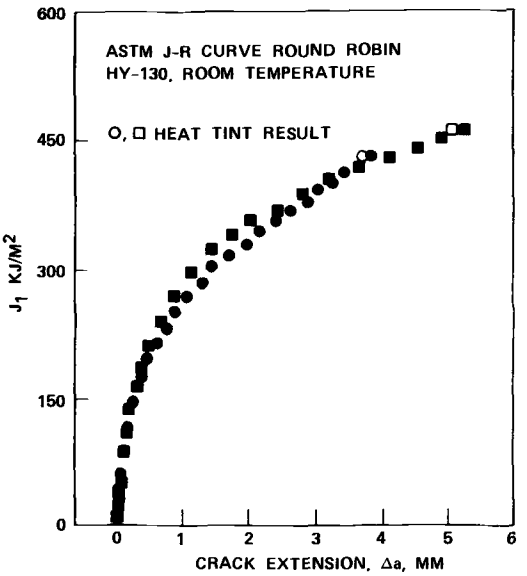

FIG. 6—*J-R curves for HY-130 at room temperature; generated as Part of the ASTM J-Integral R-Curve Round Robin Program using automated single-specimen procedure (1 kJ/m^2 = 5.7 in. ·lb/in.^{2}; 1 mm = 0.04 in.).*

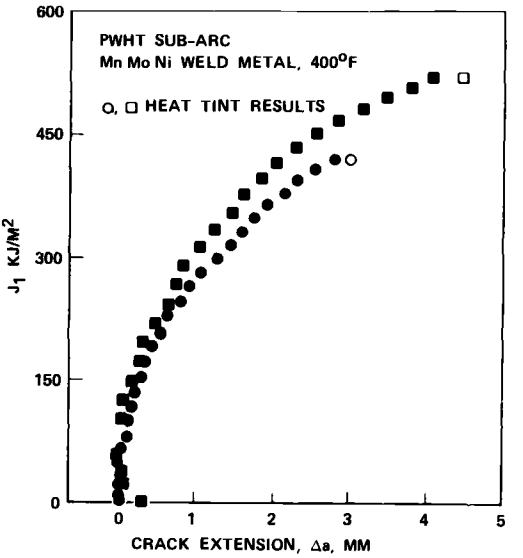

FIG. 7—*J-R curves for stress-relieved manganese-molybdenum-nickel (MnMoNi) sub-arc weld metal at 200°C (392°F); generated using automated single-specimen procedure (1 kJ/m^2 = 5.7 in. · lb/in.^{2}; 1 mm = 0.04 in.).*

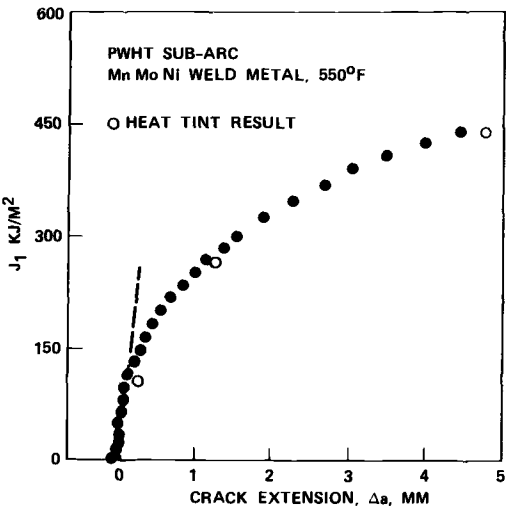

FIG. 8—*J-R curves for stress-relieved MnMoNi sub-arc weld metal at 290°C (554°F); generated using automated single-specimen procedure 1 kJ/m^2 = 5.7 in. · lb/in.^{2}; 1 mm = 0.04 in.).*

COMPACT FRACTURE TOUGHNESS SPECIMEN

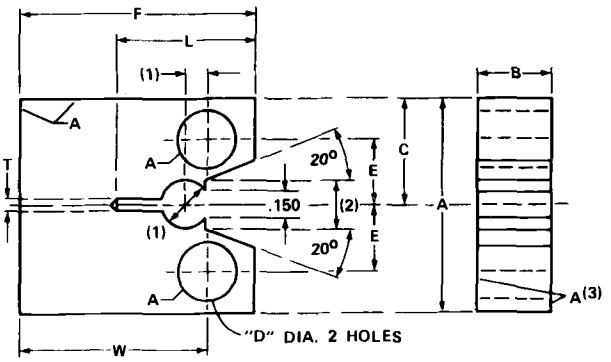

(1) 13/64" DIAMETER FOR 1TC AND 2TC SPECIMENS. OFFSET .075" 3/8" DIAMETER FOR 4TC SPECIMENS. OFFSET .150" FROM LOAD LINE.

(2) .200" FOR 1TC AND 2TC SPECIMENS.

(3) "A" SURFACES PERPENDICULAR AND PARALLEL TO WITHIN 0.002 WTIR

TABLE OF DIMENSIONS (INCHES)

SPECIMEN TYPE	A ±.010	B ±.010	C ±.005	D ±.005	E ±.005	F ±.005	L ±.005	W ±.002	T ±.010
1T	2.400	1.000	1.200	0.500	0.550	2.500	1.250	2.000	0.125
2T	4.800	2.000	2.400	1.000	1.100	5.000	2.500	4.000	0.125
3T	7.200	3.000	3.600	1.500	1.650	7.500	4.100	6.000	0.125
4T	9.600	4.000	4.800	2.000	2.200	10.000	5.600	8.000	0.125

FIG. 9—*Compact fracture specimen design used in weld metal tests. Clip gage is attached to knife edges machined in specimen load line (1 in. = 25.4 mm).*

TABLE 1—*Comparison of heat tint and compliance crack length measurements for single-specimen J-tests.*

Material	Test Temperature,[a] °C	Initial Crack: Compliance,[b] mm	Initial Crack: 9-Pt Avg ±Mean Deviation mm	Final Crack: Compliance, mm	Final Crack: 9-Pt Avg ±Mean Deviation, mm
1. HY-130	24	32.3	33.0 ± 0.34	37.4	38.0 ± 0.88
2. HY-130	24	34.6	35.1 ± 0.49	38.4	38.8 ± 0.76
3. Sub-arc weld	200	26.5	26.5 ± 0.18	29.2	29.4 ± 0.46
4. Sub-arc weld	200	26.5	26.4 ± 0.18	30.4	30.9 ± 1.3
5. Sub-arc weld	290	25.9	26.0 ± 0.12	30.3	30.8 ± 0.23

[a] $°F = \frac{°C \times 9}{5} = 32$

[b] 1 mm = 0.04 in.

was calculated as the average of nine measurements equispaced across the width of the specimen. The mean deviation of the nine measurements from the average is also shown to provide some indication of the uniformity of the crack front.

Each of the J-R curves shown in Figs. 6-8 was generated using the J-formulation corrected to account for the moving crack. In addition, the rotation correction to compliance was also used in the analysis. In each figure, both the single-specimen data points as well as the final J-value plotted with the crack extension measured by heat tinting are shown. Two additional heat tint results at intermediate crack extensions are also shown for the 290°C (554°F) weld metal test, obtained using the heat tint method on two separate specimens.

Discussion of Results and Procedure

The crack length measurements from the foregoing tests are summarized in Table 1. In the sub-arc weld metal tests, excellent agreement was found between the compliance crack length measurements and the nine-point averages both in the prediction of the absolute initial and final crack lengths as well as in the prediction of the total crack extension. Somewhat less agreement was found, however, in the prediction of the absolute crack lengths in the round-robin tests, although estimates of the total crack extension by the two methods were still quite close. The average error in compliance corresponding to the observed errors in the initial crack lengths for the two tests was 7.7 percent. The error in compliance corresponding to the observed errors in the final crack lengths was obscured due to the nonuniformity of the crack fronts.

To investigate the source of the error in the crack length measurements of the round-robin tests, the notch lengths of two sharply notched but uncracked specimens of the same geometries as used in this study were estimated from compliance measurements using the automated procedure. The results are given in Table 2. Close agreement was found between the optically measured notch length and that predicted by compliance for the machined knife edge specimen design. However, the compliance measurement significantly underestimated the actual notch length in the razor blade specimen

TABLE 2—*Comparison of measured notch length with notch length predicted by compliance for uncracked specimens.*

	Actual Notch Length,[a] mm	Predicted Notch Length, mm
Machined knife edge	21.5	21.4
Razor blade knife edge	25.6	24.6

[a] 1 mm = 0.04 in.

design, corresponding to an 8.8 percent error in compliance of $a/w = 0.504$. These results parallel the results obtained from J-tests using the two geometries, and indicate a difference in the compliance calibration equations of the specimens.

Despite the errors in the absolute values of the crack lengths in the round-robin tests, good agreement was found in all cases between the J-R curves obtained by the automated single-specimen procedure and the heat tint data points, indicating the insensitivity of the crack extension measurements to the errors just described. In addition, good reproducibility of results was found for the duplicate round-robin tests (Fig. 6), although some difference in the results of the duplicate weld metal tests at 200°C (392°F) was observed (Fig. 7). It is likely, however, that the differences in the latter are due to nonuniform crack propagation in Test 4 (see Table 1), as evidenced by the relatively large mean deviation of the optical measurement of the final crack front.

The JTEST procedure offers several advantages over more conventional techniques. Perhaps most important is the reliability and precision attainable by the complete computer control of all phases of testing. Variations in test procedures between tests can essentially be eliminated, and the possibility of losing results due to operator error can be minimized with software checks of the apparatus and prompts to the operator. Secondly, the procedure provides on-line analysis of data during the test, allowing interaction by the operator to tailor the flow of the test for optimum results. Thirdly, once the test is proceeding as desired, the system can be left unattended, reducing testing costs. Finally, data can be permanently stored on a magnetic disk for easy recall and analysis at a later date.

Conclusions

1. The specifications of equipment needed to automate the single-specimen J-test can be estimated from a statistical analysis of the elastic unloading compliance crack length measurement technique. The results show that a system with 12-bit A/D converters can be used successfully if additional amplification of the unloads over that provided by normal test control electronics is used and signal noise levels are minimized.

2. Good agreement between results obtained using the automated procedure and the more conventional heat-tinting technique was found from room temperature to 290°C (554°F). In addition, the automated procedure showed a high degree of accuracy in the prediction of absolute crack lengths for the conventional compact fracture specimen design, as well as excellent reproducibility in duplicate tests.

3. The automated procedure offers several advantages over manual techniques. These include (1) essentially exact replication of test procedure between tests, independent of operators; (2) minimization of specimen losses due to operator error; (3) analysis of data as test is being run; (4) tailoring of

test control based on intermediate results to optimize the final J-R curve; (5) reduction of testing costs due to decrease in testing and data analysis time, and requirements placed on operator; and (6) storage of all raw data on magnetic disk, allowing easy recall and reanalysis.

Acknowledgments

The authors wish to acknowledge the assistance of Dr. James A. Joyce of the U.S. Naval Academy in the formulation of the sensitivity study. Special recognition is due Dr. James E. Schwabe of the Standard Oil Co. (formerly of Babcock & Wilcox), who was responsible for the basic design of the analog hardware and the definition of the approach to automation of the test, and to Dr. Patrick C. Cain of MTS Systems Corp. for work on the initial version of software.

References

[1] Saxena, A. and Hudak, S. J., Jr., "Review and Extension of Compliance Information for Common Crack Growth Specimens," Paper 77-9E7-AFCGR-P1. Westinghouse Scientific, Pittsburgh, Pa., May 1977.

[2] Shih, C. F., DeLorenzi, H. G., and Andrews, W. R., *Journal of Testing and Evaluation*, Vol. 8, No. 5, Sept. 1980.

[3] Dixon, W. J. and Massey, F. J., Jr., *Introduction to Statistical Analysis*, McGraw-Hill, New York, 1969, p. 198.

[4] "Structural Integrity of Water Reactor Pressure Boundary Components," Progress Report Ending 30 Nov. 1977, NRL Memorandum Report 3782, F. J. Loss, Ed., Naval Research Laboratory, Washington, D.C., May 1978.

[5] Ernst, A., Paris, P. C., and Landes, J. D. in *Fracture Mechanics: 13th Conference, ASTM STP 743*, American Society for Testing and Materials, 1981, pp. 476-502.

[6] Merkle, J. G. and Corten, H. T. *Transactions*, American Society of Mechanical Engineers, *Journal of Pressure Vessel Technology*, Vol. 96, Nov. 1974, pp. 286-292.

[7] Clark, G. A. and Landes, J. D., *Journal of Testing and Evaluation*, Vol. 7, No. 5, Sept. 1979, pp. 264-269.

[8] Gudas, J. P., "Results of the J-Integral R-Curve Round Robin Program," presented at the American Society for Testing and Materials Second International Symposium on Elastic-Plastic Fracture Mechanics, Philadelphia, Pa., Oct. 1981.

Sami M. El-Soudani[1] *and John F. Knott*[2]

Quantitative Fractographic Definition and Detection of Fracture Initiation in COD/K_{Ic} Test Specimens

REFERENCE: El-Soudani, S. M. and Knott, J. F., **"Quantitative Fractographic Definition and Detection of Fracture Initiation in COD/K_{Ic} Test Specimens,"** *Elastic-Plastic Fracture: Second Symposium, Volume II—Fracture Resistance Curves and Engineering Applications, ASTM STP 803*, C. F. Shih and J. P. Gudas, Eds., American Society for Testing and Materials, 1983, pp. II-483-II-507.

ABSTRACT: One important requirement of any fracture toughness test is the ability to detect the initiation of fracture, and it is here that detailed observations of void growth ahead of the crack tip should provide background calibration for macroscopic measurements such as compliance changes, electrical resistance changes across the notch faces, or acoustic emission output. The nature of incipient crack growth process, however, is such that the use of the term "fracture initiation" requires careful definition. The problem arises in view of the complexity of a set of microscopic-scale events occurring at a crack tip upon extension. In this paper the development of a reliable single-test method for the detection of fracture initiation is described. This method is based on the use of a double-clip-gage system attached to either a fracture toughness (K_{Ic}) or a crack opening displacement (COD) test specimen. It locates the initiation point from compliance-related changes in the double-clip-gage output signals and is successful in detecting fracture initiation, independent of specimen size, under conditions of quasi-linear elastic fracture mechanics (QLEFM), elastoplastic fractures (limbo region), and fully yielded specimens (YFM). The double-clip-gage method was calibrated by quantitative scanning electron microscopy of void growth and coalescence during a series of experiments in which ductile low-alloy steel precracked specimens were unloaded from different points on the load-displacement diagram. A three-parameter microfractographic definition of fracture initiation was established at the detectable point based on: (1) maximum lineal extent of advancing microthumbnail cracks; (2) normalized areal growth increment; and (3) the percentage of advanced crack-tip length. Following its rigorous fractographic calibration, the double-clip-gage system was used as a means of checking out other methods of fracture initiation prediction. Four methods were applied simultaneously to the same specimen: the double- (or triple) clip-gage system; an acoustic emission analyzer; a potential drop system; and the Standard Offset Procedure. There was excellent agreement between the double-clip-gage system and both acoustic emission ringdown and event count indications under valid and nonvalid fracture toughness (K_{Ic}) test conditions. By

[1]Engineering specialist, Aircraft Engine Group, General Electric Co., Cincinnati, Ohio 45240.
[2]Reader, Department of Metallurgy and Materials Science, University of Cambridge, Cambridge, U.K.

comparison, the potential-drop system exhibited appreciable and, in some materials, considerable lagging, the extent of which increased with increasing plasticity. The Standard Offset Procedure agreed well with the calibrated method only in valid K_{Ic} tests, but tended to underestimate the initiation point in substandard specimens. When used as a monitoring technique for determining various measures of fracture initiation toughness in situations involving either limited or excess plasticity, the fractographically calibrated double-clip-gage method can serve as a means of developing a unified and consistent ranking of the toughness behavior of materials under widely different conditions.

KEY WORDS: fracture toughness, fracture initiation, test methods, bend tests, crack opening displacement, calibration, fractography, crack propagation, elastic-plastic fracture

This paper treats applications of quantitative microfractography in the development of background calibrations for the definition and detection of incipient crack growth during crack opening displacement/fracture toughness (COD/K_{Ic}) testing. It would be useful to be able to deduce the fracture initiation point in a precracked test specimen from its load-displacement diagram, but this has previously not been done in any convincing manner. One such attempt is the "Standard Offset Procedure" used in deducing K_{Ic} in quasi-elastic plane-strain fracture toughness testing. This procedure is based on the premise that the increment of incipient crack growth is limited to within 2 percent of the initial crack length $\bar{a}_0$ at a point during the test corresponding to the intersection of the load-displacement diagram with its secant line drawn from the origin at a slope 95 percent of the initial slope [*1*][3]; see also the ASTM Test for Plane-Strain Fracture Toughness of Metallic Materials (E 399-78a). Becuase of the relatively simple instrumentation currently required by the Standard Offset Procedure there is a tendency to oversimplify the rather complex set of events leading to the onset of crack advance, and a rigorous *microfractographic* validation of the correlation between fracture initiation and 95 percent secant slope has yet to be demonstrated.

For more ductile materials, the COD standard [*2*] locates the point of initiation of slow (or fibrous) crack growth (P_i, V_{g_i}) by the "fibrous crack length extrapolation method" [*3*], which requires the testing of several specimens followed by their subsequent optical microscopic examination to measure crack extension Δa. It also permits the use of other methods of crack growth monitoring [*2*] such as ultrasonic monitoring [*4,5*], direct current (d-c) potential-drop systems [*6–8*], and unloading experiments [*9,10*]. The use of acoustic emission (AE) for the detection of ductile crack growth has also been suggested [*11,12*].

In an attempt to provide a consistent definition of fracture initiation in K_{Ic} and COD tests, the present paper compares four methods for detecting the onset of crack extension: (1) a multiple-clip-gage system, (2) a potential-drop system, (3) a commercial (Dunegan-Endevco) AE system, and (4) the Stan-

[3]The italic numbers in brackets refer to the list of references appended to this paper.

dard Offset Procedure (Method E 399). First, a rigorous validation of the multiple-clip-gage system is made to establish the minimum detectable crack growth increment at the critical point defining initiation. Secondly, comparisons are made with the other methods to determine their sensitivity to fracture initiation.

Materials and Test Procedures

The overall test program comprised 78 COD/K_{Ic} tests of fatigue-pre-cracked three-point-bend specimens made from three groups of materials whose compositions, heat treatments, and deoxidation methods are given in Tables 1 to 3. The Al-4Zn-2Mg alloy (Table 1) was supplied as plate in thicknesses ranging from 20 to 50 mm. Two orientations were tested (see Fig. 1*a*): the longitudinal, L, and the transverse, T. Both categories of low-alloy steel (Tables 2 and 3) were cast in "keelblocks" which were subsequently sliced (after heat treatment) as shown in Fig. 1*b*. Slices 1 and 3 were used for COD/K_{Ic} tests, with three-point-bend specimen geometries covering the range 10 by 20 by 80 mm to 60 by 120 by 480 mm (the smaller specimens were cut from the broken halves of larger specimens). The reasoning behind the choice of these particular materials and range of geometries is as follows:

1. To provide a general definition of fracture initiation the analysis must deal with three basic situations: (1) quasi-elastic fracture initiation, (2) elastoplastic fracture initiation followed by the onset of general yielding, and (3) general yielding preceding the onset of slow crack growth. It was found [*13*] that Type 1 and, to a lesser extent, Type 2 fracture initiation dominated the behavior of the Al-4Zn-2Mg alloy. This gave ample opportunity for correlating the multiple-clip-gage technique with the Standard Offset Procedure. The cast steels of controlled copper and silicon content (Table 3) exhibited Type 2 initiation of fracture. The large specimens ($\gtrsim$ 30 by 60 mm in cross section) of nickel-chromium-molybdenum (Ni-Cr-Mo) steels showed mostly Type 2 with several cases of Type 1 initiation, while the smallest specimens (10 by 20 mm) produced fracture initiation of Type 3.

2. It is important to examine the response of the multiple-clip-gage detection device in situations involving widely differing fracture micromechanisms. This was demonstrated by examining the differently deoxidized modifications of Ni-Cr-Mo steels which undergo a cleavage-to-fibrous transition over

TABLE 1—*Nominal chemical composition in weight % of aluminum-zinc-magnesium alloy.*

Alloy Designation	Cu	Mn	Mg	Fe	Si	Zn	Ti	Cr	Al
Al-X[a]	0.033	0.313	2.55	0.172	0.09	4.46	0.01	0.102	balance

[a]X designates specimen orientation per Fig. 1: L for longitudinal and T for transverse.

TABLE 2—*Chemical composition*[a] *(weight %) and deoxidation (weight %) methods of cast nickel-chromium-molybdenum low-alloy steel.*

Alloy[b]	Air Melt/ Vacuum Degass[c]	Deoxidant,[d]	C	Si	Mn	P	S	Cr	Mo	Ni	Al	Ti
SA	air melt	{31.5% Al + 68.5% Si}	0.23	0.50	0.92	0.027	0.018	0.87	0.38	1.92	0.069	...
SB	air melt	100% Hypercal	0.24	0.58	0.98	0.035	0.018	0.91	0.40	2.00	0.086	...
SC	air melt	{50% Al + 50% Lanceramp 23}	0.24	0.58	0.98	0.035	0.018	0.91	0.40	2.02	0.088	...
SD	air melt	{44.5% FeTi + 55.5% Si}	0.235	0.51	0.92	0.030	0.024	0.89	0.36	1.94	0.012	0.06
SVA	vacuum degass	{31.5% Al + 68.5% Si}	0.24	0.41	0.80	0.030	0.026	0.91	0.39	2.08	0.078	...
SVB	vacuum degass	100% Hypercal	0.225	0.42	0.76	0.021	0.021	0.89	0.36	1.84	0.073	...
SVC	vacuum degass	{50% Al + 50% Lanceramp 23}	0.225	0.36	0.74	0.019	0.020	0.89	0.36	1.86	0.084	...
SVD	vacuum degass	{44.5% FeTi + 55.5% Si}	0.225	0.32	0.71	0.020	0.021	0.89	0.36	1.84	0.010	0.06

[a]Hydrogen analysis: before pouring (2 to 3) ppm, and after pouring (3 to 4) ppm.
Heat treatment: 900°C for 2½ h, furnace-cool, 880°C for 2½ h, oil-quench, temper 1 h at 640°C and air cool.
[b]Alloy designations with a single or double prime in the text were tempered at some temperature to a flow stress.
[c]After vacuum degassing heats were tapped in air whereby deoxidants were added to them.
[d]Hypercal composition: 10 to 13% Ca, 9 to 12% Ba, 38 to 40% Si, 19 to 21% Al, iron balance. Lanceramp-23 composition: an iron-base addition with approximately 20% rare-earth metals.

TABLE 3—*Chemical composition in weight % of low-alloy steels with controlled copper and silicon contents.*

Alloy Designation[a]	C	Si	Mn	P	S	Cr	Mo	Ni	Al	Cu	Sn
S1312	0.26	0.28	1.31	0.01	0.009	<.01	0.3	<.01	0.065	0.01	0.005
S1282	0.31	0.31	1.35	0.023	0.017	0.01	0.3	0.05	0.089	0.22	0.005
S1284	0.33	0.28	1.30	0.019	0.02	0.01	0.32	0.05	0.074	0.24	0.068
S1329	0.3	0.29	1.32	0.0173	0.0153	0.01	0.31	0.04	0.076	0.21	<0.01
S1314	0.3	0.29	1.32	0.0173	0.0153	0.01	0.31	0.04	0.076	0.22	0.054
S1283	0.3	0.29	1.32	0.0173	0.0153	0.01	0.31	0.04	0.076	0.02	0.078
S1313	0.3	0.29	1.32	0.0173	0.0153	0.01	0.31	0.04	0.076	0.01	<0.01
S1281	0.3	0.29	1.32	0.0173	0.0153	0.01	0.31	0.04	0.076	0.02	<0.01

[a]Heat treatment for all alloys: anneal 6 h at 930°C; furnace cool; normalize 5 h at 890°C; water-quench; temper 1 h at 650°C; water quench.

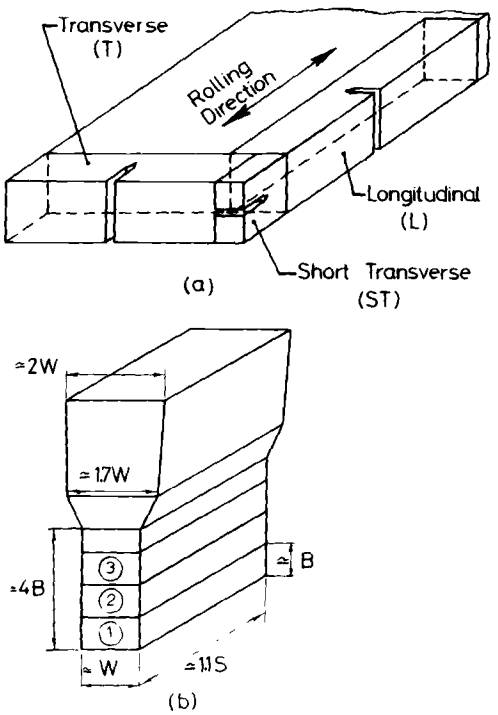

FIG. 1—*Specimen orientations for three-point-bend COD/K_{Ic} testing:* (a) *specimens from wrought aluminum alloy plate, and* (b) *specimens from cast low-alloy steel blocks. Notation:* B, W, *and* S *refer to the three-point-bend specimen thickness, width, and total span, respectively. In all cases* S = 4W.

a wide range of fracture-appearance transition [*13*] temperatures (−70 to +85°C). It was possible to carry out all testing at room temperature and still obtain different micromechanisms in the differently deoxidized steels (Table 2) with different inclusion morphologies, spacial distributions, and volume fractions. The testing of the wrought aluminum alloys also permitted the assessment of microstructures containing elongated second-phase particles and stringers of inclusions.

Specimen notation is as follows: Each COD/K_{Ic} specimen is given a serial number (from 1 to 78). Specimens 1 to 60 were tested to final failure, whereas Steel Specimens 61 to 78 were unloaded before final separation at selected points on the load-displacement diagram, subsequently broken in liquid nitrogen, and examined in the scanning electron microscope (SEM) for the determination of crack extension, Δa.

The following is a brief description of the various techniques used for the detection of fracture initiation.

Multiple-Clip-Gage System

The design of the multiple-clip-gage system is shown in Figs. 2*a* to 2*c*, where two or three clip gages are placed between their corresponding knife edges positioned at different distances from the fatigue precrack tip in a three-point-bend specimen. The outputs, $V_{g_i} = f_1(V_{g_j})$, from any pair of three clip gages placed at different elevations (Z_t at the top, Z_s near the surface, and, whenever used, Z_b below the surface) are plotted in conjunction with the load-displacement diagram $P = f_0(V_{g_s})$, where i and j are arbitrary indices identifying any given clip gage pair. The system is designed to use standard clip gages and amplifiers. The initial separations of the top and near-surface knife edge pairs are adjustable such that these clip gages operate within the linear range over their respective total displacement. It was noted that slope changes in the $V_{g_i} = f_1(V_{g_j})$ plot occur in a fairly abrupt manner, at a succession of critical points on the $[P = f_0(V_{g_s})]$ plot as illustrated schematically in Fig. 2*d*. The slope change at V_{g_A} will be shown later, using fractography, to correspond to the definition of fracture initiation, which is adopted for characterization of the "fracture initiation toughness."

Potential-Drop System

In the d-c potential-drop system a constant current is passed through the specimen, and the voltage across the crack is monitored by suitably positioned probes (see Fig. 2). The voltage drop across the crack faces, ΔV_a, depends on the net ligament area,[4] $B(W - a)$, and may be calibrated as

[4]Cracked bend specimen geometry notation: thickness = B, width = W, and average crack length = a.

a function of the a/W ratio to monitor crack growth (see, for example, Ref *14*). The same voltage drop ΔV_a also depends on the crack opening displacement at the specimen surface, V_{g_s}, which in turn is related to the dimensionless increment of crack advance $\Delta a/W$. Examples of the relationship $\Delta V_a = f_6(V_{g_s})$ are shown in Figs. 6–8.

Acoustic Emission System

Elastic wave emissions are detected using a piezoelectric transducer (D9201); see Fig. 2*a* and Ref *15*. The output voltage is amplified and fed into (1) a Dunegan 920/921 distribution module which counts the total number of AE events and displays the distribution of those events with amplitudes above a threshold setting (45 dB); (2) the Dunegan 301 totalizer module which counts the number of times the AE signal amplitude exceeds a preset threshold during any selected portion of the test (that is, ringdown count). In the establishment of fracture initiation point the following diagrams were used: Rd Count $= f_4(V_{g_s})$, Ev Count $= f_5(V_{g_s})$, and differential amplitude distribution histograms, that is, log number of events plotted as a function of event amplitude at selected time points during the test.

A Quantitative Model for the Definition of Fracture Initiation in Precracked Specimens

Scanning electron microscope examination of fractures in steel specimens Nos. 61–78 unloaded from different points on the $P = f_0(V_{g_s})$ plot and subsequently broken in liquid nitrogen revealed the following stages of crack advance (see Figs. 3*a* to 3*e*): (1) void growth; (2) coalescence of voids with each other and with the crack tip either by impingement or by shear decohesion of the intervening ligaments; (3) bursts of microscopic-scale thumbnail cracks, referred to as "microthumbnails" (see Fig. 3*a*); (4) lateral growth of microthumbnails and their coalescence into a macrothumbnail; (5) further advance of the macrothumbnail; and (6) onset of instability in the side ligaments.

In order to quantify this complex set of events which do not necessarily follow one another in a uniquely defined succession, several means of characterization are given in Figs. 3*d*–3*g*. Two such means are lineal quantities or indices characterizing crack advance, using either (1) the maximum thumbnail crack advance increment, $\Delta a_{\max}\%$, or (2) the percent original crack front length which has moved to a new position (defined conveniently in terms of specimen thickness, B, as an approximation). Thus

$$\Delta a_{\max}\% = (\Delta a/a_0) \times 100\% \tag{1}$$

$$\text{PACT}\% = \frac{\sum_i \Delta l_i}{B} \times 100\% \tag{2}$$

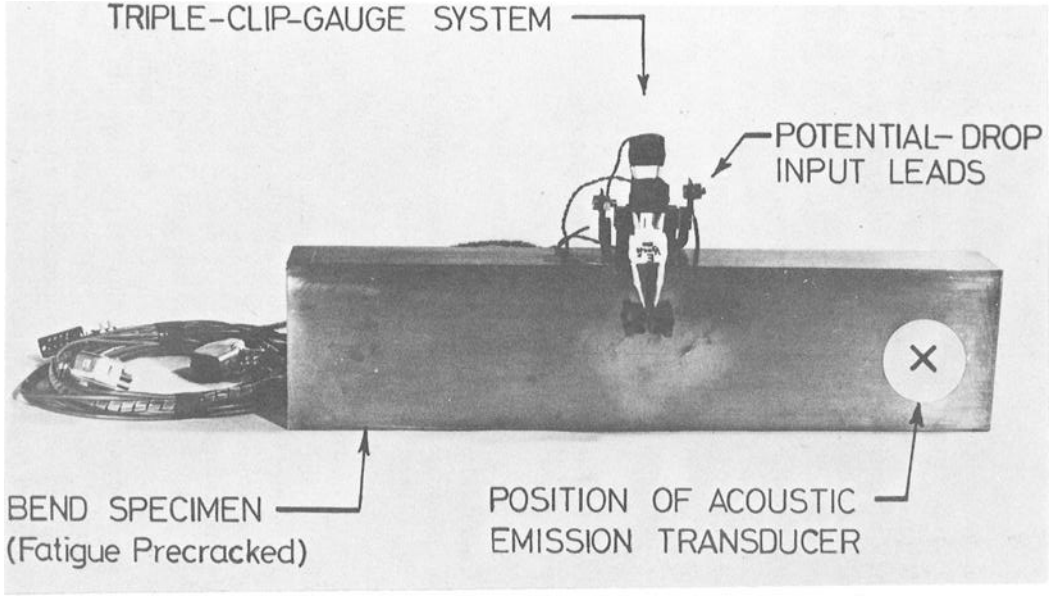

(*a*) Specimen geometry.

FIG. 2—*Equipment used for COD/K_{Ic} testing with crack growth monitoring, using simultaneously a triple-clip-gage system, a potential-drop system, and an acoustic emission analyser:* (a) *through* (c) *show specimen geometry, knife edge, and clip-gage arrangement and the potential-drop input/output-lead positions on the specimen; and* (d) *a schematic of a typical output of the double-clip-gage system.*

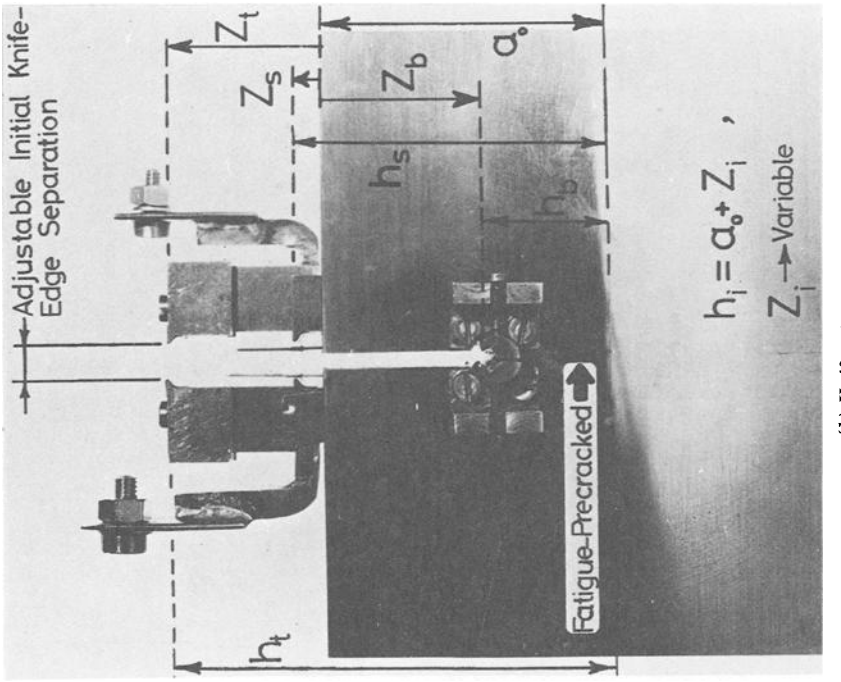

(*b*) Knife edge.

FIG. 2—*Continued.*

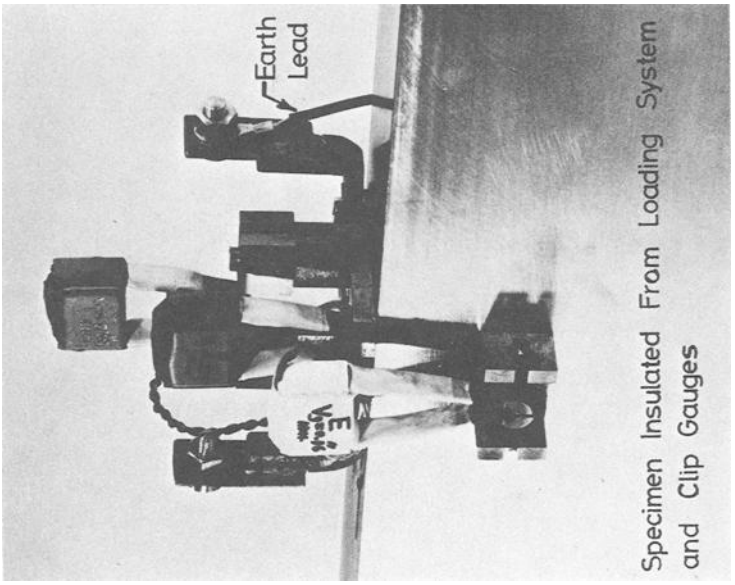

(c) Clip-gage arrangement.

FIG. 2—*Continued.*

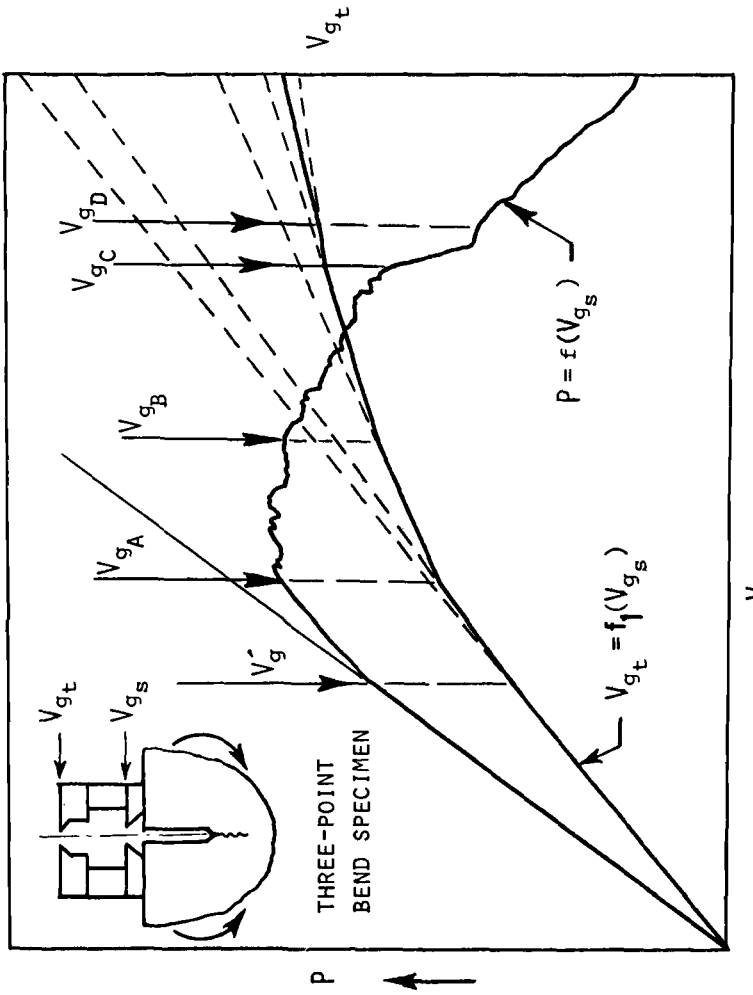

(*d*) Schematic of the double clip-gage system.

FIG. 2—*Continued.*

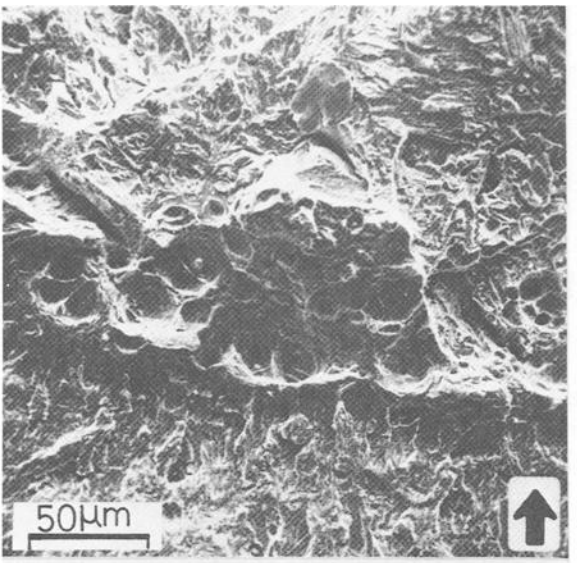

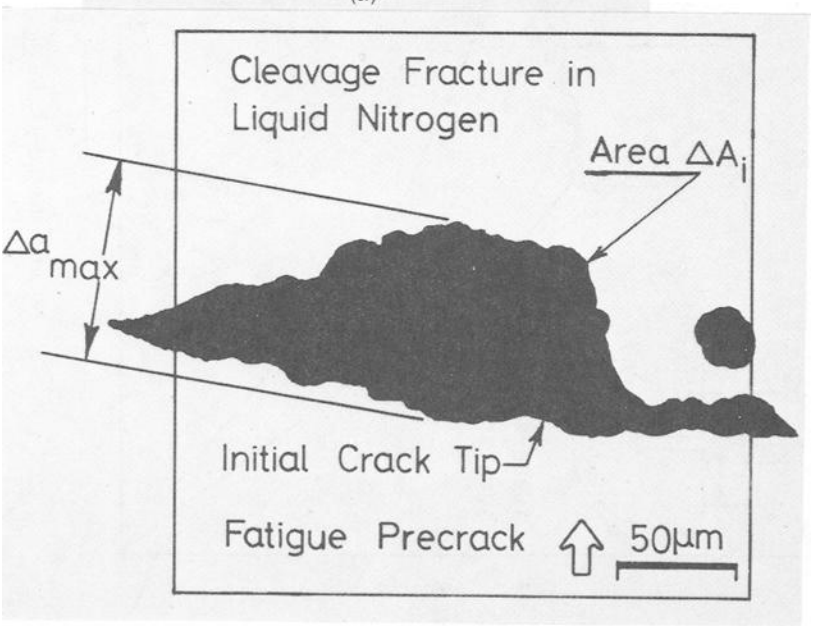

FIG. 3—*SEM evidence of incipient crack growth by local initial bursts of microscopic thumbnails in* (a) *of which a sample tracing is given in* (b), *with a model describing the succession of events leading to such microthumbnails in* (c); (d) *spectrum analysis for the quantification of microthumbnail bursts by their lineal forward extent;* (e) *another lineal method of quantification of crack advance by the projected length of extended portions of crack front;* (f) *definition of crack growth by the normalized areal advance method; and* (g) *analysis of crack-tip area fraction of voids.*

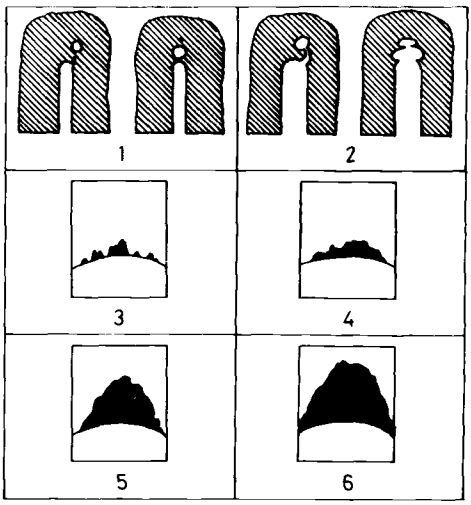

(c)

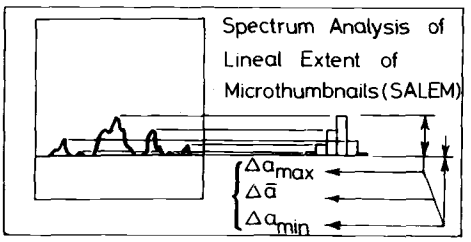

(d)

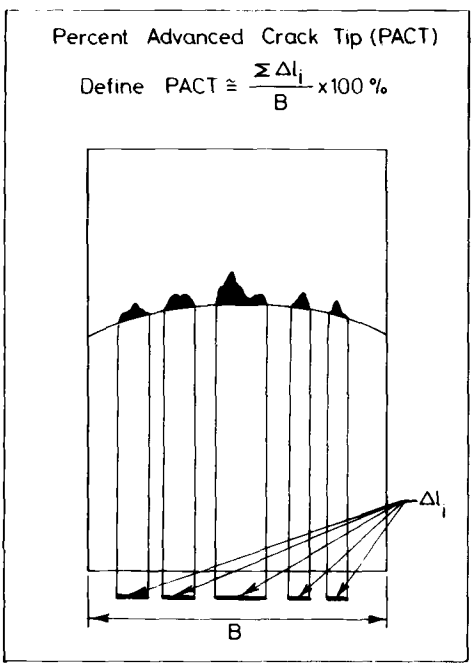

(e)

FIG. 3—*Continued.*

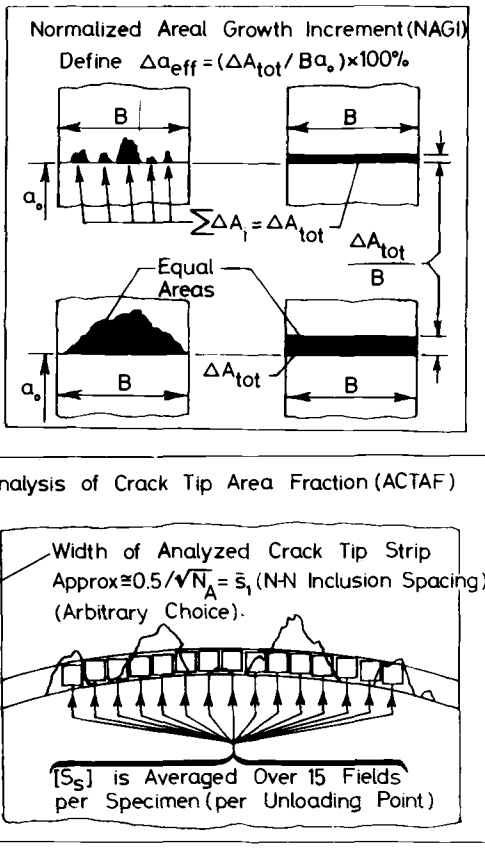

FIG. 3—*Continued.*

The two other methods rely on areal analysis of fractures. The first areal method defines the normalized areal growth increment (NAGI%) as in Fig. 3*f* by

$$\text{NAGI} = \Delta a_{\text{eff}}\% = (\Delta A_{\text{tot}}/Ba_0) \times 100\%$$

The second areal method makes use of the surface percent of voids $[S_S]\%$ measured in the immediate vicinity of the crack tip (Fig. 3*g*). It has been shown in Ref *13* that the surface percent voids is an adequate measure of their volume percent $[V_V]\%$ local to the crack tip.

All four quantities were used in assessing the resolution limit of the multiple clip-gage system.

Results of Microfractorgraphic Calibrations

Diagrams for SEM Fractographic Calibration of Fracture Initiation

The development of a fractographic calibration for fracture initiation in a given alloy system entails the preparation of superimposed plots of the type

shown in Fig. 4. The supporting detailed documentary evidence of microthumbnail crack advance as in Fig. 2*a* is given in Ref *13*. Because the $\Delta a_{max} = f_2(V_{g_s})$ curve in Fig. 4 did not cover the macrothumbnail region (Δa_{max} larger than, say, 0.5 mm), two additional alloy modifications were tested in order to confirm the overall shape of the $\Delta a_{max} = f_2(V_{g_s})$ diagrams. Only one of these diagrams is shown in Fig. 5.

From the diagrams shown in Figs. 4 and 5 and supporting fractographic evidence in Ref *13* the slope change at V_{g_A} corresponds to a sudden increase in the leading microthumbnail length from its value of $\Delta a_{max}\% \simeq 2\%$ at V_{g_A}. By contrast, the volume fraction of voids $[V_V]$ (equal to their surface fraction $[S_S]$) starts to change upon first deviation from linearity on the load-displacement diagram and undergoes a process of steady increase past V_{g_A}. At V_{g_A} the value of $[S_S]\%$ equals 1/2 to 2/3 its value during steady crack growth to final monotonic failure. The percentage of advanced crack front, measured in the SEM from composite micrographs sampling the entire crack front, gives a PACT% $\simeq$ 40 percent in alloy SVB3, together with an associated normalized areal growth increment NAGI% of $\simeq$ 0.25 percent.

Figure 6 shows correlations between initiation points as predicted by various methods, namely: V_{g_A} (double-clip-gage indication), V_{g_Q} (the Standard Offset Procedure point), $V_{g_{Rd}}$ (the ringdown count indication), $V_{g_{Ev}}$ (the event count indication), and $V_{g_{PD}}$ (the potential-drop initiation point). While there is excellent agreement between V_{g_A}, V_{g_Q}, $V_{g_{Rd}}$, and $V_{g_{Ev}}$, the predicted $V_{g_{PD}}$ was appreciably greater. Acoustic emission amplitude histograms revealed the presence of high-amplitude emission of at least two peaks or modes generated early in the process of crack growth, with both types commencing at $V_{g_{Rd}}$ and $V_{g_{Ev}}$ points. Figures 7*a* and 7*b* show typical diagrams correlating the load-displacement plots with their corresponding displacement-displacement diagrams of a triple-clip-gage system, in the wrought aluminum alloy, together with the associated potential drop traces. While the correlations are self-explanatory, the following observations are of importance for a theoretical interpretation of slope changes [*13*]: (1) The amount of slope change in $V_{g_i} = f_1(V_{g_j})$ increases with difference in clip-gage position above the center of rotation $Z_{ij} = Z_i - Z_j$. (2) The same slope changes always occurred simultaneously on both traces $V_{g_i} = f_1'(V_{g_j})$ and $V_{g_i} = f_1''(V_{g_k})$; $k \neq j$. (3) While there were long-range or major slope changes in the $V_{g_i} = f_1(V_{g_j})$ diagrams, there were also local "ripples" of a short-range nature exactly coincident with sudden small increments of load drop (clearly found in cases not reported here-see Ref *13*). The potential-drop method in Fig. 7 also continued to overestimate the fracture initiation point significantly relative to the double-clip-gage method in the Al-4Zn-2Mg alloy, with rather dubious points of transition in the low-alloy steel specimens; see Fig. 8. The initial rise at low V_g in the latter case could be due to the opening of a tightly closed fatigue precrack, where surface asperities may have been in contact. Figure 9 provides a relative measure of the variability of the initiation point given by various methods relative to that of the double clip gage as $[(V_{g_i} - V_{g_A})/V_{g_A}] \times 100$ percent.

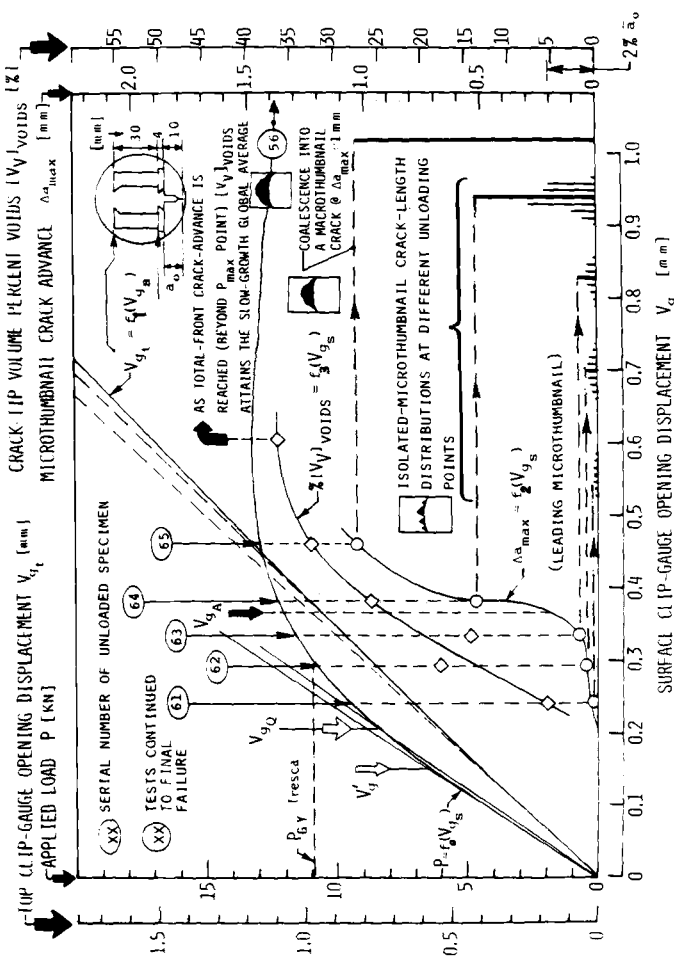

FIG. 4—*Unloading experiments in Alloy SB-1 using a series of fatigue precracked 10 by 20-mm three-point-bend specimens. Nos. 56 and 61–65. The correlation shows the coincidence of the double-clip-gage point of slope change at* V_{g_A} *with approximately 2 percent advance of the leading microthumbnail "spearhead." Note, however, the steadily increasing volume fraction of voids* V_V *shortly after the first deviation from linearity at* V_g*'. Vv tapers off to a steady-state value as* P_{max} *is approached. Note also that* V_{g_Q} *is much lower than the rapid fracture initiation point.*

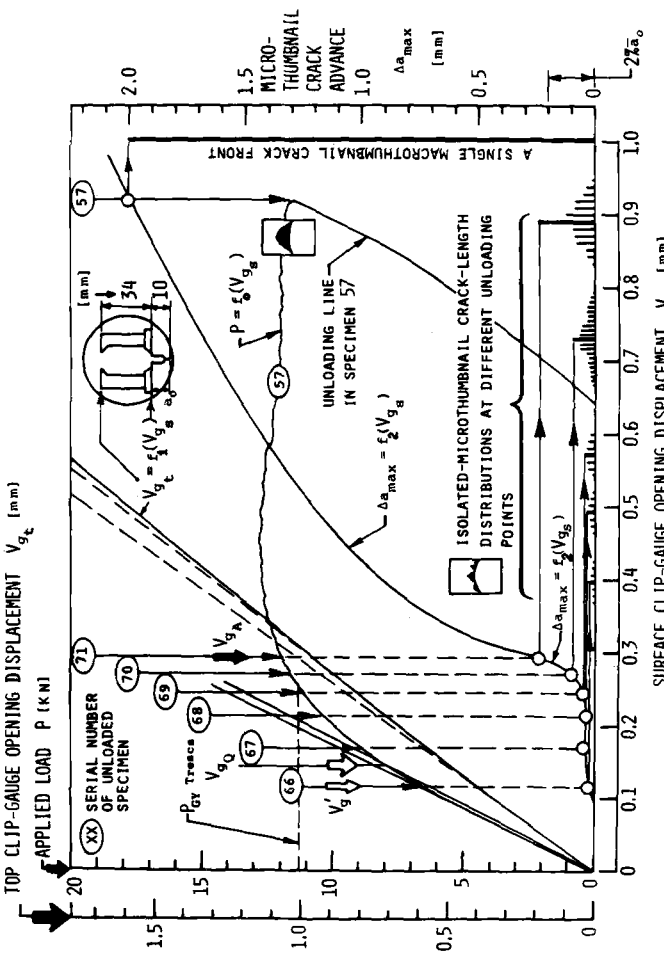

FIG. 5—*Unloading experiments in Alloy SVB-3 using a series of fatigue-precracked 10 by 20-mm three-point-bend specimens Nos. 57, and 66-71. The correlation shows the coincidence of the double-clip-gage point of slope change at* V_{g_A} *with approximately 2 percent advance of the leading microthumbnail (spearhead). Note that* V_{g_Q} *is far below the point of rapid thumbnail crack development.*

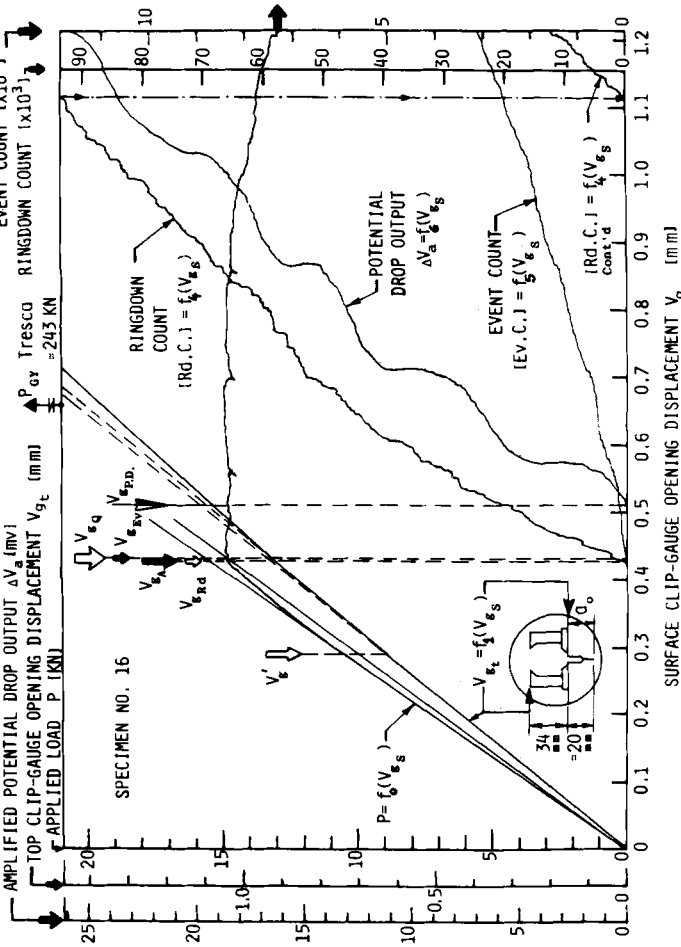

FIG. 6—*Correlation between various methods used for the detection of fracture initiation, namely, the double-clip-gage system output* $V_{g_t} = f_1(V_{g_s})$, *the potential-drop output* $\Delta V_a = f_6(V_{g_s})$, *the ringdown count* $[Rd\ C] = f_4(V_{g_s})$, *and event count* $[EV\ C] = f_5(V_{g_s})$ *in a 20 by 40-mm Al-Zn-Mg specimen, No 16. Note the lag of the potential-drop system relative to the double-clip-gage and acoustic emission systems, both of which are in good agreement with the* V_{g_Q} *point.*

While there is excellent agreement between the double clip gage, acoustic emission, and the Standard Offset Procedure in elastoplastic tests[5] as well as valid K_{Ic} tests, use of the Standard Offset Procedure in substandard or generally yielded specimens underestimates the initiation COD by a factor of up to 50 percent. At the same time, the potential drop tends to overestimate the initiation COD by a factor averaging 10 to 20 percent, and reaching as high as 50 percent.

Further work in this area should focus on developing additional evidence of the observed agreement between the double-clip-gage system and AE measurements using a broader range of materials. The potential-drop system has been used successfully by the authors in monitoring fatigue crack growth [*13,14*]. The reasons for its poor performance in monitoring monotonic crack growth in ductile materials are not obvious, although its response may be influenced by the nonuniformity of monotonic crack advance and the development of failure mechanisms ahead of the crack tip in the case of extensive plastic flow at relatively high loads.

Discussion and Conclusions

1. Comparison of the double-clip-gage device with the potential-drop or acoustic emission systems shows that for the detection of fracture initiation in single-specimen COD or K_{Ic} tests the device is more reliable and less costly. The entire AE or potential-drop systems, associated chart recorders, and digital voltmeters are replaced by an extra pair of knife edges, a clip gage, an additional clip-gage amplifier, and a single Y-Y-X recorder. The design is compact, simple to operate, employs standard clip gages, requires no temperature stabilization, and may be used over a range of temperatures.

2. Because it is a single-test method it reduces testing time and specimen costs.

3. The fracture initiation point has been validated using scanning electron microscopy of fracture surfaces. This procedure yields the following "indices of crack front advance" at the initiation point V_{g_A}: lineal advance $\Delta a_{max}\% \simeq$ 2 percent; normalized areal growth, $\Delta a_{eff}\% \simeq 0.25$ percent; and percent advanced crack tip, PACT% $\simeq$ 40 percent.

4. In terms of these indices the potential-drop system locates a transition point within 0 to +53 percent error (overestimate). Acoustic emission detects a point within −2 to +8 percent for the Al-4Zn-2Mg alloy studied. The Standard Offset Procedure predicts the initiation point with an error ranging from −3 to +15 percent in valid K_{Ic} tests, from −30 to +6 percent in the

[5]At least one of the tests using acoustic emissions in Fig. 9 was marginally valid in accordance with the ASTM Method E 399, while the remaining tests were not too remote from satisfying validity criteria. On this basis these tests have been described herein as "elastoplastic" rather than "quasi-elastic."

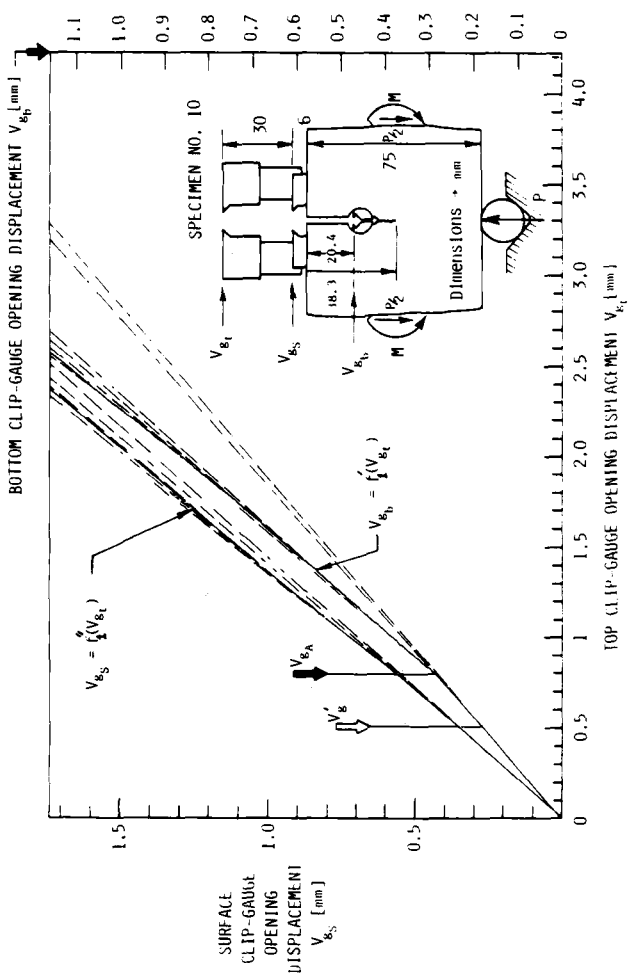
BOTTOM CLIP-GAUGE OPENING DISPLACEMENT V_{g_b} [mm]
SURFACE CLIP-GAUGE OPENING DISPLACEMENT V_{g_S} [mm]
TOP CLIP-GAUGE OPENING DISPLACEMENT V_{g_t} [mm]
$V_{g_S} = f_1(V_{g_t})$
$V_{g_b} = f_1'(V_{g_t})$
V_{g_A}
V'_g
SPECIMEN NO. 10
Dimensions : mm
30
6
75
20.4
18.3
P
M

(a)

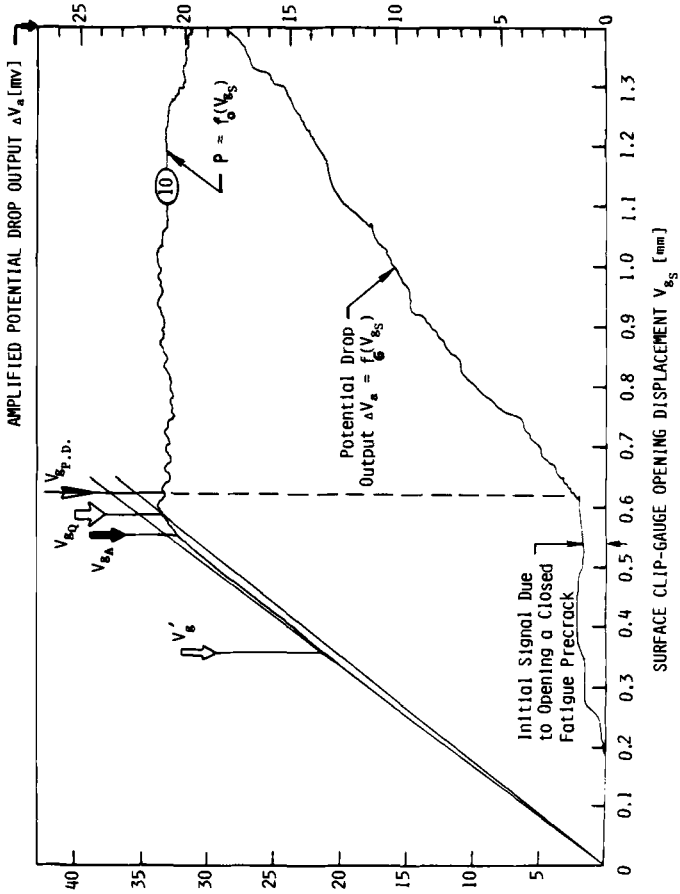

(b)

FIG. 7—*Common case of displacement-displacement and load-displacement diagram in high-strength Al-Zn-Mg alloy (Specimen No. 10) with only long-range slope changes, using a triple-clip-gage system as shown in* (a).

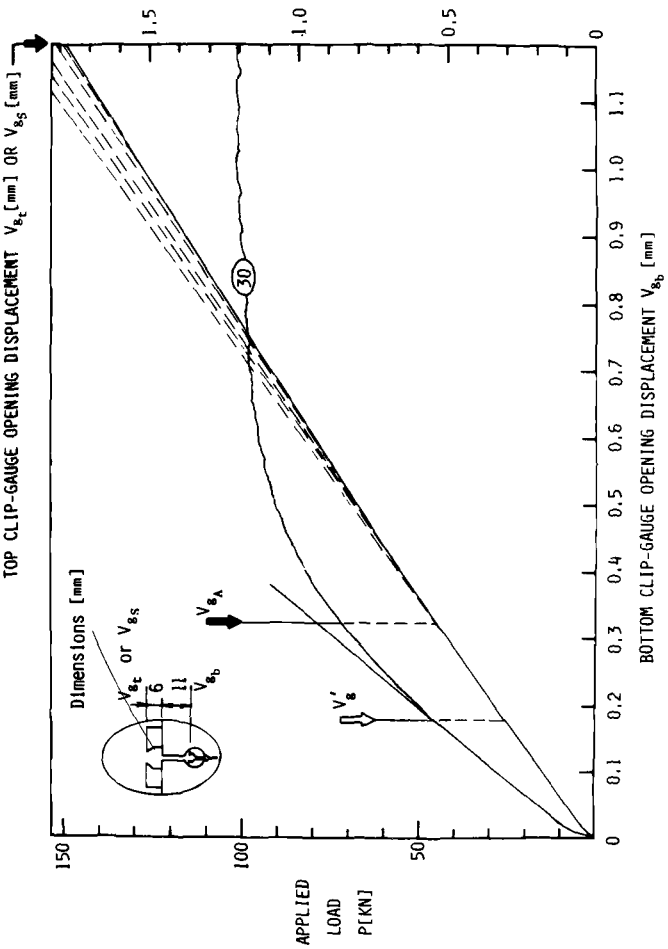
TOP CLIP-GAUGE OPENING DISPLACEMENT V_{g_t}[mm] OR V_{g_s}[mm]
1.5
1.0
0.5
0
150
100
50
APPLIED LOAD P[KN]
Dimensions [mm]
V_{g_t} or V_{g_s}
6
11
V_{g_b}
V_{g_A}
V'_g
30
0
0.1
0.2
0.3
0.4
0.5
0.6
0.7
0.8
0.9
1.0
1.1
BOTTOM CLIP-GAUGE OPENING DISPLACEMENT V_{g_b} [mm]

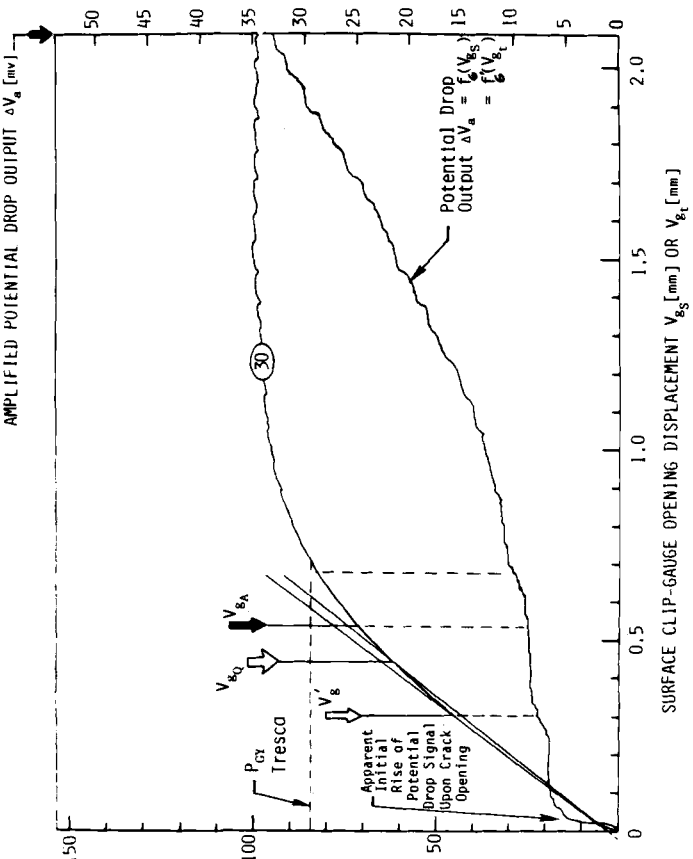

(b)

FIG. 8.—*Test data in a substandard fracture toughness specimen (30 by 60 mm) of a ductile low-alloy steel (Specimen No. 30). Beyond initiation at V_{g_A}, the slope change is almost gradual, which is also exhibited by the variations in the potential-drop trace in* (b) *with the latter lacking a clear definition of the initiation point.*

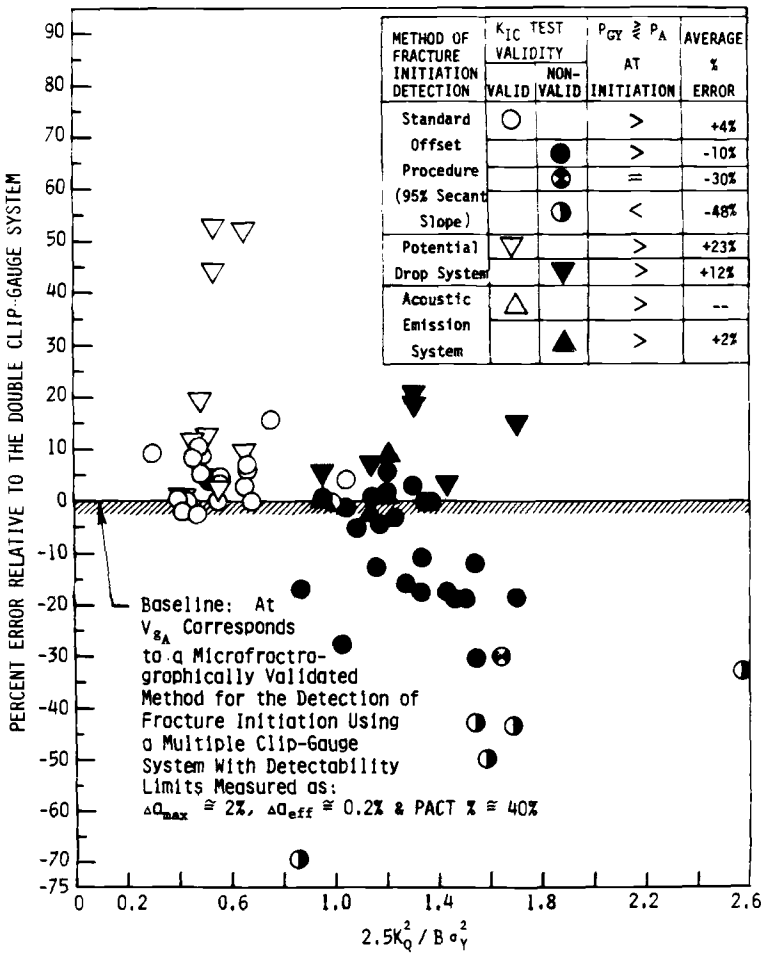

FIG. 9—*Assessment of the accuracies of various techniques for the detection of incipient crack growth in COD/K_{Ic} test specimens relative to the double- (or triple) clip-gage method which is validated by fractography (see Figs. 4 and 5).*

elastoplastic region, and from −70 to −30 percent if used in a generally yielded specimen.

Acknowledgments

This investigation was carried out in the United Kingdom at the Department of Metallurgy and Materials Science of the University of Cambridge. The authors are grateful to Professor R. W. K. Honeycombe for provision of research facilities. We wish to express our thanks to the Steel Castings Research and Trade Association and in particular to Drs. J. Jackson and K.

Selby for help with the preparation of low-alloy steel specimens. Particular thanks are also due to Dr. L. F. Coffin and the General Electric Corporate Research and Development Center for providing funds which helped in part to continue this investigation.

References

[1] Knott, J. F., *Fundamentals of Fracture Mechanics*, Butterworths, London, 1973, p. 140.
[2] "Methods for Crack Opening Displacement (COD) Testing," British Standards Institution (BSI), Draft for Development, No. 19, 1972; also BSI Draft for Public Comments, Document No. 78/71535 DC, 30 June 1978.
[3] Smith, R. F. and Knott, J. F. in *Proceedings*, Institute of Mechanical Engineers Conference on the Application of Fracture Mechanics to PV Technology, London, 1971, pp. 65-75.
[4] Klima, S. S., Fisher, D. M., and Buzzard, R. J., *Journal of Test Evaluation*, Vol. 4, 1976, pp. 397-404.
[5] Underwood, J. H., Winters, D. C., and Kendall, E. P. in *Proceedings*, Welding Institute Conference on the Detection and Measurement of Cracks, Abington, U.K., 1976, pp. 31-39.
[6] Lowes, J. M. and Fearnehough, G. D., *Engineering Fracture Mechanics*, Vol. 3, 1971, pp. 103-108.
[7] McIntyre, P. and Elliot, D., "A Technique for Monitoring Crack Extension During COD Measurement," BSC Report, MG/15/72, British Steel Corp., Rotherham, U.K.
[8] Selby, K. and Danson, P. J., "A Review of Recent Scrata Experience in COD Testing," Steel Castings Research and Trade Association Report No. 1872, Sheffield, U.K., Nov. 1977.
[9] "Proposed Recommended Practice for R-Curve Determination," *Annual Book of ASTM Standards*, American Society for Testing and Materials, Part 10, 1976, pp. 811-825.
[10] Tanaka, K. and Harrison, J. D., "An R-Curve Approach to COD and J for Austenitic Steel," Welding Institute Report No. E/73/76, Abington, U.K., 1976.
[11] Clark, G. and Knott, J. F., *Metal Science*, Vol. 11, 1977, pp. 531-536.
[12] Mishima, Y., Kishi, T., Park, K., Horiuch, R., and Saito, S. in *Proceedings*, Conference on the Physical and Metallurgical Aspects of Acoustic Emissions, London, Dec. 1977, pp. 19-21.
[13] El-Soudani, S. M., Ph.D. Thesis, University of Cambridge, U.K., 1980.
[14] Ritchie, R. O., Ph.D. Thesis, University of Cambridge, U.K., 1973.
[15] Ringshall, N. W., Ph.D. Thesis, University of Cambridge, U.K., 1978.

M. A. Khan,[1] *T. Shoji,*[1] *H. Takahashi,*[1] *and H. Niitsuma*[1]

Combined Elastic-Plastic and Acoustic Emission Methods for the Evaluation of Tearing and Cleavage Crack Extension

REFERENCE: Khan, M. A. Shoji, T., Takahashi, H., and Niitsuma, H., **"Combined Elastic-Plastic and Acoustic Emission Methods for the Evaluation of Tearing and Cleavage Crack Extension,"** *Elastic-Plastic Fracture: Second Symposium, Volume II—Fracture Resistance Curves and Engineering Applications, ASTM STP 803*, C. F. Shih and J. P. Gudas, Eds., American Society for Testing and Materials, 1983, pp. II-506–II-528.

ABSTRACT: A synergism between the acoustic emission and fracture mechanics techniques to predict failure in laboratory specimens of different structural materials is discussed. Emphasis is placed on situations in which fracture occurs by a cleavage crack propagation or controlled by the slow growth to fracture of a single crack. Results obtained during the tests indicate that acoustic emission is capable of detecting the onset of flaw growth and provide a precursor of the immediacy of fracture in a variety of steel and aluminum alloys. A new J/J_i key resistance curve procedure is developed for the evaluation of ductile fracture toughness (J_{Ic}) and tearing modulus with a single small specimen. Moreover, a new acoustic emission rating parameter for predicting tearing instability of elastic-plastic crack growth is proposed and related to the tearing modulus parameter.

KEY WORDS: elastic-plastic fracture, crack propagation, stable crack growth, structural steels, acoustic emission, cleavage fracture, tearing fracture, J contour integral

The focus of current research in elastic-plastic fracture mechanics (EPFM) is on material parameter test techniques for characterizing stable crack growth and instability conditions [*1*].[2] Both the J-integral criteria for onset of stable crack growth [*2*] and Paris tearing modulus (T) criteria [*1,3*] for stable crack growth and instability are based on the characterizing property of J for the

[1]Graduate student, associate professor, and professor, The Research Institute for Strength and Fracture Materials and associate professor, Department of Electrical Engineering, respectively, Tohoku University, Sendai 980, Japan; coauthor Khan is currently with the Pakistan Atomic Energy Commission, Islamabad, Pakistan.

[2]The italic numbers in brackets refer to the list of references appended to this paper.

crack-tip field. The work of Kumar and Shih [*4*] has shown promise that the *T*-concept can be made accessible to practical engineers and researchers as a design tool analogous to the linear elastic fracture mechanics (LEFM) toughness parameter.

In EPFM, however, some areas of uncertainty still exist. The limitations have been outlined in a specialists' meeting on plastic tearing instability [*5*] and include the following three main items.

1. The development of standard test methods for obtaining the basic material parameters with a single small specimen, especially for the irradiated conditions.
2. The prediction of instability conditions in structures, and the measurement of a fundamental *J* resistance curve that can be considered as a material property for a large amount of stable crack extension.
3. Characterization of fracture in the transition region where cleavage instability or interruption of stable crack growth by a change in fracture mode from ductile tearing to brittle (unstable) cleavage is observed.

The past few years have seen a great effort in the development of simple techniques to determine the onset of a stable crack extension. These include the unloading compliance method [*6*], the electrical potential method [*7*], the end-on ultrasonic method [*8*], the normalized *J* resistance curve procedure [*9-11*], and the acoustic emission (AE) method [*12-15*]. The AE techniques have also been used to monitor cleavage fracture [*16,17*] where a problem exists with the EPFM toughness evaluation [*18*]. The AE approach is preferred over other methods because it provides a continuous, remotely operated means of monitoring crack growth where aggressive environments or restricted accessibility impose limitations.

This study deals primarily with the limitations in EPFM methodology [*5*], with particular reference to nuclear surveillance programs. The feasibility of using the combined AE and EPFM techniques to procure the pertinent material parameters (such as J_{Ic} and tearing modulus) for different alloys from a single specimen is described. The applicability of AE for monitoring the initiation and propagation of cleavage microcracks is demonstrated. The invariance of a key *J* resistance curve for specimens of different geometries and sizes over a relatively large amount of crack extension is discussed.

Experimentation

Materials

Experiments were carried out on selected materials which exhibited either cleavage fracture, ductile-cleavage transition, large pop-in cracking, or stable ductile tearing. The materials involved in this investigation consisted of three different heats of AISI 4340 steel, turbine rotor forging steel nickel-

chromium-molybdenum-vanadium (Ni-Cr-Mo-V), a model steel [antinomy-doped nickel-chromium (Sb-doped Ni-Cr)], nuclear pressure vessel steel (SA533B), Type 304 stainless steel, and aluminum alloy 2024 T 351. The nominal chemical compositions, in percentage by weight, of the alloys studied are given in Table 1 and the mechanical properties in Table 2. The alloys had yield strengths ranging from 294 to 1790 MPa (43 to 260 ksi) at room temperature.

TABLE 1—*Chemical composition of tested alloys, % by weight.*

Material	C	Si	Mn	P	Ni	Cr	Mo	S	V	Cu
AISI 4340 steel, Heat 106	0.40	0.34	0.66	0.013	1.68	0.85	0.21	0.007	...	...
Ni-Cr-Mo-V steel	0.32	0.35	0.55	0.021	2.78	0.22	0.41	0.022	0.06	...
Ni-Cr steel	0.29	...	...	0.004	3.50	1.70	0.0035	...	...	...
AISI 4340 steel, Heat 001	0.41	0.25	0.67	0.012	1.72	0.82	0.26	0.005	...	...
AISI 4340 steel, Heat A	0.42	0.35	0.71	0.016	1.75	0.85	0.25	0.017	...	...
SA533B steel	0.17	0.20	1.48	0.011	0.58	0.16	0.52	0.006	0.003	0.13
304 stainless steel	0.06	0.63	1.22	0.031	8.41	18.05	...	0.008	...	...

	Mg	Si	Mn	Cu	Fe	Cr	Zn	Ti	Al
Al 2024 T 351	1.44	0.12	0.59	4.15	0.26	0.01	0.09	0.03	balance

TABLE 2—*Room temperature mechanical properties of steel and aluminum alloys.*

Material	Heat Treatment	Tensile Strength, MPa	0.2% Yield Strength, MPa	True Fracture Strain, %
AISI 4340 steel, Heat 106	...	950	774	...
Ni-Cr-Mo-V steel	...	700	540	22.8
Ni-Cr steel	aging for 10 h at 480°C	...	841	...
AISI 4343 steel, Heat 001	...	950	774	...
AISI 4340 steel, Heat A	tempering,			
	1 h at 200°C	1870	1790	22
	1 h at 600°C	1210	1140	30
SA533B steel	annealed for 40 h at 600°C	610	480	150
Type 304 stainless steel	...	647	294	...
Al 2024 T 351	...	489	375	14

NOTE—$°F = \frac{°C \times 9}{5} + 32.$

Fracture Test Methodology

The majority of the specimens used were of compact tension (CT) geometry having a thickness of 10, 25, 50 and 75 mm (0.4, 1, 2, and 3 in.). Some 10-mm-thick (0.4 in.) C-shape and 50-mm-thick (2 in.) bend bar (BB) specimens were also used. The details of heat treatment, size, and geometry of the specimens, and the orientation of the crack plane for each material, are given in Table 3. All tests were carried out at ambient temperature.

Elastic-plastic fracture toughness tests were carried out in an Instron-type screw-driven machine in accordance with the ASTM Test for Plane-Strain Fracture Toughness of Metallic Materials (E 399-78). Prior to testing, all specimens were fatigue precracked according to Method E 399 to crack lengths of 0.5 and 0.6 a/W, where a is the crack length and W the specimen width. Load was monitored against the displacement. A standard fracture

TABLE 3—*Summary of test matrix.*

Material	Heat Treatment	Orientation of Crack Plane[a]	Specimen Size and Geometry	a/W	Fracture Mode
AISI 4340 steel, Heat 106	...	T-L C-R	1T CT 0.5, C-shape	0.6 0.5	transgranular cleavage
Ni-Cr-Mo-V steel	as received, aged for 1000 h at 480°C	C-R C-R	1T CT 1T CT	0.5 0.5	transgranular cleavage
Ni-Cr steel	austenized for 1 h at 1025°C, tempered for 1 h at 600°C, and aged for 10 h at 480°C	C-R	modified 1T CT[b]	0.6	intergranular cleavage
AISI 4340 steel, Heat 001	...	T-L	1T CT modified 1T CT	0.6	ductile cleavage
AISI 4340 steel, Heat A	tempered for 1 h at 200°C tempered for 1 h at 600°C	C-R C-R	1T CT 0.4T CT 1T CT 0.4T CT	0.5 0.5	Ductile tearing (large pop-in)
SA533B steel	...	L-T	1T CT 2T CT 3T CT 1T BB[c] 2T BB	0.6	ductile tearing
Type 304 stainless steel	...	L-T	1T CT	0.5	ductile tearing
Al 2024 T 351	...	T-L	1T CT	0.5	ductile tearing (large pop-in)

[a]Crack plane orientation identification code; see ASTM Method E 399.
[b]12.5-mm thickness.
[c]BB = bend bar.

$$°F = \frac{°C \times 9}{5} + 32$$

mechanics clip on displacement gage was mounted on the knife edges in the load line of each specimen.

After testing, each specimen was heat-tinted and broken open in liquid nitrogen. Average measurements of initial crack length and the amounts of stable tearing were taken. The toughness was characterized by the J-integral using the method of J-calculation as per the ASTM Method for Determination of J_{Ic}, a Measure of Fracture Toughness (E 813).

Acoustic Emission Measurements

AE measurements were made with a conventional technique incorporating a piezo-electric transducer (NF Corp. AE 905S) to determine systematically the relative emission activity of different materials. The transducer is a broad-band type with a resonance frequency close to 1 MHz. The preamplified (40 dB) signals were bandpass-filtered between 2 kHz and 1 MHz, and further amplified with a variable broadband amplifier which provided an additional gain of 20 dB. These amplified signals were fed into a distribution analyzer to perform event counting of acoustic pulses according to their peak amplitude. The AE energy measuring instrumentation was used so that a measure of the energy of an emission (E_{AE}) could be obtained [*19-21*]. In some of the experiments, however, the square of the peak voltage (V^2_{o-p}) was used as a measure of energetical quantity because good correlation exists between V^2_{o-p} and energy measured with conventional energy processing equipment [*20*]. The analyses were carried out both on-line in real-time, and off-line on signals stored on magnetic tape of a modified videotape data recorder (Sony Model AV 8750). The electrical signal was also continuously monitored on an oscilloscope. Details of the detection, recording, and data handling system are given in Ref *21*.

Results

Application of Acoustic Emission to Cleavage and Tearing Fracture Monitoring

The ability of fracture mechanics to assess accurately the safety of a flawed component would be greatly enhanced if accurate flaw size could be estimated. Several researchers have expressed their disappointment in panel discussions [*22*] on the number of contributions devoted to nondestructive testing (NDT). It is generally agreed that without accurate NDT to inspect components during manufacture and in service, accurate fracture mechanics methodology would be of limited use with the present state of the art [*22*]. Therefore, the feasibility of using available AE instrumentation for the detection of cleavage and tearing crack extension in laboratory specimens of different materials should be examined.

Cleavage Fracture—Tests covered both low- and high-toughness materials. The results for Ni-Cr-Mo-V [in as-received condition and aged at 480°C (896°F) for 1000 h], AISI 4340 (Heat 106), and Ni-Cr steels which exhibit transgranular or intergranular cleavage fracture when tested at room temperature, are presented in Figs. 1 and 2. The summation of AE energy ΣE_{AE} is plotted against J. Almost all the test specimens fractured in the linear-elastic region of the load/displacement curve without any indication of stable crack growth on a macroscopic scale. The energetic emissions with a peak amplitude >1 V_{o-p}, in the main, were generated after the attainment of a load level almost half of the final fracture point. These high-amplitude signals, which are responsible for the divergence of the AE energy versus J-curve in Figs. 1 and 2, are tentatively associated with the formation of cleavage microcracks in the vicinity of the crack tip.

AE activity is the highest for Sb-doped Ni-Cr steel as shown in Fig. 2. The scanning electron microscope (SEM) studies have demonstrated that the fracture surface is predominantly intergranular cleavage (Fig. 3) where the crack runs along heavily segregated boundaries and results in a large number

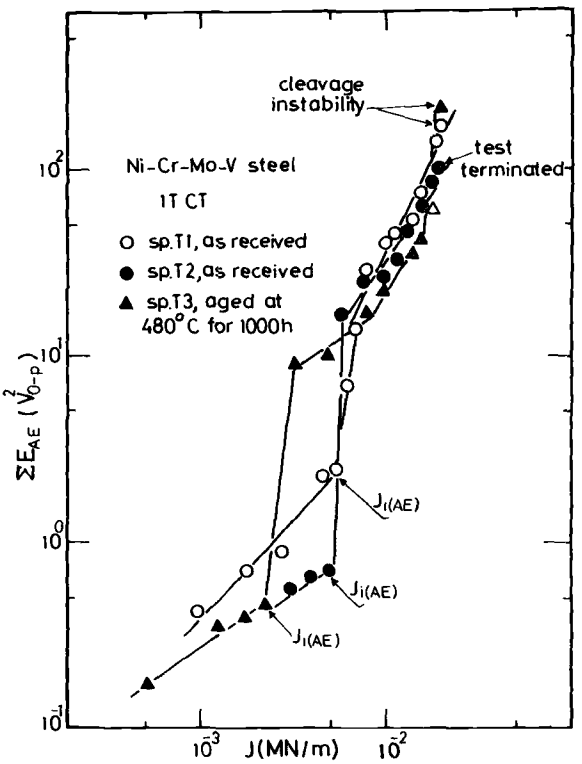

FIG. 1—*Accumulated AE energy plotted as a function of J for Ni-Cr-Mo-V steel.*

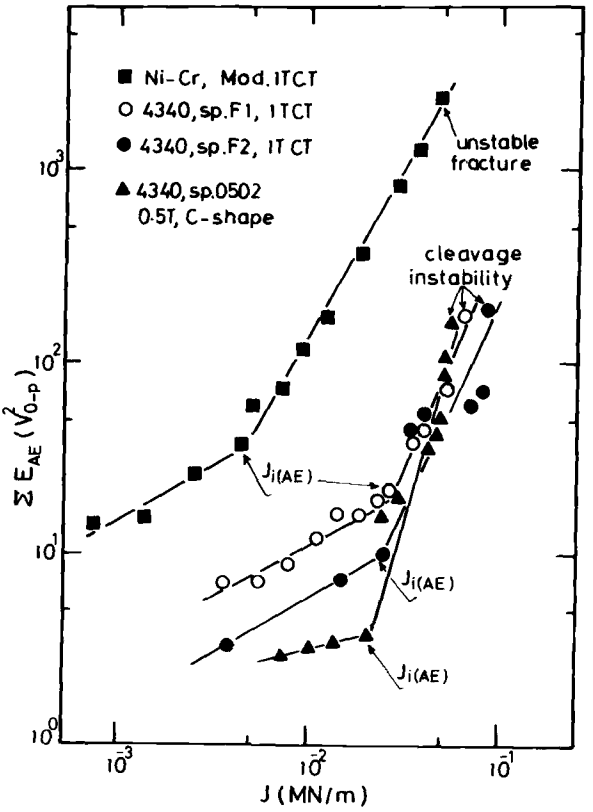

FIG. 2—*Accumulated AE energy plotted as a function of J for Ni-Cr and AISI 4340 (Heat 106) steels.*

of energetic emissions [*17*]. Furthermore, to confirm that cleavage microcracking indeed contributes to the emission of such large-amplitude signals, some of the tests were terminated immediately prior to final fast fracture [*17*]. The test on Specimen T-2 of Ni-Cr-Mo-V steel in the as-received condition was terminated after a rapid increase in AE events with large amplitude had occurred, unloaded, and fatigue postcracked at low ΔK. The cleavage microcracks were examined in the SEM. One of the cleavage microcrack locations between fatigue-precrack and postcrack regions is shown in Fig. 4. The region marked by B indicates that the specimen exhibited some plasticity before cleaving. It appears that a relatively low activity of AE just before the $J_{i(AE)}$ point is caused by cracking or decohesion of nonmetallic inclusions present in the parent phase (marked by I in Fig. 4).

These experimental results demonstrate that the AE signals serve as a precursor of transgranular or intergranular cleavage cracking. From this it implies that a conservative value of J_c corresponding to the first brittle crack

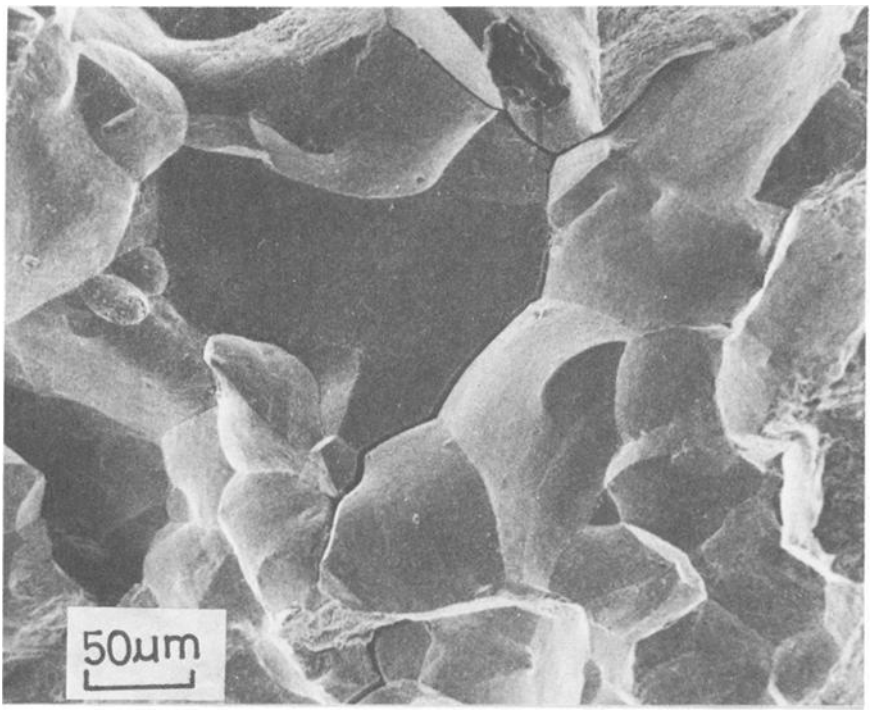

FIG. 3—*Fracture surface of Sb-doped Ni-Cr steel; crack growth occurred by intergranular cleavage.*

extension could be estimated with the AE techniques. This approach looks very promising for dealing with the problem of small specimen toughness results in the transition region where the possibility of specimen size effect exists [*18,23*].

A comparison of the J_c-values corresponding to the point of the final cleavage fracture and $J_{i(AE)}$ for different alloy steels is given in Table 4. The values of $J_{i(AE)}$ are almost identical for specimens of different geometry and size of AISI 4340 steel (Heat 106), whereas there is a considerable specimen size effect on J_c-values for cleavage fracture. However, additional work with different specimen geometries and sizes is required to draw some definite conclusions.

Tearing Fracture—The simultaneous registration of AE together with load and displacement during J resistance curve tests has been used for detection of ductile tearing in AISI 4340 (Heats A and 001) and SA533B steels and 2024 T351 aluminum alloy. Figure 5 presents the summation of AE energy ΣE_{AE} plotted against J. The high activity of AE results in two distinct regions of the curve for all the alloys investigated. The resulted bilinear nature of the ΣE_{AE} versus J curve indicates the advance of ductile crack at the point marked as $J_{i(AE)}$. Unstable crack extension for an 1T CT specimen of AISI 4340 steel

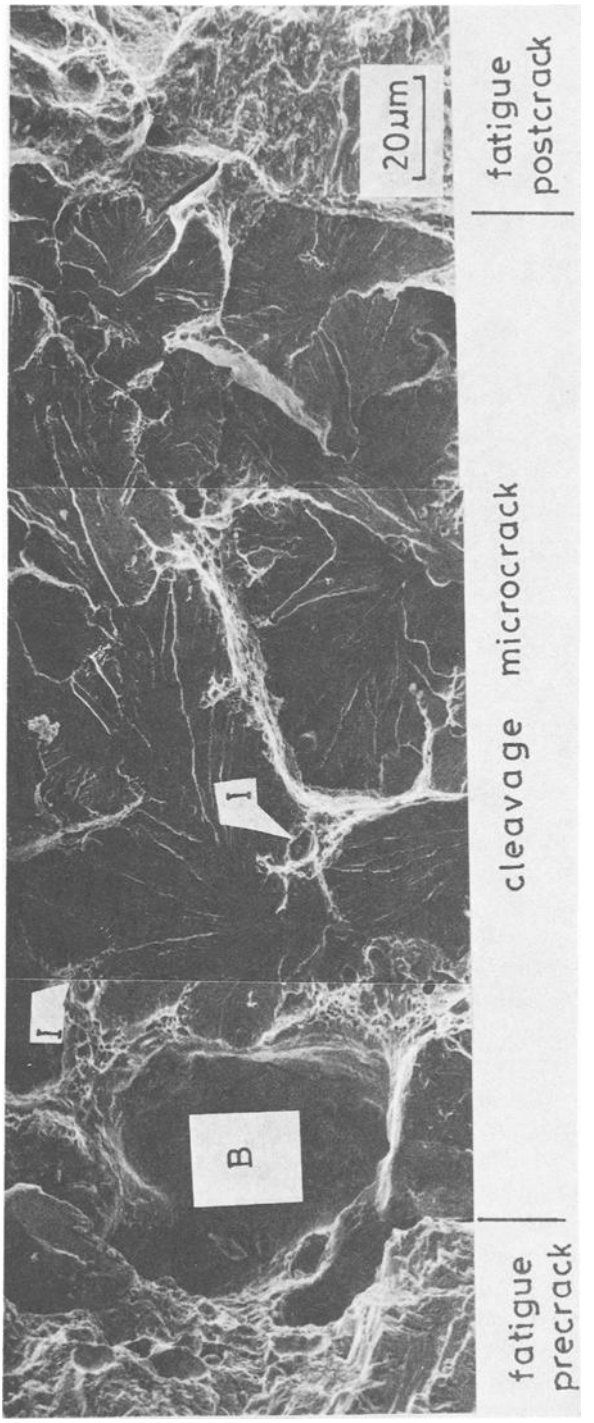

FIG. 4—*Formation of cleavage facets at the fatigue crack tip immediately prior to final fracture (material: NI-Cr-Mo-V steel).*

TABLE 4—*A comparison of the* J_c *corresponding to the final cleavage fracture and* $J_{i(AE)}$*-values for AISI 4340, Ni-Cr, and Ni-Cr-Mo-V steels.*

Material	Specimen No.	Specimen Geometry and Size	J_c, MN/m	$J_{i(AE)}$, MN/m	Remarks[c]
	F1	1T CT	0.062	0.029	TGC
	F2	1T CT	0.090	0.026	stable crack = 0.050 mm
AISI 4340	CS 0501	0.5T, C-shape	0.050	...	...
steel,	CS 0502	0.5T, C-shape	0.090	0.026	stable crack = 0.050 mm
Heat 106	CS 0504	0.5T, C-shape	0.039	0.020	TGC
Ni-Cr steel	K-1	modified 1T CT[a]	0.047	0.005	IGC
Ni-Cr-Mo-V	T-1	1T CT	0.0197	0.0054	TGC
steel (as received)	T-2	1T CT	0.019[b]	0.0050	TGC
Ni-Cr-Mo-V steel (aged at 480°C for 1000 h)	T-3	1T CT	0.020	0.0023	TCG

[a]Thickness = 10 mm.
[b]Test terminated.
[c]TGC = transgranular cleavage.
IGC = intergranular cleavage.

$$°F = \frac{°C \times 9}{5} + 32$$

[Heat A, 200°C (392°F) tempered] occurred at the maximum load level. In case of Heat 001 of 4340 steel, a stable crack extension of 1.5 to about 2 mm (0.06 to 0.08 in.) was observed prior to final cleavage fracture. A rapid increase in ΣE_{AE} clearly defines stable crack growth for both 2T CT and 2T BB specimens of SA533B steel presented in Fig. 5.

The experimental observation that high AE activity at the $J_{i(AE)}$ point corresponds to the onset of a stable crack extension needs confirmation by some standard procedure. A generally applicable method for calibration of interrupted loading test series was used to construct the crack resistance curves presented in Figs. 6 and 7. The values of J_{Ic} and $J_{i(AE)}$ determined from the J resistance curve and AE techniques are compared in Table 5 and show a reasonable agreement, although there is observed a considerable scatter in $J_{i(AE)}$ for high-toughness steels such as SA533B steel.

In some circumstances, however, it has been shown [*24,25*] that the detection of the onset of crack extension with the AE method in laboratory specimens of tough steels may not be achieved as these materials release few emissions during crack growth. Type 304 stainless steel is one example considered here. The summation of AE energy ΣE_{AE} from the tests on 1T CT specimens of Type 304 steel is plotted as a function of J in Fig. 8. Despite the large number of AE events emitted, it seems difficult to detect macrocrack initiation with the AE method in either of the two specimens. The J resistance curve in Fig. 9 is developed and a critical J-value of 0.3 to 0.4 MN/m (1700 ~ 2300

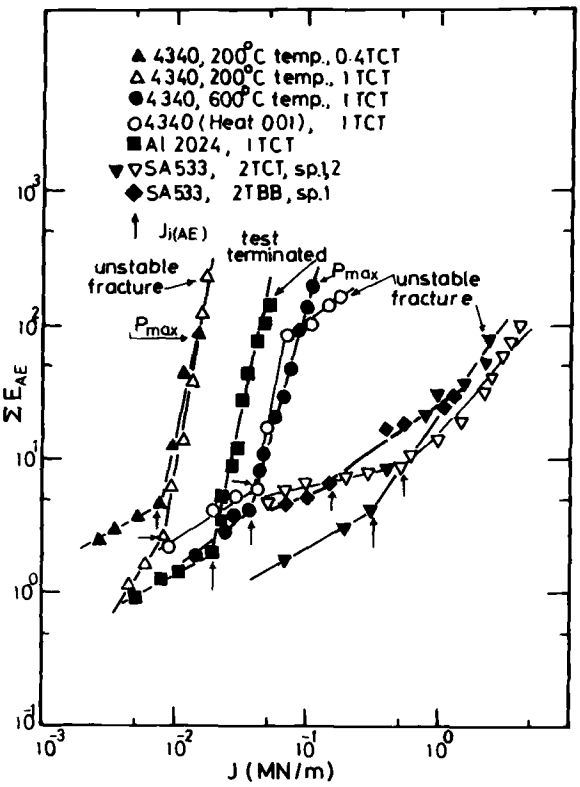

FIG. 5—*Accumulated AE energy plotted as a function of J for Al 2024, AISI 4340 steel (Heats A and 001), and SA533B steel.*

lb/in.) is deduced. An explanation based on silent crack growth in small specimens of 304 stainless steel offers one rationale. While further studies are needed to resolve such problems, it is the authors' opinion that some simple procedure (based on the J resistance curve technique) for J_{Ic} determination of high-toughness materials should be developed.

A New Approach for the Measurement of Crack Growth Resistance

The material J R-curve is an essential element of the instability analysis of elastic-plastic crack growth. The tearing modulus, T_{mat}

$$T_{mat} = (E/\sigma_Y^2)\frac{dJ}{da} \tag{1}$$

proposed by Paris and co-workers [*1*] exploits the consequences of the J-controlled crack growth—that the J resistance curve is independent of the

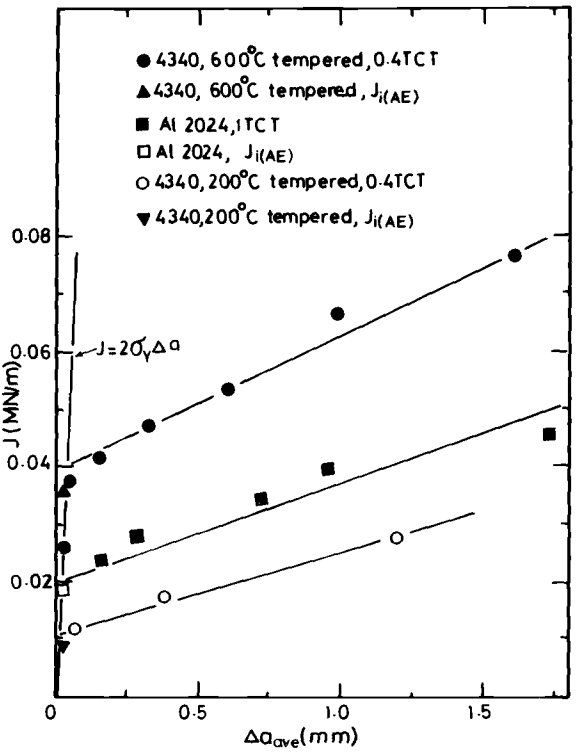

FIG. 6—J *versus* Δa *for AISI 4340 steel and Al 2024 comparing* J_{Ic} *and* $J_{i(AE)}$.

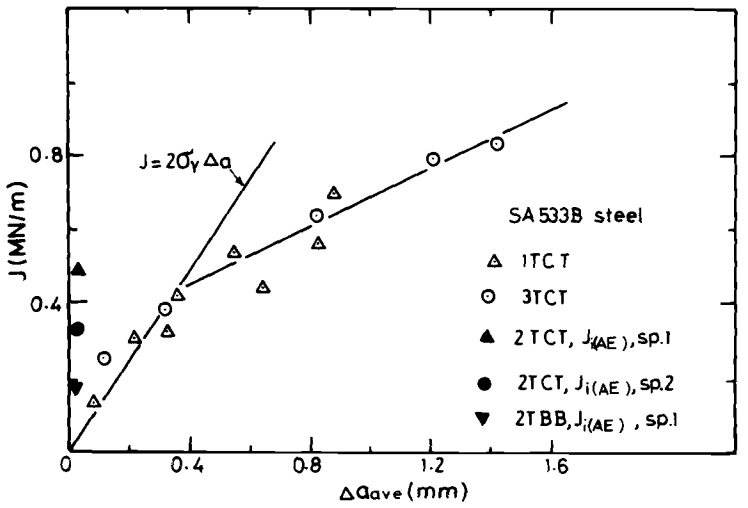

FIG. 7—J *versus* Δa *for SA533B steel comparing* J_{Ic} *and* $J_{i(AE)}$.

TABLE 5—*A comparison of J_{Ic} values determined from the AE and multispecimen J resistance curve techniques.*

Material	Heat Treatment	Specimen Size and Geometry	$J_{i(AE)}$, MN/m	$J_{i(0.2\ mm)}$, MN/m	$J_{Ic(E\ 813\text{-}81)}$, Mn/m
AISI 4340 steel, heat A	200°C tempered	0.4T CT	0.008	0.0013	0.0011
		1T CT	0.0076 ~ 0.008		
	600°C tempered	0.4T CT	0.033	0.043	0.040
		1T CT	0.034 ~ 0.036		
AISI 4340 steel, heat 001	...	1T CT modified	0.035 ~ 0.042	...	0.065
		1T CT			
		1T CT	0.32 ~ 0.50		
SA533B steel		2T CT	0.35 ~ 0.52		
		3T CT	...	0.35	0.40±0.08
		1T BB	0.18 ~ 0.40		
		2T BB	0.15		
Type 304 stainless steel	...	1T CT	...	...	0.3 ~ 0.4
Al 2024	...	1T CT	0.019	0.021	0.024

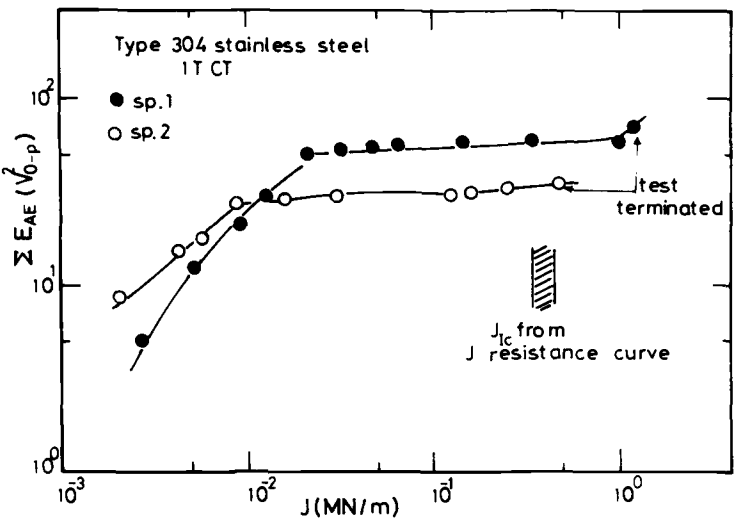

FIG. 8—*Accumulated AE energy plotted as a function of J for Type 304 stainless steel.*

size and geometry of the specimen. While single-specimen procedures for the evaluation of J_{Ic} are being considered [*2*], it is useful at this stage to develop a simpler, single-specimen procedure for estimating J_{Ic} and T_{mat}. This new approach is based on the application of a J/J_i-Δa experimental key curve [*9-11*].

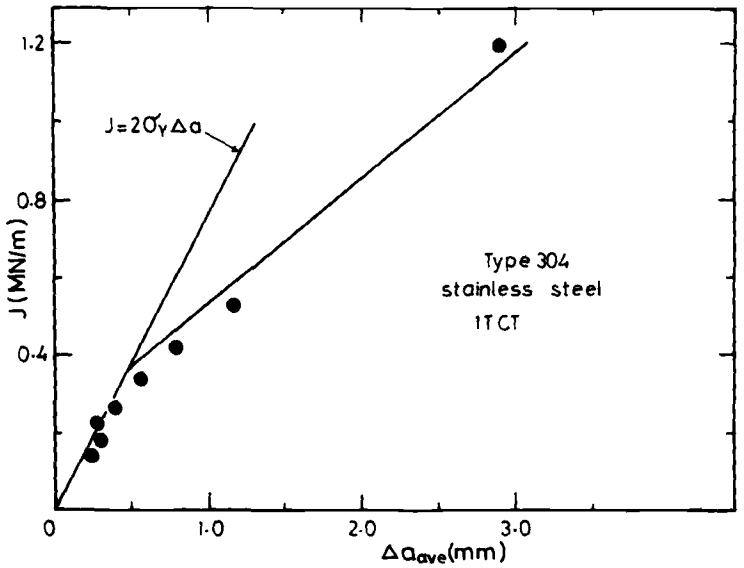

FIG. 9—J *versus crack growth for compact specimens of Type 304 stainless steel.*

It has been found convenient to treat the normalized R-curve as an average straight line for $\Delta a > 0.2$ mm (0.008 in.) [*10*]. Below this value of crack extension, the J/J_i-Δa curve appears to follow a power law as tearing progresses. The curve can be fitted approximately by the expression [*9-11*]

$$J_i = J/(\beta \Delta a + 1) \tag{2}$$

where $\beta = 857\ m^{-1}$ is the slope of the J/J_i-Δa line after the point of crack extension and is independent of material and test temperature. Equation 2 can be rewritten as

$$J = J_i + \beta \Delta a J_i \tag{3}$$

In terms of the rate of change of J with crack growth, Eq 3 reduces to

$$dJ/da = \beta J_i \tag{4}$$

where $J_i \simeq J_{Ic}$ [*9, 10*], and corresponds to a crack extension of 0.2 mm (0.008 in.). Table 6 provides some typical examples to demonstrate the usefulness of single-specimen determination of J_i-values corresponding to J_{Ic} for 2024 T351 and SA533B-1. Here, the individual values of $J_{i(\Delta a=0.2\ mm)}$ are compared with J_{Ic} determined from the R-curve method. It is shown that there is fairly good agreement between J_{Ic} and $J_{i(0.2\ mm)}$. Thus, Eqs 2 and 4 permit the use of a single specimen to predict initiation toughness (J_i) and the resistance

TABLE 6—*Some examples of single-specimen J_{Ic} determination.*

Materials	J, MN/m	Δa, mm	$J_{i(\Delta a=0.2\ mm)}$, MN/m		$J_{Ic(E\ 813\text{-}81)}$, MN/m
	0.028	0.278	0.0226		
2024 T351	0.034	0.714	0.0210	avg	0.020±0.004
(1T CT)	0.039	0.950	0.0215	0.0207	
	0.044	1.72	0.0178		
	0.380	0.32	0.298		
SA533B-1	0.630	0.81	0.372		
(3T CT)	0.795	1.20	0.392		
	0.830	1.42	0.374	avg	
				0.331	0.40±0.08
	0.30	0.21	0.254		
	0.32	0.32	0.251		
	0.415	0.36	0.317		
(1T CT)	0.44	0.64	0.284		
	0.54	0.55	0.357		
	0.56	0.82	0.329		
	0.70	0.87	0.401		

[a]Determined by equation $J_{i(\Delta a=0.2\ mm)} = J/(\beta \Delta a + 1)$.

of material to stable growth (dJ/da) from a knowledge of the J and Δa values at the point of test termination.

Currently, conclusive proof is lacking that the J resistance curve can be considered as a basic material property for a relatively large amount of crack extension. Figure 10 demonstrates the normalized J resistance curve (J/J_i versus Δa) for relatively large amounts of crack extension for different CT and BB specimen geometries and sizes. In addition to the experimental data of this study, J R-curves previously developed [*6, 10, 26-30*] are also included. Note that all the data for different geometries and sizes lie in a narrow scatterband, which indicates an invariant relationship between the critical property for crack initiation J_i and the tearing resistance dJ/da. These data support the view that the J resistance curve is independent of specimen size and geometry (CT and BB) provided validity criteria for the J resistance curve [*3, 10*] are satisfied and crack extension increments are limited to 6 percent of the unbroken ligament [*4*]. Although further work is necessary to draw any firm conclusions, it is nevertheless considered to be the most direct indication that a fundamental J R-curve can be considered a basic material property.

The experimental scatter, though seemingly large at first glance, is not unlikely because of inherent material scatter. The test data developed by the ASTM cooperative research program [*26*] for a single heat of HT 130 steel exhibited a scatter of ±20 percent on J_{Ic} and ±30 percent on dJ/da, attributed to the material inhomogeneity.

Tearing Fracture and Acoustic Rating Parameter

For materials which fracture by ductile tearing, the values of J_i and tearing modulus can be estimated conveniently from a single specimen by the J/J_i

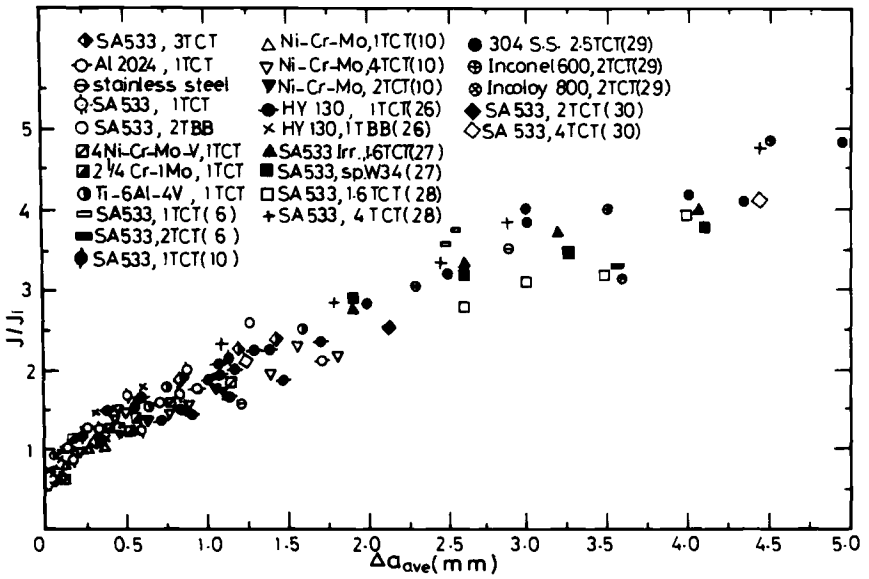

FIG. 10—J/J_i *versus* Δa *key curve for various materials.*

resistance curve technique. The use of AE along with the J/J_i key resistance curve procedure may significantly reduce the number of specimens that is required for the determination of J_{Ic} and tearing modulus.

Recently, a new AE rating parameter (severity parameter of crack) T_{ac} has been proposed [*11,32*] to estimate the ductile tearing resistance in a specimen or component, given by

$$T_{ac} = (\Sigma E_{AE}/B)/\Delta J \tag{5}$$

where B is the specimen thickness, and ΔJ the difference of J-values corresponding to P_{max} on the load/deflection curve and J_i. Furthermore, of interest here is a close relationship between T_{ac} and T_{mat}, given as

$$T_{ac} \cdot T_{mat} = k \quad \text{(a constant)} \tag{6}$$

Since T_{ac} takes into account the *in situ* changes in material properties, both T_{ac} and T_{mat} should be used for treating instability problems. A brief description of the AE rating parameter T_{ac} (presented in Eq 5) and correlation of Eq 6 is given in the Appendix. Figure 11 shows an experimental correlation between T_{ac} and T_{mat} for several steel and aluminum alloys that exhibit ductile tearing. Note that high-T_{ac} materials are materials that are most readily fractured and have low T_{mat}. For example, low-toughness materials such as quenched-and-tempered AISI 4340 steel having $T_{mat} < 10$ exhibit the highest T_{ac} where the crack instability in 0.4 and 1T CT specimens fol-

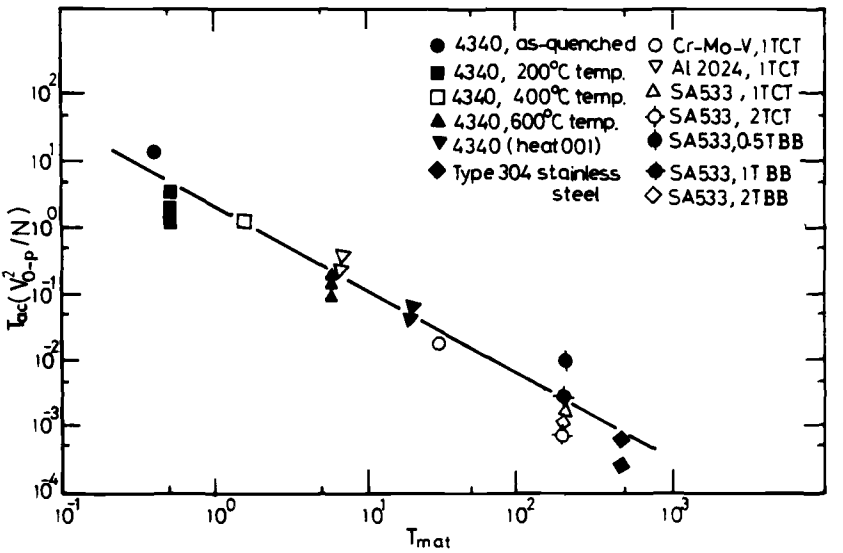

FIG. 11—*Relationship between acoustic emission rating parameter and tearing modulus for laboratory specimens.*

lowed the crack initiation almost immediately. In contrast, high-toughness materials such as Type 304 stainless steel and SA533B steel ($T_{mat} > 200$) show a minimum in T_{ac}. This indicates that the relative values of T_{ac} reflect the resistance of commercial alloys to the tearing instability.

Summary and Conclusions

Studies of cleavage and ductile stable crack extension have been carried out with EPFM and AE techniques for different steels and aluminum alloys (AISI 4340, Ni-Cr-Mo-V, Sb-doped Ni-Cr, SA533B, and Type 304 stainless steel; and Al 2024 T 351). The results have shown that many failure-related gross material properties which influence the crack propagation resistance of a material produce measurable changes in AE activity. The initial experiments on AISI 4340 (Heat 106), Ni-Cr, and Ni-Cr-Mo-V steels indicate the unique capabilities of the AE signals as a precursor of transgranular of intergranular cleavage cracking. It is shown that initiation toughness $J_{i(AE)}$ corresponding to the onset of the first brittle crack extension can be used as a conservative estimate of fracture toughness.

Further development and subsequent application of the J/J_i key resistance curve procedure for an assessment of the J_{Ic} and tearing modulus from a single specimen have been demonstrated. The evidence of the normalized key resistance curve has been taken from the experimental data for a variety of structural steels and aluminum alloys. The limited amount of data presented

support the view that the J resistance curve is a material property provided validity criteria for the curve are satisfied and crack extension increments do not exceed 6 percent of the unbroken ligament. The pursuit of AE techniques during EPFM J resistance curve studies has shown promising results in providing predictive information of the onset of a stable crack extension in ductile tearing situations.

Based on the experimental results, it is further concluded that the AE method allows for continuous monitoring of the crack growth for the whole duration of the test. A new AE rating parameter T_{ac} is proposed and related to the tearing modulus parameter to predict tearing instability of elastic-plastic crack growth.

Acknowledgments

The authors wish to thank Professor M. Suzuki of the Toyota Technological Institute for many discussions throughout the course of this investigation. Appreciation is expressed to Professor C. J. McMahon, Jr., and Dr. J. Kameda of the University of Pennsylvania for the provision of the Ni-Cr steel used in this investigation. Financial support from the Ministry of Education, Science and Cultural Affairs of Japan for one of the authors (M. A. Khan) is gratefully acknowledged.

APPENDIX

Acoustic Emission Rating Parameter, T_{ac}

To demonstrate that the AE method allows for quantitative measurements, the accumulated AE energy ΣE_{AE} is related to the area of crack advance ΔA in Fig. 12. These curves can be represented by an empirical relationship

$$\Sigma E_{AE} = \alpha(\Delta A)^{1.5} \tag{7}$$

where α depends on material's toughness and system gain.

The dependence of α on initiation toughness J_i is depicted in Fig. 13, expressed as

$$\alpha = \alpha'/J_i \tag{8}$$

where α depends on AE instrumentation.

From Eqs 7 and 8,

$$\Sigma E_{AE} \cdot J_i = \alpha'(\Delta A)^{1.5} \tag{9}$$

where $J_i \simeq J_{Ic}$.

Equation 9 indicates that it is possible to construct a single key calibration curve for different structural materials provided the toughness parameter is introduced.

Figure 14 shows $\Sigma E_{AE} \cdot J_i$ plotted versus ΔA in which most replicate tests show a fairly close agreement.

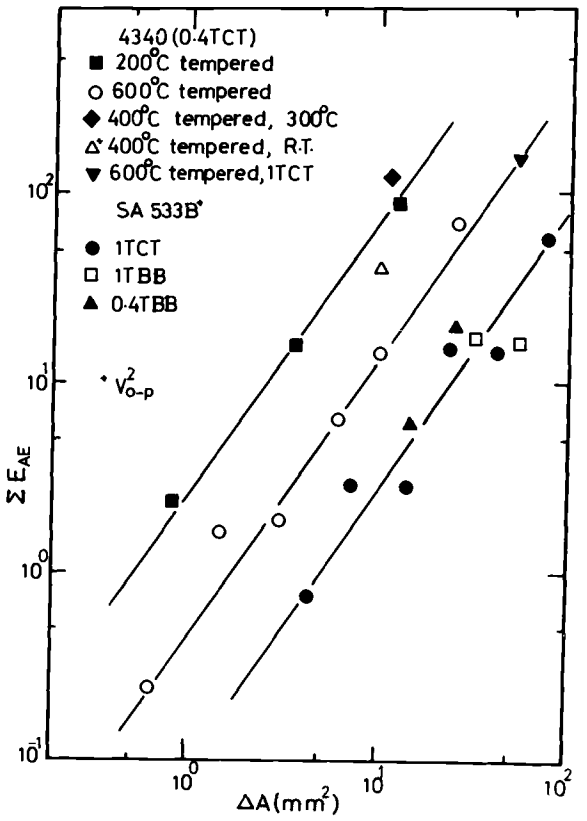

FIG. 12—*Accumulated AE energy as a function of crack area for alloy steels.*

It is possible to correlate upper-shelf toughness with changes in flow properties [*32*], though with some reservations.[3] Figure 15 shows dependence of J_i on $E/\sigma_Y{}^2$, correlated as

$$J_i = \gamma\left(\frac{E}{\sigma_Y{}^2}\right)^{1.5} \tag{10}$$

where $\sigma_Y = (\sigma_{uts} + \sigma_{ys})/2$ and Y is a constant.

From Eqs 9 and 10, we obtain

$$\frac{(\Sigma E_{AE})^{0.67}}{\Delta A}\frac{E}{\sigma_Y{}^2} = k \tag{11}$$

Equation 11 can be expressed as

[3]Segregation of solutes to surfaces, alterations in interface morphologies, carbide phase redistribution, and the presence of nonmetallic inclusions may not influence flow properties but could have a profound impact on toughness and ductility.

$$\left\{\frac{(\Sigma E_{AE})^{0.67}/B}{\Delta J}\right\}\frac{E}{\sigma_Y^2}\cdot\frac{\Delta J}{\Delta a}=k \tag{12}$$

where

$\Delta A = B\Delta a$,
B = specimen thickness,
Δa = average crack growth, and
ΔJ = difference of J-values corresponding to P_{max} on load/deflection curve and J_i.

The term

$$\left\{\frac{(\Sigma E_{AE})^{0.67}/B}{\Delta J}\right\}$$

in Eq 12 can be used in its general form $\{(\Sigma E_{AE}/B)/\Delta J\}$ and is termed an acoustic rating parameter

$$T_{ac}=\frac{\Sigma E_{AE}/B}{\Delta J} \tag{13}$$

Hence, the close relationship between the AE rating parameter T_{ac} and tearing modulus (T_{mat}) in Eq 12 can be phrased

$$T_{ac}\cdot T_{mat}=k \quad \text{(a constant)} \tag{14}$$

where k (a constant) depends only upon the AE electronic instrumentation.

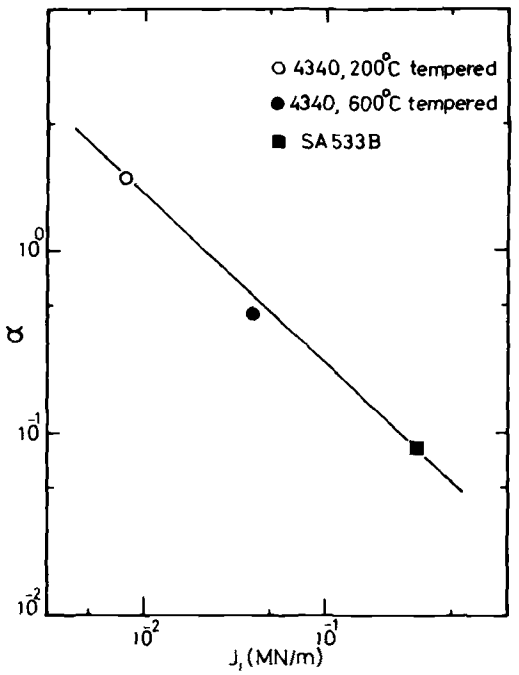

FIG. 13—*α plotted as a function of J_i for AISI 4340 and SA533B steels.*

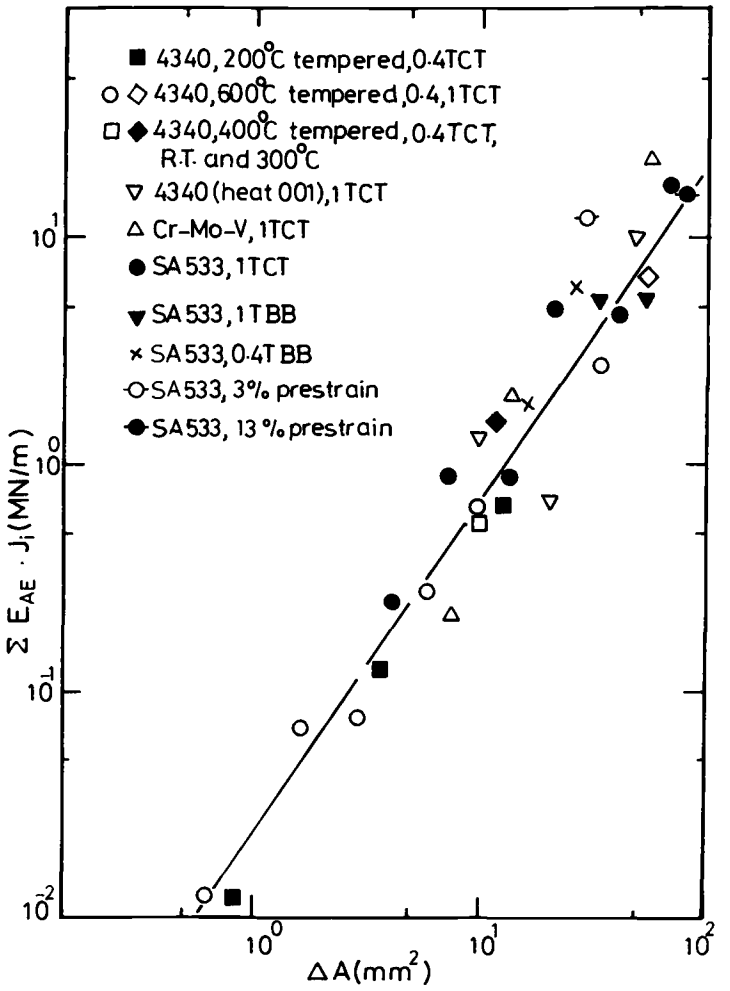

FIG. 14—($\Sigma E_{AE} \cdot J_i$) *versus stable crack growth area for different alloy steels.*

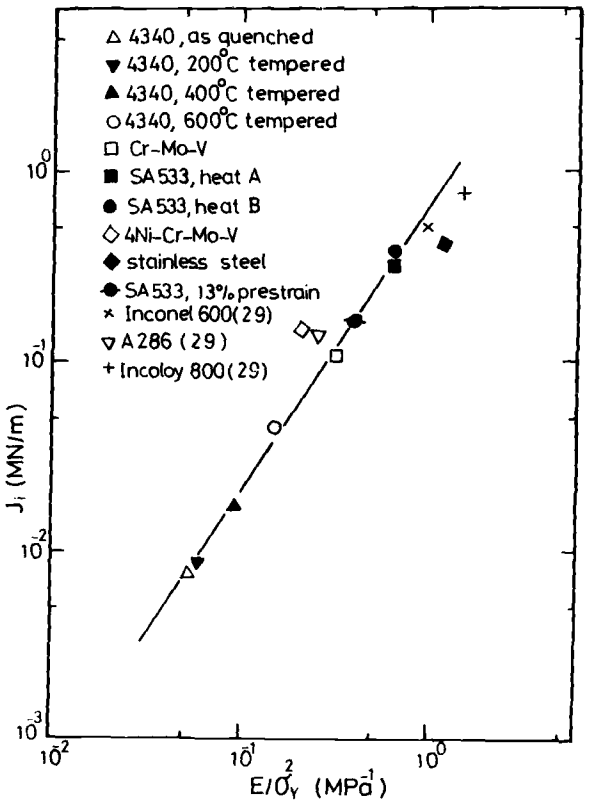

FIG. 15—J_i *plotted as a function of* E/σ_Y^2 *for various materials.*

References

[1] Paris, P. C., Tada, H., Zahoor, A., and Ernst, H. in *Elastic-Plastic Fracture, ASTM STP 668*, J. D. Landes, J. A. Begley, and G. A. Clarke, Eds., American Society for Testing and Materials, 1979, pp. 5-36.

[2] Clarke, G. A., Andrews, W. R., Begley, J. A., Donald, J. K., Embley, G. T. Landes, J. D., McCabe, D. E., and Underwood, J. H., *Journal of Testing and Evaluation*, Vol. 7, No. 1, Jan. 1979, pp. 49-56.

[3] Hutchinson, J. W. and Paris, P. C. in *Elastic-Plastic Fracture, ASTM STP 668*, J. D. Landes, J. A. Begley, and G. A. Clarke, Eds., American Society for Testing and Materials, 1979, pp. 37-64.

[4] Kumar, V. and Shih, C. F. in *Fracture Mechanics: Twelfth Conference, ASTM STP 700*, American Society for Testing and Materials, 1980, pp. 406-438.

[5] Wessel, E. in *Proceedings*, Committee on the Safety of Nuclear Installations, Specialists Meeting on Plastic Tearing Instability, Report NUREG/CP-0010, U. S. Nuclear Regulatory Commission, Washington, D. C., Jan. 1980.

[6] Vassilaros, M. G., Joyce, J. A., and Gudas, J. P. in *Fracture Mechanics: Twelfth Conference, ASTM STP 700*, American Society for Testing and Materials, 1980, pp. 251-270.

[7] Marandent, B. and Sanz, G. in *Flaw Growth and Fracture, ASTM STP 631*, American Society for Testing and Materials, 1977, pp. 462-476.

[8] Klima, S. J., Fisher, D. M., and Buzzard, R. J., *Journal of Testing and Evaluation*, Vol. 4, No. 6, 1976, pp. 397-404.
[9] Takahashi, H., Khan, M. A., and Suzuki, M., *Journal of Testing and Evaluation*, Vol. 8, 1980, pp. 63-67.
[10] Takahashi, H., Khan, M. A., and Suzuki, M., *Journal of Testing and Evaluation*, Vol. 9, 1981, pp. 14-23.
[11] Khan, M. A., Shoji, T., and Tahahashi, H., *Journal of Testing and Evaluation*, Vol. 10, Jan. 1982, pp. 3-11.
[12] Takahashi, H., Khan, M. A., Shimomura, K., and Suzuki, M. in *Proceedings*, Fourth International Acoustic Emission Symposium, High Pressure Institute, Japan, Tokyo, 1978, Session 8, pp. 24-25.
[13] Takahashi, H., Khan, M. A., Kikuchi, M., and Suzuki, M., *Experimental Mechanics*, Vol. 21, 1981, pp. 89-99.
[14] Clark, G. and Knott, J. F., *Metal Science*, Vol. 11, 1977, pp. 531-536.
[15] Khan, M. A., Shoji, T., and Takahashi, H., in *Proceedings*, Fifth International Acoustic Emission Sympsoium, The Japanese Society for Non-Destructive Inspection, Japan, Tokyo, 1980, pp. 395-410.
[16] Khan, M. A., Shoji, T., and Takahashi, H., *Res Mechanica Letters*, Vol. 1, 1981, pp. 133-138.
[17] Khan, M. A., Shoji, T., and Takahashi, H., *Metal Science*, Vol. 16, 1982, pp. 118-126.
[18] Landes, J. D. and Shaffer, D. H. in *Fracture Mechanics: Twelfth Conference, ASTM STP 700*, American Society for Testing and Materials, 1980, pp. 368-382.
[19] Harris, D. O. and Bell, R. L., *Experimental Mechanics*, Vol. 17, 1977, pp. 347-353.
[20] Lindley, T. C. and McIntyre, P. in *The Measurement of Crack Length and Shape During Fracture and Fatigue*, C. J. Beevers, Ed., Chamerleon Press, London, 1980.
[21] Niitsuma, H., Kikuchi, M., Takahashi, H., Suzuki, M., and Sato, R. in *Proceedings*, Fifth International Acoustic Emission Symposium, The Japanese Society for Non-Destructive Inspection, Japan, Tokyo, 1980, pp. 411-420.
[22] Panel Discussion, Conference on *Tolerance of Flaws in Pressurized Components*, Institution of Mechanical Engineers, London, 1978.
[23] Milne, I. and Chell, G. G. in *Elastic-Plastic Fracture, ASTM STP 668*, J. D. Landes, J. A. Begley, and G. A. Clarke, Eds., American Society for Testing and Materials, 1979, pp. 358-377.
[24] Wadley, H. N. G., Scruby, C. B., and Speake, J. H., *International Metals Reviews*, Vol. 25, 1980, pp. 41-64.
[25] Clark, G., Corderoy, D. J. H., Ringshall, N. W., and Knott, J. F., *Metal Science*, Vol. 15, No. 11412, 1981, pp. 481-491.
[26] Clarke, G. A., Landes, J. D., and Begley, J. A., *Journal of Testing and Evaluation*, Vol. 8, Sept. 1980, pp. 221-232.
[27] Loss, F. J., "Structural Integrity of Water Reactor Pressure Boundary Components," Report NUREG/CR-1783, Naval Research Laboratory, Washington, D.C., 1981.
[28] Landes, J. D. in *Proceedings*, Committee on the Safety of Nuclear Installations, Specialists Meeting on Plastic Tearing Instability, Report NUREG/CP-0010, U. S. Nuclear Regulatory Commission, Washington, D. C., Jan. 1980.
[29] Mills, W. J., *Journal of Testing and Evaluation*, Vol. 9, 1981, pp. 56-62.
[30] Zahoor, A. and Paris, P. C. in *Proceedings*, Committee on the Safety of Nuclear Installations, Specialists Meeting on Plastic Tearing Instability, Report NUREG/CP-0010, U.S. Nuclear Regulatory Commission, Washington, D.C., Jan. 1980.
[31] Khan, M. A., Shoji, T., Niitsuma, H., and Takahashi, H., *Engineering Fracture Mechanics*, Vol. 15, No. 5, 1982, pp. 645-658.
[32] Rice, J. R. and Sorensen, E. P., *Journal of the Mechanics and Physics of Solids*, Vol. 26, No. 3, June 1978, pp. 163-186.

Tadao Iwadate,[1] *Yasuhiko Tanaka,*[1] *Shin-ichi Ono,*[1] *and Juro Watanabe*[1]

An Analysis of Elastic-Plastic Fracture Toughness Behavior for J_{Ic} Measurement in the Transition Region

REFERENCE: Iwadate, T., Tanaka, Y., Ono, S., and Watanabe, J., **"An Analysis of Elastic-Plastic Fracture Toughness Behavior for J_{Ic} Measurement in the Transition Region,"** *Elastic-Plastic Fracture: Second Symposium, Volume II—Fracture Resistance Curves and Engineering Applications, ASTM STP 803*, C. F. Shih and J. P. Gudas, Eds., American Society for Testing and Materials, 1983, pp. II-531-II-561.

ABSTRACT: Fracture toughness tests were performed in the transition region for ASTM A508 Class 3 and A470 nickel-chromium-molybdenum-vanadium steels using about 300 specimens of 0.5T, 1T, 2T, and 4T compact tension (CT) specimens. The K_J-values which are converted from Jc of the smaller specimens indicated a wide scatter ranging from below the K_{Ic}-value to much higher toughness. The fracture behavior was investigated with a scanning electron microscope in detail and the sources of scatter of the toughness in small specimens were studied. The fast brittle fracture behavior in the transition regime can be divided into two regions: (1) the region where fracture occurs on a blunting line (Region I) and (2) the region where fracture occurs on an R-curve (Region II). The scatter of the K_J-values in each region is caused by the amount of crack extension contained in the specimens.

Methods to obtain the fracture toughness equivalent to the K_{Ic} from the K_J-values are presented. In Region I the lowest bound of $K_{J_{min}}$-values obtained using specimens that meet the requirement $NB \geq 3000\, Jc_{min}/\sigma_Y$ is recommended, and this method may also be used in Region II. In Region II a modified R-curve method is proposed.

KEY WORDS: steels, cleavage fracture, fractures (materials), fracture toughness, J-integral, transition effects, Weibull statistics, specimen size effects, testing technique, elastic plastic fracture

Methods for measuring the elastic-plastic fracture toughness of metals, J_{Ic}, have been examined extensively for a decade. The J-integral provides a prac-

[1]Section manager and engineers, Research Laboratory, Muroran Plant and general manager, Material Research Laboratory, respectively, The Japan Steel Works, Muroran, Japan.

tical advantage that the toughness results equivalent to the valid K_{Ic} per the ASTM Method can be obtained from smaller specimens [*1,2*].[2] A standard method draft for J_{Ic} determination developed by the ASTM E24.01.09 Task Group was published in January 1979 [*3*]. This method, however, limits determination of J_{Ic} at the temperature where stable crack extension occurs and the R-curve technique can be employed.

In the transition temperature region, an apparent problem to be solved exists with the toughness evaluation using small specimens. The fracture at the transition temperatures occurs in an unstable manner at maximum load during loading and the R-curve cannot be constructed. The toughness values evaluated by the J-integral for small specimens may give much higher toughness than the K_{Ic}-values measured by large specimens [*4-7*]. This behavior is usually explained in terms of the statistical model based on a Weibull distribution and in part the loss of constraint [*6,7*]. A method for analyzing small-specimen results to properly predict the toughness of a large specimen is proposed by Landes and Shaffer [*7*]. This approach is an attempt to describe the observed toughness behavior and is not a direct toughness measuring method.

The toughness evaluation in the transition temperature region is as important as in the upper shelf. In this paper the elastic-plastic fracture toughness test results obtained in the transition region for an ASTM A508 Class 3 nuclear pressure vessel steel and an ASTM A470 nickel-chromium-molybdenum-vanadium (Ni-Cr-Mo-V) rotor steel using about 300 specimens were analyzed. The fracture behavior was investigated with a scanning electron microscope (SEM) in detail and the sources of scatter of the toughness obtained using small specimens were studied. From the test results obtained, direct methods were proposed to measure the fracture toughness J_{Ic} corresponding to the K_{Ic} per the ASTM Method, and their usefulness was demonstrated.

Materials

The materials used in the test program were an ASTM A508 Class 3 steel, a typical commercial forging for nuclear pressure vessel components, and an ASTM A470 Class 6 Ni-Cr-Mo-V steam turbine rotor steel of commercial grade. Chemical compositions and heat treatments of the materials are presented in Table 1. The A508 Class 3 steel specimens were taken from ¼T location of a 300-mm-thick forging plate. The Ni-Cr-Mo-V steel specimens were machined so that the crack tip was located between 540 and 670 mm from the center of a 1672-mm-diameter rotor forging. Here, the specimen orientations of the A508 Class 3 and Ni-Cr-Mo-V steels were, respectively, T-L and C-R per the ASTM Test for Plane-Strain Fracture Toughness of Metallic Materials (E 399-78).

Tensile properties of the materials per the ASTM Method for Tension

[2]The italic numbers in brackets refer to the list of references appended to this paper.

TABLE 1—*Chemical composition and heat treatments of the materials.*

Material	C	Si	Mn	P	S	Ni	Cr	Mo	V
				Chemical Composition, weight %					
ASTM A508 Class 3	0.21	0.29	1.36	0.009	0.004	0.64	0.19	0.52	<0.01
ASTM A470 Class 6	0.23	0.05	0.30	0.009	0.011	3.79	1.81	0.44	0.13

		Heat Treatment
ASTM A508 Class 3	austenitize	890°C, hold 6.5 h, water quench
	temper	660°C, hold 10.5 h, air cool
	stress relieve	550°C, hold 55.0 h, furnace cool
		600°C, hold 20.5 h, furnace cool
		600°C, hold 10.5 h, furnace cool
ASTM A470 Class 6	austenitize	840°C, hold 36.0 h, water spray quench
	temper	595°C, hold 74.0 h, controlled cool
	stress relieve	570°C, hold 35.0 h, furnace cool

Testing of Metallic Materials (E 8-79) and Charpy V-notch impact properties per the ASTM Method for Notched Bar Impact Testing of Metallic Materials (E 23-72) are shown in Figs. 1 through 4. Table 2 summarizes the tensile properties at room temperature and the Charpy V-notch impact properties, and it also gives the drop weight properties of the materials per the ASTM Method of Conducting Drop-Weight Test to Determine Nil-Ductility Transition Temperature of Ferritic Steels (E 208-69). Room-temperature yield strengths of the A508 Class 3 and Ni-Cr-Mo-V steels are 480 and 767 MPa, respectively. The 50 percent ductile fracture appearance transition temperature (FATT) is −7°C for the A508 Class 3 steel and −10°C for the Ni-Cr-Mo-V steel.

Experimental Procedures

The majority of the specimens were tested in the transition region, below the temperature where upper-shelf fracture toughness behavior was first experienced. The J tests of the steels were conducted on 0.5T-CT, 1T-CT, 2T-CT, and 4T-CT specimens, recommended by the ASTM E24 Task Group, which were modified to measure the displacement at the center of loading line. The specimens having 25 percent side grooves to their original thickness were also used to evaluate the effect of constraint. The angle of the side groove was 45° and the root radius 0.25 mm. The fatigue crack length to specimen width ratio, a/w, of the specimens except for 4T-CT specimens was about 0.6. The a/w of 4T-CT specimens was about 0.55 so that the valid K_{Ic}-value per ASTM Method E 399-78 and the value of J at the fracture

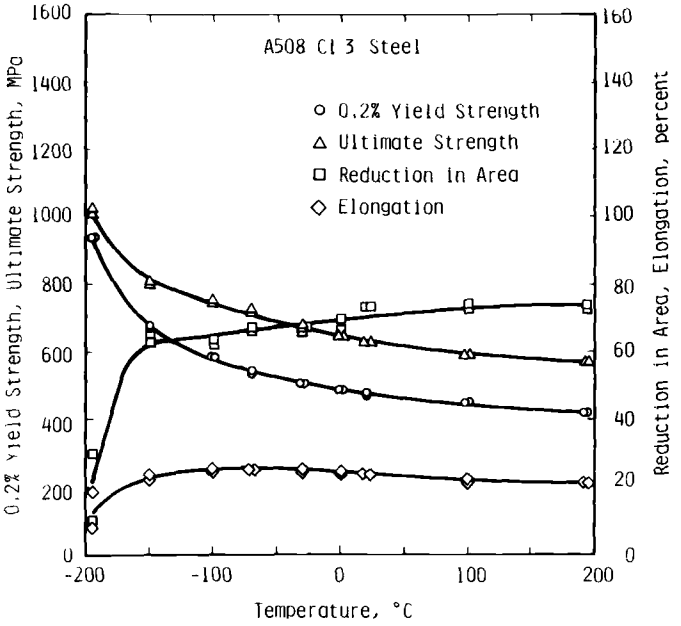

FIG. 1—*Tensile properties of A508 Class 3 pressure vessel steel.*

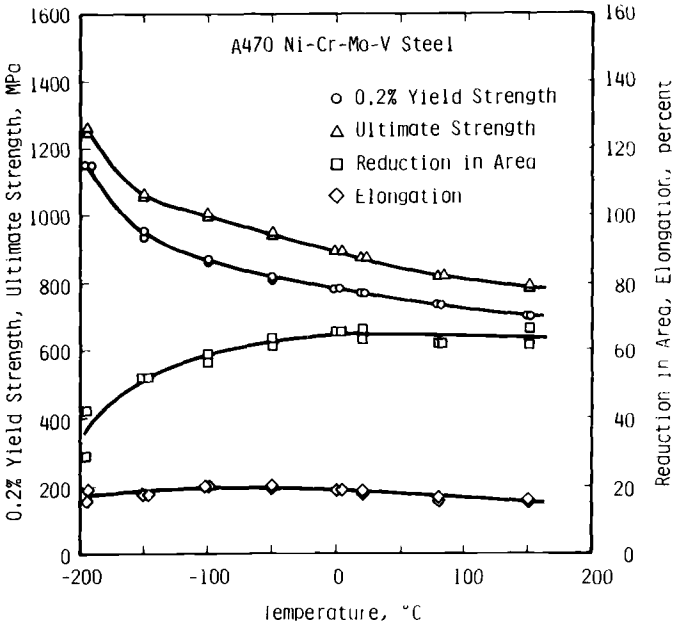

FIG. 2—*Tensile properties of A470 Ni-Cr-Mo-V rotor steel.*

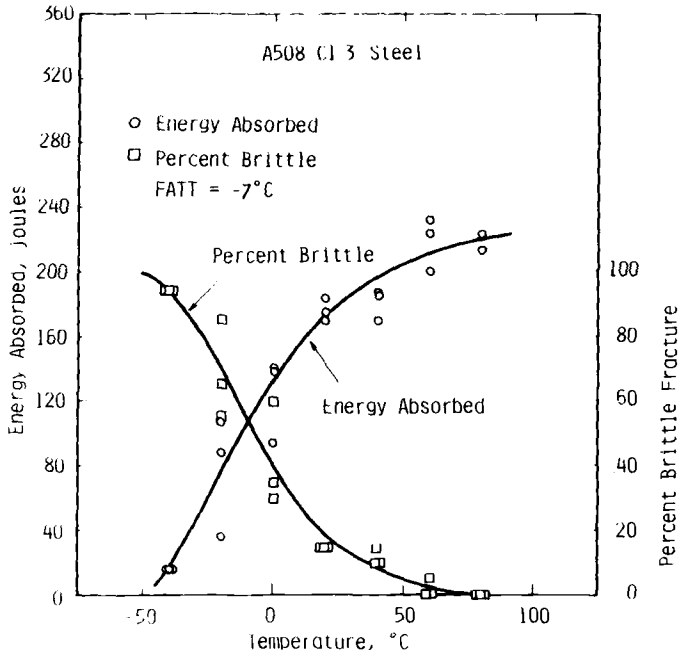

FIG. 3—*Charpy V-notch impact properties of A508 Class 3 pressure vessel steel.*

could be measured by one specimen. The final precracking stress-intensity factor, K_{max}, of the specimens was kept less than 25 MPa$\sqrt{m}$.

The value of J for fracture occurring by an instability both with and without prior stable crack growth was labeled Jc. The J-integral was calculated using the equation corrected for the tension loading component [*3*]

$$J = \frac{1 + \alpha}{1 + \alpha^2} \frac{2A}{Bb} \tag{1}$$

where

$\alpha = [(2a_o/b)^2 + 2(2a_o/b) + 2]^{1/2} - (2a_o/b + 1)$,
A = area under load versus load-point displacement record,
B = specimen thickness [for side-grooved specimens, $B = B(\text{net})$], and
b = initial uncracked ligament, $w - a_o$.

Corresponding K_J-values were calculated by converting Jc to K_J using the relationship between elastic-plastic and linear-elastic fracture mechanics parameters [*1*].

$$K_J = \left(\frac{Jc\,E}{1 - \nu^2} \right)^{1/2} \tag{2}$$

where E is Young's modulus and ν is Poisson's ratio.

At upper-shelf temperatures where the stable crack growth was fully developed, the R-curve method proposed by the ASTM E24 Task Group was employed [*3*]. The K_{Ic} tests per Method E 399-78 were also conducted using 4T-CT specimens for the A508 Class 3 steel and 3T-CT and 4T-CT specimens for the Ni-Cr-Mo-V steel to compare with K_J-values obtained by J tests.

Results and Discussion

Transition Behavior

Elastic-plastic fracture toughness tests in the transition temperature region were performed using a total of 157 specimens (68 0.5T-CT, 83 1T-CT, 4 2T-CT, and 2 4T-CT specimens) for the A508 Class 3 steel and a total of 133 specimens (62 0.5T-CT, 57 1T-CT, 8 2T-CT, and 6 4T-CT specimens) for the Ni-Cr-Mo-V steel. Figures 5 and 6 show the converted fracture toughness K_J of 0.5T-CT and 1T-CT specimens as a function of temperature for the A508

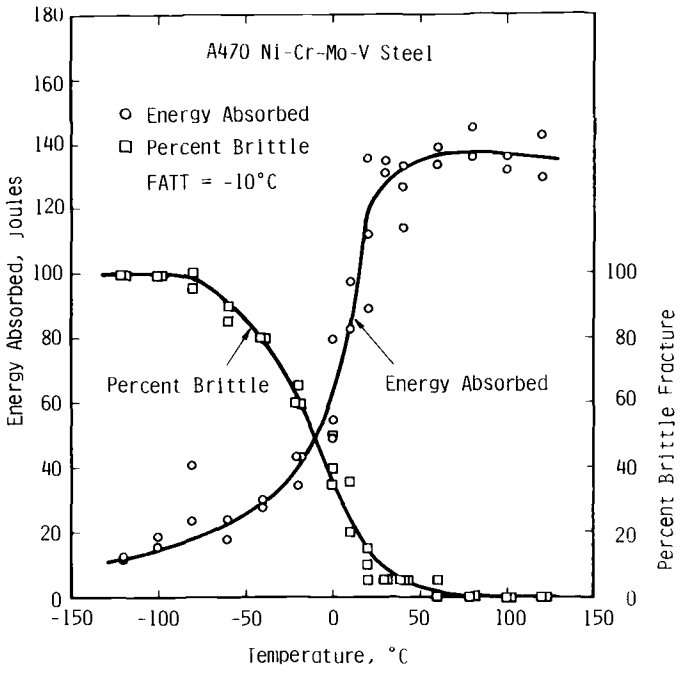

FIG. 4—*Charpy V-notch impact properties of A470 Ni-Cr-Mo-V rotor steel.*

TABLE 2—*Tensile, NDTT, and impact properties of the materials.*

Material	Tensile Properties at Room Temperature				NDTT, °C	Impact Properties	
	0.2% Offset Strength, MPa	Tensile Strength, MPa	Elongation, %	Reduction of Area, %		FATT, °C	Upper-Shelf Energy, J
ASTM A508 Class 3	480	635	27	70	−25	−7	215
ASTM A470 Class 6	767	870	18	65	−35	−10	135

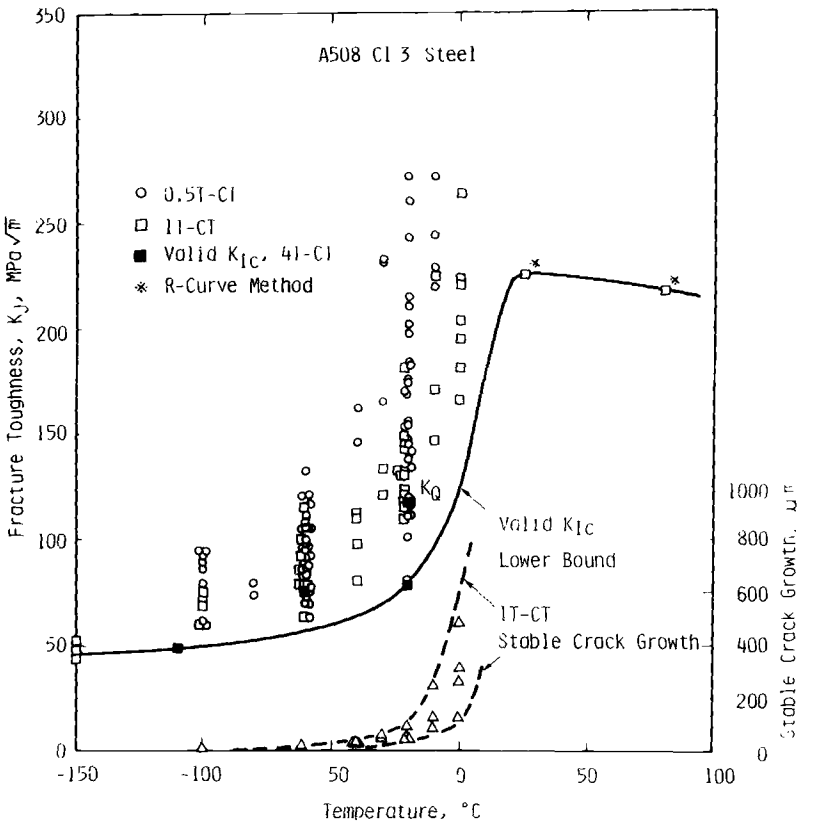

FIG. 5—K_J *calculated from* Jc *for fracture versus temperature relation for A508 Class 3 pressure vessel steel.*

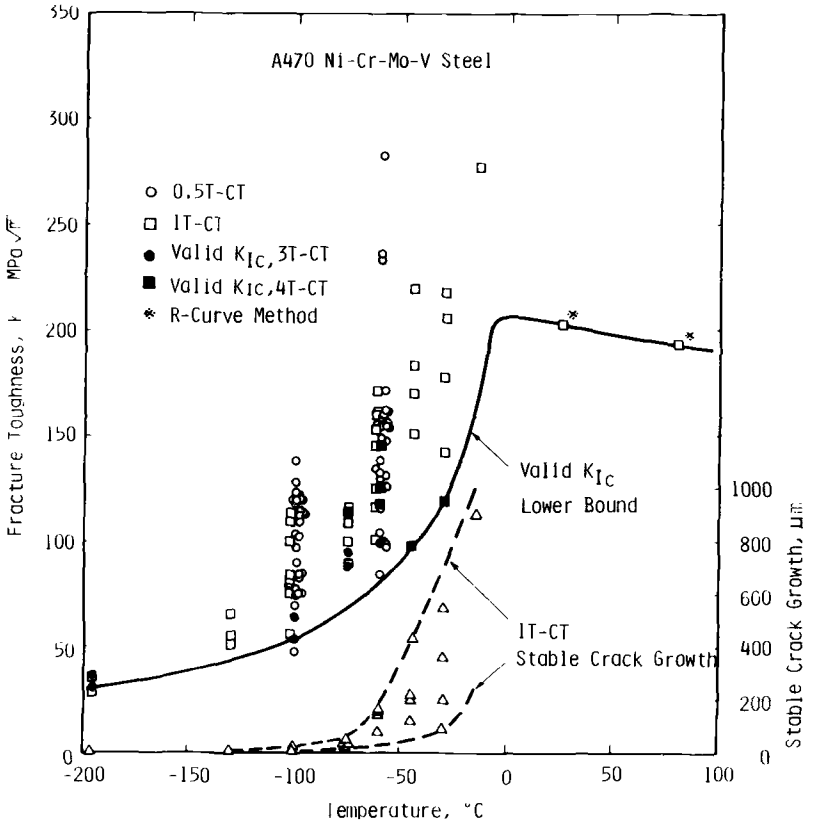

FIG. 6—K_J *calculated from* Jc *for fracture versus temperature relation for A470 Ni-Cr-Mo-V rotor steel.*

Class 3 and Ni-Cr-Mo-V steels, respectively. In these figures, the valid K_{Ic}-values obtained by large specimens were also plotted. The converted K_J-values show a great deal of scatter in particular for the smaller 0.5T-CT specimens and give the higher average of the toughness than that of valid K_{Ic}. As the temperature is increased in the transition range, the scatter becomes greater. However, the test results suggest that the lower bound of K_J-values converted from *Jc* of small specimens coincides well with the lower bound of the valid K_{Ic} up to temperatures of at least −20 and −30°C for the A508 Class 3 and Ni-Cr-Mo-V steels, respectively.

This behavior is explained in terms of the statistical model based on a Weibull distribution and the loss of constraint in smaller specimens [*6, 7*]. The materials have the statistical distribution of toughness properties which is caused by metallurgical inhomogeneity. The smaller specimens are less likely to contain the point or region of low toughness because the length of crack front is shorter than that of large specimens. Therefore, the toughness of the

smaller specimens shows a wide scatter ranging from values near to the toughness obtained by large specimens to much higher values. On the other hand, the smaller specimens have less thickness than the larger specimens, and they cannot develop the crack-tip constraint equivalent to the larger specimens, thus causing higher toughness.

Figures 7 and 8 show the effect of specimen size on the converted fracture toughness K_J of the A508 Class 3 and Ni-Cr-Mo-V steels. For both materials, as the specimen size increases, the scatter of the K_J-values becomes smaller. The lowest toughness at each specimen size is situated near or below the average of valid K_{Ic} results, while some of them coincide well with the values of K_J at the initiation of stable crack growth which were obtained using a modified R-curve technique, which is to be described in detail later in this paper. These results suggest that the scatter resulted mainly from the statistical model rather than a loss of constraint. However, the toughness results obtained using the specimens with side grooves, shown by closed points in the figures, suggest that the loss of constraint might in part cause the scatter of the toughness because the smaller specimens, 0.5T-CT, having side grooves lead to a much narrower scatter for both materials.

The toughness measured at two temperatures using 0.5T-CT specimens for the A508 Class 3 and Ni-Cr-Mo-V steels was plotted on Weibull graphs in

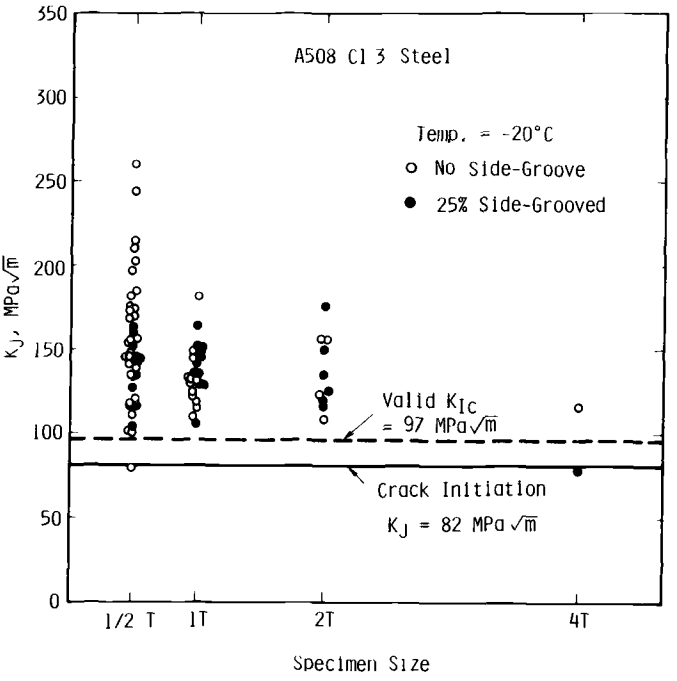

FIG. 7—*Effect of specimen size on* K_J *for fracture of A508 Class 3 steel.*

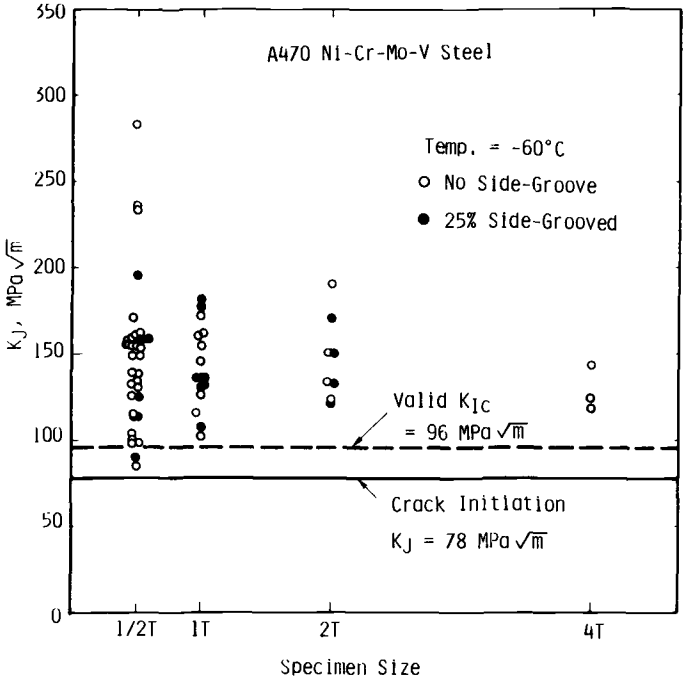

FIG. 8—*Effect of specimen size on* K_J *for fracture of A470 Ni-Cr-Mo-V steel.*

Figs. 9 and 10, respectively. The linear distribution of data points indicates that the Weibull model is an appropriate statistical model for these data. The straight lines were determined using a least-squares-fit technique. The slope at −60°C for the A508 Class 3 steel is about 2.7 whereas the slope at −20°C is about 1.9. For the Ni-Cr-Mo-V steel, the decrease of the slope with increasing temperature is very small, about 2.6 at both temperatures. Note that at the higher test temperature the stable crack was fully developed before the fast brittle fracture, whereas at the lower test temperature, only local stable cracking was observed. This suggests that the shape of the Weibull model is affected not only by the material but also by the fracture mode, and probably specimen size.

Analysis of Fracture Behavior

To investigate the scatter of the toughness evaluated by J-integral, the fracture surfaces of the specimens were examined in detail using a scanning electron microscope. Figure 11 shows examples of the fracture surfaces of the A508 Class 3 steel tested at −20 and −100°C. On the fracture surface tested at −20°C, the stable crack growth and stretch zone created prior to fast fracture is clearly observed, whereas on the fracture surface tested at −100°C a

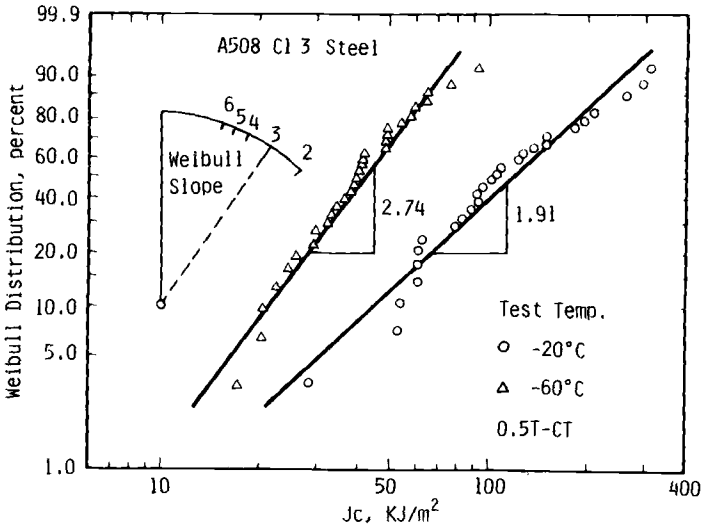

FIG. 9—*Weibull distribution versus* Jc *measured with 0.5T-CT specimens for A508 Class 3 steel.*

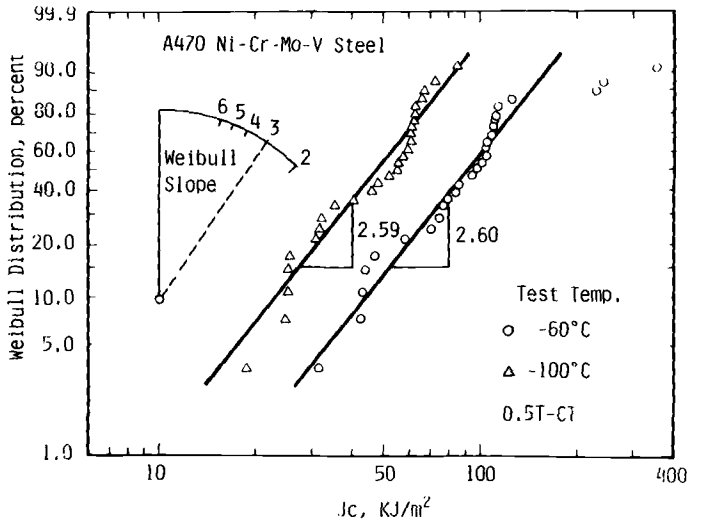

FIG. 10—*Weibull distribution versus* Jc *measured with 0.5T-CT specimens for A470 Ni-Cr-Mo-V steel.*

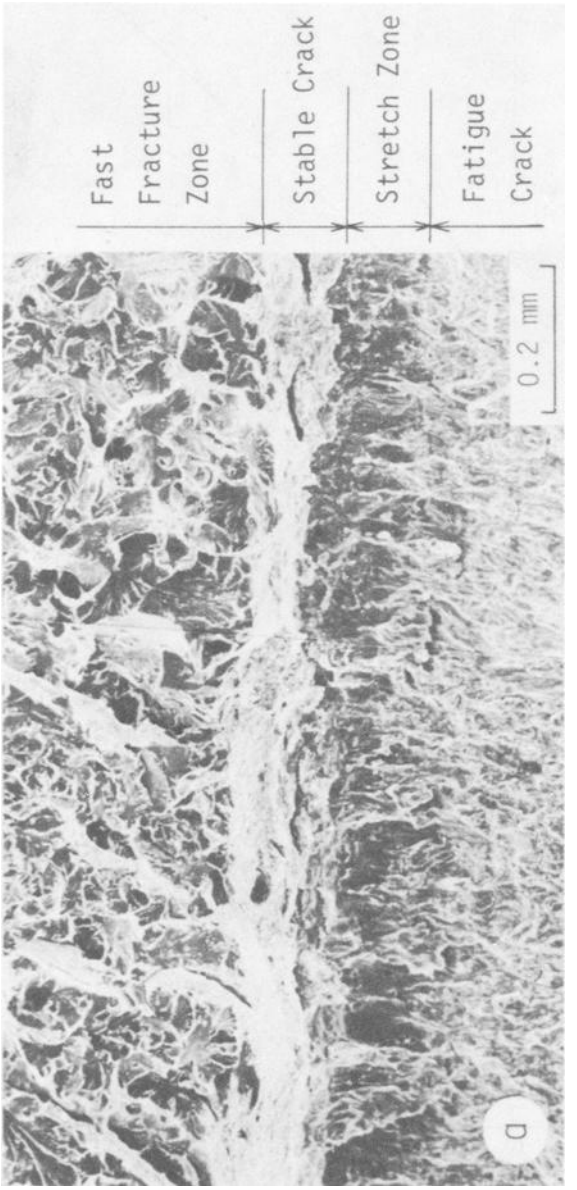
Fast
Fracture
Zone
Stable Crack
Stretch Zone
Fatigue
Crack
0.2 mm
a

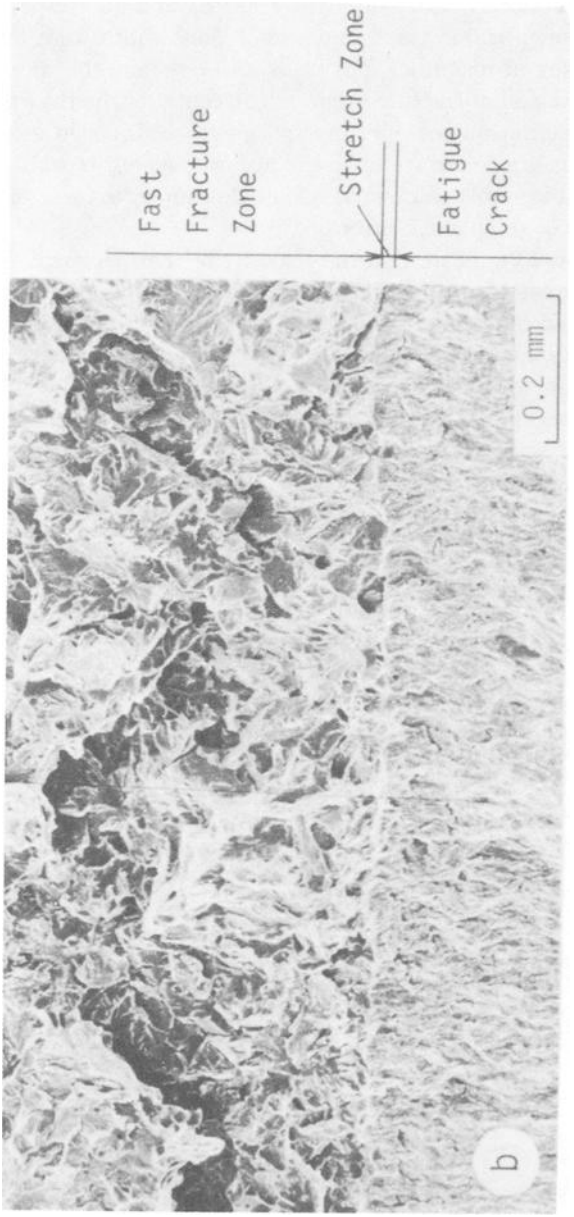

FIG. 11—*SEM fractographs of 1T-CT specimens of A508 Class 3 steel: (a) temperature = −20°C, Jc = 63.7 KJ/m²; (b) temperature = −100°C, Jc = 22.2 KJ/m².*

little stretch zone with no stable crack is observed. The stable crack growth and stretch zone width measured at various temperatures for the A508 Class 3 and Ni-Cr-Mo-V steels were plotted in Figs. 12 and 13, respectively. The uniformly developed stable crack and stretch zone width were measured on photographs taken at magnifications of 50 to 500, where the specimens were taken from the region of fracture origin or the center of the thickness. Under the scanning electron microscope, the specimen was inclined at an angle of 30° to the fatigue crack surface to obtain accurate length of stable crack and stretch zone, as the stable cracks also had angles similar to those of the stretch zone in the case of small crack extension.

Figures 12 and 13 indicate that the majority of the specimens fractured in the transition region, having a wide scatter of the toughness, contain stable crack growth, and that the amount of the crack growth increases remarkably with increasing temperature. The temperature range where the slow crack exceeds about 50 μm for 1T-CT specimens is located higher than −40°C for the A508 Class 3 steel and −75°C for the Ni-Cr-Mo-V steel. Compared with the fracture toughness versus temperature curves in Figs. 5 and 6, it is found that these temperatures are close to the temperature where the lower shelf of the valid K_{Ic} curve starts. Note that even in the lower-shelf regime where stable

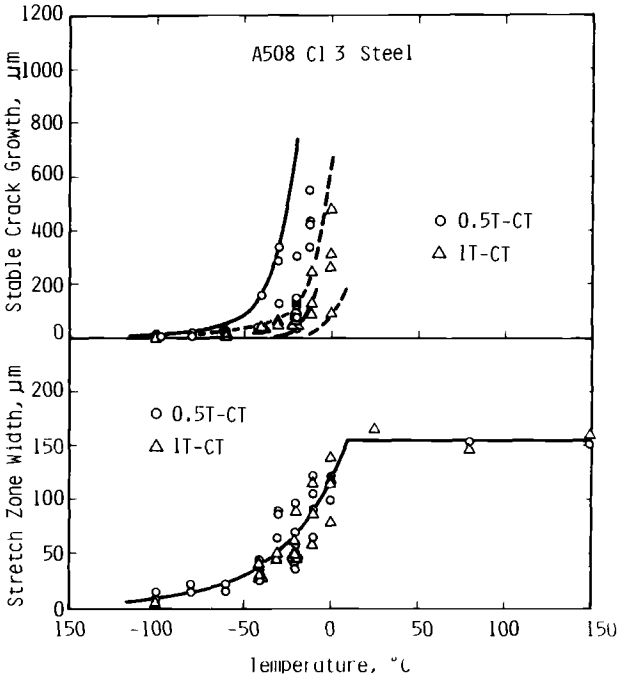

FIG. 12—*Temperature dependence of stable crack growth and stretch zone width for A508 Class 3 steel.*

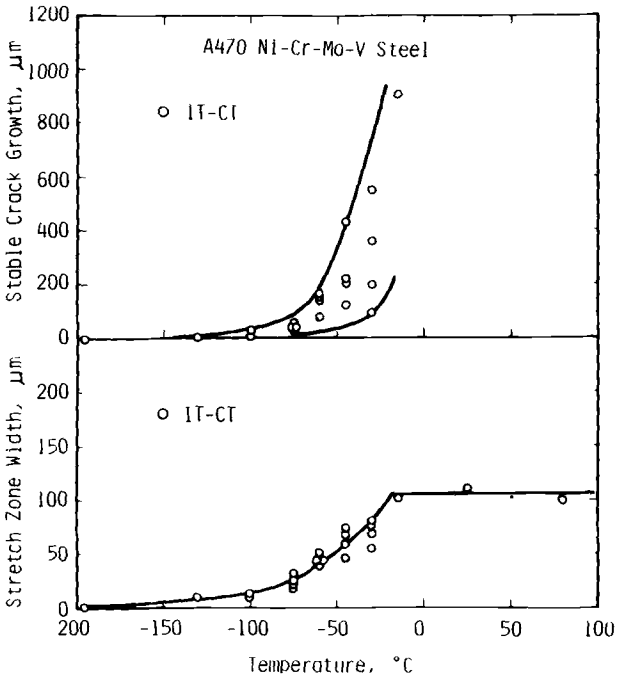

FIG. 13—*Temperature dependence of stable crack growth and stretch zone width for A470 Ni-Cr-Mo-V steel.*

crack growth is not observed, the K_J-values exhibit considerable scatter. The effect of specimen size on stable crack growth is seen in Fig. 12. The larger specimens have smaller crack extension; correspondingly, the larger specimens have smaller scatter of toughness. Figures 12 and 13 also show that the stretch zone width created at the tip of the crack increases with increasing temperature and reaches a plateau at the upper-shelf temperature. The effect of specimen size on stretch zone width cannot be observed.

The sum of the stable crack and stretch zone, that is, the crack extension Δa defined by the E24 Task Group, and the stretch zone width itself for both steels were plotted as a function of J in Figs. 14 and 15. The relationship between crack extension Δa and its corresponding J constructs an R-curve. This suggests that the fast brittle fracture occurs on an R-curve of the material, and that the scatter of the toughness is caused by the difference in crack extension contained in the specimen. The figures also indicate that the stretch zone width increases with increasing J even after the onset of stable crack growth, especially for the A508 Class 3 steel. This means that the stretch zone created before the crack initiation is continuously stretched during the following stable crack formation. The difference between the theoretical blunting line, $J = 2\sigma_Y \Delta a$, recommended by the E24 Task Group, and the actual points is

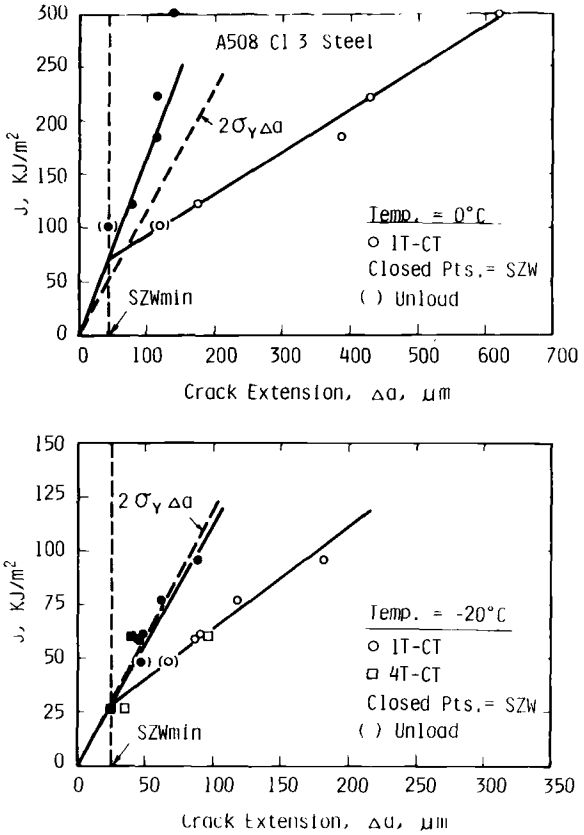

FIG. 14—J *versus crack extension and stretch zone width tested at 0 and −20°C for A508 Class 3 steel.*

also observed. This makes it impossible to determine the J_{Ic} at the initiation of stable crack growth, even with an aid of the stretch zone width measurement.

The investigation has led to a conclusion that the fracture behavior observed in the transition regime can be divided into two regions: (1) the region where fracture occurs on a blunting line (Region I) and (2) the region where fracture occurs on an R-curve (Region II), and that the scatter of the toughness of small specimens in each region is caused by the amount of crack extension contained in the specimens. Figure 16 presents a schema of these two regions. Toughness evaluation in the transition region should be examined separately in each region.

Toughness Evaluation

Fracture toughness tests using 4T-CT specimens with crack length to width ratio, $a/w = 0.55$, were performed to study the correlation between the con-

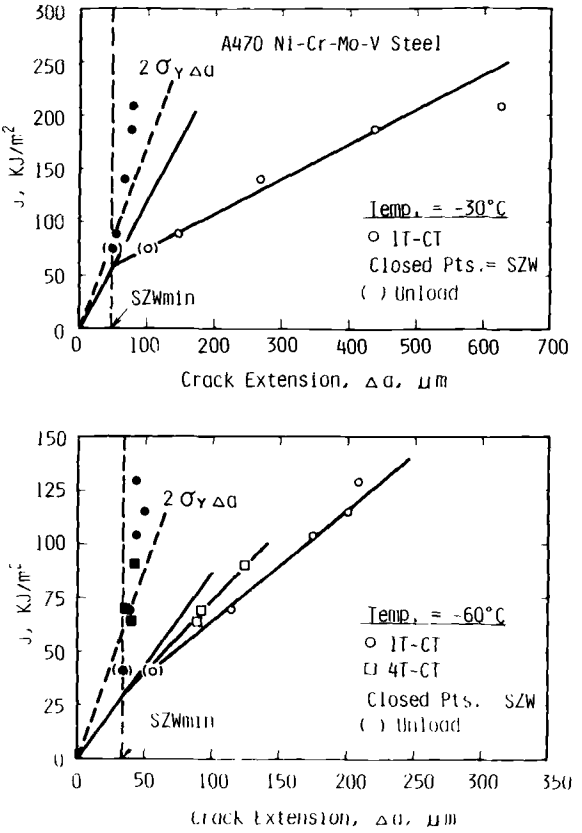

FIG. 15—J *versus crack extension and stretch zone width tested at −30 and −60°C for A470 Ni-Cr-Mo-V steel.*

verted toughness K_J and the K_{Ic} per Method E 399-78 obtained by one specimen. Test results obtained are listed in Table 3. Good coincidence between the toughness evaluated by J-integral and the valid K_{Ic} is demonstrated. Here, in all 4T-CT specimens, stable crack growth was observed, of which examples are shown in Fig. 17 and measured values are listed in Table 3.

In Region II (Fig. 16), the stable crack is fully developed, and an R-curve can be constructed. However, as mentioned earlier, the use of crack extension Δa which includes stretch zone is inadequate to determine the J_{Ic} at the incipient crack growth. Note that the crack extension which does not include the stretch zone, namely, the stable crack growth, can be easily measured by a scanning electron microscope. Therefore, if a J versus stable crack growth R-curve (modified R-curve) is constructed, the value of J at the initiation of stable crack growth can be obtained as an intersection of the R-curve and the ordinate.

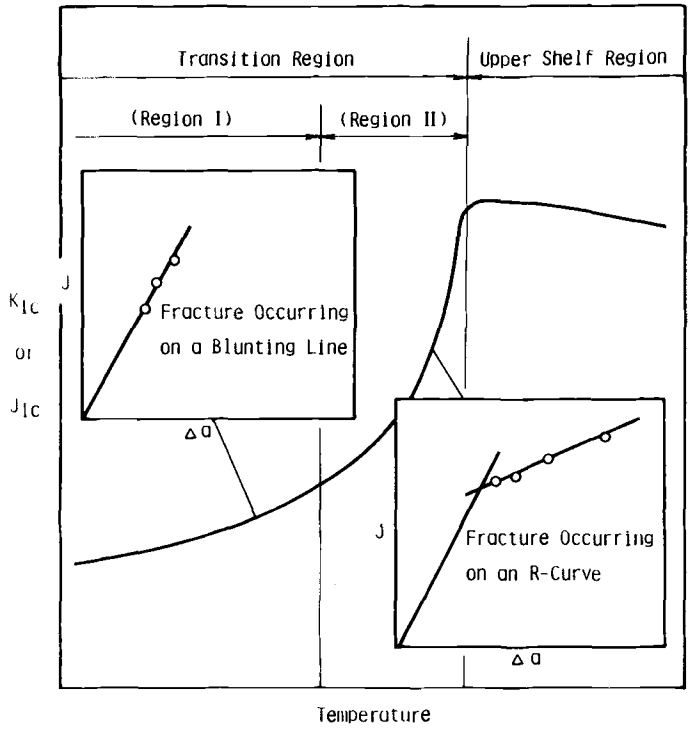

FIG. 16—*Schematic representation showing the fracture behavior in the transition region.*

TABLE 3—*Comparison between K_{Ic} and K_J-values measured with 4T-CT specimens.*

Material	No.	Temperature, °C	$B/(K_Q/\sigma_{ys})^2$	K_{Ic}, MPa$\sqrt{m}$	K_J, MPa$\sqrt{m}$	Stable Crack, μm
ASTM A508 Class 3	1	−20	2.2	108	116	56
	2[a]	−20	3.2	73	77	11
ASTM A470 Class 6	1	−30	4.5	119	120	89
	2	−45	6.7	98	99	50
	3	−60	3.7	145	144	82
	4	−60	4.3	125	125	55
	5	−60	5.6	118	120	49
	6	−75	5.3	114	114	38

[a]25% side grooved.

Figures 18 and 19 show the J versus stable crack growth R-curves of 1T-CT specimens obtained at various temperatures for both steels. The data shown in parentheses are those of the specimens unloaded before fracture. In the measurement of stable crack initiated at only local areas, the measured lengths of the crack growth were averaged along the crack front of interest. The figures suggest that four or more specimens are required to develop an R-curve, and that one of them needs the crack growth more than about 50 μm. Figures 18 and 19 also indicate that the slope of the R-curve increases with decreasing temperature. The modified R-curves obtained from various specimen sizes are shown in Figs. 20 and 21, where some of the 4T-CT specimens meet the size criterion of valid K_{Ic} required by E 399-78. Good coincidence of J_{Ic} among the specimen sizes is observed. In the Ni-Cr-Mo-V steel, the valid K_{Ic}-values give a higher toughness than the K_J-value calculated from J_{Ic}.

In Region I, the modified R-curve method cannot be applied, because the stable crack growth to construct an R-curve is not observed. The fracture in Region I is mainly controlled by a Weibull-type size effect resulting from the metallurgical inhomogeneity of the material. Larger specimens are more likely to contain weak areas, leading to lower fracture toughness. Note that the minimum toughness of small specimens coincides well with that of large specimens. In a 4T-CT specimen, the crack tip leading edge contains four times the properties controlling near-tip volume compared with one 1T-CT specimen. Therefore, the following assumption could be given. If the number of small specimens is tested so that the total length of crack front is equivalent to that of a large K_{Ic} specimen, the minimum toughness of the K_J-values would be consistent with the valid K_{Ic}. Figure 22 is a schema to show this assumption. When the thickness of a small specimen is B and the number of small specimens is N, the crack front equivalent to a large K_{Ic} specimen can be expressed as NB. Using the foregoing assumption, the number of small specimens required to measure the fracture toughness equivalent to the valid K_{Ic} per the ASTM Method can be obtained.

Figure 23 presents the results obtained with 0.5T-CT and 1T-CT specimens in Region I, plotted in terms of $K_{J_{min}}/K_{Ic}$ against the equivalent length of crack front NB normalized by Jc_{min}/σ_Y. $K_{J_{min}}$ and its corresponding Jc_{min} values are the minimum toughness among N number of specimens. K_{Ic} is the average value measured in K_{Ic} tests shown as a dotted line in Figs. 28 and 29, and σ_Y is flow stress, the mean value of the yield and ultimate tensile strengths. The normalizing parameter Jc_{min}/σ_Y in the abscissa is an elastic-plastic fracture parameter representing the crack-tip opening displacement (CTOD) which is more reasonable than a linear-elastic fracture parameter $(K_{J_{min}}/\sigma_{ys})^2$, because the use of $(K_{J_{min}}/\sigma_{ys})^2$ may require the specimen constraint, that is, the proportional specimen size equivalent to the crack front length NB. In Fig. 23, the plots were conducted in the following manner. For example, when ten specimens were tested, for $N = 1$, ten data points were

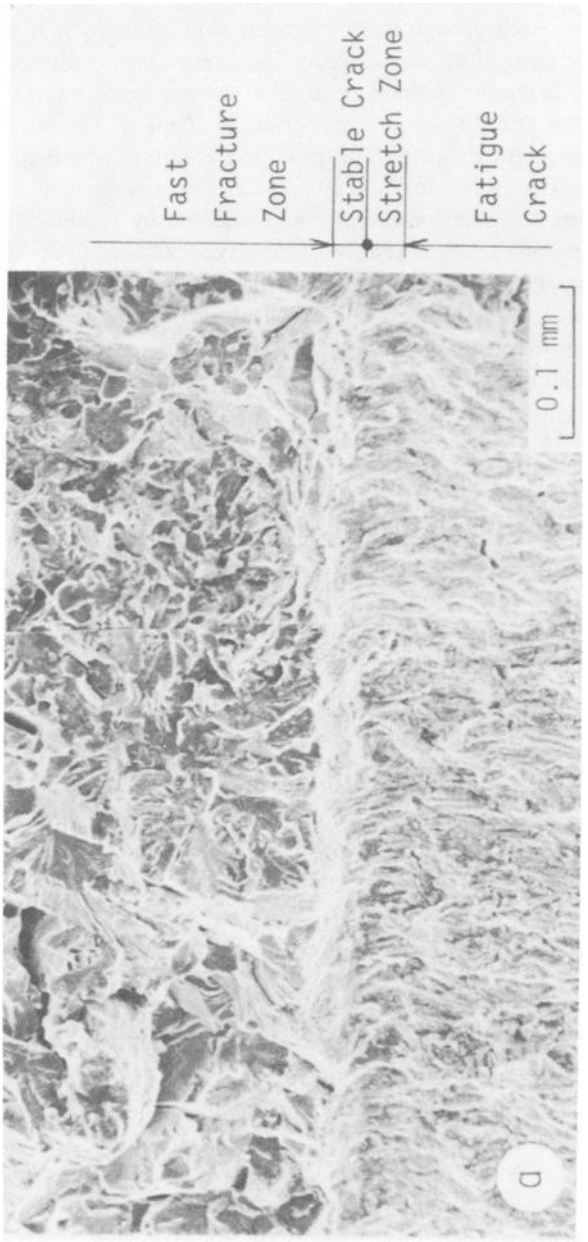
Fast
Fracture
Zone
Stable Crack
Stretch Zone
Fatigue
Crack
0.1 mm
d

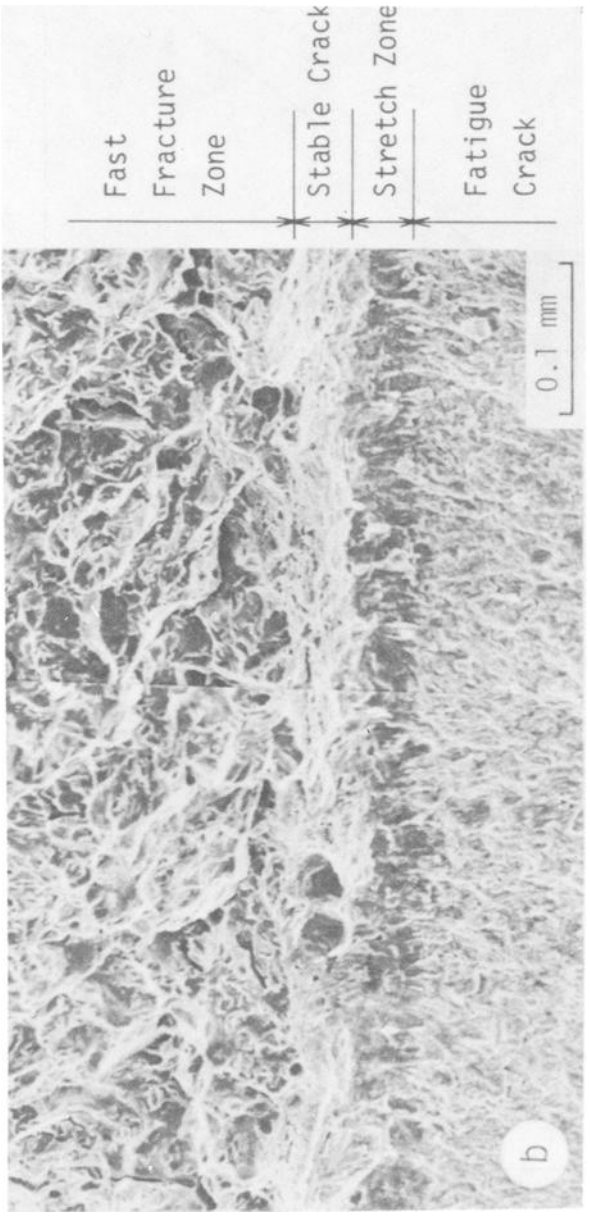

FIG. 17—*Examples of stable crack growth observed in the 4T-CT valid* K_{Ic} *specimens: (a) A508 Class 3 steel,* $K_{Ic} = 73\ MPa\sqrt{m}$, $-20°C$; (b) *A470 Ni-Cr-Mo-V steel,* $K_{Ic} = 118\ MPa\sqrt{m}$, $-60°C$.

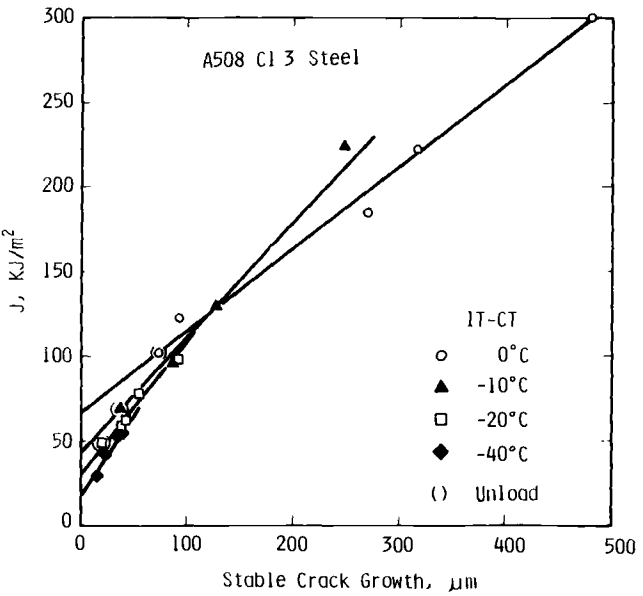

FIG. 18—J *versus stable crack growth R-curves for A508 Class 3 steel at temperatures of 0, −10, −20, and −40°C.*

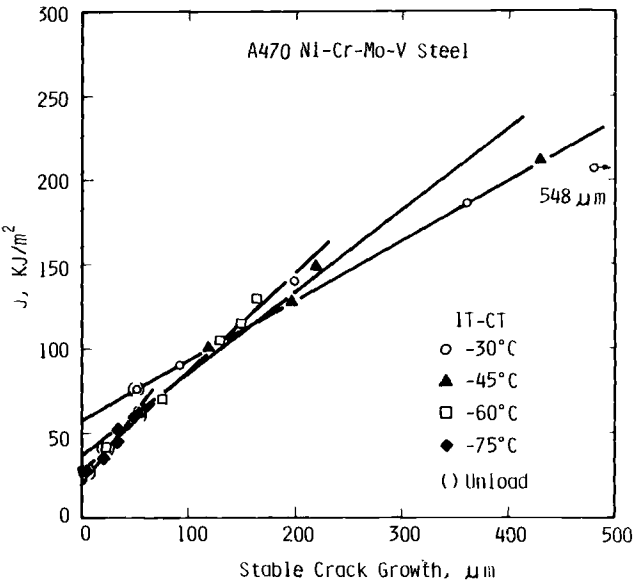

FIG. 19—J *versus stable crack growth R-curves for A470 Ni-Cr-Mo-V steel at temperatures of −30, −45, −60, and −75°C.*

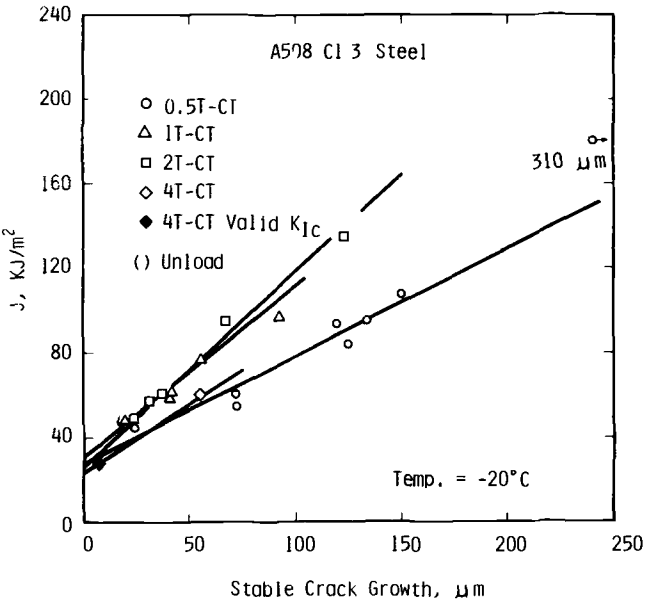

FIG. 20—J *versus stable crack growth R-curves for different specimen sizes of A508 Class 3 steel.*

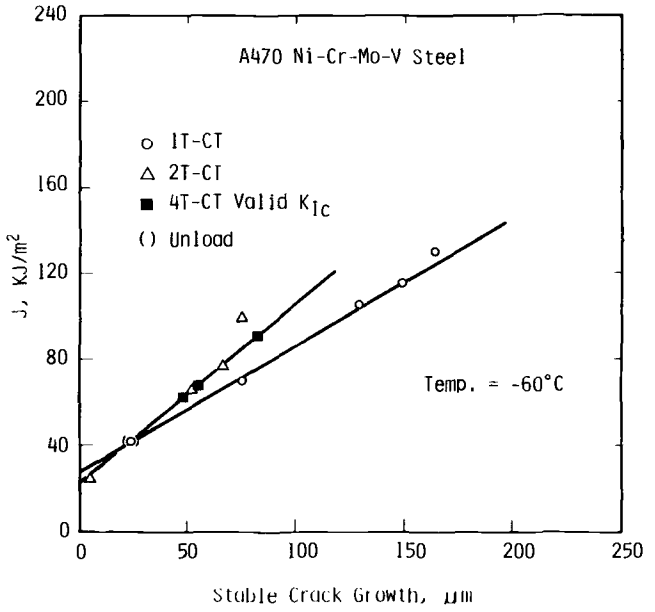

FIG. 21—J *versus stable crack growth R-curves for different specimen sizes of A470 Ni-Cr-Mo-V steel.*

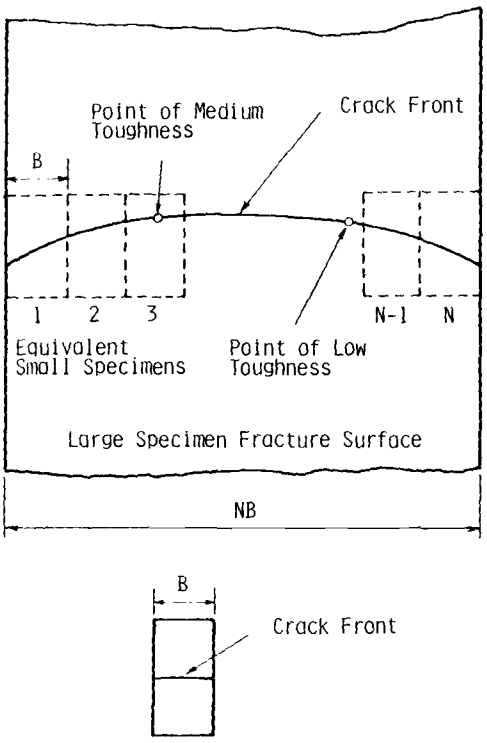

FIG. 22—*Schematic representation showing the number of small specimens required to obtain equivalent crack front length to that of a large specimen.*

plotted as $K_{J_{min}}$ or Jc_{min}. For $N = 3$, ten data points were arranged in sampling order and were divided into groups of three specimens each: first, No. 1 to No. 3, No. 4 to No. 6, and No. 7 to No. 9 specimens; second, No. 2 to No. 4, No. 5 to No. 7, and No. 8 to No. 10 specimens; and third, No. 3 to No. 5, and No. 6 to No. 8 specimens. Thus, eight minimum toughness specimens in each block were plotted as $K_{J_{min}}$ or Jc_{min}. This sequence is based upon the fact that when the preceding assumption is applied, the equivalent crack front length NB of small specimens should consist of each neighboring specimen (Fig. 22).

Figure 23 shows that the scatter of $K_{J_{min}}/K_{Ic}$-values decreases dramatically as the value of $NB/(Jc_{min}/\sigma_Y)$ increases. If the $NB/(Jc_{min}/\sigma_Y)$ value of 3000 (solid line) is chosen as the limit beyond which the scatter should be small, namely

$$NB \geq 3000 \frac{Jc_{min}}{\sigma_Y} \tag{3}$$

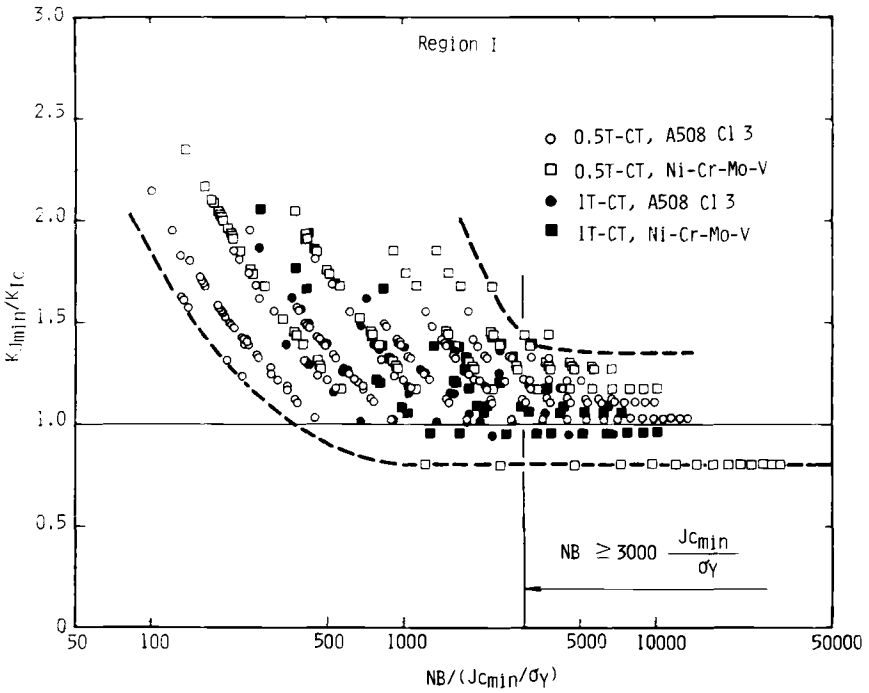

FIG. 23—*Relationship between* $K_{J_{min}}/K_{Ic}$ *and* $NB/(Jc_{min}/\sigma_Y)$ *in Region I.*

then the toughness variation of $K_{J_{min}}/K_{Ic}$ ranges from 0.8 to 1.4. This limit corresponds to about four to five times the specimen size required for K_{Ic} tests. Figure 23 also shows the much less scatter of 1T-CT specimens resulting in the limit smaller than $3000\,Jc_{min}/\sigma_Y$. This might be explained mainly by the fact that the effective crack front length, where plane-strain conditions exist, is larger in a 1T-CT specimen than in two 0.5T-CT specimens. The results obtained in Region II were also plotted in the same manner as in Fig. 23. Figure 24 shows that the limit which has the same toughness variation as in Region I is

$$NB \geq 1000 \frac{Jc_{min}}{\sigma_Y} \tag{4}$$

This limit in Region II is close to that for 1T-CT specimens in Region I (solid symbols in Fig. 23).

Figure 25 shows the scatter in valid K_{Ic}-values per ASTM E 399 obtained by this study and other investigators [*8–10*]. The figure suggests that the K_{Ic}-values can easily vary as much as ±20 percent at any K_{Ic} level. Therefore the toughness variation in $K_{J_{min}}/K_{Ic}$ specified by Eqs 3 and 4 would be acceptable

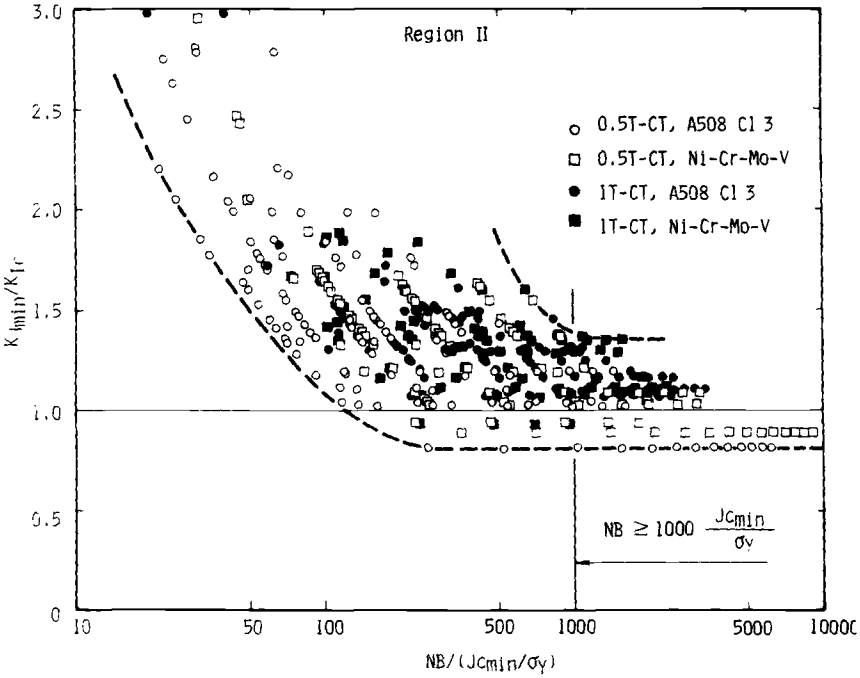

FIG. 24—*Relationship between* $K_{J_{min}}/K_{Ic}$ *and* $NB/(Jc_{min}/\sigma_Y)$ *in Region II.*

for the J test requirement. Figure 26 presents the relationship between the number of 1T-CT specimens required by Eq 3 and the fracture toughness K_{Ic}. If the flow stress of the material is 500 MPa, the number of specimens required to measure the K_{Ic} of 60 MPa$\sqrt{m}$ is more than four. When the lowest value of Jc among the four specimens meets the requirement of Eq 3, the minimum Jc-value, Jc_{min}, may be defined as J_{Ic}, but if not, one more specimen is required. Using the requirements of Eq 3 or Eq 4, the valid J_{Ic}-values in Region II can also be obtained without developing an R-curve. However, the use of Eq 4 requires a judgment whether the test temperature is located in Region II by measuring the stable crack growth with a scanning electron microscope.

Summarizing this study, the methods for J_{Ic} measurement in the entire temperature range are as follows;

Transition Region:

Region I: Statistical Method

$$\text{Requirement:} \quad NB \geq 3000 \frac{Jc_{min}}{\sigma_Y}$$

Region II: Modified R-Curve Method

Statistical Method

Requirement: $NB \geq 1000 \frac{Jc_{min}}{\sigma_Y}$ and stable crack growth

larger than 50 μm

Statistical Method

Requirement: $NB \geq 3000 \frac{Jc_{min}}{\sigma_Y}$

Upper-Shelf Region:
R-Curve Method Recommended by ASTM E24 Task Group

Figure 27 provides a schema of the methods of toughness measurement for J-integral tests. Figures 28 and 29 show the results obtained by these methods

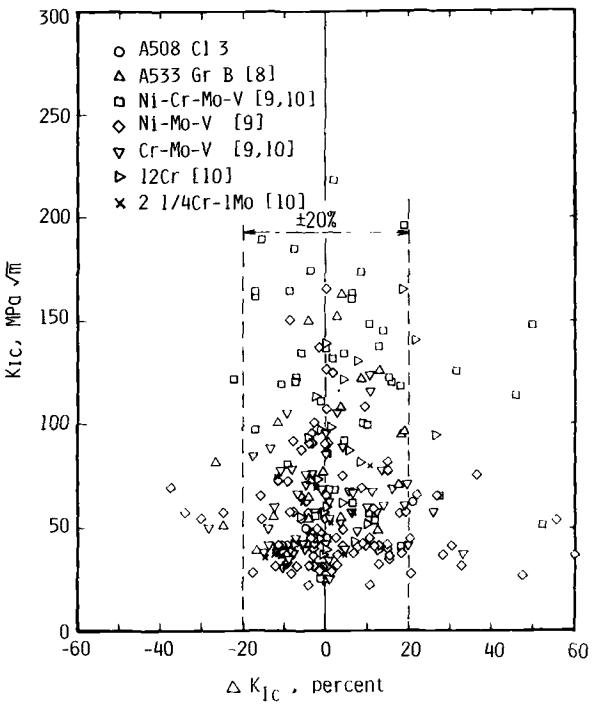

FIG. 25—*Scatter of valid K_{Ic}-values obtained in accordance with ASTM Method E 399.*

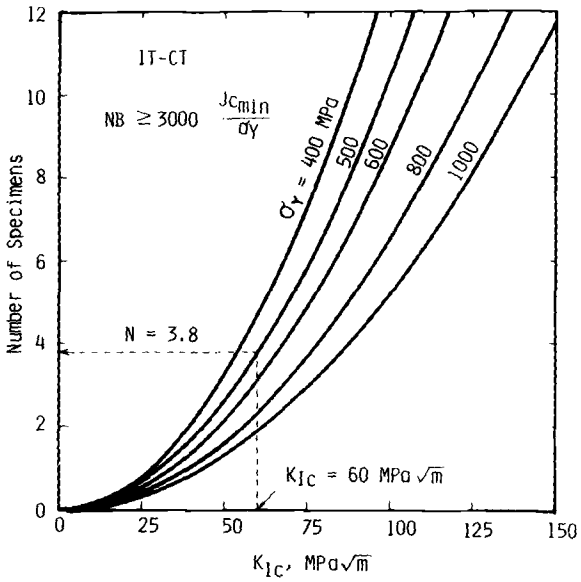

FIG. 26—*Relationship between the number of test specimens required by* NB ≥ *3000* Jc_{min}/σ_Y *and fracture toughness* K_{Ic}.

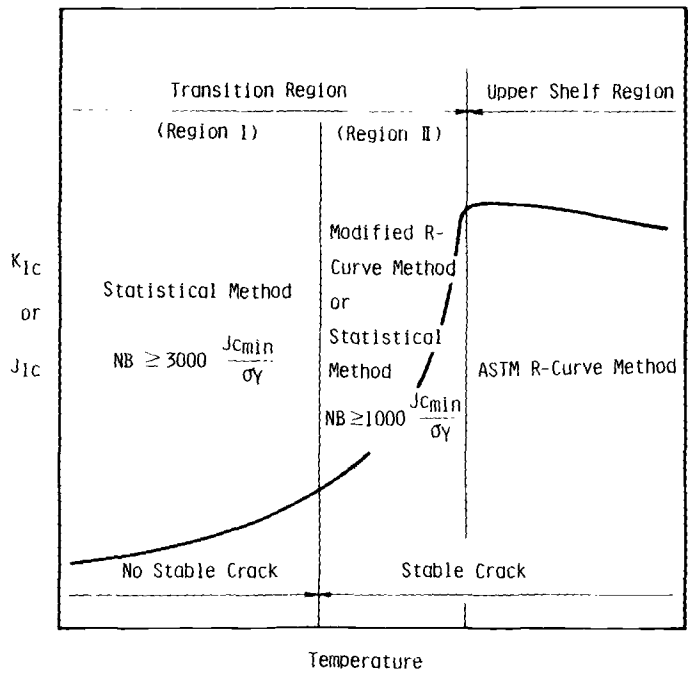

FIG. 27—*Schematic representation showing the methods for* J_{Ic} *measurement in the entire temperature range.*

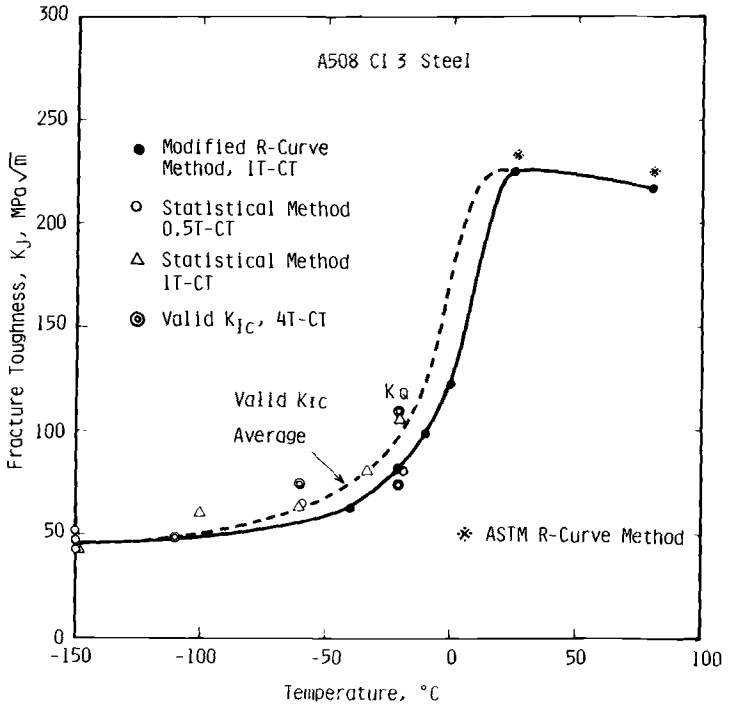

FIG. 28—*Comparison between* K_J*-values obtained by the proposed methods and the valid* K_{Ic}*-values for A508 Class 3 steel.*

for the A508 Class 3 and Ni-Cr-Mo-V steels. The K_J-values obtained by the proposed modified R-curve method coincide well with the lower bound of valid K_{Ic}, and the $K_{J_{min}}$-values obtained by the proposed statistical method agree well with the average measured by K_{Ic} tests (dotted line). Considering the statistical fracture toughness behavior in the transition temperature region, the lower-bound toughness should be referred to as the fracture toughness of the materials, because the fracture of a structure may well be controlled by the statistical distribution of toughness properties of the materials. Therefore, in Region II the modified R-curve method is recommended, and in Regions I and II the lowest bound of $K_{J_{min}}$-values obtained by the statistical method is more reliable for the toughness evaluation of structures. As a whole, the methods mentioned herein are proposed to measure the fracture toughness equivalent to the K_{Ic}-value per the ASTM Method.

Conclusions

To find the methods for measuring the elastic-plastic fracture toughness J_{Ic} in the transition region, fracture toughness tests were conducted on an ASTM A508 Class 3 nuclear pressure vessel steel and an ASTM A470 Ni-Cr-Mo-V

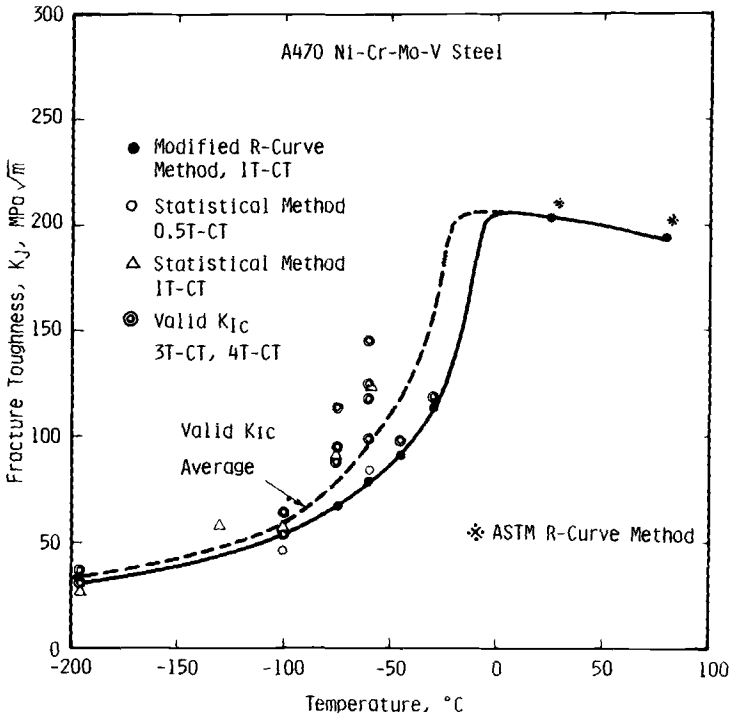

FIG. 29—*Comparsion between K_J-values obtained by the proposed methods and the valid K_{Ic}-values for A470 Ni-Cr-Mo-V steel.*

rotor steel using about 300 specimens. The results obtained in this study are summarized as follows:

1. The K_J-values which are converted from *Jc* of the smaller specimens showed a great deal of scatter, ranging from below the K_{Ic}-value to much higher toughness. This behavior is explained in terms of the statistical model based on a Weibull distribution and in part on the loss of constraint.

2. The majority of the specimens fractured in the transition region contained the stable crack growth. The fast brittle fracture behavior in the transition regime can be divided into two regions: (1) the region were fracture occurs on a blunting line (Region I) and (2) the region where fracture occurs on an R-curve (Region II). The scatter of the K_J-values in each region is caused by the amount of crack extension contained in the specimens.

3. In Region I, where the fracture occurs without stable crack growth, the lowest bound of $K_{J_{min}}$-values obtained using specimens that meet the requirement $NB \geq 3000\ Jc_{min}/\sigma_Y$ is recommended for measuring the fracture toughness of the materials. This method may also be used for toughness measurement in Region II.

4. In Region II, where the fracture occurs with stable crack growth, a J versus stable crack growth R-curve, that is, the modified R-curve, can be constructed using a SEM technique. The modified R-curve makes it possible to determine J_{Ic} at the initiation of a stable crack as an intersection of the R-curve and the ordinate. Four or more specimens are required to develop an R-curve and one of them needs crack growth of more than about 50 μm.

Acknowledgments

The authors wish to thank Dr. S. Kawaguchi, general plant manager, Muroran Plant, and Dr. K. Suzuki, manager, Research Laboratory, The Japan Steel Works, Ltd., for their encouragement during this study. They also acknowledge the cooperation of Messrs. K. Terashima and T. Kabutomori.

References

[1] Landes, J. D. and Begley, J. A. in *Fracture Analysis, ASTM STP 560*, American Society for Testing and Materials, 1974, pp. 170–186.

[2] Landes, J. D. and Begley, J. A. in *Developments in Fracture Mechanics Test Methods Standardization, ASTM STP 632*, W. R. Brown, Jr., and J. G. Kaufman, Eds., American Society for Testing and Materials, 1977, pp. 57–81.

[3] Clarke G. A. et al, *Journal of Testing and Evaluation*, Vol. 7, No. 1, Jan. 1979, pp. 49–56.

[4] Sumpter, J. D. G., *Metal Science*, Vol. 10, 1976, p. 359.

[5] Sunamoto, D., Satoh, M., Funada, T., and Tomimatsu, M., *Fracture 1977*, Vol. 3, *Proceedings*, Fourth International Conference on Fracture, Waterloo, Canada, June 1977, p. 267.

[6] Milne, I. and Chell, G. G. in *Elastic-Plastic Fracture, ASTM STP 668*, J. D. Landes, J. A. Begley, and G. A. Clarke, Eds., American Society for Testing and Materials, 1979, pp. 358–377.

[7] Landes, J. D. and Shaffer, D. H. in *Fracture Mechanics, ASTM STP 700*, American Society for Testing and Materials, 1980, pp. 368–382.

[8] Shabbits, W. O., Pryle, W. H., and Wessel, E. T., "Heavy Section Fracture Toughness Properties of A533 Grade B Class 1 Steel Plate and Submerged Arc Weldment," Technical Report No. 6, Heavy Section Steel Technology Program, Dec. 1969.

[9] Greenberg, H. D., Wessel, E. T., Clark, W. G., Jr., and Pryle, W. H., "Critical Flaw Sizes for Brittle Fracture of Large Turbine Generator Rotor Forgings," presented at the Fifth International Forgemaster Meeting, Terni, Italy, May 1970.

[10] Logsdon, W. A. in *Mechanics of Crack Growth, ASTM STP 590*, American Society for Testing and Materials, 1976, pp. 43–60.

Donald E. McCabe,[1] *John D. Landes,*[1] *and Hugo A. Ernst*[1]

An Evaluation of the J_R-Curve Method for Fracture Toughness Characterization

REFERENCE: McCabe, D. E., Landes, J. D., and Ernst, H. A., **"An Evaluation of the J_R-Curve Method for Fracture Toughness Characterization,"** *Elastic-Plastic Fracture: Second Symposium, Volume II—Fracture Resistance Curves and Engineering Applications, ASTM STP 803*, C. F. Shih and J. P. Gudas, Eds., American Society for Testing and Materials, 1983, pp. II-562–II-581.

ABSTRACT: This program involved the testing of compact specimens made from A508 Class 2A tube plate material. The objective of the program was to study specimen size and plan view dimension effects on the upper-shelf [204°C (400°F)] J_R-curve toughness behavior. Low upper-shelf Charpy toughness relative to typical reactor vessel materials was preferred.

The basis material was a 330-cm-diameter (130 in.) by 61-cm-thick (24 in.) slab of tube plate that had been rejected from service after ultrasonic inspection. There was some unwanted variability in strength and toughness properties and a careful specimen sampling plan did not entirely eliminate material variability from the test matrix. Therefore, a dimensional analysis in the form of key curves was used to categorize the material before attempting to decipher specimen geometry effects on the J_R-curve behavior. It was then possible to show that specimens of all sizes from 1T to 10T that had equal conditions of constraint would develop the same J_R-curve. The principal limitation on small specimens was that they simply lacked sufficient ligament size to sustain crack growth for full J_R-curve development.

The omega (ω) criterion was evaluated with the hope of identifying when $J-\Delta a_p$ data from specimens with short ligaments could be expected to depart from the specimen-size-independent J_R-curve. This was not successful herein from the standpoint that few specimens had sufficiently small ligaments to display this deviation. When deviation did in fact occur, it was not distinctly associated with a given value of ω.

A comparison was made between the load-displacement behavior of two 1T compact specimens having equal Charpy (CVN) toughness and J_R-curves but unequal strength properties (88 R_B versus 99 R_B). This was possible because of uniquely variable metallurgical conditions. The high-hardness specimen showed 40 percent greater load-bearing capacity. This was a good demonstration of why more than just J_R-curve behavior should be used to judge the suitability of materials for given applications. Material strength properties are contained in crack drive representations which are curves that are compared with J_R-curves. From such comparisons it is possible to predict load versus displacement and

[1]Senior engineer, advisory engineer, and senior engineer, respectively, Materials Engineering Department, Westinghouse R&D Center, Pittsburgh, Pa. 15235.

crack instability in untested configurations. Hence, part of the material flow property effect is not considered when comparing just J_R-curves.

KEY WORDS: elastic-plastic fracture, J_R-curve, A50B steel

Present American Society of Mechanical Engineers (ASME) code requirements on nuclear vessel materials [*1*][2] tend to focus attention on the transition region of fracture toughness behavior. Here linear-elastic K_{Ic} and rapid load K_{Id} toughness behaviors tend to be the parameters of dominant interest. The data in support of this approach have been largely derived from the early phases of the Heavy Section Steel Technology (HSST) experimental testing program [*2*]. This perhaps represented the first significant effort to apply fracture mechanics to pressure vessel materials and a great deal was learned. Because the tests were performed in the transition temperature range, the stable crack growth prior to brittle instability was not of any particular concern. A full range of compact specimen sizes from 1T to 12T was involved among various other specimen configurations of comparable sizes. At the time of this work, the need for upper-shelf toughness data and for crack growth measurement was not fully appreciated. In addition, it was considered that upper-shelf K_{Ic} was a measurable quantity provided that sufficiently large specimens were tested. Hence appropriate testing methods and a rational J_R-curve evaluation philosophy was not actually available for the critical early stages of the study.

In recent years, the technology of upper-shelf fracture toughness characterization has improved dramatically. The development of the J-integral to handle elastic-plastic conditions has been the major breakthrough [*3,4*]. In addition, the development and verification for the use of J has been strongly aided by the very powerful computer-related tool of numerical analysis. The conditions which ensure J-controlled crack growth are presently known qualitatively, and the framework has been established through analytical and numerical methods [*5*]. The experimental information in support of these concepts is extremely sparse, however, and one objective of the present project was to help to satisfy this shortcoming.

More recently, the J_R-curve characterization of the behavior of materials has developed as a focal point of elastic-plastic toughness studies. A major need for exploration was to demonstrate, for given specimen geometries, the conditions where geometry independence of J_R-curve behavior tends to break down. This not only applies to detection of a breakdown in conditions for J-controlled growth, but it also involves evaluation of the influence of variable constraint and consequent fracture toughness level changes.

The present project was initiated to provide experimental evidence in support of analytical concepts and to test the geometry independence aspects of

[2]The italic numbers in brackets refer to the list of references appended to this paper.

J_R-curve theory. The material chosen was A508, Class 2A, which is a material of interest to nuclear applications. Specimen design in the present report was confined to the standard compact geometry and this ranged in size from 1T [W = 5 cm (2 in.)] to 10T [W = 51 cm (20 in.)]. This program, therefore, represents something of a revisit to the HSST scope of specimen size study, except as was implied by the foregoing, all tests were made on the upper shelf of toughness behavior.

Material and Specimens

A rejected steam generator tube plate of A508-2A was selected for this study. It was a 3.4-m-diameter (136 in.) by 0.58-m-thick (24 in.) plate which had been rejected from possible service because of greater than allowable ultrasonic flaw indications within a central 1.5-m-diameter (58-in.) zone. Prior to the obtaining of specimens for a test matrix, the plate was subjected to an extensive material property survey [*6*] and, as might have been expected for such a large piece, there was high-strength-hardness properties in the skin [to about 12.7-cm (5 in.) depth] and in the rim zone [to about 51 cm (20 in.)]. The microstructures typical of this variability are shown in Fig. 1. Fracture toughness was measured using both Charpy V-notched specimens and standard 1T compact specimens. An unusual feature was that the material had high toughness at two levels of hardness which represent skin and midthickness microstructures. See Fig. 2. Above 95 R_B hardness, the extra-tough microstructure resulted from the high skin quench rate. The center slab positions are represented by 85 to 90 R_B and the improved toughness was due principally to reduced strength in spite of the less unfavorable ferrite-pearlite microstructure. This trend in toughness with location was also supported by J_R-curve data, as shown in Fig. 3. Values of nominal strength were calculated and these appear with the J_R-curves. The calculation was based on strength ratio, R_{sc}, from the ASTM Test for Plane-Strain Fracture Toughness of Metallic Materials (E 399-78a):

$$\sigma = R_{sc} \cdot \sigma_{ys} = \frac{2P}{B} \frac{(2W + a)}{(W - a)^2} \tag{1}$$

where

a = crack size updated for stable growth,
B = thickness,
P = load,
W = specimen width, and
σ_{ys} = yield strength.

Once maximum load is attained, σ_N tends to plateau with continued testing and the values shown were calculated for the latter stages of the test. Although

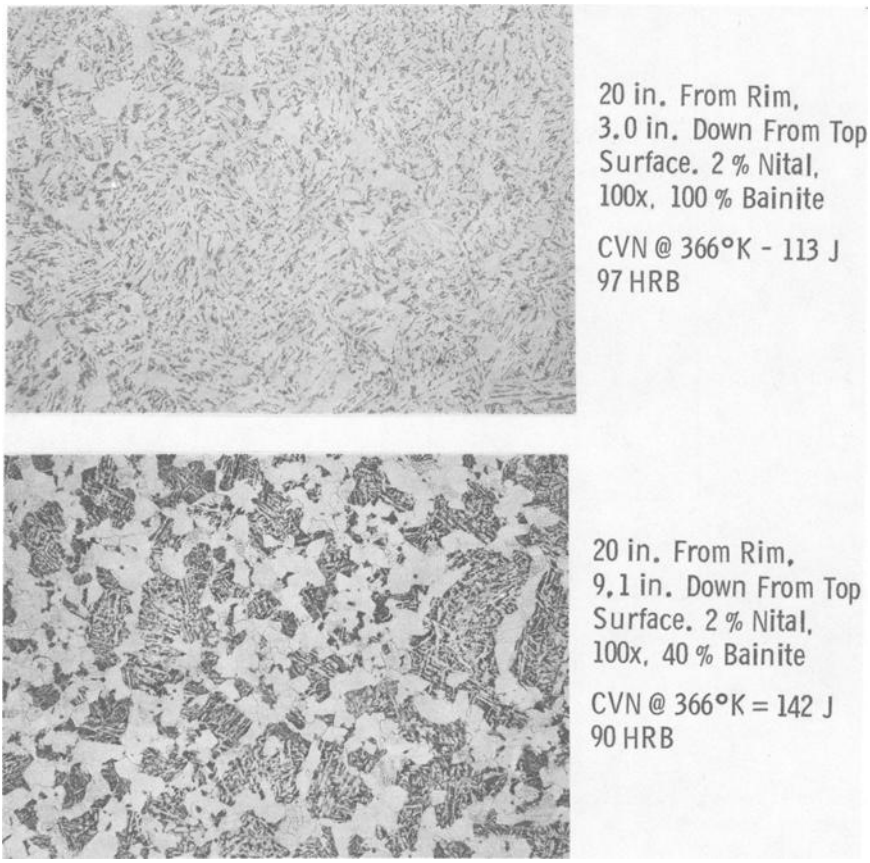

FIG. 1—*Surface and center microstructure at the 51-cm (20 in.) position on 330-cm-diameter (130 in.) by 58-cm-thick (23 in.) A508-2A tube plate. Source: Westinghouse Electric Corp.*

the trend in J_R-curve toughness appears to be consistent with that of CVN toughness in Fig. 2, a caution is that strength level identification by hardness is not necessarily an optimum mechanism for precise characterization.

For the specimen plan view study, all specimens were taken where the hardness was nominally 85 to 90 R_B and the cracks were oriented in the C-R direction of the forged piece (see ASTM Method E 399). The crack tips were positioned within an imaginary cylindrical shell zone about 66 cm (26 in.) in radially from the rim and at midthickness ± 12.7 cm (5 in.) off of the midthickness plane. Representative properties for this position are listed in Table 1.

A matrix showing the various specimen sizes and dimensions is presented in Table 2. The standard E 399 compact design specimen with all dimensions scaled proportionally is represented by a diagonal through the table from upper left to lower right. All specimens were 20 percent side-grooved (10 percent

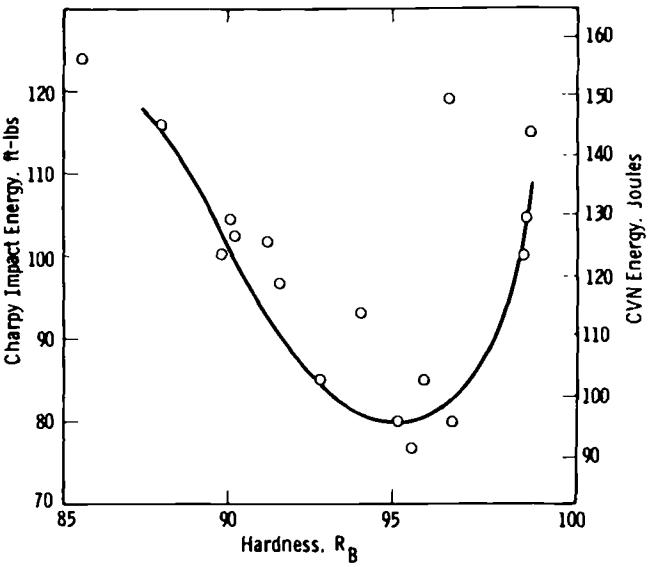

FIG. 2—*Upper-shelf Charpy energy versus hardness, R_B.*

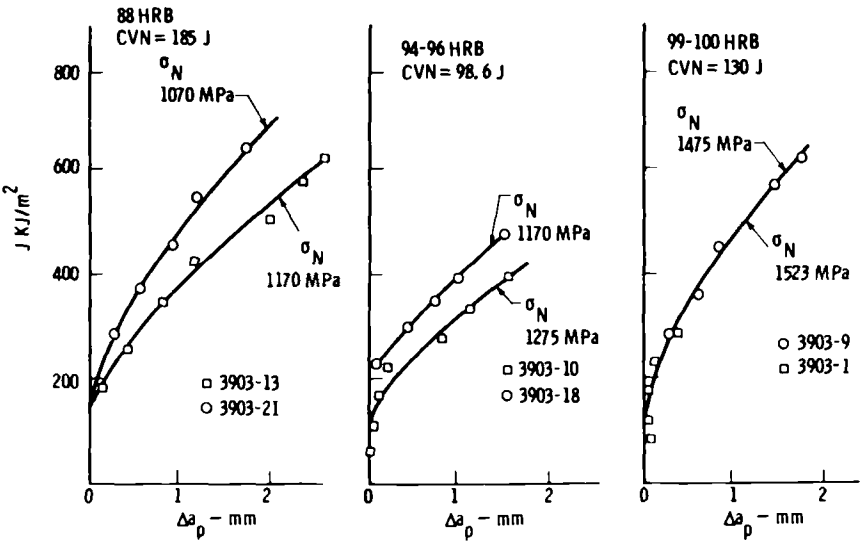

FIG. 3—*R-curves on 1T specimens; initial crack ratio 0.6.*

TABLE 1—*Tensile and Charpy properties of A508-2A at the mid-slab location where specimens were taken.*

Yield Strength		Tensile Strength		% Elongation	Reduction of Area, %	R_B	CVN[a]		FATT[b]	
ksi	MPa	ksi	MPa				ft-lb	J	°F	K
55	(380)	80	(550)	30	63	87	115	(157)	110	(396)

[a]CVN = Charpy V-notch.
[b]FATT = fracture appearance transition temperature.

TABLE 2—*Test matrix: elastic-plastic methodology to establish J_R-curves.*

Thickness, in., Gross/Net	Ligament Size, in.				
	½	1	2	4	10
0.5/0.4	$W = 2$	$W = 2$	$W = 4$	...	...
	$W = 2$	$W = 2$	...	...	
1.0/0.8	...	$W = 8$	$W = 8$	$W = 8$	$W = 20$
2.0/1.6	$W = 4$	...	$W = 4$	...	...
	...	$W = 8$	$W = 8$	...	...
4.0/3.2	...	$W = 8$	...	$W = 8$	...
10/8	...	...	...	...	$W = 20$

each side) after fatigue precracking. Figure 4 is a photograph of broken specimen halves also arranged in a matrix array. The smallest specimens shown (½T and 1XWOL) are not discussed in the present report (see Ref 7).

Experimental Conditions and Calculations

All specimens were tested at 477 K (400°F), which had been established beforehand as a temperature that is safely on the upper-shelf behavior for all possible specimen sizes. Crack growth was measured using unloading compliance and the details of the testing procedure have been covered in a companion paper [7]. In all cases, deformation theory J was obtained through crack growth correction using the following equation [8]

$$J_{i+1} = \left[J_i + \left(\frac{\eta}{b}\right)_i \frac{A_{i,i+1}}{B_N}\right]\left[1 - \left(\frac{\gamma}{b}\right)_i (a_{i+1} - a_i)\right] \tag{2}$$

where

$$\eta = 2 + 0.522(b/W)_i,$$

$$\gamma = 1 + 0.76(b/W)_i,$$

$A_{i,i+1}$ = work done on specimen between Steps i and $i + 1$, and
B_N = net thickness.

Crack growth was predicted using differential compliance from the following relationships

$$da = \frac{(W - a_0)}{2} \frac{dC}{C} \frac{1 + \alpha^2}{1 + \alpha}$$

$$\Delta a_p = \sum_{a_0}^{a_i} da \tag{3}$$

$$\alpha = \left[\left(\frac{2a}{b}\right)^2 + 2\left(\frac{2a}{b}\right) + 2\right]^{1/2} - \left[\frac{2a}{b} + 1\right]$$

The terms α and C (compliance slope) are updated at each increment for crack growth as the test proceeds. It is possible to compare materials on the

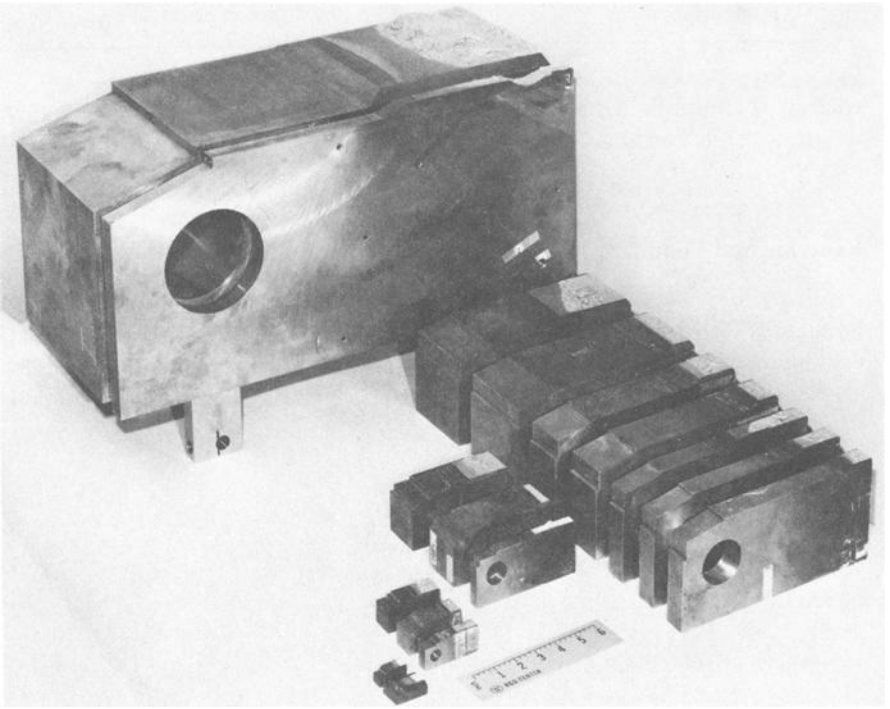

FIG. 4—*Specimen sizes tested in R-curve effects study.*

basis of nominal strength or key curve analysis [*19*], both of which are similar and can be equally effective in practice. The nominal strength can be calculated by Eq 1 and if the crack size dimension a is continuously updated for crack growth, an upper plateau value of σ_N is reached at about the onset of limit-load deformation. To be perfectly accurate, this value will sometimes rise modestly with extensive continued fully plastic deformation.

The key-curve concept is derived from dimensional analysis which defines calibration load-displacement behavior through a separation of material and dimensional variables.

For the compact specimen of unit thickness, the following describes a relationship of the acting variables

$$P = \frac{b^2}{W} F_1\left(\frac{\delta}{W} p, \frac{a}{w}\right) \tag{4}$$

Separation of variables gives

$$\frac{PW}{b^2} = F\left(\frac{\delta}{W} p\right) \cdot g\left(\frac{a}{W}\right) \tag{5}$$

The function $F(\delta_p/W)$ corresponds to the material property part of load versus plastic displacement behavior and the function $g(a/W)$ in concert with b^2 will handle specimen geometry effects. Ernst has determined the $g(a/W) - \eta$ relationship [*8*] and thus for compact specimens

$$g\left(\frac{a}{W}\right) = \exp(0.522b/W) \tag{6}$$

Introducing thickness and assuming that initial slope is a key to both elastic and plastic properties in response to side-grooving, we determine effective thickness, B_e

$$\frac{PW}{b^2 B_e} \cdot \frac{1}{g\left(\frac{a}{W}\right)} = F\left(\frac{\delta}{W} p\right) \tag{7}$$

Hence when load is normalized according to the left side of Eq 7 and plotted against normalized plastic displacement, δ_p/W, all specimen sizes and initial crack sizes should converge to a common "key curve." Again, as with Eq 1, the dimension b in Eqs 6 and 7 is updated for crack growth. Therefore, if the key curves indicate a difference between certain specimen comparisons, the implication is that the material flow properties are fundamentally different and a difference in toughness development should be expected.

J_R-Curve Results

In all, there were about 35 specimens tested for J_R-curve. Most were a priori expected to have sufficient remaining ligament sizes for valid J-controlled stable crack growth. The specimens with square to short-of-square ligaments were expected to have full plane-strain constraint and hence they would also tend to have the same J_R-curve. Figure 5 shows some representative J_R-curves and it is obvious that the results did not come out with the consistency that had been expected. To verify the accuracy of the J_R-curve data, the last data points shown on each set are duplicated (connected points) with one being crack growth from compliance indicated measurement and the other from 9-point heat tint measurement [ASTM Determination of J_{Ic}, A Measure of Fracture Toughness (E 813-81)]. To evaluate the validity of J, we can look at three proposed criteria, all of which are ligament size, b_0, related requirements, and ostensibly formulated to maintain conditions of J-controlled growth.

1. A limitation on crack growth to ensure deformation theory J [5]

$$\Delta a_p/b_0 < 0.06 \tag{8}$$

2. A limitation on the ratio of proportional strain increments compared with local nonproportional strain increments (omega [10])

$$\omega = \frac{b_0}{J}\,\frac{dJ}{da} \tag{9}$$

3. M-parameter; a limitation on crack-opening displacement relative to specimen ligament [10]

$$M_b = b_0\sigma_y/J \tag{10}$$

Table 3 lists calculated values of ω and M_b for the two conditions of (1) onset of crack growth and (2) the final values corresponding to the termination of J_R-curve development. Conservative provisional requirements have been proposed based upon the best judgment from numerical methods

$$\omega > 10$$

$$M_b > 20 \tag{11}$$

$$\Delta a_p/b_0 < 0.06$$

For crack initiation conditions, all specimen sizes met the requirements for J-controlled growth as stipulated in Eq 11. For the final data values, ω_f, $(M_b)_f$, and $\Delta a_p/b_0$, almost all specimens violated two of the three conditions. Viola-

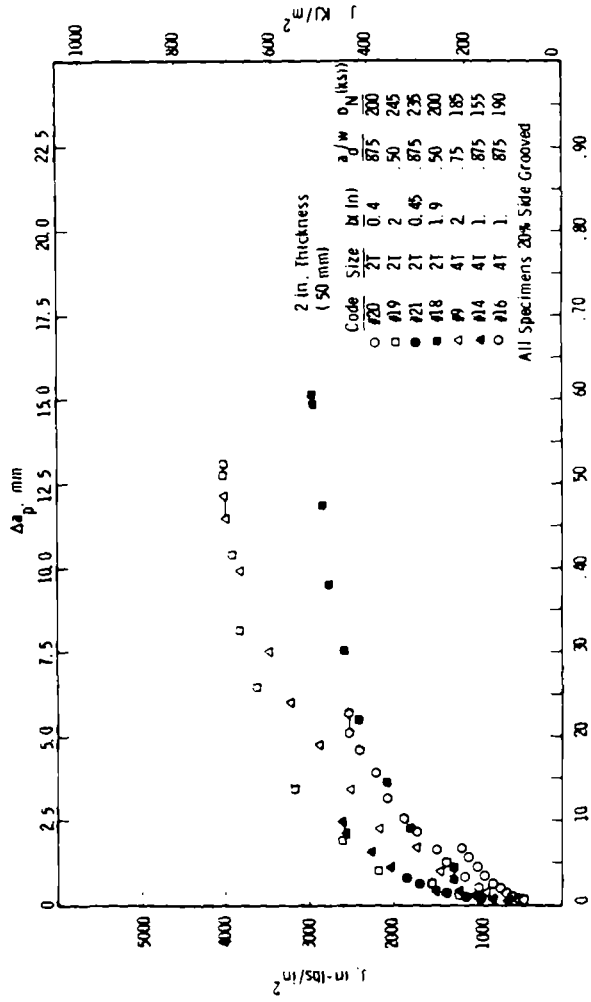

FIG. 5—*R-curves, Task II test.*

TABLE 3—*Values of* ω, M_b, *and* $\Delta a_p/b$ *at onset of growth (Subscript 0) and final data point (Subscript f).*

Code	Size	b_0, in.	ω_0	$(M_b)_0$	ω_f	$(M_b)_f$	$\Delta a_p/b_0$
1	10T	8.22	79	478	5.6[b]	92[b]	0.10[b]
2	10T	8.38	73	550	7.4[b]	91[b]	0.09[b]
3	10T	6.40	282	826	5.0	34	0.13
4	10T	8.95	113	664	5.4[b]	61[b]	0.11[b]
5	4T	3.86	181	360	1.6	35	0.19
6	4T	3.92	100	303	1.1[b]	36[b]	0.22[b]
7	4T	3.85	169	490	4.5	45	0.09
8	4T	3.89	160	495	4.2	44	0.10
9	4T	1.92	24	128	1.1	25	0.25
11	4T	1.93	48	225	1.0	27	0.27
12	4T	0.95	57	148	3.4	20	0.15
13	4T	0.89	20	83	1.9	20	0.23
14	4T	0.93	12	47	4.9	23	0.09
15	4T	0.96	39	84	3.0	22	0.12
16	4T	0.93	14	81	2.5	19	0.25
17	4T	0.92	45	128	2.0	19	0.25
18	2T	1.89	39	147	0.5	31	0.32
19	2T	1.96	109	183	0.5	25	0.27
20	2T	0.37	10	58	2.4	18	0.18
21	2T	0.45	16	31	5.7	16	0.07
23	2T	2.00	71	232	1.8	22	0.27
24	1T	0.97	13	68	3.3	18	0.28
25	1T	0.96	14	73	3.6	20	0.19
26	1T	0.98	19	62	0.4	14	0.27
27	1T	0.97	23	73	1.1	13	0.23
28	1T	0.45	18	58	0.8	13	0.22
29	1T	0.48	15	48	0.8	12	0.25
30	1T	0.48	32	56	0.9	7	0.28
31	1T	0.48	26	46	0	8	0.28

[a] 1 in. = 25.4 mm.
[b] Not final but intermediate at about 1 in. (25.4 mm) of crack growth.
$M > 25.0$
$\omega > 10$.

tion of the latter crack growth limit is arbitrary, at the discretion of the investigator. However, error in deformation theory J is presumably eliminated through the use of Eq 2.

The omega (ω) criterion of Eq 10 is obviously violated in almost all cases at the end of J_R-curve determination. Omega, however, is not a parameter that is amenable to the assignment of absolute values. Material work-hardening characteristics affect proportional-nonproportional strain relationships and hence an appropriate ω for one material may not necessarily be appropriate for another material. In addition to this, Eq 9 represents only a rather general mathematical confirmation that J-controlled conditions can in fact exist with crack growth. To set an acceptable level of omega (Eq 10 for example) is roughly equivalent to the setting of an acceptable upper limit for error in J_R-curve slope. Ernst [*12*] has shown that in approximate terms, the slope error is

roughly ($1/\omega \times 100$) in percent. Since slope change is a very subtle effect, this makes the task of detecting departure from J_R-curve due to ω violation subjective and difficult to separate from the usual J_R experimental data scatter.

The M_b factor evaluation which is employed in a proposed plane-strain J_R-curve test method was set at 20 and this is not only used on minimum ligament size, but it is also used for minimum net section thickness to develop plane-strain J_R-curve conditions. The comparison in Table 3 is for the remaining ligament, and all but a few 1T specimens were satisfactory by M_b at the end of the J_R-curve test.

To draw a conclusion from the foregoing considerations, the variability seen in J_R-curve behavior in Fig. 5 was not attributable to crack growth measurement inaccuracy or due to strongly definable violations of J-controlled growth conditions.

All specimen results were compared on the basis of their key-curve behavior, that is, Eq 7, plotting normalized load versus normalized plastic displacement, and five levels were identified. These along with the corresponding J_R-curves are plotted in Figs. 6 through 10. The nominal strengths at 1.5 percent

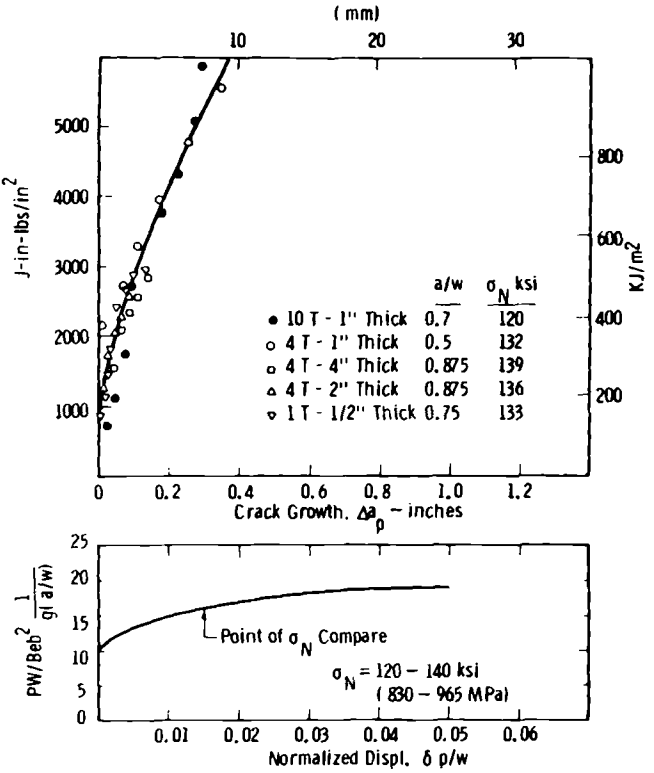

FIG. 6—*J_R-curves for material in the 830 to 965-MPa (120 to 140 ksi) nominal strength category.*

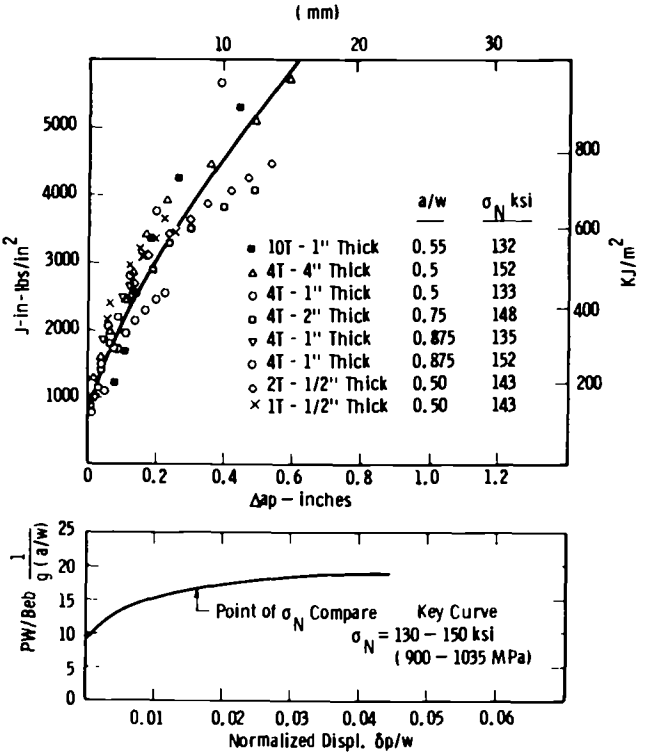

FIG. 7—*J_R-curves for material in the 900 to 1035-MPa (130 to 150 ksi) nominal strength category.*

plastic displacement (relative to W) are also indicated. It is evident from these comparisons that the J_R-curve variability in Fig. 5 was principally due to variability in material properties.

The comparison between the J_R-curves of Figs. 9 and 10 follows the Charpy toughness versus material hardness trend indicated in Fig. 2 and J_R-curve trend from 1T specimens in Fig. 3. The overall J_R-curve and key-curve behaviors are summarized in Fig. 11.

The J_R-curve data of Fig. 8 has the indication of greatest significance to the original objectives of this study. Here data from 25.4-cm-thick (10 in.) 10T specimens and 2.54-cm-thick (1 in.) 1T specimens have about the same flow properties, as indicated by key curve, and it can be seen that the J_R-curve toughness is also comparable. In this case, the extent of J_R-curve data development in small specimens appears to be truncated due to exhaustion of remaining ligament and loss in load-carrying capability of the specimen.

Table 4 lists hardnesses and nominal strengths (@ 0.015 δ_P/W) in the specimen geometry matrix format. Again, the standard E 399 geometry appears on a diagonal from top left to bottom right. Specimens to the lower left have less-than-square remaining ligaments and everything to the upper right

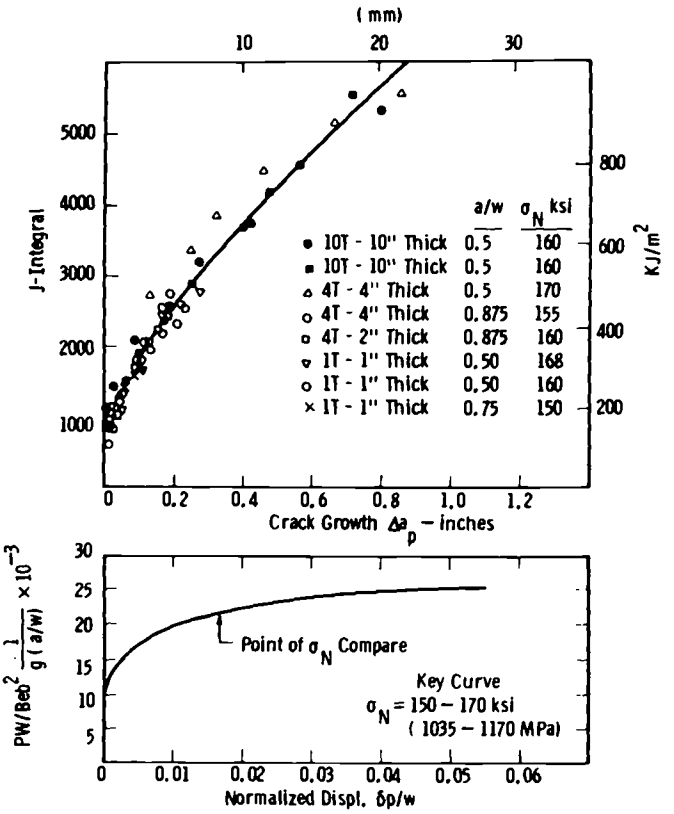

FIG. 8—*J_R-curves for material in the 1035 to 1170-MPa (150 to 170 ksi) nominal strength category.*

represents long thin ligaments. Despite the hardness variability problem, it is possible to detect some loss of constraint effects in specimens to the right of the diagonal. At about 88 R_B hardness, the nominal strength should be about 1102 MPa (160 ksi) with full plane-strain constraint. A loss of constraint is also evident from observing specimen thickness reductions as compared in Fig. 12 for matched broken halves of 4T plane-view specimens. Side-grooving 20 percent throughout the text matrix undoubtedly had promoted conditions of plane-strain constraint but the effectiveness was definitely limited as Fig. 12 illustrates.

The M_b equation referred to earlier could be calculated on the basis of thickness instead of ligament, which was used with regard to validation of J-controlled growth. This of course, is an entirely different value and the proposed ASTM J_R-curve method [*11*] currently recommends $M_B > 20$ for plane-strain J_R-curves where

$$M_B = B_N \sigma_y / J \tag{12}$$

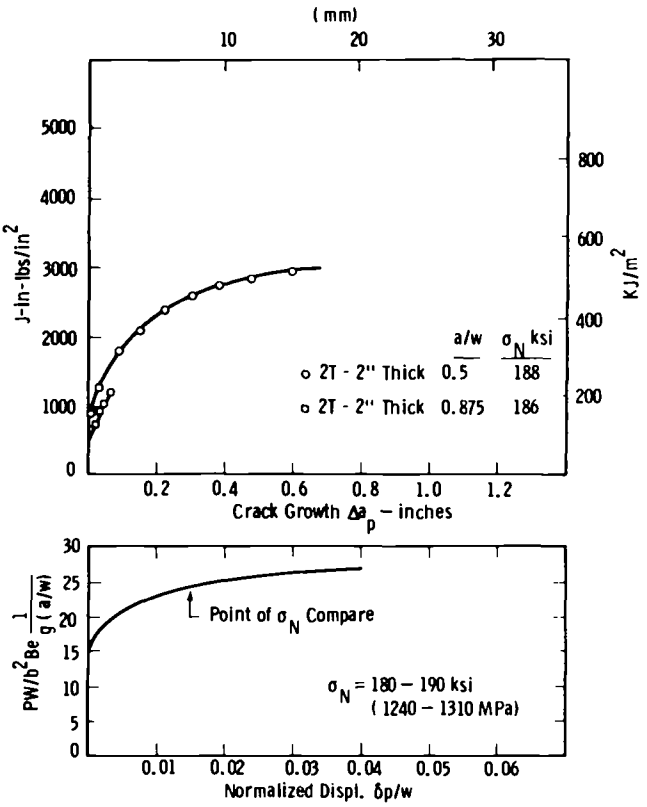

FIG. 9—*J_R-curves for material in the 1240 to 1310-MPa (180 to 190 ksi) nominal strength category.*

Table 5 lists thickness-based M_B for the various specimens at the end of J_R-curve development. The results here tend to support the proposition that plane-strain J_R-conditions exist at M_B greater than or equal to 20.

The material property screening part of this program that was discussed earlier had provided an interesting opportunity to compare the A508 material at contrasting strength levels (88 R_B and 99 R_B), both having good toughness by Charpy V evaluation (see Fig. 2). Two such specimens were found and their J_R-curves are compared in Fig. 13 (lower part). They were non-side-grooved 1T specimens with initial crack sizes of 31.597 and 31.699 mm (1.244 and 1.248 in.), so specimen dimensions are no factor in this comparison. The fracture toughness by J_R-curve appears to suggest that there is no difference. However, if we examine the test specimen behavior in terms of load versus displacement, there is a highly significant difference. The maximum load of the high-strength specimen was greater by about 40 percent, despite the identical J_R-curves. The onset of crack growth had developed much earlier on in the test. This result clearly emphasizes the importance of material strength and the fact that J_R-

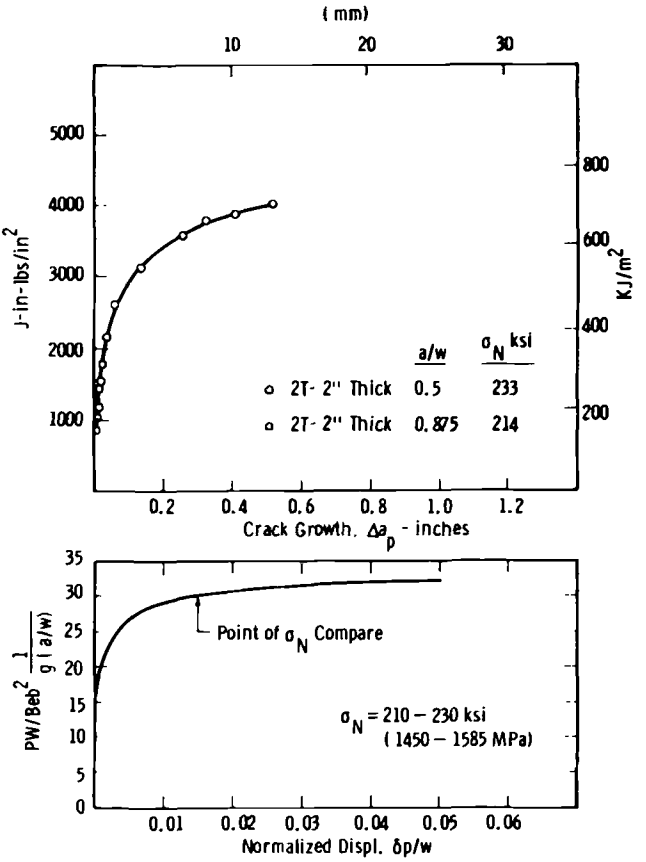

FIG. 10—*J_R-curves for material in the 1450 to 1585-MPa (210 to 230 ksi) nominal strength category.*

curves in the J-Δa_p format do not necessarily completely describe inservice performance of materials. In other words, materials are not necessarily properly selected on the basis of J_R-curve comparisons alone. Material flow property differences appear in crack drive and this in concert with J_R-curve behavior dictates the resulting load-versus-displacement behavior.

Conclusions

J_R-curves tended to be independent of specimen geometry effects when the results were categorized according to their key-curve behaviors. This separation encompasses not only differences according to metallurgical strength causes, but also differences in constraint conditions.

Side-grooving of specimens is an aid to promotion of plane-strain constraint. However, the 20 percent used here was most effective on square cross

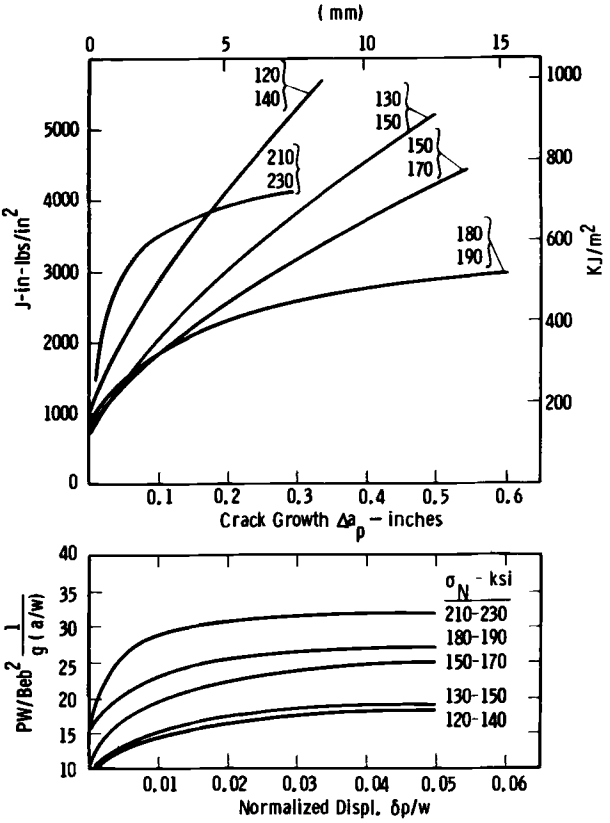

FIG. 11—*J_R-curve and key-curve summary.*

TABLE 4—*Hardness, HR_B, and nominal strength, ksi.*

Gross Thickness \ Remaining Ligament	½ in. (125 mm)	1 in. (25.4 mm)	2 in. (50.8 mm)	4 in. (101.6 mm)	10 in. (254 mm)
½ in. (12.5 mm)	84/86 133/133	86/86 143/143	88 143	...	...
1 in. (25.4 mm)	85/88 150/150	83/88/90 135/160/168	90 148	87/87 133/132	84/86 120/132
2 in. (50.8 mm)	92/98 186/214	81/87 136/160	88/92/98 148/188/233	...	...
4 in. (101.6 mm)	...	81/89 135/152	...	85/88 152/170	...
10 in. (254 mm)	...	...	...	...	88 160/160

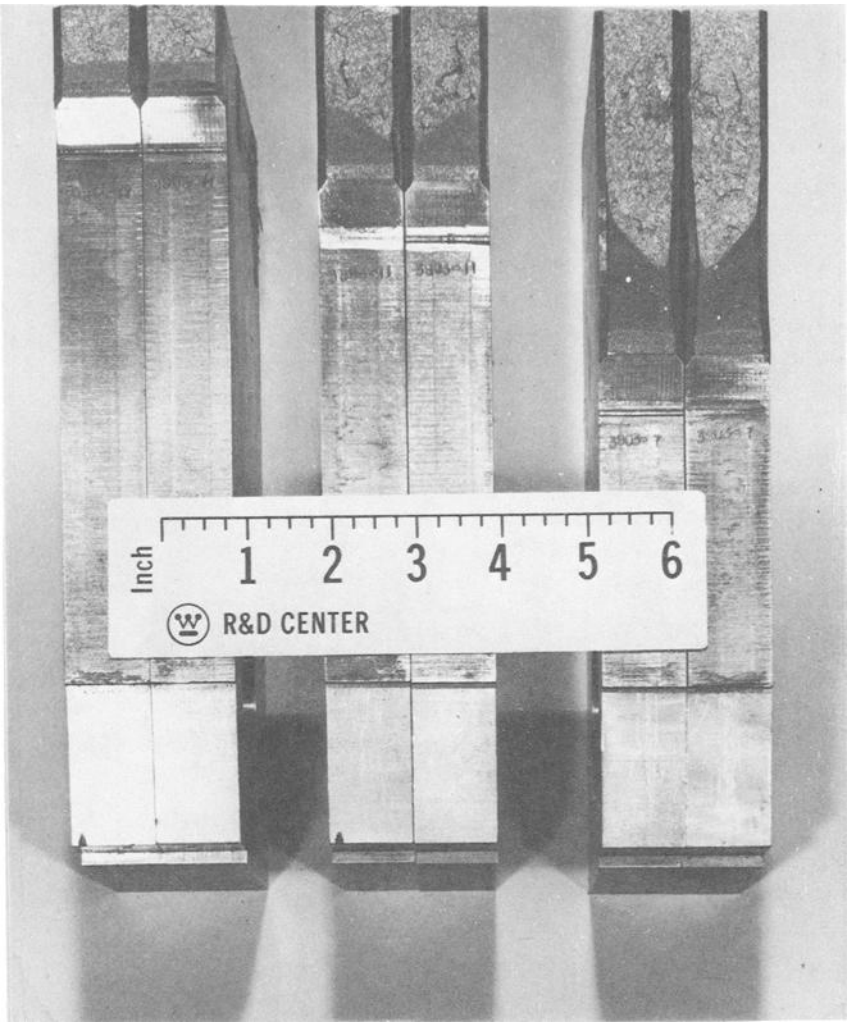

FIG. 12—*Variable-ligament-size 4T specimens, 2.54 cm (1 in.) thick.*

TABLE 5—*Values of* M_b *for thickness and plane-strain control.*

B_N \ b_0	1/2 in.	1 in.	2 in.	4 in.	10 in.
0.4 in.	9	7.5	6	...	...
0.8 in.	30	20	15	6.5	5.0
1.6 in.	75	42	30	...	...
3.2 in.	...	85	...	35	...
8 in.	...	...	...	...	80

1 in. = 25.4 mm.

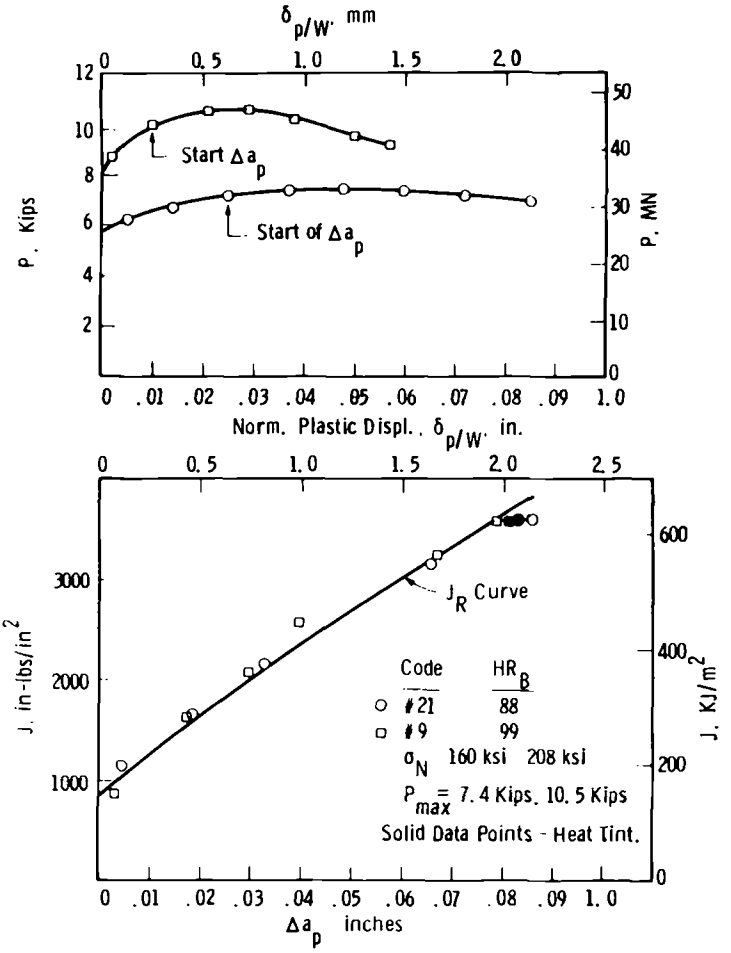

FIG. 13—*Comparison of R-curve and test record behavior.*

section or less-than-square cross section ligaments. The side-grooving of long and thin ligaments is not totally effective in promoting plane-strain constraint. A thickness-based M_B-value criterion of 20 appeared to assure plane-strain J_R-curve conditions for 20 percent side-grooved specimens.

J_R-curve behavior was shown to be almost completely dominated by strength-toughness interactions and remaining ligament conditions relating to conditions of J-controlled growth did not appear to be a factor in these tests. After substantial crack growth, the calculated ω-values tended toward unity but this was only weakly related to J_R-curve results. Since this proportional-to-nonproportional strain condition indicator was so weak, the ω-criterion does not presently appear to be usable in experimental J-validation. The parameter M_b ap-

pears to be a more sturdy evaluation method and better suited to test method applications.

Observation of load-displacement behavior of identical specimens with identical J_R-curves but having different strength levels has demonstrated the importance of crack drive considerations. Material strength in relatively ductile materials increases the load-bearing capability of components and this information is contained in crack drive relationships. Therefore, selection of materials for given applications should not be based on J_R-curve comparisons alone.

Acknowledgment

The work presented in this paper was supported by the Electric Power Research Institute (EPRI) under Contract RP1238-2. The authors would like to acknowledge Dr. D. M. Norris, Jr., EPRI project manager, who contributed to the planning of the work.

The authors would also like to acknowledge the assistance of their colleagues at Westinghouse R&D Center: W. H. Pryle, who assisted with specimen preparations; L. W. Burtner, who worked diligently on the careful testing of the specimens; and F. X. Gradich, who assisted in the equipment development.

References

[1] ASME Boiler and Pressure Vessel Code, Section III. Rules for Construction of Nuclear Power Plant Construction, Appendix G.

[2] Witt, F. J., "The USAEC Heavy Section Steel Technology Program Objectives and Status," First International Conference on Structural Mechanics in Reactor Technology, Paper G4/1. 6 Jan. 1972.

[3] Rice, J. R., *Journal of Applied Mechanics. Transactions of the American Society of Mechanical Engineers*, June 1968, pp. 379-386.

[4] Paris, P. C. in *Flaw Growth and Fracture, ASTM STP 631*, American Society for Testing and Materials, 1977, pp. 3-27.

[5] Shih, C. F., deLorenzi, H. G., and Andrews, W. R. in *Elastic-Plastic Fracture, ASTM STP 668*, J. D. Landes, J. A. Begley, and G. A. Clarke, Eds., American Society for Testing and Materials, 1979, pp. 65-120.

[6] Landes, J. D. et al, "Elastic-Plastic Methodology to Establish R-Curves and Instability Criteria," EPRI Contract No. RP 1238-2, Third Semiannual Report, Electric Power Research Institute, Palo Alto, Calif., 21 March 1980.

[7] McCabe, D. E. and Landes, J. D., this publication, pp. II-353-II-371.

[8] Ernst, H. A., Paris, P. C., and Landes, J. D. in *Fracture Mechanics—13th Conference, ASTM STP 743*, American Society for Testing and Materials, 1981.

[9] Ernst, H. A., Paris, P. C., Rossow, M., and Hutchinson, J. W. in *Fracture Mechanics, ASTM STP 677*, American Society for Testing and Materials, 1979, pp. 581-599.

[10] Hutchinson, J. W. and Paris, P. C. in *Elastic-Plastic Fracture, ASTM STP 668*, J. D. Landes, J. A. Begley, and G. A. Clarke, Eds., American Society for Testing and Materials, 1979, pp. 37-64.

[11] Gudas, J. P., "Results of the J-Integral R-Curve Round Robin Program," presented at the Second ASTM Symposium on Elastic-Plastic Fracture, Philadelphia, Pa., 6-9 Oct. 1981.

[12] Ernst, H. A., this publication, pp. I-191-I-213.

Dan A. Davis,[1] *Michael G. Vassilaros,*[1] *and John P. Gudas*[1]

Specimen Geometry and Extended Crack Growth Effects on J_I-R Curve Characteristics for HY-130 and ASTM A533B Steels

REFERENCE: Davis, D. A., Vassilaros, M. G., and Gudas, J. P., **"Specimen Geometry and Extended Crack Growth Effects on J_I-R Curve Characteristics for HY-130 and ASTM A533B Steels,"** *Elastic-Plastic Fracture: Second Symposium, Volume II—Fracture Resistance Curves and Engineering Applications, ASTM STP 803*, C. F. Shih and J. P. Gudas, Eds., American Society for Testing and Materials, 1983, pp. II-582-II-610.

ABSTRACT: An evaluation of the ductile fracture toughness and J_I-R curve properties of HY-130 and ASTM A533B-HSST-03 steels in response to systematic variations of thickness and crack length in the side-grooved compact specimen geometry was carried out. A series of 2T compact specimens was produced to varying thicknesses, and with various fatigue crack lengths. Elastic compliance J_I-R curve tests were performed, and analyses of J_{Ic}, the slope of the J_I-R curve, the accuracy of the Ernst-Paris-Landes approximation for J_I, and an assessment of the ω criterion for J-controlled crack growth were carried out. Results showed that J_{Ic} of both steels was geometry independent when validity criteria were met. Both steels displayed a clear dependence of the slope of the J_I-R curve as related to thickness/ligament ratio and degree of crack extension. A limiting thickness/ligament ratio of 1 is necessary to ensure a conservative J_I-R curve slope over the full range of crack growth. The Ernst-Paris-Landes expression was shown to accurately describe J_I to crack extension values of 0.4 b_0 for HY-130 steel. Limited evidence suggests that a minimum value of ω to guarantee J-controlled crack growth with compact specimens in HY-130 steel is 2.

KEY WORDS: elastic-plastic fracture, compact specimen geometry, J_I-R curve, J_{Ic}, tearing modulus, J-controlled crack growth

Characterization of ductile fracture properties of materials using J-integral concepts has been shown to be valid and widely applicable [*1*].[2] Development and application of single-specimen J-integral test methods [*2,3*] accelerated interest in the J-integral crack growth resistance curve. Hutchinson and Paris

[1]David W. Taylor Naval Ship R&D Center, Annapolis, Md. 21402.

[2]The italic numbers in brackets refer to the list of references appended to this paper.

[4] discussed the theoretical foundation for utilizing the J-integral approach beyond crack initiation, and defined conditions for J-controlled crack growth. Subsequently, analyses of the stability of crack growth in the J-controlled regime were conducted by Paris and co-workers [5,6]. These investigations included the development of tearing instability relationships under fully plastic conditions for several specimen geometry configurations, and the definition of the nondimensional tearing modulus parameter which incorporates the slope of the J_I-R curve [5].

Experimental validation of the tearing instability concept was performed initially by Paris and co-workers [6] using 3-point bend specimens, and subsequently by Joyce and Vassilaros [7] and Vassilaros and co-workers [8] using compact specimens. The results of 3-point bend specimen tests showed that the size of the remaining ligament affected the tearing instability behavior of the steel tested. Results of tests with compact specimens showed that in the case of very tough steels, the functional form of the J_I-R curve had to be evaluated to accurately predict the point of instability [8]. These tearing instability validation experiments pointed to the importance of evaluating the sensitivity of the J-integral R-curve to specimen geometry for both materials characterization and structural analysis applications.

Several recent investigations have been directed to evaluating effects of compact specimen geometry modifications on J_{Ic} and the J_I-R curve of steels [9-12]. Andrews and Shih [9] evaluated J_{Ic} and the slope of the J_I-R curve of ASTM A533B steel and concluded that side grooves machined to a total thickness reduction of 12.5 percent suppressed the shear lip formation. They also showed that the slope of the J_I-R curve developed with 4T compact specimens was reduced in specimens with side grooves of 50 percent total section reduction. In tests performed with HY-130 steel, Gudas and co-workers [10] showed that while J_{Ic} was independent of specimen geometry, tearing modulus values were minimized by specimen side-grooving. They also indicated that tearing modulus values for side-grooved specimens with greater than 12.5 percent total thickness reduction remained constant with increasing crack length, at the value coinciding with the lowest value measured for planar specimens. In their investigations of specimen geometry effects on J_I-R curves for A533B steel, Vassilaros et al [11] and Gudas et al [12] indicated that 20 percent side grooves produced straight fronts for tearing, and resulted in lower J_I-R curves, testing modulus values, and somewhat reduced J_{Ic}-values than those obtained for planar specimens. These investigations also suggested that the tearing modulus was unaffected by variations in thickness-to-ligament ratios of 0.63 to 3.89 and was not sensitive to changes in slip mode from planar to cross slip.

The objective of this investigation was to evaluate the ductile fracture toughness and J_I-R curve properties of HY-130 and ASTM A533B steels in response to systematic variations of thickness and crack length to ligament length ratios in the side-grooved compact specimen geometry. Additionally,

the accuracy of the Ernst-Paris-Landes expression [*13*] for J_I was experimentally evaluated. A series of 2T compact specimens was produced to varying thicknesses and with various fatigue crack lengths. Elastic compliance J_I-R curve tests were performed with both steels, and several analyses were employed to assess the variation in the ductile fracture parameters.

Experimental Procedure

ASTM A533B (HSST-03) and HY-130 structural steels were utilized in this investigation. Chemical compositions and mechanical properties for these steels are shown in Table 1.

All ductile fracture experiments utilized 2T compact specimens (Fig. 1) with maximum thicknesses of 12.5, 25.0, and 50.0 mm (0.5, 1.0 and 2.0 in.). Specimens were fatigue precracked according to the ASTM Test for Plane-Strain Fracture Toughness of Metallic Materials (E 399-78a) criteria to crack depths of approximately 0.55, 0.65, 0.75, and 0.85 a/W, where a is the crack length and W the specimen width. These combinations of specimen thickness and crack length provided the wide range of specimen thickness/ligament ratios (B/b) shown schematically in Fig. 2. Side grooves were machined into all specimens, after precracking, along the nominal crack plane to a total section reduction of 20 percent. Tests of A533B steel were conducted at 150°C (302°F) while HY-130 steel specimens were tested at room temperature, approximately 25°C (77°F).

J_I-R curve tests in this investigation were conducted using the computer-interactive unloading compliance test procedure of Joyce and Gudas [*3*]. The J-integral tests were undertaken by performing a series of approximately 10 percent unloadings during the course of a normal fracture mechanics type test. For all tests, the values of crack length and changes in crack length were calculated from compliance measurements using the expression suggested by Saxena and Hudak [*14*]. J_I was calculated according to the expression [*13*]

$$J_{(i+1)} = \left[J_i + \left(\frac{\eta}{b}\right)_i \frac{A_{i,i+1}}{B_N}\right]\left[1 - \left(\frac{\gamma}{b}\right)_i (a_{i+1} - a_i)\right] \tag{1}$$

where

η = 2 + (0.522) b/W for compact specimens,
W = specimen width,
γ = 1 + (0.76) b/W,
b_i = instantaneous length of remaining ligament,
B_N = minimum specimen thickness,
a_i = instantaneous crack length,
$A_{i,i+1}$ = area under load versus load-line displacement record between lines of constant displacement at Points i and $i + 1$.

TABLE 1—*Chemical compositions and mechanical properties for ASTM A533B-HSST-03 and HY-130 steels.*

Chemical Composition, weight %													
Material	C	Mn	P	Si	Ni	Cr	Mo	V	S	Cu	Al	Co	Ti
A533B-HSST-03	0.20	1.26	0.011	0.25	0.56	...	0.45	...	0.018	...	...	...	...
HY-130	0.12	0.73	0.005	0.028	4.94	0.46	0.51	0.047	0.003	0.02	0.02	0.02	0.06

Mechanical Properties					
Material	0.2% Offset Yield Strength, MPa (ksi)	Ultimate Tensile Strength, MPa (ksi)	Elongation in 50 mm (2 in.), %	Reduction of Area, %	CVN Impact Energy, J (ft-lb)
A533B-HSST-03 149°C (301°F)	461(67)	620(90)	22	58	87(64)
HY-130 Room Temperature	935(136)	995(144)	22	63	87(64)

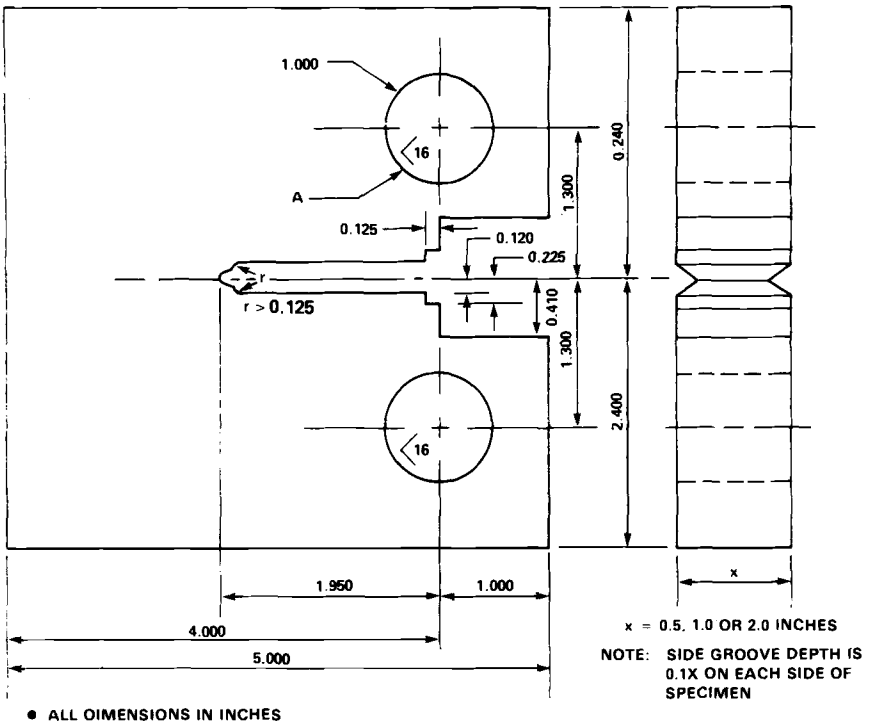

FIG. 1—*2T compact specimens tested in this investigation (25.4 mm = 1.0 in.).*

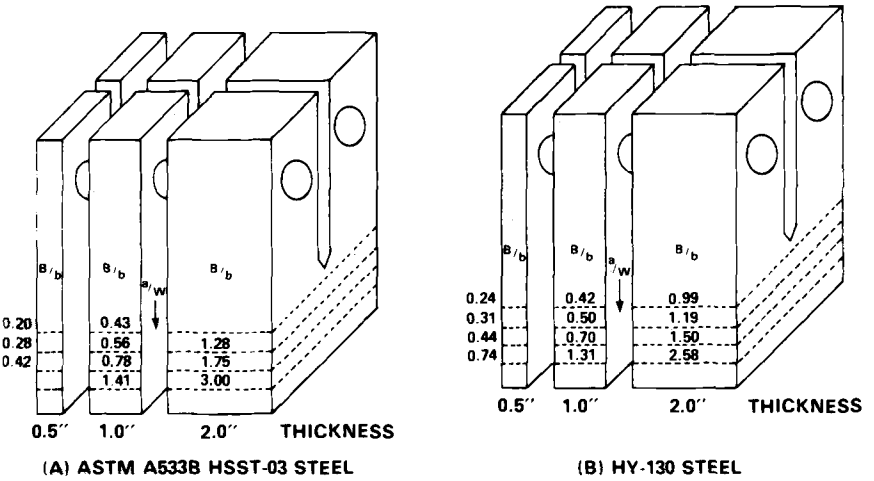

FIG. 2—*Thickness/ligament ratios for 2T compact specimens tested in this investigation (25.4 mm = 1.0 in.).*

At the conclusion of testing, specimens were heat-tinted at 380°C (716°F) for 30 min to mark the extent of crack growth. After breaking open at liquid nitrogen temperature, the crack length and crack extension were measured at nine equally spaced points across the crack front, including the two surfaces. An average value of the two surface measurements was used as a single point in computing crack dimension and crack growth.

For the 2T compact specimens tested in this investigation, J_{Ic}-values were computed according to the ASTM Determination of J_{Ic}, A Measure of Fracture Toughness (E 813-81) that is, from the intersection of the crack-opening stretch line with the least-squares fit of data points, which fell at least 0.15 mm (0.006 in.) beyond the blunting line, and did not exceed 1.5 mm (0.06 in.) in crack growth from that blunting line. The tearing moduli were calculated using the following expression [6]

$$T = \frac{E}{\sigma_y^2} \frac{dJ_I}{da} \tag{2}$$

where

T = tearing modulus,
dJ_I/da = slope of J_I versus crack extension curve,
E = elastic modulus, and
σ_y = flow stress = $\frac{\text{(yield strength + ultimate tensile strength).}}{2}$

The dJ_I/da-values in this investigation were calculated using two methods, including the least-squares linear regression fit of J_I crack extension data within the ASTM E 813-81 exclusion region, and the least-squares linear fit of J_I crack extension data which fell at least 0.15 mm (0.006 in.) beyond the blunting line to 50.0 mm (0.200 in.) of crack growth.

Results and Discussion

The purpose of the first segment of the investigation was to determine the effects of varying specimen thickness and remaining ligament on the ductile fracture properties of HY-130 and A533B steels. As part of the data analysis, each specimen test was examined for validity using criteria established in Standard E 813-81. The first of these criteria requires that specimen thickness and remaining ligament be greater than or equal to $15\,J/\sigma_y$, where J and remaining ligament relate to a specific amount of crack extension. This criterion was considered satisfied for both J_{Ic} and tearing modulus evaluations if it was met at 1.5 mm (0.060 in.) of crack extension. For evaluations of tearing modulus data determined over 5.0 mm (0.20 in.) (far field) of crack extension, results were considered valid if the $15\,J/\sigma_y$ criterion was satisfied at 5.0 mm (0.20 in.) of crack extension. Secondly, E 813-81 requires that thick-

ness and the remaining initial ligament be greater than $25 J_{Ic}/\sigma_y$. Test results in this investigation were considered for the data analysis only if they met both validity criteria. Parameters necessary to determine these validity limits for HY-130 steel are presented in Table 2, and for A533B steel in Table 3.

Test results from this investigation are presented in Table 4 for HY-130 steel, while results of A533B steel tests are given in Table 5. These tables include specimen identification, J_{Ic} (according to E 813), dJ_I/da, thickness/ligament ratio, tearing moduli measured at 1.5 mm (0.06 in.) and 5.0 mm

TABLE 2—*Validity criterion parameters for HY-130 steel compact specimens.*

		Specimen Thickness		
a/W	Data	12.5 mm (0.5 in.)	25 mm (1.0 in.)	51 mm (2.0 in.)
0.55	Specimen ID	FST-21B	FST-10	FST-5
	a_0/W	0.56	0.56	0.60
	B_N, mm (in.)	10.4 (0.41)	18.5 (0.73)	40.4 (1.59)
	b_0, mm (in.)	44.5 (1.75)	43.9 (1.73)	40.7 (1.60)
	J_{Ic}, KJ/m^2 (in.-lb/in.^{2})	115 (655)	109 (621)	129 (738)
	$25 J_{Ic}/\sigma_y$, mm (in.)	3.0 (0.12)	2.8 (0.11)	3.3 (0.13)
	Δa, b_i $15 J/\sigma_y$, mm (in.)	>5.0 (0.200)	>5.0 (0.200)	>5.0 (0.200)
	Δa, B_N $15 J/\sigma_y$, mm (in.)	>5.0 (0.200)	>5.0 (0.200)	>5.0 (0.200)
	Δa, valid by $15 J/\sigma_y$, mm (in.)	>5.0 (0.200)	>5.0 (0.200)	>5.0 (0.200)
0.65	Specimen ID	FST-17M	FST-11	FST-8
	a_0/W	0.67	0.66	0.67
	B_N, mm (in.)	10.4 (0.41)	17.3 (0.68)	40.7 (1.60)
	b_0, mm (in.)	33.5 (1.32)	34.3 (1.35)	34.0 (1.34)
	J_{Ic}, KJ/m^2(in.-lb/in.^{2})	101 (578)	118 (674)	129 (735)
	$25 J_{Ic}/\sigma_y$, mm (in.)	2.5 (0.10)	3.0 (0.12)	3.3 (0.13)
	Δa, b_i $15 J/\sigma_y$, mm (in.)	>5.0 (0.200)	>5.0 (0.200)	>5.0 (0.200)
	Δa, B_N $15 J/\sigma_y$, mm (in.)	>5.0 (0.200)	>5.0 (0.200)	>5.0 (0.200)
	Δa, valid by $15 J/\sigma_y$, mm (in.)	>5.0 (0.200)	>5.0 (0.200)	>5.0 (0.200)
0.75	Specimen ID	FST-20M	FST-15B	FST-6
	a_0/W	0.77	0.76	0.74
	B_N, mm (in.)	10.4 (0.41)	17.0 (0.67)	39.6 (1.56)
	b_0, mm (in.)	23.6 (0.93)	24.2 (0.96)	26.4 (1.04)
	J_{Ic}, KJ/m^2 (in.-lb/in.^{2})	138 (789)	109 (623)	140 (802)
	$25 J_{Ic}/\sigma_y$, mm (in.)	3.6 (0.14)	2.8 (0.11)	3.6 (0.14)
	Δa, b_i $15 J/\sigma_y$, mm (in.)	>5.0 (0.200)	>5.0 (0.200)	>5.0 (0.200)
	Δa, B_N $15 J/\sigma_y$, mm (in.)	>5.0 (0.200)	>5.0 (0.200)	>5.0 (0.200)
	Δa, valid by $15 J/\sigma_y$, mm (in.)	>5.0 (0.200)	>5.0 (0.200)	>5.0 (0.200)
0.85	Specimen ID	FST-16T	FST-14T	FST-7
	a_0/W	0.86	0.86	0.85
	B_N, mm (in.)	10.4 (0.41)	18.5 (0.73)	40.4 (1.59)
	b_0, mm (in.)	14.2 (0.56)	14.2 (0.56)	15.6 (0.62)
	J_{Ic}, KJ/m^2 (in.-lb/in.^{2})	124 (711)	129 (736)	138 (787)
	$25 J_{Ic}/\sigma_y$, mm (in.)	3.3 (0.13)	3.3 (0.13)	3.6 (0.14)
	Δa, b_i $15 J/\sigma_y$, mm (in.)	>5.0 (0.200)	>5.0 (0.200)	>5.0 (0.200)
	Δa, B_N $15 J/\sigma_y$, mm (in.)	>5.0 (0.200)	>5.0 (0.200)	>5.0 (0.200)
	Δa, valid by $15 J/\sigma_y$, mm (in.)	>5.0 (0.200)	>5.0 (0.200)	>5.0 (0.200)

TABLE 3—*Validity criterion parameters for ASTM A533B-HSST-03 steel compact specimens.*

		Specimen Thickness			
a/W	Data	12.5 mm (0.5 in.)	25 mm (1.0 in.)	51 mm (2.0 in.)	
0.55	Specimen ID	FSH-811	FSH-807		
	a_0/W	0.54	0.56		
	B_N, mm (in.)	9.4 (0.37)	18.5 (0.73)		
	b_0, mm (in.)	46.6 (1.83)	44.1 (1.74)		
	J_{Ic}, KJ/m^2 (in.-lb/in.^{2})	260 (1485)	202 (1153)	...	
	$25\,J_{Ic}/\sigma_y$, mm (in.)	11.2 (0.44)	8.6 (0.34)		
	Δa, b_i $15\,J/\sigma_y$, mm (in.)	>5.0 (0.200)	>5.0 (0.200)		
	Δa, B_N $15\,J/\sigma_y$, mm (in.)	1.27 (0.050)	3.18 (0.125)		
	Δa, valid by $15\,J/\sigma_y$, mm (in.)	1.27 (0.050)-B_N	3.18 (0.125)-B_N		
0.65	Specimen ID	FSH-815	FSH-806	FSH-800	
	a_0/W	0.64	0.67	0.66	
	B_N, mm (in.)	9.4 (0.37)	18.5 (0.73)	40.6 (1.60)	
	b_0, mm (in.)	33.8 (1.33)	33.1 (1.31)	31.6 (1.25)	
	J_{Ic}, KJ/m^2 (in.-lb/in.^{2})	159 (911)	233 (1330)	152 (867)	
	$25\,J_{Ic}/\sigma_y$, mm (in.)	6.86 (0.27)	9.91 (0.39)	6.60 (0.26)	
	Δa, b_i $15\,J/\sigma_y$, mm (in.)	>5.0 (0.200)	>5.0 (0.200)	>5.0 (0.200)	
	Δa, B_N $15\,J/\sigma_y$, mm (in.)	2.4 (0.095)	>5.0 (0.200)	>5.0 (0.200)	
	Δa, valid by $15\,J/\sigma_y$, mm (in.)	2.4 (0.095)-B_N	>5.0 (0.200)	>5.0 (0.200)	
0.75	Specimen ID	FSH-813	FSH-808	FSH-803	
	a_0/W	0.75	0.74	0.77	
	B_N, mm (in.)	9.9 (0.39)	18.8 (0.74)	40.9 (1.61)	
	b_0, mm (in.)	23.6 (0.93)	24.1 (0.95)	23.2 (0.91)	
	J_{Ic}, KJ/m^2 (in.-lb/in.^{2})	288 (1647)	233 (1330)	192 (1099)	
	$25\,J_{Ic}/\sigma_y$, mm (in.)	12.19 (0.48)	91.4 (0.36)	8.13 (0.32)	
	Δa, b_i $15\,J/\sigma_y$, mm (in.)	>5.0 (0.200)	>5.0 (0.200)	>5.0 (0.200)	
	Δa, B_N $15\,J/\sigma_y$, mm (in.)	0.8 (0.030)	>5.0 (0.200)	>5.0 (0.200)	
	Δa, valid by $15\,J/\sigma_y$, mm (in.)	0.8 (0.030)-B_N	>5.0 (0.200)	>5.0 (0.200)	
0.85	Specimen ID		FSH-809	FSH-804	FSH-802
	a_0/W		0.87	0.82	0.86
	B_N, mm (in.)		18.5 (0.73)	43.4 (1.71)	40.6 (1.60)
	b_0, mm (in.)		13.2 (0.52)	18.8 (0.74)	13.4 (0.53)
	J_{Ic}, KJ/m^2 (in.-lb/in.^{2})	..	203 (1159)	164 (938)	217 (1239)
	$25\,J_{Ic}/\sigma_y$, mm (in.)		8.6 (0.34)	7.11 (0.28)	9.14 (0.36)
	Δa, b_i $15\,J/\sigma_y$, mm (in.)		2.3 (0.090)	3.5 (0.137)[a]	1.3 (0.053)
	Δa, B_N $15\,J/\sigma_y$, mm (in.)		3.1 (0.123)[a]	3.5 (0.137)[a]	>5.0 (0.200)
	Δa, valid by $15\,J/\sigma_y$, mm (in.)		2.3 (0.090)-b_i	3.5 (0.137)[a]	1.3 (0.053)-b_i

[a]Indicates total measured crack extension (Δa) obtained in this specimen.

TABLE 4—*J_IR curve test results for HY-130 steel compact specimens.*

a/W	Data	Specimen Thickness		
		12.5 mm (0.5 in.)	25 mm (1.0 in.)	51 mm (2.0 in.)
0.55	Specimen ID	FST-21B	FST-10	FST-5
	B_N/b_0	0.24	0.42	0.99
	a_0/W	0.56	0.56	0.60
	J_{Ic}, KJ/m^2 (in.-lb/in.^{2})	115 (655)	109 (621)	129 (738)
	dJ_I/da, KJ/m^3(in.-lb/in.^{3})	7510 (10900)	8750 (12700)	5010 (7270)
	T at 1.5 mm (0.06 in.)Δa	16.1	18.8	10.8
	T at 5.0 mm (0.20 in.)Δa	6.8	7.2	5.4
	Estimated Δa, mm (in.)	25.68 (1.011)	26.18 (1.031)	30.33 (1.194)
	Measured Δa, mm (in.)	26.77 (1.054)	25.55 (1.006)	30.66 (1.207)
0.65	Specimen ID	FST-17M	FST-11	FST-8
	B_N/b_0	0.31	0.50	1.19
	a_0/W	0.67	0.66	0.67
	J_{Ic}, KJ/m^2(in.-lb/in^2)	101 (578)	118 (674)	129 (735)
	dJ_I/da, KJ/m^3(in.-lb/in.^{3})	7780 (11300)	11480 (16660)	4410 (6400)
	T at 1.5 mm (0.06 in.)Δa	16.7	24.6	9.5
	T at 5.0 mm (0.20 in.)Δa	6.9	9.9	5.7
	Estimated Δa, mm (in.)	24.69 (0.972)	26.64 (1.049)	25.45 (1.002)
	Measured Δa, mm (in.)	24.92 (0.981)	26.92 (1.060)	25.55 (1.006)
0.75	Specimen ID	FST-20M	FST-15B	FST-6
	B_N/b_0	0.44	0.70	1.50
	a_0/W	0.77	0.76	0.74
	J_{Ic}, KJ/m^2(in.-lb/in.^{2})	138 (789)	109 (623)	140 (802)
	dJ_I/da, KJ/m^3(in.-lb/in.^{3})	7260 (10400)	8740 (12520)	4140 (6020)
	T at 1.5 mm (0.06 in.)Δa	15.4	18.5	8.2
	T at 5.0 mm (0.20 in.)Δa	7.1	7.8	5.4
	Estimated Δa, mm (in.)	5.21 (0.205)	19.02 (0.749)	19.18 (0.755)
	Measured Δa, mm (in.)	5.64 (0.222)	19.41 (0.764)	19.63 (0.773)
0.85	Specimen ID	FST-16T	FST-14T	FST-7
	B_N/b_0	0.74	1.31	2.58
	a_0/W	0.86	0.86	0.85
	J_{Ic}, KJ/m^2(in.-lb/in.^{2})	124 (711)	129 (736)	138 (787)
	dJ_I/da, KJ/m^3(in.-lb/in.^{3})	7950 (11550)	6070 (8810)	4730 (6870)
	T at 1.5 mm (0.06 in.)Δa	17.1	13.0	10.2
	T at 5.0 mm (0.20 in.)Δa	6.1	6.3	5.5
	Estimated Δa, mm (in.)	9.86 (0.388)	9.42 (0.371)	11.00 (0.433)
	Measured Δa, mm (in.)	9.93 (0.391)	9.91 (0.390)	11.35 (0.447)

(0.200 in.) of crack extension, and measured and estimated crack extension values.

Prior to evaluating the effects of thickness/ligament ratio on the J_I-R curve characteristics of HY-130 steel, it is important to comment on the effects of the 20 percent side grooves machined after precracking. These side grooves acted to eliminate tunneling and provide straight crack fronts, as shown in Fig. 3, in the HY-130 steel compact specimens. This straight crack front geometry provided excellent correlation between estimated and measured crack extension values, where the difference was less than 5 percent.

TABLE 5—*J_IR-curve test results for ASTM A533B-HSST-03 steel compact specimens.*

		Specimen Thickness			
a/W	Data	12.5 mm (0.5 in.)	25 mm (1.0 in.)	51 mm (2.0 in.)	
0.55	Specimen ID	FSH-811	FSH-807		
	B_N/b_0	0.20	0.43		
	a_0/W	0.54	0.56		
	J_{Ic}, KJ/m^2 (in.-lb/in.^{2})	260 (1485)	202 (1153)		
	dJ_I/da, KJ/m^3 (in.-lb/in.^{3})	9830 (14270)	25050 (36350)	...	
	T at 1.5 mm (0.06 in.)Δa	57	146		
	T at 5.0 mm (0.20 in.)Δa	43	79		
	Estimated Δa, mm (in.)	20.09 (0.791)	16.94 (0.667)		
	Measured Δa, mm (in.)	20.88 (0.822)	17.78 (0.700)		
0.65	Specimen ID	FSH-815	FSH-806	FSH-800	
	B_N/b_0	0.28	0.56	1.28	
	a_0/W	0.64	0.67	0.66	
	J_{Ic}, KJ/m^2 (in.-lb/in.^{2})	159 (911)	233 (1330)	152 (867)	
	dJ_I/da, KJ/m^3 (in.-lb/in.^{3})	10280 (14910)	14800 (21480)	10430 (15130)	
	T at 1.5 mm (0.06 in.)Δa	60	86	61	
	T at 5.0 mm (0.20 in.)Δa	45	60	38	
	Estimated Δa, mm (in.)	15.54 (0.612)	14.07 (0.554)	16.05 (0.632)	
	Measured Δa, mm (in.)	19.79 (0.779)	15.34 (0.604)	18.97 (0.747)	
0.75	Specimen ID	FSH-813	FSH-808	FSH-803	
	B_N/b_0	0.42	0.78	1.75	
	a_0/W	0.75	0.74	0.77	
	J_{Ic}, KJ/m^2(in.-lb/in.^{2})	288 (1647)	212 (1214)	192 (1099)	
	dJ_I/da, KJ/m^3 (in.-lb/in.^{3})	11590 (16820)	6210 (9010)	13480 (19560)	
	T at 1.5 mm (0.06 in.)Δa	68	36	79	
	T at 5.0 mm (0.20 in.)Δa	34	35	54	
	Estimated Δa, mm (in.)	7.95 (0.313)	8.74 (0.344)	7.42 (0.292)	
	Measured Δa, mm (in.)	11.48 (0.452)	10.92 (0.430)	9.98 (0.393)	
0.85	Specimen ID		FSH-809	FSH-804	FSH-802
	B_N/b_0		1.41	2.30	3.00
	a_0/W		0.87	0.82	0.86
	J_{Ic}, KJ/m^2 (in.-lb/in.^{2})		203 (1159)	164 (938)	217 (1239)
	dJ_I/da, KJ/m^3 (in.-lb/in.^{3})	...	10910 (15830)	14730 (21380)	20610 (29910)
	T at 1.5 mm (0.06 in.)Δa		65	86	120
	T at 5.0 mm (0.20 in.)Δa		55	70	106
	Estimated Δa, mm (in.)		3.12 (0.123)	3.28 (0.129)	2.06 (0.081)
	Measured Δa, mm (in.)		3.35 (0.132)	3.58 (0.141)	2.64 (0.104)

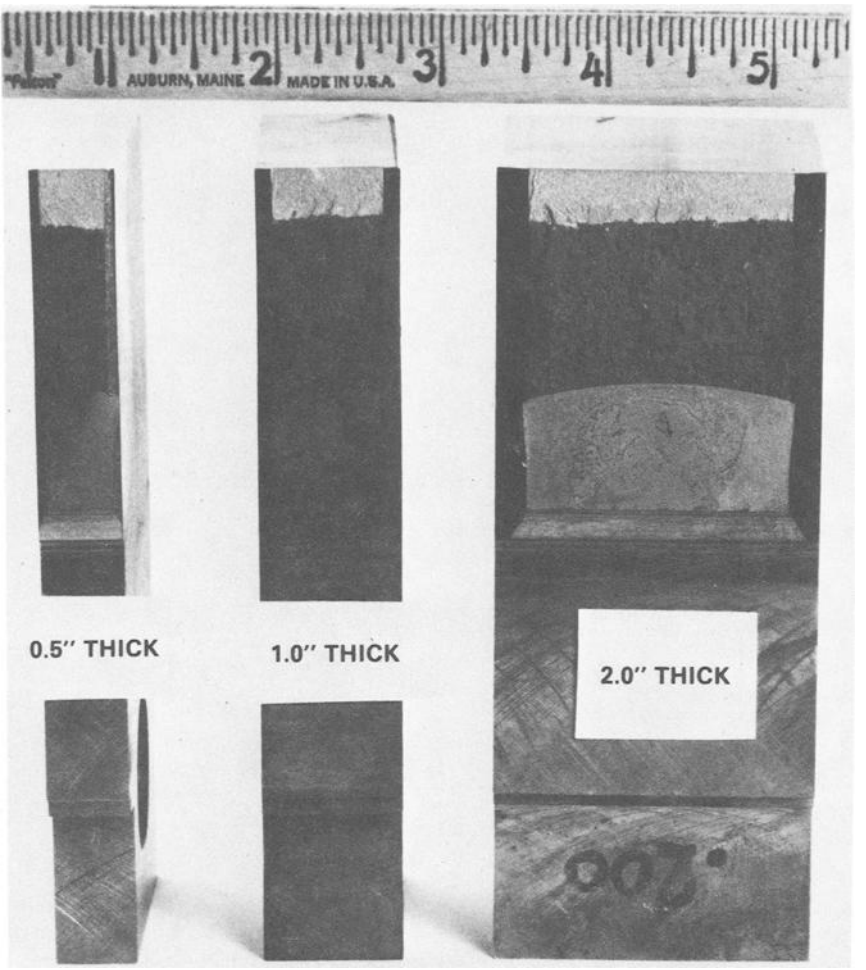

FIG. 3—*Fracture surfaces of tested 2T compact specimens of HY-130 steel with various thickness/ligament ratios (25.4 mm = 1.0 in.).*

Examination of the J_I-R curves for HY-130 steel tests, as shown in Fig. 4 [12.5 mm (0.5 in.) thick], Fig. 5 [25 mm (1.0 in.) thick], and Fig. 6 [51 mm (2.0 in.) thick], indicates that these data show minimal scatter among the specimens tested. Additionally, data in Table 2 indicate that all HY-130 steel compact specimens are valid by the requirements previously established, up to 5.0 mm (0.200 in.) of crack extension.

The plot of J_{Ic} versus net thickness/ligament ratio for HY-130 steel is presented in Fig. 7. These resutls indicate that, with a single exception, J_{Ic}-values exhibit minimal variation with increase in thickness/ligament ratio. This

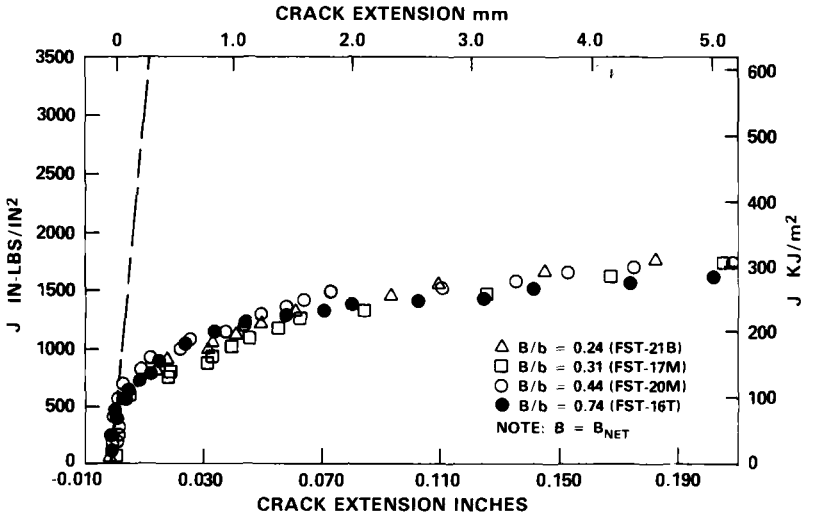

FIG. 4—J_I *versus crack extension data for 12.5-mm-thick (0.5-in.) 2T compact specimens of HY-130 steel.*

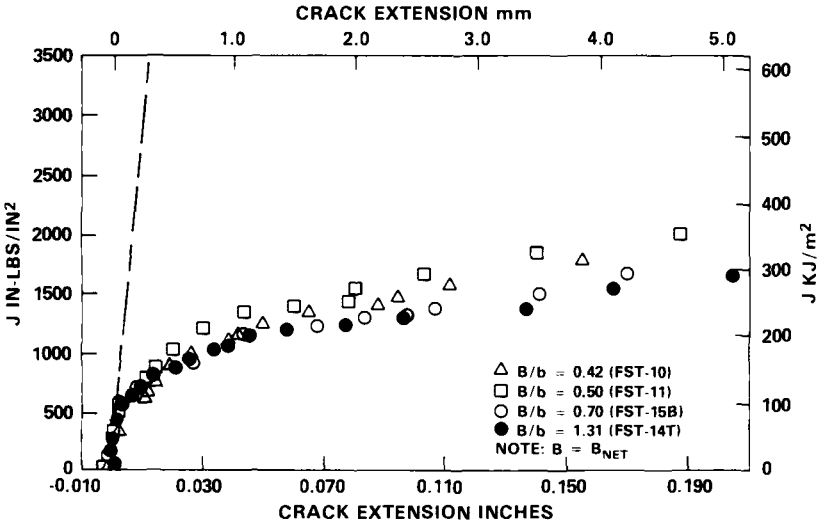

FIG. 5—J_I *versus crack extension data for 25-mm-thick (1.0 in.) 2T compact specimens of HY-130 steel.*

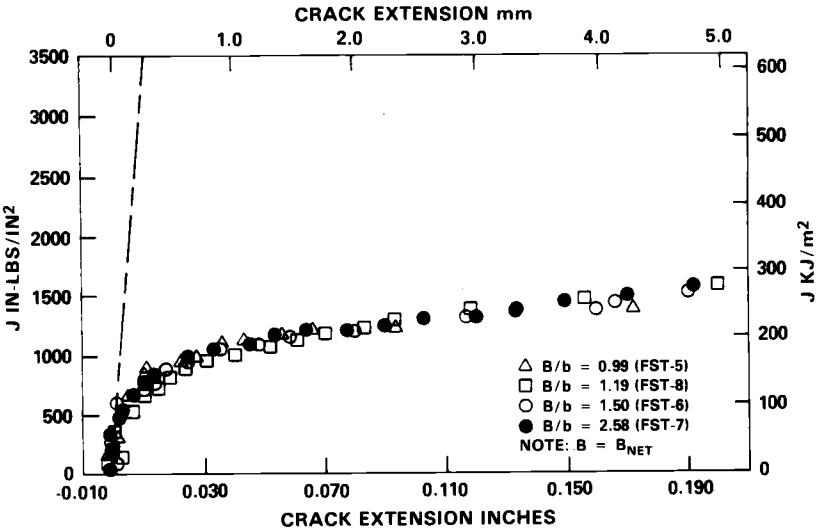

FIG. 6—J_I *versus crack extension data for 51-mm-thick (2.0 in.) 2T compact specimens of HY-130 steel.*

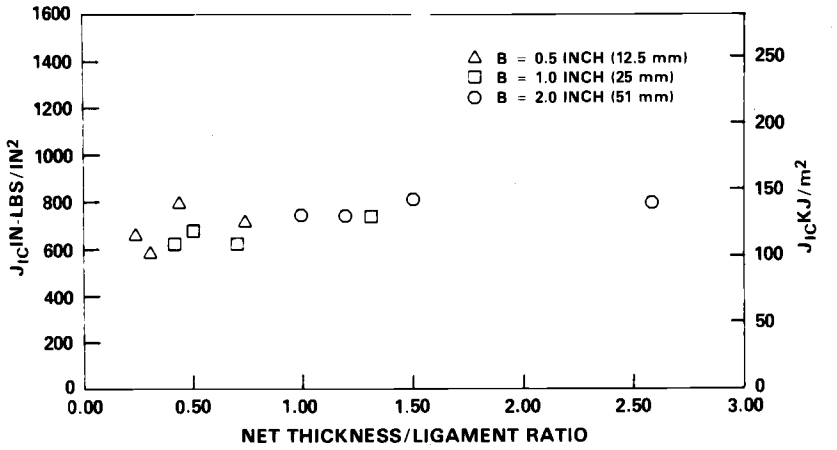

FIG. 7—J_{Ic} *versus thickness/ligament ratio data for 2T compact specimens of HY-130 steel.*

result is similar to that seen in previous investigations in which the effects of side-groove depth and ligament length were evaluated with HY-130 steel 1T compact specimens [*10,12*]. The J_{Ic}-value for one specimen, a 12.5 mm thick (0.5 in.) compact with $a/w = 0.75$, was moderately higher than the remainder of the data. Examination of the fracture surface of that specimen showed that it tends toward cross slip, which would act to force the J_I-values up and produce a higher apparent J_{Ic} for this specimen.

Tearing modulus data determined from the linear fit of J_I-R curve data to 1.5 mm (0.06 in.) of crack extension are shown in Fig. 8. These data exhibit a decreasing trend before apparently leveling off at a thickness/ligament ratio approximately equal to 1. The minimum tearing modulus values were observed in the specimens with the largest nominal thickness and net thickness/ligament ratios. Tearing modulus results from the linear fit of the J_I-R curve over an extended range of crack extension [5.0 mm (0.200 in.)] are plotted in Fig. 9. The data scatter has collapsed, and the tearing modulus values have reduced to a minimum band which is independent of the thickness/ligament ratio. It can be observed that the compact configuration with the largest specimen thickness and thickness/ligament ratio showed the smallest decrease in tearing modulus value when calculated over the extended range of crack extension.

After analyzing these tearing modulus data determined from the linear fit of J_I-R curve data, it was necessary to attempt to establish whether the trends and results produced in evaluating J_I-R curve data over 1.5-mm (0.06 in.) crack extension were actually a function of the varying specimen geometry, or merely a function of the technique used for the analysis. To this end, the J_I-R curve slope, dJ/da, and consequently the tearing modulus were reevaluated utilizing the power-law fit described by Carlson and Williams [*15*] where

$$J = A_1(\Delta a)^{A_2} \tag{3}$$

This fit was applied to the unloading compliance J_I-R curves and differentiated to give the following expression:

$$\frac{dJ_1}{da} = (A_1 \cdot A_2)\Delta a^{(A_2-1)} \tag{4}$$

and then

$$T_{MAT} = \frac{E}{\sigma_y{}^2} \cdot \frac{dJ_1}{da} = \frac{EA_1A_2}{\sigma_y{}^2} \cdot \Delta a^{(A_2-1)} \tag{5}$$

in terms of the coefficients A_1 and A_2. Tearing modulus values were then determined at several increments of crack extension, including 0.51 mm (0.02 in.), 1.27 mm (0.05 in.), 1.78 mm (0.07 in.), 2.54 mm (0.10 in.), 3.81 mm (0.15 in.), and 5.08 mm (0.20 in.) from the blunting line. Figure 10 is a plot of the various sets of calculated tearing modulus values against the net thickness/ligament ratios. The tearing modulus data developed in this analysis support results obtained using the linear fits of this data. For cases of limited crack extension of less than 1.3 mm (0.05 in.), the tearing modulus shows a decreasing trend with increasing specimen net thickness/ligament ratio. For cases of crack extension approaching 5.0 mm (0.20 in.), the in-

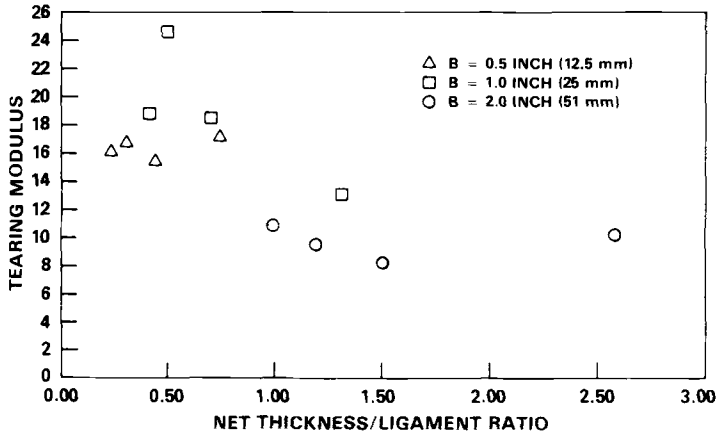

FIG. 8—*Tearing modulus* (T) *versus thickness/ligament ratio data for 2T compact specimens of HY-130 steel with* T *determined over 1.5 mm (0.06 in.) of crack extension.*

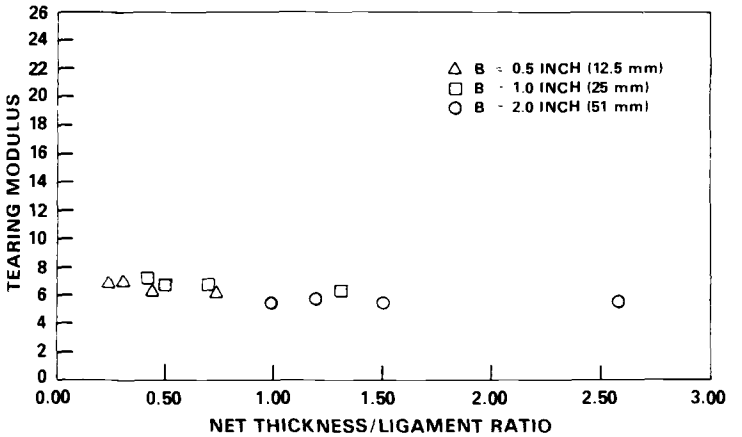

FIG. 9—*Tearing modulus* (T) *versus thickness/ligament ratio data for 2T compact specimens of HY-130 steel with* T *determined over 5.0 mm (0.200 in.) of crack extension.*

stantaneous slopes of the J_I-R curves decreased, and showed little or no dependence on net thickness/ligament ratio in the limit. This suggests that as the mode of crack extension changes from blunting to tearing, effects of this transition do cause a real elevation of the J_I-R curve under certain constraint conditions. In Fig. 10, it can be seen that sensitivity of the tearing modulus measurement is minimized where the net thickness/ligament ratio exceeds 1, for any amount of crack extension. The crack front geometries achieved where $B/b > 1$ tend toward those expected under plane-strain constraint conditions, where negligible tunneling and cross slip were observed. This

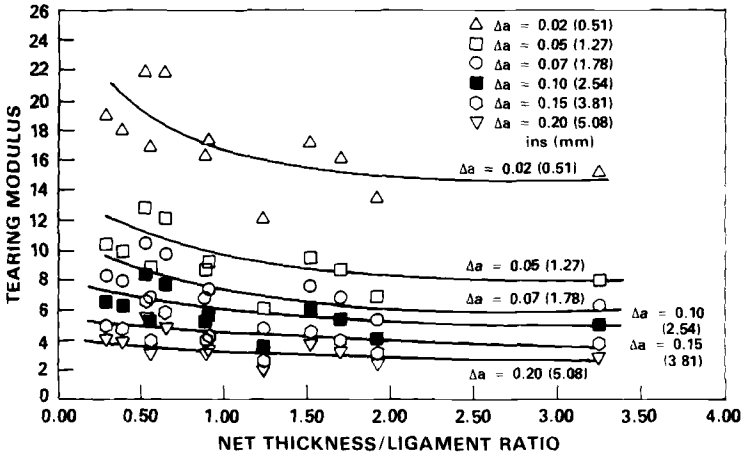

FIG. 10—*Tearing modulus versus thickness/ligament ratio data developed from a power-law fit analysis for 2T compact specimens of HY-130 steel.*

ratio of net thickness/ligament is apparently sufficient to maximize constraint, as suggested by Hertzberg [*16*], and assure plane-strain constraint. Importantly, for the cases of limited crack growth, the decreasing trend in tearing modulus values suggests that even though side grooves have produced planar crack growth, plane-strain constraint conditions do not necessarily exist.

Figure 11*a* shows fracture surfaces for several 2T compact specimens of ASTM A533B (HSST-03) steel with 20 percent side grooves. The crack fronts of these specimens are typical of those tested in this investigation, and indicate that tunneling was reduced and crack fronts were substantially straighter than those previously produced in non-side-grooved compact specimens of A533B steel, as shown in Fig. 11*b*, tested by Vassilaros et al [*8*] and also by Andrews and Shih [*9*]. However, the crack fronts were not as straight as those for the HY-130 steel compact specimens. This is reflected in the fact that the measured and estimated crack extension values (Table 5) for the A533B differ by up to 31 percent. Additionally, not all 2T compact specimens of the A533B met the previously established validity criterion. As identified in Table 3, these invalid test specimens will be included in all data plots for A533B (Figs. 16, 17, and 18) but will be denoted by "closed" symbols.

The J_I-R curves for ASTM A533B steel tests are presented in Fig. 12 [12.5 mm (0.5 in.) thick], Fig. 13 [25 mm (1.0 in.) thick], and Fig. 14 [51 mm (2.0 in.) thick], Fig. 13 [25 mm (1.0 in.) thick], and Fig. 14 [51 mm (2.0 in.) thick]. These curves exhibit significant data scatter with varying thicknesses and net thickness/ligament ratios. As previously mentioned, several A533B specimens did not meet the specified validity criterion. It should be reiterated that specimen tests satisfying the criterion of B_N, $b > 15\ J/\sigma_y$ at 1.5 mm

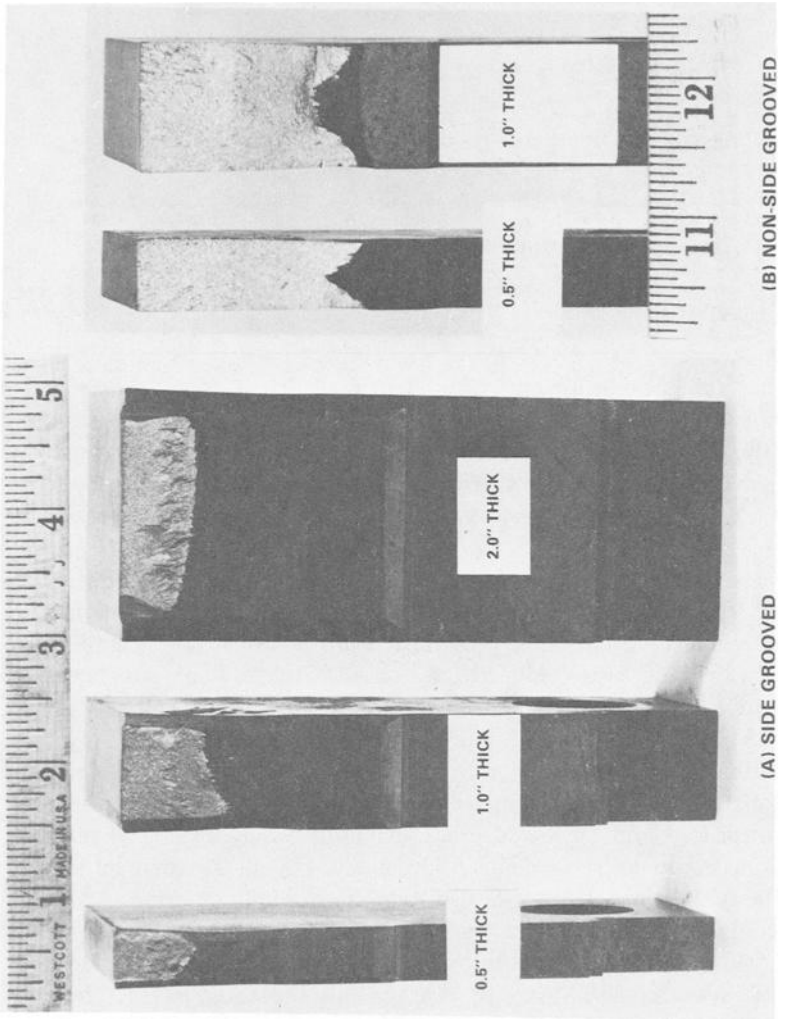

FIG. 11—*Fracture surfaces of tested 2T compact specimens of ASTM A533B steel with various thickness/ligament ratios (25.4 mm = 1.0 in.).*

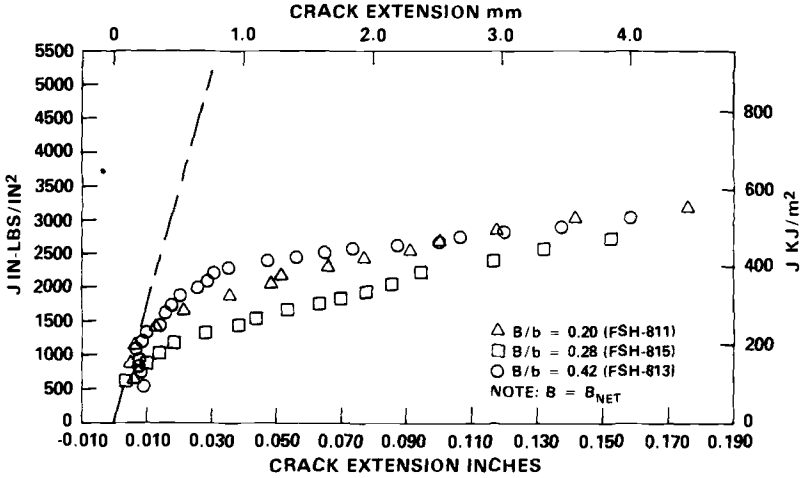

FIG. 12—J_I *versus crack extension data for 12.5-mm-thick (0.5 in.) 2T compact specimens of ASTM A533B steel.*

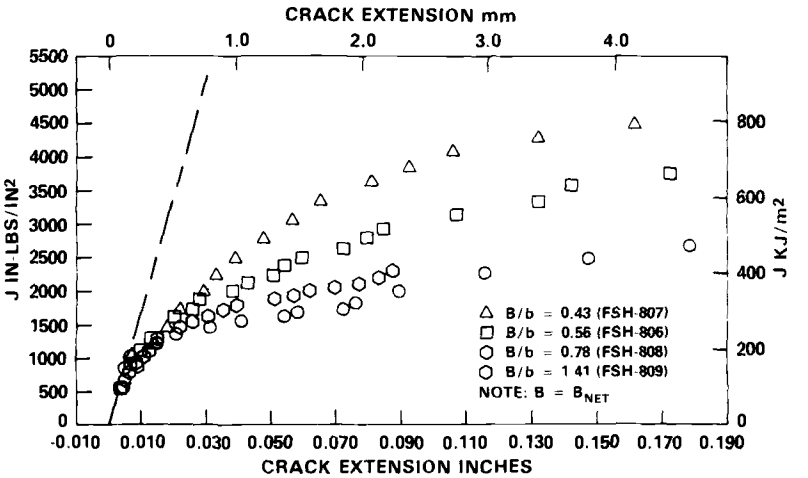

FIG. 13—J_I *versus crack extension data for 25-mm-thick (1.0 in.) 2T compact specimens of ASTM A533B steel.*

(0.06 in.) of crack growth were considered valid for J_{Ic} and near-field tearing moduli analyses. Additionally, two 25-mm-thick (1.0 in.) compact specimens (FSH-807 and FSH-806) which met those validity criteria displayed severe lateral contraction in the test section, indicating non-plane-strain fracture behavior. The lateral contraction was measured to be 3 and 5 percent of the net section reduction on these specimens. The J_I-R curves for the six remaining A533B compact specimens are shown in Fig. 15. Considering the ex-

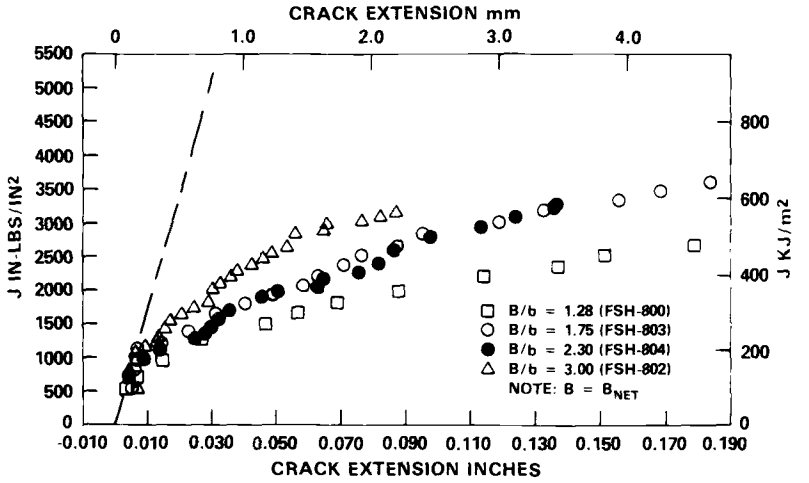

FIG. 14—J_I *versus crack extension data for 51-mm-thick (2.0 in.) 2T compact specimens of ASTM A533B steel.*

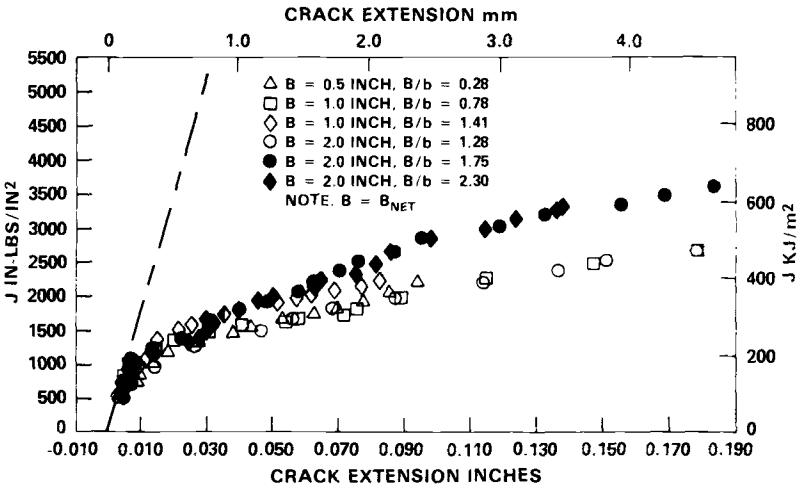

FIG. 15—J_I *versus crack extension data for 2T compact specimens of ASTM A533B steel valid according to criteria established in ASTM E 813 with negligible test section lateral contraction (25.4 mm = 1.0 in.).*

pected material scatter, as previously observed by Vassilaros [*11*] and Gudas et al [*12*] in J_I-R curve investigations on A533B steel, these "valid" J_I-R curves display similar agreement to that seen with HY-130 steel.

The J_{Ic}-values versus net thickness/ligament ratio for A533B 2T compact specimens are presented in Fig. 16. It can be seen that J_{Ic} data for this material exhibits considerable scatter which is similar to that noted by Gudas et al

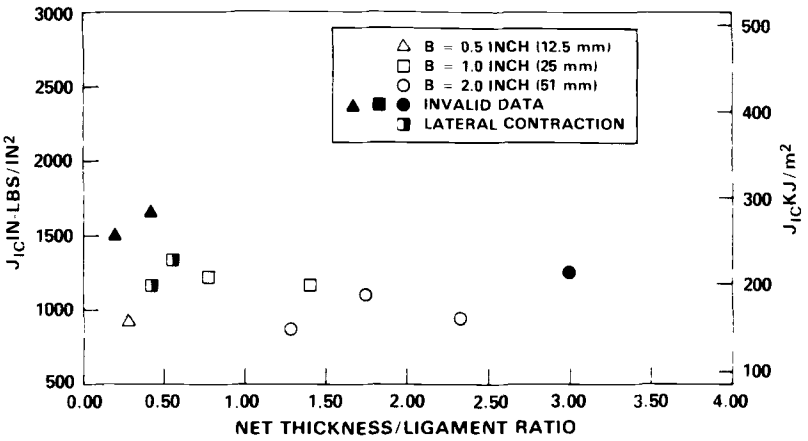

FIG. 16—J_{Ic} *versus thickness/ligament ratio data for 2T compact specimens of ASTM A533B steel.*

[*12*] in previous tests of A533B steel. Also, it can be seen that the most scatter occurs in the 12.5-mm-thick (1.0 in.) specimens, where J_I-values were elevated, but where specimen tests were invalidated by the previously established criteria. When considering only valid data, as denoted by open symbols in Fig. 16, these results indicate a relative specimen geometry independence for J_{Ic} with increasing net thickness/ligament ratio. This supports the behavior previously observed for the HY-130 steel 2T compact specimens tested with 20 percent side grooves.

Tearing modulus values determined from linear regression fits of J_I-R curve data up to 1.5 mm (0.06 in.) of crack extension for A533B steel are plotted against the 2T compact specimen thickness/ligament ratio in Figure 17. Although there is substantial scatter, there is an initially decreasing trend of tearing modulus with increasing net thickness/ligament ratio. In the case of this steel, this trend is associated with lateral contraction observed in 25-mm-thick (1.0 in.) specimens. As the net thickness/ligament ratio increased further, the tearing modulus values began to increase, as previously observed by Vassilaros [*11*] and Gudas et al [*12*]. This trend is particularly evident with the nonvalid, deeply cracked 2T compact specimen (B/b = 3.00). Analysis of A533B test data with respect to the validity criterion established in ASTM E 813 indicated that only three specimens satisfied the B_N, $b > 15\,J/\sigma_y$ (Table 3) criteria at 5.0 mm (0.20 in.) of crack extension. With this limited far-field tearing modulus data available for analysis, such an evaluation was not undertaken for A533B steel specimens.

The results of these experiments to evaluate J_{Ic} and the slope of the J_I-R curve in response to systematic variations in crack length and thickness in side-grooved 2T compact specimens point to several conclusions. First, the geometry independence of fracture toughness, J_{Ic}, has been demonstrated for

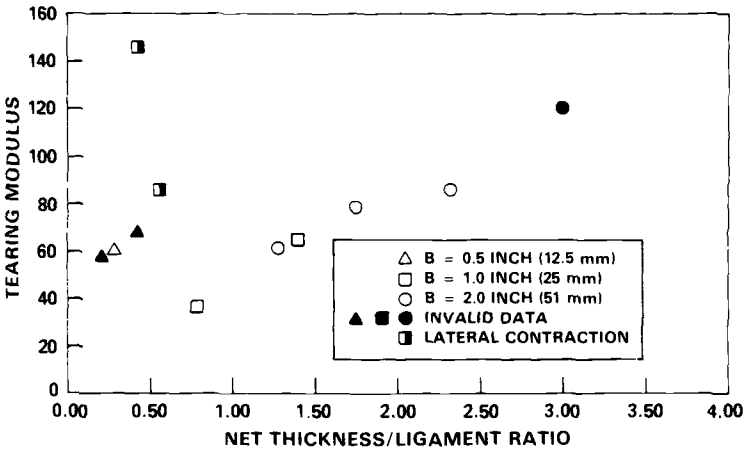

FIG. 17—*Tearing modulus* (T) *versus thickness/ligament ratio data for 2T compact specimens of ASTM A533B steel with* T *determined over 1.5 mm (0.06 in.) of crack extension.*

HY-130 steel and supported by data for A533B steels where the validity criterion established in ASTM E 813 were met. HY-130 steel showed less scatter than A533B steel as previously reported by other investigators, but both steels were insensitive to substantially changing constraint conditions when J_{Ic} was evaluated. Secondly, clear dependence of the slope of the J-integral R-curve was seen in both steels as related to the net thickness/ligament ratio, and the degree of crack extension. In the case of the HY-130 steel, the slope of the J_I-R curve was elevated in the regime of short crack extension, particularly where the net thickness/ligament ratio was less than approximately 1. Limited evidence of cross slip was also noted in this regime, even though the side grooves caused substantially planar crack growth. This dependence of the J_I-R curve slope upon constraint conditions diminshed with crack extension. In the case of A533B steel, the slope of the J_I-R curve also showed a decreasing trend for side-grooved 2T compact specimens in the regime where B/b was less than 1. The trend was complicated by the occurrence of lateral contraction in several specimens, which again pointed to the lack of full plane-strain constraint. Additionally, it is suggested that due to the significant effect lateral contraction exhibited on the J_I-R curves, a validity criterion limiting this contraction should be considered for materials such as A533B steel. ASTM A533B steel tests also showed an increase in the tearing modulus calculated for the near-field J_I-R curve [crack extension up to 1.5 mm (0.06 in.)] as crack length was increased, where $a/W > 0.75$, to produce net thickness/ligament ratios greater than 1. This increase was not seen in tests for HY-130 steel but was noted in previous investigations with A533B steel [*11,12*]. Those investigators suggested that this increasing tearing modulus trend observed for A533B steel could possibly be attributed to back-wall effects in deeply cracked compact specimens.

One of the initial goals of this investigation was to evaluate the Ernst-Paris-Landes expression [*13*] for calculating J_I-values from load-displacement records. This approximation was developed because the expressions formulated by Rice [*17*] and Merkle and Corten [*18*] to calculate J_I-values for compact specimens did not consider the contribution of crack extension. Hutchinson and Paris [*4*] proposed a method to calculate J_I considering the effect of crack growth.

Although analytically exact, these techniques required a large amount of numerical manipulation to analyze a load-displacement record. The expression developed by Ernst [*13*] et al emphasized the strict deformation theory interpretation of J_I as a function of two variables, in this case crack length and deflection, and the value of J is independent of the particular path chosen to the point of interest. This method is applicable to the single-specimen test and makes full use of the load-displacement test record. The Ernst-Paris-Landes expression for crack-growth-corrected J_I was previously given in Eq 1.

To initiate evaluation of this expression, several J_I-R curves (Figs. *18, 19,* and *20*) for previously tested HY-130 steel 2T compact specimens with maximum crack extensions approaching 25 mm (1.0 in.) were examined. J_I-values were observed to reach a maximum at crack extensions equal to approximately 40 percent of the original remaining ligament (b_0). Beyond that point, J_I-values exhibited a decreasing trend up to the maximum crack extension obtained for each test. The approach employed in this phase was to determine J_I-values for J_I-R curve points on the increasing slope portion, at a point

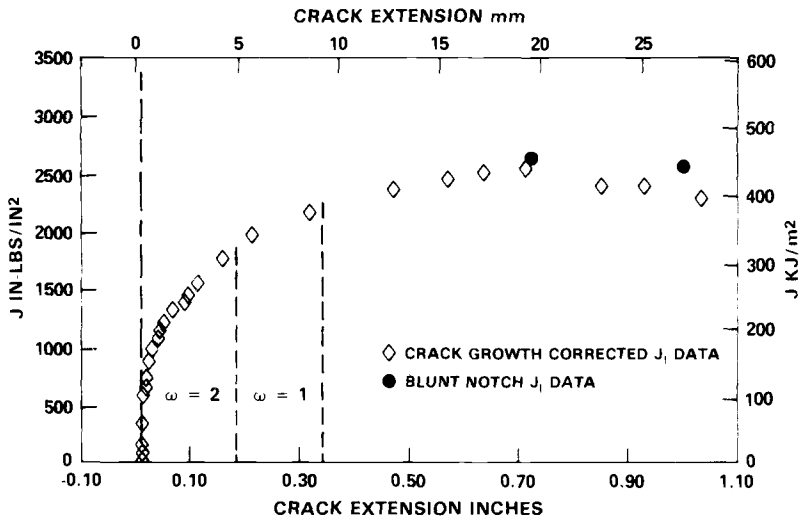

FIG. 18—*Tearing modulus* (T) *versus thickness/ligament ratio data for 2T compact specimens of ASTM A533B steel with* T *determined over 5.0 mm (0.200 in.) of crack extension.*

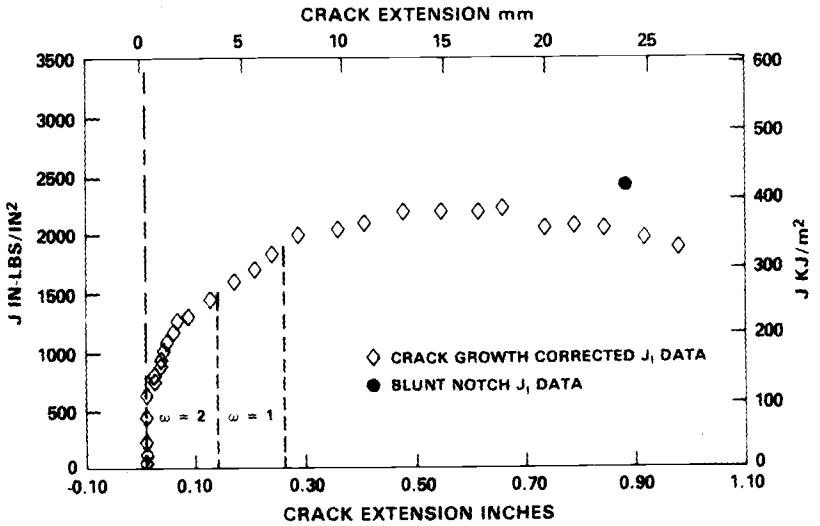

FIG. 19—J_I *versus crack extension data for a 12.5-mm-thick (0.5 in.) 2T compact specimen of HY-130 steel with* $a_0/W = 0.67$.

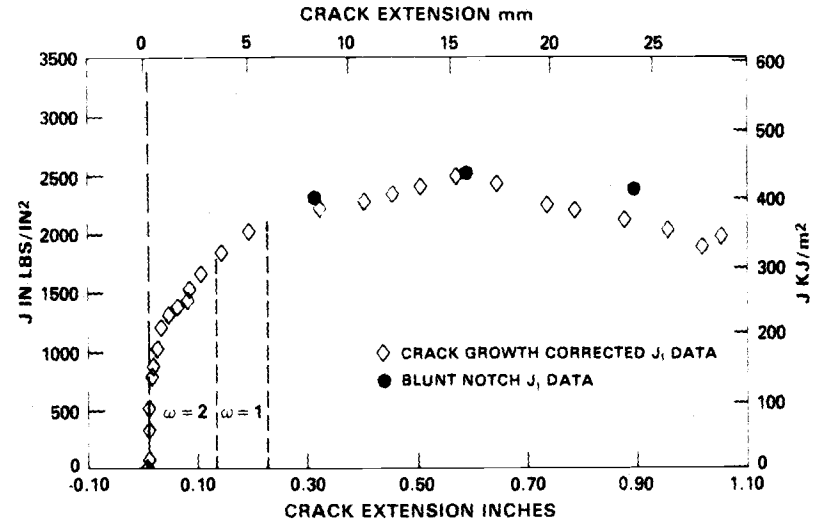

FIG. 20—J_I *versus crack extension for a 25-mm-thick (1.0 in.) 2T compact specimen of HY-130 steel with* $a_0/W = 0.56$.

approximately equal to the maximum J_I-value, and at points on the decreasing slope portion of specific J_I-R curves for comparison with crack-growth-corrected J_I-values. The experimental procedure employed was to determine the actual crack lengths corresponding to the specific crack extension points of interest on 2T compact specimens which had undergone elastic compliance tests. Blunt notches, with root radii of 1.6 mm (0.625 in.), were machined in similar 2T compact specimens to depths corresponding to those specific crack lengths. After determining the load-line crack-opening displacements (COD) taken from the elastic compliance load-displacement record that corresponded to the specific crack extensions of interest, the blunt-notch specimens were loaded to those specific COD values. J_I was then calculated at that point, using Eq 1, where the crack extension term was zero. To confirm that no crack extension existed after test, specimens were broken open in liquid nitrogen after heat tinting and the crack length was measured as per ASTM E 813. No crack extension was observed on any test specimens.

The J_I-values determined from this series of blunt-notch tests are plotted on the original J_I-R curves, shown in Figs. 18, 19, and 20, developed using the Ernst-Paris-Landes expression. These results suggest that up to the point of maximum J_I, where crack extension is approximately equal to 0.40 b_0, the Ernst-Paris-Landes expression accurately corrects J_I for crack extension. In the range of crack extension beyond 0.40 b_0, this expression apparently overcorrects J_I in 2T compact specimens of HY-130 steel. This suggests that this expression is limited in its ability to accurately correct J_I-values for cases of extended crack growth, at least for the cases of elastic-perfectly plastic materials like HY-130 steel. However, the range of accuracy demonstrated by this expression is well beyond the limits of crack extension suggested for J-controlled crack growth, which are on the order of 6 percent b_0 [*19*]. It was also observed that while J_I-values produced from these tests where not crack growth occurred did not exhibit the decreasing trend noted in the Ernst-Paris-Landes approximation, they did not continue to elevate with increasing crack extension as would be expected with an energy-related parameter. This suggests that although J-controlled crack growth, as described by Hutchinson and Paris [*4*], may extend beyond previously established limits, its dominance is clearly not applicable for cases of extensive crack growth ($>0.40\ b_0$).

The J_I-R curves shown in Figs. 18–20 were the results of attempts to produce crack extensions beyond the region of J-controlled crack growth. A parameter developed to indicate the existence of the necessary conditions for J-controlled crack growth is $\omega = (b/J)\ (dJ_I/da)$ as defined by Hutchinson and Paris [*4*]. Originally it was postulated that an ω-value much greater than 1 was necessary to assure J-controlled crack growth. This minimum value has not been ascertained, however, and values from $\omega = 40$ [*4*] to $\omega = 5$ [*20*] have been suggested.

All of the J-integral R-curves produced in this investigation were analyzed

to evaluate resultant ω-values achieved during each test. The values were calculated at closely spaced intervals of 0.12 mm (0.005 in.) of crack extension along each J_I-R curve using the instantaneous value of b, J, and dJ/da determined from the power-law fit approximation, as described earlier, generated for each J_I-R curve, up to the maximum crack extension obtained or 5.0 mm (0.200 in.) of crack extension, whichever value was lower. Tables 6 and 7 present tabulations of the crack extensions corresponding to ω-values of 20, 10, 5, 2, and 1 for each specimen of HY-130 steel and A533B steel, respectively.

For the HY-130 steel compact specimens tested in this investigation, the application of a minimum ω-criterion of 20 would restrict crack extension to 0.18 to 0.81 mm (0.007 to 0.032 in.), whereas a minimum ω-value of 5 would limit crack extension to 0.71 to 3.07 mm (0.028 to 0.121-in.) as shown in Table 6. Similarly, considering valid data as outlined in Table 3 and noted in Table 7 for A533B steel, a minimum ω-value of 20 would limit crack extension to 0.23 to 1.4 mm (0.009 to 0.45 in.), and an ω-value of 5 would limit crack extension to 0.94 to 2.54 mm (0.037 to 0.100 in.). For both steels, the amount of crack extension allowed under various ω-value limitations decreases with increasing crack length as expected. The order of this decrease places the limits of apparent J-controlled crack growth within the exclusion bands set forth in ASTM Method E 813. However, the similarity of all HY-130 J_I-R curves shown in Figs. 4-6 and several of the A533B steel J_I-R curves presented in Fig. 15 suggests that restrictive values of ω are not supported. For all HY-130 steel specimens there are no apparent perturbations of the J_I-R curves over the full range of crack extension to 5 mm (0.2 in.). In Table 6, it can be seen that ω-values at or near this point of crack extension ranged from 2.8 to 0.5.

Previously, several J_I-R curves for HY-130 steel compact specimens with extended crack growth were presented, including J_I data produced from several blunt-notch specimen tests, as shown in Figs. 18-20. Examination of these figures shows that each J_I-R curve undergoes a definite change in slope wherein the strong dependency of the J-integral value with crack extension is reduced. These figures also include the crack extension points where ω-values of 2 and 1 occur. For all three specimens shown, the apparent change in J_I-R curve behavior occurs at or near the point where $\omega = 1$. If this change in the slope of the J_I-R curve is interpreted to be loss of J-controlled crack growth, then a conservative limiting ω-value of 2 would appear to be appropriate. However, additional testing of larger specimens, various geometries, and materials with work-hardening characteristics different than HY-130 is necessary to validate this point.

Conclusions

The objective of this investigation was to evaluate the ductile fracture toughness and J_I-R curve properties of HY-130 and ASTM A533B steels in

TABLE 6—*ω-data for HY-130 steel compact specimens.*

Specimen ID	Thickness mm (in.)	a_0/W	Length of Crack Extension in mm (in.) for Specific ω-Values					ω-Values and Corresponding Maximum Crack Extension Values Used in Power-Law Fit Analysis
			ω = 20	ω = 10	ω = 5	ω = 2	ω = 1	
FST-21B	12.5 (0.5)	0.56	0.66 (0.026)	1.30 (0.051)	2.52 (0.099)	...	...	4.42 (0.174): ω = 2.73
FST-17M	12.5 (0.5)	0.67	0.53 (0.021)	1.02 (0.040)	1.96 (0.077)	...	...	4.95 (0.195): ω = 1.80
FST-20M	12.5 (0.5)	0.77	0.28 (0.011)	0.53 (0.021)	1.09 (0.043)	4.52 (0.178)	4.62 (0.182)	5.03 (0.198): ω = 0.89
FST-16T	12.5 (0.5)	0.86	0.20 (0.008)	0.38 (0.015)	0.74 (0.029)	2.54 (0.100)	3.02 (0.119)	4.88 (0.192): ω = 2.52
FST-10	25 (1.0)	0.56	0.81 (0.032)	1.60 (0.063)	3.07 (0.121)	...	...	5.16 (0.203): ω = 2.82
FST-11	25 (1.0)	0.66	0.53 (0.021)	1.07 (0.042)	2.03 (0.080)	...	...	4.57 (0.180): ω = 2.07
FST-15B	25 (1.0)	0.76	0.31 (0.012)	0.61 (0.024)	1.17 (0.046)	2.72 (0.107)	...	4.14 (0.163): ω = 1.23
FST-14T	25 (1.0)	0.86	0.18 (0.007)	0.38 (0.015)	0.71 (0.028)	1.65 (0.065)	2.97 (0.117)	4.98 (0.196): ω = 0.49
FST-5	51 (2.0)	0.60	0.43 (0.017)	0.84 (0.033)	1.60 (0.063)	3.79 (0.149)	...	4.17 (0.164): ω = 1.81
FST-8	51 (2.0)	0.67	0.53 (0.021)	1.01 (0.040)	2.01 (0.079)	4.60 (0.181)	...	4.85 (0.191): ω = 1.89
FST-6	51 (2.0)	0.74	0.28 (0.011)	0.58 (0.023)	1.12 (0.044)	2.57 (0.101)	...	4.60 (0.181): ω = 1.03
FST-7	51 (2.0)	0.85	0.20 (0.008)	0.38 (0.015)	0.76 (0.030)	1.75 (0.069)	3.15 (0.124)	5.21 (0.205): ω = 0.51

TABLE 7—*ω-data for ASTM A533B-HSST-03 steel compact specimens.*

Specimen ID	Thickness, mm (in.)	a_0/W	Length of Crack Extension in mm (in.) for Specific ω-Values					ω-Values and Corresponding Maximum Crack Extension Values Used in Power Law Fit Analysis
			$\omega = 20$	$\omega = 10$	$\omega = 5$	$\omega = 2$	$\omega = 1$	
FSH-811	12.5 (0.5)	0.54	0.74 (0.029)	1.47 (0.058)	2.87 (0.113)	...	...	5.1 (0.200): $\omega = 2.70$
FSH-815	12.5 (0.5)	0.64	0.66 (0.026)-V	1.27 (0.050)	2.52 (0.099)-V	...	...	5.33 (0.210): $\omega = 2.15$
FSH-813	12.5 (0.5)	0.75	0.38 (0.015)-V	0.71 (0.028)	1.50 (0.059)	3.40 (0.134)	...	5.39 (0.212): $\omega = 1.14$
FSH-807	25 (1.0)	0.56	1.14 (0.045)-V	2.24 (0.088)	4.32 (0.170)	...	...	4.67 (0.184): $\omega = 4.57$
FSH-806	25 (1.0)	0.67	0.64 (0.025)-V	1.30 (0.051)	2.54 (0.100)-V	...	...	5.41 (0.213): $\omega = 2.12$
FSH-808	25 (1.0)	0.74	0.51 (0.020)-V	0.76 (0.030)	1.55 (0.061)-V	3.56 (0.140)	...	4.95 (0.195): $\omega = 1.33$
FSH-809	25 (1.0)	0.87	0.23 (0.009)-V	0.46 (0.018)	0.94 (0.037)-V	2.11 (0.083)	...	3.05 (0.120): $\omega = 1.27$
FSH-800	51 (2.0)	0.66	0.64 (0.025)-V	0.79 (0.031)	2.39 (0.094)-V	...	...	4.90 (0.913): $\omega = 2.22$
FSH-803	51 (2.0)	0.77	0.43 (0.017)-V	0.91 (0.036)	1.75 (0.069)-V	3.94 (0.155)	...	5.21 (0.205): $\omega = 1.42$
FSH-804	51 (2.0)	0.82	0.41 (0.016)-V	0.84 (0.033)	1.55 (0.061)-V	...	...	3.33 (0.131): $\omega = 2.09$
FSH-802	51 (2.0)	0.86	0.31 (0.012)-V	0.61 (0.024)	1.17 (0.046)	...	...	2.21 (0.087): $\omega = 2.43$

Note—V indicates that the validity criteria established in ASTM E 813 and ASTM E 399 were met at the designated crack extension.

response to systematic variations of thickness and crack length in the side-grooved compact specimen geometry. The following conclusions are suggested from the analyses of the elastic-compliance J_I-R curve test results developed herein:

1. The fracture toughness, J_{Ic}, of both steels was shown to be geometry independent when validity criteria for thickness and remaining ligament are met.
2. Both steels displayed a clear dependence of the slope of the J_I-R curve as related to the net thickness/ligament ratio and degree of crack extension.
3. For HY-130 steel, in cases of limited crack extension, a net thickness/ligament ratio of 1 is necessary to ensure conservative J_I-R curve slopes and to preclude compact specimen geometry dependence.
4. For ASTM A533B steel, the tearing modulus values were apparently dependent on compact specimen geometry over the range of net thickness/ligament ratios evaluated.
5. The Ernst-Paris-Landes expression for J_I accurately describes this parameter in the compact specimen to crack extension values of approximately $0.4\,b_0$ for HY-130 steel.
6. Limited evidence suggests that a minimum value of ω to guarantee J-controlled crack growth in HY-130 steel is 2.

Acknowledgments

The authors wish to acknowledge the sponsorship of the Naval Sea Systems Command (H. H. Vanderveldt) and the U.S. Nuclear Regulatory Commission (Milton Vagins) in conducting this research.

References

[1] Begley, J. A. and Landes, J. D. in *Fracture Mechanics, ASTM STP 514*, American Society for Testing and Materials, 1972, pp. 1-20.
[2] Clarke, G. A., Andrews, W. K., Paris, P. C., and Schmidt, D. W. in *Mechanics of Crack Growth, ASTM STP 590*, American Society for Testing and Materials, 1976, pp. 27-42.
[3] Joyce, J. A. and Gudas, J. P. in *Elastic-Plastic Fracture, ASTM STP 668*, J. D. Landes, J. A. Begley, and G. A. Clarke, Eds., American Society for Testing and Materials, 1979, pp. 451-468.
[4] Hutchinson, J. W. and Paris, P. C. *in Elastic-Plastic Fracture, ASTM STP 668*, J. D. Landes, J. A. Begley, and G. A. Clarke, Eds., American Society for Testing and Materials, 1979, pp. 37-64.
[5] Paris, P. C., Tada, H., Zahoor, A., and Ernst, H. in *Elastic-Plastic Fracture, ASTM STP 668*, J. D. Landes, J. A. Begley, and G. A. Clarke, Eds., American Society for Testing and Materials, 1979, pp. 5-36.
[6] Paris, P. C., Tada, H., Zahoor, A., and Ernst, H. in *Elastic-Plastic Fracture, ASTM STP 668*, J. D. Landes, J. A. Begley, and G. A. Clarke, Eds., American Society for Testing and Materials, 1979, pp. 251-265.
[7] Joyce, J. A. and Vassilaros, M. G., in *Fracture Mechanics: 13th Conference, ASTM STP 743*, American Society for Testing and Materials, 1981, pp. 525-542.

[8] Vassilaros, M. G., Joyce, J. A. and Gudas, J. P. in *Fracture Mechanics: 14th Conference, ASTM STP 791*, American Society for Testing and Materials, 1983.
[9] Andrews, W. R. and Shih, C. F. in *Elastic-Plastic Fracture, ASTM STP 668*, J. D. Landes, J. A. Begley, and G. A. Clarke, Eds., American Society for Testing and Materials, 1979, pp. 426-450.
[10] Gudas, J. P., Joyce, J. A., and Davis, D. A. in *Fracture Mechanics, ASTM STP 677*, C. W. Smith Ed., American Society for Testing and Materials, 1979, pp. 474-485.
[11] Vassilaros, M. G., Joyce, J. A. and Gudas, J. P. in *Fracture Mechanics: Twelfth Conference, ASTM STP 700*, American Society for Testing and Materials, 1980, pp. 251-270.
[12] Gudas, J. P. et al, "A Summary of Recent Investigations of Compact Specimen Geometry Effects of the J_I-R Curve of High Strength Steels," NUREG/CR-1813, U.S. Nuclear Regulatory Commission, Washington, D.C., Nov. 1980.
[13] Ernst, H. et al in *Fracture Mechanics: 13th Conference, ASTM STP 743*, American Society for Testing and Materials, 1981, pp. 476-502.
[14] Saxena, A. and Hudak, S. J., *International Journal of Fracture*, Vol. 14, No. 5, Oct. 1978, pp. 453-468.
[15] Carlson, K. W. and Williams, J. A. in *Fracture Mechanics: 13th Conference. ASTM STP 743*, American Society for Testing and Materials, 1981, pp. 503-524.
[16] Hertzberg, R. W., *Deformation and Fracture Mechanics of Engineering Materials*, Wiley, New York, 1976, pp. 279-281.
[17] Rice, J. R. et al in *Progress in Flaw Growth and Fracture Toughness Testing, ASTM STP 536*, American Society for Testing and Materials, 1973, pp. 231-245.
[18] Merkle, J. and Corten, H., *Journal of Pressure Vessel Technology, Transactions*, American Society of Mechanical Engineers, 1974, pp. 286-292.
[19] Shih, C. F., deLorenzi, H. G., and Andrews, W. R. in *Elastic-Plastic Fracture, ASTM STP 668*, J. D. Landes, J. A. Begley, and G. A. Clarke, Eds., American Society for Testing and Materials, 1979, pp. 65-120.
[20] Paris, P., this publication, pp. II-5-II-40.

Pauline H. Davies[1]

An Elastic-Plastic Fracture Mechanics Study of Crack Initiation in 316 Stainless Steel

REFERENCE: Davies, P. H., **"An Elastic-Plastic Fracture Mechanics Study of Crack Initiation in 316 Stainless Steel,"** *Elastic-Plastic Fracture: Second Symposium, Volume II—Fracture Resistance Curves and Engineering Applications, ASTM STP 803*, C. F. Shih and J. P. Gudas, Eds., American Society for Testing and Materials, 1983, pp. II-611-II-631.

ABSTRACT: An experimental study of crack initiation in solution-treated 316 stainless steel was undertaken to test the validity of the elastic-plastic fracture mechanics parameters, J and crack opening displacement (COD), in the presence of extensive yield. Measurements of the J-integral are obtained for 6.4 to 25-mm-thick compact specimens using the proposed ASTM equation. The latter is shown to give results within 2 percent of those obtained using the original calibration method of Begley and Landes. However, deviations from the proposed crack blunting line, $J = 2\sigma_f \Delta a$ are found for this high work-hardening material. Midsection COD is also determined using a rubber infiltration technique. Critical values of the J-integral and COD at crack initiation are shown to be constant independent of plate thickness under plane-strain and non-plane-strain crack-tip conditions as defined by $B = 25$ to 50 (J_i/σ_f) and $B = 25\ \mathrm{COD}_i$. These results are supported by measurements of the surface crack-tip contraction.

KEY WORDS: elastic-plastic fracture, 316 stainless steel, J-integral, crack opening displacement, compact specimen, crack initiation, thickness effects

Linear elastic fracture mechanics (LEFM) has been found to give reliable estimates of defect tolerance in elastic and small-scale yielding situations. When there is extensive plasticity at the crack tip, the assumptions of linear elasticity become invalid and alternative methods of analysis must be used. Both the J-integral [*1*][2] and the crack opening displacement (COD) [*2*] have been proposed as material toughness parameters for the elastic-plastic situation.

The energy line integral, J, defined by Rice [*1*], is applicable to deforma-

[1]Research engineer, Ontario Hydro Research Division, Toronto, Ont., Canada; formerly, P. H. Hodkinson, senior research fellow, Materials Branch, Department of Civil Engineering, Royal Military College of Science, Shrivenham, Swindon, U.K.

[2]The italic numbers in brackets refer to the list of references appended to this paper.

tion-type elastic-plastic materials. J can be interpreted as the potential energy difference between two identically loaded bodies of thickness, B, having neighboring crack sizes a and $a + \Delta a$ [1]

$$J = -\frac{1}{B}\left(\frac{\partial U}{\partial a}\right)_u \tag{1}$$

where U is the absorbed strain energy under fixed displacement, u. Under linear elastic conditions, J then reduces to the fracture mechanics parameter G, the elastic strain energy release rate.

Alternatively, Wells [2] suggested that the amount by which the crack opens is a measure of work done in extending the crack and this opening, termed COD, was shown to be compatible with K and G used in LEFM

$$\text{COD} = C\frac{G}{\sigma_y} = C\frac{K^2}{E\sigma_y} \qquad \frac{\sigma}{\sigma_y} < 0.7 \tag{2}$$

where C is a constant.

From Eqs 1 and 2 the relation between J and COD is of the general form

$$J = M\sigma_y \,\text{COD} \tag{3}$$

where M is a constraint factor. Experimental evidence indicates that under plane-strain crack-tip conditions, variations in M are predominantly due to differences in the plastic flow properties of the material [3,4].

The aim of the present work has been to determine the validity of such parameters as J and COD in the presence of extensive yield and under non-plane-strain crack-tip conditions. A 316 stainless steel was selected having a high fracture toughness to yield strength ratio at room temperature, simulating many structural steels used in the upper-shelf region at higher temperatures. The results are supported by measurements of the surface crack-tip contraction to determine the extent of through-thickness yielding.

Material

The wrought 316 stainless steel was supplied as 32-mm-thick plate in the solution-annealed condition. Chemical analysis revealed a particularly low carbon content, Table 1. After machining, all specimens underwent a ½ h solution treatment at 1050°C in vacuo followed by a nitrogen quench to remove the work-hardened surface layer. Mechanical properties in the longitudinal or rolling direction were determined at a crosshead speed of 1 mm/min^{-1}, Table 2. Fracture occurred by dimpled rupture with considerable stretching.

TABLE 1—*Chemical Composition in weight % of Type 316 stainless steel.*[a]

	C	Si	Mn	S	P	Cr	Mo	Ni
Sample 1	0.01	0.2	1.6	<0.005	0.026	16.9	2.4	11.9
Sample 2	0.025	0.24	1.61	0.008	0.028	16.65	2.46	12.39

[a]Materials Quality Assurance Directorate, Bragg Laboratory, Sheffield, U.K.

TABLE 2—*Room-temperature mechanical properties of solution-treated Type 316 stainless steel.*[a]

Static Young's modulus	191×10^3 N · mm^{-2}
Poisson's ratio	0.30 (manufactured)
0.2% offset yield stress	198 N · mm^{-2}
Ultimate tensile strength	563 N · mm^{-2}
Elongation	82%
Reduction of area	81%
True strain at onset of necking	0.458

[a]Three round uniaxial test specimens, gage length = 25 mm, cross-sectional area = 25 mm^2, tensile axis in longitudinal direction.

Experimental Procedure

Three series of compact specimens of thicknesses 25.4 mm (1-1 → 1-7), 12.7 mm (2-1 → 2-6), and 6.35 mm (4-1 → 4-6) were tested. All in-plane dimensions were identical (W = 50.8 mm, $\alpha = a/W \sim 0.6$, L-T orientation), the only variable being thickness. Measurements of J for crack initiation were made using the American Society for Testing and Materials (ASTM) proposed method for a deeply cracked compact specimen [5]. For comparison, J_i for the 6.35-mm-thick specimens was also determined by direct evaluation of the calibration function $-(1/B)/(\partial U/\partial a)_u$ using a series of notched specimens (4-7 → 4-12) having a notch size range $\alpha \sim 0.5$ to 0.8 [6]. One precracked specimen of each thickness (1-2, 2-6, and 4-1) was left for determination of the COD using a rubber infiltration technique [7] as well as the surface crack-tip contraction.

Surface Preparation

After machining, the surfaces of each specimen were mechanically ground flat with fine silicon carbide prior to solution treatment. Finally, each plate was polished down to 6-μm diamond in the region immediately ahead of the notch. Particular care was taken with specimens to be used for the surface crack-tip contraction measurements, which were polished down to 1-μm diamond.

Fatigue precracking was carried out in accordance with the ASTM Test for

Plane-Strain Fracture Toughness of Metallic Materials (E 399-78a) using a maximum stress intensity for the fatigue cycle of 650 $N \cdot mm^{-3/2}$, that is, a maximum load later found to correspond to 0.27 of the limit load achieved in subsequent tests.

Experimental Apparatus

Testing was performed in an Instron 1250 static and dynamic testing machine fitted with a 200-kN tensile load cell on 10 percent full transducer range. Use of a modified compact specimen enabled both the load-line and load-pin displacement to be monitored simultaneously, the latter being required for determination of the real energy input of the system. One displacement gage was mounted at the front of the specimen along the load line and two additional displacement gages each side of the loading grips between attachable knife edges, the output of the latter being averaged to cancel any effects of misalignment.

J-Integral Tests

In the first test series, notched specimens 4-7 → 4-12 were loaded at a crosshead speed of 1 $mm \cdot min^{-1}$ to just beyond a load maximum. The remaining sets of specimens of identical crack size (except 1-2, 2-6, and 4-1) were then used to determine the crack initiation point by the heat-tinting method. Each specimen was loaded to a different displacement at a crosshead speed of 1 $mm \cdot min^{-1}$ and unloaded. After heat-tinting in a furnace at 450°C for 2 h, specimens were broken open to reveal the extent of crack growth during monotonic loading. The initial fatigue crack length and average crack extension were measured directly from the fracture surface.

COD Measurements and Surface Crack-Tip Contraction

Direct measurements of crack-tip COD were made using Specimens 1-2, 2-6, and 4-1 by infiltrating the crack with a hardening silicone rubber [7]. Liquid rubber was placed in the notch and the specimen loaded to a known displacement. After 20 min the rubber solidified and could be removed with tweezers after loading the specimen to a higher displacement. Replicas were examined under a microscope and a thin section cut from the rubber at the crack front midpoint. Measurements of COD at the original crack tip were then made to ± 0.01 mm.

For Specimens 1-2, 2-6, and 4-1 the following testing procedure was adopted. After introducing liquid rubber at the crack tip, each specimen was loaded to a given displacement at a crosshead speed of 1 mm/min^{-1}. The maximum crack-tip contraction was measured in the loaded state using a pointed micrometer. After 15 to 20 min, loading was continued to a higher

displacement and the hardened replica removed. This sequence was continued up to a load maximum.

Results and Analysis of Results

Figure 1 shows typical load-displacement curves for the 316 stainless steel compact specimens loaded to different displacements, load maxima being achieved at extremely large displacements, 10 to 12 mm. After yield the displacement-time records showed a constant slope over the linear range of the gages, 0 to 7 mm ± 0.025 mm, so that displacements greater than 7 mm were obtained by extrapolation.

Fracture surfaces of the different thickness specimens are shown in Fig. 2, from which the crack growth extension areas are easily identified. Scanning electron microscopy revealed the characteristic dimples of a fibrous fracture in all cases with no significant change in fracture mode with plate thickness. Measurements of stretch zone width at 0 deg to the fracture surface showed no significant variation for the three different-thickness plates, widths between 0.42 and 0.60 mm being obtained for all specimens at the midthickness.

Figure 3 is a summary of results given in the form of a failure analysis diagram [8]. The load is plotted as $P^{\phi} = P/0.4142\ \sigma_u WB$ where the denominator

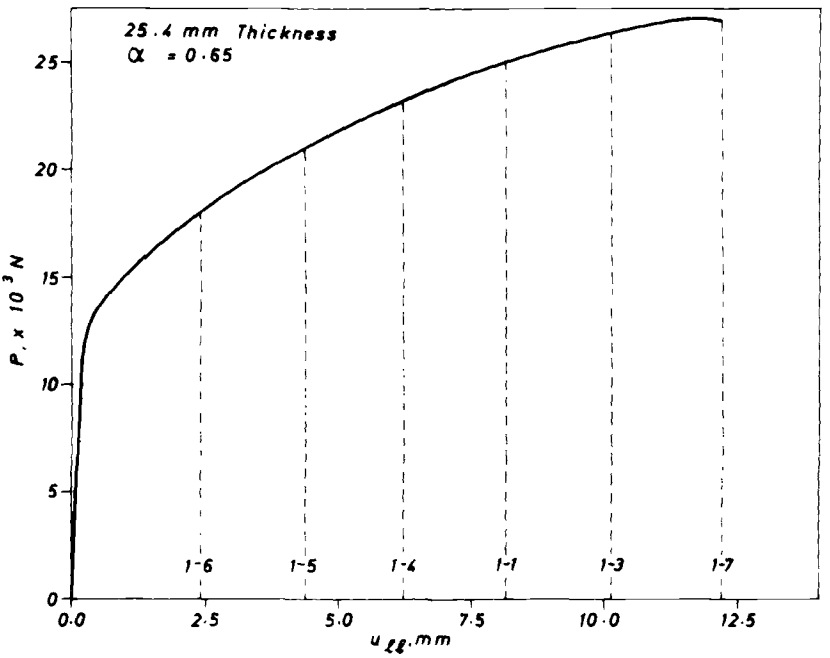

FIG. 1—*Experimental load-load line displacement curves for 25.4-mm-thick type 316 stainless steel compact specimens.*

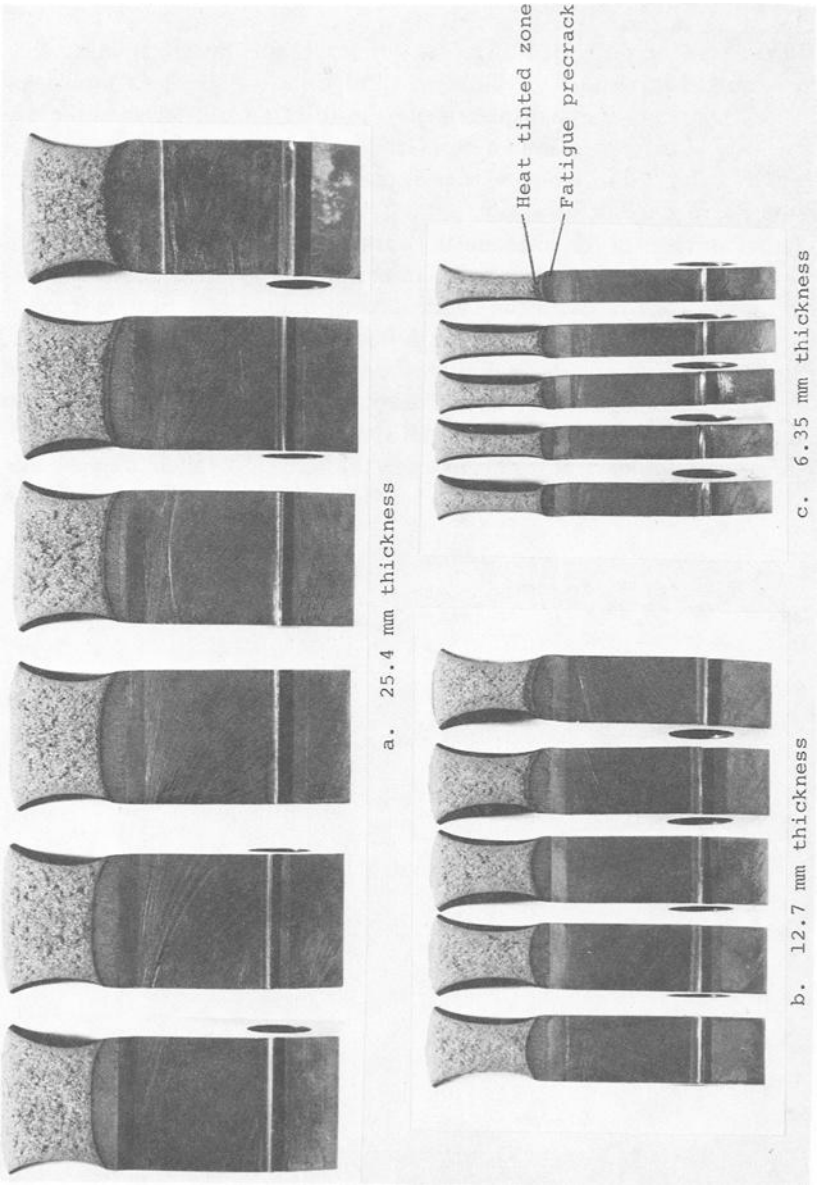

FIG. 2—*Fracture surfaces of type 316 stainless steel compact specimens.*

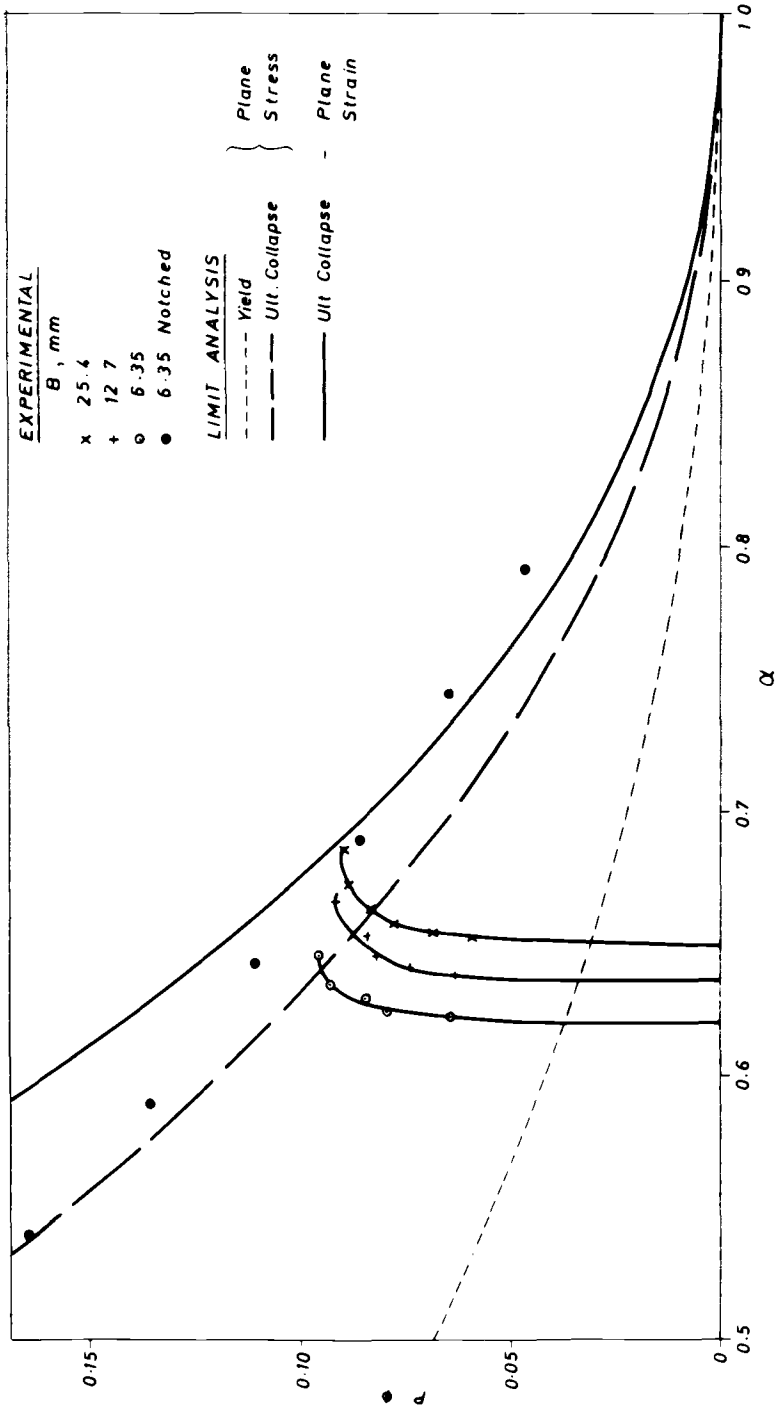

FIG. 3—*Failure analysis diagram for type 316 stainless steel compact specimens—comparison of analytical and experimental results.*

is a normalizing factor equal to the plane-stress ultimate collapse load for an uncracked compact specimen. P^{Φ}-versus-α curves for the three sets of specimens all showed an initially steep slope with little stable crack growth except close to the plastic instability load. The experimental load maximum for the 6.35-mm-thick specimen was within 3 percent of the plane-stress limit analysis solution. However, load maxima for the thicker specimens were up to 20 percent higher, results for the 25.4-mm-thick specimens being within 9 percent of the plane-strain solution [*9*]. Results for the 6.35-mm-thick notched specimens also deviated from the plane-stress solution especially at longer crack lengths, presumably due to the suppression of through-thickness yield and slow crack growth by the presence of the notch.

J-Integral

The J-integral for crack initiation was determined using the recommended interpolation procedure [*5*]. J corresponding to a given crack extension was calculated from the estimation equation of Clarke and Landes [*10*] after measuring the area under the appropriate load-load line displacement record with a planimeter

$$J = 2\frac{(1+\alpha')}{(1+\alpha'^2)}\frac{U_{ll}}{(1-\alpha)WB} \qquad \alpha \geq 0.5 \tag{4}$$

and

$$\alpha' = 2\left\{\left(\frac{a}{W-a}\right)^2 + \left(\frac{a}{W-a}\right) + \frac{1}{2}\right\}^{1/2} - 2\left(\frac{a}{W-a} + \frac{1}{2}\right)$$

Equation 4 is a simplified version of an original formulation by Merkle and Corten [*11*] which accounts for the small tension component of the compact specimen.

From Fig. 4 the results for all three thickness specimens appear to define a single curve for small crack extensions. A least-squares fit was performed on the first six data points and the last seven data points, the intersection of the former crack blunting line and the latter crack extension line defining crack initiation. The results are summarized in Table 3, where a provisional J_Q of 690 N · mm^{-1} was obtained at the intersection point.

For the 6.35-mm-thick specimens J_i was also determined by evaluation of the calibration function $-(1/B)/(\partial U/\partial a)_u$ from load-load pin displacement records of notched specimens 4-7 → 4-12 following the method of Begley and Landes [*6*] (see Appendix). From a calibration plot of $-(1/B)/(\partial U/\partial a)_u$ as a function of displacement at $\alpha = 0.62$ the J-value associated with increments of crack extension for each 6.35-mm-thick precracked specimen was obtained directly according to the final load-pin displacement. The results are pre-

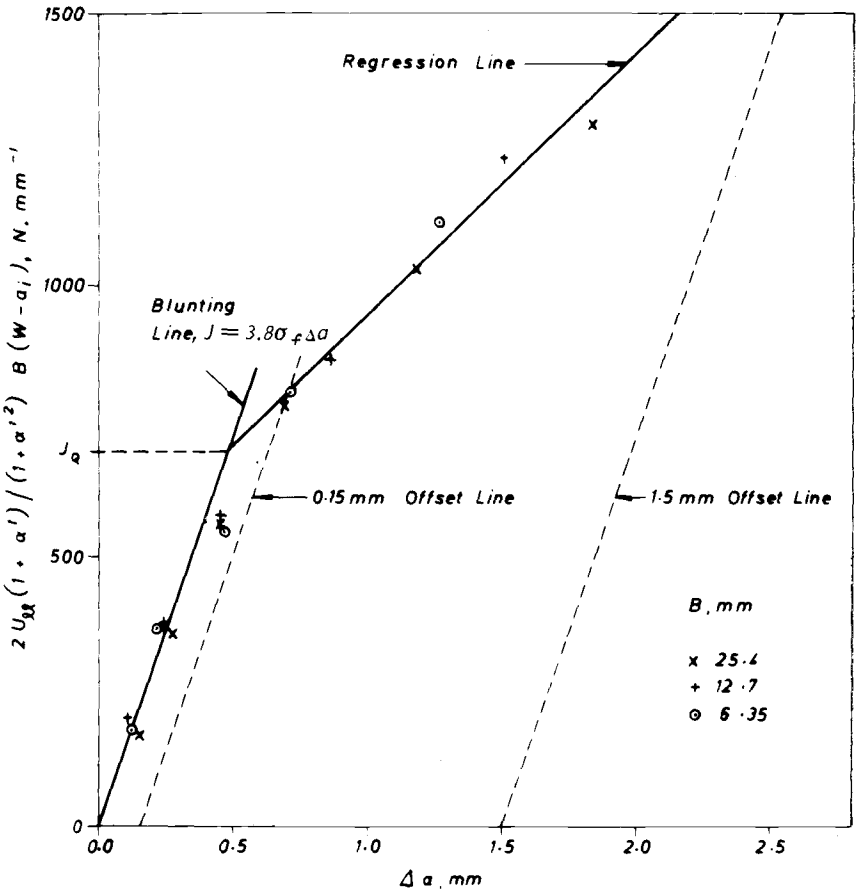

FIG. 4—*Determination of* J_i *for crack initiation for type 316 stainless steel compact specimens using an estimation equation.*

sented in Fig. 5, being very similar to Fig. 4 obtained for all three thickness specimens. In fact J determined by the estimation equation was within 2 percent of the value obtained from the calibration function for four out of five specimens.

An identical interpolation procedure was carried out as before to give a provisional J_Q at crack initiation of 590 N · mm^{-1} on the basis of four data points, Table 3, that is, 14 percent less than that calculated for all three sets of different-thickness specimens, 690 N · mm^{-1}. Equation 4 has been shown to yield an excellent estimate of J so that the difference between the two sets of results must be due solely to the number of data points in the interpolation procedure, the intersection point J_Q being particularly sensitive to the slope of the crack extension line, dJ/da. In the proposed ASTM method [5] a min-

TABLE 3—*Linear regression analysis of J-Δa curves to determine J_i for crack initiation for type 316 stainless steel compact specimens.*

	Crack Blunting Line	Crack Extension Line	Intersection
25.4 mm 12.7 mm 6.35 mm } thickness	$\frac{J}{\Delta a} = 1460\ \text{N} \cdot \text{mm}^{-2}$ or $J = 3.8\ \sigma_{flow} \Delta a$	$J = 483\ \Delta a + 464\ \text{N} \cdot \text{mm}^{-1}$ that is, $\frac{dJ}{da} = 483\ \text{N} \cdot \text{mm}^{-2}$ or $\frac{dJ}{da} = 1.3\ \sigma_{flow}$	$J_Q = 690\ \text{N} \cdot \text{mm}^{-1}$ at $\Delta a = 0.48$ mm
Estimation equation, Clarke and Landes	6 data points + 10 weighting at 0,0 $R = 0.987$	7 data points $R = 0.988$	
6.35-mm thickness $\frac{-1}{B}\left(\frac{\partial U}{\partial a}\right)_u$	$\frac{J}{\Delta a} = 1620\ \text{N} \cdot \text{mm}^{-2}$ or $J = 4.3\ \sigma_{flow} \Delta a$	$J = 615\ \Delta a + 366\ \text{N} \cdot \text{mm}^{-1}$ that is, $\frac{dJ}{da} = 615\ \text{N} \cdot \text{mm}^{-2}$ or $\frac{dJ}{da} = 1.6\ \sigma_{flow}$	$J_Q = 590\ \text{N} \cdot \text{mm}^{-1}$ at $\Delta a = 0.36$ mm
	2 data points + 10 weighting at 0,0 $R = 0.999$	2 data points $R = 1.000$	

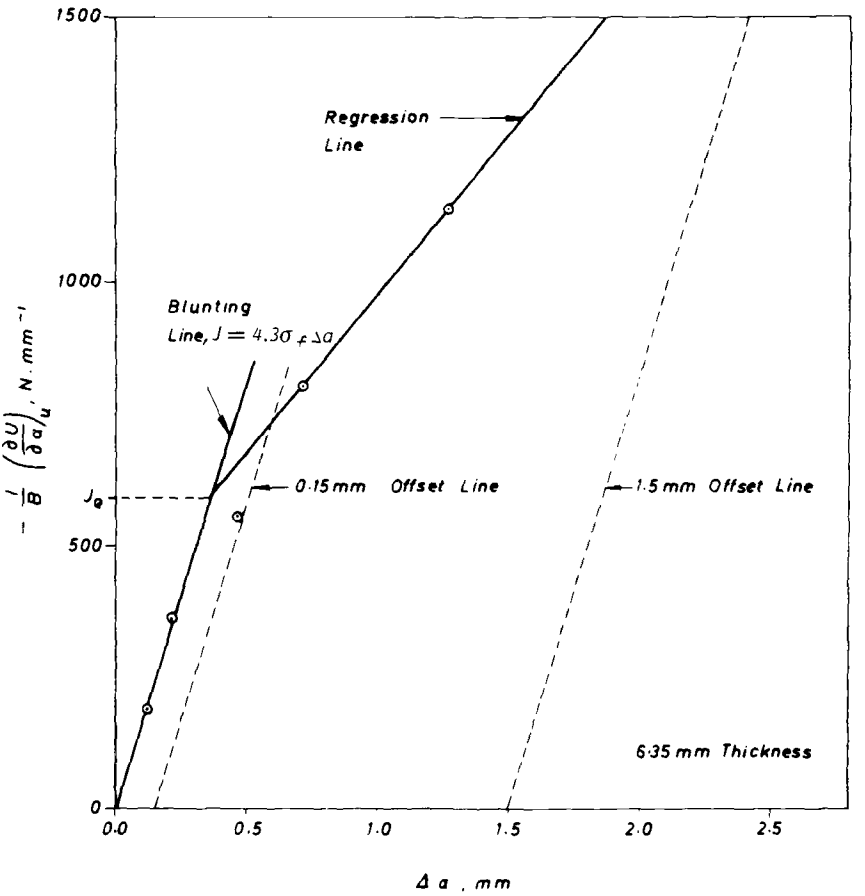

FIG. 5—*Determination of* J_i *for crack initiation for 6.35-mm-thick type 316 stainless steel compact specimens using the calibration function* $-(1/B)/(\partial U/\partial a)_u$.

imum number of four measurements of real crack extension are suggested to define the crack extension line. To ensure a reasonable spread of data points it is also suggested that these values lie between the limits of two offset lines constructed parallel to the crack blunting line at 0.15- and 1.5-mm crack extension, Figs. 4 and 5. These criteria were met in the case of all three sets of specimens taken together but not the 6.35-mm-thick specimens alone. For determination of accurate values of dJ/da and hence J_Q the use of thicker specimens covering a greater crack extension range up to a load maximum would appear preferable. In view of this the results of Fig. 4 for all three thickness specimens were considered more representative of material behavior and will be used in further discussion.

More important, the crack blunting line for 316 stainless steel differed markedly from that recommended

$$J = 2\sigma_f \Delta a \tag{5}$$

where σ_f is a flow stress taken as the average of the yield and ultimate tensile stress.

According to the proposed method [*5*], Eq 5 appears to be in good agreement with experimental results for most structural steels and aluminum alloys but not some austenitic stainless steels. For 316 stainless steel a factor of 3.8 was obtained from the results of six different specimens, Table 3, this value being in good agreement with the factor of 4 determined recently by Mills [*12*] for 304 stainless steel. This appears to reflect the higher work-hardening rate encountered with austenitic stainless steel resulting in higher apparent values for the flow stress.

Equation 5 was derived by assuming that as the crack tip opens and blunts during loading, deformation occurs along 45-deg sliplines so that the apparent crack extension is given by COD/2. For an apparent crack extension up to crack initiation of 0.48 mm, Fig. 4, and a COD_i of 1.56 mm, Fig. 6, the relation between these two parameters for 316 stainless steel is

$$\Delta a_i = 0.31\ \text{COD}_i \tag{6}$$

Thus, the slipline field ahead of the crack tip differed markedly from the 45-deg sliplines assumed in Eq 5, slip being produced at approximately 58 deg to the x-axis in 316 stainless steel. It should be noted that the stretch zone width measurements at 0 deg to the fracture surface of 0.42 to 0.60 mm were in good agreement with an apparent crack extension up to crack initiation of 0.48 mm.

The proposed validity requirement for plane-strain crack initiation [*5*] (B, $W - a \geq 25$ to $50 J_Q/\sigma_f \geq 45$ to 91 mm) was not met for any of the specimens. However, the J-Δa blunting lines and initial part of the resistance curves were in good agreement for all three specimen thicknesses, indicating that J may be useful as a material characteristic in the plane-stress regime. This supports similar results by Hickerson [*13*]. For this reason the symbol J_Q will be dropped and J_i used to denote a valid measurement of J at crack initiation under non-plane-strain conditions.

A valid plane-strain measurement, J_{Ic}, of 169 $\text{N} \cdot \text{mm}^{-1}$ was obtained by Chipperfield [*3*] using 10 to 50-mm-thick three-point-bend specimens of an annealed 316 stainless steel (T-L orientation). In comparison, Tobler et al [*14*] report a nonvalid J_Q of 597 $\text{N} \cdot \text{mm}^{-1}$ using 38-mm-thick compact specimens of a solution-annealed 316 stainless steel (T-L orientation). Finally, Bamford and Bush [*15*] obtained valid measurements of J_{Ic} of over 700 $\text{N} \cdot \text{mm}^{-1}$ using 50.8-mm-thick compact three-point-bend and center-cracked plate specimens of

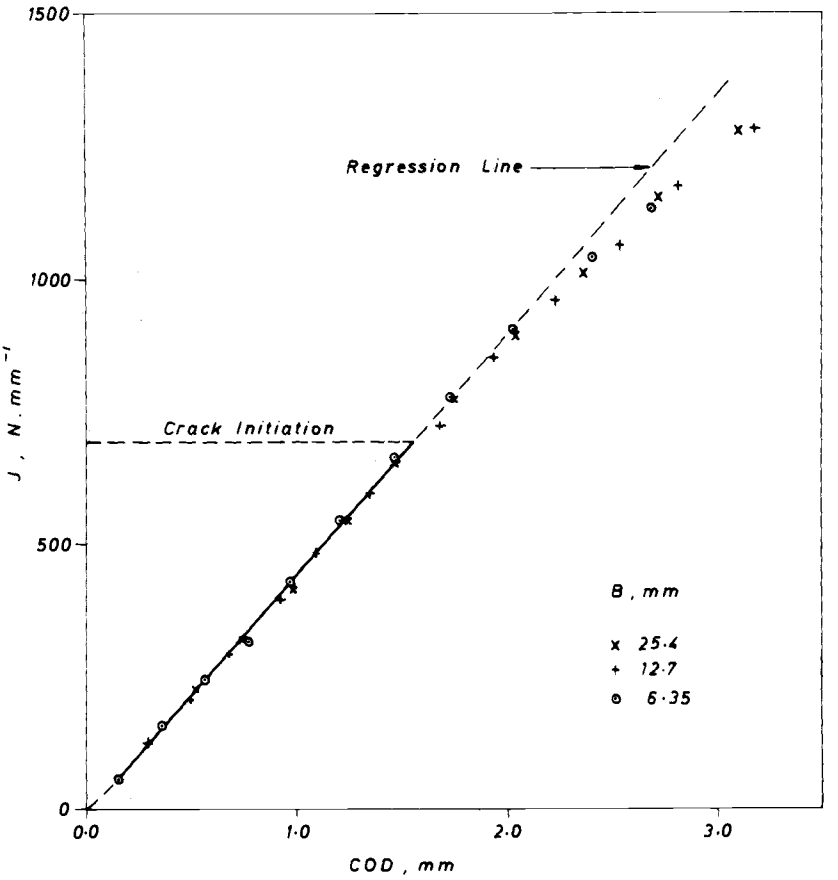

FIG. 6—*Experimental curve of the J-integral versus crack opening displacement for type 316 stainless steel compact specimens.*

annealed 316 stainless steel (axial and circumferential orientation). Unfortunately, the latter assumed the proposed ASTM crack blunting line, Eq 5, to determine a crack initiation point so that these results are probably nonconservative. However, it appears that the value of J_i of 690 N · mm^{-1} obtained here for solution-annealed 316 stainless steel is of the order of some valid measurements of J_{Ic} using thicker specimens of the same material.

Relationship Between J-Integral and COD

The experimental relationship between the J-integral and midsection COD is shown in Fig. 6, where J was calculated using the estimation Eq 4 [*10*]. Again the results from all three thickness plates were in excellent agreement,

the relationship linear over a significant range. A least-squares analysis was carried out up to crack initiation ($J_i = 690\ \mathrm{N \cdot mm^{-1}}$), giving the equation

$$J = 454\ \mathrm{COD} - 15.2\ \mathrm{N \cdot mm^{-1}}\ R = 0.999$$

that is

$$J \simeq 454\ \mathrm{COD}\ (0.15\ \mathrm{mm} < \mathrm{COD} < 1.56\ \mathrm{mm}) \tag{7}$$

or

$$J \simeq 2.3\ \sigma_y\ \mathrm{COD}$$

where 1.56 mm is the limiting value of COD_i at crack initiation. A typical rubber casting of the crack in 316 stainless steel is shown in Fig. 7, where the section was taken from the midthickness of Specimen 1-2 loaded to a load-line displacement of 7.1 mm. The measurement position of the COD is indicated, all COD measurements being made at the position of the original

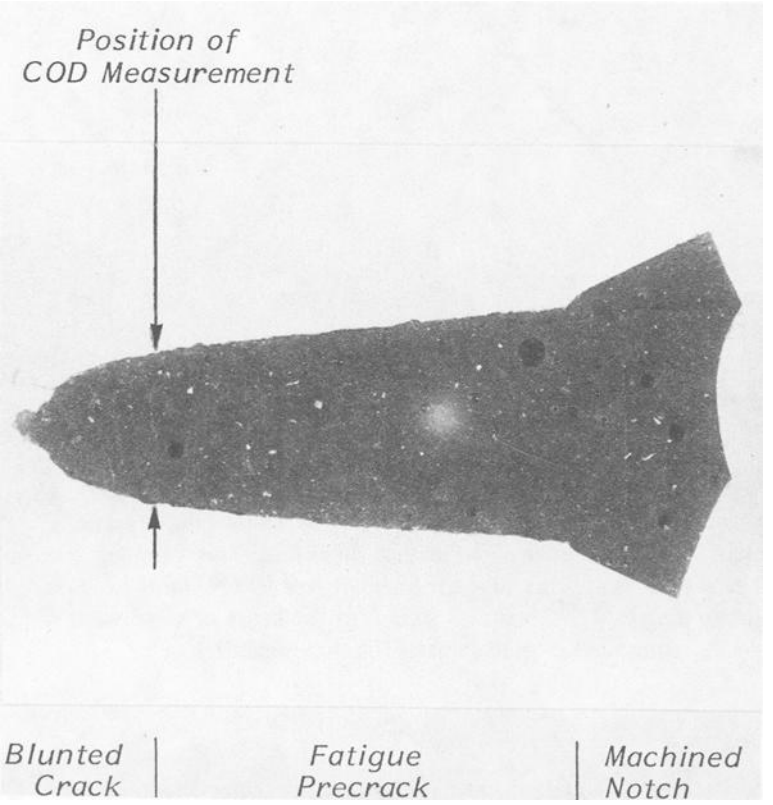

FIG. 7—*Rubber casting of crack in type 316 stainless steel at crack initiation, section at midthickness (×14).*

crack tip in the loaded state. The onset of ductile tearing from the crack tip is apparent at a COD of 1.50 mm, in good agreement with the interpolated COD_i of 1.56 mm.

During the 15 to 20 min curing of the rubber, the load relaxed 5 to 10 percent at constant displacement. However, this was not believed to have influenced the COD values obtained to any extent since the results were extremely reproducible. Also, no significant difference was found in the load-displacement curves obtained by superimposing the incremental loadings compared with the previous monotonic tests, limit loads of 27.1, 13.5, and 7.10 kN being obtained for Specimens 1-2, 2-6, and 4-1, respectively, compared with 27.2, 13.7, and 7.16 kN for Specimens 1-7, 2-2, and 4-6, respectively.

Thus, COD_i for the 316 stainless steel was found to be a constant 1.56 mm independent of plate thickness over the range 6.35 to 25.4 mm although the latter was below the suggested minimum thickness requirements [*3,16–18*] ($B \geq 25\ COD_i \geq 39$ mm). Constant values of COD_i of 0.38 mm have been obtained by Chipperfield [*3*]. However, as with the previous J measurements this value of COD_i is considerably lower than that measured in the present tests. As discussed elsewhere [*19*], this difference is believed to be due to the higher distribution of inclusions present in Chipperfield's sample of 316 material.

It is interesting to compare the experimental relation between the J-integral and COD, Eq 7, with Chipperfield's results

$$J_{Ic} = 445\ COD_i\ N \cdot mm^{-1}$$

or (8)

$$J = 1.6\sigma_y\ COD$$

Thus the relation between J and COD for 316 stainless steel appears to be a constant independent of specimen configuration and thickness. The difference in constraint factor, M, of 2.3 in the present tests and 1.6 from Chipperfield can, therefore, be accounted for solely on the basis of differences in yield stress reflecting a higher work-hardening capacity of the material tested here. These results support the suggestion of Chipperfield [*3*] that the presence of voids ahead of the crack tip in such material may well result in a reduction in constraint due to the interaction of these free surfaces with the near-tip stress field. Under such circumstances a value of M near 1 would probably be more appropriate so that any increase in constraint would then be due only to the influence of the work hardening of the material.

Crack-Tip Contraction

It has been suggested that a linear relation exists between crack-tip contraction and COD [*20,21*]. Figure 8 presents a plot of on-load w_{max} versus

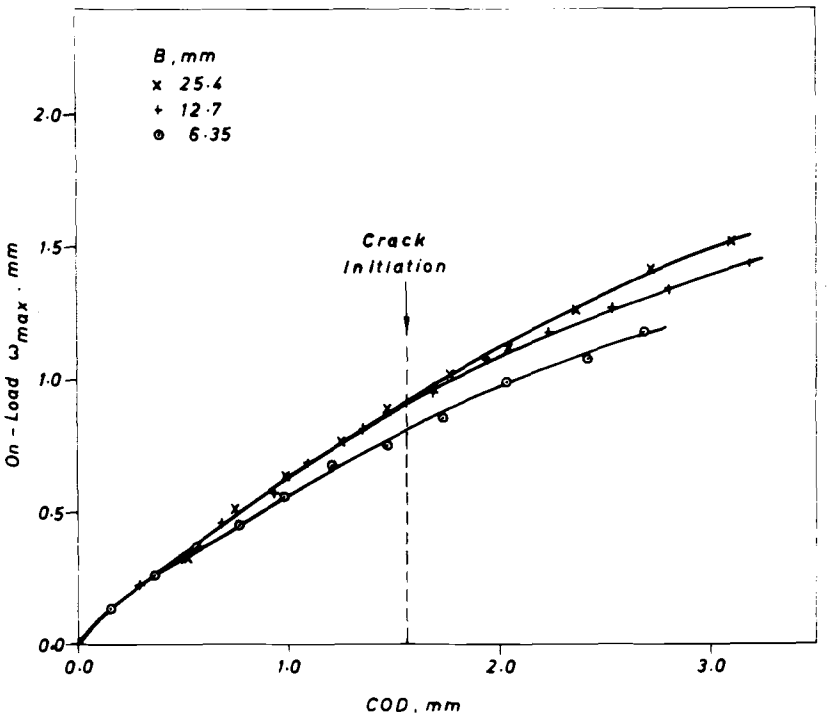

FIG. 8—*Experimental curve of on-load crack-tip contraction versus COD for type 316 stainless steel compact specimens.*

midsection COD for the three different-thickness specimens. The results deviate markedly from a linear relation at low values of COD and especially at high values of COD after crack initiation, results for the 6.4 mm thick specimens lying below those for the thicker plates. However, a linear regression analysis was performed up to crack initiation. From this the maximum crack-tip contraction on one surface was approximately one half the COD, the factors being 0.58, 0.57, and 0.47 for the 25.4, 12.7, and 6.35-mm-thick plates, respectively.

Under fully plane-stress conditions the COD may well be expected to equal the total crack-tip contraction, $2w_{max}$, assuming shear occurs preferentially on planes at 45 deg to the plate surface. However, deviations from such a model would be expected in the present case since yield has been shown to occur at an angle of 58 deg to the x-axis for 316 stainless steel. In addition, none of the specimens tested exhibited free yielding through the thickness as shown by the proportion of square fracture, 82, 68, and 57 percent for the 25.4, 12.7, and 6.35-mm-thick specimens, respectively.

From Fig. 8 it was possible to construct a plot of average through-thickness strain, $2w_{max}/B$, at crack initiation versus plate thickness, Fig. 9. This figure

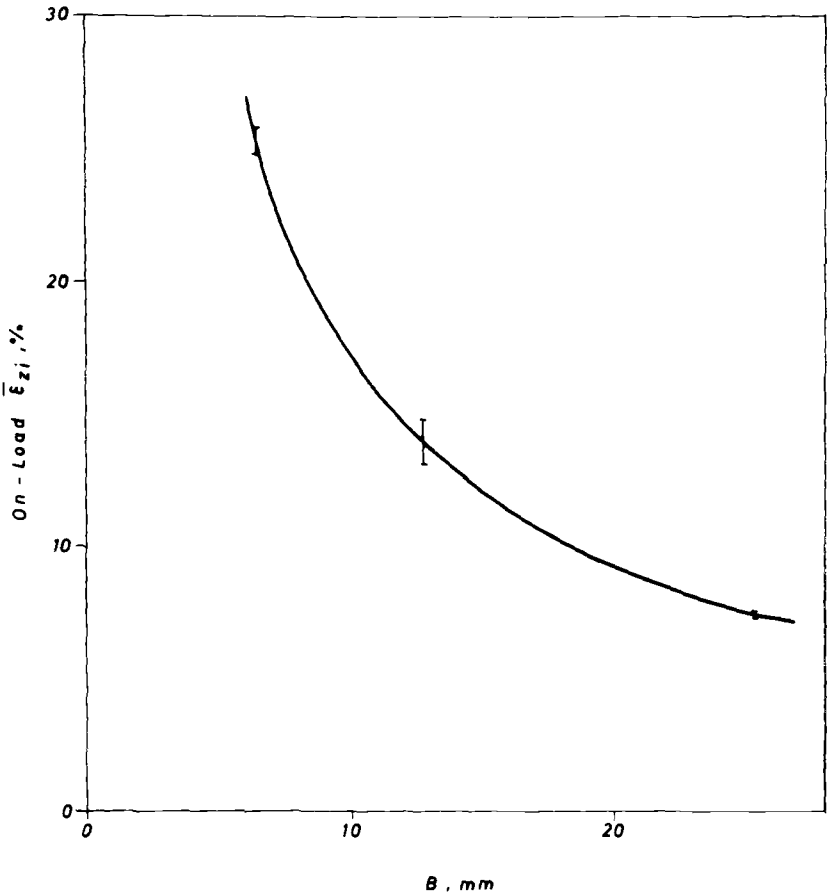

FIG. 9—*Average through-thickness strain at crack initiation versus thickness for type 316 stainless steel compact specimens.*

includes results of measurements of $\bar{\epsilon}_z$ made directly on the three sets of fracture specimens, the crack initiation point for $\bar{\epsilon}_z$ being defined by an interpolation procedure analogous to that used in the J-integral test [*19*]. It can be seen that the average through-thickness strain for the thinnest specimens increased sharply with decreasing thickness in spite of the fact that the contraction of the thicker specimens was more than that of the thinner specimens.

Discussion

For a highly ductile material such as stainless steel it was anticipated that failure would occur under plane-stress conditions. This can be demonstrated by calculating the plane-stress plastic zone size at crack initiation, $EG_{Ic}/$

$2\pi\sigma_y^2$. Using Chipperfield's value of 169 N · mm^{-1} for $J_{Ic} = G_{Ic}$, an estimated plastic zone size of 131 mm is calculated, considerably in excess of the plate thickness used here. However, from Fig. 3 it is apparent that except for the 6.35-mm-thick plates there were significant differences between the experimental and ultimate collapse loads as predicted by the plane-stress model, results for the thicker specimens deviating by up to 20 percent from the plane-stress solution.

In view of this it may seem surprising that constant values of both the J-integral and COD were obtained at crack initiation for all three plate thicknesses of 316 stainless steel. By definition, J_i represents the energy required for the production of the crack-tip stretch or process zone, that is, the region dominated by the crack-tip singularity. From scanning electron microscopy the fibrous fracture mode was essentially the same for the three different-thickness plates. Therefore, since J_i is an energy parameter it is quite possible that any reduction in crack-tip strain due to an increase in constraint may have been fully compensated by a corresponding increase in stress intensification at the crack tip as reflected by the failure analysis diagram.

The constancy of COD_i with plate thickness is more difficult to explain. It might be expected that the sharp increase in crack-tip strain for the thinner specimens as measured by $\bar{\epsilon}_z$, Fig. 9, would be reflected by higher values of COD at crack initiation. However, if the COD merely reflects midsection behavior, then the constancy of COD_i may be due to the overriding influence of voids ahead of the crack tip in the near-tip stress field as suggested by Chipperfield [*3*].

Conclusions

1. Static loading experiments on 6.35 to 25.4-mm-thick compact specimens of a solution-treated 316 stainless steel have shown that critical values of the J-integral and COD at crack initiation are constant independent of plate thickness under non-plane-strain crack-tip conditions, that is $B < 25$ to 50 (J_i/σ_f) and $B < 25\ COD_i$.

2. The ASTM proposed modified equation for the determination of J from single compact specimens [*5*] can yield values within 2 percent of those determined using the Begley and Landes calibration method.

3. The crack blunting line for 316 stainless steel

$$J = 3.8\sigma_f \Delta a$$

differed markedly from that recommended in the proposed ASTM method for J_{Ic} [*5*]. The difference has been shown to be due not only to an apparent increase in flow stress as a result of the high work-hardening capacity of stainless steel but also to the development of the slipline field ahead of the crack tip.

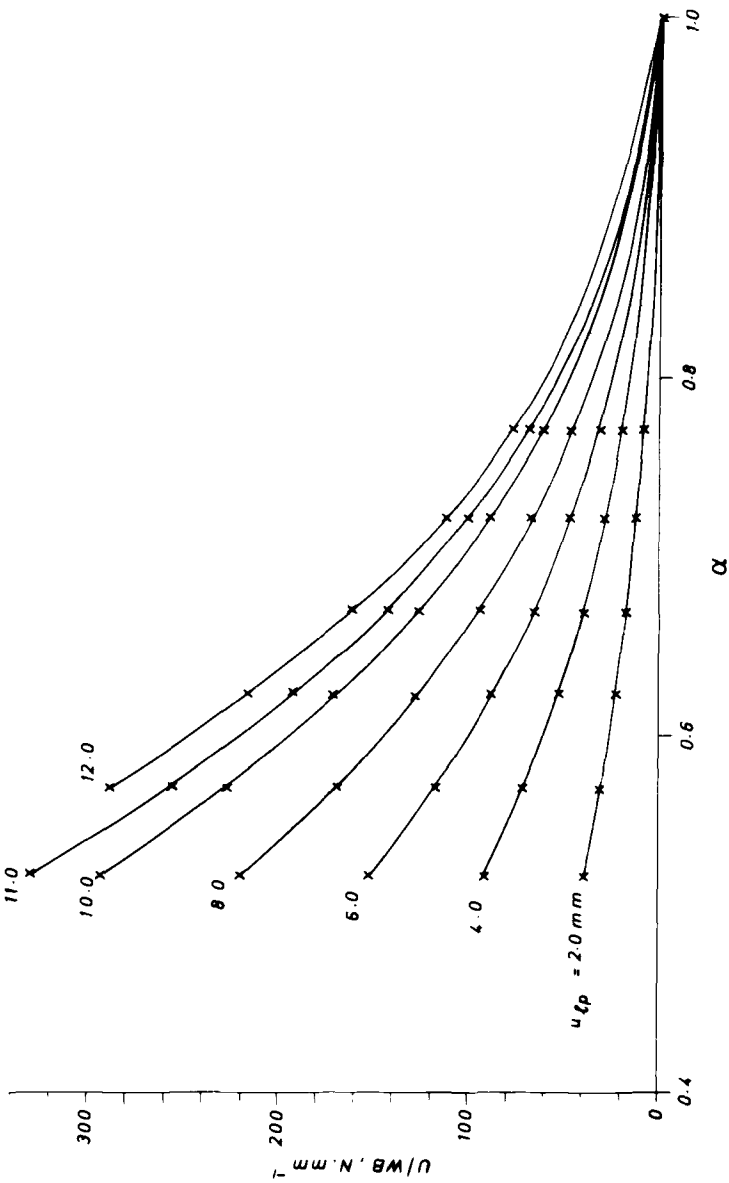

FIG. 10—*Cubic spline curve fit to experimental results of strain energy versus relative crack length for 6.35-mm-thick type 316 stainless steel compact specimens.*

4. In order to determine accurate values of dJ/da and hence J_Q at crack initiation, the use of thicker specimens covering as large a crack extension range as possible is recommended.

5. The relationship between J and COD for stainless steel

$$J \sim 454 \text{ COD N} \cdot \text{mm}^{-1} \ (0.15 \text{ mm} < \text{COD} < 1.56 \text{ mm})$$

was in excellent agreement with Chipperfield's results [3], indicating that the foregoing equation is independent of specimen configuration and thickness under both plane-strain and non-plane-strain crack-tip conditions. Alternatively, in terms of the yield stress and a constraint factor

$$J = M\sigma_y \text{ COD}$$

$$J \sim 2.3\sigma_y \text{ COD} \ (0.15 \text{ mm} < \text{COD} < 1.56 \text{ mm})$$

Variations in M have been shown to be due primarily to variations in the work-hardening capacity of the material.

6. An approximately linear relationship exists between crack-tip contraction and midsection COD for 316 stainless steel up to crack initiation, this relationship depending upon the extent of through-thickness yield.

Acknowledgments

Financial support for this work from the Ministry of Defence, Royal Military College of Science, Shrivenham, U.K., is gratefully acknowledged.

The author wishes to thank Mr. C. A. Andrasic, Materials Branch, for his computational assistance.

APPENDIX

Using the method of cubic splines a computer program was developed to fit curves to the experimental results of strain energy, U/WB, versus relative crack length, α, for each displacement and hence compute the first derivative, $-(1/B)/(\partial U/\partial a)_u$, at a given crack size. With three equally spaced internal knot positions, negative values of the first derivative were obtained. Eventually, physically acceptable results were obtained using one internal knot at $\alpha = 0.7$. The curves resulting from this procedure are shown in Fig. 10 and the residual sum of the squares for each curve is as follows:

Load-Pin Displacement, u_{lp}, mm	Residual Sum of Squares
2.0	0.00035
4.0	0.00045
6.0	0.00110

8.0	0.00509
10.0	0.00309
11.0	0.00427
12.0	0.00165

References

[1] Rice, J. R. in *Fracture—An Advanced Treatise*, Vol. 2, H. Liebowitz, Ed., Academic Press, New York, 1968, p. 191.

[2] Wells, A. A. in *Proceedings*, Symposium on Crack Propagation, Cranfield, U.K., 1961, p. 210.

[3] Chipperfield, C. G., *International Journal of Fracture*, Vol. 12, 1976, p. 873.

[4] Robinson, J. N., *International Journal of Fracture*, Vol. 12, 1976, p. 723.

[5] Clarke, G. A., Andrews, W. R., Begley, J. A., Donald, J. K., Embley, G. T., Landes, J. D., McCabe, D. E., and Underwood, J. H., *Journal of Testing and Evaluation*, Vol. 7, 1979, p. 49.

[6] Begley, J. A. and Landes, J. D. in *Fracture Toughness, ASTM STP 514*, American Society for Testing and Materials, 1972, p. 1.

[7] Robinson, J. N. and Tetelman, A. S. in *Fracture Toughness and Slow-Stable Cracking, ASTM STP 559*, American Society for Testing and Materials, 1974, p. 139.

[8] Dowling, A. R. and Townley, C. H. A., *International Journal of Pressure Vessels and Piping*, Vol. 3, 1975, p. 77.

[9] Ewing, D. J. F. and Richards, C. E., CEGB Report RD/L/N237/72, Central Electricity Generating Board, Surrey, U.K., 1972.

[10] Clarke, G. A. and Landes, J. D., *Journal of Testing and Evaluation*, Vol. 7, 1979, p. 264.

[11] Merkle, J. G. and Corten, H. T., *Transactions*, American Society of Mechanical Engineers, *Journal of Pressure Vessel Technology*, 1974, Vol. 96, p. 286.

[12] Mills, W. J., *Journal of Testing and Evaluation*, Vol. 9, 1981, p. 56.

[13] Hickerson, J. P., Jr., *Engineering Fracture Mechanics*, Vol. 9, 1977, p. 75.

[14] Tobler, R. L., Mikesell, R. P., Durcholz, R. L., Fowlkes, C. W., and Reed, R. P., "Materials Research in Support of Super-conducting Machinery," NBSIR 74-359, National Bureau of Standards, Boulder Laboratories, Boulder, Colo., 1974, p. 296.

[15] Bamford, W. H. and Bush, A. J. in *Elastic-Plastic Fracture, ASTM STP 668*, J. D. Landes, J. A. Begley, and G. A. Clarke, Eds., American Society for Testing and Materials, 1979, p. 553.

[16] Knott, J. F., *Fundamentals of Fracture Mechanics*, Butterworths, London, 1973.

[17] Green, G. and Knott, J. F., *Journal of the Mechanics and Physics of Solids*, Vol. 23, 1975, p. 187.

[18] Robinson, J. N. and Tetelman, A. S., *International Journal of Fracture*, Vol. 11, 1975, p. 453.

[19] Hodkinson, P. H., Royal Military College of Science Technical Note MAT/27, R.M.C.S., Shrivenham, Swindon, U.K., May 1980.

[20] Robinson, J. N. and Tetelman, A. S., *Engineering Fracture Mechanics*, Vol. 8, 1976, p. 301.

[21] Taira, S. and Tanaka, K., *Engineering Fracture Mechanics*, Vol. 11, 1979, p. 231.

H. W. Liu,[1] *Wan-liang Hu,*[2] *and Albert S. Kuo*[3]

Thickness Effects on the Choice of Fracture Criteria

REFERENCE: Liu, H-W., Hu, Wan-liang, and Kuo, Albert S., **"Thickness Effects on the Choice of Fracture Criteria,"** *Elastic-Plastic Fracture: Second Symposium. Volume II—Fracture Resistance Curves and Engineering Applications, ASTM STP 803*, C. F. Shih and J. P. Gudas, Eds., American Society for Testing and Materials, 1983, pp. II-632-II-656.

ABSTRACT: The stresses and strains in a cracked solid are in a complicated three-dimensional state. There are three two-dimensional limiting cases: plane strain, plane stress, and Dugdale's strip yielding case. The thickness of a plate relative to crack tip plastic zone size determines which one of these three limiting cases is predominant. The characteristics of the plane-stress and the Dugdale strip yielding crack-tip fields were investigated with the moire method together with the finite-element calculations. The state of the crack-tip stress and strain fields approaches that of plane strain for very thick plates. For a very thin plate with a very large crack-tip plastic zone, the Dugdale strip yielding model is applicable, and the crack opening displacement, crack-tip opening displacement, and thickness contraction are related to K or J and they can be used for fracture toughness measurements. When a plate thickness is in between these two extremes, there exists a characteristic plane stress crack-tip field. The correspondence of the plane-stress crack-tip fields in small-scale yielding and in general yielding was established, and the J value of a small specimen in general yielding can be obtained from the established correspondence. The value of the applied J-field of a small specimen in general yielding can be measured in terms of the applied stress and the specimen elongation.

KEY WORDS: nonlinear fracture mechanics, fracture toughness, small-scale yielding, general yielding, crack opening displacement, crack-tip opening displacement, thickness contraction, elastic-plastic fracture

Griffith [*1*][4] formulated the energy fracture criterion for brittle solids. At the onset of fracture initiation, the driving force (that is, the rate of change of the elastic strain energy of a cracking solid) is equal to the energy dissipation rate (that is, the surface energy of a brittle solid), which is a constant. Irwin

[1]Professor of materials science, Syracuse University, Department of Chemical Engineering and Materials Science, Syracuse, N.Y. 13210.
[2]Hanford Engineering Development Laboratory, Westinghouse Corp.,
[3]Fairchild Republic Co.,
[4]The italic numbers in brackets refer to the list of references appended to this paper.

[2] and Orowan [3] extended the Griffith energy criterion to metallic solids by assuming that the plastic energy dissipation rate for fracture initiation was a material constant. However, it can be shown that the plastic energy dissipation rate of a cracking infinite plate in the condition of plane strain is linearly proportional to crack length, $2a$. So is the rate of change of the elastic strain energy of the plate. The fracture criterion based on the global energy balance leads to a constant fracture stress for an infinite plate, and the fracture stress is independent of crack length. This conclusion contradicts the experimental evidence; therefore the criterion of the global energy balance for fracture initiation without the consideration of the detailed fracture processes must be fortuitous [4].

Liu [4] has shown that the stress-intensity factor, K, characterizes crack-tip stresses and strains even within the crack-tip plastic zone, r_p, if the condition of small-scale yielding (SSY) is satisfied. The very existence of this conclusion allows us to determine experimentally the minimum specimen size for valid fracture toughness measurements. But the condition of SSY is a sufficient, but not the necessary condition for the validity of the linear elastic fracture mechanics (LEFM). The necessary condition is that K should be able to characterize the crack-tip stress or strain responsible for the defined fracture process. When the applied stress or strain at the fracture process zone reaches the critical value, fracture will occur.

If it is limited to the realm of the LEFM, with the restriction to the same fracture mode and the limitation to the same thickness, the concept of the K-characterization of the crack-tip field and the assumption of the constant dissipation rate of plastic deformation energy lead to the same results. However, when it is extended beyond the realm of the LEFM, only the correct analysis will lead to the desired results. The concept of characterizing crack-tip stress and strain fields by the stress-intensity factor, K, forms a sound basis for the extension of the LEFM to nonlinear fracture mechanics. This paper ilustrates its applications. A detailed review of the global energy balance fracture theory, the sharp notch fracture theory, and the concept of characterization of crack tip field by the stress-intensity factor are given in Ref 5a.

The characteristic crack-tip stresses and strains are greatly affected by specimen thickness. When a small plastic zone at a crack tip is imbedded in a massive and thick plate, the constraint to thickness contraction induces a state of high triaxial stresses, and the state of the crack-tip field approaches that of plane strain. The maximum principal stress, σ_{max} is nearly $2.45 \times \sigma_{flow}$, and the triaxial state of stresses restrains plastic deformation. On the other hand, a very large plastic zone in a thin plate causes crack-tip necking. In this instance, extensive plastic deformation is concentrated within a thin narrow strip. Within the strip, the plate thickness contracts considerably, and the deformation approaches the Dugdale strip yielding model [6]. When specimen thickness is intermediate between these two extremes, a character-

istic plane-stress crack-tip field exists. In this case, the maximum principal stress is nearly equal to σ_{flow}.

Fracture processes are controlled by the crack-tip stresses and strains which are greatly affected by plate thickness. Therefore the choice of the fracture criteria must also be dependent on plate thickness.

This paper summarizes and synthesizes the experimental and theoretical work at Syracuse University on the effects of thickness on crack-tip stresses and crack-tip deformation, and on the choice of the fracture criteria for nonlinear fracture mechanics. Plate thicknesses less than that of plane strain were studied. The results are applicable to structures made of high-toughness materials which are less than 5 cm (2 in.) thick.

Characteristic Plane-Stress Crack-Tip Field—Small-Scale Yielding and Large-Scale Yielding Correspondence

Crack-tip strains, ϵ_{yy}, were measured by Gavigan, Ke, and Liu [7] in double-edge-cracked (DEN) specimens made of three batches 2024-0 aluminum alloy. Specimens 102 and 203 mm (4 or 8 in.) wide of three different thicknesses were tested. The measurements are shown in Fig. 1. The solid lines are plane-stress finite-element calculations. Away from the crack tip, in the region $r > t$, the measurements and the calculations agree very well; t is plate thickness. Close to the crack tip, $r < t$, the measured strains are less than the calculated values. These strains were measured on the specimen surface; however, the surface was not free to deform because the surface was coupled to the interior of the specimen, where "plane strain" constraint existed. The constraint "stiffened" the crack-tip area and it reduced strains on the surface. The constraint is a localized three-dimensional phenomenon. Beyond the crack-tip stiffened zone, the measurements clearly indicate the existence of a characteristic plane-stress crack-tip field. Figure 2 shows the measured and the calculated load-displacement, P-Δ, curves. Again, the agreement of the measurements and the calculations is very good.

Figure 3 schematically shows various regions of stress and strain fields. Region I extends from the crack tip to a distance approximately equal to half of the specimen thickness. In this region, the plane-strain stiffening effect exists, and the three-dimensional effect is clearly shown. In Region II, the plane-stress condition prevails. The stress and strain fields approach the analytical results of Hutchinson [8] and Rice and Rosengren [9].[5] Region III lies farther away from the crack tip where the material deforms elastically and the stresses and strains vary with $r^{-0.5}$. The measurements shown in Fig. 1. were all made at general yielding. However, if a specimen is large enough, the characteristic elastic field may exist. Still farther away is Region IV, where the effects of specimen geometry and type of loading dominate the

[5]This will be discussed in detail later.

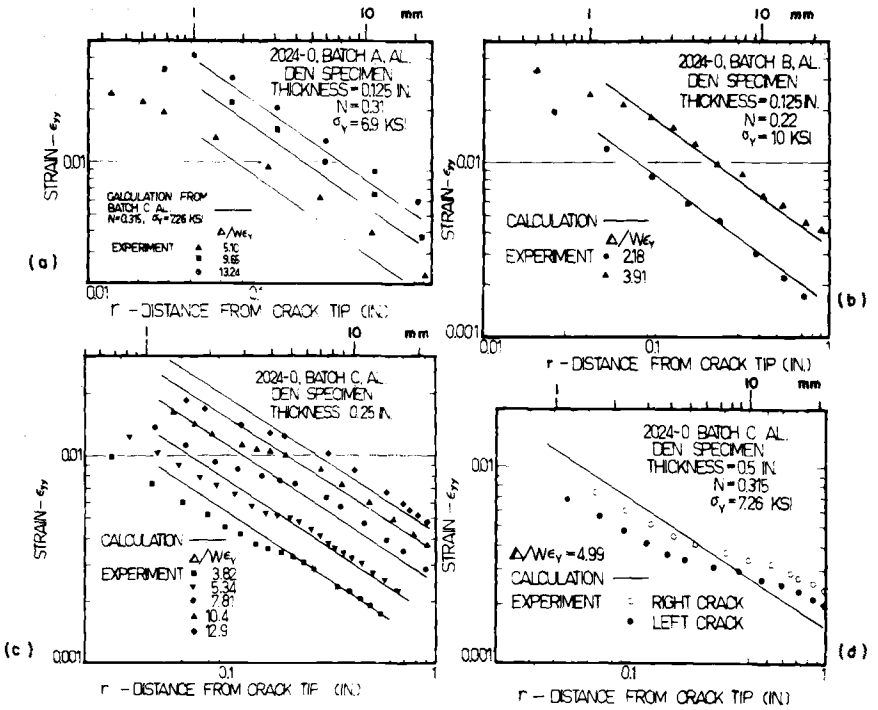

Batch	σ_Y MPa	σ_Y ksi	N	W mm	W in.	a mm	a in.	GL mm	GL in.
A	47.6	6.9	0.31	104	4.1	19.4	0.764	168	6.625
B	69	10	0.22	208	8	40.6	1.6	356	14.0
C	50	7.26	0.315	102	4	20.3	0.8	178	7.0

FIG. 1—*Comparison of calculated* ϵ_{yy} *versus experimental measurements, double-edge-notched plate, 2024-0 aluminum alloy.* Δ = *elongation of gage length, GL;* $E = 6.9 \times 10^4$ *MPa* (10^4 *ksi*); *Ref* 10.

deformation characteristics. Note that, in general, not all of these four regions are present. For example, Region III diminishes with increasing load. For a very thick single-edge-cracked (SEN) specimen, only Regions I and IV may exist.

The nature of the plane-strain stiffening effect in Region I has been discussed previously [*10*]. It is the stresses and strains in the immediate vicinity of the crack tip within the stiffened zone that cause fracture initiation. The crack-tip stiffened zone is embedded within the plane-stress crack-tip field. It is reasonable that the stresses and strains in the stiffened zone should be characterized by the intensity of the plane-stress crack-tip field. In other words, the same intensity of the plane-stress crack tip field infers the same stresses and strains in the stiffened zone, even though the exact values of the

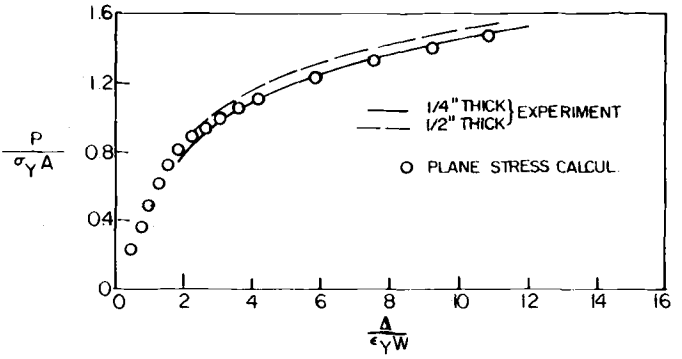

FIG. 2—*Measured and calculated load-elongation curves:* A = *area,* W = *width [10].*

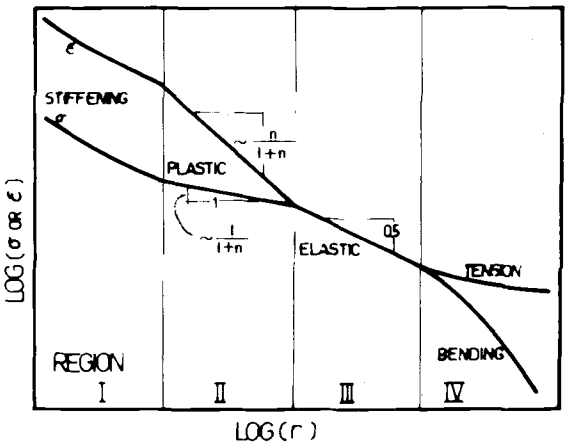

FIG. 3—*Schematic plot of stress and strain distributions ahead of a crack in logarithmic scale.*

stresses and strains in the stiffened zone are unknown. Therefore, the intensity of the plane-stress crack-tip field also characterizes the condition for crack initiation. The degree of crack-tip strengthening is affected by plate thickness; therefore this conclusion is applicable only to specimens of the same thickness. We will focus our attention on Regions II and III.

Crack-tip stresses, strains, and displacements in elastic solids can be expressed in terms of the stress-intensity factor K. In a like manner, Hutchinson [8] and Rice and Rosengren [9] have shown that crack-tip stresses, strains, and displacements can be expressed in terms of J

$$[\sigma_{ij}, \sigma_e] = \sigma_0 \left[\frac{J}{\alpha \sigma_0 \epsilon_0 I_n r} \right]^{1/(n+1)} [\tilde{\sigma}_{ij}(\theta, n), \tilde{\sigma}_e(\theta, n)]$$

$$\epsilon_{ij} = \alpha\epsilon_0 \left[\frac{J}{\alpha\sigma_0\epsilon_0 I_n r} \right]^{n/(n+1)} \tilde{\epsilon}_{ij}(\theta, n) \tag{1}$$

$$u_i - u_i^0 = \alpha\epsilon_0 \left[\frac{J}{\alpha\sigma_0\epsilon_0 I_n} \right]^{n/(n+1)} r^{1/(n+1)} \tilde{u}_i(\theta, n)$$

for a material with a power-law stress-strain relation

$$\frac{\epsilon}{\epsilon_0} = \alpha\left(\frac{\sigma}{\sigma_0} \right)^n \tag{2}$$

where σ_0 is the flow stress at the strain ϵ_0. When $\sigma_0 = \sigma_Y$ and $\epsilon_0 = \epsilon_Y$, $\alpha = 1$ and $n \geqq 1$. σ_e is the effective stress. $\tilde{\sigma}_{ij}(\theta, n)$, $\tilde{\sigma}_e(\theta, n)$, $\tilde{\epsilon}_{ij}(\theta, n)$, and $\tilde{u}_i(\theta, n)$ are functions of θ and n. They define the distributions of their corresponding components in the θ-direction. $I_n(n)$ is a function of n

$$I_n = \int_{-\pi}^{\pi} \left[\frac{n}{n+1} \tilde{\sigma}_e^{(n+1)} + (\ ) \right] d\theta \tag{3}$$

The symbol ( ) represents the additional terms in the full expression, which is given in Ref *8*. J is the well-known J-integral. It characterizes crack-tip stresses, strains, and displacements analogous to K for elastic solids.

For a nonlinear elastic solid, J can also be considered as the rate of the change of the potential energy with respect to crack increment. In the case of SSY,

$$J = G = \frac{K^2}{\bar{E}} \tag{4}$$

where $\bar{E} = E$ for plane stress and $\bar{E} = E/(1 - \nu^2)$ for plane strain. ν is Poisson's ratio.

However, the characteristic crack-tip fields given by Eq 1 are not universally valid in all the cases. Figure 4 shows the slipline fields of a double-edge-

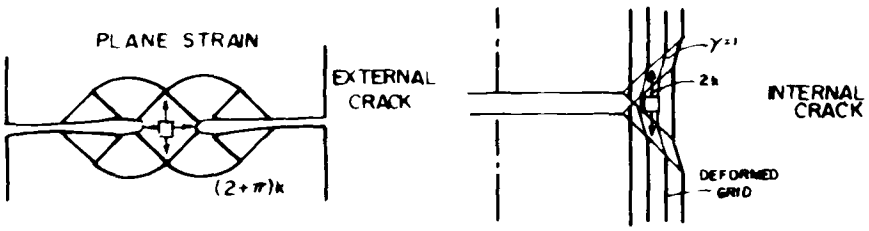

FIG. 4—*Slipline fields for fully plastic tension mode; plane strain.*

notched specimen and a single-edged-notched specimen under fully plastic tensile loads. Because of the difference in in-plane constraint, the principal tensile stress is equal to $(2 + \pi)k$ in one case and $2k$ in the other; k is the yield stress in terms of shear. The characteristic flow fields and stress fields of these two cases are grossly different. In other words, for different types of specimen geometry, the characteristic fields might be different. The same J-value might indicate different crack-tip stresses, strains, and displacements. As a result, one would expect that specimens of different geometric types would fail at different J-values. Indeed, Hancock and Cowling [*11*] tested specimens of five different geometries. The lowest and the highest values of crack-tip opening displacements at fracture, δ_c, differ by a factor of 10. δ is related to J but the relation differs for different flow fields. Taking the difference of the flow fields into consideration, Hancock and Cowling [*11*] found the corresponding extreme values of J_c to be 570 and 147 kNm^{-1} (3.25 and 0.839 ksi-in.), a difference of a factor of four.

In order to measure fracture toughness as a material property, a reference state of crack-tip field must be established. The most meaningful one is that of the small-scale yielding. With this choice, the measured fracture toughness of a small specimen in general yielding (GY) will be able to predict the fracture strength of a large structure in small-scale yielding.

Plane stress calculations are also made for the double-edge-cracked specimen and the single-edge-cracked specimen in SSY, large-scale yielding (LSY), and GY. The characterization of the crack-tip fields, the correspondence between the crack-tip fields in the state of the SSY, LSY, and GY, and their relation to the applied stress and the imposed elongation are studied.

The crack-tip stress and strain fields in specimens made of two batches of aluminum alloy in the state of SSY were studied using plane-stress finite-element analysis. A circular specimen with a crack along one of the radial lines and with boundary displacements given by the dominant terms of the linear elastic solution, that is, $u_i = (K/2\mu)(r/2\pi)^{1/2}\,\tilde{u}_i(\theta)$, serves as the reference state; see Fig. 5, μ is shear modulus. The $\sigma - \epsilon$ relations are prescribed by $\sigma = E\epsilon$ for $\sigma \leqq \sigma_Y$ and $\sigma = k\epsilon^N$ for $\sigma \geqq \sigma_Y$ and $k = E^N\sigma_Y^{(1-N)}$. $\sigma_Y =$ 69 MPa (10 ksi) and $N = 0.22$ for Batch B; and $\sigma_Y = 50$ MPa (7.26 ksi) and $N = 0.315$ for Batch C. The finite-element mesh is shown in Fig. 5. The details of the calculations are given in Ref *12*. The crack line stresses and strains for Batch C aluminum are shown in the dimensionless plots in Fig. 6. The results of nine loading steps are shown. The value of K_I ranges from 1.24 to 4.4 $\text{MPa}\sqrt{\text{m}}$ (1.13 to 4 $\text{ksi}\sqrt{\text{in.}}$).

Within r_p, the y-direction strain and stress can be expressed as

$$\epsilon_{yy} = \epsilon_{yy(r=r_p)}\left(\frac{r_p}{r}\right)^m = \frac{\epsilon_Y}{\beta}\left(\frac{r_p}{r}\right)^m$$

$$= \frac{\epsilon_Y}{\beta}\left(\gamma\frac{J}{\epsilon_Y\sigma_Y r}\right)^m = \frac{\epsilon_Y}{\beta}\left(\frac{K_I}{\sigma_Y}\right)^{2m}\left(\frac{\gamma}{r}\right)^m \qquad (9a)$$

$$\sigma_{yy} = \sigma_{yy(r=r_p)}\left(\frac{r_p}{r}\right)^{m'} = \frac{\sigma_Y}{\beta'}\left(\frac{r_p}{r}\right)^{m'}$$

$$= \frac{\sigma_Y}{\beta'}\left(\gamma\frac{J}{\epsilon_Y\sigma_Y r}\right)^{m'} = \frac{\sigma_Y}{\beta'}\left(\frac{K_I}{\sigma_Y}\right)^{2m'}\left(\frac{\gamma}{r}\right)^{m'} \quad (9b)$$

where $r_p = \gamma(K_I/\sigma_Y)^2 = \gamma J/\epsilon_Y\sigma_Y$. The value of β, β', and γ are, respectively, 1.41, 0.98, and 0.243 for Batch C aluminum, and 1.35, 0.92, and 0.281 for Batch B aluminum.

The form of Eq 9 is similar to that given by Hutchinson [8] and Rice and Rosengran [9], Eq 1. Combining Eqs 1 and 9, with $(m + m') = 1$, one obtains

$$I_n(n)/\tilde{\sigma}_{yy}(0, n)\tilde{\epsilon}_{yy}(0, n) = \beta\beta'/\gamma \quad (10)$$

Table 1 lists the values of $(\beta\beta'/\gamma)$ obtained from the finite-element calculation and the values of $(I_n/\tilde{\sigma}_{yy}\tilde{\epsilon}_{yy})$ obtained from Hutchinson's results. These two sets of values are very close to each other. The values of $\tilde{\sigma}_{yy}$ $(0, n)$ and $\tilde{\epsilon}_{yy}$ $(0, n)$ are obtained by the linear interpolation between $\tilde{\sigma}_{yy}$ $(0, 3) = 1.1$ and $\tilde{\sigma}_{yy}$ $(0, 13) = 1.2$; and $\tilde{\epsilon}_{yy}$ $(0.3) = 0.7$ and $\tilde{\epsilon}_{yy}$ $(0.13) = 0.8$; the values of I_n (n) are from the linear interpolation between I_n $(3) = 3.86$ and I_n $(5) = 3.41$.

The results for σ_{yy}, ϵ_{yy}, $\bar{\sigma}$, and $\bar{\epsilon}^p$ along the radial lines of 45, 60, and 90 deg away from the crack line are shown in Fig. 7 as solid curves. $\bar{\sigma}$ is effective stress; $\bar{\epsilon}^p$ is effective plastic strain. Similar relations as Eq 9 can also be obtained for these stresses and strains.

The state of the crack-tip stress and strain-fields in SSY serves as a reference to be compared with the crack-tip fields of specimens in LSY and GY.

DEN and SEN specimens were studied. The calculated σ_{yy}, ϵ_{yy}, $\bar{\sigma}$, and $\bar{\sigma}^p$ are shown in Figs. 7 and 8. For comparison, the results of the SSY calcula-

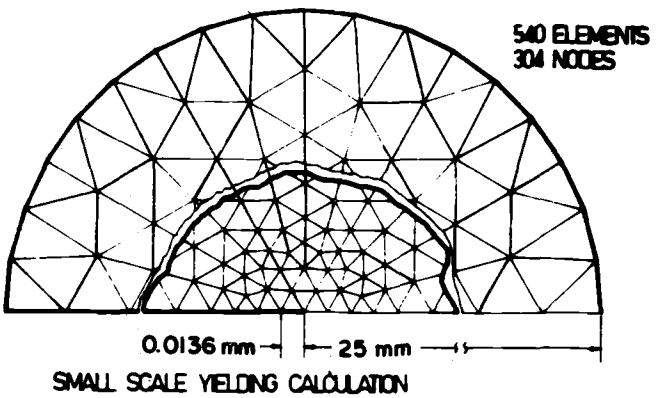

FIG. 5—*Element layout for small-scale yielding calculations.*

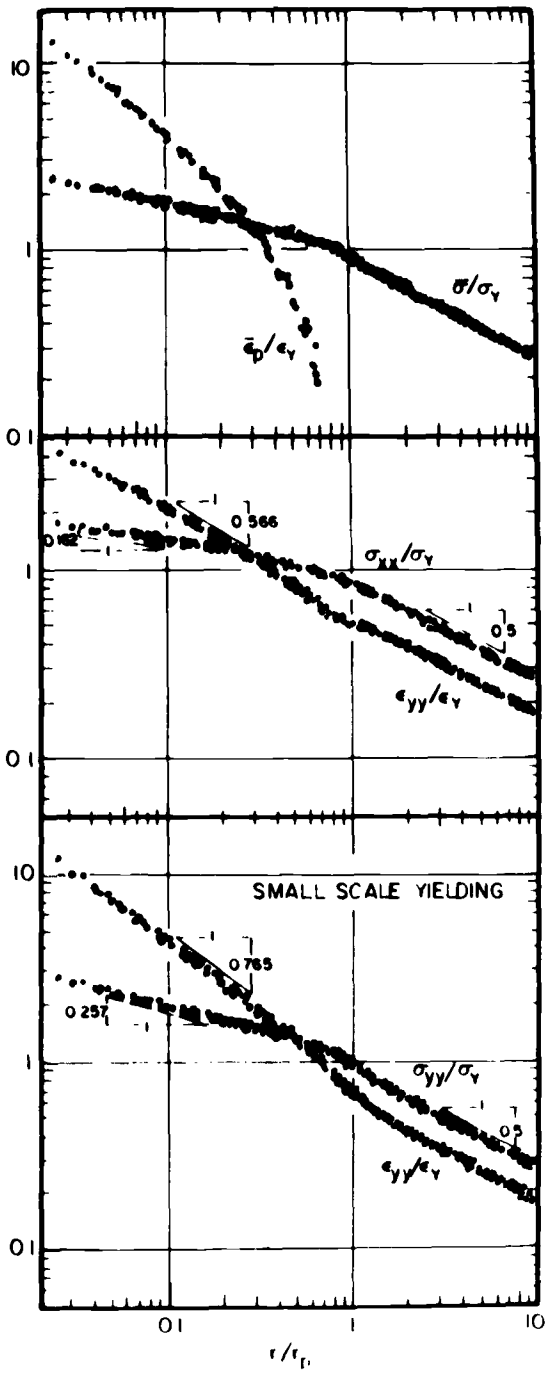

FIG. 6—*Normalized plots of crack line stresses and strains.*

TABLE 1—*Characteristic crack-tip field parameters.*

	N	n	β	β'	γ	$\beta\beta'/\gamma$	$I_n^{(n)}/\tilde{\sigma}_{yy}(0, n)\tilde{\epsilon}_{yy}(0, n)$
Batch B	0.22	4.5	1.35	0.92	0.28	4.4	4.4
Batch C	0.32	3.2	1.41	0.98	0.24	5.7	5.0

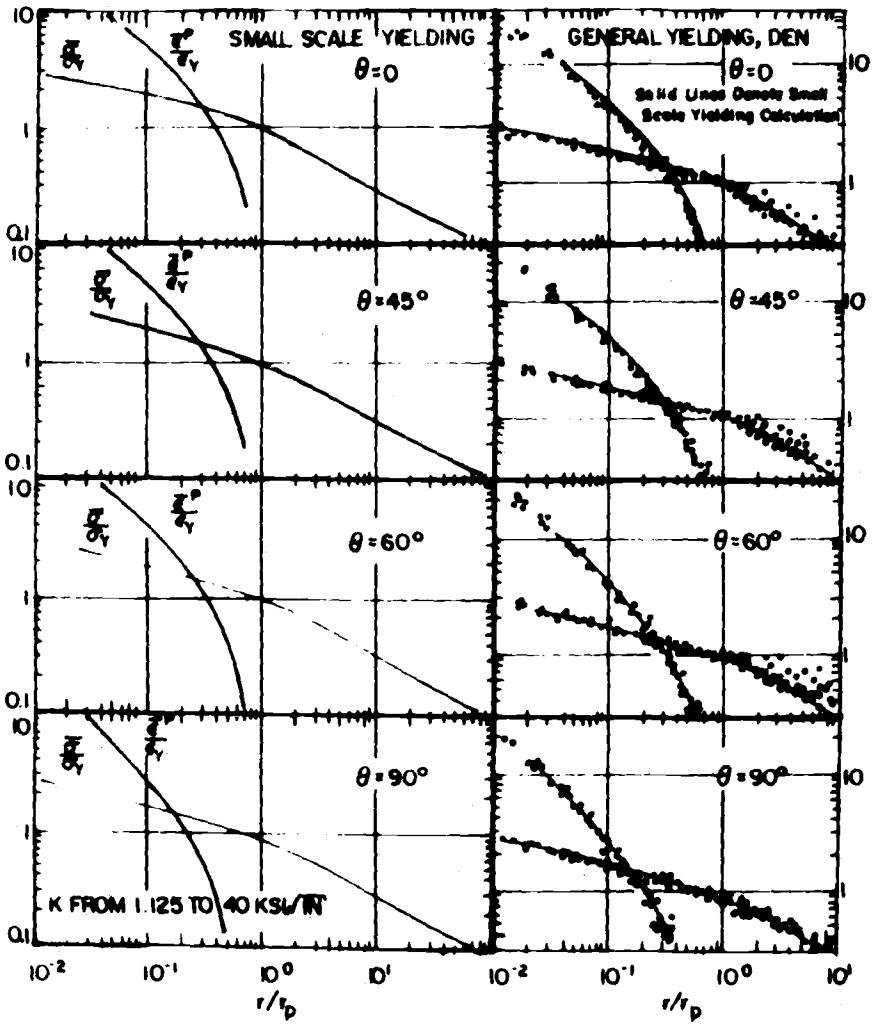

FIG. 7*a*—*Correlations of* $\bar{\sigma}$ *and* $\bar{\epsilon}^p$ *between the small-scale yielding and double-edge-notched specimen loaded in general yielding.*

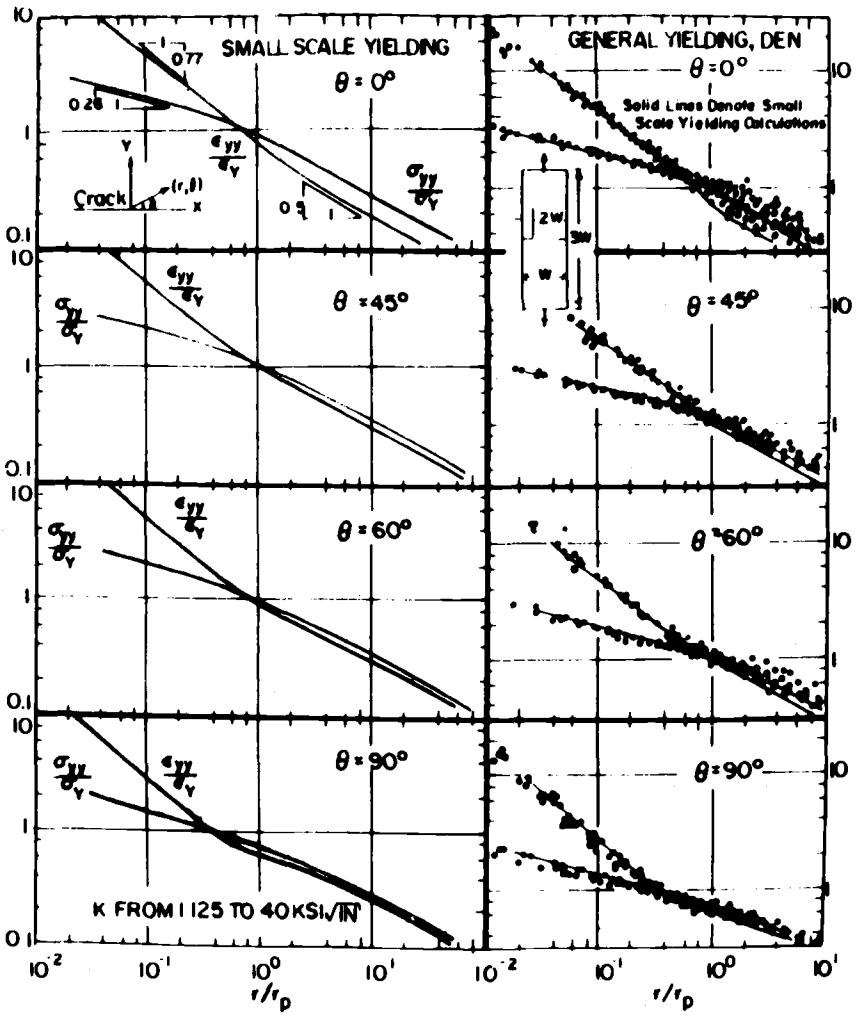

FIG. 7b—*Correlations of σ_{yy} and ϵ_{yy} between the small-scale yielding and double-edge-notched specimen loaded in general yielding.*

tions (solid curves) are also shown. The values of r_p for the specimens in LSY and GY are obtained by the linear extrapolation of effective stress, $\bar{\sigma}$, to yield stress σ_Y in a logarithmic plot of $\bar{\sigma}$ versus r. The solid lines of the SSY coincide with the data of GY. The same scaling factor r_p is applicable to all stress and strain components. Therefore, these stresses and strains can be expressed in terms of a single parameter, r_p. Since r_p is related to K or J in SSY, these stresses and strains can also be written in terms of K or J. In other words, these stresses and strains in LSY and GY are also characterized by K or J. Therefore the values of the K or J of the small specimens in GY can be

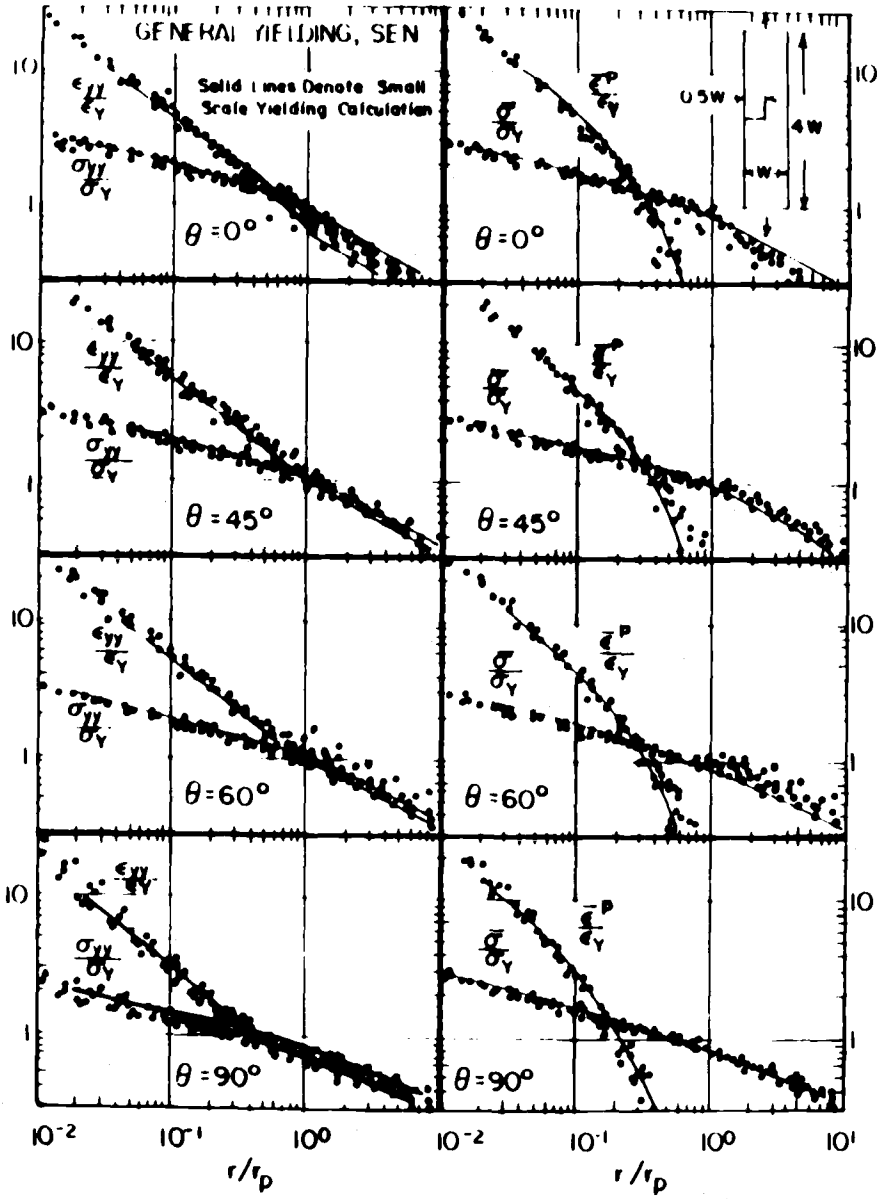

FIG. 8—*Correlations of* σ_{yy}, ϵ_{yy}, $\bar{\sigma}$, *and* $\bar{\epsilon}^p$ *between the small-scale yielding and single-edge-notched specimen loaded into the region of general yielding.*

obtained by the direct correspondence of the crack-tip fields. The values of J have also been evaluated by calculating the contour integral as defined by Rice. The values of the contour integral differ less than 10 percent from the values of J obtained by the method of direct correspondence.

The fact that the data of SSY and GY fall onto the same line means that a crack-tip field in GY does correspond uniquely to a crack-tip field in SSY. Consequently, one will be able to use a small specimen in GY to reach the crack-tip field of a large specimen in SSY at the equivalent K-value. The fracture process is controlled by the crack tip stresses and strains within the stiffened zone, and the crack tip stiffened zone is imbedded within the plane-stress zone. Thus, the stresses and strains within the stiffened zone will be the same if the intensity of the surrounding plane-stress crack-tip field is the same. Or, to state the conclusion more simply, the K or J of the plane-stress crack-tip field characterizes the stresses and strains within the stiffened zone, even though the stresses and strains within the stiffened zone are unknown. Therefore, if a small specimen in GY fractures at a K-value so defined, a very large specimen, made of the same material in SSY, will fracture at the same K-value, because the crack-tip stresses and strains are identical in both specimens. Since crack-tip stresses and strains in the stiffened zone are affected by plate thickness, this conclusion is valied only for specimens of the same thickness.

The near-tip stresses and strains correlate with K or J. In order to use the correlation for convenient fracture toughness measurements, the near-tip field must be related to the applied stress σ_∞ and the imposed elongation Δ. Figure 9 shows the correlation of the product $\sigma_{yy}\,\epsilon_{yy}$ at a certain distance r ahead of a crack tip with the product $\sigma_\infty\Delta$ for the DEN specimen. The product $\sigma_{yy}\,\epsilon_{yy}$ is linearly proportional to J. Therefore, we have

$$\frac{K^2}{E} = J = 13.4\,\sigma_\infty\Delta \qquad \text{(Batch C aluminum)}$$

$$\frac{K^2}{E} = J = 13.7\,\sigma_\infty\Delta \qquad \text{(Batch B aluminum)} \tag{11}$$

These relations can be used to measure the fracture toughnesses of the DEN specimens made of these two materials.

In a cracked elastic solid, an area exists near the crack tip bounded by r_e within which the singular terms of the characteristic crack-tip stress and strain fields are valid approximations. For metallic specimens it can be shown that if the size of $r_e \gg r_p$, K will characterize crack-tip stresses and strains even within r_p [4,5]. The very existence of this conclusion serves as the basis for the empirical determination of the minimum specimen size for valid fracture toughness measurements. The condition of $r_e \gg r_p$ is known as the

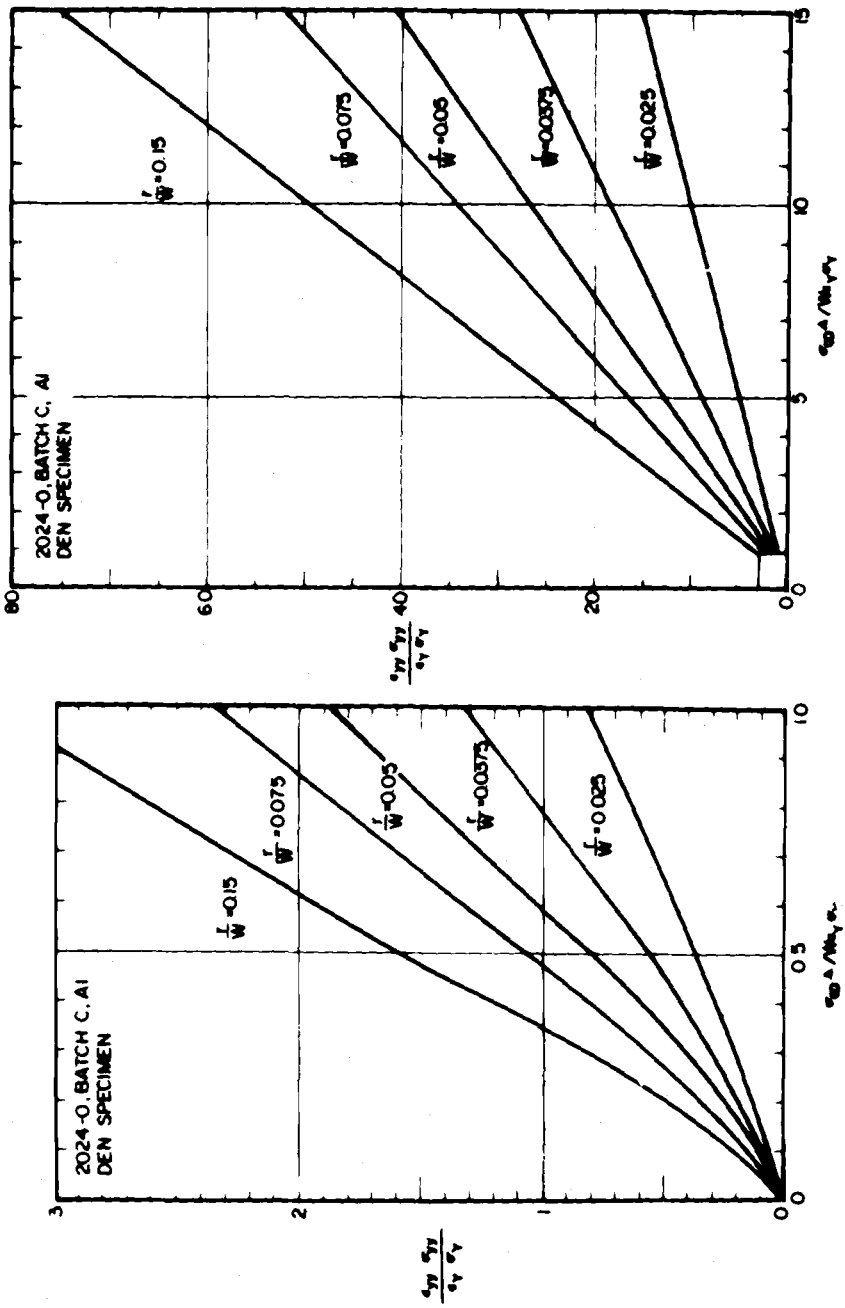

FIG. 9—*Near-field parameter, $\sigma_{yy}\epsilon_{yy}$ versus far-field parameter, $\sigma_\infty\Delta$.*

condition of small-scale yielding. Wilson has found that the size of r_e is quite small [*13*] when compared with other specimen dimensions. However, r_e is linearly proportional to specimen size; so, in principle, the condition of SSY can always be satisfied by using a large enough specimen.

The condition of $r_e \gg r_p$ could be unduly restrictive in terms of specimen size requirements. The condition of $r_e \gg r_p$ is a sufficient condition. The necessary condition for the validity of LEFM is that K would be able to characterize the crack-tip stress or strain component at the location of the defined fracture process.

Figure 10 shows the relation between the applied stress and the equivalent K-value of a DEN specimen, both in LEFM region and in the nonlinear region. The linear elastic solution is capable of characterizing the crack tip field up to $\sigma_\infty/\sigma_Y \simeq 0.6$, which gives a crack line plastic zone size $r_{p(\theta=0)} \simeq$ 6.35 mm (0.254 in.) in comparison with the crack length $a = 20.3$ mm (0.812 in.). In this case, the condition of $r_e \gg r_p$ is obviously more restrictive than necessary.

It can be concluded that the plane-stress crack-tip field of a DEN or SEN specimen in GY correlates well with the crack-tip field in SSY, and that the crack-tip field of a small specimen in GY can be expressed in terms of K or J. The correlation is substantiated by the experimental strain measurements and the measured load-elongation curve as well as by its agreement with the analytical results of Hutchinson and Rice and Rosengren. The characteristic plane-stress crack-tip field is related to the product of the applied stress and the imposed elongation. The relation can be used to measure fracture toughnesses of small specimens in GY. The size of the crack-tip stiffened zone is approximately equal to the plate thickness. In order to use the characteristic plane stress field, the plastic zone perhaps should be more than twice the plate thickness; that is, $0.25\,(K_c/\sigma_Y)^2 \geq 2t$. For a tough material, with $K_c =$ 352 MPa$\sqrt{\text{m}}$ (320 ksi$\sqrt{\text{in.}}$), $\sigma_Y = 552$ MPa (80 ksi), t could be up to 5 cm (2 in.).

Crack-Tip Opening Displacement as a Fracture Criterion

It is well known that a tensile bar necks down, when the applied strain is beyond a certain value. In a power-law material, necking takes place when the applied strain exceeds the strain-hardening exponent. Beyond the point of plasticity instability, the stress in the neck increases while the stress outside of the neck decreases.

When a very large crack-tip plastic zone takes place in a thin plate, a strip necking zone will be formed by the same kind of localized plasticity instability. The well known "strip yielding zone" is not a physical reality. It is a good approximation to the strip necking zone as shown by the moire pattern in Fig. 11. The strip necking zone is imbedded in the "diffused" plastic zone in the thin steel plate. Plastic deformation took place ahead of the strip necking zone forming the diffused plastic zone. As the strip necking zone grew into

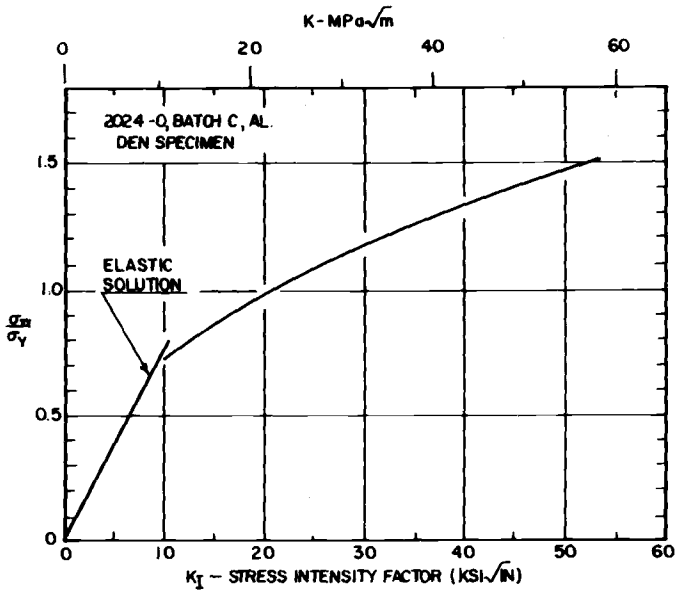

FIG. 10—*Calculated stress-intensity factor at various loading levels.*

the diffused plastic zone, the plastic deformation in the diffused zone, behind the crack tip, remained "constant," and the further plastic deformation is concentrated within the strip necking zone, and the plate thickness is greatly reduced within the strip. A strip necking zone is shown imbedded in a diffused plastic zone in Fig. 12.

Schaeffer et al [*14*] have measured crack opening displacements as well as the relative "opening displacements" between the upper and the lower boundaries of the strip necking zone. Their measurements agree very well with the calculated values according to the Dugdale strip yielding model. The Dugdale strip yielding model will be applicable when the strain and displacement in the strip overshadow the strain and displacement outside of the strip, and when the length of the strip necking zone is several times the thickness of the plate. The length of the strip necking zone, relative to plate thickness, t, is given by the parameter $\eta = (K/\sigma_Y)^2/t$. For the specimens tested by Schaeffer et al, $\eta = 48$. Furthermore, they have found that the crack opening displacements (COD's) within the strip necking zone equal the thickness contraction.

As K increases, and crack grows slowly toward a point ahead of the crack tip, the relative opening displacement at the point in the strip necking zone increases while the thickness is reduced. Once the crack tip passes the point, the plate thickness at the point stops changing. After a specimen is broken, the thickness at a point along the fracture path is the same thickness as when the crack tip first reached the point. The thickness contraction, Δt, at the

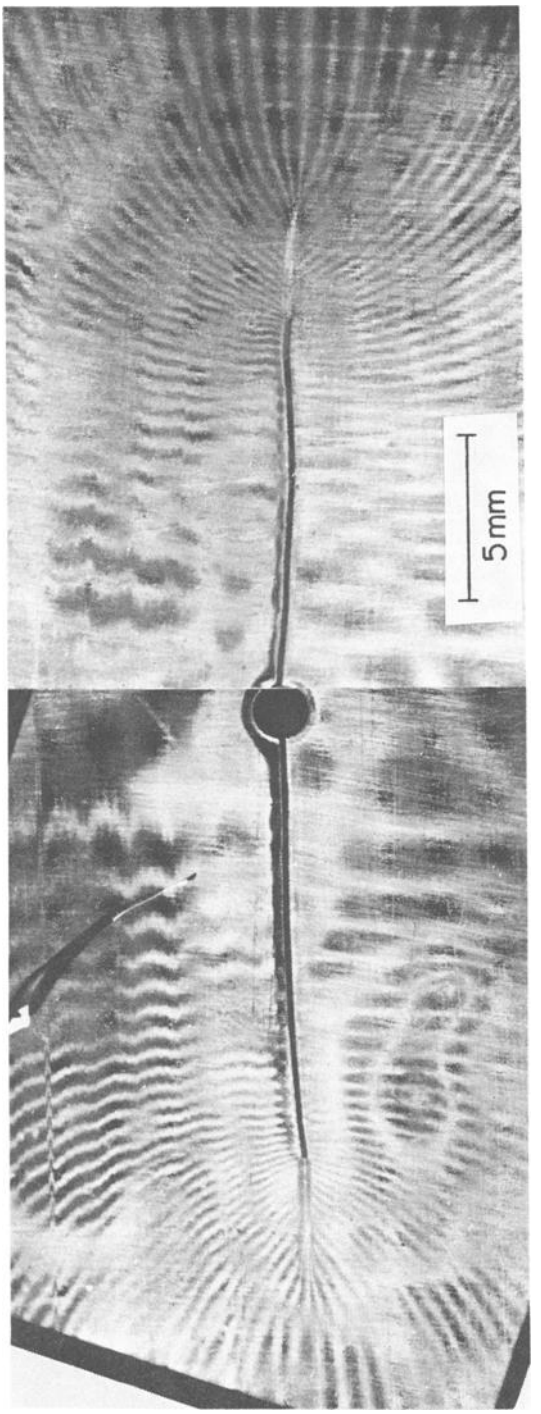

FIG. 11—*Moire pattern of a steel specimen: applied stress 379 MN/m² (55 ksi); 0.2 percent offset yield stress 627 MN/m² (91 ksi); Young's modulus 221 000 MN/m² (32 × 10⁶ psi); 0.3 mm (0.012 in.) thick; 152 mm (6 in.) wide; slot length 25.4 mm (1 in.); pitch of moire grille 1/528 mm (1/13 400 in.)* [14].

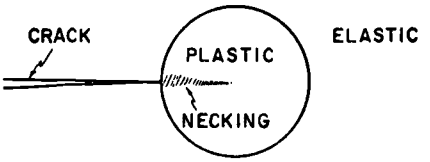

FIG. 12—*Schematic diagram of crack-tip necking.*

point equals the crack tip opening displacement (CTOD), and CTOD is directly related to the applied K. According to the Dugdale model [*15*]

$$\text{CTOD} = K^2/E\sigma_Y \tag{12}$$

for small-scale yielding. Therefore the K-values during stable crack growth can be obtained by plate thickness measurements along the fracture surface of a broken specimen. Indeed, Liu and Kuo [*16*] have measured the fracture resistance curve as well as K_c from thickness measurements in such a manner. The thickness contraction fracture toughness measurements can be used economically for screening tests.

When strip necking takes place, CTOD is the result of the stretch of the materials within the strip necking zone. In this case, the crack-tip opening displacement is a "tangible" physical quantity that can be measured directly.

Experimental observations showed that crack-tip necking began to form at η equal to about 18 [*17*]. For specimens in which η is between 18 and 48, the strip necking zone is not large enough to warrant the use of the thickness contraction as a fracture toughness measurement.

Using the moire method [*17,18*], COD's were measured in specimens made of 2024-0, 2024-T3, and 2024-T351 aluminum alloys with tensile yield strengths, 54, 310, and 383 MN/m^2 (7.8, 45, and 55.5 ksi), respectively. All specimens were 101.6-mm-wide (4.064 in.) center-cracked panels with a nominal crack length of 17.8 mm (0.712 in.). The applied stresses were about one-half the yield strengths for all of the specimens. The density of the moire grille is 528 lines/mm (13 400 lines/in.), and is capable of measuring COD of about 2.5×10^{-4} mm (10^{-5} in.), using the rotational mismatch technique [*19*]. Figure 13 shows the measured COD. The dashed lines are calculated from the Dugdale model and the solid lines from the elastic model. Figure 13*a* shows two specimens at the same K-value. Specimen 1 is much thinner than Specimen 2. The thinner specimen ($\eta = 17.5$) agrees very well with the Dugdale model, and the thicker one ($\eta = 1.12$) agrees with the elastic model. Approaching the crack tip, the difference in COD is more than a factor of two. It is not likely that the crack-tip opening displacement of Specimen 2 will be equal to that given by the Dugdale model. Similar data are

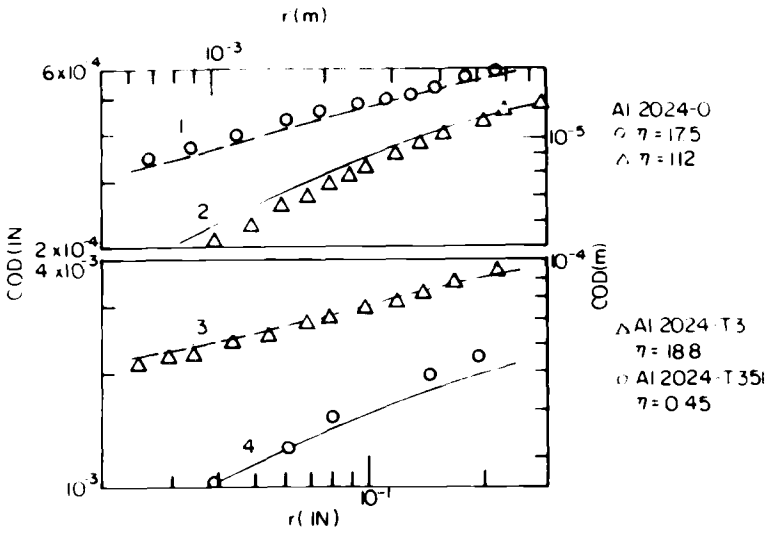

Spec No	Material	σ_Y MN/m^2	K MN/m$^{3/2}$	t mm	η $(K/\sigma_Y)^2/t$	COD Model
1	Al 2024-0	54	4 53	0 41	175	Dugdale
2	Al 2024-0	54	4 53	6 25	1 12	Elastic
3	Al 2024-T3	310	28 2	0 38	188	Dugdale
4	Al2024-T351	386	20 4	6 25	0 45	Elastic

FIG. 13—*Thickness effects on COD. Dashed line = Dugdale model; solid line = elastic model.*

shown in Fig. 13*b*. It can be concluded that when η is close to 18, the measured COD's agree exceedingly well with the Dugdale model. When η is close to one or less, the measured COD's agree well with the elastic calculations. When the COD measurements agree with the Dugdale model, the measured COD can be used to infer a CTOD according to the Dugdale model and the inferred CTOD relates to K by Eq 12. The inferred CTOD characterizes crack-tip deformation and crack-tip stresses. Therefore it is a suitable choice as a fracture criterion. It should be emphasized that no strip necking zone was observed in the thin specimens despite the fact that the COD's in these specimens agreed well with the Dugdale model, which assumes a strip yield zone.

The agreement in COD between the measurements and the Dugdale model was observed for aluminum specimens in small-scale yielding or prior to general yielding. Figure 14 shows the COD measurements in a magnesium specimen by Kobayashi et al [*20*]. All curves are beyond general yielding. The points shown in the figure were calculated in this investigation with the Dugdale model for Curve Mg-1-1Y, which was at the incipience of general yielding. The measurements agree well with the Dugdale model even in the

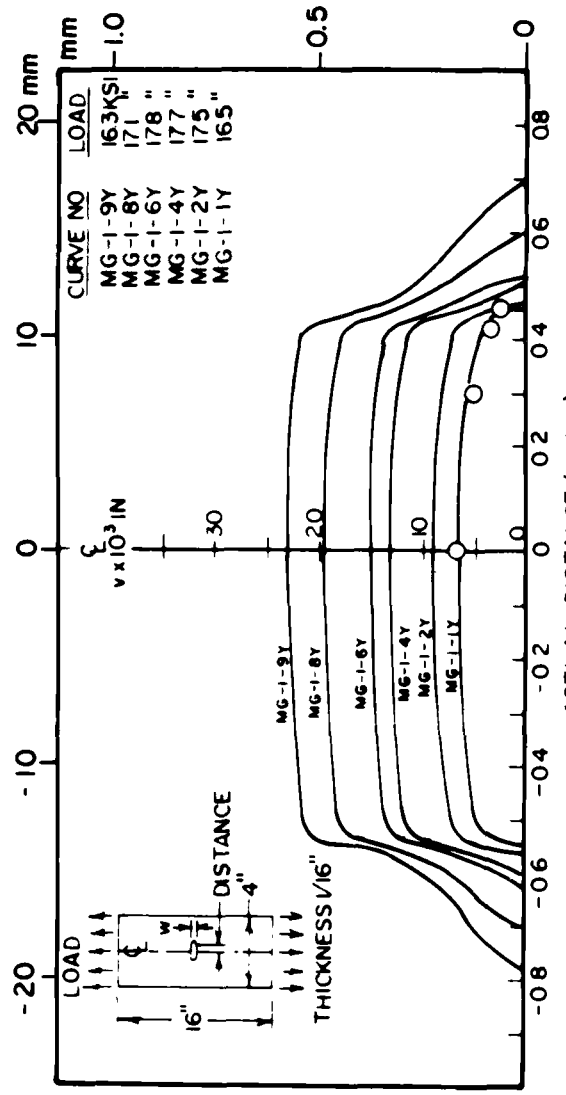

FIG. 14—*COD in magnesium (from Kobayashi et al [20]).*

general yielding condition. The agreement of the measured and the calculated COD both in SSY and in GY supports the Dugdale model for fracture toughness measurements. Figure 14 also shows that crack opening profiles are parallel once beyond general yielding. When the upper and the lower crack surfaces move apart like two rigid surfaces, the area ahead of the crack tip is stretched, and the added stretch gives more opening displacement at the crack tip. During the process of crack-tip opening stretching, the crack profile maintains its original shape, corresponding to that at the incipience of general yielding. Let $\delta\text{COD}(r)$ be the difference between the crack opening displacement at r, $\text{COD}(r)$, and the crack-tip opening displacement at the incipience of general yielding. Once beyond general yielding, the $\delta\text{COD}(r)$ remains unchanged. The total $\text{COD}(r)$ beyond general yielding is the sum of $\delta\text{COD}(r)$ and CTOD, that is

$$\text{COD}(r) = \delta\text{COD}(r) + \text{CTOD}$$

or

$$\text{CTOD} = \text{COD}(r) - \delta\text{COD}(r) \tag{13}$$

$\delta\text{COD}(r)$ can be calculated by the finite-element method. CTOD can be obtained from the measured $\text{COD}(r)$ and the calculated $\delta\text{COD}(r)$. CTOD is related to K by Eq 12.

Equation 13 is applicable to center-cracked panels. For the compact-tension specimens, an additional term should be added to account for the rigid-body rotation about a "plastic hinge." The rotational effects remain to be investigated.

The finite-element method, based on the Dugdale model, can be used to calculate $\delta\text{COD}(r)$ for plates of arbitrary shape. Hayes and William [*21*] have used the finite-element method to calculate COD and CTOD for the central-crack, double-edge-crack, single-edge-crack, and circumferential-crack specimens under various load levels up to general yielding. Basically, the Hayes and Williams method balances the stress-intensity factors contributed from the remote applied stress and the stresses in the strip yielding zone.

Equation 12 has been indiscriminantly used to relate CTOD to K without consideration of the thickness effect. The equation is applicable when $\eta \geq 18$. For specimens of lower η-values, Eq 12 needs to be modified by a parameter which is thickness dependent.

There exist several methods to measure CTOD, such as the load-line mouth opening and plastic hinge method, the linear extrapolation of a crack opening profile from an optical photograph, and rubber infiltration. None of these methods can avoid some degree of arbitrariness, either in the relation between the far-field measurement and the near-tip deformation behavior or in the relation between the measured quantity and the inferred K-value.

Perhaps some of the earlier difficulties in applying CTOD to fracture toughness measurements arise from such arbitrariness. The method and the procedure outlined in this study will help to avoid these difficulties.

Summary and Conclusions

1. The stresses and strains in a cracked solid are in a complicated three-dimensional state. There are three two-dimensional limiting cases: plane strain, plane stress, and the Dugdale strip yielding case. The parameter $\eta = (K/\sigma_Y)^2/t$ determines which one of these three limiting cases is predominant. The characteristic crack-tip fields of these three cases differ vastly.

2. The fracture process is controlled by the stresses and strains at the crack tip. Because of the difference in the characteristics of the crack tip field, there exist various regimes of fracture correlations between a small laboratory specimen in general yielding and a large engineering structure in small-scale yielding.

3. Crack tip strip necking has been observed, when $\eta = 48$. At $\eta = 48$, the measured relative opening displacements between the upper and the lower boundaries of the strip necking zone, including that at the crack tip, agree well with the calculated values according to the Dugdale strip yielding model. Furthermore, the relative opening displacement in the strip necking zone is equal to the thickness contraction. According to the Dugdale model

$$K = (E\sigma_Y \text{CTOD})^{1/2} = (E\sigma_Y \Delta t)^{1/2}$$

where Δt is the thickness contraction.

4. When $\eta = 18$, a crack-tip necking zone begins to form, and the measured crack opening displacements agree extremely well with the calculations based on the Dugdale strip yielding model. Once general yielding is reached, the upper and the lower crack surfaces move apart as two rigid surfaces. The difference between the crack opening displacement at a distance r, CTOD(r), and crack-tip opening displacement, CTOD, remains unchanged once beyond general yielding

$$\delta\text{COD}(r) = \text{COD}(r) - \text{CTOD}$$

δCOD(r) can be calculated by the finite-element method. CTOD can be obtained from the calculated δCOD(r) and the measured COD(r); and CTOD is related to K. Thus for η between 18 and 48, we have

$$K = (E\sigma_Y \text{CTOD})^{1/2}$$

$$= \{E\sigma_Y[\text{COD}(r) - \delta\text{COD}(r)]\}^{1/2}$$

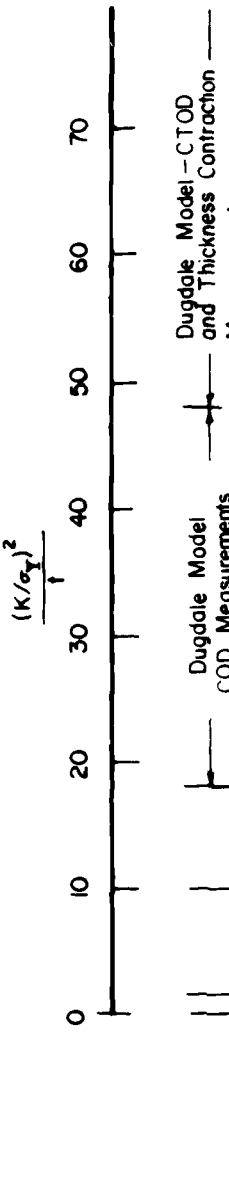

FIG. 15—*Thickness effects on the choice of fracture criteria.*

5. When r_p is several times larger than the plate thickness but it is not large enough to form the crack-tip necking zone, a characteristic plane-stress crack-tip field exists. For double-edge-notched and single-edge-notched specimens, there is a unique correspondence between the crack-tip field in a small specimen in general yielding and the crack-tip field in a very large specimen in small-scale yielding. Therefore the equivalent K-value of such a small specimen in GY can be established. Furthermore, the near-tip stresses and strains are related to the applied stress and the imposed elongation. Therefore the fracture toughnesses of such small specimens can be measured conveniently for η between 10 and 18.

In summary, as shown in Fig. 15, when η is more than 48, thickness contraction can be used to measure K; when η is between 18 and 48, the COD can be used to measure equivalent K; and when η is between 10 and 18, the correspondence between the crack-tip fields in small-scale yielding and in general yielding can be used to measure the fracture toughness of a ductile and tough material. However, the demarcations between the various regions are tentative. Additional studies are needed to establish them firmly.

Acknowledgment

The authors are indebted to Mr. Robert Heyer for his sustained support during the initial period of the research program and for his farsightedness in recognizing the importance of plastic deformation to the development of the nonlinear fracture mechanics. The authors also wish to acknowledge the financial supports by American Iron and Steel Institute (Contract No. 123) and the Army Research Office (Contract No. DAAG-78-G0069) and the assistance in manuscript preparation by Mrs. H. Turner and Mr. R. Ziemer.

References

[1] Griffith, A. A., *Philosophical Transactions of the Royal Society*, London, Series A, Vol. 221, 1921, pp. 163-198.

[2] Irwin, G. R., *Fracturing of Metals*, American Society for Metals, Cleveland, 1948, pp. 147-166.

[3] Orowan, E., *Welding Research Equipment*, Vol. 20, 1955, p. 1575.

[4] Liu, H. W. in *Symposium on Fracture Toughness Testing and its Application, ASTM STP 381*, American Society for Testing and Materials, 1965, pp. 23-26.

[5a] Liu, H. W., *International Journal of Engineering Fracture Mechanics*, Vol. 17, No. 5, 1983, pp. 425-438.

[5b] Liu, H. W., *International Journal of Fracture Mechanics*, Vol. 2, 1966, pp. 393-399.

[6] Dugdale, D. S., *Journal of the Mechanics and Physics of Solids*, Vol. 8, 1960, pp. 100-104.

[7] Gavigan, W. J., Liu, H. W., and Ke, J. S., "Local and Gross Deformation in Cracked Metallic Plates and an Engineering Ductile Fracture Analysis," ASME Paper 71-PVP-52, American Society of Mechanical Engineers, 1971.

[8] Hutchinson, J. W., *Journal of the Mechanics and Physics of Solids*, Vol. 16, 1968, p. 13; see also; Hutchinson, J. W., *Nonlinear Fracture Mechanics*, Technical University of Denmark, 1979.

[9] Rice, J. R. and Rosengren, G. F., *Journal of the Mechanics and Physics of Solids*, Vol. 16, 1968, p. 1.
[10] Hu, W. L. and Liu, H. W. in *Crack and Fracture, ASTM STP 601*, American Society for Testing and Materials, 1976, 522-534.
[11] Hancock, J. W. and Cowling, M. J., *Metal Science*, Aug.-Sept. 1980, pp. 293-304.
[12] Hu, W. L., "A Finite Element Study on Crack Tip Deformation," Ph.D. Dissertation, Solid State Science and Technology, Syracuse University, Syracuse, N.Y., 1976.
[13] Wilson, W. K., Discussion in *Current Status of Plane Strain Crack Toughness Testing of High Strength Metallic Materials, ASTM STP 410*, American Society for Testing and Materials, 1969, p. 75.
[14] Schaeffer, B. J., Liu, H. W., and Ke, J. S., *Experimental Mechanics*, April 1971, pp. 172-175.
[15] Rice, J. R. in *Fatigue Crack Propagation, ASTM STP 415*, American Society for Testing and Materials, 1967, pp. 247-309.
[16] Liu, H. W. and Kuo, A. S., *International Journal of Fracture*, Vol. 14, 1978, pp. R-109-R112.
[17] Kuo, A. S. and Liu, H. W. in *Proceedings*, 23rd Sagamore Army Material Research Conference, Plenum Press, N.Y., 1979, pp. 385-408.
[18] Kuo, A. S., "An Experimental and FEM Study on Crack Opening Displacement and Its Application to Fatigue Crack Growth," Ph.D. Dissertation, Solid State Science and Technology, Syracuse University, Syracuse, N.Y., 1976.
[19] Kuo, A. S. and Liu, H. W. in *Proceedings*, 23rd Sagamore Army Material Research Conference, Plenum Press, N.Y., 1979, pp. 385-408.
[20] Kobayashi, A. S., Engstrom, W. L., and Simon, B. R., *Experimental Mechanics*, April 1969, pp. 163-170.
[21] Hayes, D. J. and Williams, J. G., *International Journal of Fracture Mechanics*, Vol. 8, No. 3, Sept. 1972, pp. 239-256.

Ian Milne[1]

Experimental Validation of Resistance Curve Analysis

REFERENCE: Milne, I., **"Experimental Validation of Resistance Curve Analysis,"** *Elastic-Plastic Fracture: Second Symposium, Volume II—Fracture Resistance Curves and Engineering Applications, ASTM STP 803*, C. F. Shih and J. P. Gudas, Eds., American Society for Testing and Materials, 1983, pp. II-657-II-685.

ABSTRACT: The experimental evidence which supports the existence of stable ductile crack extension in metallic specimens and structures is reviewed and compared with modern failure assessment procedures. The evidence includes data from the following:

1. Materials—two aluminium alloys, mild steel, two nickel-chromium-molybdenum-vanadium forging steels, A533B and A508 pressure vessel steels, a quenched-and-tempered steel, austenitic steels, and HY-130.
2. Geometries—3-point bend specimens of various sizes, compact tension specimens plane and side-grooved, single-edge-notched tension specimens, double-edge-notched tension specimens, center-cracked tension panels, wide plate specimens, pressurized pipe geometries, and pressurized nozzle geometries with the crack located in the crotch corner,
3. Section sizes—thicknesses ranged from 2 to 700 mm in specimen geometries with crack sizes between 0.1 and 0.9 of the section.

It is concluded that for materials with a low to moderate capacity for strain hardening, an adequate engineering assessment can be obtained using a simple form of assessment such as the Central Electricity Generating Board's procedures, R6. However, for materials with a high capacity for strain hardening, total elastic plastic behavior can be predicted only by a procedure which allows for this strain hardening capacity explicitly. Nevertheless, the load capacity of such materials appears to be satisfactorily predicted using a flow stress criterion.

KEY WORDS: ductile crack extension, J_R-curves, ferritic steels, austenitic steels, aluminium alloys, flow stress, strain hardening capacity, load capacity, test specimens, pressure vessels, crotch corners, elastic-plastic fracture

When a structure is failing by ductile cracking mechanisms, the resistance to fracture can, within limits, be represented by the J-integral. When J is expressed as a function of crack extension, over the first few millimetres of crack growth, Δa, it generally increases with Δa. Thus a J-resistance curve or

[1]Research officer, Central Electricity Research Laboratories, Central Electricity Generating Board, Kelvin Avenue, Leatherhead, Surrey, U.K.

J_R-curve is obtained, and under these conditions structures are normally extremely tolerant of crack-life defects.

The procedures which have been developed to evaluate this defect tolerance fall into two distinct groups. The first group attempts as far as possible to evaluate a precise estimate of J applied to the structure and to compare this with the J_R-curve. The critical condition of the structure is then obtained by solving the equations

$$J_{App} = J_R \tag{1a}$$

$$\frac{dJ_{App}}{da} = \frac{dJ_R}{da} \tag{1b}$$

with stability being assured when $dJ_{App}/da < dJ_R/da$. Procedures which fall into this group include any procedure which uses finite-element techniques to evaluate J_{App}; the estimation scheme of Kumar, German, and Shih [*1*][2]; the tearing modulus concept developed by Paris et al [*2*]; and, in the limit of small amounts of crack extension, the instability criterion defined by Turner [*3*]. The second group of procedures can be thought of as using approximate estimates of the applied J to solve Eq 1*a* and 1*b*. These are generally presented in terms of an assessment or design line which is universally applicable to all problems regardless of geometry. Examples of these procedures include the J design line proposed by Turner [*4*] and the Central Electricity Generating Board (CEGB) procedures, colloquially known as R6, proposed by Harrison, Loosemore, Milne, and Dowling [*5*]. The crack-opening displacement design line of Burdekin and Dawes [*6*] also falls into this category, although in this case the resistance criterion is expressed in terms of crack-opening displacement rather than J. All of these procedures have been reviewed by Chell and Milne [*7*].

The following attempts to provide an experimental validation of the basic concepts inherent in any form of resistance curve analysis. This validation will be based upon the R6 procedures after first establishing that for all practical purposes these procedures will give results which are comparable to those obtained from an explicit J analysis. The validation will be carried out in three stages: first by demonstrating the validity of the R6 assessment diagram using data obtained from specimen test geometries, second by discussing the influence of geometry on the results, and third by using the procedures to predict load-crack extension behavior in pressurized structures. The materials involved in this study fall into two categories: those, like ferritic steels and some aluminium alloys, with a moderate capacity for strain hardening, and those with a high capacity for strain hardening, like austenitic stainless steels. These two classes of material will be treated separately.

[2]The italic numbers in brackets refer to the list of references appended to this paper.

Materials with a Moderate Capacity for Strain Hardening

The R6 Diagram and J-Estimates

The R6 procedures differ from a J analysis in three important respects:

1. The explicit use of a plastic collapse load: In a J analysis the plastic collapse load is normally implied from the load at which J increases rapidly.
2. The use of a flow stress criterion to define this plastic collapse load rather than a strain-hardening law.
3. The concept that, for all practical purposes, elastic-plastic effects of any geometry can be represented by a form of the infinite-plate solution of the strip yielding model normalized by the plastic collapse limit of the cracked geometry.

Despite these differences between the R6 procedures and typical methods of estimating J, for materials with a moderate capacity for strain hardening, for example, ferritic steels and some aluminium alloys, it has often been demonstrated that failure assessments made using the R6 approach will be in good agreement with those obtained using a J analysis [*8-11*]. This is demonstrated in Figs. 1*a* to 1*c*, where failure assessments lines derived from J solutions for a number of geometries have been plotted on the R6 axes using the scheme first outlined by Chell [*8*]. Here, if G is the elastic strain energy release rate at the applied load P, and P_1 is the plastic collapse load, the J assessment line is obtained by plotting $\sqrt{G/J}$ against P/P_1.

The J solutions plotted in Figs. 1*a*, 1*b*, and 1*c* were obtained from the following sources

1. Center-cracked panel, Curve 3; three-point bend, Curve 5; single-edged cracked tension, Curve 8; and double-edged cracked tension, Curve 9, were all obtained for plane strain using the J estimation scheme of Kumar et al [*1*] for an A533B steel [*10, 12*]. P_1 was derived from the general equation

$$P_1 = m\bar{\sigma}BW \tag{2}$$

where $\bar{\sigma}$ is the flow stress given by the arithmetic mean of the yield and ultimate tensile stresses, $\frac{1}{2}(\sigma_y + \sigma_u)$, and B and W are the thickness and width of the specimen, respectively. The value of m was chosen to give a plane-strain solution and is given in terms of the crack length, a, as follows [*13*]

Center-cracked panel: $m = 1.15(1 - a/w)$
Three-point bend of span S: $m = 1.456(1 - a/w)^2 W/S$
Single-edged cracked tension: $(1 - a/w) = 1.26(m + m^2)^{1/2} - m$
Double-edged cracked tension: $m = (1 - a/w)\left(1 + \ell n \dfrac{1 - a/2w}{1 - a/w}\right)$

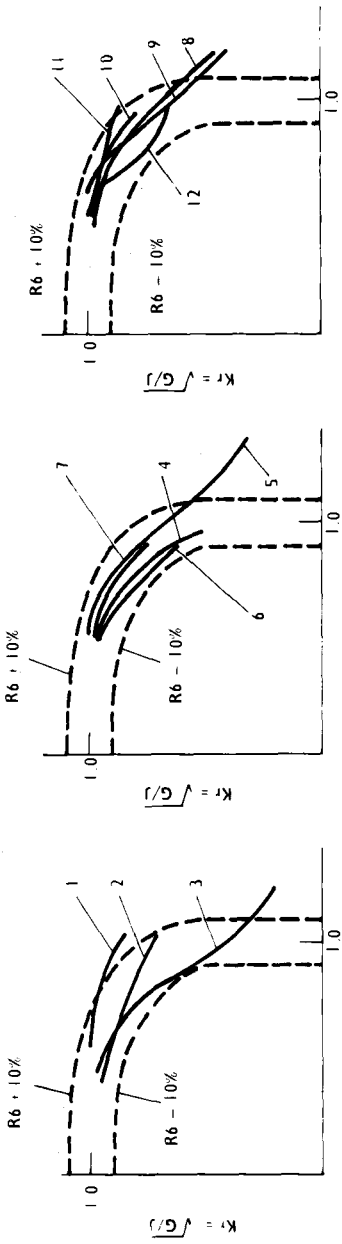

FIG. 1—*Comparison of J-estimates for various geometries with R6 diagram.*

2. Crack close to hole in plate, Curve 12, from Sumpter and Turner [*14*], with P_1 derived from the stress at which J increases rapidly.

3. Penny-shaped crack, Curve 10, from the analytical solution of Keer and Mura [*15*], following Chell [*8*]. This solution was expressed in terms of a reference stress, σ_1, which was taken as the collapse stress.

4. Center-cracked panel, Curves 1 and 2, and the crack from a hole, Curve 11, from Sumpter [*16*]; three-point bend, Curves 6 and 7, from Sumpter and Turner [*14*]; and three-point bend, Curve 4, from Hayes and Turner [*17*] were all plotted following Chell [*8*] with P_1 derived from the load or stress at which J increased rapidly.

Of the twelve J solutions plotted in Figs. 1*a* to 1*c*, two geometries were duplicated, the center-cracked panel with $a/w = 0.5$ and three-point bend with $a/w = 0.5$ (Curves 1 and 3 and 4 and 5, respectively). The J solutions for each of these geometries were obtained from different sources [*1,16,17*] but were nominally for the same material. There is clearly a considerable variation in the different J estimates for a given geometry, a factor that has been previously exposed by the round-robin exercises coordinated by Wilson and Osias [*18*] and Larsson [*19*]. These variations demonstrate an incompatibility between different J-estimates to a degree that makes them unreliable except where they have been fully validated experimentally or where rigorous external checks are applied [*7*].

The dashed lines plotted in Figs. 1*a*–1*c* have been drawn corresponding to loads 10 percent above and below the load required to define the R6 assessment line. Since in general the twelve J solutions fall within the dashed lines, the loads derived using the R6 procedures will be within 10 percent of the loads derived using these particular J solutions. Thus allowing for possible inaccuracies in the J-estimates and for the uncertainties in material properties which will be far in excess of ± 10 percent, it is clear that the R6 procedures will give as good an approximation to a J analysis as is normally needed for any real problem.

Principles of R6 Resistance Curve Analysis

When using the R6 procedures, it is necessary only to evaluate two basic parameters, S_r and K_r. For a resistance curve analysis, these parameters are evaluated as a function of postulated crack extension, Δa, under the appropriate loading conditions [*20*].

For example, under a constant applied load P

$$S_r(\Delta a) = \frac{P}{P_1(\Delta a)}$$

where P_1 is the plastic collapse load defined formerly. The parameter K_r can be defined in terms of stress-intensity factors or J as

$$K_r = \frac{K_1(\Delta a)}{K_\Omega(\Delta a)} = \sqrt{\frac{G(\Delta a)}{J_R(\Delta a)}}$$

where K_1 is the applied stress-intensity factor at load P and crack size a, $a + \Delta a$, etc., and $K_\Omega(\Delta a)$ is the resistance toughness derived from the J_R-curve. Assessment points with coordinates (S_r, K_r) are then plotted as a function of Δa, the locus of which typically has a form shown in Fig. 2. The load required to raise each point on this locus to the assessment line defines the load required to produce the relevant crack extension.

In the example shown in Fig. 2, the locus at P is well within the stable region of the diagram, so that at this load the structure would be stable. By raising the load to P^1 the crack is on the point of growing, but the structure is still stable because the locus at P^1 falls within the stable part of the diagram. Increasing the load to P^2 causes the crack to grow to a_2, the structure again remaining stable. On application of P^3 the locus becomes tangential to the assessment line at a-crack length of a_3. This is the graphical solution to Eq 1 in terms of R6 [*21*] and defines the load tolerance of the structure.

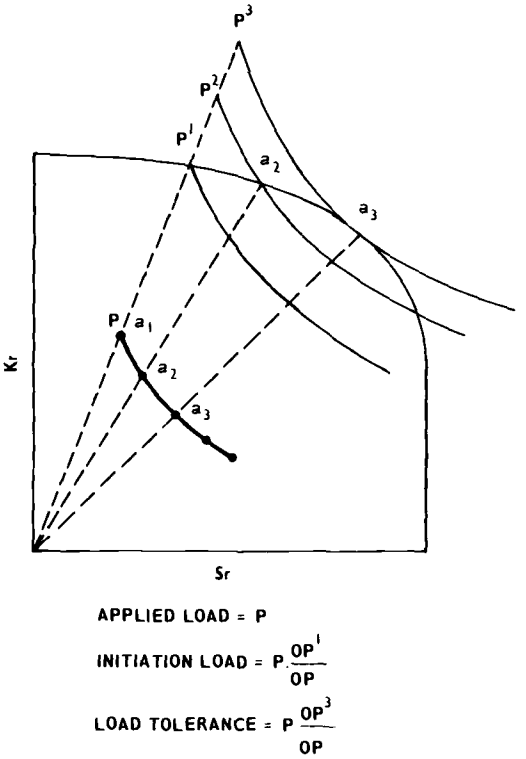

FIG. 2—*Principles of resistance curve analysis using R6.*

The parameters S_r and K_r are linear in applied load so that the graphical solution can be performed by simply scaling the load linearly up the appropriate radius. Alternatively, this scaling factor, F, can be evaluated analytically from the equation [*21*]

$$F = \frac{2}{\pi S_r} \cos^{-1} \exp - \frac{\pi^2}{8} \frac{S_r^2}{K_r^2} \tag{3}$$

The maximum load is defined where F is a maximum and is given by the product of $P \cdot F_{max}$. Note that this equation can be used only for a mechanically loaded structure where all load paths go through the origin. In the presence of residual or thermal stresses, F must be evaluated graphically or by iteration to separate the effects of the residual or thermal stresses from the mechanical stresses [*22*].

Validation Using Test Specimen Geometries

In the first paper which developed the method of performing a growth analysis [*20*] an attempt was made to predict the maximum loads obtained from a number of three-point bend and compact tension specimen (CTS) tests for a variety of steels using as far as possible the J_R data developed from each set of specimens. Since these J_R data were obtained using the Merkle-Corten or some similar form of equations, good agreement between the predicted and measured maximum loads would indicate that the R6 procedure was a satisfactory approximation to these equations. In fact, as can be seen from Table 1, the predicted maximum loads were generally within 10 or 15 percent of those measured, although for one three-point bend specimen the prediction was as much as 20 percent low. At the time, this seemed to be a satisfactory level of agreement especially since, in the original data, some of the initial crack sizes had not been precisely listed. Errors of 1 mm in crack size can have a large effect on the plastic collapse loads predicted for 12.7-mm-thick bend specimens, and it was in a specimen of this type that the 20 percent discrepancy occurred. It was noted that in all cases the maximum load was close to the plastic collapse load, so that accurate assessments of the plastic collapse loads were necessary. This was demonstrated by Bloom [*23*] when he improved the accuracy of the predictions for the four-inch (101.6 mm) side-grooved compact tension specimens of A533B by using more exact plastic collapse solutions for this geometry.

For the two nickel-chromium-molybdenum-vanadium (NiCrMoV) steels, and the A533B steel listed in Table 1, a second set of predictions was also made [*20*] using a J_R-curve drawn as a linear lower bound to the experimental J_R for these steels. These results were almost identical to those obtained using the specific test specimen data, suggesting that the fine detail of the J_R-curve is not very important in determining maximum loads. This conclusion was substantiated by the predictions for the quenched-and-tempered low-alloy steel,

TABLE 1—*Comparison of measured maximum loads with maximum loads predicted using R6 [20].*

Steel	Geometry dimensions in mm	Maximum Loads, kN	
		Measured	Predicted
Quenched-and-tempered low alloy	3-point bend $B = 10$ $W = 40$	30	27.5
Quenched-and-tempered low alloy	3-point bend $B = 40$ $W = 82$	153	150
Quenched-and-tempered low alloy	3-point bend $B = 6$ $W = 12$	4.55	4.8
A533B	CTS (side-grooved) $B = 100$ $a = 118$	650	610
A533B	CTS (side-grooved) $B = 100$ $a = 162$	135	116
NiCrMoV rotor steel	3-point bend $B = W = 12.7$	4.3	4.0
NiCrMoV rotor steel	3-point bend $B = 12.7$ $W = 25.4$	16	12.5
NiCrMoV rotor steel	CTS $B = 25.4$	60	51.3
NiCrMoV (different from above)	3-point bend $B = 12.7$ $W = 25.4$	13.6	13.5

where the J_R data were obtained from only one set of specimens, the 10 by 40-mm three-point bend specimens. These J_R data were successful in predicting the maximum loads not only of the 10 by 40-mm specimens but also of the 6 by 12-mm and 40 by 82-mm specimens to within less than 5 percent, despite there being significant differences in the shapes of the growing crack from one geometry to another.

For Bloom's analysis [*23*], J_R data from the specific specimen of interest were used to predict not only maximum loads, but total load crack extension behavior in the four-inch (101.6 mm) side-grooved specimens of A533B tested by Shih, de Lorenzi, and Andrews [*24*], two plane-sided compact tension specimens of HY-130, and a number of compact tension specimens of the aluminium alloy 2075-T651 included in the ASTM Task Group E24.06.02 predictive round-robin exercise on fracture [*25*]. Bloom succeeded in predicting the load-crack extension behavior of all of these specimens to within very small errors using the R6 procedures. It was noticeable, however, that the accuracy of the predictions beyond maximum load was reduced with increasing crack extension and as the strain hardening capacity of the material

increased. The maximum loads predicted by Bloom are plotted against the measured maximum loads in Fig. 3.

Also included in Fig. 3 are results for a second aluminium alloy, 2024-T3, using the experimental data of Schwalbe and Setz [*26*] and analyzed at the Central Electricity Research Laboratories (CERL). These specimens were 2-mm-thick center-cracked panels whose width W varied from 30 to 300 mm with crack sizes varying from 0.1 to 0.9 of the widths. For these specimens, the collapse loads were defined by Eq 2 with $m = (1 - a/w)$, as the rather thin section was expected to deform in plane stress. Using this form of collapse solution, with $\bar{\sigma} = \frac{1}{2}(\sigma_y + \sigma_u)$, the maximum loads were predicted to be uniformly 5 or 6 percent below the measured maximum loads. However, using $\bar{\sigma} = \sigma_u$, the predicted maximum loads were a much closer match to the measured ones, and occurred over the correct crack-growth interval. These results are plotted in Fig. 3. The prediction of the correct crack-growth interval is highly important, since the crack extension at maximum load varied

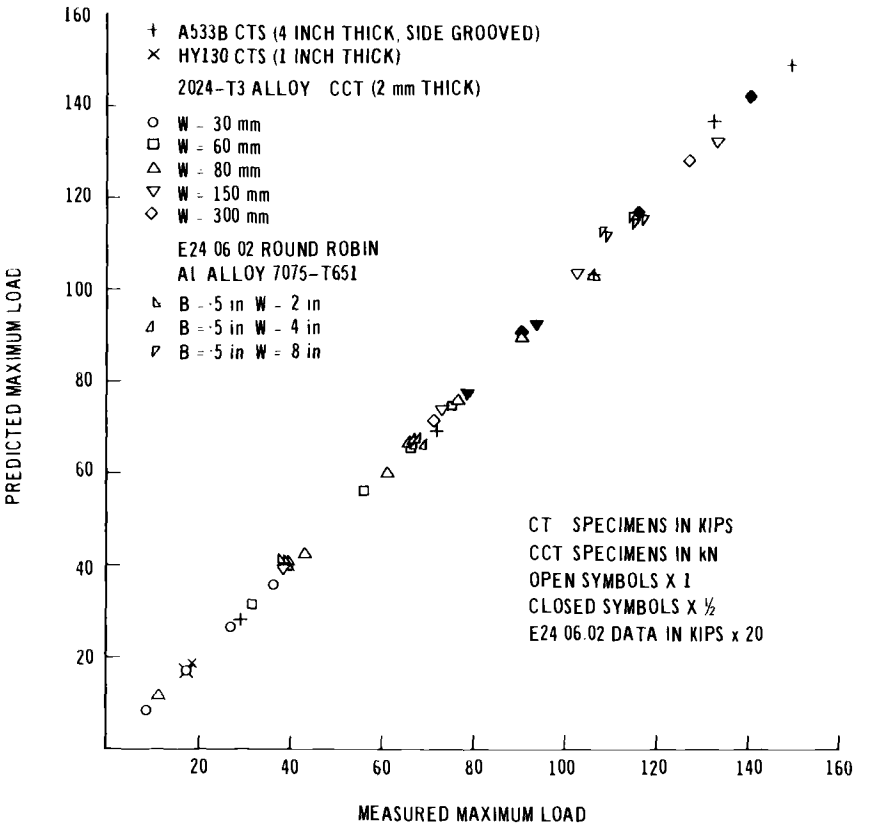

FIG. 3—*Comparison of measured maximum loads with those predicted using R6.*

from 0.527 to 27.15 mm depending on the specimen. The values of S_r at maximum load varied from 0.65 to 0.81, indicating that all the load maxima occurred in the elastic-plastic regime, so this was an excellent test of the validity of the R6 interpolation formula.

There are three possible reasons as to why the plastic collapse expression for these specimens needed to be evaluated using $\bar{\sigma} = \sigma_u$ rather than $\frac{1}{2}(\sigma_y + \sigma_u)$:

1. The R6 curve may underestimate the J solutions appropriate for this geometry and material.
2. The material may have deformed in plane strain rather than in plane stress.
3. The material may have deformed as expected, in plane stress, but the specimens behaved like simple tension specimens so that the "flow stress" became σ_u.

Reason 2 is highly unlikely since the specimens were only 2 mm thick. Reason 1 is a possibility, the 5 or 6 percent difference between the predictions using $\bar{\sigma}$ and σ_u being well within the band of uncertainty obtained by superimposing all the J solutions plotted in Figs. 1*a*-1*c*. Indeed, in Fig. 1*a*, of the three J assessment lines derived for center-cracked panels, Curves 1 and 3 were both for $a/w = 0.5$ but from two different sources. The lower of these, Curve 3, would result in maximum load predictions some 10 percent below the measured maximum loads using $\bar{\sigma}$ to define the collapse load, while the upper one, Curve 1, would produce almost exact agreement. So, since both these curves were derived for a similar material with a modest capacity for strain hardening, this would suggest that these J solutions cannot be considered to be particularly exact either. The most likely explanation for this result, however, lies in Reason 3. The tensile data would have been obtained from flat tension specimens which modeled exactly the thickness and state of strain of the cracked specimens. Thus the collapse stress for the tension specimen (σ_u) would be a good measure of the stress level which governs collapse in the cracked specimens.

It is worth noting that the crack sizes evaluated in this series of tests varied from 0.1 to 0.9 of the specimen widths [*26*], yet the results were all predictable to a high level of accuracy. This conflicts somewhat with what would be expected using the J estimates of Shih et al [*1*]. For this geometry, and also for the single-edged cracked tension geometry, these solutions show a systematic crack size dependence [*11*] when plotted on the R6 diagram, which in some circumstances implies that for shorter cracks R6 may be unconservative. The experimental results showed no such systematic dependence on crack size.

These results therefore demonstrate three things relevant to the analyses of structures made of material with a moderate capacity for strain hardening. First, the simplistic interpolation formula used in R6 provides a realistic basis for performing an elastic-plastic analysis for a wide variety of geometries,

and is consistent with the numerical, analytical, and experimental methods of estimating J for these geometries. Second, good precision can be obtained if the plastic collapse loads are accurately known. Third, there is no significant systematic effect of crack length on elastic-plastic behavior, other than that described by conventional plastic collapse expressions.

Application to Structures

In the foregoing section the R6 procedures were applied to test specimen geometries using J_R data generated from the specific test specimen geometry of interest. This did little but confirm the general applicability of the R6 assessment line to the geometries evaluated. In performing an analysis of an engineering structure, J_R data obtained from simple test specimens must be applied to more complicated structural geometries. This raises several questions concerning the effects of geometry on J_R, and assumptions involved in postulating changes in crack size (and possibly shape) in the structure. These questions will be addressed in this section by applying J_R data obtained from standard fracture toughness test specimens, compact tension specimens, and three-point bend specimens to predict maximum loads in other geometric configurations.

Uniaxially Loaded Structures

Krageloh, Issler, and Zirn [*27*] tested four specimens cut from a thick plate of A533B steel: a 50-mm-thick compact tension specimen, a 200-mm-thick compact tension specimen, a 700-mm-thick single-edged-notched tension specimen, and a 560-mm-thick double-edged notched tension specimen. J_R-curves were produced from the compact tension geometries, and these fell on the same curve with 3 mm of growth for the 50-mm specimen and up to about 10 mm of growth for the 200-mm specimen (Issler, private communication). These J_R-curves were used to produce the loci, plotted at the maximum load measured, in Fig. 4. An exact prediction would be obtained if each locus was tengential to the assessment line. The load necessary to make each of these loci tangential to the assessment line has been evaluated, and is listed in Table 2 to compare with the measured maximum loads. Each of these specimens has been reanalyzed at CERL using the plastic collapse formulas following Eq 2, and these new predictions have also been included in Table 2. There are minor differences between the two sets of predictions, no doubt reflecting different solutions used to evaluate the stress-intensity factors, as well as different plastic collapse solutions, but the results are in general compatible and in reasonable agreement with the measured values.

It is particularly interesting to see how these predictions vary with the assumptions used in the analysis. For example, for the double-edged-notched tension test specimen, Krageloh et al [*27*] used a plane-strain collapse solu-

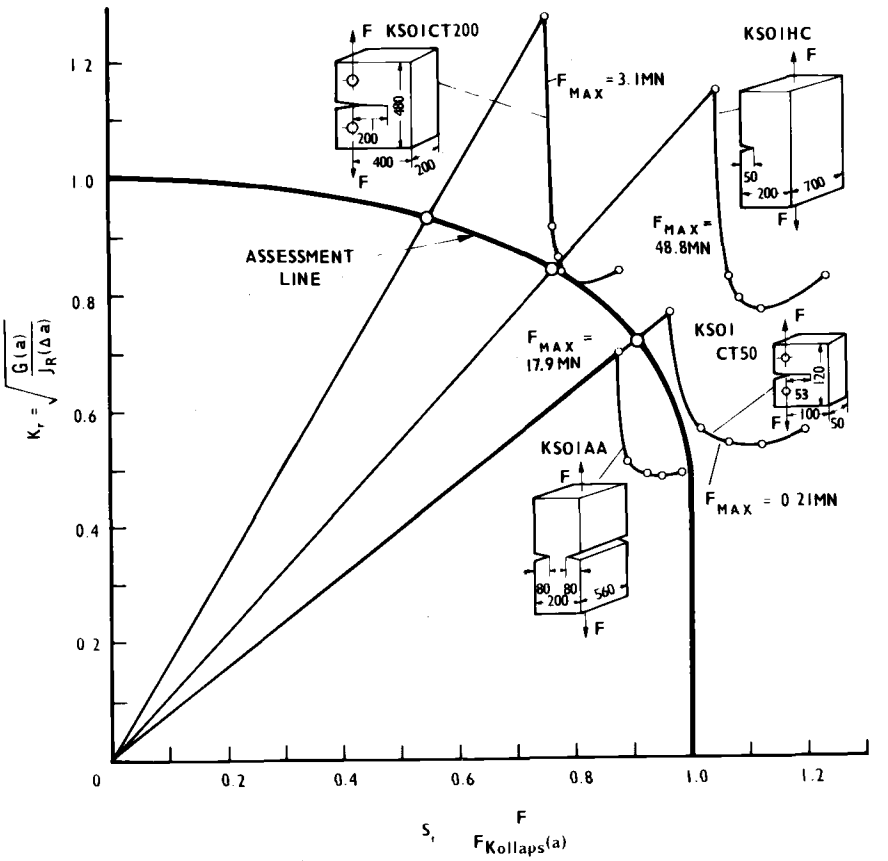

FIG. 4—*Growth loci plotted at maximum loads, F_{max}, for the geometries indicated (after Ref 27). Exact predictions are obtained when these curves are tangential to the assessment line.*

TABLE 2—*Comparison of measured and predicted maximum loads using the data of Krageloh et al [27].*

Specimen	Max Load Measured, MN	Maximum Load Predicted, kN	
		Krageloh et al [27]	CERL
DENT KS01AA	17.9	19.87	20.82 using $\bar{\sigma}$ 17.98 using σ_y
SENT KS01HC	48.8	42	44.35
CT200 KS01CT200	3.1	3.1	3.05
CT50 KS01CT50	0.21	0.206	0.221

tion similar to that defined for Eq 2. It was demonstrated, however, that the plastic collapse load was better defined by using the yield stress in this equation rather than the flow stress. This is probably because of the very high constraint in this deep double-edged-notched specimen limiting the development of plasticity and inhibiting strain hardening. The yield stress produced a very accurate prediction of the maximum load in the CERL analysis.

The large single-edged-notched tension specimen exhibited another anomaly. This is manifested in the predictions in Table 2 which suggest that R6 provides a very conservative estimate of the load capacity of this specimen. It has been reported, however, that this specimen behaved more as if it were loaded in a constrained manner than if it were pin-loaded. Alternative analyses have been performed [*11,28*] assuming the specimen to be one half of a center-cracked panel, and these produced much better agreement using either the R6 procedure or the J estimation scheme [*1*]. It is unlikely, however, that this is the total explanation for the underestimate. Plasticity is relatively unconstrained in the single-edged-notched tension specimen, making conditions for J controlled growth difficult to achieve [*29*]. The J_R data obtained from a compact tension specimen, in conditions of J controlled growth, will tend to underestimate the resistance to fracture in a tensile geometry, and lead to underestimates of the load capacity.

Clearly, as for the thin center-cracked tensile panels of aluminium alloy, these specimens of A533B did not deform precisely as expected and this was reflected in the results. No doubt this is partly because tensile data are normally obtained from round-bar specimens, and are expected to be applicable to considerably different geometries. This is admissable only if the plastic collapse solutions have been generated to take this into account, so inevitably the results will depend upon how well these factors are matched. In general, however, these results do present evidence that J_R data obtained from deeply cracked compact tension specimens is successful in predicting or underpredicting the load tolerance of other geometric configurations, with crack sizes of between 0.25 and 0.8 of the specimen width, even when the criteria for J controlled growth are violated. Again the results for the single-edged cracked tension specimen indicate that there is little in the elastic-plastic behavior of short cracked specimens which cannot be accommodated via the crack size dependence of the plastic collapse solutions.

The foregoing examples were one-dimensional in the sense that the cracks were full through-thickness cracks, the crack fronts were mainly straight, and they did not change shape significantly as they extended. Because of this the J_R-curves obtained from the small compact tension specimens were directly applicable. More generally, cracks will only partially penetrate the section and crack extension will have to be considered as two-dimensional. Garwood demonstrated this in a wide-plate tension test containing a semi-elliptical surface flaw [*30*]. The patterns of crack growth are shown schematically in Fig. 5. Initial growth was entirely through the thickness, crack extension

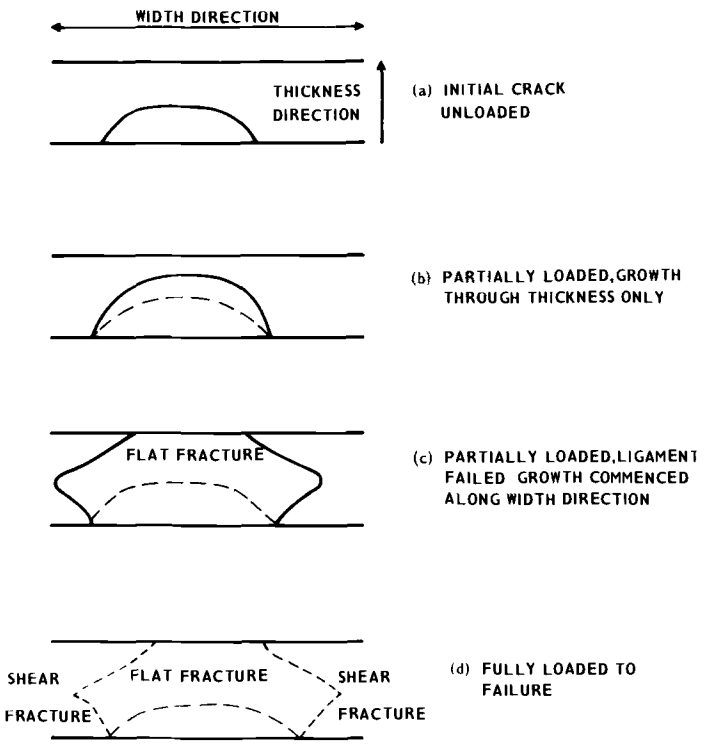

FIG. 5—*Stages of growth of semi-elliptical crack in an end-loaded wide-plate test.*

along the surface in the width direction being held up by plane-stress effects and shear-lip development. Once the crack had fully penetrated the ligament, it was free to extend along the width, but it did so in the tunneling fashion characteristic of thin-section behavior, despite the fact that the plate was 110 mm thick. Similar patterns of growth have been observed from semi-elliptical surface cracks in pressurized cylinders [*31*]. In extreme cases in pressurized cylinders, crack extension along the surface is so difficult that once the ligament has been severed the subsequent instability has caused the cracked area of the pipe to butterfly open via circumferential cracks rather than to unzip along the axial direction [*32*]. Two-dimensional patterns of crack growth make the analysis more complicated since not only should the J_R-curve used in the analysis reflect the loading configuration, but it should also take account of the changing shape of the crack.

Fortunately there are several features about the preferred pattern of growth of a surface crack, in what is predominantly a tensile stress field, which favor a pessimistic assessment. First, the initial retardation of crack growth in the surface regions results from plane-stress deformation and unconstrained plasticity. This tends to increase the J_R local to the surface and to cause shear

lips. Second, the changing aspect ratio of the crack as it grows through the thickness causes a progressive reduction in the crack driving force calibration factor and hence a higher load to maintain the crack driving force. This means that crack growth of this type is intrinsically stable. Third, since these geometries are loaded predominantly in tension, the J_R-curves obtained from bend or compact tension specimens will tend to underestimate that for the structure. This latter point was indeed observed by Garwood [*30*] for the particular A533B specimens involved. When these three features are combined with the conventional concept of J_R expressed in terms of increases in crack length, any analysis which assumes that the crack grows with a uniform shape will be pessimistic.

Pressurized Containers

Although a large number of pressure vessels have been tested to failure, the material properties necessary for a resistance curve analysis have in general not been classified to the extent needed. Nevertheless the general features experienced by a pressure vessel as it fails by ductile cracking have been known for some time and are identical to those obtained in uniaxially loaded tests. For example, Fearnehough et al [*33*] monitored the extension of through-thickness axial cracks in thin-walled pressurized pipes, demonstrating that although the pressure to initiate cracking was low, the instability pressure was close to the plastic-collapse pressure evaluated at the final crack length. This is demonstrated in Fig. 6*a*. In Fig. 6*b* the results are presented of a resistance curve analysis using the R6 procedures and as far as possible the test data of Fearnehough et al [*33*]. J_R data for the material are unknown, so the sensitivity of the predictions to two different J_R-curves was assessed

1. $J_R = 65 + 72\Delta a$
2. $J_R = 65 + 288\Delta a$

where J_R is in kNm^{-1} and Δa is in mm. Both sets of predictions were reasonably close to the observations of Fearnehough et al [*33*] despite one J_R-curve having four times the slope of the other. Note that the assumed level of J_{Ic} is rather low by the standards of present-day pressure vessel steels. However, it did compare with J_{Ic} derived from the crack-tip opening displacements that were measured at the initiation of cracking in the vessels, and the material was a carbon-manganese steel made in the 1960's, presumably of a quality which is lower than A533B steel. It is clear from this that quite large differences in J_R data have only a small effect on the predicted load capacity of the structure. This point was demonstrated by Chell and Milne [*21*] when analyzing part thickness defects in pressurized pipes.

In the Heavy Section Steel Technology (HSST) intermediate vessel program, three tests are of particular interest. The first of these, V7, involved pressurizing a vessel containing a deep crack in its wall. This test was analyzed

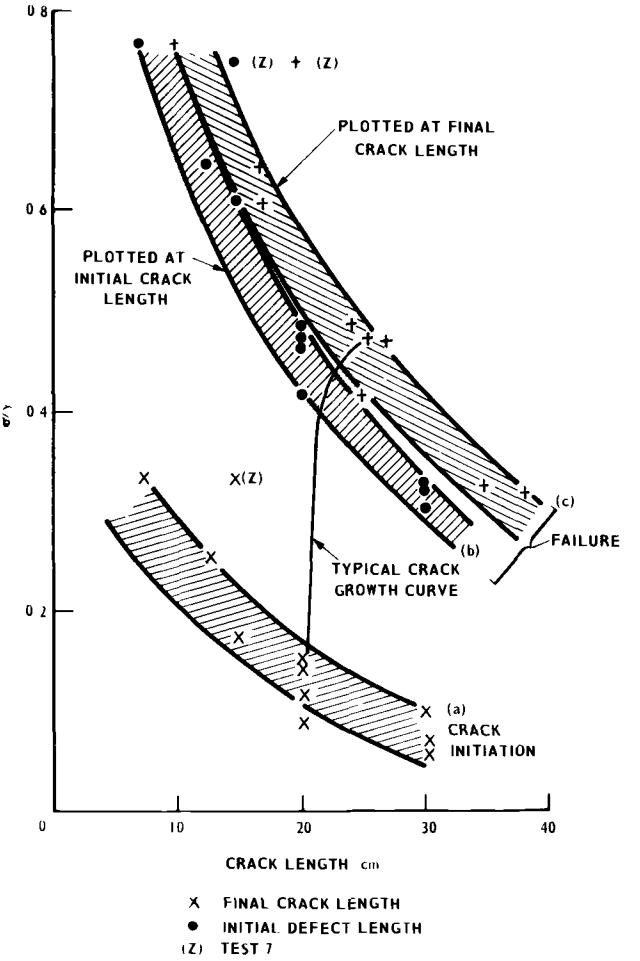

FIG. 6a—*Results of pipe burst tests showing effect of defect length and crack growth on failure (Ref 33).*

by Zahoor et al [*34*] using the tearing modulus version of resistance curve analyses [*2*]. Although the resistance curve data had to be obtained from test work on A533B unrelated to the test vessel, it was possible to demonstrate why the crack growth was stable at the pressures applied.

Vessels V5 and V9 are of more interest since these contained relatively shallow cracks in the crotch corner of nozzles which had been welded into the vessels. Details of the geometries and test data have been described by Merkle [*35*], although as for V7 appropriate J_R data are unavailable. Nevertheless, in the Appendix a resistance curve analysis is performed on each of these vessels for three different assumed J_R-curves.

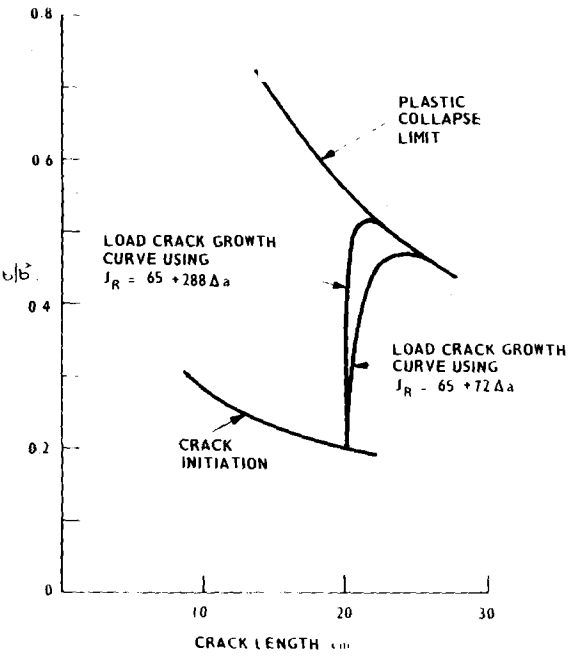

FIG. 6*b*—*Prediction of pipe burst test behavior.*

Vessel V5 was tested at 88°C. This vessel failed by leakage. In Fig. 7 three pressure crack extension curves are plotted for this vessel, as predicted from the analysis in the Appendix. As for the pressurized pipes analyzed in Figs. 6*a* and 6*b*, all three curves demonstrate crack initiation at a low pressure, and final failure at a pressure close to the collapse pressure at the final crack length. The pressures predicted for crack initiation and failure are listed in Table 3, where it is shown that they compare favorably with the measured pressures for these events. Again, it is clear that the detail of the J_R-curve has little influence on the maximum predicted pressure.

Vessel V9 was tested at 24°C. This vessel failed by cleavage after 12.7 mm of ductile crack growth. When structures are loaded in the ductile-brittle transition temperature regime, the extent of ductile cracking prior to cleavage can be allowed for using the scheme outline by Milne and Curry [*36*]. Using this scheme, the maximum pressures for this vessel could be predicted. These are listed in Table 4, along with the predicted initiation pressure, and again they compare favorably with the measured pressures for these events.

It must be admitted, of course, that the predictions obtained for these pressurized geometries were obtained using J_R data which were not related to the test vessels in any precise way. Although this is an undoubted weakness in the analyses, the facts that the assumed J_R data are representative of the materials involved and that the maximum load predictions are relatively insensi-

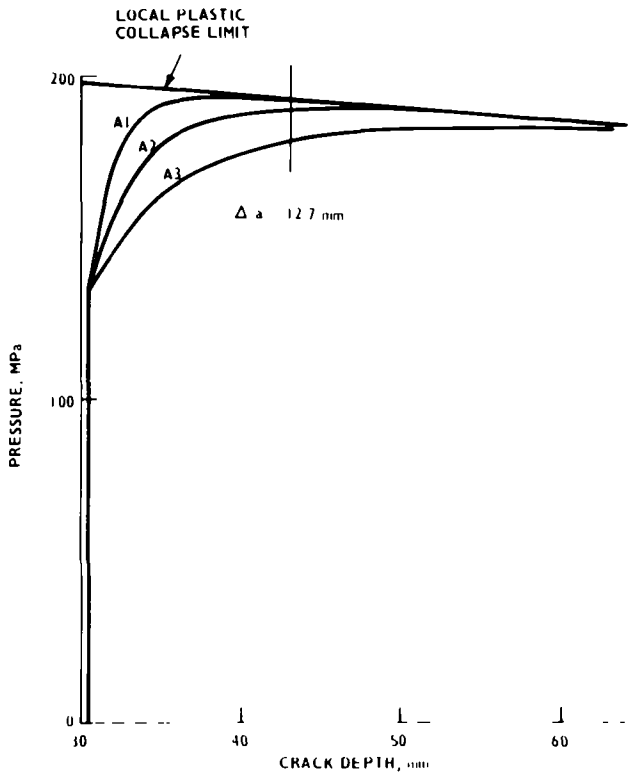

FIG. 7—*Pressure-crack size curves for HSST vessel V5.*

TABLE 3—*Comparison of measured and predicted data for HSST vessel V5 [35,37,45].*

	Measured Pressure, MPa	Predicted Pressure, MPa		
		J_R (Eq 4)	J_R (Eq 5)	J_R (Eq 6)
Crack initiation	124	134	134	134
Leakage	183	193	190	184

tive to large changes in the J_R data mean that the analyses are on the whole satisfactory [*37*]. It is therefore reasonable to claim that these results do support the basic assumption that J_R data obtained from test specimen geometries can be used to predict the load capacities of structural geometries.

Materials with a High Capacity for Strain Hardening

For these materials the effects of the high strain hardening capacity cannot be adequately represented by a simple flow stress model [*9,10*]. To cater for

TABLE 4—*Comparison of measured and predicted data for HSST Vessel V9 [35-37,45].*

	Measured Pressure, MPa	Predicted Pressure, MPa		
		J_R (Eq 4)	J_R (Eq 5)	J_R (Eq 6)
Crack initiation	145	134	134	134
Failure	185	193	189	180

such situations a strain-hardening modification to the R6 assessment line was developed [*10*]. The single R6 assessment line is replaced by a series of empirical assessment lines which depend upon the ratio of the ultimate to the yield stress, Fig. 8, according to the equations

$$S_r = \frac{\sigma}{\sigma_y} + (1 - K_r^{1/2})\left(\frac{\sigma_u}{\sigma_y} - 1\right)$$

$$K_r = \frac{\sigma}{\sigma_y}\left\{\frac{8}{\pi^2} \ln \sec \frac{\pi}{2}\frac{\sigma}{\sigma_y}\right\}^{-1/2}$$

where σ is the applied stress.

To perform an assessment, K_r and S_r are evaluated in the normal way, but S_r is referred to σ_y rather than $\bar{\sigma}$, and the assessment points are judged by reference to the particular assessment line defined by the appropriate ratio of σ_u/σ_y. It has been demonstrated that for $\sigma_u/\sigma_y \gtrsim 1.5$ an analysis performed

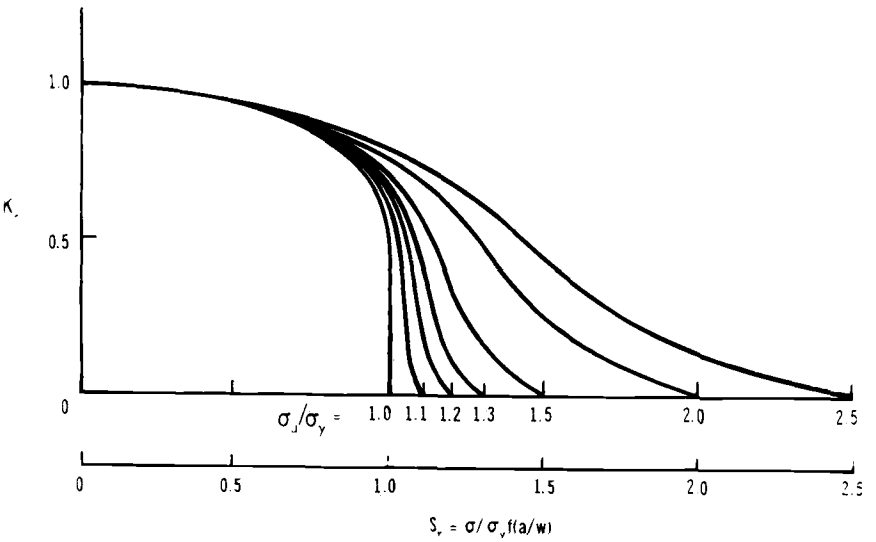

FIG. 8—*The R6 strain-hardening assessment diagram proposed by Milne [10].*

using this diagram will produce a result within a few percent of that obtained using the conventional R6 diagram [*10*]. Consequently this form of the diagram is only of practical value for materials with a high capacity for strain hardening, especially austenitic steels.

Again, as for the pressure vessel tests, most of the data available in the literature are unsuitable for experimental validation of these curves. This problem arises because of the nature of austenitic steel itself: It is a very tough steel with a high resistance to cracking, it is generally used in sections less than 50 mm thick, and it has a high capacity for strain hardening. Because of this, cracking is seldom extensive before maximum loads have been achieved and at this point the stress in the material remote from the crack has more often than not exceeded yield. As a result the plasticity measured at the loading points contains a component which is unrelated to the cracking mechanism, causing an overestimation of the J_R-curve. Thus for austenitic materials, J_R-curves can be considered reliable only if the load displacement data are corrected for effects due to plasticity remote from the crack, or alternatively by using deeply cracked specimens so that the stress level in the uncracked body is always below yield.

In the ASTM E24 predictive round-robin exercise [*25*] values of load and load-line displacements were tabulated for three compact tension specimens of 304 austenitic steel. The J_R data were also presented, but there were linear with crack growth and passed through the origin. They were clearly unreliable, suffering from some of the problems indicated in the preceding paragraph. Crack sizes were also tabulated as a function of load. From these tables, load-load line displacement curves were generated, one of which is shown in Fig. 9 along with its load-crack size curve. This shows that the crack did not grow until the maximum load had been reached.

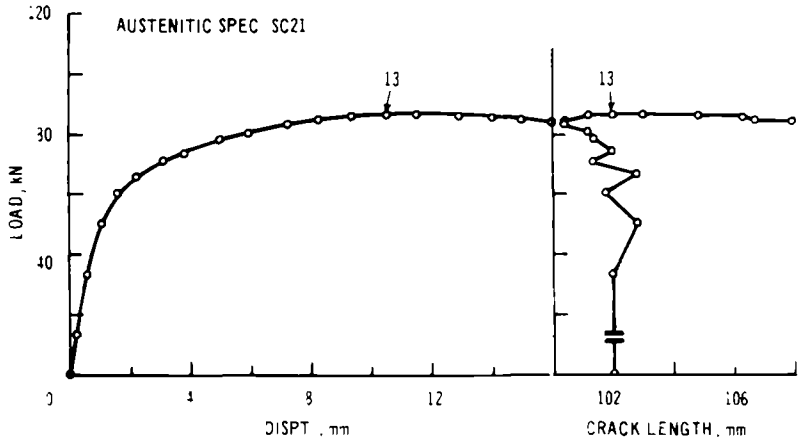

FIG. 9—*Load-load line displacement and load crack length curves for Specimen SC21, following Newman [25].*

The ratio $K_r = \sqrt{G/J}$ was calculated from these load-displacement curves as a function of applied load, P. S_r was calculated as the ratio of P/P_y, where P_y is given by Eq 2 with $\bar{\sigma} = \sigma_y$, and $m^2 + 2m(1 + a/w) = (1 - a/w)^2$, the plane-stress (Tresca) solution [*13*]. The resulting coordinates are shown plotted in Fig. 10 and compared with the assessment line derived for the appropriate ratio of σ_u/σ_y, 2.4. The elastic-plastic behavior of all three specimens analyzed is well represented by the assessment line shown.

It should be emphasized that the data plotted in Fig. 10 are mainly pre-maximum load data, and that little if any crack growth had occurred prior to this in any of the specimens. The data for SC21 and SC81 fell close together and mainly below the line, while the data for SC83 fell predominantly above the line. Although all three specimens were 12.7 mm thick, SC83 was only 50.8 mm wide. The other two specimens were twice and four times this width. Because of these differences in the shape of the crack plane, the deformation pattern in SC83 would be closer to plane strain than the other two, and this is consistent with their relative positions along the S_r-axis.

For some other specimens of this steel, Newman [*25*] listed maximum load data but not the complete load displacement data. If it is assumed that, as for the three specimens analyzed earlier, the crack extension prior to maximum load is insignificant, the maximum loads of these specimens should be predictable from the collapse loads evaluated at the original crack length.

Collapse loads were evaluated for all these specimens using first the foregoing plane-stress solution and second the plane-strain solution given by Ref *13*: $(1 - a/w) = 1.26(2m + m^2)^{1/2} - m$, with $\bar{\sigma} = \frac{1}{2}(\sigma_y + \sigma_u)$. The results are listed in Table 5 and compared with the experimental maximum loads. Clearly reasonable agreement (to within 5 percent) is obtained if it is assumed that, as was concluded from the data plotted in Fig. 10, the 203.2-mm-wide specimens deformed in plane stress, the 50.8-mm-wide specimens deformed

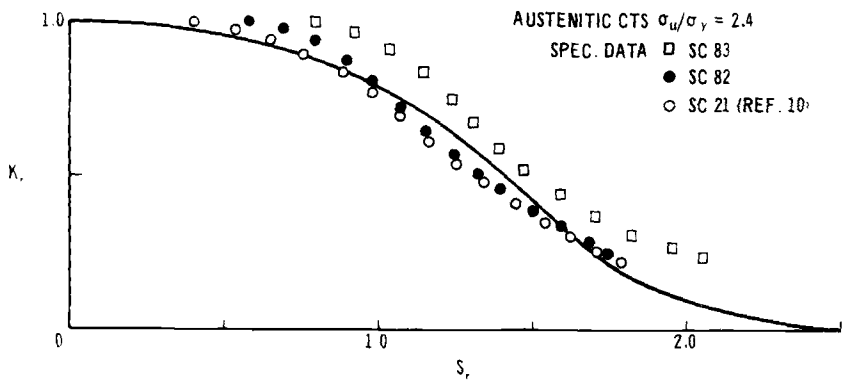

FIG. 10—*Comparison of R6 strain-hardening diagram with test data from austenitic specimens, following Newman [25].*

TABLE 5—*Comparison of maximum loads measured on CT specimens of 304 austenitic steel [25] with predicted plastic collapse loads.*

Specimen	W, mm	Maximum Loads, kN		
		Measured	Predicted Plane Strain	Predicted Plane Stress
SC23	50.8	27.3	32.0	23.0
53	50.8	25.9	30.6	22.1
83	50.8	26.8	31.7	22.7
73	50.8	27.5	32.2	23.1
33	50.8	26.9	31.0	22.4
SC22	101.6	55.1	70.9	50.8
52	101.6	50.8	67.4	48.5
82	101.6	47.8	65.1	46.8
32	101.6	51.8	67.3	49.0
72	101.6	50.62	64.6	46.5
SC21	203.2	86.8	130.1	92.9
51	203.2	85.4	129.4	93.2
81	203.2	85.3	130.4	93.1
31	203.2	96.3	139.2	100.1
71	203.2	96.1	135.4	97.5

in plane strain, and the 101.6-mm-wide specimens deformed some way between plane strain and plane stress. It therefore appears that although some form of strain-hardening solution is necessary to describe the total elastic-plastic behavior of these specimens of austenitic steel, the flow stress criterion is all that is required to describe the maximum loads.

Other experimental data on austenitic steels have been presented by Kanninen et al [*38*] on 8-mm and 25-mm-thick three-point bend specimens and 8-mm-thick center-cracked tension specimens. Although J_R data were obtained from the three-point bend specimens, the outer fiber stress in these specimens exceeded yield, so again J_R is likely to be overestimated. Nevertheless, load-crack extension curves were produced for the center-cracked panels which were similar in form to those shown in Figs. 5*a*, 5*b*, and 7. In these cases the maximum loads were slightly greater than the plastic collapse loads evaluated from $\frac{1}{2}(\sigma_y + \sigma_u)$ at the final crack size, but not by a large extent.

Discussion

The range of materials covered herein include two aluminium alloys, mild steel, two NiCrMoV forging steels, A533B pressure vessel steel, A508 forging steel, austenitic steels, a quenched-and-tempered steel, and HY130. The geometries tested included small three-point bend specimens, compact tension specimens, single-edged-notched tension specimens, double-edged-notched specimens, center-cracked panels, wide plate specimens, pressurized pipe

geometries, and pressurized nozzle geometries with the crack located in the nozzle crotch corner. The section size used in the tests ranged from 2-mm-thick panels to 700-mm-thick single-edge-notched specimens and included a 230-mm-thick section across the crotch corner of a pressure vessel with crack depths ranging from 0.1 to 0.9 of the width of the section. In all of the cases considered, there was no indication that either the resistance curve concept or the R6 procedures used for the analysis were inapplicable.

There are, however, two points which should be emphasized. The first is that for all practical purposes, most structures will fail at their plastic collapse limit when loaded mechanically in the temperature regime where cracks grow by ductile mechanisms. This plastic collapse limit must be considered in terms of the load-bearing ligament in the vicinity of the flaw. For precise predictions, an accurate measure of the plastic collapse limit is needed. This is an area where further work is required not only to develop formal plastic collapse solutions for all conceivable geometries, but also to provide a better indication of what material properties are relevant.

Plastic collapse solutions can be obtained from a number of sources, for example, slip-line field theory, J-estimates, or empirical solutions. In all cases, some judgment has to be made on the choice of material parameters. To date, a flow stress equal to $\frac{1}{2}(\sigma_y + \sigma_u)$ has proved to be adequate for most cases, even for structures made of austenitic steels if maximum loads are all that is required. It should be noted, however, that this choice will depend upon the geometry of the tension specimen and how closely it models the structure being analyzed. These factors should be taken into account by the collapse expression used.

The total elastic-plastic behavior of materials like austenitics can be predicted only using some form of strain-hardening solution. The R6 strain-hardening diagram proposed by Milne [*10*] is just one possibility and has been validated only for compact tension specimens. Other solutions based upon J would naturally be equally applicable. However, if the strain hardening law chosen to evaluate J provides a poor representation of the materials stress-strain curve, the J-estimates can be seriously in error. This important aspect of analyzing austenitic structures is frequently unrecognized but can lead to severe overestimates of J at low stress levels [*7,10*]. A further complication arises in deciding whether to use plane-strain or plane-stress solutions. There are no clear-cut rules to follow, since the stress state depends not only upon thickness but also upon the width of the uncracked ligament. Plane-stress solutions will of course tend to err on the safe side.

All of these problems are magnified when dealing with surface cracks of semi-elliptical shape where load shedding occurs in the uncracked ligament. Because of these complications—which are equally problematical for any other form of elastic-plastic analysis—the most successful form of plastic collapse solution is an empirical one. In cases where such solutions are accurate, the aforementioned procedures have been shown to be very precise in their

predictions. Of course in the absence of detailed plastic collapse formulas, the plastic limit load for any geometry can be easily underestimated, for example, by equating forces over the uncracked ligament to the flow properties of the material. Further pessimism will be generated if the flow stress is chosen to be equal to the yield stress, σ_y. Alternatively, solutions based upon J-estimates could be used, as proposed by Bloom [*11*], with S_r normalized via a reference load rather than a collapse load [*1,7,10*]. For this approach, however, different solutions have to be generated for different geometries. Moreover, the variations between different J solutions for the same geometry are not trivial [*18,19*] and the possible inaccuracies resulting from these cannot be neglected.

The second point is that the plastic collapse load is itself determined by the size of the extended crack. This is in turn determined by the original crack size and the crack growth resistance curve. Resistance curves should be generated only from bend-type specimens (three-point bend or compact tension) and care should be taken that the specimens are large enough for the curves to be size-independent. This means that shear lips should be suppressed either by using large specimens, or by side-grooving. In an analysis it is prudent to determine the sensitivity of the results to large changes in the value of the resistance curve. Confidence is increased if it can be shown that the results are relatively insensitive to this [*37*].

There is, of course, always an argument for limiting any analysis to the regime of J-controlled growth. This limit is not required if the physical models for resistance curves [*39-41*] are used as the basis of the analysis rather than rigorous J-theory [*42*]. Use of these limits, however, does not restrict the analysis, but only how far up the load-crack growth locus the rigorous J-theory is applicable. In Fig. 7, Curve A2 uses J_R data from Loss et al [*43*] and these were valid by the J-controlled growth criteria up to 1.5 mm of crack extension, that is, to within about 20 percent of the maximum predicted load. The valid range of these J_R data would be doubled by doubling the specimen size, in which case the predictions would have been valid to within 11 percent of the predicted maximum load. Clearly there is little penalty incurred by restricting the applicability of the analysis to the J-controlled growth regime, provided the data are obtained from large enough specimens.

The behavior of Vessel V9 highlights two further aspects of resistance-curve analysis. First, in the ductile-brittle transition regime, a ductile crack will grow following the J_R-curve to the point where if it extends far enough it will change mode to a cleavage crack. The extent of the ductile crack growth prior to cleavage is determined by the temperature of the material relative to its ductile-brittle transition temperature [*36*]. The ductile-brittle transition temperature is sensitive to metallurgical hardening processes, such as strain aging or irradiation embrittlement. So where there is a risk of hardening during service the degree of hardening and its effect on the ductile-brittle transition temperature should be carefully monitored. Second, despite the fact that the

final failure mode was brittle, and therefore catastrophic, the crack extension prior to the brittle failure required the pressure in the vessel to be raised to the collapse limit.

Conclusions

In this paper a considerable amount of experimental data on ductile crack extension have been analyzed covering a wide variety of materials, geometries, and section sizes. From the results of these analyses the following conclusions can be drawn.

For materials with a low to moderate capacity for strain hardening:

1. The techniques for extending the CEGB's failure assessment procedures beyond the point where ductile cracks initiate provided an adequate engineering assessment of all the geometries investigated to date.
2. Resistance curves obtained from small specimens were successful in predicting the load capacity of large specimens.
3. These resistance curves were also found to be capable of predicting load-crack extension curves for geometries other than the geometry of the specimen, including such structural geometries that occur at a pressure vessel nozzle crotch corner.
4. Large differences in resistance curve detail, for example, a factor of 4 in dJ/da, often produce only small differences in the load capacity of a structure.

For materials with a high capacity for strain hardening:

1. Prediction of total elastic plastic behavior requires a form of assessment procedure which caters explicitly for the strain-hardening capacity.
2. Nevertheless the load capacity of structures of this material appears to be satisfactorily predicted using a flow stress criterion.

Acknowledgments

This work was performed at the Central Electricity Research Laboratories and is published by permission of the Central Electricity Generating Board.

APPENDIX

Analysis of HSST Intermediate Vessel Tests V5 and V9

V5 at 88°C

Details of this vessel are described in Ref *35*, and a complete analysis is presented in Ref *37*.

Crack growth initiated at a pressure of 124 MPa and failure occurred by leakage when the crack had grown across the nozzle-shell intersection. The failure pressure was 183 MPa.

Calculation of S_r—The nozzle was designed by the area replacement method, which prevents gross yielding of the nozzle before gross yielding of the vessel. This led Merkle [*35*] to assume that gross yielding of the nozzle was coincident with gross yielding of the vessel, an assumption which was confirmed by the gages which were positioned to monitor strain at various points in the vessel, including the vessel wall and nozzle crotch corners [*35*]. The equation used by Merkle for gross yielding of a vessel, $P_{GY} = 1.04\ \sigma_y \ln R_o/R_i$ where R_o and R_i are the outer and inner radius of the vessel, respectively, gave a value of $P_{GY} = 182$ MPa for the yield stress assumed by Merkle [*35*]. This value is below the failure pressure, so for the present calculation the value was raised by 10 percent to cover the difference between flow stress and yield stress. This value of P_{GY} is of course appropriate for general yield of an uncracked nozzle. However, S_r must be evaluated by reference to the local plastic collapse load of the cracked nozzle. To correct for the presence of the crack, Milne, Loosemore, and Harrison [*44*] suggested reducing the load-bearing area by the factor $(1 - c/w)$ with $c/w = \pi al/4t(l + t)$, where a is the depth of the crack, l its length, and t the thickness of the nozzle corner [*5*]. Hence

$$S_r = \frac{P}{200(1 - c/w)}$$

where P is the applied pressure.

Calculation of K_r—The applied stress-intensity factor was obtained from Fig. 5.31 of Merkle [*45*]. Crack growth resistance data for the A508 steel in question are unavailable, so the data published in Fig. 5 of Loss et al [*43*] were used to derive three idealized J_R-curves to test the sensitivity of the results to the J_R input. The equations derived were

$$J_R(\Delta a) = 220 + 188(\Delta a) \quad (4)$$
$$J_R(\Delta a) = 220 + 94(\Delta a) \quad (5)$$
$$J_R(\Delta a) = 220 + 47(\Delta a) \quad (6)$$

where J_R is expressed in KNm^{-1} and Δa in mm.

Equation 5 is equivalent to the lower of the two curves published in Fig. 5 of Ref *43* for $\Delta a < 1.5$ mm.

The analysis was performed at an applied pressure $P = 138$ MPa as a function of crack extension by incrementing the crack 5.08 mm at a time, from the original crack size, with

$$a_0 = 30.5 \text{ mm}$$
$$l_0 = 61 \text{ mm}$$
$$t = 231.4 \text{ mm}$$
$$P = 138 \text{ MPa}$$

The crack shape was assumed to be constant with increasing Δa. Values of the load factor F were obtained as a function of Δa for each of the J_R equations, using the formula

$$F(\Delta a) = \frac{2}{\pi S_r} \cos^{-1} \exp - \left\{ \frac{\pi^2}{8} \frac{S_r^2}{K_r^2} \right\}$$

TABLE 6—*Analysis for HSST vessel V5*

a, mm	c/w	S_r	K_I, MPa$\sqrt{m}$	J_R (Eq 4)	K_r (Eq 4)	F (Eq 4)	J_R (Eq 5)	K_r (Eq 5)	F (Eq 5)	J_R (Eq 6)	K_r (Eq 6)	F (Eq 6)
30.5	0.022	0.699	200.7	220	0.908	0.973	220	0.908	0.973	220	0.908	0.973
35.5	0.028	0.710	212.7	1160	0.419	1.382	690	0.543	1.299	455	0.669	1.183
40.6	0.036	0.716	222.0	2119	0.323	1.395	1169	0.436	1.365	695	0.565	1.274
45.7	0.044	0.722	231.2	3078	0.279	1.385	1649	0.382	1.374	934	0.507	1.313
50.8	0.053	0.728	239.9	4036	0.253	1.374	2128	0.349	1.369	1174	0.469	1.329
55.9	0.062	0.736	248.7	4995	0.236	1.359	2608	0.327	1.357	1414	0.444	1.329
60.9	0.071	0.743	256.7	5935	0.224	1.346	3078	0.310	1.345	1649	0.424	1.326

The relevant data are listed in Table 6. Pressure crack extension curves were then obtained from the product of $P \cdot F(\Delta a)$ and these are plotted in Fig. 7. Also plotted in this figure is the plastic collapse locus defined by the formula $P_1 = 200(1 - c/w)$.

The maximum predicted pressures depended upon the J_R relationship but they were all close to the measured failure pressure. These are listed in Table 3, together with the relevant initiation pressures.

V9 at 24°C

This vessel behaved in an identical fashion to V5, up to a maximum pressure, coinciding again with general yield of the vessel, of 185 MPa. However, at this pressure a brittle crack initiated. The amount of ductile crack extension which occurred before the brittle fracture was 12.7 mm.

The analysis for this vessel was therefore identical to that for V5, with the J_R-curves being limited by the crack extension required to promote cleavage following the scheme outlined by Milne and Curry [*36*].

Using this scheme, the pressure crack extension curves are identical to those for V5, but are limited to 12.7 mm and this limit has been indicated in Fig. 7. For J_R given by Eq 4, cleavage is predicted after the maximum pressure is reached so for this J_R-curve the maximum pressure is as predicted for V5. For the other two J_R-curves cleavage occurred while the pressure was rising, so the maximum pressures in these cases were lower than for V5. All maximum pressure predictions were comparable to the measured failure pressure, and these together with the initiation pressures are listed in Table 4.

Assumptions

This form of analysis is subject to many uncertainties as a result of the large number of assumptions which are an inevitable feature of any analysis of a real problem. The significance of these assumptions is best evaluated by means of a sensitivity analysis. Such an analysis [*37*] has demonstrated that the two important parameters are the local plastic collapse pressure of the cracked nozzle and the resistance curve data. The first of these determines the failure pressure of the structure and the second the crack extension at failure.

References

[*1*] Kumar, V., German, M. D., and Shih, C. F., "Estimation Technique for the Prediction of Elastic Plastic Fracture of Structural Components of Nuclear Systems," General Electric Report SRD-80-094, Schenectady, N.Y., 1980.

[2] Paris, P. C., Tada, H., Zahoor, A., and Ernst, H. in *Elastic-Plastic Fracture. ASTM STP 668*, J. D. Landes, J. A. Begley, and G. A. Clarke, Eds., American Society for Testing and Materials, 1979, pp. 5-36.
[3] Turner, C. E. in *Fracture Mechanics: Twelfth Conference, ASTM STP 700*, American Society for Testing and Materials, 1980, p. 314.
[4] Turner, C. E. in *Advances in Elasto-Plastic Fracture Mechanics*, L. H. Larsson, Ed., Applied Science, London, 1979, p. 301.
[5] Harrison, R. P., Loosemore, K., Milne, I., and Dowling, A. R., "Assessment of the Integrity of Structures Containing Defects," Revision 2, CEGB Report R/H/R6 Central Electricity Generating Board, Leatherhead, Surrey, U.K., 1980.
[6] Burdekin, F. M. and Dawes, M. G. in *Proceedings*, Conference on Practical Application of Fracture Mechanics of Pressure Vessel Technology, Institution of Mechanical Engineers, London, 1971, p. 28.
[7] Chell, G. G. and Milne, I., this publication, pp. II-179-II-205.
[8] Chell, G. G. in *Elastic-Plastic Fracture, ASTM STP 668*, J. D. Landes, J. A. Begley, and G. A. Clarke, Eds., American Society for Testing and Materials, 1979, p. 581-605.
[9] Bloom, J. M. in *Proceedings*, Electric Power Research Institute Ductile Fracture Meeting, Palo Alto, Calif., Dec. 1980.
[10] Milne, I. "Failure Assessment Diagrams and *J* Estimates: A Comparison for Ferritic and Austenitic Steels," *International Journal of Pressure Vessels and Piping*, Vol. 13, 1983, pp. 107-125.
[11] Bloom, J. M., this publication, pp. II-206-II-238.
[12] Issler, L., Birk, R. and Hund, R. in *Proceedings*, 6MPa Seminar, Stuttgart, 1980, Paper 9.
[13] Haigh, J. R. and Richards, C. E. "Yield Point Loads and Compliance Functions of Fracture Mechanics Specimens," CEGB Report RD/L/M461, Central Electricity Generating Board, Leatherhead, Surrey, U.K., 1974.
[14] Sumpter, J. D. G. and Turner, C. E., *International Journal of Fracture*, Vol. 12, No. 6, 1976, p. 861.
[15] Keer, L. M. and Mura, J. in *Proceedings*, First International Conference on Fracture. T. Yokobori, T. Kawasaki, and J. L. Swedlow, Eds., Japanese Society for Strength and Fracture of Materials, Tokyo, Vol. 1, 1965, p. 99.
[16] Sumpter, J. D. G. "Elastic Plastic Fracture Analysis and Design Using the Finite Element Method," Ph.D. Thesis, Imperial College, London, 1973.
[17] Hayes, D. J. and Turner, C. E., *International Journal of Fracture*, Vol. 10, 1974, p. 17.
[18] Wilson, W. K. and Osias, J. R., *International Journal of Fracture*, Vol. 14, 1978, p. R95.
[19] Larsson, L. H. in *Proceedings*, Sixth International Conference on Structural Mechanics in Reactor Technology, Paris, 1981, Paper G 3/2.
[20] Milne, I., *Materials Science and Engineering*, Vol. 39, 1979, p. 900.
[21] Chell, G. G. and Milne, I. in CSNI Report No. 39, Nuclear Regulatory Commission Report NUREG/CP-0010 1979, p. 376.
[22] Milne, I. in *Proceedings*, Fifth International Conference on Structural Mechanics in Reactor Technology, Berlin, 1979, Paper G 1/3.
[23] Bloom, J. M., *International Journal of Pressure Vessels and Piping*, Vol. 8, 1980, p. 215.
[24] Shih, C. F., deLorenzi, H. G., and Andrews, W. R. in *Elastic-Plastic Fracture, ASTM STP 668*, J. D. Landes, J. A. Begley, and G. A. Clarke, Eds., American Society for Testing and Materials, 1979, pp. 65-120.
[25] Newman, J. C., "Predictive Round Robin on Fracture," ASTM Task Group E24.06.02 on Application of Fracture Analysis Methods, American Society for Testing and Materials, 1979.
[26] Schwalbe, K. H. and Setz, W. in *Proceedings*, Third European Conference on Fracture, Imperial College, London, 1980, p. 277.
[27] Krageloh, E., Issler, L., and Zirn, R. in *Proceedings*, 6MPa Seminar, Stuttgart, 1980, Paper 8A.
[28] Hodulak, L. and Blaunel, J. G., this publication, pp. II-103-II-114.
[29] McMeeking. R. M. and Parks, D. M. in *Elastic-Plastic Fracture, ASTM STP 668*, American Society for Testing and Materials, 1979, pp. 175-194.
[30] Garwood, S. J. in CSNI Report No. 39, NRC Report NUREG/CP-0010, Nuclear Regulatory Commission, 1979, p. 226.

[31] Hellen, R. A. J., Darlaston, B. J. L., and Connors, D. C. in *Proceedings*, Fourth International Conference on Pressure Vessel Technology, Institution of Mechanical Engineers, London, 1980, Paper C21/80.
[32] Sturm, D. and Stoppler, W. in *Proceedings*, 6MPa Seminar, Stuttgart, 1980, Paper 12.
[33] Fearnehough, G. D., Loss, G. M., Lowes, J. M., and Weiner, R. T. in *Proceedings*, Conference on Practical Applications of Fracture Mechanics to Pressure Vessel Technology, Institution of Mechanical Engineers, London, 1971, Paper C33.
[34] Zahoor, A. and Paris, P. C. in CSNI Report No. 39, NRC Report NUREG/CP-0010, Nuclear Regulatory Commission, 1979, p. 477.
[35] Merkle, J. G. in *Elastic-Plastic Fracture. ASTM STP 668*, J. D. Landes, J. A. Begley, and G. A. Clarke, Eds., American Society for Testing and Materials, 1979, pp. 674-702.
[36] Milne, I. and Curry, D. A., this publication, pp. II-278-II-290.
[37] Milne, I. in *Proceedings*, Conference on Fitness for Purpose, Validation of Welded Constructions, The Welding Institute, London, 1981, Paper 35.
[38] Kanninen, M. F., Marschall, C. W., Broek, D., Sampath, S. G., Abou-Sayed, I. S., Wilkowski, G., and Zahoor, A., Battelle Columbus Laboratories Report T-118-2, Ohio, 1980.
[39] Rice, J. R. and Sorensen, E. P., *Journal of the Mechanics and Physics of Solids*, Vol. 26, 1978, p. 163.
[40] Hermann, L. and Rice, J. R. in *Proceedings*, Conference on Micromechanisms of Crack Extension, Cambridge, U.K., 1980, Paper 1.
[41] Curry, D. A. in *International Journal of Fracture*, Vol. 15, 1979, p. R59.
[42] Hutchinson, J. W. and Paris, P. C. in *Elastic-Plastic Fracture. ASTM STP 668*, J. D. Landes, J. A. Begley, and G. A. Clarke, Eds., American Society for Testing and Materials, 1979, pp. 37-64.
[43] Loss, F., Menke, B. H., Gray, R. A., and Hawthorne, J. R. in CSNI Report No. 39, NRC Report NUREG/CP-0010, Nuclear Regulatory Commission, 1979, p. 292.
[44] Milne, I., Loosemore, K., and Harrison, R. P. in *Proceedings*, Conference on Tolerance of Flaws in Pressurized Components, Institution of Mechanical Engineers, London, 1978, Paper C106/78.
[45] Merkle, J. G., Robinson, G. C., Holz, P. P., and Smith, J. E., NRC Report ORNL/NUREG-7, Nuclear Regulatory Commission, 1977.

Cyclic Plasticity Effects and Material Characterization

Mohmed H. El Haddad[1] *and Biswajit Mukherjee*[2]

Elastic-Plastic Fracture Mechanics Analysis of Fatigue Crack Growth

REFERENCE: El Haddad, M. H. and Mukherjee, B., **"Elastic-Plastic Fracture Mechanics Analysis of Fatigue Crack Growth,"** *Elastic-Plastic Fracture: Second Symposium, Volume II—Fracture Resistance Curves and Engineering Applications, ASTM STP 803*, C. F. Shih and J. P. Gudas, Eds., American Society for Testing and Materials, 1983, pp. II-689-II-707.

ABSTRACT: Fatigue crack growth rate data are obtained for ASTM A516 Grade 70 steel subjected to elastic and elastic-plastic cyclic loading for both load-controlled and displacement-controlled test conditions. Cyclic J-integral values estimated from load versus deflection hysteresis loops and crack closure estimates are correlated with growth rate data. The cyclic J-crack growth rate data agree well with that from the linear elastic tests. The J-integral parameter is shown to be better than the linear elastic parameter K in correlating fatigue crack growth, particularly so in ductile materials such as A516 steel and at high load levels.

KEY WORDS: crack propagation, elastic and elastic-plastic fracture mechanics, J-integral, fatigue, elastic-plastic fracture

The stress-intensity parameter, K, is widely used for correlation of fatigue crack growth rates. As the stress-intensity concept is based on linear elastic analysis, its validity is restricted to situations where the size scale of the plasticity that occurs is small compared with the other significant dimensions. However, conditions may exist in which large loads and high temperature lead to extensive crack-tip plasticity. Thus, it is of practical importance to determine the rate of growth of preexisting flaws under such conditions. Hence, an elastic-plastic parameter is needed to account for the effect of plasticity on fatigue crack growth rates. The J-integral parameter appears to be a suitable candidate in this case.

[1]Assistant professor, Structural Engineering Department, Cairo University, Giza, Cairo, Egypt.
[2]Unit head, Fracture Mechanics, Ontario Hydro Research, Toronto, Ont., Canada M8Z 5S4.

A method to determine J for both load-controlled and deflection-controlled fatigue is discussed in this paper. Fatigue crack growth rate data are also obtained for compact tension specimens of A516 Grade 70 steel subjected to elastic and elastic-plastic cyclic loading. The present results are expected to play an important role in simplifying the assumptions to be employed in the elastic-plastic fracture mechanics analysis of complicated cracked components subjected to fatigue loading.

Experimental Details

Materials and Specimens

The material tested is ASTM A516 Grade 70 steel. The chemical, mechanical, and cyclic properties of the material are given in detail in a previous report [*1*][3] and are listed in Table 1. Compact tension (CT) specimens of various thicknesses were machined from two orientations, S-T and T-L, as outlined in Tables 2 and 3. Side grooves were provided for five specimens machined in the S-T orientation to ensure straight crack front shape. These orientations conform with the ASTM Test for Plane-Strain Fracture Toughness of Metallic Materials (E 399-78a). CT specimens were selected for both tension-tension and tension-compression tests since well-established compliance calibration curves are available for this specimen geometry.

Test Procedure

All tests were conducted at room temperature on an MTS testing machine. The clevis and other loading fixtures were modified so that compressive loads could be applied during cycling. Tests were carried out under load control, deflection control, and deflection control to a sloping line. Displacement was measured in all tests at the loading line and for a few tests it was measured across the crack tip to determine crack opening load. Cyclic load displacement loops at the load line were monitored to estimate cyclic J-values. Under load control, elastic-plastic conditions cause the mean deflection to increase with cycling. This behavior is related to cyclic-dependent creep, or ratcheting. Unstable deformation behavior under load control causes the crack growth rate to increase rapidly and high crack growth rate data can be obtained. Under deflection control, the maximum load reduces toward zero and the crack growth rate decreases with cycling. Deflection control to a sloping line tests were achieved automatically by means of a microprocessor. The advantage of this type of test is that it avoids the difficulties associated with simple load and deflection control tests. It also provides variable cyclic load ratios during the same test and it can be employed to obtain constant J tests.

[3]The italic numbers in brackets refer to the list of references appended to this paper.

TABLE 1—*Material properties of A516 Gr70 steel.*

Physical Properties	
yield strength, S_y	315 MPa (45.6 ksi)
tensile strength, S_u	506 MPa (73.3 ksi)
elongation in 5 cm	30%

Chemical Composition

C	Mn	S	P	Si	Cr
0.26	1.02	0.02	0.007	0.22	0.12

Cyclic Stress-Strain Curve Constants

$$\Delta\epsilon/2 = \frac{\Delta\sigma}{2E} + \left(\frac{\Delta\sigma}{2A}\right)^{1/S}$$

Room Temperature

MULTIPLE-SPECIMEN TESTS

	Cycle 2	Cycle 10	Half Life	Before Load Drop
S	0.26	0.23	0.236	0.22
A, MPa (ksi)	1158 (168)	1128 (164)	1247 (181)	1200 (174)

INCREMENTAL STEP TEST

S		0.16
A, MPa (ksi)		861 (125)

Crack lengths were measured visually with a traveling microscope with an accuracy of ± 0.01 mm. They were also estimated based on the unloading compliance technique described in detail in Ref *2*. Accurate estimates of the unloading compliance indicated by Line 1 shown in Fig. 1 were achieved by amplifying the load and displacement voltages of the initial unloading part of the unloading cycle. Signal resolution for displacement was ± 1 part in 400 of the transducer signal range and the pen displacement was 1600 times load-line displacement. Signal resolution for the load transducer was ± 1 in 400 of the transducer signal range.

The sensitivity of the load signal was such that it produced approximately 8 cm of linear pen travel on each unloading. With this technique it was possible to measure crack lengths with an accuracy of ± 0.01 cm. Figure 2 shows an

TABLE 2—*Load control tests summary.*

Specimen No.	Specimen Thickness, cm	$P_{max.}$, kN[b]	P_{min}, kN	N_f	Orientation
1	2.541	45	1	0- 8585	S-T
4	[a]2.376	35	1	0- 7074	S-T
7	[a]2.374	33	1	0-10484	S-T
8	2.538	40.5	1	0-10207	S-T
9	2.394	23	1	0- 271	S-T
		26	1	272- 958	S-T
		28	1	959- 1968	S-T
13	[a]2.354	33	1	0- 9575	S-T
14	[a]2.382	35	1	0- 8193	S-T
18	[a]2.372	34	1	0- 2397	S-T
HD3	1.269	11.75	−11.75	0-13831	T-L
	...	7.62	−7.50	13832-15210	...
	...	4.56	−4.50	15211-16224	...
HD5	1.268	27.25	−11.60	0- 71	T-L
HD8	1.270	25.40	−12.75	0- 35	T-L
	...	25.90	−13.25	35- 65	...
HD9A	1.270	6.09	−10.85	701- 723	T-L
	...	6.12	−10.81	724- 1051	...
	...	5.00	− 9.88	1052- 1145	...

[a]Side-grooved specimen thickness given is Be: $\left[Be = B - \frac{(B - Bn)^2}{B} \right]$

[b]1 kN = 224.8 lbf.

example of the change in the unloading compliance with cycling. The compliance technique employed here is shown to give excellent estimates of crack sizes compared with optical measurements as shown in Fig. 3. It is noticed in Fig. 3 that at large crack lengths, the compliance technique provides higher values for crack length. This is due to the fact that this technique gives an average value for crack length compared with the surface crack length obtained optically. The latter is usually smaller than the former as indicated by the fracture surfaces shown in Fig. 4.

Plasticity and Elastic-Plastic Criteria

Plasticity Effects

In this program, tests were conducted to determine the applicability of the J-integral methodology to crack growth behavior in the high plastic deformation range. Due to the loading conditions that were selected for the tests and ductility of the material, most test results exceeded the plasticity limit required to keep a specimen predominantly elastic as defined in the ASTM Standard Test for Constant-Load-Amplitude Fatigue Crack Growth Rates Above 10^{-8}m/Cycle (E 647-78T). However, all test data were analyzed initially according to

TABLE 3—*Deflection control tests summary (orientation of all specimens is T-L).*

Specimen No.	Specimen Thickness, cm[a]	Max σ, mm[b]	Min σ, mm	N_f
HD1	2.536	0.19	0	0- 1310
		0.23	0	1311- 4630
		0.28	0	4631-11010
		0.32	0	11011-12330
		0.37	0	12331-14660
		0.41	0	14661-17210
		0.45	0	17211-28030
HD2	2.538	0.15	−0.14	0- 90
		0.17	−0.16	91- 230
		0.18	−0.18	231- 580
		0.20	−0.19	581- 850
		0.22	−0.22	851
		0.23	−0.23	852- 1160
		0.25	−0.24	1161- 3850
		0.27	−0.27	3851- 5850
		0.28	−0.28	5851-10700
		0.37	−0.19	10701-11650
		0.30	−0.30	11651-11655
HD4	1.270	0.16	−0.16	0-16002
		0.19	−0.14	16003-17840
		0.21	−0.16	17841-28110
		0.24	−0.14	28111-33710
		0.26	−0.11	33711-40820
		0.31	−0.16	40821-43000
HD9	2.534	0.14	−0.15	0- 112
		0.18	−0.19	113- 962
		0.21	−0.22	963- 1098
		0.26	−0.22	1099- 1275
		0.30	−0.23	1276- 1681
		0.32	−0.21	1682- 1684
		0.35	−0.18	1685- 1689
		0.37	−0.16	1690- 1692
		0.40	−0.14	1693- 1697
		0.42	−0.11	1698- 1702
		0.43	−0.12	1703- 1706
		0.45	−0.14	1707- 1739
		0.51	−0.19	1740- 1742
		0.57	−0.19	1743- 1745
		0.63	−0.12	1746- 1748
		0.69	−0.19	1749- 1755
HD9A	1.270	0.46	−0.24	0- 400
		0.47	−0.23	401- 560
		0.46	−0.24	561- 700

[a]1 cm = 0.4 in.
[b]mm = 0.04 in.

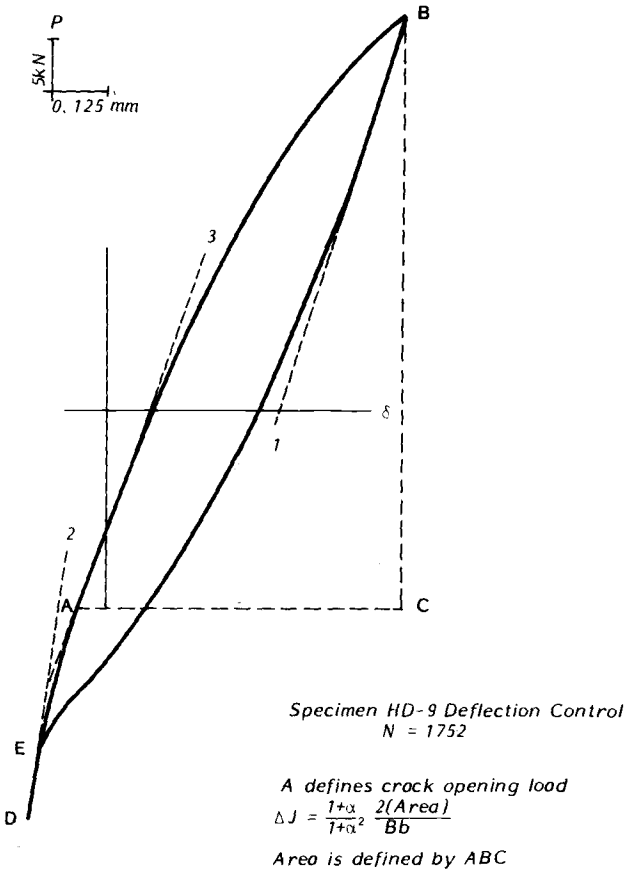

FIG. 1—*Load-line displacement curve with crack closure effect (1 kN = 224.8 lbf; 1 mm = 0.04 in.).*

the linear elastic procedures indicated in Method E 647. This is a routine procedure in our laboratory and these results are presented in Figs. 5 and 6 for information only, with the understanding that this method of analysis may be entirely inappropriate. Also shown on these plots is the American Society of Mechanical Engineers (ASME) Section XI air reference curve for low-carbon steel which has been shown to describe elastic crack growth data for A516 Gr70 steel [*3*]. Due to the existence of a large plastic zone size at the crack tip, an elastic plastic parameter such as the J-integral is needed to account for such an effect. Methods of estimation of cyclic J-integral are discussed in detail in the next section.

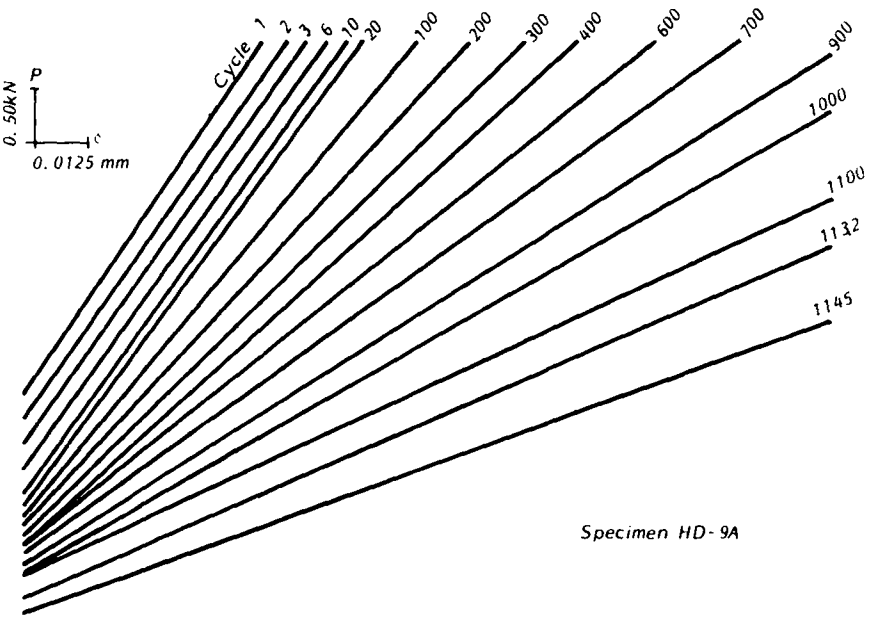

FIG. 2—*Change in unloading compliance with cycling at load control (1 kN = 224.8 lbf; 1 mm = 0.04 in.).*

Experimental Estimation of Cyclic J-Integral

Values of cyclic ΔJ were determined from areas under load versus load-line deflection curves during a rising load as indicated in Fig. 1. For the compact tension specimens tested here, the following expression was used to estimate ΔJ [4]

$$\Delta J = \frac{1 + \alpha}{1 + a^2} \frac{2A}{Bb} \tag{1}$$

where

$(1 + \alpha)/(1 + \alpha^2)$ = coefficient; function of crack length to width ratio [4],
B = thickness of the specimen,
b = uncracked ligament, and
A = area defined by ABC as indicated in Fig. 1.

As macroscopic crack closure behavior occurred, it was necessary to estimate the point at which the crack opened and to calculate ΔJ from the area above this point as indicated in Fig. 1. An attempt was made to measure crack opening and closure during cyclic plasticity tests performed here and it will be discussed in detail in the next section.

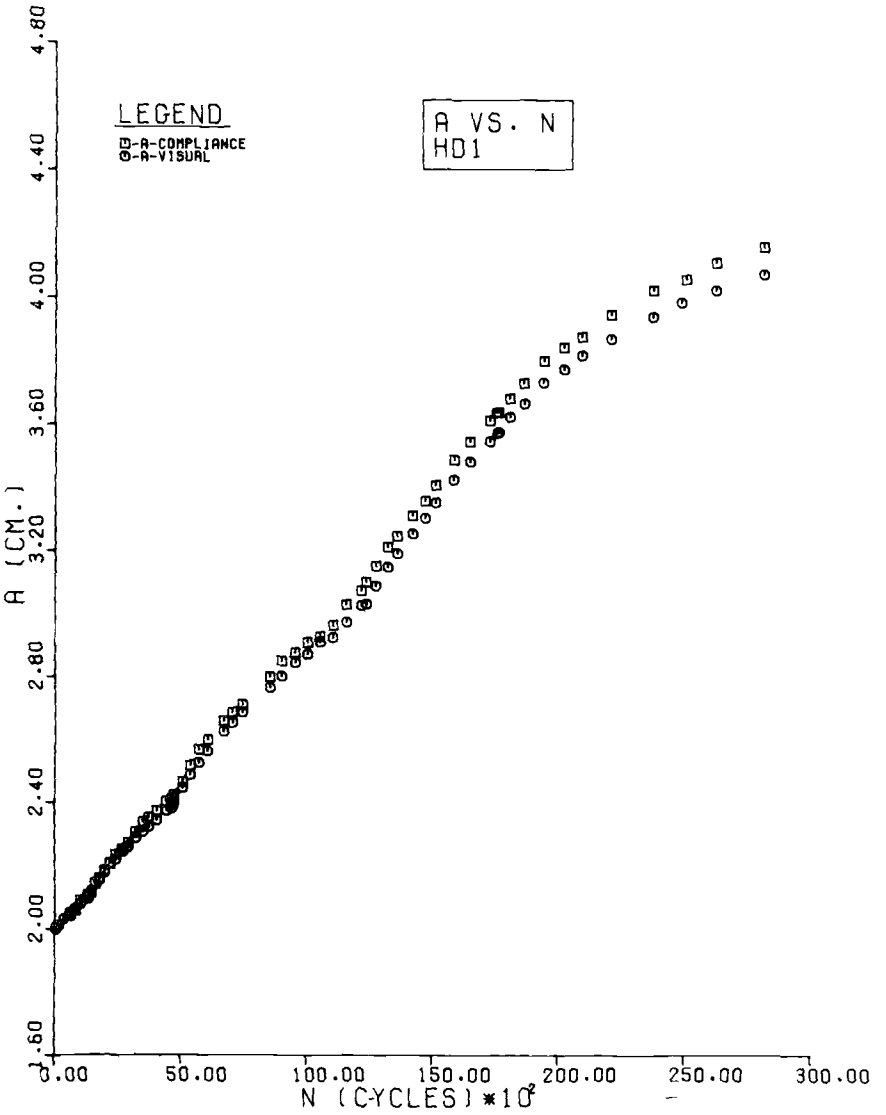

FIG. 3—*Comparison between compliance estimates and optical measurements for crack sizes (1 cm = 0.4 in.).*

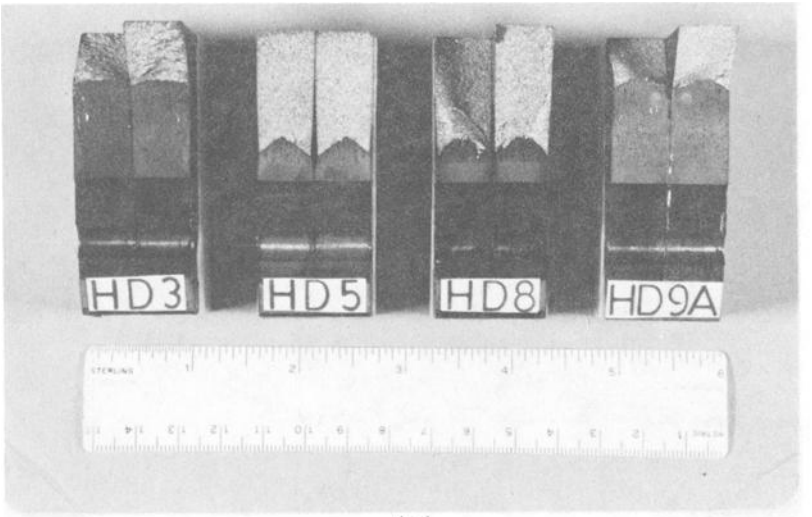

(a)

Load Control Tests

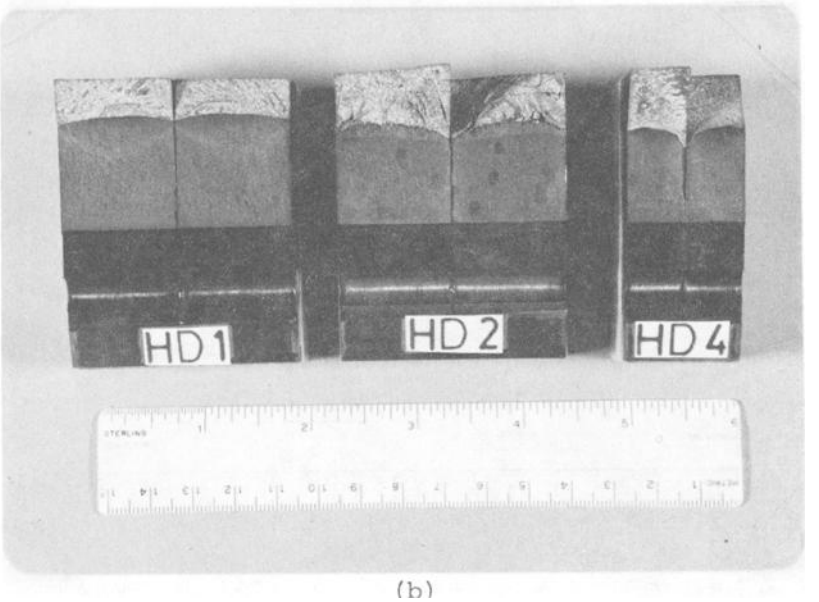

(b)

FIG. 4—*Fracture surfaces.*

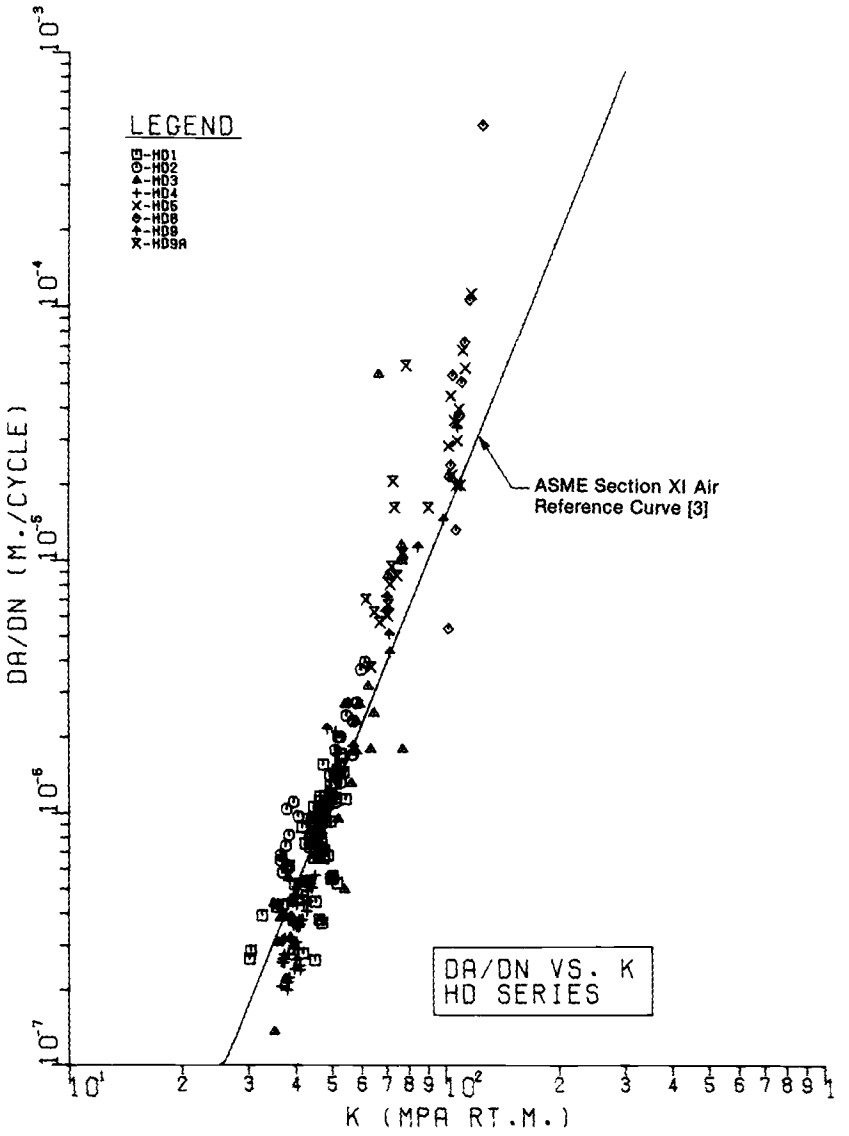

FIG. 5—*Fatigue crack growth rates as a function of* ΔK *(1 MPa = 0.145 ksi).*

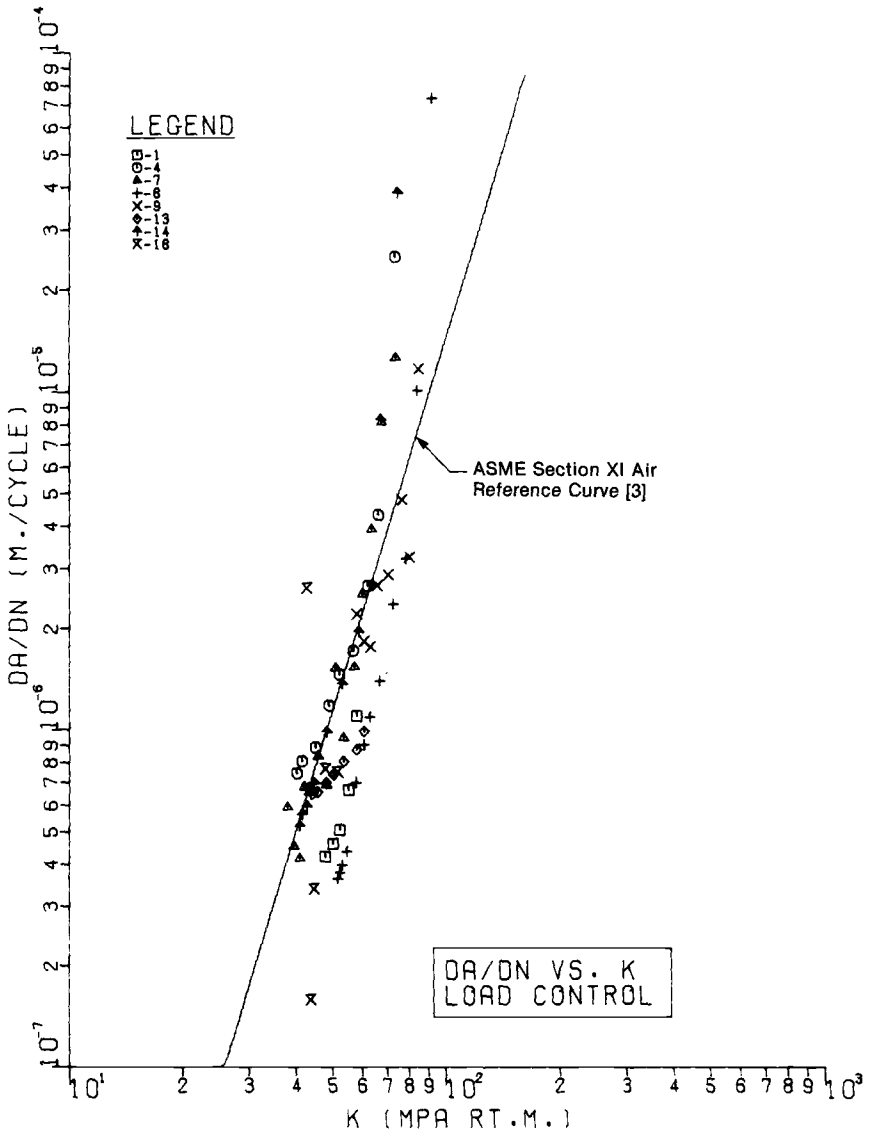

FIG. 6—*Fatigue crack growth rates as a function of* ΔK *(1 MPa = 0.145 ksi).*

Crack Opening and Closure Measurements

For cyclic plastic deformation of a cracked member where closure effects do not occur, the material behavior is expected to result in a load versus deflection hysteresis loop which is approximately symmetrical with respect to its central point. The asymmetry which does occur (see Fig. 1) is therefore due mainly to crack closure. Several attempts have been made to measure crack closure by means of strain gages near the crack tip [5] or by changes in an electric potential applied to the specimen [6] or by measuring displacement across the crack tip using a clip gage attached to the side of the specimen [7]. This last method was applied here.

Figure 7 compares the load line and crack-tip displacement measurements obtained in one of the tests. The stiffness changes in the load versus deflection hysteresis loop observed in Fig. 7 are an indication of crack closure and they correspond to the crack opening load position as shown in Fig. 7. Both hysteresis loops shown in Fig. 7 are found to result in the same estimate of crack opening load, P_{op}. It should be mentioned that the crack closure effect was eliminated by reducing the compression load and, therefore, both load-line and crack-tip displacement measurements indicated no changes in the stiff-

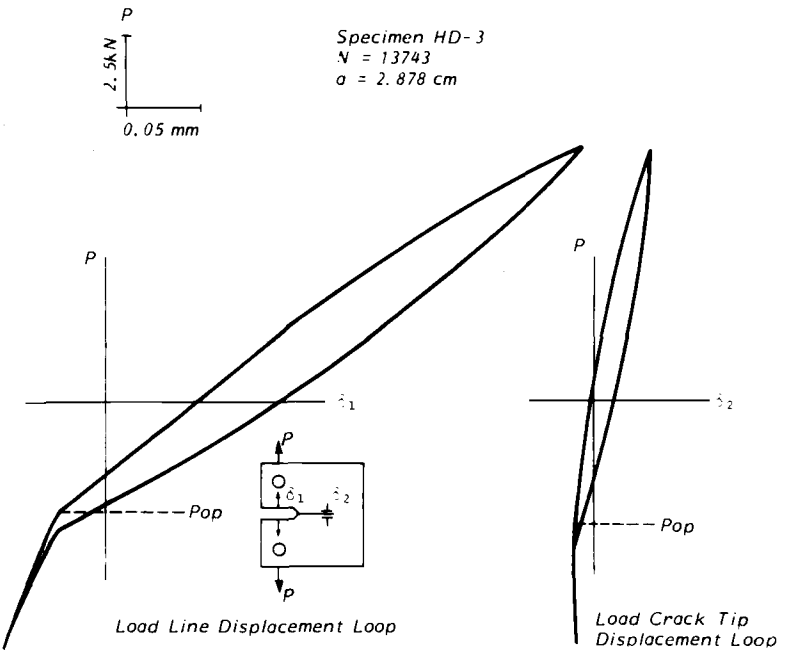

FIG. 7—*Comparison between load-line and crack-tip displacement measurements under load control (1 kn = 224.8 lbf; 1 cm = 0.4 in.; 1 mm = 0.04 in.).*

ness of the hysteresis loops. Hence, load versus load-line displacement loops are adequate to estimate crack opening point, which was found to be more convenient than the direct use of side clip gage data.

The specific procedure used to easily identify the crack opening load is shown in Fig. 1. It has been employed successfully to determine the crack opening loads [*8*]. For most of the load-line displacement hysteresis loops obtained in the present investigation, three distinct linear parts were observed as shown in Fig. 1. The first part, defined by B-1, is the unloading compliance of the cracked specimen and it was shown to accurately predict the crack size. The second line, which is defined by DE2, is shown to correspond to the unloading compliance of the uncracked specimen. This is true due to the fact that the crack is fully closed between D and E. The third part is defined by A-3 and crack opening load P_{op} was assumed to occur at Point A shown in the fig. A transition occurs between Point E, where the crack is fully closed, and at the start of crack opening at Point A.

It is also possible that the linear part defined by A-3 is absent and that a continuously curved line is observed in cases where crack sizes are very large or very large plastic deformations exist at the crack tip. Elber [*9*] proposed in that case that a tangent to the loading curve should be drawn with the same slope as the first part of the unloading line defined by B-1. Visual observation of the surface of the test specimens tested here have shown that the aforementioned procedure resulted in a very accurate estimate of crack opening loads.

An attempt was made to investigate the effect of loading conditions on the crack closure behavior. It is generally observed that for tests carried out under load control, there were no indications of crack closure. This may be due to the fact that the metal at the crack tip was subjected to cycles of plastic deformation under stress control and, therefore, a progressive increase in the mean and the maximum displacements occurred from cycle to cycle, resulting in a tensile displacement at the crack tip. As a result, the crack is expected to remain open with cycling. Also, when test conditions switched from deflection control, where crack closure has occurred, to load control, crack closure disappeared as shown in Fig. 8. It should be emphasized that this is true only in cases where the minimum displacement remains tensile. However, when the minimum displacement remains in compression as shown in Figs. 9 and 10, crack closure still occurs with cycling in load control.

The effect of material conditions at the specimen surface on crack closure was also investigated. For the deflection control test shown in Fig. 1, specimen surfaces were machined off after crack closure was observed as shown in the figure. Then the specimen was recycled at approximately the same ΔJ-value. Initially, crack closure was not observed, as shown in Fig. 9, but it did occur as crack size increased later in the fatigue life. Therefore, removing the specimen surfaces eliminated plasticity zones at the surfaces and hence eliminated crack closure. However, with cycling, crack size increased and plasticity zones redeveloped at the surfaces of the specimen and crack closure occurred once again.

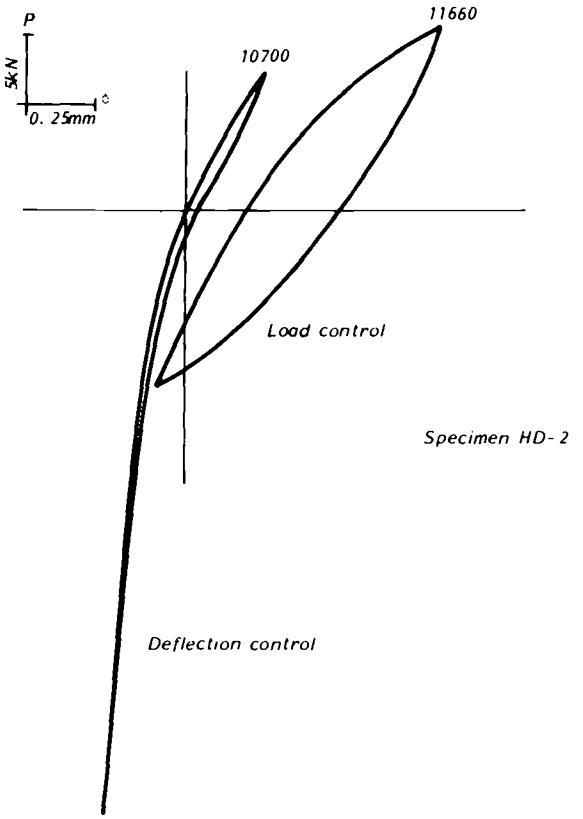

FIG. 8—*Shift from deflection control to load control (1 kN = 224.8lbf; 1 mm = 0.04 in.).*

Fatigue Crack Growth Rates as a Function of ΔJ

To examine the accuracy of the cyclic J-integral analysis just described, the crack growth data of Figs. 5 and 6 are reanalyzed based on Eq 1 and plotted in Figs. 11 and 12 as a function of $\sqrt{E \cdot \Delta J}$, where E is the Young's modulus. The data are plotted in terms of $\sqrt{E \cdot \Delta J}$ so that the relative merits of linear and nonlinear parameters can be easily compared. The data obtained from different specimen thicknesses, for different load levels, and for different test conditions show excellent agreement with the elastic crack growth line. The various complexities and lack of correlation apparent in the plots using ΔK shown in Figs. 5 and 6 are no longer present. In particular, the extent of spread in the data is less in terms of ΔJ than in terms of ΔK.

The J-integral analysis presented in the foregoing has two important features which account for the successful correlations in Figs. 11 and 12. First, the effect of plasticity is included. And second, the crack closure which is a direct reflection of the residual deformation near the crack tip is included.

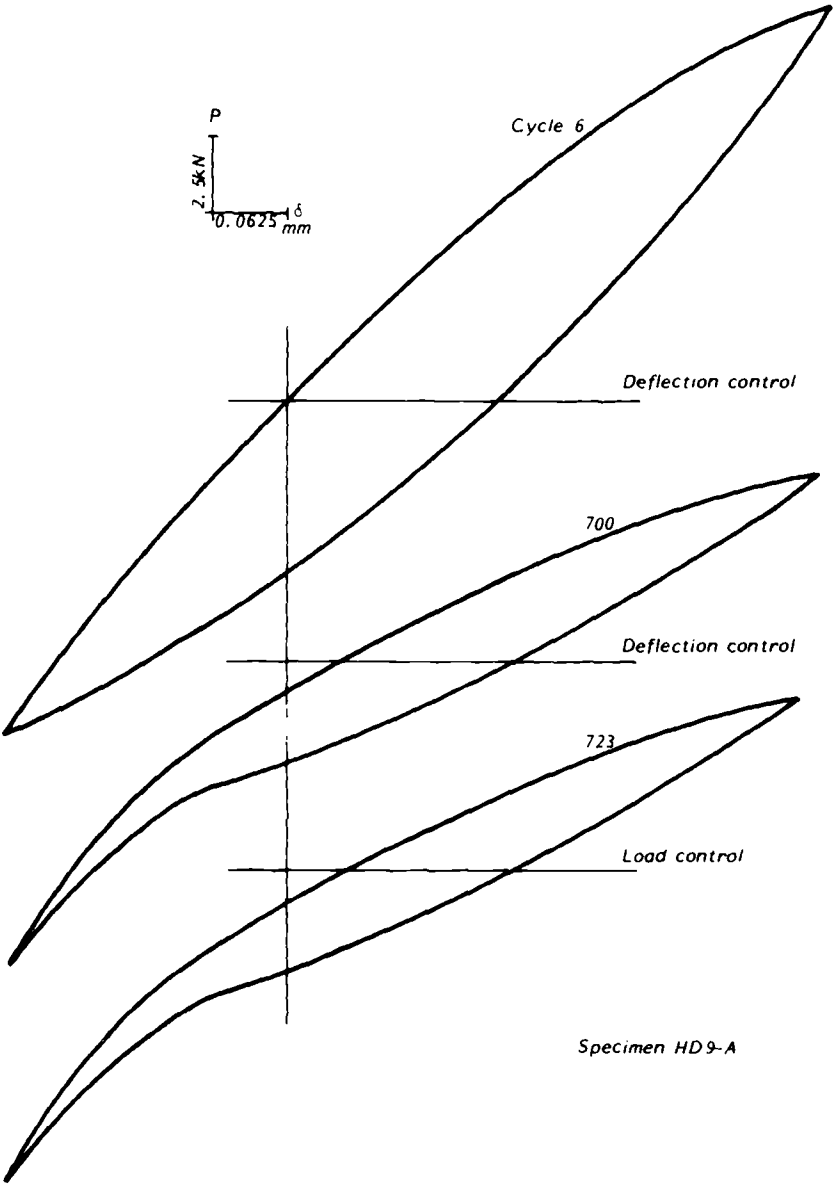

FIG. 9—*Shift from deflection control to load control (1 kN = 224.8lbf; 1 mm = 0.04 in.).*

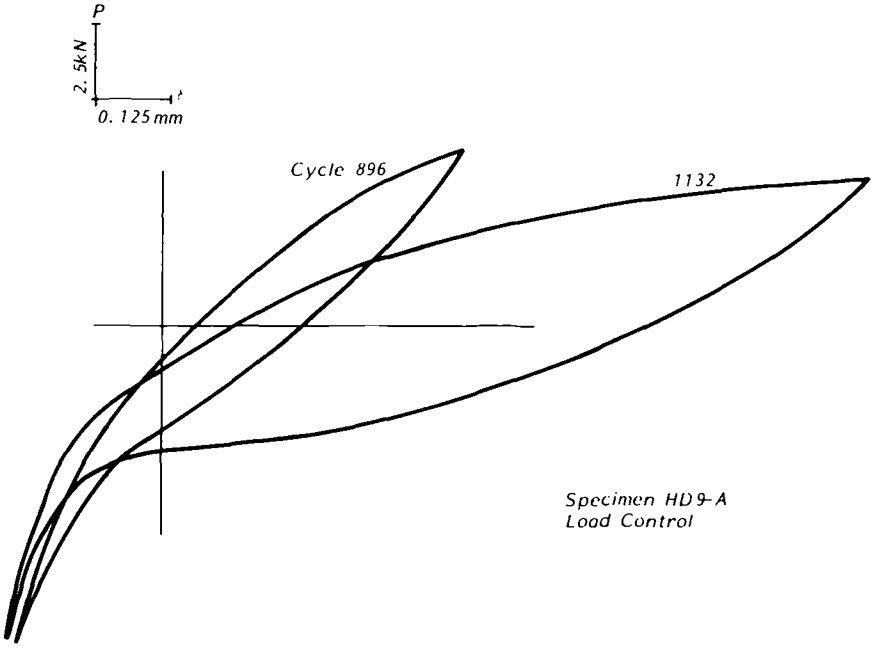

FIG. 10—*Load displacement cyclic loops for load control test (1 kN = 224.8 lbf; 1 mm = 0.04 in.).*

These two features are needed to successfully correlate the data presented. The increasing and decreasing trends in growth rates observed in load control and deflection control tests are reflected in corresponding variation with crack length of ΔJ-values from Eq 1. Otherwise, the data correlations of Figs. 11 and 12 could not be successful. Therefore, ΔJ not only works for cases when its value is monotonically increased as suggested in Ref *10*, but it also works when its value is decreased with cycling as noticed in the deflection control tests.

The data obtained here represent various test histories that may be of direct significance in demonstrating the utility of J in fatigue crack growth analysis when history-dependent effects such as crack closure are included.

Summary

Fatigue crack growth rate data were obtained for compact tension specimens of ASTM A516 Gr70 steel subjected to elastic and elastic-plastic cylic loading for both load-controlled and displacement-controlled test conditions. The following results were obtained:

1. Crack size estimates based on unloading compliance result in very accurate values, compared with optical measurements on the specimen surface.

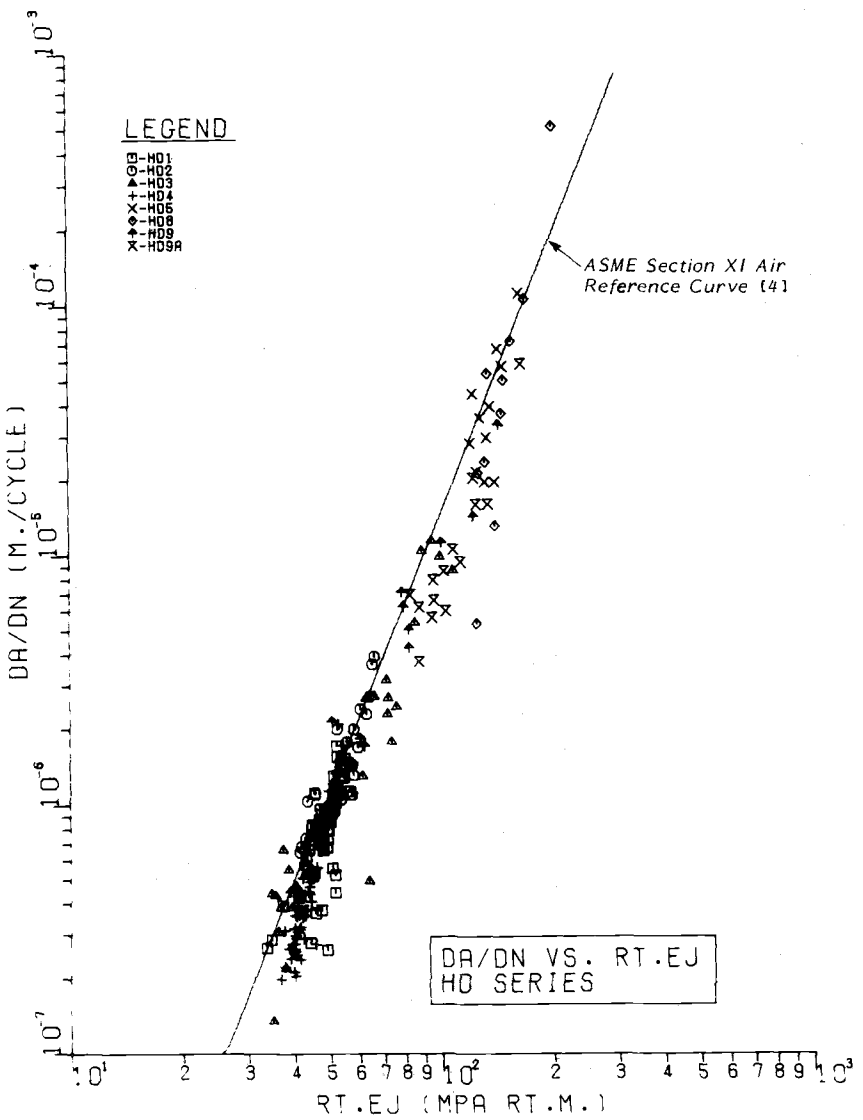

FIG. 11—*Fatigue crack growth rates as a function of* $\sqrt{E \cdot \Delta J}$ (1 MPa = 0.145 ksi).

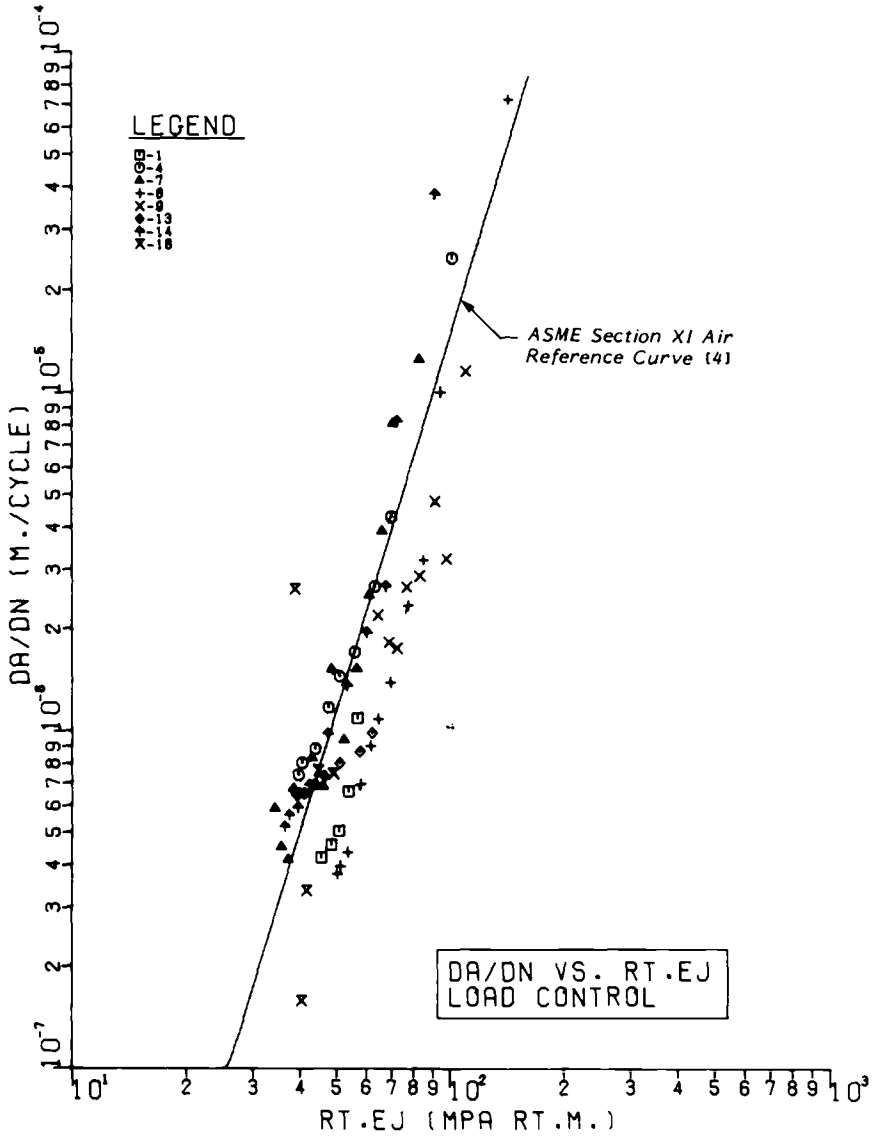

FIG. 12—*Fatigue crack growth rates as a function of* $\sqrt{E \cdot \Delta J}$ (1 MPa = 0.145 ksi).

2. Crack growth rate increases with cycling for load-controlled tests, but it decreases with cycling for displacement-controlled tests.

3. Crack closure and opening loads are successfully obtained from displacement measurement and from stiffness changes in load versus displacement loops.

4. The cyclic J-integral crack growth rate data agree well with those from the linear elastic tests.

5. The J-integral parameter is shown to be better than the linear elastic parameter K in correlating fatigue crack growth, particularly in ductile materials such as A516 steel and at high load levels.

Acknowledgment

The experiments were conducted by Mr. D. McCluskey, of Ontario Hydro Research.

References

[1] El Haddad, M. H., "Strain Controlled Fatigue Bahaviour of A516 Gr 70 Steel," Ontario Hydro Research Report No. 80-365-K, Toronto, Ont., Canada, 1980.

[2] Albrecht, P. et al, "Tentative Test Procedure for Determining the Plane Strain J-R Curve," American Society for Testing and Materials, May 1980.

[3] Mukherjee, B., "Fatigue Crack Growth in A516 Gr 70 Steel and Associated Welds," Ontario Hydro Research Report No. 80-92-K, Toronto, Ont., Canada, 1980.

[4] Clarke, G. A. and Landes, J. D., *Journal of Testing and Evaluation*, Vol. 7, No 5., Sept. 1979, pp. 264-269.

[5] Schmidt, R. A. and Paris, P. C., in *Progress in Flaw Growth and Fracture Toughness Testing, ASTM STP 536*, American Society for Testing and Materials, 1973, pp. 79-94.

[6] Shih, T. T. and Wei, R. P., "A Study of Crack Closure in Fatigue," Report No IFSM 72-25, Institute of Fracture and Solid Mechanics, Lehigh University, Bethlehem, Pa., Nov. 1972.

[7] Dowling, N. E. and Begley, J. A. in *Mechanics of Crack Growth, ASTM STP 590*, American Society for Testing and Materials, 1976, pp. 82-103.

[8] Bachmann, V. and Munz, V. in *Proceedings*, International Conference of the Society of Environmental Engineers Fatigue Group, City University, London, 5-9 April 1976.

[9] Elber, W. in *Damage Tolerance in Aircraft Structures, ASTM STP 486*, American Society for Testing and Materials, 1971, pp. 230-242.

[10] Leis, B. N. and Zahoor, A. in *Fracture Mechanics: Twelfth Conference, ASTM STP 700*, American Society for Testing and Materials, 1980, pp. 65-96.

Keisuke Tanaka,[1] *Toshihiko Hoshide,*[2] *and Machi Nakata*[3]

Elastic-Plastic Crack Propagation Under High Cyclic Stresses

REFERENCE: Tanaka, K., Hoshide, T., and Nakata, M., **"Elastic-Plastic Crack Propagation Under High Cyclic Stresses,"** *Elastic-Plastic Fracture: Second Symposium, Volume II—Fracture Resistance Curves and Engineering Applications, ASTM STP 803*, C. F. Shih and J. P. Gudas, Eds., American Society for Testing and Materials, 1983, pp. II-708-II-722.

ABSTRACT: The effects of the loading condition and the specimen geometry on the elastic-plastic crack growth in structural low-carbon steel under high cyclic stresses are investigated experimentally. The acceleration of crack growth rate, deviating from the stable relation between the rate and the J-integral range, was found to take place coincidently with the onset of the ratcheting extension of the specimen. Based on the fractographic observation, the crack growth acceleration is attributed to the incomplete reversal of plastic deformation in ratcheting extension and to the inclusion of dimple-mode fracture in crack growth. The maximum amount of crack growth acceleration through the former mechanism is predictable by considering the increase in crack-tip opening displacement. A method to evaluate the transitional behavior from stable fatigue growth to unstable fracture is proposed by introducing the concept of fatigue crack growth resistance curve.

KEY WORDS: fatigue (material), crack growth, fracture mechanics, J-integral, resistance curve, ratcheting deformation, fractography, elastic-plastic fracture

Dowling and Begley [*1*][4] first applied the J-integral to fatigue crack propagation under elastic-plastic and general yield conditions, and found that the propagation rate of a fatigue crack was expressible as the power function of the range of J-integral (ΔJ). Later, the rate versus ΔJ relation has been found to be independent of the specimen geometry and the cyclic loading conditions, and it has also been shown that the usual conversion of ΔJ to the stress-

[1]Associate professor, Department of Mechanical Engineering and Mechanics, Lehigh University, Bethlehem, Pa. 18015.

[2]Research associate, Department of Mechanical Engineering, Kyoto University, Kyoto, Japan.

[3]Engineer, Osaka-Seikosho, Sumitomo Metal Industries, Osaka, Japan.

[4]The italic numbers in brackets refer to the list of references appended to this paper.

intensity range yields the crack growth law obtained in the same material under the small-scale yielding situations [*2-5*]. The J-integral approach is further applied to the fatigue propagation of three-dimensional surface cracks [*6-8*]. Although the J-integral approach begins to be widely used, a significant acceleration of crack growth found under high cyclic stresses with positive mean stresses limits the applicability of the conventional J-integral approach [*1,3,5*].

In the present paper, the effects of the loading condition and the specimen geometry on the elastic-plastic crack growth under high cyclic stresses are investigated experimentally, and the mechanisms of crack growth acceleration are clarified based on the observations of fractography and of the plastic deformation of the specimen. The method to analyze the transitional behavior from stable to unstable fracture under high cyclic stresses is discussed by introducing the concept of the fatigue crack growth resistance curve.

Experimental Procedure

The materials used for the experiments were two structural low-carbon steels with the same designation JIS SM41B. The chemical compositions and mechanical properties as annealed are summarized in Table 1. The yield strength and the tensile strength of SM41B(I) with 0.15 weight percent carbon were slightly lower than those of SM41B(II) with 0.17 weight percent carbon. The specimens were of compact tension (CT) type and center-cracked plates (CCP). The widths W of CT specimens were 40 and 200 mm and the thicknesses B were 2, 5, and 10 mm. The ratio of the initial crack length a_0 to width was 0.45 except for the case of the specimen with $W = 200$ mm and $B = 10$ mm, which had $a_0/W = 0.33$. The width $2W$ of the CCP specimens was 30 mm and the thickness 4 mm. The initial crack length $2a_0$ was $0.2W$. The experimental data for each specimen will be described by a set of the specimen type, width, and thickness. Most experiments on the CT specimens were conducted with Material SM41B(I) and additional experiments on the CCP specimens with Material SM41B(II). The rolling direction of the materials was parallel to the crack growth direction (T-L direction).

Fatigue tests were carried out in a closed-loop servohydraulic testing machine under load-controlled conditions at the load ratio, R, of the minimum load to the maximum load ranging from -1 to 0.7. The frequency of stress cycling was varied from 0.3 to 30 Hz depending on the experimental conditions. The crack length was measured with a traveling microscope with $\times 100$ magnification. The stress-intensity factor (SIF) was calculated from the conventional equations proposed for the CT and CCP specimens ASTM Tentative Test Method for Constant-Load-Amplitude Fatigue Crack Growth Rate Above 10^{-8} m/Cycle (E647-78)].

The load versus displacement curves were recorded several times during the fatigue tests. The displacement measured was that at the loading point in

TABLE 1—*Chemical compositions and mechanical properties of test materials.*

	Weight %					Yield Strength σ_Y, MPa	Tensile Strength σ_B, MPa
	C	Si	Mn	P	S		
SM41B(I)	0.15	0.15	0.81	0.021	0.014	274	421
SM41B(II)	0.17	0.19	0.79	0.016	0.020	281	449

the CT specimens, and was the crack-opening displacement at the center of a crack in the CCP specimens [5].

The J-integral range (ΔJ) was evaluated from the loading portion of the hysteresis loop of load against displacement. For the case of the CT specimens, ΔJ was evaluated from the energy V^* of the loading curve above the crack closure point by using the modified Merkle-Corten equation [9].

$$\Delta J = \frac{1 + \alpha}{1 + \alpha^2} \frac{2V^*}{B(W - a)} \tag{1}$$

where $(1 + \alpha)/(1 + \alpha^2)$ is the known function of a/W and B is the specimen thickness. For the case of the CCP specimen, ΔJ was evaluated from

$$\Delta J = \Delta K^{*2}/E + S^*/B(W - a) \tag{2}$$

where ΔK^* was the maximum stress-intensity factor K_{max} minus the SIF value at the crack closing point K_{cl}, and S^* was the energy enclosed by the loading curve and the secant line from the closure load to the maximum load [2,5]. The first term is the elastic component of ΔJ and the latter is the plastic component. Figure 1 illustrates a cyclic hysteresis loop where S^* is indicated by the hatched area. Rice et al [10] originally proposed to use the load-point displacement in obtaining S^* instead of the opening displacement at the crack center. Recent experiments by the authors [5] indicated that the use of the crack-center opening displacement is more appropriate to evaluate the plastic component of ΔJ for CCP specimens with shallow cracks as well as deep cracks.

Fatigue Crack Propagation and Plastic Deformation

Under load-controlled cycling with a tensile mean stress, the hysteresis loop of load against displacement tended to shift horizontally and the extensional deformation, or the ratcheting deformation, was monotonically accumulated as a fatigue crack grew. The amount of the ratcheting deformation of the specimen was evaluated by the plastic component, $v_{min}{}^p$, of the displacement at the minimum load [5]. From the hysteresis loop, the point of

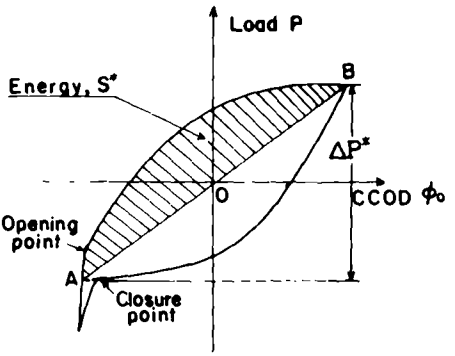

FIG. 1—*Estimate of J-integral for CCP specimen.*

crack closure was determined as the inflection point of the unloading curve [*4,5,8*]. The effective fraction U of the applied load is defined by

$$U = (P_{max} - P_{cl})/(P_{max} - P_{min}) \tag{3}$$

where P_{max} and P_{min} are the maximum and minimum loads, and P_{cl} is the load at the crack closure.

Figure 2 shows an example of the changes of $v_{min}{}^{P}$ and U with crack length for a CT specimen (W = 40 mm, B = 2 mm). The points of the yielding initiation at the back face and the general yielding observed are also indicated by BY and GY in the figure. Below the BY point, the ratcheting deformation is negligible and U increases with increasing crack length. At the BY point, U becomes unity; that is, there is no closure at the minimum load. The ratcheting deformation starts at the BY point and increases rapidly above the GY point. A similar behavior was observed for the cases of CCP specimens, although the amount of ratcheting deformation is generally smaller in CCP specimens than in CT specimens [*5*].

By neglecting ratcheting deformation, the J-integral range ΔJ was evaluated from the loading curve of the hysteresis loop as described in the preceding section. The relation between crack propagation rate da/dN and ΔJ is shown in Fig. 3*a* for CT specimens. The data obtained below BY, between BY and GY, and above GY are discriminated by the open, half-open, and solid marks, respectively. In the region below BY, the relation between da/dN (m/cycle) and ΔJ (N/m) is approximated by

$$da/dN = C(\Delta J)^m \tag{4}$$

where $C = 4.61 \times 10^{-13}$ and $m = 1.57$. This relation was also found to be valid in the cases of deflection-controlled fatigue tests of the same material [*5*].

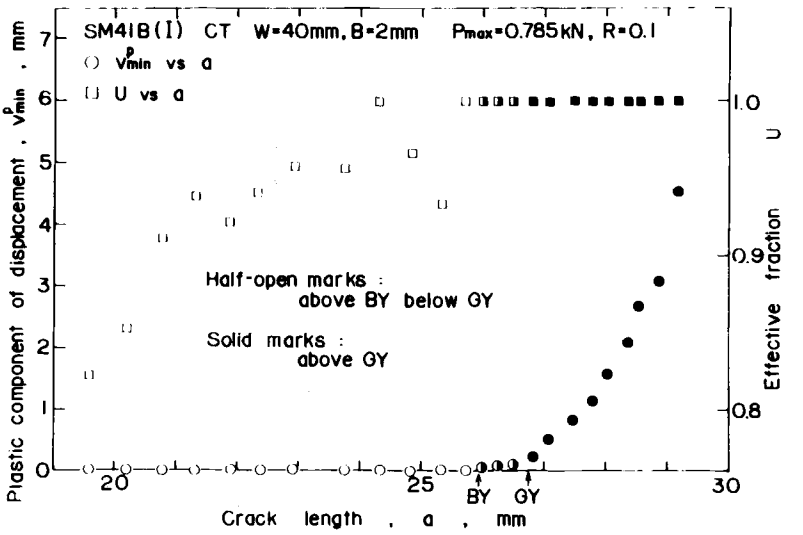

FIG. 2—*Changes of ratcheting deformation and effective fraction with crack length in CT specimen of Material SM41B(I) (*W = *40 mm,* B = *2 mm,* P_{max} = *0.785 kN,* R = *0.1).*

Above GY points, the rate becomes higher than that predicted from Eq 4. The points at BY and GY are lower with increasing R and are uniquely determined by the maximum load divided by the thickness P_{max}/B (compare the data for P_{max} = 0.785 kN, B = 2 mm; P_{max} = 1.96 kN, B = 5 mm; P_{max} = 3.92 kN, B = 10 mm). The maximum load at the BY point was found to coincide with the limit load calculated under the plane-stress condition, and that at GY was found to be above the plane-stress limit load and below the plane-strain limit load [*5*].

The relation between da/dN and ΔJ obtained for CCP specimens of Material SM41B(II) is shown in Fig. 3*b*, where σ_{max} is the maximum gross stress. A similar acceleration of the rate was observed above the general yielding, deviating from the da/dN-ΔJ relation obtained below GY, although the amount of acceleration is small near the GY point. The constants in Eq 4 obtained below GY are $C = 2.45 \times 10^{-13}$ and $m = 1.70$ for Material SM41B(II). The relation for Material SM41B(II) (the solid line) does not widely differ from that for Material SM41B(I) (the dashed line). The maximum load at the GY point for CCP specimens was about 85 percent of the calculated limit load [*5*]. As seen in the case of $R = 0.7$, the process of crack growth acceleration has two stages. The acceleration just above the GY point is not large and the da/dN-ΔJ relation tends to lie parallel to Eq 4. In the later stage, the rate accelerates rapidly. Two-stage acceleration is also detected for the other cases shown in Fig. 3.

Mechanisms of Crack Growth Acceleration

The fracture surfaces of all the tested specimens were macroscopically flat and were not accompanied with shear lips. The details of the fracture surface topography were examined with a scanning electron microscope. Figure 4 presents several examples of the micrographs taken from the fracture surface at about the middle of the specimen thickness. In the region below BY, the fracture surface has ductile striations or striation-like pattern as seen in (*a*). The micrographs (*b*), (*c*), and (*e*) taken from fracture surfaces made near GY are more or less the same as (*a*). Dimple patterns can be seen in the micrographs (*d*) and (*f*) taken from the fracture surface made well above GY. By correlating the micrographs (*e*) and (*f*) with the da/dN-ΔJ relation shown in Fig. 3*b* for the case of $R = 0.7$, it is easy to note that the initial stage of acceleration is not caused by the change of crack growth mode, and that the static mode fracture mechanism is operating in the rapid acceleration stage.

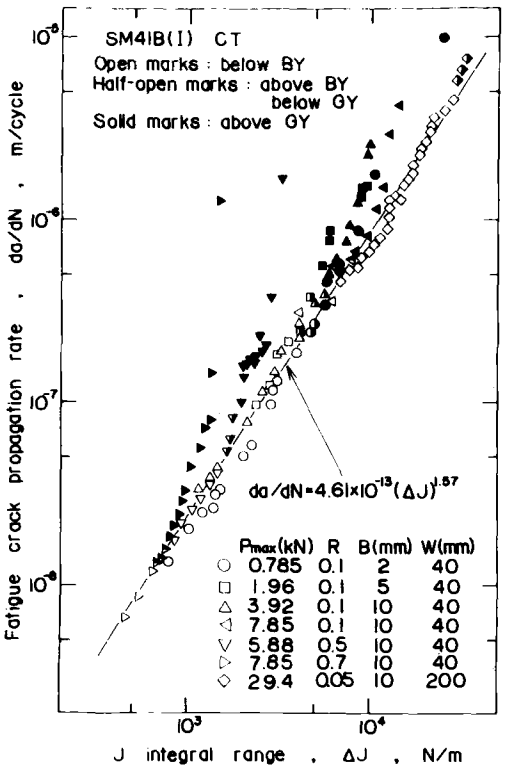

FIG. 3*a*—*Relation between crack propagation rate and J-integral range: CT specimens, Material SM41B(I).*

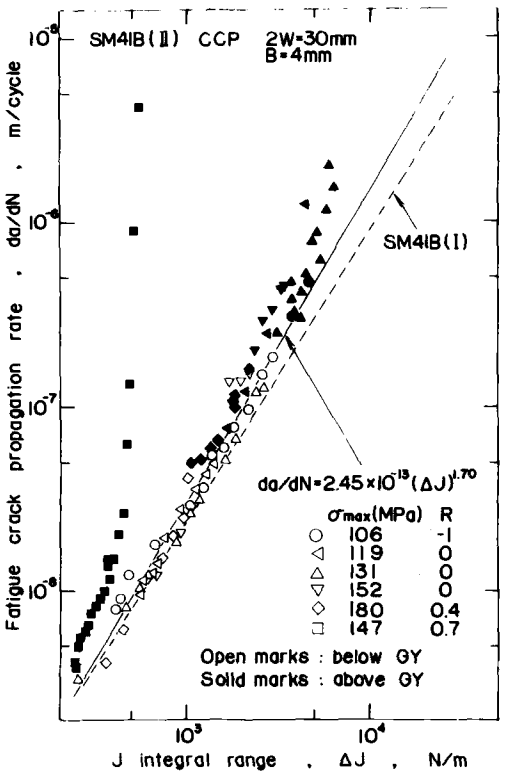

FIG. 3*b*—*Relation between crack propagation rate and J-integral range: CCP specimens, Material SM41B(II).*

Based on the observations of fractography and plastic deformation of the specimen, it can be concluded that crack growth acceleration at high cyclic stresses is ascribed to two reasons: (1) the ratcheting deformation and (2) the inclusion of static-mode fracture. The crack growth acceleration reported by Kobayashi et al [*11*] seems to correspond to that due to ratcheting deformation because they observed a striation pattern on the fracture surface as in the present study. The ratcheting deformation takes place when the plastic displacement of the specimen is not completely reversed at the minimum load to the initial value. The amount of growth acceleration caused only by ratcheting can be evaluated as follows.

The crack-tip opening displacement (CTOD) under monotonic loading has been expressed

$$\text{CTOD} = J/p\sigma_Y \tag{5}$$

where σ_Y is the yield stress and p the plastic constraint factor. Most previous experiments indicate that p is between 1 and 2 [*12*], and it was found to be

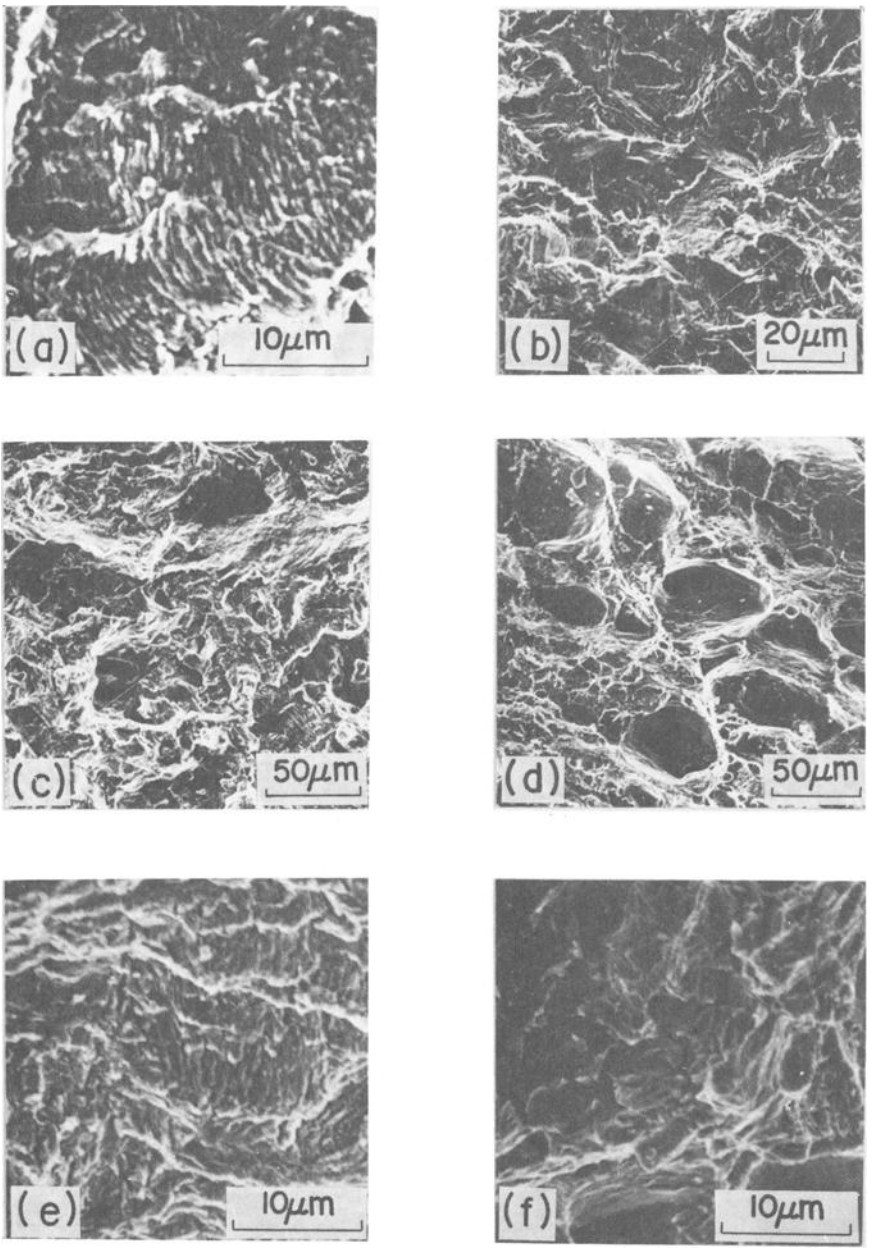

FIG. 4—*Scanning electron micrographs of fracture surfaces (growth direction is from left to right)* (a) *Below BY, SM41B(I), CT*, R = *0.1*, da/dN = *2.3* × 10^{-8} *m/cycle.* (b) *Above BY and below GY, SM41B(I), CT*, R = *0.1*, da/dN = *6.0* × 10^{-7} *m/cycle.* (c) *Just above GY, SM41B(I), CT*, R = *0.1*, da/dN = *1.0* × 10^{-6} *m/cycle.* (d) *Well above GY, SM41B(I), CT*, R = *0.1*, da/dN = *9.0* × 10^{-6} *m/cycle.* (e) *Just above GY, SM41B(II), CCP*, R = *0.7*, da/dN = *7.9* × 10^{-9} *m/cycle.* (f) *Well above GY, SM41B(II), CCP*, R = *0.7*, da/dN = *1.1* × 10^{-6} *m/cycle.*

about 1.2 at the crack initiation point for the present material, SM41B(I) [*13,14*]. Rice [*15*] proposed to double the yield stress to describe the plastic deformation under cyclic stress. Therefore, the range of CTOD, ΔCTOD, can be given by

$$\Delta\text{CTOD} = \Delta J/2p\sigma_Y \tag{6}$$

In the case when the plastic deformation is ratcheting, the reversed plastic zone may be small and the maximum estimation of ΔCTOD will be

$$\Delta\text{CTOD} = \Delta J/p\sigma_Y \tag{7}$$

In the previous study of Taira et al [*4*], it was found that the rate of fatigue crack growth was generally expressed as the power function of ΔCTOD. Therefore, if we express the da/dN-ΔJ equation, Eq 4, as the function of $\Delta J/\sigma_Y$ (m)

$$da/dN = C'(\Delta J/\sigma_Y)^m \tag{8}$$

the maximum amount of growth rate accelerated due to ratcheting can be given by

$$da/dN = C'(2)^m(\Delta J/\sigma_Y)^m \tag{9}$$

where $C' = 8.15$ for Material SM41B(I) and $C' = 56.5$ for Material SM41B(II).

In Fig. 5, the rate data for CT specimens (Fig. 3*a*) are replotted against $\Delta J/\sigma_Y$. The stretched zone widths measured in the fracture toughness of the same material [*13,14*] are plotted against J/σ_Y. The critical value of the stretched zone size was 20.5 μm [*13*]. The solid line in the figure indicates Eq 8 and the dashed line Eq 9. The data of stretched zone width lie close to the dashed line. The rate in the initial stage of acceleration due to ratcheting lies above the solid line and below the dashed line. The upper bound of acceleration due to ratcheting can be estimated by the dashed line. It is interesting to see that the crack growth acceleration due to the inclusion of the static mode fracture starts at the rate below the critical stretched zone width.

Fatigue Crack Growth Resistance Curve

The crack growth acceleration due to static mode fracture cannot be predicted from ΔJ. Since this type of acceleration in low-toughness materials is predictable from the maximum stress-intensity factor K_{max} [*16,17*] or the crack-tip opening displacement [*18*], the maximum values of J-integral or the crack-tip opening displacement should be evaluated for the present ductile materials to characterize the static mode growth.

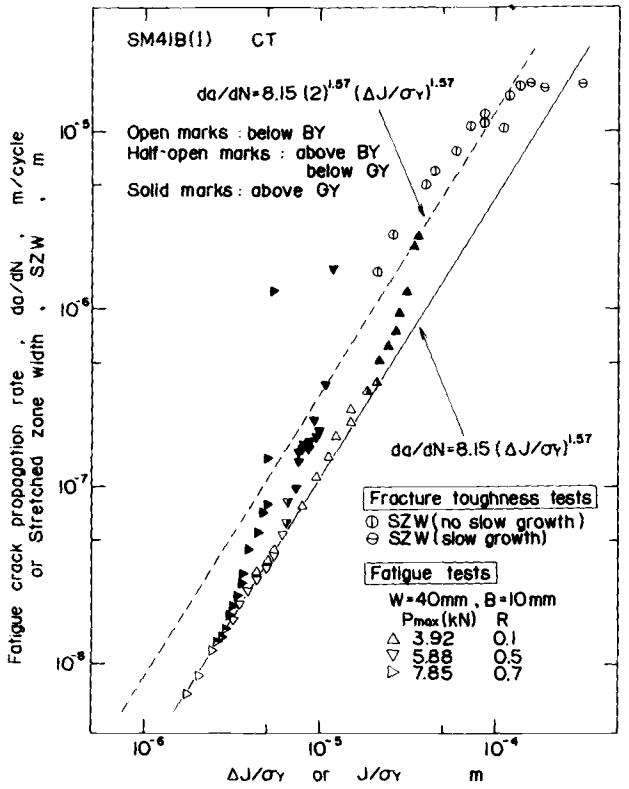

FIG. 5—*Crack propagation rate and stretched zone size plotted against J-integral divided by yield stress.*

Figure 6 illustrates schematically the loading curve AB at the crack length a_i after N_i cycles under fatigue load cycling between P_{max} and P_{min}. The range of J-integral has been evaluated from this loading curve. The accumulated deformation by ratcheting gives an additional deformation to the near-tip field. Since no theoretical analysis has been conducted for the present situation, the following approximation will be made to evaluate the maximum J-integral. It is assumed that the total deformation can be decomposed into the cyclic component and the accumulated monotonic component, and that the latter corresponds to the deformation caused by the loading curve ODB shown in Fig. 6. The maximum J-integral (J_{max}) is evaluated from Eq 1 for CT specimens by using the energy of the curve ODB as

$$J_{max} = \frac{1+\alpha}{1+\alpha^2}\frac{P_{max}v_{max}^{e}}{B(W-a)} + 2\frac{1+\alpha}{1+\alpha^2}\frac{P_{max}v_{max}^{p}}{B(W-a)} \tag{10}$$

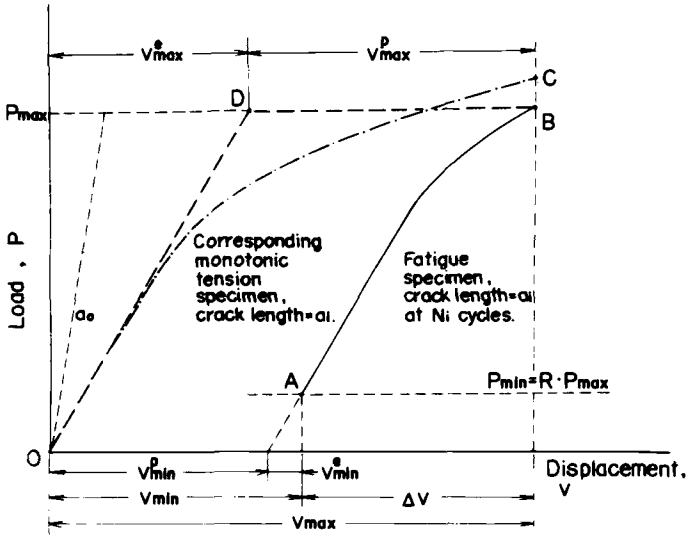

FIG. 6—*Evaluation of maximum values of J-integral and crak-tip opening displacement.*

where v_{max}^{e} and v_{max}^{p} are the elastic and plastic components of the load-point displacement at the maximum load. Since the first term is equal to $K_{max}^{2}(1 - \nu^2)/E$ [9], Eq 10 is correct for the case of small-scale yielding. Similarly, J_{max} for CCP specimens is given from the curve ODB by using Eq 2 as

$$J_{max} = \frac{K_{max}^{2}}{E} + \frac{P_{max} v_{max}^{p}}{2B(W - a)} \tag{11}$$

The relation between crack length increment per cycle Δa and J_{max} thus evaluated is shown in Fig. 7 for the cases of CT specimens. As seen in the case of $R = 0.1$, the $\Delta a - J_{max}$ relation is independent of the maximum load and the specimen thickness. The relation is composed of three stages: the stage of stable fatigue growth in the region below BY, the plateau stage near GY, and the acceleration stage due to static mode growth contribution. In the third stage, all curves tend to converge to a single curve. The J_{max}-value at the onset of the third stage is rather independent of R-value and equal to about 8×10^4 N/m. In the figure, the result of the fracture toughness tests [*13,14*] of Material SM41B(I) is shown with two segments of the dashed lines which are the blunting line and the resistance line. The fracture toughness J_{Ic} is 4.5×10^4 N/m. The J_{max}-value at the onset of the third stage is about twice that of J_{Ic}. The resistance for fatigue crack growth evaluated in term of J_{max} is larger than that for slow crack growth under monotonic loading, and the latter seems to give the lower bound of the fatigue data.

In Fig. 8, the data, obtained only above GY, together with those for CCP

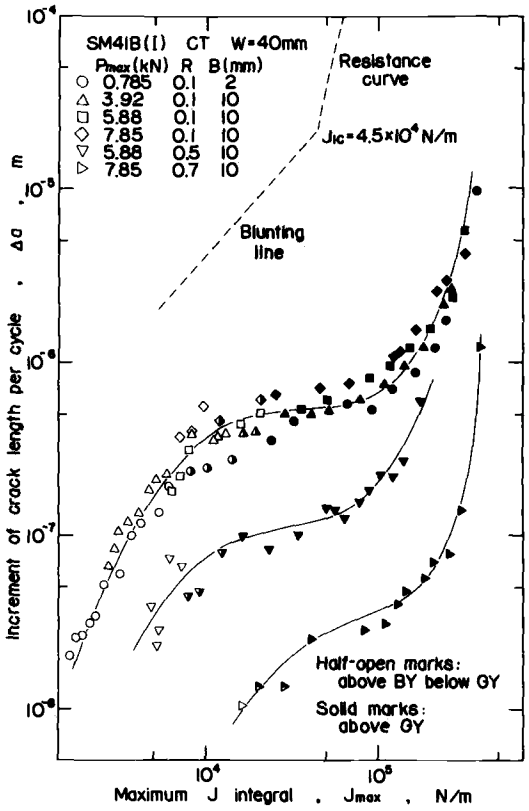

FIG. 7—*Crack length increment per cycle plotted against maximum J-integral.*

specimens are plotted in the linear scale as in the conventional resistance curve [*19*]. The relation between J_{max} and Δa is dependent on R, and the larger R-value gives the larger resistance. A similar influence of R on fatigue crack growth resistance in the small-scale yielding situation was reported by Wilhem and Ratwani [*17*]. The curve seems to be also dependent on the loading condition. A further investigation is necessary to clarify the influence of the specimen geometry on the resistance curve.

McCabe [*19*] successfully utilized the crack-tip opening displacement to generate the resistance curve for elastic-plastic crack growth under monotonic loading. Here, CTOD will be used as another parameter to express the resistance of fatigue crack growth. For the cases of CT specimens, the maximum value of CTOD, ϕ_{max}, is evaluated through the British standard method B55762, Crack Opening Displacement Testing (1979) by using

$$\phi_{max} = \frac{1-\nu^2}{E}\,\frac{K_{max}{}^2}{2\sigma_Y} + \frac{0.4(W-a)}{0.4W+0.6a}\,v_{max}{}^p \tag{12}$$

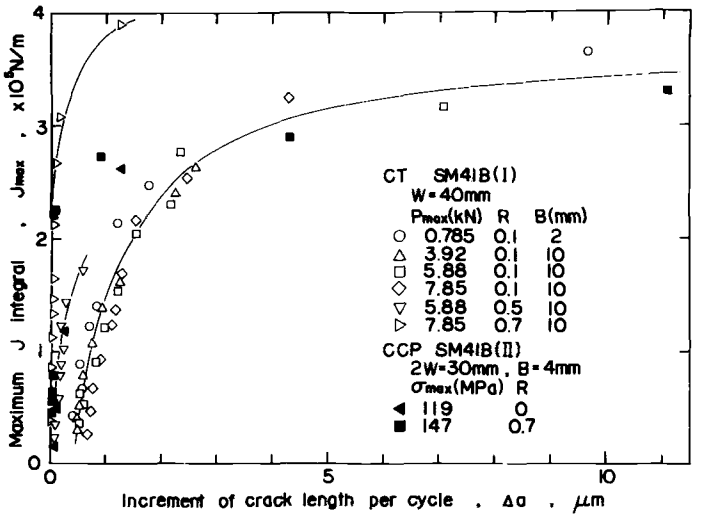

FIG. 8—*Fatigue crack growth resistance curve expressed in terms of J-integral.*

where v_{max}^{p} is the plastic component of the displacement at the maximum load and a is the current crack length. In this evaluation, the loading curve is assumed to be the dot-dash line OC shown in Fig. 5 and the maximum load does not agree with the actual value as in the method by McCabe [*19*]. Figure 9 indicates the relation between the crack length increment and ϕ_{max}, together with the data obtained in the fracture toughness test [*13,14*]. The onset of crack growth acceleration takes place at about $\phi_{max} = 2 \times 10^{-4}$ m, which is about the twice of the CTOD value at the crack initiation $\phi_i = 90$ μm. The general trend of each resistance curve expressed in terms of ϕ_{max} is similar to that expressed in terms of J_{max}. The differences in the critical parameters for fibrous crack growth between fatigue and static fracture obviously come from a direct result of ratcheting deformation. It is necessary to compare the near-tip deformation associated with the ratcheting process with the static to further clarify the differences.

Conclusions

1. The acceleration of crack growth rate, deviating from the stable relation between the rate and the J-integral range, was found to take place when the plastic yielding spread across the ligament of the specimen. Coincidently, the monotonic accumulation or ratcheting of extensional deformation of the specimen started. The onset of the acceleration is predictable by correlating the maximum load of cyclic applied loads to the limit load.

2. The crack growth acceleration at high cyclic stresses is attributed to two causes: the incomplete reversal of plastic deformation in ratcheting extension

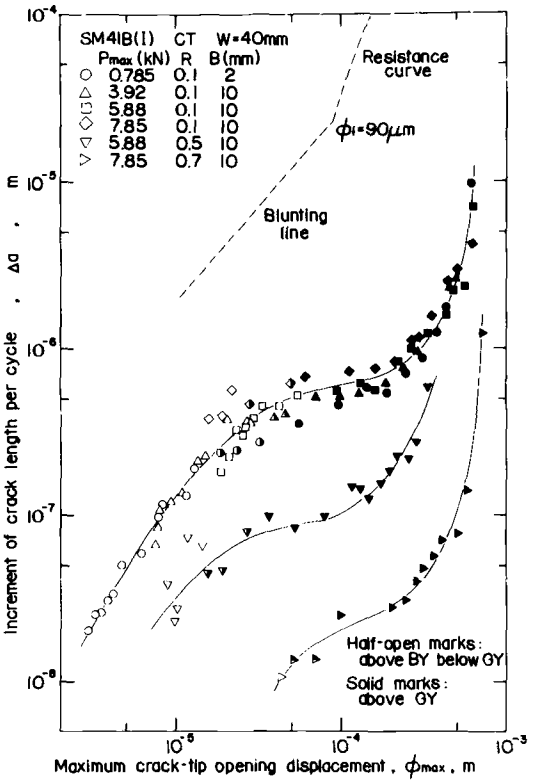

FIG. 9—*Crack length increment per cycle plotted against crack-tip opening displacement.*

and the inclusion of dimple mode fracture in crack growth. The upper bound of crack growth acceleration through the former mechanism is evaluated from the rate versus J-integral relation obtained in the stable growth region by considering the increase in crack-tip opening displacement due to the incomplete reversal of the plastic deformation of the specimen.

3. A crack growth resistance curve due to cyclic stresses was constructed where the maximum values of J-integral and the crack-tip opening displacement evaluated from the accumulated plastic deformation were used to express the resistance of the material. The onset of the inclusion of dimple mode fracture can be expressed in terms of the critical value of the maximum J-integral or the maximum crack-tip opening displacement.

References

[1] Dowling, N. E. and Begley, J. A. in *Mechanics of Crack Growth, ASTM STP 590*, American Society for Testing and Materials, 1976, pp. 82-103.

[2] Dowling, N. E. in *Cracks and Fracture, ASTM STP 601*, American Society for Testing and Materials, 1976, pp. 19-32.
[3] Dowling, N. E. in *Flaw Growth and Fracture, ASTM STP 631*, American Society for Testing and Materials, 1977, pp. 139-158.
[4] Taira, S., Tanaka, K., and Ogawa, S., *Journal of the Society of Materials Science* (Japan), Vol. 26, 1977, pp. 93-98.
[5] Hoshide, T., Tanaka, K., and Nakata, M., *Journal of the Society of Materials Science* (Japan), Vol. 31, 1982, pp. 566-572.
[6] Dowling, N. E. in *Cyclic Stress-Strain and Plastic Deformation Aspects of Fatigue Crack Growth, ASTM STP 637*, American Society for Testing and Materials, 1977, pp. 97-121.
[7] Tanaka, K., Hoshide, T., and Maekawa, O., *Engineering Fracture Mechanics*, Vol. 16, 1982, pp. 207-220.
[8] Hoshide, T. and Tanaka, K., *Transactions*, Japan Society of Mechanical Engineers, Vol. 48A, 1982, pp. 1102-1110.
[9] Clark, G. A. and Landes, J. D., *Journal of Testing and Evaluation*, Vol. 7, 1979, pp. 264-269.
[10] Rice, J. R., Paris, P. C., and Merkle, J. G. in *Progress in Flaw Growth and Fracture Toughness Testing, ASTM STP 536*, American Society for Testing and Materials, 1973, pp. 231-245.
[11] Kobayashi, H., Shibuya, E., and Nakazawa, H., *Journal of the Society of Materials Science* (Japan), Vol. 29, 1980, pp. 1049-1055.
[12] Paranjpe, S. A. and Banerjee, S., *Engineering Fracture Mechanics*, Vol. 11, 1979, pp. 43-53.
[13] Tanaka, K., Fujiyama, K., and Nakamura, K., *Journal of the Society of Materials Science* (Japan), Vol. 29, 1980, pp. 62-68.
[14] Tanaka, K., Fujiyama, K., Nakagawa, Y., Nakamura, K., and Kawabe, Y., *Journal of the Society of Materials Science* (Japan), Vol. 29, 1980, pp. 710-716.
[15] Rice, J. R. in *Fatigue Crack Propagation, ASTM STP 415*, American Society for Testing and Materials, 1967, pp. 247-311.
[16] Schwalbe, K. H., *Engineering Fracture Mechanics*, Vol. 11, 1979, pp. 331-342.
[17] Wilhem, D. P. and Ratwani, M. M., *Transactions*, American Society of Mechanical Engineers, *Journal of Engineering Materials and Technology*, Vol. 100, 1978, pp. 416-420.
[18] Barson, J. M. in *Damage Tolerance in Aircraft Structures, ASTM STP 486*, American Society for Testing and Materials, 1971, pp. 1-15.
[19] McCabe, D. E. in *Flaw Growth and Fracture, ASTM STP 631*, American Society for Testing and Materials, 1977, pp. 245-266.

John D. Landes[1] *and Donald E. McCabe*[1]

Load History Effects on the J_R-Curve

REFERENCE: Landes, J. D. and McCabe, D. E., **"Load History Effects on the J_R-Curve,"** *Elastic-Plastic Fracture: Second Symposium, Volume II—Fracture Resistance Curves and Engineering Applications, ASTM STP 803*, C. F. Shih and J. P. Gudas, Eds., American Society for Testing and Materials, 1983, pp. II-723-II-738.

ABSTRACT: The effect of load history on the J-Δa behavior of materials was studied under cyclic loading conditions. Two steels were studied, an HY-130 steel and a A508 Class 2 steel. The HY-130 steel showed little effect of the cyclic loading and the behavior was labeled "R-curve-dominated crack growth." The A508 Class 2 steel showed a significant effect of the cyclic loading and the behavior was labeled "cyclic-dominated crack growth."

KEY WORDS: fracture toughness, R-curve, cracks, crack growth, cyclic loading, J-integral, monotonic loading, elastic-plastic fracture

The application of fracture mechanics methods to the evaluation of structural integrity and life often uses the approach of determining the time required for a defect, growing in a subcritical manner, to reach a critical size whereupon the life of the component is terminated. For components subjected to cyclic loading the defect would grow in a fatigue mode until the fracture toughness of the material is reached, causing component failure [*1,2*].[2] The method for predicting the rate of fatigue crack growth in a fracture mechanics approach uses growth rate, da/dN, as a function applied stress-intensity range, ΔK, [*2,3*]. This approach has been widely documented and an ASTM standard test method has been developed [ASTM Test for Constant-Load-Amplitude Fatigue Crack Growth Rates Above 10^{-8} m/Cycle (E 647-81)].

Methods for determining fracture toughness have also been fully evaluated and several ASTM methods have been written to standardize testing. In the linear elastic plane-strain regime, K_{Ic} is used to measure initiation toughness

[1]Advisory scientist and senior engineer, respectively, Materials Engineering Department, Westinghouse R&D Center, 1310 Beulah Rd., Pittsburgh, Pa. 15235.

[2]The italic numbers in brackets refer to the list of references appended to this paper.

[ASTM Test for Plane-Strain Fracture Toughness of Metallic Materials (E 399-78a)]. Beyond the linear elastic regime, elastic-plastic test procedures have been developed to determine fracture toughness by J_{Ic} [Ref *4* and ASTM Determination of J_{Ic}, A Measure of Fracture Toughness (E 813-81)] and by R-curve techniques [*5,6*].

Although methods for measuring crack growth rate and fracture toughness have been developed independently, the approach oftentimes used involves combining the two to determine component life as if one is unaffected by the other. However, the success of the method has not been clearly demonstrated. Some studies in fact have indicated that this approach may not work [*7-9*] and have suggested that toughness measured by the ASTM test methods may be different from toughness that is developed when a cracked structure is cyclically loaded to failure.

These studies have been conducted predominantly within the linear elastic regime. However, a similar study is also needed for toughness values developed within an elastic-plastic framework. In this paper, toughness development under cyclic loading is discussed and some preliminary results for cyclic history effects are presented.

Linear Elastic Toughness

The difference in toughness values determined from a standard test procedure and those measured from cyclic loading to failure can be attributed to the manner in which a crack-like defect is developed in the toughness test specimen. Figure 1 shows schematically how this defect is developed for a

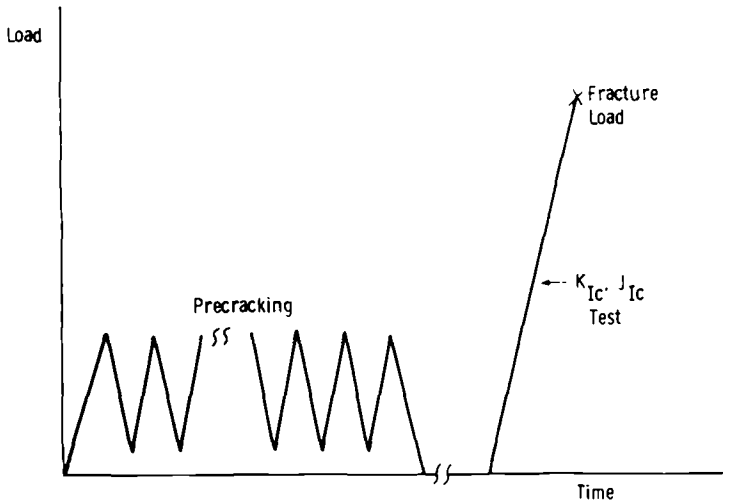

FIG. 1—*Typical fracture toughness test load history.*

toughness test. A notched specimen is subjected to low-level cyclic loads (or ΔK) until a crack of specified length is developed. The test specimen is then subjected to a monotonically increasing load, and fracture toughness is determined by a prescribed method. In all of the test procedures, the cyclic load levels must be much lower than the loads at which toughness is measured. (Methods E 399, E 813, and Ref *6*). If this requirement is not met, a consistent toughness value, taken to be a material property, cannot be guaranteed and the test result is judged to be invalid.

The load history that an actual cracked structural component might experience is not likely to be the same as that used for the toughness test specimen. In general the component may receive large cyclic loads, high level constant loads, and temperature and environment variations. The load history encountered in simply cycling a component to failure is different from the one used for the toughness test and a difference in toughness level could be possible.

Some examples of the effects of cycling a test specimen to failure are taken from the studies previously cited. Dowling [*7*] and Begley [*8*] studied the effect of cycling 7075-T651 aluminum specimens to failure, Fig. 2. For this material, the toughness developed under cyclic loading was identical to that developed under monotonic loading using the K_{Ic} test procedure.

In this same study, an ASTM A470 Class 8 chromium-molybdenum-vanadium (CrMoV) steel was cycled to failure, Fig. 3. In this case, the cyclic loading to failure increased the toughness considerably over that measured by the monotonically loaded K_{Ic} test. The result for this material was unexpected for two reasons. Not only was the toughness increased by cyclic loading to failure, but the fracture mode was changed. The A470 Class 8 steel is a high-temperature rotor steel. At room temperature, the K_{Ic} is relatively low and fracture always occurs by a cleavage mode. The fracture transition, where toughness increases greatly and the fracture mode changes a ductile tearing, occurs about 70 to 125 deg C above room temperature. The specimens cycled to failure at room temperature all failed by a plastic limit-load mechanism in a completely ductile mode. Although the testing conditions affecting this result are complex, it is noted here as an example of what can happen to toughness when a specimen is cycled to failure.

A third example is taken from the work of Troshchenko et al [*9*] as shown in Fig. 4 where two low-carbon construction steels were tested by monotonic and cyclic loading to failure. The result shows that there is a transition temperature shift under cyclic loading to lower toughness than that developed under monotonic loading.

The three examples in Figs. 2 through 4 show that toughness values developed under cyclic loading were higher, lower, or identical to toughness values developed by monotonic loading in the K_{Ic} test procedure. The conclusion taken from these results is that fracture toughness values determined by the K_{Ic} test procedure may not be the correct ones to use in the evaluation

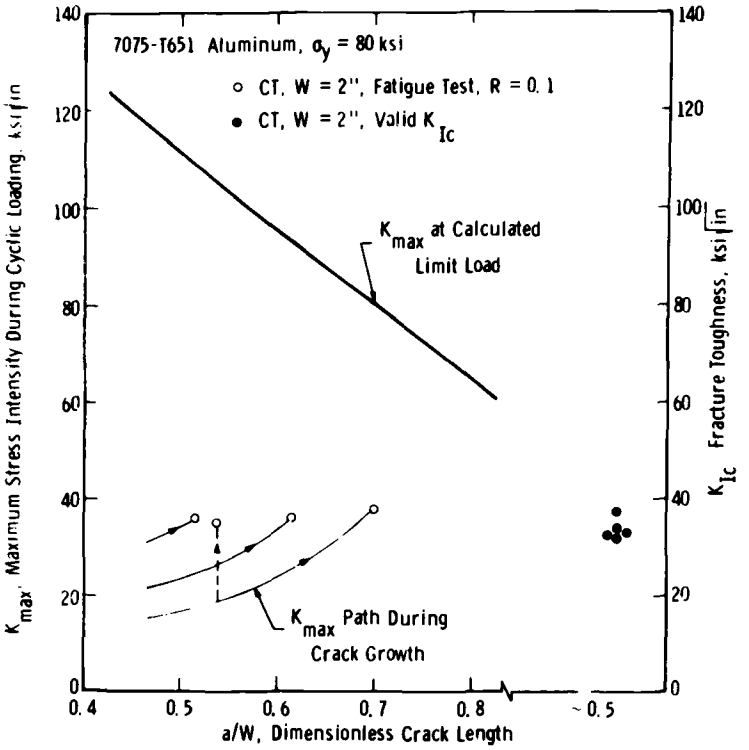

FIG. 2—*Fracture toughness failures terminating fatigue crack growth in 7075-T651 aluminum (Begley).*

of structural component life when that structure is cyclically loaded to failure. In addition, it is presently not possible to tell whether the correct toughness will be higher or lower than the measured toughness. The observations are somewhat discouraging because the procedure for evaluating component life by determining the number of cycles needed to grow a crack under fatigue to the K_{Ic}-value has been one of principal application techniques of a fracture mechanics analysis. Although this procedure may work for a number of examples, it may not work in every case.

Toughness-Crack Growth Behavior

The previous examples suggest that toughness measured in the elastic-plastic regime might also be affected by cyclic loading. Elastic-plastic toughness is often determined in an R-curve format where J is plotted as a function of ductile crack extension ([*4-6*] and Method E 813). R-curve behavior of materials is schematically illustrated in Fig. 5, showing how initiation toughness, J_{Ic}, values can be determined ([*4*] and E 813) as well as a

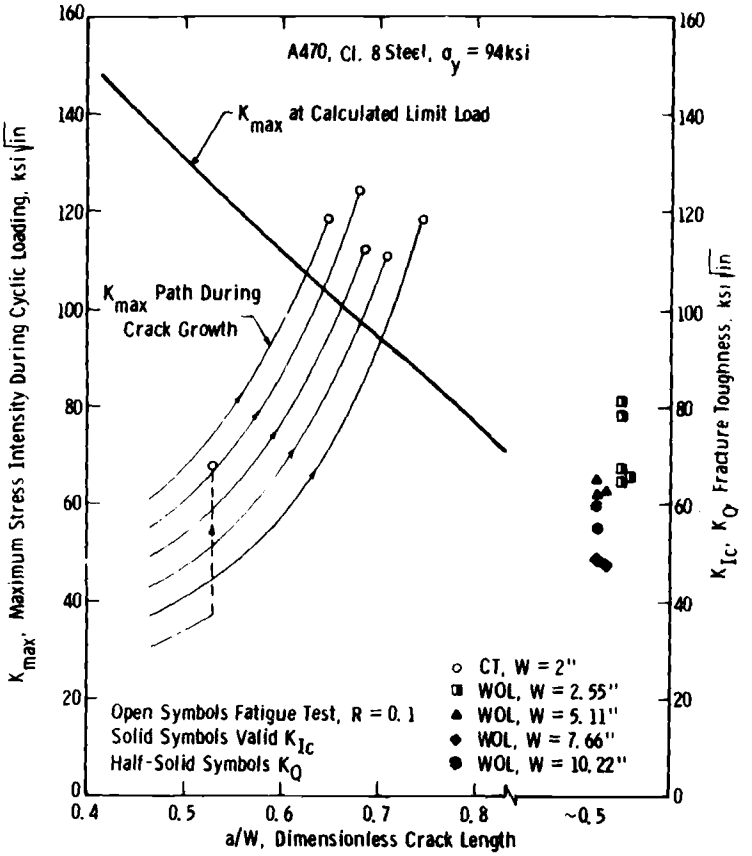

FIG. 3—*Unexpected fully plastic limit load failures following fatigue crack growth in A470 steel (Begley).*

material resistance to crack extension. These R-curves are developed by test procedures similar to the K_{Ic} test in that a crack is introduced into a notched specimen by cyclic loading at low levels and then the R-curve is developed by monotonically loading the specimen to much higher loads.

The question addressed in this work is, will crack growth be different if it is developed by cyclic loading rather than by monotonic loading? The rationale for developing a test procedure comes from an assumption of a crack at a notch subtended by a zone of plastic deformation, Fig. 6. If the remainder of the component is elastic, the boundary conditions placed on the plastic deformation zone will be displacement control. The test specimens should then be loaded in a manner where cyclic displacement is controlled rather than cyclic load.

An illustration of displacement-controlled cyclic loading which can be

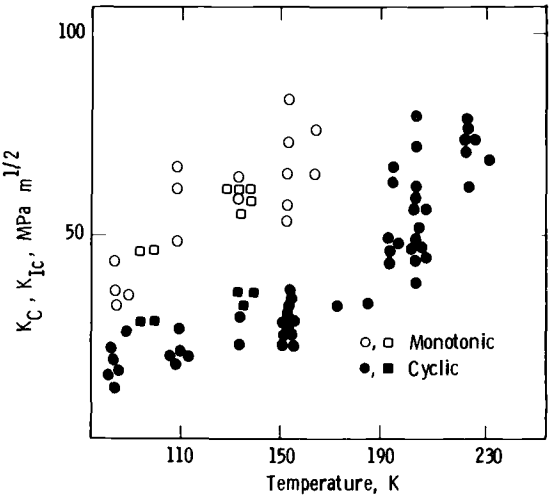

FIG. 4—K_{Ic} *versus temperature for two steels under cyclic and monotonic loading from Troshchenko et al [9].*

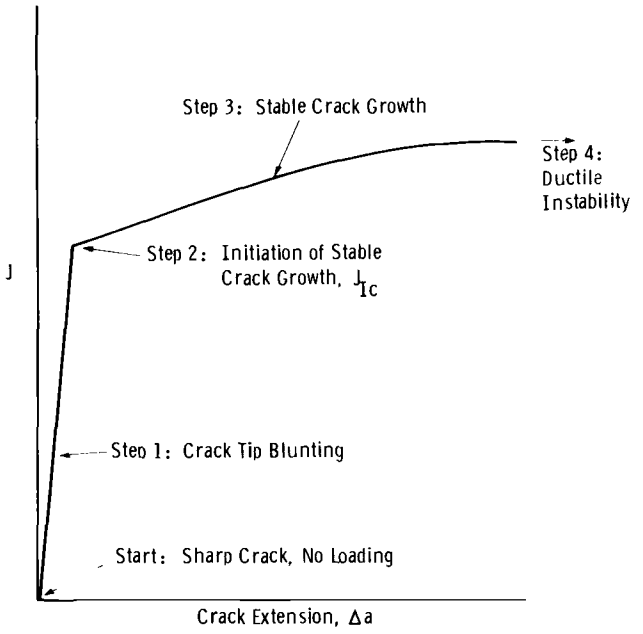

FIG. 5—*Four steps of ductile fracture process on an R-curve.*

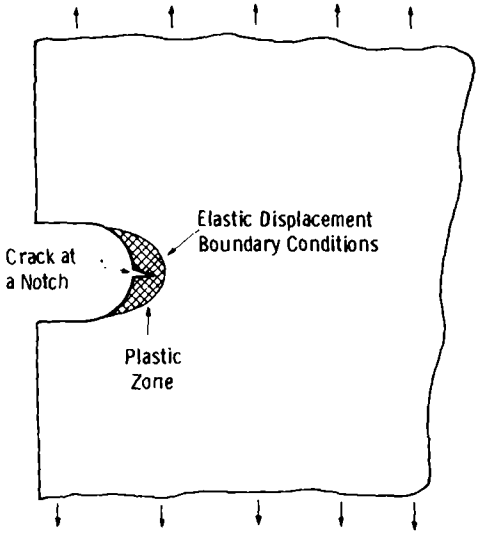

FIG. 6—*Schematic of a crack at a notch.*

used to generate crack growth is shown schematically in a load-versus-displacement record in Fig. 7. The specimen is loaded in displacement control into the plasticity range. At a prescribed displacement level, the specimen is then unloaded to a second prescribed displacement level (the example, shown in Fig. 7 is zero displacement). The specimen is then reloaded to a displacement level Δv_1 above that at the first load. It is then unloaded to Δv_2 above the displacement after the first unload. Continued cyclic loading is applied to the specimen by loading to controlled displacement increments Δv_1 and Δv_2.

Although the combinations of cyclic load history that can be applied to a specimen are numerous, a few possible examples are also illustrated in Fig. 7. If $\Delta v_1 = \Delta v_2$, a cyclic loop with a reasonably consistent size is applied to the specimen, and the type of cyclic loading is labeled "ratcheting crack" because the crack is forced open in progressively even cyclic steps. A second example is given where the first unload is to zero displacement and all succeeding unloads are to zero displacement ($\Delta v_2 = 0$). The crack is forced open to progressively larger displacements during each loading portion and then returned to zero displacement at each unload. This loading is labeled "elastic dominance" and illustrates a case where the elastic field would return the plastic displacement zone to its original position at each unload. Other control conditions could involve the displacement level for the first unload to be before J_{Ic} or after J_{Ic}.

Illustrations of actual cyclic load histories applied to specimens are shown

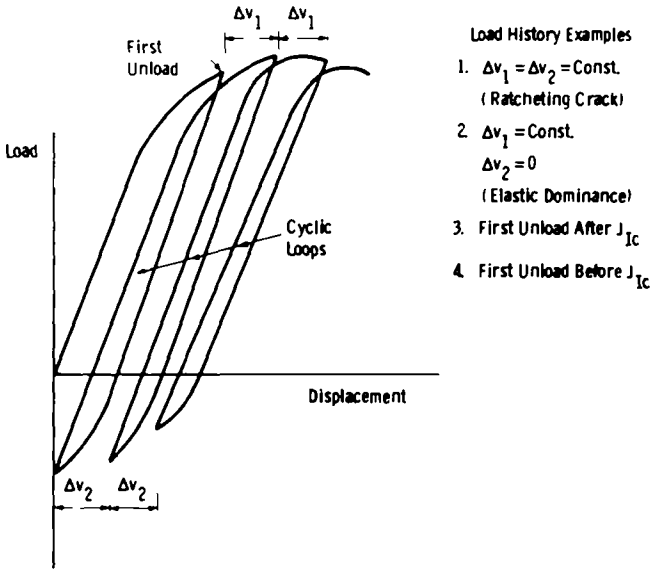

FIG. 7—*Schematic of load versus displacement for study of load history effect on the R-curve.*

in Fig. 8. Figure 8*a* shows the ratcheting crack where $\Delta v_1 = \Delta v_2$. Figure 8*b* shows elastic dominance where $\Delta v_2 = 0$. Figure 8c shows a ratcheting crack where the first unload is taken at a large displacement level well beyond J_{Ic}.

Analysis of Results

The results from these tests can be analyzed by two techniques. One method is to draw an envelope over the top of the cyclic loads so that a standard area approximations of J can be made. For this method, J is determined from the area under the curve to a given displacement level [*10*] and crack extension is determined at each unload from the elastic slope of the unload curve, Fig. 9 [*11*].

A second method of analysis is taken from the work of Dowling and Begley [*12*]. Each cyclic loop is treated individually. J is determined from the area under each loop. Crack extension is determined again from the unloading slopes, Fig. 10. (Note that a J for cyclic loading is operationally defined and may not be identical to the J-integral, which does not permit unloading).

From the first method of analysis, an R-curve can be developed. Crack extension should contain components from both the monotonic and cyclic loading portions. From the second analysis, crack extension per unload cycle, da/dN, can be determined as a function of the cyclic J, ΔJ. Again, crack growth should contain two components.

The J-versus-Δa behavior developed by the cyclic loading can be equal to

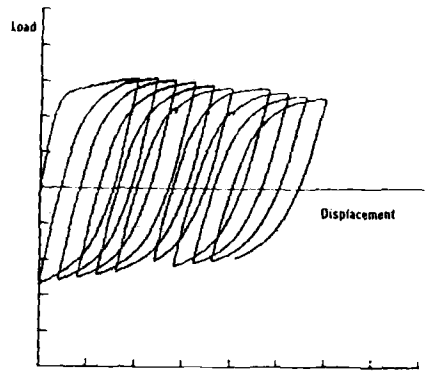

Ratcheting Crack, $\Delta v_1 = \Delta v_2 = \text{Constant}$

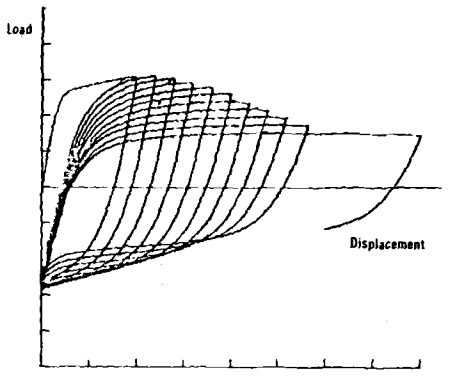

Elastic Dominance, $\Delta v_1 = \text{Constant}, \Delta v_2 = 0$

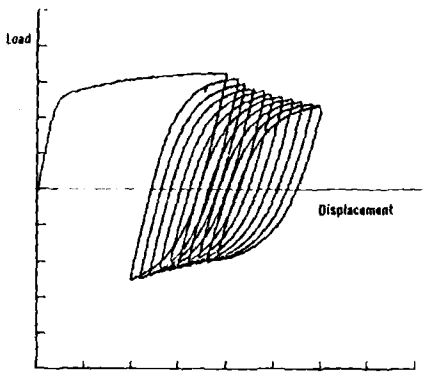

First Unload Beyond J_{IC}

FIG. 8—*Examples of load histories used for developing cyclic R-curves.*

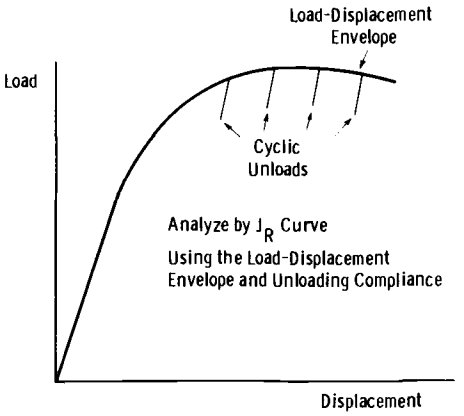

FIG. 9—*Load history effect—analysis by R-curve.*

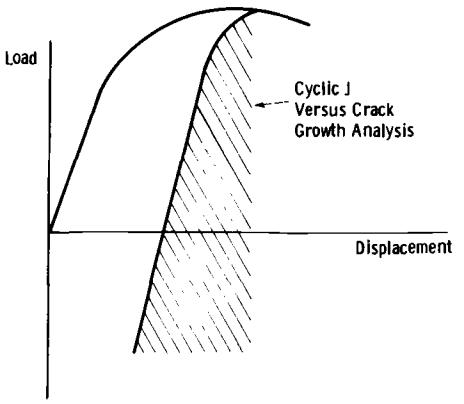

FIG. 10—*Load history effect—analysis by cyclic J.*

or lower than the one obtained from a similar specimen loaded monotonically. If a normal interaction of monotonic and cyclic loading contributions to crack extension is anticipated, the resultant curves could contain a linear summation of monotonic and cyclic components. This shown schematically in Fig. 11. If the interaction between monotonic and cyclic loading is coupled in a nonlinear way, this sample summation might not be correct and a different effect on the J-versus-Δa behavior could be observed.

Test Results

To study the effects of cyclic loading on crack growth behavior, two materials were selected for preliminary testing. The two materials, HY-130

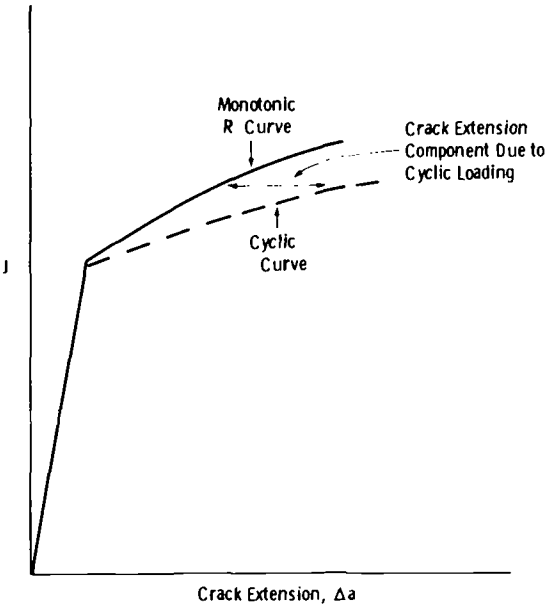

FIG. 11—*Schematic showing linear summation principle for developing a cyclic R-curve.*

steel and A508 Class 2 steel were chosen because numerous R-curves had been developed for these materials under the monotonic loading procedure in the J_{Ic} test standard (E 813). The HY-130 steel was used in a round-robin test program to study the J_{Ic} procedure [*13*]. The A508 Class 2 steel was used in a study of size effect on the R-curve [*14*].

Compact specimens of the IT-CT geometry were used in the cyclic tests. These have a specimen width of 50 mm (2 in.) and thickness of 25 mm (1 in.).

Loading conditions for these specimens are given in Table 1. For each material, two specimens were tested. Each was given a cyclic load history which was identified previously as the "ratcheting crack" case. The difference between the two specimens is the spacing of the cycles (Δv_1 and Δv_2) and hence

TABLE 1—*Cyclic R-curve test conditions—ratcheting crack.*

Material	Specimen No.	Displacement First Unload, in.	Cyclic Range, in.	Cycle Spacing, in.	Total Displacement, in.	Cycle No.
HY-130	1	0.035	0.035	0.005	0.100	13
HY-130	2	0.035	0.035	0.001	0.100	~70
A508 C1 2	94	0.060	0.060	0.010	0.200	13
A508 C1 2	92	0.100	0.060	0.002	0.250	~75

1 in. = 25.4 mm.

the total number of cycles applied. The first specimen for each material had cyclic spacing five times that of the second so the second had approximately five times as many cycles as the first to the final displacement level. The loading rate, which was essentially constant for all tests, was one which would result in a K of about 33 MPa$\sqrt{m}$/min (30 ksi$\sqrt{in.}$/min) during elastic loading.

The crack growth history resulting from the cyclic loads is shown in Fig. 12 for the HY-130 steel and in Fig. 13 for the A508 Class 2 steel. For these re-

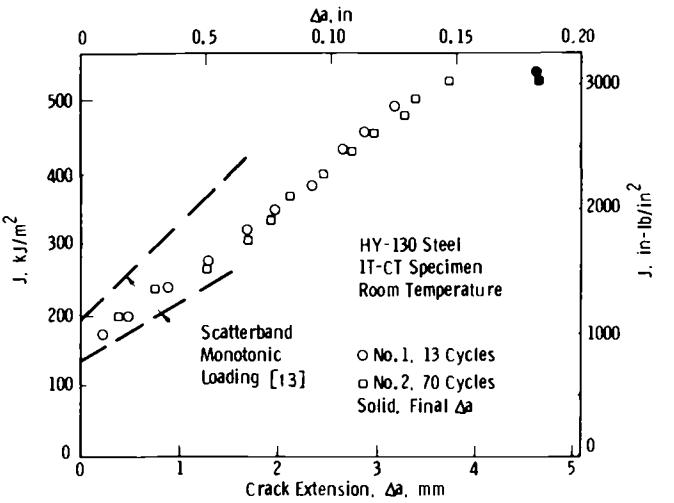

FIG. 12—J *versus* Δa *for HY-130 steel loaded cyclicly to develop the R-curve.*

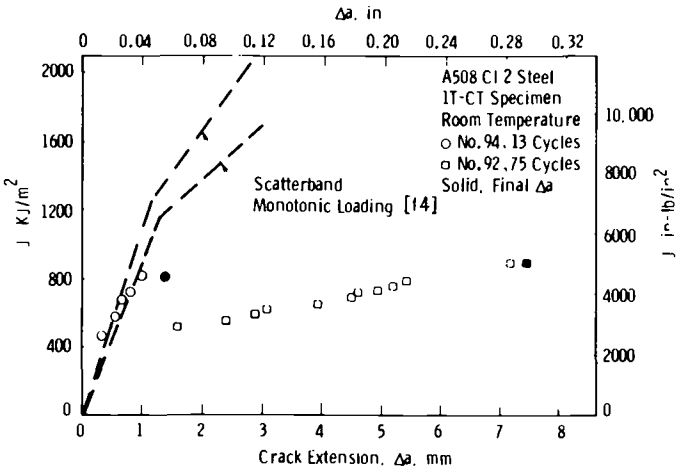

FIG. 13—J *versus* Δa *for A508 Class 2 steel loaded cyclicly to develop the R-curve.*

sults the first method of analysis was used. Each is compared with the scatterband for R-curves developed under monotonic loading. J calculations for the present results and those referenced in Figs. 12 and 13 were made using the formula in ASTM Method E 813.

The test data were also analyzed by the second method of analysis, which resulted in a da/dN-versus-ΔJ format. These results are given in Fig. 14 for the HY-130 steel and in Fig. 15 for the A508 Class 2a steel. In Fig. 14, previous results from da/dN-versus-ΔK fatigue crack growth rate data for HY-140 steel [*15*] were converted to a da/dN-versus-ΔJ format and plotted. These results did not cover the same ΔJ range as the specimens tested in this work so a linear extrapolation was shown for comparison.

An A533B steel was tested by Dowling in a da/dN-versus-ΔJ format to very large ΔJ-values [*16*]. This material is similar to A508 so the scatterband from Dowling's results on A533B is included in Fig. 15 for comparison.

Discussion of Results

The two different steels showed different responses to the cyclic loading. The results for the HY-130 steel in an R-curve format, Fig. 12, show almost

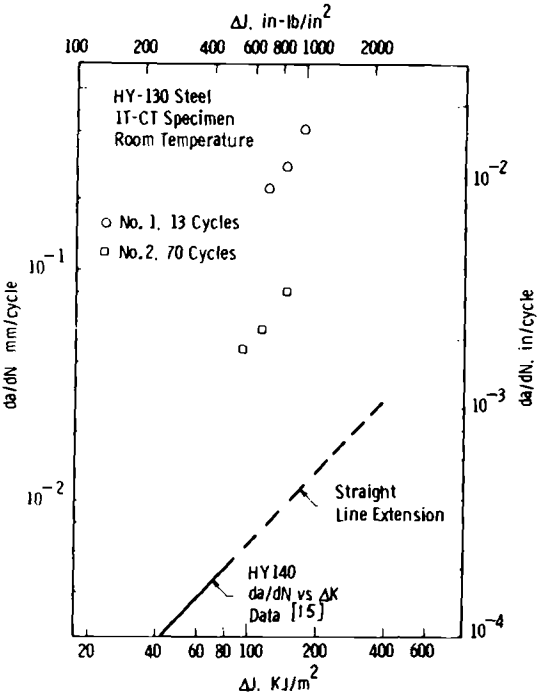

FIG. 14—da/dN *versus* ΔJ *for HY-130 steel loaded cyclicly compared with Ref* 15 da/dN *on HY-140.*

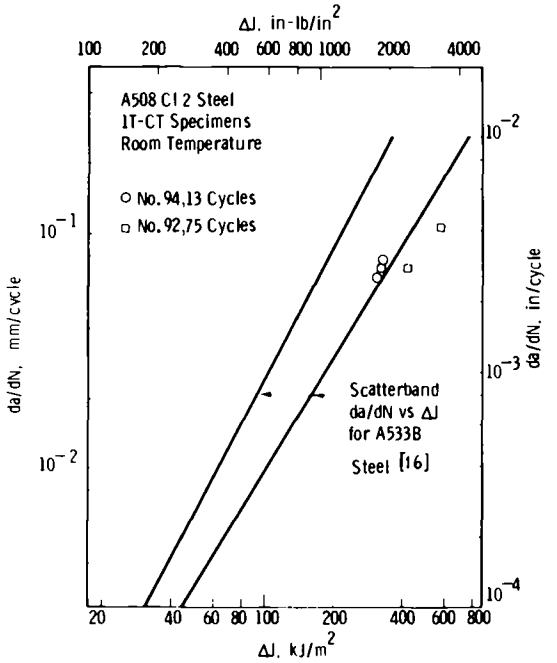

FIG. 15—da/dN *versus* ΔJ *for A508 Class 2 steel loaded cyclicly compared with Ref* 16 da/dN *on A533B.*

no influence of the cyclic loading. The results fall within the scatterband of the monotonic results and the R-curves for the two specimens are nearly identical. The results for the HY-130 steel in a *da/dN*-versus-ΔJ format, Fig. 14, show growth rates per cycle much higher than that expected from the extrapolated fatigue data. This again is evidence that at the chosen ΔJ levels, crack growth is caused mainly by the monotonic component rather than by the cyclic component. The behavior observed for this steel was labeled "R-curve-dominated crack growth."

A strong cyclic growth effect was observed for the A508 Class 2a steel. Figure 13 shows that the growth increments for the cyclically loaded A508 are much higher than that for the monotonic case. The specimen that had five times as many cycles at lower ΔJ had much more crack growth and did not follow monotonic behavior. Figure 15 shows that the resultant crack growth taken in a *da/dN*-versus-ΔJ format falls close to the scatterband of fatigue results for the A533 steel. This would suggest that the majority of crack growth came from the cyclic component of loading rather than the monotonic component. The behavior observed here was labeled "cyclic-dominated crack growth."

The linear summation model suggested for determining the influence of the cycle loading on the crack growth increments, Fig. 11, is demonstrated in

principle by these results; however, it did not result in a conclusive evaluation. For the HY-130 steel, the cyclic component contributed about one tenth of the total crack extension and the monotonic component about nine tenths. In the 4 mm (0.16 in.) of total crack extension, the contribution of the cyclic loading should be about 0.4 mm (0.016 in.). This is not a large enough component to influence the matchup to the R-curve behavior noticeably since the monotonic R-curve scatterband is about 1 mm (0.04 in.).

For the A508 Class 2 steel, the cyclic component of growth in the first specimen was about equal to the monotonic component and in the second specimen it was about ten times the monotonic component. In both cases this result is approximately observed. In the first specimen there was not enough crack extension to make a positive comparison and in the second specimen the crack extension was nearly all due to cyclic loading. Therefore, these results would verify a principle of linear summation of crack extensions only for the limiting cases.

The difference in behavior between the two steels is likely due to the relationship between the size of the cyclic loops and the overall monotonic toughness. The HY-130 steel has much lower R-curve toughness than the A508 Class 2a steel. The cyclic loops for the HY-130 were initiated at about J_{Ic} whereas for the A508 they were initiated well below J_{Ic}. The monotonic component of crack extension would develop more readily in the HY-130 steel. In the A508 Class 2 steel, the cyclic loops were larger. Therefore, it is reasonable that the HY-130 steel would have "R-curve-dominated crack growth" whereas the A508 Class 2a steel had "cyclic-dominated crack growth." The tests conducted here were to observe what types of behavior might result from cyclic loading. To develop a full understanding of the factors which control in this behavior, a greater number of tests with a larger combination of loading variables would be required.

Summary

This work studied the effect of load history on the J-Δa behavior of materials under cycle loading conditions where loading conditions were well into the elastic-plastic regime.

Results for an HY-130 steel cycled to develop ΔJ versus Δa_p show little effect of the cyclic loading. The crack extension is developed primarily from the monotonic loading component and the behavior is labeled "R-curve-dominated crack growth."

Results for an A508 Class 2 steel showed that the cyclic loading tended to dominate the crack growth rate. This behavior is labeled "cyclic-dominated crack growth."

To fully determine the effects of cyclic loading on crack growth rates, many more cases including different combinations of loading variables would be required.

References

[1] Clark, W. G., Jr., *Journal of Engineering for Industry, Transactions*, American Society of Mechanical Engineers, Feb. 1972.

[2] Clark, W. G., Jr., *Experimental Mechanics*, Vol. 11, Sept. 1971, p. 421.

[3] Paris, P. C. and Erdogan, F., *Journal of Basic Engineering*, Sept. 1963, p. 528.

[4] Clarke, G. A. et al, *Journal of Testing and Evaluation*, Vol. 7, No. 1, Jan. 1979, pp. 49-56.

[5] Landes, J. D. and Begley, J. A. in *Developments in Fracture Mechanics Test Methods Standardization, ASTM STP 632*, W. F. Brown, Jr. and J. G. Kaufman, Eds., American Society for Testing and Materials, 1977, pp. 57-81.

[6] Gudas, J. P., "Results of the J-Integral R-Curve Round Robin Program," presented at the Second ASTM Symposium on Elastic-Plastic Fracture, Philadelphia, Pa., 6-9 Oct. 1981.

[7] Dowling, N. E. in *Flaw Growth and Fracture. ASTM STP 631*, American Society for Testing and Materials, 1977, pp. 139-158.

[8] Begley, J. A., unpublished results, Westinghouse R&D Center, Pittsburgh, Pa., 1972.

[9] Troshchenko, V. T., Pokrovsky, V. V., and Prokopenko, A. V. in *Proceedings*, Fourth International Conference on Fracture, Waterloo, Ont., Canada, Vol. 3, June 1977.

[10] Rice, J. R., Paris, P. C., and Merkle, J. G. in *Progress in Flaw Growth and Fracture Toughness Testing, ASTM STP 536*, American Society for Testing and Materials, 1973, pp. 231-245.

[11] Clarke, G. A., Andrews, W. R., Paris, P. C., and Schmidt, D. W. in *Mechanics of Crack Growth, ASTM STP 590*, American Society for Testing and Materials, 1976, pp. 27-42.

[12] Dowling, N. E. and Begley, J. A. in *Mechanics of Crack Growth, ASTM STP 590*, American Society for Testing and Materials, 1976, pp. 83-104.

[13] Clarke, G. A., Landes, J. D., and Begley, J. A., *Journal of Testing and Evaluation*, Vol. 8, No. 5, Sept. 1980, pp. 221-232.

[14] Clarke, G. A., "An Evaluation of the Unloading Compliance Procedure for J Integral Testing in the Hot Cell," Final Report to Oak Ridge National Laboratories on Contract No. 7395, Oak Ridge, Tenn., 18 July 1979.

[15] Clark, W. G., Jr. and Kim, D. S., *Engineering Fracture Mechanics*, Vol. 4, 1972, pp. 499-510.

[16] Dowling, N. E. in *Cracks and Fracture. ASTM STP 601*, American Society for Testing and Materials, 1976, pp. 19-32.

William P. A. Belcher[1] *and Stephen G. Druce*[2]

Micromechanisms of Ductile Stable Crack Growth in Nuclear Pressure Vessel Steels

REFERENCE: Belcher, W. P. A. and Druce, Stephen G., **"Micromechanisms of Ductile Stable Crack Growth in Nuclear Pressure Vessel Steels,"** *Elastic-Plastic Fracture: Second Symposium, Volume II—Fracture Resistance Curves and Engineering Applications, ASTM STP 803*, C. F. Shih and J. P. Gudas, Eds., American Society for Testing and Materials, 1983, pp. II-739–II-762.

ABSTRACT: The objective of this work was to investigate the relationship between the micromechanisms of ductile crack growth, the microstructural constituent phases present in nuclear pressure vessel steel, and the observed fracture behavior as determined by impact and fracture mechanics tests.

Results from a microstructural and mechanical property comparison of an A508 Class 3 pressurized water reactor nozzle forging cutout and a 150-mm-thick A533B Class 1 plate are reported. The variation of upper-shelf toughness between the two steels and its orientation sensitivity are discussed on the basis of inclusion and precipitate distributions. Inclusion clusters in A533B, deformed to elongated disks in the rolling plane, have a profound effect on short transverse fracture properties.

Data derived using the multi-specimen J-integral method to characterize the initiation of ductile crack extension and resistance to stable crack growth are compared with equivalent Charpy results. Results of the J_R-curve analyses indicate (1) that the A533B short transverse crack growth resistance is approximately half that observed from transverse and longitudinal specimen orientations, and (2) that the A508 initiation toughness and resistance to stable crack growth are insensitive to position through the forging wall, and are higher than exhibited by A533B at any orientation in the midthickness position.

KEY WORDS: elastic-plastic fracture, J-integral fracture mechanics, crack growth tearing resistance, inclusions, steels, crack initiation toughness

Pressurized water reactor (PWR) vessels are constructed from thick-section, medium-yield-strength ferritic steels [*1,2*].[3] To ensure adequate tol-

[1]Metallurgist, National Nuclear Corporation, Ltd., Whetstone, Leicester LE8 3LH, U.K.; attached to AERE Harwell for duration of this work.

[2]Senior scientific officer, Atomic Energy Research Establishment, Harwell, Oxfordshire OX11 ORA, U.K.

[3]The italic numbers in brackets refer to the list of references appended to this paper.

erance to postulated defects under normal reactor operation and faulted conditions, these materials must exhibit a high resistance to ductile crack growth. Traditionally, this resistance has been assessed using notched impact testing, and much of our understanding of the microstructural control of ductile fracture in steels has come from this type of test. In particular, the inverse relationship between inclusion content (sulphides + oxides) and upper-shelf (that is, totally ductile) fracture energy has long been recognized. Several models of ductile fracture based on ductile void initiation and growth around inclusions have been proposed [*3–8*]. These rarely give close agreement with experimental data for the orientation dependence of toughness from materials where more than one species of inclusions are present, or where inclusions exist with a wide size distribution or are highly elongated.

Over the past 15 years there have been advances in both material fabrication and toughness assessment techniques. Secondary steelmaking and vacuum deoxidation now provide steels with low inclusion content and bulk sulfur levels less than 0.010 percent by weight [*9,10*]. Fracture mechanics has evolved to embrace quantitative defect assessment, where fracture is preceded by large-scale plasticity [*11*]. The J-integral test [*12*] is the most developed of the post-yield fracture tests and is capable of quantifying changes in material resistance during the initial stages of crack extension. In view of these developments, the work reported here was instigated to examine the relationships between the micromechanisms of ductile crack growth, the microstructural constituent phases present in modern pressure vessel steels, and their fracture behavior as determined by impact and J-integral fracture mechanics tests. The aim of the work is to improve our understanding of how material composition, steelmaking, and fabrication procedures can be optimized with respect to resistance to ductile crack growth.

Materials and Specimen Details

The A533B steel was supplied as a commercially produced, 150-mm-thick plate in a quenched-and-tempered condition, satisfying Class 1 of the appropriate American Society of Mechanical Engineers/American Society for Testing and Materials (ASME/ASTM) material specifications, and subsequently given a simulated post-weld heat treatment (PWHT). The chemical composition of the plate at surface and center positions is given in Table 1. A more detailed analysis of the through-thickness variation of principal alloying element and impurity concentrations is reported elsewhere [*13*].

The A508 Class 3 steel originated from a 500-ton ingot, which was subsequently forged into an integral nozzle and flange section for a PWR [*14*]. The material examined was from a coolant nozzle cutout subjected to the same heat-treatment conditions as the thick section (545 mm) quenched-and-tempered, post-weld heat-treated forging. Table 1 contains chemical composition data from the inner forging wall, midthickness, and outer-wall posi-

TABLE 1—*Chemical composition of the A533B Class 1 and A508 Class 3 steels.*

Material	Position	Composition								
		C	Mn	Ni	Mo	S	P	Cr	Si	Al
A533B Class 1	plate surface	0.18	1.43	0.57	0.48	0.005	0.005	0.11	0.30	0.03
	plate center	0.21	1.43	0.59	0.48	0.005	0.005	0.11	0.22	0.03
A508 Class 3	inner-wall (IW)	0.23	1.49	0.79	0.49	0.004	0.006	0.08	0.30	0.02
	midthickness (½ W)	0.19	1.43	0.75	0.47	0.002	0.006	0.08	0.29	0.03
	outer wall (OW)	0.19	1.43	0.76	0.47	0.001	0.006	0.08	0.30	0.03

tions. Tensile properties of the A533B and A508 materials tested at 290°C are given in Table 2.

Full size (that is, 10 mm thick) Charpy specimens were machined from the midthickness position of the plate and forging, in six orientations with respect to the three principal hot working directions. Each orientation is subsequently referred to by a two letter code, the first being the direction normal to the macroscopic fracture plane and the second being the direction of propagation. A specific crack plane is referred to by the direction perpendicular to that plane. The principal working directions for plate and forging are shown in the legend to Fig. 1.

Compact specimens 25 mm thick were machined from (1) the A533B material at the midthickness (½T) position in four different orientations, RW, WR, WT, and TW; and (2) the A508 material at the inner-wall (IW) midthickness (½W) and outer-wall (OW) positions in one orientation, *ar*.

Experimental Procedure

Charpy V-Notch Impact Testing

Charpy V-notch impact testing was performed between −125 and +300°C using a 300-J machine complying with the ASTM Specifications for Notched Bar Impact Testing of Metallic Materials (E23-72).

J-*Testing*

J-testing was performed at 290 ± 2°C using a 100-kN servohydraulic mechanical testing machine, operating under displacement control with a constant ram speed of 1 mm/min, using specimens precracked at room temperature to a final crack length-to-width ratio of 0.55. During each test, load, ram displacement, and load-line displacement were recorded on a multichannel recorder and a plot of load versus load-line displacement simultaneously produced. The experimental and analytical procedure, ASTM E 813-81, for cal-

TABLE 2—*Tensile properties of the A533B Class 1 and A508 Class 3 steels at 290°C.*

Material	Position	Yield Stress, σ_y MPa	Ultimate Tensile Strength, MPa	Elongation, %	σ_{flow},[a] MPa
A533B Class 1[b]	mean of 1/5T, 1/2T, 4/5T	399	545	20	472
A508 Class 3[c]	inner wall (IW)	470	650	22	560
	midthickness (1/2W)	390	550	24	470
	outer wall (OW)	390	560	20	475

[a] $\sigma_{flow} = \left(\frac{0.2\ \%\ \text{proof stress} + \text{ultimate tensile strength}}{2} \right)$.

[b] Longitudinal orientation.

[c] Orientation equivalent to A533B.

culating J and measuring the average ductile crack extension, Δa, was adopted. As is usual in these tests, a small but acceptable amount of crack tunneling was observed for both materials. Five to nine specimens, strained to varying levels of load-point displacement, were used to construct each resistance curve up to a maximum crack extension of 2.5 mm.

Measurements of the critical stretch zone width, $(SZW)_c$, prior to crack extension were obtained from the A533B TW-orientation midthickness and A508 *ar*-orientation outer-wall specimens, using a stereomicroscope.

Fractography

Fracture surfaces of compact specimens and Charpy specimens tested at 290°C were studied predominantly using a scanning electron microscope (SEM). Carbon extraction replicas, taken from Charpy specimens, were prepared for examination at higher magnification in an analytical transmission electron microscope (TEM) equipped with microdiffraction and energy-dispersive X-ray analysis (EDX) facilities.

Results

Mechanical Testing

Figure 1 shows the Charpy impact fracture energy data for the A533B Class 1 and A508 Class 3 materials.

J-integral data for small amounts of crack growth may be displayed and analyzed in several ways. The ASTM Standard Method for the Determination of J_{Ic} (E 813-81) requires a linear regression through data points displayed on linear axes of J versus Δa, with the initiation toughness, J_{Ic}, being defined as the intersection of the regression line with a blunting line given as $J = 2\sigma_{flow}\ \Delta a$, where σ_{flow} is defined as the average of the 0.2 percent proof stress and the

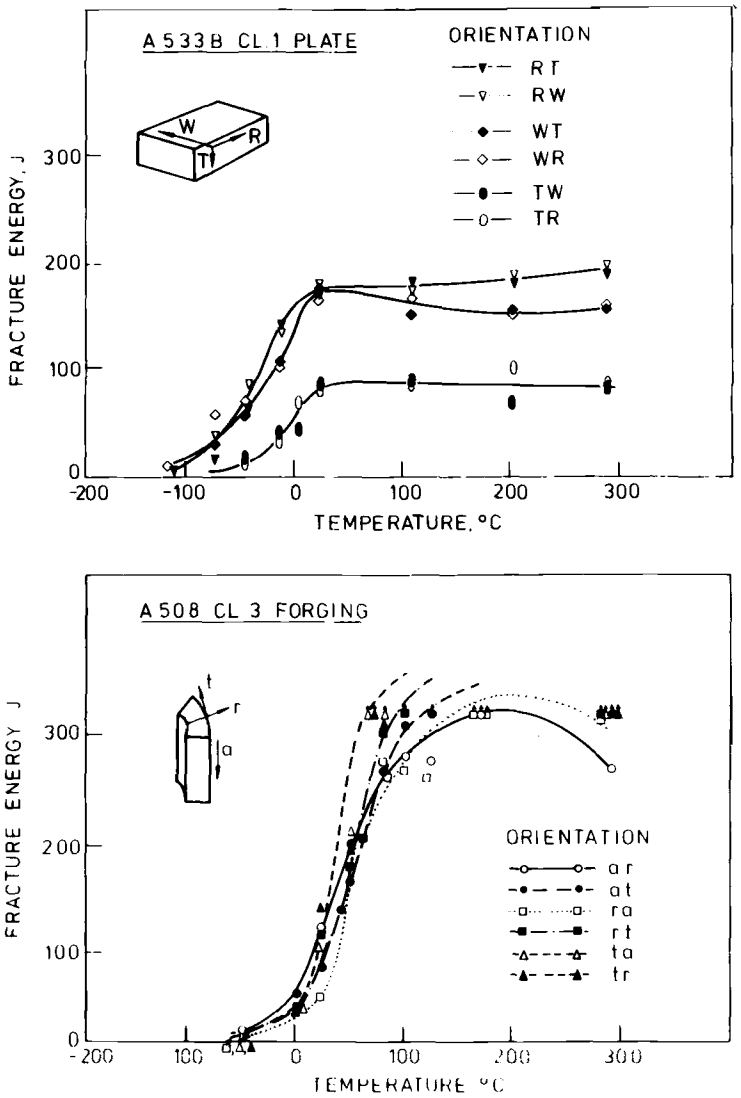

FIG. 1—*Charpy fracture energy data for A533B Class 1 and A508 Class 3 steel.*

ultimate tensile strength. Figures 2 and 3 show the data for A533B and A508, respectively, displayed in this format. The specimen thickness criterion of 25 J_{Ic}/σ_{flow}, given in E 813-81, was satisfied for all material conditions tested. Actual measurements of the $(SZW)_c$ were 0.07 and 0.10 mm for the A533B TW-orientation and the A508 OW-specimens, respectively, indicating that the $2\sigma_{flow}\,\Delta a$ blunting line overestimates stretch zone formation in these materials, with the result that J_{Ic} includes a small but significant amount of stable crack

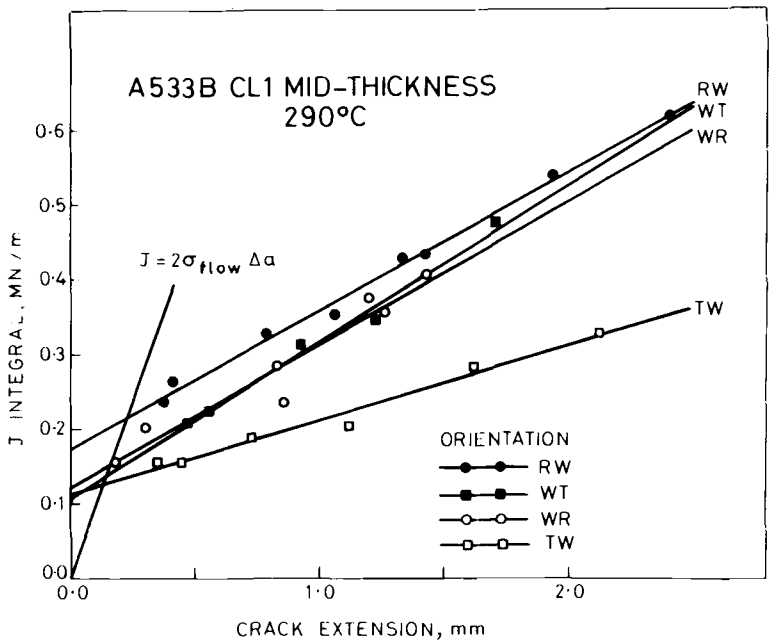

FIG. 2—J *versus* Δa *data for A533B tested at 290°C.*

growth. An alternative procedure for defining initiation, avoiding the use of a blunting line, is to extrapolate the linear regression to zero crack extension. Values of initiation toughness, defined either as the intersection with the $2\sigma_{flow}$ Δa blunting line, $J_{2\sigma_{flow}\Delta a}$, or alternatively as the extrapolation to zero crack growth, $J_{\Delta a=0}$, are given in Table 3, together with the slope of the linear regression lines and the standard errors in determinations.

Neither of the foregoing procedures accounts for the nonlinear J versus Δa behavior often found at small values of crack extension, typically below 1 mm [*15,16*]. An alternative procedure is to fit each set of data to a power-law function of the form $J = m(\Delta a)^p$, m and p being constants, and report values of J and tearing resistance, dJ/da, at specific increments of crack extension. Table 4 gives the results of this type of analysis procedure at values of 0.15, 0.5, 1.0, and 2.0-mm crack extension. A comparison of the regression coefficients led to the suggestion that both the linear and power-law curve-fitting procedures provide equally good interpretations for the test data presented, reflecting the absence of data points at very low values of ductile crack extension.

Fractography

A533B Class 1—All fracture surfaces of A533B showed a ductile, dimpled topography. As shown in Fig. 4, the fracture morphology in the T crack

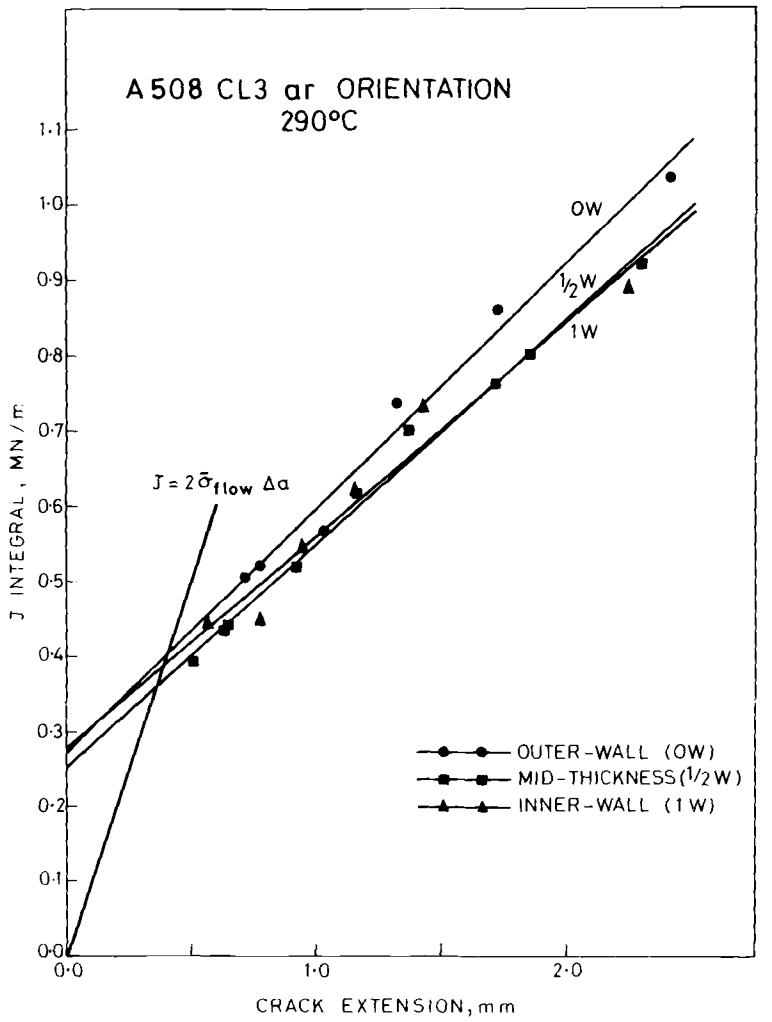

FIG. 3—J *versus* Δa *data for A508 tested at 290°C.*

plane was characterized by a stepped appearance resulting from isolated islands, comprising large shallow dimples, interconnected by walls of small dimples. Each island was associated with a cluster of either Type II manganese sulfide (MnS) inclusions, or calcium and magnesium aluminate inclusions of composition (Ca-Mg) $0.6Al_2O_3$. Quantitative analysis suggested that ~30 percent of the TW fracture surface consisted of inclusion cluster islands, which had a mean aspect ratio of 2:1, being elongated in the rolling direction, and average maximum and minimum semi-axes of 200 and 100 μm, respectively.

A marked variation in fracture surface topography was observed between

TABLE 3—*Linear regression analysis of J-integral data.*

Material	Orientation	Position	$J_{\Delta a=0}$, MNm^{-1}	$J_{2\sigma_{flow}\Delta a}$, MNm^{-1}	Standard Error of Intercept, MNm^{-1}	dJ/da, MNm^{-1}/mm	Standard Error of Slope, MNm^{-1}/mm
A533B	RW	½T	0.17	0.22	0.008	0.18	0.005
A533B	WT	½T	0.11	0.14	0.015	0.21	0.014
A533B	WR	½T	0.12	0.15	0.023	0.19	0.023
A533B	TW	½T	0.11	0.13	0.010	0.10	0.008
A508	*ar*	1W	0.28	0.37	0.038	0.28	0.029
A508	*ar*	½W	0.25	0.37	0.028	0.30	0.021
A508	*ar*	OW	0.27	0.41	0.033	0.33	0.022

TW and the other orientations, WT, WR, and RW. Figure 5 shows representative areas of the ductile crack extension in compact specimens with the three principal fracture planes. No inclusion islands are present in the specimens with W and R crack planes. Instead, the fracture surfaces are characterized by the presence of elongated dimples of high aspect ratio, extending parallel to the crack propagation direction in the RW orientation and perpendicular to this direction in the WT orientation. Figure 6 shows elongated dimples formed both at MnS and aluminate inclusions on the WT Charpy fracture surface. Elongated dimples, which could be identified as having formed at aluminate inclusions, were predominantly wider than those associated with MnS. In addition, as illustrated in Fig. 7, the RW fracture surface showed deep circular dimples associated with MnS stringer inclusions oriented perpendicular to the fracture plane.

The area occupied by large dimples on RW, WR, and WT fracture surfaces was noticeably smaller than for the TW orientation. The remaining area in all cases was populated by small dimples, 1 to 20 μm in diameter, which exhibited a more equiaxed morphology in R and W fracture planes than found for the T fracture plane.

Voids, which had opened up ahead of the propagating ductile crack at aluminate or MnS cluster inclusions and coalesced to form a large island-type void, were observed in the cleavage region of fracture surfaces of TW orientation compact specimens. Examples are shown in Fig. 8. The cleavage fracture was produced at low temperatures following the J-integral tests.

A508 Class 3—Compared with the A533B steel, Charpy specimens of all orientations in the A508 steel exhibited greater macroscopic shear lip formation, with a tendency for the ductile crack to bifurcate and propagate in two directions before finally fracturing along one of these directions. Furthermore, the degree of shear lip and crack bifurcation increased on going from the *a* to the *r* to the *t* fracture plane.

At higher magnifications, fracture surfaces showed a wide range of dimple sizes. No large elongated dimples were observed; instead, the larger dimples

TABLE 4—*Power-law regression analysis of J-integral data.*

			Δa, mm							
			0.15		0.5		1.0		2.0	
Material	Orientation	Position	J, MNm^{-1}	dJ/da, MNm^{-1}/mm	J, MNm^{-1}	dJ/da, MNm^{-1}/mm	J, MNm^{-1}	dJ/da, MNm^{-1}/mm	J, MNm^{-1}	dJ/da, MNm^{-1}/mm
A533B	RW	½T	0.15	0.49	0.27	0.26	0.38	0.18	0.53	0.13
A533B	WR	½T	0.14	0.40	0.24	0.20	0.32	0.14	0.43	0.09
A533B	WT	½T	0.10	0.41	0.21	0.26	0.32	0.20	0.50	0.15
A533B	TW	½T	0.10	0.28	0.17	0.14	0.22	0.09	0.30	0.06
A508	*ar*	1W	0.20	0.74	0.39	0.44	0.57	0.32	0.84	0.24
A508	*ar*	½W	0.19	0.73	0.38	0.44	0.57	0.33	0.85	0.25
A508	*ar*	OW	0.19	0.77	0.39	0.49	0.61	0.37	0.93	0.29

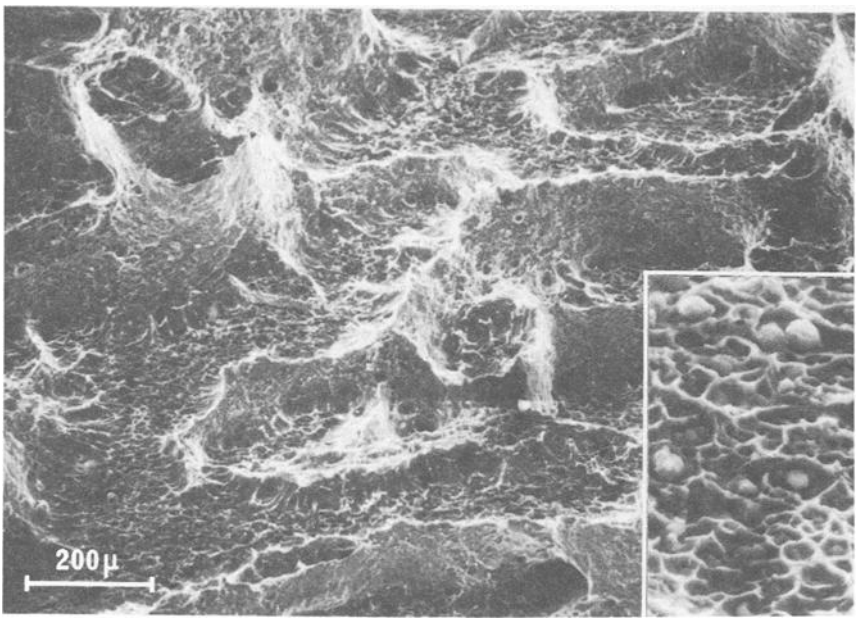

FIG. 4—*Fracture surface of A533B TW orientation showing islands of shallow dimples interconnected by walls of small dimples. Insert shows inclusions and individual voids in shallow dimples at higher magnification.*

were predominantly equiaxed and rarely >100 μm in diameter, as illustrated in Fig. 9. These were associated with MnS inclusions. As a result, compared with the A533B, the A508 specimen fracture surfaces were covered with a significantly increased proportion of medium and small-sized dimples. There appeared to be little difference in dimple characteristics either as a function of Charpy specimen orientation or compact specimen positioning in the through-thickness direction of the forging.

Extraction Replicas

Results from a micro-analytical examination of the submicron precipitates, which initiate the very small dimples (~ 1 μm) on the A508 and A533B Charpy fracture surfaces, suggest that dimples form principally at Fe_3C particles in A508 and at A*l*N/Mo_2C particle aggregates in A533B. Insufficient data have been gathered to attach statistical significance to this result, but a noticeable trend exists. Figure 10 shows small, shear dimples from the A533B, TW orientation fracture surface, each containing a submicron precipitate identified by EDX as either Mo_2C, A*l*N, or an A*l*N/Mo_2C aggregate.

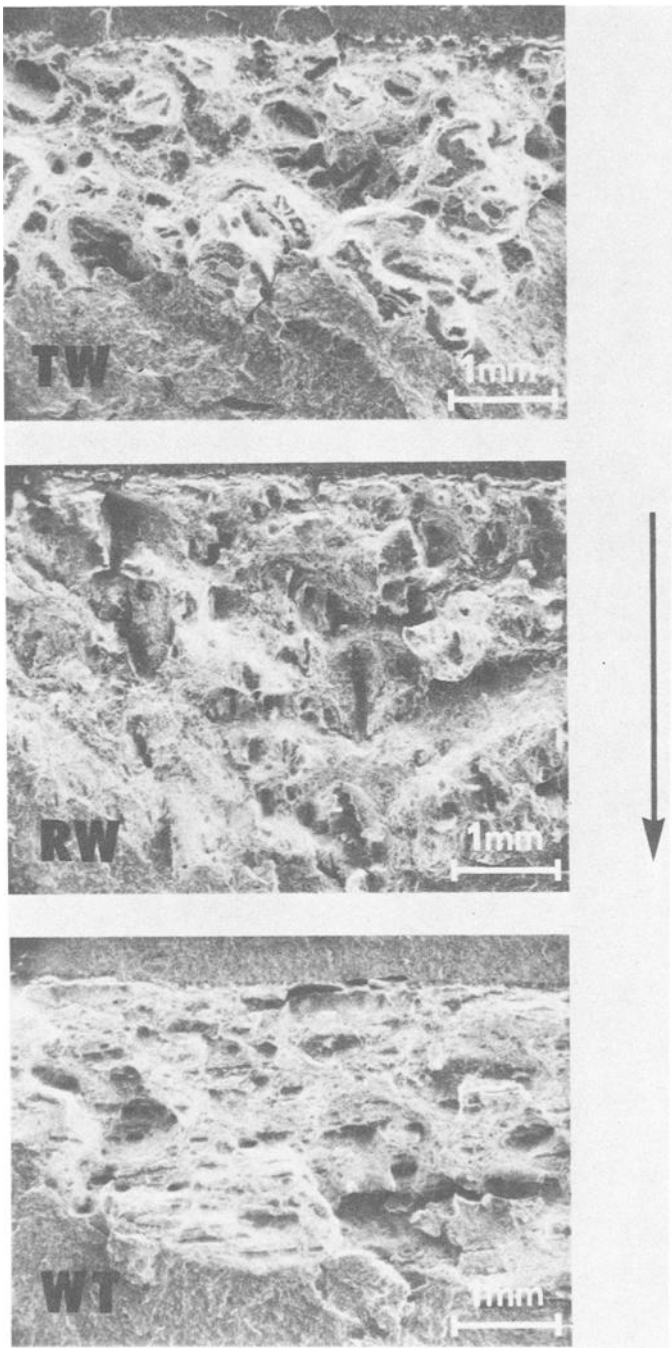

FIG. 5—*Comparison of A533B CT fracture surfaces with T, R, and W fracture planes. Direction of crack growth is indicated by arrow.*

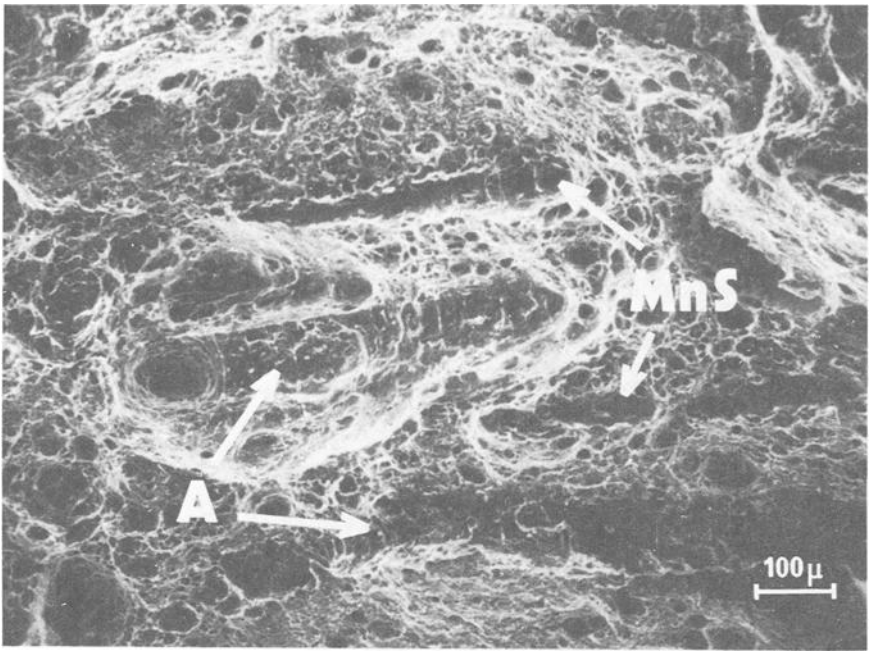

FIG. 6—*Elongated dimples on W crack plane originating from MnS and aluminate inclusions* (A).

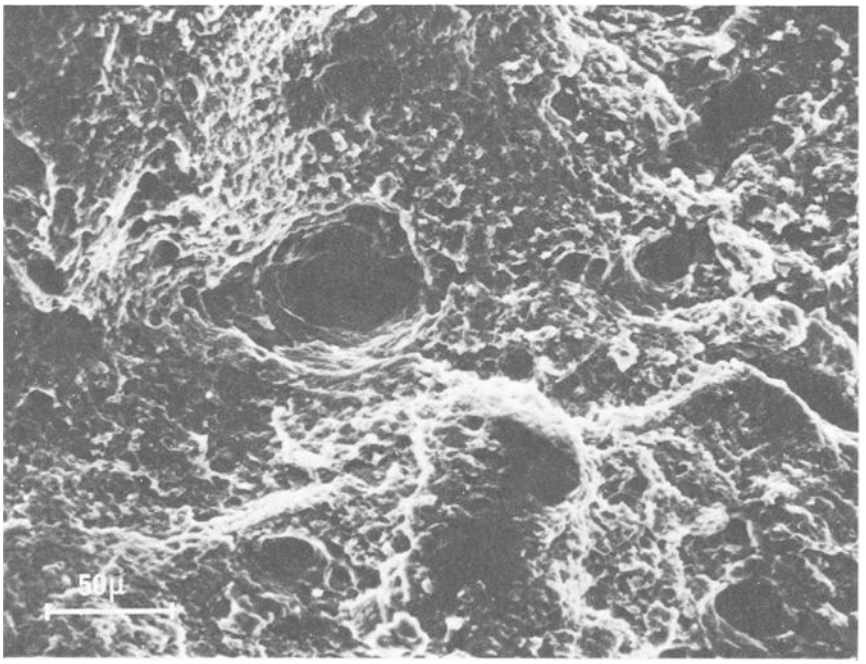

FIG. 7—*Deep circular dimples on R crack plane originating from MnS stringer inclusions.*

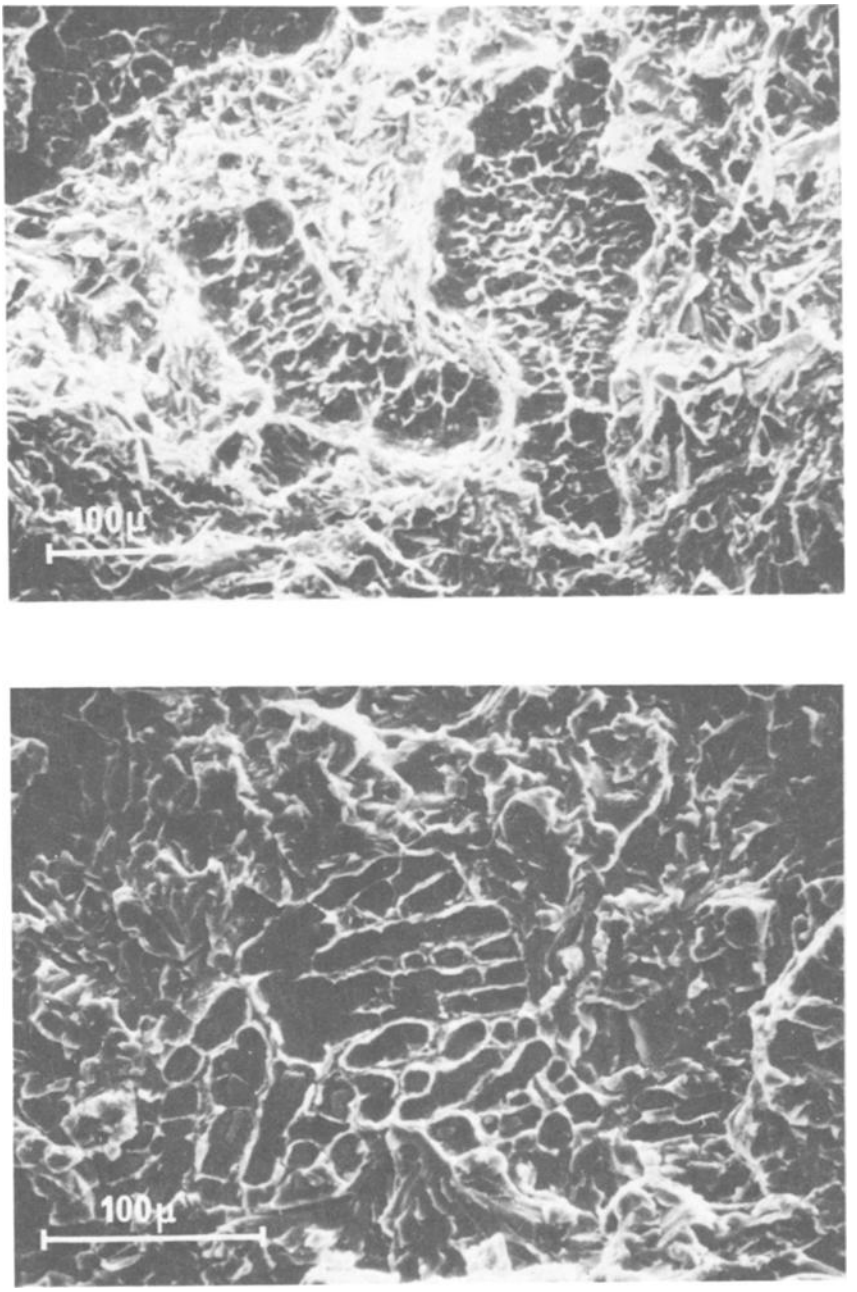

FIG. 8—*Voids surrounding cluster inclusions ahead of ductile crack tip:* (top) *aluminate cluster inclusion;* (bottom) *Type II MnS cluster inclusion.*

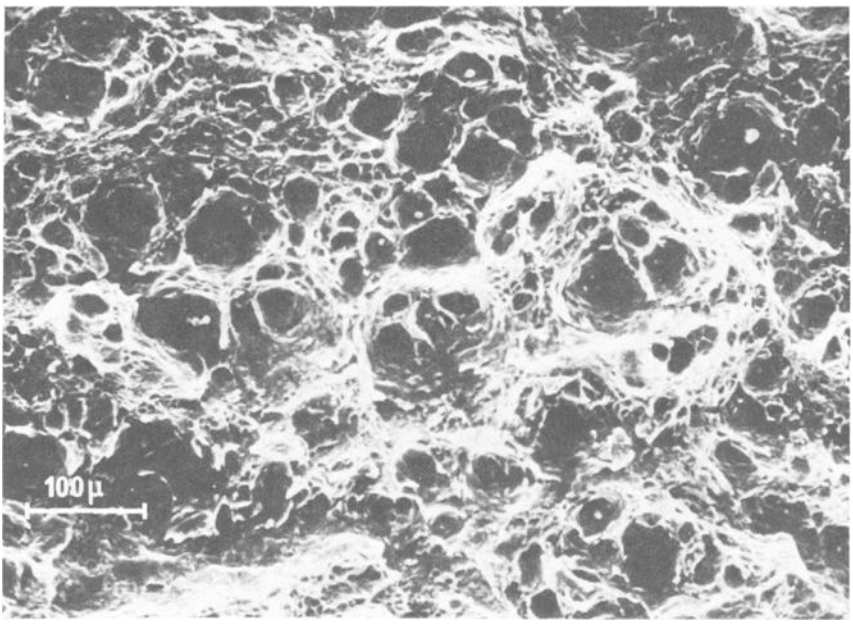

FIG. 9—*Typical fracture topography of the A508 Class 3 showing equiaxed dimples.*

Discussion

Comparison of the Charpy impact and J-integral results with those obtained from steels of the same class [*17*] shows that both the A508 and A533B materials examined in this study exhibit good ductile toughness properties. Independent of the method of analyzing the J-integral test data, Tables 3 and 4 show that the toughness of the A533B is orientation dependent and that over the range of Δa examined, the toughness of the A508 material is higher than that of A533B and is essentially independent of position in the through-thickness direction. The orientation dependence in A533B and higher upper-shelf toughness of A508 are reflected in the Charpy results (Fig. 1), which further indicate that the A508 material exhibits a reduced orientation dependence, particularly in terms of the ductile-brittle transition temperature. Further discussion of the J-integral data will be in terms of initiation, defined by $J_{\Delta a=0}$, and resistance to crack propagation, dJ/da, as determined by the linear regression analysis, Table 3.

The fractographic features previously described for A533B indicate an inclusion distribution as illustrated schematically in Fig. 11. Inclusion clusters, slightly extended in the primary rolling direction, consist either of Type II MnS or aluminates and lie parallel to the plate surface. Other MnS inclusions exist throughout the plate as elongated stringers. In the A508 material,

FIG. 10—*Transmission electron fractograph of an A533B extraction replica showing small shear dimples containing submicron precipitates identified as* (1) Mo_2C: (2) *AlN: and* (3) *AlN*/Mo_2C *aggregate.*

no inclusion clusters were found, the inclusion density was lower, and the MnS inclusions present were equiaxed. This description is consistent with metallographic studies of these materials [*13,18*]. It is clear that, despite the high degree of purity of these steels and the profuse carbide precipitation throughout the microstructure, the ductile fracture behavior is being markedly influenced by inclusion morphology and distribution.

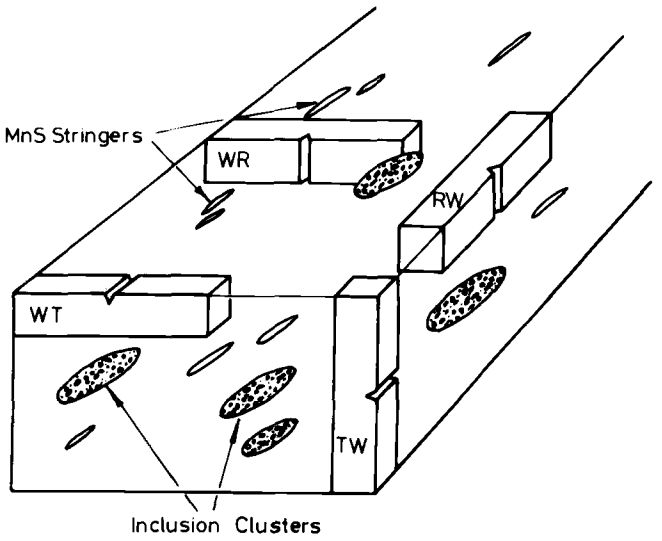

FIG. 11—*Schematic inclusion distribution in A533B plate.*

Void initiation at inclusions found in A533B and A508 steels is known to occur at low strains [*19,20*], the exact value being dependent on stress triaxiality [*21*]. Near the crack tip, the stress triaxiality is high and the contribution of void initiation to the overall ductile crack growth process may be considered negligible [*21*]. The results are therefore discussed in terms of models based on void growth and coalescence.

A533B Orientation Effects

It is well established that elongated inclusion morphologies cause marked anisotropy of tensile ductility and toughness behavior [*22*]. According to Willoughby et al [*7*], where fracture occurs by the coalescence of voids formed at elongated inclusions, the projected inclusion length in the local direction of fracture governs toughness by determining the strain intensification at the crack tip. Specifically, the model predicts that initiation toughness depends inversely on the projected inclusion length in the direction of crack advance, while resistance to crack propagation is minimized when the major inclusion axis lies in the crack plane. That is, for ductile initiation, the inclusion dimension in the direction of propagation dominates, while for propagation, inclusion dimensions both parallel and perpendicular to this direction must be considered. During Charpy testing, the upper-shelf fracture energy (USE) of A533B and A508 steels has been shown to be dominated by crack growth [*23,24*].

Therefore, on the basis of this model, making the assumption that fracture

results principally by void growth at the elongated MnS inclusions and subsequent coalescence with the crack tip, the orientation dependence of Charpy upper-shelf fracture energy would be USE (RW, RT) > USE (WT, WR) ≈ USE (TW, TR). While experimental results from the present study confirm this suggestion for fracture in the R and W crack planes, the upper-shelf energy of the TW and TR orientations is much smaller than predicted. This may be explained by the presence of MnS and aluminate inclusion clusters, whose plane is parallel to the T crack plane. In the TW orientation, the plane of crack propagation coincides with the cluster plane. In this case, the entire cluster effectively acts as a single inclusion, resulting in large voids being opened up at clusters ahead of the crack at low strains, as observed fractographically and referred to previously as islands. This mechanism results in a low energy absorbing fracture mode. When the cluster plane is normal to the plane of fracture, as for the RW, WT, and WR orientations, fractographic studies suggest that predominantly, *individual* inclusions along the line of intersection of cluster and crack planes initiate voids as the cluster is approached by the propagating crack, to form a composite void of size and shape corresponding to the sectioned cluster. Such elongated dimples, associated with calcium and magnesium aluminate inclusions, have been identified on RW, WT, and WR fracture surfaces. Had a single void resulted from all the inclusions in each cluster, then deep fissures or delaminations would have formed corresponding to the cluster size. Such features were only rarely observed, suggesting that for these orientations, all the inclusions in each cluster were not participating in void formation.

Application of the Willoughby et al concept to include the effects of a secondary population of disk-shaped inclusion clusters predicts that RT and RW orientations will show a slightly higher resistance to crack propagation than WT and WR orientations, while TW and TR orientations will be substantially lower. This prediction is in agreement with the observed Charpy results.

The J-integral data indicate a similar orientation dependence on resistance to crack growth. As shown in Table 3, dJ/da for the TW orientation is approximately half that for WT, WR, and RW orientations. If, as seems likely, the higher dJ/da value for WT compared with RW is experimentally insignificant, the tearing resistance anisotropy of A533B is predicted from inclusion cluster considerations.

The analysis of A533B data given in Table 3 indicates that the orientation dependence of initiation toughness is such that $J_{\Delta a=0}$ (RW) > $J_{\Delta a=0}$ (WT = TW = WR). Consideration of the projected length of ellipsoidal MnS inclusions in the direction of crack advance in accordance with the model of Willoughby et al predicts that $J_{\Delta a=0}$ (RW = TW ≈ WT) ≫ $J_{\Delta a=0}$ (WR). Including the effect of inclusion clusters contributing to fracture initiation predicts $J_{\Delta a=0}$ (WT) ≫ $J_{\Delta a=0}$ (RW, TW) > $J_{\Delta a=0}$ (WR). Both these suggestions do not fit experimental results and therefore the model does not explain

the initiation results with the same degree of agreement that was found for crack propagation.

An alternative mechanism has been proposed whereby void growth cannot occur at inclusions until they are enveloped by the logarithmic shear lines that are generated ahead of the blunted crack [*8*]. For inclusions aligned normal to the fracture plane, this mechanism requires a higher crack-opening displacement (or equivalently a larger value of J) than when the inclusion axis lies in the crack plane. Hence, consideration of MnS stringer inclusions suggests that $J_{\Delta a=0}$ (RW) > $J_{\Delta a=0}$ (WT = WR = TW). The contribution of inclusion clusters will be equivalent in each orientation, because the void associated with the individual cluster inclusions will always lie in the fracture plane. The combined effect of MnS stringers and cluster inclusions, analyzed on this basis, is therefore in agreement with experimental results.

From the preceding discussion, it is clear that neither of the models examined is capable of fully explaining the effect of orientation on both initiation and ductile crack growth.

While void growth and coalescence are likely to dominate the fracture process, it is possible that void initiation may be contributing a secondary effect. Recent results [*20*] suggest that cavity formation at MnS inclusions occurs by interface decohesion when the applied tensile stress axis is perpendicular to the inclusion axis, and by fracture when the tensile and inclusion axes are aligned. The latter requires a critical local stress, which is approximately 40 percent greater than that required for interfacial decohesion. In addition, the initial void size formed at a cracked MnS inclusion will be significantly smaller than when the whole interface decoheres. Although no evidence was obtained to substantiate this mechanism in the present A533B material, if such an effect was relevant, the higher initiation toughness for RW would be consistent with the greater strain required for both void nucleation and growth.

The lack of a pronounced orientation dependence in the A508 Charpy USE and the improved ductile fracture properties, compared with the A533B, derive from the significantly reduced inclusion content of the forging. All fracture surfaces of A533B and A508 revealed a duplex dimple-size distribution, indicating the role of both inclusions and carbide precipitates in the fracture process. The duplex distribution arises because sheets of tiny dimples, which are initiated at carbide precipitates, interconnect the large inclusion voids before they can coalesce. The void sheets form in response to the localization of strain between inclusion voids. Voids forming at carbide particles require a greater local strain for nucleation than voids initiating from inclusions [*25*]. A similar phenomenon has been reported in detail for a high-strength AISI 4340 steel [*26*]. The strain at which void linkage occurs will be dependent not only on precipitate and matrix characteristics, such as interfacial strength and work-hardening capacity, but also on the strain intensification between an inclusion void and the crack tip, which is a function in particular of the inclusion size, shape, orientation, and spacing ahead of

the crack [*7,27*]. Consideration of toughness parameters on the basis of inclusion variables is therefore relevant to a micromechanism which involves void sheeting effects.

In terms of the relative toughness of A508 and A533B, the increased density and size of inclusions present in A533B suggests that void sheets will link inclusion voids at lower applied strain than in A508. The submicron dimple formation at Fe_3C precipitates in A508 and at AlN/Mo_2C precipitate aggregates in A533B raises the possibility of varying toughness by altering the submicron precipitate population, using heat treatment and compositional control.

Comparison of Charpy and J-Integral Tests

Charpy upper-shelf fracture energy results and J_R-curves have qualitatively shown the same relative fracture resistance of the two materials and the same effect of varying orientation in the A533B plate. Furthermore, similar fractographic features have been observed from both types of test. These observations inspire further investigation into the quantitative relationship between the two tests. Several authors have proposed equations to relate Charpy fracture energy with fracture mechanics parameters, usually referring to crack initiation [*28*], for example, K_{Ic} or J_{Ic}. For low-strength high-toughness materials, it is known that crack initiation in the Charpy test accounts only for a small fraction of the total fracture energy [*23,24*]. Any correlation between Charpy fracture energy and fracture mechanics testing, therefore, should consider both initiation and crack growth parameters. Such a correlation is proposed as follows. The Charpy fracture energy is the energy required to initiate a crack from a blunt notch and propagate that crack across a ligament of 8 mm. Similarly the area under the J_R-curve is a measure of the energy required for fracture. Therefore evaluation of the integral $\int_0^{8mm} J \cdot da$ provides a basis for comparing the two types of test. It should be noted that, although energetically the integral $\int_0^{8mm} J \cdot da$ embodies the essence of the Charpy test, direct comparison is without rigorous theoretical foundation, since *J*-domination will not be maintained throughout the Charpy test. Table 5 gives the results of this evalua-

TABLE 5—*Comparison of Charpy fracture energy and J-integral data.*

		J-Integral Comparison	
	Charpy USE Comparison	Linear Regression	Exponential Regression
A533B RW: A533B WT	1.25:1	0.97:1	0.96:1
A533B RW: A533B TW	2.43:1	1.78:1	1.86:1
A533B WT: A533B TW	1.94:1	1.84:1	1.94:1
A508 ½W: A508 1W	0.96:1	1.02:1	1.03:1
A508 ½W: A533B RW	1.54:1	1.59:1	1.73:1

tion for specific comparisons of different materials and specimen orientations, using both the linear and exponential J versus Δa regression analyses extrapolated to $\Delta a = 8$ mm. These results suggest that this correlation can provide an approximate method for relating Charpy energy and J_R-curve toughness parameters. However, an exact correlation would not be anticipated due to the differing strain rates and geometric constraints of the two types of test.

Relationship Between Toughness and Steel Production Procedure

The results of this study indicate that despite low absolute levels of sulfur and profuse carbide precipitation, the ductile crack growth resistance of bainitic pressure vessel steels of similar strengths is principally controlled by inclusion distribution. As for steels of higher impurity concentrations, the volume fraction, morphology, and distribution of inclusions determine the relative toughness and degree of isotropy. For uniform high-isotropic toughness, inclusions should be few in number, spherical in shape, and evenly distributed throughout the section.

The remaining paragraphs provide a brief descripton of how the inclusion distribution and morphologies have been influenced by the fabrication procedures adopted for the two materials tested. The A533B plate and A508 forging examined in this study have several differences in their inclusion distributions, as described in more detail elsewhere [*13,18,24*]. The forging contains manganese sulfide inclusions with a bimodal size distribution, small spherical particles being found in the majority of the product and large amoeba-like inclusions being restricted to small areas associated with regions of macroscopic solidification segregation known as 'A' segregates. These regions occur with higher frequency closer to the inner wall of the forging. Few oxide inclusions resulting from deoxidation of the liquid steel melt were observed. In the A533B plate material, the number of inclusions >5 μm long was nearly an order of magnitude greater than for the forging. Inclusions were of two basic types, manganese sulfides, which were often elongated in the working direction, and aluminium and calcium or magnesium-containing oxides existing as clusters of individual inclusions. The density of inclusions was highest in the center regions of the plate.

Both materials were produced using electric furnaces to melt selected scrap of low impurity content and refined by sequential application of oxidizing and reducing slags. Silicon and aluminium were added for deoxidation, with final degassing being effected under vacuum by a ladle technique for the A533B and by vacuum stream degassing for the A508. The A508 specimen originated from a large ingot weighing 500 tons. The chemical composition data given in Table 1 show both steels to be low in impurities, with the A508 showing a particularly low sulfur content.

From the preceding description of the steelmaking practices, the anticipated sulfide inclusions would be Type II MnS [*29,30*]. MnS, exhibiting the

classical eutectic-like morphology, was observed in the A533B but not in the A508 material. The absence of this morphology is thought to be due to the low sulfur content, combined with spheroidization of inclusions occurring during the long high-temperature period following solidification of the 500-ton A508 ingot.

The oxide cluster inclusions found in the A533B originate from the refining and deoxidation practices. The calcium oxide (CaO) has the lowest free energy of formation among the elements usually found in steelmaking and, therefore, will not be reduced during steelmaking. Although calcium has not been intentionally added to this steel, the slags would be rich in lime and also contain some magnesium oxide (MgO). Furthermore, calcium is present in some silicon compounds, which may be used for deoxidation. Inclusions, resulting from deoxidation, are dependent on the exact procedure adopted, with the absence of silicon-containing inclusions suggesting that final deoxidation was principally by aluminium. Vacuum treatment would not be anticipated to result in any dissociation of the very stable alumina or calcium aluminates, but a ladle vacuum procedure, as used for the A533B, would reduce the average size of the remaining inclusions by allowing floatation of the larger inclusions [*31*]. The extended holding and solidification periods associated with the production of the large A508 ingot, together with the removal of the lower section of the ingot prior to forging, would explain the low oxide inclusion content of this material.

Prior to hot-working, the top and bottom regions of both the A508 and A533B ingots were removed to ensure that only material within the specified composition range was allowed in the final product. The plate material, A533B, was then hot-worked by rolling in the temperature range 950 to 1200°C to a thickness of 150 mm, the central core of the ingot, containing a high density of inclusions, becoming the midthickness region of the final product. This involved an overall reduction in ingot thickness by a factor of 6. The forging was pierced and forged by a combination of mandrel forging and upsetting to produce the required dimensions of the ring forging. During piercing, some or all of the high inclusion density region of the ingot core would be removed. The reduction in wall thickness from the pierced ingot stage to final product was a factor of 1.87. Examination of the microstructure across the wall in the through-thickness direction of the final product revealed that the degree of deformation was not homogeneous, but concentrated close to the inner wall [*24*].

Inclusion shape is controlled by the overall degree of deformation and the relative plasticity of the inclusion with respect to the steel. The relative plasticity of Types II and III MnS increases with decreasing temperature, such that in the lower temperature range of hot-working, the sulfides deform more readily than the steel matrix. Type I sulfides deform less readily than Types II or III. Alumina, calcium aluminate, and spinel MgO Al_2O_3 all behave as rigid particles at temperatures below 1200°C. Hence in the A533B plate, the

final inclusion distribution is one of elongated sulfides, together with essentially two-dimensional clusters of aluminates and sulfides, as shown schematically in Fig. 11. The small amount of hot-working in the majority of the A508 forging resulted in little shape change of the MnS inclusions and, therefore, an essentially equiaxed inclusion distribution remains in the final product. Close to the inner wall, where the degree of hot-working is substantially greater, elongated inclusions are observed.

Conclusions

Resistance to ductile crack growth has been examined at 290°C by Charpy impact and multispecimen J-integral tests in two commercially produced pressure vessel steels, containing low levels of sulfur. The conclusions are as follows:

1. Both the A533B Class 1 plate and A508 Class 3 forging examined exhibit a high resistance to ductile crack initiation and growth.
2. The A533B plate exhibits a marked orientation dependence in resistance to crack growth. The slope of the initial J-resistance curve for the short transverse (TW) orientation is approximately half that for longitudinal (RW) or long transverse (WT or WR) orientations.
3. The A508 forging shows only a small orientation dependence in Charpy upper-shelf fracture energy and little or no effect of position through the wall of the forging.
4. Charpy fracture energy results and various interpretation procedures of J-integral test data indicate that the A508 Class 3 forging exhibits superior upper-shelf toughness to all of the orientations examined in A533B Class 1 plate.
5. An approximate relationship exists between the integral of the J versus Δa resistance curve and upper-shelf Charpy fracture energy.
6. Differences in upper-shelf toughnesses of the A508 and A533B steels tested and the orientation dependence observed in A533B are attributable to the inclusion and second-phase particle distribution resulting from the steelmaking and fabrication procedures used during production. In particular, resistance to crack growth is largely dominated by inclusion distribution with thin disk-shaped clusters of inclusions being most detrimental when the crack plane coincides with the plane of the disk. Inclusion clusters largely consisting of calcium aluminates and sometimes Type II manganese sulfides or magnesium aluminates were identified in the A533B plate material.

Acknowledgments

We wish to thank Mr. R. V. Salkin of S. A. Cockerills, Belgium, for supplying the A508 Class 3 forging material and Dr. F. B. Pickering of Sheffield

Polytechnic for several useful discussions on steelmaking procedures. We wish also to acknowledge the assistance of Mr. P. R. Goggin in the design of the testing equipment.

References

[1] Steele, L. E., "Neutron Irradiation Embrittlement of Reactor Pressure Steels," Technical Report Series No 163, International Atomic Energy Agency, Vienna, 1975.
[2] Druce, S. G. and Edwards, B. C., *Nuclear Energy*, Vol. 19, 1980, pp. 347-360.
[3] Gurland, J. and Plateau, J., *Transactions*, American Society for Metals, Vol. 56, 1963, pp. 442-454.
[4] McClintock, F. A., *Journal of Applied Mechanics*, 1968, pp. 363-371.
[5] Rice, J. R. and Johnson, M. A. in *Inelastic Behaviour of Solids*, M. V. Kanninen et al, Eds., McGraw-Hill, New York, 1970, pp. 641-672.
[6] Baker, T. J. and Charles, J. A. in *Proceedings*, Conference on Effect of Second Phase Particles on the Mechanical Properties of Steel, Iron and Steel Institute, London, 1971, p. 79.
[7] Willoughby, A. A., Pratt, P. L., and Baker, T. J. in *Proceedings*, 5th International Conference on Fracture Vol. 1, Pergamon Press, Oxford, U.K., 1981, pp. 179-186.
[8] Green, G. and Knott, J. F., *Journal of Engineering Materials and Technology, Transactions*, American Society of Mechanical Engineers, Vol. 98H, 1976, p. 37.
[9] Cadiou, L., *Materiaux et Techniques*, Vol. 6, 1977, p. 341.
[10] Fernandez, S. in *Trends in Reactor Pressure Vessel and Circuit Development*, R. W. Nicholls, Ed., London, 1980, p. 315.
[11] *Post Yield Fracture Mechanics*, D. G. H. Latzko, Ed., *Applied Science*, London, 1979.
[12] Landes, J. D. and Begley, J. A. in *Post Yield Fracture Mechanics*, D. G. H. Latzko, Ed., *Applied Science*, London, 1979, p. 211.
[13] Titchmarsh, J. M., Bartlett, A. F., and Druce, S. G., "A Comprehensive Chemical and Microstructural Characterisation of a Commercial SA533B Class 1 Pressure Vessel Steel Plate," UKAEA Report AERE R-9674, Atomic Energy Research Establishment, Harwell, Oxfordshire, U.K.
[14] Onodera, S., Moritani, H., Tsuchiya, K., Tsukada, H., Widart, J., and Scailteur, A., "Mono-block Vessel Flange Forging for PWRPV 1000MWE," presented at 8th International Forgemasters Meeting, Kyoto, Japan, Oct. 1977.
[15] "Structural Integrity of Water Reactor Pressure Boundary Components," Annual Report, Fiscal Year 1979, F. J. Loss, Ed., NUREG CR-1128, Nuclear Regulatory Commission, Washington, D.C.
[16] Davis, D. A., Vassilaros, M. G., and Gudas, J. P., this publication, II-582-II-610.
[17] EPRI Report No. 933, Project 866-1, 1978, Fracture Control Corp., Calif., 1978.
[18] Titchmarsh, J. M. and Bartlett, A. F., "Comparison of the Microstructure of A508 Class 3 and SA533B Class 1 Steels Following Simulated Post Weld Heat Treatment," UKAEA Report AERE R10333, Atomic Energy Research Establishment, Harwell, Oxfordshire, U.K.
[19] Shih, C. F., Andrews, W. R., deLorenzi, H. G., Van Stone, R. H., Yukawa, S., and Wilkinson, J. P. F., EPRI Report NP-701-SR, Electric Power Research Institute, Palo Alto, Calif., Feb. 1978, pp. 6-16.
[20] Beremin, F. M., *Metallurgical Transactions*, Series A, Vol. 12A, May 1981, p. 723.
[21] Beremin, F. M. in *Proceedings*, Fifth International Conference on Fracture, Cannes, France, 1981, Vol. 2, p. 809.
[22] Francois, D. in *Advances in Elasto-Plastic Fracture Mechanics*, L. H. Larsson, Ed., Applied Science Publishers, Barking, U.K., 1980, p. 237.
[23] Norris, D. M., Reough, J. E., Moran, B. and Quinones, D. F., EPRI Report NP 961, Research Project 603, Lawrence Livermore Laboratory, Livermore, Calif., 1979.
[24] Druce, S. G., UKAEA Report AERE-R9581, Atomic Energy Research Establishment, Harwell, Oxfordshire, U.K., 1979.
[25] Knott, J. F., *Metal Science*, Vol. 14, No. 8/9, Aug./Sept. 1980, p. 327.

[26] Cox, T. B. and Low, J. R., *Metallurgical Transactions*, Vol. 5A, June 1974, p. 1457.
[27] Hancock, J. W. and Cowling, M. J., *Metal Science*, Vol. 14, No. 8/9, Aug./Sept. 1980, p. 293.
[28] Roberts, R. and Newton, C., WRC Bulletin 265, Welding Research Council, Abington, Cambridge, U.K., 1981.
[29] Sims, C. E., *Transactions*, American Institute of Mining, Metallurgical and Petroleum Engineers, Vol. 215, 1959, p. 367.
[30] Pickering, F. B. in *Inclusions*, F. B. Pickering, Ed., Institution of Metallurgists, Monograph No. 3, London, 1979, p. 47.
[31] Pickering, F. B. in *Inclusions*, F. B. Pickering, Ed., Institution of Metallurgists, Monograph No. 3, London, 1979, p. 73.

Ralph L. Tobler[1]

Ductile Fracture with Serrations in AISI 310S Stainless Steel at Liquid Helium Temperature

REFERENCE: Tobler, R. L., **"Ductile Fracture with Serrations in AISI 310S Stainless Steel at Liquid Helium Temperature,"** *Elastic Plastic Fracture: Second Symposium, Volume II—Fracture Resistance Curves and Engineering Applications. ASTM STP 803*, C. F. Shih and J. P. Gudas, Eds., American Society for Testing and Materials, 1983, pp. II-763-II-776.

ABSTRACT: Fracture toughness tests were performed on annealed austenitic stainless steel AISI 310S, immersed in liquid helium at 4 K, using 25-mm-thick compact specimens. The J_{Ic} results (360 to 380 kJ/m^2) from single- and multiple-specimen test techniques are compared and shown to be in close agreement. Attention is called to the remarkable failure process of this steel at 4 K: Crack extension occurs by ductile tearing, while the test records exhibit serrations due to repeated bursts of unstable plastic flow and arrests. The nature of this behavior is discussed, and the performance of stable austenitic AISI 310S is compared with that of related steels, including those that transform from austenite to martensite during testing at 4 K.

KEY WORDS: austenitic stainless steel, cryogenic properties of materials, fracture of materials, J-integral tests, low-temperature properties, stainless steels, elastic-plastic fracture

AISI 310S is a low-carbon (C $\leq$ 0.08 weight percent) modification of Fe-25Cr-20Ni stainless steel. This steel has an austenitic (face-centered cubic) structure, and so remains highly ductile at extreme cryogenic temperatures. Owing to its high alloy content, the austenitic structure is completely stable and does not undergo martensitic phase transformations during deformation at low temperatures. Fracture toughness data for this material at 4 K were desired to serve three purposes:

1. to evaluate the National Bureau of Standards (NBS) single-specimen J_{Ic} measurement procedure,

[1]Metallurgist, Fracture and Deformation Division, National Bureau of Standards, Boulder, Colo. 80303.

2. to illustrate the unique serrated plastic flow behavior that accompanies fracture of such materials at extreme cryogenic temperatures, and
3. to compare the toughness of a stable austenitic stainless steel with previously tested metastable stainless steels.

Materials and Specimens

The tested material was a 25.4-mm-thick plate of AISI 310S in the as-received condition: annealed at 1339 K, water-quenched, and descaled. In weight percent, the chemistry is : Fe-24.6Cr-20.4Ni-1.65Mn-0.07C-0.70 Si-0.18Mo-0.041P-0.027S. The hardness and tensile properties were measured by conventional methods [*1,2*][2] and are presented in Table 1.

Six compact fracture specimens of the T-L orientation were machined from the as-received stock. These were not side-grooved. The specimen thicknesses (B) and widths (W) were 25 and 50.8 mm, respectively. A diagram is given elsewhere [*3*].

In addition, one side-grooved specimen was prepared from a special portion of stock that had been reannealed in the laboratory: 1339 K, 1 h, water-quench. Symmetrical side grooves were machined on both faces, reducing the section thickness by 10 percent (B_{net} = 22.8 mm). The notch root radii were 0.100 mm.

Procedures

Precracking was accomplished in liquid nitrogen (76 K) or liquid helium (4 K), but the temperature of precracking had no apparent affect on results. The maximum and minimum fatigue loads were 22 and 2.2 kN, well below 40 percent of the maximum load reached in J tests. The final a/W ratio was typically 0.60 to 0.63.

Both the single-specimen and multiple-specimen test techniques were applied. In the absence of accepted standards, the measurement techniques followed those reported elsewhere [*3-5*]. In the single-specimen technique,

TABLE 1—*Mechanical properties of AISI 310S stainless steel.*[a]

Temperature, K	Yield Strength, MPa	Ultimate Strength, MPa	Elongation in 4D, %	Reduction in Area, %	Rockwell Hardness
295	251	600	43	50	R_B80
4	645	1259	36	31	NA[b]

[a]It is assumed that at 4 K Young's modulus is 206.4 GPa and Poisson's ratio is 0.293 [*2*].
[b]NA = not available.

[2]The italic numbers in brackets refer to the list of references appended to this paper.

crack extension (Δa) was inferred periodically by unloading compliance measurements made with computer-aided data analysis. One specimen was loaded extensively to obtain a well-defined J-resistance curve. Five similar specimens were also tested with periodic 10 percent unloadings, but these tests were terminated at successively lower Δa-values according to the multiple-specimen technique [5]. Displacement control was used. Each specimen was completely unloaded at the end of J testing and heat-tinted or refatigued to mark the final Δa, which was measured with a microscope at nine locations, and averaged.

Results

Loading Behavior

Figure 1 shows a typical load-versus-deflection curve for AISI 310S steel at 4 K. The behavior is fully plastic in that a limit load is reached. However, the curves are marked by serrations which become more pronounced as the test proceeds. Superimposing test records for similarly sized specimens showed that the behavior was reproducible (except for specimen No. 6), with major serrations occurring at nearly equivalent loads and deflections. Test records for this type of steel at 295 and 76 K (not reported here) do not show these serrations.

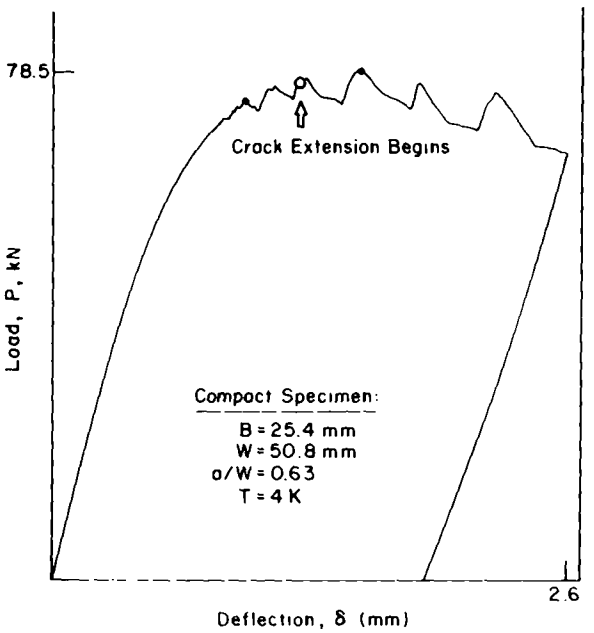

FIG. 1—*Typical load-versus-deflection curve for AISI 310S steel at 4 K.*

Fracture Mode

In appearance, the serrations of Fig. 1 resemble a type of "pop-in" phenomenon, which is frequently observed in other materials at room temperature. Such behavior is usually caused by spurts of brittle cracking and arrest. However, annealed AISI 310S steel is not at all brittle. A fractured specimen is shown in Fig. 2, and a scanning electron micrograph of the 4 K fracture surface is shown in Fig. 3. The microscopy reveals a heavily dimpled fracture surface produced by void formation, growth, and coalescence. There is no visual evidence of a change in fracture mechanism or surface markings that might be associated with the serrations of Fig. 1. Apparently, then, we have here an example of a material in which a single mechanism of crack extension (ductile tearing) is associated with first stable, then unstable loading conditions in the same test specimen. Rarely has this been observed.

J-Resistance Curves and J_{Ic}

A J-versus-Δa curve for the AISI 310S steel from the single-specimen technique is shown in Fig. 4. The curves follow a linear regression line, as assumed in the recommended procedure [5]. The recommended procedure also assumes that crack-tip-blunting behavior will conform to the equation

$$\Delta a = \frac{J}{2\sigma_f} \tag{1}$$

where σ_f is the average of the yield and ultimate strengths. Although the data for one specimen did follow this equation, the data for all other specimens deviated, owing to a slight zero shift during the early stage of blunting line development just after the first unloading (see Fig. 4). For the single-specimen technique used in this study at 4 K, the initial crack length, a_0, inferred from compliance was 3 percent lower than the value measured from broken specimens. This could be attributed to errors in the compliance function used and in the assumed value of Young's modulus (206.4 GPa) at 4 K.

Table 2 and Fig. 5 present the relevant J-integral data from the multiple-specimen technique for AISI 310S at 4 K. These data for specimens with no side grooves show little scatter, except for the outlying datum for one relatively low-toughness specimen. This low-toughness datum was excluded from further analysis so that a realistic comparison of the test techniques could be made using only specimens of comparable toughness levels. In comparison, the result from extrapolation for the multiple-specimen technique gives $J_{Ic} = 360\ \text{kJ/m}^2$, whereas the single-specimen technique indicates 380 kJ/m^2.

The J_{Ic} measurement point was traced to its location on the load-versus-deflection curve; it does not coincide with the first sizable load drop or with the attainment of maximum load, but falls intermediate between these points, as

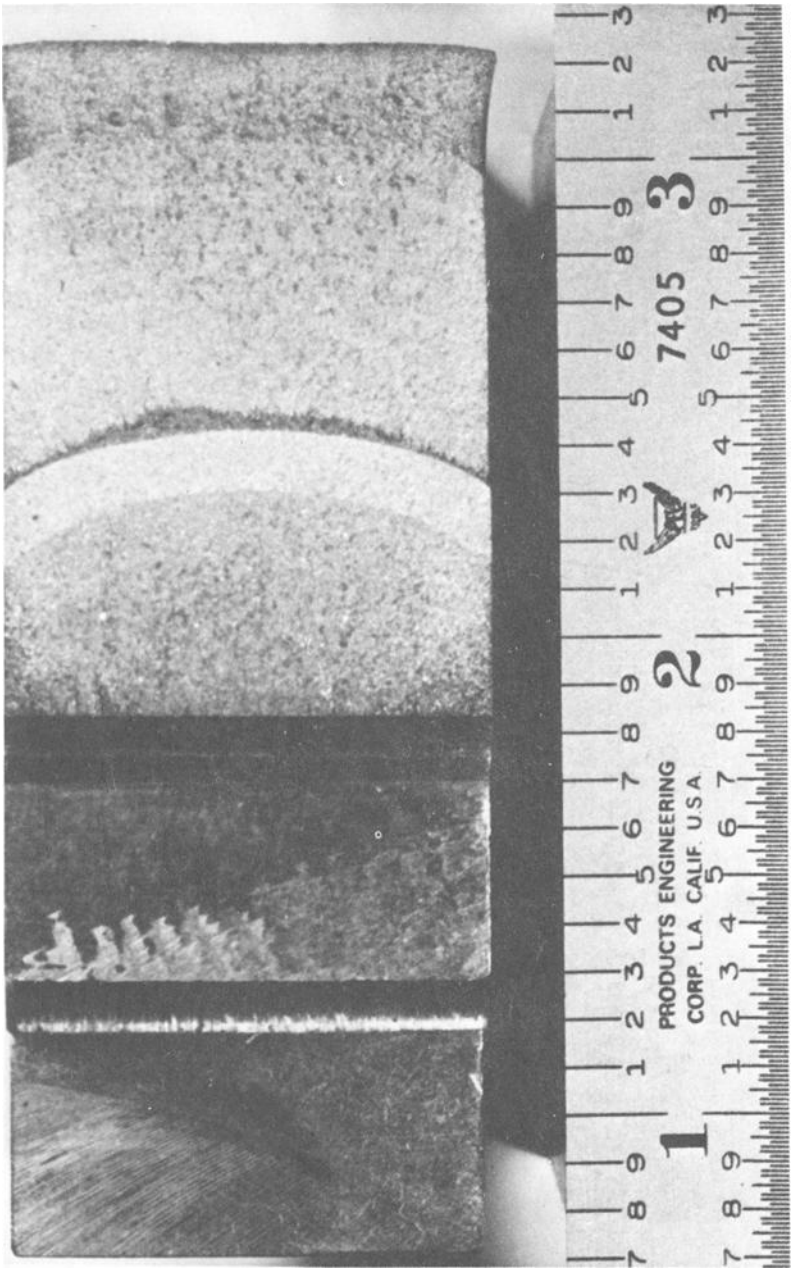

FIG. 2— *Fractured compact specimen of AISI 310S steel, tested at 4 K.*

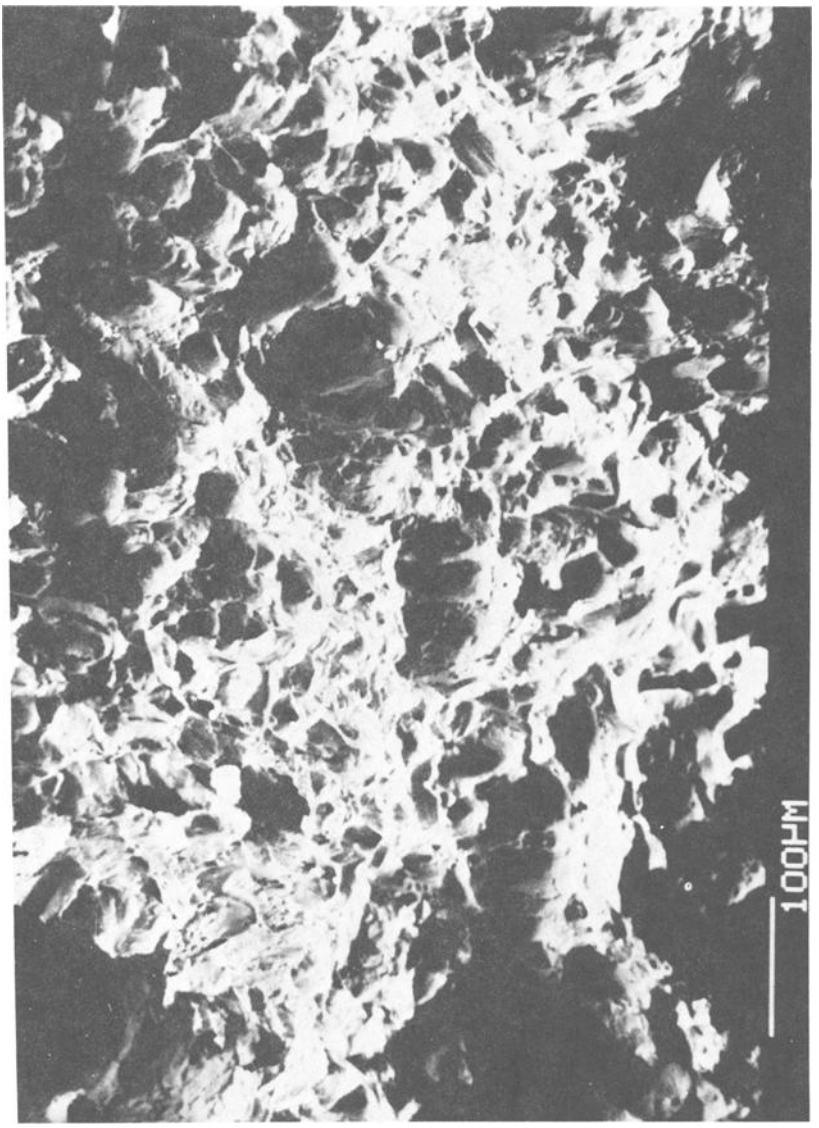

FIG. 3—*Scanning electron microscope photograph of AISI 310S compact specimen fracture surface.*

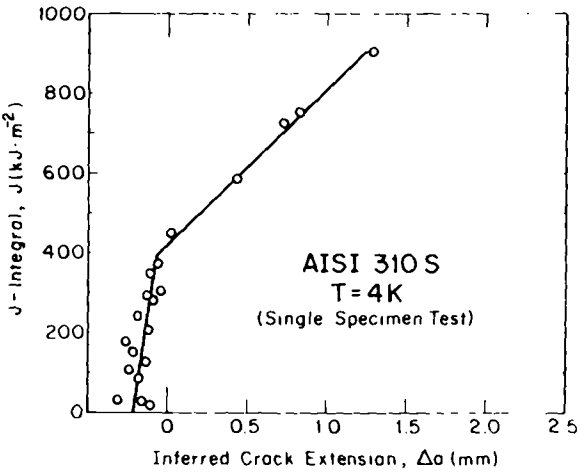

FIG. 4—*J-versus-Δa curve for AISI 310S using single-specimen technique.*

TABLE 2—*J-integral fracture results for AISI 310S at 4 K.*

Specimen No.	a_0, mm	B, mm	W, mm	J, kJ/m^2	Δa, mm
1	31.275	25.500	50.8	475	0.675
4	31.950	25.400	50.8	900	2.300
6[a]	31.325	25.450	50.8	413	1.025
7	30.325	25.400	50.8	654	1.300
8	30.375	25.400	50.8	387	0.325
10	30.675	25.475	50.8	621	1.175
x[b]	29.725	25.250	50.8	482	0.425

J_{Ic} = 360 kJ/m^2; $K_{Ic}(J)$ = 285 MPa·m$^{1/2}$ where $K_{Ic}(J)$ is estimated using $K_{Ic}(J) = (J_{Ic} \cdot E')^{1/2}$ where $E' = E/(1 - \nu^2)$ = 226 GPa

[a]Abnormally low toughness.
[b]Reannealed and side grooved (B_{net} = 22.860 mm).

shown in Fig. 1. Since the J-value at the first significant load drop (~ 327 kJ/m^2) is lower than J_{Ic}, the first load drop must be due only to unstable plastic flow, not true crack extension. This was confirmed by compliance measurements made before and after the first load drop; only a small increase of Δa was indicated, not greater than the amount predicted from Eq 1 for crack-tip blunting.

Comparisons of the measured and inferred crack extensions for the five specimens without side grooves reveal an error that increases significantly as the J test proceeds, with disagreements as high as 55 percent. This error appears to be due to a plasticity effect on measured compliance values. Since this error is less at low Δa-values, the J_{Ic} measurement from the single-

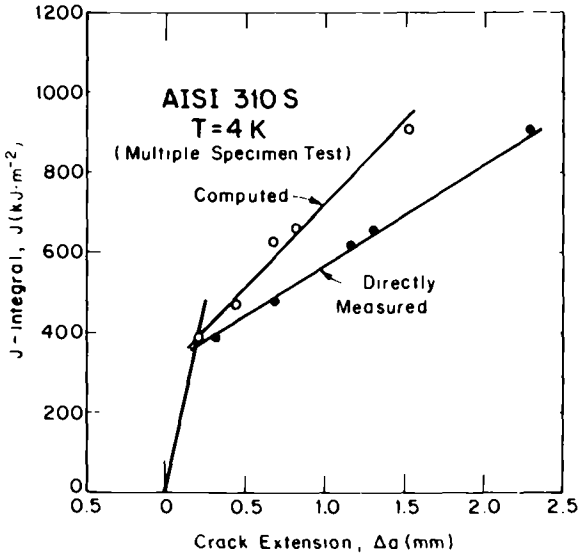

FIG. 5—*Computed and directly measured J-versus-Δa curves for AISI 310S using multiple-specimen technique.*

specimen technique is reasonably accurate (within 5 percent) of the value given by the multiple-specimen technique. However, the apparent slope of the J-Δa curve for the single-specimen technique is inaccurate, being 65 percent greater than the true slope given by the multiple-specimen technique. Therefore, our unloading compliance technique could not be used to determine the tearing modulus of the material at 4 K, which, based on the multiple-specimen technique, is 60.

K_{Ic} Estimates

The J_{Ic} data are often used to estimate the linear-elastic plane strain fracture toughness, K_{Ic}. From the single- and multiple-specimen techniques, the K_{Ic} estimates for AISI 310S steel at 4 K are 290 and 285 MPa · $m^{1/2}$, respectively. The uncertainty in J_{Ic} is ± 15 percent, which translates to an uncertainty in K_{Ic} of ± 8 percent [*1*]. Note, however, that the existence of K_{Ic} for annealed austenitic stainless steels has never been observed. To determine experimentally whether linear-elastic fracture behavior could be achieved in AISI 310S at 4 *K*, it would be necessary to test a specimen of impractical size, having a thickness of about 0.5 m

$$B \leq 2.5\left(\frac{K_{Ic}}{\sigma_y}\right)^2 = 2.5\left(\frac{285\ \text{MPa}\cdot\text{m}^{1/2}}{645\ \text{MPa}}\right)^2 \cong 0.5\ \text{m}$$

Fracture Toughness Comparisons

Although it would be interesting to compare the J_{Ic}-values for AISI 310S at 4 K and at room temperature, this is impossible because J_{Ic} data for 25-mm-thick specimens are invalid at 295 K. Comparisons must be limited to results for other stainless steels that have been similarly tested at 4 K.

Logsdon et al [*6*] also tested a heat of AISI 310S steel at 4 K, reporting a K_{Ic} estimate of 262 MPa · $m^{1/2}$ and an 819-MPa yield strength. Their result is quite consistent with ours, because K_{Ic} scales as an inverse function of the yield strength, as shown in Fig. 6. The somewhat higher strength and lower fracture toughness of the heat tested by Logsdon et al is easily explained by compositional differences.

Considerable low-temperature fracture toughness data are now available for two categories of austenitic stainless steels: (1) stable with respect to phase transformation at 4 K (for example, AISI 310S and Fe-20Cr-16Ni-6Mn-0.2N steels [*17*], and (2) metastable with respect to phase transformation at 4 K (for example, AISI 304 type steels [*3, 4*]. Figure 6 summarizes data pertaining to the effect of structural stability on fracture toughness in the iron-chromium-nickel-manganese (Fe-Cr-Ni-Mn) system. The results shown in this figure are for equivalent specimen orientation, specimen size, and test technique; all of the steels represented in this figure exhibited the dimpled fracture mode, as verified by scanning electron microscopy. We see that the data for three stable steels

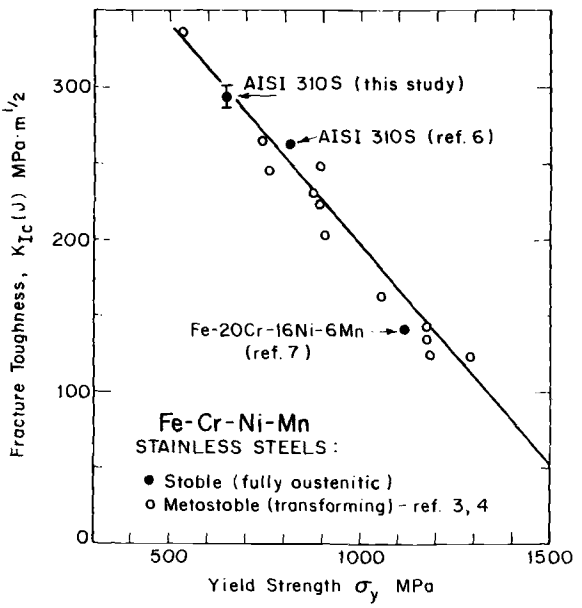

FIG. 6—*Fracture toughness versus tensile yield strength for many austenitic stainless steels, all measured at 4 K.*

fall within the scatterband for unstable steels, so that a single inverse-linear dependence on yield strength appears to govern fracture toughness, regardless of whether martensitic phase transformation takes place or not.

Side Grooves

One specimen having side grooves was J-tested, and the inferred Δa was 24 percent lower than the measured value. From Fig. 5, the error for an ungrooved specimen at the same value of measured crack extension would be 33 percent. This indicates that side grooves may improve the final Δa prediction for ductile austenitic stainless steels tested by the unloading compliance technique. Confirmation is needed using deeply side-grooved specimens.

Discussion

AISI 310S at 4 K furnishes a remarkable example of a material that fails by repeated bursts of instability and arrests, the same mechanism of failure (ductile tearing) being associated with alternating stable and unstable conditions in a single test specimen. The first few serrations in the load-displacement record result from unstable plastic deformation that causes crack-tip blunting, but no true crack extension.

Subsequent serrations at J-values exceeding J_{Ic} are presumed to be associated with both plastic flow and crack extension by ductile tearing. As discussed later, this type of ductile fracture with serrations can be expected in many ductile alloys at temperatures near absolute zero.

Mechanism of Serrated Flow

The serrations observed in tests of compact specimens at 4 K are analogous to the serrations observed in stress-strain curves during conventional unnotched tension tests. The phenomenon as it occurs in tension tests is documented in studies of a wide variety of materials at temperatures below 20 K, including stable and transforming stainless steels, aluminum, and copper alloys [*8–12*]. In tension tests of austenitic stainless steels at 4 K, the serrations begin after small initial plastic strains of about 2 percent, and the deformation propagates as a Lüders band [*8*].

Observations from our tests of AISI 310S show that the serrations at 4 K cannot be attributed to brittle cracking or to phase transformation. The most widely accepted explanation is based on adiabatic heating, as described by Basinski [*9, 10*] and later defended [*11*], although not everyone is in agreement [*12*].

The adiabatic heating model is plausible at 4 K because of the very strong changes of specific heat (large decrease) and flow strength (large increase) as temperature is lowered from room temperature to 4 K. Many materials exhibit

these trends, and serrated flow behavior is also wide-spread [*13*]. For AISI 310S, the specific heat shows a 200-fold reduction between 295 and 4 K [*14*]. Thus, the amount of thermal energy necessary to produce an appreciable adiabatic temperature rise is quite low at 4 K.

The adiabatic heating mechanism might be pictured as follows: Heating during dislocation movement causes appreciable softening, and deformation becomes unstable. Low thermal conductivity at 4 K (compared with that at 295 K) contributes to a localization of the heat to produce load instability. During instability the load drops suddenly and the plastic flow becomes localized when thermal softening due to heat generated by plastic straining is greater than the strain-rate hardening. The instability is eventually arrested at some strain and temperature where the flow process becomes stable, owing to local specimen strain hardening that distributes the load over an ever-increasing area at a time when the rise of specific heat precludes continued temperature increases. Once the flow has become stable again, the specimen cools to 4 K, and with further deformation, the process repeats.

As noted in the text, the tension and fracture test records at 295 and 76 K (not shown) do not exhibit serrations. In fact, serrations of the type occurring at 4 K are seldom observed at temperatures above 40 K. The instability criterion is satisfied only at the lowest temperatures because (1) the volume specific heat is reduced so that relatively large temperature increases are possible in straining, and (2) the flow stress is more strongly temperature dependent.

Test Methodology

According to the proposed convention [*5*], two offset lines for data qualification are drawn parallel to the blunting line at $\Delta a = 0.15$ and 1.5 mm, and data falling outside the specified interval are discounted. Although two data points in Fig. 5 do fall outside the specified interval, both lie on the linear regression line and so were used in the analysis of results.

Two errors were observed in the single-specimen J test: (1) the blunting line zero shift (Fig. 4) and (2) the false resistance curve slope owing to errors in the inferred Δa-values (Fig. 5). These errors are apparently related to plasticity effects on the compliance-versus-crack length correlation [*15*], but the cause is not yet fully understood. Further experience with the single-specimen method is needed to fully explain and compensate for these effects.

The experimental evidence for AISI 310S shows that the initiation of crack extension at 4 K occurs at a point after the first serration and before the maximum load. Therefore, taking the first load drop or the maximum load point as the J_{Ic} measurement point is an unacceptable procedure for austenitic stainless steels at 4 K. The unloading compliance technique used here enables J_{Ic} to be measured at 4 K with good accuracy, but gives an inaccurate resistance curve slope (dJ/da). The multiple-specimen technique gives both parameters accurately, but is more costly in materials and time. Normally, as many points as

desired can be obtained in the single-specimen technique. But owing to the serrated loading behavior at 4 K, few data points are obtained than usual, since unloadings cannot be performed at points of instability on the load-versus-deflection curve.

Martensitic Phase Transformation

The role of martensitic phase transformations on fracture toughness is a subject of fundamental interest, with potential practical applications in the development of austenitic stainless steels. Apparently, the effects may be different for different steel families [*16,17*]. Two opposite trends are suggested:

1. Since martensitic phases forming in metastable austenitic steels have hcp or bcc structures which are typically brittle at 4 K, it might be expected that transformations at cryogenic temperatures could reduce the fracture toughness.
2. If the martensitic phases forming in metastable steels can absorb energy that otherwise might be converted to crack extension, it might be argued that these transformations could improve fracture toughness, as in TRIP steels at 295 K [*17*].

Neither of these trends was observable in our study. From a simple comparison of stable and transforming steels having similar yield strengths (as in Fig. 5), we observed that the effects of phase transformation on toughness were negligible for the compositions studied. Unfortunately, it is not possible to vary the alloy stability while holding the composition constant. The relative stability of the Fe-Cr-Ni-Mn steels in Fig. 5 is a function of composition and is strongly dependent on nickel content. The unstable Fe-18Cr-8 to 10Ni steels featured in this comparison transformed locally to as much as 90 percent bcc martensite, as measured from X-ray examination of the 4 K fracture surfaces. Such large amounts of martensite were formed gradually with increasing plastic strain. The initial transformation began locally at slip plane intersections, and high percentages of bcc phase were detectable only after extensive plastic deformation. Significantly, the fracture surface appearance remained dimpled, as is the case for stable steels.

Conclusions

J-integral tests were performed on 25-mm-thick compact specimens of AISI 310S stainless steel immersed in liquid helium at 4 K. The major conclusions are:

1. The J_{Ic}-value for this material is 360 or 380 kJ/m^2, and the tearing modulus is 60.
2. The unloading compliance technique used here at 4 K gave a reasonably accurate J_{Ic}-value but an inaccurate J-Δa slope. Improvements to reduce the

error in inferred Δa-values and blunting line deviations are needed. Side grooves may help.

3. Serrations resembling "pop-ins" occurred in the 4 K test records of compact fracture specimens, analogous to the serrations observed in conventional tension tests of unnotched specimens. These serrations are caused by plastic flow instability and are not necessarily associated with true crack extension. Therefore, J_{Ic} should not be measured at the first "pop-in," because crack extension is not the true cause of the instability.

4. The failure mode for this AISI 310S steel at 4 K was ductile tearing. The same ductile tearing mechanism was associated with both stable and unstable regions of the load-deflection fracture test record.

5. Comparison of existing data for steels in the Fe-Cr-Ni-Mn family shows a universal rate of decrease of fracture toughness with increasing yield strength at 4 K, regardless of whether martensitic phase transformations occur. This suggests that microstructural stability does not necessarily influence toughness, at least for the range of compositions included in the comparison.

Acknowledgment

This work was supported by the Department of Energy, Office of Magnetic Fusion Energy.

References

[1] Read, D. T. and Tobler. R. L. in *Advances in Cryogenic Engineering-Materials*, Vol. 28, Plenum Press, New York, 1982, pp. 17-28.

[2] Ledbetter, H. M., Weston, W. F., and Naimon, E. R., *Journal of Applied Physics*, Vol. 46, 1975, pp. 185-194.

[3] Tobler, R. L., Read, D. T., and Reed, R. P. in *Fracture Mechanics: Thirteenth Conference. ASTM STP 743*, R. Roberts, Ed., American Society for Testing and Materials, 1981, pp. 250-268.

[4] Tobler, R. L. and Reed, R. P. in *Advances in Cryogenic Engineering-Materials*, Vol. 28, Plenum Press, New York, 1982, pp. 83-92.

[5] Clarke, G. A., Andrews, W. R., Begley, J. A., Donald, J. K., Embley, G. T., Landes, J. D., McCabe, D. E., and Underwood, J. H., *Journal of Testing and Evaluation*, Vol. 7, No. 1, 1979, pp. 49-56.

[6] Logsdon, W. A., Wells, J. M., and Kossowsky, R. in *Proceedings, Second International Conference on Mechanical Behavior of Materials*, American Society for Metals, Metals Park, Ohio, 1976, pp. 1283-1289.

[7] Reed, R. P., Tobler, R. L., Elmer, J. W., McHenry, H. I., and Yushchenko, K. A. in *Proceedings*, International Cryogenic Engineering Conference, ICEC 8, C. Rizzuto, Ed., IPC Science and Technology Press, Guildford, Surrey, U.K., 1980, pp. 797-801.

[8] Powell, G. W., Marshall, E. R., and Backofen, W. A., *Transactions, American Society for Metals*, Vol. 50, 1958, pp. 478-497.

[9] Basinski, Z. S., *Proceedings of the Royal Society*, London, Vol. A240, 1957, pp. 229-242.

[10] Basinski, Z. S., *Australian Journal of Physics*, Vol. 13, 1960, pp. 354-358.

[11] Read, D. T. and Reed, R. P. in *Advances in Cryogenic Engineering-Materials*, Vol. 26, Plenum Press, New York, 1980, pp. 91-101.

[12] Obst, B. and Pattanayak, D. in *Advances in Cryogenic Engineering-Materials*, Vol. 28, Plenum Press, New York, 1982, pp. 57-66.

[*13*] Wessel, E. T., *Transactions, American Society for Metals*, Vol. 49, 1957, pp. 149-172.
[*14*] Corsan, J. M. and Mitchem, N. I. in *Proceedings, Sixth International Cryogenic Engineering Conference*, IPC Science and Technology Press, Guildford, Surrey, U.K., 1976, pp. 342-344.
[*15*] Cheng, Y. -W., National Bureau of Standards, Boulder, Colo., private communication.
[*16*] Brickner, K. G. and Defillippi, J. D. in *Handbook of Stainless Steels*, D. Peckner and I. M. Bernstein, Eds., McGraw-Hill, New York, 1977, Chap 20.
[*17*] Gerberich, W. W., Hennings, P. L., Zackay, V. F., and Parker, E. R. in *Fracture 1969*, P. L. Pratt, Ed., Chapman and Hall, London, 1969, pp. 288-296.

Frank J. Loss,[1] *Blaine H. Menke,*[1] *Allen L. Hiser,*[1] *and Henry E. Watson*[2]

J-R Curve Characterization of Irradiated Low-Shelf Nuclear Vessel Steels

REFERENCE: Loss, F. J., Menke, B. H., Hiser, A. L., and Watson, H. E., "**J-R Curve Characterization of Irradiated Low-Shelf Nuclear Vessel Steels,**" *Elastic-Plastic Fracture: Second Symposium, Volume II—Fracture Resistance Curves and Engineering Applications, ASTM STP 803*, C. F. Shih and J. P. Gudas, Eds., American Society for Testing and Materials, 1983, pp. II-777–II-795.

ABSTRACT: The J-R curve behavior of irradiated nuclear pressure vessel steels is characterized in the ductile upper-shelf regime in order to provide a materials basis with which to assess the margin of safety against fracture for water reactor vessels exhibiting a low upper-shelf C_V energy. With the single specimen compliance technique, the R-curve is shown to follow a power-law behavior for small crack extension, and this phenomenon has led to a proposed new indexing procedure for J_{Ic}. In addition, a specimen size dependence of the R-curve has been suggested by the results of similar compact tension specimens up to 100 mm thick and which have sufficiently deep side grooves to produce a straight crack-front extension.

R-curve data are presented in terms of a J versus T instability diagram which couples material and structural parameters, thereby permitting an analysis to be made of the margin against failure in terms of J. Also, a correlation has been suggested between the R-curve parameters and C_V shelf energy; this could enhance the structural significance of C_V reactor surveillance data.

KEY WORDS: J-integral, R-curve, elastic-plastic fracture, reactor pressure vessels, fracture toughness, radiation, tearing modulus, size effect

Certain steels and weld deposits used in the beltline region of commercial nuclear pressure vessels exhibit a high sensitivity to irradiation embrittlement. As a result, the crack initiation toughness K_{Ic} is projected to be less than that required to provide an acceptable margin for certain postulated ac-

[1]Technical director, senior engineer, and mechanical engineer, respectively, Materials Engineering Associates, Inc., Lanham, Md. 20706.
[2]Supervisory mechanical engineer, Naval Research Laboratory, Washington, D.C. 20375.

cident conditions. On the other hand, within the ductile upper-shelf regime these pressure vessel steels are expected to exhibit a stable crack extension behavior with rising load up to the point of instability. Under these conditions the application of a structural integrity concept that is based upon a crack initiation philosophy could produce excessive conservatism in the analysis. Thus, the question to be addressed is one of defining the margin against failure under elastic-plastic conditions as opposed to application of a linear-elastic fracture mechanics (LEFM) concept to a situation which may not physically exist. To address this issue, the Nuclear Regulatory Commission (NRC) is sponsoring research studies to (1) formulate a structural integrity approach based upon elastic-plastic behavior, (2) characterize the toughness of low upper-shelf steels in terms compatible with the analysis procedure, and (3) verify the approach through structural tests.

In order to achieve these objectives the tearing instability approach as defined by Paris et al [*1*][3] is being explored as one means to assess structural reliability. This procedure hinges on the concept of a J-R curve which exhibits an apparent increase in J-integral toughness with stable crack extension within the upper shelf regime. As part of an NRC-coordinated program, this paper summarizes experimental research studies to define the elastic-plastic toughness trends of low upper-shelf irradiated vessel steels in terms of the J-R curve. When coupled with a tearing instability analysis, these results will permit an assessment of vessel integrity in the presence of assumed defects. The fracture behavior within the brittle-ductile transition region, which is not currently amenable to a tearing instability analysis, is not treated here.

Experimental Program

At the Naval Research Laboratory (NRL) an extensive experimental program was undertaken to characterize the fracture toughness of irradiated structural steels. Under NRC sponsorship, investigations centered on the behavior of low upper-shelf steels with special emphasis directed to weld deposits having a high sensitivity to radiation embrittlement; this sensitivity has been associated with a high residual copper impurity level in the weld. Characterization of weld deposits irradiated under the Heavy Section Steel Technology (HSST) Program [*2*] formed a central part of this effort. Here, the J-R-curve behavior of seven irradiated A533-B submerged-arc welds is being studied with compact tension (CT) specimens of 12 to 100 mm thickness. A related effort, termed the IAR program, [*3,4*], focused on embrittlement relief through periodic heat treatment (annealing). In the latter program two A533-B weld deposits containing high copper impurity levels were subjected to a cyclic pattern of irradiation (I) followed by annealing (A) and reirradia-

[3]The italic numbers in brackets refer to the list of references appended to this paper.

tion (R). Since irradiation of these welds resulted in a low upper-shelf behavior, such a sequence may be required over the vessel's lifetime in order to insure the maintenance of an adequate margin of conservatism. Under a third program, sponsored by the Electric Power Research Institute (EPRI), a fracture toughness data base of R-curve and Charpy V-notch (C_V) properties is being developed for irradiated steels used in U.S. reactor vessels, including A302-B and A533-B plate, A508-2 forging, and submerged-arc welds of these steels [5].

Because of limited irradiation space, both in test reactors and power reactors as well, it is required to minimize the size and number of fracture test specimens. For practical reasons, therefore, it has been necessary to characterize the R-curve by means of a single-specimen test procedure. To this end, we have adapted the single-specimen compliance (SSC) technique [6] for remote testing in a hot cell.

Single Specimen Compliance Procedure

The SSC technique provides a method to determine the crack extension by means of small unloadings (~ 10 percent) at regular intervals during the specimen loading. Because these unload and reload segments are conducted under elastic conditions, even though the specimen has undergone extensive plastic deformation, the change in crack length from one unloading to the next can be inferred through a change in the compliance ($EB\delta/P$) where E is Young's modulus, B the specimen thickness, and P and δ the load and load-line deflection, respectively. A 25.4-mm-thick compact tension specimen (IT-CT) was selected for the majority of the studies because it can be irradiated easily and yet its size provides sufficient mechanical constraint to infer high levels of plane-strain initiation toughness when the specimen itself exhibits elastic-plastic behavior. For example, the criterion of $b > 25\, J_{Ic}/\sigma_f$ given in ASTM Test for J_{Ic}, a Measure of Fracture Toughness (E 813-81) will permit measurement of J_{Ic} of approximately 500 kJ/m^2 for irradiated material where b and σ_f are the unbroken ligament and flow stress, respectively.

The SSC method as developed by NRL is described in Refs 7 and 8. A CT specimen conforming to the geometry of the ASTM Test for Plane-Strain Fracture Toughness of Metallic Materials (E 399-78) is employed. However, the notch region has been modified to permit the mounting of razor knife edges for the measurement of load-line displacement with a clip gage. In addition, a crack length-to-width ratio (a/W) > 0.5 was used for some tests. The J-value can be calculated at any point on the load versus load-line displacement record using the relationship [9]

$$J_{(i+1)} = \left[J_i + \left(\frac{\eta}{b}\right)_i \frac{A_{i,i+1}}{B}\right]\left[1 - \left(\frac{\gamma}{b}\right)_i (a_{i+1} - a_i)\right] \qquad (1)$$

where

$\eta = 2 + (0.522)\, b/W$,
$\gamma = 1 + (0.76)\, b/W$,
a = crack length, and
$A_{i,i+1}$ = incremental area under the load versus load-line displacement record.

Equation 1 incorporates a correction for crack extension; a separate correction for specimen rotation is also applied [5].

Application of this method with CT specimens having thicknesses of 12 to 41 mm (0.5T- to 1.6-CT) has produced R-curves whose points have a typical accuracy of ± 0.25 mm in predicted crack extension versus that measured optically, provided the crack front is straight and the steel is relatively free from metallurgical inhomogeneity [8]. The scatter in predicted crack extension increments on an individual R-curve has been generally ± 0.08 mm. Thus, the SSC technique presents an attractive procedure for R-curve determination.

A typical R-curve produced with the SSC technique, as illustrated in Fig. 1, is normally restricted to a small crack extension (Δa) in order to maintain a region of "J-dominance." This requirement has been formulated by Hutchinson and Paris [10] as $\omega \gg 1$ where $\omega = (b/J)(dJ/da)$. However, R-curves associated with longer crack extension, which would violate the ω-criterion, may be necessary for a given structural analysis. In addition, proposed validity criteria, including that of ω, are still topics of research. Therefore, R-curves have been developed here which sometimes exceed current crack extension limitations with the expectation that the data may prove useful for future analyses.

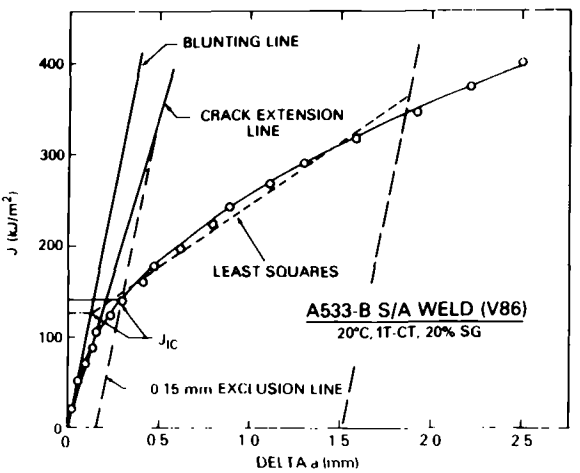

FIG. 1—*Power-law R-curve described with the SSC approach. The indexing procedure for* J_{Ic} *proposed by the authors is compared with that of ASTM E 813 (least squares).*

The R-curve format in Fig. 1 is in accordance with that of ASTM E 813: J_{Ic} is defined by the intersection of a linear regression fit to the data (that is, the dashed line between the 0.15 and 1.5-mm exclusion lines) with the blunting line, $J = 2\sigma_f \Delta a$. The use of a least-squares fit of the data stemmed from the ASTM J_{Ic} standard which emphasizes a multiple-specimen procedure. On the other hand, the SSC procedure permits an R-curve to be generated with one specimen. The latter is not only cost-effective from a materials point of view but, more importantly, minimizes the variability in the R-curve over that produced by a multiple-specimen procedure typically involving five or more specimens. Using this technique, Loss and co-workers [*4*] have demonstrated that the R-curve is nonlinear for small amounts of crack extension (for example, 2 mm) in structural steels. Consequently, the R-curve in the region between the 0.15 and 1.5-mm exclusion lines is more correctly described in terms of a power law, $J = C\Delta a^n$, where C and n are constants chosen to optimize the curve fit.

As a consequence of the power-law R-curve it is clear that the tearing modulus of the material, T_m, defined as (E/σ_f^2) (dJ/da), is not constant for small crack extensions as was originally envisioned [*1*]. In view of this, the J_{Ic}-value computed with a linear regression fit of the data assumes a degree of arbitrariness which was not apparent when the R-curve was considered as linear in the region between 0.15 and 1.5-mm exclusion lines. For example, if the 1.5-mm exclusion line had been chosen as a larger value, then the least-squares fit of the data would necessarily produce a higher value of J_{Ic}.

To circumvent the potential difficulties associated with the least-squares procedure, Loss and co-workers [*4*] have formulated a new indexing procedure for J_{Ic} which more clearly represents the physical behavior. Specifically, J_{Ic} is taken as that value of J where the power-law R-curve crosses the 0.15-mm exclusion line. This is an engineering approach, analogous to that for the 0.2 percent yield stress, and permits a small, but measurable crack extension at the J_{Ic} point. However, it should be noted that for the reactor vessel steels discussed here the magnitude of J_{Ic} given by the authors' method is nearly identical to that of ASTM E 813 for reactor vessel steels, as illustrated in Fig. 1. To address materials having a toughness higher than that illustrated in Fig. 1, it is proposed to define an allowable crack extension at the J_{Ic} point in terms of the crack opening displacement. In this case J_{Ic} would be the point in Fig. 1 where the R-curve crosses a crack extension line, defined as $J = {}^4/_3\sigma_f \Delta a$, provided that the crack extension has first exceeded the 0.15-mm exclusion line [*4*].

Effect of Side Grooves

The crack-front extension in a CT specimen normally exhibits a tunneled shape which results from the lack of mechanical constraint at the free surfaces. The latter permits plastic deformation at these locations at the expense of

crack extension. Just the opposite is true in a more highly constrained configuration (for example, the specimen midthickness). Currently there is disagreement as to whether the tunneling in a laboratory specimen is representative of the crack-front behavior in a large structure. In addition, this phenomenon results in a three-dimensional effect which may not be properly accounted for by the two-dimensional form of the J-integral. It has been shown that a 20 percent total side groove depth will eliminate the tunneling in CT specimens having thicknesses of 12 to 100 mm. Also, the R-curves produced with a straight crack-front extension exhibit slopes (dJ/da) lower than those associated with tunneled crack extension [*8*]. Thus, it is possible that side-grooved specimens may more accurately represent the behavior of a thick section such as the wall of a nuclear vessel. For this reason the experimental programs were conducted with specimens having 20 percent side grooves. In this case the net thickness B_n is used in place of B in Eq 1. This is an approximation which is generally accepted in the absence of an exact relationship.

Instability Analysis

An instability concept is illustrated schematically in Fig. 2 in terms of structural parameters (applied J_a and T_a) and the material characteristics (J-R curve). The material resistance curve reflects the power-law behavior depicted in Fig. 1. The structural loading line represents a simple case of a surface flaw in a cylindrical shell, where a is the crack depth. The loading of the cylinder and the related response of the material are illustrated by the arrows; instabil-

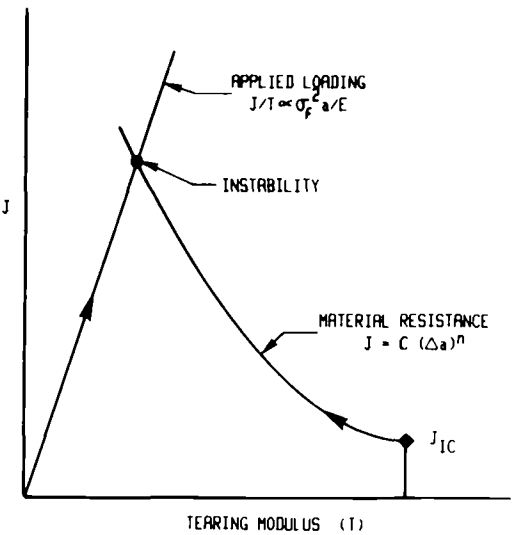

FIG. 2—*Instability diagram illustrating the interaction of material and structural parameters.*

ity is achieved when $T_a > T_m$, as denoted by the intersection of the two curves. Application of this diagram requires an accurate computational procedure for J_a and T_a under elastic-plastic conditions as well as a characterization of the R-curve which considers the possible specimen versus structural geometry dependence of this quantity. The preceding areas are current topics of research and the verification of the tearing instability concept will require structural tests. (Further discussion of this subject is given in Ref *11*.) From a materials point of view, however, this concept provides a valuable insight as to the structural significance of changes in R-curve behavior, such as the toughness degradation associated with radiation embrittlement.

In a subsequent section, R-curve data are presented in the format of a J versus T diagram to better assess the significance of the trends observed with the vessel steels that exhibit a low upper-shelf behavior. For reference to the structural behavior, a value of 8.8 kJ/m^2 is taken for the slope of the applied loading line. In fact, it is believed that the loading associated with a surface flaw in a cylindrical section will produce a slope much greater than this for flaws on the order of 25 mm in depth [*11*]. Consequently, this reference point for the structural input is an illustrative example that incorporates a degree of conservatism.

Curve Trends with Irradiation

IAR Welds

An example of the change in the R-curve with irradiation is illustrated in Fig. 3. This result, selected from the IAR program [*4*], illustrates the behavior of a weld deposit containing a high copper impurity level (0.35 percent copper). The shaded band represents the results of several specimens irradiated to a fluence of 12×10^{18} neutrons (n)/cm^2 > 1 MeV. Note that J_{Ic} has decreased by 50 percent from the value associated with the unirradiated material. If expressed in terms of K_{Ic}, this implies a twofold reduction in the critical crack size for initiation. Near the end of a 30-to-40-year lifetime, a typical pressurized water reactor vessel can accumulate a fluence significantly greater than this at the inside wall, with a concurrent degradation in J_{Ic}. Inferring a K_{Ic}-value from J_{Ic}, using the relationship $K_{Jc} = [EJ_{Ic}]^{1/2}$, results in a value of approximately 117 MPa$\sqrt{m}$ for the irradiated material.

The tearing modulus exhibits a somewhat greater effect of irradiation than does J_{Ic}. Because of the variation of T_m with crack extension, an average value of tearing modulus, T_{avg}, has been defined in the region between the exclusion lines (similar to the least-squares fit shown in Fig. 1). On this basis T_{avg} has decreased by a factor of 2.5 for the fluence illustrated. Additional data are contained in Refs *7* and *8*.

The variation in T_{avg} with temperature is shown in Fig. 4 for another weld deposit in the IAR program. The inverse relationship shown here between

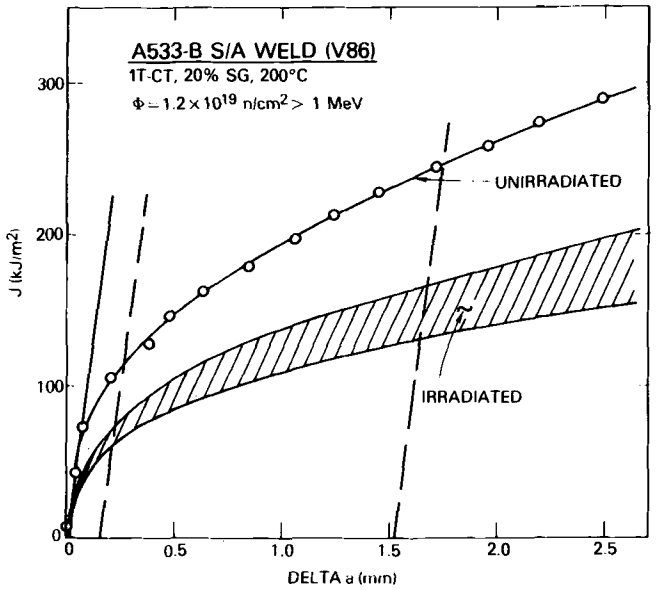

FIG. 3—*Comparison of R-curve trends between unirradiated and irradiated conditions.*

T_{avg} and temperature is sufficiently pronounced such that it must be considered in a structural analysis which uses the instability diagram (Fig. 2). (This behavior is not consistent with a temperature-independence in C_V shelf energy as is often depicted for these steels.) While not an integral part of the current theme, Fig. 4 also illustrates the recovery in toughness with annealing. The fact that subsequent reirradiations, following annealing, do not result in further embrittlement over that observed with the initial irradiation (1), suggests that periodic annealing can limit the degree of embrittlement encountered during the vessel's lifetime.

HSST Low-Shelf Weld Deposits

Seven different A533-B submerged-arc weld deposits, representing commercial practice, have been irradiated to fluences of 6 to 20 $\times$ 10^{18} n/cm^2 > 1 MeV under the HSST program [*2*]. These irradiations were designed to achieve a low upper-shelf behavior, that is, a C_V upper shelf below 68 J. This goal was largely attained in that the C_V shelf levels for the irradiated welds ranged from 54 to 81 J.

A summary of R-curve trends for these welds, developed with 1.6T-CT specimens (41 mm thick), is presented in Fig. 5. The J_{Ic}-values lie between 55 and 90 kJ/m^2, which is similar to the results obtained for the welds in the IAR program. The R-curves in Fig. 5 exhibit a power-law behavior similar to

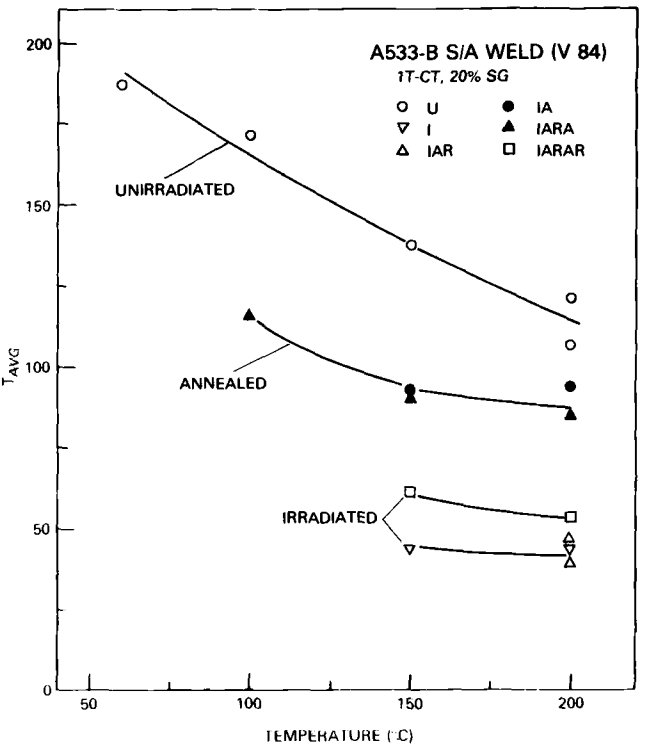

FIG. 4—*Variation of average tearing modulus with temperature.*

observations by the authors with smaller-size specimens [*4*]. In these tests, large crack extensions were achieved (~20 mm), representing the first data of this type for irradiated steels. The ω-values range from approximately 10 at a crack extension of 1.5 mm to unity near 6 mm of crack extension. Thus, the proposed region of J-dominance, in terms of ω, is violated somewhere between these crack extension increments. The data also illustrate the low values T_m (proportional to R-curve slope) that were observed at large Δa values. In fact, one curve actually exhibits a negative slope. This is believed to be a consequence of exceeding the limit of applicability of the correction for crack extension, contained in Eq 1. There is a marked decrease between the average value of tearing modulus, as evaluated within the exclusion lines, (T_{avg}) and T_m at, say, 6 mm of crack extension. Consequently, the use of T_{avg} to project structural integrity, where large crack extensions are anticipated, may not yield a conservative result. Also, because of the flattening of the R-curve at large Δa, a power-law fit is no longer appropriate in this region.

The majority of tests illustrated in Fig. 5 were conducted at 200°C; other tests were performed at somewhat lower temperatures, though still within the

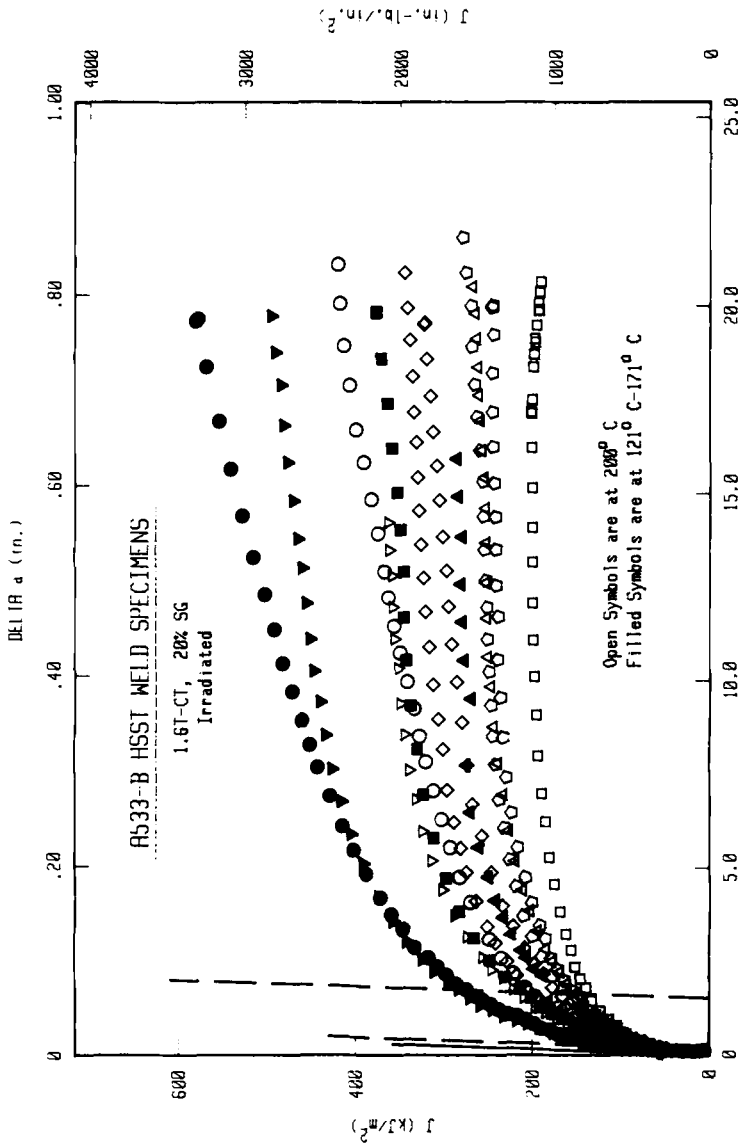

FIG. 5—*Comparison of postirradiation R-curve trends developed with 1.6T-CT specimens for six different HSST submerged-arc weld deposits.*

upper-shelf regime. A comparison of T_{avg}-values obtained from these results corroborates the inverse relationship between temperature and R-curve slope shown in Fig. 4. Other than this temperature dependence, no definitive relationship is apparent between the R-curve levels and the mechanical properties or irradiation conditions. This is not intended to be a generalization for all conditions since the commonality of the data is due, in part, to the relatively narrow range of C_V energies which is represented. In addition, the variation in fluence (3:1) among the welds, coupled with differences in sensitivity to irradiation stemming from the different copper levels (0.16 to 0.40 percent), tends to mask the embrittlement trends.

Size Effects

The effects of specimen size on the R-curve have been investigated with similar CT specimens having 20 percent side grooves (0.5T- to 4T-CT). Figure 6 compares R-curves developed by four different laboratories using IT- and 4T-CT specimens cut from the same A533-B steel plate (HSST plate 02) and side-grooved by 20 percent; no difference in R-curve behavior is indicated. This result again demonstrates that power-law form of the R-curve for larger-size specimens. Figure 7 compares R-curves developed with three different-size specimens cut from an irradiated weld deposit. In this case the 4T-CT specimen has produced a curve which lies above those developed with the smaller-size specimens. This result is opposite to the expected behavior: Because of its higher constraint, the larger specimen should produce the lower R-curve. Finally, Fig. 8 compares R-curves for another HSST weld deposit in the pre- and post-irradiated conditions. With the irradiated material, identical R-curves have been defined by the 1.6T- and 4T-CT specimens. For the unirradiated material, however, a somewhat higher R-curve has been produced with the larger-size specimen.

These preliminary results suggest that, for certain tests, a specimen size independence of the R-curve exists; in other cases the results suggest that the smaller specimens produce lower R-curves that would be defined with larger specimens. An explanation of this inconsistent behavior is not currently available and this topic warrants further investigation. In the authors' opinion the differences in R-curves are neither the result of metallurgical variability (since data from small specimens have exhibited little scatter) nor are they due to other sources of experimental data scatter (since the SSC technique has produced little scatter). Differences in ω also should not contribute to the variability in the R-curves since the criterion of $\omega \gg 1$ is satisfied in the region of crack extension where differences in the R-curve are observed.

Data Compilation and Correlations

Figure 9 summarizes R-curve data from IT-CT specimens obtained from programs at NRL sponsored by the NRC and EPRI. Trends are illustrated

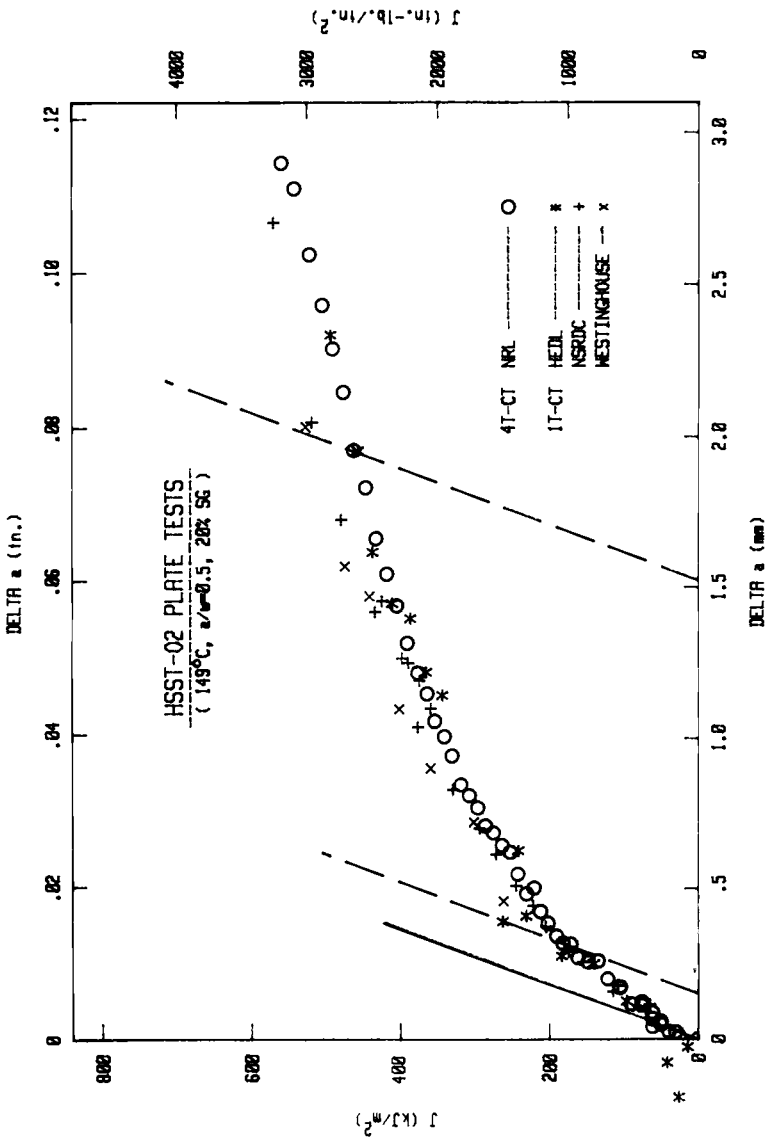

FIG. 6—*Comparison of R-curves measured for four laboratories using different-size specimens cut from a plate of A533-B steel.*

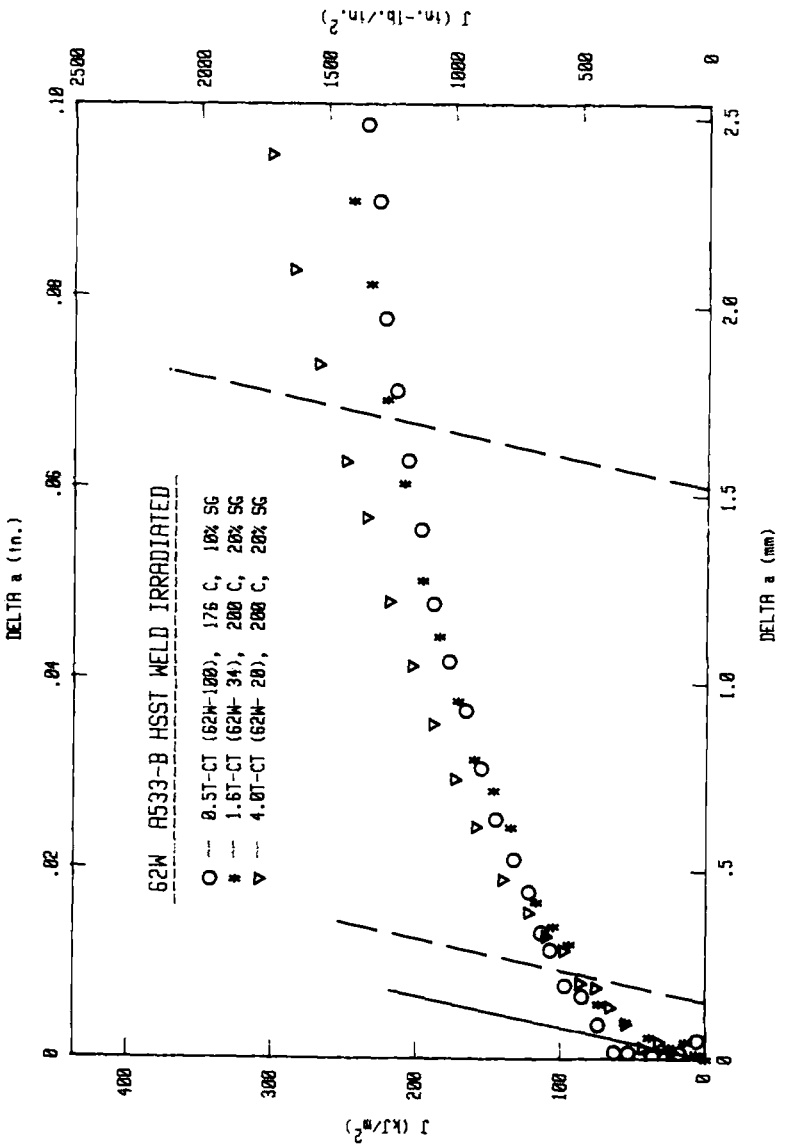

FIG. 7—*Comparison of R-curves defined by three different-size specimens cut from an irradiated A533-B weld deposit.*

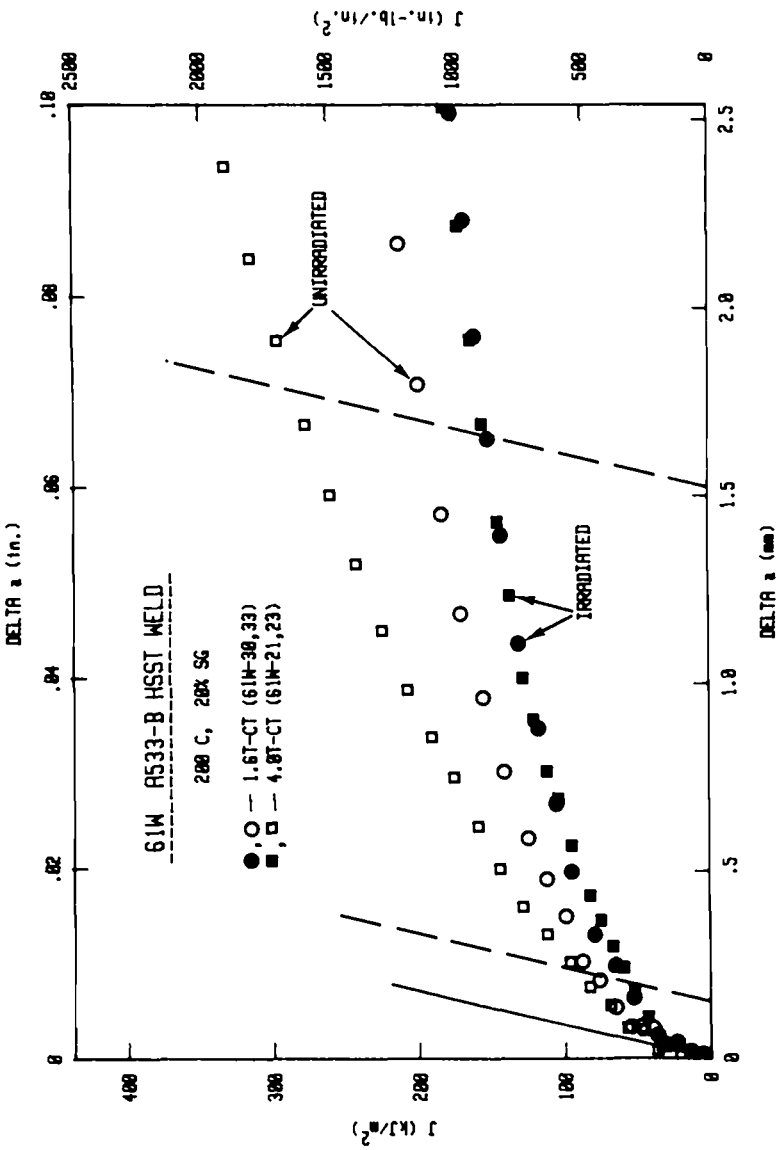

FIG. 8—*Comparison of R-curves for an A533-B weld deposit in the pre- and post-irradiated conditions using two different-size specimens.*

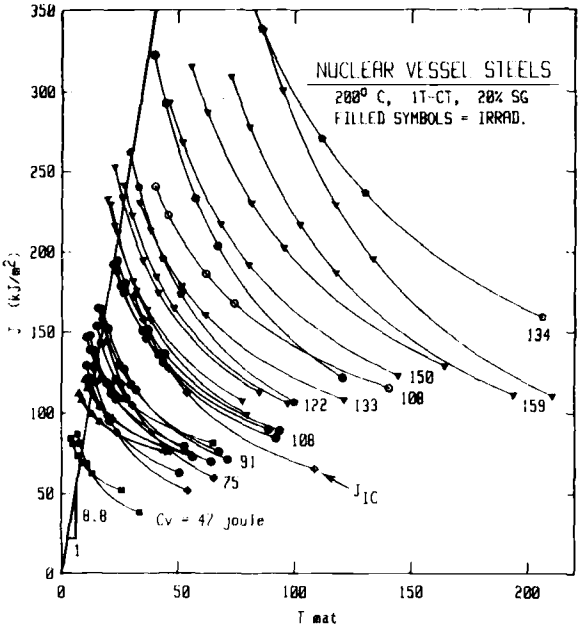

FIG. 9—*R-curve trends for a range of reactor vessel steels. Selected C_V shelf energies are indexed.*

from eight reactor vessel steels including A533-B and A302-B plate, A508-2 forging, and welds of these steels. The results from the HSST welds, however, have not been included here because of a possible specimen size dependence. This compilation is the first of its type and encompasses the range of materials and toughness levels expected in U.S. reactor vessels, with the exception of the very high toughness which is characteristically exhibited by some A508-2 forgings.

The R-curves for all materials in Fig. 9, unirradiated as well as irradiated, are shown to follow a power-law relationship. The lowest points on each R-curve represent J_{Ic}; subsequent points, in increasing order, denote crack extension increments of 0.75, 1.0, 1.6, and 2.0 mm. It is clear that the R-curve levels generally increase with C_V shelf energy. This trend provides the first indication that a correlation with C_V shelf energy may be possible. If verified, this observation will significantly enhance the usefulness of reactor surveillance data, which are often based on the results of C_V tests. It must be cautioned, however, that the R-curves are temperature dependent (Fig. 4) so that the trends in Fig. 9 are strictly applicable only at 200°C.

To project a general assessment of vessel integrity, the R-curve data in Fig. 9 have been grouped (approximately) into regions according to C_V shelf energy (Fig. 10); lines representing a fixed crack extension have also been plotted. This formulation is the first generalization of R-curve data for low-

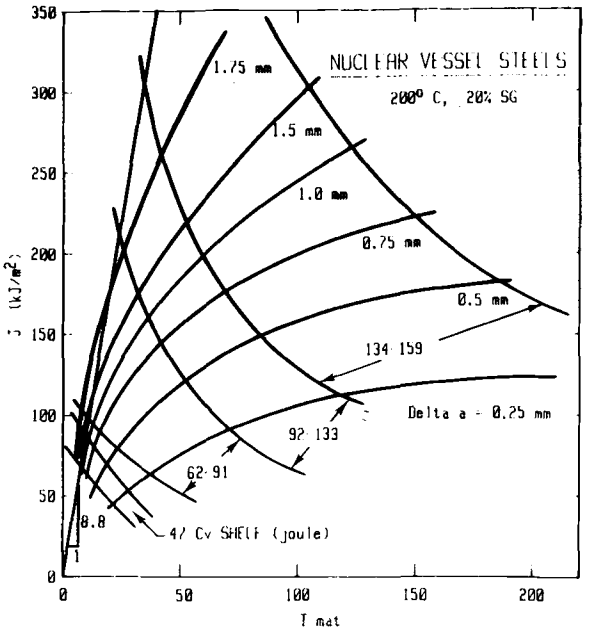

FIG. 10—*Generalization of trends in Fig. 9 in terms of C_V shelf energy and stable crack extension (Δa).*

shelf reactor vessel steels in a format suitable for a tearing instability analysis. While this interpretation is preliminary and subject to verification through bona fide structural tests, a scheme is presented for coupling the loading parameters, J_a and $(J/T)_a$, associated with a given flawed condition with the material response so as to predict both the margin of safety against instability at a given J level as well as the amount of stable crack extension to be expected.

Another correlation between the R-curve data base and C_V shelf energy is presented in Fig. 11. Here, J at a (J/T) value of 8.8 kJ/m^2 is plotted against C_V shelf energy, and a correlation between the two quantities is apparent. (This correlation includes data from steels exhibiting high R-curves which are above the region illustrated in Fig. 9. Because of the large crack extension associated with the latter, a power-law fit of the data was not used.) The IT-CT data band in Fig. 11 was constructed without benefit of the data from the HSST tests (1.6T- and 4T-CT), and some of these data do not exactly match the projection, thereby suggesting a specimen size effect. However, it is not believed that the unirradiated 4T-CT data requires construction of a correlation band wider than shown in Fig. 11. Note that the results for most of the irradiated 4T-CT tests lie inside the band while just the opposite is true for the unirradiated tests of these same welds. The behavior of the 4T-CT

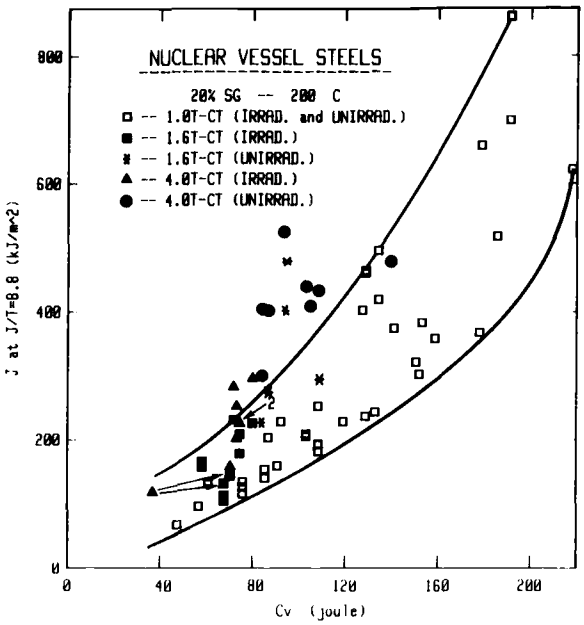

FIG. 11—*Correlation between C_V shelf energy and a fixed value of* J/T.

tests suggests that a size effect may result because of a different degree of plasticity between the different size specimens. If correct, the size effect would be more pronounced for the unirradiated specimens, which are presumed to undergo more extensive plastic deformation than their irradiated counterparts, which exhibit a lower toughness.

From the correlation illustrated in Fig. 11 it is presumed that a similar behavior will exist between C_V shelf energy and other values of $(J/T)_a$. Recall that a value of 8.8 kJ/m^2 for this quantity was chosen somewhat arbitrarily to represent a factor of safety in the loading of a cylindrical section containing a flaw. The R-curves which form the basis for the correlation in Fig. 11 may exceed the region of J dominance. For these larger Δa-values, questions remain as to the validity of the IT-CT data in terms of ω. In addition, beyond this region of crack extension the power-law fit is not appropriate so that the curves in Fig. 9 should not be extrapolated to obtain instability points at larger values of $(J/T)_a$. Nevertheless, the current correlation appears to be sufficiently well established to permit a tearing instability analysis of reactor vessels for J_a levels approaching 350 kJ/m^2 in connection with steels having low upper-shelf energy.

Conclusions

The principal conclusions of this study are:

1. The SSC technique has been demonstrated as an effective method to characterize the J-R curve of irradiated steels.

2. The J-R curves from different-size specimens obey a power-law relationship for crack extension increments less than 2 mm, for low-shelf steels. This observation has led the authors to propose a new indexing procedure for J_{Ic}. The curvature in the R curve also demonstrates that the tearing modulus varies with crack extension and is not constant as was presumed earlier.

3. The first R-curve data base has been developed for irradiated vessel steels having low shelf energy. In terms of an average tearing modulus the data exhibit an inverse relationship with test temperature. This is not consistent with a temperature insensitivity of C_V upper shelf energy which is often shown for these steels.

4. In certain cases a specimen size independence of the R-curve has been demonstrated with side-grooved CT specimens having thicknesses between 12 and 100 mm. In other cases, R-curves defined with 4T-CT specimens were above those measured with smaller-size specimens, thereby suggesting a size effect.

5. R-curve data have been presented in the format of a J versus T instability diagram which couples material and structural parameters and thereby permits an initial assessment to be made of the margin against failure in terms of the applied J; the amount of stable crack extension to be expected is also predicted.

6. A correlation has been suggested between the R-curve parameters and C_V upper-shelf energy. If verified, this finding could enhance the significance of C_V reactor surveillance data with respect to structural integrity.

Acknowledgment

Sponsorship of this research by the U.S. Nuclear Regulatory Commission is gratefully acknowledged. The authors are also indebted to the Electric Power Research Institute for their support of related R-curve studies reported here.

References

[1] Paris, P. C., Tada, H., Zahoor, A., and Ernst, H. in *Elastic-Plastic Fracture, ASTM STP 668*, J. D. Landes, J. A. Begley, and G. A. Clarke, Eds., American Society for Testing and Materials, 1979, pp. 5-36.

[2] Whitman, G. D., "Heavy Section Steel Technology Program, Quarterly Progress Report for April-June 1976," ORNL/NUREG/TM-49, Oak Ridge National Laboratory, Oak Ridge, Tenn., Oct. 1976.

[3] Hawthorne, J. R., Watson, H. E., and Loss, F. J. in *Effects of Radiation on Materials—*

Tenth International Symposium, ASTM STP 725, American Society for Testing and Materials, 1981, pp. 63-75.

[4] Loss, F. J., Menke, B. H., Gray, R. A., Jr., and Watson, H. E. in *Effects of Radiation on Materials—Tenth International Symposium, ASTM STP 725*, American Society for Testing and Materials, 1981, pp. 77-91.

[5] "NRL-EPRI Research Program (RP886-2), Evaluation and Prediction of Neutron Embrittlement in Reactor Pressure Vessel Materials, Annual Report for CY 1978," J. R. Hawthorne, Ed., NRL Report 8327, Naval Research Laboratory, Washington, D.C., 30 Aug. 1979.

[6] Clarke, G. A., Andrews, W. R., Paris, P. C., and Schmidt, D. W. in *Mechanics of Crack Growth, ASTM STP 590*, American Society for Testing and Materials, 1976, pp. 27-42.

[7] "Structural Integrity of Water Reactor Pressure Boundary Components, Quarterly Progress Report for the Period April-June 1979," F. J. Loss, Ed., NUREG/CR-0943, NRL Memorandum Report 4064, Naval Research Laboratory, Washington, D.C., 28 Sept. 1979.

[8] "Structural Integrity of Water Reactor Pressure Boundary Components, Annual Report, Fiscal Year 1979," F. J. Loss, Ed., NUREG/CR-1128, NRL Memorandum Report 4122, Naval Research Laboratory, Washington, D.C., 31 Dec. 1979.

[9] Ernst, H., Paris, P. C., and Landes, J. D. in *Fracture Mechanics* (Thirteenth Conference), *ASTM STP 743*, American Society for Testing and Materials, 1981, pp. 476-502.

[10] Hutchinson, J. W. and Paris, P. C. in *Elastic-Plastic Fracture, ASTM STP 668*, J. D. Landes, J. A. Begley, and G. A. Clarke, Eds., American Society for Testing and Materials, 1979, pp. 37-64.

[11] "Resolution of the Reactor Vessel Materials Toughness Safety Issue," R. E. Johnson, Ed., NUREG-0744, U.S. Nuclear Regulatory Commission, Washington, D.C., Sept. 1981.

Manuel Freitas[1] *and Dominique Francois*[1]

Initiation of Fatigue Cracks Around Inclusions in Rolling Fatigue

REFERENCE: Freitas, M. and Francois, D., **"Initiation of Fatigue Cracks Around Inclusions in Rolling Fatigue,"** *Elastic-Plastic Fracture: Second Symposium, Volume II—Fracture Resistance Curves and Engineering Applications, ASTM STP 803*, C. F. Shih and J. P. Gudas, Eds., American Society for Testing and Materials, 1983, pp. II-796–II-807.

ABSTRACT: The cyclic behavior of E52 100 quenched and tempered rolling bearing steel displayed strain-hardening according to the law $\Delta\sigma/2 = 5790\ (\Delta\epsilon_p/2)^{0.137}$. The fatigue life was found to be given by the formula $\Delta\epsilon/2 = 0.0073\ (2N_f)^{-0.36} + 0.0145\ (2N_f)^{-0.062}$.

The cyclic strain-hardening law was used in a finite-element bidimensional incremental elastoplastic analysis to compute the plastic deformation around inclusions in the Herzian stress field produced by a rolling ball. Three types of inclusions were studied: alumina, titanium nitride, and spinel. The maximum plastic strain region was found to be inclined with respect to the rolling direction as observed in rolling bearings. This strain distribution provided an explanation for the relative harmfulness of the various inclusions. The strain amplitude found could be used to predict the number of cycles for fatigue crack initiation at inclusions using the experimental fatigue life law.

KEY WORDS: rolling fatigue, bearing steel, low cycle fatigue, elastic-plastic fracture

In rolling fatigue the role of inclusions is of prime importance [*1–3*].[2] Many authors have demonstrated the improvement in fatigue properties which results from a cleaner material, obtained, for instance, by vacuum or slag remelting [*2,4,5*].

In pure rolling the stress field was studied by Hertz [*6*]. He showed that the region where the tangential stress is maximum is located below the surface. Micrographic observations reveal without any ambiguity that the fatigue cracks are nucleated at inclusions below the surface [*4,5*] in association with

[1]Research student and director, respectively, Université de Technologie de Compiègne, Laboratoire de Recherche sur les déFaillances d'Origine Mécanique et Physico-Chimique, B. P. 233-60206-Compiègne Cedex, France; coauthor Francois is currently at École Centrale des Arts et Manufactures, Grande Voie des Vignes, 92 290 Chatenay-Malabry, France.

[2]The italic numbers in brackets refer to the list of references appended to this paper.

structural modifications of the martensite, white phases, and butterflies, inclined at 45 deg with respect to the surface.

The interpretation of the phenomenon must be related to the mechanical properties of the inclusions and thus to their chemical nature, to their shape and dimensions, and to the mechanical properties of the martensitic matrix. The attempts made to rationalize the classification of the inclusions according to their harmfulness are not adequate [*1, 7–9*]. Neither the size effect nor the internal stresses induced by the difference between the thermal expansion coefficients of the matrix and of the inclusions can explain quantitatively the observed phenomena. The authors do not take into account the cyclic behavior of the material nor the Hertzian stress field.

The fatigue crack initiation which usually takes place at the surface can now be predicted by the consideration of a tiny fictitious specimen which consumes its lifetime when submitted to the local cyclic plastic deformations in a strain concentration region [*10*]. The fatigue initiation time is then a function of the local strain range, itself depending upon the cyclic behavior of the material, and upon the plastic fatigue life [Manson-Coffin law].

The present study uses this approach, linking the crack initiation at inclusions in rolling fatigue with the local plastic behavior of the matrix. It attempts to bring a rational explanation to the role of inclusions by a precise study of the cyclic properties of the matrix followed by the best possible analysis of the strain and stress fields near the inclusions.

Experimental Procedure

Material Tested

An E52 100 rolling bearing steel was studied. It was slag-remelted, giving a low inclusion count. The chemical composition is given in the first Table 1.

The steel was austenized at 850°C for 20 min in a neutral salt bath, quenched in oil at 20°C and annealed at 180°C for 2 h and then air-cooled.

The hardness obtained was HRC 61.5. The residual austenite fraction was 10 percent.

Specimens

The specimens used were hourglass shaped with a minimum radius of 5 mm and a radius of curvature of 30 mm, machined out of a 15-mm-diameter bar. They were machined before heat treatment and finally longitudinaly rectified.

Equipment and Procedure

The fatigue tests were carried out on a 250-kN servohydraulic Mayes ESH 4 C fatigue machine, using total diametral strain control. The diametral strain was

TABLE 1—*Chemical composition of the steel, %.*

C	Mn	Si	S	P	Mo	Cr	Ni
1.01	0.27	0.14	0.002	0.009	0.02	1.45	0.05

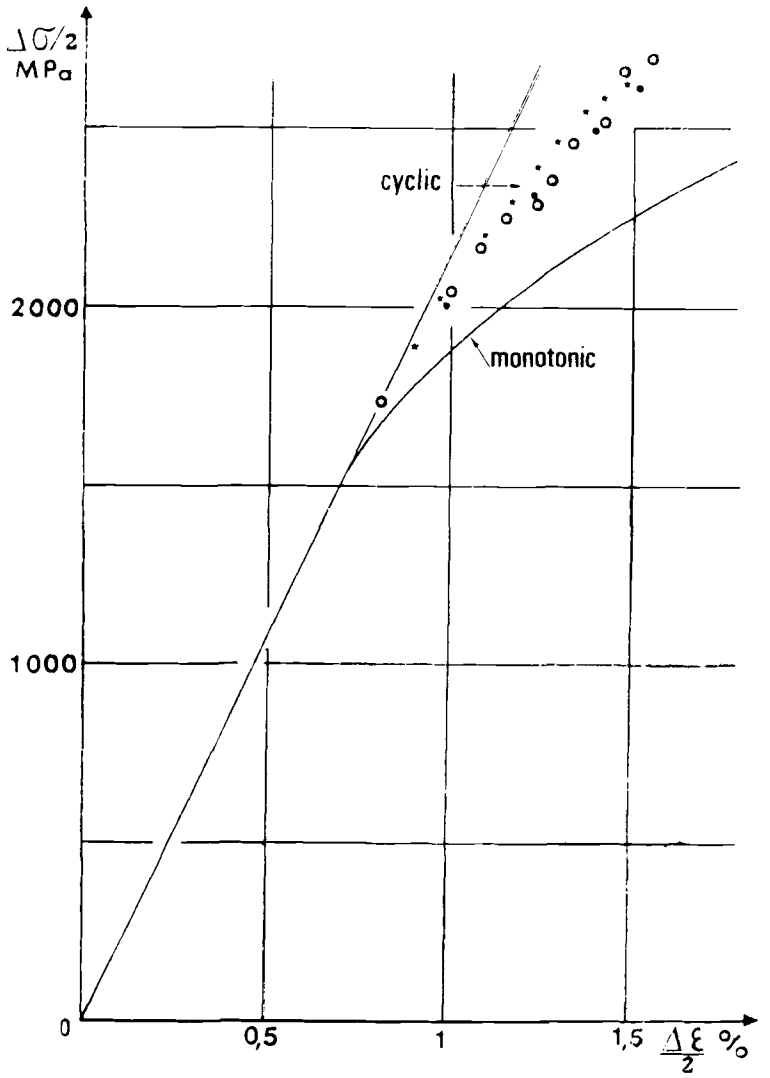

FIG. 1—*Monotonic and cyclic strain hardening.*

measured with a linear variable differential transformer (LVDT) extensometer. The cycles were sinusoidal around zero mean strain at a frequency of 0.01 to 1 Hz. The load and the displacement were continuously recorded. The following tests were performed:

1. fatigue tests at a prescribed strain range until fracture,
2. fatigue tests at increasing levels of strain ranges, and
3. fatigue tests using programmed blocks of increasing and decreasing strain ranges.

Results

Hysteresis loops were obtained with an increasing maximum stress corresponding to a cyclic strain-hardening behavior, obeying the law

$$\Delta\sigma/2 = 5790\,(\Delta\epsilon_p/2)^{0.137}$$

where the stress is expressed in MPa, and $\Delta\epsilon_p$ is the amplitude of the plastic strain. This is shown in Fig. 1, which was obtained by the three methods just listed.

Figure 2 shows fatigue life, the strain amplitude being divided into the plastic and elastic strain amplitudes. The corresponding law is

$$\Delta\epsilon/2 = 0.0073\,(2N_f)^{-0.36} + 0.0145\,(2N_f)^{-0.062}$$

For all practical purposes the first term can be dropped.

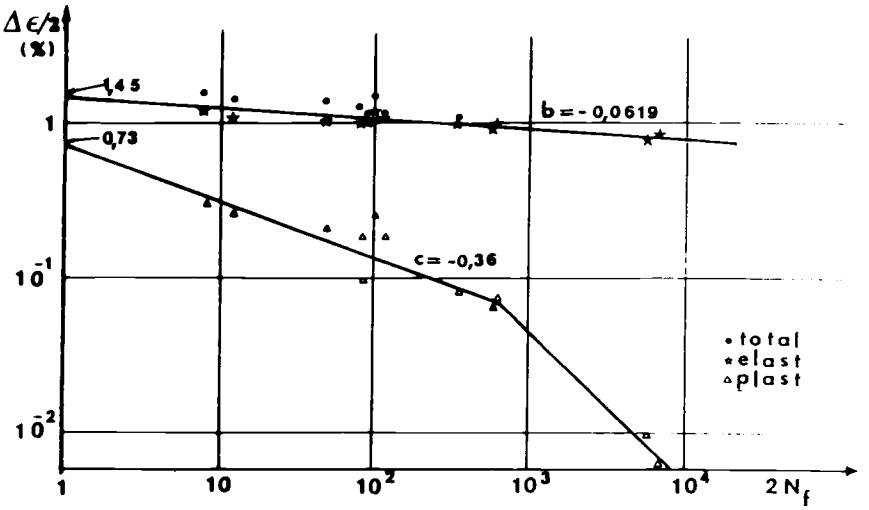

FIG. 2—*Fatigue life divided into the plastic and the elastic parts.*

Elastoplastic Analysis

Owing to the unusual behavior of this steel, for which the plastic line remains always below the elastic line on the fatigue life diagram, and thus to the very little influence indeed of the plastic deformation, it was nevertheless decided to carry out an elastoplastic computation of the strain distribution around inclusions. There are at least two reasons for doing so: First, it was felt that it could provide an explanation as to why the butterflies are inclined with respect to the surface; second, the incremental nature of plasticity could, in this complicated loading situation, create a large cumulative plastic strain. This might have a large influence on the prediction of the harmfulness of the various inclusions and it could also, by adding to the elastic strain amplitude, reduce the number of cycles for initiation.

Hertz [*6*] was the first to give a formulation of the stresses due to the pressure exerted by an elastic body against another one. The materials were assumed to be homogeneous and isotropic, and the loading static. The maximum stress region is located below the surface at a distance which is a function of the applied load and of the radii of curvature of the bodies in contact. Other authors [*11*] completed this work by giving the stresses along the contact area with or without gliding.

In a ball bearing the variation of the stresses in the region where the Hertzian stress is maximum is shown in Fig. 3 as a function of the horizontal distance to the ball. They represent the boundary conditions which will be imposed upon a small zone of the matrix containing fatigue initiating inclusions of average size $r = 0.050$ mm. A numerical analysis is then carried out using a finite-element program allowing elastoplastic behavior and which uses an explicit calculation [*12*]. The analysis is a bidimensional one in plane strain, the inclusion being represented by an elongated cylinder. The calculation uses the cyclic strain-hardening law as given in the foregoing, incremental plasticity, isotropic hardening, and the von Mises criterion. It is carried out in five steps of stress increment. The network is shown in Fig. 4.

The elastic constants of the inclusions are those given in the literature [*7-9*]. Three types of inclusions were studied: alumina Al_2O_3, titanium nitride TiN, and spinel Al_2O_3-MgO (Table 2).

The Hertzian stresses are a function of the load and of the contact area; the maximum imposed pressure was varied between 2500 and 5000 MN/m^2

$$P_{max} = (2\,q\,\Delta/\pi)^{1/2}/\Delta$$

with

$$\Delta = 4\,R\,(I - \nu^2)/E$$

where

q = load on the ball,
R = ball radius,

ν = Poisson's ratio, and
E = Young's modulus.

The calculation assumed that the ball was alternately rolling in both directions, that is, imposing as boundary conditions in Fig. 3 shear stresses of one sign or the other.

Results of the Numerical Analysis

Figure 5 is a map giving the cumulative plastic deformations during the loading for a ball rolling from left to right on a horizontal bearing with respect to the figure. Were the ball rolling in the other direction the maximum deformation zone would be shifted by 60 deg. The maximum deformation is found at the interface. For a ball pressure equal to 3500 MN/m^2 it reaches 0.13 percent, a value higher than the strain range corresponding to the stress range

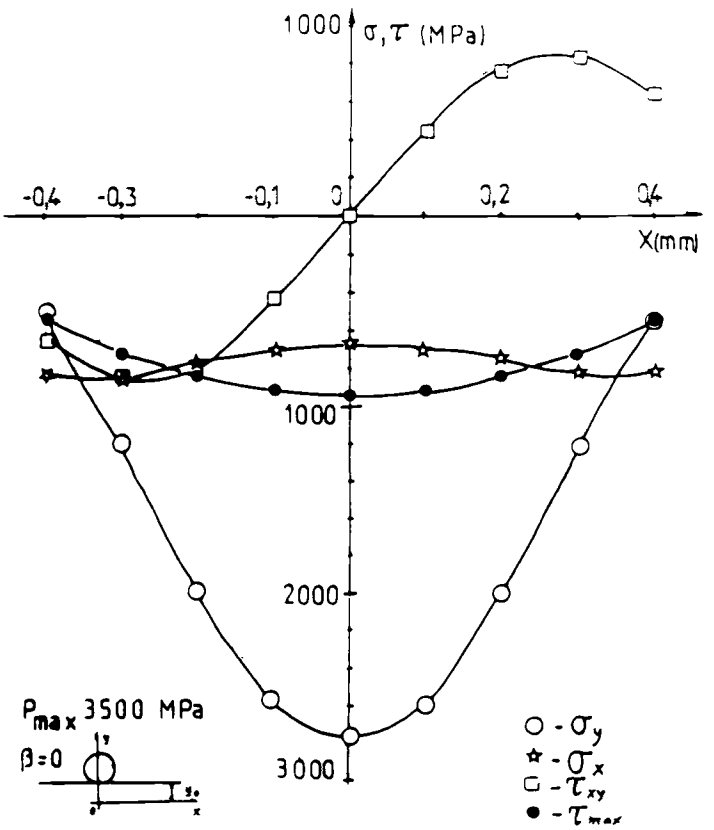

FIG. 3—*Hertzian stress field at the inclusion site.*

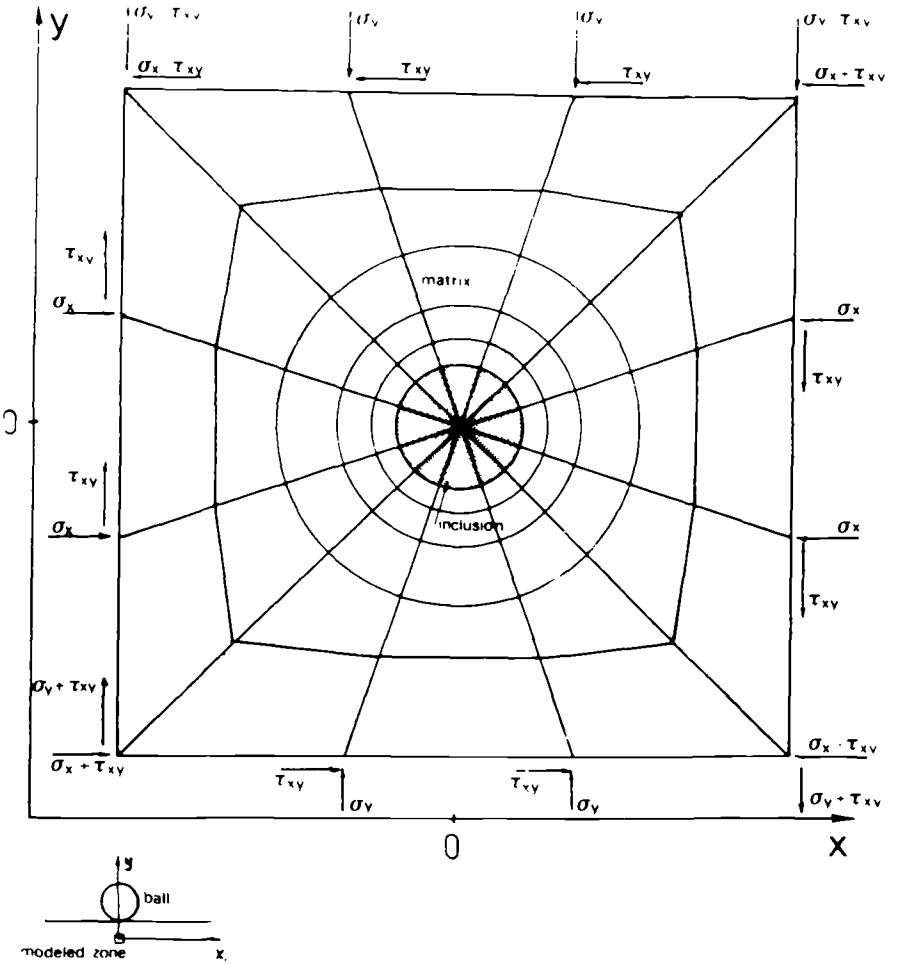

FIG. 4—*Network and boundary conditions for the numerical calculation around the inclusion.*

TABLE 2—*Elastic constants of the inclusions.*

Nature	Elastic Constants, MPa	Reference
Al_2O_2	397 000	[7-9]
TiN	317 000	[7-9]
Al_2O_3-Mgo	271 000	[7-9]

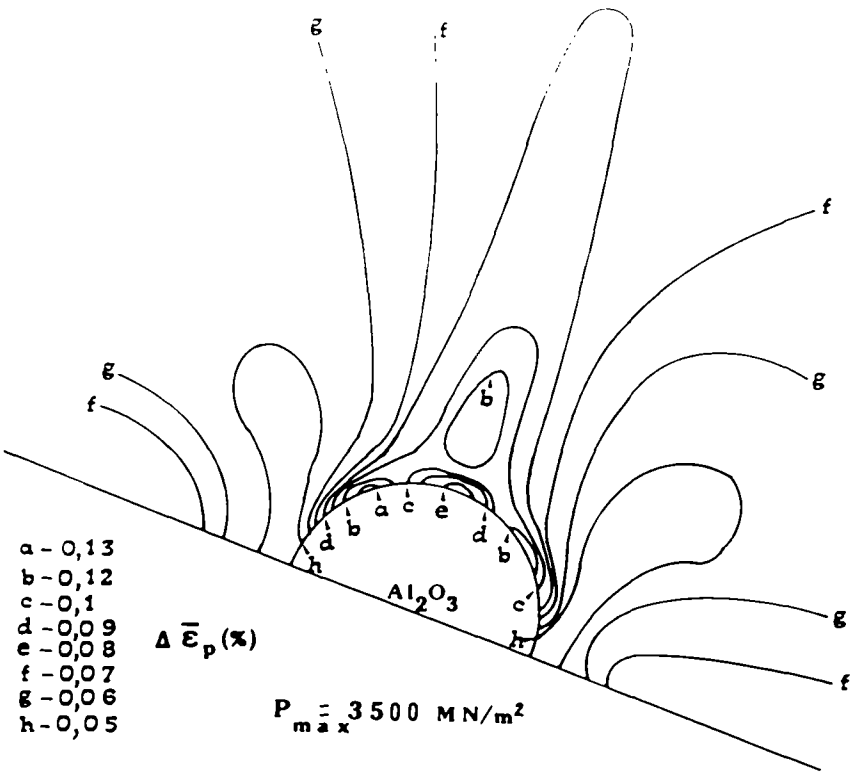

FIG. 5—*Lines of constant plastic strain amplitudes around an alumina inclusion, for an applied load equal to 3500 MN/m².*

according to the cyclic stress-strain law. The difference is due to the cumulative nature of the plastic strain. In Fig. 6 is shown its variation as a function of the maximum Hertzian pressure for the three types of inclusions. Figure 7 shows the variation of the plastic deformation along the interface between the inclusion and the matrix for a ball pressure equal to 3500 MPa. These figures indicate that, more than the amplitude of the maximum plastic deformation, it is the nature of the inclusion which influences its localization. It is highly localized for the alumina whereas it is much more spread out for the spinel.

Correlations with the Fatigue Life

Having computed the strain amplitude around inclusions in bearing steels, a crack initiation criterion must be chosen. The fatigue life law was experimentally found for zero average stress and strain. The ball bearings work under high compressive mean stress. A modification of the fatigue life law was

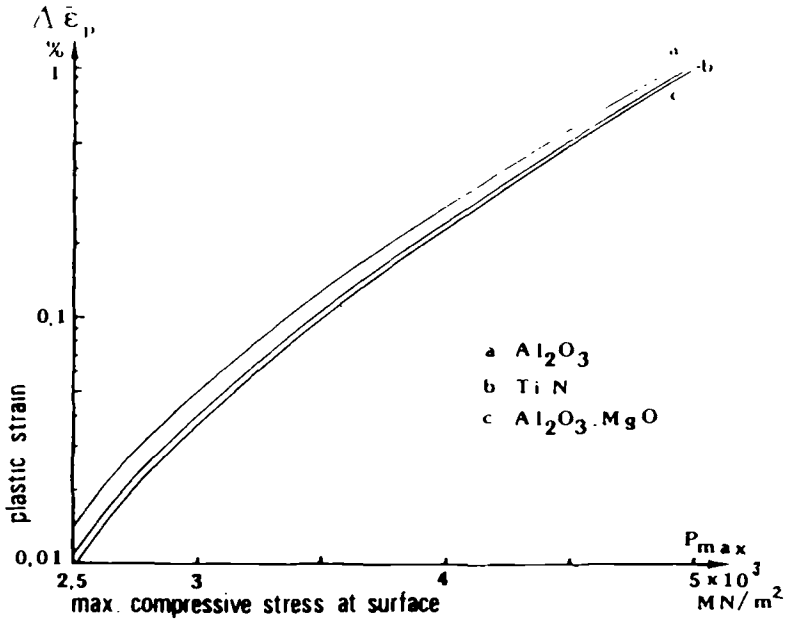

FIG. 6—*Maximum plastic strain amplitude near various inclusions as a function of the applied load on the bearing surface.*

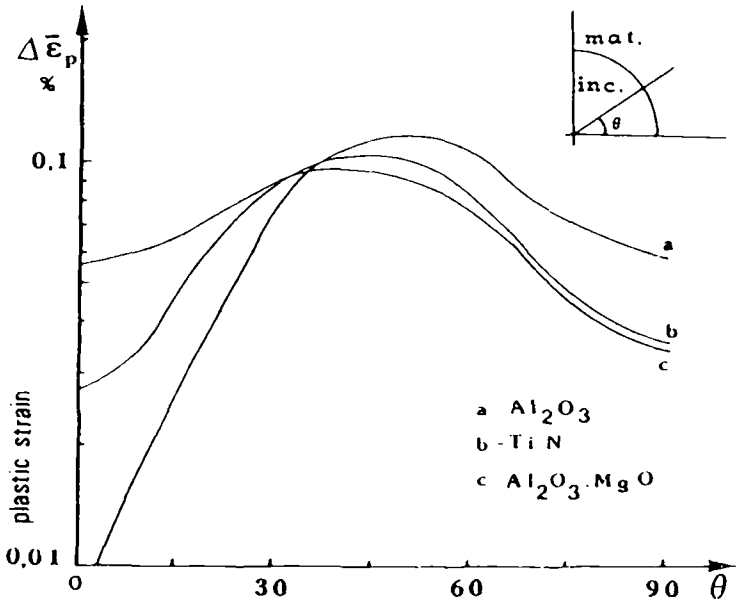

FIG. 7—*Angular distribution of the plastic strain amplitude around various inclusions.*

then used to take into account those conditions as proposed by Antolovich et al [*13*]

$$\Delta\epsilon/2 = (\sigma_f'/E)(1 - \sigma_m/\sigma_r)^{1/2}(2N_f)^b + (\epsilon_f' - \epsilon_m)(2N_f)^c$$

where

σ_f' = fatigue strength coefficient,
σ_m = mean stress,
σ_r = fracture strength,
ϵ_f' = fatigue ductility coefficient, and
ϵ_m = mean strain.

It is then possible to compute the fatigue life N_f knowing $\Delta\epsilon$, σ_m, and ϵ_m. With an average stress $\sigma_m \sim -1100$ MN/m^2, the mean stress correction factor $(1 - \sigma_m/\sigma_r)^{1/2}$ was approximately 1.2 in our case, leading to a multiplication of the fatigue life by a factor of 19.

A comparison was made between these results and the measured fatigue lives of ball bearings as published in the literature [*2,3,14-16*]. For instance, for $P_{max} = 3500$ MN/m^2 the calculation yields 20 to 50 $\times$ 10^6 cycles for initiation compared with 20 to 60 $\times$ 10^6 cycles for fracture given in the literature.

For $P_{max} = 5000$ MN/m^2 the calculation yields 0.8 to 2 $\times$ 10^6 cycles for initiation compared with 1 to 10 $\times$ 10^6 cycles for fracture. It should be noted that the measured fatigue lives include the number of cycles for initiation and for propagation.

As indicated in Figs. 6 and 7, it is expected that the alumina inclusions will produce more severe damage because of the larger strain amplitude and the higher strain localization which they produce, and the harmfulness of the inclusions thus obtained is in good agreement with published results [*14,15*].

Discussion

It is remarkable that for such a hard steel the cycling produces hardening instead of softening. This is due to the transformation of the residual austenite in martensite in the tensile part of the cycles [*17*].

The cyclic behavior was obtained for a steel which might be slightly different from that of the matrix whose carbon and chromium content might be different because of carbides. The presence of a few inclusions, even in a clean slag-remelted steel, could also affect the results. However, among all specimens broken, only three showed initiation on inclusions.

In the elastoplastic computation the inclusion was imbedded in an homogeneous stress field whereas the Hertzian field gives stress gradients. To minimize the effect, the distance between the boundaries and the inclusion was such that the Hertzian stress gradient was less than 0.1 percent.

The internal stresses induced around the inclusions by quenching, consid-

ered by other authors [*7–9*], were not included in the calculation. It is believed that they are quickly washed out during the first few cycles by the plastic deformation. The observed cracks always follow the direction of the computed plastic strains and not that of the residual stresses.

It must be recognized that the computation which is carried out in plane strain is inaccurate because the inclusions which are rather spherical or ellipsoidal are badly represented by cylinders.

The unsymmetrical plastic deformation which was found around the inclusions is in agreement with the orientation of the observed butterflies, which are inclined at 45 deg to the bearing surface. Their orientation with respect to the rolling direction is also well explained. It comes from a memory effect of the material which remembers the shear stresses that are applied at the beginning of plastification. In fact loading with no evolution of the rolling stresses yields plastic deformations at 90 deg from the vertical axis.

The observed fatigue cracks in ball bearings are initiated at the boundary of the butterflies of the white phase. We were unable to include this transformation in our computation as very little is known about its conditions of occurrence and about the properties of the white phase.

In spite of the limitations, we found results which are in good agreement with the published fatigue lives and which give a classification of the harmfulness of the inclusion that corresponds to what is known [*14,15*]. The usual pressures applied in rolling fatigue experiments are between 3500 and 5000 MN/m^2, yielding elastic strain amplitudes which are larger than the plastic strain amplitudes. Under those conditions, use of Basquin's law is sufficient to make predictions.

If the calculation is carried out using simply the Hertzian stresses at the inclusion site, the fatigue life is found to be larger than 10^9 cycles for a ball pressure of 3500 MN/m^2. This is what is expected since the stress concentration at the inclusion is ignored. On the other hand, use of the computed stress range at the inclusion interface, forgetting about the plastic strain range, also yields too high a value (3×10^8 cycles). It is only by adding the plastic strain range (0.065 percent) that a better agreement is found with experimental rolling fatigue life. Use could be made of Neuber's stress concentration factor for rough predictions.

Conclusions

The following conclusions were reached:

1. The E52 100 rolling bearing steel, quenched and tempered, displays a cyclic strain-hardening behavior described by the formula

$$\Delta\sigma/2 = 5790\,(\Delta\epsilon_p/2)^{0.137}$$

2. The fatigue life law has an elastic component which is always higher than the plastic component. It is described by the formula

$$\Delta\epsilon/2 = 0.0073\,(2N_f)^{-0.36} + 0.0145\,(2N_f)^{-0.062}$$

3. The non-symmetry of the plastic deformation with respect to the rolling direction was explained.

4. A classification of the harmfulness of the various inclusions finds a rational basis according to their Young's modulus.

5. A good prediction of the fatigue life of the ball bearings can be achieved.

Acknowledgments

This work was carried out under contract of DGRST and with a contribution from Creusot-Loire and in cooperation with Ecole Centrale de Lyon and the Technical University of Lisbon (CEMUL).

References

[1] Vincent, L., Coquillet, B., Guiraldenq, P., Boucher, A., and Rabbe, P., *Memoires Scientifiques de la Revue de Metallurgie,*, Vol. 73, 1976, p. 303.

[2] Johnson, R. F., and Sewel, J. F., *Journal of the Iron and Steel Institute*, Vol. 196, 1960, p. 414.

[3] Uhrus, L. O., Iron and Steel Institute Special Report No. 77, 1963, p. 104.

[4] Tricot, R., Monnot, J., and Lhuansi, M., *Metals Engineering Quarterly*, Vol. 12, 1972, p. 39.

[5] Styri, H. in *Proceedings, Symposium on New Methods for Particle Size Determination in the Subsieve Range, ASTM STP 51* American Society for Testing and Materials, 1951, p. 682.

[6] Hertz, H., *Journal für die Reine und Angewandte Mathematik*, Vol. 92, 1881, p. 155.

[7] Brooksbank, D., and Andrews, K. W., *Journal of the Iron and Steel Institute*, Vol. 206, 1968, p. 595.

[8] Brooksbank, D., and Andrews, K. W., *Journal of the Iron and Steel Institute.* Vol. 207, 1969, p. 474.

[9] Brooksbank, D., and Andrews, K. W., *Journal of the Iron and Steel Institute*, Vol. 210, 1972, p. 246.

[10] Baux, A. and Lieurade, J. P. in *Flaw Growth and Fracture. ASTM-STP 631*, American Society for Testing and Materials, 1977, p. 96.

[11] Seely, F. B. and Smith, J. O. in *Advanced Mechanics of Materials*, 2nd ed., Wiley, London, 1952.

[12] Nayak, G. C. and Zienkievicz, O. C., *International Journal for Numerical Methods in Engineering*, Vol. 5, 1972, p. 113.

[13] Antolovich, S. D., Anderson, A. F., and Zagray, K. in *Fracture 1977 (Advances in Research on the Strength and Fracture of Materials)*, D.M.R. Taplin, Ed. Pergamon Press, New York, 1978.

[14] Okamoto, K. and Shikoh, S., Nippon Steel Technical Report Overseas No. 2, Jan. 1973.

[15] Sugimo, K., Miyamoto, K. and Nagumo, M., *Transactions, Iron and Steel Institute of Japan*, Vol. 11, 1971, p. 9.

[16] Schlicht, H., *Wear*, Vol. 12, 1968, p. 149.

[17] de Freitas, M. and Francois, D., *Communication aux Journées Métallurgiques d'Automne 1981*, Société Française de Métallurgie (in press).

Index

This Index combines entries for both volumes of STP 803. "I" denotes entries for Volume I, and "II" denotes entries for Volume II.

D

K

L

M

N

O

P

T